

# Central and Eastern United States Seismic Source Characterization for Nuclear Facilities

Volume 2: Chapters 5 to 7



U.S. Nuclear Regulatory Commission  
Office of Nuclear Regulatory Research  
Washington DC 20555  
NUREG-2115



U.S. Department of Energy  
1000 Independence Avenue SW  
Washington, DC 20585  
Report # DOE/NE-0140



Electric Power Research Institute  
3420 Hillview Avenue  
Palo Alto, CA 94304  
Report # 1021097



## AVAILABILITY OF REFERENCE MATERIALS IN NRC PUBLICATIONS

### NRC Reference Material

As of November 1999, you may electronically access NUREG-series publications and other NRC records at NRC's Public Electronic Reading Room at <http://www.nrc.gov/reading-rm.html>.

Publicly released records include, to name a few, NUREG-series publications; *Federal Register* notices; applicant, licensee, and vendor documents and correspondence; NRC correspondence and internal memoranda; bulletins and information notices; inspection and investigative reports; licensee event reports; and Commission papers and their attachments.

NRC publications in the NUREG series, NRC regulations, and *Title 10, Energy*, in the Code of *Federal Regulations* may also be purchased from one of these two sources.

1. The Superintendent of Documents  
U.S. Government Printing Office  
Mail Stop SSOP  
Washington, DC 20402-0001  
Internet: [bookstore.gpo.gov](http://bookstore.gpo.gov)  
Telephone: 202-512-1800  
Fax: 202-512-2250
2. The National Technical Information Service  
Springfield, VA 22161-0002  
[www.ntis.gov](http://www.ntis.gov)  
1-800-553-6847 or, locally, 703-605-6000

A single copy of each NRC draft report for comment is available free, to the extent of supply, upon written request as follows:

Address: U.S. Nuclear Regulatory Commission  
Office of Administration  
Publications Branch  
Washington, DC 20555-0001

E-mail: [DISTRIBUTION.SERVICES@NRC.GOV](mailto:DISTRIBUTION.SERVICES@NRC.GOV)

Facsimile: 301-415-2289

Some publications in the NUREG series that are posted at NRC's Web site address <http://www.nrc.gov/reading-rm/doc-collections/nuregs> are updated periodically and may differ from the last printed version. Although references to material found on a Web site bear the date the material was accessed, the material available on the date cited may subsequently be removed from the site.

### Non-NRC Reference Material

Documents available from public and special technical libraries include all open literature items, such as books, journal articles, and transactions, *Federal Register* notices, Federal and State legislation, and congressional reports. Such documents as theses, dissertations, foreign reports and translations, and non-NRC conference proceedings may be purchased from their sponsoring organization.

Copies of industry codes and standards used in a substantive manner in the NRC regulatory process are maintained at—

The NRC Technical Library  
Two White Flint North  
11545 Rockville Pike  
Rockville, MD 20852-2738

These standards are available in the library for reference use by the public. Codes and standards are usually copyrighted and may be purchased from the originating organization or, if they are American National Standards, from—

American National Standards Institute  
11 West 42<sup>nd</sup> Street  
New York, NY 10036-8002  
[www.ansi.org](http://www.ansi.org)  
212-642-4900

Legally binding regulatory requirements are stated only in laws; NRC regulations; licenses, including technical specifications; or orders, not in NUREG-series publications. The views expressed in contractor-prepared publications in this series are not necessarily those of the NRC.

The NUREG series comprises (1) technical and administrative reports and books prepared by the staff (NUREG-XXXX) or agency contractors (NUREG/CR-XXXX), (2) proceedings of conferences (NUREG/CP-XXXX), (3) reports resulting from international agreements (NUREG/IA-XXXX), (4) brochures (NUREG/BR-XXXX), and (5) compilations of legal decisions and orders of the Commission and Atomic and Safety Licensing Boards and of Directors' decisions under Section 2.206 of NRC's regulations (NUREG-0750).



# Central and Eastern United States Seismic Source Characterization for Nuclear Facilities

## Cosponsors

### **U.S. Department of Energy**

1000 Independence Avenue SW  
Washington, DC 20585

R. H. Lagdon, Jr.  
Chief of Nuclear Safety  
Office of the Under Secretary for Nuclear Security, S-5

M.E. Shields  
Project Manager  
Office of Nuclear Energy, NE-72

### **Electric Power Research Institute**

3420 Hillview Avenue  
Palo Alto, CA 94304

J. F. Hamel  
Program Manager  
Advanced Nuclear Technology

### **U.S. Nuclear Regulatory Commission**

Office of Nuclear Regulatory Research  
Washington DC 20555

R.G. Roche-Rivera  
NRC Project Manager

*This document was **not** developed under a 10CFR50  
Appendix B program.*

## **DISCLAIMER OF WARRANTIES AND LIMITATION OF LIABILITIES**

### **EPRI DISCLAIMER**

THIS DOCUMENT WAS PREPARED AS AN ACCOUNT OF WORK SPONSORED OR COSPONSORED BY THE ELECTRIC POWER RESEARCH INSTITUTE, INC. (EPRI). NEITHER EPRI, ANY MEMBER OF EPRI, ANY COSPONSOR BELOW, NOR ANY PERSON ACTING ON BEHALF OF ANY OF THEM:

(A) MAKES ANY WARRANTY OR REPRESENTATION WHATSOEVER, EXPRESS OR IMPLIED, (I) WITH RESPECT TO THE USE OF ANY INFORMATION, APPARATUS, METHOD, PROCESS, OR SIMILAR ITEM DISCLOSED IN THIS DOCUMENT, INCLUDING MERCHANTABILITY AND FITNESS FOR A PARTICULAR PURPOSE, OR (II) THAT SUCH USE DOES NOT INFRINGE ON OR INTERFERE WITH PRIVATELY OWNED RIGHTS, INCLUDING ANY PARTY'S INTELLECTUAL PROPERTY, OR (III) THAT THIS DOCUMENT IS SUITABLE TO ANY PARTICULAR USER'S CIRCUMSTANCE; OR

(B) ASSUMES RESPONSIBILITY FOR ANY DAMAGES OR OTHER LIABILITY WHATSOEVER (INCLUDING ANY CONSEQUENTIAL DAMAGES, EVEN IF EPRI OR ANY EPRI REPRESENTATIVE HAS BEEN ADVISED OF THE POSSIBILITY OF SUCH DAMAGES) RESULTING FROM YOUR SELECTION OR USE OF THIS DOCUMENT OR ANY INFORMATION, APPARATUS, METHOD, PROCESS, OR SIMILAR ITEM DISCLOSED IN THIS DOCUMENT.

### **DOE DISCLAIMER**

THIS REPORT WAS PREPARED AS AN ACCOUNT OF WORK SPONSORED BY AN AGENCY OF THE UNITED STATES GOVERNMENT. NEITHER THE UNITED STATES GOVERNMENT NOR ANY AGENCY THEREOF, NOR ANY OF THEIR EMPLOYEES, MAKES ANY WARRANTY, EXPRESS OR IMPLIED, OR ASSUMES ANY LEGAL LIABILITY OR RESPONSIBILITY FOR THE ACCURACY, COMPLETENESS, OR USEFULNESS OF ANY INFORMATION, APPARATUS, PRODUCT, OR PROCESS DISCLOSED, OR REPRESENTS THAT ITS USE WOULD NOT INFRINGE PRIVATELY OWNED RIGHTS. REFERENCE HEREIN TO ANY SPECIFIC COMMERCIAL PRODUCT, PROCESS, OR SERVICE BY TRADE NAME, TRADEMARK, MANUFACTURER, OR OTHERWISE DOES NOT NECESSARILY CONSTITUTE OR IMPLY ITS ENDORSEMENT, RECOMMENDATION, OR FAVORING BY THE UNITED STATES GOVERNMENT OR ANY AGENCY THEREOF. THE VIEWS AND OPINIONS OF AUTHORS EXPRESSED HEREIN DO NOT NECESSARILY STATE OR REFLECT THOSE OF THE UNITED STATES GOVERNMENT OR ANY AGENCY THEREOF.

### **NRC DISCLAIMER**

THIS REPORT WAS PREPARED AS AN ACCOUNT OF WORK SPONSORED BY AN AGENCY OF THE U.S. GOVERNMENT. NEITHER THE U.S. GOVERNMENT NOR ANY AGENCY THEREOF, NOR ANY EMPLOYEE, MAKES ANY WARRANTY, EXPRESSED OR IMPLIED, OR ASSUMES ANY LEGAL LIABILITY OR RESPONSIBILITY FOR ANY THIRD PARTY'S USE, OR THE RESULTS OF SUCH USE, OF ANY INFORMATION, APPARATUS, PRODUCT, OR PROCESS DISCLOSED IN THIS PUBLICATION, OR REPRESENTS THAT ITS USE BY SUCH THIRD PARTY WOULD NOT INFRINGE PRIVATELY OWNED RIGHTS. THE STATEMENTS, FINDINGS, CONCLUSIONS AND RECOMMENDATIONS ARE THOSE OF THE AUTHOR(S) AND DO NOT NECESSARILY REFLECT THE VIEW OF THE US NUCLEAR REGULATORY COMMISSION.

## SPONSORS' ACKNOWLEDGMENTS

---

The project sponsors would like to acknowledge the following individuals for directing the project:

Coppersmith Consulting, Inc.  
2121 N. California Blvd., #290  
Walnut Creek, CA 94596

Technical Integration (TI) Lead  
K.J. Coppersmith

Savannah River Nuclear Solutions, LLC  
Savannah River Site  
Building 730-4B, Room 313  
Aiken, SC 29808

CEUS SSC Project Manager  
L.A. Salomone

This document describes research sponsored by the Electric Power Research Institute (EPRI), U.S. Department of Energy (U.S. DOE) under Award Number DE-FG07-08ID14908, and the U.S. Nuclear Regulatory Commission (U.S. NRC) under Award Number NCR-04-09-144.

---

This publication is a corporate document that should be cited in the literature in the following manner:

*Technical Report: Central and Eastern United States Seismic Source Characterization for Nuclear Facilities.* EPRI, Palo Alto, CA, U.S. DOE, and U.S. NRC: 2012.



# AUTHORS

---

This document was prepared by the following investigators:

<b>Technical Integration Lead</b>	Kevin J. Coppersmith
<b>Project Manager</b>	Lawrence A. Salomone
<b>Technical Integration Team</b>	Chris W. Fuller Laura L. Glaser Kathryn L. Hanson Ross D. Hartleb William R. Lettis Scott C. Lindvall Stephen M. McDuffie Robin K. McGuire Gerry L. Stirewalt Gabriel R. Toro Robert R. Youngs
<b>Database Manager</b>	David L. Slayter
<b>Technical Support</b>	Serkan B. Bozkurt Randolph J. Cumbest Valentina Montaldo Falero Roseanne C. Perman Allison M. Shumway Frank H. Syms Martitia (Tish) P. Tuttle, Paleoliquefaction Data Resource



---

**This document has been  
reproduced from the best available copy.**

---



# ABSTRACT

---

This report describes a new seismic source characterization (SSC) model for the Central and Eastern United States (CEUS). It will replace the *Seismic Hazard Methodology for the Central and Eastern United States*, EPRI Report NP-4726 (July 1986) and the *Seismic Hazard Characterization of 69 Nuclear Plant Sites East of the Rocky Mountains*, Lawrence Livermore National Laboratory Model, (Bernreuter et al., 1989). The objective of the CEUS SSC Project is to develop a new seismic source model for the CEUS using a Senior Seismic Hazard Analysis Committee (SSHAC) Level 3 assessment process. The goal of the SSHAC process is to represent the center, body, and range of technically defensible interpretations of the available data, models, and methods. Input to a probabilistic seismic hazard analysis (PSHA) consists of both seismic source characterization and ground motion characterization. These two components are used to calculate probabilistic hazard results (or seismic hazard curves) at a particular site. This report provides a new seismic source model.

## Results and Findings

The product of this report is a regional CEUS SSC model. This model includes consideration of an updated database, full assessment and incorporation of uncertainties, and the range of diverse technical interpretations from the larger technical community. The SSC model will be widely applicable to the entire CEUS, so this project uses a ground motion model that includes generic variations to allow for a range of representative site conditions (deep soil, shallow soil, hard rock). Hazard and sensitivity calculations were conducted at seven test sites representative of different CEUS hazard environments.

## Challenges and Objectives

The regional CEUS SSC model will be of value to readers who are involved in PSHA work, and who wish to use an updated SSC model. This model is based on a comprehensive and traceable process, in accordance with SSHAC guidelines in NUREG/CR-6372, *Recommendations for Probabilistic Seismic Hazard Analysis: Guidance on Uncertainty and Use of Experts*. The model will be used to assess the present-day composite distribution for seismic sources along with their characterization in the CEUS and uncertainty. In addition, this model is in a form suitable for use in PSHA evaluations for regulatory activities, such as Early Site Permit (ESPs) and Combined Operating License Applications (COLAs).

## Applications, Values, and Use

Development of a regional CEUS seismic source model will provide value to those who (1) have submitted an ESP or COLA for Nuclear Regulatory Commission (NRC) review before 2011; (2) will submit an ESP or COLA for NRC review after 2011; (3) must respond to safety issues resulting from NRC Generic Issue 199 (GI-199) for existing plants and (4) will prepare PSHAs to meet design and periodic review requirements for current and future nuclear facilities. This work replaces a previous study performed approximately 25 years ago. Since that study was

---

completed, substantial work has been done to improve the understanding of seismic sources and their characterization in the CEUS. Thus, a new regional SSC model provides a consistent, stable basis for computing PSHA for a future time span. Use of a new SSC model reduces the risk of delays in new plant licensing due to more conservative interpretations in the existing and future literature.

### **Perspective**

The purpose of this study, jointly sponsored by EPRI, the U.S. Department of Energy (DOE), and the NRC was to develop a new CEUS SSC model. The team assembled to accomplish this purpose was composed of distinguished subject matter experts from industry, government, and academia. The resulting model is unique, and because this project has solicited input from the present-day larger technical community, it is not likely that there will be a need for significant revision for a number of years. See also Sponsors' Perspective for more details.

### **Approach**

The goal of this project was to implement the CEUS SSC work plan for developing a regional CEUS SSC model. The work plan, formulated by the project manager and a technical integration team, consists of a series of tasks designed to meet the project objectives. This report was reviewed by a participatory peer review panel (PPRP), sponsor reviewers, the NRC, the U.S. Geological Survey, and other stakeholders. Comments from the PPRP and other reviewers were considered when preparing the report. The SSC model was completed at the end of 2011.

### **Keywords**

Probabilistic seismic hazard analysis (PSHA)  
Seismic source characterization (SSC)  
Seismic source characterization model  
Central and Eastern United States (CEUS)

# CONTENTS

---

Abstract.....	vii
Contents .....	ix
List of Figures .....	xxiii
List of Tables .....	lxxvii
Executive Summary .....	lxxxv
Participatory Peer Review Panel Final Report Dated October 24, 2011 .....	xcv
Project Acknowledgements .....	ciii
Sponsor’s Perspective .....	cv
Abbreviations .....	cix
<b>1 INTRODUCTION .....</b>	<b>1-1</b>
1.1 Background and History .....	1-1
1.1.1 EPRI-SOG and LLNL Projects .....	1-2
1.1.2 Development of the SSHAC Process .....	1-2
1.1.3 Implementation of the SSHAC Methodology .....	1-3
1.1.4 Regional SSC Model for Nuclear Facilities.....	1-3
1.1.5 Differences from USGS National Seismic Hazard Mapping Project.....	1-4
1.2 Purpose of the CEUS SSC Project .....	1-5
1.2.1 Implementation of SSHAC Level 3 Process .....	1-6
1.2.2 Goals: Stability and Longevity .....	1-8
1.2.3 Interface with Ground Motion Models.....	1-8
1.3 Study Region.....	1-10
1.4 Products of Project .....	1-10
1.4.1 Seismic Source Model for Study Region .....	1-10
1.4.2 Hazard Input Document .....	1-12
1.4.3 Documentation of Technical Bases for All Assessments .....	1-12
1.4.4 Other Key Products.....	1-13
1.4.4.1 Data Evaluation and Data Summary Tables .....	1-13

---

1.4.4.2 Database of Geologic, Geophysical, and Seismological Data.....	1-13
1.4.4.3 Earthquake Catalog with Uniform Moment Magnitudes .....	1-13
1.4.4.4 Updated Paleoseismicity Data and Guidance .....	1-14
1.4.4.5 Recommendations for Future Applications of SSC Model .....	1-14
<b>2 SSHAC LEVEL 3 ASSESSMENT PROCESS AND IMPLEMENTATION .....</b>	<b>2-1</b>
2.1 Goals and Activities of a SSHAC Assessment Process .....	2-2
2.1.1 Evaluation .....	2-4
2.1.2 Integration .....	2-4
2.2 Roles of CEUS SSC Project Participants.....	2-5
2.3 CEUS SSC Project Organization .....	2-7
2.4 Key Tasks and Activities.....	2-9
2.4.1 Database Development.....	2-9
2.4.2 Identification of Significant Issues .....	2-10
2.4.3 Workshop #1—Key Issues and Available Data .....	2-10
2.4.4 Workshop #2—Alternative Interpretations .....	2-12
2.4.5 Working Meetings .....	2-13
2.4.6 SSC Sensitivity Model Development .....	2-14
2.4.7 Workshop #3—Feedback.....	2-15
2.4.8 SSC Preliminary Model Development .....	2-16
2.4.9 Finalization and Review of SSC Draft and Final Model .....	2-17
2.4.10 Documentation.....	2-19
2.4.10.1 Development of the Hazard Input Document .....	2-19
2.4.10.2 Development of Earlier Draft Report.....	2-19
2.4.10.3 Draft Report Review .....	2-19
2.4.10.4 Final Report Development .....	2-20
2.5 Participatory Peer Review Panel .....	2-20
2.5.1 Roles and Responsibilities .....	2-20
2.5.2 Reviews and Feedback .....	2-20
2.5.3 Fulfillment of SSHAC-Prescribed Scope of Review of Both Technical and Process Issues .....	2-21
2.6 Consistency of CEUS SSC Assessment Process with SSHAC Guidelines .....	2-22
<b>3 EARTHQUAKE CATALOG .....</b>	<b>3-1</b>
3.1 Goals for the Earthquake Catalog Development.....	3-1
3.1.1 Completeness .....	3-1

3.1.2	Uniformity of Catalog Processing .....	3-2
3.1.3	Catalog Review .....	3-3
3.2	Catalog Compilation .....	3-4
3.2.1	Continental-Scale Catalogs.....	3-5
3.2.2	Regional Catalogs.....	3-7
3.2.3	Catalogs from Special Studies .....	3-7
3.2.4	Focal Depth Data .....	3-8
3.2.5	Nontectonic Events .....	3-9
3.2.6	Identification of Unique Earthquake Entries.....	3-9
3.3	Development of a Uniform Moment Magnitude Earthquake Catalog.....	3-11
3.3.1	Approach for Uniform Magnitude and Unbiased Recurrence Estimation .....	3-11
3.3.2	Estimation of $E[M]$ for the CEUS SSC Project Catalog.....	3-19
3.3.2.1	Effect of Magnitude Rounding on Statistical Tests .....	3-19
3.3.2.2	Moment Magnitude Data .....	3-20
3.3.2.3	Estimation of $E[M]$ from Body-Wave Magnitudes.....	3-22
3.3.2.4	Estimation of $E[M]$ from $M_L$ Magnitudes .....	3-28
3.3.2.5	Estimation of $E[M]$ from $M_S$ Magnitudes .....	3-29
3.3.2.6	Estimation of $E[M]$ from $M_C$ and $M_D$ Magnitudes .....	3-30
3.3.2.7	Estimation of $E[M]$ from the Logarithm of Felt Area .....	3-32
3.3.2.8	Estimation of $E[M]$ from the Maximum Intensity, $I_0$ .....	3-32
3.3.2.9	Uniform Moment Magnitude Catalog of $E[M]$ and $N^*$ Values.....	3-36
3.4	Identification of Independent Earthquakes .....	3-37
3.5	Catalog Completeness .....	3-39
<b>4</b>	<b>CONCEPTUAL SEISMIC SOURCE CHARACTERIZATION FRAMEWORK .....</b>	<b>4-1</b>
4.1	Needs for a Conceptual SSC Framework .....	4-2
4.1.1	Logic Tree Approach to Representing Alternatives and Assessing Uncertainties.....	4-2
4.1.1.1	Examples of Logic Trees .....	4-3
4.1.1.2	Assigning Weights to Logic Tree Branches .....	4-3
4.1.2	Data Identification and Evaluation .....	4-5
4.1.2.1	“Generic” Data Identification to Address Indicators of a Seismic Source.....	4-5
4.1.2.2	Data Evaluation for Particular Seismic Sources: Data Evaluation and Data Summary Tables.....	4-7
4.1.3	Methodology for Identifying Seismic Sources.....	4-9

---

4.1.3.1 Hazard-Informed Approach .....	4-11
4.1.3.2 Conclusions Regarding the Hazard Significance of Various SSC Issues .....	4-13
4.1.3.3 Criteria for Defining Seismic Sources .....	4-14
4.2 Master Logic Tree.....	4-18
4.2.1 Description of Logic Tree Elements.....	4-18
4.2.2 RLME Source Logic Tree.....	4-20
4.2.3 Mmax Zones Logic Tree .....	4-22
4.2.4 Seismotectonic Zones Branch.....	4-24
<b>5 SSC MODEL: OVERVIEW AND METHODOLOGY.....</b>	<b>5-1</b>
5.1 Overview of Spatial and Temporal Models .....	5-1
5.1.1 Spatial Model Considerations.....	5-1
5.1.2 Considerations Regarding Temporal Models .....	5-3
5.1.3 Perspective on CEUS SSC Models.....	5-4
5.2 Maximum Earthquake Magnitude Assessment.....	5-5
5.2.1 Approaches to Mmax Estimation in the CEUS .....	5-6
5.2.1.1 Bayesian Mmax Approach.....	5-8
5.2.1.2 Kijko Approach to Mmax Assessment .....	5-17
5.2.1.3 Weights for the Alternative Mmax Approaches .....	5-20
5.2.1.4 Example Mmax Distributions .....	5-20
5.2.2 Other Mmax Issues .....	5-21
5.3 Earthquake Recurrence Assessment.....	5-22
5.3.1 Smoothing to Represent Spatial Stationarity.....	5-22
5.3.2 Smoothing Approach .....	5-23
5.3.2.1 Development of Penalized-Likelihood Approach and Formulation .....	5-23
5.3.2.2 Application of the Model and Specification of Model Parameters.....	5-36
5.3.2.3 Exploration of Model Results in Parameter Space.....	5-40
5.3.2.4 Consideration of Constant b-Value Kernel Approaches.....	5-42
5.3.2.5 Comparison to EPRI-SOG Approach.....	5-45
5.3.2.6 Assessment of the Lombardi Study .....	5-46
5.3.3 Estimation of Recurrence for RLME Sources .....	5-47
5.3.3.1 Estimation of Occurrence Rates for the Poisson Model .....	5-48
5.3.3.2 Estimation of Occurrence Rates for a Renewal Model.....	5-51
5.3.3.3 Incorporating Uncertainty in the Input.....	5-52
5.3.3.4 RLME Magnitude Distribution .....	5-53

---

5.4 Assessment of Future Earthquake Characteristics .....	5-54
5.4.1 Tectonic Stress Regime .....	5-55
5.4.2 Sense of Slip/Style of Faulting .....	5-55
5.4.3 Strike and Dip of Ruptures .....	5-55
5.4.4 Seismogenic Crustal Thickness .....	5-56
5.4.5 Fault Rupture Area.....	5-57
5.4.6 Rupture Length-to-Width Aspect Ratio.....	5-57
5.4.7 Relationship of Rupture to Source Zone Boundaries.....	5-58
5.5 Predicted Seismic Moment Rate.....	5-58
<b>6 SSC MODEL: RLME SOURCES AND MMAX ZONES BRANCH .....</b>	<b>6-1</b>
6.1 RLME Sources .....	6-1
6.1.1 Charlevoix.....	6-3
6.1.1.1 Evidence for Temporal Clustering.....	6-4
6.1.1.2 Localizing Tectonic Features .....	6-4
6.1.1.3 Geometry and Style of Faulting .....	6-5
6.1.1.4 RLME Magnitude.....	6-7
6.1.1.5 RLME Recurrence.....	6-8
6.1.2 Charleston .....	6-10
6.1.2.1 Evidence for Temporal Clustering.....	6-11
6.1.2.2 Localizing Feature .....	6-12
6.1.2.3 Geometry and Style of Faulting .....	6-12
6.1.2.4 RLME Magnitude.....	6-15
6.1.2.5 RLME Recurrence .....	6-17
6.1.3 Cheraw Fault .....	6-22
6.1.3.1 Evidence for Temporal Clustering.....	6-23
6.1.3.2 Geometry and Style of Faulting .....	6-24
6.1.3.3 RLME Magnitude.....	6-25
6.1.3.4 RLME Recurrence.....	6-26
6.1.4 Meers Fault.....	6-28
6.1.4.1 Evidence for Temporal Clustering.....	6-29
6.1.4.2 Localizing Feature .....	6-29
6.1.4.3 Geometry and Style of Faulting .....	6-30
6.1.4.4 RLME Magnitude.....	6-31
6.1.4.5 RLME Recurrence.....	6-34

---

6.1.5 Reelfoot Rift–New Madrid Fault System .....	6-35
6.1.5.1 Evidence for Temporal Clustering.....	6-40
6.1.5.2 Geometry and Style of Faulting .....	6-42
6.1.5.3 RLME Magnitude.....	6-44
6.1.5.4 RLME Recurrence .....	6-47
6.1.6 Reelfoot Rift—Eastern Rift Margin Fault .....	6-50
6.1.6.1 Evidence for Temporal Clustering.....	6-53
6.1.6.2 Geometry and Style of Faulting .....	6-53
6.1.6.3 RLME Magnitude.....	6-54
6.1.6.4 RLME Recurrence .....	6-56
6.1.7 Reelfoot Rift—Marianna .....	6-57
6.1.7.1 Evidence for Temporal Clustering.....	6-58
6.1.7.2 Geometry and Style of Faulting .....	6-59
6.1.7.3 RLME Magnitude.....	6-60
6.1.7.4 RLME Recurrence .....	6-61
6.1.8 Reelfoot Rift—Commerce Fault Zone .....	6-62
6.1.8.1 Evidence for Temporal Clustering.....	6-63
6.1.8.2 Geometry and Style of Faulting .....	6-64
6.1.8.3 RLME Magnitude.....	6-65
6.1.8.4 RLME Recurrence .....	6-66
6.1.9 Wabash Valley .....	6-68
6.1.9.1 Evidence for Temporal Clustering.....	6-69
6.1.9.2 Geometry and Style of Faulting .....	6-69
6.1.9.3 RLME Magnitude.....	6-72
6.1.9.4 RLME Recurrence .....	6-73
6.2 Mmax Distributed Seismicity Source Zones.....	6-74
6.2.1 Definition of Mmax Zones .....	6-74
6.2.2 Criteria for Defining the MESE/NMESE Boundary .....	6-75
6.3 Maximum Magnitude Distributions for Mmax Distributed Seismicity Sources.....	6-76
6.3.1 Maximum Observed Earthquake Magnitude .....	6-76
6.3.2 Mmax Distributions .....	6-77
6.4 Recurrence Parameters.....	6-78
6.4.1 Rate and b-Value Maps for Single Zone and Two Zones .....	6-78
6.4.2 Comparison of Recurrence Parameters to Catalog .....	6-79

---

<b>7 SSC MODEL: SEISMOTECTONIC ZONES BRANCH .....</b>	<b>7-1</b>
7.1 Approaches and Data Used to Define Seismotectonic Zones .....	7-1
7.2 RLME Sources in the Seismotectonic Zones Branch .....	7-4
7.3 Seismotectonic Source Zones .....	7-4
7.3.1 St. Lawrence Rift Zone (SLR) .....	7-4
7.3.1.1 Background .....	7-5
7.3.1.2 Basis for Defining Seismotectonic Zone .....	7-11
7.3.1.3 Basis for Zone Geometry .....	7-12
7.3.1.4 Basis for Zone Mmax.....	7-12
7.3.1.5 Future Earthquake Characteristics .....	7-13
7.3.2 Great Meteor Hotspot Zone (GMH) .....	7-15
7.3.2.1 Background .....	7-16
7.3.2.2 Basis for Defining Seismotectonic Zone .....	7-18
7.3.2.3 Basis for Zone Geometry .....	7-19
7.3.2.4 Basis for Zone Mmax.....	7-19
7.3.2.5 Future Earthquake Characteristics .....	7-20
7.3.3 Northern Appalachian Zone (NAP) .....	7-21
7.3.3.1 Background .....	7-21
7.3.3.2 Basis for Defining Seismotectonic Zone .....	7-23
7.3.3.3 Basis for Zone Geometry .....	7-24
7.3.3.4 Basis for Zone Mmax.....	7-24
7.3.3.5 Future Earthquake Characteristics .....	7-25
7.3.4 Paleozoic Extended Crust (PEZ).....	7-25
7.3.4.1 Background .....	7-26
7.3.4.2 Basis for Defining Seismotectonic Zone .....	7-32
7.3.4.3 Basis for Zone Geometry .....	7-33
7.3.4.4 Basis for Zone Mmax.....	7-34
7.3.4.5 Future Earthquake Characteristics .....	7-36
7.3.5 Illinois Basin Extended Basement Zone (IBEB) .....	7-37
7.3.5.1 Background .....	7-38
7.3.5.2 Basis for Defining Seismotectonic Zone .....	7-38
7.3.5.3 Basis for Zone Geometry .....	7-40
7.3.5.4 Basis for Zone Mmax.....	7-41
7.3.5.5 Future Earthquake Characteristics .....	7-41
7.3.6 Reelfoot Rift Zone (RR).....	7-42

---

7.3.6.1 Background .....	7-42
7.3.6.2 Basis for Defining Seismotectonic Zone .....	7-46
7.3.6.3 Basis for Zone Geometry.....	7-46
7.3.6.4 Basis for Zone Mmax.....	7-47
7.3.6.5 Future Earthquake Characteristics .....	7-48
7.3.7 Extended Continental Crust–Atlantic Margin Zone (ECC-AM).....	7-48
7.3.7.1 Background .....	7-49
7.3.7.2 Basis for Defining Seismotectonic Zone .....	7-53
7.3.7.3 Basis for Geometry.....	7-54
7.3.7.4 Basis for Mmax.....	7-54
7.3.7.5 Future Earthquake Characteristics .....	7-55
7.3.8 Atlantic Highly Extended Crust Zone (AHEx).....	7-55
7.3.8.1 Basis for Defining Seismotectonic Zone .....	7-56
7.3.8.2 Basis for Geometry.....	7-57
7.3.8.3 Basis for Mmax.....	7-57
7.3.8.4 Future Earthquake Characteristics .....	7-57
7.3.9 Extended Continental Crust–Gulf Coast Zone (ECC-GC) .....	7-58
7.3.9.1 Basis for Defining Seismotectonic Zone .....	7-58
7.3.9.2 Basis for Zone Geometry.....	7-59
7.3.9.3 Basis for Zone Mmax.....	7-62
7.3.9.4 Future Earthquake Characteristics .....	7-63
7.3.9.5 Possible Paleoliquefaction Features in Arkansas, Louisiana, and Mississippi.....	7-64
7.3.10 Gulf Coast Highly Extended Crust Zone (GHEx) .....	7-65
7.3.10.1 Basis for Defining Seismotectonic Zone .....	7-66
7.3.10.2 Basis for Zone Geometry.....	7-66
7.3.10.3 Basis for Zone Mmax.....	7-66
7.3.10.4 Future Earthquake Characteristics .....	7-67
7.3.11 Oklahoma Aulacogen Zone (OKA).....	7-68
7.3.11.1 Basis for Defining Seismotectonic Zone .....	7-69
7.3.11.2 Basis for Zone Geometry.....	7-69
7.3.11.3 Basis for Zone Mmax.....	7-70
7.3.11.4 Future Earthquake Characteristics .....	7-70
7.3.12 Midcontinent-Craton Zone (MidC) .....	7-70
7.3.12.1 Background .....	7-71

7.3.12.2 Basis for Defining Seismotectonic Zone .....	7-76
7.3.12.3 Basis for Zone Geometry.....	7-77
7.3.12.4 Basis for Zone Mmax.....	7-77
7.3.12.5 Future Earthquake Characteristics .....	7-77
7.4 Maximum Magnitude Distributions for Seismotectonic Distributed Seismicity Sources.....	7-78
7.4.1 Maximum Observed Earthquake Magnitude .....	7-78
7.4.2 Mmax Distributions .....	7-79
7.5 Recurrence Parameters.....	7-80
7.5.1 Rate and b-Value Maps for Single Zone and Two Zones .....	7-80
7.5.2 Comparison of Recurrence Parameters to Catalog .....	7-80
<b>8 DEMONSTRATION HAZARD CALCULATIONS.....</b>	<b>8-1</b>
8.1 Background on Demonstration Hazard Calculations.....	8-1
8.2 Demonstration Hazard Calculations .....	8-2
8.2.1 Central Illinois Site .....	8-4
8.2.2 Chattanooga Site .....	8-5
8.2.3 Houston Site .....	8-6
8.2.4 Jackson Site .....	8-7
8.2.5 Manchester Site.....	8-9
8.2.6 Savannah Site .....	8-9
8.2.7 Topeka Site.....	8-10
<b>9 USE OF THE CEUS SSC MODEL IN PSHA .....</b>	<b>9-1</b>
9.1 Overview .....	9-1
9.2 Hazard Input Document (HID) .....	9-2
9.3 Implementation Instructions.....	9-2
9.3.1 Simplifications to Seismic Sources.....	9-2
9.3.1.1 Charleston RLME .....	9-3
9.3.1.2 Charlevoix RLME .....	9-3
9.3.1.3 Cheraw RLME .....	9-4
9.3.1.4 Commerce Fault Zone RLME .....	9-5
9.3.1.5 Eastern Rift Margin North RLME .....	9-5
9.3.1.6 Eastern Rift Margin South RLME.....	9-5
9.3.1.7 Marianna RLME .....	9-6
9.3.1.8 Meers RLME .....	9-6

9.3.1.9 New Madrid Fault System RLME.....	9-7
9.3.1.10 Wabash Valley RLME.....	9-7
9.3.1.11 Background Sources .....	9-8
9.3.2 Accessing the SSC Model and Components from the Website .....	9-8
9.3.3 Accessing Project Databases.....	9-9
9.3.4 Use of SSC Model with Site-Specific Refinements .....	9-10
9.4 Hazard Significance.....	9-10
9.4.1 Data Available to Evaluate the Precision of Seismic Hazard Estimates.....	9-10
9.4.2 Observed Imprecision in Seismic Hazard Estimates .....	9-11
9.4.2.1 Area Seismic Sources .....	9-11
9.4.2.2 RLME Seismic Sources.....	9-12
9.4.2.3 Ground Motion Equations.....	9-15
9.4.2.4 Site Response.....	9-19
9.4.3 Conclusions on the Precision in Seismic Hazard Estimates .....	9-19
<b>10 REFERENCES .....</b>	<b>10-1</b>
<b>11 GLOSSARY OF KEY TERMS .....</b>	<b>11-1</b>
<b>A DESCRIPTION OF THE CEUS SSC PROJECT DATABASE.....</b>	<b>A-1</b>
A.1 Data Sources .....	A-2
A.2 Project Database Design and Management.....	A-3
A.3 Workflow and Data Assessment.....	A-3
A.3.1 Workflow.....	A-3
A.3.2 Digital Data.....	A-4
A.3.3 Nondigital Data .....	A-4
A.4 Use of Project Database in Model Development .....	A-5
A.5 Metadata.....	A-5
A.6 Database Delivery Format.....	A-6
<b>B EARTHQUAKE CATALOG DATABASE .....</b>	<b>B-1</b>
B.1 CEUS SSC Uniform Moment Magnitude Earthquake Catalog.....	B-1
B.2 Moment Magnitude Data.....	B-2
B.3 Approximate Moment Magnitude Data .....	B-3
B.4 CEUS SSC Project Data .....	B-3

<b>C DATA EVALUATION TABLES.....</b>	<b>C-1</b>
Introduction .....	C-2
<b>D DATA SUMMARY TABLES .....</b>	<b>D-1</b>
Introduction .....	D-2
<b>E CEUS PALEOLIQUEFACTION DATABASE, UNCERTAINTIES ASSOCIATED WITH PALEOLIQUEFACTION DATA, AND GUIDANCE FOR SEISMIC SOURCE CHARACTERIZATION.....</b>	<b>E-i</b>
E.1 Development of the Paleoliquefaction Database .....	E-1
E.1.1 Database Structure .....	E-1
E.1.2 Regional Data Sets .....	E-4
E.2 Uncertainties Associated with Paleoliquefaction Data .....	E-24
E.2.1 Collection of Paleoliquefaction Data .....	E-24
E.2.2 Uncertainties Related to Interpretation of Paleoliquefaction Data.....	E-35
E.2.3 Recommendations for Future Research .....	E-43
E.3 Guidance for the Use of Paleoliquefaction Data in Seismic Source Characterization.....	E-44
E.4 Glossary.....	E-46
E.5 References .....	E-49
E.5.1 References Cited in Paleoliquefaction Database .....	E-49
E.5.2 References Cited in Appendix E .....	E-54
<b>F WORKSHOP SUMMARIES .....</b>	<b>F-1</b>
WORKSHOP 1: KEY ISSUES AND AVAILABLE DATA	
DAY 1–TUESDAY, JULY 22, 2008 .....	F-1
DAY 2–WEDNESDAY, JULY 23, 2008 .....	F-10
REFERENCES.....	F-17
WORKSHOP 2: ALTERNATIVE INTERPRETATIONS	
DAY 1–WEDNESDAY, FEBRUARY 18, 2009 .....	F18
DAY 2–THURSDAY, FEBRUARY 19, 2009.....	F-24
DAY 3–FRIDAY, FEBRUARY 20, 2009 .....	F-29
REFERENCES .....	F-34
WORKSHOP 3: FEEDBACK	
DAY 1–TUESDAY, AUGUST 25, 2009 .....	F-42
DAY 2–WEDNESDAY, AUGUST 26, 2009.....	F-49

---

<b>G BIOGRAPHIES OF PROJECT TEAM.....</b>	<b>G-1</b>
EPRI MANAGEMENT .....	G-2
PROJECT MANAGER.....	G-2
TI TEAM.....	G-3
TECHNICAL SUPPORT .....	G-7
DATABASE MANAGER .....	G-9
PARTICIPATORY PEER REVIEW PANEL .....	G-9
SPONSOR REVIEWERS .....	G-14
<b>H CEUS SSC MODEL HAZARD INPUT DOCUMENT (HID) .....</b>	<b>H-1</b>
H.1 Introduction .....	H-1
H.2 Seismic Source Model Structure and Master Logic Tree.....	H-1
H.3 Mmax Zones Distributed Seismicity Sources .....	H-2
H.3.1 Division of Study Region .....	H-2
H.3.2 Location of Boundary of Mesozoic Extension .....	H-2
H.3.3 Magnitude Interval Weights for Fitting Earthquake Occurrence Parameters .....	H-2
H.3.4 Mmax Zones .....	H-2
H.3.5 Seismogenic Crustal Thickness .....	H-2
H.3.6 Future Earthquake Rupture Characteristics .....	H-3
H.3.7 Assessment of Seismicity Rates .....	H-3
H.3.8 Degree of Smoothing Applied in Defining Spatial Smoothing of Seismicity Rates .....	H-3
H.3.9 Uncertainty in Earthquake Recurrence Rates.....	H-3
H.3.10 Uncertainty in Maximum Magnitude.....	H-4
H.4 Seismotectonic Zones.....	H-4
H.4.1 Alternative Zonation Models .....	H-4
H.4.2 Magnitude Interval Weights for Fitting Earthquake Occurrence Parameters .....	H-4
H.4.3 Seismotectonic Zones .....	H-5
H.4.4 Seismogenic Crustal Thickness.....	H-5
H.4.5 Future Earthquake Rupture Characteristics .....	H-5
H.4.6 Assessment of Seismicity Rates .....	H-5
H.4.7 Degree of Smoothing Applied in Defining Spatial Smoothing of Seismicity Rates .....	H-5
H.4.8 Uncertainty in Earthquake Recurrence Rates .....	H-5
H.4.9 Uncertainty in Maximum Magnitude .....	H-6
H.5 RLME Sources .....	H-6

H.5.1 Charlevoix RLME Seismic Source Model .....	H-6
H.5.2 Charleston RLME Seismic Source Model.....	H-7
H.5.3 Cheraw RLME Seismic Source Model.....	H-9
H.5.4 Meers RLME Seismic Source Model .....	H-11
H.5.5 New Madrid Fault System RLME Seismic Source Model.....	H-12
H.5.6 Eastern Rift Margin Fault RLME Seismic Source Model .....	H-14
H.5.7 Marianna Zone RLME Seismic Source Model .....	H-15
H.5.8 Commerce Fault RLME Seismic Source Model.....	H-16
H.5.9 Wabash Valley RLME Seismic Source Model .....	H-18
<b>/ PPRP REVIEW COMMENTS .....</b>	<b>I-1</b>
CORRESPONDENCE—CONTENTS.....	I-3
Participatory Peer Review Panel (PPRP) Letters.....	I-3
Technical Integration (TI) Team and Project Manager (PM) Response to PPRP Letters .....	I-4
<b>J MAGNITUDE-RECURRENCE MAPS FOR ALL REALIZATIONS AND ALL SOURCE-ZONE CONFIGURATIONS .....</b>	<b>J-1</b>
<b>K SCR DATABASE USED TO DEVELOP MMAX PRIOR DISTRIBUTIONS .....</b>	<b>K-1</b>
K.1 SCR Earthquake Catalog .....	K-1
K.2 SCR Crustal Domains .....	K-3
<b>L QUALITY ASSURANCE.....</b>	<b>L-1</b>
L.1 BACKGROUND.....	L-1
L.2 CEUS SSC PROJECT .....	L-2
L.2.1 Introduction.....	L-2
L.3 BEST BUSINESS PRACTICES.....	L-3
L.3.1 General.....	L-3
L.4 CEUS SSC EARTHQUAKE CATALOG DEVELOPMENT .....	L-3
L.4.1 External Review of Earthquake Catalog.....	L-3
L.4.2 Simulation Testing .....	L-4
L.4.3 Checks for Consistency in Magnitude Conversion from Intensity .....	L-4
L.4.4 Use of Verified Computer Programs.....	L-4
L.5 RECURRENCE ANALYSIS AND SPATIAL SMOOTHING .....	L-4
L.5.1 Introduction.....	L-4
L.5.2 Recurrence Comparisons at the Source-Zone Level.....	L-5

---

L.5.3 Recurrence Comparisons for Portions of a Source Zone .....	L-5
L.5.4 Examination of Recurrence Maps .....	L-5
L.5.5 Test with a Synthetic Catalog Homogeneous Seismicity .....	L-5
L.5.6 Test for the Adequacy of Eight Maps to Represent Epistemic Uncertainty .....	L-6
L.6 HAZARD CALCULATION SOFTWARE.....	L-6
L.6.1 Introduction .....	L-6
L.6.2 Test for the Treatment of Variable b.....	L-6
L.6.3 Test for the Treatment of Dipping Ruptures Within a Source Zone .....	L-6
L.6.4 Tests for Treatment of Epistemic Uncertainty from Sources that Make Small Contribution to Hazard .....	L-6

# LIST OF FIGURES

---

Figure 1.3-1 Map showing the study area and test sites for the CEUS SSC Project.....	1-15
Figure 2.3-1 CEUS SSC Project organization .....	2-33
Figure 2.3-2 Lines of communication among the participants of the CEUS SSC Project.....	2-34
Figure 2.4-1 Essential activities associated with a SSHAC Level 3 or 4 project (Coppersmith et al., 2010) .....	2-35
Figure 3.2-1 Areal coverage of the primary earthquake catalog sources. Top: GSC catalog (Halchuk, 2009); bottom: USGS seismic hazard mapping catalog (Petersen et al., 2008). Red line denotes boundary of study region. Blue line denotes portion of each catalog used for development of project catalog. ....	3-57
Figure 3.2-2 Histogram of $M_L$ magnitudes from the GSC SHEEF catalog for the time period 1600-1899 and the region east of longitude $-105^\circ$ and south of latitude $53^\circ$ .....	3-58
Figure 3.2-3 Histogram of $M_L$ magnitudes from the GSC SHEEF catalog for the time period 1900-1929 and the region east of longitude $-105^\circ$ and south of latitude $53^\circ$ .....	3-59
Figure 3.2-4 Histogram of $M_L$ magnitudes from the GSC SHEEF catalog for the time period 1930-1979 and the region east of longitude $-105^\circ$ and south of latitude $53^\circ$ .....	3-60
Figure 3.2-5 Histogram of $M_L$ magnitudes from the GSC SHEEF catalog for the time period 1980-2007 and the region east of longitude $-105^\circ$ and south of latitude $53^\circ$ .....	3-61
Figure 3.2-6 Histogram of $M_L$ magnitudes from the revised catalog with GSC as the source for the time period 1928-1979 .....	3-62
Figure 3.2-7 Map of the CEUS SSC Project catalog showing earthquakes of uniform moment magnitude $E[M]$ 2.9 and larger. Colored symbols denote earthquakes not contained in the USGS seismic hazard mapping catalog.....	3-63
Figure 3.3-1 Illustration of equivalence of the $M^*$ and $\gamma^2$ corrections to remove bias in earthquake recurrence relationships estimated from magnitudes with uncertainty .....	3-64
Figure 3.3-2 Approximate moment magnitudes from Atkinson (2004b) compared to values of $M$ given in Table B-2 in Appendix B for earthquakes in common .....	3-65
Figure 3.3-3 Approximate moment magnitudes from Boatwright (1994) compared to values of $M$ given in Table B-2 in Appendix B for earthquakes in common .....	3-66
Figure 3.3-4 Approximate moment magnitudes from Moulis (2002) compared to values of $M$ given in Table B-2 in Appendix B for earthquakes in common .....	3-67
Figure 3.3-5 Difference between $M_N$ reported by the GSC and $M_N$ or $m_{Lg(f)}$ reported by the Weston Observatory catalog as a function of time .....	3-68
Figure 3.3-6 Spatial distribution of earthquakes with body-wave ( $m_b$ , $m_{bLg}$ , $M_N$ ) and $M$ magnitudes in the CEUS SSC Project catalog for the Midcontinent region. Color codes indicate the source of the body-wave magnitudes.....	3-69
Figure 3.3-7 $m_b$ - $M$ data for the earthquakes shown on Figure 3.3-6. Red curve shows the preferred offset fit $M = m_b - 0.28$ . ....	3-70

Figure 3.3-8 Residuals from offset fit shown on Figure 3.3-7 plotted against earthquake year .....	3-71
Figure 3.3-9 Spatial distribution of earthquakes with body wave ( $m_b$ , $m_{bLg}$ , $M_N$ ) and $M$ magnitudes in the CEUS SSC Project catalog for the northeastern portion of the study region. Color codes indicate the source of the body-wave magnitudes. ....	3-72
Figure 3.3-10 $m_b$ - $M$ data for the earthquakes shown on Figure 3.3-9. Red curve shows the preferred offset fit $M = m_b - 0.42$ . ....	3-73
Figure 3.3-11 Residuals from offset fit shown on Figure 3.3-10 plotted against earthquake year .....	3-74
Figure 3.3-12 Residuals for GSC data from offset fit shown on Figure 3.3-10 plotted against earthquake year .....	3-75
Figure 3.3-13 Residuals for WES data from offset fit shown on Figure 3.3-10 plotted against earthquake year .....	3-76
Figure 3.3-14 Residuals for data from sources other than GSC or WES from offset fit shown on Figure 3.3-10 plotted against earthquake year .....	3-77
Figure 3.3-15 Difference between body-wave magnitudes reported by LDO and those by other sources as a function of year .....	3-78
Figure 3.3-16 Spatial distribution of earthquakes with reported GSC body-wave magnitudes. Red and blue symbols indicate earthquakes with both $m_b$ and $M$ magnitudes for $m_b \geq 3.5$ . Dashed line indicates the portion of the study region considered the "Northeast" for purposes of magnitude scaling. ....	3-79
Figure 3.3-17 $M$ - $m_b$ as a function of time for $m_b$ data from the GSC shown on Figure 3.3-16 .....	3-80
Figure 3.3-18 Plot of magnitude differences $m_{bLg} - m(3 \text{ Hz})$ for the OKO catalog .....	3-81
Figure 3.3-19 Final $m_b$ - $M$ data set. Vertical dashed lines indicate the magnitude range used to develop the scaling relationship. Diagonal line indicates a one-to-one correlation. ....	3-82
Figure 3.3-20 Spatial distribution of earthquakes in the CEUS SSC Project catalog with instrumental $M_L$ magnitudes .....	3-83
Figure 3.3-21 Spatial distribution of earthquakes in the CEUS SSC Project catalog with instrumental $M_L$ magnitudes and $M$ magnitudes .....	3-84
Figure 3.3-22 $M_L$ - $M$ data from the CEUS SSC Project catalog and robust regression fit to the data .....	3-85
Figure 3.3-23 Relationship between $M_N$ and $M_L$ for the GSC data .....	3-86
Figure 3.3-24 Data from the northeastern portion of the study region with $M_L$ and $M_C$ or $M_D$ magnitude from catalog sources other than the GSC .....	3-87
Figure 3.3-25 Data from the northeastern portion of the study region with $M_L$ and $M$ magnitudes from sources other than the GSC .....	3-88
Figure 3.3-26 Spatial distribution of earthquakes in the CEUS SSC Project catalog with $M_S \geq 3$ magnitudes .....	3-89
Figure 3.3-27 $M_S$ - $M$ data from the CEUS SSC Project catalog and quadratic polynomial fit to the data .....	3-90
Figure 3.3-28 Spatial distribution of earthquakes in the CEUS SSC Project catalog with $M_C \geq 2.5$ magnitudes .....	3-91

Figure 3.3-29 Spatial distribution of earthquakes in the CEUS SSC Project catalog with $M_C \geq 2.5$ and $M$ magnitudes .....	3-92
Figure 3.3-30 Spatial distribution of earthquakes in the CEUS SSC Project catalog with $M_D \geq 3$ magnitudes .....	3-93
Figure 3.3-31 Spatial distribution of earthquakes in the CEUS SSC Project catalog with both $M_D$ and $M$ magnitudes .....	3-94
Figure 3.3-32 $M_C$ - $M$ data from the CEUS SSC Project catalog and linear regression fit to the data .....	3-95
Figure 3.3-33 Spatial distribution of earthquakes with reported $M_C$ and $M_D$ magnitudes .....	3-96
Figure 3.3-34 Comparison of $M_C$ and $M_D$ magnitudes for the LDO and WES catalogs .....	3-97
Figure 3.3-35 Comparison of $M_C$ with $M_D$ for at least one of the two magnitude types reported in the OKO catalog .....	3-98
Figure 3.3-36 Comparison of $M_C$ with $M_D$ for at least one of the two magnitude types reported in the CERI catalog .....	3-99
Figure 3.3-37 Comparison of $M_C$ with $M_D$ for at least one of the two magnitude types reported in the SCSN catalog .....	3-100
Figure 3.3-38 Comparison of $M_C$ with $M_D$ for at least one of the two magnitude types reported in other catalogs for earthquakes in the Midcontinent portion of the study region .....	3-101
Figure 3.3-39 Relationship between $M$ and $M_C$ , $M_D$ , or $M_L$ for the Midcontinent portion of the study region .....	3-102
Figure 3.3-40 Comparison of $M_C$ and $M_D$ magnitudes with $M_L$ magnitudes for the region between longitudes $105^\circ\text{W}$ and $100^\circ\text{W}$ .....	3-103
Figure 3.3-41 Comparison of $m_b$ magnitudes with $M_L$ magnitudes for the region between longitudes $105^\circ\text{W}$ and $100^\circ\text{W}$ .....	3-104
Figure 3.3-42 Comparison of $m_b$ magnitudes with $M_C$ and $M_D$ magnitudes for the region between longitudes $105^\circ\text{W}$ and $100^\circ\text{W}$ .....	3-105
Figure 3.3-43 Spatial distribution of earthquake with $\ln(\text{FA})$ in the CEUS SSC Project catalog .....	3-106
Figure 3.3-44 Catalog $\ln(\text{FA})$ - $M$ data and fitted model .....	3-107
Figure 3.3-45 Spatial distribution of earthquakes in the CEUS SSC Project catalog with reported values of $I_0$ .....	3-108
Figure 3.3-46 $I_0$ and $M$ data for earthquakes in the CEUS SSC Project catalog. Curves show locally weighted least-squares fit (Loess) to the data and the relationship published by Johnston (1996b) .....	3-109
Figure 3.3-47 $I_0$ and $m_b$ data from the NCEER91 catalog. Plotted are the relationships between $I_0$ and $m_b$ developed by EPRI (1988) (EPRI-SOG) and Sibol et al. (1987) .....	3-110
Figure 3.3-48 Categorical model fits of $I_0$ as a function and $M$ for earthquakes in the CEUS SSC Project catalog .....	3-111
Figure 3.3-49 Results from proportional odds logistic model showing the probability of individual intensity classes as a function of $M$ .....	3-112
Figure 3.3-50 Comparison of $I_0$ and $m_b$ data from the CEUS SSC Project catalog for those earthquakes with reported values of $M$ ( $M$ set) and the full catalog (full set). Locally weighted least-squares fits to the two data sets are shown along with the	

relationship use to develop the EPRI (1988) catalog and the Sibol et al. (1987) relationship used in the NCEER91 catalog.....	3-113
Figure 3.3-51 Linear fits to the data from Figure 3.3-50 for $I_0 \geq V$ .....	3-114
Figure 3.3-52 Comparison of $I_0$ and $m_b$ data from the project, with $m_b$ adjusted for the difference in $m_b$ to M scaling .....	3-115
Figure 3.3-53 Linear fits to the data from Figure 3.3-52 for $I_0 \geq V$ .....	3-116
Figure 3.3-54 Composite $I_0$ –M data set used for assessment of $I_0$ scaling relationship.....	3-117
Figure 3.3-55 Linear and inverse sigmoid models fit to the project data for $I_0 > IV$ .....	3-118
Figure 3.4-1 Illustration of process used to identify clusters of earthquakes (from EPRI, 1988, Vol. 1): (a) local and extended time and distance windows, (b) buffer window, and (c) contracted window.....	3-119
Figure 3.4-2 Identification of secondary (dependent) earthquakes inside the cluster region through Poisson thinning (from EPRI, 1988, Vol. 1).....	3-120
Figure 3.4-3 Comparison of dependent event time and distance windows with results for individual clusters in the project catalog .....	3-121
Figure 3.5-1 Earthquake catalog and catalog completeness regions used in EPRI-SOG (EPRI, 1988) .....	3-122
Figure 3.5-2 CEUS SSC Project earthquake catalog and modified catalog completeness regions .....	3-123
Figure 3.5-3 Plot of year versus location for the CEUS SSC Project earthquake catalog. Red lines indicate the boundaries of the catalog completeness time periods.....	3-124
Figure 3.5-4 (1 of 7) “Stepp” plots of earthquake recurrence rate as a function of time for the individual catalog completeness regions shown on Figure 3.5-2.....	3-125
Figure 3.5-4 (2 of 7) “Stepp” plots of earthquake recurrence rate as a function of time for the individual catalog completeness regions shown on Figure 3.5-2.....	3-126
Figure 3.5-4 (3 of 7) “Stepp” plots of earthquake recurrence rate as a function of time for the individual catalog completeness regions shown on Figure 3.5-2.....	3-127
Figure 3.5-4 (4 of 7) “Stepp” plots of earthquake recurrence rate as a function of time for the individual catalog completeness regions shown on Figure 3.5-2.....	3-128
Figure 3.5-4 (5 of 7) “Stepp” plots of earthquake recurrence rate as a function of time for the individual catalog completeness regions shown on Figure 3.5-2.....	3-129
Figure 3.5-4 (6 of 7) “Stepp” plots of earthquake recurrence rate as a function of time for the individual catalog completeness regions shown on Figure 3.5-2.....	3-130
Figure 3.5-4 (7 of 7) “Stepp” plots of earthquake recurrence rate as a function of time for the individual catalog completeness regions shown on Figure 3.5-2.....	3-131
Figure 4.1.1-1 Example logic tree from the PEGASOS project (NAGRA, 2004) showing the assessment of alternative conceptual models on the logic tree. Each node of the logic tree represents an assessment that is uncertain. Alternative branches represent the alternative models or parameter values, and the weights associated with each branch reflect the TI Team’s relative degree of belief that each branch is the correct model or parameter value. ....	4-40
Figure 4.1.1-2 Example logic tree from the PVHA-U (SNL, 2008) project showing the treatment of alternative conceptual models in the logic tree .....	4-41

Figure 4.2.1-1 Master logic tree showing the Mmax zones and seismotectonic zones alternative conceptual models for assessing the spatial and temporal characteristics of future earthquake sources in the CEUS.....	4-42
Figure 4.2.2-1 Example of a logic tree for RLME sources. Shown is the tree for the Marianna RLME source.....	4-43
Figure 4.2.2-2 Map showing RLME sources, some with alternative source geometries (discussed in Section 6.1). .....	4-44
Figure 4.2.3-1 Logic tree for the Mmax zones branch of the master logic tree .....	4-45
Figure 4.2.3-2 Subdivision used in the Mmax zones branch of the master logic tree. Either the region is considered one zone for purposes of Mmax or the region is divided into two zones as shown: a Mesozoic-and-younger extension (MESE) zone and a non-Mesozoic-and-younger zone (NMESE). In this figure the “narrow” MESE zone is shown .....	4-46
Figure 4.2.3-3 Subdivision used in the Mmax zones branch of the master logic tree. Either the region is considered one zone for purposes of Mmax or the region is divided into two zones as shown: a Mesozoic-and-younger extension (MESE) zone and a non-Mesozoic-and-younger zone (NMESE). In this figure the “wide” MESE zone is shown .....	4-47
Figure 4.2.4-1(a) Logic tree for the seismotectonic zones branch of the master logic tree .....	4-48
Figure 4.2.4-1(b) Logic tree for the seismotectonic zones branch of the master logic tree .....	4-49
Figure 4.2.4-2 Seismotectonic zones shown in the case where the Rough Creek Graben is not part of the Reelfoot Rift (RR), and the Paleozoic Extended Zone is narrow (PEZ-N) .....	4-50
Figure 4.2.4-3 Seismotectonic zones shown in the case where the Rough Creek Graben is part of the Reelfoot Rift (RR-RCG), and the Paleozoic Extended Zone is narrow (PEZ-N).....	4-51
Figure 4.2.4-4 Seismotectonic zones shown in the case where the Rough Creek Graben is not part of the Reelfoot Rift (RR), and the Paleozoic Extended Crust is wide (PEZ-W) .....	4-52
Figure 4.2.4-5 Seismotectonic zones shown in the case where the Rough Creek Graben is part of the Reelfoot Rift (RR-RCG), and the Paleozoic Extended Crust is wide (PEZ-W) .....	4-53
Figure 5.2.1-1 Diagrammatic illustration of the Bayesian Mmax approach showing (a) the prior distribution, (b) the likelihood function, and (c) the posterior distribution. The posterior distribution is represented by a discrete distribution (d) for implementation in hazard analysis.....	5-72
Figure 5.2.1-2 Diagrammatic illustration of the Bayesian Mmax approach showing (a) the prior distribution, (b) the likelihood function, and (c) the posterior distribution. The posterior distribution is represented by a discrete distribution (d) for implementation in hazard analysis.....	5-73
Figure 5.2.1-3 Median values of $m_{\max-obs}$ as a function of maximum magnitude, $m^u$ , and sample size $N$ , the number of earthquakes $\geq M$ 4.5.....	5-74
Figure 5.2.1-4 Histograms of $m_{\max-obs}$ for extended and non-extended superdomains .....	5-75

---

Figure 5.2.1-5 Histograms of $m_{\max-obs}$ for Mesozoic-and-younger extended (MESE) superdomains and for older extended and non-extended (NMESE) superdomains .....	5-76
Figure 5.2.1-6 Histograms of $m_{\max-obs}$ for Mesozoic-and-younger extended (MESE) superdomains and for older extended and non-extended (NMESE) superdomains using age of most recent extension for the age classification .....	5-77
Figure 5.2.1-7 Histograms of $m_{\max-obs}$ for Mesozoic-and-younger extended (MESE) superdomains and for older extended and non-extended (NMESE) superdomains using final sets indicated by asterisks in Tables 5.2.1-1 and 5.2.1-2.....	5-78
Figure 5.2.1-8 Histograms of $m_{\max-obs}$ for combined (COMB) superdomains using final sets indicated by asterisks in Table 5.2.1-3 .....	5-79
Figure 5.2.1-9 Bias adjustments from $m_{\max-obs}$ to $m^u$ for the three sets of superdomain analysis results presented in Table 5.2.1-4.....	5-80
Figure 5.2.1-10 Results of simulations of estimates of Mmax using the Bayesian approach for earthquake catalogs ranging in size from 1 to 1,000 earthquakes. True Mmax is set at the mean of the prior distribution.....	5-81
Figure 5.2.1-11 Comparison of the Kijko (2004) estimates of $m^u$ for given values of $m_{\max-obs}$ and $N$ , the number of earthquakes of magnitude $\geq 4.5$ . Also shown is the median value of $m_{\max-obs}$ for given $m^u$ obtained using Equation 5.2.1-2. ....	5-82
Figure 5.2.1-12 Behavior of the cumulative probability function for $m^u$ (Equation 5.2.1-9) for the K-S-B estimator and a value of $m_{\max-obs}$ equal to 6 .....	5-83
Figure 5.2.1-13 Example Mmax distribution assessed for the Mesozoic-and-younger extended Mmax zone for the case where the zone is "narrow" (MESE-N). Distributions are shown for the Kijko approach and for the Bayesian approach using either the Mesozoic-and-younger extended prior distribution or the composite prior distribution. The final composite Mmax distribution, which incorporates the relative weights, is shown by the red probability distribution. ....	5-84
Figure 5.2.1-14 Example Mmax distribution assessed for the Northern Appalachian seismotectonic zone (NAP). Distributions are shown for the Kijko approach and for the Bayesian approach using either the Mesozoic-and-younger extended prior distribution or the composite prior distribution. Note that the Kijko results are shown in this example for illustration, even though they have zero weight. The final composite Mmax distribution, which incorporates the relative weights, is shown by the red probability distribution.....	5-85
Figure 5.3.2-1 Likelihood function for rate per unit area in a Poisson process, for multiple values of the earthquake count $N$ : (a) arithmetic scale, and (b) logarithmic scale used to illustrate decreasing COV as $N$ increases .....	5-86
Figure 5.3.2-2 Likelihood function for $b$ -value of an exponential magnitude distribution, for multiple values of the earthquake count $N$ . The value of $b$ is normalized by the maximum-likelihood estimate, which is derived from Equation 5.3.2-5. ....	5-87
Figure 5.3.2-3 Histogram of magnitudes in the earthquake catalog used in this section. The minimum magnitude shown (M 2.9) is the lowest magnitude used in these recurrence calculations.....	5-88

---

Figure 5.3.2-4 Objectively determined values of the penalty function for $\ln(\text{rate})$ for Case A magnitude weights. Source zones are sorted from smallest to largest. See list of abbreviations for full source-zone names. ....	5-89
Figure 5.3.2-5 Objectively determined values of the penalty function for beta for Case A magnitude weights .....	5-90
Figure 5.3.2-6 Objectively determined values of the penalty function for $\ln(\text{rate})$ for Case B magnitude weights .....	5-91
Figure 5.3.2-7 Objectively determined values of the penalty function for beta for Case B magnitude weights. Source zones are sorted from smallest to largest.....	5-92
Figure 5.3.2-8 Objectively determined values of the penalty function for $\ln(\text{rate})$ for Case E magnitude weights .....	5-93
Figure 5.3.2-9 Objectively determined values of the penalty function for beta for Case E magnitude weights. Source zones are sorted from smallest to largest.....	5-94
Figure 5.3.2-10 Mean map of rate and $b$ -value for ECC-AM calculated using Case A magnitude weights .....	5-95
Figure 5.3.2-11 Mean map of rate and $b$ -value for ECC-GC calculated using Case A magnitude weights .....	5-96
Figure 5.3.2-12 Mean map of rate and $b$ -value for ECC-AM calculated using Case B magnitude weights .....	5-97
Figure 5.3.2-13 Mean map of rate and $b$ -value for ECC-GC calculated using Case B magnitude weights .....	5-98
Figure 5.3.2-14 Mean map of rate and $b$ -value for ECC-AM calculated using Case E magnitude weights .....	5-99
Figure 5.3.2-15 Mean map of rate and $b$ -value for ECC-GC calculated using Case E magnitude weights .....	5-100
Figure 5.3.2-16 Sensitivity of seismic hazard at Manchester site to the strength of the prior on $b$ .....	5-101
Figure 5.3.2-17 Sensitivity of seismic hazard at Topeka site to the strength of the prior on $b$ .....	5-102
Figure 5.3.2-18 Sensitivity of seismic hazard at Manchester site to the choice of magnitude weights .....	5-103
Figure 5.3.2-19 Sensitivity of seismic hazard at Topeka site to the choice of magnitude weights.....	5-104
Figure 5.3.2-20 Sensitivity of seismic hazard from source NAP at Manchester site to the eight alternative recurrence maps for Case B magnitude weights .....	5-105
Figure 5.3.2-21 Sensitivity of seismic hazard from source MID-C–A at Topeka site to the eight alternative recurrence maps for Case B magnitude weights .....	5-106
Figure 5.3.2-22 Mean recurrence-parameter map for the study region under the highest weighted source-zone configuration in the master logic tree. See Sections 6.3 and 7.5 for all mean maps. ....	5-107
Figure 5.3.2-23 Map of the uncertainty in the estimated recurrence parameters, expressed as the coefficient of variation of the rate (left) and the standard deviation of the $b$ -value (right) for the study region, under the highest weighted source-zone configuration in the master logic tree. See Appendix J for all maps of uncertainty. ....	5-108

---

Figure 5.3.2-24 First of eight equally likely realizations of the recurrence-parameter map for the study region under the highest weighted source-zone configuration in the master logic tree. See Appendix J for maps of all realizations for all source-zone configurations.....	5-109
Figure 5.3.2-25 Eighth of eight equally likely realizations of the recurrence-parameter map for the study region under the highest weighted source-zone configuration in the master logic tree. See Appendix J for maps of all realizations for all source-zone configurations.....	5-110
Figure 5.3.2-26 Map of geographic areas considered in the exploration of model results.....	5-111
Figure 5.3.2-27 Comparison of model-predicted earthquake counts for the USGS Eastern Tennessee area using Case A magnitude weights. The error bars represent the 16%–84% uncertainty associated with the data, computed using the Weichert (1980) procedure.....	5-112
Figure 5.3.2-28 Comparison of model-predicted earthquake counts for the USGS Eastern Tennessee area using Case B magnitude weights.....	5-113
Figure 5.3.2-29 Comparison of model-predicted earthquake counts for the USGS Eastern Tennessee area using Case E magnitude weights.....	5-114
Figure 5.3.2-30 Comparison of model-predicted earthquake counts for the central New England area using Case A magnitude weights.....	5-115
Figure 5.3.2-31 Comparison of model-predicted earthquake counts for the central New England area using Case B magnitude weights.....	5-116
Figure 5.3.2-32 Comparison of model-predicted earthquake counts for the central New England area using Case E magnitude weights.....	5-117
Figure 5.3.2-33 Comparison of model-predicted earthquake counts for the Nemaha Ridge area using Case A magnitude weights.....	5-118
Figure 5.3.2-34 Comparison of model-predicted earthquake counts for the Nemaha Ridge area using Case B magnitude weights.....	5-119
Figure 5.3.2-35 Comparison of model-predicted earthquake counts for the Nemaha Ridge area using Case E magnitude weights.....	5-120
Figure 5.3.2-36 Comparison of model-predicted earthquake counts for the Miami, FL, area using Case A magnitude weights.....	5-121
Figure 5.3.2-37 Comparison of model-predicted earthquake counts for the Miami, FL, area using Case B magnitude weights.....	5-122
Figure 5.3.2-38 Comparison of model-predicted earthquake counts for the Miami, FL, area using Case E magnitude weights.....	5-123
Figure 5.3.2-39 Comparison of model-predicted earthquake counts for the St. Paul, MN, area using Case A magnitude weights.....	5-124
Figure 5.3.2-40 Comparison of model-predicted earthquake counts for the St. Paul, MN, area using Case B magnitude weights.....	5-125
Figure 5.3.2-41 Comparison of model-predicted earthquake counts for the St. Paul, MN, area using Case E magnitude weights.....	5-126
Figure 5.3.2-42 Recurrence parameters for the ECC-AM, MID-C–A, and NAP seismotectonic source zones and Case A magnitude weights computed using an objective adaptive kernel approach.....	5-127

Figure 5.3.3-1 Likelihood distribution for rate parameter $\lambda$ derived using Equation 5.3.3-1 for $N = 2$ and $T = 2,000$ years. Top: normalized probability density function for $\lambda$ . Bottom: resulting cumulative distribution function. Dashed lines show the cumulative probability levels for the Miller and Rice (1983) discrete approximation of a continuous probability distribution.....	5-128
Figure 5.3.3-2 Uncertainty distributions for the age of Charleston RLMEs.....	5-129
Figure 5.4.4-1 Spatial distribution of earthquakes in the CEUS SSC Project catalog. Solid lines indicate the boundaries of the seismotectonic source zones (narrow interpretation) .....	5-130
Figure 5.4.4-2 Spatial distribution of earthquakes in the CEUS SSC Project catalog with good quality depth determinations used for assessing crustal thickness. Solid lines indicate the boundaries of the seismotectonic source zones (narrow interpretation).....	5-131
Figure 5.4.4-3 Distribution of better-quality focal depths in Mmax source zones .....	5-132
Figure 5.4.4-4 (1 of 3) Distribution of better-quality focal depths in seismotectonic source zones .....	5-133
Figure 5.4.4-4 (2 of 3) Distribution of better-quality focal depths in seismotectonic source zones .....	5-134
Figure 5.4.4-4 (3 of 3) Distribution of better-quality focal depths in seismotectonic source zones .....	5-135
Figure 6.1-1 Map showing the RLME sources characterized in the CEUS SSC model. Detailed alternatives to the source geometries are shown on figures associated with each RLME discussion. ....	6-111
Figure 6.1-2a Map showing the RLME sources and seismicity from the CEUS SSC earthquake catalog. Some of the RLMEs occur in regions of elevated seismicity, but others do not. ....	6-112
Figure 6.1-2b Close-up of the Wabash Valley and New Madrid/Reelfoot Rift RLME sources and seismicity from the CEUS SSC earthquake catalog. Some of the RLMEs occur in regions of elevated seismicity, but others do not. ....	6-113
Figure 6.1.1-1 Logic tree for the Charlevoix RLME source .....	6-114
Figure 6.1.1-2 Seismicity and tectonic features of the Charlevoix RLME.....	6-115
Figure 6.1.1-3 Magnetic and gravity anomaly maps of the Charlevoix RLME.....	6-116
Figure 6.1.2-1a Logic tree for the Charleston RLME source.....	6-117
Figure 6.1.2-1b Logic tree for the Charleston RLME source.....	6-118
Figure 6.1.2-2 Charleston RLME source zones with (a) total magnetic anomaly and (b) residual isostatic gravity data .....	6-119
Figure 6.1.2-3 Postulated faults and tectonic features in the Charleston region .....	6-120
Figure 6.1.2-4 Postulated faults and tectonic features in the local Charleston area .....	6-121
Figure 6.1.2-5a Postulated faults and tectonic features in the Charleston region with Charleston RLME source zones .....	6-122
Figure 6.1.2-5b Postulated faults and tectonic features in the local Charleston area with Charleston RLME source zones .....	6-123
Figure 6.1.2-6 Schematic diagram showing contemporary, maximum, and minimum constraining age sample locations.....	6-124

---

Figure 6.1.2-7 Charleston space-time diagram of earthquakes interpreted from paleoliquefaction, contemporary-ages-only scenario .....	6-125
Figure 6.1.2-8 Charleston space-time diagram of earthquakes interpreted from paleoliquefaction, all-ages scenario .....	6-126
Figure 6.1.2-9 Distribution of liquefaction from earthquake A, contemporary-ages-only scenario .....	6-127
Figure 6.1.2-10 Distribution of liquefaction from earthquake B, contemporary-ages-only scenario .....	6-128
Figure 6.1.2-11 Distribution of liquefaction from earthquake C, contemporary-ages-only scenario .....	6-129
Figure 6.1.2-12 Distribution of liquefaction from earthquake D, contemporary-ages-only scenario .....	6-130
Figure 6.1.2-13 Distribution of liquefaction from earthquake E, contemporary-ages-only scenario .....	6-131
Figure 6.1.2-14 Distribution of liquefaction from earthquake A, all-ages scenario .....	6-132
Figure 6.1.2-15 Distribution of liquefaction from earthquake B, all-ages scenario .....	6-133
Figure 6.1.2-16 Distribution of liquefaction from earthquake C, all-ages scenario .....	6-134
Figure 6.1.2-17 Distribution of liquefaction from earthquake D, all-ages scenario .....	6-135
Figure 6.1.2-18 Distribution of liquefaction from earthquake E, all-ages scenario.....	6-136
Figure 6.1.2-19 Uncertainty distributions for the age of Charleston RLMEs.....	6-137
Figure 6.1.3-1 Logic tree for the Cheraw fault RLME source .....	6-138
Figure 6.1.3-2 Map (c) and hillshade relief images (a, b, and d) showing location of mapped Cheraw fault, possible northeast extension, and paleoseismic locality.....	6-139
Figure 6.1.3-3 Cheraw RLME source relative to (a) total magnetic anomaly and (b) residual isostatic gravity data.....	6-140
Figure 6.1.4-1 Meers fault location.....	6-141
Figure 6.1.4-2 Logic tree for the Meers fault source .....	6-142
Figure 6.1.5-1 Logic tree for the NMFS RLME source .....	6-143
Figure 6.1.5-2 Map showing seismicity and major subsurface structural features in the New Madrid region .....	6-144
Figure 6.1.5-3 Map showing geomorphic and near-surface tectonic features in the New Madrid region and locations of NMFS RLME fault sources .....	6-145
Figure 6.1.5-4 Rupture segments (a) and models (b) for the New Madrid faults from Johnston and Schweig (1996) and (c) the NMFS RLME fault sources .....	6-146
Figure 6.1.5-5 Map of NMSZ showing estimated ages and measured sizes of liquefaction features .....	6-147
Figure 6.1.5-6 Earthquake chronology for NMSZ from dating and correlation of liquefaction features at sites (listed at top) along N-S transect across region .....	6-148
Figure 6.1.5-7 Probability distributions for the age of the AD 900 and AD 1450 NMFS RLMEs .....	6-149
Figure 6.1.5-8 Liquefaction fields for the 1811-1812, AD 1450, and AD 900 earthquakes as interpreted from spatial distribution and stratigraphy of sand blows .....	6-150

Figure 6.1.6-1a Logic tree for the Reelfoot Rift–Eastern Rift Margin South RLME source. Two options for the southern extent of the ERM-S are considered: ERM-SCC includes the Crittenden County fault zone, and ERM-SRP includes the postulated zone of deformation based on fault picks identified in a high-resolution seismic profile along the Mississippi River.....	6-151
Figure 6.1.6-1b Logic tree for the Reelfoot Rift–Eastern Rift Margin North RLME source.....	6-152
Figure 6.1.6-2 Map showing structural features and paleoseismic investigation sites along the eastern margin of the Reelfoot rift. The inset map shows the locations of inferred basement faults that border and cross the Reelfoot rift (Csontos et al., 2008) and the inferred Joiner Ridge–Meeman-Shelby fault (JR-MSF; Odum et al., 2010). .....	6-153
Figure 6.1.6-3 Maps showing surficial geology and locations of subsurface investigations at (a) Meeman-Shelby Forest State Park locality and (b) Union City site (MSF and UC on Figure 6.1.6-2). Modified from Cox et al. (2006) and Odum et al. (2010). .....	6-154
Figure 6.1.6-4 Figure showing the timing of events along the eastern Reelfoot rift margin. Modified from Cox (2009). .....	6-155
Figure 6.1.7-1 Logic tree for the Reelfoot rift–Marianna RLME source .....	6-156
Figure 6.1.7-2 Map showing tectonic features and locations of paleoliquefaction sites in the vicinity of Marianna, Arkansas .....	6-157
Figure 6.1.7-3 Map showing liquefaction features near Daytona Beach lineament southwest of Marianna, Arkansas.....	6-158
Figure 6.1.8-1 Logic tree for the Commerce Fault Zone RLME source.....	6-159
Figure 6.1.8-2 Map showing tectonic features, seismicity, and paleoseismic localities along the Commerce Fault Zone RLME source .....	6-160
Figure 6.1.8-3 Location of the Commerce geophysical lineament and Commerce Fault Zone RLME source relative to the (a) regional magnetic anomaly map and (b) regional gravity anomaly map.....	6-161
Figure 6.1.8-4 Space-time diagram showing constraints on the location and timing of late Pleistocene and Holocene paleoearthquakes that may be associated with the Commerce Fault Zone RLME source .....	6-162
Figure 6.1.9-1 Logic tree for the Wabash Valley RLME source .....	6-163
Figure 6.1.9-2 Map showing seismicity, subsurface structural features, paleoearthquake energy centers, and postulated neotectonic deformation in the Wabash Valley region of southern Illinois and southern Indiana .....	6-164
Figure 6.1.9-3 Wabash Valley RLME source relative to (a) magnetic anomaly, and (b) residual isostatic gravity data .....	6-165
Figure 6.2-1 Map showing the two M <sub>max</sub> zones for the “narrow” interpretation of the Mesozoic-and-younger extended zone .....	6-166
Figure 6.2-2 Map showing the two M <sub>max</sub> zones for the “wide” interpretation of the Mesozoic-and-younger extended zone .....	6-167
Figure 6.3.1-1 Distributions for $m_{max-obs}$ for the M <sub>max</sub> distributed seismicity source zones ..	6-168
Figure 6.3.2-1 M <sub>max</sub> distributions for the study region treated as a single M <sub>max</sub> zone .....	6-169
Figure 6.3.2-2 M <sub>max</sub> distributions for the MESE-N M <sub>max</sub> zone .....	6-170

---

Figure 6.3.2-3 Mmax distributions for the MESE-W Mmax zone .....	6-171
Figure 6.3.2-4 Mmax distributions for the NMESE-N Mmax zone.....	6-172
Figure 6.3.2-5 Mmax distributions for the NMESE-W Mmax zone.....	6-173
Figure 6.4.1-1 Mean map of rate and b-value for the study region under the source-zone configuration, with no separation of Mesozoic extended and non-extended; Case A magnitude weights .....	6-174
Figure 6.4.1-2 Mean map of rate and b-value for the study region under the source-zone configuration, with no separation of Mesozoic extended and non-extended; Case B magnitude weights .....	6-175
Figure 6.4.1-3 Mean map of rate and b-value for the study region under the source-zone configuration, with no separation of Mesozoic extended and non-extended; Case E magnitude weights .....	6-176
Figure 6.4.1-4 Mean map of rate and b-value for the study region under the source-zone configuration, with separation of Mesozoic extended and non-extended, narrow geometry for MESE; Case A magnitude weights .....	6-177
Figure 6.4.1-5 Mean map of rate and b-value for the study region under the source-zone configuration, with separation of Mesozoic extended and non-extended, narrow geometry for MESE; Case B magnitude weights .....	6-178
Figure 6.4.1-6 Mean map of rate and b-value for the study region under the source-zone configuration, with separation of Mesozoic extended and non-extended, narrow geometry for MESE; Case E magnitude weights .....	6-179
Figure 6.4.1-7 Mean map of rate and b-value for the study region under the source-zone configuration, with separation of Mesozoic extended and non-extended, wide geometry for MESE; Case A magnitude weights .....	6-180
Figure 6.4.1-8 Mean map of rate and b-value for the study region under the source-zone configuration, with separation of Mesozoic extended and non-extended, wide geometry for MESE; Case B magnitude weights .....	6-181
Figure 6.4.1-9 Mean map of rate and b-value for the study region under the source-zone configuration, with separation of Mesozoic extended and non-extended, wide geometry for MESE; Case E magnitude weights .....	6-182
Figure 6.4.2-1 Comparison of model-predicted earthquake counts for study region using Case A magnitude weights. The error bars represent the 16%–84% uncertainty associated with the data, computed using the Weichert (1980) procedure. ....	6-183
Figure 6.4.2-2 Comparison of model-predicted earthquake counts for study region using Case B magnitude weights. The error bars represent the 16%–84% uncertainty associated with the data, computed using the Weichert (1980) procedure. ....	6-184
Figure 6.4.2-3 Comparison of model-predicted earthquake counts for study region using Case E magnitude weights. The error bars represent the 16%–84% uncertainty associated with the data, computed using the Weichert (1980) procedure. ....	6-185
Figure 6.4.2-4 Comparison of model-predicted earthquake counts for MESE-N using Case A magnitude weights. The error bars represent the 16%–84% uncertainty associated with the data, computed using the Weichert (1980) procedure. ....	6-186
Figure 6.4.2-5 Comparison of model-predicted earthquake counts for MESE-N using Case B magnitude weights. The error bars represent the 16%–84% uncertainty associated with the data, computed using the Weichert (1980) procedure. ....	6-187

---

Figure 6.4.2-6 Comparison of model-predicted earthquake counts for MESE-N using Case E magnitude weights. The error bars represent the 16%–84% uncertainty associated with the data, computed using the Weichert (1980) procedure. ....	6-188
Figure 6.4.2-7 Comparison of model-predicted earthquake counts for MESE-W using Case A magnitude weights. The error bars represent the 16%–84% uncertainty associated with the data, computed using the Weichert (1980) procedure. ....	6-189
Figure 6.4.2-8 Comparison of model-predicted earthquake counts for MESE-W using Case B magnitude weights. The error bars represent the 16%–84% uncertainty associated with the data, computed using the Weichert (1980) procedure. ....	6-190
Figure 6.4.2-9 Comparison of model-predicted earthquake counts for MESE-W using Case E magnitude weights. The error bars represent the 16%–84% uncertainty associated with the data, computed using the Weichert (1980) procedure. ....	6-191
Figure 6.4.2-10 Comparison of model-predicted earthquake counts for NMESE-N using Case A magnitude weights. The error bars represent the 16%–84% uncertainty associated with the data, computed using the Weichert (1980) procedure. ....	6-192
Figure 6.4.2-11 Comparison of model-predicted earthquake counts for NMESE-N using Case B magnitude weights. The error bars represent the 16%–84% uncertainty associated with the data, computed using the Weichert (1980) procedure. ....	6-193
Figure 6.4.2-12 Comparison of model-predicted earthquake counts for NMESE-N using Case E magnitude weights. The error bars represent the 16%–84% uncertainty associated with the data, computed using the Weichert (1980) procedure. ....	6-194
Figure 6.4.2-13 Comparison of model-predicted earthquake counts for NMESE-W using Case A magnitude weights. The error bars represent the 16%–84% uncertainty associated with the data, computed using the Weichert (1980) procedure. ....	6-195
Figure 6.4.2-14 Comparison of model-predicted earthquake counts for NMESE-W using Case B magnitude weights. The error bars represent the 16%–84% uncertainty associated with the data, computed using the Weichert (1980) procedure. ....	6-196
Figure 6.4.2-15 Comparison of model-predicted earthquake counts for NMESE-W using Case E magnitude weights. The error bars represent the 16%–84% uncertainty associated with the data, computed using the Weichert (1980) procedure. ....	6-197
Figure 7.1-1 Seismotectonic zones shown in the case where the Rough Creek graben is not part of the Reelfoot rift (RR) and the Paleozoic Extended Crust is narrow (PEZ-N) .....	7-83
Figure 7.1-2 Seismotectonic zones shown in the case where the Rough Creek graben is part of the Reelfoot rift (RR_RCG) and the Paleozoic Extended Crust is narrow (PEZ-N).....	7-84
Figure 7.1-3 Seismotectonic zones shown in the case where the Rough Creek graben is not part of the Reelfoot rift (RR) and the Paleozoic Extended Crust is wide (PEZ-W).....	7-85
Figure 7.1-4 Seismotectonic zones shown in the case where the Rough Creek graben is part of the Reelfoot rift (RR_RCG) and the Paleozoic Extended Crust is wide (PEZ-W) .....	7-86
Figure 7.1-5 Example of comparing seismotectonic zones with magnetic map developed as part of the CEUS SSC Project. ....	7-87
Figure 7.1-6 Example of comparing seismotectonic zones with isostatic gravity map developed as part of the CEUS SSC Project .....	7-88

Figure 7.1-7 Map of seismicity based on the earthquake catalog developed for the CEUS SSC Project.....	7-89
Figure 7.1-8 Map showing example comparison of seismotectonic zones with seismicity. Note the non-uniform spatial distribution of seismicity within the zones. Spatial smoothing of <i>a</i> - and <i>b</i> -values accounts for these spatial variations. ....	7-90
Figure 7.3-1 Logic tree for the seismotectonic zones branch of the master logic tree.....	7-91
Figure 7.3.1-1 Significant earthquakes and paleoseismology of the SLR seismotectonic zone .....	7-92
Figure 7.3.1-2 Tectonic features of the SLR seismotectonic zone.....	7-93
Figure 7.3.1-3 Magnetic and gravity anomaly maps of the SLR seismotectonic zone.....	7-94
Figure 7.3.2-1 Significant earthquakes and paleoseismic study area in the region of the GMH seismotectonic zone.....	7-95
Figure 7.3.2-2 Igneous rocks attributed to the GMH seismotectonic zone .....	7-96
Figure 7.3.2-3 Relocated hypocentral depths and crustal depth of the GMH seismotectonic zone .....	7-97
Figure 7.3.2-4 Magnetic and gravity anomaly maps of the GMH seismotectonic zone .....	7-98
Figure 7.3.3-1 Seismicity of the NAP seismotectonic zone.....	7-99
Figure 7.3.3-2 Magnetic and gravity anomaly maps of the NAP seismotectonic zone .....	7-100
Figure 7.3.4-1 Seismicity and tectonic features of the PEZ seismotectonic zone .....	7-101
Figure 7.3.4-2 Magnetic and gravity anomaly maps of the PEZ seismotectonic zone.....	7-102
Figure 7.3.5-1 Map showing seismicity, subsurface Paleozoic and basement structures, and postulated energy centers for prehistoric earthquakes.....	7-103
Figure 7.3.5-2 Map showing alternative boundaries for Precambrian (proto-Illinois basin) rift basins.....	7-104
Figure 7.3.5-3 Maps showing the IBEB source zone boundaries, seismicity, and prehistoric earthquake centers relative to (a) regional magnetic anomalies and (b) regional gravity anomalies.....	7-105
Figure 7.3.6-1 Map of seismicity and geomorphic features and faults showing evidence for Quaternary neotectonic deformation and reactivation. Inset map shows basement structures associated with the Reelfoot rift. ....	7-106
Figure 7.3.6-2 Maps showing geophysical anomalies in the Reelfoot rift region .....	7-107
Figure 7.3.7-1 Mesozoic basins within the ECC-AM zone .....	7-108
Figure 7.3.7-2 Seismicity within the ECC-AM and AHEX zones .....	7-109
Figure 7.3.7-3 Magnetic and gravity data for ECC-AM and AHEX zones .....	7-110
Figure 7.3.7-4 Estimated locations of the 1755 M 6.1 Cape Ann earthquake .....	7-111
Figure 7.3.8-1 Correlation of interpreted transitional crust with the East Coast magnetic anomaly .....	7-112
Figure 7.3.9-1 The ECC-GC seismotectonic zone.....	7-113
Figure 7.3.10-1 The GHEX seismotectonic zone.....	7-114
Figure 7.3.11-1 The OKA seismotectonic zone and regional gravity and magnetic data .....	7-115
Figure 7.3.12-1 Simplified tectonic map showing the distribution of principal basement faults, rifts, and sutures in the Midcontinent.....	7-116

---

Figure 7.3.12-2 Maps showing major basement structural features relative to (a) regional magnetic anomalies and (b) regional gravity anomalies .....	7-117
Figure 7.3.12-3 Seismic zones and maximum observed earthquakes in the MidC zone .....	7-118
Figure 7.3.12-4 Alternative MidC source zone configurations.....	7-119
Figure 7.4.1-1 (1 of 3) Distributions for $m_{\max-obs}$ for the seismotectonic distributed seismicity source zones.....	7-120
Figure 7.4.1-1 (2 of 3) Distributions for $m_{\max-obs}$ for the seismotectonic distributed seismicity source zones.....	7-121
Figure 7.4.1-1 (3 of 3) Distributions for $m_{\max-obs}$ for the seismotectonic distributed seismicity source zones.....	7-122
Figure 7.4.2-1 Mmax distributions for the AHEX seismotectonic zone.....	7-123
Figure 7.4.2-2 Mmax distributions for the ECC_AM seismotectonic zone.....	7-124
Figure 7.4.2-3 Mmax distributions for the ECC_GC seismotectonic zone.....	7-125
Figure 7.4.2-4 Mmax distributions for the GHEX seismotectonic zone .....	7-126
Figure 7.4.2-5 Mmax distributions for the GMH seismotectonic zone .....	7-127
Figure 7.4.2-6 Mmax distributions for the IBEB seismotectonic zone .....	7-128
Figure 7.4.2-7 Mmax distributions for the MidC-A seismotectonic zone .....	7-129
Figure 7.4.2-8 Mmax distributions for the MidC-B seismotectonic zone .....	7-130
Figure 7.4.2-9 Mmax distributions for the MidC-C seismotectonic zone .....	7-131
Figure 7.4.2-10 Mmax distributions for the MidC-D seismotectonic zone .....	7-132
Figure 7.4.2-11 Mmax distributions for the NAP seismotectonic zone .....	7-133
Figure 7.4.2-12 Mmax distributions for the OKA seismotectonic zone.....	7-134
Figure 7.4.2-13 Mmax distributions for the PEZ_N seismotectonic zone.....	7-135
Figure 7.4.2-14 Mmax distributions for the PEZ_W seismotectonic zone .....	7-136
Figure 7.4.2-15 Mmax distributions for the RR seismotectonic zone .....	7-137
Figure 7.4.2-16 Mmax distributions for the RR_RCG seismotectonic zone .....	7-138
Figure 7.4.2-17 Mmax distributions for the SLR seismotectonic zone .....	7-139
Figure 7.5.1-1 Mean map of rate and $b$ -value for the study region under the source-zone configuration with narrow interpretation of PEZ, Rough Creek Graben associated with Midcontinent; Case A magnitude weights.....	7-140
Figure 7.5.1-2 Mean map of rate and $b$ -value for the study region under the source-zone configuration with narrow interpretation of PEZ, Rough Creek Graben associated with Midcontinent; Case B magnitude weights.....	7-141
Figure 7.5.1-3 Mean map of rate and $b$ -value for the study region under the source-zone configuration with narrow interpretation of PEZ, Rough Creek Graben associated with Midcontinent; Case E magnitude weights.....	7-142
Figure 7.5.1-4 Mean map of rate and $b$ -value for the study region under the source-zone configuration with narrow interpretation of PEZ, Rough Creek graben associated with Reelfoot rift; Case A magnitude weights.....	7-143

---

Figure 7.5.1-5 Mean map of rate and $b$ -value for the study region under the source-zone configuration with narrow interpretation of PEZ, Rough Creek graben associated with Reelfoot rift; Case B magnitude weights.....	7-144
Figure 7.5.1-6 Mean map of rate and $b$ -value for the study region under the source-zone configuration with narrow interpretation of PEZ, Rough Creek graben associated with Reelfoot rift; Case E magnitude weights.....	7-145
Figure 7.5.1-7 Mean map of rate and $b$ -value for the study region under the source-zone configuration with wide interpretation of PEZ, Rough Creek graben associated with Midcontinent; Case A magnitude weights.....	7-146
Figure 7.5.1-8 Mean map of rate and $b$ -value for the study region under the source-zone configuration with wide interpretation of PEZ, Rough Creek Graben associated with Midcontinent; Case B magnitude weights.....	7-147
Figure 7.5.1-9 Mean map of rate and $b$ -value for the study region under the source-zone configuration with wide interpretation of PEZ, Rough Creek Graben associated with Midcontinent; Case E magnitude weights.....	7-148
Figure 7.5.1-10 Mean map of rate and $b$ -value for the study region under the source-zone configuration with wide interpretation of PEZ, Rough Creek graben associated with Reelfoot rift; Case A magnitude weights.....	7-149
Figure 7.5.1-11 Mean map of rate and $b$ -value for the study region under the source-zone configuration with wide interpretation of PEZ, Rough Creek graben associated with Reelfoot rift; Case B magnitude weights.....	7-150
Figure 7.5.1-12 Mean map of rate and $b$ -value for the study region under the source-zone configuration with wide interpretation of PEZ, Rough Creek graben associated with Reelfoot rift; Case E magnitude weights.....	7-151
Figure 7.5.2-1 Comparison of model-predicted earthquake counts for AHEX using Case A magnitude weights. No earthquake counts are shown because this source zone contains no seismicity. ....	7-152
Figure 7.5.2-2 Comparison of model-predicted earthquake counts for AHEX using Case B magnitude weights. No earthquake counts are shown because this source zone contains no seismicity.. ....	7-153
Figure 7.5.2-3 Comparison of model-predicted earthquake counts for AHEX using Case E magnitude weights. No earthquake counts are shown because this source zone contains no seismicity. ....	7-154
Figure 7.5.2-4 Comparison of model-predicted earthquake counts for ECC_AM using Case A magnitude weights. The error bars represent the 16%–84% uncertainty associated with the data, computed using the Weichert (1980) procedure. ....	7-155
Figure 7.5.2-5 Comparison of model-predicted earthquake counts for ECC_AM using Case B magnitude weights. Error bars as in Figure 7.5.2-4. ....	7-156
Figure 7.5.2-6 Comparison of model-predicted earthquake counts for ECC_AM using Case E magnitude weights. Error bars as in Figure 7.5.2-4. ....	7-157
Figure 7.5.2-7 Comparison of model-predicted earthquake counts for ECC_GC using Case A magnitude weights. Error bars as in Figure 7.5.2-4. ....	7-158
Figure 7.5.2-8 Comparison of model-predicted earthquake counts for ECC_GC using Case B magnitude weights. Error bars as in Figure 7.5.2-4. ....	7-159
Figure 7.5.2-9 Comparison of model-predicted earthquake counts for ECC_GC using Case E magnitude weights. Error bars as in Figure 7.5.2-4. ....	7-160

---

Figure 7.5.2-10 Comparison of model-predicted earthquake counts for GHEX using Case A magnitude weights. Error bars as in Figure 7.5.2-4. ....	7-161
Figure 7.5.2-11 Comparison of model-predicted earthquake counts for GHEX using Case B magnitude weights. Error bars as in Figure 7.5.2-4. ....	7-162
Figure 7.5.2-12 Comparison of model-predicted earthquake counts for GHEX using Case E magnitude weights. Error bars as in Figure 7.5.2-4. ....	7-163
Figure 7.5.2-13 Comparison of model-predicted earthquake counts for GMH using Case A magnitude weights. Error bars as in Figure 7.5.2-4. ....	7-164
Figure 7.5.2-14 Comparison of model-predicted earthquake counts for GMH using Case B magnitude weights. Error bars as in Figure 7.5.2-4. ....	7-165
Figure 7.5.2-15 Comparison of model-predicted earthquake counts for GMH using Case E magnitude weights. Error bars as in Figure 7.5.2-4. ....	7-166
Figure 7.5.2-16 Comparison of model-predicted earthquake counts for IBEB using Case A magnitude weights. Error bars as in Figure 7.5.2-4. ....	7-167
Figure 7.5.2-17 Comparison of model-predicted earthquake counts for IBEB using Case B magnitude weights. Error bars as in Figure 7.5.2-4. ....	7-168
Figure 7.5.2-18 Comparison of model-predicted earthquake counts for IBEB using Case E magnitude weights. Error bars as in Figure 7.5.2-4. ....	7-169
Figure 7.5.2-19 Comparison of model-predicted earthquake counts for MidC-A using Case A magnitude weights. Error bars as in Figure 7.5.2-4. ....	7-170
Figure 7.5.2-20 Comparison of model-predicted earthquake counts for MidC-A using Case B magnitude weights. Error bars as in Figure 7.5.2-4. ....	7-171
Figure 7.5.2-21 Comparison of model-predicted earthquake counts for MidC-A using Case E magnitude weights. Error bars as in Figure 7.5.2-4. ....	7-172
Figure 7.5.2-22 Comparison of model-predicted earthquake counts for MidC-B using Case A magnitude weights. Error bars as in Figure 7.5.2-4. ....	7-173
Figure 7.5.2-23 Comparison of model-predicted earthquake counts for MidC-B using Case B magnitude weights. Error bars as in Figure 7.5.2-4. ....	7-174
Figure 7.5.2-24 Comparison of model-predicted earthquake counts for MidC-B using Case E magnitude weights. Error bars as in Figure 7.5.2-4. ....	7-175
Figure 7.5.2-25 Comparison of model-predicted earthquake counts for MidC-C using Case A magnitude weights. Error bars as in Figure 7.5.2-4. ....	7-176
Figure 7.5.2-26 Comparison of model-predicted earthquake counts for MidC-C using Case B magnitude weights. Error bars as in Figure 7.5.2-4. ....	7-177
Figure 7.5.2-27 Comparison of model-predicted earthquake counts for MidC-C using Case E magnitude weights. Error bars as in Figure 7.5.2-4. ....	7-178
Figure 7.5.2-28 Comparison of model-predicted earthquake counts for MidC-D using Case A magnitude weights. Error bars as in Figure 7.5.2-4. ....	7-179
Figure 7.5.2-29 Comparison of model-predicted earthquake counts for MidC-D using Case B magnitude weights. Error bars as in Figure 7.5.2-4. ....	7-180
Figure 7.5.2-30 Comparison of model-predicted earthquake counts for MidC-D using Case E magnitude weights. Error bars as in Figure 7.5.2-4. ....	7-181
Figure 7.5.2-31 Comparison of model-predicted earthquake counts for NAP using Case A magnitude weights. Error bars as in Figure 7.5.2-4. ....	7-182

---

Figure 7.5.2-32 Comparison of model-predicted earthquake counts for NAP using Case B magnitude weights. Error bars as in Figure 7.5.2-4. ....	7-183
Figure 7.5.2-33 Comparison of model-predicted earthquake counts for NAP using Case E magnitude weights. Error bars as in Figure 7.5.2-4. ....	7-184
Figure 7.5.2-34 Comparison of model-predicted earthquake counts for OKA using Case A magnitude weights. Error bars as in Figure 7.5.2-4. ....	7-185
Figure 7.5.2-35 Comparison of model-predicted earthquake counts for OKA using Case B magnitude weights. Error bars as in Figure 7.5.2-4. ....	7-186
Figure 7.5.2-36 Comparison of model-predicted earthquake counts for OKA using Case E magnitude weights. Error bars as in Figure 7.5.2-4. ....	7-187
Figure 7.5.2-37 Comparison of model-predicted earthquake counts for PEZ_N using Case A magnitude weights. Error bars as in Figure 7.5.2-4. ....	7-188
Figure 7.5.2-38 Comparison of model-predicted earthquake counts for PEZ_N using Case B magnitude weights. Error bars as in Figure 7.5.2-4. ....	7-189
Figure 7.5.2-39 Comparison of model-predicted earthquake counts for PEZ_N using Case E magnitude weights. Error bars as in Figure 7.5.2-4. ....	7-190
Figure 7.5.2-40 Comparison of model-predicted earthquake counts for PEZ_W using Case A magnitude weights. Error bars as in Figure 7.5.2-4. ....	7-191
Figure 7.5.2-41 Comparison of model-predicted earthquake counts for PEZ_W using Case B magnitude weights. Error bars as in Figure 7.5.2-4. ....	7-192
Figure 7.5.2-42 Comparison of model-predicted earthquake counts for PEZ_W using Case E magnitude weights. Error bars as in Figure 7.5.2-4. ....	7-193
Figure 7.5.2-43 Comparison of model-predicted earthquake counts for RR using Case A magnitude weights. Error bars as in Figure 7.5.2-4. ....	7-194
Figure 7.5.2-44 Comparison of model-predicted earthquake counts for RR using Case B magnitude weights. Error bars as in Figure 7.5.2-4. ....	7-195
Figure 7.5.2-45 Comparison of model-predicted earthquake counts for RR using Case E magnitude weights. Error bars as in Figure 7.5.2-4. ....	7-196
Figure 7.5.2-46 Comparison of model-predicted earthquake counts for RR_RCG using Case A magnitude weights. Error bars as in Figure 7.5.2-4. ....	7-197
Figure 7.5.2-47 Comparison of model-predicted earthquake counts for RR_RCG using Case B magnitude weights. Error bars as in Figure 7.5.2-4. ....	7-198
Figure 7.5.2-48 Comparison of model-predicted earthquake counts for RR_RCG using Case E magnitude weights. Error bars as in Figure 7.5.2-4. ....	7-199
Figure 7.5.2-49 Comparison of model-predicted earthquake counts for SLR using Case A magnitude weights. Error bars as in Figure 7.5.2-4. ....	7-200
Figure 7.5.2-50 Comparison of model-predicted earthquake counts for SLR using Case B magnitude weights. Error bars as in Figure 7.5.2-4. ....	7-201
Figure 7.5.2-51 Comparison of model-predicted earthquake counts for SLR using Case E magnitude weights. Error bars as in Figure 7.5.2-4. ....	7-202
Figure 8.1-1 Map showing the study area and seven test sites for the CEUS SSC Project ....	8-28
Figure 8.1-2 Mean VS profile for shallow soil site.....	8-29
Figure 8.1-3 Mean VS profile for deep soil site.....	8-30

---

Figure 8.1-4 Mean amplification factors for shallow soil site .....	8-31
Figure 8.1-5 Mean amplification factors for deep soil site .....	8-32
Figure 8.2-1a Central Illinois 10 Hz rock hazard: mean and fractile total hazard .....	8-33
Figure 8.2-1b Central Illinois 1 Hz rock hazard: mean and fractile total hazard .....	8-34
Figure 8.2-1c Central Illinois PGA rock hazard: mean and fractile total hazard .....	8-35
Figure 8.2-1d Central Illinois 10 Hz rock hazard: total and contribution by RLME and background .....	8-36
Figure 8.2-1e Central Illinois 1 Hz rock hazard: total and contribution by RLME and background .....	8-37
Figure 8.2-1f Central Illinois PGA rock hazard: total and contribution by RLME and background .....	8-38
Figure 8.2-1g Central Illinois 10 Hz rock hazard: contribution by background source .....	8-39
Figure 8.2-1h Central Illinois 1 Hz rock hazard: contribution by background source .....	8-40
Figure 8.2-1i Central Illinois PGA rock hazard: contribution by background source .....	8-41
Figure 8.2-1j Central Illinois 10 Hz rock hazard: comparison of three source models .....	8-42
Figure 8.2-1k Central Illinois 1 Hz rock hazard: comparison of three source models .....	8-43
Figure 8.2-1l Central Illinois PGA rock hazard: comparison of three source models .....	8-44
Figure 8.2-1m Central Illinois 10 Hz shallow soil hazard: total and total and contribution by RLME and background .....	8-45
Figure 8.2-1n Central Illinois 1 Hz shallow soil hazard: total and contribution by RLME and background .....	8-46
Figure 8.2-1o Central Illinois PGA shallow soil hazard: total and contribution by RLME and background .....	8-47
Figure 8.2-1p Central Illinois 10 Hz deep soil hazard: total and contribution by RLME and background .....	8-48
Figure 8.2-1q Central Illinois 1 Hz deep soil hazard: total and contribution by RLME and background .....	8-49
Figure 8.2-1r Central Illinois PGA deep soil hazard: total and contribution by RLME and background .....	8-50
Figure 8.2-1s Central Illinois 10 Hz hazard: comparison of three site conditions .....	8-51
Figure 8.2-1t Central Illinois 1 Hz hazard: comparison of three site conditions .....	8-52
Figure 8.2-1u Central Illinois PGA hazard: comparison of three site conditions .....	8-53
Figure 8.2-1v Central Illinois 10 Hz rock hazard: sensitivity to seismotectonic vs. Mmax zones .....	8-54
Figure 8.2-1w Central Illinois 1 Hz rock hazard: sensitivity to seismotectonic vs. Mmax zones .....	8-55
Figure 8.2-1x Central Illinois 10 Hz rock hazard: sensitivity to Mmax for source IBEB .....	8-56
Figure 8.2-1y Central Illinois 1 Hz rock hazard: sensitivity to Mmax for source IBEB .....	8-57
Figure 8.2-1z Central Illinois 10 Hz rock hazard: sensitivity to smoothing options .....	8-58
Figure 8.2-1aa Central Illinois 1 Hz rock hazard: sensitivity to smoothing options .....	8-59
Figure 8.2-1bb Central Illinois 10 Hz rock hazard: sensitivity to eight realizations for source IBEB, Case A .....	8-60

---

Figure 8.2-1cc Central Illinois 10 Hz rock hazard: sensitivity to eight realizations for source IBEB, Case B.....	8-61
Figure 8.2-1dd Central Illinois 10 Hz rock hazard: sensitivity to eight realizations for source IBEB, Case E.....	8-62
Figure 8.2-1ee Central Illinois 1 Hz rock hazard: sensitivity to eight realizations for source IBEB, Case A.....	8-63
Figure 8.2-1ff Central Illinois 1 Hz rock hazard: sensitivity to eight realizations for source IBEB, Case B.....	8-64
Figure 8.2-1gg Central Illinois 1 Hz rock hazard: sensitivity to eight realizations for source IBEB, Case E.....	8-65
Figure 8.2-2a Chattanooga 10 Hz rock hazard: mean and fractile total hazard.....	8-66
Figure 8.2-2b Chattanooga 1 Hz rock hazard: mean and fractile total hazard.....	8-67
Figure 8.2-2c Chattanooga PGA rock hazard: mean and fractile total hazard.....	8-68
Figure 8.2-2d Chattanooga 10 Hz rock hazard: total and contribution by RLME and background.....	8-69
Figure 8.2-2e Chattanooga 1 Hz rock hazard: total and contribution by RLME and background.....	8-70
Figure 8.2-2f Chattanooga PGA rock hazard: total and contribution by RLME and background.....	8-71
Figure 8.2-2g Chattanooga 10 Hz rock hazard: contribution by background source.....	8-72
Figure 8.2-2h Chattanooga 1 Hz rock hazard: contribution by background source.....	8-73
Figure 8.2-2i Chattanooga PGA rock hazard: contribution by background source.....	8-74
Figure 8.2-2j Chattanooga 10 Hz rock hazard: comparison of three source models.....	8-75
Figure 8.2-2k Chattanooga 1 Hz rock hazard: comparison of three source models.....	8-76
Figure 8.2-2l Chattanooga PGA rock hazard: comparison of three source models.....	8-77
Figure 8.2-2m Chattanooga 10 Hz shallow soil hazard: total and contribution by RLME and background.....	8-78
Figure 8.2-2n Chattanooga 1 Hz shallow soil hazard: total and contribution by RLME and background.....	8-79
Figure 8.2-2o Chattanooga PGA shallow soil hazard: total and contribution by RLME and background.....	8-80
Figure 8.2-2p Chattanooga 10 Hz deep soil hazard: total and contribution by RLME and background.....	8-81
Figure 8.2-2q Chattanooga 1 Hz deep soil hazard: total and contribution by RLME and background.....	8-82
Figure 8.2-2r Chattanooga PGA deep soil hazard: total and contribution by RLME and background.....	8-83
Figure 8.2-2s Chattanooga 10 Hz hazard: comparison of three site conditions.....	8-84
Figure 8.2-2t Chattanooga 1 Hz hazard: comparison of three site conditions.....	8-85
Figure 8.2-2u Chattanooga PGA hazard: comparison of three site conditions.....	8-86
Figure 8.2-2v Chattanooga 10 Hz rock hazard: sensitivity to seismotectonic vs. Mmax zones.....	8-87

---

Figure 8.2-2w Chattanooga 1 Hz rock hazard: sensitivity to seismotectonic vs. Mmax zones .....	8-88
Figure 8.2-2x Chattanooga 10 Hz rock hazard: sensitivity to Mmax for source PEZ-N .....	8-89
Figure 8.2-2y Chattanooga 1 Hz rock hazard: sensitivity to Mmax for source PEZ-N .....	8-90
Figure 8.2-2z Chattanooga 10 Hz rock hazard: sensitivity to smoothing options .....	8-91
Figure 8.2-2aa Chattanooga 1 Hz rock hazard: sensitivity to smoothing options .....	8-92
Figure 8.2-2bb Chattanooga 10 Hz rock hazard: sensitivity to eight realizations for source PEZ-N, Case A .....	8-93
Figure 8.2-2cc Chattanooga 10 Hz rock hazard: sensitivity to eight realizations for source PEZ-N, Case B .....	8-94
Figure 8.2-2dd Chattanooga 10 Hz rock hazard: sensitivity to eight realizations for source PEZ-N, Case E .....	8-95
Figure 8.2-2ee Chattanooga 1 Hz rock hazard: sensitivity to eight realizations for source PEZ-N, Case A .....	8-96
Figure 8.2-2ff Chattanooga 1 Hz rock hazard: sensitivity to eight realizations for source PEZ-N, Case B .....	8-97
Figure 8.2-2gg Chattanooga 1 Hz rock hazard: sensitivity to eight realizations for source PEZ-N, Case E .....	8-98
Figure 8.2-3a Houston 10 Hz rock hazard: mean and fractile total hazard .....	8-99
Figure 8.2-3b Houston 1 Hz rock hazard: mean and fractile total hazard .....	8-100
Figure 8.2-3c Houston PGA rock hazard: mean and fractile total hazard .....	8-101
Figure 8.2-3d Houston 10 Hz rock hazard: total and contribution by RLME and background .....	8-102
Figure 8.2-3e Houston 1 Hz rock hazard: total and contribution by RLME and background .....	8-103
Figure 8.2-3f Houston PGA rock hazard: total and contribution by RLME and background ..	8-104
Figure 8.2-3g Houston 10 Hz rock hazard: contribution by background source .....	8-105
Figure 8.2-3h Houston 1 Hz rock hazard: contribution by background source .....	8-106
Figure 8.2-3i Houston PGA rock hazard: contribution by background source .....	8-107
Figure 8.2-3j Houston 10 Hz rock hazard: comparison of three source models .....	8-108
Figure 8.2-3k Houston is 1 Hz rock hazard: comparison of three source models .....	8-109
Figure 8.2-3l Houston PGA rock hazard: comparison of three source models .....	8-110
Figure 8.2-3m Houston 10 Hz shallow soil hazard: total and contribution by RLME and background .....	8-111
Figure 8.2-3n Houston 1 Hz shallow soil hazard: total and contribution by RLME and background .....	8-112
Figure 8.2-3o Houston PGA shallow soil hazard: total and contribution by RLME and background .....	8-113
Figure 8.2-3p Houston 10 Hz deep soil hazard: total and contribution by RLME and background .....	8-114
Figure 8.2-3q Houston 1 Hz deep soil hazard: total and contribution by RLME and background .....	8-115

---

Figure 8.2-3r Houston PGA deep soil hazard: total and contribution by RLME and background .....	8-116
Figure 8.2-3s Houston 10 Hz hazard: comparison of three site conditions .....	8-117
Figure 8.2-3t Houston 1 Hz hazard: comparison of three site conditions .....	8-118
Figure 8.2-3u Houston PGA hazard: comparison of three site conditions .....	8-119
Figure 8.2-3v Houston 10 Hz rock hazard: sensitivity to seismotectonic vs. Mmax zones ....	8-120
Figure 8.2-3w Houston 1 Hz rock hazard: sensitivity to seismotectonic vs. Mmax zones ....	8-121
Figure 8.2-3x Houston 10 Hz rock hazard: sensitivity to Mmax for source GHEX.....	8-122
Figure 8.2-3y Houston 1 Hz rock hazard: sensitivity to Mmax for source GHEX.....	8-123
Figure 8.2-3z Houston 10 Hz rock hazard: sensitivity to smoothing options .....	8-124
Figure 8.2-3aa Houston 1 Hz rock hazard: sensitivity to smoothing options .....	8-125
Figure 8.2-3bb Houston 10 Hz rock hazard: sensitivity to eight realizations for source GHEX, Case A .....	8-126
Figure 8.2-3cc Houston 10 Hz rock hazard: sensitivity to eight realizations for source GHEX, Case B .....	8-127
Figure 8.2-3dd Houston 10 Hz rock hazard: sensitivity to eight realizations for source GHEX, Case E .....	8-128
Figure 8.2-3ee Houston 1 Hz rock hazard: sensitivity to eight realizations for source GHEX, Case A .....	8-129
Figure 8.2-3ff Houston 1 Hz rock hazard: sensitivity to eight realizations for source GHEX, Case B .....	8-130
Figure 8.2-3gg Houston 1 Hz rock hazard: sensitivity to eight realizations for source GHEX, Case E .....	8-131
Figure 8.2-4a Jackson 10 Hz rock hazard: mean and fractile total hazard.....	8-132
Figure 8.2-4b Jackson 1 Hz rock hazard: mean and fractile total hazard.....	8-133
Figure 8.2-4c Jackson PGA rock hazard: mean and fractile total hazard.....	8-134
Figure 8.2-4d Jackson 10 Hz rock hazard: total and contribution by RLME and background .....	8-135
Figure 8.2-4e Jackson 1 Hz rock hazard: total and contribution by RLME and background .....	8-136
Figure 8.2-4f Jackson PGA rock hazard: total and contribution by RLME and background ..	8-137
Figure 8.2-4g Jackson 10 Hz rock hazard: contribution by background source .....	8-138
Figure 8.2-4h Jackson 1 Hz rock hazard: contribution by background source .....	8-139
Figure 8.2-4i Jackson PGA rock hazard: contribution by background source .....	8-140
Figure 8.2-4j Jackson 10 Hz rock hazard: comparison of three source models .....	8-141
Figure 8.2-4k Jackson is 1 Hz rock hazard: comparison of three source models.....	8-142
Figure 8.2-4l Jackson PGA rock hazard: comparison of three source models .....	8-143
Figure 8.2-4m Jackson 10 Hz shallow soil hazard: total and contribution by RLME and background .....	8-144
Figure 8.2-4n Jackson 1 Hz shallow soil hazard: total and contribution by RLME and background .....	8-145

Figure 8.2-4o Jackson PGA shallow soil hazard: total and contribution by RLME and background .....	8-146
Figure 8.2-4p Jackson 10 Hz deep soil hazard: total and contribution by RLME and background .....	8-147
Figure 8.2-4q Jackson 1 Hz deep soil hazard: total and contribution by RLME and background .....	8-148
Figure 8.2-4r Jackson PGA deep soil hazard: total and contribution by RLME and background .....	8-149
Figure 8.2-4s Jackson 10 Hz hazard: comparison of three site conditions .....	8-150
Figure 8.2-4t Jackson 1 Hz hazard: comparison of three site conditions .....	8-151
Figure 8.2-4u Jackson PGA hazard: comparison of three site conditions .....	8-152
Figure 8.2-4v Jackson 10 Hz rock hazard: sensitivity to seismotectonic vs. Mmax zones ....	8-153
Figure 8.2-4w Jackson 1 Hz rock hazard: sensitivity to seismotectonic vs. Mmax zones ....	8-154
Figure 8.2-4x Jackson 10 Hz rock hazard: sensitivity to Mmax for source ECC-GC .....	8-155
Figure 8.2-4y Jackson 1 Hz rock hazard: sensitivity to Mmax for source ECC-GC .....	8-156
Figure 8.2-4z Jackson 10 Hz rock hazard: sensitivity to smoothing options .....	8-157
Figure 8.2-4aa Jackson 1 Hz rock hazard: sensitivity to smoothing options .....	8-158
Figure 8.2-4bb Jackson 10 Hz rock hazard: sensitivity to eight realizations for source ECC-GC, Case A .....	8-159
Figure 8.2-4cc Jackson 10 Hz rock hazard: sensitivity to eight realizations for source ECC-GC, Case B .....	8-160
Figure 8.2-4dd Jackson 10 Hz rock hazard: sensitivity to eight realizations for source ECC-GC, Case E .....	8-161
Figure 8.2-4ee Jackson 1 Hz rock hazard: sensitivity to eight realizations for source ECC-GC, Case A .....	8-162
Figure 8.2-4ff Jackson 1 Hz rock hazard: sensitivity to eight realizations for source ECC-GC, Case B .....	8-163
Figure 8.2-4gg Jackson 1 Hz rock hazard: sensitivity to eight realizations for source ECC-GC, Case E .....	8-164
Figure 8.2-5a Manchester 10 Hz rock hazard: mean and fractile total hazard .....	8-165
Figure 8.2-5b Manchester 1 Hz rock hazard: mean and fractile total hazard .....	8-166
Figure 8.2-5c Manchester PGA rock hazard: mean and fractile total hazard .....	8-167
Figure 8.2-5d Manchester 10 Hz rock hazard: total and contribution by RLME and background .....	8-168
Figure 8.2-5e Manchester 1 Hz rock hazard: total and contribution by RLME and background .....	8-169
Figure 8.2-5f Manchester PGA rock hazard: total and contribution by RLME and background .....	8-170
Figure 8.2-5g Manchester 10 Hz rock hazard: contribution by background source.....	8-171
Figure 8.2-5h Manchester 1 Hz rock hazard: contribution by background source.....	8-172
Figure 8.2-5i Manchester PGA rock hazard: contribution by background source.....	8-173
Figure 8.2-5j Manchester 10 Hz rock hazard: comparison of three source models.....	8-174

---

Figure 8.2-5k Manchester 1 Hz rock hazard: comparison of three source models .....	8-175
Figure 8.2-5l Manchester PGA rock hazard: comparison of three source models .....	8-176
Figure 8.2-5m Manchester 10 Hz shallow soil hazard: total and contribution by RLME and background.....	8-177
Figure 8.2-5n Manchester 1 Hz shallow soil hazard: total and contribution by RLME and background .....	8-178
Figure 8.2-5o Manchester PGA shallow soil hazard: total and contribution by RLME and background .....	8-179
Figure 8.2-5p Manchester 10 Hz deep soil hazard: total and contribution by RLME and background .....	8-180
Figure 8.2-5q Manchester 1 Hz deep soil hazard: total and contribution by RLME and background .....	8-181
Figure 8.2-5r Manchester PGA deep soil hazard: total and contribution by RLME and background .....	8-182
Figure 8.2-5s Manchester 10 Hz hazard: comparison of three site conditions .....	8-183
Figure 8.2-5t Manchester 1 Hz hazard: comparison of three site conditions.....	8-184
Figure 8.2-5u Manchester PGA hazard: comparison of three site conditions .....	8-185
Figure 8.2-5v Manchester 10 Hz rock hazard: sensitivity to seismotectonic vs. Mmax zones .....	8-186
Figure 8.2-5w Manchester 1 Hz rock hazard: sensitivity to seismotectonic vs. Mmax zones .....	8-187
Figure 8.2-5x Manchester 10 Hz rock hazard: sensitivity to Mmax for source NAP .....	8-188
Figure 8.2-5y Manchester 1 Hz rock hazard: sensitivity to Mmax for source NAP .....	8-189
Figure 8.2-5z Manchester 10 Hz rock hazard: sensitivity to smoothing options .....	8-190
Figure 8.2-5aa Manchester 1 Hz rock hazard: sensitivity to smoothing options.....	8-191
Figure 8.2-5bb Manchester 10 Hz rock hazard: sensitivity to eight realizations for source NAP, Case A.....	8-192
Figure 8.2-5cc Manchester 10 Hz rock hazard: sensitivity to eight realizations for source NAP, Case B.....	8-193
Figure 8.2-5dd Manchester 10 Hz rock hazard: sensitivity to eight realizations for source NAP, Case E.....	8-194
Figure 8.2-5ee Manchester 1 Hz rock hazard: sensitivity to eight realizations for source NAP, Case A.....	8-195
Figure 8.2-5ff Manchester 1 Hz rock hazard: sensitivity to eight realizations for source NAP, Case B.....	8-196
Figure 8.2-5gg Manchester 1 Hz rock hazard: sensitivity to eight realizations for source NAP, Case E.....	8-197
Figure 8.2-6a Savannah 10 Hz rock hazard: mean and fractile total hazard.....	8-198
Figure 8.2-6b Savannah 1 Hz rock hazard: mean and fractile total hazard.....	8-199
Figure 8.2-6c Savannah PGA rock hazard: mean and fractile total hazard.....	8-200
Figure 8.2-6d Savannah 10 Hz rock hazard: total and contribution by RLME and background .....	8-201

---

Figure 8.2-6e Savannah 1 Hz rock hazard: total and contribution by RLME and background .....	8-202
Figure 8.2-6f Savannah PGA rock hazard: total and contribution by RLME and background .....	8-203
Figure 8.2-6g Savannah 10 Hz rock hazard: contribution by background source .....	8-204
Figure 8.2-6h Savannah 1 Hz rock hazard: contribution by background source .....	8-205
Figure 8.2-6i Savannah PGA rock hazard: contribution by background source .....	8-206
Figure 8.2-6j Savannah 10 Hz rock hazard: comparison of three source models .....	8-207
Figure 8.2-6k Savannah is 1 Hz rock hazard: comparison of three source models.....	8-208
Figure 8.2-6l Savannah PGA rock hazard: comparison of three source models .....	8-209
Figure 8.2-6m Savannah 10 Hz shallow soil hazard: total and contribution by RLME and background .....	8-210
Figure 8.2-6n Savannah 1 Hz shallow soil hazard: total and contribution by RLME and background .....	8-211
Figure 8.2-6o Savannah PGA shallow soil hazard: total and contribution by RLME and background .....	8-212
Figure 8.2-6p Savannah 10 Hz deep soil hazard: total and contribution by RLME and background .....	8-213
Figure 8.2-6q Savannah 1 Hz deep soil hazard: total and contribution by RLME and background .....	8-214
Figure 8.2-6r Savannah PGA deep soil hazard: total and contribution by RLME and background .....	8-215
Figure 8.2-6s Savannah 10 Hz hazard: comparison of three site conditions .....	8-216
Figure 8.2-6t Savannah 1 Hz hazard: comparison of three site conditions .....	8-217
Figure 8.2-6u Savannah PGA hazard: comparison of three site conditions .....	8-218
Figure 8.2-6v Savannah 10 Hz rock hazard: sensitivity to seismotectonic vs. Mmax zones .....	8-219
Figure 8.2-6w Savannah 1 Hz rock hazard: sensitivity to seismotectonic vs. Mmax zones ..	8-220
Figure 8.2-6x Savannah 10 Hz rock hazard: sensitivity to Mmax for source ECC-AM.....	8-221
Figure 8.2-6y Savannah 1 Hz rock hazard: sensitivity to Mmax for source ECC-AM.....	8-222
Figure 8.2-6z Savannah 10 Hz rock hazard: sensitivity to smoothing options .....	8-223
Figure 8.2-6aa Savannah 1 Hz rock hazard: sensitivity to smoothing options .....	8-224
Figure 8.2-6bb Savannah 10 Hz rock hazard: sensitivity to eight realizations for source ECC-AM, Case A .....	8-225
Figure 8.2-6cc Savannah 10 Hz rock hazard: sensitivity to eight realizations for source ECC-AM, Case B .....	8-226
Figure 8.2-6dd Savannah 10 Hz rock hazard: sensitivity to eight realizations for source ECC-AM, Case E .....	8-227
Figure 8.2-6ee Savannah 1 Hz rock hazard: sensitivity to eight realizations for source ECC-AM, Case A .....	8-228
Figure 8.2-6ff Savannah 1 Hz rock hazard: sensitivity to eight realizations for source ECC-AM, Case B .....	8-229

---

Figure 8.2-6gg Savannah 1 Hz rock hazard: sensitivity to eight realizations for source ECC-AM, Case E .....	8-230
Figure 8.2-7a Topeka 10 Hz rock hazard: mean and fractile total hazard.....	8-231
Figure 8.2-7b Topeka 1 Hz rock hazard: mean and fractile total hazard.....	8-232
Figure 8.2-7c Topeka PGA rock hazard: mean and fractile total hazard.....	8-233
Figure 8.2-7d Topeka 10 Hz rock hazard: total and contribution by RLME and background .....	8-234
Figure 8.2-7e Topeka 1 Hz rock hazard: total and contribution by RLME and background...	8-235
Figure 8.2-7f Topeka PGA rock hazard: total and contribution by RLME and background ...	8-236
Figure 8.2-7g Topeka 10 Hz rock hazard: contribution by background source .....	8-237
Figure 8.2-7h Topeka 1 Hz rock hazard: contribution by background source .....	8-238
Figure 8.2-7i Topeka PGA rock hazard: contribution by background source .....	8-239
Figure 8.2-7j Topeka 10 Hz rock hazard: comparison of three source models .....	8-240
Figure 8.2-7k Topeka is 1 Hz rock hazard: comparison of three source models.....	8-241
Figure 8.2-7l Topeka PGA rock hazard: comparison of three source models .....	8-242
Figure 8.2-7m Topeka 10 Hz shallow soil hazard: total and contribution by RLME and background .....	8-243
Figure 8.2-7n Topeka 1 Hz shallow soil hazard: total and contribution by RLME and background .....	8-244
Figure 8.2-7o Topeka PGA shallow soil hazard: total and contribution by RLME and background .....	8-245
Figure 8.2-7p Topeka 10 Hz deep soil hazard: total and contribution by RLME and background .....	8-246
Figure 8.2-7q Topeka 1 Hz deep soil hazard: total and contribution by RLME and background .....	8-247
Figure 8.2-7r Topeka PGA deep soil hazard: total and contribution by RLME and background .....	8-248
Figure 8.2-7s Topeka 10 Hz hazard: comparison of three site conditions.....	8-249
Figure 8.2-7t Topeka 1 Hz hazard: comparison of three site conditions .....	8-250
Figure 8.2-7u Topeka PGA hazard: comparison of three site conditions .....	8-251
Figure 8.2-7v Topeka 10 Hz rock hazard: sensitivity to seismotectonic vs. Mmax zones ....	8-252
Figure 8.2-7w Topeka 1 Hz rock hazard: sensitivity to seismotectonic vs. Mmax zones.....	8-253
Figure 8.2-7x Topeka 10 Hz rock hazard: sensitivity to Mmax for source MidC-A .....	8-254
Figure 8.2-7y Topeka 1 Hz rock hazard: sensitivity to Mmax for source MidC-A .....	8-255
Figure 8.2-7z Topeka 10 Hz rock hazard: sensitivity to smoothing options.....	8-256
Figure 8.2-7aa Topeka 1 Hz rock hazard: sensitivity to smoothing options .....	8-257
Figure 8.2-7bb Topeka 10 Hz rock hazard: sensitivity to eight realizations for source MidC-A, Case A.....	8-258
Figure 8.2-7cc Topeka 10 Hz rock hazard: sensitivity to eight realizations for source MidC-A, Case B.....	8-259

---

Figure 8.2-7dd Topeka 10 Hz rock hazard: sensitivity to eight realizations for source MidC-A, Case E.....	8-260
Figure 8.2-7ee Topeka 1 Hz rock hazard: sensitivity to eight realizations for source MidC-A, Case A.....	8-261
Figure 8.2-7ff Topeka 1 Hz rock hazard: sensitivity to eight realizations for source MidC-A, Case B.....	8-262
Figure 8.2-7gg Topeka 1 Hz rock hazard: sensitivity to eight realizations for source MidC-A, Case E.....	8-263
Figure 9.3-1 1 Hz sensitivity to rupture orientation at Savannah for the Charleston regional source.....	9-24
Figure 9.3-2 10 Hz sensitivity to rupture orientation at Savannah for the Charleston regional source.....	9-25
Figure 9.3-3 1 Hz sensitivity to seismogenic thickness at Manchester for the Charlevoix area source.....	9-26
Figure 9.3-4 10 Hz sensitivity to seismogenic thickness at Manchester for the Charlevoix area source.....	9-27
Figure 9.3-5 1 Hz sensitivity to rupture orientation (dip) at Manchester for the Charlevoix area source.....	9-28
Figure 9.3-6 10 Hz sensitivity to rupture orientation (dip) at Manchester for the Charlevoix area source.....	9-29
Figure 9.3-7 1 Hz sensitivity to seismogenic thickness at Topeka for the Cheraw fault source.....	9-30
Figure 9.3-8 10 Hz sensitivity to seismogenic thickness at Topeka for the Cheraw fault source.....	9-31
Figure 9.3-9 1 Hz sensitivity to rupture orientation (dip) at Topeka for the Cheraw fault source.....	9-32
Figure 9.3-10 10 Hz sensitivity to rupture orientation at Topeka for the Cheraw fault source.....	9-33
Figure 9.3-11 1 Hz sensitivity to seismogenic thickness at Jackson for the Commerce area source.....	9-34
Figure 9.3-12 10 Hz sensitivity to seismogenic thickness at Jackson for the Commerce area source.....	9-35
Figure 9.3-13 1 Hz sensitivity to seismogenic thickness at Jackson for the ERM-N area source.....	9-36
Figure 9.3-14 10 Hz sensitivity to seismogenic thickness at Jackson for the ERM-N area source.....	9-37
Figure 9.3-15 1 Hz sensitivity to seismogenic thickness at Jackson for the ERM-S area source.....	9-38
Figure 9.3-16 10 Hz sensitivity to seismogenic thickness at Jackson for the ERM-S area source.....	9-39
Figure 9.3-17 1 Hz sensitivity to seismogenic thickness at Jackson for the Marianna area source.....	9-40
Figure 9.3-18 10 Hz sensitivity to seismogenic thickness at Jackson for the Marianna area source.....	9-41

---

Figure 9.3-19 1 Hz sensitivity to seismogenic thickness at Topeka for the Meers fault and OKA area sources .....	9-42
Figure 9.3-20 1 Hz sensitivity to seismogenic thickness at Houston for the Meers fault and OKA area sources .....	9-43
Figure 9.3-21 10 Hz sensitivity to seismogenic thickness at Topeka for the Meers fault and OKA area sources .....	9-44
Figure 9.3-22 10 Hz sensitivity to seismogenic thickness at Houston for the Meers fault and OKA area sources .....	9-45
Figure 9.3-23 1 Hz sensitivity to rupture orientation at Houston for the OKA area source .....	9-46
Figure 9.3-24 10 Hz sensitivity to rupture orientation at Houston for the OKA area source .....	9-47
Figure 9.3-25 1 Hz sensitivity to rupture orientation (dip) at Topeka for the OKA area source .....	9-48
Figure 9.3-26 1 Hz sensitivity to rupture orientation (dip) at Houston for the OKA area source .....	9-49
Figure 9.3-27 10 Hz sensitivity to rupture orientation (dip) at Topeka for the OKA area source .....	9-50
Figure 9.3-28 10 Hz sensitivity to rupture orientation (dip) at Houston for the OKA area source .....	9-51
Figure 9.3-29 1 Hz sensitivity to rupture orientation (dip) at Topeka for the Meers fault source .....	9-52
Figure 9.3-30 1 Hz sensitivity to rupture orientation (dip) at Houston for the Meers fault source .....	9-53
Figure 9.3-31 10 Hz sensitivity to rupture orientation (dip) at Topeka for the Meers fault source .....	9-54
Figure 9.3-32 10 Hz sensitivity to rupture orientation (dip) at Houston for the Meers fault source .....	9-55
Figure 9.3-33 1 Hz sensitivity to seismogenic thickness at Jackson for the NMFS fault sources .....	9-56
Figure 9.3-34 10 Hz sensitivity to seismogenic thickness at Jackson for the NMFS fault sources .....	9-57
Figure 9.3-35 1 Hz sensitivity to seismogenic thickness at Central Illinois for the Wabash Valley area source.....	9-58
Figure 9.3-36 10 Hz sensitivity to seismogenic thickness at Central Illinois for the Wabash Valley area source.....	9-59
Figure 9.3-37 1 Hz sensitivity to rupture orientation (dip) at Central Illinois for the Wabash Valley area source.....	9-60
Figure 9.3-38 10 Hz sensitivity to rupture orientation (dip) at Central Illinois for the Wabash Valley area source.....	9-61
Figure 9.3-39 1 Hz sensitivity to fault ruptures vs. point source for the Central Illinois site from the Mid C–A background source .....	9-62
Figure 9.3-40 10 Hz sensitivity to fault ruptures vs. point source for the Central Illinois site from the Mid C–A background source .....	9-63
Figure 9.4-1 $COV_{MH}$ from EPRI (1989) team sources vs. ground motion amplitude for seven test sites: PGA (top), 10 Hz SA (middle), and 1 Hz SA (bottom) .....	9-64

Figure 9.4-2 $COV_{MH}$ from EPRI (1989) team sources vs. seismic hazard (i.e., annual frequency of exceedance) for seven test sites: PGA (top), 10 Hz SA (middle), and 1 9-Hz SA (bottom).....	9-65
Figure 9.4-3 $COV_{MH}$ from seismic source experts (PEGASOS project) vs. amplitude (top) and annual frequency (bottom).....	9-66
Figure 9.4-4 $COV_K$ and $COV_{MH}$ from Charleston alternatives for PGA, plotted vs. PGA amplitude (top) and hazard (bottom). $COV_{MH}$ is the total COV of mean hazard; see Table 9.4-2 for other labels for curves. ....	9-67
Figure 9.4-5 $COV_K$ and $COV_{MH}$ from Charleston alternatives for 10 Hz, plotted vs. 10 Hz amplitude (top) and hazard (bottom). $COV_{MH}$ is the total COV of mean hazard; see Table 9.4-2 for other labels for curves. ....	9-68
Figure 9.4-6 $COV_K$ and $COV_{MH}$ from Charleston alternatives for 1 Hz, plotted vs. 1 Hz amplitude (top) and hazard (bottom). $COV_{MH}$ is the total COV of mean hazard; see Table 9.4-2 for other labels for curves. ....	9-69
Figure 9.4-7 $COV_K$ and $COV_{MH}$ of total hazard from New Madrid for 1 Hz, plotted vs. 1 Hz amplitude (top) and hazard (bottom). $COV_{MH}$ is the total COV; see the text for other labels for curves. ....	9-70
Figure 9.4-8 PGA hazard curves for Manchester test site .....	9-71
Figure 9.4-9 $COV_{MH}$ of PGA hazard at Manchester site from ground motion equation vs. PGA.....	9-72
Figure 9.4-10 COV of PGA hazard at Manchester site from ground motion equation vs. hazard .....	9-73
Figure 9.4-11 COV of 10 Hz hazard at Manchester site from ground motion equations vs. hazard.....	9-74
Figure 9.4-12 COV of 1 Hz hazard at Manchester site from ground motion equations vs. hazard .....	9-75
Figure 9.4-13 1 Hz spectral acceleration hazard curves for Manchester test site .....	9-76
Figure 9.4-14 $COV_{MH}$ of PGA hazard at Chattanooga from ground motion equation vs. hazard .....	9-77
Figure 9.4-15 $COV_{MH}$ of 10 Hz hazard at Chattanooga from ground motion equation vs. hazard .....	9-78
Figure 9.4-16 $COV_{MH}$ of 1 Hz hazard at Chattanooga site from ground motion equation vs. hazard.....	9-79
Figure 9.4-17 PGA hazard curves for Savannah test site.....	9-80
Figure 9.4-18 $COV_{MH}$ of PGA hazard at Savannah site from ground motion equations vs. hazard.....	9-81
Figure 9.4-19 $COV_{MH}$ of 10 Hz hazard at Savannah site from ground motion equations vs. hazard.....	9-82
Figure 9.4-20 $COV_{MH}$ of 1 Hz hazard at Savannah site from ground motion equations vs. hazard.....	9-83
Figure 9.4-21 PGA hazard curves for Columbia site .....	9-84
Figure 9.4-22 $COV_{MH}$ of PGA hazard at Columbia from ground motion equations vs. hazard .....	9-85

Figure 9.4-23 COVMH of 10 Hz hazard at Columbia from ground motion equations vs. hazard .....	9-86
Figure 9.4-24 COVMH of 1 Hz hazard at Columbia from ground motion equations vs. hazard .....	9-87
Figure 9.4-25 COVMH of PGA hazard at Chattanooga (New Madrid only) vs. hazard .....	9-88
Figure 9.4-26 COVMH of 10 Hz hazard at Chattanooga (New Madrid only) vs. hazard.....	9-89
Figure 9.4-27 COVMH of 1 Hz hazard at Chattanooga (New Madrid only) vs. hazard.....	9-90
Figure 9.4-28 COVMH for PGA and 1 Hz SA vs. ground motion amplitude resulting from alternative ground motion experts, PEGASOS project.....	9-91
Figure 9.4-29 COVMH for PGA and 1 Hz SA vs. mean hazard from alternative ground motion experts, PEGASOS project.....	9-92
Figure 9.4-30 COVHAZ from ground motion equations vs. mean hazard for Chattanooga.....	9-93
Figure 9.4-31 COVMH from ground motion equations vs. mean hazard for Central Illinois ....	9-94
Figure 9.4-32 COVMH from soil experts vs. PGA and 1 Hz SA, PEGASOS project .....	9-95
Figure 9.4-33 COVMH from soil experts vs. mean hazard for PGA and 1 Hz SA, PEGASOS project.....	9-96
Figure 9.4-34 COVMH resulting from site response models vs. mean hazard for four sites, 1 Hz (top) and 10 Hz (bottom).....	9-97
Figure 11-1 Geologic time scale (Walker and Geissman, 2009).....	11-10
Figure A-1 GEBCO elevation data for the CEUS study area (BODC, 2009). .....	A-22
Figure A-2 CEUS SSC independent earthquake catalog.....	A-24
Figure A-3 Bedrock geology and extended crust after Kanter (1994).....	A-26
Figure A-4 Crustal provinces after Rohs and Van Schmus (2007) .....	A-28
Figure A-5 Geologic map of North America.....	A-31
Figure A-6 Locations of geologic cross sections in the CEUS .....	A-33
Figure A-7 Precambrian crustal boundary after Van Schmus et al. (1996).....	A-35
Figure A-8a Precambrian geology and features after Reed (1993).....	A-37
Figure A-8b Explanation of Precambrian geology and features after Reed (1993) .....	A-38
Figure A-9 Precambrian provinces after Van Schmus et al. (2007) .....	A-40
Figure A-10 Precambrian units after Whitmeyer and Karlstrom (2007).....	A-42
Figure A-11 Surficial materials in the conterminous United States after Soller et al. (2009).....	A-44
Figure A-12 Basement and sediment thickness in the USGS Crustal Database for North America. Symbol size represents overlying sediment thickness (km); symbol color represents basement thickness (km). .....	A-46
Figure A-13 Top of basement P-wave seismic velocity in the USGS Crustal Database for North America .....	A-47
Figure A-14 Sediment thickness for North America and neighboring regions .....	A-49
Figure A-15 Physiographic divisions of the conterminous United States after Fenneman and Johnson (1946) .....	A-51
Figure A-16 CEUS SSC free-air gravity anomaly grid. Shaded relief with 315-degree azimuth and 30-degree inclination applied.....	A-54

---

Figure A-17 CEUS SSC free-air gravity anomaly grid. Shaded relief with 180-degree azimuth and 30-degree inclination applied.....	A-55
Figure A-18 CEUS SSC complete Bouguer gravity anomaly grid with free-air gravity anomaly in marine areas. Shaded relief with 315-degree azimuth and 30-degree inclination applied.....	A-56
Figure A-19 CEUS SSC complete Bouguer gravity anomaly grid with free-air gravity anomaly in marine areas. Shaded relief with 180-degree azimuth and 30-degree inclination applied.....	A-57
Figure A-20 CEUS SSC residual isostatic gravity anomaly grid. Shaded relief with 315-degree azimuth and 30-degree inclination applied.....	A-58
Figure A-21 CEUS SSC residual isostatic gravity anomaly grid Shaded relief with 180-degree azimuth and 30-degree inclination applied.....	A-59
Figure A-22 CEUS SSC regional isostatic gravity anomaly grid .....	A-60
Figure A-23 CEUS SSC first vertical derivative of residual isostatic gravity anomaly grid.....	A-61
Figure A-24 CEUS SSC first vertical derivative of Bouguer gravity anomaly grid with free-air anomaly in marine areas .....	A-62
Figure A-25 CEUS SSC complete Bouguer (with marine free-air) gravity anomaly grid low pass filtered at 240 km .....	A-63
Figure A-26 CEUS SSC complete Bouguer (with marine free-air) gravity anomaly grid high pass filtered at 240 km. Shaded relief with 315-degree azimuth and 30-degree inclination applied.....	A-64
Figure A-27 CEUS SSC complete Bouguer (with marine free-air) gravity anomaly grid high pass filtered at 240 km. Shaded relief with 180-degree azimuth and 30-degree inclination applied.....	A-65
Figure A-28 CEUS SSC complete Bouguer (with marine free-air) gravity anomaly grid high pass filtered at 120 km. Shaded relief with 315-degree azimuth and 30-degree inclination applied.....	A-66
Figure A-29 CEUS SSC complete Bouguer (with marine free-air) gravity anomaly grid high pass filtered at 120 km. Shaded relief with 180-degree azimuth and 30-degree inclination applied.....	A-67
Figure A-30 CEUS SSC complete Bouguer (with marine free-air) gravity anomaly grid upward continued to 40 km .....	A-68
Figure A-31 CEUS SSC complete Bouguer (with marine free-air) gravity anomaly grid minus the complete Bouguer (with marine free-air) gravity anomaly upward continued to 40 km. Shaded relief with 315-degree azimuth and 30-degree inclination applied.....	A-69
Figure A-32 CEUS SSC complete Bouguer (with marine free-air) gravity anomaly grid minus the complete Bouguer (with marine free-air) gravity anomaly upward continued to 40 km. Shaded relief with 180-degree azimuth and 30-degree inclination applied.....	A-70
Figure A-33 CEUS SSC complete Bouguer (with marine free-air) gravity anomaly grid upward continued to 100 km.....	A-71
Figure A-34 CEUS SSC complete Bouguer (with marine free-air) gravity anomaly grid minus the complete Bouguer (with marine free-air) gravity anomaly anomaly	

---

upward continued to 100 km. Shaded relief with 315-degree azimuth and 30-degree inclination applied.....	A-72
Figure A-35 CEUS SSC complete Bouguer (with marine free-air) gravity anomaly grid minus the complete Bouguer (with marine free-air) gravity anomaly upward continued to 100 km. Shaded relief with 180-degree azimuth and 30-degree inclination applied.....	A-73
Figure A-36 CEUS SSC horizontal derivative of residual isostatic gravity anomaly grid .....	A-74
Figure A-37 CEUS SSC horizontal derivative of first vertical derivative of residual isostatic gravity anomaly grid.....	A-75
Figure A-38 Corrected heat flow values from the SMU Geothermal Laboratory Regional Heat Flow Database (2008).....	A-77
Figure A-39 CEUS SSC total intensity magnetic anomaly grid (Ravat et al., 2009). Shaded relief with 315-degree azimuth and 30-degree inclination applied.....	A-80
Figure A-40 CEUS SSC total intensity magnetic anomaly grid (Ravat et al., 2009). Shaded relief with 180-degree azimuth and 30-degree inclination applied.....	A-81
Figure A-41 CEUS SSC differentially reduced to pole magnetic anomaly grid (Ravat, 2009). Shaded relief with 315-degree azimuth and 30-degree inclination applied.....	A-82
Figure A-42 CEUS SSC differentially reduced to pole magnetic anomaly grid (Ravat, 2009). Shaded relief with 180-degree azimuth and 30-degree inclination applied.....	A-83
Figure A-43 CEUS SSC tilt derivative of differentially reduced to pole magnetic anomaly grid (degrees) (Ravat, 2009).....	A-84
Figure A-44 CEUS SSC horizontal derivative of tilt derivative of differentially reduced to pole magnetic anomaly grid (radians) (Ravat, 2009) .....	A-85
Figure A-45 CEUS SSC tilt derivative of differentially reduced to pole magnetic anomaly grid (Ravat, 2009).....	A-86
Figure A-46 CEUS SSC amplitude of analytic signal magnetic anomaly grid (Ravat, 2009).....	A-87
Figure A-47 CEUS SSC paleoliquefaction database .....	A-89
Figure A-48 CEUS SSC compilation of seismic reflection and seismic refraction lines.....	A-91
Figure A-49 USGS National Seismic Hazard Maps (Petersen et al., 2008).....	A-93
Figure A-50 USGS NSHM ground motion hazard at spectral acceleration of 1 hz with 2% probability of exceedance in 50 years (Petersen et al., 2008).....	A-94
Figure A-51 USGS NSHM ground motion hazard at spectral acceleration of 1 hz with 5% probability of exceedance in 50 years (Petersen et al., 2008).....	A-95
Figure A-52 USGS NSHM ground motion hazard at spectral acceleration of 1 hz with 10% probability of exceedance in 50 years (Petersen et al., 2008).....	A-96
Figure A-53 USGS NSHM ground motion hazard at spectral acceleration of 3 hz with 2% probability of exceedance in 50 years (Petersen et al., 2008).....	A-97
Figure A-54 USGS NSHM ground motion hazard at spectral acceleration of 3 hz with 5% probability of exceedance in 50 years (Petersen et al., 2008).....	A-98
Figure A-55 USGS NSHM ground motion hazard at spectral acceleration of 3 hz with 10% probability of exceedance in 50 years (Petersen et al., 2008).....	A-99
Figure A-56 USGS NSHM ground motion hazard at spectral acceleration of 5 hz with 2% probability of exceedance in 50 years (Petersen et al., 2008).....	A-100

---

Figure A-57 USGS NSHM ground motion hazard at spectral acceleration of 5 hz with 5% probability of exceedance in 50 years (Petersen et al., 2008).....	A-101
Figure A-58 USGS NSHM ground motion hazard at spectral acceleration of 5 hz with 10% probability of exceedance in 50 years (Petersen et al., 2008).....	A-102
Figure A-59 USGS NSHM peak ground acceleration with 2% probability of exceedance in 50 years (Petersen et al., 2008).....	A-103
Figure A-60 USGS NSHM peak ground acceleration with 5% probability of exceedance in 50 years (Petersen et al., 2008).....	A-104
Figure A-61 USGS NSHM peak ground acceleration with 10% probability of exceedance in 50 years (Petersen et al., 2008).....	A-105
Figure A-62 Deformation of the North American Plate interior using GPS station data (Calais et al., 2006) .....	A-107
Figure A-63 Stress measurement update for the CEUS (Hurd, 2010) .....	A-110
Figure A-64 CEUS SSC Project study area boundary .....	A-112
Figure A-65 USGS Quaternary fault and fold database (USGS, 2006).....	A-114
Figure A-66 Quaternary features compilation for the CEUS (Crone and Wheeler, 2000; Wheeler, 2005; USGS, 2010).....	A-116
Figure A-67 CEUS Mesozoic rift basins after Benson (1992) .....	A-118
Figure A-68 CEUS Mesozoic rift basins after Dennis et al. (2004).....	A-120
Figure A-69 CEUS Mesozoic rift basins after Schlische (1993) .....	A-122
Figure A-70 CEUS Mesozoic rift basins after Withjack et al. (1998) .....	A-124
Figure A-71 RLME zones for the CEUS .....	A-126
Figure A-72 Mesozoic and non-Mesozoic zones for the CEUS, wide interpretation .....	A-128
Figure A-73 Mesozoic and non-Mesozoic zones for the CEUS, narrow interpretation .....	A-129
Figure A-74 CEUS seismotectonic zones model A.....	A-130
Figure A-75 CEUS seismotectonic zones model B.....	A-131
Figure A-76 CEUS seismotectonic zones model C .....	A-132
Figure A-77 CEUS seismotectonic zones model D .....	A-133
Figure E-1 Map of CEUS showing locations of regional data sets included in the CEUS SSC Project paleoliquefaction database, including New Madrid seismic zone and surrounding region; Marianna, Arkansas, area; St. Louis region; Wabash Valley seismic zone and surrounding region; Arkansas-Louisiana-Mississippi region; Charleston seismic zone; Atlantic Coastal region and the Central Virginia seismic zone; Newburyport, Massachusetts, and surrounding region; and Charlevoix seismic zone and surrounding region. ....	E-68
Figure E-2 Diagram illustrating size parameters of liquefaction features, including sand blow thickness, width, and length; dike width; and sill thickness, as well as some of the diagnostic characteristics of these features. ....	E-69
Figure E-3 Diagram illustrating sampling strategy for dating of liquefaction features as well as age data, such as <sup>14</sup> C maximum and <sup>14</sup> C minimum, used to calculate preferred age estimates and related uncertainties of liquefaction features.....	E-70
Figure E-4 GIS map of New Madrid seismic zone and surrounding region showing portions of rivers searched for earthquake-induced liquefaction features by M.	

---

Tuttle, R. Van Arsdale, and J. Vaughn and collaborators (see explanation); information contributed for this report. Map projection is USA Contiguous Albers Equal Area Conic, North America Datum 1983.....	E-71
Figure E-5 GIS map of New Madrid seismic zone and surrounding region showing locations of liquefaction features for which there are and are not radiocarbon data. Map projection is USA Contiguous Albers Equal Area Conic, North America Datum 1983. ....	E-72
Figure E-6 GIS map of New Madrid seismic zone and surrounding region showing locations of liquefaction features that are thought to be historical or prehistoric in age or whose ages are poorly constrained. Map projection is USA Contiguous Albers Equal Area Conic, North America Datum 1983.....	E-73
Figure E-7 GIS map of New Madrid seismic zone and surrounding region showing preferred age estimates of liquefaction features; features whose ages are poorly constrained are excluded. Map projection is USA Contiguous Albers Equal Area Conic, North America Datum 1983. ....	E-74
Figure E-8 GIS map of New Madrid seismic zone and surrounding region showing measured thicknesses of sand blows. Map projection is USA Contiguous Albers Equal Area Conic, North America Datum 1983.....	E-75
Figure E-9 GIS map of New Madrid seismic zone and surrounding region showing preferred age estimates and measured thicknesses of sand blows. Map projection is USA Contiguous Albers Equal Area Conic, North America Datum 1983. ....	E-76
Figure E-10 GIS map of New Madrid seismic zone and surrounding region showing measured widths of sand dikes. Map projection is USA Contiguous Albers Equal Area Conic, North America Datum 1983.....	E-77
Figure E-11 GIS map of New Madrid seismic zone and surrounding region showing preferred age estimates and measured widths of sand dikes. Map projection is USA Contiguous Albers Equal Area Conic, North America Datum 1983. ....	E-78
Figure E-12 GIS map of New Madrid seismic zone and surrounding region illustrating preferred age estimates and measured thicknesses of sand blows as well as preferred age estimates and measured widths of sand dikes for sites where sand blows do not occur. Map projection is USA Contiguous Albers Equal Area Conic, North America Datum 1983. ....	E-79
Figure E-13 GIS map of Marianna, Arkansas, area showing seismicity and locations of paleoliquefaction features relative to mapped traces of Eastern Reelfoot rift margin fault, White River fault zone, Big Creek fault zone, Marianna escarpment, and Daytona Beach lineament. Map projection is USA Contiguous Albers Equal Area Conic, North America Datum 1983. ....	E-80
Figure E-14 (A) Trench log and (B) ground-penetrating radar profile, showing vertical sections of sand blows and sand dikes at Daytona Beach SE2 site along the Daytona Beach lineament southwest of Marianna, Arkansas. Vertical scale of GPR profile is exaggerated (modified from Al-Shukri et al., 2009).....	E-81
Figure E-15 GIS map of Marianna, Arkansas, area showing locations of liquefaction features for which there are and are not radiocarbon data. Map projection is USA Contiguous Albers Equal Area Conic, North America Datum 1983. ....	E-82
Figure E-16 GIS map of Marianna, Arkansas, area showing locations of liquefaction features that are thought to be historical or prehistoric in age or whose ages are poorly constrained. To date, no liquefaction features thought to have formed during	

---

1811-1812 earthquakes have been found in area. Map projection is USA Contiguous Albers Equal Area Conic, North America Datum 1983.....	E-83
Figure E-17 GIS map of Marianna, Arkansas, area showing preferred age estimates of liquefaction features; features whose ages are poorly constrained are excluded. Map projection is USA Contiguous Albers Equal Area Conic, North America Datum 1983.....	E-84
Figure E-18 GIS map of Marianna, Arkansas, area showing measured thicknesses of sand blows. Map projection is USA Contiguous Albers Equal Area Conic, North America Datum 1983.....	E-85
Figure E-19 GIS map of Marianna, Arkansas, area showing preferred age estimates and measured thicknesses of sand blows. Map projection is USA Contiguous Albers Equal Area Conic, North America Datum 1983.....	E-86
Figure E-20 GIS map of Marianna, Arkansas, area showing measured widths of sand dikes. Map projection is USA Contiguous Albers Equal Area Conic, North America Datum 1983.....	E-87
Figure E-21 GIS map of Marianna, Arkansas, area showing preferred age estimates and measured widths of sand dikes. Map projection is USA Contiguous Albers Equal Area Conic, North America Datum 1983.....	E-88
Figure E-22 GIS map of St. Louis, Missouri, region showing seismicity and portions of rivers searched for earthquake-induced liquefaction features by Tuttle and collaborators; information contributed for this report. Map projection is USA Contiguous Albers Equal Area Conic, North America Datum 1983.....	E-89
Figure E-23 GIS map of St. Louis, Missouri, region showing locations of liquefaction features, including several soft-sediment deformation structures, for which there are and are not radiocarbon data. Map projection is USA Contiguous Albers Equal Area Conic, North America Datum 1983.....	E-90
Figure E-24 GIS map of St. Louis, Missouri, region showing locations of liquefaction features that are thought to be historical or prehistoric in age or whose ages are poorly constrained. Map projection is USA Contiguous Albers Equal Area Conic, North America Datum 1983.....	E-91
Figure E-25 GIS map of St. Louis, Missouri, region showing preferred age estimates of liquefaction features; features whose ages are poorly constrained, including several that are prehistoric in age, are not shown. Map projection is USA Contiguous Albers Equal Area Conic, North America Datum 1983.....	E-92
Figure E-26 GIS map of St. Louis, Missouri, region showing measured thicknesses of sand blows at similar scale as used in Figure E-8 of sand blows in New Madrid seismic zone. Note that few sand blows have been found in St. Louis region. Map projection is USA Contiguous Albers Equal Area Conic, North America Datum 1983.....	E-93
Figure E-27 GIS map of St. Louis, Missouri, region showing preferred age estimates and measured thicknesses of sand blows. Map projection is USA Contiguous Albers Equal Area Conic, North America Datum 1983.....	E-94
Figure E-28 GIS map of St. Louis, Missouri, region showing measured widths of sand dikes at similar scale as that used in Figure E-10 for sand dikes in New Madrid seismic zone. Map projection is USA Contiguous Albers Equal Area Conic, North America Datum 1983.....	E-95

---

Figure E-29 GIS map of St. Louis, Missouri, region showing measured widths of sand dikes at similar scale as that used in Figures E-42 and E-48 for sand dikes in the Newburyport and Charlevoix regions, respectively. Map projection is USA Contiguous Albers Equal Area Conic, North America Datum 1983.....	E-96
Figure E-30 GIS map of St. Louis, Missouri, region showing preferred age estimates and measured widths of sand dikes. Map projection is USA Contiguous Albers Equal Area Conic, North America Datum 1983.....	E-97
Figure E-31 GIS map of Wabash Valley seismic zone and surrounding region showing portions of rivers searched for earthquake-induced liquefaction features (digitized from McNulty and Obermeier, 1999). Map projection is USA Contiguous Albers Equal Area Conic, North America Datum 1983.....	E-98
Figure E-32 GIS map of Wabash Valley seismic zone and surrounding region showing measured widths of sand dikes at similar scale as that used in Figures E-10 and E-11 for sand dikes in New Madrid seismic zone. Map projection is USA Contiguous Albers Equal Area Conic, North America Datum 1983.....	E-99
Figure E-33 GIS map of Wabash Valley region of Indiana and Illinois showing preferred age estimates and paleoearthquake interpretation. Map projection is USA Contiguous Albers Equal Area Conic, North America Datum 1983.....	E-100
Figure E-34 GIS map of Arkansas-Louisiana-Mississippi (ALM) region showing paleoliquefaction study locations. Map projection is USA Contiguous Albers Equal Area Conic, North America Datum 1983.....	E-101
Figure E-35 GIS map of Charleston, South Carolina, region showing locations of paleoliquefaction features for which there are and are not radiocarbon dates. Map projection is USA Contiguous Albers Equal Area Conic, North America Datum 1983.....	E-102
Figure E-36 GIS map of Charleston, South Carolina, region showing locations of historical and prehistoric liquefaction features. Map projection is USA Contiguous Albers Equal Area Conic, North America Datum 1983.....	E-103
Figure E-37 Map of Atlantic coast region showing areas searched for paleoliquefaction features by Gelinias et al. (1998) and Amick, Gelinias, et al. (1990a). Rectangles indicate 7.5-minute quadrangles in which sites were investigated for presence of paleoliquefaction features. The number of sites investigated is shown within that quadrangle, if known. Orange and yellow indicate quadrangles in which paleoliquefaction features were recognized.....	E-104
Figure E-38 Map of Central Virginia seismic zone region showing portions of rivers searched for earthquake-induced liquefaction features by Obermeier and McNulty (1998).....	E-105
Figure E-39 GIS map of Newburyport, Massachusetts, and surrounding region showing seismicity and portions of rivers searched for earthquake-induced liquefaction features (Gelinias et al., 1998; Tuttle, 2007, 2009). Solid black line crossing map represents Massachusetts–New Hampshire border. Map projection is USA Contiguous Albers Equal Area Conic, North America Datum 1983.....	E-106
Figure E-40 GIS map of Newburyport, Massachusetts, and surrounding region showing locations of liquefaction features for which there are and are not radiocarbon dates. Map projection is USA Contiguous Albers Equal Area Conic, North America Datum 1983.....	E-107

---

Figure E-41 GIS map of Newburyport, Massachusetts, and surrounding region showing locations of liquefaction features that are thought to be historical or prehistoric in age or whose ages are poorly constrained. Map projection is USA Contiguous Albers Equal Area Conic, North America Datum 1983.....	E-108
Figure E-42 GIS map of Newburyport, Massachusetts, and surrounding region showing measured widths of sand dikes. Map projection is USA Contiguous Albers Equal Area Conic, North America Datum 1983.....	E-109
Figure E-43 GIS map of Newburyport, Massachusetts, and surrounding region showing preferred age estimates and measured widths of sand dikes. Map projection is USA Contiguous Albers Equal Area Conic, North America Datum 1983.....	E-110
Figure E-44 Map of Charlevoix seismic zone and adjacent St. Lawrence Lowlands showing mapped faults and portions of rivers along which reconnaissance and searches for earthquake-induced liquefaction features were performed. Charlevoix seismic zone is defined by concentration of earthquakes and locations of historical earthquakes northeast of Quebec City. Devonian impact structure in vicinity of Charlevoix seismic zone is outlined by black dashed line. Taconic thrust faults are indicated by solid black lines with sawteeth on upper plate; Iapetan rift faults are shown by solid black lines with hachure marks on downthrown side (modified from Tuttle and Atkinson, 2010).....	E-111
Figure E-45 GIS map of Charlevoix seismic zone and surrounding region showing locations of liquefaction features, including several soft-sediment deformation structures, for which there are and are not radiocarbon data. Note the location of 1988 M 5.9 Saguenay earthquake northwest of the Charlevoix seismic zone. Map projection is USA Contiguous Albers Equal Area Conic, North America Datum 1983.....	E-112
Figure E-46 GIS map of Charlevoix seismic zone and surrounding region showing locations of liquefaction features that are modern, historical, or prehistoric in age, or whose ages are poorly constrained. Map projection is USA Contiguous Albers Equal Area Conic, North America Datum 1983.....	E-113
Figure E-47 GIS map of Charlevoix seismic zone and surrounding region showing preferred age estimates of liquefaction features; features whose ages are poorly constrained are excluded. Map projection is USA Contiguous Albers Equal Area Conic, North America Datum 1983.....	E-114
Figure E-48 GIS map of Charlevoix seismic zone and surrounding region showing measured widths of sand dikes. Map projection is USA Contiguous Albers Equal Area Conic, North America Datum 1983.....	E-115
Figure E-49 GIS map of Charlevoix seismic zone and surrounding region showing preferred age estimates and measured widths of sand dikes. Map projection is USA Contiguous Albers Equal Area Conic, North America Datum 1983.....	E-116
Figure E-50 Photograph of moderate-sized sand blow (12 m long, 7 m wide, and 14 cm thick) that formed about 40 km from epicenter of 2001 M 7.7 Bhuj, India, earthquake (from Tuttle, Hengesh, et al., 2002), combined with schematic vertical section illustrating structural and stratigraphic relations of sand blow, sand dike, and source layer (modified from Sims and Garvin, 1995).....	E-117
Figure E-51 Tree trunks buried and killed by sand blows, vented during 1811-1812 New Madrid earthquakes (from Fuller, 1912).....	E-118

---

Figure E-52 Large sand-blow crater that formed during 2002 M 7.7 Bhuj, India, earthquake. Backpack for scale. Photograph: M. Tuttle (2001).....	E-119
Figure E-53 Sand-blow crater that formed during 1886 Charleston, South Carolina, earthquake. Photograph: J.K. Hillers (from USGS Photograph Library).....	E-120
Figure E-54 Photograph of sand blow and related sand dikes exposed in trench wall and floor in New Madrid seismic zone. Buried soil horizon is displaced downward approximately 1 m across two dikes. Clasts of soil horizon occur within dikes and overlying sand blow. Degree of soil development above and within sand blow suggests that it is at least several hundred years old and formed prior to 1811-1812 New Madrid earthquakes. Organic sample (location marked by red flag) from crater fill will provide close minimum age constraint for formation of sand blow. For scale, each colored intervals on shovel handle represents 10 cm. Photograph: M. Tuttle.....	E-121
Figure E-55 Sand dikes, ranging up to 35 cm wide, originate in pebbly sand layer and intrude overlying diamicton, These features were exposed in cutbank along Cahokia Creek about 25 km northeast of downtown St. Louis (from Tuttle, 2000). .....	E-122
Figure E-56 Photograph of small diapirs of medium sand intruding base of overlying deposit of interbedded clayey silt and very fine sand, and clasts of clayey silt in underlying medium sand, observed along Ouelle River in Charlevoix seismic zone. Sand diapirs and clasts probably formed during basal erosion and foundering of clayey silt due to liquefaction of the underlying sandy deposit. Red portion of shovel handle represents 10 cm (modified from Tuttle and Atkinson, 2010). .....	E-123
Figures E-57 (A) Load cast formed in laminated sediments of Van Norman Lake during 1952 Kern County, California, earthquake. Photograph: J. Sims (from Sims, 1975). (B) Load cast, pseudonodules, and related folds formed in laminated sediment exposed along Malbaie River in Charlevoix seismic zone. Sand dikes crosscutting these same laminated sediments occur at a nearby site. For scale, each painted interval of the shovel handle represents 10 cm (modified from Tuttle and Atkinson, 2010).....	E-124
Figure E-58 Log of sand blow and uppermost portions of related sand dikes exposed in trench wall at Dodd site in New Madrid seismic zone. Sand dikes were also observed in opposite wall and trench floor. Sand blow buries pre-event A horizon, and a subsequent A horizon has developed in top of sand blow. Radiocarbon dating of samples collected above and below sand blow brackets its age between 490 and 660 yr BP. Artifact assemblage indicates that sand blow formed during late Mississippian cultural period (300–550 yr BP or AD 1400–1670) (modified from Tuttle, Collier, et al., 1999). .....	E-125
Figures E-59 (A) Photograph of earthquake-induced liquefaction features found in association with cultural horizon and pit exposed in trench wall near Blytheville, Arkansas, in New Madrid seismic zone. Photograph: M. Tuttle. (B) Trench log of features shown in (A). Sand dike formed in thick Native American occupation horizon containing artifacts of early Mississippian cultural period (950–1,150 yr BP). Cultural pit dug into top of sand dike contains artifacts and charcoal used to constrain minimum age of liquefaction features (modified from Tuttle and Schweig, 1995).....	E-126
Figure E-60 In situ tree trunks such as this one buried and killed by sand blow in New Madrid seismic zone offer opportunity to date paleoearthquakes to the year and season of occurrence. Photograph: M. Tuttle. ....	E-127

---

Figure E-61 Portion of dendrocalibration curve illustrating conversion of radiocarbon age to calibrated date in calendar years. An example, 2-sigma radiocarbon age of 2,280–2,520 BP is converted to calibrated date of 770–380 BC (from Tuttle, 1999).....	E-128
Figure E-62 Empirical relation developed between A horizon thickness of sand blows and years of soil development in New Madrid region. Horizontal bars reflect uncertainties in age estimates of liquefaction features; diamonds mark midpoints of possible age ranges (from Tuttle et al., 2000).....	E-129
Figure E-63 Diagram illustrating earthquake chronology for New Madrid seismic zone for past 5,500 years based on dating and correlation of liquefaction features at sites (listed at top) across region from north to south. Vertical bars represent age estimates of individual sand blows, and horizontal bars represent event times of 138 yr BP (AD 1811-1812); 500 yr BP ± 150 yr; 1,050 yr BP ± 100 yr; and 4,300 yr BP ± 200 yr (modified from Tuttle, Schweig, et al., 2002; Tuttle et al., 2005). .....	E-130
Figure E-64 Diagram illustrating earthquake chronology for New Madrid seismic zone for past 2,000 years, similar to upper portion of diagram shown in Figure E-63. As in Figure E-63, vertical bars represent age estimates of individual sand blows, and horizontal bars represent event times. Analysis performed during CEUS SSC Project derived two possible uncertainty ranges for timing of paleoearthquakes, illustrated by the darker and lighter portions of the colored horizontal bars, respectively: 503 yr BP ± 8 yr or 465 yr BP ± 65 yr, and 1,110 yr BP ± 40 yr or 1055 ± 95 yr (modified from Tuttle, Schweig, et al., 2002).....	E-131
Figure E-65 Maps showing spatial distributions and sizes of sand blows and sand dikes attributed to 500 and 1,050 yr BP events. Locations and sizes of liquefaction features that formed during AD 1811-1812 (138 yr BP) New Madrid earthquake sequence shown for comparison (modified from Tuttle, Schweig, et al., 2002).....	E-132
Figure E-66 Liquefaction fields for 138 yr BP (AD 1811-1812); 500 yr BP (AD 1450); and 1,050 yr BP (AD 900) events as interpreted from spatial distribution and stratigraphy of sand blows (modified from Tuttle, Schweig, et al., 2002). Ellipses define areas where similar-age sand blows have been mapped. Overlapping ellipses indicate areas where sand blows are composed of multiple units that formed during sequence of earthquakes. Dashed ellipse outlines area where historical sand blows are composed of four depositional units. Magnitudes of earthquakes in 500 yr BP and 1,050 yr BP are inferred from comparison with 1811-1812 liquefaction fields. Magnitude estimates of December (D), January (J), and February (F) main shocks and large aftershocks taken from several sources; rupture scenario from Johnston and Schweig (1996; modified from Tuttle, Schweig, et al., 2002). .....	E-133
Figure E-67 Empirical relation between earthquake magnitude and epicentral distance to farthest known sand blows induced by instrumentally recorded earthquakes (modified from Castilla and Audemard, 2007).....	E-134
Figure E-68 Distances to farthest known liquefaction features indicate that 500 and 1,050 yr BP New Madrid events were at least of M 6.7 and 6.9, respectively, when plotted on Ambraseys (1988) relation between earthquake magnitude and epicentral distance to farthest surface expression of liquefaction. Similarity in size distribution of historical and prehistoric sand blows, however, suggests that paleoearthquakes were comparable in magnitude to 1811-1812 events or M ~7.6 (modified from Tuttle, 2001).....	E-135
Figure H-1-1 Region covered by the CEUS SSC model.....	H-44

---

Figure H-2-1 Master logic tree for the CEUS SSC model .....	H-45
Figure H-3-1 Logic tree for the Mmax zones branch of the master logic tree.....	H-46
Figure H-3-2 Mesozoic extended (MESE-W) and non-extended (NMESE-W) Mmax zones for the “wide” interpretation .....	H-47
Figure H-3-3 Mesozoic extended (MESE-N) and non-extended (NMESE-N) Mmax zones for the “narrow” interpretation .....	H-48
Figure H-4-1(a) Logic tree for the seismotectonic zones branch of the master logic tree.....	H-49
Figure H-4-1(b) Logic tree for the seismotectonic zones branch of the master logic tree.....	H-50
Figure H-4-2 Seismotectonic zones shown in the case where the Rough Creek Graben is not part of the Reelfoot Rift (RR) and the Paleozoic Extended zone is narrow (PEZ-N).....	H-51
Figure H-4-3 Seismotectonic zones shown in the case where the Rough Creek Graben is part of the Reelfoot Rift (RR-RCG) and the Paleozoic Extended zone is narrow (PEZ-N).....	H-52
Figure H-4-4 Seismotectonic zones shown in the case where the Rough Creek Graben is not part of the Reelfoot Rift (RR) and the Paleozoic Extended zone is wide (PEZ-W) .....	H-53
Figure H-4-5 Seismotectonic zones shown in the case where the Rough Creek Graben is part of the Reelfoot Rift (RR-RCG) and the Paleozoic Extended zone is wide (PEZ-W) .....	H-54
Figure H-5-1 Logic tree for the RLME source branch of the master logic tree .....	H-55
Figure H-5-2 Location of RLME sources in the CEUS SSC model .....	H-56
Figure H-5.1-1 Logic tree for Charlevoix RLME source .....	H-57
Figure H-5.1-2 Charlevoix RLME source geometry .....	H-58
Figure H-5.2-1(a) Logic tree for Charleston RLME source .....	H-59
Figure H-5.2-1(b) Logic tree for Charleston RLME source .....	H-60
Figure H-5.2-2 Charleston RLME alternative source geometries.....	H-61
Figure H-5.3-1 Logic tree for Cheraw RLME source.....	H-62
Figure H-5.3-2 Cheraw RLME source geometry.....	H-63
Figure H-5.4-1 Logic tree for Meers RLME source .....	H-64
Figure H-5.4-2 Meers RLME source geometries .....	H-65
Figure H-5.5-1 Logic tree for NMFS RLME source.....	H-66
Figure H-5.5-2 New Madrid South (NMS) fault alternative RMLE source geometries: Blytheville Arch-Bootheel Lineament (BA-BL) and Blytheville Arch-Blytheville fault zone (BA-BFZ) .....	H-67
Figure H-5.5-3 New Madrid North (NMN) fault alternative RMLE source geometries: New Madrid North (NMN_S) and New Madrid North plus extension (NMN_L).....	H-68
Figure H-5.5-4 Reelfoot Thrust (RFT) fault alternative RMLE source geometries: Reelfoot thrust (RFT_S) and Reelfoot thrust plus extensions (RFT_L) .....	H-69
Figure H-5.6-1 Logic tree for ERM-S RLME source .....	H-70
Figure H-5.6-2 Logic tree for ERM-N RLME source .....	H-71
Figure H-5.6-3 ERM-S RLME source geometries.....	H-72

---

Figure H-5.6-4 ERM-N RLME source geometry .....	H-73
Figure H-5.7-1 Logic tree for Marianna RLME source .....	H-74
Figure H-5.7-2 Marianna RLME source geometry .....	H-75
Figure H-5.8-1 Logic tree for Commerce Fault Zone RLME source .....	H-76
Figure H-5.8-2 Commerce RLME source geometry .....	H-77
Figure H-5.9-1 Logic tree for Wabash Valley RLME source .....	H-78
Figure H-5.9-2 Wabash Valley RLME source geometry .....	H-79
Figure J-1 Map of the rate and $b$ -value for the study region under the Mmax zonation, with no separation of Mesozoic extended and non-extended; Case A magnitude weights: Realization 1 .....	J-2
Figure J-2 Map of the rate and $b$ -value for the study region under the Mmax zonation, with no separation of Mesozoic extended and non-extended; Case A magnitude weights: Realization 2 .....	J-3
Figure J-3 Map of the rate and $b$ -value for the study region under the Mmax zonation, with no separation of Mesozoic extended and non-extended; Case A magnitude weights: Realization 3 .....	J-4
Figure J-4 Map of the rate and $b$ -value for the study region under the Mmax zonation, with no separation of Mesozoic extended and non-extended; Case A magnitude weights: Realization 4 .....	J-5
Figure J-5 Map of the rate and $b$ -value for the study region under the Mmax zonation, with no separation of Mesozoic extended and non-extended; Case A magnitude weights: Realization 5 .....	J-6
Figure J-6 Map of the rate and $b$ -value for the study region under the Mmax zonation, with no separation of Mesozoic extended and non-extended; Case A magnitude weights: Realization 6 .....	J-7
Figure J-7 Map of the rate and $b$ -value for the study region under the Mmax zonation, with no separation of Mesozoic extended and non-extended; Case A magnitude weights: Realization 7 .....	J-8
Figure J-8 Map of the rate and $b$ -value for the study region under the Mmax zonation, with no separation of Mesozoic extended and non-extended; Case A magnitude weights: Realization 8 .....	J-9
Figure J-9 Map of the coefficient of variation of the rate and the standard deviation of the $b$ -value for the study region under the Mmax zonation, with no separation of Mesozoic extended and non-extended; Case A magnitude weights .....	J-10
Figure J-10 Map of the rate and $b$ -value for the study region under the Mmax zonation, with no separation of Mesozoic extended and non-extended; Case B magnitude weights: Realization 1 .....	J-11
Figure J-11 Map of the rate and $b$ -value for the study region under the Mmax zonation, with no separation of Mesozoic extended and non-extended; Case B magnitude weights: Realization 2 .....	J-12
Figure J-12 Map of the rate and $b$ -value for the study region under the Mmax zonation, with no separation of Mesozoic extended and non-extended; Case B magnitude weights: Realization 3 .....	J-13

---

Figure J-13 Map of the rate and $b$ -value for the study region under the Mmax zonation, with no separation of Mesozoic extended and non-extended; Case B magnitude weights: Realization 4.....	J-14
Figure J-14 Map of the rate and $b$ -value for the study region under the Mmax zonation, with no separation of Mesozoic extended and non-extended; Case B magnitude weights: Realization 5.....	J-15
Figure J-15 Map of the rate and $b$ -value for the study region under the Mmax zonation, with no separation of Mesozoic extended and non-extended; Case B magnitude weights: Realization 6.....	J-16
Figure J-16 Map of the rate and $b$ -value for the study region under the Mmax zonation, with no separation of Mesozoic extended and non-extended; Case B magnitude weights: Realization 7.....	J-17
Figure J-17 Map of the rate and $b$ -value for the study region under the Mmax zonation, with no separation of Mesozoic extended and non-extended; Case B magnitude weights: Realization 8.....	J-18
Figure J-18 Map of the coefficient of variation of the rate and the standard deviation of the $b$ -value for the study region under the Mmax zonation, with no separation of Mesozoic extended and non-extended; Case B magnitude weights .....	J-19
Figure J-19 Map of the rate and $b$ -value for the study region under the Mmax zonation, with no separation of Mesozoic extended and non-extended; Case E magnitude weights: Realization 1.....	J-20
Figure J-20 Map of the rate and $b$ -value for the study region under the Mmax zonation, with no separation of Mesozoic extended and non-extended; Case E magnitude weights: Realization 2.....	J-21
Figure J-21 Map of the rate and $b$ -value for the study region under the Mmax zonation, with no separation of Mesozoic extended and non-extended; Case E magnitude weights: Realization 3.....	J-22
Figure J-22 Map of the rate and $b$ -value for the study region under the Mmax zonation, with no separation of Mesozoic extended and non-extended; Case E magnitude weights: Realization 4.....	J-23
Figure J-23 Map of the rate and $b$ -value for the study region under the Mmax zonation, with no separation of Mesozoic extended and non-extended; Case E magnitude weights: Realization 5.....	J-24
Figure J-24 Map of the rate and $b$ -value for the study region under the Mmax zonation, with no separation of Mesozoic extended and non-extended; Case E magnitude weights: Realization 6.....	J-25
Figure J-25 Map of the rate and $b$ -value for the study region under the Mmax zonation, with no separation of Mesozoic extended and non-extended; Case E magnitude weights: Realization 7.....	J-26
Figure J-26 Map of the rate and $b$ -value for the study region under the Mmax zonation, with no separation of Mesozoic extended and non-extended; Case E magnitude weights: Realization 8.....	J-27
Figure J-27 Map of the coefficient of variation of the rate and the standard deviation of the $b$ -value for the study region under the Mmax zonation, with no separation of Mesozoic extended and non-extended; Case E magnitude weights .....	J-28

---

Figure J-28 Map of the rate and $b$ -value for the study region under the Mmax zonation, with separation of Mesozoic extended and non-extended; Case A magnitude weights: Realization 1.....	J-29
Figure J-29 Map of the rate and $b$ -value for the study region under the Mmax zonation, with separation of Mesozoic extended and non-extended; Case A magnitude weights: Realization 2.....	J-30
Figure J-30 Map of the rate and $b$ -value for the study region under the Mmax zonation, with separation of Mesozoic extended and non-extended; Case A magnitude weights: Realization 3.....	J-31
Figure J-31 Map of the rate and $b$ -value for the study region under the Mmax zonation, with separation of Mesozoic extended and non-extended; Case A magnitude weights: Realization 4.....	J-32
Figure J-32 Map of the rate and $b$ -value for the study region under the Mmax zonation, with separation of Mesozoic extended and non-extended; Case A magnitude weights: Realization 5.....	J-33
Figure J-33 Map of the rate and $b$ -value for the study region under the Mmax zonation, with separation of Mesozoic extended and non-extended; Case A magnitude weights: Realization 6.....	J-34
Figure J-34 Map of the rate and $b$ -value for the study region under the Mmax zonation, with separation of Mesozoic extended and non-extended; Case A magnitude weights: Realization 7.....	J-35
Figure J-35 Map of the rate and $b$ -value for the study region under the Mmax zonation, with separation of Mesozoic extended and non-extended; Case A magnitude weights: Realization 8.....	J-36
Figure J-36 Map of the coefficient of variation of the rate and the standard deviation of the $b$ -value for the study region under the Mmax zonation, with separation of Mesozoic extended and non-extended; Case A magnitude weights .....	J-37
Figure J-37 Map of the rate and $b$ -value for the study region under the Mmax zonation, with separation of Mesozoic extended and non-extended; Case B magnitude weights: Realization 1.....	J-38
Figure J-38 Map of the rate and $b$ -value for the study region under the Mmax zonation, with separation of Mesozoic extended and non-extended; Case B magnitude weights: Realization 2.....	J-39
Figure J-39 Map of the rate and $b$ -value for the study region under the Mmax zonation, with separation of Mesozoic extended and non-extended; Case B magnitude weights: Realization 3.....	J-40
Figure J-40 Map of the rate and $b$ -value for the study region under the Mmax zonation, with separation of Mesozoic extended and non-extended; Case B magnitude weights: Realization 4.....	J-41
Figure J-41 Map of the rate and $b$ -value for the study region under the Mmax zonation, with separation of Mesozoic extended and non-extended; Case B magnitude weights: Realization 5.....	J-42
Figure J-42 Map of the rate and $b$ -value for the study region under the Mmax zonation, with separation of Mesozoic extended and non-extended; Case B magnitude weights: Realization 6.....	J-43

---

Figure J-43 Map of the rate and $b$ -value for the study region under the Mmax zonation, with separation of Mesozoic extended and non-extended; Case B magnitude weights: Realization 7.....	J-44
Figure J-44 Map of the rate and $b$ -value for the study region under the Mmax zonation, with separation of Mesozoic extended and non-extended; Case B magnitude weights: Realization 8.....	J-45
Figure J-45 Map of the coefficient of variation of the rate and the standard deviation of the $b$ -value for the study region under the Mmax zonation, with separation of Mesozoic extended and non-extended; Case B magnitude weights .....	J-46
Figure J-46 Map of the rate and $b$ -value for the study region under the Mmax zonation, with separation of Mesozoic extended and non-extended; Case E magnitude weights: Realization 1.....	J-47
Figure J-47 Map of the rate and $b$ -value for the study region under the Mmax zonation, with separation of Mesozoic extended and non-extended; Case E magnitude weights: Realization 2.....	J-48
Figure J-48 Map of the rate and $b$ -value for the study region under the Mmax zonation, with separation of Mesozoic extended and non-extended; Case E magnitude weights: Realization 3.....	J-49
Figure J-49 Map of the rate and $b$ -value for the study region under the Mmax zonation, with separation of Mesozoic extended and non-extended; Case E magnitude weights: Realization 4.....	J-50
Figure J-50 Map of the rate and $b$ -value for the study region under the Mmax zonation, with separation of Mesozoic extended and non-extended; Case E magnitude weights: Realization 5.....	J-51
Figure J-51 Map of the rate and $b$ -value for the study region under the Mmax zonation, with separation of Mesozoic extended and non-extended; Case E magnitude weights: Realization 6.....	J-52
Figure J-52 Map of the rate and $b$ -value for the study region under the Mmax zonation, with separation of Mesozoic extended and non-extended; Case E magnitude weights: Realization 7.....	J-53
Figure J-53 Map of the rate and $b$ -value for the study region under the Mmax zonation, with separation of Mesozoic extended and non-extended; Case E magnitude weights: Realization 8.....	J-54
Figure J-54 Map of the coefficient of variation of the rate and the standard deviation of the $b$ -value for the study region under the Mmax zonation, with separation of Mesozoic extended and non-extended; Case E magnitude weights .....	J-55
Figure J-55 Map of the rate and $b$ -value for the study region under the Mmax zonation, with separation of Mesozoic extended and non-extended; Case A magnitude weights: Realization 1.....	J-56
Figure J-56 Map of the rate and $b$ -value for the study region under the Mmax zonation, with separation of Mesozoic extended and non-extended; Case A magnitude weights: Realization 2.....	J-57
Figure J-57 Map of the rate and $b$ -value for the study region under the Mmax zonation, with separation of Mesozoic extended and non-extended; Case A magnitude weights: Realization 3.....	J-58

---

Figure J-58 Map of the rate and $b$ -value for the study region under the Mmax zonation, with separation of Mesozoic extended and non-extended; Case A magnitude weights: Realization 4.....	J-59
Figure J-59 Map of the rate and $b$ -value for the study region under the Mmax zonation, with separation of Mesozoic extended and non-extended; Case A magnitude weights: Realization 5.....	J-60
Figure J-60 Map of the rate and $b$ -value for the study region under the Mmax zonation, with separation of Mesozoic extended and non-extended; Case A magnitude weights: Realization 6.....	J-61
Figure J-61 Map of the rate and $b$ -value for the study region under the Mmax zonation, with separation of Mesozoic extended and non-extended; Case A magnitude weights: Realization 7.....	J-62
Figure J-62 Map of the rate and $b$ -value for the study region under the Mmax zonation, with separation of Mesozoic extended and non-extended; Case A magnitude weights: Realization 8.....	J-63
Figure J-63 Map of the coefficient of variation of the rate and the standard deviation of the $b$ -value for the study region under the Mmax zonation, with separation of Mesozoic extended and non-extended; Case A magnitude weights .....	J-64
Figure J-64 Map of the rate and $b$ -value for the study region under the Mmax zonation, with separation of Mesozoic extended and non-extended; Case B magnitude weights: Realization 1.....	J-65
Figure J-65 Map of the rate and $b$ -value for the study region under the Mmax zonation, with separation of Mesozoic extended and non-extended; Case B magnitude weights: Realization 2.....	J-66
Figure J-66 Map of the rate and $b$ -value for the study region under the Mmax zonation, with separation of Mesozoic extended and non-extended; Case B magnitude weights: Realization 3.....	J-67
Figure J-67 Map of the rate and $b$ -value for the study region under the Mmax zonation, with separation of Mesozoic extended and non-extended; Case B magnitude weights: Realization 4.....	J-68
Figure J-68 Map of the rate and $b$ -value for the study region under the Mmax zonation, with separation of Mesozoic extended and non-extended; Case B magnitude weights: Realization 5.....	J-69
Figure J-69 Map of the rate and $b$ -value for the study region under the Mmax zonation, with separation of Mesozoic extended and non-extended; Case B magnitude weights: Realization 6.....	J-70
Figure J-70 Map of the rate and $b$ -value for the study region under the Mmax zonation, with separation of Mesozoic extended and non-extended; Case B magnitude weights: Realization 7.....	J-71
Figure J-71 Map of the rate and $b$ -value for the study region under the Mmax zonation, with separation of Mesozoic extended and non-extended; Case B magnitude weights: Realization 8.....	J-72
Figure J-72 Map of the coefficient of variation of the rate and the standard deviation of the $b$ -value for the study region under the Mmax zonation, with separation of Mesozoic extended and non-extended; Case B magnitude weights .....	J-73

---

Figure J-73 Map of the rate and $b$ -value for the study region under the Mmax zonation, with separation of Mesozoic extended and non-extended; Case E magnitude weights: Realization 1.....	J-74
Figure J-74 Map of the rate and $b$ -value for the study region under the Mmax zonation, with separation of Mesozoic extended and non-extended; Case E magnitude weights: Realization 2.....	J-75
Figure J-75 Map of the rate and $b$ -value for the study region under the Mmax zonation, with separation of Mesozoic extended and non-extended; Case E magnitude weights: Realization 3.....	J-76
Figure J-76 Map of the rate and $b$ -value for the study region under the Mmax zonation, with separation of Mesozoic extended and non-extended; Case E magnitude weights: Realization 4.....	J-77
Figure J-77 Map of the rate and $b$ -value for the study region under the Mmax zonation, with separation of Mesozoic extended and non-extended; Case E magnitude weights: Realization 5.....	J-78
Figure J-78 Map of the rate and $b$ -value for the study region under the Mmax zonation, with separation of Mesozoic extended and non-extended; Case E magnitude weights: Realization 6.....	J-79
Figure J-79 Map of the rate and $b$ -value for the study region under the Mmax zonation, with separation of Mesozoic extended and non-extended; Case E magnitude weights: Realization 7.....	J-80
Figure J-80 Map of the rate and $b$ -value for the study region under the Mmax zonation, with separation of Mesozoic extended and non-extended; Case E magnitude weights: Realization 8.....	J-81
Figure J-81 Map of the coefficient of variation of the rate and the standard deviation of the $b$ -value for the study region under the Mmax zonation, with separation of Mesozoic extended and non-extended; Case E magnitude weights.....	J-82
Figure J-82 Map of the rate and $b$ -value for the study region under the seismotectonic zonation, with narrow interpretation of PEZ; Case A magnitude weights: Realization 1.....	J-83
Figure J-83 Map of the rate and $b$ -value for the study region under the seismotectonic zonation, with narrow interpretation of PEZ; Case A magnitude weights: Realization 2.....	J-84
Figure J-84 Map of the rate and $b$ -value for the study region under the seismotectonic zonation, with narrow interpretation of PEZ; Case A magnitude weights: Realization 3.....	J-85
Figure J-85 Map of the rate and $b$ -value for the study region under the seismotectonic zonation, with narrow interpretation of PEZ; Case A magnitude weights: Realization 4.....	J-86
Figure J-86 Map of the rate and $b$ -value for the study region under the seismotectonic zonation, with narrow interpretation of PEZ; Case A magnitude weights: Realization 5.....	J-87
Figure J-87 Map of the rate and $b$ -value for the study region under the seismotectonic zonation, with narrow interpretation of PEZ; Case A magnitude weights: Realization 6.....	J-88

---

Figure J-88 Map of the rate and $b$ -value for the study region under the seismotectonic zonation, with narrow interpretation of PEZ; Case A magnitude weights: Realization 7.....	J-89
Figure J-89 Map of the rate and $b$ -value for the study region under the seismotectonic zonation, with narrow interpretation of PEZ; Case A magnitude weights: Realization 8.....	J-90
Figure J-90 Map of the coefficient of variation of the rate and the standard deviation of the $b$ -value for the study region under the seismotectonic zonation, with narrow interpretation of PEZ; Case A magnitude weights.....	J-91
Figure J-91 Map of the rate and $b$ -value for the study region under the seismotectonic zonation, with narrow interpretation of PEZ; Case B magnitude weights: Realization 1.....	J-92
Figure J-92 Map of the rate and $b$ -value for the study region under the seismotectonic zonation, with narrow interpretation of PEZ; Case B magnitude weights: Realization 2.....	J-93
Figure J-93 Map of the rate and $b$ -value for the study region under the seismotectonic zonation, with narrow interpretation of PEZ; Case B magnitude weights: Realization 3.....	J-94
Figure J-94 Map of the rate and $b$ -value for the study region under the seismotectonic zonation, with narrow interpretation of PEZ; Case B magnitude weights: Realization 4.....	J-95
Figure J-95 Map of the rate and $b$ -value for the study region under the seismotectonic zonation, with narrow interpretation of PEZ; Case B magnitude weights: Realization 5.....	J-96
Figure J-96 Map of the rate and $b$ -value for the study region under the seismotectonic zonation, with narrow interpretation of PEZ; Case B magnitude weights: Realization 6.....	J-97
Figure J-97 Map of the rate and $b$ -value for the study region under the seismotectonic zonation, with narrow interpretation of PEZ; Case B magnitude weights: Realization 7.....	J-98
Figure J-98 Map of the rate and $b$ -value for the study region under the seismotectonic zonation, with narrow interpretation of PEZ; Case B magnitude weights: Realization 8.....	J-99
Figure J-99 Map of the coefficient of variation of the rate and the standard deviation of the $b$ -value for the study region under the seismotectonic zonation, with narrow interpretation of PEZ; Case B magnitude weights.....	J-100
Figure J-100 Map of the rate and $b$ -value for the study region under the seismotectonic zonation, with narrow interpretation of PEZ; Case E magnitude weights: Realization 1.....	J-101
Figure J-101 Map of the rate and $b$ -value for the study region under the seismotectonic zonation, with narrow interpretation of PEZ; Case E magnitude weights: Realization 2.....	J-102
Figure J-102 Map of the rate and $b$ -value for the study region under the seismotectonic zonation, with narrow interpretation of PEZ; Case E magnitude weights: Realization 3.....	J-103

---

Figure J-103 Map of the rate and $b$ -value for the study region under the seismotectonic zonation, with narrow interpretation of PEZ; Case E magnitude weights: Realization 4.....	J-104
Figure J-104 Map of the rate and $b$ -value for the study region under the seismotectonic zonation, with narrow interpretation of PEZ; Case E magnitude weights: Realization 5.....	J-105
Figure J-105 Map of the rate and $b$ -value for the study region under the seismotectonic zonation, with narrow interpretation of PEZ; Case E magnitude weights: Realization 6.....	J-106
Figure J-106 Map of the rate and $b$ -value for the study region under the seismotectonic zonation, with narrow interpretation of PEZ; Case E magnitude weights: Realization 7.....	J-107
Figure J-107 Map of the rate and $b$ -value for the study region under the seismotectonic zonation, with narrow interpretation of PEZ; Case E magnitude weights: Realization 8.....	J-108
Figure J-108 Map of the coefficient of variation of the rate and the standard deviation of the $b$ -value for the study region under the seismotectonic zonation, with narrow interpretation of PEZ; Case E magnitude weights.....	J-109
Figure J-109 Map of the rate and $b$ -value for the study region under the seismotectonic zonation, with narrow interpretation of PEZ; Case A magnitude weights: Realization 1.....	J-110
Figure J-110 Map of the rate and $b$ -value for the study region under the seismotectonic zonation, with narrow interpretation of PEZ; Case A magnitude weights: Realization 2.....	J-111
Figure J-111 Map of the rate and $b$ -value for the study region under the seismotectonic zonation, with narrow interpretation of PEZ; Case A magnitude weights: Realization 3.....	J-112
Figure J-112 Map of the rate and $b$ -value for the study region under the seismotectonic zonation, with narrow interpretation of PEZ; Case A magnitude weights: Realization 4.....	J-113
Figure J-113 Map of the rate and $b$ -value for the study region under the seismotectonic zonation, with narrow interpretation of PEZ; Case A magnitude weights: Realization 5.....	J-114
Figure J-114 Map of the rate and $b$ -value for the study region under the seismotectonic zonation, with narrow interpretation of PEZ; Case A magnitude weights: Realization 6.....	J-115
Figure J-115 Map of the rate and $b$ -value for the study region under the seismotectonic zonation, with narrow interpretation of PEZ; Case A magnitude weights: Realization 7.....	J-116
Figure J-116 Map of the rate and $b$ -value for the study region under the seismotectonic zonation, with narrow interpretation of PEZ; Case A magnitude weights: Realization 8.....	J-117
Figure J-117 Map of the coefficient of variation of the rate and the standard deviation of the $b$ -value for the study region under the seismotectonic zonation, with narrow interpretation of PEZ; Case A magnitude weights.....	J-118

---

Figure J-118 Map of the rate and $b$ -value for the study region under the seismotectonic zonation, with narrow interpretation of PEZ; Case B magnitude weights: Realization 1.....	J-119
Figure J-119 Map of the rate and $b$ -value for the study region under the seismotectonic zonation, with narrow interpretation of PEZ; Case B magnitude weights: Realization 2.....	J-120
Figure J-120 Map of the rate and $b$ -value for the study region under the seismotectonic zonation, with narrow interpretation of PEZ; Case B magnitude weights: Realization 3.....	J-121
Figure J-121 Map of the rate and $b$ -value for the study region under the seismotectonic zonation, with narrow interpretation of PEZ; Case B magnitude weights: Realization 4.....	J-122
Figure J-122 Map of the rate and $b$ -value for the study region under the seismotectonic zonation, with narrow interpretation of PEZ; Case B magnitude weights: Realization 5.....	J-123
Figure J-123 Map of the rate and $b$ -value for the study region under the seismotectonic zonation, with narrow interpretation of PEZ; Case B magnitude weights: Realization 6.....	J-124
Figure J-124 Map of the rate and $b$ -value for the study region under the seismotectonic zonation, with narrow interpretation of PEZ; Case B magnitude weights: Realization 7.....	J-125
Figure J-125 Map of the rate and $b$ -value for the study region under the seismotectonic zonation, with narrow interpretation of PEZ; Case B magnitude weights: Realization 8.....	J-126
Figure J-126 Map of the coefficient of variation of the rate and the standard deviation of the $b$ -value for the study region under the seismotectonic zonation, with narrow interpretation of PEZ; Case B magnitude weights.....	J-127
Figure J-127 Map of the rate and $b$ -value for the study region under the seismotectonic zonation, with narrow interpretation of PEZ; Case E magnitude weights: Realization 1.....	J-128
Figure J-128 Map of the rate and $b$ -value for the study region under the seismotectonic zonation, with narrow interpretation of PEZ; Case E magnitude weights: Realization 2.....	J-129
Figure J-129 Map of the rate and $b$ -value for the study region under the seismotectonic zonation, with narrow interpretation of PEZ; Case E magnitude weights: Realization 3.....	J-130
Figure J-130 Map of the rate and $b$ -value for the study region under the seismotectonic zonation, with narrow interpretation of PEZ; Case E magnitude weights: Realization 4.....	J-131
Figure J-131 Map of the rate and $b$ -value for the study region under the seismotectonic zonation, with narrow interpretation of PEZ; Case E magnitude weights: Realization 5.....	J-132
Figure J-132 Map of the rate and $b$ -value for the study region under the seismotectonic zonation, with narrow interpretation of PEZ; Case E magnitude weights: Realization 6.....	J-133

---

Figure J-133 Map of the rate and $b$ -value for the study region under the seismotectonic zonation, with narrow interpretation of PEZ; Case E magnitude weights: Realization 7.....	J-134
Figure J-134 Map of the rate and $b$ -value for the study region under the seismotectonic zonation, with narrow interpretation of PEZ; Case E magnitude weights: Realization 8.....	J-135
Figure J-135 Map of the coefficient of variation of the rate and the standard deviation of the $b$ -value for the study region under the seismotectonic zonation, with narrow interpretation of PEZ; Case E magnitude weights.....	J-136
Figure J-136 Map of the rate and $b$ -value for the study region under the seismotectonic zonation, with wide interpretation of PEZ; Case A magnitude weights: Realization 1 ...	J-137
Figure J-137 Map of the rate and $b$ -value for the study region under the seismotectonic zonation, with wide interpretation of PEZ; Case A magnitude weights: Realization 2 ...	J-138
Figure J-138 Map of the rate and $b$ -value for the study region under the seismotectonic zonation, with wide interpretation of PEZ; Case A magnitude weights: Realization 3 ...	J-139
Figure J-139 Map of the rate and $b$ -value for the study region under the seismotectonic zonation, with wide interpretation of PEZ; Case A magnitude weights: Realization 4 ...	J-140
Figure J-140 Map of the rate and $b$ -value for the study region under the seismotectonic zonation, with wide interpretation of PEZ; Case A magnitude weights: Realization 5 ...	J-141
Figure J-141 Map of the rate and $b$ -value for the study region under the seismotectonic zonation, with wide interpretation of PEZ; Case A magnitude weights: Realization 6 ...	J-142
Figure J-142 Map of the rate and $b$ -value for the study region under the seismotectonic zonation, with wide interpretation of PEZ; Case A magnitude weights: Realization 7 ...	J-143
Figure J-143 Map of the rate and $b$ -value for the study region under the seismotectonic zonation, with wide interpretation of PEZ; Case A magnitude weights: Realization 8 ...	J-144
Figure J-144 Map of the coefficient of variation of the rate and the standard deviation of the $b$ -value for the study region under the seismotectonic zonation, with wide interpretation of PEZ; Case A magnitude weights.....	J-145
Figure J-145 Map of the rate and $b$ -value for the study region under the seismotectonic zonation, with wide interpretation of PEZ; Case B magnitude weights: Realization 1 ...	J-146
Figure J-146 Map of the rate and $b$ -value for the study region under the seismotectonic zonation, with wide interpretation of PEZ; Case B magnitude weights: Realization 2 ...	J-147
Figure J-147 Map of the rate and $b$ -value for the study region under the seismotectonic zonation, with wide interpretation of PEZ; Case B magnitude weights: Realization 3 ...	J-148
Figure J-148 Map of the rate and $b$ -value for the study region under the seismotectonic zonation, with wide interpretation of PEZ; Case B magnitude weights: Realization 4 ...	J-149
Figure J-149 Map of the rate and $b$ -value for the study region under the seismotectonic zonation, with wide interpretation of PEZ; Case B magnitude weights: Realization 5 ...	J-150
Figure J-150 Map of the rate and $b$ -value for the study region under the seismotectonic zonation, with wide interpretation of PEZ; Case B magnitude weights: Realization 6 ...	J-151
Figure J-151 Map of the rate and $b$ -value for the study region under the seismotectonic zonation, with wide interpretation of PEZ; Case B magnitude weights: Realization 7 ...	J-152
Figure J-152 Map of the rate and $b$ -value for the study region under the seismotectonic zonation, with wide interpretation of PEZ; Case B magnitude weights: Realization 8 ...	J-153

---

Figure J-153 Map of the coefficient of variation of the rate and the standard deviation of the $b$ -value for the study region under the seismotectonic zonation, with wide interpretation of PEZ; Case B magnitude weights.....	J-154
Figure J-154 Map of the rate and $b$ -value for the study region under the seismotectonic zonation, with wide interpretation of PEZ; Case E magnitude weights: Realization 1 ...	J-155
Figure J-155 Map of the rate and $b$ -value for the study region under the seismotectonic zonation, with wide interpretation of PEZ; Case E magnitude weights: Realization 2 ...	J-156
Figure J-156 Map of the rate and $b$ -value for the study region under the seismotectonic zonation, with wide interpretation of PEZ; Case E magnitude weights: Realization 3 ...	J-157
Figure J-157 Map of the rate and $b$ -value for the study region under the seismotectonic zonation, with wide interpretation of PEZ; Case E magnitude weights: Realization 4 ...	J-158
Figure J-158 Map of the rate and $b$ -value for the study region under the seismotectonic zonation, with wide interpretation of PEZ; Case E magnitude weights: Realization 5 ...	J-159
Figure J-159 Map of the rate and $b$ -value for the study region under the seismotectonic zonation, with wide interpretation of PEZ; Case E magnitude weights: Realization 6 ...	J-160
Figure J-160 Map of the rate and $b$ -value for the study region under the seismotectonic zonation, with wide interpretation of PEZ; Case E magnitude weights: Realization 7 ...	J-161
Figure J-161 Map of the rate and $b$ -value for the study region under the seismotectonic zonation, with wide interpretation of PEZ; Case E magnitude weights: Realization 8 ...	J-162
Figure J-162 Map of the coefficient of variation of the rate and the standard deviation of the $b$ -value for the study region under the seismotectonic zonation, with wide interpretation of PEZ; Case E magnitude weights.....	J-163
Figure J-163 Map of the rate and $b$ -value for the study region under the seismotectonic zonation, with wide interpretation of PEZ; Case A magnitude weights: Realization 1 ...	J-164
Figure J-164 Map of the rate and $b$ -value for the study region under the seismotectonic zonation, with wide interpretation of PEZ; Case A magnitude weights: Realization 2 ...	J-165
Figure J-165 Map of the rate and $b$ -value for the study region under the seismotectonic zonation, with wide interpretation of PEZ; Case A magnitude weights: Realization 3 ...	J-166
Figure J-166 Map of the rate and $b$ -value for the study region under the seismotectonic zonation, with wide interpretation of PEZ; Case A magnitude weights: Realization 4 ...	J-167
Figure J-167 Map of the rate and $b$ -value for the study region under the seismotectonic zonation, with wide interpretation of PEZ; Case A magnitude weights: Realization 5 ...	J-168
Figure J-168 Map of the rate and $b$ -value for the study region under the seismotectonic zonation, with wide interpretation of PEZ; Case A magnitude weights: Realization 6 ...	J-169
Figure J-169 Map of the rate and $b$ -value for the study region under the seismotectonic zonation, with wide interpretation of PEZ; Case A magnitude weights: Realization 7 ...	J-170
Figure J-170 Map of the rate and $b$ -value for the study region under the seismotectonic zonation, with wide interpretation of PEZ; Case A magnitude weights: Realization 8 ...	J-171
Figure J-171 Map of the coefficient of variation of the rate and the standard deviation of the $b$ -value for the study region under the seismotectonic zonation, with wide interpretation of PEZ; Case A magnitude weights.....	J-172
Figure J-172 Map of the rate and $b$ -value for the study region under the seismotectonic zonation, with wide interpretation of PEZ; Case B magnitude weights: Realization 1 ...	J-173

---

Figure J-173 Map of the rate and $b$ -value for the study region under the seismotectonic zonation, with wide interpretation of PEZ; Case B magnitude weights: Realization 2 ...	J-174
Figure J-174 Map of the rate and $b$ -value for the study region under the seismotectonic zonation, with wide interpretation of PEZ; Case B magnitude weights: Realization 3 ...	J-175
Figure J-175 Map of the rate and $b$ -value for the study region under the seismotectonic zonation, with wide interpretation of PEZ; Case B magnitude weights: Realization 4 ...	J-176
Figure J-176 Map of the rate and $b$ -value for the study region under the seismotectonic zonation, with wide interpretation of PEZ; Case B magnitude weights: Realization 5 ...	J-177
Figure J-177 Map of the rate and $b$ -value for the study region under the seismotectonic zonation, with wide interpretation of PEZ; Case B magnitude weights: Realization 6 ...	J-178
Figure J-178 Map of the rate and $b$ -value for the study region under the seismotectonic zonation, with wide interpretation of PEZ; Case B magnitude weights: Realization 7 ...	J-179
Figure J-179 Map of the rate and $b$ -value for the study region under the seismotectonic zonation, with wide interpretation of PEZ; Case B magnitude weights: Realization 8 ...	J-180
Figure J-180 Map of the coefficient of variation of the rate and the standard deviation of the $b$ -value for the study region under the seismotectonic zonation, with wide interpretation of PEZ; Case B magnitude weights.....	J-181
Figure J-181 Map of the rate and $b$ -value for the study region under the seismotectonic zonation, with wide interpretation of PEZ; Case E magnitude weights: Realization 1 ...	J-182
Figure J-182 Map of the rate and $b$ -value for the study region under the seismotectonic zonation, with wide interpretation of PEZ; Case E magnitude weights: Realization 2 ...	J-183
Figure J-183 Map of the rate and $b$ -value for the study region under the seismotectonic zonation, with wide interpretation of PEZ; Case E magnitude weights: Realization 3 ...	J-184
Figure J-184 Map of the rate and $b$ -value for the study region under the seismotectonic zonation, with wide interpretation of PEZ; Case E magnitude weights: Realization 4 ...	J-185
Figure J-185 Map of the rate and $b$ -value for the study region under the seismotectonic zonation, with wide interpretation of PEZ; Case E magnitude weights: Realization 5 ...	J-186
Figure J-186 Map of the rate and $b$ -value for the study region under the seismotectonic zonation, with wide interpretation of PEZ; Case E magnitude weights: Realization 6 ...	J-187
Figure J-187 Map of the rate and $b$ -value for the study region under the seismotectonic zonation, with wide interpretation of PEZ; Case E magnitude weights: Realization 7 ...	J-188
Figure J-188 Map of the rate and $b$ -value for the study region under the seismotectonic zonation, with wide interpretation of PEZ; Case E magnitude weights: Realization 8 ...	J-189
Figure J-189 Map of the coefficient of variation of the rate and the standard deviation of the $b$ -value for the study region under the seismotectonic zonation, with wide interpretation of PEZ; Case E magnitude weights.....	J-190
Figure K-1 Comparison of relationships between number of reporting stations and moment magnitude presented in Johnston et al. (1994) and Johnston (1996b).....	K-41
Figure K-2 Comparison of relationships between isoseismal areas and moment magnitude presented in Johnston et al. (1994) and Johnston (1996b).....	K-42

# LIST OF TABLES

Table 2.2-1 Technical Meetings Conducted as Part of the CEUS SSC Project .....	2-29
Table 2.2-2 Contributors to the CEUS SSC Project.....	2-30
Table 3.2-1 Summary of Earthquakes Added–USGS Earthquake Catalog by Time Period.....	3-44
Table 3.2-2 Summary of Earthquakes Added–USGS Earthquake Catalog by Source.....	3-45
Table 3.3-1 Conversion Relationships Used–Develop Uniform Moment Magnitudes E[M] .....	3-46
Table 3.4-1 Comparison of CEUS SSC Catalog Declustering Results Obtained Using the EPRI (1988) Approach with the Gardner Knopoff (1974) Approach .....	3-47
Table 3.5-1 Probability of Detection and Equivalent Periods of Completeness for the CEUS for Magnitude Weighting Case A .....	3-48
Table 3.5-2 Probability of Detection and Equivalent Periods of Completeness for the CEUS for Magnitude Weighting Case B .....	3-51
Table 3.5-3 Probability of Detection and Equivalent Periods of Completeness for the CEUS for Magnitude Weighting Case E .....	3-54
Table 4.1.2-1 Sample table indicating particular types of data that can be considered in the identification and characterization of seismic sources (Table 2, ANSI/ANS-2.27- 2008).....	4-26
Table 4.1.2-2 Sample table identifying the types of data that can be considered for characterizing different types of seismic sources, and an evaluation of the relative usefulness or credibility of the various data types (Budnitz et al., 1997) .....	4-27
Table 4.1.2-3 Table showing the “generic” (not source-specific) evaluation of data to address indicators of a unique seismic source. The table indicates the TI Team’s assessment of the types of data that can be used to address the indicators and their relative usefulness.....	4-28
Table 4.1.2-4 Example of Data Evaluation Table for the Illinois Basin–Extended Basement Zone (IBEB).....	4-34
Table 4.1.2-5 Example of Data Summary Table for the Extended Continental Crust– Atlantic Margin (ECC-AM) and Atlantic Highly Extended Crust (AHEX) Zones .....	4-35
Table 4.1.3-1 Criteria Used to Define the Seismotectonic Zones and Mmax Zones .....	4-37
Table 4.2.2-1 RLME Sources .....	4-38
Table 4.2.4-1 Seismotectonic Zones .....	4-39
Table 5.2.1-1 Mesozoic-and-Younger Extended Superdomains (MESE) .....	5-60
Table 5.2.1-2 Older Extended and Non-Extended Superdomains (NMESE) .....	5-61
Table 5.2.1-3 Composite SCR Superdomains (COMP).....	5-62
Table 5.2.1-4 Results of Analyses of Updated SCR Superdomains .....	5-63

---

Table 5.2.1-5 Source Zones, $P(m^u > 8\frac{1}{4})$ Values, and Weights on Kijko (2004) K-S-B Estimates .....	5-64
Table 5.2.1-6 Mmax Distributions for the Two Example Seismic Sources .....	5-65
Table 5.3.2-1 Alternative Cases Considered for the Magnitude-Dependent Weights .....	5-65
Table 5.3.3-1 Miller and Rice (1983) Discrete 5-Point Approximation to a Continuous Probability Distribution and the Modified Form Used in This Study .....	5-65
Table 5.4-1 Assessment of Default Characteristics of Future Earthquakes in the CEUS .....	5-66
Table 5.4-2 Characteristics of Future Earthquakes for Individual Seismic Sources .....	5-68
Table 5.4-3 Estimates of $D_{90}$ for Individual Seismic Source Zones .....	5-71
Table 6.1-1 Summary of Data Used to Assess RLME Recurrence Frequencies .....	6-80
Table 6.1.1-1 Charlevoix RLME Recurrence Frequency .....	6-83
Table 6.1.2-1 Summary of Interpreted Charleston Earthquake Ages and Sizes from “Contemporary Ages Only” Scenario .....	6-84
Table 6.1.2-2 Summary of Interpreted Charleston Earthquake Ages and Sizes from “All Ages” Scenario .....	6-84
Table 6.1.2-3 Charleston Liquefaction Feature Ages Used to Assess Ages of Prehistoric Earthquakes .....	6-85
Table 6.1.2-4 Charleston RLME Recurrence Frequency for Poisson Model .....	6-86
Table 6.1.2-5 Charleston RLME Recurrence Frequency for Renewal Model .....	6-87
Table 6.1.3-1 Range of Cheraw Fault Estimated Magnitudes (M) .....	6-88
Table 6.1.3-2 Cheraw RLME In-Cluster Recurrence Frequency .....	6-89
Table 6.1.3-3 Cheraw RLME In-Cluster Slip Rates .....	6-89
Table 6.1.3-4 Cheraw RLME Out-of-Cluster Recurrence Frequency .....	6-90
Table 6.1.3-5 Cheraw RLME Out-of-Cluster Slip Rates .....	6-90
Table 6.1.4-1 Range of Estimated Meers Fault Earthquake Magnitudes (M) .....	6-91
Table 6.1.4-2 Meers RLME In-Cluster Recurrence Frequency .....	6-91
Table 6.1.4-3 Meers RLME Out-of-Cluster Recurrence Frequency .....	6-91
Table 6.1.5-1 Preferred Ages for Paleoearthquakes in the New Madrid Region <sup>1</sup> .....	6-92
Table 6.1.5-2 Magnitude Comparisons for New Madrid 1811-1812 Earthquake Sequence .....	6-93
Table 6.1.5-3 Liquefaction Constraints on Age of AD 1450 NMFS RLME .....	6-94
Table 6.1.5-4 Liquefaction Constraints on Age of AD 900 NMFS RLME .....	6-95
Table 6.1.5-5 NMFS In-Cluster RLME Recurrence Frequency—Poisson Model .....	6-96
Table 6.1.5-6 NMFS In-Cluster RLME Recurrence Frequency—Renewal Model .....	6-96
Table 6.1.5-7 NMFS Out-of-Cluster RLME Recurrence Frequency—Poisson Model .....	6-96
Table 6.1.6-1 Range of ERM-S Estimated Magnitudes (M) .....	6-97
Table 6.1.6-2 Range of ERM-N Estimated Magnitudes (M) .....	6-98
Table 6.1.6-3 ERM-S RLME Recurrence Frequency .....	6-98
Table 6.1.6-4 ERM-N RLME Recurrence Frequency .....	6-99
Table 6.1.7-1 Marianna RLME Recurrence Frequency .....	6-99

Table 6.1.8-1 Range of Commerce Fault Zone RLME Estimated Magnitudes (M) .....	6-100
Table 6.1.8-2 Commerce Fault Zone RLME Recurrence Frequency .....	6-101
Table 6.1.9-1 Liquefaction Evidence for Prehistoric Earthquakes in the Southern Illinois Basin .....	6-102
Table 6.1.9-2 Wabash RLME Recurrence Frequency .....	6-109
Table 6.2-1 Alternative Mmax Zonation Models .....	6-109
Table 6.3.2-1 Maximum Magnitude Distributions for Mmax Distributed Seismicity Sources .....	6-110
Table 7.1-1 Data Summary and Data Evaluation Tables for Seismotectonic Zones in Appendices C and D .....	7-81
Table 7.4.2-1 Maximum Magnitude Distributions for Seismotectonic Distributed Seismicity Sources .....	7-82
Table 8.1-1 Description of Seven Test Sites .....	8-13
Table 8.2.1-1 Mean and Select Fractiles for Rock Hazard at Central Illinois: Digital Data for Figures 8.2-1a through 8.2-1c .....	8-14
Table 8.2.2-1 Mean and Select Fractiles for Rock Hazard at Chattanooga: Digital Data for Figures 8.2-2a through 8.2-2c .....	8-16
Table 8.2.3-1 Mean and Select Fractiles for Rock Hazard at Houston: Digital Data for Figures 8.2-3a through 8.2-3c .....	8-18
Table 8.2.4-1 Mean and Select Fractiles for Rock Hazard at Jackson: Digital Data for Figures 8.2-4a through 8.2-4c .....	8-20
Table 8.2.5-1 Mean and Select Fractiles for Rock Hazard at Manchester: Digital Data for Figures 8.2-5a through 8.2-5c .....	8-22
Table 8.2.6-1 Mean and Select Fractiles for Rock Hazard at Savannah: Digital Data for Figures 8.2-6a through 8.2-6c .....	8-24
Table 8.2.7-1 Mean and Select Fractiles for Rock Hazard at Topeka: Digital Data for Figures 8.2-7a through 8.2-7c .....	8-26
Table 9.4-1 Available Information for Determining the Precision of Mean Hazard .....	9-21
Table 9.4-2 Summary of an Example Logic Tree Representing Uncertainties for the Charleston Seismic Zone .....	9-21
Table 9.4-3 Basic Weights Given in EPRI (2004) for Ground Motion Equations .....	9-22
Table 9.4-4 Ground Motion Equations and Weights Used in USGS 2008 National Hazard Map for CEUS .....	9-23
Table 9.4-5 Minimum COV <sub>MH</sub> Values Observed in Seismic Hazard .....	9-23
Table A-1 CEUS SSC GIS Database .....	A-7
Table B-1 Earthquake Catalog .....	B-6
Table B-2 Moment Magnitude Data .....	B-312
Table B-3 Approximate Moment Magnitude Data .....	B-324
Table C-5.4 Data Evaluation Future Earthquake Characteristics .....	C-3
Table C-6.1.1 Data Evaluation Charlevoix RLME .....	C-9
Table C-6.1.2 Data Evaluation Charleston RLME .....	C-14
Table C-6.1.3 Data Evaluation Cheraw Fault RLME .....	C-30

Table C-6.1.4 Data Evaluation Oklahoma Aulacogen RLME .....	C-36
Table C-6.1.5 Data Evaluation Reelfoot Rift–New Madrid Fault System RLMEs .....	C-42
Table C-6.1.6 Data Evaluation Reelfoot Rift–Eastern Margin Fault(s) RLMEs.....	C-51
Table C-6.1.7 Data Evaluation Reelfoot Rift–Marianna RLME .....	C-62
Table C-6.1.8 Data Evaluation Reelfoot Rift–Commerce Fault Zone RLME .....	C-67
Table C-6.1.9 Data Evaluation Wabash Valley RLME .....	C-75
Table C-7.3.1 Data Evaluation St. Lawrence Rift Zone .....	C-83
Table C-7.3.2 Data Evaluation Great Meteor Hotspot Zone .....	C-92
Table C-7.3.3 Data Evaluation Northern Appalachian Zone.....	C-99
Table C-7.3.4 Data Evaluation Paleozoic Extended Crust Zone .....	C-105
Table C-7.3.5 Data Evaluation Illinois Basin-Extended Basement Zone .....	C-112
Table C-7.3.6 Data Evaluation Reelfoot Rift Zone.....	C-124
Tables C-7.3.7/7.3.8 Data Evaluation Extended Continental Crust—Atlantic.....	C-131
Tables C-7.3.9/7.3.10 Data Evaluation Extended Continental Crust—Gulf Coast .....	C-138
Table C-7.3.12 Data Evaluation Midcontinent-Craton Zone .....	C-146
Table D-5.4 Data Summary Future Earthquake Characteristics.....	D-3
Table D-6.1.1 Data Summary Charlevoix RLME .....	D-10
Table D-6.1.2 Data Summary Charleston RLME.....	D-17
Table D-6.1.3 Data Summary Cheraw Fault RLME .....	D-35
Table D-6.1.4 Data Summary Oklahoma Aulacogen RLME.....	D-38
Table D-6.1.5 Data Summary Reelfoot Rift–New Madrid Seismic Zone (NMSZ) Region.....	D-44
Table D-6.1.9 Data Summary Wabash Valley RLME .....	D-92
Table D-7.3.1 Data Summary St. Lawrence Rift Zone (SLR) .....	D-121
Table D-7.3.2 Data Summary Great Meteor Hotspot Zone (GMH).....	D-141
Table D-7.3.3 Data Summary Northern Appalachian Zone (NAP) .....	D-151
Table D-7.3.4 Data Summary Paleozoic Extended Crust Zone.....	D-163
Table D-7.3.7 Data Summary Extended Continental Crust Zone—Atlantic Margin (ECC-AM).....	D-191
Table D-7.3.9 Data Summary Extended Continental Crust Zone—Gulf Coast (ECC-GC).....	D-225
Table D-7.3.12 Data Summary Midcontinent-Craton Zone (MidC) .....	D-240
Table E-1.2-1. Summary of Information on Liquefaction Features in Regional Data Sets.....	E-5
Table E-1.2-2 Summary of Type and Prevalence of Paleoliquefaction Features .....	E-7
Table E-2.1.3. Summary of Dating Techniques Used in Paleoliquefaction Studies.....	E-30
Table E-2.2. Uncertainties Related to Interpretation of Paleoearthquake Parameters .....	E-36
Table 1: Key Questions and Topics That Workshop 2 Presenters Were Asked to Address .....	F-35
Table H-3-1 Weighted Alternative Seismogenic Crustal Thickness Values for Mmax Zones .....	H-20
Table H-3-2 Aleatory Distributions for Characterization of Future Earthquake Ruptures for Mmax Zones .....	H-20

---

Table H-3-3 Maximum Magnitude Distributions for Mmax Distributed Seismicity Sources ....	H-20
Table H-4-1 Seismotectonic Source Zones .....	H-21
Table H-4-2 Weighted Alternative Seismogenic Crustal Thickness Values for Seismotectonic Zones .....	H-21
Table H-4-3 Aleatory Distributions for Characterization of Future Earthquake Ruptures for Seismotectonic Zones .....	H-22
Table H-4-4 Maximum Magnitude Distributions for Seismotectonic Distributed Seismicity Sources .....	H-24
Table H-5.1-1 Charlevoix RLME Magnitude Distribution .....	H-25
Table H-5.1-2 Annual Frequencies for Charlevoix RLME Events Data Set 1: 1870 and 1663 .....	H-25
Table H-5.1-3 Annual Frequencies for Charlevoix RLME Events Data Set 2: 3 Earthquakes in 6–7 kyr BP .....	H-25
Table H-5.1-4 Annual Frequencies for Charlevoix RLME Events Data Set 3: 4 Earthquakes in 9.5–10.2 kyr BP .....	H-26
Table H-5.2-1 Charleston RLME Magnitude Distribution .....	H-26
Table H-5.2-2 Annual Frequencies for Charleston RLME Events Poisson Model, 2,000- Year Time Period Earthquakes 1886, A, B, and C .....	H-26
Table H-5.2-3 Annual Frequencies for Charleston RLME Events Poisson Model, 5,500- Year Time Period Earthquakes 1886, A, B, and C .....	H-27
Table H-5.2-4 Annual Frequencies for Charleston RLME Events Poisson Model, 5,500- Year Time Period Earthquakes 1886, A, B, C, and D .....	H-27
Table H-5.2-5 Annual Frequencies for Charleston RLME Events Poisson Model, 5,500- Year Time Period Earthquakes 1886, A, B, C, and E .....	H-27
Table H-5.2-6 Annual Frequencies for Charleston RLME Events Poisson Model, 5,500- Year Time Period Earthquakes 1886, A, B, C, D, and E .....	H-28
Table H-5.2-7 Annual Frequencies for Charleston RLME Events BPT Renewal Model, $\alpha$ = 0.3, 2,000-Year Time Period Earthquakes 1886, A, B, and C .....	H-28
Table H-5.2-8 Annual Frequencies for Charleston RLME Events BPT Renewal Model, $\alpha$ = 0.5, 2,000-Year Time Period Earthquakes 1886, A, B, and C .....	H-28
Table H-5.2-9 Annual Frequencies for Charleston RLME Events BPT Renewal Model, $\alpha$ = 0.7, 2,000-Year Time Period Earthquakes 1886, A, B, and C .....	H-29
Table H-5.2-10 Annual Frequencies for Charleston RLME Events BPT Renewal Model, $\alpha$ = 0.3, 5,500-Year Time Period Earthquakes 1886, A, B, and C .....	H-29
Table H-5.2-11 Annual Frequencies for Charleston RLME Events BPT Renewal Model, $\alpha$ = 0.5, 5,500-Year Time Period Earthquakes 1886, A, B, and C .....	H-29
Table H-5.2-12 Annual Frequencies for Charleston RLME Events BPT Renewal Model, $\alpha$ = 0.7, 5,500-Year Time Period Earthquakes 1886, A, B, and C .....	H-30
Table H-5.2-13 Annual Frequencies for Charleston RLME Events BPT Renewal Model, $\alpha$ = 0.3, 5,500-Year Time Period Earthquakes 1886, A, B, C, and D .....	H-30
Table H-5.2-14 Annual Frequencies for Charleston RLME Events BPT Renewal Model, $\alpha$ = 0.5, 5,500-Year Time Period Earthquakes 1886, A, B, C, and D .....	H-30

Table H-5.2-15 Annual Frequencies for Charleston RLME Events BPT Renewal Model, $\alpha$ = 0.7, 5,500-Year Time Period Earthquakes 1886, A, B, C, and D .....	H-31
Table H-5.2-16 Annual Frequencies for Charleston RLME Events BPT Renewal Model, $\alpha$ = 0.3, 5,500-Year Time Period Earthquakes 1886, A, B, C, and E.....	H-31
Table H-5.2-17 Annual Frequencies for Charleston RLME Events BPT Renewal Model, $\alpha$ = 0.5, 5,500-Year Time Period Earthquakes 1886, A, B, C, and E.....	H-31
Table H-5.2-18 Annual Frequencies for Charleston RLME Events BPT Renewal Model, $\alpha$ = 0.7, 5,500-Year Time Period Earthquakes 1886, A, B, C, and E.....	H-32
Table H-5.2-19 Annual Frequencies for Charleston RLME Events BPT Renewal Model, $\alpha$ = 0.3, 5,500-Year Time Period Earthquakes 1886, A, B, C, D, and E .....	H-32
Table H-5.2-20 Annual Frequencies for Charleston RLME Events BPT Renewal Model, $\alpha$ = 0.5, 5,500-Year Time Period Earthquakes 1886, A, B, C, D, and E .....	H-32
Table H-5.2-21 Annual Frequencies for Charleston RLME Events BPT Renewal Model, $\alpha$ = 0.7, 5,500-Year Time Period Earthquakes 1886, A, B, C, D, and E .....	H-33
Table H-5.3-1 Cheraw RLME Magnitude Distribution .....	H-33
Table H-5.3-2 Annual Frequencies for Cheraw RLME Events In-Cluster Case, Data Set: 2 Earthquakes in 20–25 kyr .....	H-33
Table H-5.3-3 Annual Frequencies for Cheraw RLME Events In-Cluster Case, Data Set: 3 Earthquakes in 20–25 kyr .....	H-34
Table H-5.3-4 Slip Rates for Cheraw Fault In-Cluster Case, Data Set: 3.2–4.1 m in 20–25 kyr .....	H-34
Table H-5.3-5 Annual Frequencies for Cheraw RLME Events Out-of-Cluster Case, Time Between Clusters .....	H-34
Table H-5.3-6 Slip Rates for Cheraw Fault Out-of-Cluster Case, Data Set: 7–8 m in 0.4–2.0 myr .....	H-35
Table H-5.4-1 Meers RLME Magnitude Distribution .....	H-35
Table H-5.4-2 Annual Frequencies for Meers RLME Events In-Cluster Case.....	H-35
Table H-5.4-3 Annual Frequencies for Meers RLME Events Out-of-Cluster Case.....	H-36
Table H-5.5-1 NMFS RLME Magnitude Distribution .....	H-36
Table H-5.5-2 Annual Frequencies for NMFS RLME Events In-Cluster Case, Poisson Model .....	H-36
Table H-5.5-3 Annual Frequencies for NMFS RLME Events In-Cluster Case, BPT Model, $\alpha$ = 0.3 .....	H-37
Table H-5.5-4 Annual Frequencies for NMFS RLME Events In-Cluster Case, BPT Model, $\alpha$ = 0.5 .....	H-37
Table H-5.5-5 Annual Frequencies for NMFS RLME Events In-Cluster Case, BPT Model, $\alpha$ = 0.7 .....	H-37
Table H-5.5-6 Annual Frequencies for NMFS RLME Events Out-of-Cluster Case, Poisson Model.....	H-38
Table H-5.6-1 ERM-S RLME Magnitude Distribution.....	H-38
Table H-5.6-2 ERM-N RLME Magnitude Distribution.....	H-38
Table H-5.6-3 Annual Frequencies for ERM-S RLME Events Data Set: 2 Earthquakes in 17.7–21.7 kyr .....	H-39

---

Table H-5.6-4 Annual Frequencies for ERM-S RLME Events Data Set: 3 Earthquakes in 17.7–21.7 kyr .....	H-39
Table H-5.6-5 Annual Frequencies for ERM-S RLME Events Data Set: 4 Earthquakes in 17.7–21.7 kyr .....	H-39
Table H-5.6-6 Annual Frequencies for ERM-N RLME Events Data Set: 1 Earthquake in 12–35 kyr .....	H-40
Table H-5.6-7 Annual Frequencies for ERM-N RLME Events Data Set: 2 Earthquakes in 12–35 kyr .....	H-40
Table H-5.7-1 Marianna RLME Magnitude Distribution .....	H-40
Table H-5.7-2 Annual Frequencies for Marianna RLME Events Data Set: 3 Earthquakes in 9.6–10.2 kyr.....	H-41
Table H-5.7-3 Annual Frequencies for Marianna RLME Events Data Set: 4 Earthquakes in 9.6–10.2 kyr.....	H-41
Table H-5.8-1 Commerce RLME Magnitude Distribution.....	H-41
Table H-5.8-2 Annual Frequencies for Commerce RLME Events Data Set: 2 Earthquakes in 18.9–23.6 kyr.....	H-42
Table H-5.8-3 Annual Frequencies for Commerce RLME Events Data Set: 3 Earthquakes in 18.9–23.6 kyr.....	H-42
Table H-5.9-1 Wabash RLME Magnitude Distribution .....	H-42
Table H-5.9-2 Annual Frequencies for Wabash RLME Events Data Set: 2 Earthquakes in 11–13 kyr.....	H-43
PPRP Comment Response Table .....	(Appendix I)
Table K-1 SCR Earthquake Catalog.....	K-5
Table K-2 SCR Domains Updated from Johnston et al. (1994) .....	K-34



## EXECUTIVE SUMMARY

---

The Central and Eastern United States Seismic Source Characterization for Nuclear Facilities (CEUS SSC) Project was conducted over the period from April 2008 to December 2011 to provide a regional seismic source model for use in probabilistic seismic hazard analyses (PSHAs) for nuclear facilities. The study replaces previous regional seismic source models conducted for this purpose, including the Electric Power Research Institute–Seismicity Owners Group (EPRI-SOG) model (EPRI, 1988, 1989) and the Lawrence Livermore National Laboratory model (Bernreuter et al., 1989). Unlike the previous studies, the CEUS SSC Project was sponsored by multiple stakeholders—namely, the EPRI Advanced Nuclear Technology Program, the Office of Nuclear Energy and the Office of the Chief of Nuclear Safety of the U.S. Department of Energy (DOE), and the Office of Nuclear Regulatory Research of the Nuclear Regulatory Commission (NRC). The study was conducted using Senior Seismic Hazard Analysis Committee (SSHAC) Study Level 3 methodology to provide high levels of confidence that the data, models, and methods of the larger technical community have been considered and the center, body, and range of technically defensible interpretations have been included.

The regional seismic source characterization (SSC) model defined by this study can be used for site-specific PSHAs, provided that appropriate site-specific assessments are conducted as required by current regulations and regulatory guidance for the nuclear facility of interest. This model has been designed to be compatible with current and anticipated ground-motion characterization (GMC) models. The current recommended ground-motion models for use at nuclear facilities are those developed by EPRI (2004, 2006a, 2006b). The ongoing Next Generation Attenuation–East (NGA-East) project being supported by the NRC, DOE, and EPRI will provide ground-motion models that are appropriate for use with the CEUS SSC model. The methodology for a SSHAC Level 3 project as applied to the CEUS SSC Project is explained in the SSHAC report (Budnitz et al., 1997), which was written to discuss the evolution of expert assessment methodologies conducted during the previous three decades for purposes of probabilistic risk analyses. The methodological guidance provided in the SSHAC report was intended to build on the lessons learned from those previous studies and, specifically, to arrive at processes that would make it possible to avoid the issues encountered by the previous studies (NRC, 2011).

The SSHAC assessment process, which differs only slightly for Level 3 and 4 studies, is a technical process accepted in the NRC’s seismic regulatory guidance (Regulatory Guide 1.208) for ensuring that uncertainties in data and scientific knowledge have been properly represented in seismic design ground motions consistent with the requirements of the seismic regulation 10 CFR Part 100.23 (“Geologic and Seismic Siting Criteria”). Therefore, the goal of the SSHAC assessment process is the proper and complete representation of knowledge and uncertainties in the SSC and GMC inputs to the PSHA (or similar hazard analysis). As discussed extensively in

the SSHAC report (Budnitz et al., 1997) and affirmed in NRC (2011), a SSHAC assessment process consists of two important sequential activities, *evaluation* and *integration*. For a Level 3 assessment, these activities are conducted by the Technical Integration (TI) Team under the leadership of the TI Lead. As described in NRC (2011),

The fundamental goal of a SSHAC process is to carry out properly and document completely the activities of evaluation and integration, defined as:

*Evaluation:* The consideration of the complete set of data, models, and methods proposed by the larger technical community that are relevant to the hazard analysis.

*Integration:* Representing the center, body, and range of technically defensible interpretations in light of the evaluation process (i.e., informed by the assessment of existing data, models, and methods).

Each of the assessment and model-building activities of the CEUS SSC Project is associated with the evaluation and integration steps in a SSHAC Level 3 process. Consistent with the requirements of a SSHAC process, the specific roles and responsibilities of all project participants were defined in the Project Plan, and adherence to those roles was the responsibility of the TI Lead and the Project Manager. The technical assessments are made by the TI Team, who carry the principal responsibility of evaluation and integration, under the technical leadership of the TI Lead. The Database Manager and other technical support individuals assist in the development of work products. Resource and proponent experts participate by presenting their data, models, and interpretations at workshops and through technical interchange with the TI Team throughout the project. The Participatory Peer Review Panel (PPRP) is responsible for a continuous review of both the SSHAC process being followed and the technical assessments being made. The project management structure is headed by the Project Manager, who serves as the liaison with the sponsors and the PPRP and manages the activities of all participants. The SSHAC Level 3 assessment process and implementation is discussed in depth in Chapter 2 of this report.

Each of the methodology steps in the SSHAC guidelines (Budnitz, 1997) was addressed adequately during the CEUS SSC Project. Furthermore, the project developed a number of enhancements to the process steps for conducting a SSHAC Study Level 3 project. For example, the SSHAC guidelines call for process steps that include developing a preliminary assessment model, calculating hazard using that model in order to identify the key issues, and finalizing the model in light of the feedback provided from the hazard calculations and sensitivity analyses. Because of the regional nature of the project and the multitude of assessments required, four rounds of model-building and three rounds of feedback were conducted. These activities ensured that all significant issues and uncertainties were identified and that the appropriate effort was devoted to the issues of most significance to the hazard results. A comparison of the activities conducted during the CEUS SSC Project with those recommended in the SSHAC guidelines themselves (Section 2.6) led to the conclusion that the current standards of practice have been met for a SSHAC Study Level 3 process—both those that are documented in the SSHAC report and those that resulted from precedents set by projects conducted since the SSHAC report was issued.

The catalog of past earthquakes that have occurred in a region is an important source of information for the quantification of future seismic hazards. This is particularly true in stable continental regions (SCRs) such as the CEUS where the causative mechanisms and structures for the occurrence of damaging earthquakes are generally poorly understood, and the rates of crustal deformation are low such that surface and near-surface indications of stresses in the crust and the buildup and release of crustal strains are difficult to quantify. Because the earthquake catalog is used in the characterization of the occurrence of future earthquakes in the CEUS, developing an updated earthquake catalog for the study region was an important focus of the CEUS SSC Project. The specific goals for earthquake catalog development and methods used to attain those goals are given in Chapter 3.

The earthquake catalog development consists of four main steps: catalog compilation, assessment of a uniform size measure to apply to each earthquake, identification of dependent earthquakes (catalog declustering), and assessment of the completeness of the catalog as a function of location, time, and earthquake size. An important part of the catalog development process was review by seismologists with extensive knowledge and experience in catalog compilation. The result is an earthquake catalog covering the entire study region for the period from 1568 through the end of 2008. Earthquake size is defined in terms of the moment magnitude scale (Hanks and Kanamori, 1979), consistent with the magnitude scale used in modern ground-motion prediction equations (GMPEs) for CEUS earthquakes. A significant contribution of the CEUS SSC Project is the work conducted to develop an updated and consistent set of conversion relationships between various earthquake size measures (instrumental magnitudes and intensity) and moment magnitude.

The conceptual SSC framework described in Chapter 4 was developed early in the CEUS SSC Project in order to provide a consistent approach and philosophy to SSC by the TI Team. This framework provides the basic underpinnings of the SSC model developed for the project, and it led to the basic structure and elements of the master logic tree developed for the SSC model. In considering the purpose of the CEUS SSC Project, the TI Team identified three attributes that are needed for a conceptual SSC framework:

1. A systematic, documented approach to treating alternatives using logic trees, including alternative conceptual models for future spatial distributions of seismicity (e.g., stationarity); alternative methods for expressing the future temporal distribution of seismicity (e.g., renewal models, Poisson models); and alternative data sets for characterizing seismic sources (e.g., paleoseismic data, historical seismicity data).
2. A systematic approach to identifying applicable data for the source characterization, evaluating the usefulness of the data, and documenting the consideration given to the data by the TI Team.
3. A methodology for identifying seismic sources based on defensible criteria for defining a seismic source, incorporating the lessons learned in SSC over the past two decades, and identifying the range of approaches and models that can be shown to be significant to hazard.

Each of these needs was addressed by the methodology used in the project. For example, the need for a systematic approach to identifying and evaluating the data and information that underlie the source characterization assessments was met by the development of Data Summary

and Data Evaluation tables. These tables were developed for each seismic source to document the information available at the time of the CEUS SSC assessments (the Data Summary tables) and the way those data were used in the characterization process (the Data Evaluation tables). Given the evolution of approaches to identifying seismic sources, it is appropriate to provide a set of criteria and the logic for their application in the CEUS SSC Project. In the project, unique seismic sources are defined to account for distinct differences in the following criteria:

- Earthquake recurrence rate
- Maximum earthquake magnitude (M<sub>max</sub>)
- Expected future earthquake characteristics (e.g., style of faulting, rupture orientation, depth distribution)
- Probability of activity of tectonic feature(s)

Rather than treat these criteria as operating simultaneously or without priority, the CEUS SSC methodology works through them sequentially. Further, because each criterion adds complexity to the seismic source model, it is applied only if its application would lead to hazard-significant changes in the model. In this way, the model becomes only as complex as required by the available data and information.

The CEUS SSC master logic tree is tied to the conceptual SSC framework that establishes the context for the entire seismic source model. The master logic tree depicts the alternative interpretations and conceptual models that represent the range of defensible interpretations, and the relative weights assessed for the alternatives. By laying out the alternatives initially, the subsequent detailed source evaluations were conducted within a framework that ensures consistency across the sources. Important elements of the master logic tree are as follows:

- Representation of the sources defined based on paleoseismic evidence for the occurrence of repeated large-magnitude earthquakes (RLMEs, defined as two or more earthquakes with  $M \geq 6.5$ ).
- Alternatives to the spatial distribution of earthquakes based on differences in maximum magnitudes (M<sub>max</sub> zones approach).
- Representation of uncertainty in spatial stationarity of observed seismicity based on smoothing of recurrence parameters.
- Representation of possible differences in future earthquake characteristics (e.g., style, seismogenic thickness, and orientation of ruptures), which lead to definition of seismotectonic zones in the logic tree (seismotectonic zones approach).

The methodologies used by the project to make the SSC assessments are discussed in Chapter 5. The heart of any SSC model for PSHA is a description of the future spatial and temporal distribution of earthquakes. Continued analysis of the historical seismicity record and network monitoring by regional and local seismic networks has led to acceptance within the community that the general spatial patterns of observed small- to moderate-magnitude earthquakes provide predictive information about the spatial distribution of future large-magnitude earthquakes. The analyses leading to this conclusion have focused on whether the observed patterns of earthquakes

have varied through time; therefore, in effect, this is an assessment of uncertainty in whether small- to moderate-magnitude earthquakes have been relatively stationary through time. However, the available data on larger-magnitude earthquakes and their relationship to the spatial distribution of smaller earthquakes based on the observed record are quite limited. These data are not sufficient to allow confidence in the predictions generated by empirical spatial models. For this reason, geologic and geophysical data are needed to specify the locations of future earthquakes in addition to the observed patterns of seismicity.

Detailed studies in the vicinity of large historical and instrumental earthquakes, and liquefaction phenomena associated with them, coupled with field and laboratory studies of geotechnical properties, are leading to a stronger technical basis for (1) placing limits on the locations of paleoearthquakes interpreted by the distribution of liquefaction phenomena and (2) defining their magnitudes. In some cases, the paleoseismic evidence for RLMEs is compelling, and the TI Team has included the RLME source in the SSC model. The locations of RLME sources notwithstanding, the spatial distribution of distributed seismicity sources has advanced in PSHA largely because of the assumption of spatial stationarity, and the SSC and hazard community uses approaches to “smooth” observed seismicity to provide a map that expresses the future spatial pattern of recurrence rates. The CEUS SSC model is based largely on the assumption, typical in PSHA studies, that spatial stationarity of seismicity is expected to persist for a period of approximately 50 years.

Estimating  $M_{max}$  in SCRs such as the CEUS is highly uncertain despite considerable interest and effort by the scientific community over the past few decades.  $M_{max}$  is defined as the upper truncation point of the earthquake recurrence curve for individual seismic sources, and the typically broad distribution of  $M_{max}$  for any given source reflects considerable epistemic uncertainty. Because the maximum magnitude for any given seismic source in the CEUS occurs rarely relative to the period of observation, the use of the historical seismicity record provides important but limited constraints on the magnitude of the maximum event. Because of the independent constraints on earthquake size, those limited constraints are used to estimate the magnitudes of RLME. For distributed seismicity source zones, two approaches are used to assess  $M_{max}$ : the Bayesian approach and the Kijko approach. In the Bayesian procedure (Johnston et al., 1994), the prior distribution is based on the magnitudes of earthquakes that occurred worldwide within tectonically analogous regions. As part of the CEUS SSC Project, the TI Team pursued the refinement and application of the Bayesian  $M_{max}$  approach because it provides a quantitative and repeatable process for assessing  $M_{max}$ .

The TI Team also explored alternative approaches for the assessment of  $M_{max}$  that provide quantitative and repeatable results, and the team identified the approach developed by Kijko (2004) as a viable alternative. While the Kijko approach requires fewer assumptions than the Bayesian approach in that it uses only the observed earthquake statistics for the source, this is offset by the need for a relatively larger data sample in order to get meaningful results. Both approaches have the positive attribute that they are repeatable given the same data and they can be readily updated given new information. The relative weighting of the two approaches for inclusion in the logic tree is source-specific, a function of the numbers of earthquakes that are present within the source upon which to base the  $M_{max}$  assessment: sources with fewer earthquakes are assessed to have little or no weight for the Kijko approach, while those with

larger numbers of events are assessed higher weight for the Kijko approach. In all cases, because of the stability of the Bayesian approach and the preference for “analogue” approaches within the larger technical community, the Bayesian approach is assessed higher weight than the Kijko approach for all sources.

A major effort was devoted to updating the global set of SCR earthquakes and to assessing statistically significant attributes of those earthquakes following the approach given in Johnston et al. (1994). In doing so, it was found that the only significant attribute defining the prior distribution is the presence or absence of Mesozoic-or-younger extension. The uncertainty in this assessment is reflected in the use of two alternative priors: one that takes into account the presence or absence of crustal domains having this attribute, and another that combines the entire CEUS region as a single SCR crustal domain with a single prior distribution. The use of the Bayesian—and Kijko—approach requires a definition of the largest observed magnitude within each source, and this assessment, along with the associated uncertainty, was incorporated into the Mmax distributions for each seismic source. Consideration of global analogues led to the assessment of an upper truncation to all Mmax distributions at 8¼ and a lower truncation at 5½. The broad distributions of Mmax for the various seismic source zones reflect the current epistemic uncertainty in the largest earthquake magnitude within each seismic source.

The CEUS SSC model is based to a large extent on an assessment that spatial stationarity of seismicity will persist for time periods of interest for PSHA (approximately the next 50 years). Stationarity in this sense does not mean that future locations and magnitudes of earthquakes will occur exactly where they have occurred in the historical and instrumental record. Rather, the degree of spatial stationarity varies as a function of the type of data available to define the seismic source. RLME sources are based largely on paleoseismic evidence for repeated large-magnitude ( $M \geq 6.5$ ) earthquakes that occur in approximately the same location over periods of a few thousand years. On the other hand, patterns of seismicity away from the RLME sources within the Mmax and seismotectonic zones are defined from generally small- to moderate-magnitude earthquakes that have occurred during a relatively short (i.e., relative to the repeat times of large events) historical and instrumental record. Thus, the locations of future events are not as tightly constrained by the locations of past events as for RLME sources. The spatial smoothing operation is based on calculations of earthquake recurrence within one-quarter-degree or half-degree cells, with allowance for “communication” between the cells. Both *a*- and *b*-values are allowed to vary, but the degree of variation has been optimized such that *b*-values vary little across the study region.

The approach used to smooth recurrence parameters is a refinement of the penalized-likelihood approach used in EPRI-SOG (EPRI, 1988), but it is designed to include a number of elements that make the formulation more robust, realistic, and flexible. These elements include the reformulation in terms of magnitude bins, the introduction of magnitude-dependent weights, catalog incompleteness, the effect of Mmax, spatial variation of parameters within the source zone, and the prior distributions of *b*. A key assessment made by the TI Team was the weight assigned to various magnitude bins in the assessment of smoothing parameters (Cases A, B, and E). This assessment represents the uncertainty in the interpretation that smaller magnitudes define the future locations and variation in recurrence parameters. Appropriately, the penalized-likelihood approach results in higher spatial variation (less smoothing) when the low-magnitude

bins are included with high weight, and much less variation (higher smoothing) in the case where the lower-magnitude bins are given low or zero weight. The variation resulting from the final set of weights reflects the TI Team's assessment of the epistemic uncertainty in the spatial variation of recurrence parameters throughout the SSC model.

The earthquake recurrence models for the RLME sources are somewhat simpler than those for distributed seismicity sources because the magnitude range for individual RLMEs is relatively narrow and their spatial distribution is limited geographically such that spatial variability is not a concern. This limits the problem to one of estimating the occurrence rate in time of a point process. The data that are used to assess the occurrence rates are derived primarily from paleoseismic studies and consist of two types: data that provide estimated ages of the paleoearthquakes such that the times between earthquakes can be estimated, and data that provide an estimate of the number of earthquakes that have occurred after the age of a particular stratigraphic horizon. These data are used to derive estimates of the RLME occurrence rates and their uncertainty.

The estimation of the RLME occurrence rates is dependent on the probability model assumed for the temporal occurrence of these earthquakes. The standard model applied for most RLME sources in this study is the Poisson model, in which the probability of occurrence of an RLME in a specified time period is completely characterized by a single parameter,  $\lambda$ , the rate of RLME occurrence. The Poisson process is “memoryless”—that is, the probability of occurrence in the next time interval is independent of when the most recent earthquake occurred, and the time between earthquakes is exponentially distributed with a standard deviation equal to the mean time between earthquakes. For two RLME sources (Reelfoot Rift–New Madrid fault system and the Charleston source), the data are sufficient to suggest that the occurrence of RLMEs is more periodic in nature (the standard deviation is less than the mean time between earthquakes). For these RLME sources a simple renewal model can also be used to assess the probability of earthquake occurrence. In making an estimate of the probability of occurrence in the future, this model takes into account the time that has elapsed since the most recent RLME occurrence.

The CEUS SSC model has been developed for use in future PSHAs. To make this future use possible, the SSC model must be combined with a GMC model. At present, the GMPEs in use for SCRs such as the CEUS include limited information regarding the characteristics of future earthquakes. In anticipation of the possible future development of GMPEs for the CEUS that will make it possible to incorporate similar types of information, a number of characteristics of future earthquakes in the CEUS are assessed. In addition to characteristics that might be important for ground motion assessments, there are also assessed characteristics that are potentially important to the modeling conducted for hazard analysis. Future earthquake characteristics assessed include the tectonic stress regime, sense of slip/style of faulting, strike and dip of ruptures, seismogenic crustal thickness, fault rupture area versus magnitude relationship, rupture length-to-width aspect ratio, and relationship of ruptures to source boundaries.

Chapters 6 and 7 include discussions of the seismic sources that are defined by the Mmax zones and the seismotectonic zones branches of the master logic tree. Because of convincing evidence for their existence, both approaches include RLME sources. The rarity of repeated earthquakes relative to the period of historical observation means that evidence for repeated events comes

largely from the paleoseismic record. By identifying the RLMEs and including them in the SSC model, there is no implication that the set of RLMEs included is in fact the total set of RLMEs that might exist throughout the study region. This is because the presently available studies that locate and characterize the RLMEs have been concentrated in certain locations and are not systematic across the entire study region. Therefore, the evidence for the existence of the RLMEs is included in the model where it exists, but the remaining parts of the study region are also assessed to have significant earthquake potential, which is evidenced by the inclusion of moderate-to-large magnitudes in the Mmax distributions for every Mmax zone or seismotectonic zone.

In Chapter 6, each RLME source is described in detail by the following factors: (1) evidence for temporal clustering, (2) geometry and style of faulting, (3) RLME magnitude, and (4) RLME recurrence. The descriptions document how the data have been evaluated and assessed to arrive at the various elements of the final SSC model, including all expressions of uncertainty. The Data Summary and Data Evaluation tables (Appendices C and D) complement the discussions in the text, documenting all the data that were considered in the course of data evaluation and integration process for each particular seismic source.

Alternative models for the distributed seismicity zones that serve as background zones to the RLME sources are either Mmax zones or seismotectonic zones. The Mmax zones are described in Chapter 6 and are defined according to constraints on the prior distributions for the Bayesian approach to estimating Mmax. The seismotectonic zones are described in Chapter 7 and are identified based on potential differences in Mmax as well as future earthquake characteristics. Each seismotectonic zone in the CEUS SSC model is described according to the following attributes: (1) background information from various data sets; (2) bases for defining the seismotectonic zone; (3) basis for the source geometry; (4) basis for the zone Mmax (e.g., largest observed earthquake); and (5) future earthquake characteristics. Uncertainties in the seismotectonic zone characteristics are described and are represented in the logic trees developed for each source.

For purposes of demonstrating the CEUS SSC model, seismic hazard calculations were conducted at seven demonstration sites throughout the study region, as described in Chapter 8. The site locations were selected to span a range of seismic source types and levels of seismicity. The results from the seismic hazard calculations are intended for scientific use to demonstrate the model, and they should not be used for engineering design. Mean hazard results are given for a range of spectral frequencies (PGA, 10 Hz, and 1 Hz) and for a range of site conditions. All calculations were made using the EPRI (2004, 2006) ground-motion models such that results could be compared to understand the SSC effects alone. Sensitivity analyses were conducted to provide insight into the dominant seismic sources and the important characteristics of the dominant seismic source at each site. The calculated mean hazard results are compared with the results using the SSC model from the 2008 U.S. Geological Survey national seismic hazard maps and the SSC model from the Combined Operating License applications for new nuclear power reactors. The hazard results using the CEUS SSC model given in Chapter 8 are reasonable and readily understood relative to the results from other studies, and sensitivities of the calculated hazard results can be readily explained by different aspects of the new model. The TI Team concludes that the SSC model provides reasonable and explainable calculated seismic hazard

results, and the most important aspects of the SSC model to the calculated hazard (e.g., recurrence rates of RLME sources, recurrence parameters for distributed seismicity sources,  $M_{max}$ ) and their uncertainties have all been appropriately addressed.

Presumably, the GMC model input to the PSHA calculations will be replaced in the future by the results of the ongoing NGA-East project. The calculated hazard at the demonstration sites in Chapter 8 comes from the regional CEUS SSC model and does not include any local refinements that might be necessary to account for local seismic sources. Depending on the regulatory guidance that is applicable for the facility of interest, additional site-specific studies may be required to provide local refinements to the model.

To assist future users of the CEUS SSC model, Chapter 9 presents a discussion on the use of the model for PSHA. The basic elements of the model necessary for hazard calculations are given in the Hazard Input Document (HID). This document provides all necessary parameter values and probability distributions for use in a modern PSHA computer code. The HID does not, however, provide any justification for the values, since that information is given in the text of this report.

Chapter 9 also describes several simplifications to seismic sources that can be made to increase efficiency in seismic hazard calculations. These simplifications are recommended on the basis of sensitivity studies of alternative hazard curves that represent a range of assumptions on a parameter's value. Sensitivities are presented using the test sites in this study. For applications of the seismic sources from this study, similar sensitivity studies should be conducted for the particular site of interest to confirm these results and to identify additional simplifications that might be appropriate. For the seismic sources presented, only those parameters that can be simplified are discussed and presented graphically. The sensitivity studies consisted of determining the sensitivity of hazard to logic tree branches for each node of the logic tree describing that source. The purpose was to determine which nodes of the logic tree could be collapsed to a single branch in order to achieve more efficient hazard calculations without compromising the accuracy of overall hazard results.

Finally, this report provides a discussion of the level of precision that is associated with seismic hazard estimates in the CEUS. This discussion addresses how seismic hazard estimates might change if the analysis were repeated by independent experts having access to the same basic information (geology, tectonics, seismicity, ground-motion equations, site characterization). It also addresses how to determine whether the difference in hazard would be significant if this basic information were to change and that change resulted in a difference in the assessed seismic hazard. This analysis was performed knowing that future data and models will continue to be developed and that a mechanism for evaluating the significance of that information is needed. Based on the precision model evaluated, if an alternative assumption or parameter is used in a seismic hazard study, and it potentially changes the calculated hazard (annual frequency of exceedence) by less than 25 percent for ground motions with hazards in the range  $10^{-4}$  to  $10^{-6}$ , that potential change is within the level of precision at which one can calculate seismic hazard. It should be noted, however, that a certain level of precision does not relieve users from performing site-specific studies to identify potential capable seismic sources within the site region and vicinity as well as to identify newer models and data. Also, this level of precision does not relieve users from fixing any errors that are discovered in the CEUS SSC model as it is

---

*Executive Summary*

implemented for siting critical facilities. In addition, NRC has not defined a set value for requiring or not requiring siting applicants to revise or update PSHAs.

Included in the report are appendices that summarize key data sets and analyses: the earthquake catalog, the Data Summary and Data Evaluation tables, the paleoliquefaction database, the HID, and documentation important to the SSHAC process. These data and analyses will assist future users of the CEUS SSC model in the implementation of the model for purposes of PSHA. The entire report and database will be provided on a website after the Final Project Report is issued.

The TI Team, Project Manager, and Sponsors determined the approach for quality assurance on the CEUS SSC Project in 2008, taking into account the SSHAC assessment process and national standards. The approach was documented in the CEUS SSC Project Plan dated June 2008 and discussed in more detail in the CEUS SSC Report (Appendix L). Beyond the assurance of quality arising from the external scientific review process, it is the collective, informed judgment of the TI Team (via the process of evaluation and integration) and the concurrence of the PPRP (via the participatory peer review process), as well as adherence to the national standard referred to in Appendix L, that ultimately lead to the assurance of quality in the process followed and in the products that resulted from the SSHAC hazard assessment framework.

October 24, 2011

Cliff Munson  
Senior Technical Advisor  
Office of New Reactors  
U.S. Nuclear Regulatory Commission  
Washington, DC 20555

Robert Roche  
Project Manager  
Office of Nuclear Regulatory Research  
U.S. Nuclear Regulatory Commission  
Washington, DC 20555

Richard H. Lagdon, Jr.  
Chief of Nuclear Safety  
Office of the Under Secretary for Nuclear  
Security, S-5  
U.S. Department of Energy  
1000 Independence Avenue SW  
Washington, DC 20585

Thomas P. Miller  
Senior Technical Advisor  
Office of Nuclear Energy, NE-72/GTN  
U.S. Department of Energy  
1000 Independence Avenue SW  
Washington, DC 20585

Jeffrey F. Hamel  
Advanced Nuclear Technology Program  
Manager  
Electric Power Research Institute  
3420 Hillview Avenue  
Palo Alto, CA 94304

Gentlemen:

Reference: *Central and Eastern United States Seismic Source Characterization for Nuclear Facilities Project: Participatory Peer Review Panel Final Report*

## **Introduction**

This letter constitutes the final report of the PPRP<sup>1</sup> (“the Panel”) for the *Central and Eastern United States Seismic Source Characterization for Nuclear Facilities Project* (the “CEUS SSC Project” or “the Project”). The eight Panel members (Jon P. Ake, Walter J. Arabasz, William J. Hinze, Annie M. Kammerer, Jeffrey K. Kimball, Donald P. Moore, Mark D. Petersen, J. Carl Stepp) participated in the Project in a manner fully consistent with the SSHAC Guidance.<sup>2</sup> The Panel was actively engaged in all phases and activities of the Project’s implementation, including final development of the Project Plan and planning of the evaluation and integration activities, which are the core of the SSHAC assessment process.

---

<sup>1</sup> Participatory Peer Review Panel

<sup>2</sup> Budnitz, R. J., G. Apostolakis, D. M. Boore, L. S. Cluff, K. L. Coppersmith, C. A. Cornell, and P. A. Morris, 1997. *Recommendations for Probabilistic Seismic Hazard Analysis: Guidance on Uncertainty and the Use of Experts* (known as the “Senior Seismic Hazard Analysis Committee Report,” or the “SSHAC Guidance”). NUREG/CR-6372, U. S. Nuclear Regulatory Commission. TIC; 235076. Washington, DC.

The Panel's involvement, described more fully later in this letter, also included review of analyses performed by the Project to support the evaluation and integration processes, review of interim evaluation and integration products, and review of the interim draft project report and the final project report. Additionally, panel members participated in specific analyses as resource experts, and panel members were observers in or participated as resource experts in eight of the eleven Technical Integrator Team (TI Team) working meetings held to implement the integration phase of the assessment process. We want to express our appreciation for the opportunity to participate in the CEUS SSC Project in this way.

In the remainder of this letter we provide our observations and conclusions on key elements of the project implementation process, and we summarize our reviews of the draft and final project reports. As we explain in our comments, assurance that the center, body, and range of the technically-defensible interpretations ("CBR of the TDI")<sup>3</sup> have been properly represented in the CEUS SSC Model fundamentally comes from implementing the structure and rigor of the SSHAC Guidance itself. We are aware that the SSHAC Guidance is accepted by the Nuclear Regulatory Commission and the Department of Energy for developing seismic hazard models that provide reasonable assurance, consistent with the seismic safety decision-making practices of these agencies, of compliance with their seismic safety policies and regulatory requirements. For these reasons, we describe aspects of the SSHAC Guidance to provide context for our observations and conclusions.

### **Project Plan: Conformity to the SSHAC Assessment Process**

The SSHAC Guidance recognizes that observed data, available methods, models, and interpretations all contain uncertainties. These uncertainties lead to alternative scientific analyses and interpretations. In other words, experts in the broad technical community do not hold a single interpretation. Accepting this scientific situation, the SSHAC assessment process is designed to engage the scientific community in an orderly assessment of relevant data, methods, models, and interpretations that constitute current scientific knowledge as the basis for development of a seismic hazard model that represents the CBR of the TDI.

The assessment process is carried out by means of two main activities: *evaluation* and *integration*.<sup>4</sup> In implementation, the evaluation activities are structured to inform the integration activities. The evaluations are carried out by means of workshops in which the TI Team engages proponents of alternative interpretations that represent the range of relevant current community knowledge. Resource experts in the various relevant data sets are also engaged. The workshops have the dual purposes of, first, evaluating the degree to which alternative interpretations are supported by observed data and, second, defining uncertainties in the degree to which the interpretations are defensible, given the observed data. Integration is carried out by individual evaluator experts or evaluator expert teams (Level 4 process) or by a Technical Integrator (TI) Team (Level 3 process) who, informed by the evaluation activities, characterize the range of

---

<sup>3</sup> See Section 2.1 in the CEUS SSC Final Report for discussion of concepts relating to the center, body, and range of the "technically-defensible interpretations" vs. the center, body, and range of the "informed technical community."

<sup>4</sup> For an excellent discussion of this two-stage process, see *Practical Implementation Guidelines for SSHAC Level 3 and 4 Hazard Studies*, USNRC NUREG-XXXX, Draft for Review, Office of Nuclear Regulatory Research, May 2011.

defensible alternative interpretations in an integrated hazard model and assess the scientific uncertainty distribution. Based on our review of the Project Plan and our subsequent discussions with the Project Team, we concurred that the Plan conformed with the SSHAC Guidance, incorporating lessons learned from fourteen years experience using the Guidance, and that the planned implementation was structured to properly carry out the SSHAC assessment process for development of the CEUS SSC Model.

### **SSHAC Level 3 Assessment Process**

The SSHAC Guidance describes implementation processes for four levels of assessment depending on the scientific complexity of the assessment and the intended use of the assessed hazard model. For an assessment such as the regional SSC model for the Central and Eastern United States, which will be used at many sites for making safety and licensing decisions for nuclear facilities, the SSHAC Guidance recommends using an assessment Level 3 or Level 4.

There are process differences between a Level 3 and Level 4 implementation, but the objective is the same: to obtain from multiple proponent experts information that supports an informed assessment of the range of existent relevant interpretations and associated uncertainties that together represent current community knowledge and to perform an informed assessment of the CBR of the TDI. We understand that within the SSHAC assessment process “technically defensible” means that observed data are sufficient to support evaluation of the interpretation and the corresponding uncertainty.

In a Level 4 assessment process a TI Team facilitates the assessment, identifying and engaging proponent and resource experts, performing supporting analyses, and conducting knowledge evaluation workshops and assessment integration working meetings. Multiple experts or teams of experts perform as evaluators of the range of existent interpretations and as integrators of the hazard model. The individual evaluator experts or evaluator expert teams take ownership of their individual or team assessments. In a Level 3 assessment all of these activities are consolidated under a single TI Team consisting of a TI Lead, multiple evaluator experts representing the scope of required scientific expertise, and experienced data and hazard analysts.

As we noted earlier in this report, assurance that the CBR of the TDI is properly represented in a hazard model comes from rigorously implementing the SSHAC assessment process itself. We note that an important lesson learned from multiple implementations of the SSHAC Guidance over the past fourteen years is that the Level 3 and Level 4 assessment processes provide comparably high assurance that the relevant scientific knowledge and the community uncertainty distribution are properly assessed and represented in the hazard model. The Level 3 assessment is significantly more integrated and cohesive and is more efficient to implement. These considerations led us to endorse use of the Level 3 assessment for implementation of the CEUS SSC Project in our Workshop No. 1 review letter. During the course of the Project we observed that the higher level of cohesiveness inherent in the Level 3 assessment process leads to significantly improved communication, facilitating the experts’ performance of their technical work.

## **Overall Project Organization**

A complex project with multiple sponsors such as the CEUS SSC Project cannot be successful unless it is well organized and energetically managed so that the various participants understand the interconnectedness of their activities and perform their technical work as a cohesive group. In this regard the adopted project management structure allowed the Project Manager to provide integrated overall project leadership, manage the database development activities, and effectively maintain communication with the PPRP and project sponsors while allowing TI Team lead to concentrate on the structural and technical activities of the assessment as the Project unfolded. We conclude that the project organization was effective overall and particularly so with regard to facilitating the TI Team's implementation of the assessment process.

## **Implementing the SSHAC Level 3 Assessment Process**

Irrespective of the level of implementation, evaluation and integration are the main activities of a SSHAC assessment. The evaluation activities aim to identify and evaluate all relevant available data, models, methods, and scientific interpretations as well as uncertainties associated with each of them. The integration activities, informed by the evaluations, aim to represent the CBR of the TDI in a fully integrated SSC model.

### ***Evaluation***

Consistent with the SSHAC Guidance the evaluation phase of the CEUS SSC project accomplished a comprehensive evaluation of the data, models, methods, and scientific interpretations existent in the larger technical community that are relevant to the SSC model. In significant part the process was carried out in three structured workshops, each focusing on accomplishing a specific step in the evaluation process.

The first workshop (WS-1) focused on evaluations of relevant geological, geophysical, and seismological datasets (including data quality and uncertainties) and on identification of hazard-significant data and hazard-significant SSC assessment issues. It became clear that a number of issues relating to the earthquake catalog, the paleoliquefaction data set, the potential-field geophysical data, updating procedures for assessing maximum earthquake magnitude, and development of procedures for assessing earthquake recurrence would require focused analyses. These analyses were appropriately carried out within the TI Team working interactively with appropriate resource experts recognized by the larger scientific and technical community.

WS-2 focused on evaluations of the range of alternative scientific interpretations, methods, and models within the larger scientific community and on corresponding uncertainties. WS-3 focused on evaluations of hazard feedback derived at seven representative test locations using a preliminary CEUS SSC model. Specifically, the workshop focused on the identification of the key issues of most significance to completing the SSC model assessment.

Experience has shown that evaluations to gain understanding of the quality of various data sets and uncertainties associated with them are essential for fully informing an SSC assessment. We observed that in WS-1 resource experts for the various data sets did a high-quality job of describing the data sets and giving their perspective about the data quality and associated uncertainties. We conclude that the understanding of data quality and uncertainties gained in WS-1 together with continued interactions between the TI Team and data resource experts

significantly informed the TI Team’s evaluations. The TI Team’s evaluations of the data quality and uncertainties are well documented in the innovative “Data Summary Tables” and “Data Evaluation Tables” included in the Project Report. Importantly, the TI Team continued to effectively engage data resource experts in productive analyses of potential-field geophysical data, the earthquake catalog, development of the paleoearthquake data set (including an integrated assessment of the paleoliquefaction data in order to extend the earthquake catalog), the development of methods for assessing maximum earthquakes, and the development of earthquake recurrence analyses. All of these focused analyses strongly informed the assessment process. Moreover, documentation of the analyses resulted in stand-alone products of the Project that will serve future users of the CEUS SSC Model.

The compilation and evaluation of potentially relevant methods, models, and alternative scientific interpretations representing the community knowledge and corresponding uncertainties must be considered the core process activity of any SSHAC assessment. This step was largely carried out in WS-2. Success in defining the community knowledge depends on fully engaging proponent experts representing the range of methods, models, and interpretations existent at the time. Full engagement means that the proponent experts completely and clearly describe their interpretations and the data that support them and provide their individual evaluations of corresponding uncertainties. We observed that the actions taken by the Project and TI Team to explain the workshop goals and to guide participants toward meeting those goals was very productive. We conclude that the workshop was highly successful in meeting the stated goals and that it fully met the expectation of the SSHAC Guidance with respect to evaluating the range of alternative scientific interpretations. The discussions during the workshop and between the TI Team and Panel following the workshop evolved the “SSC Framework” concept, which provided transparent criteria that framed the TI Team’s systematic identification and assessment of seismic sources throughout the CEUS.

Feedback from hazard calculations and sensitivity analyses is an important step in a SSHAC assessment to understand the importance of elements of the model and inform the final assessments. For development of a regional SSC model to be used for site-specific probabilistic seismic hazard analyses (PSHAs) at many geographically distributed sites, feedback based on the preliminary model is particularly important. Following WS-2 a preliminary SSC model termed “the SSC sensitivity model,” was developed and used for hazard sensitivity calculations that were evaluated in WS-3. While the SSC sensitivity model was clearly preliminary, the evaluation of sensitivity results that took place in WS-3 provided important feedback for completing analyses and for supporting the TI Team’s development of the preliminary CEUS SSC model. The Panel was able to review the preliminary model and provide feedback in a subsequent project briefing meeting on March 24, 2010.

Together the three workshops provided the TI Team interactions with the appropriate range of resource and proponent experts. These experts were carefully identified to present, discuss, and debate the data, models, and methods that together form the basis for assuring that the CBR of the TDI have been properly represented in the hazard model. Experts representing academia, government, and private industry participated. The TI Team also reached out to a wide range of experts as they developed the database and performed the integration activities to develop the SSC model. The Panel participated throughout this process, and is satisfied that the TI Team fully engaged appropriate experts to accomplish the goals of a SSHAC Guidance.

### ***Integration***

Consistent with the SSHAC Guidance, integration is the process of assessing the CBR of the TDI and representing the assessment in the SSC model. Informed by the evaluation process, the integration process includes representation of the range of defensible methods, models, and interpretations of the larger technical community together with new models and methods developed by analyses during the evaluation and integration process.

For the CEUS SSC Project, development of the earthquake catalog, methods for assessing and representing maximum earthquake magnitudes, and methods for earthquake recurrence assessment continued during the integration process. The Panel reviewed all the analyses at various stages of development and provided comments and recommendations. The TI Team performed the integration process by means of eleven working meetings. Members of the Panel participated in most of these working meetings as observers or resource experts. The full Panel participated in the discussions during both feedback meetings and provided formal comments and recommendations following the meetings. We observed that the integration process was thorough and that it acceptably complied with the SSHAC Guidance. Based on our participation and observations we conclude that the integrated CEUS SSC Model appropriately represents the center, body, and range of current methods, models and technically defensible interpretations.

### **PPRP Engagement**

Consistent with the SSHAC Guidance, the Panel was fully engaged in peer-review interactions with the TI Team and the Project Manager of the CEUS SSC Project throughout the entire project period—from development of the Project Plan in early to mid 2008 through production of the Final Project Report in mid to late 2011.<sup>5</sup> The Panel provided both written and oral peer-review comments on both technical and process aspects at many stages of the Project's evolution. Key PPRP activities, leading up to this final report, have included:

- Review of the Project Plan.
- Formulation of a PPRP implementation plan, specifically for the CEUS SSC Project, to ensure adherence to the general guidance provided by SSHAC and NUREG-1563 for the scope and goals of a PPRP review.
- Involvement in *each* of the three Project workshops, including advising in the planning stage; participating collectively as a review panel during the workshop (and individually as resource experts when requested by the TI Team), providing timely comments on technical and process issues; and submitting a written report of the Panel's observations and recommendations following each workshop.
- Development and implementation of a process, together with the TI Team, to document the resolution of recommendations made in PPRP formal communications.
- Participation as observers (and occasionally as resource experts when requested by the TI Team) in eight of the TI Team's 11 working meetings.
- Peer-review and written comments, including several informal reports, on the TI Team's intermediate work products, particularly early versions of the CEUS SSC Model.

---

<sup>5</sup> See CEUS SSC Final Report: Section 2.5, Table 2.2-1, and Appendix I

- Direct interaction with the TI Team and Project Manager in more than 20 teleconferences and four face-to-face briefings—in addition to the three workshops and eight working meetings of the TI Team noted above.
- Extensive, critical peer-review of the Project’s 2010 Draft Report and 2011 Final Report.

The Panel, collectively and individually, fully understood the SSHAC Guidance for a structured participatory peer review and the requirements for a Level 3 assessment process; had full and frequent access to information and interacted extensively with the TI Team and Project Manager throughout the entire project; provided peer-review comments at numerous stages; and, as documented within the Final Project Report, was fully engaged to meet its peer-review obligations in an effective way.

## **Project Report**

The SSHAC Guidance makes clear that adequate documentation of process and results is crucial for their understanding and use by others in the technical community, by later analysis teams, and by the project sponsors. The Panel understood what was needed to conform to the SSHAC requirements, and it was committed to ensuring that the documentation of technical details associated with the CEUS SSC Model in the Project Report was clear and complete. The Panel was equally committed to ensuring the transparency of process aspects of the project, both in implementation and in description in the Project Report.

The Panel provided lengthy compilations of review comments (see Appendix I of the Project Report) for both the 2010 Draft Report and the 2011 Final Report. These included hundreds of comments, categorized as general, specific, relating to clarity and completeness, or editorial. The massive amount of detail provided by the TI Team in the Project Report and the intensiveness of the Panel’s review comments both reflect great diligence and a mutual understanding by the TI Team and the PPRP of the thoroughness and high quality of documentation expected in the Project Report.

The Project Manager and the TI Lead provided review criteria to the Panel for both the draft and final versions of the Project Report. The criteria for reviewing the Draft Report<sup>6</sup> covered the range of technical and process issues consistent with requirements of the SSHAC Guidance, including draft implementation guidance (see footnote #4). Key criteria, among others, include sufficiency of explanatory detail; adequate consideration of the full range of data, models, and methods—and the views of the larger technical community; adequate justification of the data evaluation process, logic-tree weights, and other technical decisions; proper treatment of uncertainties; and conformance to a SSHAC Level 3 assessment process. To be clear, the PPRP is charged with judging the adequacy of the documented *justification* for the CEUS SSC Model and its associated logic-tree weights. The TI Team “owns” the Model and logic-tree weights.

Criteria for reviewing the Final Report focused on reaching closure to comments made on the Draft Report and ensuring that no substantive issues remained unresolved. To that end, among its many review comments on the Final Report the Panel identified “mandatory” comments, which the TI Team was required to address in the final version of the Project Report.

---

<sup>6</sup> See PPRP report dated October 4, 2010, in Appendix I of CEUS SSC Final Report

The Panel made thorough, extensive efforts in its documented reviews of the 2010 Draft Report and the 2011 Final Report (as well as in many related interactions with the TI Team) to ensure a high-quality Project Report that fully meets SSHAC requirements for clear, complete, and transparent documentation of all aspects of the CEUS SSC Project. We are pleased to confirm that implementation of the CEUS SSC Project fully conformed with the SSHAC Guidance and that the resulting CEUS SSC Model properly meets the SSHAC goal of representing the center, body, and range of technically-defensible interpretations.

This concludes our PPRP Final Report for the CEUS SSC Project.



Jon P. Ake



Walter J. Arabasz



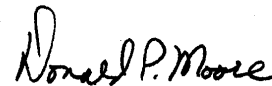
William J. Hinze



Annie M. Kammerer



Jeffrey K. Kimball



Donald P. Moore



Mark D. Petersen



J. Carl Stepp

Copy:

Lawrence A. Salomone

Kevin J. Coppersmith

Brent Gutierrez

# PROJECT ACKNOWLEDGMENTS

---

This study was sponsored by the Electric Power Research Institute (EPRI) Advanced Nuclear Technology Action Plan Committee, the U.S. Department of Energy (DOE) Office of Nuclear Energy and Office of the Chief of Nuclear Safety, and the U.S. Nuclear Regulatory Commission (NRC) Office of Nuclear Regulatory Research. Technical experts from the DOE, NRC, U.S. Geological Survey, Defense Nuclear Facility Safety Board, industry, and academia participated in the study as part of the Technical Integration (TI) Team or as members of the Participatory Peer Review Panel (PPRP). Any statements, opinions, findings, conclusions, or recommendations expressed in this material are those of the authors and do not necessarily reflect those of the participating or sponsoring agencies.

Jeffrey F. Hamel was the EPRI Advanced Nuclear Technology Program Manager. Lawrence A. Salomone of Savannah River Nuclear Solutions, LLC, served as the Project Manager for the study. Kevin J. Coppersmith of Coppersmith Consulting Inc., served as the lead for the TI Team. J. Carl Stepp of Earthquake Hazards Solutions, and Walter J. Arabasz, Research Professor Emeritus of Geology and Geophysics at the University of Utah, served as Co-chairmen for the PPRP. The entire Central and Eastern United States Seismic Source Characterization Project Team and their roles are discussed in Section 2 and are shown on the project organization chart (Figure 2.3-1) of the report.

The authors of the report wish to acknowledge the contributions of the following people: the resource experts who participated in Workshop 1, the proponent experts who participated in Workshop 2, and the technical experts who provided valuable insights, perspective, and references throughout the study. The names of all these contributors are listed in Table 2.2-2.

In addition, the authors of the report appreciate the support of Geraldine Moore-Butler as administrative assistant and Nancy L. Sutherland as technical editor for the project. This report was assembled at AMEC.

Page intentionally left blank

## SPONSORS' PERSPECTIVE

---

This report describes a new seismic source characterization model for the Central and Eastern United States (CEUS) for use in probabilistic seismic hazard analysis (PSHA) for nuclear facilities. PSHA has become a generally accepted procedure for supporting seismic design, seismic safety and decision making for both industry and government. Input to a PSHA consists of seismic source characterization (SSC) and ground motion characterization (GMC); these two components are necessary to calculate probabilistic hazard results (or seismic hazard curves) at a particular geographic location.

The 1986 Electric Power Research Institute and Seismicity Owners Group (EPRI-SOG) study included both an SSC and GMC component. Recent applications for new commercial reactors have followed U.S. Nuclear Regulatory Commission (NRC) regulatory guidance (RG 1.208) by using the EPRI-SOG source model as a starting point and updating it as appropriate on a site-specific basis. This CEUS SSC Project has developed a new SSC model for the CEUS to replace the SSC component of the EPRI-SOG study.

The CEUS SSC Project was conducted using a Senior Seismic Hazard Analysis Committee (SSHAC) Level 3 process, as described in the NRC publication, *Recommendations for Probabilistic Seismic Hazard Analysis: Guidance on Uncertainty and Use of Experts* (NUREG/CR-6372). The goal of the SSHAC process is to represent the center, body, and range of technically defensible interpretations of the available data, models, and methods. The CEUS SSC model is applicable to any site within the CEUS and can be used with the EPRI 2004/2006 GMC model to calculate seismic hazard at any site of interest. Long-term efforts to replace the EPRI 2004/2006 GMC model with the Next Generation Attenuation Relationships for Central and Eastern North America obtained from the NGA-East Project is scheduled for completion in 2014.

The updated CEUS SSC model provides industry and government with the following: a new model for the commercial nuclear industry to perform PSHAs for future reactor license applications; the NRC to support its review of early site permit (ESP) and construction and operating license (COL) applications; and the U.S. Department of Energy (DOE) to support modern PSHAs to meet design and periodic review requirements for its current and future nuclear facilities. Specific benefits of the model are as follows:

- **Consistency:** For many sites, seismic sources at distances up to 300 km (186 mi.) or more significantly contribute to hazard at some spectral frequencies. Consequently, seismic hazard models for many sites have significant geologic overlap. If done separately, there is a likelihood of conflicting assessments for the same regions. A regional source model allows for consistent input into a PSHA. An updated conceptual SSC framework that provides a

consistent basis for identifying and characterizing seismic sources in the CEUS has been developed. The NRC will no longer need to review each time each applicant's regional SSC model when the accepted CEUS SSC model is used. This will avoid lengthy review of the regional SSC model in ESP and COL applications for sites within the CEUS that use the accepted regional CEUS SSC model to develop its site-specific SSC model.

- **Stability:** This CEUS SSC model was developed using the accepted state-of-practice SSHAC methodology that involved the following tasks:
  - Development of a comprehensive database and new tools for documenting the data consideration process.
  - Multiple workshops to identify applicable data, debate alternative hypotheses, and discuss feedback.
  - Multiple working meetings by the Technical Integration (TI) Team to develop the SSC model and fully incorporate uncertainties.
  - Technical advancements in a number of areas, such as developing a uniform earthquake catalog, developing an updated approach for assessing maximum magnitude, compiling data evaluation tables, incorporating paleoseismic data, and using spatial smoothing tools.
  - Participatory peer review, including four panel briefings, multiple interactions, and periodic formal feedback.
  - Proper documentation of all process and technical aspects of the project.

Experience has shown that stability is best achieved through proper and thorough characterization of our knowledge and uncertainties, coupled with the involvement of the technical community, regulators, and oversight groups.

- **Greater Longevity:** An explicit goal of the SSHAC methodology is to represent the center, body, and range of the technically defensible interpretations of the available data, models, and methods. Using the SSHAC process provides reasonable assurance that this goal has been achieved. Representing the center, body, and range of interpretations at the time of the study means that as new information is acquired and various interpretations evolve as a result, the current thinking at any point is more likely to be addressed in the study. As new information becomes available, an existing SSC will require periodic reviews to evaluate the implications of the new findings. The need for updates to a particular study is now better understood as a result of findings of the CEUS SSC Project sensitivity studies to determine the significance of source characteristics.
- **Cost and Schedule Savings:** The CEUS SSC model can be used to perform a PSHA at any geographic location within the CEUS. It is applicable at any point within the CEUS, subject to site-specific refinements required by facility-specific regulations or regulatory guidance. Having stable, consistent input into a regional PSHA will reduce the time and cost required to complete a commercial nuclear site's ESP or COL licensing application, prepare a DOE site's PSHA, and develop design input for new commercial and DOE mission-critical nuclear facilities.

- **Advancement of Science:** The CEUS SSC Project provides new data, models, and methods. This information was shared at three workshops with international observers as a means to provide technology transfer for application in other regions. The CEUS SSC earthquake catalog, which merges and reconciles several catalogs and provides a uniform moment magnitude for all events, and the CEUS SSC paleoliquefaction database provide a new baseline for future research and updates. New approaches used in this project for spatial smoothing of recurrence parameters, assessment of maximum magnitude, and systematical documentation of all data considered and evaluated also benefit future research and PSHA updates.

The sponsors of the CEUS SSC Project are utilities and vendors on the EPRI Advanced Nuclear Technology Action Plan Committee, the DOE Office of Nuclear Energy, the DOE Office of the Chief of Nuclear Safety, and the NRC Office of Nuclear Regulatory Research. Technical experts from the DOE, NRC, U.S. Geological Survey (USGS), and Defense Nuclear Facility Safety Board (DNFSB) participated in the study as part of the TI Team or as members of the Participatory Peer Review Panel (PPRP).

The product of the CEUS SSC Project is a robust peer-reviewed regional CEUS SSC model for use in PSHAs. This model will be applicable to the entire CEUS, providing an important baseline for future research and updates. The CEUS SSC Project demonstrates that a SSHAC Level 3 approach can achieve the goals of considering the knowledge and uncertainties of the larger technical community within a robust and transparent framework. The value of the new CEUS SSC model has been enhanced by the participation of key stakeholders from industry, government, and academia who were part of the CEUS SSC Project Team.

Looking forward, the NRC will publish NUREG-2117 (2012), *Practical Implementation Guidelines for SSHAC Level 3 and 4 Hazard Studies* that provides SSHAC guidance on the need to update a regional model. The guidance covers updating both regional and site-specific assessments. It addresses the “refinement” process of starting with a regional model and refining it for site-specific applications.

Page intentionally left blank

# ABBREVIATIONS

---

AD	anno domini (in the year of the Lord)
AFE	annual frequency of exceedance
AIC	Akaike information criterion
ALM	Alabama-Louisiana-Mississippi (zone of possible paleoseismic features)
AM	Atlantic Margin (seismotectonic zone)
AHEX	Atlantic Highly Extended Crust (seismotectonic zone)
ANSS	U.S. Advanced National Seismic System
ANT	Advanced Nuclear Technology
APC	Action Plan Committee
BA	Blytheville arch
BC	before Christ
BCFZ	Big Creek fault zone
BFZ	Blytheville fault zone
BL	Bootheel lineament
BMA	Brunswick magnetic anomaly
BP	before present
BPT	Brownian passage time
BTP	Branch Technical Position
CAD	computer-aided design

---

*Abbreviations*

CBR	center, body, and range
CCFZ	Crittenden County fault zone
CDZ	Commerce deformation zone
CENA	Central and Eastern North America
CERI	Center for Earthquake Research and Information
CEUS	Central and Eastern United States
CFZ	Commerce fault zone
CFR	Code of Federal Regulations
CGL	Commerce geophysical lineament
CGRGC	Cottonwood Grove–Rough Creek graben
CI	confidence interval
CNWRA	Center for Nuclear Waste Regulatory Analysis
COCORP	Consortium for Continental Reflection Profiling
COCRUST	Consortium for Crustal Reconnaissance Using Seismic Techniques
COL	combined construction and operating license
COLA	combined operating license application
COMP	composite prior, composite superdomain
CON	contemporary (with earthquake occurrence)
COV	coefficient of variation
CPT	cone penetration test
CVSZ	Central Virginia seismic zone
D&G	Dewey and Gordon (1984 catalog)
DEM	digital elevation model

DNFSB	Defense Nuclear Facilities Safety Board
DOE	U.S. Department of Energy
DWM	Division of Waste Management
ECC	Extended Continental Crust
ECC-AM	Extended Continental Crust–Atlantic Margin (seismotectonic zone)
ECC-GC	Extended Continental Crust–Gulf Coast (seismotectonic zone)
ECFS	East Coast fault system
ECFS-C	East Coast fault system—central segment
ECFS-N	East Coast fault system—northern segment
ECFS-S	East Coast fault system—southern segment
EC-SFS	East Coast–Stafford fault system
ECMA	East Coast magnetic anomaly
ECRB	East Continent rift basin
ECTM	Eastern Canada Telemetered Network
E[M]	expected moment magnitude listed in the CEUS SSC catalog for an earthquake
ENA	eastern North America
EP	Eau Plain shear zone
EPRI	Electric Power Research Institute
EPRI-SOG	Electric Power Research Institute–Seismicity Owners Group
ERM	Eastern rift margin
ERM-N	Eastern rift margin—north
ERM-RP	Eastern rift margin—river (fault) picks
ERM-S	Eastern rift margin—south

---

*Abbreviations*

ERM-SCC	Eastern rift margin—south/Crittenden County
ERM-SRP	Eastern rift margin—south/river (fault) picks
ERRM	Eastern Reelfoot Rift Margin
ESP	early site permit
ESRI	Environmental Systems Research Institute
ETSZ	Eastern Tennessee seismic zone
EUS	Eastern United States
FAFC	Fluorspar Area fault complex
FGDC	Federal Geographic Data Committee
ft	foot or feet
FTP	file transfer protocol
ft/s	feet per second
ft/yr	feet per year
FWLA	Fugro William Lettis & Associates
FWR	Fort Wayne rift
Ga	billion years ago
GC	Gulf Coast
GCVSZ	Giles County, Virginia, seismic zone
GHEX	Gulf Coast Highly Extended Crust (seismotectonic zone)
GIS	geographic information system
GLTZ	Great Lakes tectonic zone
GMC	ground-motion characterization (model)
GMH	Great Meteor Hotspot (seismotectonic zone)

GMPE	ground-motion prediction equation
GMRS	ground-motion response spectra
GPR	ground-penetrating radar
GPS	global positioning system
GSC	Geological Survey of Canada
Gyr	gigayears ( $10^9$ years)
HF	Humboldt fault
HID	hazard input document
$I_0$	maximum intensity
IAEA	International Atomic Energy Agency
IBEB	Illinois Basin Extended Basement (seismotectonic zone)
IPEEE	Individual Plant Examination for External Events
IRM	Iapetan rifted margin
ISC	International Seismological Centre
ITC	informed technical community
ka	thousand years ago
K-Ar	potassium-argon
km	kilometer(s)
km <sup>2</sup>	square kilometer(s)
km/sec	kilometers per second
K-S	Kijko-Sellevoll
K-S-B	Kijko-Sellevoll-Bayes
kyr	thousand years

---

*Abbreviations*

LDO	Lamont-Doherty Earth Observatory (catalog)
LHS	Latin hypercube sampling
LLNL	Lawrence Livermore National Laboratory
ln(FA)	logarithm of felt area (with felt area measured in km <sup>2</sup> )
LS	least squares
LSA	La Salle anticlinal belt
LWLS	locally weighted least squares
m	meter(s)
M	magnitude
M, M <sub>w</sub>	moment magnitudes
Ma	million years ago
MAR	Marianna (RLME source)
m <sub>b</sub>	body-wave magnitude (short period)
m <sub>bLg</sub>	body-wave magnitude determined from higher-mode (L <sub>g</sub> ) surface waves
M <sub>C</sub>	coda magnitude
MCMC	Markov Chain Monte Carlo
M <sub>D</sub>	duration magnitude
MESE	Mesozoic and younger extended crust
MESE-N	Mesozoic-and-younger extended crust or Mmax zone that is “narrow”
MESE-W	Mesozoic-and-younger extended crust or Mmax zone that is “wide”
mi.	mile(s)
mi. <sup>2</sup>	square mile(s)
MIDC	midcontinent

MidC	Midcontinent-Craton (seismotectonic zone)
Mfa	felt-area magnitude
$M_L$	local magnitude
$M_{\max}$ , Mmax	maximum magnitude
MMI	modified Mercalli intensity
mm/yr	millimeters per year
$M_N$	Nuttli magnitude
$M_o$	Scalar seismic moment
MRS	Midcontinent rift system
m/s	meters per second
$M_S$	surface-wave magnitude
MSF	Meeman-Shelby fault
$M_w$	
Myr	million years
NAD83	North American Datum of 1983
NAP	Northern Appalachian (seismotectonic zone)
Nd	neodymium
NEDB	National Earthquake Database
NEI	Nuclear Energy Institute
NEIC	National Earthquake Information Center
NF	Niagara fault zone
NMESE	Non-Mesozoic and younger extended crust
NMESE-N	Mesozoic-and-younger extended crust or Mmax zone that is “narrow”

---

*Abbreviations*

NMESE-W	Mesozoic-and-younger extended crust or Mmax zone that is “wide”
NMFS	New Madrid fault system
NMN	New Madrid North fault
NMS	New Madrid South fault
NMSZ	New Madrid seismic zone
NN	New Madrid north (fault segment as designated by Johnston and Schweig, 1996)
NOAA	National Oceanic and Atmospheric Administration
NPP	nuclear power plant(s)
NR	Nemaha Ridge
NRC	U.S. Nuclear Regulatory Commission
NRHF	Nemaha Ridge–Humboldt fault
NSHMP	National Seismic Hazard Mapping Project
NW	New Madrid west (fault segment as designated by Johnston and Schweig, 1996)
OKA	Oklahoma aulacogen (seismotectonic zone)
OKO	Oklahoma Geological Survey Leonard Geophysical Observatory (catalog)
OSL	optically stimulated luminescence
$P_a$	probability of activity (of being seismogenic)
PEZ	Paleozoic Extended Crust (seismotectonic zone)
PGA	peak ground acceleration
PM	Project Manager
PPRP	Participatory Peer Review Panel
PSHA	probabilistic seismic hazard analysis
PVHA	probabilistic volcanic hazard analysis

RCG	Rough Creek graben
RF	Reelfoot fault
RFT	Reelfoot thrust (fault)
RLME	repeated large-magnitude earthquake (source)
RR	Reelfoot rift zone
RS	Reelfoot South (fault segment)
SA	spectral acceleration
SCL	St. Charles lineament
SCML	south-central magnetic lineament
SCR	stable continental region
SCSN	South Carolina Seismic Network
SEUS	Southeastern United States (catalog)
SEUSSN	Southeastern United States Seismic Network
SGFZ	Ste. Genevieve fault zone
SHmax	maximum horizontal stress, compression, or principal stress
SLR	St. Lawrence rift (seismotectonic zone)
SLTZ	Spirit Lake tectonic zone
SLU	Saint Louis University (catalog)
SNM	Sanford et al. (2002 catalog)
SOG	Seismicity Owners Group
SPT	standard penetration test
SRA	Stover, Reagor, and Algermissen (1984 catalog)
SRTM	Shuttle Radar Topography Mission

---

*Abbreviations*

SSC	seismic source characterization
SSE	safe shutdown earthquake
SSHAC	Senior Seismic Hazard Analysis Committee
Str&Tur	Street and Turcotte (1977 catalog)
SUSN	Southeastern United States Network
TC	technical community
TFI	technical facilitator/integrator
TI	technical integration
USGS	U.S. Geological Survey
USNSN	U.S. National Seismograph Network
UTC	Coordinated Universal Time
$V_P/V_S$	ratio of P-wave velocity to S-wave velocity
WES	Weston Observatory (catalog)
WIPP	Waste Isolation Pilot Project
WQSZ	Western Quebec seismic zone
WRFZ	White River fault zone
WUS	Western United States
WVFS	Wabash Valley fault system
WVSZ	Wabash Valley seismic zone
WWSSN	World-Wide Standardized Seismograph Network

# 5

## CHAPTER 5

### SSC MODEL: OVERVIEW AND METHODOLOGY

---

#### 5.1 Overview of Spatial and Temporal Models

The heart of any SSC model for PSHA is a description of the future spatial and temporal distribution of earthquakes. The earliest PSHA models identified seismic source zones within which the spatial distribution of earthquakes was assumed to be uniform. The temporal distribution of earthquakes was assumed to follow a Poisson process, and the sizes of earthquakes within the zones were assumed to follow an exponential distribution. In more tectonically active areas such as the WUS, the recognition of active faults allowed the spatial models to evolve such that they were able to include the fault sources as well as the background source zones within which they lie. Further, the development of fault-specific paleoseismic data regarding the timing, amount of slip per earthquake, and geologic slip rate provided a new class of temporal models that could use this information directly in the PSHA.

In the meantime, the evolution of spatial and temporal models within stable continental regions (SCRs) such as the CEUS has taken place differently and more slowly. Despite continued geologic investigations, the search for the causative faults giving rise to observed seismicity has yielded very few cases where a definitive argument can be made for having identified an active fault in the sense that this is commonly identified in the WUS. With notable exceptions such as the Meers fault and the Cheraw fault, the best-defined cases of localized seismicity and deformation occur in the New Madrid region, where individual fault-like sources can be called out and characterized. Even in locales such as Charleston, where geologic and geophysical studies have continued over the decades, uncertainties persist regarding the unique association of the observed historical seismicity and the one or more causative faults that are responsible.

##### 5.1.1 *Spatial Model Considerations*

Continued analysis of the historical seismicity record and network monitoring by regional and local seismic networks has led to acceptance within the community that the general spatial patterns of observed small-to-moderate magnitude earthquakes provide predictive information about the spatial distribution of future large-magnitude earthquakes. The analyses leading to this conclusion have focused on whether the observed patterns of earthquakes have varied through time; therefore, in effect, this is an assessment of whether small- to moderate-magnitude earthquakes have been relatively stationary through time. Studies such as those by Kafka (2007, 2009) suggest that this has generally been the case and that we can with some level of confidence use the spatial pattern of smaller earthquakes to predict the future pattern of smaller earthquakes.

However, the available data on larger-magnitude earthquakes and their relationship to the spatial distribution of smaller earthquakes based on the observed record is quite limited and not sufficient to allow an empirical spatial model to arrive at such a conclusion with confidence. We have some cases like Charlevoix and New Madrid where a spatial concentration of smaller-magnitude earthquakes is occurring generally within the region of larger historical earthquakes. However, we also have counter-examples like the Eastern Tennessee seismic zone, which is defined by a highly concentrated zone of small to moderate earthquakes without any larger events in the historical record. Likewise, the Charleston region is associated with a pattern of observed seismicity that is not particularly remarkable for drawing attention to the location of the 1886 earthquake.

Perhaps the most dramatic finding in recent years is paleoseismic evidence for the occurrence of prehistoric large-magnitude earthquakes in the CEUS. For obvious reasons, the earliest paleoseismic studies occurred in the locales of large historical earthquakes (e.g., New Madrid, Charleston), and subsequent studies moved to other regions (e.g., Wabash Valley, Charlevoix, Eastern Tennessee). With a few exceptions, the paleoseismic information developed at these locations appears to be related to secondary shaking effects such as liquefaction rather than observed fault displacements. As a result, uncertainties exist about both the locations and sizes of the earthquakes. Detailed studies of historical and instrumental earthquakes, and liquefaction phenomena associated with them, coupled with field and laboratory studies of geotechnical properties, are leading to a stronger technical basis for placing limits on the locations of paleoearthquakes interpreted by the distribution of liquefaction phenomena and for defining their magnitudes. In some cases, the paleoseismic evidence for repeated large-magnitude earthquakes is so compelling that the TI Team has concluded that a RLME source must be included in the SSC model. In other cases, there is suggestive evidence of potential liquefaction earthquakes, such as the postulated Alabama-Louisiana-Mississippi (ALM) zone. In that situation, consideration is given to possible evidence for a prehistoric earthquake, but inclusion as an RLME source is not warranted (see Section 7.3.9 for a discussion). The establishment of several RLME sources as spatial components of the CEUS SSC model is an important advancement over previous studies and reflects the evolution taking place within the technical community.

Notwithstanding the locations of RLME sources, the spatial distribution of distributed seismicity sources has advanced in PSHA based largely on the assumption of spatial stationarity, as discussed in Section 5.3.2.1 of this report. For example, the EPRI-SOG project and the U.S. National Seismic Hazard Mapping Project (Petersen et al., 2008) use different approaches to “smooth” observed seismicity to provide a map that expresses the future spatial pattern of seismicity. In reality, the  $a$ -values, or rates per unit area, and  $b$ -values are subject to the smoothing operation, and various calculation approaches are carried out. Because of the support in the community for these approaches to representing the future spatial distribution of seismicity, they have been explored thoroughly as part of the CEUS SSC Project. Various adaptive kernels were evaluated along with the penalized maximum-likelihood approach that is a refinement of the approach used in the EPRI-SOG project. The refined approach subdivides the region into one-quarter-degree cells and specifies the degree of “communication” between adjacent cells. As discussed in Section 5.3.1, the approach was selected because, although it is based on the same conceptual model of spatial stationarity as the kernel approach, it offers the

ability to allow for spatial variability in both  $a$ - and  $b$ -values, and it was found to provide comparable results to the adaptive kernel when a constant  $b$ -value was assumed.

### **5.1.2 Considerations Regarding Temporal Models**

For purposes of SSC model assessments, the “temporal” issue concerns both the sizes of future earthquakes as well as their frequency of occurrence (average rate and aperiodicity). With time and study the earthquake research community in the WUS has developed information that suggests that the assumption of an exponential distribution of magnitudes may not be appropriate for individual faults. Poissonian models are memoryless and do not incorporate information about the timing or size of prior earthquakes. Studies of fault displacements, including the timing and displacement per event, and physical notions of strain accumulation and release provide information for modeling where a source currently resides in the seismic cycle. Such “real-time” and “renewal” models have found their way into some SSC model assessments where the dominant sources are highly active plate-boundary faults.

In contrast to plate-boundary SSC models, the fundamental information source for the assessment of temporal models in the CEUS is the catalog of historical and instrumental earthquakes. Though uneven in coverage and incomplete back through time, the catalog is the cornerstone for assessing recurrence rates for most seismic sources in the CEUS. Thus, significant effort was devoted to developing an earthquake catalog for the CEUS SSC Project with moment magnitudes for all earthquakes and for analyzing its completeness as a function of time and location. Beyond the catalog, in the CEUS, the modeling of temporal behavior has benefited most from paleoseismic investigations at the RLME sources. An ever-increasing database of paleoliquefaction studies, which have been compiled as part of the CEUS SSC Project (Appendix E), provides information on the approximate sizes and timing of large-magnitude events. In effect, these studies extend the historical observations back a few thousand years. Despite their uncertainties, the studies provide clues about the nature of the repeated pattern of larger earthquakes through time at individual seismic sources. A number of studies conducted within SCRs including the CEUS have concluded that large earthquakes are not evenly spaced in time, but rather occur as “clusters” of earthquakes that are separated from other clusters by long “intercluster” periods of quiescence.

For each RLME source, the available data were evaluated in order for the TI Team to assess whether temporally clustered behavior has been observed and, if so, whether the source is currently within or outside of a temporal cluster. In either case, the temporal behavior is modeled as a Poisson process. The TI Team further evaluated the available data to assess whether the application of a renewal model would be appropriate for the RLME sources. The physical underpinning of a renewal model is a quasi steady state loading process applied to a fault. These models have been given relatively high weight in characterizing earthquake occurrences on plate boundary faults, even though there may not be a well-developed paleoseismic history (e.g., Working Group, 2003). Two of the RLME sources defined by the TI team have reasonably well-developed paleoseismic histories: New Madrid and Charleston. However, the physical process of steady state loading being applied to these sources is more problematic. In addition, the specific causative faults associated with the New Madrid RLME sources are only moderately understood and the fault or faults associated with the Charleston RLME source are poorly understood.

Therefore, giving due consideration to the larger technical community's views regarding recurrence models for these RLME sources, the TI team concluded that applying the renewal model to these two RLME sources should have some weight, although it is relatively low. For all of the other RLME sources, the available data were judged not to be sufficient to allow for the application of such models with any confidence. The methodology for characterizing RLME recurrence is given in Section 5.3.3 and the specific data and recurrence assessments related to the Charleston and New Madrid RLME sources are given in Sections 6.1.2 and 6.1.5, respectively.

For distributed seismic source zones, the earthquake catalog provides the fundamental basis for assessing recurrence and, as described previously, for describing its future spatial distribution. Consistent with common practice in the assessment of seismicity within large seismic sources, the observed seismicity is assessed to follow a truncated exponential magnitude distribution (e.g. Cornell and Van Marke, 1969) and Poissonian behavior.

### **5.1.3 Perspective on CEUS SSC Models**

At the time of the preparation of this report, there were a number of promising research areas pertaining to spatial and temporal models that had not reached the level where they could be included in the SSC model with confidence. Examples include models proposed as part of the ongoing debate on "characteristic" earthquakes or, simply stated, the tendency for a specific fault to generate earthquake magnitudes that are not exponentially distributed in magnitude. The TI Team reviewed this continuing dialogue within the community, but concluded that the models were not applicable to the kinds of sources being characterized in the CEUS. Models of fault-specific behavior were not judged to be applicable in the CEUS unless and until seismogenic faults were identified and data regarding their behavior was gathered. Rather, the intent of the RLME sources is to model only the recurrence of repeated large earthquakes in a specific location. As such, the RLME sources represent a source of seismic hazard that is in addition to the hazard resulting from the occurrence of distributed seismicity modeled by the distributed seismicity sources. The addition of the RLME recurrence with that derived from observed seismicity within the distributed seismicity sources allows for a departure from the general truncated exponential recurrence behavior in specific locations. This simple approach to incorporating the data available in the CEUS is described in Sections 5.3.3.4 and 6.1.

Another area of ongoing research with potential implications for recurrence behavior relates to geodetic strain rate measurements. No doubt, the systematic gathering of geodetic data throughout the CEUS for purposes of identifying and analyzing tectonic strain is crucial for the understanding of contemporary deformation processes. Its importance is acknowledged and its promise in the decades ahead is undeniable. However, in 2010, the CEUS technical community's understanding of the meaning of a short-term (few decades) strain signal relative to seismic source characteristics is embryonic. The spatial distribution and temporal stability of such strains is not known, and there is no clear method for translating these strain signals into spatial and temporal SSC models. One need only witness the ongoing debates in the WUS on the discrepancies between long-term geologic slip rates and short-term geodetic strain rates to lose confidence that, in the complete absence of geologic slip rates, the geodetic results can be used.

As a corollary, the types of analyses carried out in the WUS to “test” the reasonableness of a seismic source model are generally not applicable in the CEUS. For example, the integrated moment rate derived for a region from the summed fault slip rates (derived from geologic studies) cannot be developed and, as a result, cannot be compared to the observed moment rate for the same region based on the seismicity record. Likewise, given the generally sparse geodetic networks and short period of observation, the uncertainties in attempting to compare the recurrence rates for seismic sources derived from seismicity with those developed from geodetic data are unacceptably large. It is acknowledged in this report that local well-studied areas such as the central New Madrid region may eventually provide clues or even constraints on the temporal behavior of seismic sources. Research in these areas is encouraged, but the current data do not allow for direct incorporation into the CEUS SSC model.

## 5.2 Maximum Earthquake Magnitude Assessment

This section describes the methodology that was used in the CEUS SSC Project to assess  $M_{max}$  for all seismic sources. Estimating  $M_{max}$  in SCRs such as the CEUS is highly uncertain despite considerable interest and effort by the scientific community over the past few decades.  $M_{max}$  is defined as the upper truncation point of the earthquake recurrence curve for individual seismic sources, and the typically broad distribution for any given source reflects considerable epistemic uncertainty. Because the maximum magnitude for any given seismic source in the CEUS occurs rarely relative to the period of observation, the use of the historical seismicity record provides important but limited constraints on the magnitude of the maximum event. At annual frequencies of interest for conventional buildings (approximately  $10^{-2}$  to  $10^{-3}$ /yr), the hazard results are usually not particularly sensitive to the maximum magnitude. However, at annual frequencies of interest for nuclear facilities ( $10^{-3}$  to  $10^{-7}$ ), the influence of  $M_{max}$  can be very significant. For this reason, focus on the  $M_{max}$  issue has been driven by PSHAs conducted for nuclear facilities.

In view of the importance of  $M_{max}$  revealed by the EPRI-SOG project (EPRI, 1988), a major study sponsored by EPRI was carried out in the early 1990s to attempt to quantify the knowledge and uncertainties in  $M_{max}$  for purposes of PSHA (Johnston et al., 1994). The approach advocated in the EPRI  $M_{max}$  study is based on analogies between the CEUS and other SCR areas. To develop the analogies, two key activities needed to be conducted: (1) development of a worldwide seismicity catalog of moderate to large earthquakes with systematic moment magnitudes for all events, and (2) identification and characterization of the regions worldwide that can be considered analogous tectonically to the CEUS. The results of those efforts were the first of their kind and led to considerable advances in the research (e.g., Johnston, 1996a).

The EPRI  $M_{max}$  study also focused on the use of a Bayesian procedure for estimating  $M_{max}$ , in which the prior distribution is based on the earthquake magnitudes of events that occurred worldwide within tectonically analogous regions. At the time the study was conducted, there was considerable focus on the occurrence of large earthquakes within formerly rifted or extended crust. For example, the 1811-1812 New Madrid earthquakes were interpreted to have occurred within the Reelfoot rift, which exhibits evidence of multiple episodes of extension but is currently within a compressive stress regime. Despite the anecdotal evidence for the occurrence of the largest SCR earthquakes within extended crust, the statistical analyses in Johnston et al. (1994) did not provide strong evidence that any particular tectonic characteristic—or

combination of characteristics—is correlated with maximum earthquake size. The best correlations at the time suggested that sites of major Paleozoic and younger extension appeared to have the potential for a larger  $M_{max}$  (i.e., a higher mean of the prior distribution), but the analyses also indicated that the standard deviation of the prior distribution was larger.

From the beginning of the CEUS SSC Project, the TI Team pursued the refinement and application of the Bayesian  $M_{max}$  approach (Johnston et al., 1994). An evaluation of alternative approaches to assessing  $M_{max}$  in the CEUS (Wheeler, 2009) concluded that the Bayesian  $M_{max}$  approach, as well as other approaches that were based on tectonic analogues, was worthy of pursuit within the technical community. The Bayesian  $M_{max}$  approach has the advantage that it provides a quantitative and repeatable process for assessing  $M_{max}$ . The approach is described below in Section 5.2.1.1 along with the updates to the Johnston et al. (1994) characterization of  $M_{max}$  for SCRs. The TI Team also explored alternative approaches for the assessment of  $M_{max}$  that provide quantitative and repeatable results, and the team identified the approach developed by Kijko(2004) as a viable alternative. In his evaluation of statistical approaches for estimating  $M_{max}$ , Wheeler (2004) noted that problems of small samples and rare large earthquakes continue to hinder testing of statistical models in SCRs. Nevertheless, the Kijko (2004) approach requires fewer assumptions than the Bayesian approach in that it uses only the observed earthquake statistics for the source, but this is offset by the need for a relatively larger data sample in order to get meaningful results. The Kijko (2004) approach is described in Section 5.2.1.2.

### **5.2.1 Approaches to $M_{max}$ Estimation in the CEUS**

The CEUS SSC model incorporates two types of seismic sources: RLME sources and distributed-seismicity source zones of various types. The RLME sources are characterized by their sizes and recurrence rates derived primarily from the paleoseismic record and, despite variations in the seismic source zone configurations, are assumed to always exist in the model. RLME sources include those in the New Madrid area, Wabash Valley, Charleston, Charlevoix, and Meers fault, among others. Because of the independent constraints on earthquake size, those constraints are used to estimate the magnitudes of RLMEs, and the assessment of  $M_{max}$  discussed here is not applicable to RLME sources. Rather, this discussion is applicable to the distributed-seismicity source zones, which exist in different forms depending on whether the  $M_{max}$  zones or the seismotectonic zones branches of the master logic tree are being followed.

The assessment of  $M_{max}$  for distributed seismicity sources (source zones) in the CEUS SSC Project has been designed to incorporate the uncertainties in both the conceptual models and the parameter values associated with each model. Based on the review and evaluation of the Bayesian method and consideration of other methods that exist within the larger technical community, it was decided that the assessment would need to include alternative conceptual models for  $M_{max}$ . In particular, it was decided that alternative prior distributions should be considered for the Bayesian approach, and that an alternative to the Bayesian approach should be considered.

The TI Team decided to use two alternative approaches as a basis for estimating the  $M_{max}$  distributions for distributed seismicity sources: (1) the Bayesian procedure, which uses the prior

distributions from an update and evaluation of the global SCR data; and (2) the Kijko (2004) procedure, which uses the observed seismicity within a region to provide a direct (or posterior) assessment of  $M_{max}$ . The Bayesian approach is representative of a category of approaches that rely on drawing analogies to tectonically comparable regions in order to estimate the  $M_{max}$  for the source of interest. These approaches are based on the ergodic assumption that one can substitute time (the short period of observation) for space (other SCRs). The Kijko approach is representative of an alternative category of models that rely on the observations of seismicity entirely within the zone of interest. Because the occurrence of  $M_{max}$  is typically rare relative to the period of observation, these approaches assume a particular frequency distribution of earthquake sizes and, to be able to apply them with confidence to larger or very active regions, rely on significant numbers of observed earthquakes to provide stable estimates.

Both the Bayesian and Kijko approaches have their pros and cons. They both have the positive attribute that they are repeatable given the same data and that they can readily be updated given new information. The Bayesian approach is arguably more stable because of the use of a prior distribution that, even in the absence of a significant number of earthquakes in the zone of interest, can still provide a result. However, the prior distributions for  $M_{max}$  are developed based on analogies to other “tectonically comparable” regions, which can be a source of uncertainty, and based on evaluation of those regions relative to a highly uncertain set of characteristics that are postulated to be important to  $M_{max}$ . The advantage of the Kijko approach is that it does not require the identification of analogue regions or assessments of the characteristics of those regions. However, as applied the approach relies on the assumption that the distribution of earthquake magnitudes follows a doubly truncated exponential distribution. Moreover, the approach does not provide stable results when the number of observed earthquakes is low.

From the standpoint of their specific use in the CEUS SSC model, there are other considerations in evaluating the two approaches. The key difference between the Kijko approach and the Bayesian approach is that the Kijko approach does not have a prior distribution; it uses only the earthquakes within the source of interest. The prior distribution is based on analogies to other parts of the world and the assumption that those events are applicable to the estimation of maximum magnitudes within the source of interest. A potential problem is that the global SCR database includes earthquakes from RLME sources (e.g., New Madrid, Charleston, and perhaps others worldwide that we suspect might have RLMEs). In the CEUS SSC model, however, the Bayesian approach is being applied to non-RLME sources, so we are possibly overestimating  $M_{max}$  by using RLMEs globally to develop our prior distributions. The Kijko approach has some appeal because, by definition, it uses only data from the CEUS and only the earthquake catalog that does not include RLMEs. Care must be taken to avoid instability due to small numbers of earthquakes, but this can be accomplished by examining the statistics of the calculations, as provided for in the Kijko approach, and by giving the approach less weight when numbers of events are too low for stable estimates. Also, the seismic sources of interest in the CEUS SSC model tend to be larger regions with a significant number of earthquakes, thus mitigating the likelihood of instability.

The application of the Bayesian and Kijko approaches to assessing Mmax for the CEUS SSC Project is described below in Sections 5.2.1.1 and 5.2.1.2. The approach to weighting the alternative approaches for particular seismic sources is described in Section 5.2.1.3.

### 5.2.1.1 Bayesian Mmax Approach

The Bayesian Mmax approach is illustrated on Figure 5.2.1-1. The approach is based on estimating Mmax by drawing analogies to regions that are comparable to the CEUS (i.e., SCRs) and using that information to establish *prior* distributions on Mmax for distributed seismicity sources (source zones) in the CEUS. Part (a) of Figure 5.2.1-1 shows the *prior* distribution developed by Johnston et al. (1994) for extended continental crust. The prior distribution is then updated with source-specific information about the number and sizes of observed earthquakes. The update is expressed as a *likelihood* function, part (b) of Figure 5.2.1-1, which is zero for all values below the maximum observed magnitude, has a peak near the maximum observed, and then becomes essentially constant at larger magnitudes. The prior distribution is then convolved with the likelihood function to arrive at a *posterior* distribution of Mmax, shown in part (c) of the figure. The continuous posterior distribution is then represented by a discrete distribution for use in hazard analysis, as shown in part (d).

The likelihood function used to update the prior is derived from the earthquake recurrence model applied to the source region. The model used in this study is an exponential distribution for the sizes of earthquakes occurring with a source region. This is the standard model applied to regions where multiple individual sources contribute to the occurrence of earthquakes. The likelihood function for possible values of Mmax,  $m^u$ , based on the exponential model is (e.g., Johnston, 1994) is

$$L[m^u] = \begin{cases} 0 & \text{for } m^u < m_{\max-obs} \\ [1 - \exp\{-b \ln(10)(m^u - m_0)\}]^{-N} & \text{for } m^u \geq m_{\max-obs} \end{cases} \quad (5.2.1-1)$$

where  $b$  is the Gutenberg-Richter  $b$ -value,  $N$  is the number of recorded earthquakes with magnitudes equal to or larger than a minimum value  $m_0$ , and  $m_{\max-obs}$  is the largest recorded earthquake. The likelihood function has two effects on the prior. The first is to truncate the lower tail of the prior distribution at the value of the maximum observed earthquake. The shape of the likelihood function is controlled by the value of  $N$ , the number of earthquakes between  $m_0$  and  $m_{\max-obs}$ . In most cases, the value of  $N$  is small such that the likelihood function is relatively flat with a small peak at  $m^u$  equal to  $m_{\max-obs}$ , as shown in part (b) of Figure 5.2.1-1. As a result, the primary effect is to produce a posterior distribution with a similar shape to the prior, as shown in part (c) of Figure 5.2.1-1. When  $N$  becomes large, the likelihood function becomes very peaked at  $m_{\max-obs}$  and has a major effect on the prior distribution. Figure 5.2.1-2 repeats the example of Figure 5.2.1-1 with the value of  $N$  increased from 2 to 10. In this case, the posterior distribution also becomes very peaked near  $m_{\max-obs}$ . It is important to note that the influence of size of  $N$  is relative to the magnitude range  $m_0$  to  $m_{\max-obs}$ . Because of the exponential distribution of magnitude sizes, increasing  $N$  by reducing  $m_0$  for a given value of  $m_{\max-obs}$  has no effect on the

likelihood function as long as the increase in  $N$  is consistent with the  $b$ -value of the source region.

Because typical applications involve small values of  $N$ , the shape of the posterior  $M_{\max}$  distribution is similar to that of the prior. Thus, specification of the prior distribution is of primary importance in defining the  $M_{\max}$  distribution. The Johnston et al. (1994)  $M_{\max}$  prior distributions were developed from a study of SCR earthquakes. The process involved subdividing the SCR into tectonic domains on the basis of characteristics such as crustal extension, crustal age, age of major deformation, state of stress, and orientation of predominant structural grain relative to stress. A catalog of SCR earthquakes was developed in which moment magnitudes were assessed for each earthquake. The SCR earthquake catalog was then used to assess the largest observed earthquake in each domain. The mean and standard deviation of these values for specified subsets of the SCR domains provided normal distributions for  $m_{\max-obs}$ . The last step in converting the distribution for  $m_{\max-obs}$  into a prior distribution for  $m^u$  was to make a bias correction to account for the fact that  $m_{\max-obs}$  is in nearly all cases less than  $m^u$ . The bias correction is based on the assumption that the size distribution of earthquakes in a source region corresponds to a truncated exponential distribution between a specified minimum magnitude  $m_0$  and the maximum magnitude for the region,  $m^u$ . Using this assumption, the cumulative probability distribution for the largest earthquake in a sample of size  $N$  given a specified value of  $m^u$  is (Johnston et al., 1996):

$$F[m_{\max-obs}] = \left[ \frac{1 - \exp\{-b \ln(10)(m_{\max-obs} - m_0)\}}{1 - \exp\{-b \ln(10)(m^u - m_0)\}} \right]^N \quad \text{for } m_0 \leq m_{\max-obs} \leq m^u \quad (5.2.1-2)$$

Figure 5.2.1-3 shows median (50th percentile) values of  $m_{\max-obs}$  as a function of  $m^u$  and  $N$ . These values were used to make a bias adjustment from  $m_{\max-obs}$  to  $m^u$  by selecting a value of  $m^u$  such that the median value of the maximum observed,  $\hat{m}_{\max-obs}$ , equals the actual observed value. An example is illustrated on Figure 5.2.1-3 for the case in which the value of  $m_{\max-obs}$  equal to 5.7 for a sample size of 10 earthquakes equal to or larger than  $m_0$  of 4.5. The  $N = 10$  curve shown on Figure 5.2.1-3 indicates that a  $m^u$  value of 6.3 produces a value of  $\hat{m}_{\max-obs}$  equal to 5.7. Thus a magnitude of 6.3 represents the bias-adjusted value of  $m^u$  for the source.

The relationships shown on Figure 5.2.1-3 indicate that for a given value of  $N$ , the value of  $\hat{m}_{\max-obs}$  reaches an asymptotic level as  $m^u$  increases. Thus it is not possible to make meaningful bias corrections for large values of  $m_{\max-obs}$  unless the sample size is large. This fact led Johnston et al. (1994) to use domain pooling to increase the sample size. Tectonic domains that had the same characteristics (e.g., same type of crust, same age, same state of stress) were combined into a "superdomain" under the assumption that the common set of characteristics would correlate with a common value of  $m^u$ . The mean value of  $m_{\max-obs}$  in a set of superdomains was then bias-adjusted to produce a mean value of  $m^u$  using the average sample size in the superdomains. This bias adjusted value of  $m^u$  along with the standard deviation of  $m_{\max-obs}$  was used as a prior distribution for  $M_{\max}$ .

Given the importance of the prior distribution in most applications of the Bayesian Mmax approach, the CEUS SSC Project focused its efforts on development of updated prior distributions. This involved updating the SCR data sets and performing new statistical analyses.

The SCR data sets used to develop the Johnston et al. (1994) Mmax prior distributions consist of the SCR earthquake catalog and the set of SCR domains. The SCR earthquake catalog was updated for this study. The principal source for this update was the catalog published by Schulte and Mooney (2005) that extended the SCR catalog of Johnston et al. (1994) from the end of 1990 to the end of 2003 as well as added additional earthquakes for the earlier time period identified in the literature. Earthquakes occurring in SCRs for the period 2004 through 2008 were added from the Harvard Moment Tensor (HMT) catalog. All earthquakes were assigned moment magnitudes and magnitude uncertainties based on the values given in Johnston et al. (1994) and Schulte and Mooney (2003). These values were updated using the relationships and assessments presented in Johnston (1996a, 1996b) as well as data from the CEUS SSC catalog for earthquakes in the CEUS. Moment magnitudes from the HMT catalog were assigned a nominal uncertainty of 0.1-magnitude unit standard deviation. Moment magnitudes for specific earthquakes, such as the 1811-1812 New Madrid sequence and the 1886 Charleston earthquake, were assigned according to the current literature. Appendix K presents the updated SCR earthquake catalog.

Updating the basis for Johnston et al.'s (1994) division of the SCR crust into 255 tectonic domains was beyond the scope of this project. However, the assignments of age, stress state, and stress structure angles to the 255 SCR domains were reviewed and updated using recent information. Appendix Table K-2 lists the 255 SCR domains defined by Johnston et al. (1994) and the updated domain characteristics defined for each. The boundaries of these domains are included in the Project database.

The updated SCR catalog was then used to assess the value of  $m_{\max-obs}$  for each domain and the sample size  $N$  representing the number of earthquakes  $\geq M$  4.5. Following the approach of Johnston et al. (1994), an equivalent sample size corrected for completeness is obtained for each domain. Johnston et al. (1994) estimated catalog completeness intervals for various portions of the SCR. These were used to define the completeness-corrected equivalent earthquake count for each domain based on the catalog completeness period for magnitudes equal to  $m_{\max-obs}$ . The typical case is that for magnitudes smaller than  $m_{\max-obs}$  the catalog completeness periods are shorter than those for  $m_{\max-obs}$ . Assuming that earthquake occurrence rates are stationary in time for the period covered by the catalog, then the maximum likelihood estimate of the rate of earthquakes of magnitude  $m_i$  is given by the number of earthquakes,  $N(m_i)$  in the completeness period for  $m_i$  divided by the length of the completeness period,  $T_C(m_i)$ . An estimate of the total number of earthquakes of the smaller magnitude that would have been recorded in the completeness period for  $m_{\max-obs}$  is then given by the estimated rate of occurrence for magnitude  $m_i$  multiplied by  $T_C(m_{\max-obs})$ :

$$N_{\text{Completeness Corrected}}(m_i) = N_{\text{In period } T_C(m_i)} \times \frac{T_C(m_{\max-obs})}{T_C(m_i)} \quad (5.2.1-3)$$

The values of  $N_{\text{Completeness Corrected}}(m_i)$  are then summed to provide the completeness-corrected sample size for each domain. These values are listed in Appendix Table K-2.

The updated domain data set was then used to assess appropriate prior distributions. The first step reviewed was the development of the superdomains by pooling domains with the same characteristics. Johnston et al. (1994) found that separation of the domains into extended and non-extended crust was the most meaningful initial classification. They then used other domain characteristics to develop superdomains within these two classes. For the non-extended crust domains, the characteristics used were crustal age, stress state, and whether the predominant structures within a domain are favorably oriented with respect to stress (labeled as source stress angle). These three attributes were used to group the 146 non-extended domains into a small number of superdomains. The characterization of the extended crust domains included additional factors such as the type of crust adjacent to the domain, the presence or absence of cross structures, and the presence or absence of multiple features. These additional characteristics were used by Johnston et al. (1994) to assign the 109 extended domains to superdomains. The result of using more characteristics to define extended crust superdomains was to increase the number of possible superdomains at the expense of reducing the sample size in each. Therefore, it was decided to use the same three characteristics—age, stress, and source stress angle—as the basis for defining both extended and non-extended superdomains. This provided a consistent basis for superdomain definition and also increased the average sample size in the extended superdomains. The result was 15 active (i.e., containing earthquakes) non-extended superdomains and 15 active extended superdomains. Figure 5.2.1-4 shows histograms of  $m_{\text{max-obs}}$  for the extended and non-extended superdomains.

The significance of the extended and non-extended superdomain classifications was examined by comparing the statistics of  $m_{\text{max-obs}}$  for the two classes. The results indicated that the extended and non-extended superdomain sites had similar mean values of  $m_{\text{max-obs}}$ . Applying a Student's *t*-test (with the Welsh modification for unequal variances) to compare the two samples yielded a very high probability (*p*-value) of 0.99 that the two populations from which the samples were drawn (extended superdomains and non-extended superdomains) have the same mean. This suggested that the classification scheme for Mmax priors for extended and non-extended crust needed to be revisited.

Examination of the values of  $m_{\text{max-obs}}$  in the extended crust superdomain set suggested that the larger values of  $m_{\text{max-obs}}$  occurred in the domains with Mesozoic and younger ages. Accordingly, an alternative grouping of superdomains was tested in which extended superdomains of Mesozoic and younger ages formed one group, designated MESE, and the older extended and the non-extended superdomains formed the second group, designated NMESE. Figure 5.2.1-5 shows histograms of  $m_{\text{max-obs}}$  for these two sets of superdomains. Application of the Student's *t*-test to these two samples yielded a lower *p*-value of 0.46, suggesting that it is more likely that the two populations have different mean values.

Building on the concept that a relatively young age of extension is an important factor, a new age classification was assigned to each extended domain based on the age of the most recent

extension episode. These age assignments are listed in Appendix Table K-2. The resulting sets of superdomains containing the Mesozoic and younger extended superdomains (MESE) are listed in Table 5.2.1-1, and those containing older extended and non-extended superdomains (NMESE) are listed in Table 5.2.1-2. Figure 5.2.1-6 shows histograms of  $m_{\max-obs}$  for the revised superdomains. Using these two classifications resulted in a further reduction in the  $p$ -value obtained from the Student's  $t$ -test to 0.31.

An additional step taken was to remove from the samples those superdomains for which the stress classification is “Unknown” as it is likely that they would be classified as either compressive or extensive with more data. The “Unknown” source–stress angle classification was retained because it includes cases where there is no clear structural grain in the domain. In addition, superdomains made up of a single domain or those with a single earthquake were removed, assuming that the information was too limited to assess  $m_{\max-obs}$  for these cases. The set of superdomains used in the final test are flagged in Tables 5.2.1-1 and 5.2.1-2.

Figure 5.2.1-7 shows histograms of  $m_{\max-obs}$  for this final set of superdomains. Application of the Student's  $t$ -test to these two samples yielded a  $p$ -value of 0.09, indicating a reasonable likelihood that the mean  $m_{\max-obs}$  values for the two populations are different.

The fact that the computed  $p$ -value for the two samples listed in Table 5.2.1-1 is not as low as conventional values used to indicate statistical significance (e.g., a value of 0.05) indicates that in fact the distinction between Mesozoic and younger extension and older extension and non-extension is not important to the assessment of Mmax. Therefore, a second grouping of domains into superdomains was performed using only age, stress, and source stress angle. The resulting composite superdomains (COMP) are listed in Table 5.2.1-3 and the assignment of each of the domains to these combined superdomains is indicated on Appendix Table K-2. Figure 5.2.1-8 shows a histogram of  $m_{\max-obs}$  for the combined superdomains.

The remaining step in computing the priors was to compute the mean and standard deviation of  $m_{\max-obs}$  and perform a bias correction to adjust the mean of  $m_{\max-obs}$  to the mean of  $m^u$ . The SCR catalog contains many earthquakes whose moment magnitudes were estimated from macroseismic data and are, therefore, subject to considerable uncertainty. It is important to capture the impact of this uncertainty on the estimates of the mean and standard deviation of  $m_{\max-obs}$ . The process used to compute the statistics of  $m_{\max-obs}$  for each group of superdomains is as follows.

The updated SCR catalog was used to construct an earthquake catalog for each superdomain. As discussed in Section 3.3.1, it is important to take into account the background distribution for earthquake size in computing the statistics of earthquake sizes. Assuming that earthquake size conforms to a truncated exponential distribution, then the density function for earthquake magnitude is exponential in shape— $f_M(m) \propto \exp(-\beta m)$ , where  $\beta$  is the Gutenberg-Richter  $b$ -value expressed in natural log units [ $\beta = b \times \ln(10)$ ]. If it is assumed that uncertainty in the observed value of magnitude can be represented by a normal distribution,  $f_{\hat{M}|M} \sim N(M, \sigma)$ , then using Bayes's Theorem, the distribution for the true size of an observed earthquake is proportional to the product of the normal and exponential distributions. The result is a normal

distribution centered on the expected magnitude  $E[\mathbf{M}]$  given by Equation 3.3-5 (repeated below for ease of reference).

$$E[\mathbf{M}] = \hat{\mathbf{M}} - \beta\sigma^2[\mathbf{M}|\hat{\mathbf{M}}] \quad (5.2.1-4)$$

In Equation 5.2.1-4,  $\hat{\mathbf{M}}$  is the observed value of magnitude for the earthquake and  $\sigma$  is the standard deviation of the estimate. Thus, for the case of direct observation of moment magnitude from data, the effect is to shift the expected value of the true magnitude from  $\hat{\mathbf{M}}$  to  $E[\mathbf{M}]$  by the amount  $-\beta\sigma^2$ . However, as discussed in Section 3.3.1, the estimation of moment magnitude using regressions against other size measures (other magnitude scales or shaking intensity measures) directly produces the estimate  $E[\mathbf{M}]$ . This situation applies to the majority of the earthquakes in the SCR database. The magnitudes listed in Table K-1 are values of  $E[\mathbf{M}]$ . In the cases where the magnitudes were estimated from correlations with other size measures, then the values listed in Table K-1 are taken directly from the source. In the case where actual moment magnitudes are observed, then  $E[\mathbf{M}]$  is obtained using Equation 5.2.1-4. The value of  $\beta$  used was estimated from the combined catalog of earthquakes in the superdomains, allowing for differences in the rate of activity and average catalog completeness among the superdomains.

Using the values of  $E[\mathbf{M}]$  and  $\sigma[\mathbf{M}]$  for earthquakes in the SCR database, a catalog of earthquakes associated with each superdomain was simulated and the statistics of  $m_{\max-obs}$  for the superdomain set was computed. The simulation process was repeated 10,000 times to generate a composite estimate of the mean and standard deviation of  $m_{\max-obs}$  for the three sets of superdomains listed in Tables 5.2.1-1, 5.2.1-2, and 5.2.1-3. The results are listed in Table 5.2.1-4. The mean values of  $m_{\max-obs}$  were then adjusted to a mean value of  $m^u$  by applying the bias correction process given by Equation 5.2.1-2 and illustrated on Figure 5.2.1-9. The average sample sizes and  $b$ -values for each group of superdomains are also listed in Table 5.2.1-3. Figure 5.2.1-9 shows the three bias adjustment curves and Table 5.2.1-4 lists the resulting values of mean  $m^u$ . After evaluation the results of the above analysis, as well as considering the meaning of prior distributions, it was assessed that the uncertainty in assigning prior distributions for maximum magnitude to the CEUS sources should incorporate two alternative conceptual models: a “two-priors” distribution model and a “single-prior” (composite) distribution model. These alternatives are described below.

#### 5.2.1.1.1 Two-Priors Distribution Model

The results of the updated statistical analysis show that the most significant separation of the SCR database is between superdomains that show Mesozoic-and-younger extension and those that do not. The data used are based on the domains in the SCR database, defined by their most recent age of extension and known characteristics of tectonic stress, and on those superdomains with more than one domain and more than a single earthquake. This subdivision shows reasonable statistical significance (i.e., there is a relatively low  $p$ -value of 0.09, indicating that based on the difference in the mean values, there is a low probability that the two data sets came

from the same data population), but the statistical significance is not strong. Using the bias-adjusted values listed in Table 5.2.1-4, the Mmax priors for the “two-prior” model are as follows:

	Mean Mmax	Sigma
Mesozoic and younger extension (MESE):	7.35	0.75
Non-Mesozoic and younger extension (NMESE):	6.70	0.61

These prior distributions are assigned to the applicable Mmax zones of the CEUS SSC study area, whose boundary and uncertainty have been appropriately accounted for in the SSC model (Section 6.2.1). Also, each seismotectonic zone is assigned one of these prior distributions (or both are assigned with associated weights) to obtain its appropriate prior distributions.

#### 5.2.1.1.2 Composite-Prior Distribution Model

This model assumes that a single, composite-prior distribution is appropriate throughout the region covered by the CEUS SSC seismic source model. The composite prior represents the concept that the characteristics within SCRs that control Mmax cannot be identified with confidence, despite our considerable effort to do so. Therefore, the only distinction made is that the applicable global database must be from SCRs (as defined in Johnston et al., 1994), but no subdivisions are imposed beyond that. This alternative conceptual model is consistent with the relatively weak statistical significance of any subdivision of the SCR as indicators of Mmax. Using the values listed in Table 5.2.1-4, the prior distribution for the composite data set is as follows:

	Mean Mmax	Sigma
Composite (COMP):	7.20	0.64

#### 5.2.1.1.3 Relative Weights

The “two-priors” model is assessed to have slightly higher weight (0.6) than the “composite-prior” model (0.4). Higher weight reflects the fact that there is some statistical significance to the separation of the data into the two Mmax zones, as well as an expectation that the locations of geologically recent crustal extension should have ample faults of sufficient dimensions for larger earthquakes. However, a stronger weight than 0.6 is not assessed because the statistical significance of the separation is not strong and could only be evaluated after multiple domains were combined into superdomains to increase sample size for statistical evaluation.

#### 5.2.1.1.4 Truncation of the Prior Distributions

The Mmax prior distributions described above are represented by unbounded normal distributions. However, there is likely an upper limit to the size of earthquakes that can occur in the CEUS and a bound on the minimum size of the maximum magnitude, as well.

The upper tail of the maximum magnitude distributions for all distributed seismicity seismic sources is truncated at  $M 8\frac{1}{4}$ . This value is selected primarily on the basis of empirical data. **M 8**

$M_{8\frac{1}{4}}$  envelopes the largest magnitude events ever recorded in SCRs. The largest events reported in the SCR earthquake database include the 1668  $M$  7.87 Yellow Sea China earthquake, the  $M$  7.8 New Madrid earthquake, and the 1819  $M$  7.8 Kutch earthquake (Appendix K).  $M_{8\frac{1}{4}}$  also approximates the largest crustal earthquakes recorded anywhere in the world outside of subduction zones, including the 1905  $M_w$  8.1–8.5 Bulnay earthquake (375 km rupture length) (Prentice et al., 2010), the 1949  $M$  8.1 Queen Charlotte earthquake (300–490 km rupture length) (Bostwick, 1984; Rogers, 1986), and the 1957  $M$  8.0–8.1 Gobi Altay earthquake (260 km rupture length; Prentice et al., 2010). The estimated rupture lengths for these earthquakes are comparable to or significantly longer than the rupture lengths of the largest strike-slip crustal earthquakes included in the Wells and Coppersmith (1994) and Hanks and Bakun (2002) worldwide databases that are used to develop empirical relationships for magnitude and fault rupture parameters. The Bulnay earthquake is poorly recorded, and estimates of magnitude are based on physical dimensions of the rupture ( $M$  8.1, Schwartz et al., 1998) and analysis of historical Wiechert seismograms ( $M$  8.2–8.5; Schlupp and Cisternas, 2007). Published magnitude estimates for the 1957 Gobi Altay earthquake range from  $M$  7.8–8.3 (Prentice et al., 2010), with a preferred value of  $M$  8.1 (USGS Earthquake Database, 2010; Choi et al., 2009). Based on these empirical observations of the largest crustal events that have occurred anywhere in the world, our estimate of  $M_{8\frac{1}{4}}$  as the upper-bound truncation of the maximum magnitude distribution reasonably captures the epistemic uncertainty in maximum magnitude. This value is larger than the magnitude of any observed SCR earthquakes.

The prior distributions are also truncated at the minimum magnitude that is assessed to be technically defensible, given a consideration of the observed magnitudes of earthquakes that have occurred with SCRs worldwide. Review of the values of  $m_{\max-obs}$  listed in Tables 5.2.1-1, 5.2.1-2, and 5.2.1-3 for the superdomains used to develop the prior distributions indicates a minimum value of 5.5. Conceptually, this value should be increased slightly by the bias adjustment described above. However, bias adjustments are typically small at these low magnitudes (Figure 5.2.1-9). In addition, the parameter being assessed is the minimum of a distribution, which should be below the minimum observed. Therefore, it was assessed that an appropriate lower truncation point for the prior distributions is  $M_{5\frac{1}{2}}$ .

#### 5.2.1.1.5 Addressing Criticism of the Bayesian Approach

Kijko et al. (2009) have criticized the use of the Bayesian approach for estimation of  $M_{\max}$  as producing results that are biased low. They demonstrate the issue by performing simulations of catalogs of earthquakes generated from an exponential distribution with a known  $M_{\max}$  (set at the mean of a hypothetical  $M_{\max}$  prior distribution) and then estimating the  $M_{\max}$  using the posterior distribution generated from the product of the prior with the sample likelihood function (e.g., the lower right-hand plots on Figures 5.2-1 and 5.2-2). Discussions with the lead author (A. Kijko, pers. comm., 2011) indicate that Kijko et al. (2009) use the mode of the posterior as the point estimate of  $M_{\max}$ . However, the application of the Bayesian Approach for  $M_{\max}$  estimation in the CEUS SSC Project uses the full posterior distribution. A better point estimate of this result is the mean of the posterior rather than the mode. The effect of the use of the mode versus the mean can be clearly seen by comparing the posterior distributions on Figures 5.2.1-1 and 5.2.1-2. On Figure 5.2.1-1, the sample size is small and the posterior distribution has a shape very similar to the prior with only a minor shift in the mode. The shift in the mean between the

prior and the posterior is even less. On Figure 5.2.1-2, the sample size is large and the likelihood function has dramatically affected the shape of the posterior such that the mode occurs at the maximum observed value. However, the posterior distribution does extend to magnitudes larger than the maximum observed such that the mean would be a larger value.

The effect of use of the mode of the posterior, as in Kijko et al. (2009), versus the mean of the posterior, a more appropriate point estimate of the results used in the CEUS SSC Project, is illustrated on Figure 5.2.1-10. A prior distribution for maximum magnitude with a mean of 6.9 and a standard deviation of 0.5 was assumed. Various size samples of exponentially distributed earthquakes were then simulated from an exponential distribution of magnitudes truncated at the mean of the prior, 6.9. For each sample the likelihood function was used to develop a posterior distribution. The mean and the mode of this posterior were then computed. The process was repeated for 1000 simulations of each sample size. The average values of the mean and mode for each sample size are plotted on Figure 5.2.1-10. These results confirm the conclusion of Kijko et al. (2009) that the mode of the posterior is a biased estimate of  $M_{\max}$ , with the bias to smaller values. However, the mean of the posterior does not display any significant bias. Therefore, it is concluded that the application of the Bayesian approach using the full posterior distribution should not lead to biased estimates of  $M_{\max}$ .

#### 5.2.1.1.6 Application to CEUS Distributed Seismicity Sources

The application of the Bayesian  $M_{\max}$  approach requires development of the likelihood function Equation 5.2.1-1 from the assessment of the maximum observed earthquake in each source and the number of earthquakes larger than a specified minimum magnitude. The assessment of these parameters was based on the project earthquake catalog (Chapter 3), and descriptions of the largest earthquakes in each source are provided in Chapters 6 and 7. The minimum magnitude used for the earthquake counts is  $M$  4.7, as this is at the lower limit of one of the magnitude intervals used in the earthquake catalog analysis and there is a focus on earthquakes of significance for a hazard analysis. The magnitude estimates for the earthquakes in the CEUS catalog are subject to uncertainty. This uncertainty was incorporated into the assessment of  $m_{\max-obs}$  using the procedure described above for the SCR domains by simulating 100,000 sets of earthquake magnitudes for the domain catalogs, selecting the largest magnitude for each simulated catalog, and then binning these values in 0.1-magnitude units to develop a distribution for  $m_{\max-obs}$ . In some cases, there is uncertainty in assigning the largest observed earthquake to a particular source, due to uncertainty in location for earthquakes near source boundaries. This uncertainty was incorporated by developing alternative catalogs including or excluding the particular earthquake, developing simulated distributions for  $m_{\max-obs}$  for each case, and then combining the results to produce a composite distribution.

The uncertainty distribution for  $m_{\max-obs}$  was incorporated into the assessment of  $M_{\max}$  distributions for the distributed seismicity sources by developing a likelihood function for each possible value of  $m_{\max-obs}$  using Equation 5.2.1-1, using this likelihood function with the appropriate prior to develop a posterior  $M_{\max}$  distribution, and then weighting this posterior by

the probability assigned to the value of  $m_{\max-obs}$ . The sum of these weighted posteriors represents the composite Mmax distribution for the source.

### 5.2.1.2 Kijko Approach to Mmax Assessment

The Kijko approach (Kijko, 2004) provides an assessment of Mmax based on only the observed distribution of earthquakes in a region. As described in Kijko (2004), the cumulative distribution for  $m_{\max-obs}$  in a source zone is given by

$$F_{m_{\max-obs}}(m) = \begin{cases} 0 & m < m_0 \\ [F_M(m)]^N & m_0 \leq m \leq m^u \\ 1 & m > m^u \end{cases} \quad (5.2.1-5)$$

where  $F_M(m)$  is the cumulative probability distribution for magnitude and parameters  $m_0$ ,  $m^u$ , and  $N$  as defined above in Section 5.2.1.1. Kijko (2004) shows that the expected value of  $m_{\max-obs}$  is given by the expression

$$E(M_{\max-obs}) = \int_{m_0}^{m^u} m \frac{dF_{\max-obs}(m)}{dm} dm \quad (5.2.1-6)$$

Integration by parts yields

$$E(M_{\max-obs}) = m^u - \int_{m_0}^{m^u} F_{m_{\max-obs}}(m) dm \quad (5.2.1-7)$$

which leads to the expression:

$$m^u = E(M_{\max-obs}) + \int_{m_0}^{m^u} F_{m_{\max-obs}}(m) dm \quad (5.2.1-8)$$

Kijko (2004) presents three alternative relationships for the application of Equation 5.2.1-8. The first is based on application of the truncated exponential distribution for  $F_M(m)$ , leading to the distribution for  $F_{m_{\max-obs}}(m)$  given by Equation 5.2.1-2. This is designated the K-S (Kijko-Sellevoll) estimator by Kijko (2004). The second relationship incorporates uncertainty in  $\beta$  (the  $b$ -value) and takes the form

$$F_{m_{\max-obs}}(m) = \begin{cases} 0 & m < m_0 \\ \left[ C_\beta \left\{ 1 - \left( \frac{p}{p+m-m_0} \right)^q \right\} \right]^N & m_0 \leq m \leq m^u \\ 1 & m > m^u \end{cases} \quad (5.2.1-9)$$

where  $p = \bar{\beta} / \sigma_\beta^2$ ,  $q = (\bar{\beta} / \sigma_\beta)^2$ , and  $C_\beta = \left[ 1 - \{p / (p + m^u - m_0)\}^q \right]^{-1}$ . This second formulation is designated the K-S-B (Kijko-Sellevoll-Bayes) estimator by Kijko (2004). The third formulation makes no assumption about the form of the magnitude distribution. Instead, it used a kernel density estimation technique to estimate the form of the magnitude distribution from the observed magnitudes. This form, designated the N-P-G form in Kijko (2004) was not investigated for application in the CEUS SSC. Its intended use is to cases where characteristic earthquake type behavior is observed. In the CEUS SSC model, known earthquakes of this type are modeled by a separate set of RLME sources. With these earthquakes addressed by separate sources, the remaining earthquakes in the Project catalog display an approximately exponential distribution, which are addressed by the K-S and K-S-B estimators.

The behavior of the K-S and K-S-B estimators as a function of  $m_{\max-obs}$  and  $N$  is shown on Figure 5.2.1-11. The values of  $m^u$  were computed by iteratively solving Equation 5.2.1-8 until convergence. Note that the estimates for the K-S estimator reach a point where the iterative solutions do not converge. The K-S-B estimator converges for all values of  $m^u$  tried. Also shown on Figure 5.2.1-11 is the relationship between  $m^u$  and the median value given by Equation 5.2.1-2, indicating that the bias adjustment used in developing the Bayesian priors is nearly equivalent to the Kijko (2004) estimators of  $m^u$ . This is not surprising given that they are based on similar formulations.

The relationships shown on Figure 5.2.1-11 indicate that the Kijko estimators for the expected value of  $m^u$  are subject to the same need for large values of  $N$  as the bias adjustment relationship used to develop the Bayesian priors. In order to apply the approach to situations where  $N$  is small, an additional constraint must be used. This constraint is supplied by the assumption of a limiting size for CEUS earthquakes that was used to truncate the Bayesian prior distributions in Section 5.2.1.1. Kijko (2004) presents the following relationship for the cumulative probability function for  $m^u$ :

$$P(m^u < z) = F(m^u) = 1 - F_{m_{\max-obs}}(m_{\max-obs} | z) \quad (5.2.1-10)$$

Figure 5.2.1-12 shows the behavior of Equation 5.2.1-10 as a function of  $N$ . For values of  $N$  below about 100, the value of  $F(m^u)$  reaches a limiting value less than 1.0 as  $m^u$  approaches infinity ( $\infty$ ). Kijko (2004) discusses this limiting value of  $F(m^u)$  as an indicator of the probability that the K-S or K-S-B estimator provides meaningful results.

As indicated by Figure 5.2.1-12, the cumulative distribution function  $F(m^u)$  does not provide a complete probability distribution for  $m^u$  in the unbounded case. However, if a limiting value for  $m^u$  is imposed, then  $F(m^u)$  can be truncated at this point and renormalized to produce a probability distribution for  $m^u$ .

While this approach allows one to construct a proper probability distribution for  $m^u$  regardless of the value of  $N$  and  $m_{\text{max-obs}}$ , it involves truncation of substantial probability mass for most practical applications. The truncated probability mass is given by  $P(m^u > 8\frac{1}{4})$  calculated using Equation 5.2.1-10. The assessment was made that the point where the truncated probability mass equals the remaining probability mass,  $P(m^u > 8\frac{1}{4}) = 0.5$ , represents the limit of applicability of the Kijko Mmax approach.

The application of a lower truncation point for Mmax distributions at  $M 5\frac{1}{2}$  requires a modification of the approach. The first step is to compute the unbounded cumulative distribution function  $F(m^u)$  using Equation 5.2.1-10. This distribution is modified by imposing the requirement that  $m^u$  must be  $\geq 5\frac{1}{2}$  by computing its derivative, removing the probability mass below  $5\frac{1}{2}$ , if any, and then renormalizing. The effective result is to increase the value of  $P(m^u > 8\frac{1}{4})$  for those cases where the maximum observed magnitude is less than  $5\frac{1}{2}$ .

After a variety of exploratory calculations and considerations, the following key constraints were made in the application of the Kijko approach to assessment of Mmax for the CEUS SSC model:

- The K-S-B approach (Kijko, 2004) that incorporates the uncertainty in  $b$ -value for the exponential distribution will be used, with an upper truncation at  $M 8\frac{1}{4}$  and a lower truncation at  $M 5\frac{1}{2}$ .
- Uncertainties in the magnitude of the largest earthquake in each source are assessed using the approach described in Section 5.2.1.1.5.
- For those sources with a maximum observed magnitude derived from the paleoseismic record, the Kijko approach cannot be used because the approach assumes a complete record (historical earthquakes are adjusted for catalog completeness). We have no approach to formally evaluate the completeness of the paleoseismic record. An exploratory calculation using, for example, the four earthquakes identified for the Illinois Basin Extended Basement (IBEB) source, which has the largest number of observed paleoseismic earthquakes for any seismic source in the model, confirms that a high value of  $F(m^u > 8\frac{1}{4})$  results from consideration of these events. Therefore, giving zero weight to the Kijko approach is reasonable.
- The weighting scheme for the use of the Bayesian approach versus the Kijko approach should be source-specific (to account for the numbers and magnitudes of observed earthquakes). In no case should the Kijko approach be given higher weight than the Bayesian approach, considering the higher reliance on the Bayesian approach (and similar analogy-based approaches) by the technical community.

### 5.2.1.3 Weights for the Alternative Mmax Approaches

Because the probability that Mmax is much greater than 8 is a measure of the statistical stability of the Kijko approach—and is noted by its author as providing a measure of whether the approach is producing meaningful Mmax estimates—it is used as an index for weighting the Kijko versus Bayesian approaches. At values of  $P(m^u > 8^{1/4}) = 0.5$  and higher, the Kijko approach is assessed to have zero weight. Likewise, at  $P(m^u > 8^{1/4}) = 0$ , where Kijko's approach is at its strongest with large numbers of larger earthquakes, the Kijko approach is assessed to have equal weight (0.5) relative to the Bayesian approach. With these endpoints, a linear relationship is developed that provides the weight for the Kijko approach as a function of the calculated value of  $P(m^u > 8^{1/4})$  for the source of interest.

Using the linear relationship between  $P(m^u > 8^{1/4})$  values and the Kijko weights, the calculated weights for the Kijko approach for the various source zones are shown in Table 5.2.1-5. Using the assumptions discussed previously and the cutoff of a  $P(m^u > 8^{1/4})$  value equal to or greater than 0.5, it can be seen that the Kijko approach is given zero weight for several sources: for some sources, the Kijko approach is given zero weight because the paleoseismic record is used to constrain the size of the maximum observed event; for others, zero weight is given because of the high  $P(m^u > 8^{1/4})$  values.

### 5.2.1.4 Example Mmax Distributions

Using the Bayesian and Kijko approaches in the manner described in this section, Mmax distributions were developed for both the Mmax zones (Section 6.2.3) and for the seismotectonic zones (Section 7.4.2). An example of how these distributions are displayed is given on Figures 5.2.1-13 and 5.2.1-14. As a reminder, in the master logic tree, the Mmax zones approach is assessed a weight of 0.4, versus 0.6 for the seismotectonic zones approach. Given the Mmax zones approach, the weight assessed for a single, composite zone is 0.4, versus 0.6 for two Mmax zones. Given two Mmax zones, the weight assessed for the “narrow” interpretation of Mesozoic and younger extended zone (MESE-N) configuration is 0.8, versus a weight of 0.2 assessed for the “wide” interpretation (MESE-W).

Figure 5.2.1-13 shows the Mmax distribution for the Mesozoic and younger extended zone (MESE-N), which is one of the Mmax zones. Shown in all of the plots, regardless of the assessed weights, are the results for the Kijko approach, the Bayesian approach using the composite prior distribution, and the Bayesian approach using a MESE or non-MESE prior distribution. The weights assessed for the Kijko approach in Table 5.2.1-5 are functions of the  $P(m^u > 8^{1/4})$  value and whether paleoseismic data is used to define the size of the maximum observed magnitude. As discussed in Section 5.2.1.1.3, the weight assessed for the “two-priors” model is 0.6, and to the “composite” model, 0.4. Mmax estimates for each of these prior distributions are given along with their weights, which are the product of the Kijko versus Bayesian weights and the two-priors versus composite-prior weights. The final composite Mmax distribution is shown by the thick red histogram that reflects the probability mass function at 0.1-magnitude increments.

A second example of Mmax distribution is shown on Figure 5.2.1-14 for the Northern Appalachian (NAP) seismotectonic zone. The same convention is used in the labeling and

display of the results for the Kijko and Bayesian approaches. In this case, the weight assessed for the Kijko approach is zero, based on a  $P(m^u > 8^{1/4})$  being greater than 0.5. The results of the Kijko approach are shown simply for purposes of comparison, but they are not incorporated into the final composite Mmax distribution, shown in red.

For use in the hazard calculations, the maximum magnitude distributions for each source are then represented by a five-point discrete approximation to an arbitrary continuous distribution developed by Miller and Rice (1983). (The use of a discrete representation of a continuous distribution is described in more detail in Section 5.3.3.1.3.) The distributions for the two example sources are listed in Table 5.2.1-6.

### **5.2.2 Other Mmax Issues**

One of the key uncertainties regarding the assessment of Mmax for seismic sources in the CEUS is spatial variation of Mmax throughout any given seismic source. That is, is it realistic to assume that a single Mmax distribution developed for a seismic source applies to all locations within that source? To a large extent, this issue is resolved within more active regions where active faults have been identified and Mmax can be assessed on a fault-specific basis using approaches such as fault rupture dimensions. In SCRs like the CEUS, however, the physical bases for specifying differences in Mmax spatially are not known with confidence. Unless specific faults can be identified that are the causative structures, the use of fault dimensions to constrain Mmax is problematic. The tectonic history of a region and the presence of significant geologic structures suggest that such structures might host future larger earthquakes, but no systematic studies have been conducted to show that the presence or absence of older geologic structures leads to differences in Mmax potential. Further, many SCRs show evidence of significant older geologic structures, but they show no evidence of large earthquake occurrence (Johnston et al., 1994). Also, in his inventory and evaluation of possible Mmax approaches, Wheeler (2009, pp. 12-13) cites the difficulties in using local geologic structures to estimate Mmax when there is no direct geologic evidence for young faulting.

Using current approaches, the broad distributions of Mmax developed for seismic sources in the CEUS are assumed to be entirely epistemic and applicable throughout the source of interest. If the spatial variation of Mmax were known, that is, if it were possible to say that one part of the source should have a higher Mmax than another part, then that variation could be captured as aleatory variability. The result might be two epistemic distributions—one for regions marked by higher Mmax and one for regions with lower Mmax—and both distributions could be narrower than the current distribution for the entire source. At present, if there is a basis for identifying a spatial variation in Mmax, that information is used in the CEUS SSC Project to identify a separate seismic source (see Section 4.2.3). The Mmax distributions for the seismic sources in the CEUS developed for the Mmax zones (Section 6.3.2) and for the seismotectonic zones (Section 7.4.2) are quite broad in many cases to reflect the current uncertainties that exist with the estimation of Mmax within an SCR. It is hoped that the estimation of Mmax will continue to be a focus of research efforts in the scientific community, and that those efforts will lead to reductions in the epistemic uncertainties that currently exist.

## 5.3 Earthquake Recurrence Assessment

### 5.3.1 Smoothing to Represent Spatial Stationarity

The CEUS SSC model is based to a large extent on an assessment that spatial stationarity of seismicity will persist for time periods of interest for PSHA (approximately the next 50 years for engineered structures). Stationarity in this sense does not mean that future locations and magnitudes of earthquakes will occur exactly where they have occurred in the historical and instrumental record. Rather, the degree of spatial stationarity varies as a function of the type of data available to define the seismic source. RLME sources are based largely on paleoseismic evidence for repeated large-magnitude ( $M \geq 6.5$ ) earthquakes that occur in approximately the same location over periods of a few thousand years. Uncertainties in the locations and sizes of these events are a function of the types of data available (e.g., fault-specific repeated displacements on the Meers fault, and shaking effects over a relatively small region for the Marianna source). Because the record that defines the RLME sources spans a relatively long time period and records large-magnitude events, repeated events for these sources are expected to occur within a restricted location defined by the RLME source.

On the other hand, patterns of seismicity away from the RLME sources within the Mmax and seismotectonic zones are defined from generally small- to moderate-magnitude earthquakes that have occurred during a relatively short (i.e., relative to the repeat times of large events) historical and instrumental record. Thus the locations of future events are not as tightly constrained by the locations of past events as for RLME sources. As discussed below in Section 5.3.2, the spatial smoothing operation is based on calculations of earthquake recurrence within one-quarter-degree or half-degree cells, with allowance for “communication” between the cells. Both  $a$ - and  $b$ -values are allowed to vary, but the degree of variation has been optimized such that  $b$ -values vary little across the study region. Also,  $a$ -values are neither “spiky,” reflecting too strong of a reliance on the exact locations and rate densities of observed events, nor too smooth, reflecting the belief that the observed record does not provide a spatial constraint on rate density variation. Likewise, the recurrence calculation considers weighting of magnitudes in the recurrence rate calculations; thus moderate events are assigned more weight than smaller events.

Ultimately, any smoothing operation of seismicity is founded on expert judgment related to the expected future distribution of moderate- to large-magnitude events. The CEUS SSC model gives strong consideration to locations of RLME sources as being spatially stationary through the future time periods of interest. The smoothing operation within the distributed seismicity zones results in variations in  $a$ - and  $b$ -values over scales that were judged by the TI Team to be reasonable, given the technical community’s views on spatial stationarity and the relationship between observed small- to moderate-magnitude seismicity and future moderate- to large-magnitude seismicity.

## 5.3.2 Smoothing Approach

### 5.3.2.1 Development of Penalized-Likelihood Approach and Formulation

#### 5.3.2.1.1 Model for the Penalized-Likelihood Function of Recurrence Parameters

This section introduces and discusses the formulation for the calculation of earthquake recurrence parameters for one source zone (or one cell within a source zone) under very simple assumptions, then reformulates and expands the formulation to include a number of elements that make the formulation more robust, realistic, and flexible. These elements include the reformulation in terms of magnitude bins, and the introduction of magnitude-dependent weights, catalog incompleteness, the effect of maximum earthquake magnitude ( $M_{\max}$ ), spatial variation of parameters within the source zone, and the prior distributions of  $b$ .

The first model to consider is the basic model, first presented by Aki (1965) and others. In this formulation, the number of earthquakes with magnitudes in the interval between  $m$  and  $m + dm$  that occur in a source zone, within a time period of duration  $T$ , follows a Poisson probability distribution, with mean given by the following expression:

$$n(m \leq M < m + dm) = AT\nu\beta e^{-\beta(m-m_0)} dm \quad m \geq m_0 \quad (5.3.2-1)$$

where  $A$  is the area of the source zone (in units of equatorial degrees squared),  $T$  is the time period of interest (i.e., the duration of the catalog in years),  $\nu$  is the rate per unit time and per unit area for earthquakes with magnitude greater than or equal to  $m_0$  (the lowest magnitude considered in the recurrence analysis), and  $\beta$  is the slope of the exponential magnitude-recurrence law (i.e., the  $b$ -value times  $\ln[10]$ ). In addition, it is assumed that the number of earthquakes in non-overlapping magnitude intervals is independent, so that earthquake occurrences in time represent a marked Poisson process.

Before going further, it is useful to make some comments about the above formulation. First,  $M_{\max}$  is not considered at this early stage. Second, the magnitude  $m_0$  is not the same as the lower-bound magnitude considered in the hazard integration; it is typically much smaller. This project uses  $m_0$  equal to moment magnitude 2.9. Finally, many of the assumptions in this initial formulation will be relaxed later in this section. Still, this initial formulation serves as a building block for the more general formulation and is helpful because it lends itself to the development of useful insights about the methodology.

Data input to this first simplified model consist of the list of earthquake magnitudes in the catalog; i.e.,  $m_1, m_2, \dots, m_N$ , where  $N$  is the number of earthquakes in the catalog. In this project, these magnitudes are all moment magnitudes, and some of them may have been converted to moment magnitude from the magnitude, epicentral intensity, or felt area in the primary catalogs (see Section 3.3). In addition, the catalog is considered complete over the time period  $T$ , for all magnitudes above  $m_0$ . A somewhat surprising feature of the Poisson process is that the occurrence times of these earthquakes are immaterial, as long as the earthquakes occurred within

the time period  $T$  of the catalog. This property is actually a natural consequence of the “lack of memory” property of the Poisson process.

The likelihood function for the model parameters takes the form

$$\ell(\nu, \beta) = \prod_{i=1}^N (\nu AT \beta e^{-\beta(m_i - m_0)}) \exp \left[ -\nu A \int_{m_0}^{\infty} T \beta e^{-\beta(m - m_0)} dm \right] \quad (5.3.2-2)$$

where all multiplicative constants that are independent of the parameters have been omitted because they do not affect the results. In this equation and in the equations that follow, index  $i$  denotes the earthquakes in the catalog and  $N$  denotes the number of such earthquakes. Note that the integral is equal to  $T$  in this special case because  $T$  is independent of magnitude (and can be moved out of the integral) and the exponential probability density function integrates to unity. This simplification does not apply in the more realistic case to be considered later, where the completeness time depends on magnitude.

In general, the likelihood function indicates the degree of consistency between the parameters that one wants to estimate (in this case,  $\nu$  and  $\beta$ ) and the available data (in this case, the number of earthquakes and their magnitudes during a time period  $T$ ). If the data are abundant, the likelihood function has a narrow shape, indicating low uncertainty. If the data are scarce, the likelihood function has a broad shape, indicating high uncertainty. In the context of the maximum-likelihood method, one chooses the parameters that maximize the likelihood function and one estimates the uncertainty using the second derivatives of the natural log of the likelihood, evaluated at the point of maximum likelihood.

To derive Equation 5.3.2-2, one can formulate the Poisson likelihood function for each small interval of width  $dm$ , using Equation 5.3.2-1, multiply these likelihoods, and then compute the limit of this product as  $dm$  approaches 0, taking into account that when  $dm$  is very small, the number of earthquakes in an interval is either 0 or 1.

Note that the integral in Equation 5.3.2-2 is equal to  $T$  in this special case because  $T$  is independent of magnitude (and can be moved out of the integral) and what remains inside the integral (i.e., the exponential probability density function) integrates to unity. This simplification does not apply in the more realistic case to be considered later, where the completeness time depends on magnitude. If we apply this simplification, we note that the likelihood function is separable into a product of factors that depend on the rate  $\nu$  and factors that depend on the exponential slope  $\beta$ , i.e.,

$$\ell(\nu, \beta) = (\nu AT)^N e^{-\nu AT} \times \prod_{i=1}^N (\beta e^{-\beta(m_i - m_0)}) \quad (5.3.2-3)$$

Note that the  $\nu$ -dependent portion and the  $\beta$ -dependent portions of the likelihood function are separable. This separability is lost later, as the formulation is made more robust and realistic.

The first ( $\nu$ -dependent) portion in the above equation is the traditional likelihood for a Poisson distribution. The second ( $\beta$ -dependent) portion is the traditional likelihood for an exponential distribution.

This separability also implies that the maximum-likelihood estimates of  $\nu$  and  $\beta$  are decoupled in this simple case. In particular, by taking the logarithm of the above expression, differentiating with respect to each parameter, making the result equal to 0, and solving for the parameter, we obtain the following well-known results for the maximum-likelihood estimates of  $\nu$  and  $\beta$ :

$$\nu_{ML} = \frac{N}{AT} \quad (5.3.2-4)$$

$$\frac{1}{\beta_{ML}} = \frac{1}{N} \sum_{i=1}^N (m_i - m_0) \quad (5.3.2-5)$$

The last result was first derived independently by Aki (1965) and Utsu (1965). Note that in the case where  $N = 0$ , the maximum-likelihood estimate of the rate  $\nu$  is zero. On the other hand, if one is working with the entire likelihood function (in order to represent an epistemic uncertainty), one sees that the  $\nu$ -dependent portion of the likelihood in Equation 5.3.2-3 for  $N = 0$  follows an exponential distribution, which happens to have a mean value of  $1/(AT)$  (i.e., the value in Equation 5.3.2-4 corresponding to  $N = 1$ ). Thus, consideration of the full-likelihood function for  $\nu$  gives rise to a natural “floor” in regions of low seismicity.

Note also that this likelihood function for the Poisson portion has sharper peaks (i.e., lower coefficient of variation, or COV) when  $N$  is large, indicating that only a narrow range of values of  $\nu$  are consistent with the catalog. In contrast, the distribution is broad when  $N$  is small (becoming as broad as the exponential distribution when  $N = 0$ ). This is illustrated on Figure 5.3.2-1.

Similarly, Figure 5.3.2-2 shows the likelihood function for the  $b$ -value, for different values of  $N$ . Again, the COV decreases as  $N$  increases.

Equation 5.3.2-3 is in fact easier to derive than the equivalent 5.3.2-2. One begins by introducing the standard assumptions that the number of earthquakes follows a Poisson distribution, independent of the magnitudes, and that the magnitudes are exponential and independent identically distributed (iid). Equation 5.3.2-3 then follows automatically as the product of the Poisson probability mass function and the  $N$  exponential probability density functions (again, omitting multiplicative constants that are independent of the parameters  $\nu$  and  $\beta$ ).

This simple formulation of the magnitude-recurrence model is useful as a starting point but is not always robust and sufficient in practice. The remainder of this section describes the various modifications to the formulation, in order to make it more robust and flexible.

The first difficulty arises from the continuous nature of the above formulation, which assumes that the exponential assumption applies at both small and large scales. In practice, the exponential assumption may not apply at small scales (i.e., over differences of a few tenths of a magnitude units, or less), for a number of reasons. Most importantly, some of the earthquake magnitudes in the catalog have been effectively binned into integer epicentral intensity and then converted to magnitude. Other possible causes include problems in the conversion to moment magnitude, edge effects, or the phenomenon investigated by Lombardi (2003).

This deviation from exponentiality is illustrated by Figure 5.3.2-3, which shows a histogram of the magnitudes in the earthquake catalog developed in Chapter 3 and used later in this section for the calculation of recurrence parameters. Focusing on the left portion of this figure (say, magnitudes lower than 3.5), one notices that the data deviate substantially from a smooth exponential shape. These deviations are not consistent with the exponential model, given the very large earthquake counts in these bins. These large earthquake counts mean that the continuous formulation of the likelihood may incorrectly interpret the local slope of the histogram around magnitude 3 as containing information about the exponential slope  $\beta$ .

In order to avoid these potential problems, the likelihood function is reformulated in terms of the earthquake counts in discrete magnitude bins, with bin sizes appropriately selected so that magnitudes converted from intensity fall in the middle of these bins.

Considering bins of  $\delta$  magnitude units (i.e., first bin between magnitudes  $m_0$  and  $m_0 + \delta$ , second bin between  $m_0 + \delta$  and  $m_0 + 2\delta$ , etc.), one can write the likelihood function

$$\ell(\nu, \beta) = \prod_{k=1}^{\infty} (\nu A T p_k)^{n_k} \exp \left[ -\nu A \sum_{k=1}^{\infty} T p_k \right] \quad (5.3.2-6)$$

where  $n_k$  is the number of earthquakes in the  $k$ -th magnitude bin ( $m_0^k \leq m < m_0^{k+1}$ ),

$$p_k = p_k(\beta) = \exp[-\beta(m_0^k - m_0)] - \exp[-\beta(m_0^{k+1} - m_0)] \quad (5.3.2-7)$$

is the probability mass associated with the  $k$ -th magnitude bin, and  $m_0^k = m_0 + (k-1)\delta$  is the magnitude at the lower end of the  $k$ -th magnitude bin. One can obtain Equation 5.3.2-6 from Equation 5.3.2-2 by replacing each occurrence of the exponential density  $\beta \exp[-\beta(m - m_0)]$  with the value of  $p_k$  for the magnitude bin where  $m$  falls. By working with earthquake counts in discrete bins, sensitivity to small-scale deviations from the exponential model (i.e., deviations at scales of a few tenths of a magnitude unit or smaller) is removed, resulting in a more robust formulation. We note that the expression for the likelihood function in Equation 5.3.2.6 is still a separable function of  $\nu$  and  $\beta$ , although one cannot easily solve for  $\beta_{ML}$ .

Perhaps the best known example of this discrete-magnitude formulation for the likelihood function is the paper by Weichert (1980). The discrete-magnitude formulation was also used in the EPRI-SOG project.

It is also worth noting that the number  $n_k$  in Equation 5.3.2-6 is not necessarily an integer number. This project accounts for the effect of uncertainty in magnitude by calculating an “event factor” for each earthquake (see Chapter 3). Thus,  $n_k$  represents the sum of the event factors for all the earthquakes in the  $k$ -th magnitude bin.

A second modification is required because the assessment may result in a lower weight for lower magnitude bins. For instance, the magnitude-recurrence law may deviate from exponential, or the magnitude-conversion models or completeness model may be less reliable for lower magnitudes. The USGS (Petersen et al., 2008) use of alternative low-magnitude cutoffs may be viewed as a special case of magnitude-dependent (or magnitude- and time-dependent) weights. One can represent these weights by the quantities  $w_1, w_2, \dots$  (indexed by  $k$ , the magnitude-bin number; note also that these weights do not necessarily add to 1, and the resulting weighted-likelihood function is

$$\ell(\nu, \beta) = \prod_{k=1}^{\infty} (\nu A T p_k)^{n_k w_k} \exp \left[ -\nu A \sum_{k=1}^{\infty} T p_k w_k \right] \quad (5.3.2-8)$$

The introduction of weights, resulting in Equation 5.3.2-8, is equivalent to raising the portion of the likelihood function associated with magnitude bin  $k$  to a power  $w_k \leq 1$ . Raising to a power less than 1 has the effect of flattening this portion of the likelihood, without shifting the location of its peak. For instance, if there are  $n_1$  earthquakes in the first magnitude bin, and this bin is given a weight of 0.1, the associated portion of the likelihood becomes flatter (as if it had only  $n_1/10$  earthquakes), but the location of its peak remains unchanged (recall Figures 5.3.2-1 and 5.3.2-2).

We note that the summation in the above equation cannot be simplified after the introduction of the weights. As a result, it is impossible to obtain the maximum-likelihood estimates of  $\nu$  and  $\beta$  in closed form.

A third modification is necessary to account for magnitude-dependent catalog completeness. Following EPRI-SOG (1986), earthquakes in magnitude bin  $k$  are counted if they occurred after a certain date  $t_{0,k}$ , even if the catalog is not fully complete after that date, and the associated catalog duration is characterized by the Equivalent Period of Completeness, which is defined as

$$T_{E,k} = \int_{t_{0,k}}^{\text{present}} P_D(t; k) dt \quad (5.3.2-9)$$

where  $P_D(t; k)$  is the detection probability for magnitudes in bin  $k$  at time  $t$ . The detection probabilities and equivalent periods of completeness are calculated in Section 3.5 using the EPRI-SOG methodology for determining completeness (which includes a penalized-likelihood analysis of recurrence). For the purposes of this discussion, it is assumed that the equivalent period of completeness is the same within the source zone under consideration and for all magnitudes in a certain magnitude bin. In the final model to be developed here, it will be assumed that the equivalent periods of completeness are constant within each cell comprising the source zone. Another assumption in this derivation is that all earthquakes under consideration (which have magnitudes  $m_1, m_2, \dots, m_N$ ) occurred after their corresponding dates  $t_{0,k(m_i)}$ .

After introducing magnitude-dependent completeness, the likelihood function becomes

$$\ell(\nu, \beta) = \prod_{k=1}^{\infty} (\nu A T_{E,k} p_k)^{n_k w_k} \exp \left[ -\nu A \sum_{k=1}^{\infty} T_{E,k} p_k w_k \right] \quad (5.3.2-10)$$

A fourth modification is necessary to account for maximum magnitude  $M_{\max}$ . In the case of a single  $M_{\max}$  value, Equation 5.3.2.7 is modified by considering that portions of a magnitude bin, or the entire bin, may be above  $M_{\max}$ , resulting in the expression

$$p_k(M_{\max}) = \begin{cases} \exp[-\beta(m_0^k - m_0)] - \exp[-\beta(m_0^{k+1} - m_0)] & \text{for } m_0^{k+1} < M_{\max} \\ \exp[-\beta(m_0^k - m_0)] - \exp[-\beta(M_{\max} - m_0)] & \text{for } m_0^k < M_{\max} < m_0^{k+1} \\ 0 & \text{for } M_{\max} < m_0^k \end{cases} \quad (5.3.2-11)$$

There should be a normalizing constant in the above equation, but this constant is very nearly equal to unity (because  $m_0$  is 2.9 and  $M_{\max}$  is 5.5 or greater) and can be neglected in this case. For the case where there is epistemic uncertainty in  $M_{\max}$  (which is represented in this project by a five-point discrete distribution), one can use the expected value (with respect to  $M_{\max}$ ) of the  $p_k$  given by Equation 5.3.2-11; that is,

$$p_k = E_{M_{\max}} [p_k(M_{\max})] \quad (5.3.2-12)$$

where  $E_{M_{\max}} [\bullet]$  denotes the expect-value operation with respect to uncertainty in  $M_{\max}$ . Another consequence of introducing  $M_{\max}$  is that the number of magnitude bins becomes finite. In the equations that follow,  $Q$  will denote the highest bin with a nonzero value of  $p_k$ .

Up to this point, the formulation does not include spatial variation of parameters within a source zone. Consideration of spatial variation is necessary in this project because the assumption of geographically constant rate and  $b$ -value is not necessarily applicable to some of the large source zones developed in Chapter 4. There are two commonly used approaches to introduce spatial

variation of seismicity within a source zone; namely, the penalized-likelihood (EPRI-SOG, 1986) and kernel approaches (e.g., Frankel, 1995; Stock and Smith, 2002). This project uses the penalized-likelihood approach, with a number of methodological refinements. A discussion of the two approaches and their merits is presented in Section 5.3.2.4.

The first step in the penalized-likelihood approach is to divide the source zones into cells for the purposes of the recurrence-model evaluation and hazard calculations. This division is often done along parallels and meridians. This project uses a cell dimension of one-quarter degree by one-quarter degree. For source zones of large dimensions, the cell size is increased to one-half degree by one-half degree for computational efficiency. Cells near source-zone boundaries have smaller areas and irregular shapes, generated so that the geometry of a source zone is honored in the recurrence and hazard calculations, without any quantization error.

The likelihood function is then formulated separately for each cell in the source zone. The joint likelihood function for the values of  $\nu$  and  $\beta$  in all  $M$  cells within the source zone takes the form:

$$\ell(\mathbf{v}, \boldsymbol{\beta}) = \prod_{j=1}^M \left\{ \prod_{k=1}^Q \left( \nu_j A_j T_E(k, j) p(k, j) \right)^{n(k, j) w_k} \exp \left[ -\nu_j A_j \sum_{k=1}^Q T_E(k, j) p(k, j) w_k \right] \right\} \quad (5.3.2-13)$$

where vectors  $\mathbf{v}, \boldsymbol{\beta}$  contain the values of  $\nu$  and  $\beta$  in all cells within the source zone,  $j$  is the index for the cells ( $j=1, \dots, M$ ). Also, the notation has been changed slightly from previous equations, so that  $T_E(k, j)$ ,  $n(k, j)$ , and  $p(k, j)$  are the equivalent period of completeness, earthquake count, and truncated-exponential bin probability (Equation 5.3.2.12) for magnitude bin  $k$  and cell  $k$ .

Because cells are small and most cells do not contain enough earthquakes to allow the reliable estimation of  $\nu_j$  and  $\beta_j$  using these earthquakes alone, and because very large variations in  $\nu$  and  $\beta$  (particularly the latter) between adjacent cells are not considered physically realistic, one introduces penalty functions that penalize those solutions where  $\nu$  and  $\beta$  have large variations between adjacent cells. Thus the solution to the penalized-likelihood problem represents an optimal compromise between consistency with the data (as indicated by a high value of the likelihood) and smoothness (as indicated by a low value of the penalty function). For a given value of the smoothing parameters, the likelihood has a stronger effect on the solution in cells where data are abundant because only a narrow range of values are consistent with the data.

This project utilizes a penalty function based on the Laplacian operator, which represents a generalization of the second derivative to multiple dimensions, and is commonly used in applications of this kind (e.g., Fukuda and Johnson, 2008). For a function  $f(x, y)$  in two dimensions, the Laplacian operator and its lowest-order finite difference approximation are given by

$$\begin{aligned}
\Delta f &= \frac{\partial^2 f}{\partial x^2} + \frac{\partial^2 f}{\partial y^2} \approx \\
&\approx 2 \left( \frac{f(x - \Delta x, y) / 2 - f(x, y) + f(x + \Delta x, y) / 2}{\Delta x^2} \right) + \\
&\quad 2 \left( \frac{f(x, y - \Delta y) / 2 - f(x, y) + f(x, y + \Delta y) / 2}{\Delta y^2} \right) \\
&= -2 \left( \frac{f(x, y) - \bar{f}^x(x, y)}{\Delta x^2} \right) - 2 \left( \frac{f(x, y) - \bar{f}^y(x, y)}{\Delta y^2} \right)
\end{aligned} \tag{5.3.2-14}$$

where  $\bar{f}^x(x, y)$  is the average value of  $f$  in the two cells adjacent to the  $(x, y)$  cell in the  $x$  direction. In the special case of  $\Delta x = \Delta y$ , the finite-difference Laplacian at  $(x, y)$  is proportional to the difference between  $\bar{f}^x(x, y)$  and the average of the values in the four adjoining cells (not counting diagonal cells that share a vertex with the cell under consideration). This project defines the Laplacian in terms of distances in kilometers (rather than in degrees) because this makes more physical sense, resulting in  $\Delta x / \Delta y = \cos(\text{Latitude})$  and yielding a slightly more complicated expression for the finite-difference Laplacian. Based on the above, and assuming a normal distribution for variations in  $\beta$  between a cell and its neighbors, the penalty function for  $\beta$  over the entire source zone is of the form

$$f_\beta(\boldsymbol{\beta}; \sigma_{\Delta\beta}) = \prod_{j=1}^M \frac{1}{\sqrt{2\pi}\sigma_{\Delta\beta}} \exp \left[ -\frac{1}{2} \left( \frac{\Delta\beta_j}{\sigma_{\Delta\beta}} \right)^2 \right] \tag{5.3.2-15}$$

where the product extends over all cells,  $\sigma_{\Delta\beta}$  controls the degree of smoothing, and

$$\Delta\beta_j = -\frac{1}{2} \left\{ \left( \frac{\beta(x_j, y_j) - \bar{\beta}^x(x_j, y_j)}{\cos^2(\text{Latitude}_j)} \right) + \left( \frac{\beta(x_j, y_j) - \bar{\beta}^y(x_j, y_j)}{1} \right) \right\} \tag{5.3.2-16}$$

Because  $\Delta y$  is constant, it can be absorbed into  $\sigma_{\Delta\beta}$ . The change from a factor of 2 to a factor of  $\frac{1}{2}$  in the definition of  $\Delta\beta_j$  is introduced for the sake of consistency with the EPRI-SOG formulation, and its effect is absorbed into  $\sigma_{\Delta\beta}$ . For a cell at the edges of the source zone,  $\bar{\beta}^x(x_j, y_j)$  or  $\bar{\beta}^y(x_j, y_j)$  is calculated using only cells on one side.

The penalty term  $f_\nu(\mathbf{v}; \sigma_{\Delta\nu})$  for the rate is constructed in the same manner, except that the Laplacian term  $\Delta\nu_j$  is calculated in terms of  $\ln(\nu)$  instead of  $\nu$  itself.

It is useful to consider the effect of  $\sigma_{\Delta\beta}$  (and the corresponding  $\sigma_{\Delta\nu}$  for rate), which control the degree of smoothing. A lower value favors solutions with less variation between adjacent cells. In the limit, infinitesimally small values of  $\sigma_{\Delta\nu}$  and/or  $\sigma_{\Delta\beta}$  lead to constant  $\nu$  and/or  $\beta$  throughout the source zone. At the other extreme, very large values of  $\sigma_{\Delta\nu}$  and  $\sigma_{\Delta\beta}$  is equivalent to determining  $\nu$  and  $\beta$  separately for each cell, considering only the earthquakes in that cell, without any consideration of spatial continuity.

The two penalty terms,  $f_\nu(\mathbf{v}; \sigma_{\Delta\nu})$  and  $f_\beta(\mathbf{\beta}; \sigma_{\Delta\beta})$ , multiply the likelihood function in Equation 5.3.2-13, favoring solutions that are consistent with the data and, simultaneously, show less variation between parameters  $\ln(\nu)$  and  $\beta$  in adjacent cells. One can fix the penalty terms  $\sigma_{\Delta\nu}$  and  $\sigma_{\Delta\beta}$  and then solve the penalized-likelihood problem. In this case one can view the penalty terms as prior distributions on the degree of smoothness of  $\ln(\nu)$  and  $\beta$ .

Alternatively, one can solve simultaneously for the optimal values of  $\nu$ ,  $\beta$ , and  $\sigma_{\Delta\nu}$  and  $\sigma_{\Delta\beta}$ . In this case,  $\sigma_{\Delta\nu}$  and  $\sigma_{\Delta\beta}$  are often called hyperparameters. Larger values of these hyperparameters reduce the penalizing effect of the exponential penalty term in Equation 5.3.2-15 and tend to increase the value of the penalized likelihood (by allowing a very close match between model predictions and data in each individual cell). At the same time, these larger values of  $\sigma_{\Delta\beta}$  in the denominator of Equation 5.3.2-15 tend to decrease the value of the penalized likelihood. The value of  $\sigma_{\Delta\beta}$  at which this optimal balance is achieved depends on the earthquake data, in particular, how many earthquakes there are and how they are distributed in latitude-longitude-magnitude space. This project will refer to the estimates of  $\sigma_{\Delta\nu}$  and  $\sigma_{\Delta\beta}$  obtained using this approach as the objective estimates of these hyperparameters. They are objective in the sense that they are determined automatically from the data, using the mechanism described above.

This optimal balance between the exponential term and the denominator in Equation 5.3.2-15, which leads to the objective estimate of the smoothing parameter, arises frequently in statistics. Perhaps the best known example is the calculation of the standard deviation of normally distributed data using the method of maximum likelihood.

EPRI-SOG (1986) used a similar formulation for the penalty terms, except that the cosine term is not included, the average of neighboring cells includes diagonal cells that share a vertex with the cell under consideration, and the smoothing parameters are assessed by the expert teams on the basis of their evaluations, aided by statistical tests. The presence of the cosine term is justified on physical arguments (see above); the omission of the diagonal terms makes the definition consistent with the standard finite-difference definition of the Laplacian operator.

Following EPRI-SOG (1986), this project introduces an additional penalty term, in the form of a prior distribution for  $\beta_j$ . The product of the prior distributions for all cells in the source zone takes the form

$$f'_{\beta}(\boldsymbol{\beta}) = \prod_{j=1}^M \frac{1}{\sqrt{2\pi}\sigma_{\beta}} \exp\left[-\frac{1}{2}\left(\frac{\beta_j - \beta_{\text{prior}}}{\sigma_{\beta}}\right)^2\right] \quad (5.3.2-17)$$

It may be possible to determine  $\beta_{\text{prior}}$  and  $\sigma_{\beta}$  objectively, but this was not done in this project. Instead,  $\beta_{\text{prior}}$  was specified as the value of  $\beta$  obtained for the entire study region (see regional  $b$ -values obtained in Section 3.5), and  $\sigma_{\beta}$  was selected on the basis of the EPRI-SOG (1986) experience and sensitivity runs.

There is a subtle difference between Equations 5.3.2-15 and 5.3.2-17. The former favors solutions with spatially uniform  $\beta$ , regardless of the value of  $\beta$ , while the latter promotes values of  $\beta$  near  $\beta_{\text{prior}}$ .

The complete penalized-likelihood, which may also be viewed as a posterior distribution, is constructed as the product of the joint likelihood for all the cells in the source zone (Equation 5.3.2-13), the smoothness penalty terms (Equation 5.3.2-15 and its counterpart for  $\ln(\nu)$ ), and the prior distribution of  $\beta$  (Equation 5.3.2-17). We write this quantity as

$$p(\mathbf{X}) = \ell(\mathbf{v}, \boldsymbol{\beta}) f_{\nu}(\mathbf{v}; \sigma_{\Delta\nu}) f_{\beta}(\boldsymbol{\beta}; \sigma_{\Delta\beta}) f'_{\beta}(\boldsymbol{\beta}) \quad (5.3.2-18)$$

where

$$\mathbf{X} = [\mathbf{v}, \boldsymbol{\beta}, \sigma_{\Delta\nu}, \sigma_{\Delta\beta}] \quad (5.3.2-19)$$

is the complete vector of parameters and hyperparameters. It will be called the state vector in the section that follows.

Equation 5.3.2-18 cannot be solved analytically for the penalized maximum-likelihood estimates of the parameters. Furthermore, we need more than point estimates of the recurrence parameters. Modern PSHA requires an assessment of the epistemic uncertainty associated with these estimates—including correlations between the recurrence parameters of cells in the same geographical region, which may jointly affect the hazard at one site. Therefore, this project needs to characterize the entire multidimensional joint distribution of  $\mathbf{X}$  (this distribution is given by Equation 5.3.2-18 times a normalizing constant). An additional, practical requirement is that one must represent the epistemic uncertainty in a computationally efficient manner. This can be accomplished by means of a small number of alternative “maps” of the recurrence parameters. Sections 5.3.2.1.2 and 5.3.2.1.3 present an approach to fulfill this need.

### 5.3.2.1.2 Modeling the Joint Distribution of Recurrence Parameters

The approach used to generate alternative maps of the recurrence parameters uses a technique known as Markov Chain Monte Carlo (MCMC), in particular, the Metropolis algorithm (Metropolis et al., 1953). MCMC is frequently used to generate multiple realizations from a complex multi-dimensional probability distribution by constructing a Markov chain that has this distribution as its limiting or stationary distribution. In this case, the distribution of interest is given by Equation 5.3.2-18 (times a constant). This distribution represents the central tendency and epistemic uncertainty of the vector  $\mathbf{X} = [\mathbf{v}, \boldsymbol{\beta}, \sigma_{\Delta v}, \sigma_{\Delta \beta}]$ , which contains the recurrence parameters for all cells, plus the two hyperparameters. The number of dimensions of  $\mathbf{X}$  is  $2M + 2$ , where  $M$  is the number of cells in the source zone.

A Markov chain is a discrete-time<sup>1</sup> probabilistic model with states  $\mathbf{X}^{(1)}, \mathbf{X}^{(2)}, \mathbf{X}^{(3)}, \mathbf{X}^{(4)}, \dots$ , in which the conditional probability distribution of the state at time  $t+1$  (denoted  $\mathbf{X}^{(t+1)}$ ), given the states at earlier times, depends only on the immediately previous state ( $\mathbf{X}^{(t)}$ ). This conditional probability distribution of  $\mathbf{X}^{(t+1)}$  given  $\mathbf{X}^{(t)}$  is known as the transition probability. If a Markov chain meets certain requirements, it possesses a limiting or stationary distribution, which will be reached asymptotically after many realizations, regardless of the initial state. A mechanical analogy is a linear damped oscillator under harmonic loading. After a sufficiently long time, the oscillator will reach a steady-state amplitude (and, as a consequence, a steady-state probability distribution for the instantaneous displacement), regardless of its initial conditions. Further details on Markov chains may be found in Parzen (1962).

MCMC constructs a discrete-time Markov chain with the following properties: (a) the Markov chain has a stationary or limiting distribution, and (b) this limiting distribution is equal to the joint distribution of interest (i.e., the penalized likelihood function  $p(\mathbf{X})$  given by Equation 5.3.2-18). Thus, one can use this sequence to obtain realizations from that distribution. A number of initial realizations are discarded because they are affected by the initial conditions. Then, a number of realizations are generated and summary statistics are calculated from them.

In the Metropolis MCMC algorithm, a new realization  $\mathbf{X}^{(t+1)}$  is generated from  $\mathbf{X}^{(t)}$  by the following two-step procedure: (1) generate a new candidate state  $\mathbf{X}'$  by drawing from a trial distribution  $q(\mathbf{X}'|\mathbf{X}^{(t)})$  that depends only on  $\mathbf{X}^{(t)}$  and is symmetrical (i.e.,  $q(\mathbf{X}'|\mathbf{X}^{(t)}) = q(\mathbf{X}^{(t)}|\mathbf{X}')$ ), and (2) accept the new trial state with probability

$$P_{\text{accept}} = \min\left(1, \frac{p(\mathbf{X}')}{p(\mathbf{X}^{(t)})}\right) \quad (5.3.2-20)$$

If the new state is accepted (i.e., if a standard uniform random number generator draws a value lower than  $P_{\text{accept}}$ ),  $\mathbf{X}'$  becomes the new state  $\mathbf{X}^{(t+1)}$ . Otherwise, the new state  $\mathbf{X}^{(t+1)}$  is equal to  $\mathbf{X}^{(t)}$ .

---

<sup>1</sup> The word “time” is not used in a strict chronological sense here. Instead it is used to represent a sequence of discrete realizations of a mathematical process.

In this project, the Metropolis algorithm is implemented locally, as follows. For each cell  $j$ , trial values of  $\ln(\nu_j)$  and  $\beta_j$  are drawn from uniform distributions centered at the current values of these parameters, the penalized likelihood function is calculated for these trial values, and the values are accepted or rejected using Equation 5.3.2-20 and a random-number generator. The only portions of the penalized likelihood that are reevaluated each time are the likelihood function for cell  $j$ , the penalty terms for cell  $j$  and for its neighboring cells within the source zone, and the prior distribution of  $\beta_j$ . After going through all cells, trial values of the hyperparameters  $\sigma_{\Delta\nu}$  and  $\sigma_{\Delta\beta}$  are drawn in a similar manner, the penalized likelihood is recalculated, and the values are accepted or rejected. In this step, only the smoothness-penalty terms for all cells are recalculated. This process is repeated a large number of times.

The widths of the uniform distributions are controlled by the analyst. These widths affect the acceptance rate, which in turn affects the numerical efficiency of the algorithm. Recommendations as to the optimal acceptance rates vary; a common recommendation is values in the range between 20% and 40% (e.g., Ntzoufras, 2009). After discarding some of the initial realizations of  $\mathbf{X}^{(i)}$ , one generates a large number of realizations to represent the joint distribution of the state vector  $\mathbf{X} = [\mathbf{v}, \boldsymbol{\beta}, \sigma_{\Delta\nu}, \sigma_{\Delta\beta}]$ . The section that follows describes the approach to obtain eight equally likely realizations of  $\mathbf{X}$  (i.e., eight alternative maps to represent the joint distribution of  $\nu$  and  $\beta$  and the two hyperparameters), including their correlation structure.

### 5.3.2.1.3 Development of Alternative Recurrence Maps

The approach presented below constructs alternative maps of the recurrence parameters  $\nu$  and  $\beta$  that jointly represent the central tendency and statistical uncertainty in the recurrence parameters, including correlations between the recurrence parameters of cells in the same geographical region (which may jointly affect the hazard at one site). At the same time, the number of alternative recurrence maps must be kept small for the sake of efficiency in the hazard calculations. The approach used here is a combination of well known techniques.

The first step in this formulation is to generate many realizations of the state vector  $\mathbf{X} = [\mathbf{v}, \boldsymbol{\beta}, \sigma_{\Delta\nu}, \sigma_{\Delta\beta}]$  using the MCMC algorithm described above and then use these realizations to calculate the mean vector  $\mathbf{m}_X$  and the covariance matrix  $\mathbf{S}_X$  of  $\mathbf{X}$ . This covariance matrix contains information about the marginal variance of  $\nu$  and  $\beta$  in each cell, the correlation between  $\nu$  and  $\beta$  in each cell, as well as the correlation between parameters in neighboring cells.

The second step is to perform an eigenvalue decomposition of the covariance matrix  $\mathbf{S}_X$ . Because this matrix is a covariance matrix, it is positive-semi-definite, so that all eigenvalues are positive or zero. Let  $\alpha_1^2, \alpha_2^2, \dots, \alpha_{2M+2}^2$  be the eigenvalues of  $\mathbf{S}_X$ , ordered from largest to smallest, and let  $\boldsymbol{\phi}_1, \boldsymbol{\phi}_2, \dots, \boldsymbol{\phi}_{2M+2}$  be the associated eigenvectors.

An important property of this eigenvalue decomposition is that of orthogonality, meaning that the dot product of  $\varphi_r$  and  $\varphi_s$  is equal to 1 if  $r = s$  and 0 if  $r \neq s$ . Taking advantage of orthogonality, one can show that a random vector  $\tilde{\mathbf{X}}$  constructed using the following randomized linear combination of the eigenvalues

$$\tilde{\mathbf{X}} = \mathbf{m}_X + \sum_{k=1}^{2M+2} \varepsilon_k \boldsymbol{\varphi}_k \quad (5.3.2-21)$$

where  $\varepsilon_1, \varepsilon_2, \dots, \varepsilon_{2M+2}$  are independent random variables with mean zero and variances  $\alpha_1^2, \alpha_2^2, \dots, \alpha_{2M+2}^2$ , has mean  $\mathbf{m}_X$  and covariance matrix  $\mathbf{S}_X$ . This implies that a synthesized realization of  $\tilde{\mathbf{X}}$  generated using Equation 5.3.2-21 has the correlation properties of the random vector  $\mathbf{X} = [\mathbf{v}, \boldsymbol{\beta}, \sigma_{\Delta v}, \sigma_{\Delta \beta}]$  that we want to simulate. This technique, based on the eigenvalue decomposition of the covariance matrix, is used in many disciplines, under a variety of names; e.g., Karhunen–Loève expansion, principal component analysis, and empirical orthogonal functions (see, for example, Preisendorfer, 1988).

In many applications of this technique, only a few terms are required in Equation 5.3.2-21 because the eigenvalues decrease rapidly in size. This is not the case in this application, and it may be necessary to use a large number of terms (up to a few hundred) in the summation in order to represent 99% of the total variance of  $\mathbf{X}$ .

The third step is to generate eight realizations of the  $\varepsilon$ 's and then use these to generate realizations of  $\tilde{\mathbf{X}}$  using Equation 5.2.2-21, with each realization representing an alternative recurrence map. This is done using a technique known as Latin Hypercube sampling or LHS (Iman and Conover, 1980). The technique will be described in the context of Equation 5.3.2-21, where we want to generate eight realizations of the random vector  $\boldsymbol{\varepsilon} = [\varepsilon_1, \varepsilon_2, \dots, \varepsilon_{2M+2}]$  and we want these realizations to provide a good representation of the underlying distributions, despite the small number of realizations. We also assume, for the sake of convenience, that the components of  $\boldsymbol{\varepsilon}$  have normal distributions (this assumption and its implications are discussed later). The process is as follows:

1. Divide the sample space of each normally distributed  $\varepsilon_j$  into eight intervals, with each interval containing an equal probability of 1/8. These intervals will have unequal lengths.
2. Within each interval  $z$  ( $z=1, 2, \dots, 8$ ), generate a random value  $\varepsilon_{jz}$  that follows the conditional distribution within the interval. The resulting values form a sequence with  $\varepsilon_{j1} < \varepsilon_{j2} < \dots < \varepsilon_{j8}$ .
3. For each  $j$ , generate an independent random permutation of  $\varepsilon_{j1}, \varepsilon_{j2}, \dots, \varepsilon_{j8}$ . After this permutation,  $\varepsilon_{j1}, \varepsilon_{j2}, \dots, \varepsilon_{j8}$  are no longer an increasing sequence. The result is eight random realizations of the random vector  $\boldsymbol{\varepsilon} = [\varepsilon_1, \varepsilon_2, \dots, \varepsilon_{2M+2}]$ . Because the eight values for each  $j$  were drawn from the eight equal-probability intervals, the distribution of  $\varepsilon_j$  is well

approximated by the eight realizations. Because of the random permutations, the correlation coefficient between the eight realizations of any two  $\varepsilon_{j_1}$  and  $\varepsilon_{j_2}$  has an expected value of 0 and is likely to be low.

4. Generate eight alternative realizations of  $\tilde{\mathbf{X}}$  using the eight permuted  $\varepsilon$  vectors and Equation 5.3.2-21.
5. Convert each realization of  $\tilde{\mathbf{X}}$  (actually, all but its last two elements) into values of  $\nu$  and  $b$  for each cell in the source zone, and use these two values to calculate  $\nu(5)$ , the rate of earthquakes above magnitude 5.

The resulting eight alternative maps represent the uncertainty in recurrence parameters that results from the limited duration of the catalog. If the smoothing parameters are treated as uncertain and estimated objectively from the data, the eight alternative maps also include the uncertainty about the appropriate values of the smoothing parameters.

This approach presented below constructs the alternative realizations of  $\nu$  and  $\beta$  as linear combinations of normally distributed random quantities. Thus, it produces normally distributed quantities. This normal distribution is consistent with the distribution shapes of  $\nu$  and  $\beta$  shown in Figures 5.3.2-1 and 5.3.2-2, which approach normal shapes as the number of earthquakes approaches 10. Although there may be a few earthquakes in each cell, the presence of the penalty terms tends to “pool” the data from many adjacent cells, resulting in a larger value of the “effective” earthquake count.

The initial implementation of this approach required that the number of realizations be a power of 2 because the first few epsilons were sampled using two-point distributions. This number was set to 8 because 4 was considered insufficient and 16 imposed a high computational burden for the hazard calculations. In the present Latin Hypercube implementation, the restriction of a power of 2 no longer exists, but the choice of eight realizations was retained. Tests indicate that eight realizations, together with Latin Hypercube sampling, provide an adequate representation of the mean and fractiles of the hazard.

### 5.3.2.2 Application of the Model and Specification of Model Parameters

#### 5.3.2.2.1 Calculations

Calculations were performed for all the seismotectonic and Mmax-region source zones identified in Chapter 4. The catalog had all dependent earthquakes removed; earthquakes associated with the RLME sources were also removed from this catalog to avoid double-counting (see Chapter 3).

The MCMC formulation was used to generate a large number of realizations (typically 15 million), of which roughly the first 25% were discarded because they were affected by the initial conditions. The evolution of recurrence parameters at a few points was examined in each run to verify that this number was sufficient, in the sense that the system had reached a steady state. In some instances, this number had to be increased and sometimes the width of the MCMC trial

distribution had to be altered. The cell sizes for all seismotectonic source zones except MidC was 0.25 degrees in order to have the ability to resolve any sharp gradients in parameters that may occur in the more active regions. For reasons of computational efficiency, the cell size for MidC and for the Mmax source zones was set to 0.5 degrees. Tests with MidC indicated similar results for both cell sizes.

In addition to the algorithmic inputs described above, one must specify the weights for the various magnitude bins, the degree of spatial smoothing (including the option of objective smoothing), and the mean value and standard deviation of the prior distribution on  $b$ . Section 5.3.2.1.1 provides details on how these quantities enter the calculations and the rationale for their use.

Table 5.3.2.1 shows the five cases that were initially considered for the weights to the magnitude bins. These five alternative sets of weights span a wide range, in order to investigate the effect of giving lower weights to the lower-magnitude bins. Case E was introduced later, as an intermediate case between Cases C and D, because Case E was considered too extreme.

Some of the reasons for giving lower weights to the lower magnitude bins were discussed earlier. For instance, the magnitude-recurrence law may deviate from exponential, or the magnitude-conversion models or completeness model may be less reliable for lower magnitudes. In this regard, it is useful to remember that only earthquakes with magnitudes greater than 5 (4 if the CAV filter is being used) are important for seismic hazard and risk for nuclear facilities. The only reason for considering lower magnitudes is that the  $M > 4$  data alone are not sufficient for determining both the magnitude-recurrence law and the spatial distribution for earthquakes of engineering interest. Because the magnitude weights also affect the degree of smoothing<sup>2</sup>, one must also consider the issue of spatial stationarity; i.e., whether the spatial pattern of past, small, earthquakes is representative of the spatial pattern of future, hazard-significant, earthquakes. Cases A through E were designed to cover a broad range of alternatives regarding magnitude weights.

Based on calculations performed earlier in the project, only Cases A, B, and E were retained. The reasons for dropping Cases C and D were that case C was very similar to Case B and that Case E was considered too extreme, relying almost entirely on magnitudes 4.3 and greater, and leading to nearly spatially uniform seismicity. The three remaining cases (Cases A, B, and E) were examined and compared in terms of their fit to the magnitude-recurrence data and their degree of smoothing. Preference for the three cases was nearly equal, except that Case E was given slightly more weight because this case is more sensitive to data in the magnitude bins that that control seismic hazard. The resulting weights are 0.3, 0.3, and 0.4, for Cases A, B, and E, respectively.

The mean value for the prior distribution of  $\beta$  (Equation 5.3.2.17) was calculated separately for Cases A, B, and E above, by performing a maximum-likelihood recurrence analysis for the entire study region, and assuming constant  $b$ . Details of these calculations are contained in Section 3.5

---

<sup>2</sup> When objective smoothing is used, the cases where the lower bins are downweighted result in smoother seismicity. This effect will be discussed and explained later in this section.

Two values were considered for the strength of the prior distribution of  $\beta$ , which is specified by the standard deviation  $\sigma_b = \sigma_\beta / \ln(10)$ . The first value is 0.6 (in units of  $b$ ), which corresponds to a “moderate prior” in the EPRI-SOG (1988) project; we will also refer to this value as a moderate prior for  $b$ . The second value is 0.3 (in units of  $b$ ), and we will refer to it as a strong prior. We also considered a weak prior (1.2, in units of  $b$ ) in earlier stages of the project, but this value was not considered credible because there is a general consensus in the TI Team that spatial variation in  $b$  should be mild.

For all source zones except SLR, the smoothing parameters were determined using the objective approach. For each source zone, and for each of the magnitude-bin weights and strengths of the prior on  $b$  considered, the smoothing parameters  $\sigma_{\Delta v}$  and  $\sigma_{\Delta\beta}$  were allowed to vary, allowing the catalog data themselves to determine their optimal values and associated uncertainty for each source zone in an objective manner. Figures 5.3.2-4 through 5.3.2-9 show the values of the smoothing parameters and their  $\pm$  one-sigma ranges for magnitude-weight Cases A, B, and E, using a moderate prior for  $b$ .

On Figures 5.3.2-4 through 5.3.2-9, the source zones are sorted by size, with the small seismotectonic zones on the left side, and the Midcontinent and the Mmax zones on the right-hand side. The EPRI-SOG equivalent values (adjusted for differences in cell size) are provided for the sake of reference; the equivalence is only approximate because of some of the differences mentioned earlier between the two formulations of smoothing and because of potential limitations in the adjustment for size.

On Figure 5.3.2-4, the small- and moderate-size seismotectonic zones show a broad variation in the objectively determined values of  $\sigma_{\Delta v}$ : zones with high seismicity such as Reelfoot Rift show higher values (less smoothing), while zones with low seismicity such as AHEX show lower values (more smoothing). The large MidC and Mmax zones show similar values as the active zones. Relative to the EPRI-SOG values, the objectively determined values indicate less smoothing, except for the seismotectonic zones with low seismicity. Comparing Figures 5.3.2-6 and 5.3.2-8, to Figure 5.3.2-4 we note that the objective approach assigns significantly more smoothing to the cases where the lower-magnitude bins are downweighted. The reason for this is that the effective number of earthquakes in a source-zone is diminished when the low-magnitude data are down-weighted. The objective approach compensates for this smaller sample size by imposing more smoothing, thereby reducing spatial resolution.

On Figure 5.3.2-5, there is zone-to-zone variation in the objectively determined values of  $\sigma_{\Delta b}$ , there is a trend with size, but no trend with seismicity. It is important to notice that there is significantly more smoothing on  $b$  than for EPRI-SOG, indicating that the data favor a very mild geographical variation in  $b$ . Comparing Figure 5.3.2-7 and 5.3.2-9 to Figure 5.3.2-3, we note that the objective approach assigns slightly higher smoothing on  $b$  for the cases in which the low-magnitude bins are downweighted.

Figures 5.3.2-10 and 5.3.2-11 illustrate the effect of smoothing and seismic activity by comparing the results for the extended-crust source zones ECC-AM and ECC-GC, for case-A magnitude weights and moderate prior on  $b$ . ECC-AM has higher activity and the objective

procedure assigns to it low smoothing for rates (high  $\sigma_{\Delta v}$ ). In contrast, ECC-GC has low activity and the objective procedure assigns to it approximately 10 times more smoothing for rates. Note that the scales for activity rate are different in the two figures.

It is also useful to compare the above figures to Figures 5.3.2-12 through 5.3.2-15, which show results for the same source zones, for Case B and E magnitude weights and moderate prior on  $b$ . Because the effective number of earthquakes is smaller, the objective procedure compensates by increasing the smoothing on rate. The effect is much more pronounced in ECC-AM.

Figures 5.3.2-10 through 5.3.2-15 show that, by considering three alternative sets of magnitude weights together with an objective approach for smoothing, we are effectively sampling a broad range of smoothing parameters for rate. To further appreciate this, it is useful to examine the mean recurrence maps for Cases A, B, and E that will be presented in Sections 6.4 and 7.5.

For the SLR source zone, the approach described above led to underestimation of the observed rates for magnitude 4.3 and higher. To obtain an adequate fit it was necessary to remove the prior distribution on  $\beta$  and to constrain the smoothing on  $\beta$ . This constraint was introduced by specifying a prior distribution of  $\sigma_{\Delta\beta}$  with a median of 0.01 and a COV of 30%, which appears as an additional multiplicative term in Equation 5.3.2-18. The need for this different treatment is that SLR appears to have a  $b$ -value that is substantially lower than that of the region as a whole, and that portions of SLR (particularly in the Charlevoix area) appear have even lower  $b$ -values. This is consistent with the experience of Petersen et al. (2008), who assign a lower  $b$ -value to Charlevoix. Figures 5.3.2-10 through 5.3.2-15, and all other figures shown later in this section and in Chapter 7 reflect this modified approach for the treatment of the SLR source zone.

#### 5.3.2.2.2 Sensitivity to Magnitude Weights, Strength of Prior, and Alternative Maps

The six sets of recurrence maps obtained above were used to perform sensitivity calculations in order to quantify and illustrate the effect of the strength of the prior on  $b$  and magnitude weights, and alternative recurrence maps. Calculations were performed for the host zones under the most likely source-zone configuration. These calculations were also performed at other demonstration sites, but only representative results will be shown here.

Figures 5.3.2-16 and 5.3.2-17 show the sensitivity to the strength of the prior on  $b$ , for the Manchester and Topeka sites. These results show essentially no effect on hazard, a result that was observed at other demonstration sites and for both PGA and 1 Hz SA. As a consequence of these comparisons, the strong prior on  $b$  is deemed unnecessary and is eliminated from further consideration.

Figures 5.3.2-18 and 5.3.2-19 show the sensitivity to magnitude weights for the same two sites. These results indicate a moderate effect on hazard, particularly in areas of low seismicity. Finally, Figures 5.3.2-20 and 5.3.2-21 show the effect of the eight alternative recurrence maps on the hazard at the same two sites, for Case B magnitude weights. In both cases, the effect is important.

Based on the above comparisons, only the moderate prior on  $b$  will be considered (except for SLR, where no prior is used), and the logic-tree branches associated with magnitude weights and the eight alternative realizations will be retained.

### 5.3.2.2.3 Resulting Maps

Figure 5.3.2-22 shows the map of mean recurrence parameters for the most-likely source-zone map in the logic tree. Figure 5.3.2-23 shows the associated uncertainties, in the form of COV of the rate and standard deviation of the  $b$ -value. Figures 5.3.2-24 and 5.3.2-25 show two realizations of the equally likely recurrence maps. Although the last two maps show areas of no activity (i.e., white areas), it is important to note that no region has a mean rate of zero (i.e., these white areas “move” from one map to another), and that these white areas almost always occur in areas of no seismicity. Note also that the areas of high activity change little between the mean map and the two realizations, indicating that the uncertainty in rate (in the form of the COV) is low in regions with abundant data.

Maps of mean recurrence parameters for all source-zone configurations are shown in Sections 6.4 (for Mmax zones) and 7.5 (for seismotectonic zones). All realizations of the alternative maps are shown in Appendix J.

### 5.3.2.3 Exploration of Model Results in Parameter Space

This section explores the recurrence parameters obtained in the previous section by examining and discussing the results obtained at a few specific locations and comparing the recurrence parameters to the catalog data. The purpose of these comparisons is to demonstrate consistency with the data under a variety of conditions and to gain insights into the behavior of the model developed here. These comparisons will focus on the higher-weighted branches of the master logic tree (namely, the seismotectonic zonation with the narrow interpretation of PEZ and Rough Creek graben in the Midcontinent). Figure 5.3.2-26 shows the local areas considered in these comparisons.

#### 5.3.2.3.1 Regions of High Activity

The first region to consider is East Tennessee, which is represented by the same polygon used by Petersen et al. (2008; see Figure 5.3.2-26). The purpose of this comparison is to demonstrate that the penalized-likelihood formulation does not cause unwarranted dilution of highly localized seismicity.

Figures 5.3.2-27 through 5.3.2-29 compare the observed seismicity within the polygon to the expected counts within the same polygon, as calculated from the recurrence maps source zone PEZ-N, which is the host zone for this polygon. For each recurrence map, the expected counts are calculated by (1) calculating the expected rate for each magnitude bin using the values of  $\nu$  and  $\beta$  for the cells covered by the polygon, taking into account that some cells are only partially contained within the polygon and accounting for  $M_{\max}$  (recall Equations 5.3.2-11 and 5.3.2-12),

(2) multiplying this rate by the equivalent period of completeness for that bin, and (3) summing the expected counts, beginning at the highest bin. The observed counts do not take integer values because they represent effective counts. The error bars on the data represent the 16%–84% range of statistical uncertainty and are calculated using the approach by Weichert (1980). Each of the eight curves represents expected counts (i.e., rate times equivalent period of completeness) for one of the eight equally weighted alternative maps. Figures 5.3.2-27 through 5.3.2-29 use the maps for magnitude-weight Cases A, B, and E, respectively.

Figures 5.3.2-27 and 5.3.2-28 show a close agreement between model and data for Cases A and B. As anticipated, the results for Case A show a better fit to the low-magnitude data, while the results for Case B show a better fit for magnitude 4.3 and higher. Both figures also show that the eight curves are closely spaced, indicating low uncertainty in recurrence parameters in areas of high activity.

The results for Case E on Figure 5.3.2-29 shows lower rates, with the expected counts slightly below the error bars for the  $M$  4.3–5.0 magnitude bin. Because the objective smoothing imposes more smoothing for Case E, it is not surprising that the expected counts within a small region of high activity are somewhat lower than the observed counts. Nonetheless, the expected counts from Cases A, B, and E—taken as an ensemble—are consistent with the data, especially when the error bars are taken into account.

Figures 5.3.2-30 and 5.3.2-32 show similar results for a  $3^\circ \times 2^\circ$  rectangular region in central New England, comprising Massachusetts and southern Vermont and New Hampshire (see Figure 5.3.2-26). This region overlaps the NAP and ECC-AM seismotectonic zones, which are used to calculate the expected counts. Again, there is good agreement between model and data and the uncertainty in recurrence is low.

#### 5.3.2.3.2 *Nemaha Ridge Area*

The Nemaha Ridge in Kansas and Oklahoma has experienced two  $M > 5.0$  earthquakes in historical times, despite being in an area of moderate seismicity in the Midwest. The geometry considered (see Figure 5.3.2-26) is a rough average of the geometries considered by the EPRI-SOG (1988) project for the Nemaha Ridge.

Figures 5.3.2-33 through 5.3.2-35 compare seismicity and recurrence parameters in the same manner used above. The two earthquakes in the  $M$  5.0–5.7 interval (the highest intervals with data) are the April 24, 1867, and April 9, 1952, earthquakes. Figures 5.3.2-33 and 5.3.2-34 (Cases A and B) show predicted rates that are at or slightly below the one-sigma error bars, indicating marginal agreement with the data. Figure 5.3.2-35 (Case E), shows less agreement. The explanation for this result is that the effect of giving lower weights to the first two magnitude bins—which one would have expected to produce a better fit for the higher bins—is counteracted by higher smoothing.

Although the rates of  $M > 5$  earthquakes for this region are slightly underestimated, it is important to keep in mind that the TI team, after reviewing the literature on the Nemaha Ridge,

did not see a justification for identifying the Nemaha Ridge as a distinct seismotectonic zone. Two  $M > 5$  earthquakes in this region are not sufficient to change that assessment.

#### 5.3.2.3.3 *Regions of Low Activity*

Kernel methods have a tendency to predict very low rates in regions with few or no recorded earthquakes because the commonly used Gaussian kernel function decays very rapidly at distances greater than twice the kernel width. This problem is discussed by Frankel et al. (1996), where the problem is avoided by introducing an alternative “floor” based on a constant weight.

The penalized-likelihood approach developed here does not have this problem. As indicated in Section 5.3.2.1.2 and illustrated on Figure 5.3.2-1 for the simple formulation considered at first, the likelihood function for zero observed earthquakes allows for nonzero rates and has a mean rate of  $1/AT$ , which acts as a natural floor for the activity rate. This result also applies to one cell, if there is no penalty function linking the cell’s parameters with its neighbors’. Introduction of the penalty function has two effects on this floor. On the one hand, it increases the effective area in the denominator, thereby reducing the mean rate. On the other hand, it also elevates the rate if there is activity near the cell under consideration. Examination of the maps on Figure 5.3.2-16 and those in Sections 6.4 and 7.5 suggests that the rates do not drop rapidly as one moves into regions of very low activity, as happens with the Gaussian kernel (where the rate decays as  $\exp[-1/2(x/\sigma)^2]$ , where  $x$  is the distance to the closest earthquake and  $\sigma$  is the kernel size).

Figures 5.3.2-36 through 5.3.2-38 compare seismicity and recurrence parameters for a  $3^\circ \times 2^\circ$  rectangular region in the southern Florida Peninsula near Miami (see Figure 5.3.2-26). There is good agreement between the recurrence curves and the one earthquake in the catalog. The mean annual rate of  $M$  5 or greater is approximately 0.01 earthquakes (for an area of approximately 5.5 squared equatorial degrees). These figures also show a large spread between the alternative recurrence curves (especially for the reduced-magnitude weights), indicating a high uncertainty in rates.

Figures 5.3.2-39 through 5.3.2-41 provide similar comparisons for a  $3^\circ \times 2^\circ$  rectangular region in northern Minnesota, around St. Paul (see Figure 5.3.2-26). Although there are no earthquakes within this area, the model predicts activity rates that are comparable to those obtained for Miami.

These two sets of results demonstrate the effect of a natural floor that arises from consideration of the full likelihood function for the rate. This natural floor has the advantage that it does not require any external assumptions regarding the spatial extent that should be used to determine the floor rate.

#### 5.3.2.4 *Consideration of Constant $b$ -Value Kernel Approaches*

In addition to the penalized-likelihood approach, this project evaluated kernel approaches as alternatives for the calculation of recurrence parameters. Both fixed size (e.g., Frankel, 1995) and adaptive (e.g., Stock and Smith, 2002) were evaluated and exercised in the early stages of this

project. In the end, only the penalized-likelihood approach was retained in the logic tree. The rationale for this decision is provided below.

The first consideration is the specification of kernel size. In most applications of the kernel method for PSHA applications (e.g., Petersen et al., 2008), the kernel size is fixed spatially and is assessed subjectively, although methods exist for the objective selection of kernel size (e.g., Silverman, 1986). The adaptive kernel approach of Stock and Smith (2002) is partially objective. It begins with an arbitrary kernel size, and then it applies a location-dependent adjustment that depends on the density of data. This approach can be made fully objective, as illustrated below. In contrast to the approach used in most previous PSHA applications, the penalized-likelihood approach employed in this project is objective, in the sense that it determines the optimal degree of smoothing for each source zone (recall Figures 5.3.2-4 through 5.3.2-9), finding the best tradeoff between statistical precision and spatial resolution. This consideration of objectivity is not as important as those that follow, however. Although objective approaches are desirable, there are situations in PSHA where informed judgment is required because the data and statistical models are not sufficient.

The second consideration is adaptability. Fixed kernel approaches cannot provide higher spatial resolution where data are abundant and lower resolution where data are sparse. The adaptive kernel approach provides adaptability by performing an initial calculation of rate and then adjusting the kernel size for each location based on the result of this calculation. The penalized-likelihood approach provides adaptability because the likelihood function is narrower where data are abundant and broader where data are sparse (recall Figures 5.3.2-1 and 5.3.2-2). As a result, the relative effect of the penalty terms (which tends to reduce roughness in the recurrence parameters) is weaker where data are abundant and stronger where data are sparse. The comparisons shown earlier for East Tennessee demonstrate the adaptability of the penalized-likelihood approach.

The third consideration is that of geographical variation of  $b$ . The kernel approaches (both fixed and adaptive), as they have been implemented so far for PSHA, do not allow for geographical variation in  $b$ . In contrast, the penalized-likelihood approach allows for geographical variation in  $b$ . Furthermore, smoothing on rate and on  $b$  is controlled by separate smoothing parameters, allowing for more variation in rate and less variation in  $b$ , as the data and the technical community's intuition suggest. This ability to allow variation in  $b$  is important for large source zones thousands of kilometers across and encompassing different tectonic settings, such as those in the Mmax branches of the master logic tree. For these large source zones, some geographical variation in  $b$  should not be precluded a priori.

The fourth consideration is the quantification of epistemic uncertainty. The two kernel approaches, as they have been implemented so far for PSHA, provide a simplistic representation of epistemic uncertainty in rate and  $b$ . This representation essentially treats the source zone as having constant rate and  $b$  for the purposes of calculating uncertainty, and then assigns the resulting COV in rate and standard deviation in  $b$  to the entire source zone. This approach underestimates the true uncertainty. It is possible to obtain more realistic estimates of the uncertainty by using bootstrapping (i.e., fitting the kernel model to multiple synthetic catalogs), but the number of alternative maps required to obtain a stable estimate of the uncertainty in

hazard is likely to be large. The penalized-likelihood approach combined with MCMC provides a realistic representation of uncertainty in the hazard because it samples the entire penalized-likelihood function for the cells, thereby providing an estimate of the uncertainty in both rate and  $b$  for each cell, and the associated correlations. In particular, this uncertainty, as measured by the COV, is higher in regions of low activity than in regions of high activity (again, recall Figures 5.3.2-1 and 5.3.2-2). In addition, the penalized-likelihood approach also incorporates the epistemic uncertainty in the smoothing parameters, as represented by the error bars on Figures 5.3.2-4 through 5.3.2-9). Considering multiple kernel sizes in the logic tree (e.g., Petersen et al., 2008) also captures this uncertainty, but in a subjective manner. Furthermore, the penalized-likelihood approach combined with MCMC and with the eigenvalue-based sampling scheme presented here provides an efficient representation of epistemic uncertainty (including correlations between cells) by means of eight alternative maps.

A fifth consideration is the rates in regions of very low seismicity. The fixed kernel approach, and to a lesser extent the adaptive kernel approach, yield very low estimates in these regions. This problem may be resolved by the introduction of a somewhat artificial floor level, or by using a different kernel shape. The penalized-likelihood approach, on the other hand, provides a natural floor that is consistent with the data (or lack thereof) in these regions. This floor is based on the understanding that the observation of zero earthquakes during a certain time interval does not necessarily imply a rate of zero, but it does imply that the rate is unlikely to be moderate or high.

In relation to these regions of low seismicity, there may be valid economical and structural-engineering reasons for imposing minimum design values in building codes—and these values may exceed the hazard computed from the natural or artificial floor values discussed here. These considerations are the responsibility of code-writing committees and should be kept separate from the process of estimating recurrence parameters and computing seismic hazard.

A sixth consideration is that the choice between penalized likelihood and kernel smoothing is a choice between statistical tools, not a choice between different conceptual models regarding the spatial distribution of future seismicity. Both approaches implement the same conceptual model, but apply different statistical tools—each with its own strengths and weaknesses, as discussed above.

To illustrate this last point, it is useful to compare the result from the penalized-likelihood and kernel-smoothing methods for selected source zones (and magnitude-weight Case A), using the same catalog and completeness model. Figure 5.3.2-42 shows the recurrence parameters calculated for three of the seismotectonic zones, spanning a broad range of source-zone size and rate density). These results were obtained using an initial kernel size calculated by cross-validation (Silverman, 1986), and then applying an adaptive-kernel (Stock and Smith, 2002). This approach is an objective and adaptive implementation of the Gaussian kernel method. Comparison of the rates on Figure 5.3.2-42 to the corresponding portions of Figure 5.3.2-22 shows a good agreement in most regions, particularly in regions of high activity such as portions of NAP and regions of moderately low activity such as portions of ECC-AM. The main difference is in the areas of very low activity (e.g., central Texas, northern North Dakota, offshore areas in the northeast of the study region), where the kernel approach predicts

essentially zero rates but the penalized-likelihood approach predicts low (but nonzero) rates. Another fundamental difference is that the kernel approach, as currently implemented, does not produce spatially variable estimates of uncertainty such as those shown on Figure 5.3.2-23.

All these considerations led the project TI Team to the decision to retain only the penalized-likelihood approach (together with MCMC and eigenvalue-based sampling) for the purpose of calculating recurrence parameters and their uncertainty.

### 5.3.2.5 Comparison to EPRI-SOG Approach

The penalized-likelihood approach used in this project has a number of elements in common with the EPRI-SOG (1988) methodology, but there are also substantial differences in implementation. This section summarizes and discusses the common elements and the differences in the calculation of recurrence parameters between this project and the EPRI-SOG project.

The basic formulation of the problem is the same for this project and the EPRI-SOG project. Both projects divide a source zone into rectangular cells, (using partial cells at the edges to honor the geometry of the source zone), both projects formulate the likelihood function for  $\nu$  and  $\beta$  in each cell using magnitude bins, both projects introduce penalty functions (in terms of  $\ln[\nu]$  and  $\beta$ ) that increase continuity between cells, and both projects introduce a prior distribution for  $\beta$ .

There are some differences in the way the penalty terms are computed. In particular, this project uses the standard form of the finite-difference Laplacian operator, using a slight adjustment to correct for the effect of latitude on the East-West size of the finite-difference grid. In contrast, the EPRI-SOG project uses the difference between a cell and the average of all its neighbors (which is not too different from the average of the Laplacians computed along the longitude-latitude grid and along a grid rotated 45 degrees from it, without correcting in either case for difference in the size of the finite-difference grid). The effect of these differences is believed to be small, and the approach used in this project is preferable because it is isotropic with respect to distances in kilometers. There are also differences in parameterization (i.e., this project uses standard deviations  $\sigma_{\Delta\nu}$  and  $\sigma_{\Delta\beta}$ , while the EPRI-SOG project uses quantities that multiply the squared difference between a cell and its neighbors), but these differences are of no consequence.

The main difference between this project and the EPRI-SOG project is in the treatment of epistemic uncertainty. This project captures epistemic uncertainty by working with the full penalized likelihood function, which contains all information about the “center, body, and range” of the distribution of recurrence parameters, as well as information about the correlation between recurrence parameters in nearby cells. This penalized likelihood function is sampled using Markov Chain Monte Carlo (MCMC), which generates many realizations of the recurrence parameters. These realizations are then used to construct eight representative realizations by computing the covariance matrix of the recurrence parameters, and then using a Karhunen–Loève expansion of this covariance matrix, together with Latin Hypercubes to generate a set of eight realizations that represent the mean and epistemic uncertainty in recurrence parameters. In contrast, the EPRI-SOG methodology works only with the maximum penalized likelihood

estimates of the recurrence parameters. The EPRI-SOG study implemented a “bootstrapping” procedure in its software (i.e., generating multiple synthetic catalogs and performing the maximum penalized likelihood calculations for each catalog) to quantify uncertainty, but this procedure was never used by the EPRI-SOG (1988) project in production calculations that went all the way to hazard (and it is believed to be impossible in practice, due to the number of alternative recurrence maps required).

Another difference relates to the smoothing parameters  $\sigma_{\Delta v}$  and  $\sigma_{\Delta\beta}$ . This project calculated optimal values of these parameters using an objective approach, while the EPRI-SOG project specified multiple values of the equivalent smoothing parameters using expert opinion (aided by statistical diagnostics). This project also treated  $\sigma_{\Delta v}$  and  $\sigma_{\Delta\beta}$  as free hyperparameters in the MCMC, thereby capturing their epistemic uncertainty and the effect of that uncertainty on the uncertainty in  $\mathbf{v}$  and  $\boldsymbol{\beta}$ .

There is also a small difference in the treatment of magnitude uncertainty in the catalog. This project counts earthquakes by using “event factors” different from unity, as discussed earlier. In contrast, the EPRI-SOG project uses a uniform magnitude  $M^*$  different from the best-estimate magnitude. Analysis and numerical tests in Chapter 3 indicates that the two approaches are equivalent in principle, but the use of event factors is preferable because it avoids edge effects at the lower magnitudes.

An area in common is the calculation of completeness times. Prior to performing recurrence calculations for each team, source zone, and smoothing option, the EPRI-SOG (1988) project performed a coupled recurrence and completeness analysis, using a zoneless penalized maximum-likelihood formulation for recurrence, together with certain assumptions regarding completeness (e.g., the detection probability does not decrease with time or with magnitude). This project followed the same approach, using the same EPRI-SOG formulation and software, but using the new catalog and an updated map of the completeness region. These calculations are documented in Section 3.5.

### 5.3.2.6 Assessment of the Lombardi Study

In a study of the 1990–2001  $M > 1.9$  Southern California earthquakes, Lombardi (2003) observes that the catalog of all events (i.e., main shocks and aftershocks combined) follows an exponential magnitude distribution, but the catalog of main shocks deviate from exponential, with flattening at low magnitudes. Lombardi then proposes the following model: (a) the magnitude distribution for the population of all events is exponential, and (b) the magnitude distribution of main events may be constructed as the distribution of the maximum of  $N$  independent identically distributed (iid) exponential magnitudes, where  $N$  is the number of events in a cluster (as determined by the declustering algorithm). This model predicts a main-shock magnitude-recurrence curve that deviates from exponential in the  $M$  1.9–2.5 range, and this deviation is observed in the data.

One physical problem with this model is the assumption of iid magnitudes within a cluster. One would expect that the same physical factors that introduce tight spatial and temporal clustering of earthquakes would also introduce correlation in their magnitudes.

There are also a number of alternative explanations for the observed deviation from exponentially distributed main shocks. One possible explanation is that the 1900–2001 Southern California catalog may not be complete down to  $M$  1.9. In fact, Felzer (2008) finds that the lowest complete magnitudes for Southern California during the period 1993–1997 are in the  $M$  2.7–3.0 range and that completeness down to magnitudes near 2.0 was only achieved during the period 2000–2007. Another possible explanation is edge effects associated with incomplete clusters that include some aftershocks with  $M < 1.9$  and a main event with  $M > 1.9$  (and for which  $N$  has been underestimated).

Even if the observed deviation from exponentiality were real and not an artifact of incompleteness or edge effects, there are a number of reasons why it would not have large practical implications for this project. The reason for this is that this deviation is localized, extending only over the lowest 0.3- to 0.5-magnitude units. This project (and, to a lesser degree, EPRI-SOG) use alternative sets of magnitude weights to allow for deviations from exponentiality and other problems that may arise with magnitudes near the cutoff. Recall that magnitude-weight Cases B and E (which, together, carry 70% of the total probability in the logic tree) give 10% and 0% weight to the first magnitude bin (see Table 5.3.2-1). In addition, the formulation of the likelihood function in terms of magnitude bins does not work with the local slope of the magnitude-recurrence data, reducing the effect of any localized deviations from exponentiality. Finally, the completeness analysis for magnitude-weight Cases A and B would likely compensate for any deviation from exponentiality by altering the completeness times.

In summary, even if the deviations from main shock exponentiality postulated by Lombardi (2003) were real, they would have no effect on the  $b$ -values computed in this project.

### **5.3.3 Estimation of Recurrence for RLME Sources**

The earthquake recurrence models for the RLME sources are somewhat simpler than those described in Section 5.3.2 in that the magnitude range for individual RLMEs is relatively narrow and their spatial distribution is limited geographically such that spatial variability is not an issue. (Note that for simplicity in this section and later in the report, the term *RLME* is used to refer to the actual past earthquakes and the forecast future occurrences; the term *RLME source* is used to refer to the seismic source used to model the spatial and temporal distribution of the RLMEs.) This limits the problem to one of estimating the occurrence rate in time of a point process. The data that is used to assess the occurrence rates are derived primarily from paleoseismic studies and consist of two types. In many cases, the data provide estimated ages of the paleoearthquakes such that the times between earthquakes can be estimated. In other cases, the data provide an estimate of the number of earthquakes that have occurred post the age of a particular stratigraphic horizon. These data can be easily used to derive estimates of the RLME occurrence rates and their uncertainty.

The estimation of the RLME occurrence rates is dependent on the probability model assumed for the temporal occurrence of these earthquakes. The standard model applied in most PSHA studies and the one adopted for most RLME sources in this study is the Poisson model in which the probability of occurrence of an RLME in a specified time period is completely characterized by a single parameter,  $\lambda$ , the rate of RLME occurrence. The approaches used to assess  $\lambda$  and its uncertainty are described in Section 5.3.3.1. The principal features of the Poisson process are that it is “memoryless”—the probability of occurrence in the next time interval is independent of when the most recent earthquake occurred, and the time between earthquakes is exponentially distributed with a standard deviation equal to the mean time between earthquakes.

For two RLME sources, the data are sufficient to suggest that the occurrence of RLMEs is more periodic in nature (the standard deviation is less than the mean time between earthquakes). For these RLME sources a simple renewal model can also be used to assess the probability of earthquake occurrence. This model takes into account the time that has elapsed since the most recent RLME occurrence in making an estimate of the probability of occurrence in the future. The probability of occurrence for renewal models is time-dependent in that the probability of occurrence in the next time interval is dependent upon the elapsed time since the most recent earthquake. The approaches used to assess the RLME occurrence probabilities for a renewal model are presented in Section 5.3.3.2.

#### 5.3.3.1 Estimation of Occurrence Rates for the Poisson Model

The estimation of the uncertainty distribution for the rate parameter  $\lambda$  of a Poisson process uses the following general framework:

- Define a likelihood function that represents the probability of seeing the observed sample of data given a specified rate parameter  $\lambda$ .
- Compute the likelihood values for a full range of the rate parameter  $\lambda$ .
- Normalize these likelihood values to create a probability distribution for  $\lambda$ .
- Incorporate uncertainty in the input data by repeating the process for the weighted alternative data sets and computing a weighted combination of the resulting probability distributions for  $\lambda$ .
- Represent the resulting probability distribution by a discrete approximation for implementation in hazard analysis.

The likelihood functions used to implement this process depend upon the type of paleoseismic data available. The recurrence data fall into two general categories. In the first, the data consist of an estimate of the number of earthquakes that have occurred after the deposit of a datable stratigraphic horizon, but estimates of the actual ages of the individual earthquakes are not available. These type of data are analogous to the assessments made for historical seismicity where the data consist of the number of earthquakes that have occurred within the period of catalog completeness. The second type of paleoseismic data are estimates of the actual ages of individual earthquakes. If these data are available, they provide estimates of the intervals between individual earthquakes that can be used to assess the average recurrence interval of

RLMEs. The following subsections describe the mathematical formulation used to assess earthquake recurrence rates from these two general types of paleoseismic data.

### 5.3.3.1.1 Earthquake Count in a Time Interval

The data available in this case is an estimate of the number of earthquakes,  $N$ , that have occurred in a known time interval  $T$ . For a Poisson model, the probability of observing  $N$  events in time interval  $T$  is given by

$$f(N) = \frac{(\lambda T)^N \exp\{-\lambda T\}}{N!} \quad (5.3.3-1)$$

This leads to the likelihood function for a rate parameter of  $\lambda_i$  given the observed data  $(N, T)$ :

$$L(\lambda_i | N, T) = \frac{(\lambda_i T)^N \exp\{-\lambda_i T\}}{N!} \quad (5.3.3-2)$$

Figure 5.3.3-1 shows the relative likelihood based probability distribution developed using Equation 5.3.3-1 for the case where  $N$  equals two earthquakes and  $T$  equals 2,000 years. The resulting normalized uncertainty distribution for  $\lambda$  is in fact a gamma distribution with a mean value of  $(N+1)/T$  (e.g., Benjamin and Cornell, 1970). The mean differs from the maximum likelihood estimate of  $\lambda$ , which is  $N/T$  due to the skewness of the normalized likelihood distribution. In the case where the observed count is zero, the mean estimate of  $\lambda$  from the normalized likelihood function would be  $1/T$ . This is analogous to the “natural floor” in the seismicity-based estimates of earthquake recurrence rates discussed in Section 5.3.2.1.1.

### 5.3.3.1.2 Earthquake Recurrence Intervals

The data available in this case are estimates of the occurrence times of a sequence of  $N+1$  earthquakes obtained from dating of paleoseismic features or known occurrence times from the historical record. The estimated dates for the  $N+1$  earthquakes provide  $N$  values of the times between earthquakes,  $t_i$ , plus the open interval since the most recent RLME,  $t_0$ . The Poisson process produces an exponential distribution for the time between occurrences:

$$f(t) = \lambda \exp\{-\lambda t\} \quad (5.3.3-3)$$

$$F(t) = 1 - \exp\{-\lambda t\}$$

This leads to the likelihood function for a rate parameter of  $\lambda_i$  given the observed data  $(t_i, i = 1, N, t_0)$ :

$$L(\lambda_i | t_i, t_0) = \prod_{i=1}^N f(t_i) \times [1 - F(t_0)] = \lambda_i^N \exp\left\{-\lambda_i \times \left[\sum_{i=1}^N t_i + t_0\right]\right\} \quad (5.3.3-4)$$

The form of the likelihood function indicates that specification of the dates for the intermediate events is not needed as the term  $\sum_{i=1}^N t_i + t_0$  is equal to the elapsed time since the oldest earthquake

in the sequence. The likelihood function given by Equation 5.3.3-4 is equivalent in form to that given by Equation 5.3.3-2 and leads to the same gamma-shaped uncertainty distribution for  $\lambda$  with mean  $(N + 1) / \left( \sum_{i=1}^N t_i + t_0 \right)$ .

The maximum likelihood estimate of  $\lambda$  from Equation 5.3.3-4 is  $N / \left( \sum_{i=1}^N t_i + t_0 \right)$ . This differs from a common practice of using the inverse of the average of the recurrence intervals due to the inclusion of the length of the open interval  $t_0$  in the denominator. However, neglecting the open interval is ignoring information. The use of Equation 5.3.3-4 is considered more appropriate because it incorporates all of the available information.

### 5.3.3.1.3 Representation of Continuous Distribution for $\lambda$ by a Discrete Approximation

The logic tree structure is generally used to represent uncertainty in the inputs to a PSHA. In a logic tree, uncertainty distributions are represented by a (small) set of discrete alternatives with assigned probability weights. Miller and Rice (1983) provide a set of discrete approximations for arbitrary continuous probability distributions. Their five-point approximation was chosen to represent the distributions for  $\lambda$  developed for the RLME sources. The Miller and Rice (1983) five-point discrete approximation is given in Table 5.3.3-1. The first column indicates the location of the five discrete values for the variable in terms of their cumulative probability levels in the defined continuous distribution. These are illustrated by the five horizontal dashed lines in the lower panel of Figure 5.3.3-1. The second column lists the probability weights to be assigned to the five discrete values of the variable. The number of decimal points in the probability weights given in Miller and Rice (1983) perhaps implies too high a degree of precision. For application in the CEUS project, these probability weights are approximated by the values listed in the third column.

Application of the five-point approximation given above to the example shown on Figure 5.3.3-1 yields a discrete distribution with  $\bar{\lambda} = 0.00149$  and  $\sigma_{\lambda} = 0.000849$ . The values for the continuous gamma distribution are  $\bar{\lambda} = 0.0015$  and  $\sigma_{\lambda} = 0.000866$ , indicating that the discrete approximation does a good job of capturing the first two moments of the skewed continuous parameter distribution.

### 5.3.3.1.4 Use of Fault Slip Rates

In a few cases, the data used to estimate occurrence rates for RLMEs is in the form of fault slip rate. In these cases the value of  $\lambda$  is obtained by converting the fault slip rate into a moment rate and then dividing by the seismic moment of an RLME, i.e.:

$$\lambda = \frac{SA\mu}{M_o(RLME)} \quad (5.3.3-5)$$

where  $S$  is the fault slip rate,  $A$  is the total area of the fault surface,  $\mu$  is crustal rigidity (taken to be  $3 \times 10^{11}$  dynes/cm<sup>2</sup>), and  $\overline{M}_o$  (RLME) is the average seismic moment of an RLME. The fault slip rate is computed by dividing the cumulative fault offset,  $D_{cum}$ , by the length of time over which it occurred,  $T$ :

$$S = \frac{D_{cum}}{T} \quad (5.3.3-6)$$

### 5.3.3.2 Estimation of Occurrence Rates for a Renewal Model

A renewal model for the occurrence probability of earthquakes is applied when the data suggest a more periodic behavior for the occurrence times between earthquakes than implied by the Poisson model. There are a variety of distributions that have been used to model the variability in the time between events, such as the lognormal, Weibull, and gamma distributions. Recently, Matthews et al. (2002) have proposed a model based on the inverse Gaussian distribution for inter-arrival times of repeated large ruptures on a fault. This model, termed the Brownian Passage Time (BPT) model was used by the Working Group (2003) to assess the probabilities of large earthquakes in the San Francisco Bay area. Ellsworth et al. (1999) and Matthews et al. (2002) propose that the BPT model is more representative of the physical process of strain buildup and release on a seismic source than the other distribution forms that have been used for renewal models (e.g., the lognormal). Based on these arguments, the BPT model was used in this analysis.

For the BPT model, the time interval between earthquakes,  $t$ , is distributed with probability density given by

$$f(t) = \left( \frac{\mu}{2\pi\alpha^2 t^3} \right)^{1/2} \exp\left( -\frac{(t-\mu)^2}{2\mu\alpha^2 t} \right) \quad (5.3.3-7)$$

and cumulative probability given by

$$F(t) = \Phi[u_1(t)] + e^{2/\alpha^2} \Phi[-u_2(t)]$$

$$u_1(t) = \left( \sqrt{t/\mu} - \sqrt{\mu/t} \right) / \alpha \quad (5.3.3-8)$$

$$u_2(t) = \left( \sqrt{t/\mu} + \sqrt{\mu/t} \right) / \alpha$$

where  $\mu$  is the mean inter-arrival time (repeat time),  $\alpha$  is the aperiodicity coefficient (COV of  $t$ ), and  $\Phi(\cdot)$  is the standard normal cumulative probability function.

Given a sample of  $N$  time intervals and one open interval since the most recent earthquake,  $t_0$ , the likelihood function for the observed data set is given by

$$L(\mu, \alpha) = \prod_{i=1}^N f(t_i) \times [1 - F(t_0)] \quad (5.3.3-9)$$

with  $f(t)$  and  $F(t)$  given by Equation 5.3.3-7 and 5.3.3-8, respectively. Because of the very limited size of the data samples for the RLME sources where the model is applied, estimation of the aperiodicity coefficient,  $\alpha$ , is highly uncertain. Therefore, the value of  $\alpha$  is constrained to values reported from examination of larger data sets. Based on examination of a number of data sets, the Working Group (2003) developed an uncertainty distribution for the aperiodicity coefficient for the BTP model consisting of three weighted values for  $\alpha$  of 0.3 (weight 0.2), 0.5 (weight 0.5), and 0.7 (weight 0.3). The Working Group (2003) weighted distribution was adopted to constrain the value of  $\alpha$ .

The process described in Section 5.3.3.1 was used to develop a likelihood-based distribution for  $\mu$  given a specified value of  $\alpha$ . A broad range of values for  $\mu$  were input into Equation 5.3.3-9 to compute likelihood values. These likelihoods were then normalized to form a probability distribution for  $\mu$  for each of the three values of  $\alpha$ . This distribution was then represented by the discrete five-point approximation from Miller and Rice (1983) described above.

For the renewal recurrence model, the probability of an earthquake in the next time interval  $\Delta t$  is given by the expression:

$$P_{renewal}(\text{event in time } t_0 \text{ to } t_0 + \Delta t) = \frac{F(t_0 + \Delta t) - F(t_0)}{1 - F(t_0)} \quad (5.3.3-10)$$

The basic PSHA formulation used to assess the site hazard assumes that the occurrence of individual earthquakes conforms to a Poisson process. In order to combine the hazard from earthquakes defined by a renewal process into the total hazard, an equivalent Poisson rate is defined such that a Poisson process will give a probability of at least one earthquake in time interval  $\Delta t$  that is equal to the probability given by Equation 5.3.3-10. The equivalent Poisson rate,  $\lambda_{renewal}$ , is given by the expression:

$$\lambda_{renewal} = -\ln[1 - P_{renewal}(\text{event in time } t_0 \text{ to } t_0 + \Delta t)] / \Delta t \quad (5.3.3-11)$$

A time period of 60 years was chosen as the time period of interest for application (20-year license life plus 40-year plant design life). The time  $t_0$  was set at January 1, 2011. The corresponding values of  $\lambda_{renewal}$  computed from the five weighted values of  $\mu$  were then used as a discrete uncertainty distribution for the rate of RLMEs. Distributions are developed for each value of  $\alpha$ , resulting in a total of 15 weighted alternative RLME rates.

### 5.3.3.3 Incorporating Uncertainty in the Input

The typical uncertainties encountered in characterizing the occurrence rates for RLME sources are uncertainties in the data set (i.e., specification of the number of earthquakes and the time span of their occurrence) and uncertainties in the actual ages of individual earthquakes or the age of the offset stratigraphic horizon used to define the time span.

Uncertainties in the appropriate data set are handled by creating a probability distribution for occurrence rate for each data set and then including these alternatives in the seismic source model logic tree as weighted alternatives. Examples of this are the alternative time periods of

complete paleoseismic reporting (e.g., 2,000 vs. 5,500 years) and the alternative number of RLME earthquakes that are evident in the data for the Charleston RLME, discussed in Section 6.1. A number of the other RLME source models also include alternative estimates of the number of RLMEs that have occurred in the recent past as discrete alternative models in the seismic source model logic tree.

Uncertainty in the age of individual earthquakes or the age of the offset marker horizon are typically expressed as a 90% or 95% confidence interval on the before present (BP) age, or as an age range (e.g., 10,000 to 12,000 years for the age of a marker horizon). This type of uncertainty is incorporated into the uncertainty distribution for the RLME rate parameter by simulating values of the age of the  $i^{\text{th}}$  RLME or of the total time span  $T$  from the expressed uncertainty distribution. The resulting values of  $t_i$  or  $T$  are then used to develop a likelihood based continuous probability distribution for the rate parameter. The process is then repeated multiple times and the resulting probability distributions averaged to produce a composite continuous distribution for the rate parameter. This composite distribution is then represented by the five-point discrete approximation described above.

For two of the RLME sources the available paleoseismic data consists of multiple samples providing constraints on the timing of past RLME occurrences. For the Charleston RLME, two types of data are used. One consists of samples whose ages are considered to be contemporary with the earthquake occurrence, denoted as CON ages. Each sample has its own age estimate with associated uncertainties. A distribution for the age of the associated RLME was developed by computing the relative likelihood that a range of possible ages produced the sample of age dates, assuming that the uncertainty in each age can be approximated by a normal distribution with the specified uncertainty ranges. These relative likelihoods were then normalized to produce a probability distribution for the RLME age. Figure 5.3.3-2 shows the resulting distributions for the ages of the five most recent Charleston RLMEs preceding the 1886 earthquake, labeled as “Con Ages.”

The second type of sample data for the Charleston RLME is those that provide constraints on the event age in terms of representing points in time either before or after each earthquake occurrence. This additional age data was used to modify the CON age distributions by simulating ages from the CON age distribution and from the distribution for the constraining sample age and rejecting those simulations that violate the age constraints. The resulting earthquake age distributions are shown on Figure 5.3.3-2 as the “All Ages” distributions.

These two sets of age distributions were then used to develop uncertainty distributions for the RLME occurrence rate.

#### 5.3.3.4 RLME Magnitude Distribution

The RLME sources are intended to model the repeated occurrence of large earthquakes of similar size. The expected magnitude of the RLME is estimated from various sources of data and its uncertainty is expressed by a probability distribution in the RLME source logic tree. In addition, it is anticipated that there will be variability in the actual magnitude of each earthquake when it occurs, requiring the need for specifying an aleatory uncertainty for earthquake magnitude. For

this study, a simple uniform distribution is assumed, which implies maximum uncertainty. The width of this distribution is set to be the expected RLME magnitude  $\pm 1/4$ -magnitude units, resulting in a range of  $1/2$ -magnitude units. A  $1/2$ -magnitude unit range implies a factor of 3 range in source dimensions and over a factor of 5 range in seismic moment. The  $1/2$ -magnitude range was chosen as a typical representation of the variability of repeated large earthquakes occurring on a single source (e.g., Youngs and Coppersmith, 1985).

## **5.4 Assessment of Future Earthquake Characteristics**

The CEUS SSC model has been developed for use in future PSHAs. To make this future use possible, the SSC model must be combined with a ground-motion characterization (GMC) model. At present, the ground-motion prediction equations (GMPEs) in use for SCRs such as the CEUS include limited information regarding the characteristics of future earthquakes. In contrast, GMPEs for active tectonic environments often include multiple characteristics, including style of faulting as defined by sense of fault slip and distance to the fault rupture. In anticipation of the possible future development of GMPEs for the CEUS that will make it possible to incorporate similar types of information, a number of characteristics of future earthquakes in the CEUS are assessed in this section. In addition to characteristics that might be important for ground-motion assessments, there are also assessed characteristics that are potentially important to the modeling conducted for hazard analysis. For example, assuming that the PSHA models earthquakes as finite fault ruptures, information is then needed about the relationship between magnitude of the earthquake and rupture dimensions, length-to-width aspect ratios, and the relationship between the rupture and the seismic source zone boundaries.

The assessment by the TI Team of future earthquake characteristics was carried out in two parts. In the first, a set of characteristics believed to be representative of the entire CEUS study region was assessed. This set of characteristics is termed “default” because, in the absence of local data for a particular region, it would provide a basis for use in the PSHA calculations. The default characteristics and their assessed values are given in Table 5.4-1. The second assessment involved making estimates of the future earthquake characteristics for the individual seismic sources. These assessments were made by the TI Team by evaluating source-specific data. A summary of the source-specific assessments is given in Table 5.4-2. A brief description of the future earthquake characteristics is given below.

The assessment of future earthquake characteristics for the entire CEUS study region is given in Table 5.4-1. Also included in Table 5.4-1 are representative references to data and interpretations that have been evaluated in the assessment of these characteristics. It should be noted that these references usually cite local or site-specific studies, and not evaluations across the entire CEUS SSC study region, because such studies are not available on a regional scale. In addition, the references only provide data for consideration by TI Team members in their assessments of the future earthquake characteristics; the assessed values in column 2 of the table are based on the assessments by the TI Team of the default characteristics that represent the current state of scientific knowledge” for the CEUS in the absence of source-specific information.

In the characterization of individual seismic sources, if source-specific data suggest a difference from the default case, the characteristics were assessed for that particular source. The source-

specific assessments summarized in Table 5.4-2 are discussed for each RLME source and Mmax source in Chapter 6 and for each seismotectonic zone in Chapter 7. The discussions in Chapters 6 and 7 include a description of the assessments of the future earthquake characteristics, as well as the technical bases for the weights applied to the alternatives. As indicated in Table 5.4-2, those assessments that are the same as the default assessments are shown as italics; those assessments that are different from the default assessments due to source-specific information are shown in plain text.

Subsequent to the finalization of the model for developing the HID and hazard calculations, minor revisions to the future earthquake characteristics were made to the ECC-AM and ECC-GC sources. The final characteristics are given in Table 5.4-2. These characteristics have little to no effect on the hazard, given the ground motion models that were used for the hazard calculations. However, future users of the CEUS SSC model should consider the characteristics given in Table 5.4-2 to be the final assessments for the CEUS SSC model.

The Data Evaluation table for the assessment of default characteristics of future earthquakes in the CEUS is presented in Appendix Table C-5.4, and the Data Summary table in Appendix Table D-5.4. Each of the future earthquake characteristics is described below.

#### **5.4.1 Tectonic Stress Regime**

Some GMPEs provide different relationships as a function of compressional or extensional tectonic stress regimes. A variety of data sets, including the stress data compiled for the project by Zoback (2010), indicate the CEUS study region lies within a contemporary tectonic stress regime that is compressional.

#### **5.4.2 Sense of Slip/Style of Faulting**

Sense of slip of future earthquakes, which defines the style of faulting, is assessed based on a variety of data sets, including earthquake focal mechanisms, stress indicators, and the relationship between stress orientations and the geologic structure. The result of the assessment given in Table 5.4-1 is aleatory variability, which reflects the expected relative frequency of strike-slip versus reverse faulting averaged across the study region.

#### **5.4.3 Strike and Dip of Ruptures**

It is assumed that the GMPE for the CEUS will be capable of incorporating information about the characteristics of earthquake sources, modeled as finite faults in much the same manner as earthquake sources are modeled in the WUS. Therefore, Table 5.4-1 includes a number of assessment results that address the expected geometry of future ruptures and, in some cases, the relationship of the geometry to earthquake magnitude. A key attribute of the geometry is the strike and dip (i.e., orientation) of the rupture surfaces. Assessment of the strike of future rupture surfaces was made using information from earthquake focal mechanisms, the structural grain of major fold and fault systems—unless the grain is judged to have no relationship to contemporary earthquake properties; and tectonic stress data in regard to the orientations and magnitudes of

principal stresses. Assessment of the dip of future rupture surfaces was dependent on style of faulting and derived from empirical data related to observed ruptures and evaluations of physical properties.

#### **5.4.4 Seismogenic Crustal Thickness**

From the standpoint of high-frequency energy release and seismic hazard, an important consideration is the geometry of the rupture within the seismogenic part of the crust. The thickness of the seismogenic crust (also called the seismogenic layer or seismogenic zone) varies spatially, but the results of the assessment shown in Table 5.4-1 represent an epistemic assessment of the average crustal thickness across the study region. This distribution can be modified locally to account for unusually thick or thin seismogenic crust at the scale of an individual seismic source. The assessment of seismogenic crustal thickness is based on the focal depth distributions of well-studied earthquakes, usually those lying within local or regional seismic networks, such that hypocentral depth can be determined with a high degree of confidence. However, uncertainties in focal depth across the study region vary considerably as a function of available hypocenter information.

Given a focal depth distribution, physical considerations given by various researchers suggest that the base of the seismogenic zone is identified as lying near the base of the observed focal depths. For example, Scholz (1998) identifies the 300°C isotherm as corresponding to the onset of dislocation creep in quartz, which he interprets to control the seismic/aseismic transition zone by Scholz (1998). Tanaka (2004) and Tanaka and Ito (2002) compares high-quality thermal measurements and seismicity depth data to examine the concept that temperature is a fundamental parameter for determining the thickness of the seismogenic zone. Their gridded heat flow or geothermal gradient and  $D_{90}$ , the depth above which 90% of earthquakes occur, correlated well with each other. The evaluated temperatures for  $D_{90}$  range between 250°C and 450°C. The consistency of temperature for  $D_{90}$  over a large depth interval almost all over the Japanese Islands leads these researchers to conclude that temperature is the dominant factor governing the focal depth in the crust. However, other evaluators have used criteria, such as the 95<sup>th</sup> percentile of the focal depth distribution. Given these alternative interpretations, and the uncertainty in focal depth assessments across the the study region, the generic and zone-specific assessments of crustal thickness presented in Tables 5.4-1 and 5.4-2 were made.

As discussed in Chapter 8, uncertainty in crustal thickness is not a significant contributor to uncertainty in seismic hazard in the CEUS because the current ground motion prediction equations have only limited sensitivity to depth. However, in anticipation of future advances in the characterization of ground motions for CEUS earthquakes, additional analysis of focal depth data are presented. Given the assumption that the criterion of  $D_{90}$  is the correct interpretation of the base of the seismogenic layer, a high-quality focal depth data set was compiled based on those earthquakes having the best-resolved focal depths. The calculation of  $D_{90}$  is made for each of the seismic source zones. The assessment of seismogenic thickness and its uncertainty is, in turn, a function of the number of earthquake focal depths that exist for each source. A bootstrapping approach was used that uses the assumption that the random uncertainty in the focal depth of any given earthquake is about  $\pm 2$  km and the uncertainty in the actual thickness is a function of the number of number of earthquakes that define  $D_{90}$ .

Figure 5.4.4-1 shows the spatial distribution of earthquakes in the CEUS SSC Project catalog with  $E[M]$  magnitudes of 2.2 and greater. Figure 5.4.4-2 shows the spatial distribution of earthquakes in the CEUS SSC Project database having the best-resolved focal depths. This include smaller earthquakes for which  $E[M]$  magnitudes were not computed. In general, the spatial distribution of earthquakes with better quality depth determinations is similar to that of the full catalog. However, some areas, such as the Gulf Coast region and the upper Great Plains have limited coverage.

Figure 5.5.4-3 shows histograms of focal depth for earthquakes within the Mmax source zones and Figure 5.5.4-4 shows histograms of focal depth for earthquakes within the seismotectonic source zones. Several of the seimotectonic source zones have limited to very limited data (AHEX, ECC-GC, GHEX, and OKA). Assessment of  $D_{90}$  for these sources was therefore based on assumed similarity with other sources. As discussed in Section 3.2.4, an attempt was made to identify fixed depth earthquakes. Dips in the histograms for a number of source zones at depths of 5, 10, and 18 km indicates that for some of the earthquakes flagged fixed depths may not be fixed. However, adding synthetic data to representing estimates of the number of missing earthquakes did not result in a significant difference in the estimate of  $D_{90}$ .

Bootstrap samples of focal depths were drawn from the observed focal depth distributions for each source zone. A normally distributed random depth error with a standard deviation of 2 km was added to each focal depth. The bootstrap samples were then used to compute an uncertainty distribution for  $D_{90}$ . Table 5.4-3 lists the results of the analyses. The uncertainty range for  $D_{90}$  is typically  $\pm 1$  km about the observed value. Three of the source zones (AHEX, GHEX, and OKA) have too few good quality focal depths to make an assessment and the results for ECC-GC may also be too broad due to the limited sample size.

The results presented in Table 5.4-3 can be used as part of use of the CEUS SSC model in site-specific applications and to incorporate potential advancements on ground motion modeling.

#### **5.4.5 Fault Rupture Area**

In the hazard analysis, each event is associated with a moment magnitude from the recurrence relationship and, as a result, can be associated with a rupture area that is a function of that magnitude. A variety of empirical relationships between magnitude and rupture area have been proposed in the literature, most leading to very similar results for crustal earthquakes. Because of those similarities, it was judged sufficient to use a single relationship to represent the range of estimates. The relationship used (Somerville et al., 2001) was developed specifically for application in eastern North America, thus it is deemed to be applicable to the CEUS for this assessment. In the future, consideration should be given for updating this assessment with more recent relationships such as that given by Leonard (2010).

#### **5.4.6 Rupture Length-to-Width Aspect Ratio**

Given a rupture area, the shape of the rupture must be defined within the seismogenic crust. Based on an evaluation of observed ruptures for moderate-to-large earthquakes, an assessment

was made of the length-to-width aspect ratio. For smaller rupture areas, the aspect ratio is assessed to be equi-dimensional or one-to-one. For progressively larger rupture areas, the downdip width of the rupture surface, which varies depending on dip angle, will eventually involve the entire seismogenic crustal thickness. At still larger rupture areas, only rupture length will increase, leading to progressively larger aspect ratios. Such a model will result in large aspect ratios for large strike-slip earthquakes and somewhat lower aspect ratios for the same-magnitude reverse earthquakes, which is consistent with empirical observations. For the smaller equi-dimensional ruptures, the depth of the rupture surface is related to the focal depth distribution, following the approach given in NAGRA (2004, p. 174). That approach uses the focal depth distribution as a basis for the relative likelihood of the center point of ruptures occurring at any particular depth. Given the small magnitudes of these earthquakes, the effect of this assumption on hazard is small.

#### **5.4.7 Relationship of Rupture to Source Zone Boundaries**

For a finite-fault SSC model, the locations of future earthquakes are defined by an epicenter and an associated rupture, the geometry of which is represented by the assessment results as discussed above in Sections 5.4.3 through 5.4.6. The event epicenters lie within the seismic source zone of interest, but it is also possible that the associated ruptures may propagate outside the source zone, depending on the properties assessed for the source boundary. If the source boundary is assessed as “leaky,” then ruptures will be allowed to extend beyond the boundary; if they are “strict,” the ruptures will be confined within the boundary. The earthquake epicenter is assumed to lie at the midpoint of the rupture length. Therefore, a leaky rupture would entail no more than 50% of the rupture length (for the particular case where the epicenter is located at the zone boundary). The assessment of whether a boundary is leaky or strict is related to the orientation of rupture surfaces and the expected orientation of ruptures in the adjacent seismic source zones. Sharp source boundaries defined by distinct changes in expected rupture geometries are likely to be strict boundaries. For example, a boundary of a seismic source zone that marks the distinct change in orientation of future earthquake ruptures would likely be assessed as having a strict boundary so that ruptures from one source with a particular orientation are not modeled with that orientation in the adjacent source. In all cases, the lengths of ruptures that are assessed to occur within seismic sources are checked to be sure that their rupture dimensions would not exceed the dimensions allowed within the source (and rupture across the source boundary, as applicable) for the earthquake magnitudes that are assessed. Across the region, the general continuity of expected rupture orientations results in the default assessment of leaky boundaries for most seismic source zones.

### **5.5 Predicted Seismic Moment Rate**

The CEUS SSC seismic source model developed in Chapters 4, 5, and 6 provides an assessment of earthquake recurrence rates for the entire CEUS study region. These recurrence rates were used to compute the predicted mean seismic moment rate for the study region. The table below summarizes these results. Two thirds of the seismic moment rate results from the recurrence of New Madrid RLMEs. The remaining contribution is evenly split between the remaining RLME sources and the distributed seismicity sources.

Predicted Seismic Moment Rate for CEUS SSC Model

Source	Seismic Moment Rate (dyne-cm/year)
Distributed Seismicity	$3.2 \times 10^{24}$
New Madrid RLME	$1.0 \times 10^{25}$
Remaining RLMEs	$3.4 \times 10^{24}$
Total	$1.7 \times 10^{25}$

Johnston et al. (1994) assessed a seismic moment rate for the SCR region of North America both including and excluding the New Madrid 1811-1812 earthquake sequence. Their assessment is listed in the table below in terms of seismic moment rate per  $10^5 \text{ km}^2$ . Also listed are the mean moment rates predicted using the CEUS SSC model and the area encompassed by the CEUS SSC seismic source model of  $7.8 \times 10^6 \text{ km}^2$ . The results are similar excluding the New Madrid earthquakes and with a factor of 2 including the New Madrid earthquakes. Johnston et al. (1994) used moment magnitudes **M** 8.1–8.3. The characterization of the New Madrid RLME for the CEUS SSC model results in a mean magnitude for these earthquakes in updated magnitude assessments for these earthquakes are approximately **M** 7.5. The one-half magnitude difference in the moment magnitudes assigned to these earthquakes translates into approximately a factor of 5 in seismic moment. Thus, the difference in seismic moment rate assigned to the New Madrid sequence based on magnitude assessments for the three earthquakes easily accounts for differences in the estimated moment rate for the CEUS. Based on these comparisons it is concluded that the seismic moment rate predicted by the CEUS SSC model is consistent with the values estimated by Johnston et al. (2004).

Seismic Moment Rates for the SCR Portion of North America

Comparison Case	Seismic Moment Rate Density (dyne-cm/year/ $10^5 \text{ km}^2$ )	
	Johnston et al. (1994)	CEUS SSC Model
Including New Madrid	$4.5 \times 10^{23}$	$2.2 \times 10^{23}$
Excluding New Madrid	$1.07 \times 10^{23}$	$0.8 \times 10^{23}$

**Table 5.2.1-1  
Mesozoic-and-Younger Extended Superdomains (MESE)**

Superdomain Number	Total Area (km <sup>2</sup> )	No. of Domains	Type	Age	Stress	Source Stress Angle	$m_{\max-obs}$ From Catalog	Number of Earthquakes $M \geq 4.5$
SE01*	1326660	6	EC	CZ	C	F	6.3	65.8
SE02*	4369994	15	EC	CZ	C	NF	7.9	871.7
SE03*	2125357	7	EC	CZ	C	UK	7.3	32.9
SE04	1651160	1	EC	CZ	E	NF	6.2	16.1
SE05	2149008	4	EC	CZ	U	UK	5.2	4
SE06*	4057142	10	EC	MZ	C	F	7.3	63.2
SE07*	5323365	21	EC	MZ	C	NF	7.8	557.2
SE08*	3638444	8	EC	MZ	C	UK	6.5	21.9
SE09	1272700	1	EC	MZ	E	F	6.2	4
SE10*	1279577	4	EC	MZ	E	NF	5.9	13
SE11	1196907	2	EC	MZ	E	UK	5.2	1
SE12	4314292	14	EC	MZ	U	UK	5.6	8
SE13	31132	1	EC	PC	C	F	0	0
SE14	507439	2	EC	PC	C	NF	5.5	8.5
SE15	22629	1	EC	PC	E	UK	6.5	2
SE16	556326	3	EC	PC	U	UK	5.4	1
SE17	82782	1	EC	PZ	C	F	5.5	4.1
SE18	570732	4	EC	PZ	C	NF	6.5	8.2
SE19	27315	1	EC	PZ	C	UK	5.3	3
SE20	1257982	3	EC	PZ	U	UK	6.1	11.3

\* Indicates superdomain used to develop prior distribution.

C—Compressive

F—Favorable orientation

PC—Precambrian

CZ—Cenozoic

MZ—Mesozoic

PZ—Paleozoic

E—Extensive

NE—Non-extended crust

U—Unknown

EC—Extended crust

NF—Unfavorable orientation

**Table 5.2.1-2**  
**Older Extended and Non-Extended Superdomains (NMESE)**

Superdomain Number	Total Area (km <sup>2</sup> )	No. of Domains	Type	Age	Stress	Source Stress Angle	$m_{\max-obs}$ From Catalog	Number of Earthquakes $M \geq 4.5$
SE13	31132	1	E	PC	C	F	0	0
SE14*	507439	2	E	PC	C	NF	5.5	8.5
SE15	22629	1	E	PC	E	UK	6.5	2
SE16	556326	3	E	PC	U	UK	5.4	1
SE17	82782	1	E	PZ	C	F	5.5	4.1
SE18*	570732	4	E	PZ	C	NF	6.5	8.2
SE19	27315	1	E	PZ	C	UK	5.3	3
SE20	1257982	3	E	PZ	U	UK	6.1	11.3
SN01	33900	1	NE	MZ	C	F	0	0
SN02*	805784	2	NE	MZ	C	NF	6.2	46.5
SN03*	835876	2	NE	MZ	C	UK	6.4	92.6
SN04	599472	3	NE	MZ	U	UK	5	2
SN05*	9759298	16	NE	PC	C	F	6.7	225.2
SN06*	19633024	17	NE	PC	C	NF	7.3	277.8
SN07*	34329412	38	NE	PC	C	UK	6.8	765.6
SN08*	1519341	3	NE	PC	E	F	5.7	22
SN09*	1689145	3	NE	PC	E	NF	6.6	401.2
SN10*	2039146	3	NE	PC	E	UK	5.6	13.4
SN11	9474115	20	NE	PC	U	UK	6.4	37.1
SN12*	2592956	7	NE	PZ	C	F	6.4	294.4
SN13*	1870538	6	NE	PZ	C	NF	6.4	75.9
SN14*	6518060	16	NE	PZ	C	UK	6.8	110.4
SN15	3645521	9	NE	PZ	U	UK	5.7	12.7

\* Indicates superdomain used to develop prior distribution.

C—Compressive

F—Favorable orientation

PC—Precambrian

CZ—Cenozoic

MZ—Mesozoic

PZ—Paleozoic

E—Extensive

NE—Non-extended crust

U—Unknown

EC—Extended crust

NF—Unfavorable orientation

**Table 5.2.1-3  
Composite SCR Superdomains (COMP)**

Superdomain Number	Total Area (km <sup>2</sup> )	Number of Domains	Type	Age	Stress	Source Stress Angle	$m_{\max-obs}$ From Catalog	Number of Earthquakes $M \geq 4.5$
SD01*	1326660	6	NA	CZ	C	F	6.3	65.8
SD02*	4369994	15	NA	CZ	C	NF	7.9	871.7
SD03*	2125357	7	NA	CZ	C	UK	7.3	32.9
SD04	1651160	1	NA	CZ	E	NF	6.2	16.1
SD05	2149008	4	NA	CZ	U	UK	5.2	4
SD06*	4091042	11	NA	MZ	C	F	7.3	63.2
SD07*	6129149	23	NA	MZ	C	NF	7.8	603.7
SD08*	4474320	10	NA	MZ	C	UK	6.5	114.5
SD09	1272700	1	NA	MZ	E	F	6.2	4
SD10*	1279577	4	NA	MZ	E	NF	5.9	13
SD11	1196907	2	NA	MZ	E	UK	5.2	1
SD12	4913764	17	NA	MZ	U	UK	5.6	10
SD13*	9790430	17	NA	PC	C	F	6.7	225.2
SD14*	20140460	19	NA	PC	C	NF	7.3	286.3
SD15*	34329412	38	NA	PC	C	UK	6.8	765.6
SD16*	1519341	3	NA	PC	E	F	5.7	22
SD17*	1689145	3	NA	PC	E	NF	6.6	401.2
SD18*	2061775	4	NA	PC	E	UK	6.5	15.4
SD19	10030441	23	NA	PC	U	UK	6.4	38.1
SD20*	2675738	8	NA	PZ	C	F	6.4	298.5
SD21*	2441270	10	NA	PZ	C	NF	6.5	84.1
SD22*	6545375	17	NA	PZ	C	UK	6.8	113.4
SD23	4903503	12	NA	PZ	U	UK	6.1	24

\* Indicates superdomain used to develop prior distribution.

C—Compressive

F—Favorable orientation

PC—Precambrian

CZ—Cenozoic

MZ—Mesozoic

PZ—Paleozoic

E—Extensive

NE—Non-extended crust

U—Unknown

EC—Extended crust

NF—Unfavorable orientation

**Table 5.2.1-4**  
**Results of Analyses of Updated SCR Superdomains**

<b>Superdomain Set</b>	<b>Average Number of Earthquakes <math>\geq 4.5</math></b>	<b>Average <i>b</i>-value</b>	<b>Mean <math>m_{\max-obs}</math></b>	<b>Standard Deviation</b>	<b>Bias Adjusted Mean <math>m^u</math></b>
MESE	232	0.85	7.05	0.75	7.35
NMESE	180	1.02	6.48	0.61	6.70
COMP	248	0.94	6.88	0.64	7.20

**Table 5.2.1-5**  
**Source Zones,  $P(m^u > 8\frac{1}{4})$  Values, and Weights on Kijko (2004)**  
**K-S-B Estimates**

Source	$P(m^u > 8\frac{1}{4})$	Weight Assigned to Kijko Approach
Study Region (paleo eq)	0.84	0
MESE-N	0.44	0.06
MESE-W (paleo eq)	0.83	0
NMESE-N (paleo eq)	0.87	0
NMESE-W	0.27	0.23
AHEX	1	0
ECC-AM	0.45	0.05
ECC-GC	0.78	0
GHEX	0.8	0
GMH	0.81	0
IBEB (paleo eq)	0.72	0
MidC-A	0.26	0.24
MidC-B	0.26	0.24
MidC-C	0.26	0.24
MidC-D	0.26	0.24
NAP	0.58	0
OKA	0.69	0
PEZ-N	0.65	0
PEZ-W	0.49	0.01
RR	0.67	0
RR-RCG	0.43	0.07
SLR	0.48	0.02

Note: "Paleo eq" indicates that the zone uses paleoseismic evidence to constrain the size of the largest observed earthquake in that zone. In those cases, the Kijko approach is assigned zero weight.

**Table 5.2.1-6**  
**Mmax Distributions for the Two Example Seismic Sources**

Weight	Maximum Magnitude for:	
	MESE-N	NAP
0.101	6.1	5.8
0.244	6.3	6.4
0.310	6.6	6.9
0.244	7.0	7.5
0.101	7.8	8.0

**Table 5.3.2-1**  
**Alternative Cases Considered for the Magnitude-Dependent Weights**

Case	<b>M 2.9–3.6</b>	<b>M 3.6–4.3</b>	<b>M 4.3–5.0</b>	<b>M 5.0–5.7</b>	<b>M 5.7–6.4</b>	<b>M &gt; 6.4</b>
A (wt = 0.3)	1	1	1	1	1	1
B (wt = 0.3)	0.1	1	1	1	1	1
C	0	1	1	1	1	1
D	0	0.1	1	1	1	1
E (wt = 0.4)	0	0.3	1	1	1	1

Note: The cases used in the final calculations and the weights assigned to them are shown in bold.

**Table 5.3.3-1**  
**Miller and Rice (1983) Discrete 5-Point Approximation to a Continuous Probability Distribution and the Modified Form Used in This Study**

Cumulative Probability Level of Continuous Distribution	Assigned Probability Weight	Modified Probability Weight
0.034893	0.10108	0.101
0.211702	0.24429	0.244
0.5	0.30926	0.310
0.788298	0.24429	0.244
0.965107	0.10108	0.101

**Table 5.4-1**  
**Assessment of Default Characteristics of Future Earthquakes in the CEUS**

<b>Future Earthquake Characteristic</b>	<b>TI Team Assessments (Relative frequencies or weighted alternatives)</b>	<b>References<sup>1</sup></b>
Tectonic Stress Regime	Compressional	Zoback (2010)
Sense of Slip/Style of Faulting	Treat as aleatory (relative frequency): <ul style="list-style-type: none"> <li>• 2:1 strike-slip:reverse</li> </ul>	Focal mechanisms: New Madrid (Shumway, 2008; Horton et al., 2005) Eastern Tennessee (Chapman et al., 1997) Central Virginia (Kim and Chapman, 2005) St. Lawrence (S. Mazzotti, Wksp 2) Southern Great Lakes (Dineva et al., 2004) Wabash Valley (Kim, 2003) Pennsylvania (Seeber et al., 1998) CEUS (Zoback, 2010; Heidbach et al., 2008; van Lanen and Mooney, 2007) Charleston (P. Talwani, Wksp 2) Zoback (1992)
Strike and Dip of Ruptures	Aleatory distribution: <ul style="list-style-type: none"> <li>• N50W (0.2)</li> <li>• N-S (0.2)</li> <li>• N35E (0.4)</li> <li>• N60E (0.1)</li> <li>• E-W (0.1)</li> </ul> Dip is a function of sense of slip: <ul style="list-style-type: none"> <li>• Strike-slip (90°–60°) (uniform)</li> <li>• Reverse (30°–60°) (uniform)</li> <li>• Either direction (50:50)</li> </ul>	van Lanen and Mooney (2007) Sibson and Xie (1998) Zoback (1992) Marshak and Paulsen (1997) (NW trends)

<b>Future Earthquake Characteristic</b>	<b>TI Team Assessments (Relative frequencies or weighted alternatives)</b>	<b>References<sup>1</sup></b>
Seismogenic Crustal Thickness	Epistemic distribution: <ul style="list-style-type: none"> <li>• 13 km (0.4)</li> <li>• 17 km (0.4)</li> <li>• 22 km (0.2)</li> </ul>	Sibson (1984, 2007) van Lanen and Mooney (2007) for ENA Mai et al. (2005) Atkinson (2004a) Sykes et al. (2008) P. Talwani (Wksp 2)
Fault Rupture Area	Function of magnitude: <ul style="list-style-type: none"> <li>• Use Somerville et al. relation for ENA</li> </ul>	Somerville et al. (2001)
Rupture Length-to-Width Aspect Ratio	Function of rupture area: <ul style="list-style-type: none"> <li>• 1:1 for smaller ruptures</li> <li>• With progressively larger areas, when rupture width equals seismogenic crustal thickness, extend only the length</li> </ul>	Wesnousky (2008) Toro approach in NAGRA (2004)
Relationship of Rupture to Source Zone Boundaries	<ul style="list-style-type: none"> <li>• Epicenter is at center of rupture length (map view)</li> <li>• All boundaries are “leaky”; rupture is allowed to extend beyond boundary. (Note: If boundary is “strict,” rupture cannot extend beyond boundary, although epicenter can be near boundary)</li> </ul>	

1. References provide insight into the assessment of characteristics; however, they do not uniquely define them for purposes of the CEUS SSC study. Those assessments were made by the TI Team.

**Table 5.4-2**  
**Characteristics of Future Earthquakes for Individual Seismic Sources**

Source	Sense of Slip <sup>1</sup>	Rupture Strike <sup>1</sup>	Rupture Dip <sup>1</sup>	Source Boundaries	Seismogenic Crustal Thickness <sup>2</sup>
<b>RLME Sources</b>					
Charlevoix	Reverse	Uniform 0°–360°	Uniform 40°–60°	Leaky	25 km (0.8) 30 km (0.2)
Charleston—Large	Strike-slip	NE parallel to long axis (0.8) NW parallel to short axis (0.2)	90°	Strict	13 km (0.4) 17 km (0.4) 22 km (0.2)
Charleston—Local	Strike-slip	NE parallel to long axis	90°	Strict	13 km (0.4) 17 km (0.4) 22 km (0.2)
Charleston—Narrow	Strike-slip	NE parallel to long axis	90°	Leaky at ends	13 km (0.4) 17 km (0.4) 22 km (0.2)
Cheraw	Normal-oblique	On fault trace (NE)	50° NW (0.6) 65° NW (0.4)	Strict	13 km (0.4) 17 km (0.4) 22 km (0.2)
Commerce	Strike-slip	NE parallel to long axis of zone	90°	Leaky at ends	13 km (0.4) 15 km (0.4) 17 km (0.2)
ERM-N	Strike-slip	NE parallel to long axis of zone	90°	Leaky at ends	13 km (0.4) 15 km (0.4) 17 km (0.2)
ERM-S	Strike-slip	NE parallel to long axis of zone	90°	Leaky at ends	13 km (0.4) 15 km (0.4) 17 km (0.2)
Marianna	Strike-slip	NE 45° (0.5) NE 45° (0.5)	90°	Leaky at ends	13 km (0.4) 15 km (0.4) 17 km (0.2)
Meers—Fault	Strike-slip (0.5) Reverse (0.5)	On fault	Strike-slip 90° Reverse 40° SW	Strict	15 km (0.5) 20 km (0.5)
Meers—Random in OKA	Reverse oblique	Parallel to long axis of zone	Uniform 40°–90°	Strict	15 km (0.5) 20 km (0.5)
NMFS	NMN, NMS: Strike-slip RMT: reverse	On fault	NMN, NMS: 90° RFT: 40° SW	Strict	13 km (0.4) 15 km (0.4) 17 km (0.2)

Source	Sense of Slip <sup>1</sup>	Rupture Strike <sup>1</sup>	Rupture Dip <sup>1</sup>	Source Boundaries	Seismogenic Crustal Thickness <sup>2</sup>
Wabash Valley	2/3 Strike-slip 1/3 Reverse	Strike parallel to the long axis of the zone (0.8) N50W (0.1) N20W (0.1)	2/3 Strike-slip, 90° 1/3 Reverse, 40°–60° Strike-slip, 90° Reverse, 40°	Leaky	17 km (0.7) 22 km (0.3)
<b>Seismotectonic Zones</b>					
AHEX	2/3 Strike-slip 1/3 Reverse	N50W (0.1) N-S (0.1) N25E (0.4) N60E (0.3) E-W (0.1)	Strike-slip (90°–60°) (uniform) Reverse (30°–60°) (uniform)	Leaky	8 km (0.5) 15 km (0.5)
ECC-AM	2/3 Strike-slip 1/3 Reverse	N50W (0.2) N-S (0.2) N35E (0.4) N60E (0.1) E-W (0.1)	Strike-slip (90°–60°) (uniform) Reverse (30°–60°) (uniform)	Leaky	13 km (0.6) 17 km (0.3) 22 km (0.1)
ECC-GC	2/3 Strike-slip 1/3 Reverse	Uniform 0° to 360°	Strike-slip (90°–60°) (uniform) Reverse (30°–60°) (uniform)	Leaky	13 km (0.6) 17 km (0.3) 22 km (0.1)
GHEX	2/3 Strike-slip 1/3 Reverse	Uniform 0° to 360°	Strike-slip (90°–60°) (uniform) Reverse (30°–60°) (uniform)	Leaky	8 km (0.5) 15 km (0.5)
GMH	4/5 Reverse 1/5 Strike-slip	N50W (0.4) N20W (0.4) E-W (0.2)	Strike-slip (90°–60°) (uniform) Reverse (30°–60°) (uniform)	Leaky	25 km (0.5) 30 km (0.5)
IBEB	SS (0.1) RO (0.1) R (0.3) SS (0.2) SS (0.3)	N50W (0.1) N20W (0.1) N-S (0.3) E-W (0.2) N40E (0.3)	90° 70 E (0.5), 70 W (0.5) 40E/W (0.4); 70E/W (0.3) 90° 90°	Strict	13 km (0.4) 17 km (0.4) 22 km (0.2)

Source	Sense of Slip <sup>1</sup>	Rupture Strike <sup>1</sup>	Rupture Dip <sup>1</sup>	Source Boundaries	Seismogenic Crustal Thickness <sup>2</sup>
PEZ	2/3 Strike-slip 1/3 Reverse	N50W (0.2) N-S (0.2) N35E (0.4) N60E (0.1) E-W (0.1)	<i>Strike-slip (90°–60°) (uniform)</i> <i>Reverse (30°–60°) (uniform)</i>	Leaky	13 km (0.4) 17 km (0.4) 22 km (0.2)
MidC	2/3 Strike-slip 1/3 Reverse	<i>N50W (0.2)</i> <i>N-S (0.2)</i> <i>N35E (0.4)</i> <i>N60E (0.1)</i> <i>E-W (0.1)</i>	<i>Strike-slip (90°–60°) (uniform)</i> <i>Reverse (30°–60°) (uniform)</i>	Strict	13 km (0.4) 17 km (0.4) 22 km (0.2)
NAP	1/3 Strike-slip 2/3 Reverse	N50W (0.2) N-S (0.2) N35E (0.4) N60E (0.1) E-W (0.1)	<i>Strike-slip (90°–60°) (uniform)</i> <i>Reverse (30°–60°) (uniform)</i>	Leaky	13 km (0.4) 17 km (0.4) 22 km (0.2)
OKA	Reverse Oblique	Parallel to long axis of zone	Uniform 45°–75°	<i>Leaky</i>	15 km (0.5) 20 km (0.5)
RR and RR-RCG	SS (0.2) R (0.35) SS (0.5) SS (0.2) SS (0.2)	N50W (0.2) N10W(0.35) E-W (0.05) N30E (0.2) N55E (0.2)	90° 70 E/W (0.5), 40 E/W (0.5) 90° 90° 90°	Strict	13 km (0.4) 15 km (0.4) 17 km (0.2)
SLR	1/3 Strike-slip 2/3 Reverse	N25E (0.2) N40E (0.2) N70E (0.2) N50W (0.15) N70W (0.15) N-S (0.05) E-W (0.05)	<i>Strike-slip (90°–60°) (uniform)</i> <i>Reverse (30°–60°) (uniform)</i>	Leaky	25 km (0.5) 30 km (0.5)

Note: Default characteristics are indicated in italics.

1. Weights reflect aleatory variability; weights are therefore relative frequencies.

2. Weights reflect epistemic uncertainty; weights are therefore relative credibility that the given thickness is correct.

**Table 5.4-3**  
**Estimates of  $D_{90}$  for Individual Seismic Source Zones**

<b>Seismic Source Zone</b>	<b>5<sup>th</sup> Percentile <math>D_{90}</math> (km)</b>	<b><math>D_{90}</math> from Observed Focal Depths (km)</b>	<b>95<sup>th</sup> Percentile <math>D_{90}</math> (km)</b>
MESE-N	16	17	18
MESE-W	17	18	19
NMESE-N	17	18	19
NMESE-W	15	16	17
AHEX	—	—	—
ECC-AM	11	12	13
ECC-GC	12	16	20
GHEX	—	—	—
GMH	22	23	24
IBEB	18	19	21
MIDC-A	15	16	17
MIDC-B	15	16	17
MIDC-C	15	16	17
MIDC-D	15	16	17
NAP	15	17	20
OKA	—	—	—
PEZ-N	18	19	20
PEZ-W	18	19	20
RR	12	13	14
RR-RCG	12	13	14
SLR	19	20	21

Note: Cells with “—” indicate source zones with too few earthquakes from which to obtain an estimate.

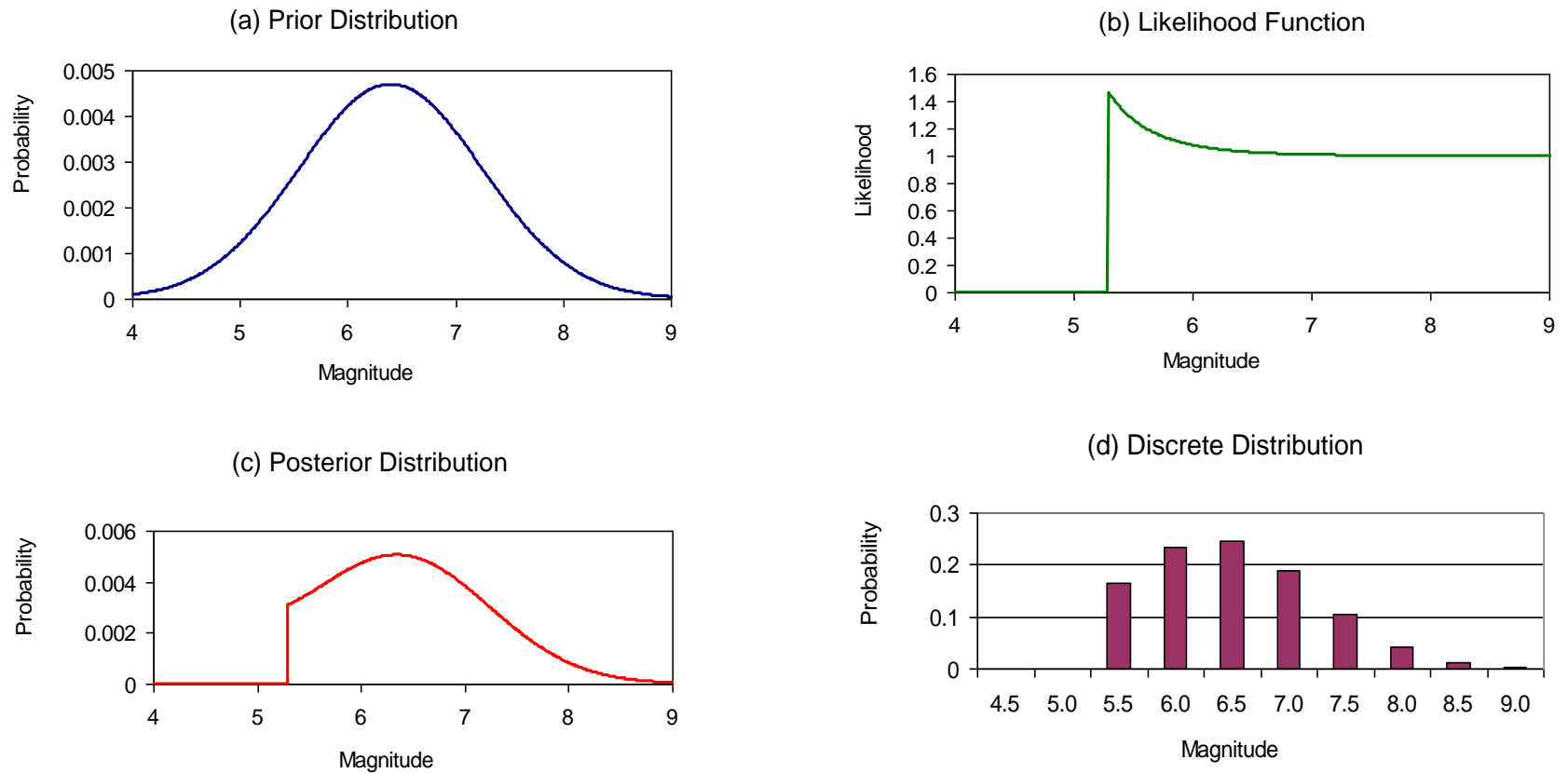


**Figure 5.2.1-1**  
Diagrammatic illustration of the Bayesian Mmax approach showing (a) the prior distribution, (b) the likelihood function, and (c) the posterior distribution. The posterior distribution is represented by a discrete distribution (d) for implementation in hazard analysis.

Notes: Prior is normal distribution with mean  $M$  6.4 and standard deviation 0.85. Likelihood function is based on two observed earthquakes larger than  $M$  4.5, with the largest being 5.3.

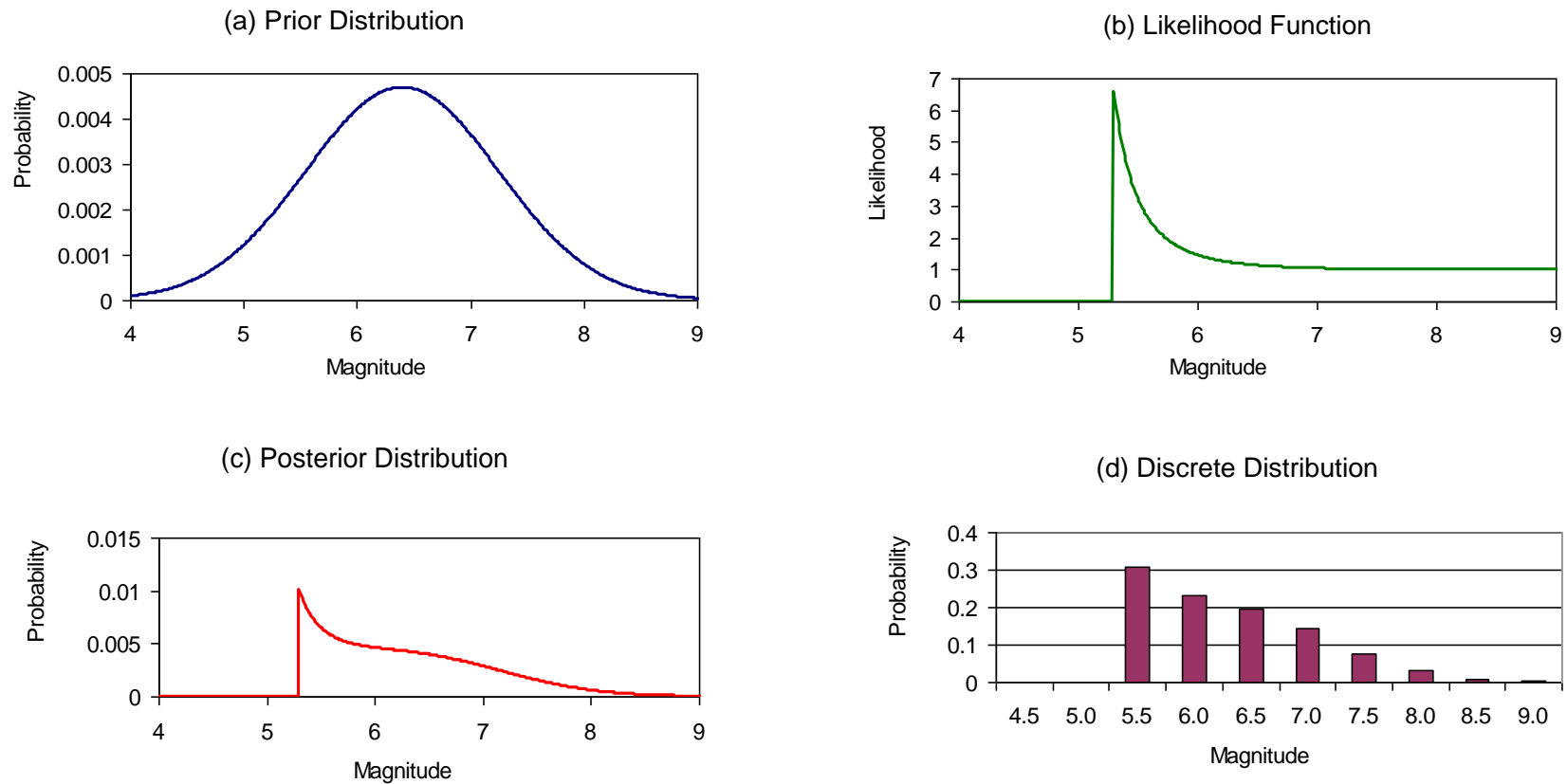


**Figure 5.2.1-2**  
Diagrammatic illustration of the Bayesian Mmax approach showing (a) the prior distribution, (b) the likelihood function, and (c) the posterior distribution. The posterior distribution is represented by a discrete distribution (d) for implementation in hazard analysis.

Notes: Prior is normal distribution with mean M 6.4 and standard deviation 0.85. Likelihood function is based on 10 observed earthquakes larger than M 4.5, with the largest being 5.3.

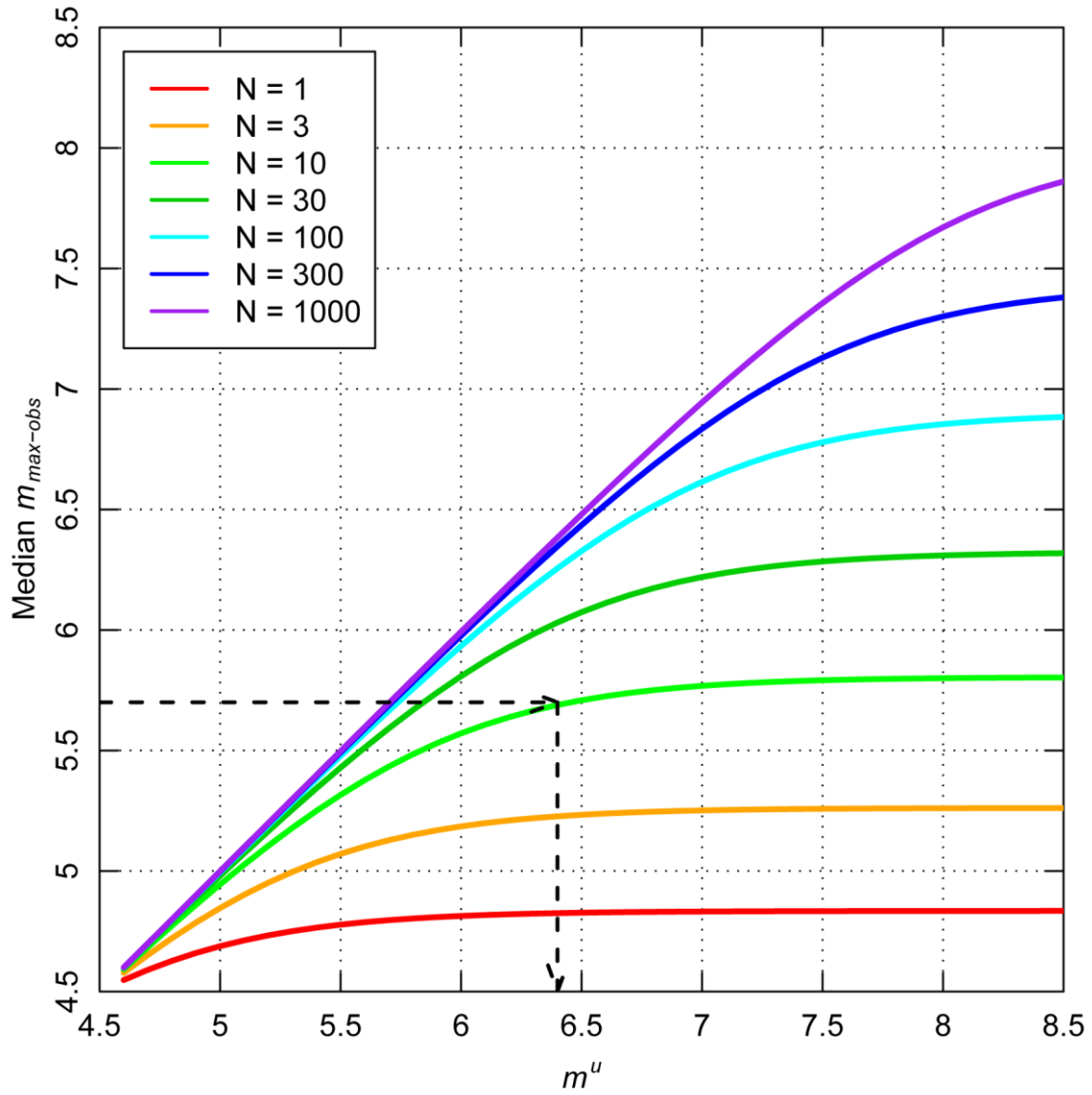


**Figure 5.2.1-3**  
Median values of  $m_{\max-obs}$  as a function of maximum magnitude,  $m^u$ , and sample size  $N$ , the number of earthquakes  $\geq M$  4.5

Note: Dashed lines show bias correction for a  $m_{\max-obs}$  of 5.7 with a sample size of 10.

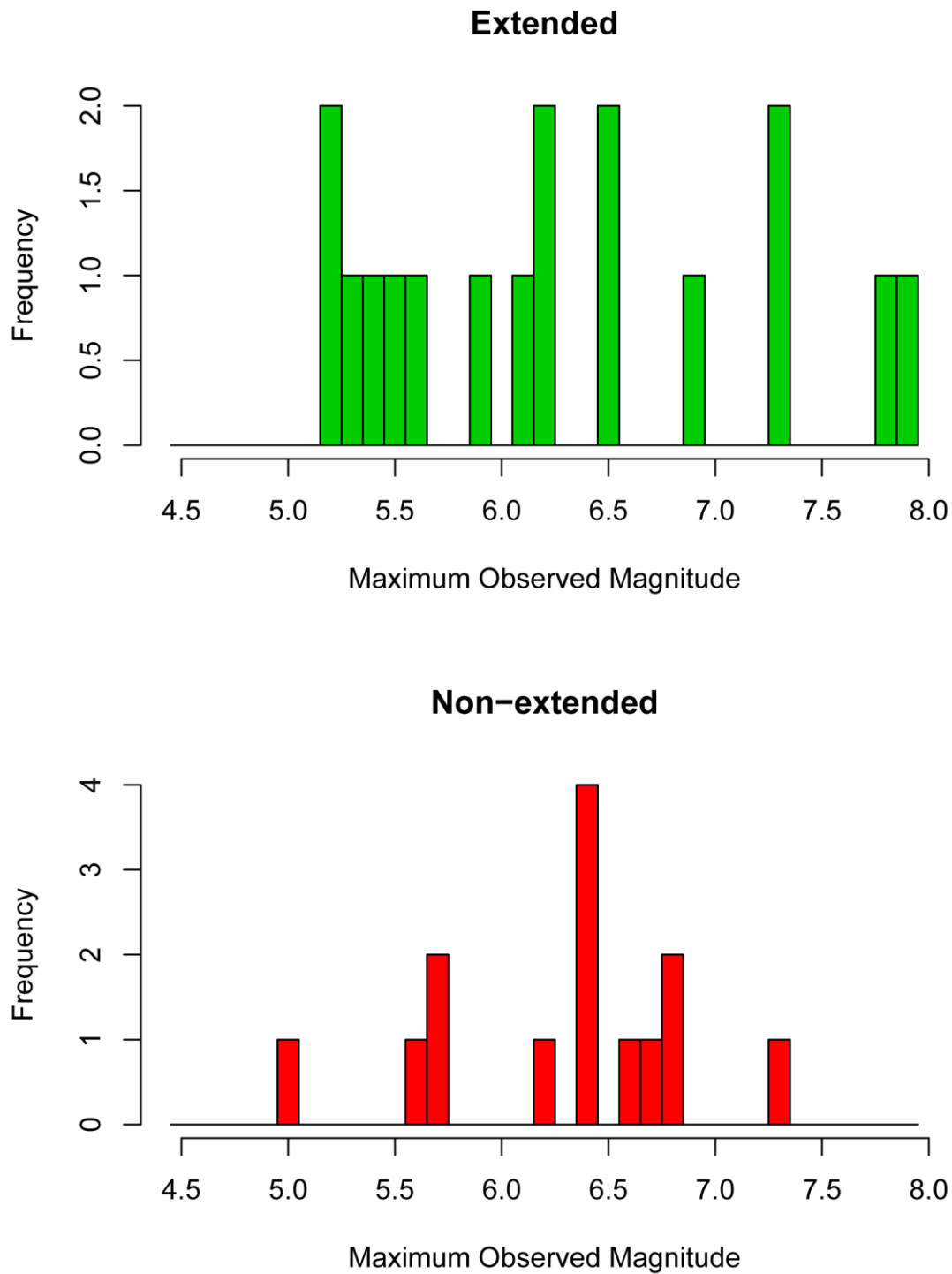
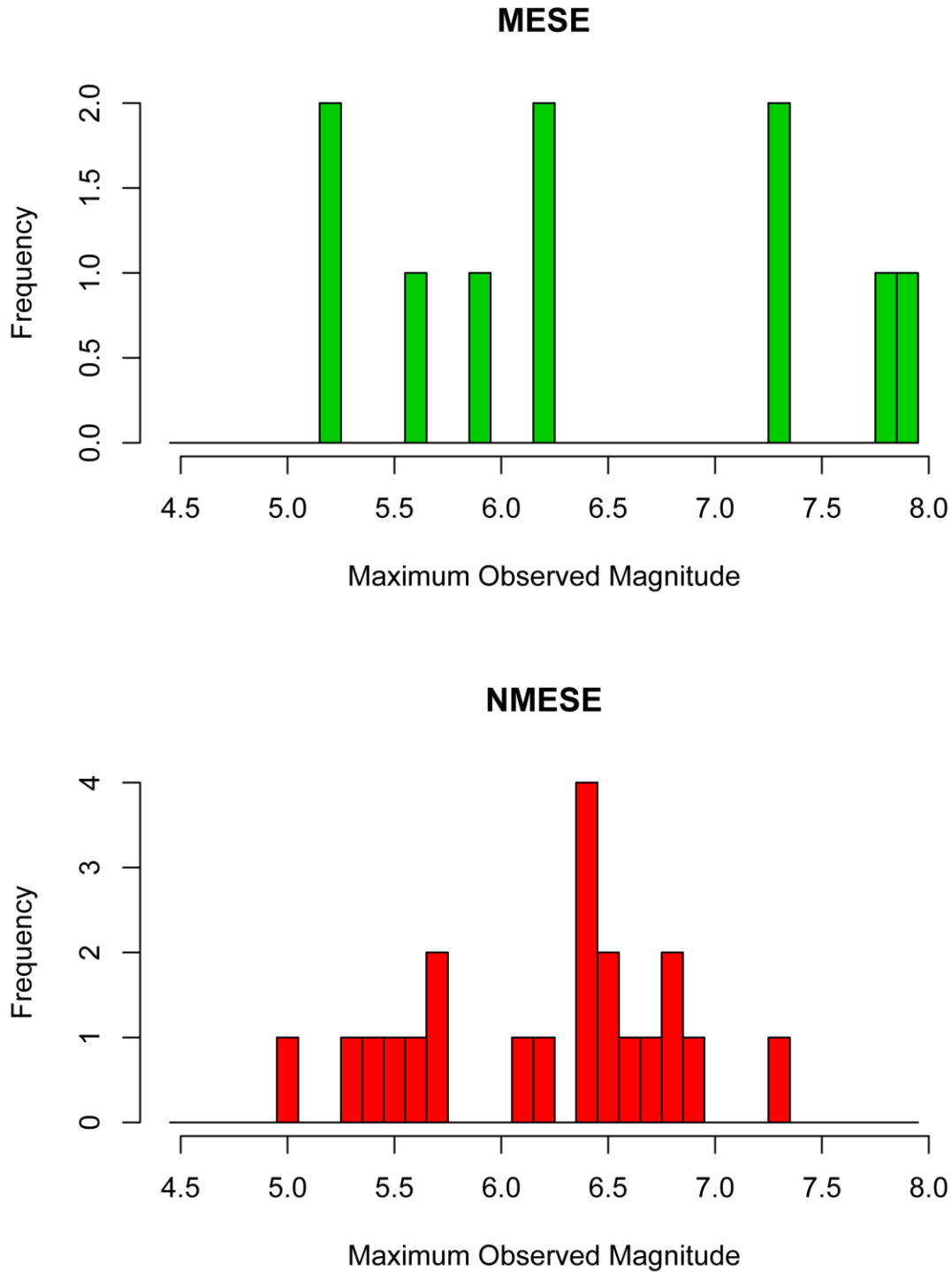
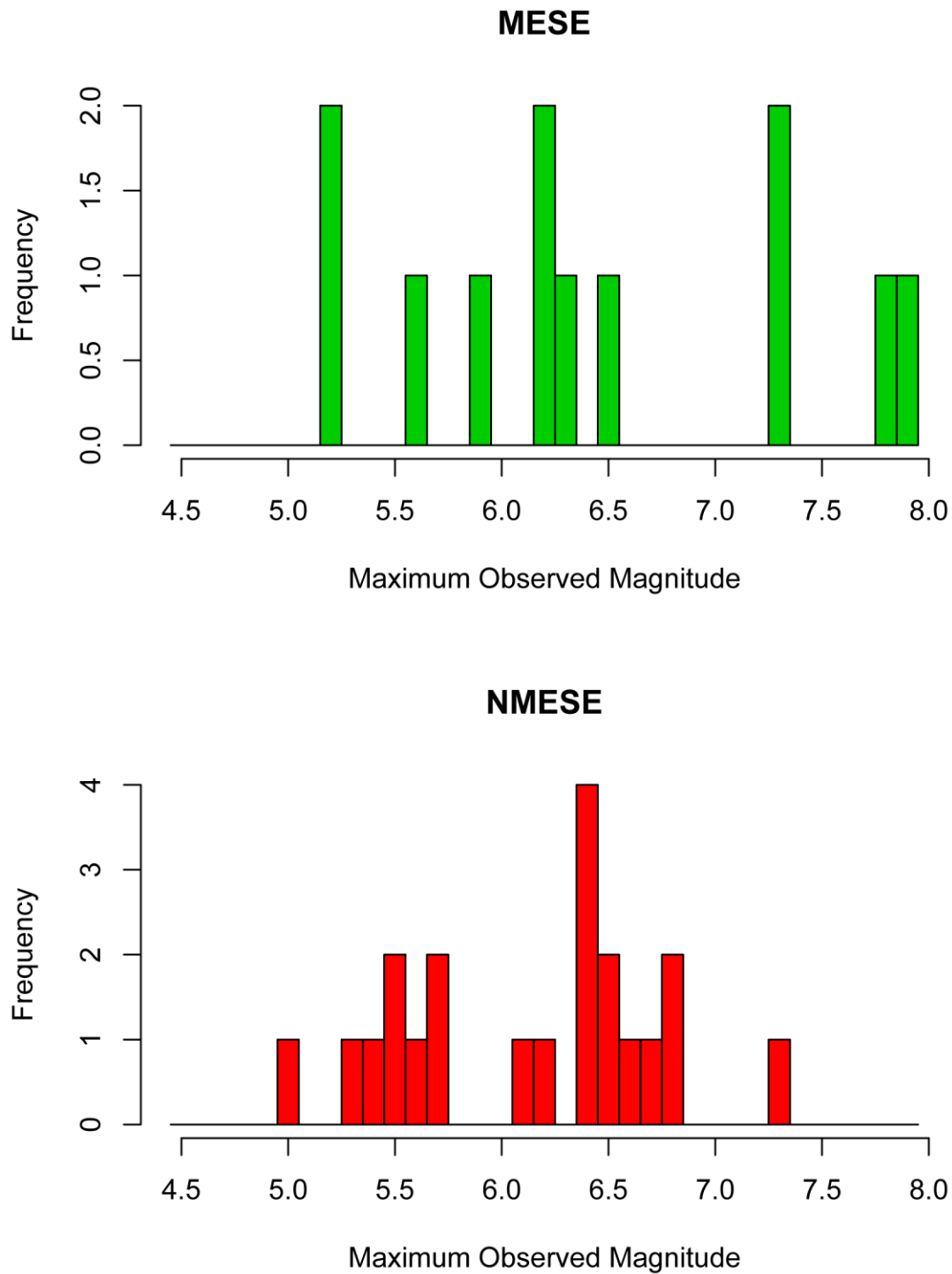


Figure 5.2.1-4  
Histograms of  $m_{\max-obs}$  for extended and non-extended superdomains



**Figure 5.2.1-5**  
Histograms of  $m_{\max-obs}$  for Mesozoic-and-younger extended (MESE) superdomains and for older extended and non-extended (NMESE) superdomains



**Figure 5.2.1-6**  
Histograms of  $m_{\max-obs}$  for Mesozoic-and-younger extended (MESE) superdomains and for older extended and non-extended (NMESE) superdomains using age of most recent extension for the age classification

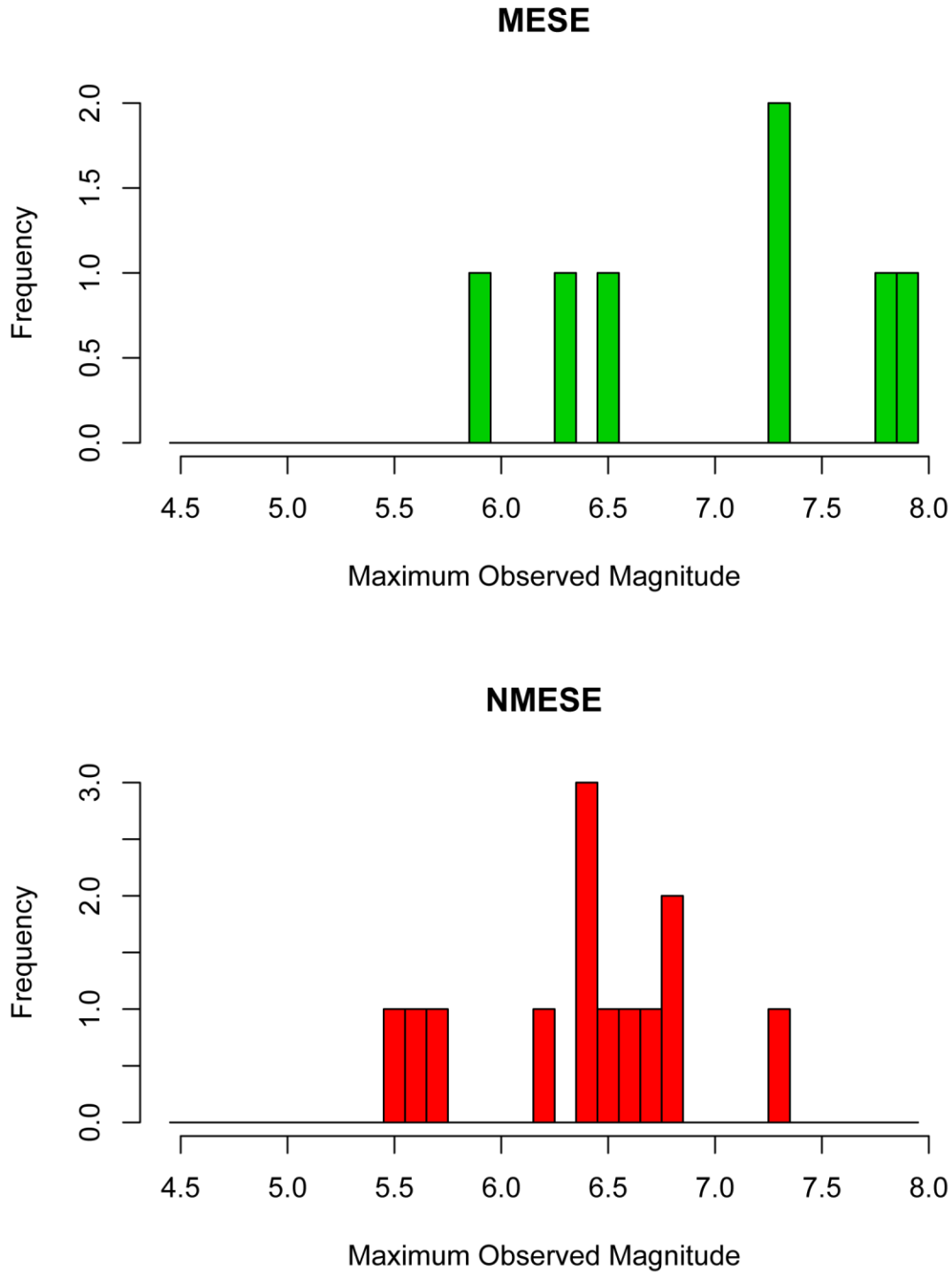


**Figure 5.2.1-7**  
Histograms of  $m_{\max-obs}$  for Mesozoic-and-younger extended (MESE) superdomains and for older extended and non-extended (NMESE) superdomains using final sets indicated by asterisks in Tables 5.2.1-1 and 5.2.1-2

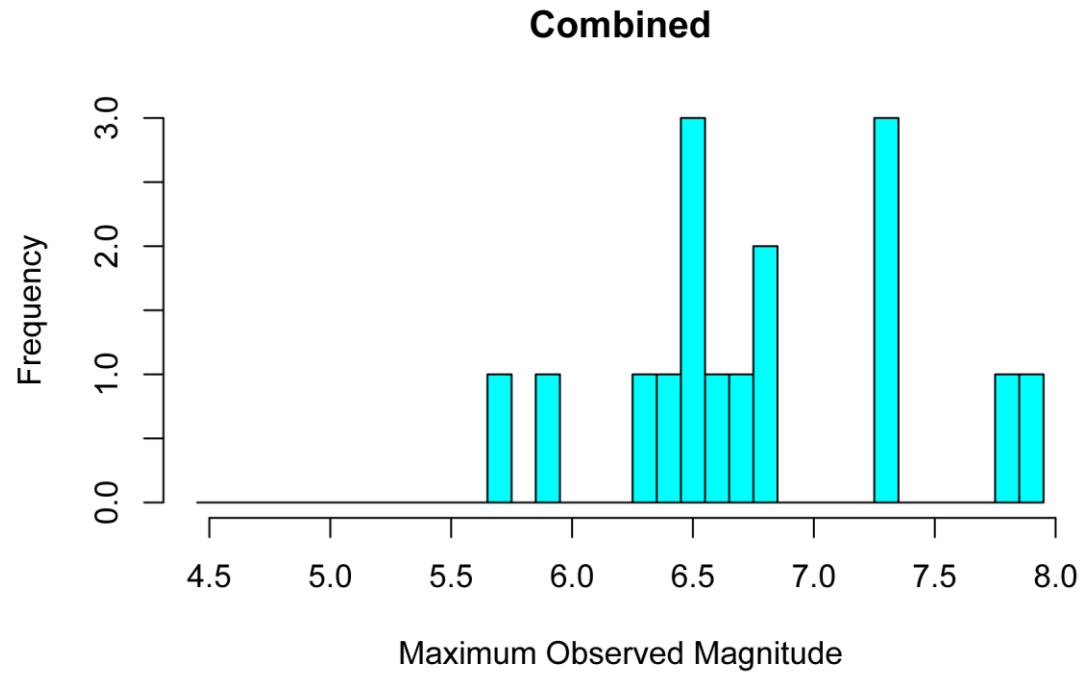


**Figure 5.2.1-8**  
Histograms of  $m_{\text{max-obs}}$  for combined (COMB) superdomains using final sets indicated by asterisks in Table 5.2.1-3

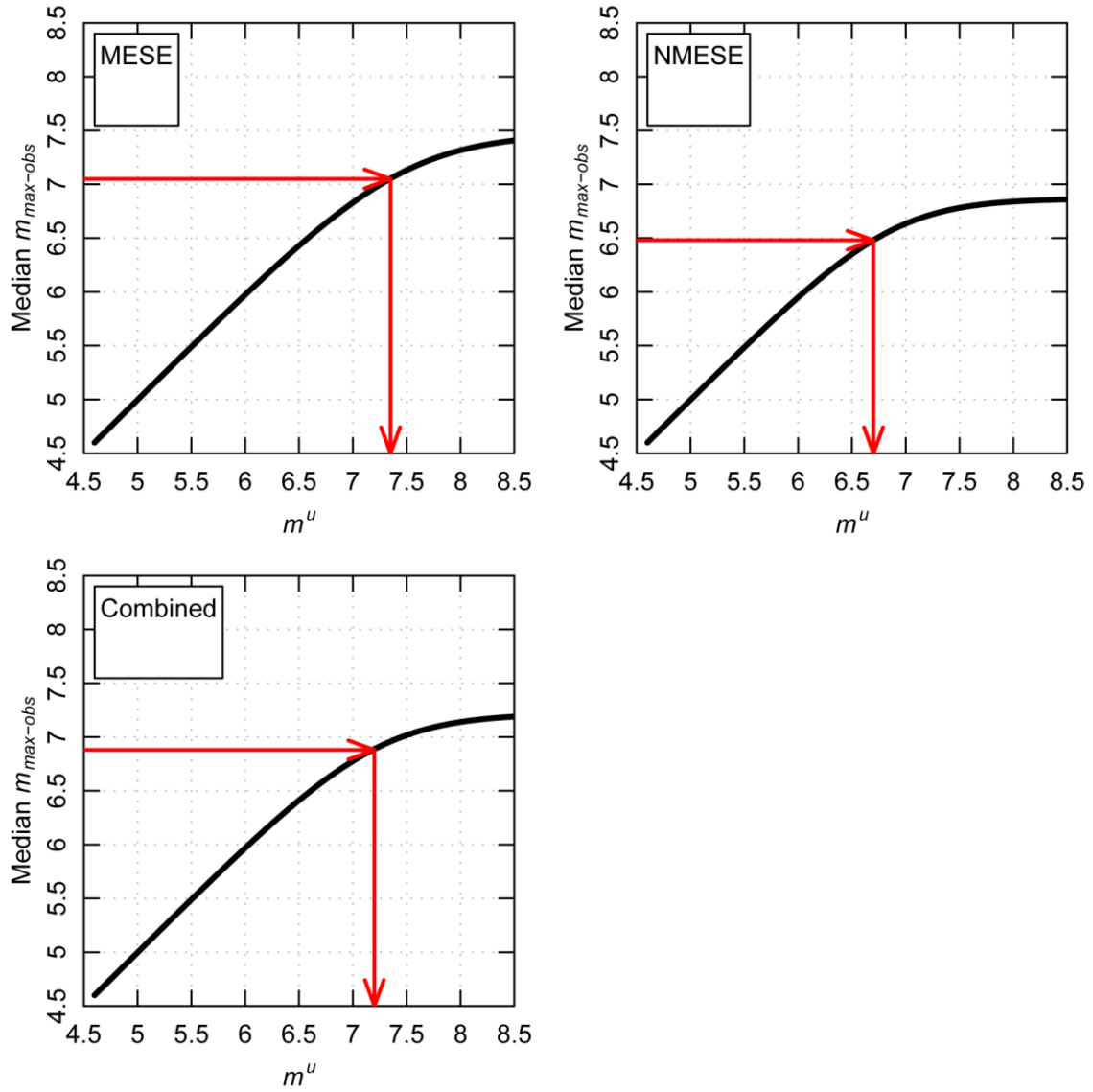


**Figure 5.2.1-9**  
Bias adjustments from  $m_{\max-obs}$  to  $m^u$  for the three sets of superdomain analysis results presented in Table 5.2.1-4

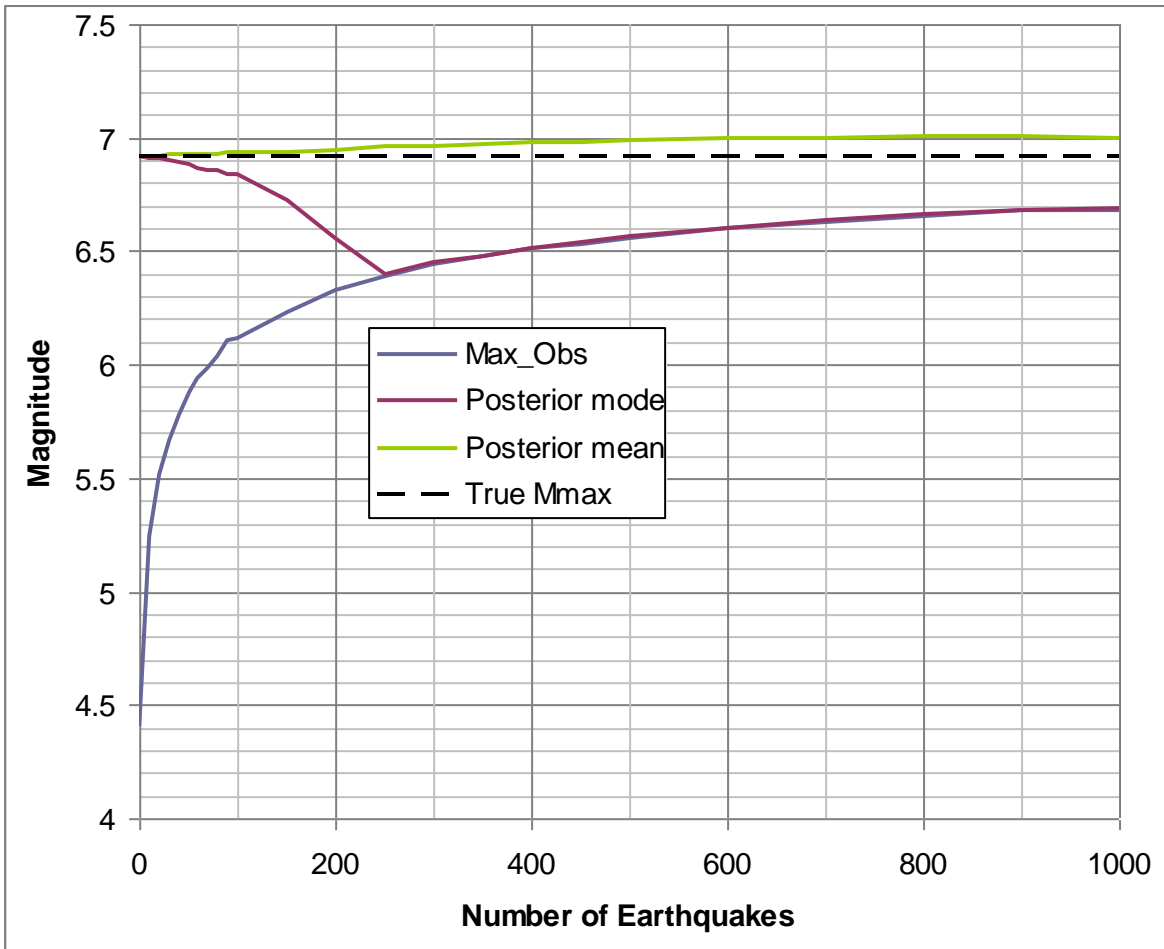


**Figure 5.2.1-10**  
Results of simulations of estimates of Mmax using the Bayesian approach for earthquake catalogs ranging in size from 1 to 1,000 earthquakes. True Mmax is set at the mean of the prior distribution.

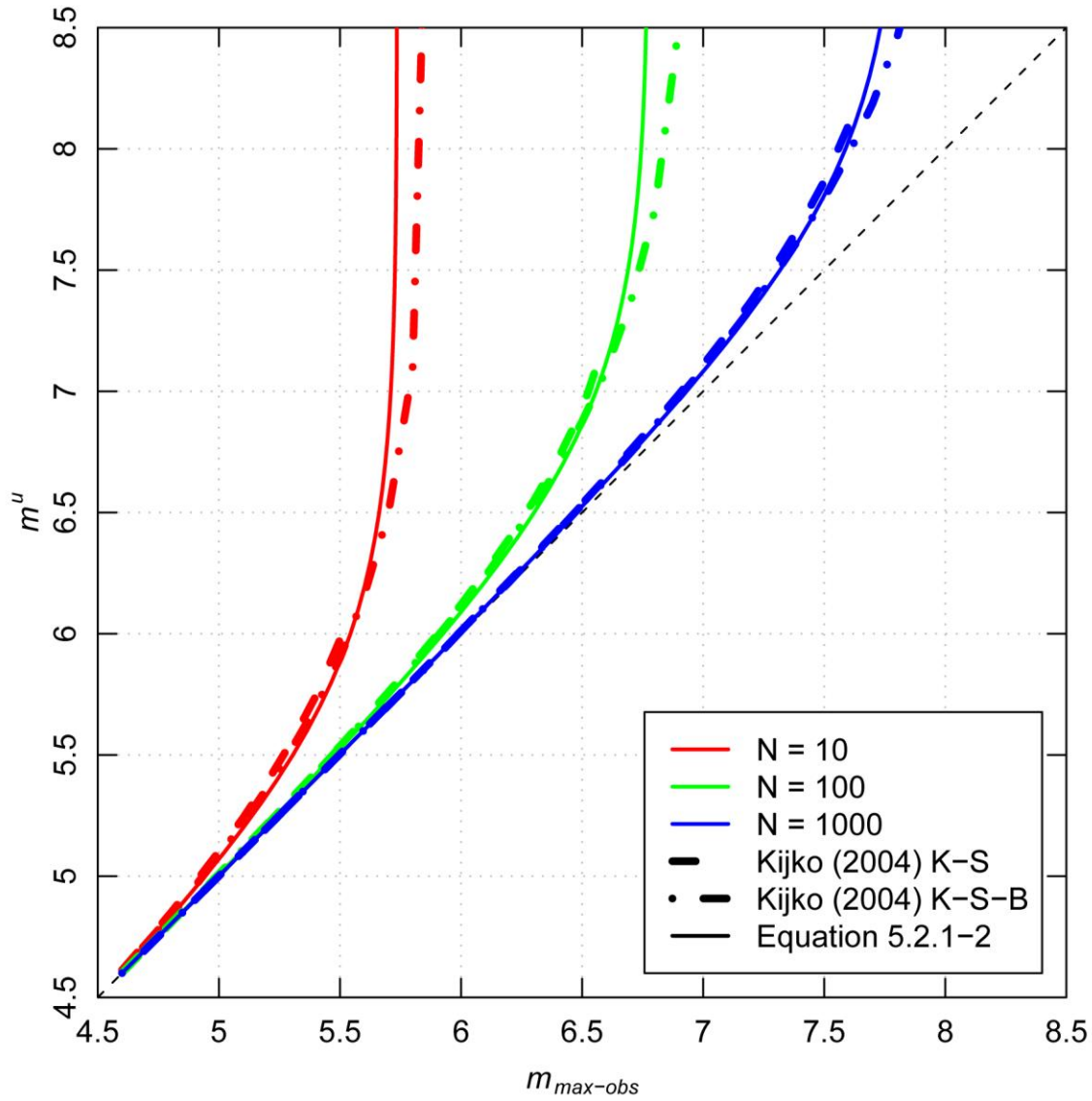


**Figure 5.2.1-11**  
 Comparison of the Kijko (2004) estimates of  $m^u$  for given values of  $m_{\max-obs}$  and  $N$ , the number of earthquakes of magnitude  $\geq 4.5$ . Also shown is the median value of  $m_{\max-obs}$  for given  $m^u$  obtained using Equation 5.2.1-2.

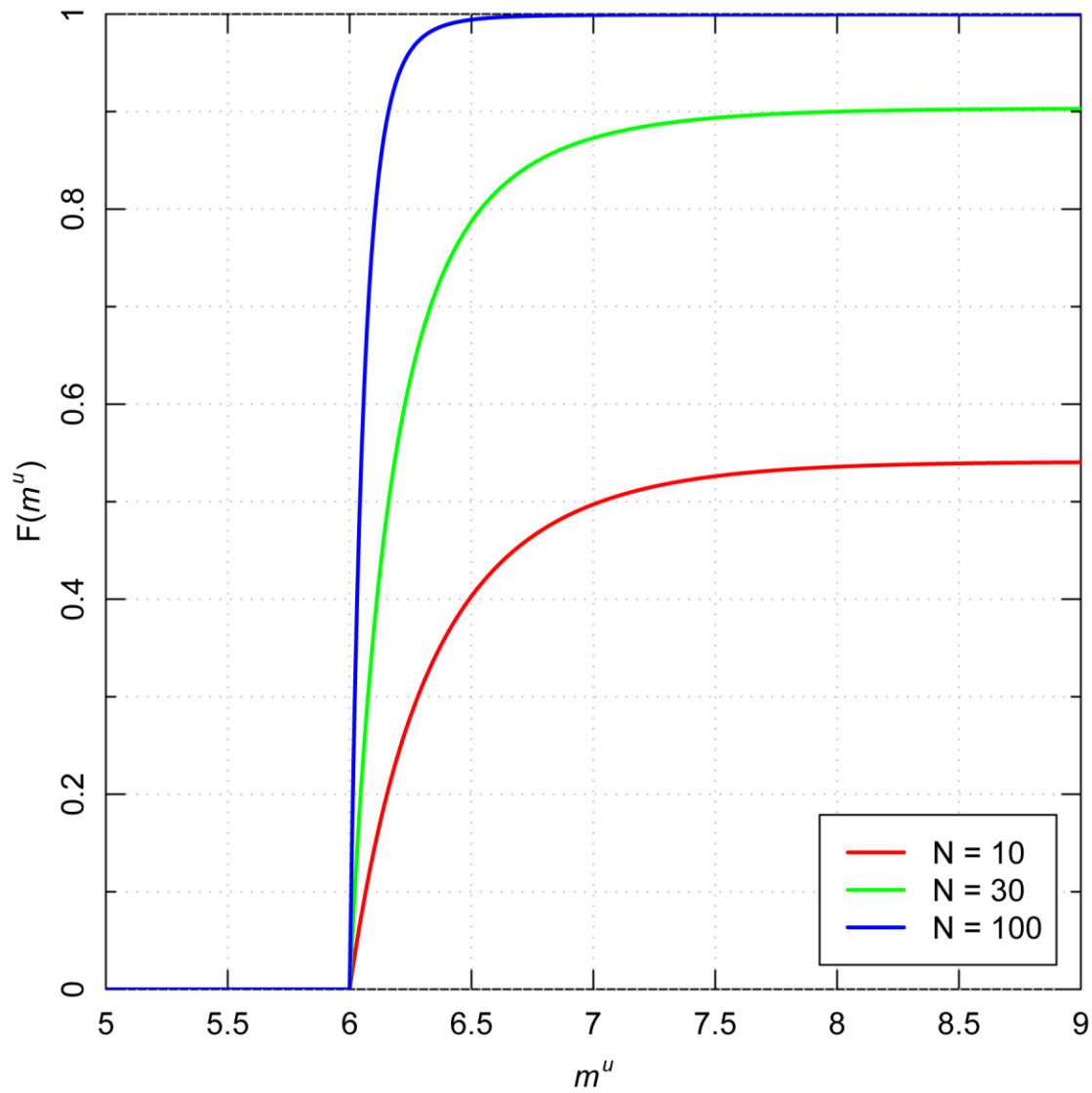


**Figure 5.2.1-12**  
Behavior of the cumulative probability function for  $m^u$  (Equation 5.2.1-9) for the K-S-B estimator and a value of  $m_{\max-obs}$  equal to 6

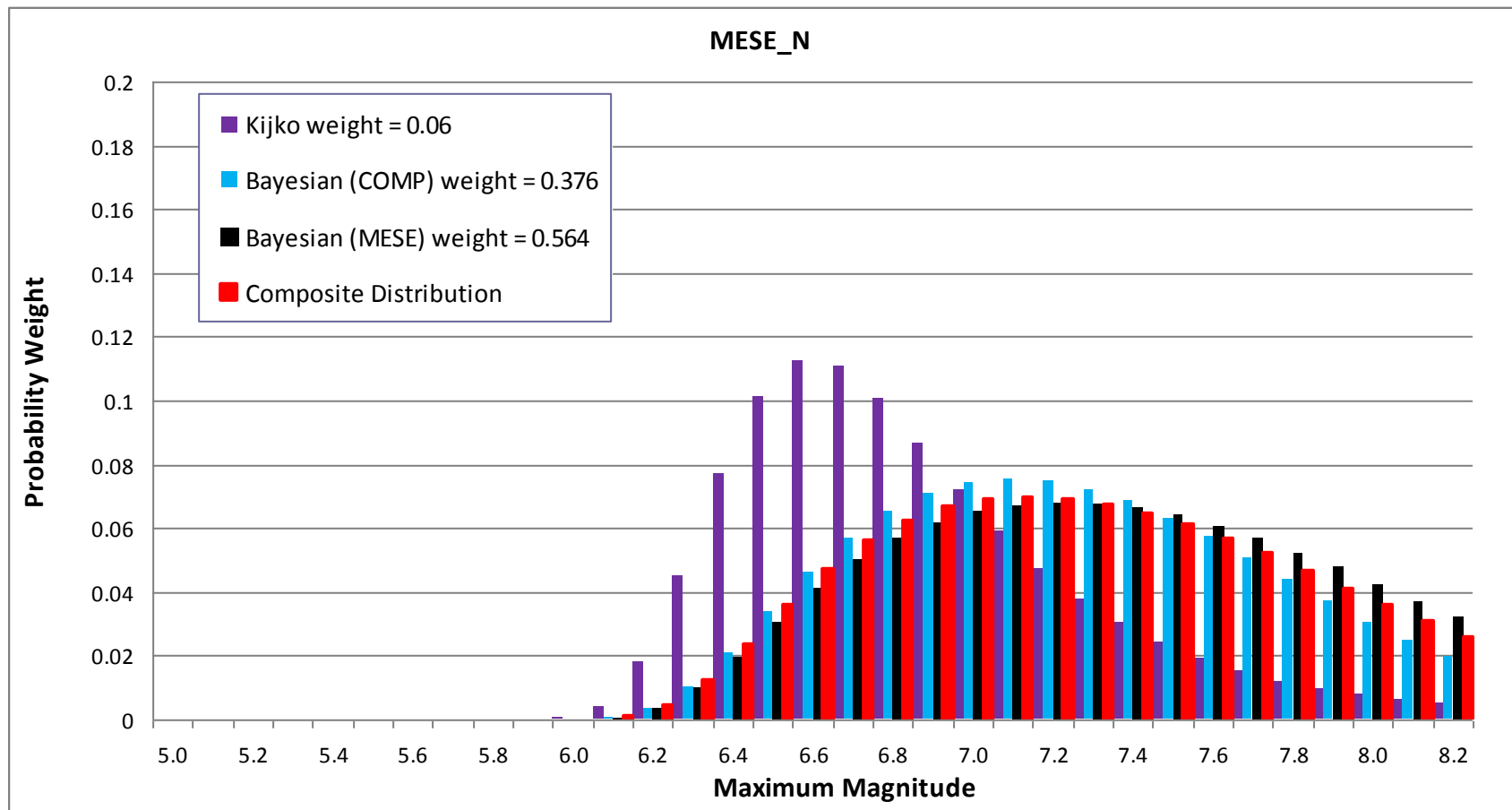


**Figure 5.2.1-13**  
 Example Mmax distribution assessed for the Mesozoic-and-younger extended Mmax zone for the case where the zone is “narrow” (MESE-N). Distributions are shown for the Kijko approach and for the Bayesian approach using either the Mesozoic-and-younger extended prior distribution or the composite prior distribution. The final composite Mmax distribution, which incorporates the relative weights, is shown by the red probability distribution.

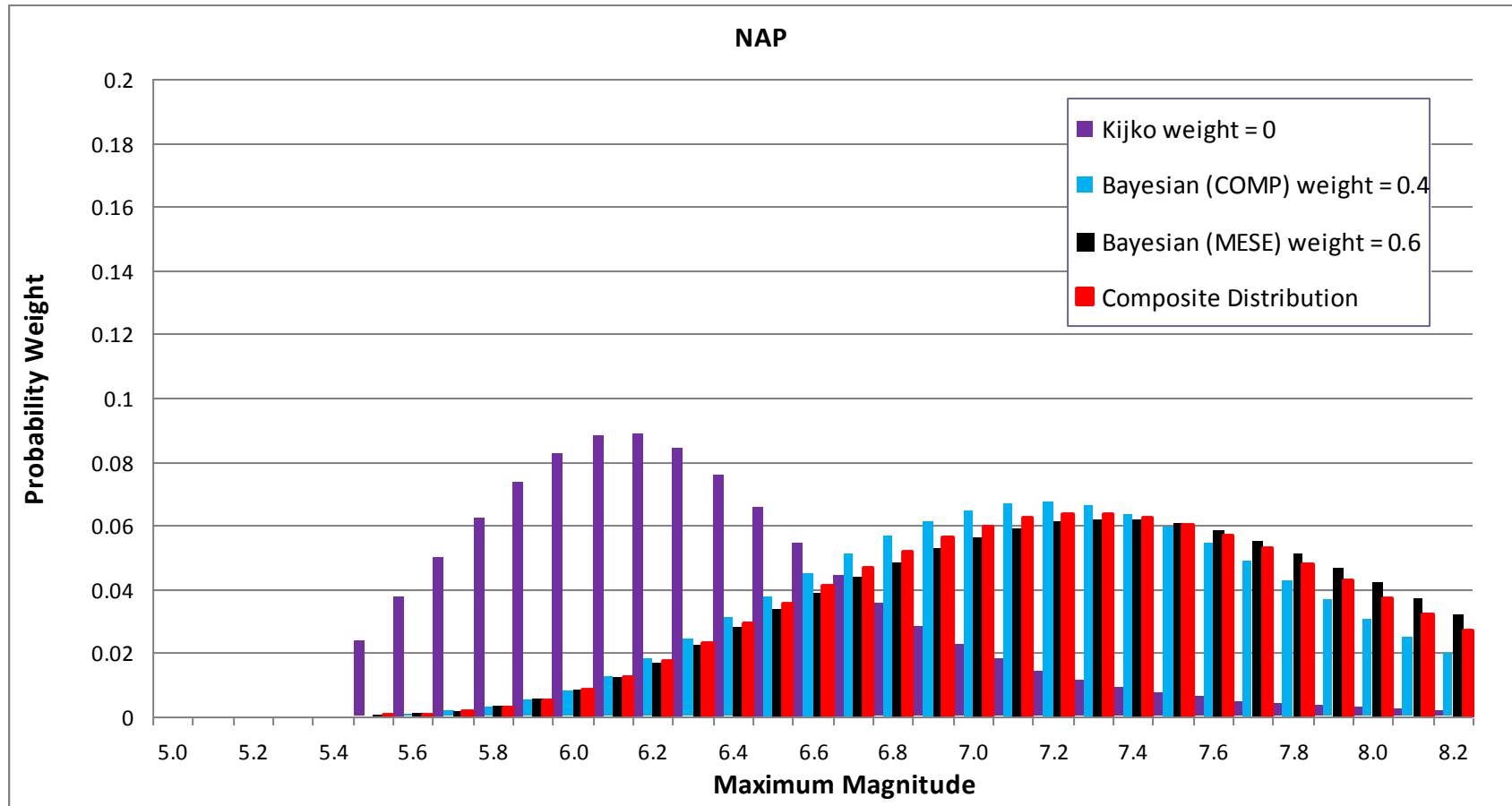


**Figure 5.2.1-14**  
Example Mmax distribution assessed for the Northern Appalachian seismotectonic zone (NAP). Distributions are shown for the Kijko approach and for the Bayesian approach using either the Mesozoic-and-younger extended prior distribution or the composite prior distribution. Note that the Kijko results are shown in this example for illustration, even though they have zero weight. The final composite Mmax distribution, which incorporates the relative weights, is shown by the red probability distribution.

### Likelihood Function for Rate Per Unit Area $\nu$

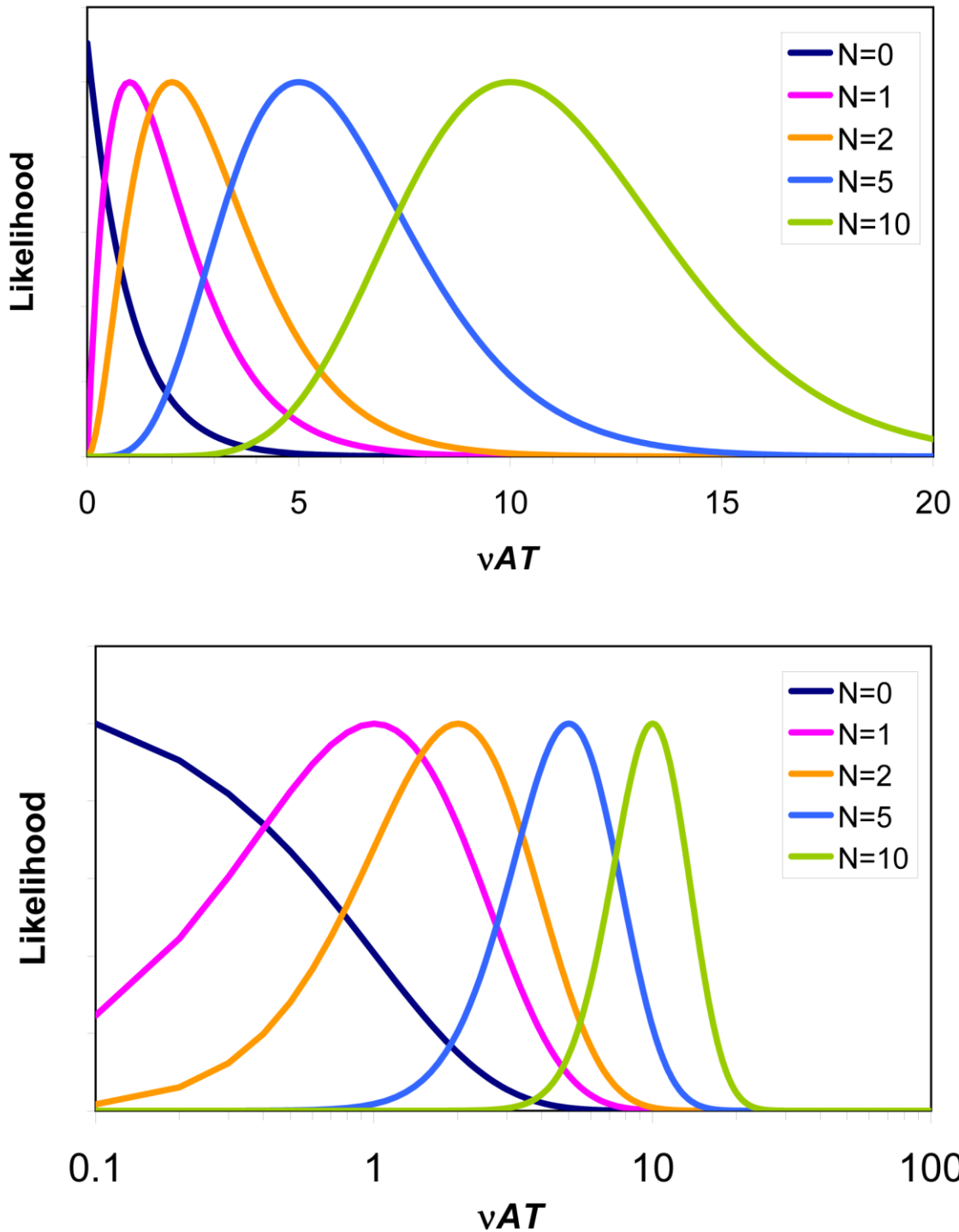
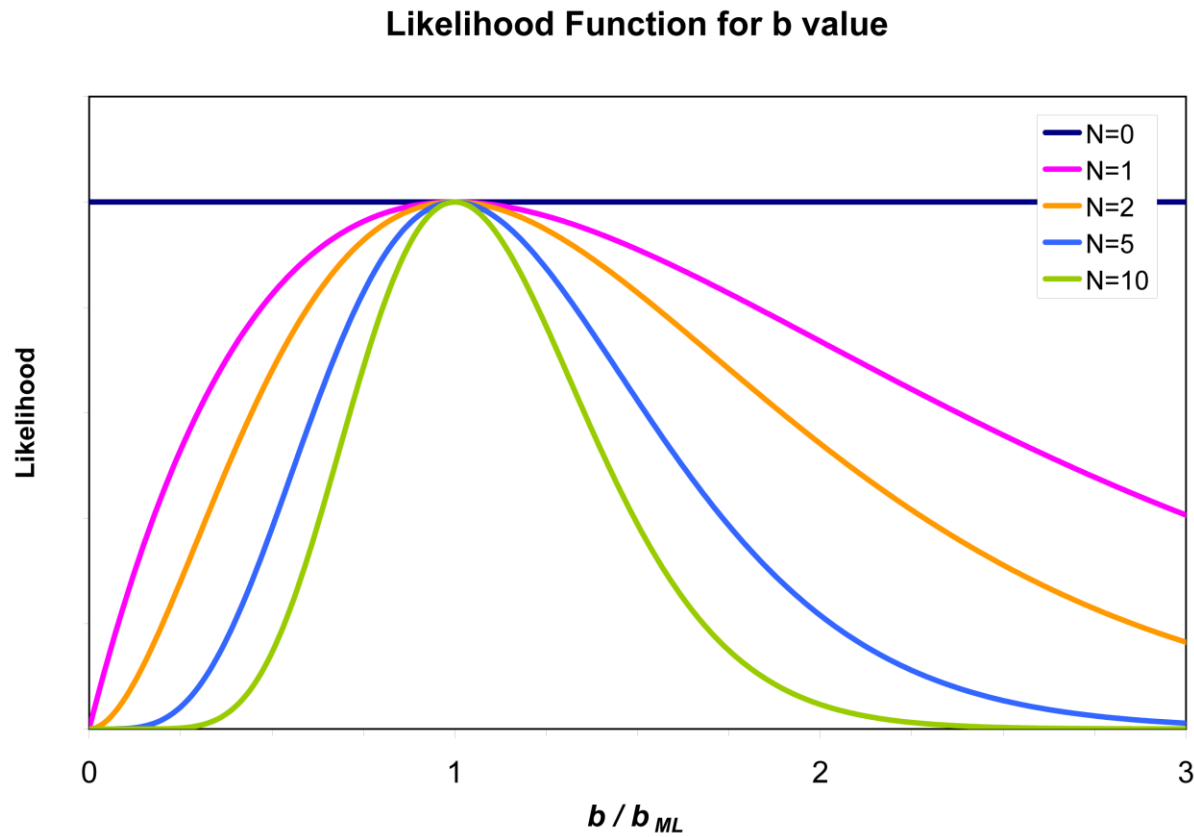
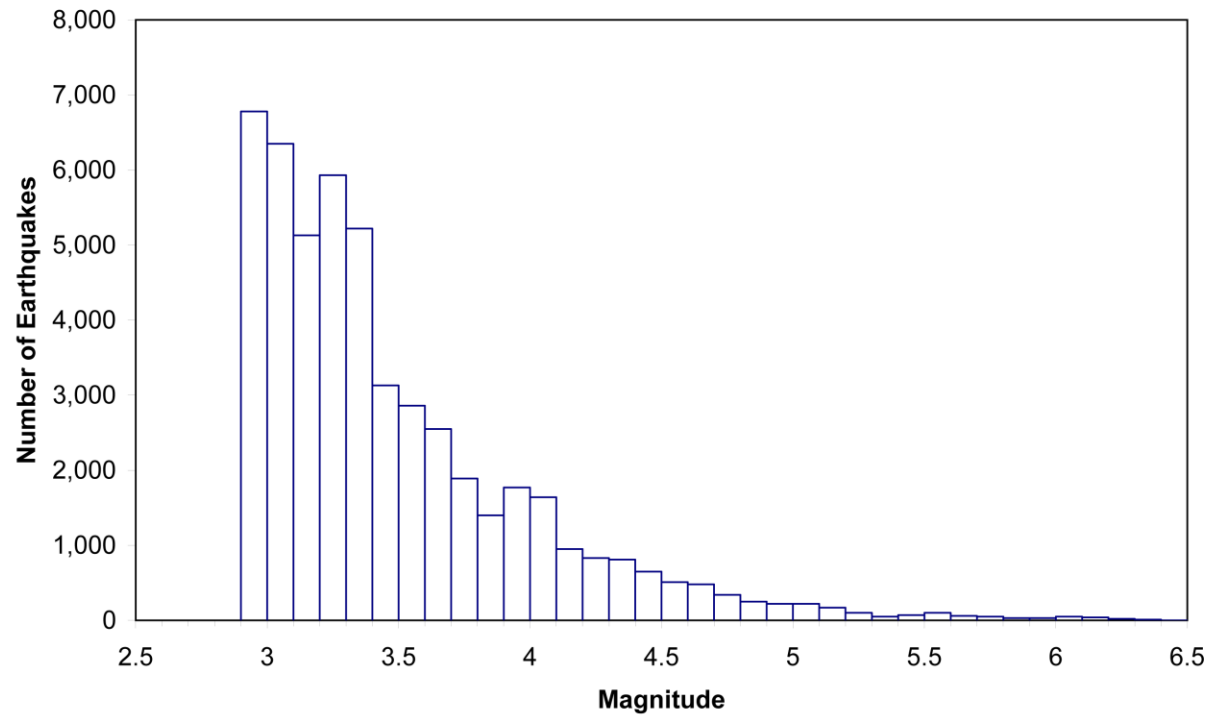


Figure 5.3.2-1  
Likelihood function for rate per unit area in a Poisson process, for multiple values of the earthquake count  $N$ : (a) arithmetic scale, and (b) logarithmic scale used to illustrate decreasing COV as  $N$  increases



**Figure 5.3.2-2**  
Likelihood function for  $b$ -value of an exponential magnitude distribution, for multiple values of the earthquake count  $N$ . The value of  $b$  is normalized by the maximum-likelihood estimate, which is derived from Equation 5.3.2-5.

### Histogram of Magnitudes in Project Catalog



**Figure 5.3.2-3**  
Histogram of magnitudes in the earthquake catalog used in this section. The minimum magnitude shown (M 2.9) is the lowest magnitude used in these recurrence calculations.

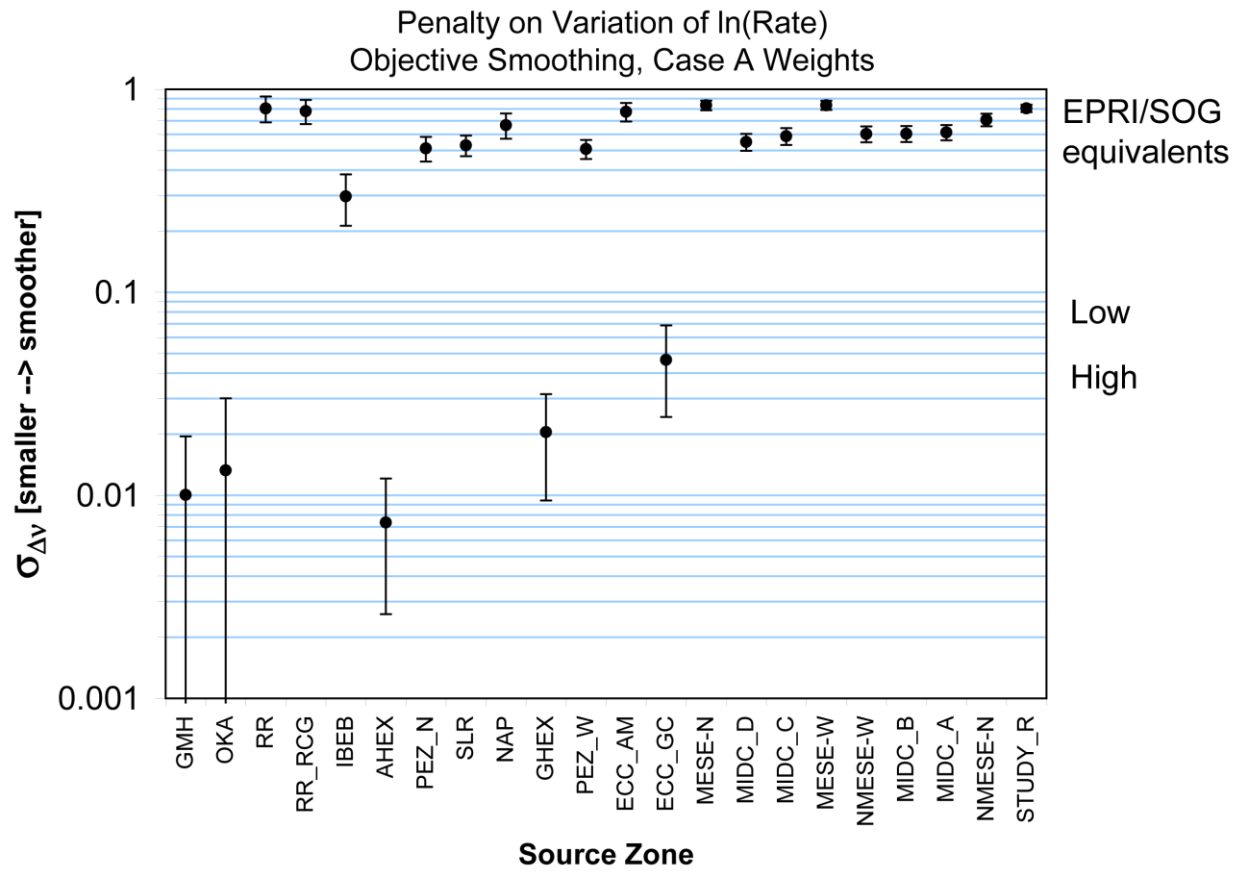


**Figure 5.3.2-4**  
Objectively determined values of the penalty function for  $\ln(\text{rate})$  for Case A magnitude weights. Source zones are sorted from smallest to largest. See list of abbreviations for full source-zone names.

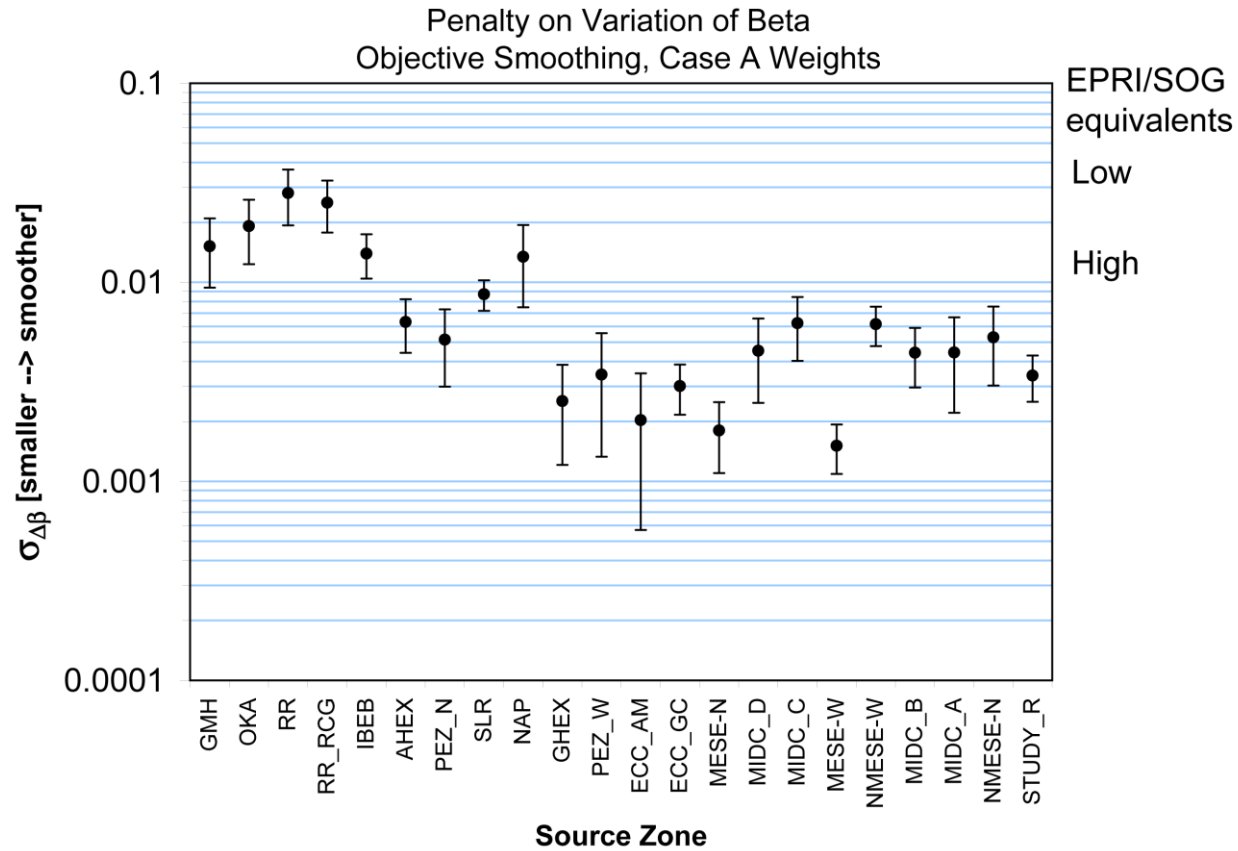


**Figure 5.3.2-5**  
Objectively determined values of the penalty function for beta for Case A magnitude weights

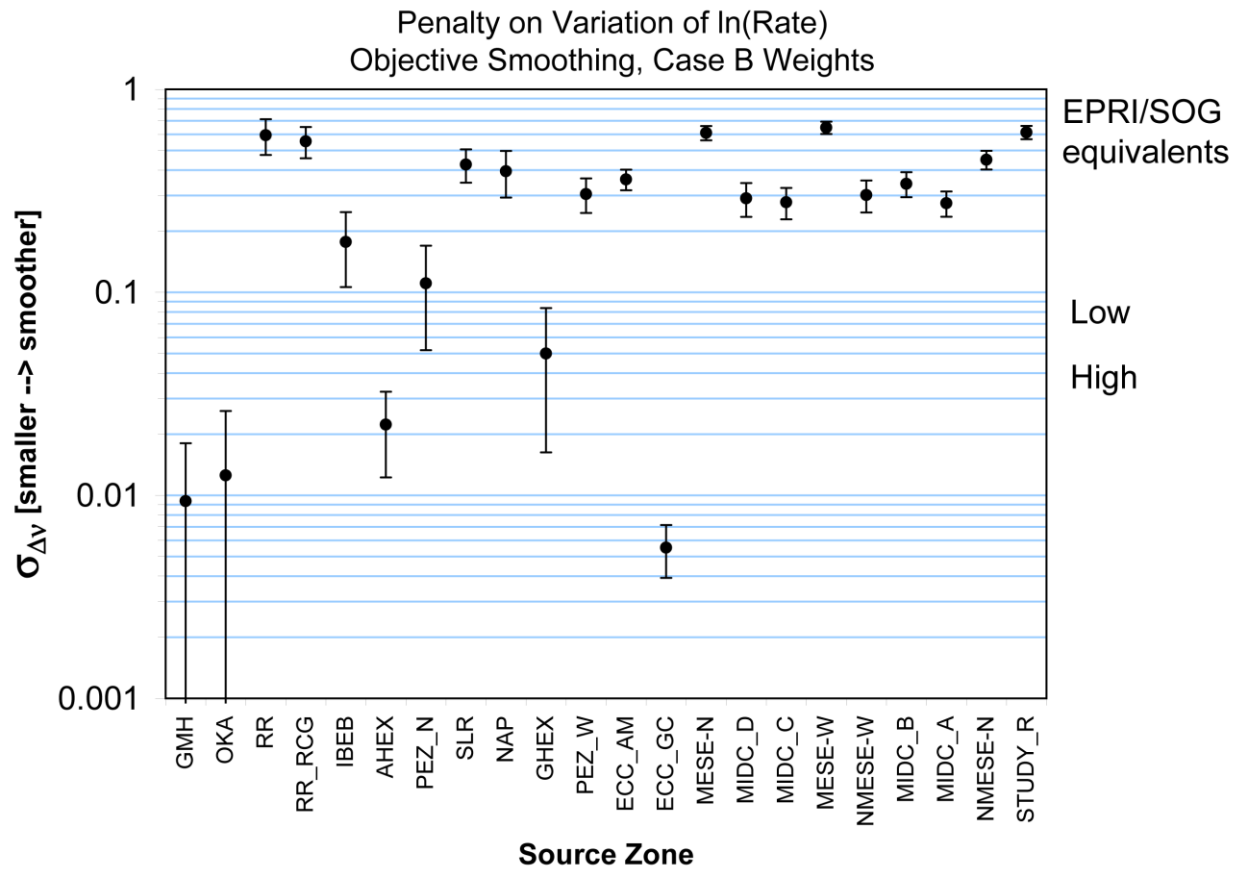
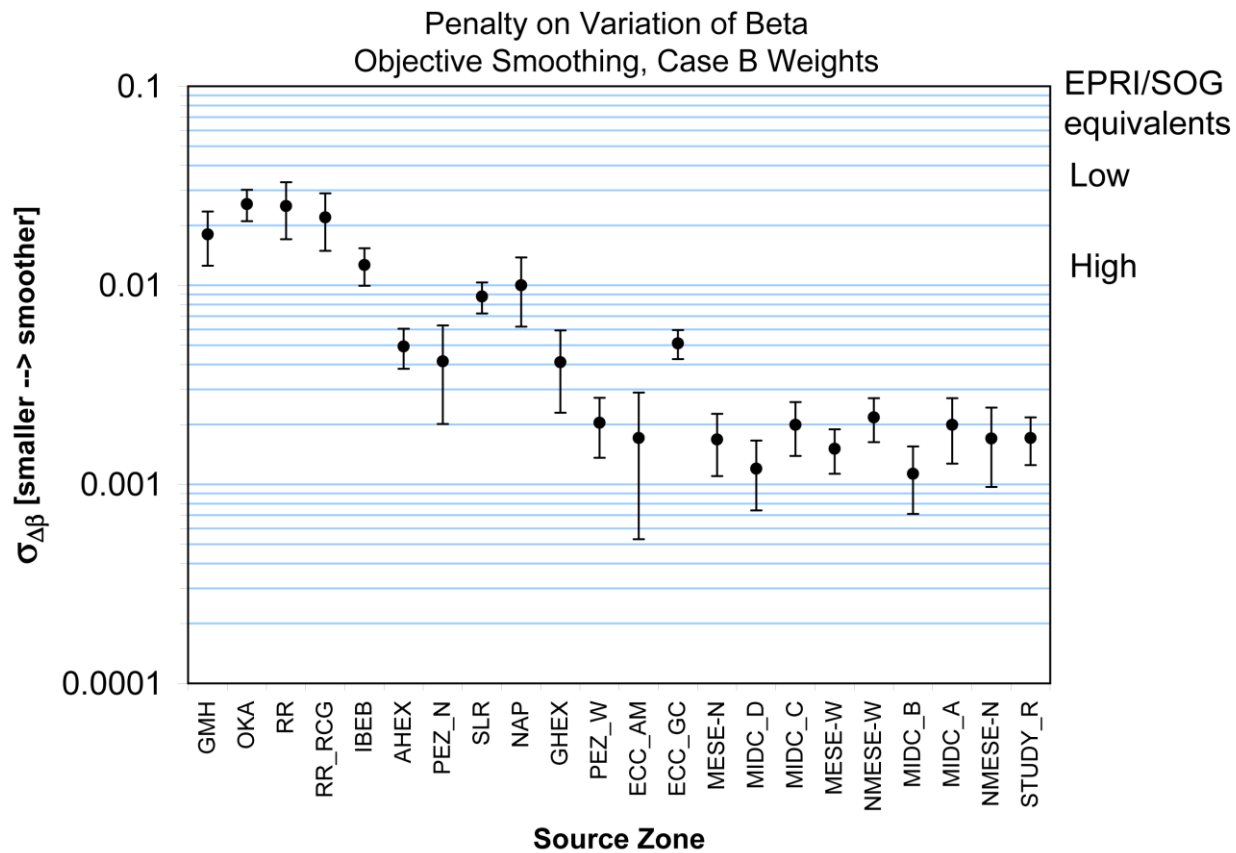


Figure 5.3.2-6  
Objectively determined values of the penalty function for  $\ln(\text{rate})$  for Case B magnitude weights



**Figure 5.3.2-7**  
 Objectively determined values of the penalty function for beta for Case B magnitude weights. Source zones are sorted from smallest to largest.

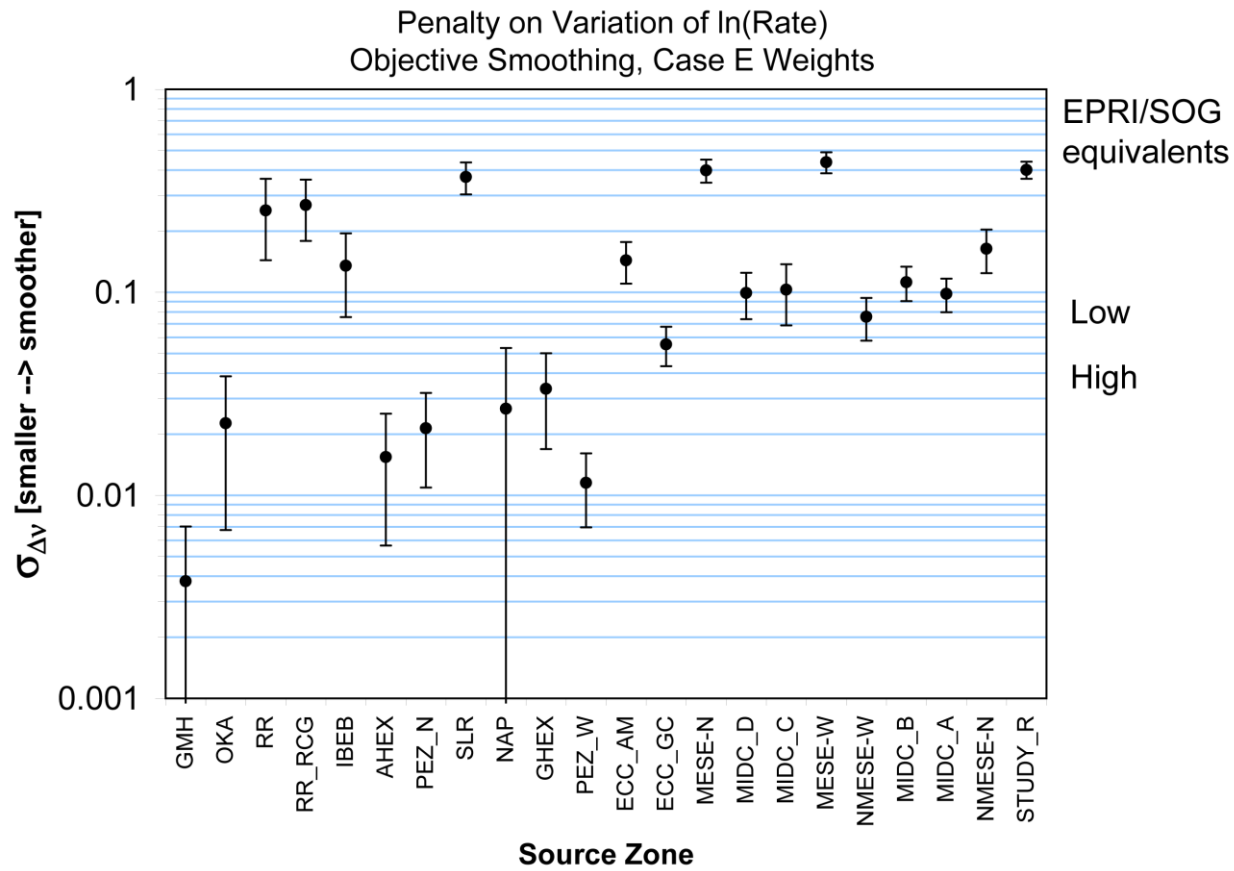
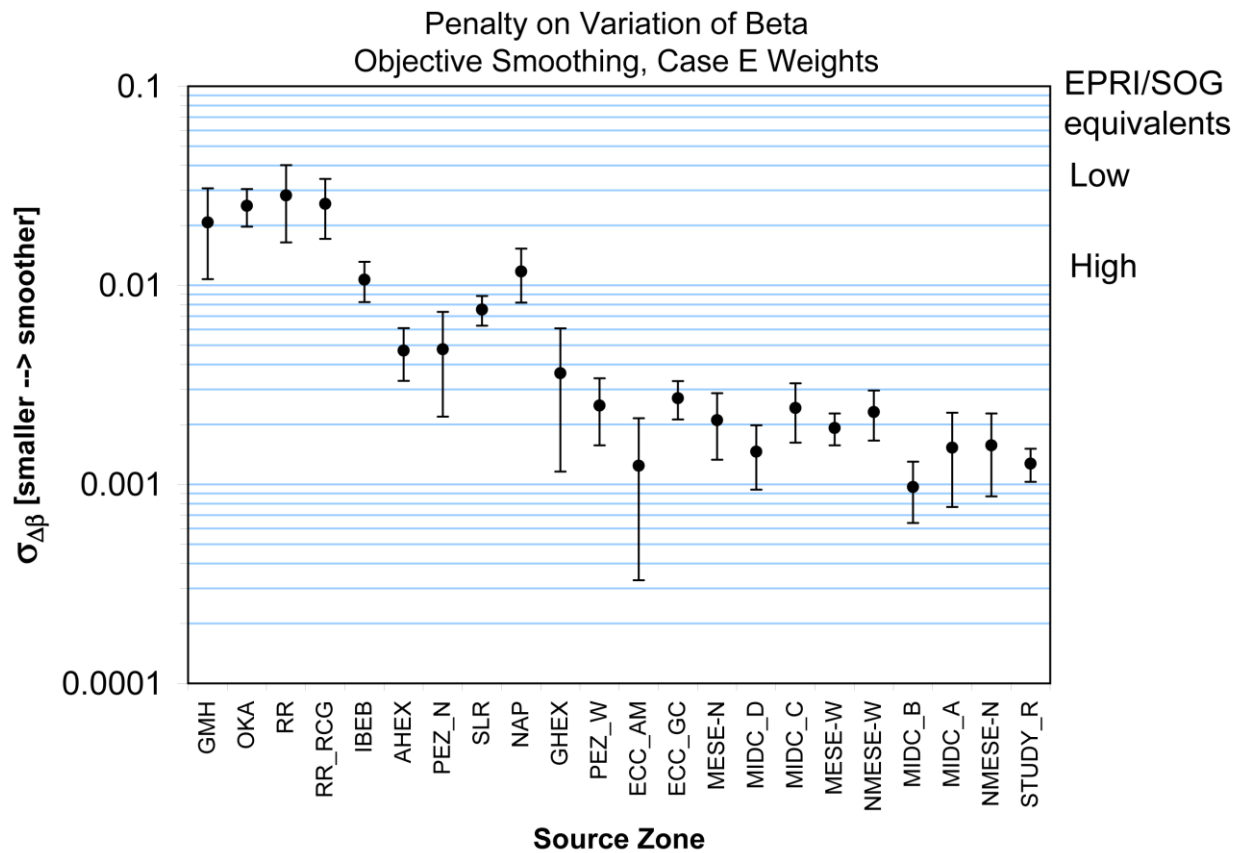
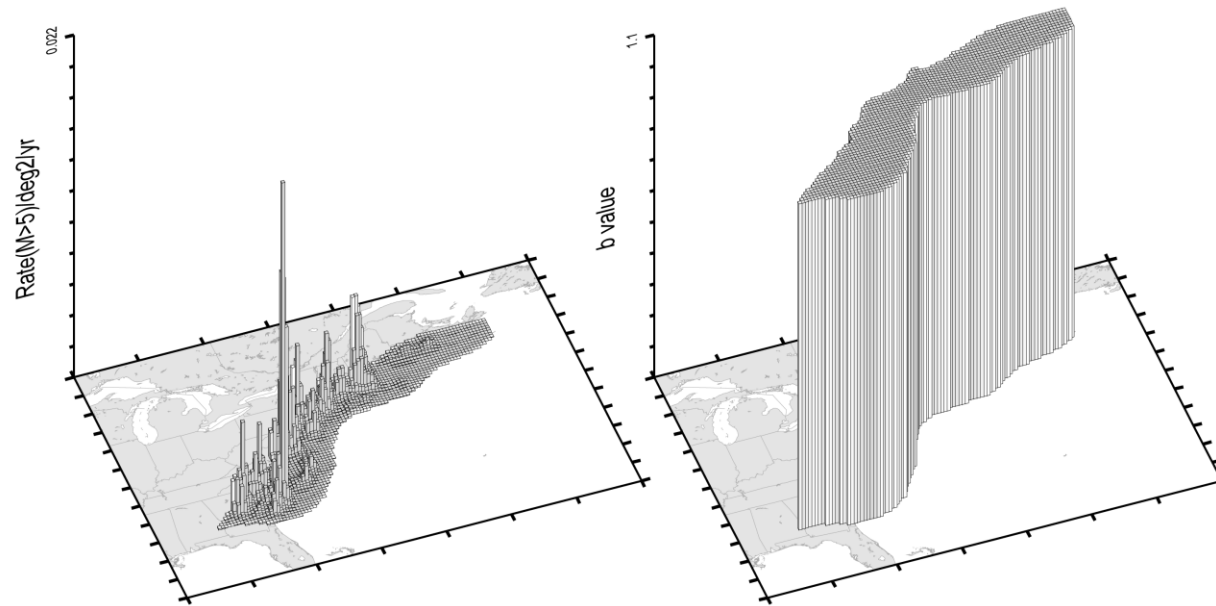


Figure 5.3.2-8  
Objectively determined values of the penalty function for  $\ln(\text{rate})$  for Case E magnitude weights



**Figure 5.3.2-9**  
 Objectively determined values of the penalty function for beta for Case E magnitude weights. Source zones are sorted from smallest to largest.



**Figure 5.3.2-10**  
Mean map of rate and *b*-value for ECC-AM calculated using Case A magnitude weights

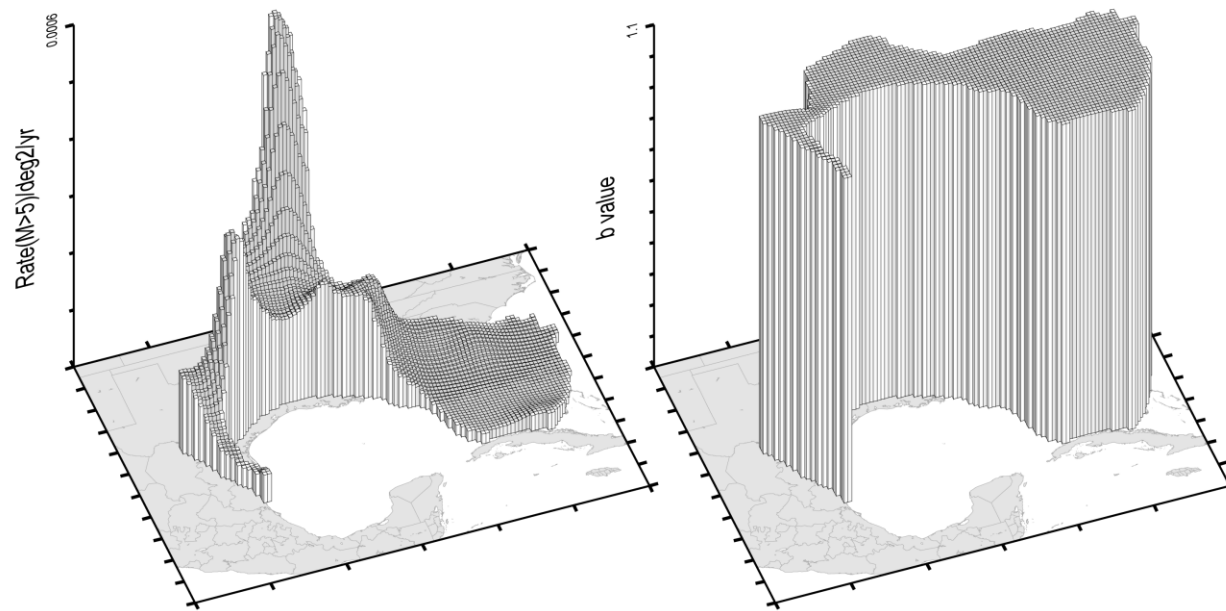


**Figure 5.3.2-11**  
Mean map of rate and *b*-value for ECC-GC calculated using Case A magnitude weights

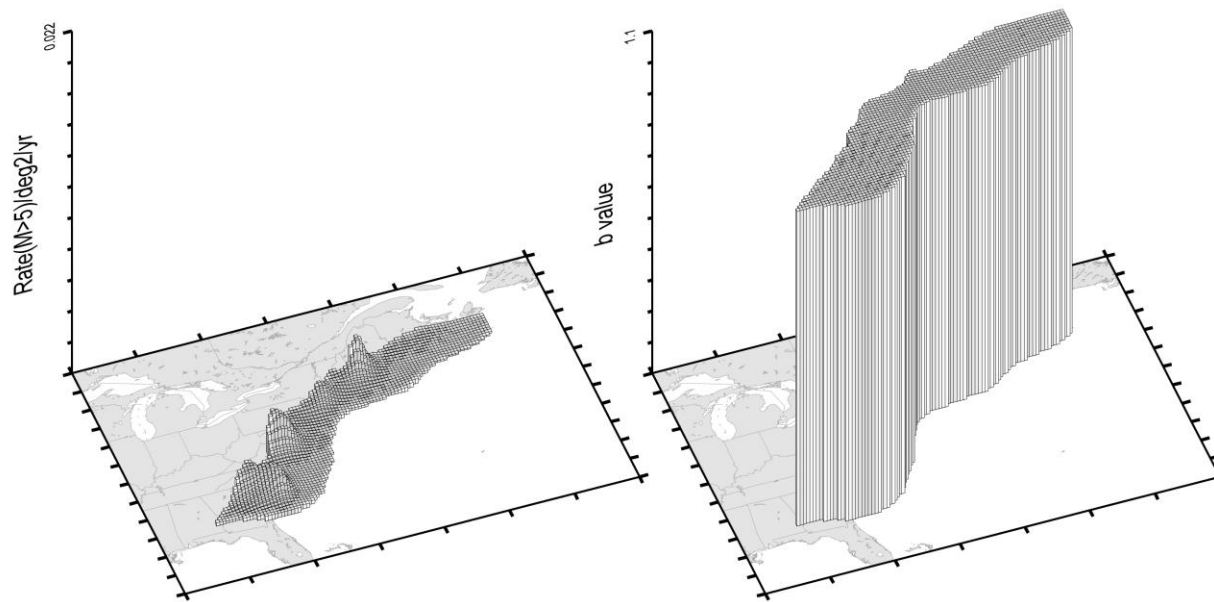


**Figure 5.3.2-12**  
Mean map of rate and *b*-value for ECC-AM calculated using Case B magnitude weights

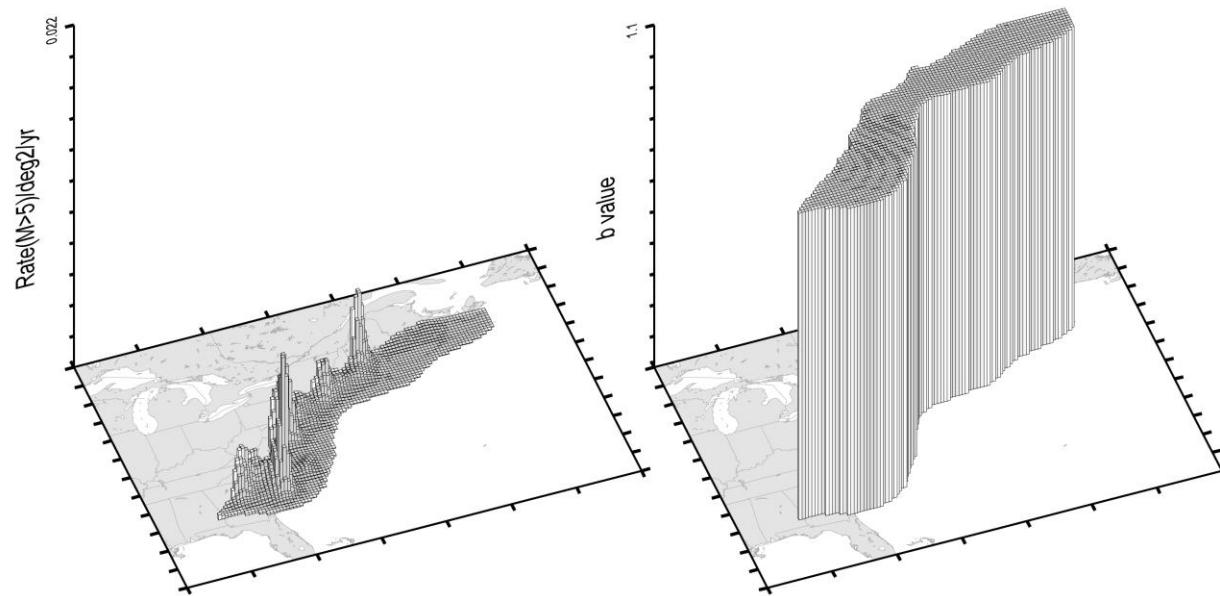


**Figure 5.3.2-13**  
Mean map of rate and *b*-value for ECC-GC calculated using Case B magnitude weights

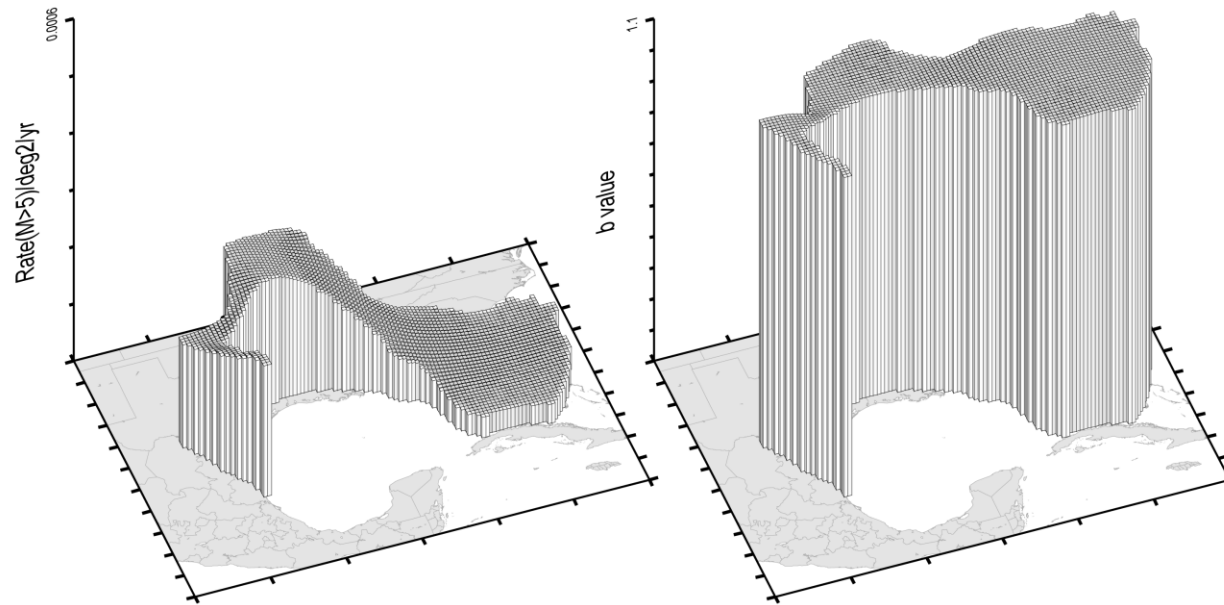


**Figure 5.3.2-14**  
Mean map of rate and *b*-value for ECC-AM calculated using Case E magnitude weights

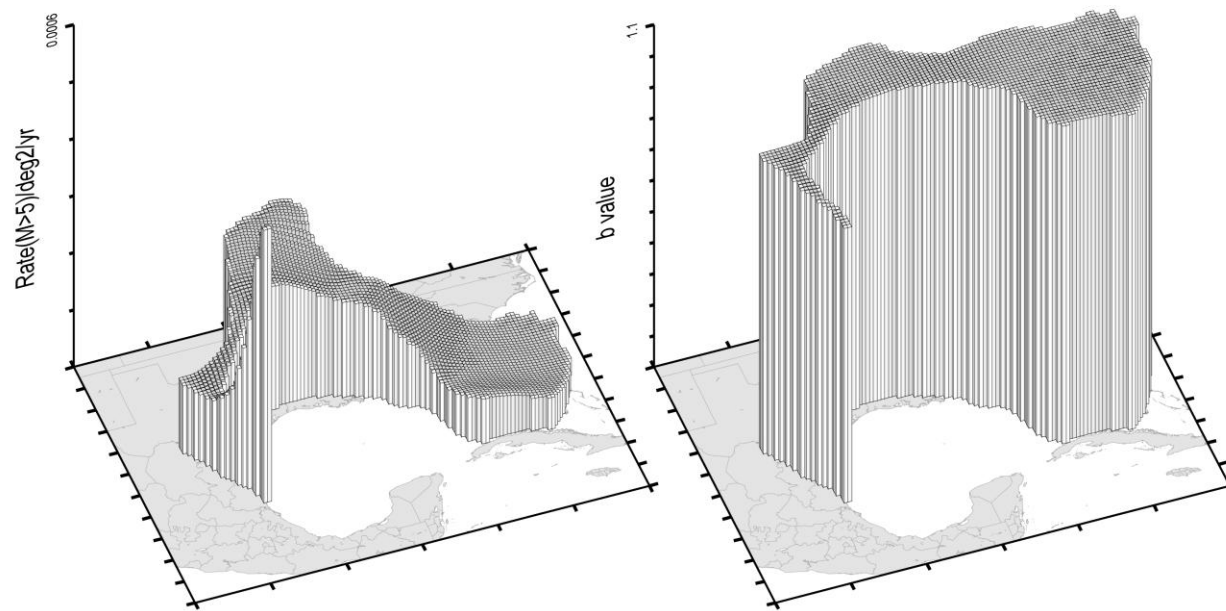


**Figure 5.3.2-15**  
Mean map of rate and  $b$ -value for ECC-GC calculated using Case E magnitude weights

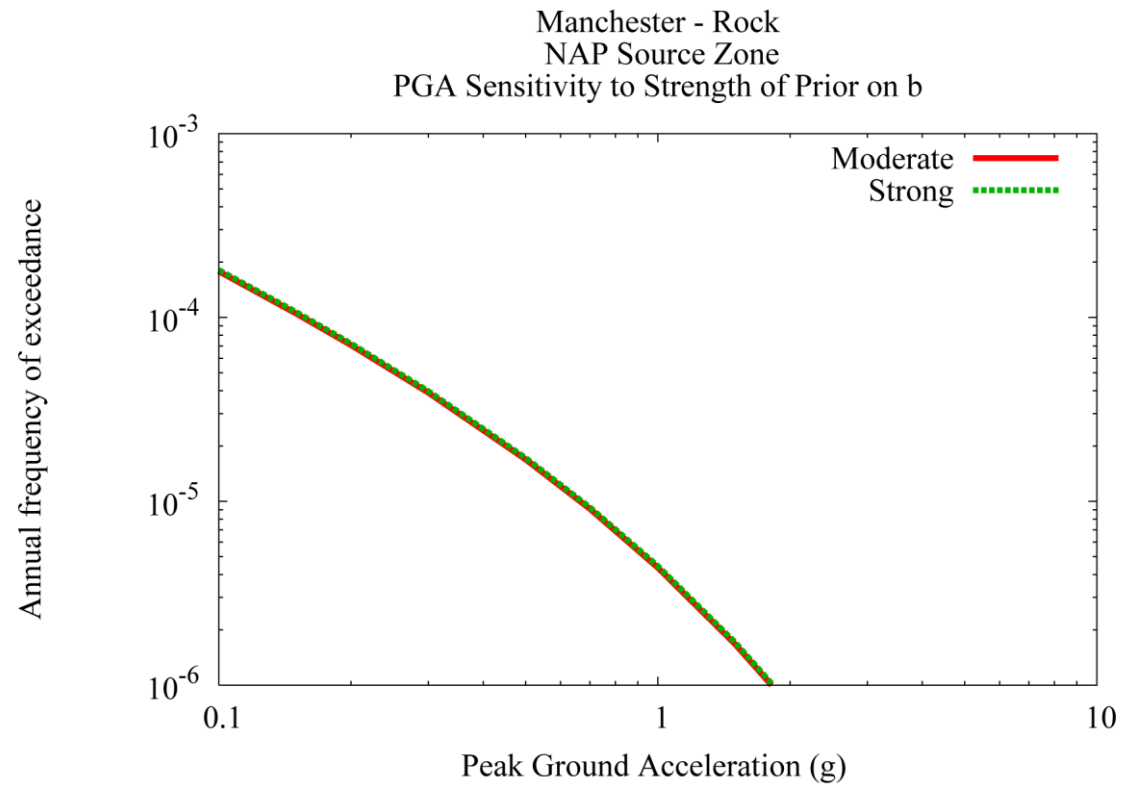


**Figure 5.3.2-16**  
Sensitivity of seismic hazard at Manchester site to the strength of the prior on b

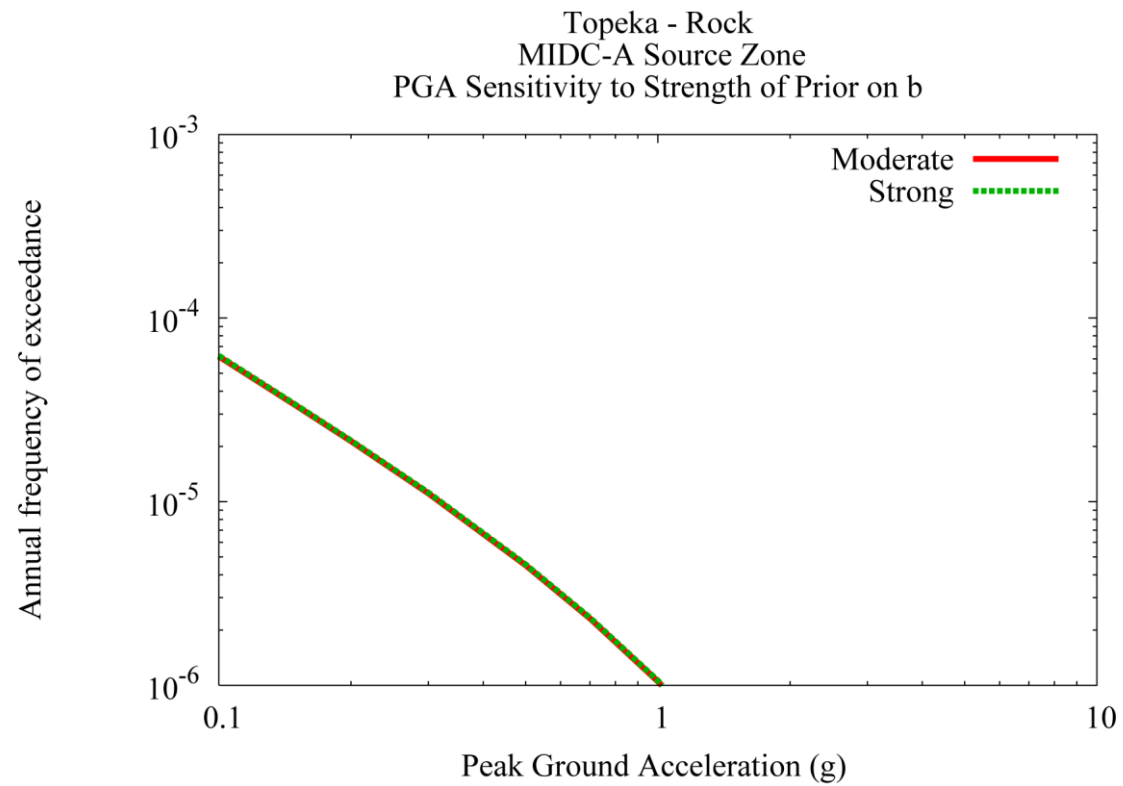


**Figure 5.3.2-17**  
Sensitivity of seismic hazard at Topeka site to the strength of the prior on b

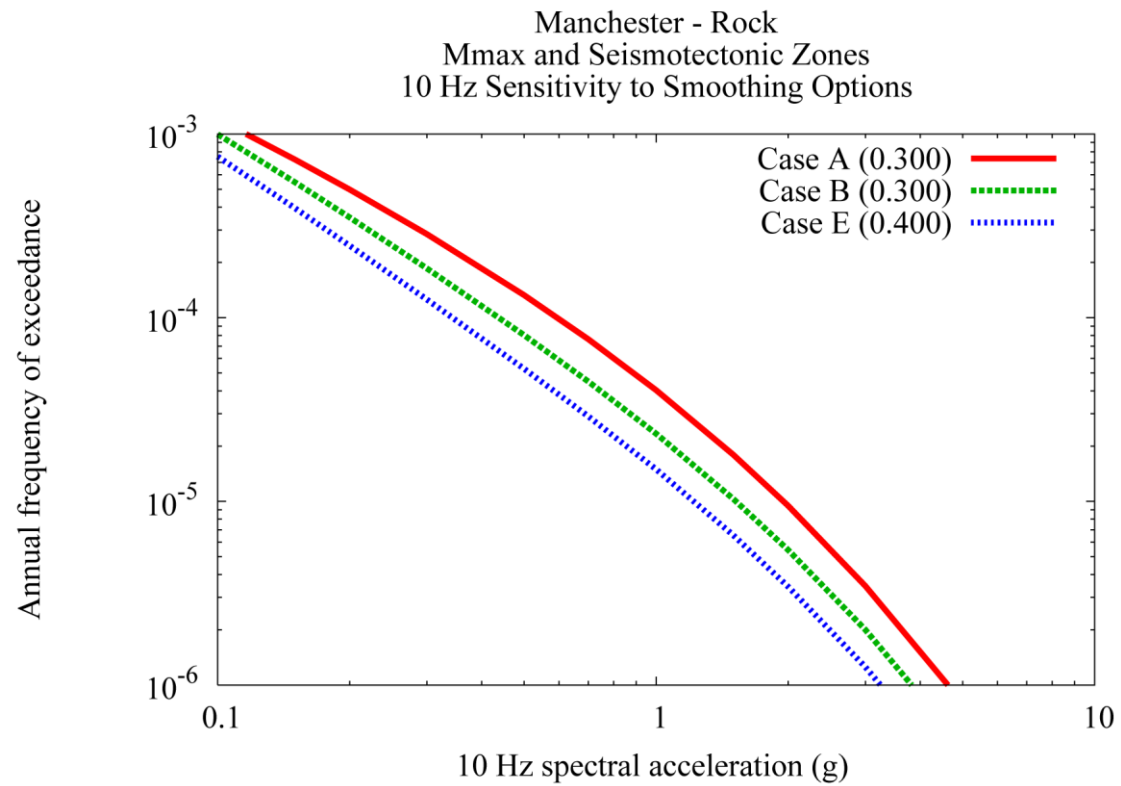


**Figure 5.3.2-18**  
Sensitivity of seismic hazard at Manchester site to the choice of magnitude weights

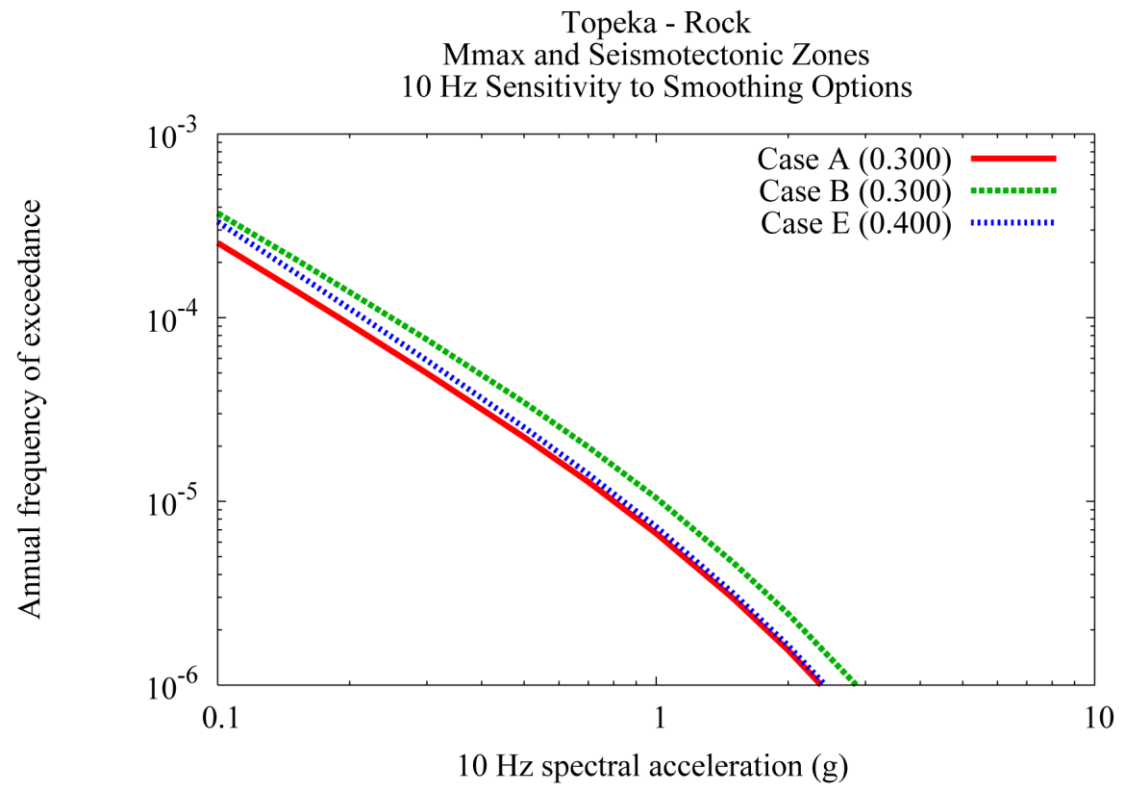


**Figure 5.3.2-19**  
Sensitivity of seismic hazard at Topeka site to the choice of magnitude weights

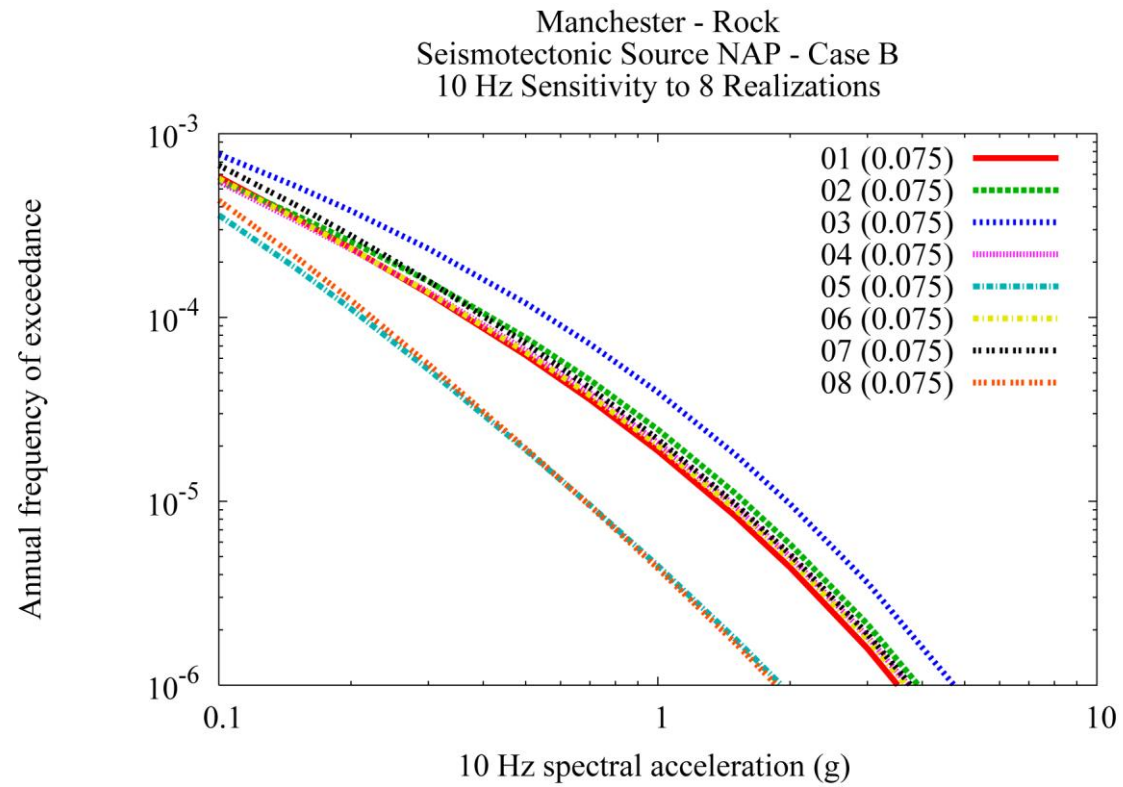


**Figure 5.3.2-20**  
Sensitivity of seismic hazard from source NAP at Manchester site to the eight alternative recurrence maps for Case B magnitude weights

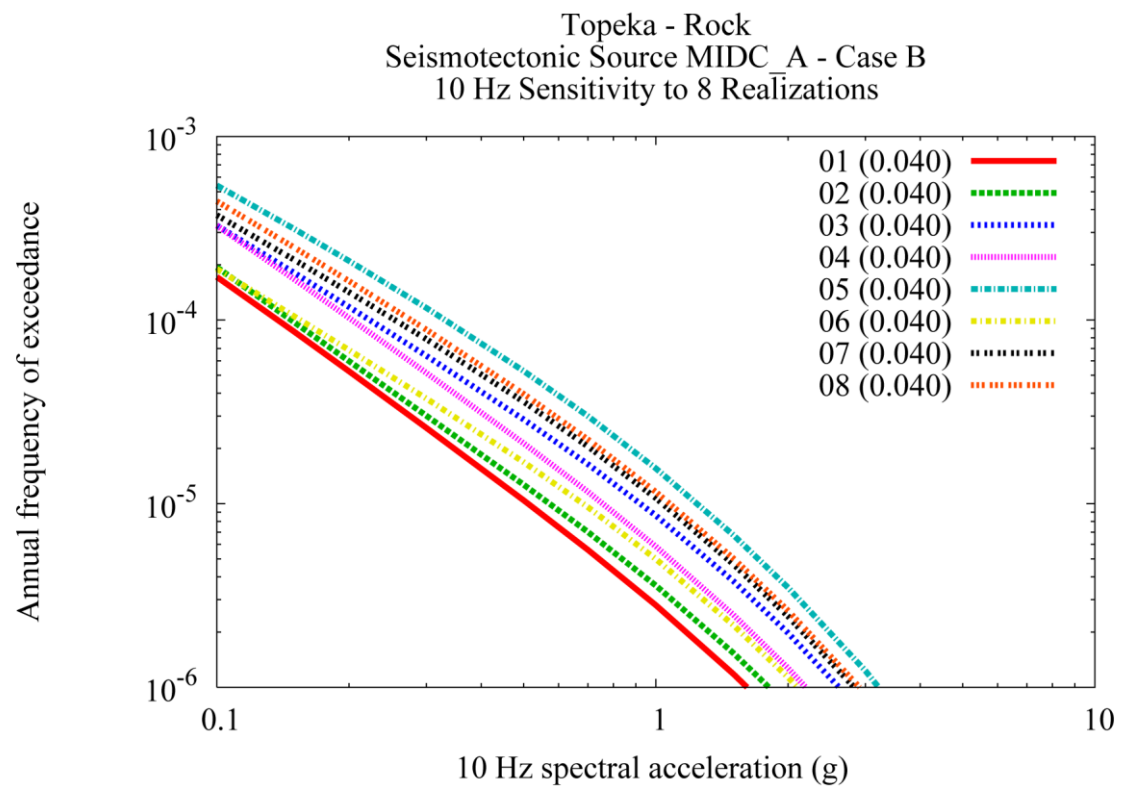


**Figure 5.3.2-21**  
Sensitivity of seismic hazard from source MID-C-A at Topeka site to the eight alternative recurrence maps for Case B magnitude weights

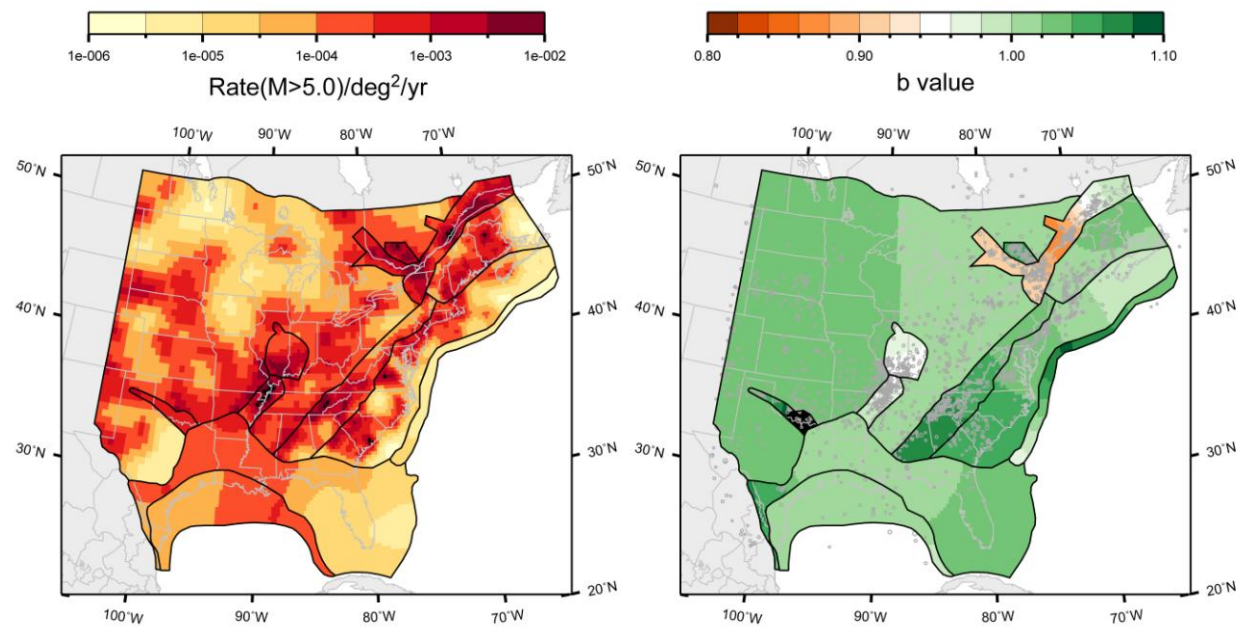


**Figure 5.3.2-22**  
Mean recurrence-parameter map for the study region under the highest weighted source-zone configuration in the master logic tree. See Sections 6.3 and 7.5 for all mean maps.

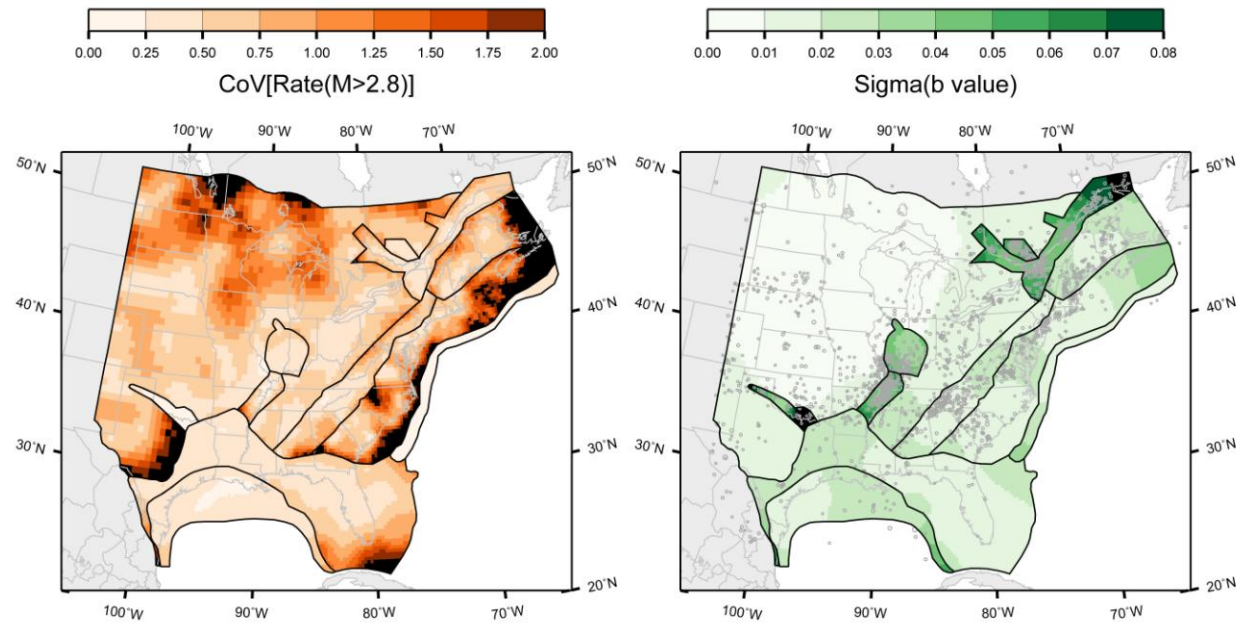


**Figure 5.3.2-23**  
Map of the uncertainty in the estimated recurrence parameters, expressed as the coefficient of variation of the rate (left) and the standard deviation of the  $b$ -value (right) for the study region, under the highest weighted source-zone configuration in the master logic tree. See Appendix J for all maps of uncertainty.

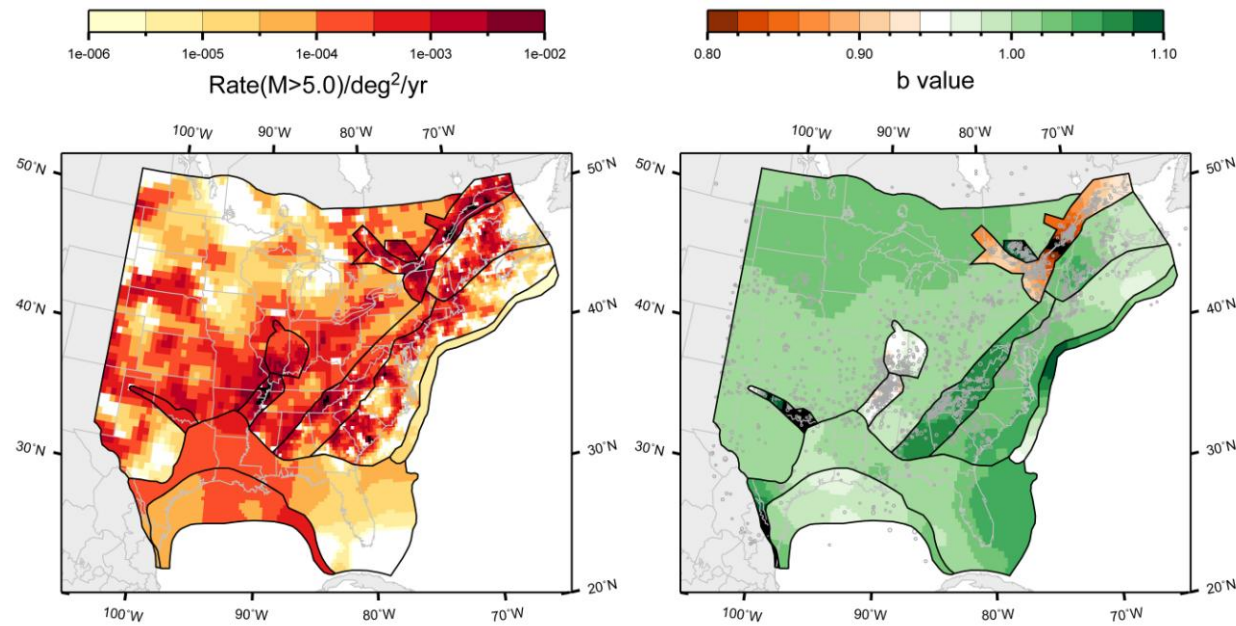


**Figure 5.3.2-24**  
First of eight equally likely realizations of the recurrence-parameter map for the study region under the highest weighted source-zone configuration in the master logic tree. See Appendix J for maps of all realizations for all source-zone configurations.

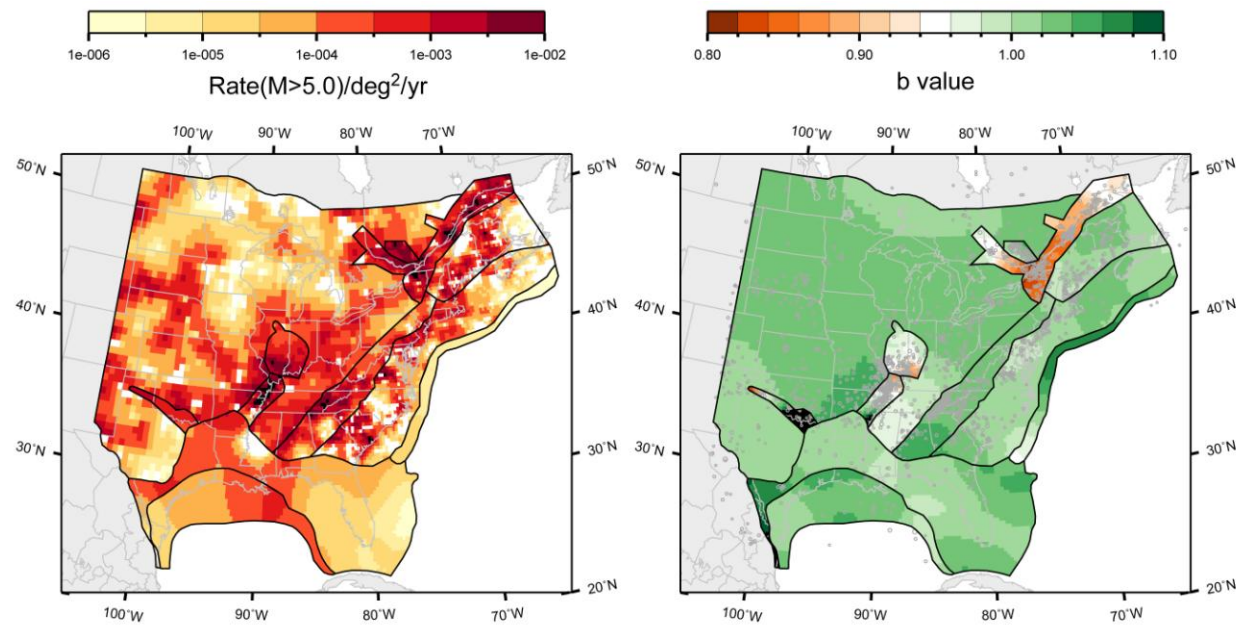


**Figure 5.3.2-25**  
Eighth of eight equally likely realizations of the recurrence-parameter map for the study region under the highest weighted source-zone configuration in the master logic tree. See Appendix J for maps of all realizations for all source-zone configurations.

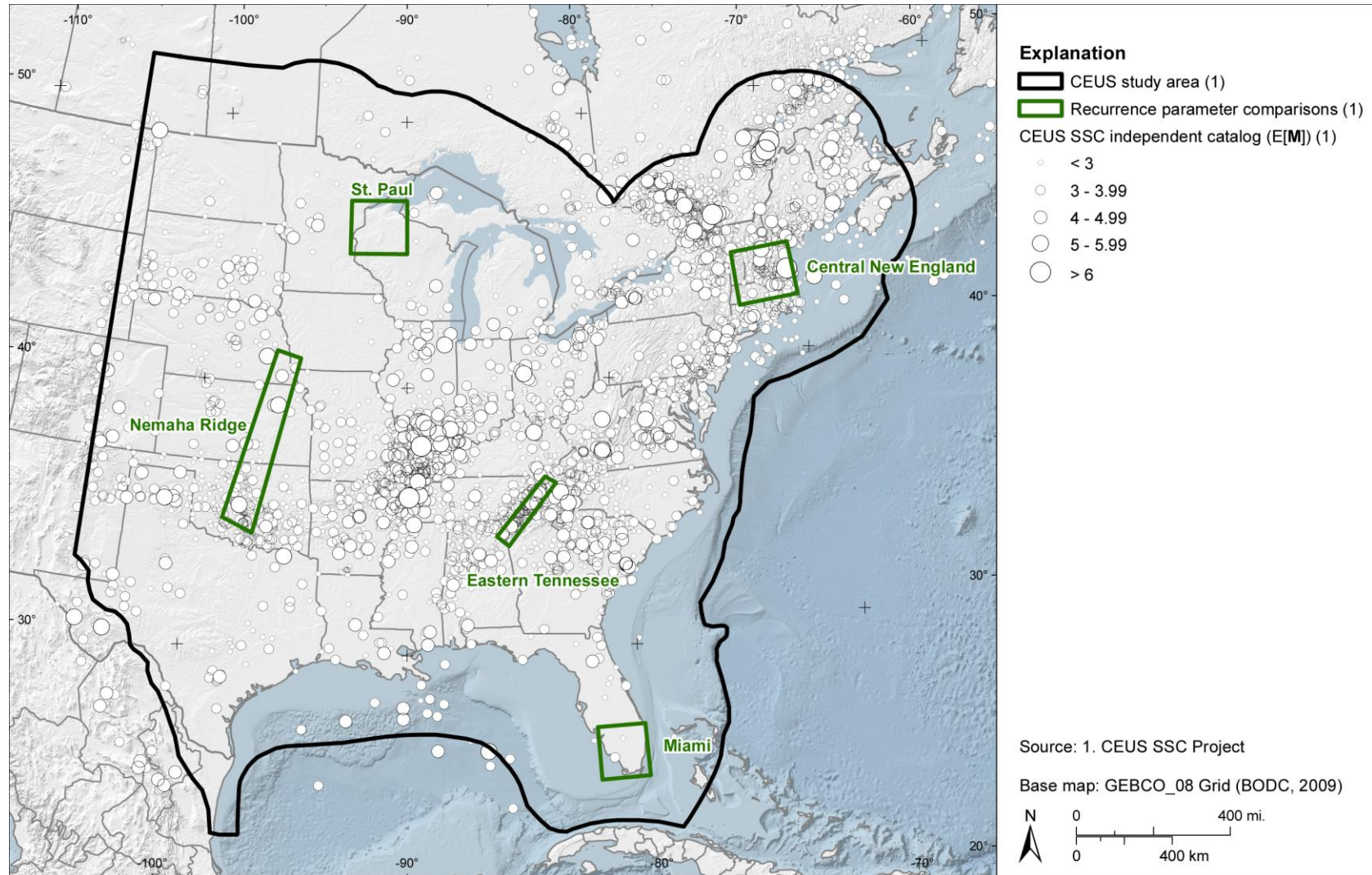


**Figure 5.3.2-26**  
Map of geographic areas considered in the exploration of model results

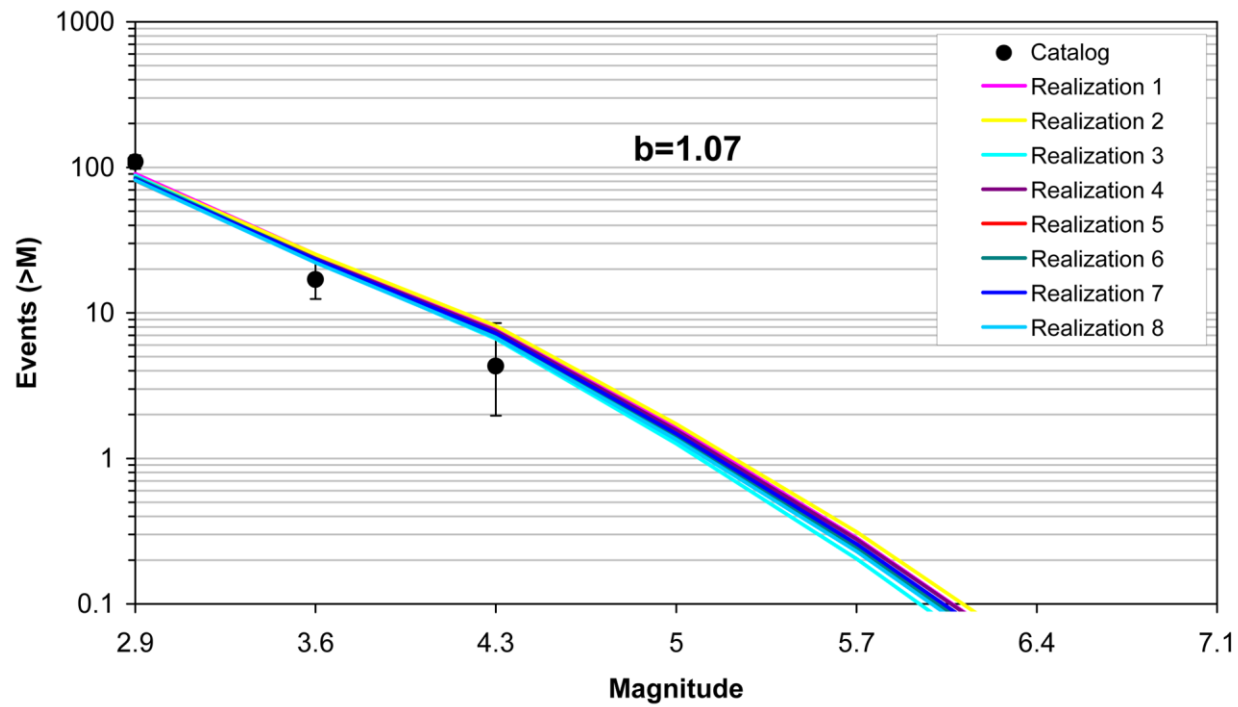


**Figure 5.3.2-27**  
Comparison of model-predicted earthquake counts for the USGS Eastern Tennessee area using Case A magnitude weights. The error bars represent the 16%–84% uncertainty associated with the data, computed using the Weichert (1980) procedure.

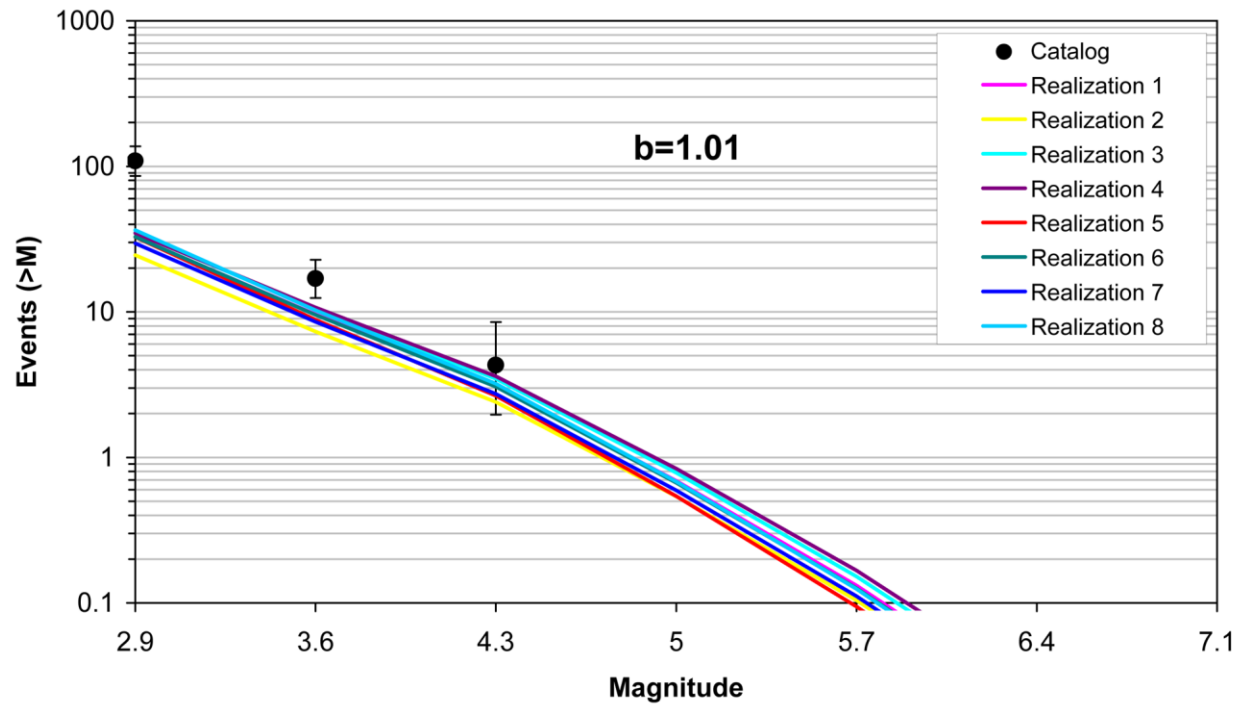


Figure 5.3.2-28  
Comparison of model-predicted earthquake counts for the USGS Eastern Tennessee area using Case B magnitude weights

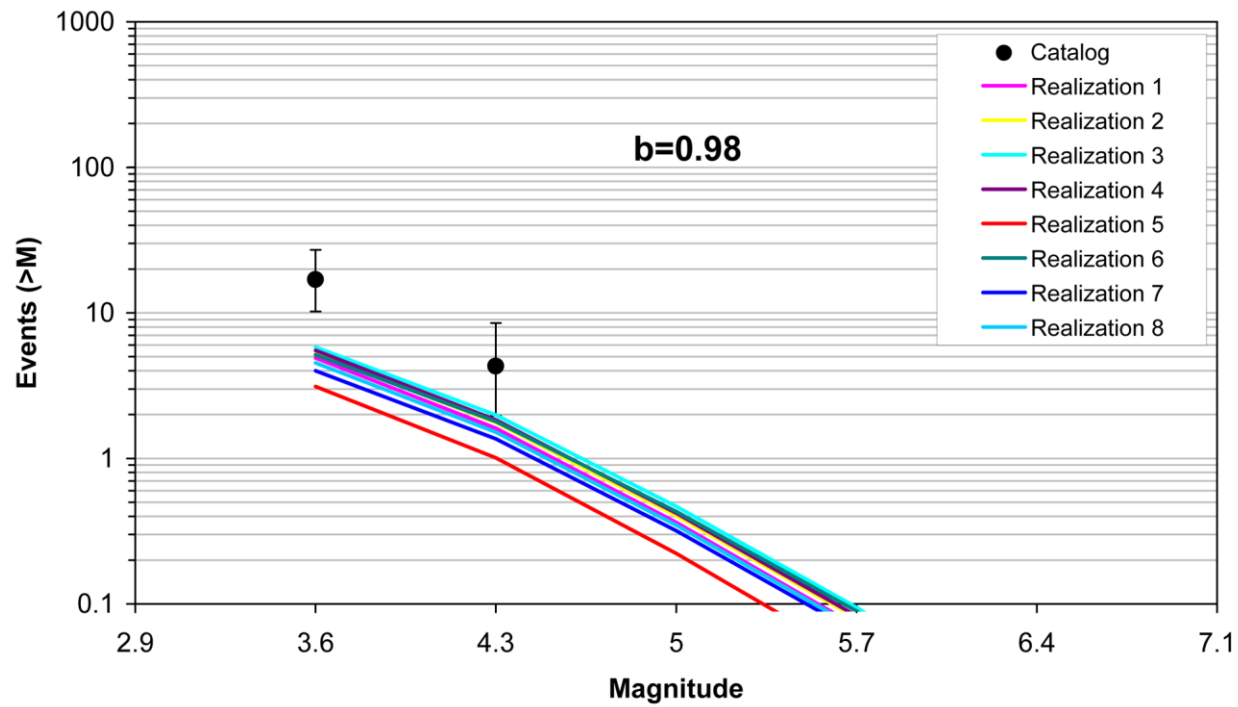


Figure 5.3.2-29  
Comparison of model-predicted earthquake counts for the USGS Eastern Tennessee area using Case E magnitude weights

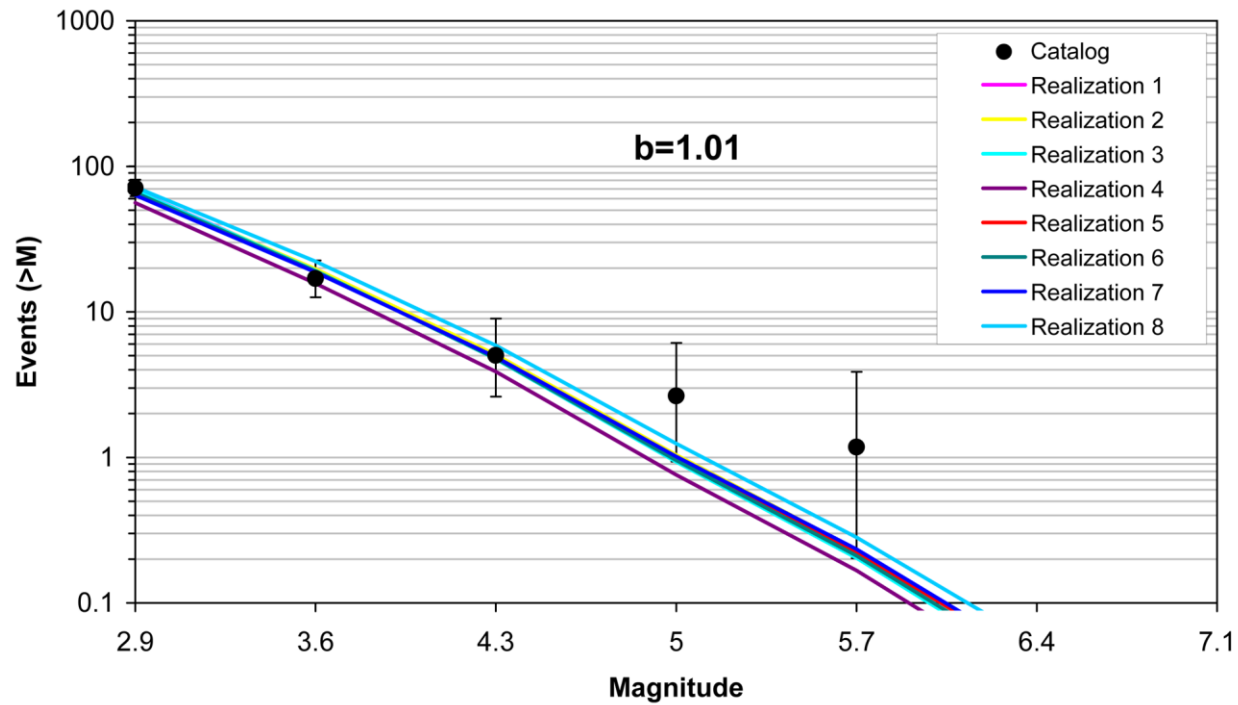


Figure 5.3.2-30  
Comparison of model-predicted earthquake counts for the central New England area using Case A magnitude weights

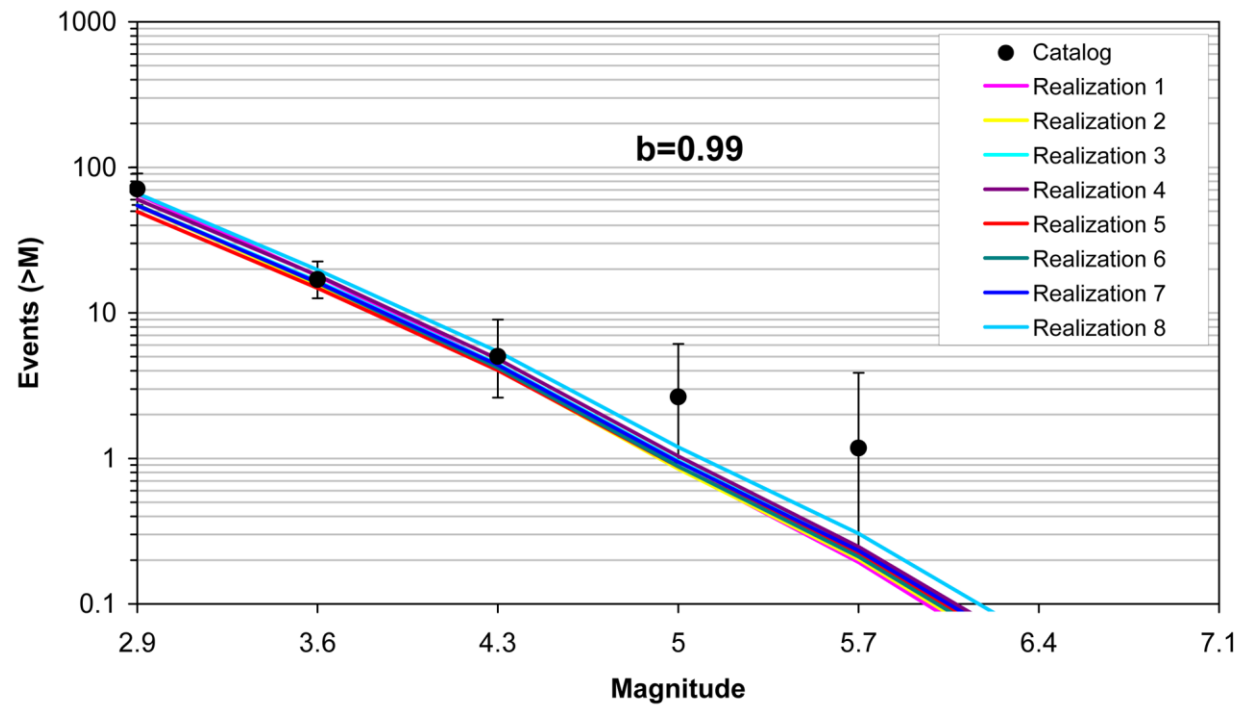


Figure 5.3.2-31  
Comparison of model-predicted earthquake counts for the central New England area using Case B magnitude weights

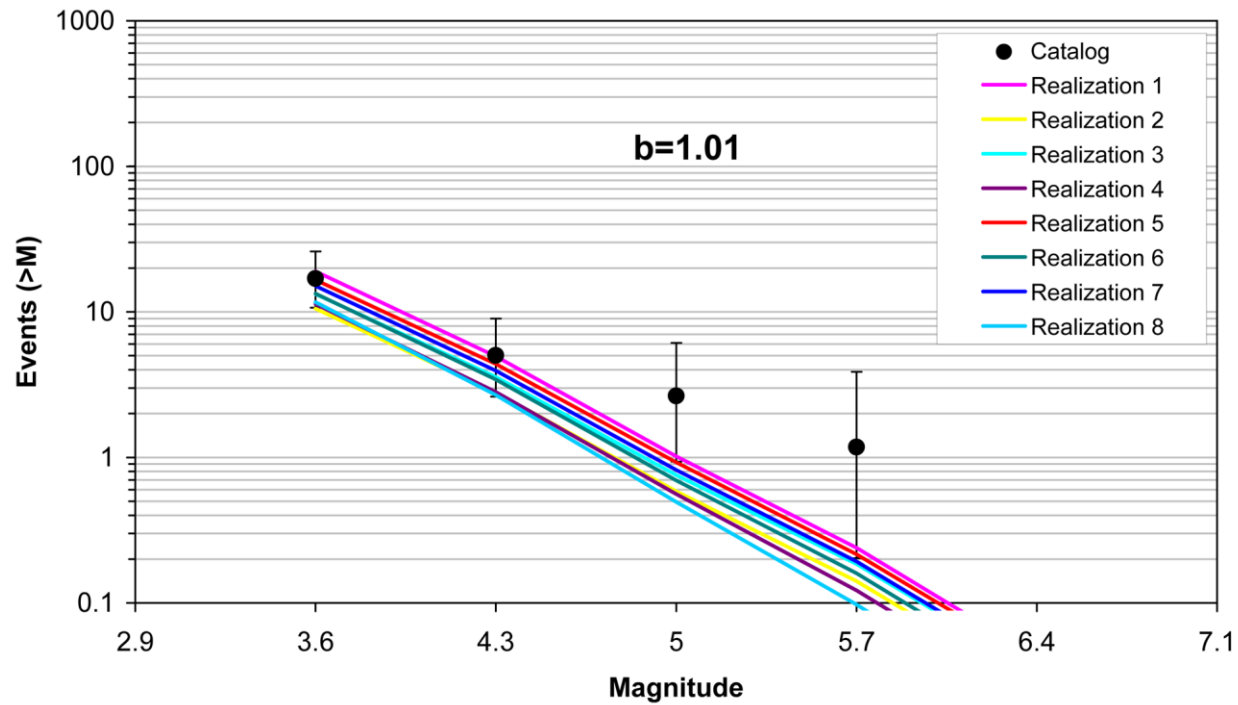


Figure 5.3.2-32  
Comparison of model-predicted earthquake counts for the central New England area using Case E magnitude weights

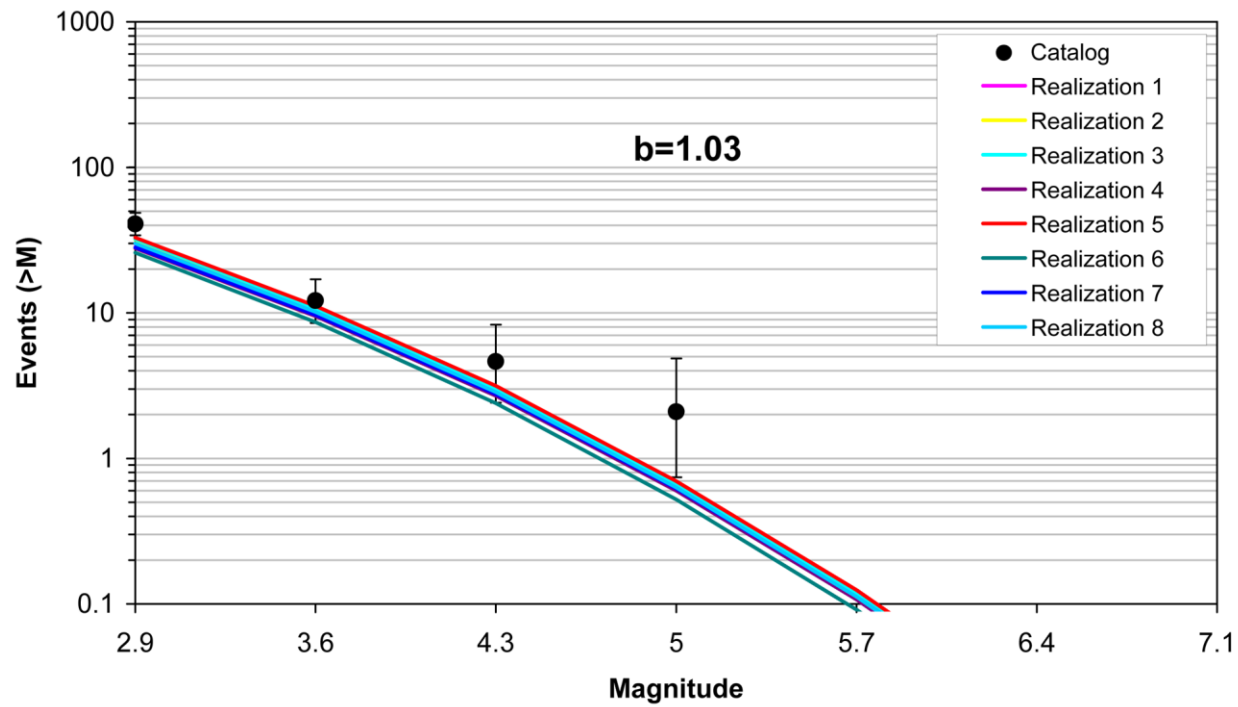


Figure 5.3.2-33  
Comparison of model-predicted earthquake counts for the Nemaha Ridge area using Case A magnitude weights

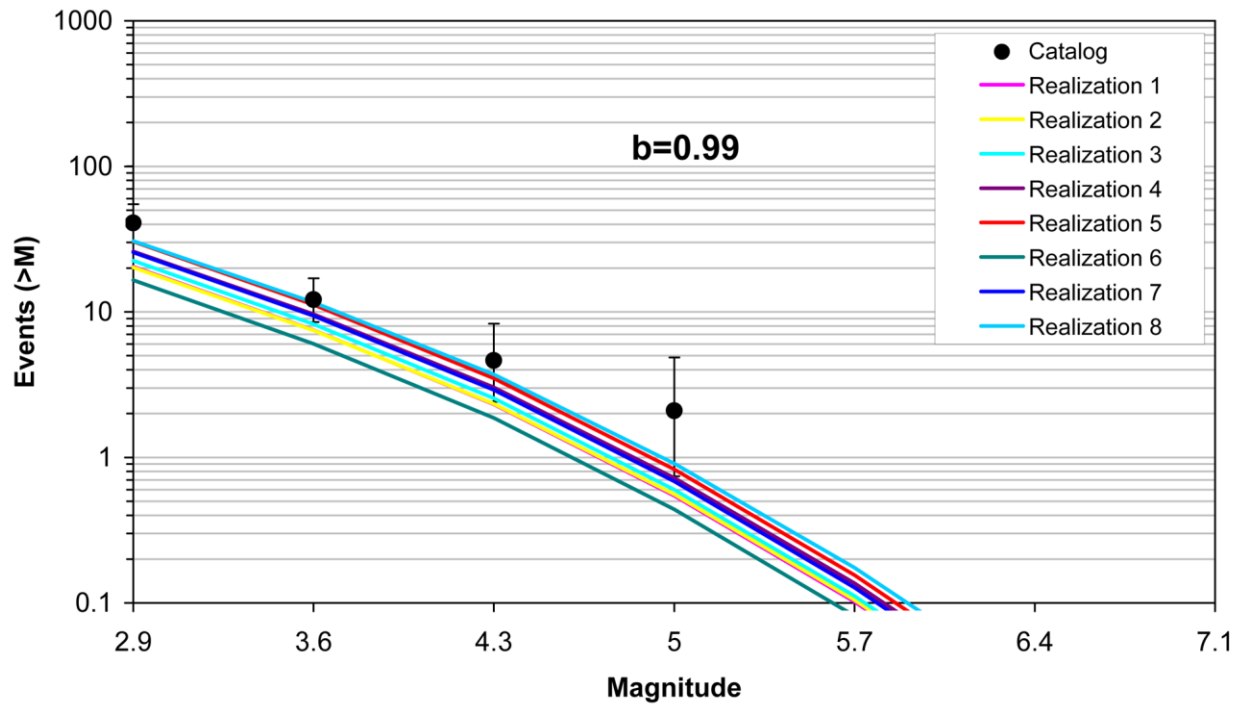


Figure 5.3.2-34  
Comparison of model-predicted earthquake counts for the Nemaha Ridge area using Case B magnitude weights

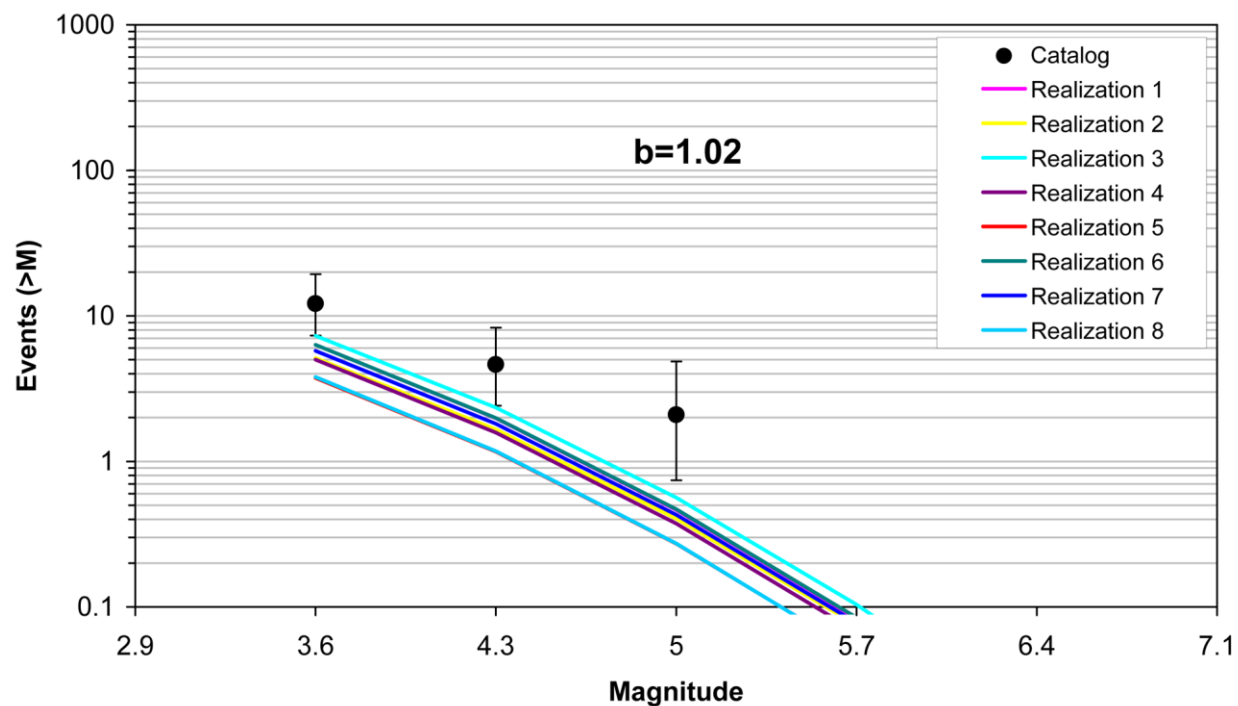


Figure 5.3.2-35  
Comparison of model-predicted earthquake counts for the Nemaha Ridge area using Case E magnitude weights

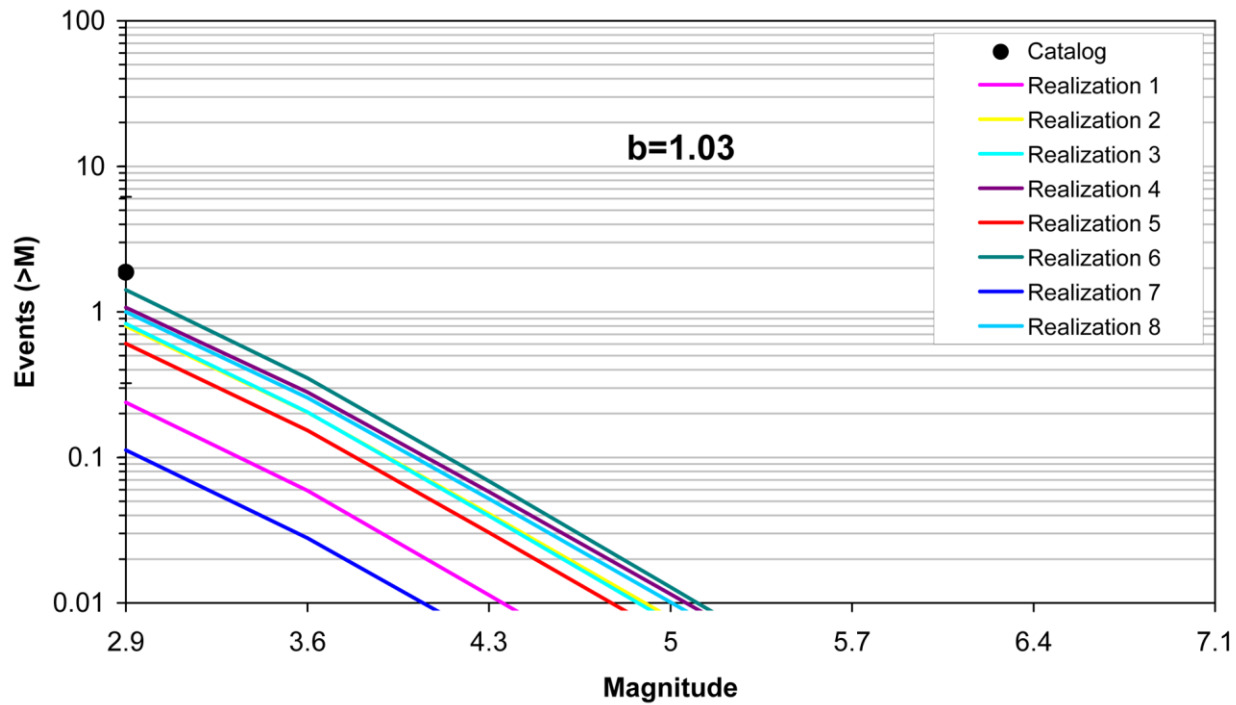


Figure 5.3.2-36  
Comparison of model-predicted earthquake counts for the Miami, FL, area using Case A magnitude weights

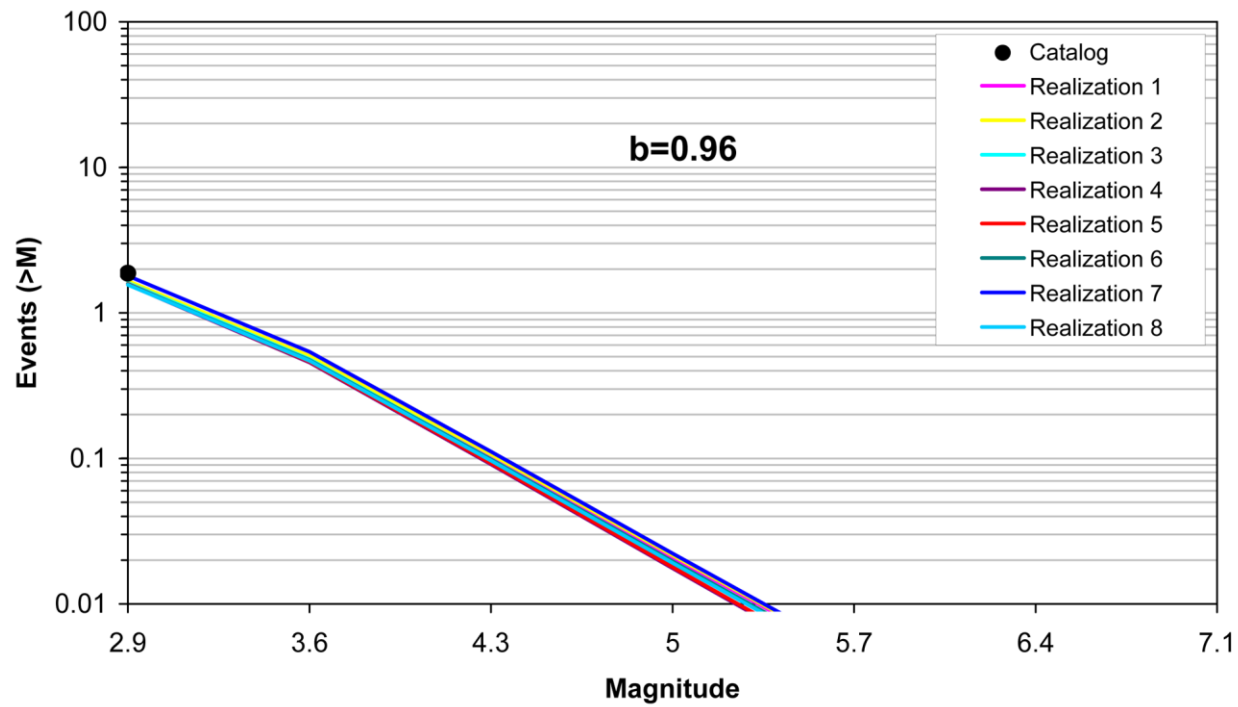


Figure 5.3.2-37  
Comparison of model-predicted earthquake counts for the Miami, FL, area using Case B magnitude weights

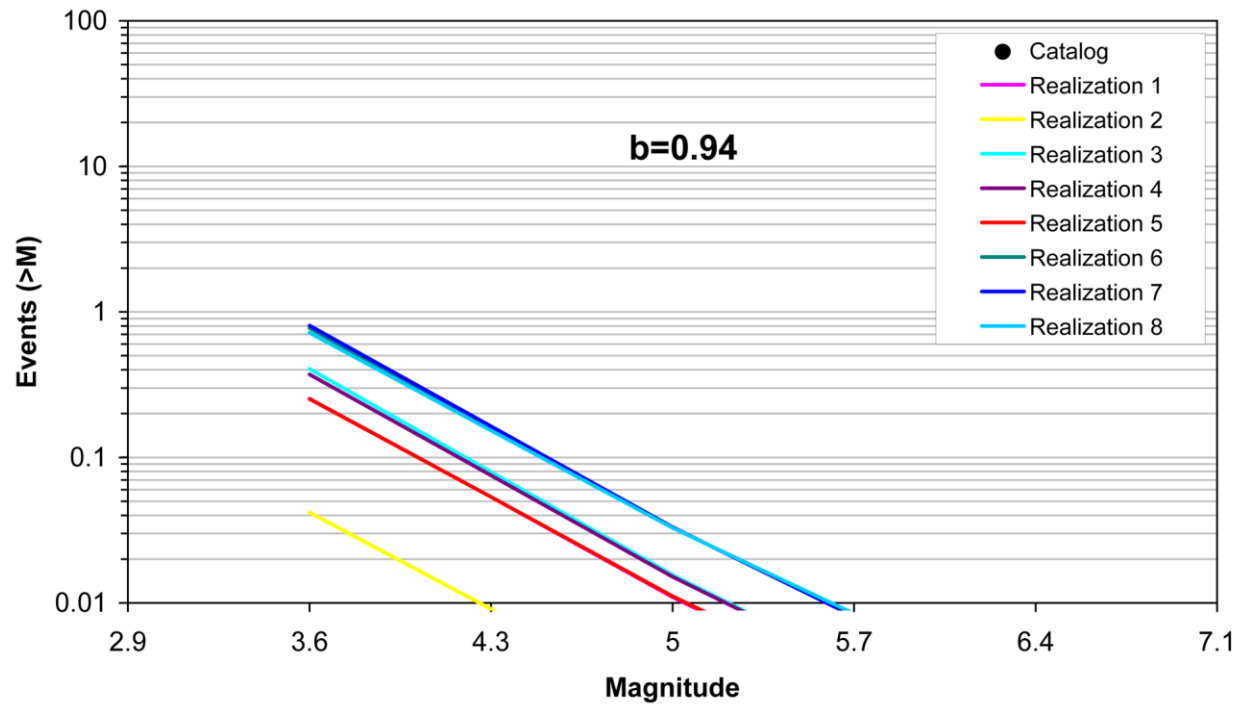


Figure 5.3.2-38  
Comparison of model-predicted earthquake counts for the Miami, FL, area using Case E magnitude weights

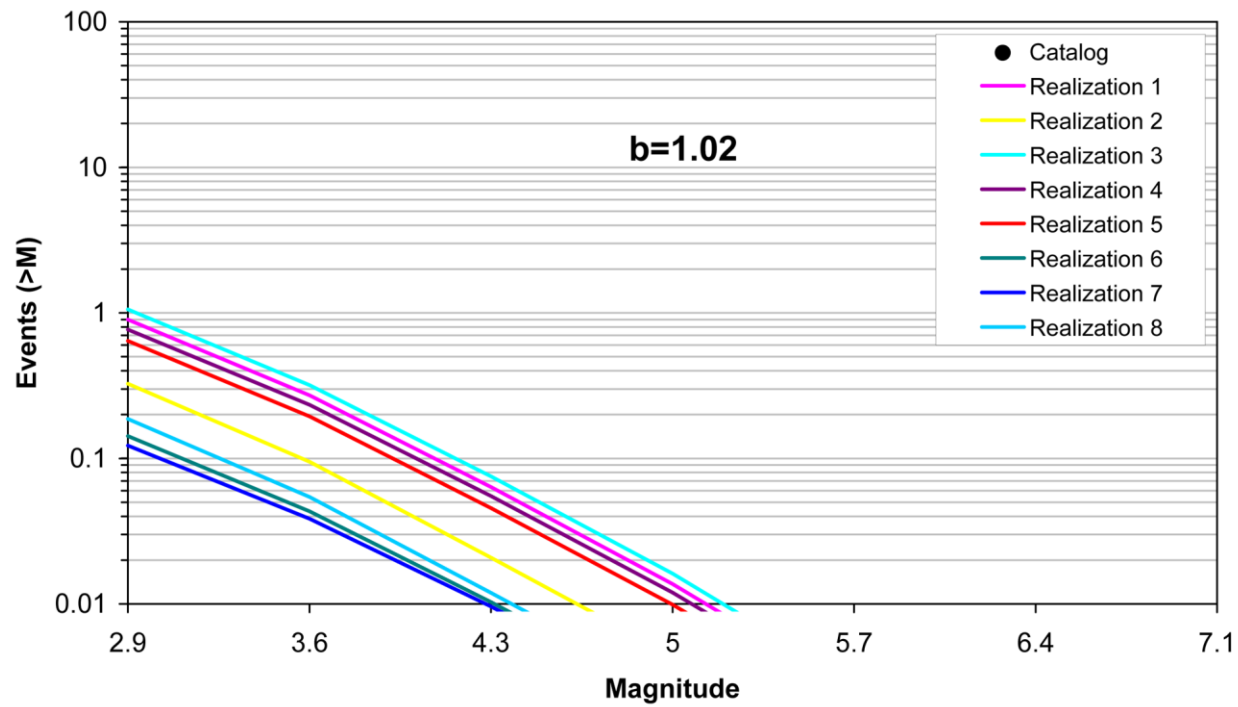


Figure 5.3.2-39  
Comparison of model-predicted earthquake counts for the St. Paul, MN, area using Case A magnitude weights

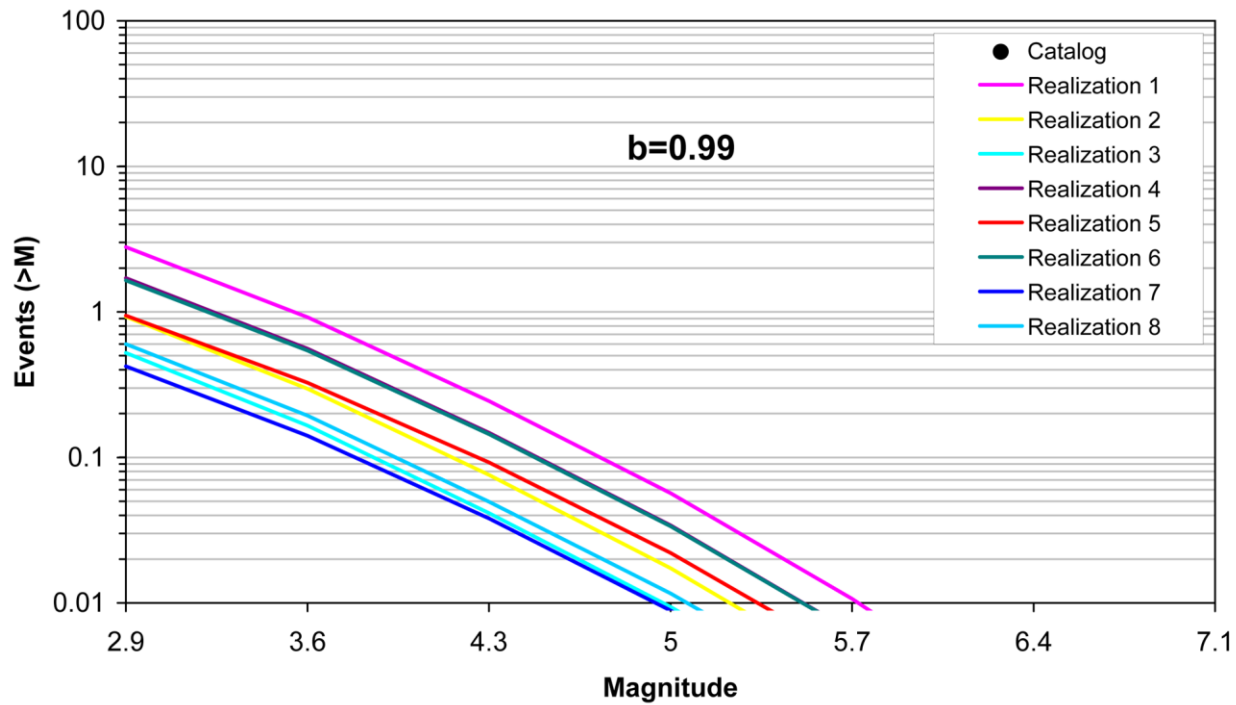


Figure 5.3.2-40  
Comparison of model-predicted earthquake counts for the St. Paul, MN, area using Case B magnitude weights

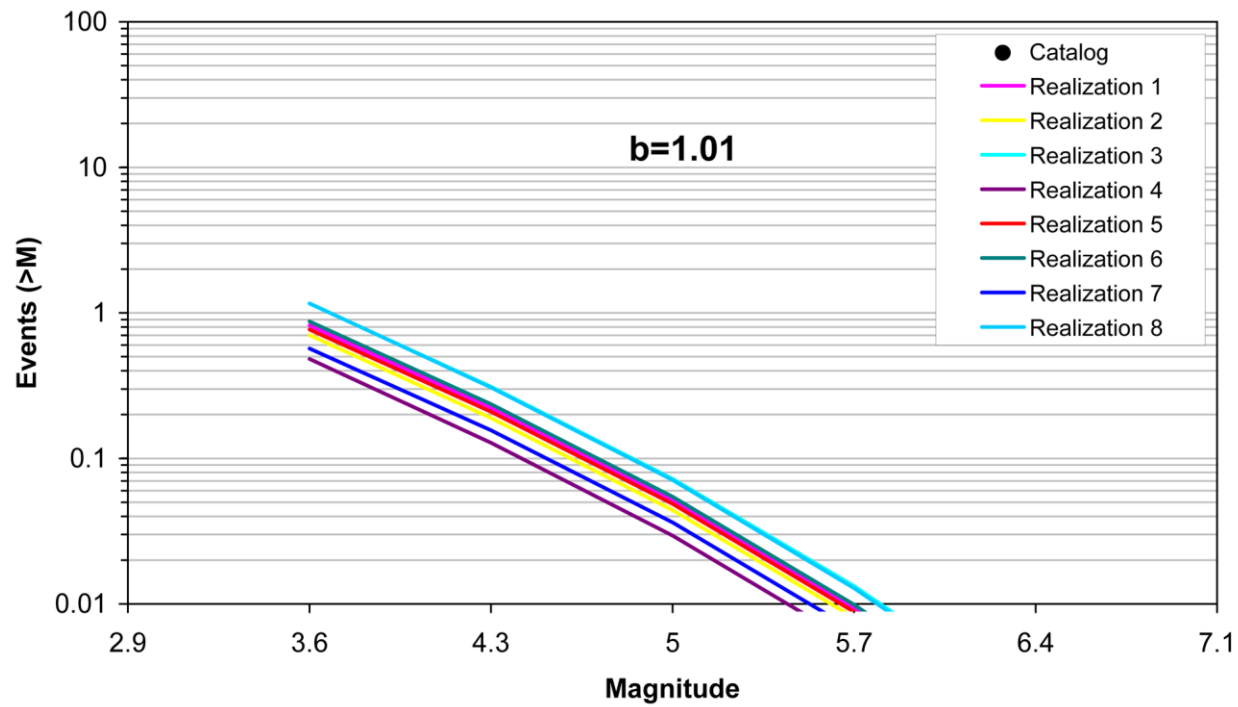
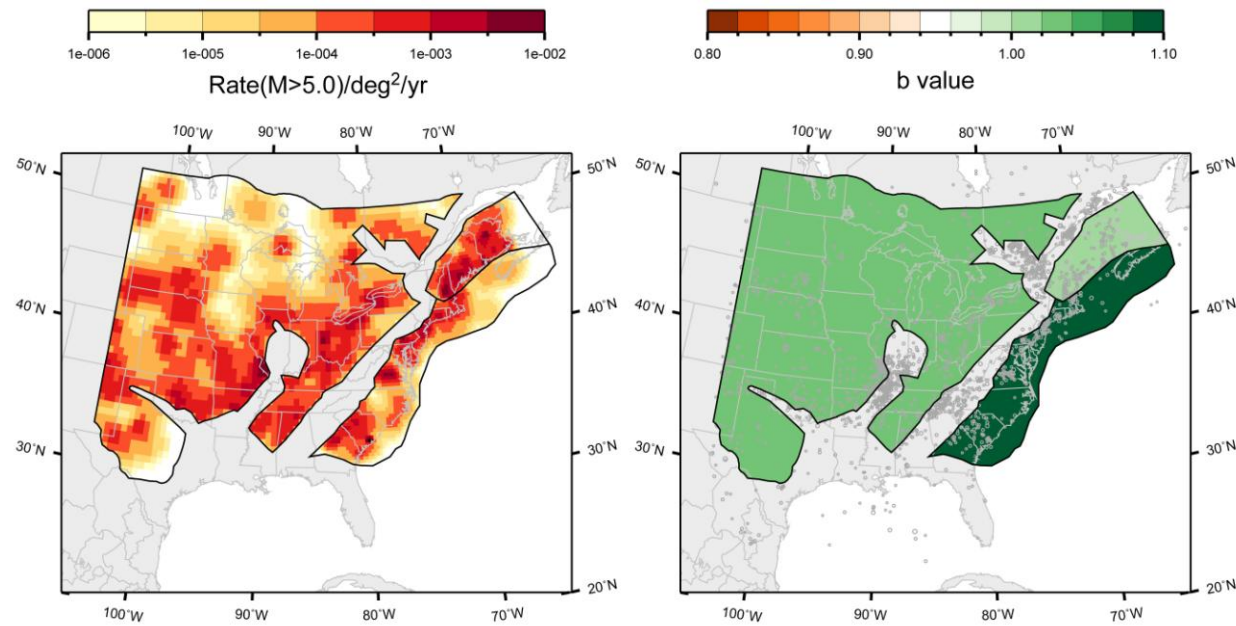
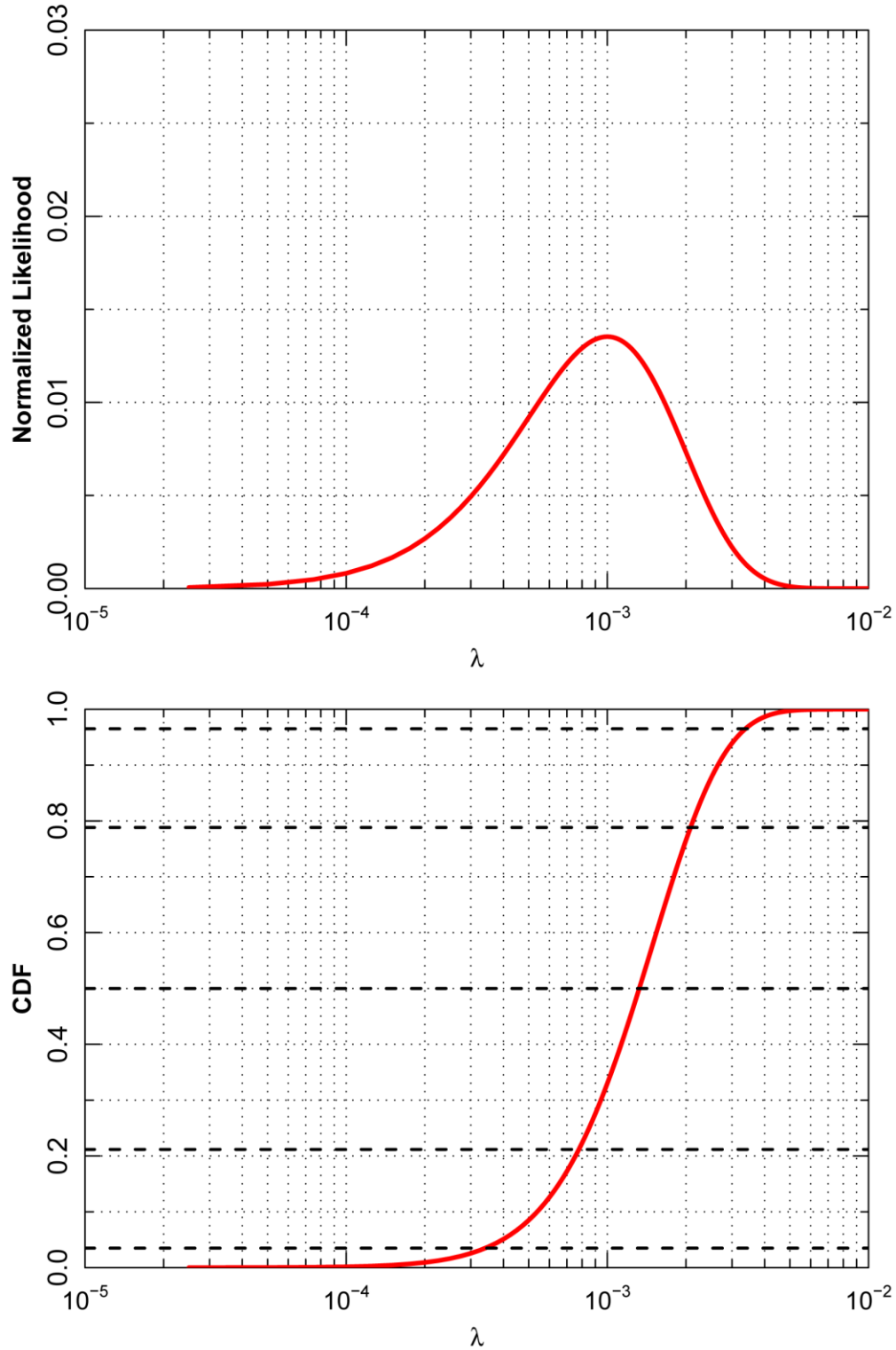


Figure 5.3.2-41  
Comparison of model-predicted earthquake counts for the St. Paul, MN, area using Case E magnitude weights



**Figure 5.3.2-42**  
Recurrence parameters for the ECC-AM, MID-C-A, and NAP seismotectonic source zones and Case A magnitude weights computed using an objective adaptive kernel approach



**Figure 5.3.3-1**  
Likelihood distribution for rate parameter  $\lambda$  derived using Equation 5.3.3-1 for  $N = 2$  and  $T = 2,000$  years. Top: normalized probability density function for  $\lambda$ . Bottom: resulting cumulative distribution function. Dashed lines show the cumulative probability levels for the Miller and Rice (1983) discrete approximation of a continuous probability distribution.

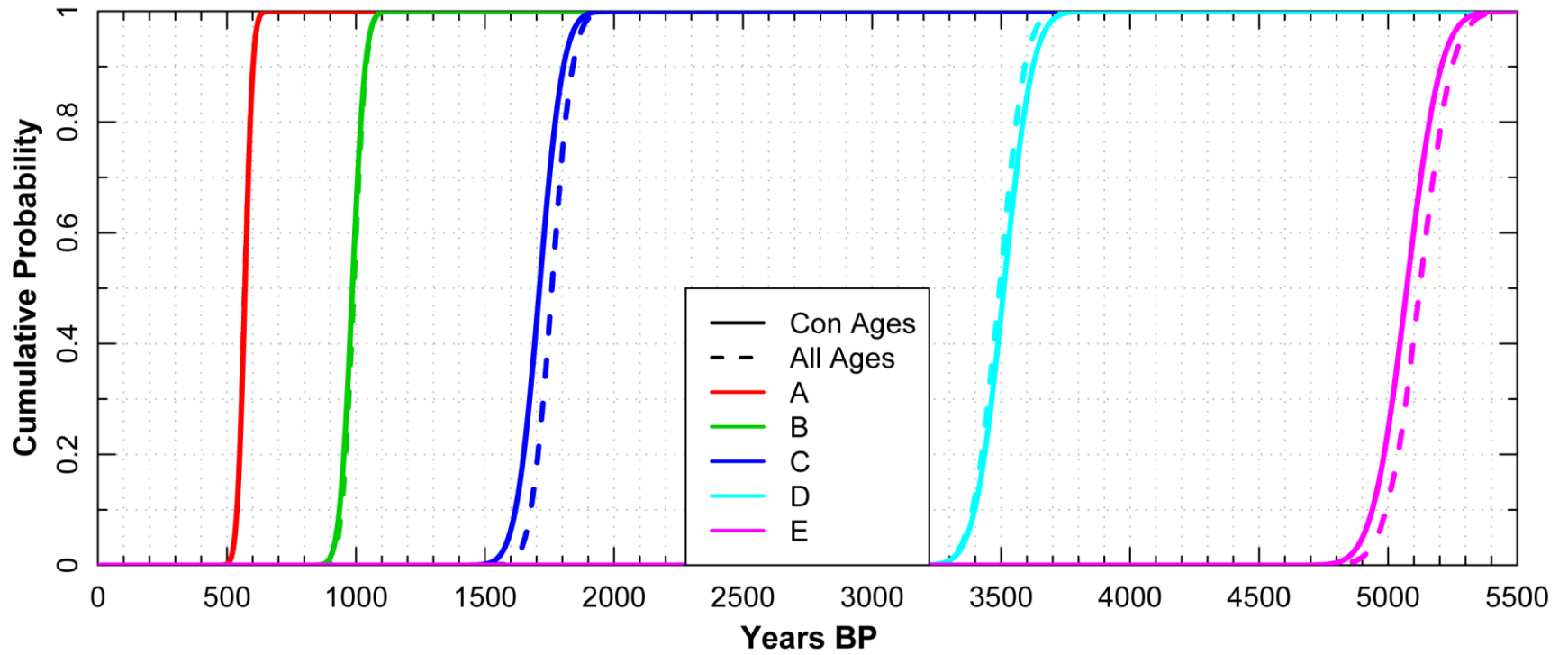
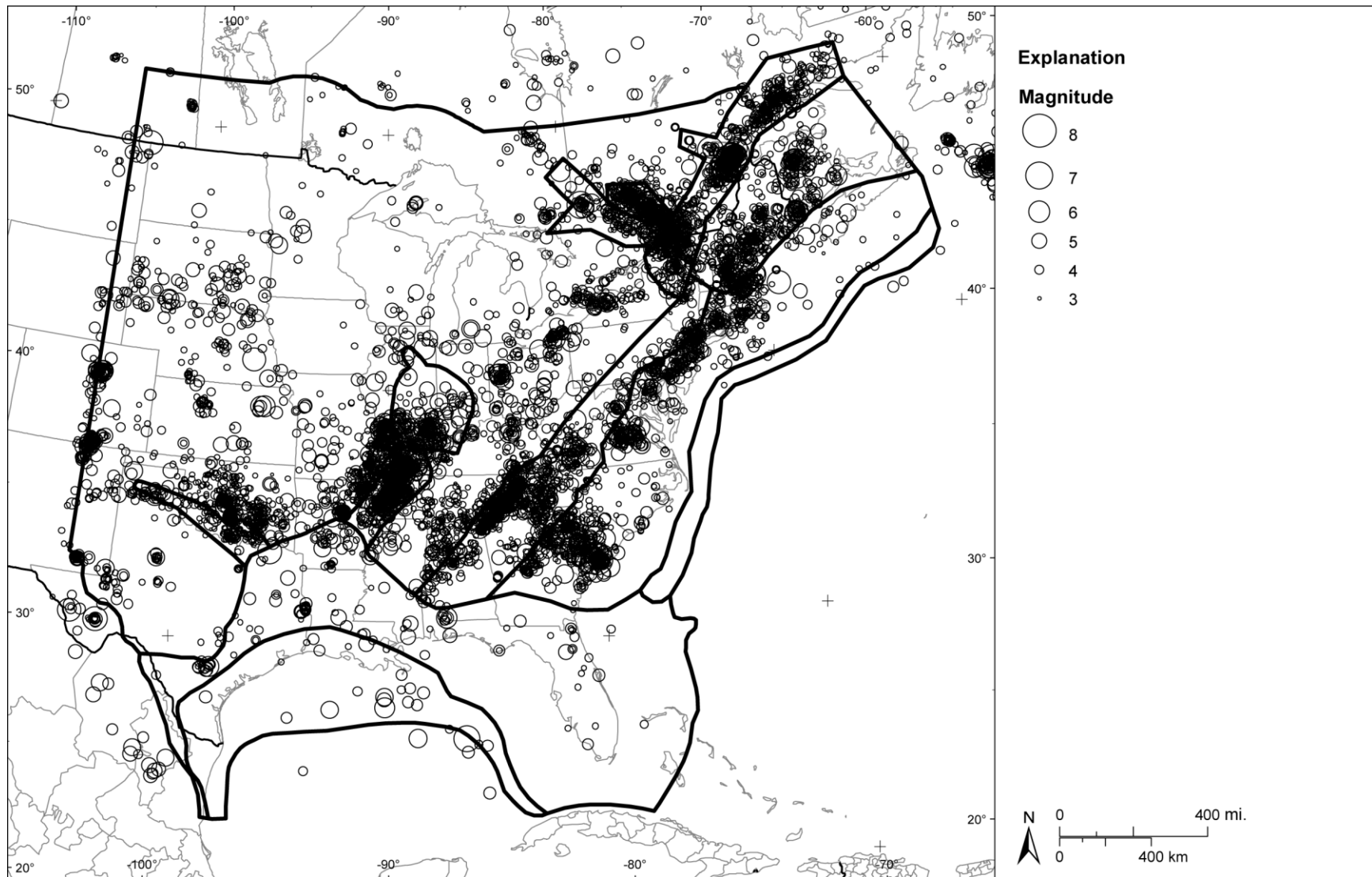
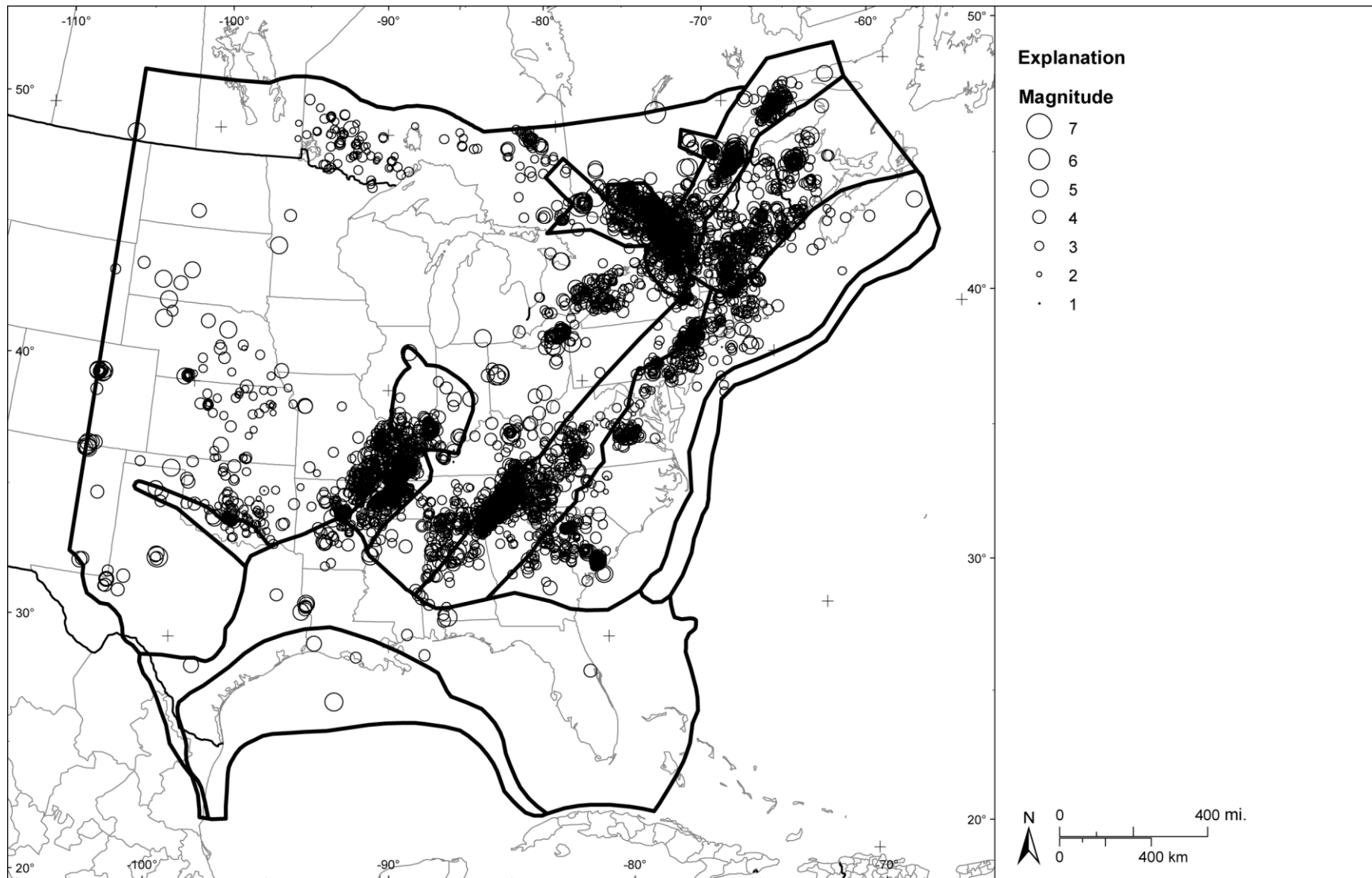


Figure 5.3.3-2  
Uncertainty distributions for the age of Charleston RLMEs



**Figure 5.4.4-1**  
Spatial distribution of earthquakes in the CEUS SSC Project catalog. Solid lines indicate the boundaries of the seismotectonic source zones (narrow interpretation).



**Figure 5.4.4-2**  
Spatial distribution of earthquakes in the CEUS SSC Project catalog with good quality depth determinations used for assessing crustal thickness. Solid lines indicate the boundaries of the seismotectonic source zones (narrow interpretation).

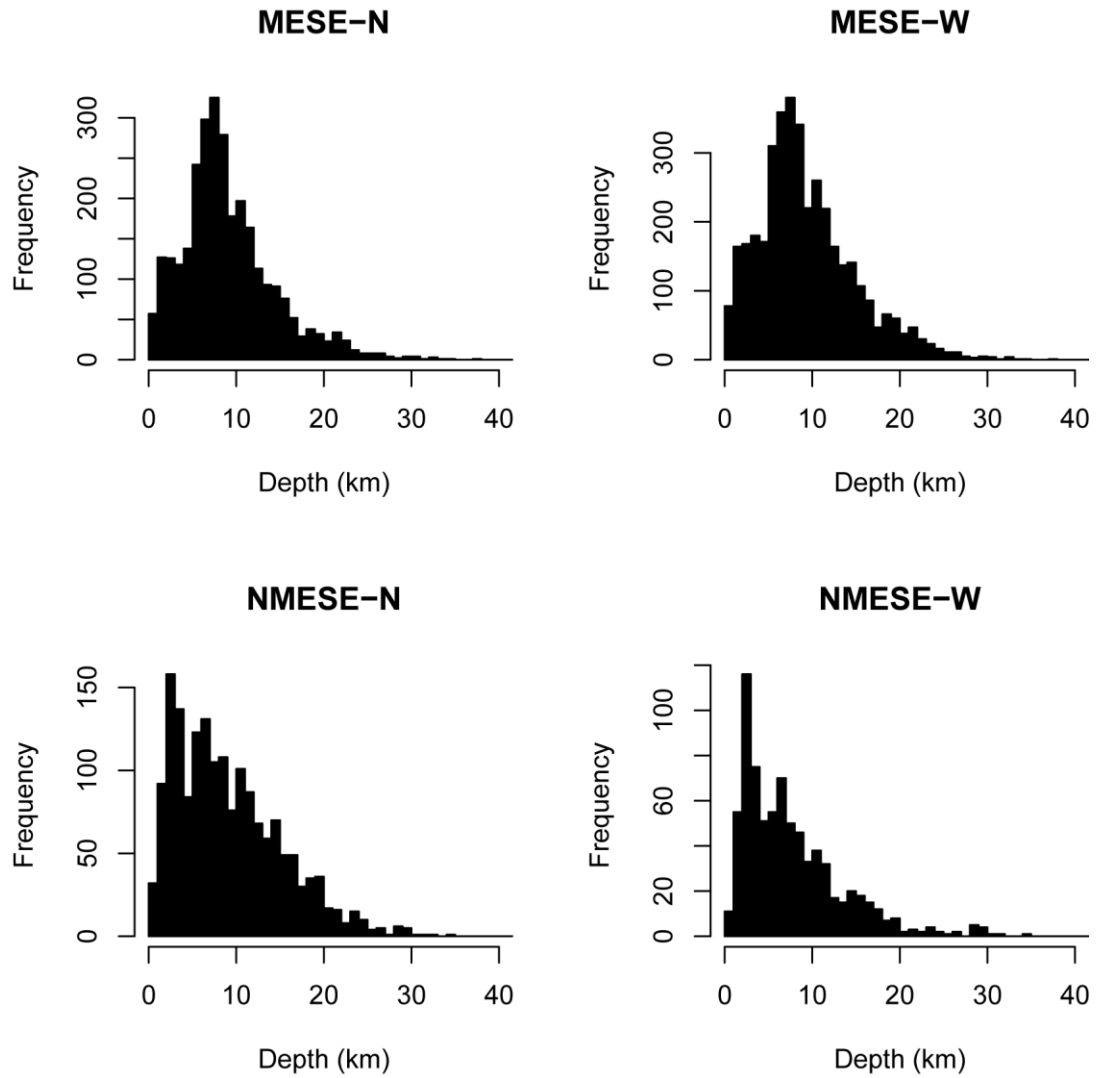


**Figure 5.4.4-3**  
Distribution of better-quality focal depths in Mmax source zones

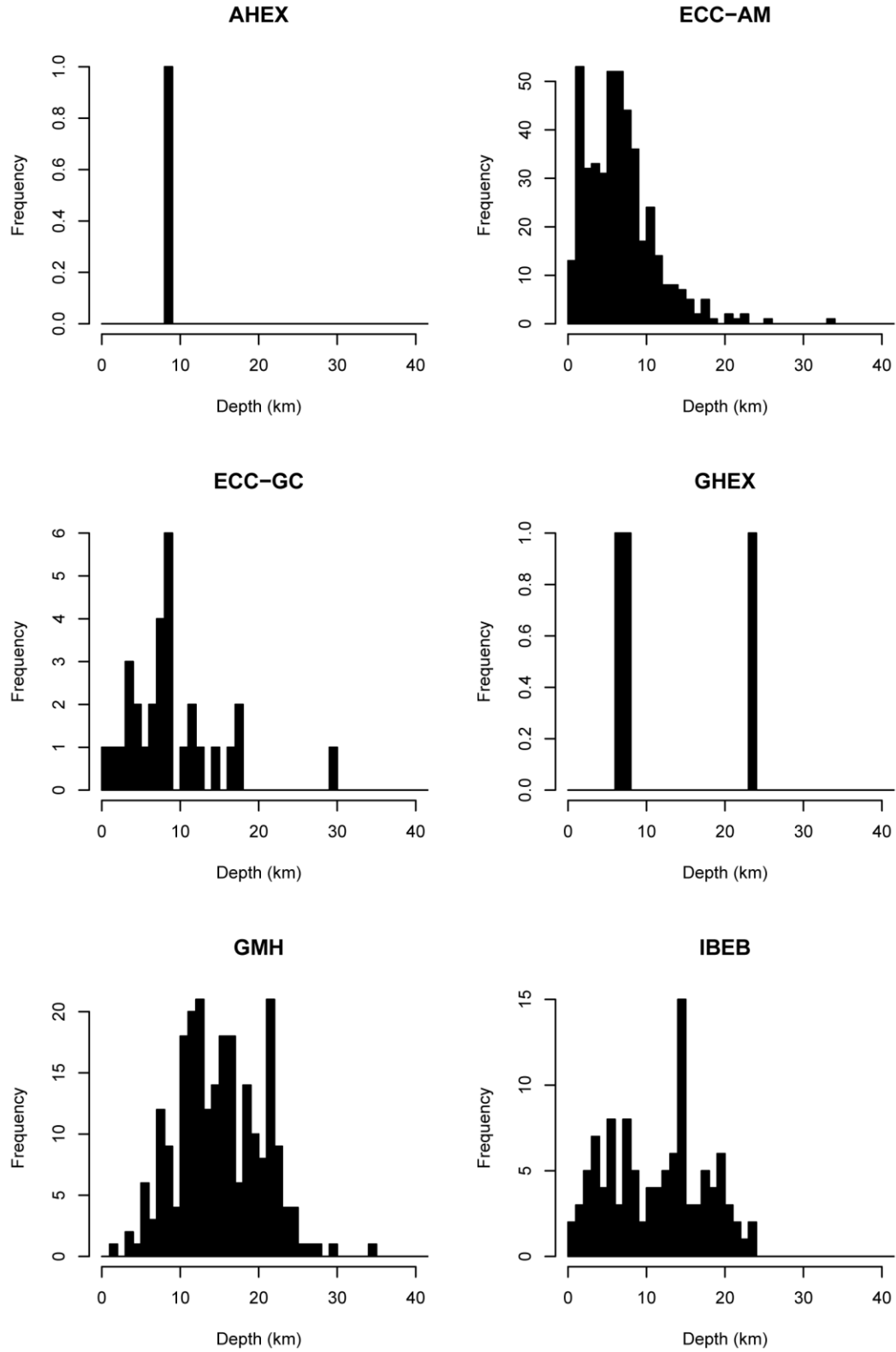


**Figure 5.4.4-4 (1 of 3)**  
**Distribution of better-quality focal depths in seismotectonic source zones**

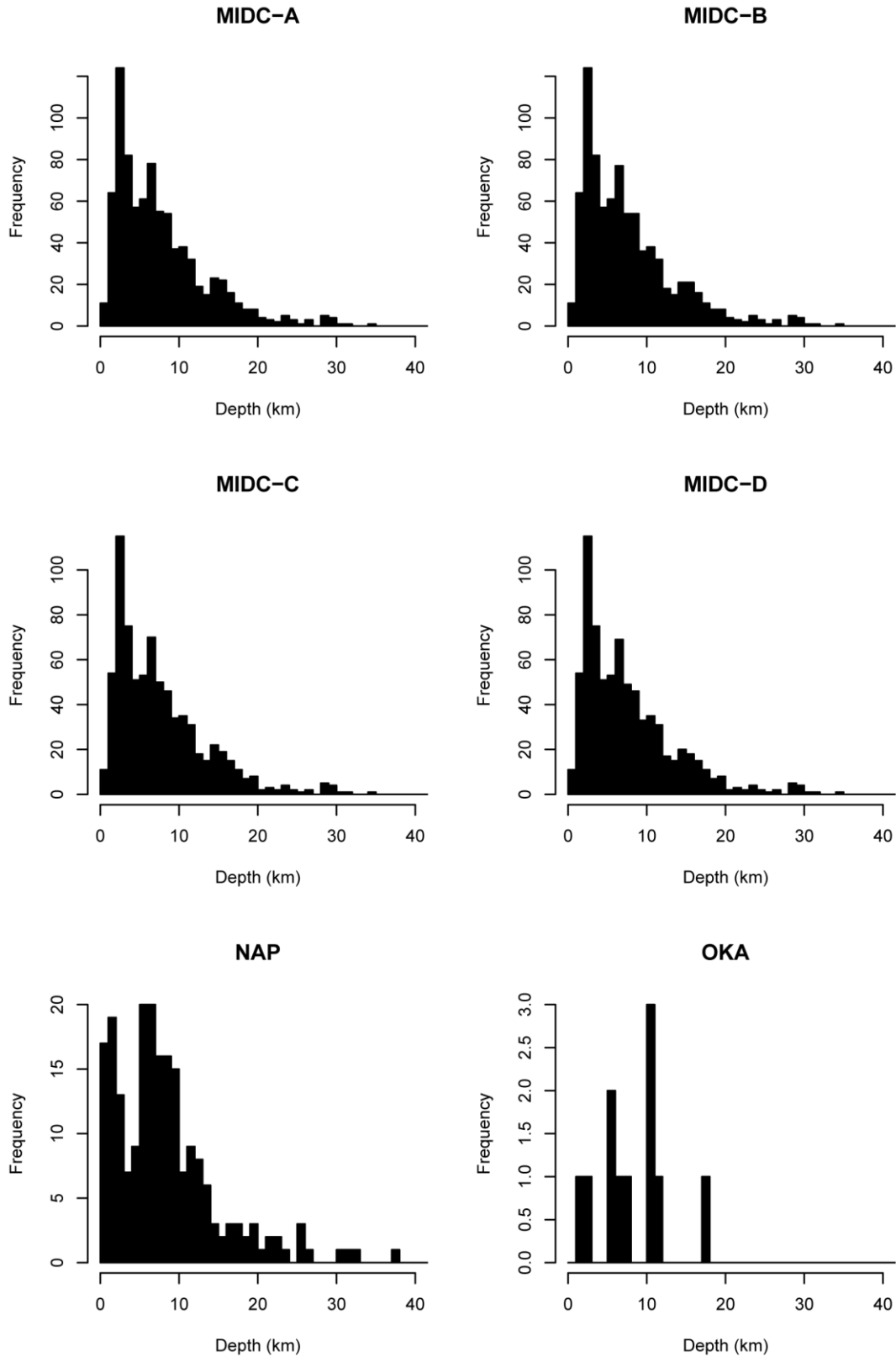


**Figure 5.4.4-4 (2 of 3)**  
**Distribution of better-quality focal depths in seismotectonic source zones**

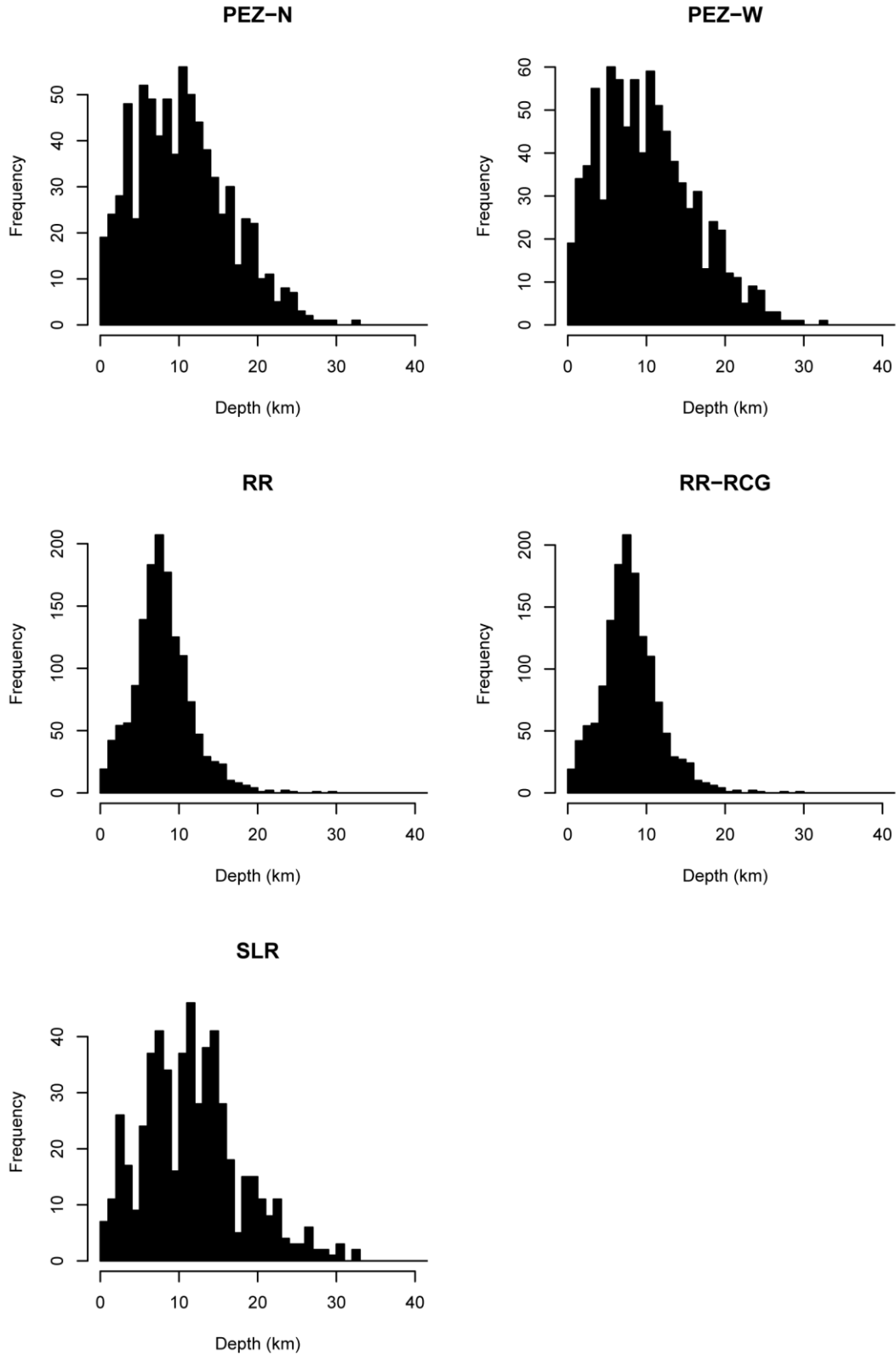


**Figure 5.4.4-4 (3 of 3)**  
Distribution of better-quality focal depths in seismotectonic source zones



# 6

## CHAPTER 6

# SSC MODEL: RLME SOURCES AND MMAX ZONES BRANCH

---

As discussed in Section 4.2, the two major branches of the master logic tree define two approaches to characterizing the spatial and temporal distribution of seismic sources: the Mmax zones approach and the seismotectonic zones approach. As discussed in Section 4.2.1, the “Mmax zones” model involves (1) the direct use of observed seismicity by spatial smoothing of distributed seismicity and (2) the inclusion of RLMEs that are defined primarily by paleoseismic evidence. The Mmax zones are defined solely by differences in the prior distribution of Mmax, using the Bayesian approach. In contrast, the “seismotectonic zones” model (described in Chapter 7), which also includes the RLMEs, involves the use of additional seismotectonic data to define the spatial variation in the characteristics of future earthquakes. This chapter defines both the RLME sources and the Mmax zones. Section 6.1 describes each of the RLME sources; Section 6.2 describes the alternative interpretations of the Mmax zones; Section 6.3 discusses the assessment of maximum magnitude for the Mmax zones; and Section 6.4 describes the spatial smoothing of recurrence parameters within the Mmax zones.

### 6.1 RLME Sources

By definition, RLME sources are the locations of repeated (more than one) large-magnitude ( $M \geq 6.5$ ) earthquakes in the historical or paleoearthquake record. Because of the rarity of RLMEs relative to the period of historical observation, evidence for these earthquakes comes largely from the paleoearthquake record. For example, paleoearthquakes identified by interpretations of paleoliquefaction features and fault displacement (paleoseismic) studies combined with those in the historical record result in the catalog of large-magnitude earthquakes in the central New Madrid region and at Charleston. At Charlevoix, RLMEs are observed in the historical record and are supplemented by the paleoearthquake record. For the Meers and Cheraw faults as well as the Wabash Valley source, there are no large-magnitude earthquakes in the historical record. The RLMEs for these sources are characterized by evaluating repeated surface-faulting displacements identified in trenches across the faults and, for the Wabash Valley source, by interpreting the geographic distribution of paleoliquefaction features.

The RLME sources considered for the CEUS SSC model are listed in Table 4.2.2-1 and shown on Figure 6.1-1, which is an overview map. Detailed maps of the RLME sources, along with their alternative geometries, are given in the individual subsections describing each of the 11 RLME sources (Sections 6.1.1 through 6.1.9). The relationship of the RLME sources to observed historical seismicity is enigmatic. Some of the RLME sources are associated with elevated

seismicity (Figures 6.1-2a and 6.1-2b), such as the central New Madrid faults (Figure 6.1-2b) and Charlevoix, but others occur within areas of moderate levels of seismicity (e.g., Charleston and Wabash Valley) or even relatively low levels of seismicity (e.g., Cheraw fault). Data evaluation tables for each of the 11 RLME sources are in Appendix C. Six data summary tables for the 11 sources are in Appendix D; a single data summary table (D-6.1.5) is provided for the combined New Madrid region sources described in Sections 6.1.5 to 6.1.8.

By identifying the RLME sources and including them in the SSC model, there is no implication that the set of RLME sources included is, in fact, the total set of RLME sources that might exist throughout the study region. This is because the presently available studies that have located and characterized the RLME sources have been concentrated in certain locations, not conducted systematically across the entire study region. If it were possible to identify all RLME sources throughout the study region, in much the same way that major faults are identified in a plate-boundary tectonic setting, then the earthquake potential of the remaining region might be assessed as being secondary to the RLME sources. This type of conclusion cannot be drawn in the CEUS, based on current knowledge. Therefore, the evidence for the existence of the RLME sources is included in the model, but the remaining parts of the study region are also assessed to have potentially significant earthquake potential, which is characterized using either Mmax zones (Section 6.2) or seismotectonic zones (Section 7.3).

The intent of the RLME sources is to model only the recurrence of repeated large earthquakes in a specific location. As such, the RLME sources represent a source of seismic hazard that is in addition to the hazard resulting from the occurrence of distributed seismicity modeled by the distributed seismicity sources—the Mmax zones. In essence, the RLME sources act as fault-like seismic sources embedded in large areal seismic source zones. They allow for a departure from the general truncated exponential recurrence behavior in specific locations. The expected magnitude of the RLMEs that occur in each RLME source is represented by an *epistemic* distribution assessed from the available information for each source. As described in Section 5.3.3.4, given a specific value for the expected RLME magnitude, the size of individual RLMEs is modeled by a uniform *aleatory* distribution over the range of  $\pm 0.25$  magnitude units about the expected value. The assessment of the size and magnitude distribution for the RLME sources is independent of the assessment of the maximum magnitude distribution for the distributed seismicity sources. As a result, there is overlap in the magnitude ranges in most cases. This introduces a small degree of “double counting” in the area covered by the RLME sources. However, the earthquakes in the CEUS SSC earthquake catalog that are identified as RLMEs are not included in the calculation of earthquake recurrence rates for the distributed seismicity sources.

The assessment of RLME recurrence rates is based on paleoseismic data gathered at each location and the methodology described in Section 5.3.3. Table 6.1-1 presents a summary of the specific methods and data used for each RLME source. The descriptions of the data and the assessment of relative weights assigned to alternative data sets are discussed in the following sections.

### 6.1.1 Charlevoix

Repeated historical earthquakes have occurred within the Charlevoix region of the lower St. Lawrence (Figure 6.1-2a), including the February 5, 1663, **M** 7 (E[**M**] 7.00)<sup>1</sup>; December 6, 1791, **M** 5.8 (E[**M**] 5.50); October 17, 1860, **M** 6 (E[**M**] 6.08); October 20, 1870, **M** 6.5 (E[**M**] 6.55); and March 1, 1925, **M** 6.3 (E[**M**] 6.18) earthquakes (Lamontagne et al., 2008). Only two of these earthquakes, the 1663 and 1870 earthquakes, are considered RLME earthquakes. The rest are considered to be part of seismicity occurring in the distributed seismicity sources. In addition, paleoseismic investigations have identified evidence of paleoearthquakes throughout the Holocene (Tuttle and Atkinson, 2010; Doig, 1991; Fillion et al., 1991) that are spatially restricted to the Charlevoix area (Tuttle and Atkinson, 2010).

Several explanations have been offered for why RLMEs occur within the Charlevoix seismic zone. Adams and Basham (1991) attribute seismicity of the SLR system to earthquakes occurring on rift structures in the regional stress field of southeast-to-east compression, recognizing that a Devonian impact structure also exists in the general area and may be related to the spatial concentration of seismicity in the Charlevoix area. The observation that seismicity continues beyond the impact structure (crater) with orientations indicative of reactivation of rift faults led Adams and Basham (1991) to de-emphasize the role of impact structures. Lamontagne and Ranalli (1997) correlate large-magnitude Charlevoix earthquakes to reactivation of rift faults in response to the regional stress field. They interpret variations in orientation and style of faulting for small-magnitude earthquakes to reactivation of impact-related faults and fractures in response to local stress and/or strength conditions. In another paper, Lamontagne and Ranalli (1996) attribute earthquakes in the Charlevoix seismic zone to some or all of the following circumstances:

- Fracturing above the brittle-ductile transition at depths of at least 25 km (15.5 mi.).
- High pore-fluid pressure at mid- to lower crustal depths where hydration reactions are not favored.
- Low coefficients of friction related to highly fractured zones at depth, as opposed to thick fault gouges made of clay minerals.

Results of two-dimensional stress modeling account for the spatial pattern of observed seismicity as stress concentration due to the interaction of the crater (local zone of weakness) and rift faults (large-scale weak zone) (Baird et al., 2009). Smaller-magnitude, more frequent seismicity occurs within the impact crater, and infrequent larger-magnitude earthquakes are localized along rift faults (Baird et al., 2009). Mazzotti and Adams (2005) have also observed that the discrepancy between modeled seismic moment and strain rates derived from earthquake statistics may represent a short-term process such as postglacial rebound.

A summary of the investigations evaluated for the Charlevoix seismic zone is provided in Appendix Table D-6.1.1, and information used in the CEUS SSC Project to characterize this

---

<sup>1</sup> Magnitudes are reported in the magnitude scale designated in the cited publication. E[**M**] denotes the value of the expected moment magnitude listed in the CEUS SSC catalog for the earthquake. It is reported to two decimal places to indicate that it is a calculated value. See the discussion in Section 3.3.1.

RLME zone is presented in Appendix Table C-6.1.1. The logic tree for the Charlevoix RLME source is shown on Figure 6.1.1-1.

#### 6.1.1.1 Evidence for Temporal Clustering

The first node of the logic tree (Figure 6.1.1-1) addresses the issue of temporal clustering of earthquakes in the present tectonic stress regime (see Section 5.1.2). The historical earthquakes identified as RLMEs are the February 5, 1663,  $M$  7 (E[ $M$ ] 7.00), and the October 20, 1870,  $M$  6.5 (E[ $M$ ] 6.55), earthquakes. Recently, Tuttle and Atkinson (2010) reported evidence, based on a minimum magnitude to produce paleoliquefaction features, for three or more  $M \geq 6.2$  earthquakes during the past 10,000 years. These earthquakes include one historical earthquake possibly associated with either the 1663, 1870, or 1925 earthquake, and two prehistoric earthquakes occurring approximately 5,000 and 10,000 years ago. The available information on the size and location of these earthquakes and the geologic evidence for long-term slip rates or recurrence intervals are insufficient to evaluate whether the Charlevoix RLME source exhibits evidence for temporal clustering. Therefore, this node of the logic tree is not applicable to the Charlevoix RLME source.

#### 6.1.1.2 Localizing Tectonic Features

The late Proterozoic–early Paleozoic SLR, which passes through the Charlevoix RLME source zone, is attributed to the opening of the Iapetus Ocean (Tremblay and Lemieux, 2001) and is characterized within the SLR seismotectonic zone in Section 7.3.1. The St-Laurent fault strikes N20-50E and dips 60–70 degrees to the southeast, forming a northeast-trending, southeast-dipping half graben oriented parallel to the main axis of the SLR system (Tremblay and Lemieux, 2001). High-resolution seismic profiles in the St. Lawrence estuary indicate that the Laurentian Channel trough transitions from a half graben to a graben structure from southwest to northeast (Tremblay et al., 2003).

Two major fault orientations (N40-70W and N20-40E) are found outside the Charlevoix impact zone, with minor fault sets trending east to west to N80W and north to south to N20E (Lemieux et al., 2003). Fault rocks consist of fault breccia, cataclastite, foliated gouge, and pseudotachylyte with a minimum thickness of 20 m (66 ft.) near Sault-au-Cochon (Tremblay and Lemieux, 2001). Fault rocks exposed at Cap-Tourmente consist of zones of protocataclasite, cataclasite, and fault breccia 10–15 m (33–49 ft.) thick (Tremblay and Lemieux, 2001). Changes in strain rate, pressure, temperature, and fluid conditions are required for formation of cataclastic rocks, pseudotachylytes, and fault gouge within the same environment, suggesting that a single, progressive tectonic event along the SLR resulted in this distribution of fault rocks (Lemieux et al., 2003). The St-Laurent fault crosses the Charlevoix impact crater without any major deflection in strike or without any fault offsets within or at the boundaries of the structure, indicating that impact-related faulting did not significantly alter the orientation of preexisting structures and that reactivation of the St-Laurent fault is younger than the impact structure (Tremblay and Lemieux, 2001).

Within the Charlevoix impact crater the St-Laurent fault is also characterized by a well-developed and extensive series of cataclastic rock, gouge, and pseudotachylyte, as well as polymictic clastic matrix breccias restricted to the impact crater (Tremblay and Lemieux, 2001). Fragments of cataclastic breccia are present, suggesting recurrent brecciation during incremental faulting events associated with the St-Laurent fault. Fault orientations are more scattered within the impact crater but are similar to the northwest- and northeast-trending faults of the entire rift system (Lemieux et al., 2003). The spread of orientations within the central portion of the crater is attributed to the impact-related polygonal pattern of normal faults, whereas the northwest and northeast fault sets represent the youngest reactivation of the SLR (Lemieux et al., 2003).

The SLR system has experienced multiple stages of reactivation. Stratigraphic evidence of Ordovician growth faulting during late stages of the Taconic orogeny in platform deposits near Charlevoix includes major variations in thickness laterally within the Ordovician section, the presence of slump deformation features induced by faulting in almost all stratigraphic units, the preservation of pseudotachylyte within synsedimentary breccias, and the occurrence of fault breccia clasts (Lemieux et al., 2003). Tremblay et al. (2003) speculate that additional episodes of reactivation of faulting in the SLR system are younger than the Devonian-age Charlevoix impact crater. Truncation of Devonian impact-related structures by northeast-southwest and northwest-southeast faults is consistent with Mesozoic fault reactivation due to rifting of the North Atlantic region (Lemieux et al., 2003). Tremblay et al. (2003) attribute some fault throw along the SLR system to the opening of the Central Atlantic in the Jurassic and/or seafloor spreading of the North Atlantic during the Cretaceous.

Because the occurrence of RLMEs in the Charlevoix zone cannot be associated with a specific feature, future RLMEs are modeled as occurring randomly within the RLME source zone, as indicated on the second node of the logic tree (Figure 6.1.1-1).

### 6.1.1.3 Geometry and Style of Faulting

The geometry of the Charlevoix RLME source, shown on Figure 6.1.1-2, is defined to encompass the locations of earthquakes with  $M > 6$ , mapped rift faults, and the Charlevoix impact crater. Gravity and magnetic data sets delineate Grenville and Appalachian crust (Figure 6.1.1-3) and were not used to constrain the geometry for the Charlevoix RLME source. Lamontagne (1999) observed that small to moderate earthquakes of the Charlevoix seismic zone occur between, not along, rift faults and extend northeast of the impact structure as a result of the asymmetric placement of rift faults through the crater (Baird et al., 2009). Large-magnitude earthquakes are thought to occur along weakened rift faults that concentrate stress into the crater (Baird et al., 2009). The geometry for the Charlevoix RLME source zone was modified from the Charlevoix source zone of the GSC H model (Adams et al., 1996; Adams and Halchuck, 2003). Tuttle and Atkinson (2010) consider a narrower geometry for the Charlevoix seismic zone that is more localized along rift faults. A single geometry for the Charlevoix RLME source that envelops both interpretations is used, as indicated by the third node of the logic tree shown on Figure 6.1.1-1.

The location of causative faults within the Charlevoix RLME source is uncertain. In addition, using a relationship between magnitude and rupture length (e.g., Leonard, 2010), the lengths of

ruptures that would be associated with the postulated RLMEs are in the range of 30–80 km (19–50 mi.), similar to the 30 by 85 km (19 by 53 mi.) dimensions of the RLME source. Given the small source size and uncertain fault locations, the boundaries of the Charlevoix RLME source are leaky, allowing ruptures to extend beyond the source boundary by 50 percent.

Hypocentral depths for earthquakes in the Charlevoix seismic zone occur as deep as 29 km (18 mi.), although most earthquakes occur between 8 and 15 km (5 and 9.5 mi.) (Lamontagne and Ranalli, 1996). Comparing this depth distribution to rheological models of the region, Lamontagne and Ranalli (1996) attribute earthquakes in the Charlevoix seismic zone to one or more of the following: faulting above the brittle-ductile transition at depths of at least 25 km (15.5 mi.); high pore-fluid pressure below the onset of ductility for hydrated feldspar at about 350°C; and a low coefficient of friction, possibly related to unhealed zones of intense fracturing. The distribution of spatially clustered earthquakes within the Charlevoix seismic zone indicates that very few earthquakes have occurred on the same fractures with similar focal mechanisms, implying that these fault zones occur in highly fractured rocks (Lamontagne and Ranalli, 1997). The thickness of seismogenic crust is modeled with equal weight on 25 and 30 km (16 and 19 mi.), as shown on the fourth node of the logic tree (Figure 6.1.1-1).

Tremblay et al. (2003) observe several orientations of faulting within the Charlevoix RLME source. Northeast-trending longitudinal faults parallel to the main axis of the rift show three trends (N25E, N40E, and N70E) and generally dip between 60 and 90 degrees to the southeast, although a minor number dip to the northwest. Crosscutting transverse faults show two trends (N70W and N50W) and dip to the northeast or southwest; these orientations are consistent with the horst-and-graben geometry of the SLR system. Both sets of faults are high-angle faults with dip angles averaging 75–80 degrees. The pitch of fault lineations is greater than 70 degrees, indicating that most structures are dip-slip faults (Tremblay et al., 2003). Lemieux et al. (2003) observed the largest variation in fault trends within the central portion of the impact crater, which still displayed a dominant northwest-southeast orientation.

Lamontagne (1999) observed that faulting style inferred from focal mechanisms within the Charlevoix RLME source indicates reverse to oblique-reverse faulting on fault planes with highly variable orientations, and he assumed that these ruptures occur on preexisting southeast-dipping faults. Adams and Basham (1991) report that structural complexity in the form of distributed fracturing and ring faulting within the impact crater may be responsible for more varied focal mechanisms within Charlevoix. Focal mechanisms for earthquakes of magnitude  $\geq 3$  show reverse faulting, whereas smaller-magnitude earthquakes indicate some strike-slip and normal faulting, suggesting that local stress conditions affect rupture style (Lamontagne and Ranalli, 1997). Fault-plane solutions for recent small earthquakes located within the Charlevoix seismic zone are predominantly reverse events on steeply dipping planes, but a number of events have a significant strike-slip component, some on northwest-striking planes and some on more shallowly dipping planes (Lamontagne, 1987; Adams et al., 1989; Wetmiller and Adams, 1990).

Analysis by Li et al. (1995) of rupture directions for two **M** 4 events indicates that focal mechanisms have east-dipping planes. Bent (1992) determined a reverse mechanism for the 1925  $M_s$  6.2 (E[**M**] 6.18) Charlevoix earthquake with a strike of  $N42^\circ \pm 7^\circ E$ , dip of  $53^\circ \pm 7^\circ$ , and rake of  $105^\circ \pm 10^\circ$  and favors a southeast-dipping solution based on observed seismicity and mapped

faults. Dips for the January 11, 1986,  $M_N$  4.0 ( $E[M]$  3.40) and the March 18, 1987,  $M_N$  3.3 ( $E[M]$  2.79) earthquakes range between 42 and 59 degrees to the south (Lamontagne and Ranalli, 1997). Because of the variability exhibited in mapped structures and focal mechanisms, future ruptures for the Charlevoix RLME source are modeled as randomly oriented reverse events with dips between 45 and 60 degrees in either direction.

#### 6.1.1.4 RLME Magnitude

The February 5, 1663, earthquake is the largest observed historical earthquake within the Charlevoix seismic zone. Lamontagne et al. (2008) use a best estimate for the magnitude of  $M$  7. This estimate is based on felt effects in Quebec City, Trois-Rivières, Montreal, Boston, and New York and on reported landsliding along the St. Lawrence, Shipshaw, Betsiamites, Pentecote, Batiscan, and Saint-Maurice rivers (Lamontagne et al., 2008; Gouin, 2001). Using similar observations of intensity from felt reports and accounts of landsliding and liquefaction, Ebel (1996) assigned a magnitude of  $M \geq 7.0 \pm 0.5$  to the 1663 Charlevoix earthquake and concluded that the magnitude of the 1663 event is somewhat larger than the 1925 Charlevoix earthquake. Ebel (2006b) later postulated that, if the total length of the Charlevoix seismic zone (70 km, or 43.5 mi.) produced a single rupture approaching  $M$  7.5 during the 1663 event, all modern seismicity represents aftershocks from this event. Ebel (2009) notes that this rupture length could produce a main-shock magnitude of  $M$  7.1–7.5. He interpreted MMI VI reports at Roxbury, Massachusetts, as a  $m_{bLg}$  7.5 ( $M$  7.8) using an intensity-attenuation relationship, and as a  $M$  7.5 using recent ground-motion attenuation relationships. These lines of evidence led him to assign a magnitude of  $M$  7.5  $\pm$  0.3 to the 1663 Charlevoix event. Recent discussions with Ebel (pers. comm., 2009) indicate that he prefers a magnitude of 7.2–7.5.

Paleoliquefaction features occurring along the Gouffre, Malbaie, and Ouelle rivers (Figure 6.1.1-2) in the Charlevoix area (Appendix E, Section 1.2.8.1) provide evidence of three generations of earthquake-induced liquefaction within the last 10,000 years (Tuttle and Atkinson, 2010). The spatial distribution of these features and the lack of paleoliquefaction evidence to the south in the Trois Rivières area can be attributed to paleoearthquakes of  $M \geq 6.2$  in the Charlevoix seismic zone (Tuttle and Atkinson, 2010). The prehistoric earthquakes are considered RLMEs ( $M \geq 6.5$ ) given the range of magnitudes ( $M$  6.2–7.0) capable of explaining the spatial distribution of observed liquefaction features (Tuttle and Atkinson, 2010). Recent work by Locat (2008) places the  $M$  7 1663 earthquake near Saguenay, based on the distribution of largely undated landslide deposits throughout the region and subaqueous mass movements in the St. Lawrence estuary, Saguenay fjord, and nearby lakes. This work illustrates the role of landsliding, in addition to liquefaction, in recording paleoearthquakes in the region. However, better constraints on timing of events are required for correlating deformation with specific events and geotechnical studies of susceptibility are required for determining the location and magnitude of those events. Consequently, the results of the Locat (2008) study were not used in the characterization of the 1663 Charlevoix earthquake.

Based on the information above, the distribution for RLME magnitude tabulated below was developed. This magnitude distribution places most of the weight on the preferred magnitude from Lamontagne et al. (2008) and incorporates uncertainty from the paleoliquefaction record and recent estimates from Ebel (2009). Aleatory variability in the size of an individual

Charlevoix RLME is modeled as a uniform distribution of  $\pm 0.25$  **M** units centered on the expected RLME magnitude value (Section 5.3.3.4).

Expected Charlevoix RLME Magnitude (M)	Weight
6.75	0.2
7.0	0.5
7.25	0.2
7.5	0.1

#### 6.1.1.5 RLME Recurrence

The remaining nodes of the Charlevoix RLME logic tree address uncertainties in the specification of the annual frequency of RLMEs.

##### *Recurrence Methods and Data*

Paleoseismic investigations provide evidence of persistent earthquake activity through the Holocene. Filion et al. (1991) interpreted two earthquake-induced landslides by dating tree rings in the base of flow materials of dammed lakes along the Rivière du Gouffre, which is located within the Charlevoix seismic zone. Doig (1990) identified silt layers in lakes as recording earthquake-induced landslides and inferred a variable recurrence rate for the Charlevoix seismic zone: a recurrence interval of 120 years from 320 BC to AD 800; 270 years from AD 800 to 1500; and 75 years from AD 1500 to the present. Some silt layers in the section were correlated with historical earthquakes from 1638, 1663, 1791, 1870, and 1925 (Doig, 1990). These observations are difficult to quantitatively incorporate within earthquake recurrence calculations since silt layers may be due to nontectonically induced landslides; however, if the cause is tectonic, these silt layers can be attributed to either local moderate-sized earthquakes or distant large-magnitude earthquakes. Assigning a magnitude, location, and recurrence for the features identified by Doig (1990) would require a detailed chronology of regional landslide features and geotechnical assessments of their strength. Therefore, the recurrence for the Charlevoix RLME source is modeled from the 1663 and 1870 earthquakes and two prehistoric earthquakes identified by Tuttle and Atkinson (2010), which does include geotechnical assessments of liquefaction potential of host sediments in the evaluation of magnitude and location for these paleoearthquakes.

Tuttle and Atkinson (2010) provide evidence of at least three Holocene paleoearthquakes in Charlevoix with  $M \geq 6.2$ , including one historical event with a bracketed age of at least 540 yr BP. Tuttle and Atkinson (2010) argue that the 540 yr BP features could be assigned to one of three historical Charlevoix earthquakes since 1660. This set of liquefaction features is therefore included in the recurrence assessment as either the 1663 or 1870 earthquake. Two prehistoric paleoearthquakes are included in the assessment of Charlevoix RLME recurrence. The oldest

generation of features interpreted as having been formed by paleoearthquakes includes pseudonodules and related folds along the Malbaie River, and pillars and convolute bedding along the Gouffre River formed between 10,120 and 9,410 yr BP (Tuttle and Atkinson, 2010). A paleoearthquake of intermediate age is identified by sand dikes and load casts formed since 5,040 yr BP (Tuttle and Atkinson, 2010). Dionne (2001) reports evidence of a sea-level lowstand of 10 m (33 ft.) along the south shore of the St. Lawrence estuary between 6 and 7 ka based on the elevations of intertidal or subtidal deposits overlying the erosional surface of marine clay and covered by emergent organic layers. This lowstand may have reduced the completeness of the paleoliquefaction record during that time, indicating that the three events observed by Tuttle and Atkinson (2010) in the past 10 kyr should be viewed as a minimum.

The available data suggest three possible alternatives for assessing the RLME recurrence rates: the historical record and the two alternative geologic records of 6–7 kyr and 9.5–10.2 kyr. The alternatives for the number of RLMEs in each time period are the 1870 and 1663 earthquakes in the historical period (data set 1); the 1870 and 1663 earthquakes with one paleoearthquake in 6–7 kyr (data set 2); and the 1870 and 1663 earthquakes with two paleoearthquakes in 9.5–10.2 kyr (data set 3). The assessment of RLME recurrence puts the greatest weight on the 6–7 kyr geologic record [0.6] because geologic conditions affecting the susceptibility of sediments are not likely to have changed since the sea level lowstand at 6–7 ka and thus the geological record is expected to be reasonably complete. The longer, 10 kyr, geologic record may be affected by incompleteness in the period before 6–7 ka, and is thus given lower weight [0.2], one-third of the weight assigned to the shorter geologic period. The historic period is also given lower weight [0.2] because it contains a small sample (two earthquakes) and the short recurrence interval between the 1663 and 1870 earthquakes could have occurred by chance (e.g., with approximately 10 percent probability for a Poisson process with the average return period based on the 6–7 kyr record).

The three alternative data sets represent two types of data. Data set 1 consists of earthquakes with known times of occurrence and is analyzed by the “Earthquake Recurrence Intervals” approach, while data sets 2 and 3 represent “Earthquake Counts in a Time Interval.” The common logic tree format used for the RLME sources includes a node for Recurrence Method and a node for Recurrence Data. The weights assigned to the three alternative data sets are used to assign the weights to the branches for these two nodes in the RLME logic tree. For the Recurrence Method node, the “Earthquake Recurrence Intervals” approach is assigned a weight of 0.2, the weight assigned to data set 1, and the “Earthquake Count in a Time Interval” approach is assigned a weight of 0.8, the sum of the weights assigned to data sets 2 and 3. For the Recurrence Data node on the “Earthquake Recurrence Intervals” branch, data set 1 then gets a conditional weight of 1.0. For the Recurrence Data node on the “Earthquake Count in a Time Interval” branch, data set 2 gets a conditional weight of 0.75 ( $= [0.6]/[0.8]$ ) and data set 3 gets a conditional weight of 0.25 ( $= [0.2]/[0.8]$ ).

### *Earthquake Recurrence Model*

As discussed in Section 5.3.3, the Poisson model is used as the default earthquake recurrence model, with a weight of 1.0 for the Charlevoix RLME source, as there are not sufficient data to justify including an alternative model.

### RLME Annual Frequency

The final node of the logic tree addresses the uncertainty distributions for the annual frequency of RLMEs. These distributions were developed using the methodology described in Section 5.3.3.1. For data set 1 the relative likelihood of various values of the recurrence rate parameter was developed using Equation 5.3.3-4 and the observations of one closed recurrence interval between the 1663 and 1870 earthquakes and one open interval post the 1870 earthquake. The resulting relative-likelihood-based distribution was represented by the five-point discrete distribution listed in Table 6.1.1-1. For data set 2 the relative-likelihood-based distribution was developed using Equation 5.3.3-2, with  $N$  equal to three earthquakes and  $T$  uniformly distributed between 6 and 7 kyr. The distribution for data set 3 was also developed using Equation 5.3.3-2, with  $N$  equal to four earthquakes and  $T$  uniformly distributed between 9.5 and 10.2 kyr. The resulting distributions for RLME recurrence frequency are listed in Table 6.1.1-1.

#### 6.1.2 Charleston

The September 1 (August 31 local time), 1886, E[**M**] 6.90, earthquake that occurred in the Charleston, South Carolina, area is the largest historical earthquake ever recorded in the Eastern United States. This earthquake produced modified Mercalli intensity (MMI) X shaking in the epicentral area near Charleston, and was felt as far away as Chicago (Johnston, 1996c). Strong ground shaking during the 1886 Charleston earthquake resulted in extensive liquefaction, which was expressed primarily as sand-blow craters at the ground surface (Dutton, 1889). Because no primary tectonic surface rupture has been identified as the causative structure for the 1886 earthquake, a combination of geologic, geophysical, geomorphic, and instrumental seismicity data have been used by multiple investigators to suggest several different faults as the potential source for Charleston-area seismicity (e.g., Behrendt et al., 1981; Talwani, 1982; Hamilton et al., 1983; Behrendt and Yuan, 1987; Marple and Talwani, 2000; Weems and Lewis, 2002; Talwani and Katuna, 2004; Dura-Gomez and Talwani, 2009; Talwani and Dura-Gomez, 2009; Chapman and Beale, 2008, 2010).

The existence of pre-1886 sand-blow craters and other paleoliquefaction features that occur throughout coastal South Carolina also provides evidence for prior strong ground motions during prehistoric large earthquakes in the region (e.g., Obermeier et al., 1989; Weems and Obermeier, 1990; Amick et al., 1990a, 1990b; Talwani and Schaeffer, 2001; Talwani et al., 2008). Paleoliquefaction studies conducted in coastal South Carolina since the 1980s provide evidence that the Charleston seismic source exhibits RLMEs and appears to be confined to the Charleston area. Based on the strong field evidence for RLMEs derived from the study of liquefaction and paleoliquefaction features, the Charleston seismic zone is characterized as an RLME source. Appendix Table D-6.1.2 (data summary table) lists the references that were reviewed to characterize the Charleston RLME source, and Appendix Table C-6.1.2 (data evaluation table) lists the data that were explicitly used to constrain the characterization of this RLME source. Neither the 1886 nor the prehistoric (i.e., pre-1886) earthquakes in the Charleston area can be definitively attributed to any specific fault or fault zone at the present time.

### 6.1.2.1 Evidence for Temporal Clustering

The first node of the logic tree (Figure 6.1.2-1) addresses the issue of temporal clustering of earthquakes in the present tectonic stress regime (see Section 5.1.2). The rates of deformation suggested by paleoliquefaction data and the lack of surface features that would be expected if those deformation rates persisted over the long term lead to the conclusion that either the recent sequence of earthquakes is an isolated occurrence in time, or such sequences occur as clusters with long intercluster periods of seismic quiescence. The recurrence behavior of the large earthquakes in the Charleston seismic zone therefore may be highly variable through time, such that periods of activity alternate with periods of quiescence. Section 5.1.2 provides a definition and discussion of the temporally clustered earthquake model.

Geologic and geomorphic observations suggest that inter-event times of large earthquakes in the Charleston seismic zone since the mid-Holocene (approximately hundreds to a few thousand years; see Section 6.1.2.5) are not characteristic of the region over longer-term periods. For example, based on reprocessed seismic reflection data, Chapman and Beale (2008, 2010) note evidence of a steeply dipping, down-to-the-east normal fault with approximately 200 m (656 ft.) of vertical offset in early Mesozoic sedimentary and volcanic rocks. They also report that overlying Cretaceous and Tertiary coastal plain sediments show approximately 10 m (33 ft.) of reverse up-to-the-east minor reverse displacement. Based on the minor amounts of Cretaceous- and-younger vertical separation associated with subsurface faults in the Charleston area, the mid-Holocene to modern seismicity rates inferred from the paleoliquefaction record are not interpreted to be indicative of the longer-term behavior of the Charleston seismic zone.

Additionally, geomorphic observations suggest that the high rate of recurrence of large earthquakes within the Charleston seismic zone inferred from mid-Holocene to modern seismicity is not indicative of the longer-term behavior of the Charleston seismic zone. A protracted period of large earthquakes recurring on the order of hundreds to a few thousand years apart would produce tectonic landforms with clear geomorphic expression, such as those present in regions of the world with comparably high rates of moderate to large earthquakes. For example, faults in the Eastern California shear zone with submillimeter-per-year slip rates and recurrence intervals on the order of about 5,000 years have clear expression in the landscape (Rockwell et al., 2000). The fact that such landforms are not evident in the Charleston area suggests that the Charleston source may have a recurrence rate that is highly variable through time. Therefore, sequences of earthquakes spaced about 500 to 1,000 years apart may be followed by quiescent intervals of many thousands of years.

Based on the geologic and geomorphic lines of evidence discussed above, the high rate of mid-Holocene to modern seismicity in the Charleston seismic zone is not interpreted to be a long-lived phenomenon. However, because no data definitively demonstrate whether the Charleston seismic zone is currently in or out of a temporal cluster, the Charleston RLME seismic source is modeled as “in” a temporal cluster with a weight of 0.9 and “out” of a temporal cluster with a weight of 0.1 in this study (Figure 6.1.2-1).

### 6.1.2.2 Localizing Feature

The second node of the Charleston RLME source logic tree indicates whether future earthquakes in the Charleston seismic zone will be associated with a specific localizing tectonic feature (Figure 6.1.2-1). As described in Section 6.1.2.3, numerous faults are postulated in the Charleston area, but there is no direct evidence that any structure is an active tectonic feature. Moreover, the 1886 earthquake is not definitively attributed to any particular fault or fault zone. Therefore, the “Random in Zone” option is given a 1.0 weight in the model. This modeling decision reflects the interpretation that future Charleston earthquakes will not necessarily occur on any known fault or fault zone, but rather somewhere within the alternative configurations for the Charleston RLME source shown on Figure 6.1.2-2.

### 6.1.2.3 Geometry and Style of Faulting

The third through fifth nodes of the Charleston RLME source logic tree address parameters that characterize source geometry, seismogenic crustal thickness, and rupture orientation for the Charleston RLME seismic source zones (Figure 6.1.2-1). The source characterization for Charleston comprises the following three alternative configurations (Figure 6.1.2-2):

- Charleston Local—The small “local” configuration includes the 1886 meizoseismal area (Bollinger, 1977); the preponderance of 1886 liquefaction features (e.g., Dutton, 1889; Talwani and Schaeffer, 2001); instrumentally located earthquakes in the Middleton Place–Summerville seismic zone (Madabhushi and Talwani, 1993); and numerous postulated faults (e.g., Weems and Lewis, 2002; Talwani and Katuna, 2004; Bartholomew and Rich, 2007; Talwani and Dura-Gomez, 2009).
- Charleston Narrow—The “narrow” configuration contains postulated north-northeast-striking structures, including the postulated Woodstock fault (Talwani, 1982); the southern segment of the postulated East Coast fault system (Marple and Talwani, 2000); and one interpretation of the location of Chapman and Beale’s (2009) “fault C.”
- Charleston Regional—The large “regional” configuration envelops most of coastal South Carolina, including the preponderance of pre-1886 paleoliquefaction features and postulated faults, and extends offshore to include the Helena Banks fault zone (Behrendt and Yuan, 1987).

For seismogenic crustal thickness, the fourth node of the logic tree (Figure 6.1.2-1), the three alternative Charleston source configurations adopt values and weights (shown in brackets) of 15 km (9 mi.) [0.2], 20 km (12 mi.) [0.4], and 25 km (16 mi.) [0.4]. Seismogenic crustal thickness in the Charleston area is not well constrained, but available data are consistent with these values. Bollinger (1983) indicates that seismogenic thickness in the Charleston area is poorly constrained, but he estimates a value of 12 km (7.5 mi.) for the 1886 earthquake on the basis of empirical scaling relations. Dura-Gomez and Talwani’s (2009) relocated small-magnitude earthquakes in the Charleston area indicates depths to 16 km (10 mi.), with most hypocenters between 3 and 13 km (2 and 8 mi.) depth. Moreover, the CEUS SSC Project default values for seismogenic crustal thickness are consistent with those used in previous SSCs for Charleston. Bollinger (1992) adopts depths of 14 and 25 km (8.5 and 15.5 mi.) for his “Local Charleston”

and “SC Piedmont and Coastal Plain” zones, respectively. Chapman and Talwani (2002) adopt a value of 25 km (15.5 mi.) in their source characterization developed for the South Carolina Department of Transportation. Silva et al. (2003) adopt values of 16 and 20 km (10 and 12.5 mi.) depth, inferred from contemporary seismicity.

The remaining data used to constrain each of these three alternative configurations are summarized below and are shown on Figures 6.1.2-3, 6.1.2-4, 6.1.2-5a, and 6.1.2-5b. Additional descriptions of the data constraining the Charleston model are provided in Appendix Table C-6.1.2.

### *Charleston Local Source*

The Charleston Local source configuration is an approximately 100 by 50 km (60 by 30 mi.) northeast-elongated zone centered on the 1886 Charleston meizoseismal area (area of greatest damage) (Figures 6.1.2-5a and 6.1.2-5b). The Charleston Local source completely incorporates the 1886 earthquake MMI X isoseismal (Bollinger, 1977); the majority of identified Charleston-area tectonic features and inferred fault intersections (e.g., Weems and Lewis, 2002; Talwani and Katuna, 2004; Bartholomew and Rich, 2007; Talwani and Dura-Gomez, 2009); and the majority of reported 1886 liquefaction features (e.g., Dutton, 1889; Talwani and Schaeffer, 2001). The Charleston Local source also envelops instrumentally located earthquakes in the Middleton Place–Summerville seismic zone (Tarr et al., 1981; Tarr and Rhea, 1983; Madabhushi and Talwani, 1993). The Charleston Local source excludes the northern extension of the southern segment of the postulated East Coast fault system (Marple and Talwani, 2000) because this system extends well north of the meizoseismal zone and is included in the Charleston Narrow source geometry. The Charleston Local source also excludes outlying liquefaction features, because liquefaction occurs as a result of strong ground shaking that may extend well beyond the extent of the causative fault.

In summary, the Charleston Local source configuration envelops (1) the meizoseismal area of the 1886 earthquake; (2) the area containing the majority of local tectonic features (although many have large uncertainties associated with their existence and activity); (3) the Middleton Place–Summerville seismic zone; and (4) the area of greatest density of 1886 liquefaction and prehistoric liquefaction. These four observations suggest that future earthquakes having magnitudes comparable to that of the 1886 Charleston earthquake most likely will occur within the volume of crust defined by the Charleston Local source configuration. Therefore, because a preponderance of evidence supports the interpretation that the seismic source for the 1886 Charleston earthquake is located in a relatively restricted area defined by the Charleston Local source, the Charleston Local source is given a relatively high weight of 0.50 in the model.

Future ruptures in the Charleston Local source are oriented northeast, parallel to the long axis of the zone and the regional structural grain of the Appalachian orogen. Future ruptures are modeled as occurring on vertical strike-slip faults. All boundaries of the Charleston Local source are strict, such that ruptures are not allowed to extend beyond the zone boundaries.

### *Charleston Narrow Source*

The Charleston Narrow source configuration is an approximately 65 by 30 km (40 by 20 mi.), north-northeast-oriented source (Figures 6.1.2-5a and 6.1.2-5b). The geometry of the Charleston Narrow source is constrained on the basis of postulated faults and tectonic features in the Charleston area, including (1) the proposed Woodstock fault (Talwani, 1982); (2) the zone of river anomalies (Marple and Talwani, 1993) and the southernmost portion of the southern segment of the proposed East Coast fault system (Marple and Talwani, 2000); (3) the proposed Woodstock, Ashley River, Sawmill Branch, Lincolnvillle, and Charleston faults (Talwani and Dura-Gomez, 2009); and (4) one interpretation of the location of “fault C” by Chapman and Beale (2009), based on reprocessed seismic reflection lines. These postulated faults and tectonic features strike generally northeast and are located in the same narrowly constrained area. However, the Charleston Narrow source is not modeled as any particular fault, but rather as an area that represents the possibility that one or more of these features may exist and may be active. As described below in Section 6.1.2.5 (Recurrence), the Brownian Passage Time (BPT) renewal model is applied with low weight to the Charleston Narrow source configuration because it is the most “fault-like” of the alternative configurations.

The northeast and southwest extents of the narrow source are defined by fault mapping from Dura-Gomez and Talwani (2009) and Talwani and Dura-Gomez (2009). Marple and Talwani’s (2000) depiction of the southern segment of the East Coast fault system extends northeast beyond the narrow source configuration. However, according to Dura-Gomez and Talwani (2009) and Talwani and Dura-Gomez (2009), evidence for the existence and activity of the East Coast fault system is greatest in the south (within the narrow source configuration) and decreases northeastward (beyond the narrow source configuration). The northeast and southwest boundaries of the Charleston Narrow source configuration are leaky, such that ruptures that initiate within the zone are allowed to extend beyond the zone boundaries in those directions, but by no more than 50 percent of the rupture length beyond the boundary.

The Charleston Narrow source configuration includes postulated faults with varying degrees of evidence of existence, none of which has clear evidence for Neogene activity. The Charleston Narrow source configuration is given a 0.30 weight in the CEUS SSC model.

Future ruptures in the Charleston Narrow source are oriented north-northeast, parallel to the long axis of the zone. Future ruptures are modeled as occurring on vertical strike-slip faults. As described above, the northeast and southwest boundaries of the Charleston Narrow source are leaky, whereas the northwest and southeast boundaries of the Charleston Narrow source are strict, and ruptures are not allowed to extend beyond the zone boundaries to the northwest and southeast.

### *Charleston Regional Source*

The Charleston Regional source configuration is an approximately 260 by 150 km (160 by 95 mi.) source that entirely envelops both the local and narrow zones. The regional source extends to the northeast and southwest to capture the preponderance of prehistoric paleoliquefaction features; to the southeast to include the offshore Helena Banks fault zone (Behrendt and Yuan,

1987); and inland to capture earthquakes in the Bowman seismic zone (Tarr et al., 1981; Tarr and Rhea, 1983; Smith and Talwani, 1985). The elongation and orientation of the Charleston Regional source is roughly parallel to the regional structural grain of the Appalachian orogen as well as to the elongation of 1886 isoseismals (Bollinger, 1977; Figures 6.1.2-5a and 6.1.2-5b).

The large area covered by the Charleston Regional source reflects the uncertainty associated with the seismic source or sources that produced the 1886 and prehistoric earthquakes. The size of the regional source configuration is based partially on consideration of the liquefaction magnitude-bound relation developed for the CEUS (Olson et al., 2005b; Olson, 2009) and the mapped extent of paleoliquefaction features. The inlandmost paleoliquefaction features are found along the Edisto River, approximately 80 km (50 mi.) from the coast (Figures 6.1.2-3 and 6.1.2-5a; Obermeier, 1996, figure 7.6) and typically are smaller than those found nearer the coast. The regional source extends inland of these features, however, in recognition of the fact that liquefaction susceptibility generally decreases further inland due to material properties and saturation level. The regional source extends offshore because, based on the distribution of liquefaction and paleoliquefaction features, the possibility of an offshore seismic source cannot be precluded. Moreover, the regional source extends offshore to include the northeast-striking Helena Banks fault system, as is clearly shown by multiple seismic reflection profiles, and is interpreted to exhibit Late Miocene offset (Behrendt et al., 1983). Furthermore, the occurrence of at least one light-magnitude earthquake in 2002 (November 11, E[M] 3.98) suggests a possible spatial association of seismicity with the mapped trace of the Helena Banks fault system.

The preponderance of evidence supports the interpretation that the seismic source for Charleston RLMEs is located in a relatively restricted area defined by either the Charleston Local or Narrow source configurations. The larger volume of crust represented by the Charleston Regional source configuration allows for the possibility that Charleston RLMEs are produced by a fault or faults beyond the 1886 meizoseismal zone and beyond the area containing the majority of postulated Charleston faults. The Charleston Regional source configuration is given a 0.20 weight in the CEUS SSC model.

For future rupture orientations in the Charleston Regional source configuration, two alternatives exist: (1) future ruptures oriented parallel to the long axis of the source (northeast) with 0.80 weight, and (2) future ruptures oriented parallel to the short axis of the source (northwest) with 0.20 weight. In these and all cases for Charleston, future ruptures are modeled as occurring on vertical strike-slip faults. All boundaries of the Charleston Regional source are strict, such that ruptures are not allowed to extend beyond the zone boundaries.

#### 6.1.2.4 RLME Magnitude

The sixth node of the Charleston RLME source logic tree defines the magnitude of future large earthquakes in the Charleston RLME source, and assigned weights (Figure 6.1.2-1). Estimates for magnitude are based on estimates of magnitude for the 1886 Charleston earthquake and on geotechnical estimates of magnitudes of prehistoric earthquakes in coastal South Carolina.

### *Estimates of 1886 Earthquake Magnitude*

Estimates for the magnitude of the 1886 Charleston earthquake typically are in the high-6 to mid-7 range, with more modern estimates generally nearer the low end of this range. For example, a geotechnical assessment of 1886 liquefaction data led Martin and Clough (1994) to estimate **M** 7–7.5 for the 1886 Charleston earthquake. Johnston (1996c) estimates **M**  $7.3 \pm 0.26$  for the earthquake, based on isoseismal area regressions accounting for eastern North America anelastic attenuation. The best estimate by Bakun and Hopper (2004) is **M** 6.9, with a 95 percent confidence level corresponding to a range of **M** 6.4–7.1, based on isoseismal area regression, including empirical site corrections. Most recently, Talwani (2009) studied empirical fault length–magnitude relationships and geotechnical assessments of the 1886 and prehistoric Charleston earthquakes and derives a best estimate of **M** 7.0 for the 1886 earthquake. The CEUS SSC earthquake catalog assigns  $E[M]$  6.90 to the 1886 Charleston earthquake.

### *Geotechnical Estimates of Prehistoric Earthquake Magnitudes*

Geotechnical estimates for the magnitudes of prehistoric earthquakes typically are based on one or more of the following factors: (1) empirical relations between size of paleoliquefaction features (e.g., dike width) and magnitude; (2) characterization of in situ sediment properties and the degree of strong ground motion required to liquefy those sediments; (3) distance separating the most distal paleoliquefaction feature from a known or assumed earthquake location; and (4) areal extent of the paleoliquefaction field produced by a single earthquake. Dike widths and other paleoliquefaction-feature dimensional data are lacking for the Charleston region, so magnitude estimates for prehistoric Charleston earthquakes are based on in situ soil properties and the spatial distribution of paleoliquefaction features. Geotechnical estimates for the magnitudes of prehistoric earthquakes in the Charleston seismic zone vary widely, but typically are in the high-5 to high-7 range. These widely varying magnitude estimates reflect the uncertainties associated with the use of paleoliquefaction data (see Appendix E, CEUS Paleoliquefaction Database, Uncertainties Associated with Paleoliquefaction Data, and Guidance for Seismic Source Characterization).

Hu et al. (2002a, 2002b) describe methodologies and provide estimates for the magnitudes of prehistoric Charleston earthquakes based on geotechnical estimates of in situ soil properties. They report magnitude estimates ranging from **M** 6.8 to 7.8 for “large” regional Charleston earthquakes, and from **M** 5.5 to 7.0 for possible “moderate” local earthquakes at Georgetown, South Carolina. A subsequent study by Leon et al. (2005), which includes two of the same three coauthors as Hu et al. (2002a, 2002b), presents lower magnitude estimates for prehistoric Charleston earthquakes. Leon (2003) and Leon et al. (2005) present geotechnical assessments of magnitude for Charleston prehistoric earthquakes that account for the effects of sediment aging. Their magnitude estimates range from **M** 5.5 to 7.2 for “large” regional Charleston earthquakes and from **M** 4.3 to 6.4 for possible “moderate” local earthquakes at Bluffton and Georgetown, South Carolina. Using standard penetration test, cone penetration test, and shear-wave velocity data, Gassman et al. (2009) suggest a preferred magnitude range of **M** 6.7–7.0 for prehistoric, historic, and future earthquakes in the Charleston seismic zone. Based on the interpretation of prehistoric Charleston earthquakes developed as part of the CEUS SSC Project (see Section 6.1.2.5—Recurrence), paleoliquefaction fields are similar to the 1886 earthquake liquefaction

field in location and extent. As such, the prehistoric earthquakes that formed these fields likely had magnitudes similar to the 1886 earthquake.

### Charleston RLME Magnitude

The Charleston RLME source magnitude distribution for future large earthquakes is based on assessment of the currently available data, interpretations of the range of magnitude estimates for the 1886 and prehistoric Charleston earthquakes, and the assumption that future large earthquakes will have magnitudes similar to these earthquakes. The magnitude distribution includes a total of five discrete magnitude values from **M** 6.7 to 7.5, each separated by 0.2 **M** units (Figure 6.1.2-1). It includes a discrete value of **M** 7.3 to represent Johnston’s (1996c) mean estimate for the 1886 earthquake, as well as a higher value of **M** 7.5 to capture a low probability that future large earthquakes in the Charleston seismic source will be greater than **M** 7.3. To represent Bakun and Hopper’s (2004) best estimate of the 1886 Charleston earthquake magnitude, the Charleston RLME source magnitude distribution includes a discrete value of **M** 6.9. The magnitude distribution also includes a lower value of **M** 6.7 to capture a low probability that future large earthquakes in the Charleston seismic source will be less than **M** 6.9.

The resulting RLME magnitude distribution is tabulated below. This distribution results in a weighted mean magnitude of **M** 7.1 for the Charleston RLME seismic source. Aleatory variability in the size of an individual Charleston RLME is modeled as a uniform distribution of  $\pm 0.25$  **M** units centered on the expected RLME magnitude value (Section 5.3.3.4).

<b>Expected Charleston RLME Magnitude (M)</b>	<b>Weight</b>
6.7	0.1
6.9	0.25
7.1	0.3
7.3	0.25
7.5	0.1

### 6.1.2.5 RLME Recurrence

The remaining nodes of the Charleston RLME source logic tree (i.e., nodes seven through twelve) address the uncertainty modeling of the of Charleston RLMEs (Figure 6.1.2-1). Section 1.2.6 of Appendix E provides additional information on paleoliquefaction features in coastal South Carolina.

### *Recurrence Method*

The recurrence data for the Charleston RLME source consists of ages of past RLMEs estimated from the paleoliquefaction record. Therefore, node seven of the logic tree indicates that recurrence for the Charleston RLME source is based solely on the “Earthquake Recurrence Intervals” approach.

### *Time Period*

The eighth node of the Charleston RLME source logic tree assesses length and completeness of the paleoliquefaction record, which are sources of epistemic uncertainty in the CEUS SSC (Figure 6.1.2-1). The paleoliquefaction record along the South Carolina coast extends from 1886 to the mid-Holocene, approximately 5,500 yr BP (Talwani and Schaeffer, 2001). The consensus of scientists who have evaluated these data is that the paleoliquefaction record of earthquakes is complete only for approximately the past 2,000 years and that liquefaction events likely are missing from the older portions of the record (Talwani and Schaeffer, 2001). For this reason, this study places more weight on the paleoseismic record from the most recent 2,000 years of record. The perception that the paleoseismic record may be incomplete from 2,000 to 5,500 yr BP is based on the argument that past fluctuations in sea level have produced intervals of low water table conditions, and thus low liquefaction susceptibility, during which large earthquakes may not be represented in the paleoliquefaction record (Talwani and Schaeffer, 2001). While this assertion may be true, it is also possible that the paleoliquefaction record may be complete back to the mid-Holocene (Talwani and Schaeffer, 2001). Based on these arguments, the approximately 2,000-year record of Charleston earthquakes is given a 0.80 weight in the model, and the approximately 5,500-year record is given a 0.20 weight.

### *Earthquake Count*

The ninth node of the Charleston logic tree addresses the uncertainty in the number of RLMEs that have occurred in the Charleston RLME source (Figure 6.1.2-1). Alternative interpretations of the distribution of paleoliquefaction features include a total of four large earthquakes in the past approximately 2,000 years and between four and six large earthquakes in the past approximately 5,500 years. The alternative characterizations represented in the logic tree are based on (1) interpreted length of the paleoliquefaction record, (2) interpreted types of constraining ages, and (3) evaluations of the area distribution and interpretations of which of the prehistoric liquefaction features were caused by large-magnitude earthquakes centered in the Charleston area and which were caused by moderate-magnitude local earthquakes.

Talwani and Schaeffer (2001) combine previously published data with their own studies of paleoliquefaction features in the South Carolina coastal region to derive possible earthquake recurrence histories for the region. They estimate recurrence intervals of approximately 550 to 1,000 years and interpret the possibility of both moderate- and large-magnitude earthquakes (roughly  $M$  6+ and 7+, respectively). The CEUS SSC Project supplements Talwani and Schaeffer’s (2001) compilation of Charleston paleoliquefaction data with data from other studies (e.g., Noller and Forman, 1998; Talwani et al., 2008) (see Section 1.2.6 of Appendix E).

Talwani and Schaeffer (2001) identify individual earthquake episodes based on regional correlations of prehistoric sand-blow craters with overlapping calibrated radiocarbon ages having 1-sigma (68.3 percent confidence interval) error bands. The standard in paleoseismology, however, is to use calibrated radiocarbon ages with 2-sigma (95.4 percent confidence interval) error bands (e.g., Grant and Sieh, 1994). Likewise, in paleoliquefaction studies, to more accurately reflect the uncertainties in radiocarbon dating and age estimates of paleoliquefaction features, Tuttle (2001) advises the use of calibrated radiocarbon dates with 2-sigma error bands (as opposed to narrower 1-sigma error bands). On Tuttle's (2001) recommendation, the CEUS SSC Project recalibrated and reported the conventional radiocarbon ages presented in Talwani and Schaeffer (2001) with 2-sigma error bands (see Appendix E and the CEUS SSC paleoliquefaction database). This recalibration was performed with the radiocarbon calibration program OxCal version 4.1 (Bronk Ramsey, 2009) using the radiocarbon calibration curve of Stuiver et al. (1998). The recalibrated 2-sigma radiocarbon ages form the basis of the CEUS SSC Project analyses of the timing, location, and magnitude of paleoearthquakes that induced liquefaction in the vicinity of Charleston, South Carolina.

For the Charleston data set, two types of radiocarbon ages are used to constrain the timing of formation of prehistoric sand-blow craters, namely contemporary (or "con") radiocarbon ages, and radiocarbon ages that provide maximum or minimum age constraints on a sand-blow crater (Figure 6.1.2-6). Contemporary ages are those ages interpreted by Talwani and Schaeffer (2001) as closely approximating the time of formation of the sand-blow crater. The data for determining contemporary ages include fragile twigs or stems that became entrained in fine-grained deposits within crater deposits during or very soon after crater formation, and that are thus approximately equivalent in age with time of formation of the feature. Maximum and minimum ages are provided by carbon samples collected from stratigraphic positions below and above a paleoliquefaction feature, respectively. Typically, the estimated ages of paleoliquefaction features from maximum/minimum pairs of radiocarbon samples are broader than those provided by contemporary radiocarbon ages. For this reason, contemporary ages are preferred.

Another reason for preferring contemporary age constraints concerns the specific geologic environment in which the Charleston region sand-blow craters are found. The vast majority of the sand-blow craters are located on the crests of beach ridges in geologic units that are tens to hundreds of thousands of years old or more (McCartan et al., 1984; Obermeier, 1996). Moreover, LiDAR data indicate that the vast majority of these sand-blow craters features are located on local topographic highs, representing areas removed from active deposition that are characterized by ongoing soil formation, stripping, and reworking processes. Considering the geologic environment where the sand-blow craters occur, it is unclear exactly what radiocarbon ages from maximum/minimum samples collected from stratigraphic positions above and below the paleoliquefaction features may mean. However, as described below, the timing of prehistoric earthquakes in the Charleston region is largely constrained by contemporary ages, with the maximum/minimum ages primarily used as possible evidence for constraining spatial extent, and thus the magnitude, of some of the prehistoric liquefaction fields.

Figures 6.1.2-7 and 6.1.2-8 are space-time diagrams showing the 2-sigma radiocarbon age constraints on paleoliquefaction features in the Charleston region as vertical lines, and interpreted earthquakes as colored horizontal bars. Age constraints from samples, or pairs of

samples, used to define each earthquake are shown as vertical colored bars. Appendix E provides a detailed description of the methodologies and uncertainties associated with interpreting prehistoric earthquakes from paleoliquefaction data.

Figure 6.1.2-7 shows the prehistoric earthquake scenario based on contemporary age constraints only. Figures 6.1.2-9 through 6.1.2-13 show in map view the spatial distribution of paleoliquefaction features associated with each interpreted earthquake in the “contemporary ages only” scenario. In this scenario, four large-magnitude regional earthquakes (1886, A, B, and C) have occurred in the past approximately 2,000 years. Two additional earthquakes (D and E) occurred in the past approximately 5,500 years. Yet, based on the possibly limited spatial extent of the liquefaction fields associated with earthquakes D and E, it is unclear from the “contemporary ages only” scenario whether earthquakes D and E were large-magnitude regional earthquakes with liquefaction fields similar to that produced by the 1886 earthquake, or whether they were moderate-magnitude local earthquakes. Table 6.1.2-1 summarizes the age constraints and sizes (regional or local) of interpreted prehistoric Charleston earthquakes A through E from the “contemporary ages only” scenario.

Figure 6.1.2-8 shows the prehistoric earthquake scenario based on contemporary and maximum/minimum age constraints (the “all ages” scenario). In this figure, the maximum/minimum age constraints are shown as vertical dashed lines to differentiate them from the solid vertical lines that represent contemporary age constraints. Unpaired maximum or minimum age constraints are shown as up or down arrows, respectively, and typically are not useful for interpreting prehistoric earthquakes. Figures 6.1.2-14 through 6.1.2-18 show in map view the spatial distribution of paleoliquefaction features associated with each interpreted earthquake in the “all ages” scenario. The results of the “contemporary ages only” and “all ages” scenarios are nearly identical in terms of the timing of past earthquakes in coastal South Carolina.

However, there are potentially important differences between the two scenarios with respect to the interpreted geographic extent of liquefaction in prehistoric earthquakes D and E. Specifically, earthquakes D and E in the “contemporary ages only” scenario may have produced localized liquefaction fields (Figures 6.1.2-13 and 6.1.2-14) and therefore may have been moderate-magnitude earthquakes. The “all ages” scenario, however, indicates that earthquake D and possibly earthquake E produced regional liquefaction fields (Figures 6.1.2-17 and 6.1.2-18) and, therefore, likely were large magnitude. Table 6.1.2-2 summarizes the age constraints and sizes (regional or local) of interpreted prehistoric Charleston earthquakes A through E.

The ninth node of the Charleston logic tree shows weights for the possible combinations of prehistoric large earthquakes for the approximately 2,000-year and 5,500-year records (Figure 6.1.2-1). Earthquake chronologies based on the “contemporary ages only” scenario are assigned a weight of 0.80 because, as discussed above, contemporary ages provide the best approximations of the timing of formation of Charleston area sand-blow craters. Earthquake chronologies based on the “all ages” scenario are assigned a weight of 0.20 because, as discussed above, it is unclear exactly what radiocarbon ages from maximum/minimum samples collected from stratigraphic positions above and below the paleoliquefaction features may mean.

### Earthquake Recurrence Model

The tenth node of the Charleston RLME source logic tree defines the earthquake recurrence models used for the regional, local, and narrow source zones (Figure 6.1.2-1). For the regional and local sources, only the Poisson model is used. For the more “fault-like” narrow source zone, the Poisson model is assigned 0.90 weight, and the BPT renewal model is assigned 0.10 weight. Use of the BPT renewal model requires specification of the coefficient of variation of the repeat time for RLMEs, parameter  $\alpha$ . As discussed in Section 5.3.3, the uncertainty distribution for  $\alpha$  developed by Working Group (2003) was adopted. This distribution is shown on the eleventh node of the Charleston RLME source logic tree (Figure 6.1.2-1). Section 5.3.3 provides additional information regarding the use of the earthquake recurrence models.

### RLME Annual Frequency

The final (twelfth) node of the logic tree addresses the uncertainty distributions for the annual frequency of RLMEs (Figure 6.1.2-1). These distributions were developed using the methodology described in Sections 5.3.3.1 and 5.3.3.2. For the Poisson model, the relative likelihood of various values of the recurrence rate parameter was developed using Equation 5.3.3-4 and the observations of the time intervals between the selected paleoearthquakes and the open interval post the 1886 earthquake. For the renewal model, the relative likelihoods of various values of the mean recurrence interval for RLMEs were developed using Equations 5.3.3-7, 5.3.3-8, and 5.3.3-9 for each set of past RLMEs and specified value of coefficient of variation. The resulting parameters were then used to compute the equivalent annual frequency of RLMEs using Equations 5.3.3-10 and 5.3.3-11.

The data used for the recurrence rate calculations are the time intervals between individual RLMEs for the renewal model case, and the age of the oldest RLME for the Poisson case. These are calculated from the age estimates for each past RLME. With the exception of the 1886 earthquake, these ages are estimated from two types of data, as described above, and are subject to uncertainty. One type of data consists of age dates for samples whose ages are considered to be contemporary with the earthquake occurrence, denoted as CON ages. Each sample has its own age estimate with associated uncertainty. Table 6.1.2-3 lists the sample age data used for each prehistoric earthquake. These data are shown on Figures 6.1.2-7 and 6.1.2-8. For this analysis, the range in CON ages of the samples listed in Table 6.1.2-3 was treated as a two-sigma uncertainty estimate. The uncertainty was approximated by a normal distribution with mean equal to the center of the age range and standard deviation equal to  $\frac{1}{4}$  of the uncertainty range. For the  $i^{\text{th}}$  sample associated with RLME A, the probability distribution for the true age of earthquake A is then given by the normal probability distribution:

$$f(A|A_i) = \exp\left(-\frac{(A - \mu_{A_i})^2}{2\sigma_{A_i}^2}\right) \quad (6.1.2-1)$$

where  $\mu_{A_i}$  and  $\sigma_{A_i}^2$  are the mean and variance of the age of sample  $A_i$ , respectively. The likelihood for the age of A, given all of the associated sample ages, then becomes

$$L(A|A_{1..n}) = \prod_{i=1}^n f(A|A_i) \quad (6.1.2-2)$$

Equation 6.1.2-2 was used to compute the relative likelihood of possible ages for each RLME using the associated liquefaction feature age data in Table 6.1.2-2. These relative likelihoods were then normalized by their sum to produce the uncertainty distributions for the age of each RLME shown on Figure 6.1.2-19 with the label “Con Ages.”

The second type of data associated with the Charleston RLMEs is samples that provide constraints on the event age in terms of representing points in time either before or after each earthquake occurrence. These additional age data, labeled in Table 6.1.2-2 as either “B” for before the earthquake or “A” for after the earthquake, were used to modify the CON age distributions by simulating ages from the CON age distributions shown on Figure 6.1.2-19 and from a normal distribution for the constraining feature age, and rejecting those simulations that violate the age constraints. The process was repeated until 10,000 possible ages were obtained for each RLME; these were then ranked to produce the cumulative distributions labeled “All Ages” on Figure 6.1.2-19.

The uncertainty distributions for RLME annual frequency were then computed by repeatedly simulating samples of RLME dates from the age distributions shown on Figure 6.1.2-19 and computing a relative likelihood distribution for RLME rate from each sample. The resulting distributions were then combined to produce a composite distribution for RLME rate, assigning 0.8 weight to RLME ages sampled from the Con Ages distributions and 0.2 weight to ages from the All Ages distributions. These composite distributions were then represented by five-point discrete approximations. The resulting distributions for RLME recurrence frequency are listed in Tables 6.1.2-4 and 6.1.2-5 for the Poisson and Renewal models, respectively.

### 6.1.3 Cheraw Fault

The Cheraw fault trends northeast and is located on the High Plains in southeastern Colorado, approximately 140 km (85 mi.) east of the Rocky Mountain range front (Crone and Machette, 1995; Crone, Machette, Bradley, et al., 1997; Crone and Wheeler, 2000; Figure 6.1-1). The fault, which has a down-to-the-northwest throw, lies on the western side of the Las Animas arch, a relatively low-relief, 300 km (183 mi.) long, positive structural feature in southeastern Colorado (Curtis, 1988). The crest of the arch lies approximately 20–40 km (12–24 mi.) east of the Cheraw fault.

Crone, Machette, Bradley, et al. (1997) note that the total throw of the fault is not substantial (only tens of meters are demonstrable) and that the fault does not appear to have a long history of recurrent movement. From interpretation of a structure-contour map of the top of the Lower Cretaceous Dakota Sandstone presented by Sharps (1976), Crone, Machette, Bradley, et al. (1997) estimate 6–8 m (20–26 ft.) of down-to-the-northwest throw, which is comparable to the amount of throw on early Quaternary alluvial deposits.

The Cheraw fault, which is mapped for a distance of 46 km (28 mi.), forms a subtle, northwest-facing scarp that can be traced for at least 30 km (18 mi.; Kirkham and Rogers, 1981; Crone,

Machette, Bradley, et al., 1997). Based on the following, Kirkham and Rogers (1981) concluded that the Cheraw fault has been active in the Quaternary: the presence of this scarp, vegetation lineaments, linear ponds, sinkholes, and dissolution pits along the fault trace; the apparent ponding of alluvium against the scarp where the scarp interrupts the gradient of local drainages; and the apparent displacement of the middle Rocky Flats Alluvium.

The fault was first recognized during regional geologic mapping by the USGS (Scott, 1970; Sharps, 1976; Kirkham and Rogers, 1981; Scott et al., 1978). Further paleoseismic field investigations of the Cheraw fault conducted by the USGS provided evidence for multiple surface-faulting earthquakes during the late Pleistocene and Holocene (Crone and Machette, 1995; Crone, Machette, Bradley, et al., 1997). Based on the results of these studies, the Cheraw fault is characterized as an RLME fault source.

Characterization of the Cheraw fault is based on references cited in the following subsections and in Appendix Tables C-6.1.3 Data Evaluation and D-6.1.3 Data Summary. The logic tree for the Cheraw RLME source is shown on Figure 6.1.3-1. Locations of tectonic features and key localities where detailed paleoseismic investigations have been conducted to evaluate the location and activity of the Cheraw fault are shown on Figure 6.1.3-2. The location of the Cheraw fault relative to total magnetic anomaly and residual isostatic gravity data is shown on Figure 6.1.3-3.

#### 6.1.3.1 Evidence for Temporal Clustering

The first node of the logic tree (Figure 6.1.3-1) addresses the issue of temporal clustering of earthquakes in the present tectonic stress regime (see Section 5.1.2). The Cheraw fault lies within a seismically quiescent region of eastern Colorado, but has evidence for two to three surface ruptures in the past 20–25 kyr (Crone, Machette, Bradley, et al., 1997). Crone, Machette, Bradley, et al. (1997) concluded that three surface-rupturing earthquakes (at about 8, 12, and 20–25 ka) are recorded in a trench excavated across the Cheraw fault. The evidence for the penultimate earthquake as presented by Crone, Machette, Bradley, et al. (1997) is not as definitive as the evidence for the earliest and latest earthquakes (Dr. A. Crone, USGS, electronic comm., April 21, 2010). Based on both review of the trench logs and data used to support the interpretation of three earthquakes reported by Crone, Machette, Bradley, et al. (1997) and communications with Dr. A. Crone, the likelihood that the latest Pleistocene displacement on the Cheraw fault is the result of two surface ruptures is given a weight of 0.4, and the published interpretation of three earthquakes is given a slightly higher weight (0.6).

Crone, Machette, Bradley, et al. (1997) speculate that earthquakes older than about 25 kyr must have occurred before about 100 ka because of the time needed to incise, widen, and backfill the paleo-stream channel that is now filled with latest Pleistocene deposits (Crone and Wheeler, 2000). The cumulative vertical offset on the Cretaceous shale is 3.2–4.1 m (10.5–13.5 ft.), which is the total offset of the two or three late Quaternary earthquakes (Crone, Machette, Bradley, et al., 1997). Crone and others (Crone, Machette, and Bowman, 1997; Crone, Machette, Bradley, et al., 1997) suggest that these earthquakes may be part of a pattern of temporal clustering of earthquakes in which one or more earthquakes occur in a short period of time (10–15 kyr) and that the interval of high activity is bounded by longer intervals (>100 kyr) of inactivity.

Based on the geomorphic and geologic lines of evidence described above, the within-cluster branch of the logic tree is given a weight of 0.9, and the out-of-cluster branch is given a weight of 0.1 (Figure 6.1.3-1). There is no evidence to suggest the Cheraw fault is out of a cluster based on the fact that the time elapsed since the last Holocene earthquake (approximately 8,000 years; Crone, Machette, Bradley, et al., 1997) is not longer than the mean intracluster recurrence rate for two or three earthquakes in 20–25 kyr (approximately 13,158 or 8,333 years). This weighting is consistent with the weightings for other RLMEs that exhibit clustered behavior (e.g., New Madrid seismic zone, Meers fault).

### 6.1.3.2 Geometry and Style of Faulting

The Cheraw fault is well expressed as a topographic feature on the Shuttle Radar Topography Mission (SRTM) topographic data along its entire 46 km (28 mi.) long mapped extent; a subtle northwest-facing scarp is present along at least 30 km (18 mi.; Crone, Machette, Bradley, et al., 1997). Dan Clark (Geoscience Australia) recently suggested that the fault may extend farther to the northeast, based on review of the Shuttle Radar Topographic Mission (SRTM) data, but no field investigation of this possible extension has been conducted (Dr. A. Crone, USGS, electronic comm., March 3, 2010). The possible northeast extension (approximately 16 km [10 mi.]) parallels and appears to coincide in part with a railway line. Thus, it is not certain if the feature is a culture feature or a culturally modified tectonic feature.

The second and third branches of the logic tree indicate that the Cheraw RLME source is modeled as a fault source and that two alternative total lengths of the fault are considered. The topographically well-expressed 46 km (28 mi.) long fault is given highest weight (0.8); the longer (extended) length of 62 km (38 mi.), which is based solely on interpretation of SRTM topographic data, is given much lower weight (0.2) pending confirmation by field investigations.

Based on the paleoseismic evidence for multiple surface ruptures on the Cheraw fault, it likely extends to seismogenic depths. There is little seismicity within the vicinity of the Cheraw fault from which to assess the thickness of seismogenic crust. The generic distribution of 13 km (weight of 0.4), 17 km (weight of 0.4), and 22 km (weight of 0.2) is used.

The downdip geometry of the Cheraw fault is not well known. In the near-surface trench exposures, the main fault dips steeply (70–80 degrees) to the northwest. The dip at depth, however, is uncertain. Crone and Wheeler (2000) give an average dip of 66 degrees based on the average dip of the main fault as mapped by Crone, Machette, Bradley, et al. (1997) in the only exposure of the fault, a 3–4 m (10–13 ft.) deep trench. The USGS characterization of the fault for use in the National Seismic Hazard Maps uses a dip of 60 degrees (2002 National Seismic Hazards—Fault Parameters database). Based on the observation of a steeply dipping main fault near the ground surface and analogy to well-documented seismogenic normal faults with dips of approximately 50 degrees at seismogenic depth in the Western United States, the following dip values and associated weights are used in this study to characterize the Cheraw fault: 50°NW (0.6), 65°NW (0.4).

The sense of motion on the Cheraw fault is not well known, but it is inferred to be a down-to-the-northwest normal fault based on the attitude of the faults exposed in the trench across the scarp

(Crone, Machette, Bradley, et al., 1997). No compelling evidence of lateral slip was observed on the Cheraw fault, and normal displacement is consistent with the attitude (steeply dipping to the northwest) and orientation (northeast-southwest strike) of the fault scarp in the prevailing stress field of the Midcontinent (east-northeast to northeast maximum horizontal stress direction) (Dr. A. Crone, USGS, electronic comm., January 11, 2010).

### 6.1.3.3 RLME Magnitude

The magnitude distribution for the Cheraw RLME source is defined using magnitude estimates from empirical relationships relating earthquake magnitude to fault rupture characteristics. Potential rupture lengths, rupture areas, and displacement-per-event data from trenching investigations are considered. The following relationships are used:

- Wells and Coppersmith (1994)—surface rupture length, subsurface rupture length, maximum displacement, average displacement, and rupture area for all faults.
- Somerville et al. (2001)—rupture area.

The rupture characteristics that were used in these relationships were defined as described below.

#### *Rupture Length*

Two alternative rupture lengths are considered: 46 km (28.5 mi.), the total length of the well documented Quaternary faulting, and 30 km (18.5), the length of the fault with geomorphic expression of recent faulting.

#### *Average and Maximum Displacement*

Paleoseismic trenching investigations provide data for estimating a cumulative post-25 ka vertical displacement of approximately 3.2–4.1 m (10.5–13.5 ft.) (similar to the 3.3 m [10.8 ft.] estimated from the drilling results at this site [Crone and Machette, 1995]) and displacement per event of approximately 1.5 m (5 ft.); 1.1–1.6 m (3.6–5.2 ft.); and 0.5–1.1 m (1.6–3.6 ft.), respectively, for the three most recent earthquakes (oldest to youngest) (Crone, Machette, Bradley, et al., 1997). However, as discussed in Section 6.1.3.4, the evidence for the penultimate earthquake is not conclusive, and the displacements measured for this earthquake and the younger earthquake may have occurred in a single earthquake. Based on these observations, the average slip per earthquake at this site would range from 1.1 to 2.1 m (3.6 to 6.9 ft.); the maximum slip during a single earthquake would range from 1.6 m (5.2 ft.) to as much as 2.6 m (8.5 ft.).

The trench site was selected because it is along a part of the fault where a prominent scarp is present on deposits incised into and therefore, younger than Rocky Flats Alluvium. Given the location of the site along the central part of the Quaternary fault and the prominence of the scarp at this locality, it is likely that these measured vertical offsets represent maximum rather than average displacements. However, since there is insufficient information to judge whether the

displacements per earthquake measured at the sole trench site along the Cheraw fault represent average or maximum values, both relationships are considered.

### *Rupture Area*

Potential rupture area for the Cheraw fault rupture was estimated using rupture length, fault dip, and down-dip fault width estimates for the Cheraw fault. Empirical relationships defined by Wells and Coppersmith (1994) for all slip types and by Somerville et al. (2001) for CEUS earthquakes are used to estimate magnitude from fault area.

Based on the resulting magnitudes from these parameters (rupture length, displacement per event, and rupture area; see Table 6.1.3-1), the maximum magnitude distribution tabulated below was assigned to the Cheraw fault.

<b>Expected Cheraw RLME Magnitude (M)</b>	<b>Weight</b>
6.8	0.3
7.0	0.3
7.2	0.3
7.4	0.1

### 6.1.3.4 RLME Recurrence

The remaining nodes of the Cheraw RLME logic tree address the uncertainties in modeling the recurrence rate of Cheraw RLMEs

#### *Recurrence Method*

Two types of data are available for assessing the recurrence frequency of Cheraw RLMEs. The first is the average slip rate of the fault and the second is the number and timing of previous RLMEs, allowing application of the “Earthquake Recurrence Intervals” approach. These two approaches are considered equally viable for assessing RLME annual frequency and are given equal weight in the Cheraw RLME source logic tree (Figure 6.1.3-1).

#### *Recurrence Data*

The average latest Pleistocene to Holocene slip rate on the Cheraw fault is on the order of 0.14–0.18 mm/yr; more rigorous calculations based on timing and displacement data inferred from the trench excavation allow for a range of values between 0.23 and 0.09 mm/yr (Crone and Wheeler, 2000). These slip rate values apply to periods of time when the fault is in an active phase. During that time, two or three surface rupturing earthquakes have occurred, with the oldest occurring

20-25 ka. As outlined above in Section 6.1.3.1, the evidence for the penultimate earthquake reported by Crone, Machette, Bradley, et al. (1997) is less definitive than the evidence for the earliest and latest earthquakes, but the three-event scenario is still slightly favored by Dr. Crone, one of the principal investigators for the trenching investigation. Based on review of the data and discussions with Dr. Crone, the published interpretation of three earthquakes is therefore slightly favored (weight of 0.6) over two (weight of 0.4).

A long-term average slip rate can be estimated for the Cheraw fault. Drilling results from the USGS investigations show that about 7–8 m (23–26 ft.) of throw has occurred on the Cheraw fault since deposition of an alluvial deposit tentatively correlated with the early Pleistocene Rocky Flats Alluvium estimated to be 1.2 Ma (Crone and Wheeler, 2000). These data yield a best-estimate long-term slip rate of  $\leq 0.007$  mm/yr (Crone and Wheeler, 2000). It is noted, however, that subsequent work on the Rocky Flats Alluvium along the Colorado Front Range using terrestrial cosmogenic nuclide dating techniques has shown that the age of Rocky Flats Alluvium ranges between about 400 ka and 2 Ma, with age increasing with distance from the range front (Riihimaki et al., 2006). The long-term average slip rate thus could be a factor of two higher or lower than the best-estimate rate if a broader age uncertainty is considered.

Because of the temporal clustering of earthquakes, it may not be appropriate to characterize the rate of movement on the fault using the long-term average. If it is assumed that the total displacement occurred in two intervals of clustered behavior comparable to the recent one from approximately 25 to 8 ka, the interval of time between the clusters could be several hundred thousand years.

#### *Earthquake Recurrence Model*

As discussed in Section 5.3.3, the Poisson model is used as the default earthquake recurrence model with weight 1.0 for the Cheraw RLME source as there are not sufficient data to justify including an alternative model.

#### *RLME Annual Frequency*

The final node of the logic tree addresses the uncertainty distributions for the annual frequency of RLMEs. These distributions were developed using the methodology described in Section 5.3.3.1.

For the “in-cluster” case and the “Earthquake Recurrence Intervals” approach, the relative likelihood of various values of the recurrence rate parameter was developed using Equation 5.3.3-4 and the observation of one or two closed recurrence intervals and one open interval post the 20-25 ka earthquake. Thus the value of  $\sum_{i=1}^N t_i + t_0$  was assumed to be uniformly distributed between 20 and 25 ka with  $N$  either 1 or 2. The resulting discrete uncertainty distributions for RLME annual frequency are listed in Table 6.1.3-2.

For the in-cluster slip-rate case, the fault slip rates were assessed by dividing the late Quaternary vertical offset by the age of the oldest earthquake in the trench. Uncertainty in the offset was incorporated by sampling from a uniform distribution between 3.2 and 4.1 m (10.5 and 13.5 ft.), and uncertainty in the age was incorporated by sampling from a uniform distribution between 20 and 25 ka. The results of 10,000 simulations were ranked to produce a cumulative distribution for slip rate. Because the range of results was narrow (0.13 to 0.20 mm/year), the three-point approximation developed by Keefer and Bodily (1983) was used to define the discrete distribution for recurrence rate listed in Table 6.1.3-3.

“Out-of-cluster” RLME recurrence rates for the Cheraw fault are based on the estimated elapsed time between the Holocene/late Pleistocene earthquakes and the penultimate earthquake cluster. Longer recurrence intervals of either 200, 350, or 500 kyr are expected based on the geomorphic evidence for a minimum period of at least 100 kyr between the oldest earthquake recorded in the trench and the previous earthquake, and the observation that only two or three surface-rupturing earthquakes (similar in size to the recent surface-rupturing earthquakes) have occurred. These values are assigned equal weight and were inverted to produce RLME frequencies. The resulting distribution for out-of-cluster RLME frequency is listed in Table 6.1.3-4.

The out-of-cluster slip rate for the Cheraw fault was assessed by dividing the total offset of the Rocky Flats Alluvium by its estimated age. The total offset is assumed to be uniformly distributed between 7 and 8 m (23 and 26 ft.). The age of the alluvium is most likely between 1.2 and 2 Ma, but could be as young as 0.4 Ma. A trapezoidal probability density function with uniform probability between 1.2 and 2 Ma, tapering to zero at 0.4 Ma, was used to represent this uncertainty. A distribution for long-term slip rate was developed by repeatedly sampling from the offset and age distributions and ranking the resulting values of slip rate. The results were then approximated using the Miller and Rice (1983) five-point discrete approximation to produce the out-of-cluster slip-rate distribution listed in Table 6.1.3-5.

#### **6.1.4 Meers Fault**

The Meers fault in southwestern Oklahoma (Figure 6.1.4-1) is the southern boundary of the Wichita frontal fault system, which separates the early Paleozoic Anadarko basin to the northeast from the late Paleozoic (Carboniferous) Arbuckle-Wichita-Amarillo uplift of the Ouachita orogeny to the southwest (Jones-Cecil, 1995; McConnell, 1989). During the Carboniferous, predominately oblique, left-lateral, and reverse slip along the Wichita frontal fault system uplifted the Wichita and related mountains and generated about 10 km (6 mi.) of total structural relief. Slip on the Meers fault contributed to approximately 2 km (1 mi.) of down-to-the-north vertical offset (Jones-Cecil, 1995).

Paleoseismic studies of the Meers fault conducted in the late 1980s and the 1990s documented late Cenozoic reactivation of the Meers fault, including two Holocene surface-rupturing events with left-lateral reverse slip (Crone and Luza, 1990; Kelson and Swan, 1990; Swan et al., 1993). Based on the evidence for RLMEs, the Meers fault is characterized as an RLME source. Appendix Table D-6.1.4 lists the references that were reviewed in developing the characterization of the Meers RLME source, and Appendix Table C-6.1.4 lists the data that were

explicitly used in constraining the characterization. Figure 6.1.4-2 shows the Meers RLME source logic tree.

#### 6.1.4.1 Evidence for Temporal Clustering

The first node of the logic tree (Figure 6.1.4-2) addresses the issue of temporal clustering of earthquakes in the present tectonic stress regime (see Section 5.1.2). Based on stratigraphic relations observed within trenches, soil pits, and hand auger samples, Swan et al. (1993) demonstrated that the Meers fault experienced two surface-rupturing earthquakes within the last approximately 3,000–4,000 years. However, based on observations of offset ridge crests across the fault, it is also apparent that there have been previous earthquakes on the fault (Crone and Luza, 1990; Ramelli and Slemmons, 1986; Swan et al., 1993). Swan et al. (1993) used correlations between soils observed along the Meers fault and more distant, dated soils to argue that any previous earthquakes along the Meers fault occurred prior to 200–500 ka. Based on these observations, the Meers fault appears to exhibit clustered earthquake behavior. Accordingly, the Meers fault can be classified currently as either “in” or “out” of an earthquake cluster.

The in-cluster branch of the logic tree is given a weight of 0.8 and the out-of-cluster branch a weight of 0.2. The weights reflect that there is no evidence to suggest the Meers fault is out of a cluster, based on the fact that the time elapsed since the last Holocene event (approximately 1,500 years) (Swan et al., 1993) is shorter than the weighted mean intracluster recurrence rate (approximately 2,300 years); see discussion of recurrence rates below. The weights also reflect that there is no evidence of current activity along the fault (i.e., seismicity).

#### 6.1.4.2 Localizing Feature

The second branch of the logic tree (Figure 6.1.4-2) describes whether future earthquakes associated with the Meers fault structure are expected to be localized along the Meers fault scarp (“Fault” on the logic tree), or whether they may occur along other structures within the Oklahoma aulacogen with the same rates as observed on the Meers (“Random in Zone” on the logic tree). The inclusion of this branch on the logic tree represents the interpretation that, while none of the other faults associated with the Oklahoma aulacogen and Arbuckle-Wichita-Amarillo uplift have observed Quaternary faulting (e.g., Crone and Wheeler, 2000; Ham et al., 1964; Hanson et al., 1997; Swan et al., 1993; Wheeler and Crone, 2001; Williamson, 1996), there is the possibility that Meers-like earthquakes (e.g., similar magnitudes and recurrence rates) could occur on other faults within the aulacogen.

Meers-like ruptures within the aulacogen are allowed only on the out-of-cluster branch of the logic tree, reflecting the interpretation that the spatial migration of Meers-like earthquakes will occur only if the Meers fault is out of a cluster (i.e., there can be only one Meers-like structure active within the aulacogen at any given time). This interpretation is based on the fact that there is no evidence of Quaternary activity on other faults within the aulacogen. On the out-of-cluster branch we give a low weight of 0.1 to the possibility of migrating Meers-like earthquakes

because there are no observations supporting the existence of other active faults within the aulacogen.

#### 6.1.4.3 Geometry and Style of Faulting

The third through fifth branches of the logic tree describe the source geometry and style of faulting (Figure 6.1.4-2).

The surface trace of the Meers fault is easily identified on aerial photographs for a total distance of approximately 26 km (16 mi.) as a south-down topographic escarpment (Ramelli et al., 1987; Crone, 1994). The scarp over much of this distance has been visited by various researchers and is attributed to Holocene rupture along the Meers fault (e.g., Crone and Luza, 1990; Kelson and Swan, 1990; Ramelli and Slemmons, 1990; Ramelli et al., 1987; Swan et al., 1993; Crone, 1994). In addition to this prominent scarp along the Meers fault, an approximately 11 km (6.8 mi.) southeast extension of the Meers fault scarp (Figure 6.1.4-1) was identified by Ramelli et al. (1987) and Ramelli and Slemmons (1990) by analyzing low-sun-angle aerial photography. The southeast extension is more subtle and discontinuous than the originally identified 26 km (16 mi.) long scarp. Ramelli and Slemmons (1990) argue that the southeastern continuation of the scarp shares the same history of events on the Meers fault, judging by its alignment with the original scarp, the consistent down-to-south separation across the scarp, its proximity to the original scarp, and the presence of a small drainage channel aligned parallel to the scarp and across the pattern of local drainage networks. However, Ramelli and Slemmons (1990) also acknowledge uncertainty in the structural relationship between the northwest and southeast scarps due to a left step in the scarp near the junction of the two scarp strands, and due to the absence of a scarp across East Cache Creek (Figure 6.1.4-1). In addition, field evaluation of the southeast extension of the scarp has not been possible because the scarp traverses the Fort Sill Military Reservation, where access is restricted (Ramelli and Slemmons, 1990; Ramelli et al., 1987; Crone, 1994).

One researcher (Cetin, 2003) has suggested that the Meers fault scarp also extends 30 km (19 mi.) to the northwest of the prominent scarp described above (Figure 6.1.4-1). Cetin (2003) proposed this extension based on what he describes as “displaced terrace deposits of Pleistocene age, displaced, buried and/or overthickened soil horizons, fault-related colluvium deposits (colluvial wedges) found near and only on the downthrown side of the fault, active seepage near the fault, deflection of stream alignments and the land use pattern along the fault.” However, as summarized by Wheeler and Crone (2003), the evidence presented by Cetin (2003) for Quaternary faulting is not conclusive.

To account for the potential northwest extension, the characterization of the Meers fault used here includes two alternate interpretations of the extent of the active Meers fault trace (third branch on logic tree). The alternate interpretations for fault length are (1) the approximately 37 km (23 mi.) trace as defined by Ramelli and Slemmons (1990) and Ramelli et al. (1987); and (2) an extended trace that includes the approximately 30 km (19 mi.) extension defined by Cetin (2003). The interpretations are given weights of 0.9 and 0.1, respectively. The low weight for the extended trace reflects that Cetin’s (2003) hypothesized northwest extension is not supported by robust, well-documented evidence and not widely supported by the expert community.

When Meers-like earthquakes are allowed to migrate off the fault on the out-of-cluster branch, the earthquakes are limited to occurring within the Oklahoma aulacogen.

The seismogenic thickness for the Meers fault is modeled as either 15 km or 20 km (9.3 mi. or 12 mi.) with equal weights. These depths are based on the depth distribution of seismicity within Oklahoma (Luza and Lawson, 1993).

The Meers fault is well recognized as a down-to-the-south oblique fault dominated by left-lateral slip (e.g., Swan et al., 1993; Wheeler and Crone, 2003). Based on trench exposures and a shallow seismic reflection survey, the Meers fault in the shallow subsurface (to over 150 m [490 ft.] depth) is thought to be near-vertical to slightly northeastward-dipping (Crone and Luza, 1990; Miller et al., 1990; Ramelli and Slemmons, 1990; Swan et al., 1993). However, regional well data, seismic reflection data, and comparison of the Meers fault to other faults in the Wichita frontal fault system suggest that at depth the Meers fault dips approximately 40 degrees to the southwest (Good et al., 1983; McConnell, 1989). Given the uncertainty as to what the best single dip is to characterize the Meers for future earthquake ruptures, a vertical and 40-degree southwest dip are given equal weights for earthquakes on the Meers fault. When Meers-like earthquakes are allowed for the out-of-cluster branch of the logic tree, they are characterized with a strike of N60W (i.e., approximately parallel to the faults of the Amarillo-Wichita-Arbuckle uplifts) and a random dip between 90 and 40 degrees to the southwest.

The uncertainty in the Meers fault dip also drives uncertainty as to whether the fault is best characterized as an oblique normal or reverse fault. An oblique-reverse interpretation is preferred based on the observations in the shallow subsurface (Swan et al., 1993). The obliquity of slip along the fault is not well constrained because of the lack of robust horizontal and vertical control points in the same trenches that can be used to estimate net slip. Published estimates of horizontal-to-vertical slip ratios have ranged from 1.3:1 (Kelson and Swan, 1990; Swan et al., 1993) to greater than 5:1 (Crone and Luza, 1990).

#### 6.1.4.4 RLME Magnitude

The sixth branch of the logic tree describes the earthquake magnitudes for the Meers RLME (Figure 6.1.4-2).

The Meers fault RLME source is modeled using a maximum moment earthquake model where the earthquake magnitude is characterized using a distribution of characteristic magnitudes representing epistemic uncertainty in the potential magnitude of future earthquakes. The magnitude distribution was defined using magnitude estimates from empirical relationships relating earthquake magnitude to fault rupture characteristics. The following relationships were used:

- Wells and Coppersmith (1994)—rupture length, maximum displacement, average displacement, and rupture area for strike-slip, reverse, and all faults.
- Hanks and Bakun (2002)—rupture area.
- Ellsworth (2003)—rupture area.

- Somerville et al. (2001, 2005)—rupture area.

The rupture characteristics that were used in these relationships were defined as described below.

### *Rupture Length*

Three rupture lengths for the Meers fault were used to estimate earthquake: 26 km, 37 km and 67 km (16 mi., 23 mi., and 42 mi.). The 26 km (16 mi.) length is based on the widely accepted extent of Holocene rupture along the Meers fault. The 37 km (23 mi.) length includes the southeast extension to the Meers fault that was mapped by Ramelli and Slemmons (1990) and Ramelli et al. (1987) using low-sun angle photography (see Section 6.1.4.1). The 67 km (42 mi.) extent takes into account the approximately 30 km (19 mi.) long northwest extension of the fault proposed by Cetin (2003).

### *Average and Maximum Displacement*

Only the study by Swan et al. (1993) is used to constrain displacement estimates because it is the only study to have recognized and explicitly measured displacements for the two Holocene events. Based on the results of their investigations, Swan et al. (1993) estimated that the average net slip per event along the fault is between 1.75 and 3 m (5.74 and 9.8 ft.), and the maximum net displacement is 3.5 to 5.25 m (12 and 17.2 ft.). These estimates are poorly constrained because Swan et al. (1993) were able to measure displacement at only a few locations; they measured only one net displacement (as opposed to just vertical or horizontal) and based most of the estimates on stratigraphic offsets of alluvial and colluvial material as well as paleochannel thalwegs exhumed in trenches, both of which can be difficult to use in developing accurate displacement estimates.

### *Rupture Area*

Potential rupture area for the Meers fault rupture was estimated using rupture length, fault dip, and downdip fault width estimates for the Meers fault. A lower-bound rupture area of 390 km<sup>2</sup> (151 mi.<sup>2</sup>) was calculated using the 26 km (16 mi.) estimate of Holocene rupture length (Ramelli and Slemmons, 1990; Ramelli et al., 1987), a fault dip of 90 degrees, and a downdip fault width of 15 km (9.3 mi.) based on the depth distribution of observed seismicity in the Oklahoma region (Luza and Lawson, 1993). The fault dip of 90 degrees was used for the minimum-bound estimate for the following reasons:

- There have been no studies that have reconciled the discrepancy between the shallow, near-vertical northeast dip of the fault and the deeper, moderate southwest dip of the fault (Crone and Luza, 1990; McConnell, 1989; Miller et al., 1990; Ramelli and Slemmons, 1990; Swan et al., 1993).
- There are few direct measurements of the Meers fault dip at depth (Crone, 1994; McConnell, 1989).
- This estimate is meant to be a minimum bound. An upper-bound rupture area of 1,150 km<sup>2</sup> was calculated using the 37 km (23 mi.) estimate of Holocene rupture length (Ramelli and

Slemmons, 1990; Ramelli et al., 1987); a fault dip of 40 degrees southwest; and a downdip fault width of 20 km (12 mi.), based on the depth distribution of observed seismicity in the Oklahoma region (Luza and Lawson, 1993).

Estimated magnitude ranges from these relationships and fault characteristics are presented in Table 6.1.4-1. Note that the Wells and Coppersmith (1994) displacement relationships for reverse faults were not used because they are reported as not significant at the 95 percent probability level. Based on these estimates, the following distribution for the expected RLME magnitude for the Meers fault was developed:

<b>Expected Meers RLME Magnitude (M)</b>	<b>Weight</b>
6.6	0.1
6.7	0.45
6.9	0.3
7.3	0.1
7.4	0.05

The above distribution reflects the following preferences.

- Magnitudes from the 26 km (16 mi.) rupture length estimate were given the highest weight because (1) the scarp is best expressed along the 26 km (16 mi.) long segment, potentially suggesting that Holocene ruptures were restricted to this length; and (2) rupture length is the most robust directly measurable characteristic of the Holocene ruptures compared to estimates of displacement and area, which require more assumptions to derive.
- Magnitudes from the 37 km (23 mi.) rupture length estimate were given moderate weight because (1) future earthquakes may extend along the entire 37 km of the scarp, and (2) there is no available information on the timing of events along the extended scarp.
- Magnitudes from the 67 km (42 mi.) rupture length estimate were given the lowest weight because there is no evidence that a rupture has occurred along this entire length.
- Magnitudes from the 390 km<sup>2</sup> (151 mi.<sup>2</sup>) rupture area are given low to moderate weight because they reflect a reasonable interpretation of the potential rupture area of the Holocene earthquakes yet are a less direct measure of the Holocene events than the rupture length.
- Magnitudes from the 1,150 km<sup>2</sup> (444 mi.<sup>2</sup>) rupture area are given low weight because it is unlikely that any of the Holocene ruptures have the maximum bound area (i.e., maximum length, maximum depth, and shallow dip).
- Magnitudes from the displacement estimates are given low weights because the displacements are poorly constrained by the data collected by Swan et al. (1993).

#### 6.1.4.5 RLME Recurrence

The remaining branches of the logic tree describe the assessment of RLME recurrence rates.

##### *Recurrence Method*

The data available for assessing the recurrence rate of the Meers RLMEs provide assessments of the timing of past earthquakes. Thus the “Earthquake Recurrence Intervals” approach is used with weight 1.0 (Figure 6.1.4-2).

##### *Recurrence Data*

Recurrence rates are determined using inter-event times from the Holocene ruptures for (1) the out-of-cluster branch when earthquakes occur randomly within the OKA zone, and (2) the in-cluster branch when earthquakes occur on the Meers fault trace. For the out-of-cluster branch when the earthquakes occur on the Meers fault trace, the time elapsed between the last pre-Holocene earthquake and the Holocene earthquake cluster is used to define the recurrence rate. All recurrence rates are determined from the results of the Swan et al. (1993) study because it is both the most detailed study and the only study to have recognized and dated two Holocene earthquakes on the Meers fault.

Out-of-cluster recurrence rates for the Meers fault are based on the estimated elapsed time between the Holocene earthquakes and the penultimate earthquake cluster. Swan et al. (1993) estimated that the elapsed time between the Holocene cluster and the next most recent earthquake was between 200 and 500 kyr.

Intracluster recurrence rates for the Meers fault are based on estimates of the time elapsed since the first Holocene earthquake and the number of observed events in the Holocene. The date of the first Holocene earthquake is constrained by eight radiocarbon ages presented by Swan et al. (1993). From this suite of ages, the tightest constraining minimum and maximum ages are used to define the uncertainty in the date of the first Holocene earthquake. For example, four radiocarbon ages between approximately 7,000 and 3,000 yr BP constrain the maximum age of the earthquake, but only the tightest constraining age (2,918 calibrated years BP) is used.

The maximum age of the earthquake is constrained by sample PITT-0478 of Swan et al. (1993). This sample was collected at the “Valley” site of Swan et al. (1993; Figure 6.1.4-1) from an alluvial deposit near the bottom of the trench that was clearly offset by the fault. The calibrated radiocarbon age for this sample is 2,918 yr BP. The minimum age of the earthquake is constrained by sample PITT-0478 of Swan et al. (1993). This sample was collected at the “Southeast Poned Alluvium” site of Swan et al. (1993; Figure 6.1.4-1) from an alluvial deposit interpreted to have ponded against the fault scarp after the first Holocene earthquake. The calibrated radiocarbon age for this sample is 2,093 yr BP.

### *Earthquake Recurrence Model*

As discussed in Section 5.3.3, the Poisson model is used as the default earthquake recurrence model with weight 1.0 for the Meers RLME source as there are not sufficient data to justify including an alternative model.

### *RLME Annual Frequency*

The final node of the logic tree addresses the uncertainty distributions for the annual frequency of RLMEs (Figure 6.1.4-2). These distributions were developed using the methodology described in Section 5.3.3.1. For the in-cluster case, the relative likelihood of various values of the recurrence rate parameter was developed using Equation 5.3.3-4 and the observations of one closed recurrence interval between the ~1,500 ka and the ~2,900 ka earthquakes and one open interval post the ~1,500 ka earthquake. The value of  $\sum_{i=1}^N t_i + t_0$  was assessed to be uniformly distributed between 2,153 and 2,968 years, with  $N$  equal to 1. The resulting relative-likelihood-based distribution was represented by the five-point discrete distribution listed in Table 6.1.4-2.

For the out-of-cluster case, the range of return periods for clusters of 200–500 kyr was represented by three equally likely values of 200, 350, and 500 kyr. These return periods are inverted to produce the distribution for out-of-cluster RLME frequency listed in Table 6.1.4-3. The weighting reflects the evaluation that there is no evidence to support a preferred return period.

### **6.1.5 Reelfoot Rift–New Madrid Fault System**

The New Madrid region is the source of the 1811-1812 New Madrid earthquake sequence, which includes the three largest earthquakes to have occurred in historical time in the CEUS. Extensive geologic, geophysical, and seismologic studies have been conducted to characterize the location and extent of the likely causative faults of each of these earthquakes and to assess the maximum magnitude and recurrence of earthquakes in this region. Appendix Table D-6.1.5 provides a summary of recent publications pertinent to the identification and characterization of seismic sources in this region. Based on the results of these studies, a system of faults within the New Madrid seismic zone (NMSZ) in the northern Reelfoot rift has been identified as an RLME source (herein referred to as the New Madrid fault system [NMFS] RLME source). Appendix Table C-6.1.5 lists the data that were explicitly used to constrain the characterization of this RLME source. The logic tree showing the characterization of the NMFS RLME sources is shown on Figure 6.1.5-1.

Models that have been proposed to explain the origin of stresses driving active deformation in the CEUS and specifically in the NMSZ are summarized in Appendix Table D-6.1.5. Several of these provide explanations for localization of seismicity and recurrence of large-magnitude earthquakes in the NMSZ, as follows:

- The presence of a rift pillow underlying the Reelfoot rift (Mooney et al., 1983) causes local stress concentration (Grana and Richardson, 1996).
- A weak subhorizontal detachment fault exists in the lower crust above the rift pillow that causes local stress concentration (Stuart et al., 1997).
- High local heat flow creates high ductile strain rates in the upper mantle and lower crust, causing seismicity in the upper crust (Liu and Zoback, 1997).
- Glacial unloading north of the NMSZ at the close of the Wisconsinan increased seismic strain rates in the NMSZ and initiated the Holocene seismicity (Grollmund and Zoback, 2001). Modeling studies by Grollmund and Zoback (2001) show that the removal of the Laurentide ice sheet approximately 20,000 years ago (ka) changed the stress field in the vicinity of New Madrid, causing seismic strain rates to increase by about three orders of magnitude. The modeling predicts that the high rate of seismic energy release observed during late Holocene time is likely to continue for the next few thousand years (Grollmund and Zoback, 2001).
- Some local or regional perturbation of the stress field, pore pressure, or thermal state is responsible for triggering viscous relaxation of a weak lower-crustal zone within an elastic lithosphere. This may cause a sequence of fault ruptures in short recurrence intervals. A likely explanation for this perturbation is recession of the Laurentian ice sheet approximately 14 ka (Kenner and Segall, 2000; Kenner, 2003). Kenner and Segall (2000) and Kenner (2003) suggest that this model explains the apparently contradictory observations of the Holocene increase in seismic strain rate in the NMSZ relative to long-term geologic and geomorphic observations that do not support steady-state deformation at these rates. Model predictions mostly are consistent with earthquake magnitude, coseismic slip, recurrence intervals, cumulative offset, and surface deformation rates in the NMSZ. In particular, the computed interseismic strain rates may be undetectable with available geodetic data, implying that low observed rates of strain accumulation cannot rule out future large-magnitude earthquakes.
- Low-permeability seals form around the fault zone as stress accumulates, raising the pore pressure until an earthquake happens. Temporal clustering may reflect the evolution of pore fluid pressure in a fault zone (Crone et al., 2003).
- Accelerated late Wisconsinan and Holocene denudation above the NMSZ due to the confluence of the Mississippi and Ohio rivers stepping north to Thebes Gap, perhaps in combination with the retreating Laurentide forebulge, may have been sufficient to initiate Holocene seismicity by causing a perturbation in the local stress field (the Kenner and Segall model [2000]; Van Arsdale et al., 2007).
- Descent of the ancient Farallon slab into the deep mantle beneath central North America as inferred from high-resolution seismic tomography induces a highly localized flow and stresses directly below the NMSZ. This localization arises because of structural variability in the Farallon slab and the low viscosity of the sublithospheric upper mantle. It is hypothesized that the mantle-flow-induced surface depression and associated local focusing of bending stresses in the upper crust may operate analogously to previous crustal loading scenarios, with one difference being that the slab-related loads reside in the mantle (Forte et al., 2007).

- Fault weakening can lead to repeated earthquakes on intraplate faults (Lyakhovsky et al., 2001). The predicted patterns vary with the weakening history. Clusters of large intraplate earthquakes can result from fault weakening and healing, and the clusters can be separated by long periods of quiescence. Stress triggering and migration cause spatiotemporal clustering of earthquakes (Li et al., 2009).
- Strain in the NMSZ over the past several years has accumulated too slowly to account for seismicity over the past approximately 5,000 years, hence excluding steady-state fault behavior. Fault loading, strength, or both may vary with time in the plate interior. Time variations in stress could be due to local loading and unloading from ice sheets or sediments or to earthquakes on other faults (Calais and Stein, 2009).
- The NMSZ is associated with a local, northeast-southwest-trending, low-velocity anomaly in the lower crust and upper mantle, instead of a high-velocity intrusive body as proposed in previous studies. The low-velocity anomaly is on the edge of a high-velocity lithospheric block, consistent with the notion of stress concentration near rheological boundaries. This lithospheric weak zone may shift stress to the upper crust when loaded, thus leading to repeated shallow earthquakes (Zhang et al., 2009b).
- Stress changes are caused by the Quaternary denudation/sedimentation history of the Mississippi valley. Flexural stresses are sufficient to trigger earthquakes in a continental crust at failure equilibrium. The resulting viscoelastic relaxation leads to failure again on the main fault (lower-strength threshold) and neighboring faults. In the absence of significant far-field loading, this process can only maintain seismic activity for a few thousand years (Calais et al., 2009).

The principal seismic activity within the upper Mississippi embayment is interior to the Reelfoot rift along the NMSZ. The NMSZ consists of three principal trends of seismicity: two northeast-trending arms and a connecting northwest-trending arm (Figure 6.1.5-2). This seismicity pattern has been interpreted as a northeast-trending right-lateral strike-slip fault system with a compressional left-stepover zone (Russ, 1982; Chiu et al., 1992; Schweig and Ellis, 1994), referred to as the NMFS. The south arm is coincident with the subcrop Blytheville arch; the central arm is coincident with the subcrop Pascola arch and surface Lake Country uplift; and the north arm trends at a low angle to the western margin of the Reelfoot rift (Figures 6.1.5-2 and 6.1.5-3). Johnston and Schweig (1996) identify the following fault segments within the central fault system of the NMSZ: Blytheville arch (BA); Blytheville fault zone (BFZ); Bootheel lineament (BL); New Madrid West (NW); New Madrid North (NN); Reelfoot fault (RF); Reelfoot South (RS; Figure 6.1.5-4). They outline three rupture scenarios associating each of the three 1811-1812 earthquakes with fault segments (individually or in various combinations) using historical accounts and geologic evidence. Their interpretation is consistent with the spatial distribution and source characteristics of contemporary NMSZ seismicity (Hough and Martin, 2002).

The December 16, 1811, earthquake (referred to variously by different authors as the D1, D16, or NM1 earthquake) is believed to have occurred on the south arm of seismicity (possibly the Cottonwood Grove–Ridgley fault system) associated with the BA, a major crustal transpressional fault structure identified from seismic reflection data (Figure 6.1.5-2). Mueller et al. (2004) and Bakun and Hopper (2004a) infer a location for this earthquake on the northern end of the BA

(just south of the intersection of the BL and the BFZ (also referred to as the Cottonwood Grove fault). Two alternative geometries for the main fault rupture are outlined by Johnston and Schweig (1996): BA/BL (preferred) or BA/BFZ (Figure 6.1.5-4). More recent studies by Guccione et al. (2005) have documented evidence for multiple faulting earthquakes along the central part of the BL, and it is recommended that the BL be renamed the Bootheel fault (Figure 6.1.5-3). Along the central part of the BL, a less than 10.2 ka Pleistocene braidstream sand has been displaced vertically approximately 3 m (10 ft.) and an approximately 2.4 ka Holocene paleochannel has been displaced horizontally at least 13 m (43 ft.; Guccione et al., 2005).

The causative fault for the January 23, 1812, earthquake (referred to variously by different authors as the J1, J23, or NM2 earthquake) is generally inferred to be the northern seismicity arm of the NMSZ (segment NN; Figure 6.1.5-4). Baldwin et al. (2002) suggest that the North Farrenburg lineament may be associated with NN and represent the surface expression of coseismic rupture from the January 23, 1812, earthquake. Johnston and Schweig (1996) also consider an alternative scenario in which the source for the January 23, 1812, earthquake is the west-trending zone of seismicity that lies along the trend of the RF (S#3 on Figure 6.1.5-4b). In this alternative model, both the NN and RF ruptured in the February 7, 1812, earthquake.

Microearthquake data from the northeastern NMSZ show three alignments that extend from New Madrid, Missouri, into western Kentucky and southern Illinois that may represent extensions of the NMSZ and therefore alternative locations for the NM2 rupture (Braile et al., 1986; Wheeler, 1997; Woolery and Street, 2002; Shumway, 2008) (Figure 6.1.5-2). Braile et al. (1997) identified two parallel trends of concentrated seismicity approximately 70 and 90 km (43.5 and 56 mi.) long that extend north-northeast from the central NMSZ to within 14.4 km (9 mi.) of the Illinois/Kentucky border (Wheeler, 1997; Woolery and Street, 2002). Shumway (2008) identifies these two parallel trends and a third, shorter alignment (approximately 40 km [25 mi.] long) running east-northeast from just south of Charleston, Missouri, to just north of Bardwell, Kentucky.

Mueller et al. (2004) and Hough et al. (2005) infer that the J23 (NM2) main shock may have been a remotely triggered earthquake with a location some 200–250 km (124–155 mi.) north of the New Madrid earthquake in the Wabash Valley of southern Illinois and Indiana. Bakun and Hopper (2004a) discount more northerly locations, based on the absence of 1811-1812 liquefaction features that would indicate a source in that region. They follow Johnston and Schweig (1996) in assigning the NM2 earthquake to the NN segment. Cramer et al. (2006) suggest that unilateral rupture within the New Madrid fault zone could have led to extraordinary strong ground motions to the east.

The February 7, 1812, earthquake (referred to variously by different authors as the F1, F7, or NM3 earthquake) occurred on the RF, which connects the two other fault zones through the stepover region (Johnston and Schweig, 1996). The Reelfoot scarp is the surface expression of a west-dipping reverse fault that lies within the left-stepping restraining bend between two dextral strike-slip arms of the NMSZ (Russ, 1982; Sexton and Jones, 1986; Kelson et al., 1992, 1996; Schweig and Ellis, 1994) (Figure 6.1.5-3). The fault and associated fold are defined by microearthquakes (Pujol et al., 1997); seismic reflection profiles (Sexton and Jones, 1986; Odum et al., 1998; Van Arsdale et al., 1999); surface topography; shallow trench excavations (Russ,

1982; Kelson et al., 1992, 1996; Mueller et al., 1999); and borehole data (Mihills and Van Arsdale, 1999; Champion et al., 2001). Using the constraints on fault geometry derived from interpretation of microearthquakes and seismic reflection profiles and the amounts of surface deformation based on geomorphic and trenching investigations, the slip rate for the RF is estimated (Mueller et al., 1999; Van Arsdale, 2000; Champion et al., 2001) (Appendix Table D-6.1.5). Mueller and Pujol (2001) use these constraints on geometry, slip rate, and displacement during historical and prehistoric earthquakes to estimate the rate of late Holocene moment release and the magnitudes of earthquakes for the two most recent strain cycles.

Maximum magnitudes in the New Madrid region are based largely on the analysis of intensity data from the 1811-1812 earthquake sequence (Johnston, 1996b; Johnston and Schweig, 1996; Hough et al., 2000; Mueller et al., 2004; Bakun and Hopper, 2004a; Hough and Page, 2011) and, to a lesser degree, on magnitude assessments inferred from paleoliquefaction features (Tuttle, Schweig, et al., 2002) (Appendix Table D-6.1.5). Cramer (2001) calculates the range of magnitudes (M 6.5–7.8) for fault segments that capture the range of uncertainty in the dimensions of the segment rupture (length and width ( $\leq 19$  km [11.8 mi.]) of the seismogenic crust) and choice of magnitude/area relationship (Wells and Coppersmith [1994] or Somerville and Saikia [2000] area-magnitude relationships). Mueller and Pujol (2001) provide an additional assessment of past earthquake magnitudes through detailed mapping of the geometry and area of the RF, combined with estimates of fault slip rate, recurrence, and displacement in individual earthquakes to estimate the rate of late Holocene moment release (Appendix Table D-6.1.5).

Constraints on the recurrence of large-magnitude earthquakes in the NMSZ come from paleoliquefaction studies (Saucier, 1991; Tuttle, 1999, 2001; Craven, 1995a; Li et al., 1998; Tuttle and Schweig, 1996, 2000, 2001; Tuttle, Lafferty, and Schweig, 1998; Tuttle, Collier, et al., 1999; Tuttle et al., 2000; Tuttle, Schweig, et al., 2002; and Tuttle and Wolf, 2003; Appendix E) and from evaluation of fault-related deformation along the Reelfoot scarp (Kelson et al., 1992, 1996). The age constraints for these earthquakes are summarized in Table 6.1.5-1. Findings from these studies indicate that major earthquakes occurred in the New Madrid region in ~AD 900 (900–1,200 yr BP relative to AD 1950) and ~AD 1450 (350–650 yr BP relative to AD 1950) (Figures 6.1.5-5 and 6.1.5-6; Tuttle and Schweig, 2001; Tuttle, Schweig, et al., 2002).

Saucier (1991) presents evidence for a significant earthquake in the northern part of the New Madrid region in AD 489 (1461 yr BP)  $\pm$  50 yr (Appendix E). Tuttle et al. (2005) recognized a New Madrid event about 2350 BC  $\pm$  200 yr that included several large, closely timed earthquakes, but state that the paleoearthquake record may be incomplete before AD 300 and that additional research is needed to assess whether the rate of earthquakes during the past 1,200 years is typical of the longer-term behavior. Tuttle, Schweig, et al. (2002) note that, given uncertainties in dating liquefaction events, the recurrence time between the three most recent New Madrid earthquakes (AD 900, AD 1450, and 1811-1812) may have been as short as 200 years or as long as 800, with an average of 500 years. Tuttle (2001) notes that similarities in the size and spatial distributions of historical (1811-1812) and paleoliquefaction features indicate that the NMSZ was the likely source of the two paleoearthquakes that are recognized regionally. Saucier (1989) first recognized compound sand blows that formed during the 1811-1812 earthquake sequence. Tuttle, Schweig, et al. (2002) document evidence that prehistoric sand blows, like those formed during the 1811-1812 earthquakes, probably are compound structures

resulting from multiple earthquakes closely clustered in time (i.e., earthquake sequences). The current preferred age estimates of earthquakes from 2-sigma radiocarbon maximum and minimum age constraints and, in some instances, archeological data as outlined in Appendix E are given in Table 6.1.5-1.

### 6.1.5.1 Evidence for Temporal Clustering

The first node of the logic tree (Figure 6.1.5-1) addresses the issue of temporal clustering of earthquakes in the present tectonic stress regime (see Section 5.1.2).

Various observations suggest that the high rate of seismicity within the NMSZ in the Holocene is not characteristic of the region over longer-term periods. Schweig and Ellis (1994) note that extensive seismic reflection data in the New Madrid seismic zone show relatively small cumulative fault offsets in the post-Cretaceous Mississippi embayment sediments (e.g., Hamilton and Zoback, 1982). Van Arsdale (2000) concluded based on seismic reflection and trench data that slip rates on the RF during the Holocene are at least four orders of magnitude higher than during the Pleistocene.

Other geomorphic observations also suggest that the NMSZ became more active within the past few thousand years and that this activity is part of the most recent cluster of large earthquakes. Longer-term geomorphic records suggest that periods of clustered activity within the NMSZ are interspersed with longer intervals of inactivity (Holbrook et al., 2006). The concept that the locus of seismicity and active faulting may shift or migrate within the Reelfoot rift region was suggested by McBride, Nelson, and Stephenson (2002) to explain the changes in rates of activity for faults of the Fluorspar Area fault complex within the northern Reelfoot rift, and more recently by others to explain the apparent discrepancies between long-term deformation rates on faults within the NMSZ (McKenna et al., 2007) and the evidence for possible temporally clustered earthquakes in the southern part of the rift near Marianna, Arkansas (Tuttle, 2009).

Geodetic data suggest that present strain accumulation across the NMSZ is near zero (Calais et al., 2005; Smalley et al. 2005) and that strain has accumulated too slowly to account for the paleoseismicity recorded over the past approximately 5,000 years, thereby ruling out steady-state fault behavior (Newman et al., 1999; Calais and Stein, 2009; Calais et al., 2009; Li et al., 2007, 2009; McKenna et al., 2007).

Alternative interpretations of geodetic strain in the region of the NMSZ have been reported in the literature. Using analysis of geodetic measurements from a permanent GPS array in mid-America that was installed in the mid- to late 1990s, Smalley et al. (2005) suggest relatively rapid rates of strain of the order of  $10^{-7}$  per year, comparable in magnitude to those across active plate boundaries, and consistent with known active faults in the region. Relative convergence across the RF estimated from this study is  $\sim 2.7 \pm 1.6$  mm/year. Relative fault-parallel, right-lateral motion of  $\sim 1$  mm/year was measured across the southern right-lateral strike-slip fault zone, which is highlighted by a prominent northeast-trending and vertical zone of microseismicity and right-lateral focal mechanisms. Surface velocities at distances beyond a few fault dimensions (far-field) from active faults, however, do not differ significantly from zero. According to Smalley et al. (2005), it is not certain whether the driving force behind the current

surface velocities is related to post-1811-1812 seismic processes or to the accumulation of a locally sourced strain. Others speculate that the recent small earthquakes in the NMSZ are aftershocks of the large earthquakes of 1811-1812 (Ebel et al., 2000; Stein and Newman, 2004; McKenna et al., 2007). The geodetic data indicate, however, that aseismic slip is almost certainly required across faults (or shear zones) within the upper few kilometers of the surface (Smalley et al., 2005).

More recent interpretation of geodetic results in the NMSZ shows motions between 0 and 1.4 mm/yr, and two opposing interpretations of these data are suggested (Calais and Stein, 2009). As outlined by Calais and Stein, the upper bound is consistent with steady-state behavior, in which strain accumulates at a rate consistent with a repeat time for  $M \sim 7$  earthquakes of about 600–1,500 years, as seen in the earthquake record. The lower bound cannot be reconciled with this record, which implies that the recent cluster of large-magnitude earthquakes does not reflect long-term fault behavior and may be ending. New analysis suggests strain rates lower than  $1.3 \times 10^{-9}$ /yr, less than predicted by a model in which large earthquakes occur because the NMSZ continues to be loaded as a deeper weak zone relaxes (e.g., Kenner and Segall, 2000). At a steady state, a rate of 0.2 mm/yr implies a minimum repeat time of 10 kyr for low  $M = 7$  earthquakes having approximately 2 m (6.5 ft.) of coseismic slip and a repeat time of longer than 100 kyr for  $M = 8$  earthquakes.

In summary, geodetic and geologic observations suggest that both temporal clustering and spatial migration of seismicity occurs within the Reelfoot rift, and various researchers have argued that the NMSZ faults are not presently accumulating strain at a rate consistent with that recorded by the late Holocene paleoliquefaction record and that they may be entering a less active period (e.g., Calais and Stein, 2009; McKenna et al., 2007). A recent review by the Independent Expert Panel on New Madrid Seismic Zone Earthquake Hazards of the current national seismic hazard maps in the region of the NMSZ considered claims that the apparent lack of current deformation may indicate that the process driving NMSZ earthquakes has ceased, but members of the panel and other experts consider such claims unlikely (NMSZ Expert Panel, 2011). This possibility is acknowledged but is given relatively low weight in the source model for several reasons: the relatively short geodetic record, uncertainties in the potential variability in strain accumulation over such short periods, and gaps in the state of knowledge regarding the relationship between the crustal motion measured by space geodesy and the elastic strain that is released by earthquakes. The NMSZ Expert Panel (2011) notes that the integration of GPS data in NMSZ seismic hazard analysis is limited by two main factors: (1) limitations of the existing GPS data and (2) lack of physical understanding of how stress accumulation on faults is related to surface deformation in intracontinental regions. Three options are considered in the CEUS SSC source characterization (Figure 6.1.5-1):

- The recent behavior of all three of the faults in the NMFS as inferred from paleoliquefaction studies (in a period of clustered earthquakes) is interpreted to be representative of the rate of future earthquakes (i.e., the recent period of activity for the three faults will continue into the future at the same rate; weight of 0.9).
- The NMSZ is shutting down as suggested by geodetic observations that show little or none of the interseismic motion expected before a future large earthquake (i.e., out of a period of clustered earthquakes; Newman et al., 1999; Calais et al., 2005). In this case, the hazard is

modeled by the underlying seismotectonic zone (Reelfoot rift zone) on the seismotectonic branch of the master logic tree or by global spatial smoothing of seismicity on the Mmax branch of the logic tree (weight of 0.05).

- Only the Reelfoot thrust (RFT) fault, which shows geomorphic evidence of an earlier phase of activity inferred from fluvial geomorphology (Holbrook et al., 2006), is considered to be in an active phase. In this case, the RFT is currently producing RLMEs at a lower rate (weight of 0.05).

### 6.1.5.2 Geometry and Style of Faulting

Fault sources included in the characterization of the NMFS RLME source are (1) the New Madrid South (NMS) fault; (2) the New Madrid North (NMN) fault; and (3) the RFT (Figure 6.1.5-4c). The first two levels of the logic tree (Figure 6.1.5-1) for these sources address the uncertainty in the technical community regarding the location and extent of the causative faults that ruptured during the 1811-1812 earthquake sequence. This uncertainty is represented by alternative geometries for the NMS, NMN, and RFT faults. The locations of the faults that make up the New Madrid characteristic earthquake sources are shown on Figures 6.1-2b, 6.1.5-3, and 6.1.5-4.

For the NMS fault source, two alternatives are considered, as described by Johnston and Schweig (1996): (1) the BA-BL (Blytheville arch-Bootheel lineament), and (2) the BA-BFZ (Blytheville arch-Blytheville fault zone). Although modern seismicity is occurring primarily along the BFZ, Johnston and Schweig (1996) present arguments suggesting that the BA-BL is the most likely location for the main NM1(D1) earthquake and that major NM1(D1) aftershocks occurred on the BFZ (the northeast extension of the Cottonwood Grove fault). Recent studies by Guccione et al. (2005) document that the presence of recent surface deformation and an offset Holocene channel across the BL (Bootheel fault). Therefore, slightly greater weight is given to BA/BL (weight of 0.6) (total length of 133 km [82.5 mi.]) than to BA-BFZ (weight of 0.4) (total length of 115 km [72 mi.]).

Two alternative total lengths are considered for the NMN fault source: NMN-S and NMN-L. The first, which is given the highest weight (0.7), allows for rupture of the 56.4 km (35 mi.) fault segment (NN; Figure 6.1.5-4) as defined by Johnston and Schweig (1996). Cramer (2001) uses a similar value (59 km [36.7 mi.]) as the length of this fault source. The alternative, NMN-L, which has a total length of 95 km (59 mi.), allows for the fault to extend north, including the westernmost of two trends of northeast-aligned seismicity noted by Wheeler (1997) and Shumway (2008; Figure 6.1.5-2). McBride et al. (2003) observe evidence in seismic profiles for reactivation of northeast-trending structures near Olmstead, Illinois, along the trend of the westernmost seismicity alignment. They conclude that the graben structure in this area has been reactivated as a fault-propagation fold that apparently affects Holocene sediments near the ground surface. Wheeler et al. (1997) and other researchers argue for a structural northern boundary to the rift in this region (see Appendix Table D-6.1.5). The northern extension (NMN-L; Figure 6.1.5-4c) is not as well defined by seismicity as the NMN-S segment is. Also, the recurrence interval of large-magnitude earthquakes in the northern Mississippi embayment appears significantly longer than the recurrence interval for NMSZ earthquakes based on

paleoliquefaction studies. Given these observations, the longer (97 km [60.3 mi.]) fault length (NMN-L) is given less weight (0.3) than the shorter (60 km [37.3 mi.]) fault length (NMN-S).

Johnston and Schweig (1996) conclude from historical accounts that the NM3 (F1) earthquake occurred on the RF, and they identify three possible segments of the fault: a central 32 km (19.9 mi.) long reverse fault defined by the RF scarp between the two northeast-trending strike-slip faults; a 35 km (21.7 mi.) long segment, Reelfoot South (RS), that extends to the southeast; and a 40 km (24 mi.) long segment west of the New Madrid North fault (Figure 6.1.5-4a). Seismicity and geomorphic data indicate that the southeast segment is slightly shorter (25–28 km [15.5–17.4 mi.]) than indicated by Johnston and Schweig (Van Arsdale et al., 1999; Mueller and Pujol, 2001). Cramer (2001) uses a total length of 60 km (37.3 mi.) for the RF. The alternative fault rupture scenarios of Johnston and Schweig (1996) include rupture of a 40 km (24 mi.) long northwest fault segment (Figure 6.1.5-4b).

Cramer (2001) assigns a length of 33 km (20.5 mi.) to this segment, which he refers to as the west arm. Mueller and Pujol (2001) note that this westerly arm is imaged as a vertical fault that terminates the RFT. They interpret the westerly arm as a left-lateral strike-slip fault kinematically linked to the RFT. Bakun and Hopper (2004) suggest a preferred epicenter location at the northern end of the RS segment. Hough and Martin (2002) show a slightly different geometry for the northwestern portion of the fault and do not interpret the historical 1811-1812 earthquake ruptures to have extended to the rift margin on the southeast. Van Arsdale et al. (1999) and Mueller and Pujol (2001) argue that the RF is continuous from New Madrid southeast to near Dyersburg, Tennessee. Alternatively, Csontos and Van Arsdale (2008) conclude that two segments of the fault, which they refer to as the Reelfoot North and Reelfoot South faults, are discrete segments that may not rupture as one fault. These two faults differ in strike, dip, depth, area, and basement displacement; further, the Reelfoot South fault does not have a surface scarp. Csontos and Van Arsdale (2008) note that the Reelfoot North fault is symmetric from its maximum fold amplitude of 11 m (36 ft.) northwest of Reelfoot Lake (Champion et al., 2001). They believe that the fold amplitude (scarp height) diminishes to near zero at the eastern edge of the Mississippi River floodplain, and that this is not consistent with what would be expected if the RF had ruptured over its entire 70 km (43.5 mi.) of mapped bedrock length as one plane during its Holocene history.

Two alternative fault geometries are included in this study: (1) the RFT-S fault that is based on the observed length of concentrated seismicity that is consistent with a reverse fault geometry (i.e., Chiu et al. 1992; Mueller and Pujol, 2001; Hough and Martin, 2002; Csontos and Van Arsdale, 2008); and (2) a longer fault (RFT-L) that allows for extensions to the northwest (the northwest segment of Johnston and Schweig [1996] and Cramer [2001]) and to the southeast to the margin of the Reelfoot rift. The shorter length (46.2 km [28.6 mi.]), which has geomorphic and seismologic evidence for reverse slip is given higher weight (0.7) than the alternative, longer fault (RFT-L; 82.8 km [51.3 mi.]) (weight of 0.3), which also includes the western fault segment that shows evidence for strike-slip movement.

Recent analysis and relocation of 19 earthquakes ( $M \leq 3.6$ ) in the northeastern part of the NMSZ, using a velocity model of the Mississippi embayment with appropriate depths to bedrock beneath seismic stations, shows that only 2 of the earthquakes occurred at depths between 13 and

15 km (8.1 and 9.3 mi.; Shumway, 2008). Herrmann and Ammon (1997) show depths of up to 16 km (10 mi.) for earthquakes in the Reelfoot rift. Based on these data, the following distribution for seismogenic crustal thickness is used to characterize the New Madrid fault system RLME sources: 13 km (8.1 mi.; weight of 0.3), 15 km (9.3 mi.; weight of 0.5), and 17 km (10.6 mi.; weight of 0.2).

The style of faulting for each of the fault sources is based on geologic and seismologic observations. The NMS fault is modeled as an oblique right-lateral strike-slip fault based on the following: focal mechanisms (Herrmann and Canas, 1978; Chiu et al., 1992); geologic evidence for a right-laterally offset Holocene channel along the Bootheel fault (Guccione et al., 2005); and the near-surface expression of flower structures associated with strike-slip and oblique movement of deeper, reactivated boundary faults as interpreted from seismic profile data (Odum et al., 1995). The RFT fault is modeled as a reverse fault dipping an average of 40 degrees southwest (the average being measured from near the surface to seismogenic depth) (Herrmann and Canas, 1978; Chiu et al., 1992, Mueller and Pujol, 2001; Van Arsdale, 2009). It is noted that the western end of the RFT-L may be steeper and more strike-slip, but for this regional assessment that has not been explicitly modeled. The NMN fault is modeled as a right-lateral strike-slip fault based on focal mechanisms (Shumway, 2008) and apparent right-lateral deflections of drainages and geophysical anomalies (Baldwin et al., 2002).

### 6.1.5.3 RLME Magnitude

Seismic source characterizations of the New Madrid seismic source zone typically consider the 1811-1812 earthquakes to represent the maximum earthquake for this source. Table 6.1.5-2 summarizes recent estimates of the magnitude of the New Madrid 1811-1812 main shocks.

Bakun and Hopper (2004b) provide preferred estimates of the locations and moment magnitudes and their uncertainties for the three largest earthquakes in the 1811-1812 sequence near New Madrid. Their preferred intensity magnitude  $M_I$ , which is their preferred estimate of  $M$ , is 7.6 (6.8–7.9 at the 95 percent confidence interval) for the December 16, 1811, earthquake (NM1); 7.5 (6.8–7.8 at the 95 percent confidence interval) for the January 23, 1812, earthquake (NM2); and 7.8 (7.0–8.1 at the 95 percent confidence interval) for the February 7, 1812, earthquake (NM3). The intensity magnitude  $M_I$  is the mean of the intensity magnitudes estimated from individual MMI assignments. In their analysis, Bakun and Hopper (2004b) consider two alternative eastern North America (ENA) intensity attenuation models, which they refer to as models 1 and 3. As indicated in Table 6.1.5-2, these two models give significantly different results for larger-magnitude earthquakes. Bakun and Hopper state that because these models are empirical relations based almost exclusively on  $M < 6$  calibration earthquakes, “there is no way to confidently predict which relation better represents the MMI distance data for  $M > 7$  earthquakes in ENA” (Bakun and Hopper, 2004b, p. 66). They present arguments supporting their preference for model 3, but do not discount the results based on model 1.

Dr. Susan Hough (written comm., August 23, 2004) concluded that there are insufficient data regarding the calibration of ENA earthquakes larger than  $M > 7$  to rely strictly on ENA models as was done in Bakun and Hopper (2004b). She offered arguments to support  $M$  7.6 (her preferred estimate of the size of the 2003 Bhuj earthquake) as a reasonable upper bound for the

largest of the earthquakes in the 1811-1812 New Madrid earthquake sequence, which is consistent with the estimates cited by Hough et al. (2000) and Mueller et al. (2004).

More recently, Hough has conducted new analyses and has revisited the intensity assignments, developing a set of “consensus intensities” for the four largest earthquakes in the New Madrid earthquake sequence (the three main shocks and a fourth large aftershock) based on independent assignments from four experts with experience in analysis of historical earthquakes: Duncan Agnew, Paola Albini, Kenneth Burke, and Stacey Martin (Hough and Page, 2011). The consensus intensity values are systematically (almost universally) lower than those estimated by Hough et al. (2000). Using the method developed by Bakun and Wentworth (1997) and two CEUS attenuation relations developed by Bakun et al. (2003) and Bakun and Hopper (2004), Hough and Page (2011) estimate magnitudes using the consensus values as well as the independent assignments by the four experts. The magnitude values are lower than those estimated by Hough et al. (2000).

Tuttle, Hengesh, et al. (2002) discuss the  $M_w$  7.7 Bhuj earthquake in the Kachchh region of India as a potential analog for the New Madrid earthquakes based on similarities in the tectonic and geologic settings between the two regions as well as on the extent and scale of paleoliquefaction that occurred in the Bhuj earthquake relative to the paleoliquefaction features in the NMSZ region. Tuttle, Hengesh, et al. (2002) note that if the Ambraseys (1988) relationship between magnitude and distance to the farthest liquefaction formed during an earthquake reflects intraplate earthquakes, then the Bhuj earthquake, which has a slightly shorter maximum distance to liquefaction than the NMSZ earthquakes, supports an estimate of  $M_w \geq 7.6$  for the size of the 1811-1812 earthquakes.

Mueller et al. (2004) use instrumentally recorded locations of recent earthquakes (assumed by Mueller et al. to be aftershocks of the 1811-1812 sequence) and models of elastic stress change to develop a kinematically consistent rupture scenario for the main-shock earthquakes of the 1811-1812 New Madrid sequence. In general, the estimated magnitudes for NM1 and NM3 used in their analysis ( $M = 7.3$  and  $M = 7.5$ , respectively) are consistent with those previously published by Hough et al. (2000). Mueller et al.’s results (2004) suggest that the NM1 and NM3 main shocks occurred on two contiguous faults: the strike-slip Cottonwood Grove fault and the RFT, respectively. The locations of the NM1 and NM3 earthquakes on the Cottonwood Grove and RFT, respectively, are relatively well constrained. In contrast to the earlier Hough et al. study (2000) that located the NM2 earthquake on the NN, Mueller et al. (2004) suggest a more northerly location for the NM2 earthquake, possibly as much as 200 km (124.3 mi.) to the north in the Wabash Valley of southern Indiana and Illinois. Hough et al. (2005) also infer a similar more northerly location.

Using Bakun and Wentworth’s method (1997), Mueller et al. (2004) obtain an optimal location for the NM2 main shock at  $88.43^\circ\text{W}$ ,  $36.95^\circ\text{N}$  and a magnitude of  $M$  6.8. They note that the location is not well constrained and could be fit almost as well by locations up to 100 km (62 mi.) northwest or northeast of the optimal location. Mueller et al. (2004) conclude that the three earthquakes on the contiguous faults increased stress near fault intersections and end points, in areas where present-day microearthquakes have been interpreted as evidence of primary main-shock rupture. They suggest that their interpretation is consistent with established

magnitude/fault area results, and does not require exceptionally large fault areas or stress drop values for the New Madrid main shocks.

With respect to the location of the NM2 earthquake, Bakun and Hopper (2004b) also discuss the paucity of MMI assignments available for this earthquake to the west of the NMSZ and the resulting uncertainty in its location. They note that the two MMI sites closest to the NMSZ provide nearly all of the control on the location of this earthquake and that, based on these two sites, a location northeast of their preferred site is indicated. They indicate, however, that the lack of 1811-1812 liquefaction observations in western Kentucky, southern Illinois, and southern Indiana precludes an NM2 location in those areas. Bakun and Hopper (2004b) follow Johnston and Schweig (1996) in selecting a preferred location on the NMN fault. Dr. Steve Obermeier confirmed that liquefaction features in the Wabash Valley region that would support the more northerly location preferred by Mueller et al. (2004) are absent (S. Obermeier, pers. comm., August 24, 2004). He noted that he had looked specifically in the area mentioned in the Yearby Land account that was cited by Mueller et al. (2004) and observed evidence for only small sand blows and dune sands, but did not see features of the size and origin described in that account.

Dr. Arch Johnston (written comm., August 31, 2004) indicated that the earlier estimates of Johnston (1996b) are likely to be high by about 0.2–0.3 magnitude units. More recently, Johnston expressed concerns regarding the estimation of magnitude for the 1811-1812 earthquakes from intensity data and indicated that he is working on developing revised estimates based on the assumption that the seismicity represents aftershocks from the 1811-1812 earthquakes (pers. comm., February 16, 2010). This analysis is not yet complete.

A review of published estimates (e.g., Bakun and Hopper, 2004b; Mueller et al., 2004; Hough and Page, 2011) indicates that uncertainty and differing views remain within the research community regarding the size and location of the 1811-1812 earthquakes. Based on review of the publications described in the preceding paragraphs and on communications with Drs. Bakun, Hough, and Johnston, the maximum magnitude for the NMFS faults (NMN, NMS, and RFT faults) is assessed as follows.

- Equal weight (one-third) is given to estimates based on Bakun and Hopper (2004b), Hough and Page (2011), and the Johnston revisions (written comm., August 31, 2004) to Johnston (1996b).
- Results from both intensity attenuation relations (models 1 and 3) in the Bakun and Hopper estimate (2004b) are used. Based on Bakun and Hopper's preference for model 3, weights of 0.75 and 0.25 are assigned to model 3 and model 1, respectively.
- In the case of the Hough and Page estimates (2011), which also use the Bakun and Hopper (2004b) attenuation models, similar weights of 0.75 and 0.25, are assigned to values based on model 3 and model 1, respectively.

The resulting RLME magnitude distribution for each of the three faults is given in the table below. Rupture sets 1 and 2 correspond to the revised Johnston estimates (1996b); rupture sets 3 and 4 correspond to the Bakun and Hopper estimates (2004b); and rupture sets 5 and 6 correspond to the Hough and Page estimates (2011).

As discussed in the following section, the present interpretation of the paleoearthquake data is that the two prehistoric earthquake ruptures that occurred before the 1811-1812 sequence also consisted of multiple large-magnitude earthquakes. Therefore, for this assessment, the modeled earthquake scenario includes rupture of multiple (two to three) fault sources. Furthermore, the arguments for the high- versus low-magnitude assessments for the individual faults are considered to be highly correlated. Therefore, six alternative sets of ruptures were produced from the distributions developed previously for each fault, as shown in the logic tree on Figure 6.1.5-1 and tabulated below.

Rupture Set	Expected NMFS RLME Magnitude for:			Weight
	NMS	RFT	NMN	
1	7.9	7.8	7.6	0.167
2	7.8	7.7	7.5	0.167
3	7.6	7.8	7.5	0.25
4	7.2	7.4	7.2	0.083
5	6.9	7.3	7.0	0.25
6	6.7	7.1	6.8	0.083

The magnitudes tabulated above represent the uncertainty distribution for the expected magnitude for the RLME for each fault within the NMFS. The size of the next RLME is assumed to vary randomly about the expected value following a uniform distribution over the range of  $\pm 0.25$  magnitude units (Section 5.3.3.4).

#### 6.1.5.4 RLME Recurrence

The remaining nodes of the NMFS RLME source logic tree address the assessment of earthquake recurrence rates.

##### *Recurrence Method*

The data available for assessing the recurrence rate of the NMFS RLMEs provide assessments of the timing of past earthquakes. Thus the “Earthquake Recurrence Intervals” approach is used with weight 1.0 (Figure 6.1.5-1).

##### *Recurrence Data*

The best constraints on recurrence of NMFS RLME sources derive from paleoliquefaction studies throughout the New Madrid region and from paleoseismic investigations of the RF scarp and associated fold. Using studies of hundreds of earthquake-induced paleoliquefaction features at more than 250 sites, Tuttle, Schweig, et al. (2002, 2005) concluded that (1) the fault system

responsible for the New Madrid seismicity generated sequences of two to three very large earthquakes in ~2350 BC, ~AD 900, ~AD 1450, as well as in 1811 and 1812; (2) given uncertainties in dating liquefaction features, the time between the past three earthquakes may be as short as 200 years or as long as 800 years, with an average of 500 years; (3) the paleoliquefaction record between 2350 BC and AD 900 is probably incomplete; and (4) some of the prehistoric sand blows are compound structures, resulting from multiple earthquakes (i.e., earthquake sequences) occurring closely spaced in time.

Out-of-cluster recurrence rates for the NMFS are based on dates presented in Holbrook et al. (2006). Holbrook et al. (2006) present a reconstruction of Holocene Mississippi River channels from maps of floodplain strata to identify channel perturbations reflective of major displacements on the RFT. This evaluation, in combination with the paleoliquefaction chronology developed by Tuttle et al. (2002, 2005), provides evidence of temporal clustering of earthquakes in a compressive Midcontinent intraplate on short-term cycles (months), as well as evidence for longer-term reactivation cycles ( $10^4$ – $10^6$ ). The study makes a case for a ~1,000-year cluster of earthquakes with  $10^2$  year spacing on the RF, beginning with a coseismic slip event near the end of the middle Holocene at ~2200 to ~1600 BC. This Holocene cluster appears separated from the modern episode of seismicity (beginning ~AD 900) by at least 1,700 years of tectonic quiescence.

### *Earthquake Recurrence Model*

The Poisson and renewal recurrence models are given weights of 0.75 and 0.25, respectively (Figure 6.1.5-1). As discussed in Section 5.1.2, the renewal model is considered more appropriate on a physical basis if a fault is responding to quasi-steady-state loading, producing more periodic occurrences of large earthquakes. This would suggest that a weight of 0.5 or larger be applied to the renewal model. However, it is not clear that such a physical process applies to the NMFS, even though there is evidence for periodic occurrence of large earthquakes. Therefore, the weight assigned to the renewal model is reduced to 0.25.

### *RLME Annual Frequency*

The final node of the logic tree addresses the uncertainty distributions for the annual frequency of RLMEs (Figure 6.1.5-1). These distributions were developed using the methodology described in Sections 5.3.3.1 and 5.3.3.2. For the Poisson model, the relative likelihood of various values of the recurrence rate parameter was developed using Equation 5.3.3-4 and the observations of the time intervals between the selected paleoearthquakes and the open interval post the 1812 earthquakes. For the renewal model, the relative likelihoods of various values of the mean recurrence interval for RLMEs were developed using Equations 5.3.3-7, 5.3.3-8, and 5.3.3-9 for each set of past RLMEs and specified value of coefficient of variation. The resulting parameters were then used to compute the equivalent annual frequency of RLMEs using Equations 5.3.3-10 and 5.3.3-11.

The data used for the recurrence rate calculations are the time intervals between individual RLMEs for the renewal model case and the age of the oldest RLME for the Poisson case. These are calculated from the age estimates for each past RLME. With the exception of the 1811-1812

earthquakes, these ages are estimated from two types of data, as described above. Uncertainty distributions for the ages of the two previous RLME sequences were developed from age dating of liquefaction features. Tables 6.1.5-3 and 6.1.5-4 list liquefaction features associated with the AD 900 and 1450 RLMEs, respectively (see the CEUS SSC Project paleoliquefaction database, Appendix E). The second and third columns list the minimum and maximum ages for these features defined as time before January 1, 2011. The ages were chosen based on the age range for the liquefaction features. The remaining columns of each table list possible ages for the two RLME sequences. The cells in each row contain an “X” when the age range for the liquefaction feature is in conflict with the RLME age at the top of the column. For example, the second feature in Table 6.1.5-3, “MarkedT01-01,” has an age range of 511–591 years before January 1, 2011. Those columns of the table with RLME ages outside of this range are marked with an “X.” The first feature, “Tyr01-01” has an age range of 211–711 years, which allows all of the possible ages listed in the column headings. Thus, no cells are marked with an “X” for this feature.

The last row of Tables 6.1.5-3 and 6.1.5-4 lists the number of liquefaction features whose age estimates are inconsistent with the specified RLME ages. As indicated, there are no RLME ages that do not conflict with at least one liquefaction feature age range. However, there are possible RLME ages where the number of liquefaction feature age conflicts is small compared to the total number of features. For example, age estimates for the AD 1450 RLME in the range of 511–590 years are in conflict with the ages for 2–4 liquefaction features, while age estimates outside this range are in conflict with 6–8 features. Similarly, age estimates for the AD 900 RLME in the range of 1,011–1,211 years are in conflict with the ages for 1–4 liquefaction features, while age estimates outside this range are in conflict with the ages for 7 or more liquefaction features.

The data listed in Tables 6.1.5-3 and 6.1.5-4 were used to construct distributions for the age of the two RLMEs. The limits of possible ages were defined based on the age limits that are inconsistent with the ages of four or fewer liquefaction features. This age range was chosen because the number of feature age inconsistencies grows quickly outside this range. A trapezoidal probability density function was constructed using these age limits and assigning equal probability to ages that were in conflict with the ages of fewer features. The assigned probability density functions and the resulting cumulative distribution functions for RLME age are shown on Figure 6.1.5-7.

The uncertainty distributions for in-cluster RLME annual frequency were then computed by repeatedly simulating samples of RLME dates from the age distributions shown on Figure 6.1.5-7 and computing a relative likelihood distribution for RLME rate from each sample. The resulting distributions were then combined to produce a composite distribution for RLME rate. These composite distributions were then represented by five-point discrete approximations. The resulting distributions for RLME recurrence frequency are listed in Tables 6.1.2-5 and 6.1.2-6 for the Poisson and Renewal models, respectively.

The out-of-cluster RLME rate for the NMFS was estimated from the data presented in Holbrook et al. (2006), who indicate initiation of NMFS clusters of large earthquakes 1,000 years ago (the start of the current cluster) and 4,000 years ago (the start of the previous cluster). These data correspond to one closed interval and one open interval. Using the likelihood formulation of

Equation 5.3.3.4, the distribution for out-of-cluster RLME frequency listed in Table 6.1.5-7 was developed.

The paleoliquefaction data gathered in the New Madrid region indicates that the prehistoric earthquakes have occurred in sequences closely spaced in time that are similar to the 1811-1812 sequence. Figure 6.1.5-8 shows the estimated earthquake sizes and locations for the 1811-1812 sequence (from Johnston and Schweig, 1996) and the two previous sequences. These data indicate that the RF has ruptured in all three sequences, but the NMN and NMS sources may not have produced large earthquakes in all three sequences. The available data allow for the possibility that the third earthquakes on the NMN and NMS sources may have been dependent earthquakes, on the order of a unit magnitude smaller than the main earthquakes. However, it is also possible that the paleoliquefaction record is not completely known for these earthquakes and they may have been comparable in size to the larger historical earthquakes. These observations were used to construct two alternative scenarios for the relative frequency of earthquake sequences on the central New Madrid fault sources, one in which all three components produce large earthquakes in each RLME sequence and one in which the NN component ruptures in two out of three RLME sequences. During preliminary model development, it was found that these two alternatives produced minimal difference in computed hazard. Therefore, the recurrence model presented here only includes the alternative of all three components.

### **6.1.6 Reelfoot Rift—Eastern Rift Margin Fault**

Several studies have concluded that the eastern Reelfoot rift margin is a fault zone characterized by recurrent movement in the Quaternary, with the most recent earthquake at some localities occurring within the Holocene (e.g., Crone, 1992; Luzietti et al., 1992; Crone and Schweig, 1994; Cox et al., 2006). Based on the results of these studies and preliminary results of seismic surveys along the Mississippi River that show evidence for near-surface faulting (Dr. B. Magnani, Center for Earthquake Research and Information, U. of Memphis, pers. comm., May 29, 2009), two independent sources of RLMEs, referred to as the Eastern Rift Margin South (ERM-S) and North (ERM-N) RLME sources, are included in the seismic source model. Uncertainties in the location, rate, and size of earthquakes that may occur on these two RLME sources are outlined in logic trees (Figures 6.1.6-1a and 6.1.6-1b). Locations of tectonic features and key localities where detailed geophysical surveys and subsurface explorations have been conducted to evaluate the location and activity of faults and paleoliquefaction features along the eastern margin of the Reelfoot rift zone are shown on Figure 6.1.6-2 and discussed below. Additional information used to identify and characterize RLME sources along the eastern margin of the Reelfoot rift zone is summarized in Appendix Tables C-6.1.6 and D-6.1.5.

The Crittenden County fault zone (CCFZ), located in northeastern Arkansas about 25 km (15.5 mi.) northwest of Memphis, Tennessee, is a northeast-trending zone of high-angle (up-to-the-northwest throw) reverse faulting that extends at least 32 km (20 mi.; Crone, 1992). The CCFZ, which has no known surface expression, was one of the first structures along the southeastern Reelfoot rift margin to be identified from interpretation of seismic profiles as a potential source of damaging earthquakes (Crone, 1992; Luzietti et al., 1992; Williams et al., 1995). The CCFZ roughly coincides with the southeastern margin of the northeast-trending Reelfoot rift (Figure 6.1.6-2). Based on this coincidence, Crone (1992) suggests that preexisting, west-dipping normal

faults within the rift may have been reactivated as reverse faults with up-to-the-west movement during the Late Miocene and Tertiary.

A history of recurrent fault movement from the Mesozoic into the Quaternary is interpreted by Williams et al. (1995) using seismic data (Vibroseis, Mini-Sosie, shotgun, and weight drop) and drillhole data. High-resolution seismic-reflection and refraction data show deformed and faulted beds of Pleistocene (and possibly Holocene) age above the deeper, well-imaged CCFZ in Eocene and older strata. The possible association of these shallow deformation features with the CCFZ suggests that recurrent movement may have occurred on the fault zone in the Quaternary (Williams et al., 1995). However, the lack of a clear connection between the near-surface faults that disrupt the Quaternary section and the main flexure and faults at depth leads to some uncertainty in the interpretation of the shallow faults. The sense of vertical offset in Quaternary deposits is opposite to the net structural relief in the underlying rift and on the deeper structure. Reflections from the Quaternary-Eocene unconformity show warping, dip, or interruptions in places over the CCFZ that suggest a length of at least 16 km (10 mi.) of near-surface deformation; this deformation may represent Quaternary or Holocene movement (Luzietti et al., 1992).

Williams et al. (1995) interpret one seismic profile to show that the unconformity between Eocene and overlying Quaternary deposits (referred to as the QE unconformity) has 5 m (16.5 ft.) of relief and is faulted approximately 2 m (6.5 ft.), both down to the west across one trace of the CCFZ. A second profile shows a fault with approximately 1 m (3.3 ft.) of down-to-the-east throw. The deformation extends into the overlying deposits, and a Holocene reflector is deformed by a rootless, second-order structure that is interpreted to be a bending-moment fault formed in response to the monoclinical bulge caused by the subjacent main reverse fault or an oblique-slip component in a strike-slip regime (Williams et al., 1995). Mihills and Van Arsdale (1999) also suggest that Holocene uplift may be associated with the CCFZ.

Chiu et al. (1997) report a distinct seismicity lineation that appears to be associated with the southeastern Reelfoot rift margin approximately 25 km (15.5 mi.) to the northeast of the CCFZ. They noted that focal mechanisms suggest that minor faulting on this margin is characterized by right-lateral strike-slip with high-angle thrust faulting. The faulting is generally consistent with an east-west-oriented, maximal, horizontal, compressional stress, similar to the regional stress regime. Based on analysis of intensity data, Hough and Martin (2002) conclude that a large aftershock of the December 11, 1811, New Madrid earthquake ( $M 6.1 \pm 0.2$ ) occurred within the southwestern one-third to one-half of this band of seismicity.

Paleoseismic and geomorphic investigations along the eastern margin of the Reelfoot rift from Meeman-Shelby Forest State Park (approximately 25 km [15.5 mi.] north of Memphis) to the Tennessee-Kentucky border are presented by Cox and others (Cox, Van Arsdale, and Harris, 2001; Cox, Van Arsdale, et al., 2001; Cox, Van Arsdale, and Larsen, 2002; Cox et al., 2006) (Figure 6.1.6-2). The results of these investigations show that the southeastern rift margin coincides with a 150 km (93 mi.) long linear topographic scarp from near Memphis to the Tennessee-Kentucky line; S-wave reflection profiles, auger data, and trench excavations reveal late Wisconsinan-Holocene surface faulting and late Holocene liquefaction associated with this fault-line scarp (Cox, Van Arsdale, and Harris, 2001; Cox, Van Arsdale, et al., 2001; Cox, Van

Arsdale, and Larsen, 2002; Cox et al., 2006). Cox, Van Arsdale, and Harris (2001), following Fisk (1944), refer to this fault as the Big Creek fault. Cox, Van Arsdale, et al. (2001) and other researchers (e.g., Csontos et al., 2008) subsequently refer to this zone of faults as the southeastern or eastern Reelfoot rift margin fault system. Based on variation in sense of throw along strike and flower-structure geometry observed in seismic profiles, Cox and others (Cox, Van Arsdale, et al. 2001; Cox, Van Arsdale, and Larsen, 2002) conclude that this fault is a strike-slip fault and is currently accommodating right-lateral strain along the boundary of the hanging wall of the RFT. Significant right-lateral offset (8–15 m [26.2–49.2 ft.]) and vertical ( $\geq 3$  m [9.8 ft.]) of up-to-the-west throw) displacement of a late Pleistocene fluvial channel (approximately 20 ka) is inferred from stratigraphic and structural relationships observed in paleoseismic trenches at the Porter Gap locality (Cox, Van Arsdale, and Larsen, 2002). This offset is the result of multiple (at least two) surface faulting earthquakes, the most recent being between 2,000 and 2,500 years ago (Cox, Van Arsdale, and Larsen, 2002; Cox et al., 2006).

Evidence for Holocene faulting also is observed in paleoseismic trenches at the Meeman-Shelby Forest paleoseismic site, and constraints on timing of the most recent earthquakes at this site and the Porter Gap site allow for the possibility of a single late Holocene rupture of  $\geq 80$  km (50 mi.) (Cox et al., 2006; Figure 6.1.6-2). Paleoliquefaction surveys along the Hatchie and Obion rivers near Covington and Dyersburg, Tennessee, to date have not identified paleoliquefaction features of this age, but the ages of some prehistoric liquefaction features along the two rivers have not yet been constrained (Dr. M. Tuttle, pers. comm., March 5, 2010). Along the northern part of the fault zone at the Union City site, seismic profiling and push-core transect data suggest only 1.5 m (5 ft.) of down-to-the-northwest faulting of early Wisconsinan Roxana Loess, with no discernable deformation of late Wisconsinan Peoria Loess (Cox et al., 2006). Cox et al. (2006) speculate that this segment turned off (or activity decelerated significantly) in the late Pleistocene-Holocene on the northeastern part of the fault zone north of the intersection of the RFT and the eastern margin of the rift.

One of the key structures identified in seismic data in the vicinity of the Meeman-Shelby Forest paleoseismic trenching locality is a high-angle (about 75 degrees), west-dipping reverse fault that Williams et al. (2001) identified and named the Meeman Shelby fault (MSF; Figure 6.1.6-3a). Cox and others (Cox, Van Arsdale, and Larsen, 2002; Cox et al., 2006) correlate this fault pick with a northeast-trending fault along the bluff escarpment. As imaged in a high-resolution Mini-Sosie seismic reflection line, the MSF displaces Paleozoic and Cretaceous units 70 and 40 m (230 and 131 ft.), respectively; deformation of the overlying Eocene strata is expressed primarily as an up-to-the-west fold with amplitude of about 50 m (164 ft.) at the base (Williams et al., 2001). Similar structures (i.e., having up-to-the-west folding) are observed in seismic profiles along the CCFZ, which lies approximately 18 km (11 mi.) to the west at its northernmost mapped location, and along a N33°E trend, approximately 33 km (20.5 mi.) northeast of the Meeman-Shelby vibroseis line (Williams et al., 2001). In a more recent paper, Odum et al. (2010) reevaluated the Mini-Sosie seismic reflection line and now suggest that the MSF is a N13°W trending fault that correlates with the eastern boundary fault of Joiner Ridge, a 10–15 km (6.2–9.3 mi.) wide by approximately 50 km (31 mi.) long structure defined by the uplift of the Pliocene-Pleistocene unconformity surface (Csontos et al., 2008).

The westernmost pick of the MSF as imaged on the Mini-Sosie line also lines up with a series of three fault picks identified in a high-resolution seismic survey conducted along the Mississippi River from Caruthersville, Missouri, to Helena, Arkansas (Dr. B. Magnani, CERI, U. of Memphis, pers. comm., May 29, 2009) (Figure 6.1.6-2). A line drawn through these fault picks (ERM-RP) projects along an approximately N30°E trend through the original Meeman-Shelby fault pick identified by Williams et al. (2001). Although there is currently no independent evidence that a fault of this trend is present at this location, a similar N30°E trend is exhibited by the postulated Memphis and Ellendale faults, which Van Arsdale et al. (2002) describe as possible Quaternary (and Holocene in the case of the Ellendale fault) active structures.

#### 6.1.6.1 Evidence for Temporal Clustering

The first node of the logic tree addresses the issue of temporal clustering of earthquakes in the present tectonic stress regime (Figure 6.1.6-1). The available data regarding number and timing of recent earthquakes and long-term slip rates for the ERM sources are not sufficient to evaluate whether the ERM RLME sources exhibit evidence for temporal clustering. Therefore, this branch of the tree is not applicable to the Reelfoot rift ERM-S and ERM-N RLME sources.

#### 6.1.6.2 Geometry and Style of Faulting

The primary basis for characterizing two independent RLME sources along the eastern margin of the rift is the apparent differences in the timing and recency of late Pleistocene and Holocene surface deformation inferred from paleoseismic investigations (Cox, Van Arsdale, and Harris, 2001; Cox, Van Arsdale, et al., 2001; Cox, Van Arsdale, and Larsen, 2002; Cox et al., 2006). Based on the evidence for cumulative slip, as well as on the timing and recency of faulting along the rift margin, Cox, Van Arsdale, and Harris (2001) suggest that lateral slip on the southeastern rift margin (ERM-S) is greatest southwest of the restraining bend (adjacent to the Reelfoot thrust hanging wall). In this area, 25 m (82 ft.) of reverse separation underlies the bluff along the southern part of the margin. On the northern segment (ERM-N), the rift margin is characterized by a less prominent scarp (9 m [29.5 ft.] high) and a lack of seismicity.

The location of late Quaternary faulting has been identified at only a few localities where detailed paleoseismic trenches, geophysical surveys, and drilling have been conducted (Figure 6.1.6-2). The zone of bedrock faulting associated with the Reelfoot rift margin, however, is considerably wider. In the vicinity of the CCFZ, the zone of basement faults may be on the order of 4–8 km (2.5–5 mi.) wide (Hildenbrand, 1982; Crone, 1992). Csontos and Van Arsdale (2008) show the zone to be as much as 10–12 km (6.2–7.5 mi.) wide north of Memphis (Figure 6.1.6-2 inset). Uncertainty in the width of the zone of faulting and location of future ruptures along this margin is therefore represented by a zone rather than a single fault.

The location, and extent, of the ERM-N is based primarily on Cox, Van Arsdale, et al. (2001). The ERM-N source zone is centered on the pronounced topographic escarpment and lineament identified by Cox, Van Arsdale, et al. (2001; Figure 6.1.6-3b). The basis for the dashed extension of the ERM-N into Kentucky as shown by Cox et al. (2006) is not discussed in that publication, and this feature is not topographically expressed in the digital elevation model data. Cox, Van

Arsdale, and Harris (2001) speculate that a basement fault may have controlled the emplacement of the Big Foot pluton that appears to coincide with a boundary between two drainage basin asymmetry domains to the north of Union City. There is no supporting data to demonstrate that a Quaternary fault is present; thus in the absence of topographic evidence for the extension of the fault to the north, the dashed extension is not included directly in the characterization of the ERM-N RLME source. However, the northern end of the ERM-N is treated as a leaky boundary (i.e., it is not a barrier to future fault ruptures) allowing ruptures to propagate further to the northeast along the dashed extension.

The location of the ERM-S segment is based on faults observed in paleoseismic trenches, geophysical surveys, and alignments of geomorphic features (Cox et al., 2006). Based on the orientation of the ERM fault in the current stress field, on the linear geometry of the fault system inferred from geomorphology, and on focal mechanisms of minor faulting along the margin, the predominant sense of slip for this fault system is considered to be right-lateral strike-slip with a component of reverse slip. Cox et al. (2006) interpret Holocene right-lateral slip on the basis of focal plane mechanisms of contemporary seismicity and evidence for right-lateral offset of late Pleistocene channel deposits.

To the south of the Meeman-Shelby Forest State Park area, evidence for latest Pleistocene to Holocene activity is noted for the CCFZ (Williams et al., 1995) and possibly for a N30°E trend defined by the fault picks identified in the recent river seismic survey (ERM-RP) (Dr. B. Magnani, Center for Earthquake Research and Information, U. of Memphis, pers. comm., May 29, 2009). These two alternatives are included as the southern extension of the ERM-S (Figure 6.1-2b). The validity and continuity of the ERM-RP as a continuous fault have not been confirmed. For this reason, this alternative (ERM-SRP) is given less weight (0.4) than the ERM-SCC (weight of 0.6), which is a known fault having Quaternary and possible Holocene activity.

Within the zones associated with the ERM-N, the ERM-SCC and ERM-SRP faults are distributed uniformly throughout the zone subparallel to the preferred fault traces; the faults are modeled as vertical strike-slip faults. Both the northeastern and southwestern ends of the zones are modeled as leaky to allow for uncertainty in the extent of possible reactivated faults along the rift margin.

The probability distribution used to model seismogenic thickness for the NMFS RLME source (Section 6.1.5.2), which is consistent with analysis of focal mechanisms along the ERM (Chiu et al., 1997), is used to model the ERM RLME sources: 13 km (8 mi.; weight of 0.3), 15 km (9.3 mi.; weight of 0.5), and 17 km (10.6 mi.; weight of 0.2).

### 6.1.6.3 RLME Magnitude

There are little (ERM-S) or no (ERM-N) data except for possible fault length that provide direct constraints on the magnitude of prehistoric earthquakes along the southeastern margin of the Reelfoot rift.

The ERM-S source extends for a distance of approximately 114 km (71 mi.). The fault is similar in length and style of faulting to the New Madrid South fault (discussed in Section 6.1.5). There

are only limited paleoseismic data from which to identify the length of fault ruptures or the size of individual displacements for prehistoric earthquakes on this fault zone. Information on timing of earthquakes shown on Figure 6.1.6-4, which is discussed below in Section 6.1.6.4, allows for the possibility of a  $\geq 80$  km (50 mi.) long rupture between the Porter Gap and Meeman-Shelby Forest sites, but does not preclude shorter ruptures (Cox et al., 2006). Vertical displacement of 0.5 m (1.6 ft.) and right-lateral offset of 0–2 m (0–6.6 ft.) during the most recent earthquake at the Porter Gap site are reported by Cox et al. (2006).

Ruptures of  $\leq 80$  or 114 km ( $\leq 50$  or 71 mi.), assuming seismogenic depths ranging from 13 to 17 km (8.1 to 10.5 mi.), yield magnitude estimates ranging from  $\leq \mathbf{M} 7.0/ \mathbf{M} 7.4$  (Wells and Coppersmith [1994] magnitude-length and magnitude-area relationships) to  $\leq \mathbf{M} 7.4/ \mathbf{M} 7.6$  (Somerville et al. [2001] magnitude-area relationship, median) (Table 6.1.6-1). Displacements of 0.5 or 2.1 m (1.5 or 6.9 ft.) (calculated oblique slip) would suggest magnitudes of  $\mathbf{M} 6.5$ – $7.1$  to as much as  $\mathbf{M} 6.7$ – $7.3$  based on empirical relationships for magnitude from maximum or average displacement, respectively (Table 6.1.6-1).

Given the uncertainty in the dimensions of paleoruptures, a wide range of values that capture the range in RLME magnitude estimates suggested by limited fault-specific data and analogy to the NMS fault is used to characterize the southern segments of the ERM south of the intersection with the Reelfoot rift. The resulting distribution for the expected RLME magnitude is tabulated below.

<b>Expected ERM-S RLME Magnitude (M)</b>	<b>Weight</b>
6.7	0.15
6.9	0.2
7.1	0.2
7.3	0.2
7.5	0.2
7.7	0.05

The ERM-N segment is approximately 73 km (45.5 mi.) long, which is more comparable in length to the New Madrid North (NMN) fault. There are no data on paleoearthquake rupture dimensions that can be used to estimate magnitude. Ruptures of 73 km (45.5 mi.), assuming a seismogenic depth ranging from 13 to 17 km (8 to 10.6 mi.), yield magnitude estimates ranging from  $\mathbf{M} 7.0$  (Wells and Coppersmith [1994] magnitude-area relationship) to  $\mathbf{M} 7.4$  (Somerville et al. [2001] magnitude-area relationship, median) (Table 6.1.6-2). A distribution similar to that used for the ERM-S, but with a lower maximum value based on the shorter total length, is used to characterize the ERM-N. The distribution is tabulated below.

Expected ERM-N RLME Magnitude (M)	Weight
6.7	0.3
6.9	0.3
7.1	0.3
7.4	0.1

#### 6.1.6.4 RLME Recurrence

The remaining nodes of the ERM RLME logic trees address the estimation of recurrence rate of RLMEs.

##### *Recurrence Method*

The data available for assessing the recurrence frequency of ERM RLMEs consist of the number of earthquakes that postdate a specific geologic stratum. Therefore, the “Earthquake Count in a Time Interval” approach is used to assess RLME recurrence frequency.

##### *Recurrence Data*

Paleoseismic investigations indicate that several paleoearthquakes have occurred along and within the southeastern part of the Reelfoot rift. Figure 6.1.6-4 is a summary diagram showing the relative timing and slip information inferred from paleoseismic investigations at the Porter Gap and Meeman-Shelby Forest localities on the ERM-S. The youngest calibrated radiocarbon ages of sediments predating the latest faulting earthquake (~0.5 m [1.6 ft.] vertical displacement) are 4,100–3,900 yr BP at Shelby County and 2,790–2,740 yr BP at Porter Gap (Cox et al., 2006). Radiocarbon ages from sediments postdating the latest faulting are 2,120–1,800 yr BP at Shelby County and 945–765 yr BP at Porter Gap. Minor liquefaction adjacent to the fault observed at the Porter Gap site is similar in age to widespread liquefaction features in the New Madrid region that are associated with an earthquake that occurred 2,750 yr BP ± 150 yr (Appendix E). An interpreted offset Wisconsinan paleochannel at Porter Gap records an unknown number of surface faulting earthquakes. It is assumed that at least two and possibly four earthquakes of a size similar to the recent earthquake have occurred at this locality in the past approximately 20 kyr. The infrared stimulated luminescence analysis ages of samples from the offset channel fill are 19,600 yr BP ± 1,900 yr and 19,900 yr BP ± 1,740 yr (Cox et al., 2006).

The recurrence data for the ERM RLME sources are more limited than for the NMFS RLME source. Except for the Porter Gap locality along the ERM-S segment that has a reported slip rate based on an offset channel, the recurrence data for the other segments of the ERM RLME source consists of an estimated number of earthquakes within a time period (inter-earthquake intervals or elapsed time intervals are not well constrained). There is no specific information regarding the timing of recent earthquakes on the CCFZ or inferred ERM-RP faults.

The northern segment of the southeastern rift margin fault system (ERM-N) appears to be less active than the segment to the south. Paleoseismic data from the Union City site are insufficient to estimate the timing or number of earthquakes that formed the 9 m (29.5 ft.) high scarp. The most recent faulting at a site near Union City along the northern segment of the fault appears to postdate Sangamon–early Wisconsinan terrace deposits (60–35 ka), but predate late Wisconsinan Peoria Loess (?) (ca. 24–12 ka; Cox, Van Arsdale, et al., 2001). Paleoliquefaction features in Kentucky dated at 11,300 yr BP  $\pm$  200 years (Appendix E) could be related to an earthquake on the ERM-N. However, these features are approximately 40 km (25 mi.) north of the northeastern end of the ERM-N source, and their correlation to the most recent earthquake recorded at the Union City site is uncertain. Based on these observations, one or possibly two earthquakes have occurred on the ERM-N fault source since 12–35 ka. Due to uncertainty in what fault produced the paleoliquefaction features in western Kentucky, highest weight (0.9) is given to the evidence for a single earthquake on the ERM-N at the Union City site since 12–35 ka.

### *Earthquake Recurrence Model*

As discussed in Section 5.3.3, the Poisson model is used as the default earthquake recurrence model with weight 1.0 for the ERM-S and ERM-N RLME sources as there are not sufficient data to justify including an alternative model.

### *RLME Annual Frequency*

The final node of the logic tree addresses the uncertainty distributions for the annual frequency of RLMEs (Figure 6.1.6-1). These distributions were developed using the methodology described in Section 5.3.3.1. The relative-likelihood-based distribution was developed using Equation 5.3.3-2.

For the ERM-S RLME source, the number of past earthquakes,  $N$ , was set at two, three, or four. The interpretation of the data does not favor one of these three values, so they are given equal weight in the RLME logic tree (Figure 6.1.6-1a). The time period  $T$  is treated as uniformly distributed over the range of 17.7–21.7 kyr. The resulting distributions for RLME recurrence frequency are listed in Table 6.1.6-3.

For the ERM-N RLME source, the number of past earthquakes,  $N$ , was set at one or two, with weights of 0.9 and 0.1, respectively, as indicated above (Figure 6.1.6-1b). The time period  $T$  is treated as uniformly distributed over the range of 12–35 kyr. The resulting distributions for RLME recurrence frequency are listed in Table 6.1.6-4.

### **6.1.7 Reelfoot Rift—Marianna**

Earthquake-induced liquefaction features, including large sand blows comparable in size to the NMSZ sand blows, have been identified near Marianna, Arkansas, about 75 km (46.5 mi.) southwest of Memphis, Tennessee (Tuttle et al., 2006; Al-Shukri et al., 2005, 2006, 2009). These sand blows, which are located 80 km (50 mi.) south of the southwestern end of the NMSZ, formed between about 5 and 10 ka and predate paleoearthquakes attributed to the NMSZ. The

presence of the features suggest a nearby source of Holocene RLMEs in the southeastern part of the Reelfoot rift outside of the NMSZ, which is herein referred to as the Marianna (MAR) RLME source. Paleoliquefaction features used to define the MAR source zone also are at least 30 km (19 mi.) south of the southern limits of the ERM RLME sources (Figures 6.1-2b and 6.1.6-2). The possibility that some of the earthquakes that triggered paleoliquefaction in the Marianna area originated on faults associated with the ERM RLME sources is considered as discussed below. A logic tree outlining the source characterization parameters for the MAR RLME source is shown on Figure 6.1.7-1. Data and observations used to characterize the MAR RLME source are summarized in Appendix Tables C-6.1.7 and D-6.1.7. Figures 6.1.7-2 and 6.1.7-3 show the locations of paleoliquefaction sites and structural features in the Marianna region in the southern part of the Reelfoot rift.

Tuttle et al. (2006) observed that a large sand blow at the Daytona Beach site near Marianna, which formed about 3500 BC (5,500 yr BP), may correlate with smaller sand blows to the northeast and southwest up to 175 km (108.7 mi.) away. Al Shukri et al. (2005) identified an earthquake at the Nancy 1 site near Marianna that occurred shortly after 4,850–4,800 yr BP. Al-Shukri et al. (2009) identified additional older paleoliquefaction features at the Daytona Beach Southeast site: those that formed about 10 ka and others that possibly predate 10 ka. A compound sand blow that formed about 4800 BC (6,800 yr BP) at the St. Francis 500 site may have formed as the result of several very large, closely timed earthquakes.

The location(s) of the earthquake source(s) responsible for these paleoliquefaction features is not known, but the size of the sand blows implies strong ground shaking at Marianna (Al-Shukri et al., 2005). A fault zone associated with the eastern Reelfoot rift margin is judged as a likely source for several reasons: its great length (approximately 300 km [186.5 mi.]); history of seismic activity; late Wisconsinan–early Holocene fault movement in western Tennessee; and structural relationship to the New Madrid fault system (Tuttle et al., 2006). Other potential fault sources in the vicinity of Marianna include the Big Creek fault zone and the White River fault zone.

A northwest-trending lineament defined by sand blows extends from the Daytona Beach locality to the northwest and southeast; the lineament initially defined to be approximately 10 km (6 mi.) in length (Tuttle et al., 2006) has been extended to a total length of 17 km (10.5 mi.) based on additional trenching and ground-penetrating radar surveys (Al Shukri et al., 2009; Al Quadi, 2010) (Figures 6.1.7-2 and 6.1.7-3). Its length, linear morphology, and parallelism to the nearby White River fault zone support the interpretation that the lineament may be fault controlled rather than related solely to lateral spreading (Al-Shukri et al., 2009). Al-Shukri et al. (2009) also identified a fracture in a trench exposure with a strike of N50°W (subparallel to the lineament) that crosscuts the sand blows. Although suggestive of being structurally controlled, further work is needed to verify by geologic and/or geophysical studies that strata below the sand layer that liquefied are faulted.

#### 6.1.7.1 Evidence for Temporal Clustering

The first node of the logic tree for the MAR RLME source (Figure 6.1.7-1) addresses the issue of temporal clustering of earthquakes in the present tectonic stress regime. Available published and

unpublished information on the timing of paleoearthquakes in the Marianna region that is compiled in the paleoliquefaction database (Section 6.1.7.4) indicates that four earthquakes occurred during the time period from approximately 10 to 4.8 ka and that no late Holocene paleoliquefaction features have been identified to date. Tuttle (2009) cites the absence of late Holocene earthquakes in the southern rift as possible evidence that the locus of activity within the Reelfoot rift migrates over periods of 5–15 kyr. The data, while suggestive of possible temporal clustering, do not clearly demonstrate that the causative structures are in a period of inactivity. It also is unclear whether some of the paleoliquefaction features are due to earthquakes that originated on the Eastern Rift Margin (ERM) RLME source described above in Section 6.1.6. These uncertainties are represented by the equal weight assigned to the “in” versus “out” of a cluster models. In the case of the “out-of-a-cluster” model, the characterization defaults to the background (either the Mesozoic-and-younger Mmax zone or the Reelfoot rift seismotectonic zone).

### 6.1.7.2 Geometry and Style of Faulting

The location of the causative structure(s) for the earthquakes that produced the Marianna paleoliquefaction features is not well constrained based on the present state of knowledge, but there is evidence to indicate that at least some of the features are related to earthquakes on a local fault. The MAR RLME zone used for this study encompasses the paleoliquefaction sites that have been used to define the northwest-trending Daytona Beach lineament as well as the more distant Nancy and St. Francis sites near Marianna and Marianna Gap, respectively. The zone includes structures that have been considered as possible sources of the earthquakes that produced the paleoliquefaction, including the ERM RLME faults, Big Creek fault, and White River fault (Tuttle et al., 2006).

Northeast-trending faults, including possible structures related to the ERM faults and the subparallel Big Creek fault, are likely to be reactivated as predominantly strike-slip faults with a reverse component, based on focal mechanisms recorded in the southern Reelfoot rift (Chiu et al., 1997) and general orientation within the present north-northeast-directed maximum horizontal stress field (Zoback, 1992b). The eastern Reelfoot rift margin affects the regional drainage pattern in both the St. Francis basin and the Western Lowlands (Spitz and Schumm, 1997). The Big Creek fault zone parallels the Reelfoot rift margin and marks the boundary between south-trending Wisconsinan valley-train deposits and southwest-trending Holocene meander-belt deposits (Fisk, 1944; Krinitzsky, 1950).

The northwest-trending White River fault zone (WRFZ) is characterized as a steeply dipping, predominantly strike-slip fault with a small up-to-the-southwest component of reverse slip (Fisk, 1944; Krinitsky, 1950). Schumm and Spitz (1996) and Spitz and Schumm (1997) show the WRFZ as a left-lateral strike-slip fault. Schumm and Spitz (1996) note that the WRFZ is defined by numerous geologic and topographic features, which include a northwest-trending magnetic lineament, northwest-trending basement faults within the Western Lowlands, northwest-trending Paleozoic faults in the Ozark Uplands, extremely angular northwest-trending salients in the valley margins, tributaries to the L'Anguille River that form a drainage pattern parallel to the WRFZ, and the breach and offset of the southern end of Crowley's Ridge that may be structurally controlled. Schumm and Spitz (1996) observe that many of the anomalous features

are located on Pleistocene and Holocene deposits, indicating that much of the suggested deformation may be as young as Holocene in age. Csontos et al. (2008) describe the WRFZ as an up-to-the-south fault, based on gravity, magnetic (Hildenbrand and Hendricks, 1995; Langenheim and Hildenbrand, 1997), and seismic reflection data (Howe, 1985).

Based on these observations, two equally weighted orientations that subparallel the sides of the MAR zone are used to model fault ruptures: vertical, northeast-trending strike-slip faults and vertical northwest-trending strike-slip faults. The faults suggested as possible sources for the earthquakes that generated the Marianna paleoliquefaction features extend beyond the boundaries of the MAR zone. Uncertainties in the location of the epicenters and extent of paleoearthquakes in this region are accounted for by assuming that all boundaries to the MAR zone are leaky.

The probability distribution used to model seismogenic thickness for the Reelfoot rift as a whole (see Section 7.3.6) and other RLME sources in the Reelfoot rift (e.g., the New Madrid fault system and the ERM RLME sources [Sections 6.1.5.2 and 6.1.6.2]) is used to model the MAR RLME zone: 13 km (8 mi.; weight of 0.3), 15 km (9.3 mi.; weight of 0.5), and 17 km (10.5 mi.; weight of 0.2). This distribution also is consistent with seismogenic depths of between 14 and 16 km (8.7 and 10 mi.) for well-located earthquakes along the southeastern margin of the rift.

### 6.1.7.3 RLME Magnitude

The magnitudes of RLMEs in the MAR zone are not well constrained. The size of the largest paleoliquefaction features observed in trenches and imaged by ground penetrating radar surveys are comparable to the largest paleoliquefaction features observed in the NMSZ.

The maximum magnitude probability distribution for the MAR RLME magnitude gives relatively equal weight to a range of values estimated for the New Madrid South (NMS) fault based on the estimated size of the December 16, 1811, earthquake. The resulting distribution is tabulated below.

<b>Expected Marianna RLME Magnitude (M)</b>	<b>Weight</b>
6.7	0.15
6.9	0.2
7.1	0.2
7.3	0.2
7.5	0.2
7.7	0.05

#### 6.1.7.4 RLME Recurrence

The remaining branches of the logic tree describe the assessment of RLME recurrence rates.

##### *Recurrence Method*

The data available for assessing the recurrence rate of the Marianna RLMEs provide assessments of the timing of past earthquakes. Thus the “Earthquake Recurrence Intervals” approach is used with weight 1.0 (Figure 6.1.7-1).

##### *Recurrence Data*

Four ages of paleoliquefaction features are known from paleoliquefaction studies to date (Appendix E). Estimated event ages (BP = before 1950) are as follows:

Nancy1— 4,825 yr BP $\pm$ 25 yr (4.8 ka)
Nancy2—5,460 yr BP $\pm$ 130 yr and 5,620 yr BP $\pm$ 40 yr (5.5 ka and 5.6 ka)
Daytona Beach—5,440 yr BP $\pm$ 130 yr (5.4 ka)
Daytona Beach SE2—9,855 yr BP $\pm$ 295 yr and one event before that (9.9 ka and before 9.9 ka)
St. Francis 500—6,805 yr BP $\pm$ 95 yr (6.8 ka)

Sand blows of similar age (5.5 ka) at Nancy2 and Daytona Beach probably formed during the same earthquake. Slightly older sand blows at Nancy2 (5.6 ka) could also have formed during the same earthquake. Because the age estimates of these sand blows are based on close maximum age constraints, the 4.8 and 5.5 ka sand blows could not have formed during the 6.8 ka earthquake (recorded at St. Francis 500). It also seems unlikely that the 9.9 ka sand blow formed during the 6.8 ka earthquake.

The most likely sequence of earthquakes along the Daytona Beach lineament includes earthquakes at 4.8 ka, 5.5 ka, and 9.9 ka, and another earthquake before that during the late Wisconsinan. The 6.8 ka earthquake recorded at the St. Francis site looks like an additional earthquake and may be related to an earthquake sequence resulting from multiple ruptures near the intersection of the ERM and the WRFZ. The two equally weighted data sets consist of either three or four earthquakes, with the oldest occurring approximately 9.9 ka.

### Earthquake Recurrence Model

As discussed in Section 5.3.3, the Poisson model is used as the default earthquake recurrence model with weight 1.0 for the Marianna RLME source as there are not sufficient data to justify including an alternative model.

### RLME Annual Frequency

The final node of the logic tree addresses the uncertainty distributions for the annual frequency of RLMEs. These distributions were developed using the methodology described in Section 5.3.3.1. The relative likelihood of various values of the recurrence rate parameter was developed using Equation 5.3.3-4 and the observations of two or three closed recurrence intervals and one

open interval post the 9.9 ka earthquake. The value of  $\sum_{i=1}^N t_i + t_0$  was assumed to be uniformly

distributed between 9.6 kyr and 10.2 kyr with  $N$  equal to either 2 or 3. The resulting relative-likelihood-based distributions were represented by the five-point discrete distribution listed in Table 6.1.7-1.

### 6.1.8 Reelfoot Rift—Commerce Fault Zone

The Commerce geophysical lineament (CGL) is a 600 km long (373 mi.), 5–10 km (3–6 mi.) wide, northeast-trending gravity and magnetic anomaly that trends subparallel to and west of the Reelfoot rift (Hildenbrand and Hendricks, 1995). Recent studies have identified surface geomorphic anomalies, paleoseismic evidence for latest Pleistocene to Holocene tectonic deformation, and geologic structures coincident with the vertical surface projection of the CGL in southeastern Missouri along what is referred to as the Commerce section of the CGL (Baldwin et al., 2006). The following lines of evidence, both direct and indirect, for Quaternary fault activity along the Commerce section of the CGL in southeast Missouri, have been reported in the published literature as outlined by Baldwin et al. (2006) and Givler and Baldwin (2009).

- Anomalous west-flowing drainages on Crowley's Ridge (Cox, 1988; Fischer-Boyd and Schumm, 1995).
- Displacement of late Tertiary and Pleistocene to Holocene deposits (Harrison and Schultz, 1994; Harrison et al., 1999, 2002) along northeast-striking faults favorably oriented to be reactivated in the present-day stress field.
- Paleoliquefaction features within the Western Lowlands of southeastern Missouri that, in part, coincide with the CGL (Vaughn, 1991, 1992, 1994).
- Presence of diffuse contemporary seismicity in partial alignment with the CGL (Harrison and Schultz, 1994; Langenheim and Hildenbrand, 1997).
- Geophysical evidence of Tertiary and Quaternary deformation coincident with the surface traces of previously mapped bedrock faults in the Bloomfield Hills and Benton Hills (Stephenson et al., 1999; Odum et al., 2002).

- Evidence of late Pleistocene to early Holocene deformation on the Idalia Hill fault zone based on geomorphic mapping, acquisition of seismic reflection, and ground-penetrating radar data, coupled with paleoseismic trenching and borehole information collected at the South Holly Ridge site, near Idalia, Missouri (Baldwin et al., 2006).
- Preliminary results of ongoing investigations of the Penitentiary fault, an apparent en echelon continuation of the Commerce fault to the northeast into southern Illinois, also provide evidence in multiple seismic lines of interpreted latest Pleistocene and possible early Holocene (?) faulting. The continuation of the Penitentiary fault to the northeast is poorly constrained; the geomorphic expression of a reactivated fault-line scarp is not apparent to the north (Odum et al., 2002; Baldwin et al., 2008; Givler and Baldwin, 2009).

Based on these observations, an RLME fault source that encompasses faults and probable fault-related geomorphic features exhibiting evidence of repeated late Pleistocene and Holocene activity is included in the source model. A logic tree summarizing the characterization of this RLME source, referred to as the Commerce Fault Zone RLME source, is shown on Figure 6.1.8-1. The Commerce Fault Zone RLME source is modeled as a strike-slip fault zone extending south from the northern limit of the mapped Penitentiary fault (Tamms, Illinois) to the southern end of the paleoseismic sites near Qulin Ridge (Qulin, Missouri), where evidence for Quaternary activity (paleoliquefaction and anomalous stream deflections) has been documented (approximately at the Missouri-Arkansas border), a distance of about 120 km (75 mi.; Figure 6.1.8-2). Evidence for late Quaternary deformation and repeated latest Pleistocene to Holocene faulting along the CGL also is observed to the north in southern Illinois and Indiana. This deformation is considered in the characterization of the Wabash Valley RLME source (discussed in Section 6.1.9).

Locations of tectonic features and key localities where detailed geophysical surveys and subsurface explorations have been conducted to evaluate the location and activity of faults and paleoliquefaction features along the Commerce Fault Zone RLME source are shown on Figure 6.1.8-2 and are discussed below. Additional information used to identify and characterize an RLME source along the Commerce section of the CGL is summarized in Appendix Tables C-6.1.8 and D-6.1.8.

#### 6.1.8.1 Evidence for Temporal Clustering

The first node of the logic tree for the Commerce Fault Zone RLME source (Figure 6.1.8-1) addresses the issue of temporal clustering of earthquakes. Early studies (Vaughn, 1994; Harrison et al., 2002) near Qulin Ridge and the English Hills, respectively, suggested that there may be evidence for two late Holocene earthquakes on structures related to the CGL, which could imply that the fault/fault zone is in a more active period of deformation. However, as noted below in Section 6.1.8.4, the liquefaction and secondary faulting used to document these Holocene earthquakes may be related to strong ground motion from earthquakes occurring elsewhere in the Reelfoot rift. There is no evidence to support large-magnitude earthquakes along the Idalia Hill or Penitentiary faults directly southwest and northeast of the English Hills as would be expected if large-magnitude earthquakes had ruptured the fault zone in the late Holocene. The available data regarding number and timing of recent earthquakes and long-term slip rates for the

Commerce Fault Zone RLME source are not sufficient to evaluate whether this RLME source exhibits evidence for temporal clustering. Therefore, this branch of the tree is not applicable to this source.

### 6.1.8.2 Geometry and Style of Faulting

The Commerce Fault Zone RLME source is modeled as a fault zone that encompasses late Pleistocene and possible Holocene active faults identified from geophysical, geomorphologic, and geologic data that are coincident with CGL defined by gravity and magnetic anomalies (Hildenbrand and Hendricks, 1995; Figure 6.1.8-3). Specific features used to define this RLME source are the Penitentiary fault (Givler and Baldwin, 2009; Baldwin et al., 2008); the Commerce fault (Palmer, Hoffman, et al., 1997; Palmer, Shoemaker, et al., 1997; Harrison and Schultz, 1994; Harrison et al., 2002); the Idalia Hill fault zone (Baldwin et al., 2006); and faults imaged in seismic data near Qulin Ridge (Stephenson et al., 1999) that align with an anomalous deflection of the St. Francis River (Fischer-Boyd and Schumm, 1995; Figure 6.1.8-2).

At most of the sites where detailed geophysical and subsurface paleoseismic studies have been conducted, deformation occurs across a broad zone up to a kilometer or slightly more in width. In some areas, such as in the English Hills where north-northeast-striking faults at Thebes Gap appear to splay north from the Commerce fault, the zone of Quaternary faulting encompasses the entire width of the CGL (e.g., Harrison et al., 1999; Figure 6.1.8-2). A zone the width of the entire CGL is therefore used to capture the uncertainty in the location of deformation that may be related to the Commerce Fault Zone RLME source. In the hazard analysis, future ruptures are distributed uniformly within this zone.

Recent analysis and relocation of 19 earthquakes ( $M \leq 3.6$ ) in the northeastern part of the NMSZ, using a velocity model of the Mississippi embayment with appropriate depths to bedrock beneath seismic stations, show that 2 of the earthquakes occurred at depths between 13 and 15 km (8 and 9.3 mi.; Shumway, 2008). Herrmann and Ammon (1997) show depths of up to 16 km (10 mi.) for earthquakes in the Reelfoot rift. Based on these data, the following distribution for seismogenic crustal thickness is used to characterize the Commerce Fault Zone RLME source: 13 km (8 mi.; weight of 0.3), 15 km (9.3 mi.; weight of 0.5), and 17 km (10.6 mi.; weight of 0.2).

The Commerce Fault Zone RLME source is modeled as a zone of vertical strike-slip faulting based on the following geologic and seismologic observations:

- The style of neotectonic and older deformation in the Thebes Gap area is consistent with strike-slip deformation along near-vertical structures (Harrison et al., 1999).
- Near-vertical faults and complex flower-like structures are observed in seismic data at multiple locations along the CGL (Stephenson et al., 1999; Harrison et al., 1999; Baldwin et al., 2006, 2008).
- The regional northeast strike of the faulting is favorably oriented for right-lateral transpressive slip in the present north-northeast-directed maximum horizontal stress field (Zoback, 1992).

- Focal mechanism analysis of a **M** 3.85 (E[**M**] 3.83) earthquake (February 5, 1994) along the northward-projected trend of the Commerce fault zone shows motion was primarily right-lateral strike-slip along a north-northeast azimuth (Herrmann and Ammon, 1997).

Ruptures within the Commerce Fault Zone RLME source are modeled as striking N47°E, subparallel to the Commerce and Penitentiary faults within the zone. The northwest and southeast boundaries are fixed based on the width of the CGL as defined from geophysical data and mapped faults. The northeast and southwest boundaries of the zone are considered leaky boundaries to allow for ruptures to extend along the trend of the CGL into adjacent less well studied areas where there is not a sufficient paleoseismic record to demonstrate or preclude recent activity along a similar rheological boundary.

### 6.1.8.3 RLME Magnitude

The Commerce Fault Zone RLME source extends for a distance of approximately 120 km (75 mi.). There are only limited paleoseismic data from which to identify the length of fault ruptures or the size of individual displacements for prehistoric earthquakes on this fault zone. Information on timing of earthquakes shown on Figure 6.1.8-4, which is discussed below in Section 6.1.8.4, allows for the possibility of a rupture involving the entire fault source (120 km [75 mi.]) in a single earthquake or possibly two or more smaller earthquakes. A late Pleistocene earthquake may have ruptured the southern half (55–63 km [34–39 mi.]). Baldwin et al. (2006) cite evidence for 2.0–2.2 m (6.6–7.2 ft.) of separation of a late Pleistocene–early Holocene colluvium/paleosol in trenches across the Idalia Hill fault zone; this separation may represent tectonic slip (possibly combined vertical and horizontal slip) during the most recent surface faulting earthquake at that site.

Ruptures of 55–65 km (37–40 mi.) or 120 km (75 mi.)—the southern half or entire length, respectively—assuming a seismogenic depth ranging from 13–17 km (8–10.5 mi.), yield magnitude estimates ranging from **M** 6.9–**M** 7.5 (Wells and Coppersmith, 1994) for a magnitude-area and magnitude-length relationships to **M** 7.2–**M** 7.7 (Somerville et al., 2001) for magnitude-area relationship, median. A displacement of 2.0–2.2 m (6.6–7.2 ft.) would suggest magnitudes of **M** 7.0–7.1 and **M** 7.2–7.3 based on empirical relationships for magnitude from maximum or average displacement, respectively (Wells and Coppersmith, 1994; Table 6.1.8-1). Smaller ruptures, however, cannot be precluded, based on the available data.

Given the uncertainty in the dimensions of paleo-ruptures, and the broad range of uncertainty considered even for 1811-1812 earthquakes, of which the NMN (NM2 earthquake) may be an analog for the Commerce source (see Table 6.1.5-2), the distribution tabulated below that captures a wide range in RLME magnitude estimates is used.

<b>Expected Commerce Fault Zone RLME Magnitude (M)</b>	<b>Weight</b>
6.7	0.15
6.9	0.2
7.1	0.2
7.3	0.2
7.5	0.2
7.7	0.05

#### 6.1.8.4 RLME Recurrence

The remaining branches of the logic tree describe the assessment of RLME recurrence rates.

##### *Recurrence Method*

The data available for assessing the recurrence rate of the Commerce Fault Zone RLME provides assessments of the timing of past earthquakes. Thus the “Earthquake Recurrence Intervals” approach is used with weight 1.0 (Figure 6.1.8-1).

##### *Recurrence Data*

The ages of earthquakes interpreted from stratigraphic and structural relations observed in trenches and from paleoliquefaction earthquakes at sites along the Commerce section of the CGL are shown on Figure 6.1.8-4. The colored bars show possible rupture scenarios (i.e., ruptures that are permitted by the timing of earthquakes documented at the four paleoseismic localities). The paleoseismic investigation localities are ordered from south to north.

Paleoliquefaction studies in the Western Lowlands along the southern part of the Commerce section of the CGL provide evidence for at least four poorly constrained prehistoric earthquakes, which are related to the NMSZ and/or structures associated with the CGL (Vaughn, 1994; Tuttle, Lafferty, and Schweig, 1998; Tuttle, Chester, et al., 1999) (Figure 6.1.8-2). Vaughn (1994) estimates the timing of four prehistoric earthquakes that, from oldest to youngest, occurred at about (1) 23,000–17,000 yr BP; (2) 13,400–9,000 yr BP, (3) AD 240–1020; and (4) AD 1440–1540. In the CEUS SSC paleoliquefaction database, these are assigned the following ages: 22,750 yr BP  $\pm$  650 yr; 12,600 yr BP  $\pm$  200 yr; 1,050 yr BP  $\pm$  150 yr; and 500 yr BP  $\pm$  150 yr. The two most recent earthquakes of Vaughn (1994) likely are related to paleoearthquakes associated with seismic sources within the NMSZ (Tuttle, Schweig, et al., 2002). Baldwin et al. (2006) note that the two earlier paleoliquefaction earthquakes may correlate to earthquakes on nearby CGL structures, based on the earthquake’s apparent older age and greater size. The timing of these earthquakes is compatible with the timing of poorly constrained earthquakes

interpreted at the South Holly Ridge site on the Idalia fault, approximately 30 km (19 mi.) to the northeast.

At the South Holly Ridge site, analysis of trench, borehole, and ground-penetrating radar data constrains the timing of the most recent earthquake on the Idalia fault to between the latest Pleistocene—about 18 ka—and early Holocene (pre-7.7 ka). Evidence for a penultimate earthquake predates 23–18 ka (Baldwin et al., 2006).

Evidence of Quaternary and probable Holocene deformation involving near-surface faults in the Benton Hills and Thebes Gap areas has been documented by Harrison and Schultz (1994); Harrison et al. (1999); Palmer, Hoffman, et al. (1997); Palmer, Shoemaker, et al. (1997); Stephenson et al. (1999); and Odum et al. (2002) (see Data Summary table D-6.1.5; Figure 6.1.8-2). Harrison et al. (1999) document evidence for four episodes of Quaternary faulting: one in late- to post-Sangamon, pre- to early Roxana time (between 60 and 50 ka); one in syn- or post-Roxana, pre-Peoria time (between 35 and 25 ka); and two to possibly three in post-Peoria time (<17 ka). At least two earthquakes may have occurred in the latest Holocene (just after 2-sigma calibrated calendar ages of 3747–3369 BC and AD 639–968) (Harrison et al., 2002). The youngest in the Benton Hills may represent secondary tectonic deformation correlative with a NMSZ earthquake (Harrison et al., 1999).

The timing of recent earthquakes on the Penitentiary fault are not well constrained at this time; preliminary analysis of data from paleoseismic investigations indicates latest Pleistocene and possible early Holocene faulting (Givler and Baldwin, 2009).

The possibility that most or the entire Commerce Fault Zone RLME source ruptured during an earthquake approximately 23,000 yr BP is permitted, but not required by the available data. The syn- or post-Roxana period of deformation observed on structures in the English Hills broadly overlaps with earthquakes recorded at the South Holly Ridge site on the Idalia Hill fault (Baldwin et al., 2006), with paleoliquefaction in the Western Lowlands near Qulin (Vaughn, 1994), and possibly with poorly constrained earthquakes on the Penitentiary fault (Baldwin et al., 2008). The available data also suggest the possibility of an earthquake involving only the southern part of the fault; the latest Pleistocene earthquake observed at the South Holly Ridge site (18,500–7,600 yr BP) broadly overlaps with the paleoliquefaction in the Western Lowlands (Vaughn, 1994).

The middle to late Holocene deformation earthquakes observed in the English Hills, however, are not evident on the easternmost fault strands of the Idalia Hill fault at the South Holly Ridge site, approximately 30 km (19 mi.) to the south or at the Penitentiary site about 19 km (12 mi.) to the north (Baldwin et al., 2006, 2008). Thus it is not clear that the middle to late Holocene earthquakes recorded on faults within the English Hills and by paleoliquefaction in the Western Lowlands near Qulin are related to large-magnitude earthquakes on faults within the Commerce Fault Zone RLME source. The preferred interpretation (weight 0.75) is that two earthquakes have occurred in the past 23 kyr with the possibility (weight 0.25) that the count is three earthquakes.

### Earthquake Recurrence Model

As discussed in Section 5.3.3, the Poisson model is used as the default earthquake recurrence model with weight 1.0 for the Commerce Fault Zone RLME source as there are not sufficient data to justify including an alternative model.

### RLME Annual Frequency

The final node of the logic tree addresses the uncertainty distributions for the annual frequency of RLMEs (Figure 6.1.8-1). These distributions were developed using the methodology described in Section 5.3.3.1. The relative likelihood of various values of the recurrence rate parameter was developed using Equation 5.3.3-4 and the observations of one or two closed

recurrence intervals and one open interval. The value of  $\sum_{i=1}^N t_i + t_0$  was assumed to be uniformly

distributed between 18.9 and 23.6 kyr with  $N$  equal to either 1 or 2. The resulting relative-likelihood-based distributions were represented by the five-point discrete distribution listed in Table 6.1.8-2.

### 6.1.9 Wabash Valley

Mapping and dating of liquefaction features throughout most of the southern Illinois basin and in parts of Indiana, Illinois, and Missouri have identified energy centers for at least eight Holocene and latest Pleistocene earthquakes having estimated moment magnitudes of  $M$  6 to  $\sim 7.8$  (Obermeier et al., 1991; Munson et al., 1997; Pond and Martin, 1997; Obermeier, 1998; McNulty and Obermeier, 1999; Tuttle, Chester, et al., 1999) (Table 6.1.9-1). The proximity of the energy centers for the two largest earthquakes inferred from the paleoliquefaction data (referred to as the Vincennes and Skelton paleoearthquakes), both of which are located within 25–40 km (15.5–25 mi.) of Vincennes, Indiana, suggests that there is a source of RLMEs ( $\sim M = 6.7$ – $7.8$ ) in the Wabash Valley region. These two paleoearthquakes are located in the general vicinity of the most numerous and strongest historical earthquakes ( $M$  4–5.5) in the lower Wabash Valley of Indiana and Illinois (Obermeier, 1998). A logic tree outlining the characterization of the Wabash Valley RLME source for this study is presented on Figure 6.1.9-1. Other prehistoric earthquakes identified from paleoliquefaction studies in southern Illinois and southern Indiana are considered in the characterization of the Illinois basin-extended basement seismotectonic zone (Section 7.3.5) and the modification of the Mmax priors.

The locations of tectonic features and the key localities in the Wabash Valley region of southern Illinois and southern Indiana where studies have been conducted to evaluate evidence for tectonic surface deformation, the location and activity of faults, and extent of paleoliquefaction features are shown on Figure 6.1.9-2 and are discussed below. Figure 6.1.9-3 shows the Wabash RLME source relative to total magnetic anomaly and residual isostatic gravity data. Additional information used to identify and characterize the Wabash Valley RLME source is summarized in Appendix Tables C-6.1.9 and D-6.1.9).

### 6.1.9.1 Evidence for Temporal Clustering

The first node of the logic tree for the Wabash Valley RLME source considers the issue of temporal clustering of earthquakes in the present tectonic stress regime (Figure 6.1.9-1). The paleoliquefaction evidence used to identify the Wabash Valley RLME source, which is discussed in Section 6.1.9.4, includes two earthquakes in the latest Pleistocene to Holocene. The record is not sufficient to recognize periods of temporal clustering (i.e., faster or slower rates of activity). Therefore, this branch of the tree is not applicable to the Wabash Valley RLME source.

### 6.1.9.2 Geometry and Style of Faulting

The geometry of the Wabash Valley RLME source zone is based on consideration of a variety of structural, geologic, geomorphic, and paleoseismologic observations and hypotheses as outlined below.

- A broad flexure (bend or stepover) in bedrock structure has been postulated to concentrate stress in this region (Hildenbrand and Ravat, 1997). This bend or stepover lies near the northern terminus of an approximately 600 km (375 mi.) long magnetic and gravity lineament, referred to as the Commerce geophysical lineament (CGL), which extends from Vincennes, Indiana, far into Arkansas. Late Quaternary faulting recently has been identified near this lineament, close to the Missouri-Illinois border (Langenheim and Hildenbrand, 1997) (see discussion of the Commerce Fault Zone RLME source, Section 6.1.8). Wheeler and Cramer (2002) discuss the concept of a left stepover functioning as a restraining bend if the CGL is acting as a right-lateral strike-slip fault in the current tectonic environment.
- McBride and Kolata (1999) note a possible relationship between the most deformed region of the Precambrian basement yet to be identified beneath the Illinois basin (the Enterprise subsequence) and some of the largest twentieth-century earthquakes in the central Midcontinent. This region roughly coincides with the area of the broad flexure in the CGL.
- Morphometric analysis of the land surface, detailed geologic mapping, and structural analysis of bedrock in the Wabash Valley generally indicate westward tilting of the modern land surface, preferred channel migration to the west side of the valley (see inset on Figure 6.1.9-2), a convex longitudinal profile of the Wabash River where it crosses the La Salle anticlinal belt, and increased river incision into the floodplain downstream of the anticlinal belt. These geomorphic anomalies occur along the western edge of the CGL in the restraining bend region (Fraser et al., 1997).
- Evaluation of recently acquired industry seismic-reflection profile data from southern Illinois provides additional insights as to the causative structures for recent earthquakes. McBride et al. (1997) and McBride, Hildenbrand, et al. (2002) report a northeast-trending zone of dipping reflectors and diffractions that they interpret as a zone of intrusions or a zone of deformation, or both. McBride, Kolata, et al. (2002) suggest that the zone, which lies along the CGL, may represent thrust faults deep within crystalline basement, faults that may be subject to reactivation. The largest instrumentally recorded earthquake in the Illinois basin, which occurred on November 9, 1968, had a moment magnitude of  $M$  5.4 (Johnston, 1996a) or  $m_{BLg}$  5.5 (McBride, Hildenbrand, et al., 2002) ( $E[M]$  5.32). Its focal mechanism has a nodal plane that is subparallel to the zone of dipping reflections, a midcrustal hypocenter that

is located within the zone, and a seismic moment that corresponds to a rupture zone approximately the same size as one of the reflectors. McBride et al. (1997) and McBride, Hildenbrand, et al., (2002) note that earthquakes may be nucleating along compressional structures in crystalline basement and thus may occur in parts of the basin where there are no obvious surface faults or folds. They conclude that shallow Paleozoic structures are “decoupled” from deeper, possibly seismogenic, structures. The results of their study suggest that a seismogenic source just north of the New Madrid seismic zone in the Wabash Valley area consists, in part, of thrusts in the basement localized along igneous intrusions that are locally coincident with the CGL.

- McBride et al. (2007) further evaluate major structures within the Illinois basin, including the Wabash Valley fault system (WVFS) and the La Salle anticlinal belt (LSA). Based on results of reprocessing seismic reflection profiles, combined with earthquake hypocenter parameters, three distinct seismotectonic environments are defined in the upper crust in the southern portion of the Illinois basin. First, a fault pattern that appears to correspond to the steep nodal plane of a strike-slip mechanism earthquake (April 3, 1974,  $m_b$  4.7,  $E[M]$  4.29) is interpreted to be a deeply buried rift zone or zone of intense normal faulting underpinning a major Paleozoic depocenter of the Illinois basin (Fairfield basin). Second, a similar earthquake (June 10, 1987,  $m_b$  5.2,  $E[M]$  4.95) and its well-located aftershocks define a narrow zone of deformation that occurs along and parallel to the frontal thrust of the LSA. Third, the hypocenter of the largest earthquake in the study area (November 9, 1968,  $m_b$  5.5,  $E[M]$  5.32) as outlined above may be spatially associated with a prominent zone of dipping middle crustal reflections, just west of the WVFS, which have been interpreted as a deeply buried blind thrust.
- Holocene activity is evidenced on faults within the WVFS. The WVFS is a linear northeast-southwest band of narrow graben structures that lie within the southern part of the Illinois basin (Bristol and Treworgy, 1979; Treworgy, 1981; Sexton et al., 1986; Kolata and Nelson, 1991; Rene and Stanonis, 1995; Bear et al., 1997; Hildenbrand and Ravat, 1997; Woolery, 2005). The WVFS consists of a series of high-angle normal faults and strike-slip faults with trends between N15°E and N50°E. These faults lie within and form the borders of the northeast-trending Grayville graben. The Grayville graben (~20 km [~12.5 mi.] wide, ~0.7 km [~0.4 mi.] maximum basement relief, and <40 km [25 mi.] long) underlying the Wabash Valley developed during late Precambrian-Cambrian (Iapetan) rifting, perhaps in response to stress concentrations generated by a bend in the Reelfoot–Rough Creek–Rome rift system (Hildenbrand and Ravat, 1997). Although some workers (e.g., Sexton et al., 1986) have suggested that the WVFS may be a northward extension of the Reelfoot rift, others have noted that both the dike pattern and mapped WVFS terminate near the Reelfoot–Rough Creek–Rome rift system (Hildenbrand and Ravat, 1997) and that fault displacements of the WVFS decrease southward in the direction of the NMSZ (Bear et al., 1997). The WVFS offsets the Pennsylvanian and older units with vertical offsets of as much as 145 m (480 ft.) along the faults (Nelson, 1995; Bristol and Treworgy, 1979). Woolery (2005) describes high-angle deformation associated with one of the faults in the WVFS, the Hovey Lake fault, extending above the Paleozoic bedrock and into upper Quaternary sediment. Time-displacement calculations from the data show approximately 10.5 m (34.4 ft.) of offset on the top-of-bedrock horizon, located 7.7 m (25.3 ft.) below ground surface, suggesting fault movement at this site as late as ~37 ka. More recent Holocene deformation is evidenced by

folding and faulting of sediments across the Uniontown scarp, a prominent scarp on the floodplain of the Ohio River that is interpreted to be associated with the Hovey Lake fault (Counts et al., 2009a, 2009b; Van Arsdale et al., 2009).

- Analysis of the June 18, 2002,  $M_w$  4.6 (E[**M**] 4.38) earthquake, which occurred on a steeply dipping fault within the WVFS at a depth of about 18 km (11 mi.), may suggest that buried faults associated with a possible Precambrian rift system are being reactivated by the contemporary east/east-northeast-trending regional horizontal compressive stress (Kim, 2003). The source mechanism determined from regional waveform analysis is predominantly strike-slip along near-vertical nodal planes (dips 82 and 84 degrees), striking 28 and 297 degrees. The close proximity of the epicenter to the trace of the Caborn fault (WVFS) and good agreement between the strike and dip of that fault and source mechanism for the June 2002 earthquake suggest that the earthquake occurred on that fault.
- Analysis of geodetic data in the southern Illinois basin suggests systematic northwestward motion of about 0.5–0.7 mm/yr (0.02–0.03 in.) with respect to the Stable North American Reference Frame. Block models, which assume boundaries along the Cottonwood Grove fault system–Rough Creek graben and the WVFS, indicate marginal block velocities with possible strike-slip motion along the WVFS, and east-west motions along the CGRCG (Hamburger et al., 2008).

The causative structures for the paleoearthquakes are not known. The Wabash Valley RLME source zone encompasses the structural features, postulated neotectonic deformation, and locations of the inferred energy centers for the Vincennes and Skelton earthquakes described above (Figure 6.1.9-2). Characteristics for future earthquake ruptures in the WV RLME source zone are given in Table 5.4-2.

Given the uncertainty in the location of the causative faults, the boundaries of the Wabash Valley RLME source zone are modeled as leaky.

Two alternative depths are used to estimate the seismogenic thickness of the crust in the Wabash Valley RLME source zone: 17 km (10.6 mi.; weight of 0.7) and 22 km (13.7 mi.; weight of 0.3). Higher weight is assigned to the shallower depth based on the evidence for reactivations of structures in the upper 15–17 km (9.3–10.6 mi.) of crust as inferred from recent seismicity (McBride et al., 2007). This depth is more likely to represent the average depth of seismogenic crust throughout the RLME source zone. The greater seismogenic thickness is consistent with the focal depth of the 1968 earthquake, which is postulated to have ruptured a reverse fault in the basement in the Fairfield basin, a localized basin within the southern Illinois basin.

Earthquakes in the in the Wabash Valley RLME source zone are modeled as a mixture of vertical strike-slip and reverse (with a random dip in the range of 40–60 degrees) based on the focal mechanisms for recent earthquakes (Figure 6.1.9-2). Due to the wide range in style, orientation, and focal depth of recent earthquakes and variability of structural trends within the zone, the aleatory variability in future earthquakes within the Wabash Valley RLME source is expected to be as follows:

strike—parallel to the long axis of the zone [0.8]
2/3 strike-slip, 90 degrees
1/3 reverse, uniform 40–60 degrees to the west
N50°W [0.1] strike-slip, 90 degrees
N20°W [0.1] reverse, uniform 40–60 degrees to the west

### 6.1.9.3 RLME Magnitude

The magnitude assessments for the Wabash Valley RLME source are based on recent analysis of paleoliquefaction features associated with the Vincennes and Skelton energy centers in the vicinity of the lower Wabash Valley of southern Illinois and Indiana. The magnitude of the largest paleoearthquake in the lower Wabash Valley (the Vincennes-Bridgeport earthquake), which occurred  $6,011 \pm 200$  yr BP, was estimated to be  $\geq \mathbf{M}$  7.5 using the magnitude-bound method (Obermeier, 1998). Use of a more recently developed magnitude-bound curve for the CEUS based on a value of  $\mathbf{M} \sim 7.6\text{--}7.7$  for the largest of the 1811-1812 New Madrid earthquakes (reduced from the higher  $\mathbf{M}$  8 used in the older curve) gives a lower estimate of  $\mathbf{M}$  7.1–7.3 depending on the minimum (115 km [71.5 mi.]) and maximum (153 km [95 mi.]) distance, respectively, of distal paleoliquefaction features related to this paleoearthquake (Olson et al., 2005b). The lower-bound relationship developed by Castilla and Audemard (2007) from a worldwide database gives a range of  $\mathbf{M}$  7.0–7.3 for the same minimum and maximum distance values.

Estimates based on a suite of geotechnical analyses (cyclic stress and energy stress methods) range from  $\mathbf{M}$  7.5 to 7.8 (summarized in Obermeier et al., 1993). The highest value of  $\mathbf{M}$  7.8 is based on geotechnical studies using the energy-acceleration method (a possibly flawed energy method, see Table 6.1.9-1) (Pond and Martin, 1997). A reanalysis of this earthquake has been done by Green et al. (2004a, 2004b; Green et al., 2005) using more recent ground-motion attenuation relationships for the central United States, review of approximately 50 boring logs presented by Pond and Martin (1996) to select appropriate standard penetration test values for the reanalysis, and the most recent magnitude scaling factors suggested by Youd et al. (2001). Using the cyclic stress method, the best estimate of the magnitude for the Vincennes-Bridgeport earthquake based on all these solutions ranges from  $\mathbf{M}$  7+ to 7.5. The energy-based solution developed by Green (2001) that circumvents the use of the magnitude scaling factor, which is a significant, questionable factor in the use of the cyclic stress method in the central United States, gives a value of  $\mathbf{M} \sim 7.5$  for each of the four newer ground-motion attenuation relationships (Green et al., 2004b). The more recent evaluations by Green et al. (2005) have considered the influence of aging effects on liquefaction susceptibility and concluded that for moderately susceptible sites like those in southern Illinois, the small changes expected given the types of sediments would have little influence on the interpretation of paleomagnitude (Obermeier et al., 2001; Obermeier, pers. comm., August 2003).

The next largest earthquake, the Skelton paleoearthquake, occurred  $12,000 \pm 1,000$  yr BP (Hajic et al., 1995; Munson et al., 1997; Obermeier, 1998). The magnitude of this earthquake is estimated to be **M** 7.1–7.3 by Munson et al. (1997; using a magnitude-bound approach) or **M** 7.3 by Pond and Martin (1997; using a possibly flawed energy-stress method; see Table 6.1.9-1). Olson et al. (2005b) gives an estimate of **M** 6.7 for this paleoearthquake, and the lower-bound relationship of Castilla and Audemard (2007) would yield a value of **M** 6.3. The estimated values of the size of the epicentral area of this paleoearthquake are clearly minimums, as deposits of an age that would preserve a record of this earthquake are not widespread.

The difference in the estimated sizes of the Vincennes and Skelton paleoearthquakes is on the order of 0.5 to 1 magnitude units. This probably represents a combination of the aleatory variability in the size of individual Wabash RLMEs and epistemic uncertainties in the approaches and data used to estimate the magnitudes of the prehistoric earthquakes. Therefore, a broad probability distribution is used to capture the range in uncertainty in the magnitude of earthquakes in the Wabash Valley RLME. This distribution is tabulated below.

<b>Expected Wabash Valley RLME Magnitude (M)</b>	<b>Weight</b>
6.75	0.05
7.0	0.25
7.25	0.35
7.5	0.35

#### 6.1.9.4 RLME Recurrence

The remaining branches of the logic tree describe the assessment of RLME recurrence rates.

##### *Recurrence Method*

The data available for assessing the recurrence rate of the Wabash Valley RLMEs provide assessments of the timing of past earthquakes. Thus the “Earthquake Recurrence Intervals” approach is used with weight 1.0 (Figure 6.1.9-1).

##### *Recurrence Data*

The available data for characterizing the recurrence rate of Wabash Valley RLMEs are the estimated ages for the Vincennes-Bridgeport and Skelton paleoearthquakes described above.

### Earthquake Recurrence Model

As discussed in Section 5.3.3, the Poisson model is used as the default earthquake recurrence model with weight 1.0 for the Wabash Valley RLME source as there are not sufficient data to justify including an alternative model.

### RLME Annual Frequency

The final node of the logic tree addresses the uncertainty distributions for the annual frequency of RLMEs. These distributions were developed using the methodology described in Section 5.3.3.1. The relative likelihood of various values of the recurrence rate parameter was developed using Equation 5.3.3-4 and the observations of one closed recurrence interval between the Vincennes-Bridgeport and Skelton paleoearthquakes and one open interval post the Vincennes-

Bridgeport paleoearthquake. The value of  $\sum_{i=1}^N t_i + t_0$  was assumed to be uniformly distributed

between 11 and 13 kyr with  $N$  equal to 1. The resulting relative-likelihood-based distributions were represented by the five-point discrete distribution listed in Table 6.1.9-2.

## 6.2 Mmax Distributed Seismicity Source Zones

In the Mmax zones branch of the master logic tree, the two components of the SSC model are the RLME sources and the Mmax distributed seismicity sources or, simply, Mmax zones. As discussed in the criteria for identifying seismic sources (Section 4.1.3.3), after earthquake recurrence rate, the most important criterion for identifying a seismic source is potential differences in Mmax. The Mmax zones branch considers only this parameter in defining alternative zonation models.

### 6.2.1 Definition of Mmax Zones

The Bayesian approach to estimating Mmax, described in Section 5.2.1.1, uses a prior distribution that is defined based on a statistical analysis of the global SCR database. The statistical analyses carried out for the CEUS SSC Project indicate only a marginally significant difference in prior distributions between Mesozoic-and-younger extended crust (MESE) and non-Mesozoic-and-younger crust (NMESE). For example, the  $p$ -value associated with the separation of these two data sets is 0.14 (see Section 5.2), which indicates that there is a 14 percent chance that the two data sets were derived from the same population, such that they would be expected to have the same mean value. To account for the uncertainty in whether the SCR database can be separated with confidence into two prior distributions, two alternatives are considered in the Mmax zones model: (1) two Mmax zones that are defined by two prior distributions (MESE and NMESE), and (2) a single Mmax zone that represents a single prior distribution. The first model is assigned slightly higher weight (0.6) than the single zone model (0.4). Preference is given to the first model because there is marginal statistical significance for the separation of the SCR database into the two parts, but there is also a reasonable likelihood that there is no reliable separation of the SCR database with confidence.

Alternative configurations for the two Mmax zones are shown on Figures 6.2-1 and 6.2-2. The separation reflects the assessment of those parts of the study region that show evidence of Mesozoic-and-younger extension (MESE) and those parts that do not (NMESE). Criteria used to make this assessment are described in Section 6.2.2. The uncertainty in that assessment is represented by the two alternatives: (1) the “narrow” MESE that is distinguished by clear major Mesozoic-and-younger extensional features, and (2) the “wide” MESE whose western boundary is drawn to include more questionable evidence for such features. Because of the more technically defensible evidence for the narrow interpretation, it is assigned a weight of 0.8, and the wide interpretation is assigned a weight of 0.2.

### **6.2.2 Criteria for Defining the MESE/NMESE Boundary**

The breakup of the supercontinent of Pangaea into Laurasia to the north and Gondwana to the south resulted in Mesozoic extension of the crust and consequent development of the Atlantic Ocean (Triassic), the passive Atlantic margin (Jurassic), and the Gulf of Mexico (from Triassic to Jurassic). As a result of this extension, both the Atlantic and Gulf Coast margins generally consist of three crustal domains. For the Atlantic margin, the domains comprise rifted continental crust of Appalachian origin lying principally beneath the Coastal Plain and continental shelf, oceanic crust underlying the continental rise, and the intervening 50–100 km (30–60 mi.) wide zone of transitional, or rift-stage, crust (Klitgord et al., 1988; Holbrook, Reiter, et al., 1994). Crustal domains in the Gulf of Mexico region consist of thick transitional crust, thin transitional crust, and newly formed oceanic crust (Buffler and Sawyer, 1985; Marton and Buffler, 1994; Salvador, 1991a, 1991b; Sawyer et al., 1991). Mesozoic extension associated with opening of the Atlantic Ocean and Gulf of Mexico also resulted in extensional reactivation of Paleozoic structures within the St. Lawrence rift, Reelfoot rift, and Northern Appalachians (Tremblay et al., 2003; Lemieux et al., 2003; Wheeler, 1997; Faure et al., 2006). Lesser amounts of Mesozoic extension may have occurred within the Rough Creek and Grayville grabens (Wheeler, 1997; Wheeler and Cramer, 2002). The extent of possible Mesozoic reactivation of older Iapetan rift structures inferred to be present in basement rock beneath the Appalachian detachment or older basement structures cratonward of the well-defined Mesozoic rifts is not well constrained.

Cretaceous-and-younger extension also occurred in response to thermal processes and related uplift in the northeastern United States and eastern Canada as portions of the North American Plate rode over Cretaceous hotspots (McHone, 1996; Cox and Van Arsdale, 1997, 2002; Morgan, 1983; Crough, 1981; Sleep, 1990).

The cratonward limit of significant Mesozoic-and-younger extension is inferred from a variety of geologic, geophysical, and seismologic data. Criteria used to define this boundary are listed below, ordered from most diagnostic to least definitive for identifying Mesozoic-and-younger extension.

1. Grabens and sedimentary rift basins of Mesozoic age.
2. Mesozoic-and-younger plutons.
3. Extensive distributed brittle normal faults and basaltic (tholeiitic) dikes of Mesozoic-and-younger age.

4. Evidence for Mesozoic-and-younger regional uplift and unroofing with associated normal faulting or fault reactivation.
5. Localized extensional reactivation of pre-Mesozoic structures.
6. Favorably oriented older extensional faults (e.g., Iapetan rift faults proximal to regions of Mesozoic rifting).

Regions that generally meet the first three to four criteria are included in the MESE-narrow (MESE-N) zone. This zone includes the ECC-AM, ECC-GC, AHEX, GHEX, RR, SLR, NAP, GMH, and PEZ-N seismotectonic zones described in Section 7.0 (Table 6.2-1). A description of the geologic observations and data that demonstrate Mesozoic-and-younger extension in these zones, and the basis for the definition of the cratonward limit (boundary) of the respective units used to define the MESE-N boundary are provided in Section 7.0.

The MESE-wide (MESE-W) boundary encompasses regions that have less definitive evidence for significant Mesozoic-and-younger extension. These regions include areas that have known or possible Iapetan-rift faults that may have been reactivated during the Mesozoic (e.g., the Rough Creek and Grayville grabens, Rome Trough-Kentucky River fault system) and older Precambrian compressional structures, such as the Clarendon-Linden fault and Central Metasedimentary Belt boundary structure in western New York and Ontario, Canada, that have evidence of extensional reactivation during latest Precambrian/early Paleozoic Iapetan rifting, but have less definitive evidence for Mesozoic reactivation. The MESE-W zone differs from the MESE-N in that it adopts the wide alternative geometries for the Paleozoic Extended Zone (PEZ-W); Reelfoot rift (with Rough Creek graben, RR-RCG); and the Illinois Basin Extended Basement (IBEB) zone (Table 6.2-1). Due to the limited Mesozoic deformation or lack of clear evidence of significant Mesozoic extension in these regions, low weight (0.2) is assigned to this alternative boundary. The boundaries of these zones are discussed in the descriptions of these seismotectonic source zones in Section 7.0.

### **6.3 Maximum Magnitude Distributions for Mmax Distributed Seismicity Sources**

This section presents the Mmax distributions for the Mmax distributed seismicity sources. The methodology used to develop these distributions is presented in Section 5.2.1. The steps involved are identification of the maximum observed earthquake in each distributed seismicity source (described in Section 6.3.1) and then application of the quantitative approaches developed in Section 5.2.1 to produce the composite Mmax distributions (described in Section 6.3.2).

#### **6.3.1 Maximum Observed Earthquake Magnitude**

The maximum observed earthquake magnitude,  $m_{\max-obs}$ , represents the size of the largest non-RLME observed to have occurred within each source. The value of this magnitude is used in developing the likelihood function for the Bayesian Mmax approach (Section 5.2.1.1) and is a parameter of the Kijko approach (Section 5.2.1.2). Two sources are used to assess  $m_{\max-obs}$ . One is the CEUS SSC earthquake catalog developed for this study (Section 3); the other is the

compilation of identified paleoearthquakes that are not associated with RLME sources. The latter consists of the four non-RLMEs that have been identified in southern Illinois/southern Indiana. These earthquakes are discussed in Section 7.3.5. These earthquakes have estimated magnitudes of **M** 6.2–6.3 and represent the largest non-RLMEs in the study region.

The largest historical non-RLMEs identified in the project catalog are listed below by Mmax zone.

Mmax Distributed Source	Largest Historical Earthquake	
	Date	E[M]
Study Region	September 16, 1732	6.25
MESE-N	September 16, 1732	6.25
MESE-W	September 16, 1732	6.25
NMESE-N	May 31, 1897	5.91
NMESE-W	May 16, 1909	5.72

The 1732 earthquake occurred in the St. Lawrence region; the 1897 earthquake occurred in Giles County, Virginia; and the 1909 earthquake occurred at the border of North Dakota, Montana, and Canada.

Uncertainty in  $m_{\max-obs}$  was incorporated into the Mmax assessment using the procedure described in Section 5.2.1.1.6. The uncertainties in the magnitudes for the catalog of historical earthquakes or paleoearthquakes for each source were used to develop simulated catalogs of earthquake magnitudes. The largest values for each simulation were then used to develop a distribution for  $m_{\max-obs}$ . Figure 6.3.1-1 shows the resulting distributions for  $m_{\max-obs}$ . The blue curve on each plot shows the distribution developed for  $m_{\max-obs}$ , and the red vertical line indicates the nominal observed magnitude. The phrase “paleo” in the plot legend indicates that the set of paleoearthquakes is the controlling set for determining  $m_{\max-obs}$  and was the set used to develop the Mmax distributions. The 1882 E[M] 5.58 earthquake, which is discussed in Section 7.3, occurred very near the boundary between the ECC-GC and OKA seismotectonic zones, and the uncertainty in its location is addressed by including alternative locations. To be consistent with the assessments for the seismotectonic zones, the 1882 earthquake is considered to have occurred in either the MESE zones or the NMESE zones. However, because this earthquake is not the largest historical earthquake in either zone, the alternative locations have only a small effect on the distributions for  $m_{\max-obs}$ .

### 6.3.2 Mmax Distributions

Mmax distributions were developed for each Mmax distributed seismicity source using the Bayesian and Kijko methods. For the Bayesian Mmax approach, the alternative priors described

in Section 5.2.1.1 were used. For the study region, only the composite prior is used, as the single source zone model is based on no difference between Mesozoic extended and non-extended crust. The remaining Mmax zones are assigned the composite prior with weight 0.4, and either the MESE or NMESE prior with weight 0.6. Figures 6.3.2-1 through 6.3.2-5 show the resulting Mmax distributions obtained by each method. Indicated in the legend of each figure are the weights assigned to the individual Mmax methods following the weighting approach described in Section 5.2.1.1. The final weighted composite distributions are indicated by the thick red bars on each plot.

The Mmax distributions for the study region and the MESE-W and NMESE-N Mmax zones utilize the paleoearthquake record to define the distribution for  $m_{\max-obs}$ . Because the number of paleoearthquakes is small, the Kijko method is assigned zero weight in these cases. The Kijko method is given appreciable weight (0.23) only for the NMESE-W Mmax zone.

The continuous distributions shown on Figures 6.3.2-1 through 6.3.2-5 were used to construct five-point discrete approximations for use in hazard analyses. These distributions are listed in Table 6.3.2-1. The differences in the distributions for NMESE-N and NMESE-W reflect the presence or absence of the Wabash Valley paleoearthquakes within the boundary of the source zone.

## 6.4 Recurrence Parameters

The recurrence parameters (i.e., rate and  $b$ -values) for the Mmax zones were calculated using the methodology and parameters described in Section 5.3.2. Briefly, this methodology divides the source zone into cells of dimensions a quarter or half degree and then calculates the rate and  $b$ -value in each cell using the likelihood function of the data in that cell, together with penalty functions that tend to smooth the cell-to-cell variation in the rate or the  $b$ -value. In addition, this procedure characterizes epistemic uncertainty in the recurrence parameters by generating eight alternative maps of the recurrence parameters.

### 6.4.1 Rate and $b$ -Value Maps for Single Zone and Two Zones

Figures 6.4.1-1 through 6.4.1-9 show the mean recurrence maps for the three alternative configurations of the Mmax zones distributed seismicity source zones and the three choices of magnitude weights (i.e., Cases A, B, and E). Maps of the calculated uncertainties in recurrence parameters, as well as alternative recurrence maps that represent that uncertainty (eight alternative maps for each source-zone configuration), are shown in Appendix J.

The maps in this section show more pixelation than the maps in Section 7. This is because the cell size had to be increased to half a degree to overcome computer run-time limitations.

### **6.4.2 Comparison of Recurrence Parameters to Catalog**

Figures 6.4.2-1 through 6.4.2-15 compare the expected counts from the recurrence maps for each source zone to the observed earthquake counts within the zone. The error bars on the data represent the 16–84 percent range of statistical uncertainty in the counts and are calculated using the approach by Weichert (1980). Each of the eight curves represents expected counts (i.e., rate times equivalent period of completeness) for one of the eight equally weighted alternative maps, taking Mmax into account.

These comparisons indicate a good agreement between predicted and observed rates. The only exception is the MESE-N source zone, for which the recurrence model has a slight tendency to underestimate the rates for magnitude 5.7 and higher. This is the result of deviations of the data from the exponential magnitude distribution. The actual discrepancy is smaller than it appears in the figures. If one were to consider the effect of uncertainty in Mmax on the recurrence curves, the curves would spread out at these higher magnitudes, with some of the curves coming closer to the data.

**Table 6.1-1**  
**Summary of Data Used to Assess RLME Recurrence Frequencies**

RLME Source	Recurrence Method	Recurrence Data
Charlevoix	Earthquake recurrence intervals Equation 5.3.3-4	Data Set 1 $N = 1, \sum_{i=1}^N t_i + t_0 = 348 \text{ yr}$
	Earthquake count in a time interval Equation 5.3.3-2	Data Set 2 $N = 3, T$ uniformly distributed between 6 and 7 kyr Data Set 3 $N = 4, T$ uniformly distributed between 9.5 and 10.2 kyr
Charleston	Earthquake recurrence intervals Equation 5.3.3-4 for Poisson case Equation 5.3.3-9 for renewal model case	Earthquake data defining intervals 1886 Earthquake Earthquake A: 95% interval on Con age 523 to 618 yr BP 95% interval on All age 523 to 617 yr BP Earthquake B: 95% interval on Con age 910 to 1,063 yr BP 95% interval on All age 920 to 1,065 yr BP Earthquake C: 95% interval on Con age 1,569 to 1,854 yr BP 95% interval on All age 1,637 to 1,888 yr BP Earthquake D: 95% interval on Con age 3,338 to 3,684 yr BP 95% interval on All age 3,334 to 3,642 yr BP Earthquake E: 95% interval on Con age 4,868 to 5,277 yr BP 95% interval on All age 4,924 to 5,320 yr BP

RLME Source	Recurrence Method	Recurrence Data
Cheraw Fault	Earthquake recurrence intervals Equation 5.3.3-4	In-cluster data $N = 1 \text{ or } 2, \sum_{i=1}^N t_i + t_0 \text{ uniformly distributed between 20 and 25 kyr}$ Out-of-cluster assessment 200, 350, or 500 kyr cluster recurrence interval
	Slip rate Equation 5.3.3-5	In-cluster data $D$ uniformly distributed between 3.2 and 4 m; $T$ uniformly distributed between 20 and 25 kyr Out-of-cluster data $D$ uniformly distributed between 3.2 and 8 m; $T$ between 0.4 and 2 Myr (uniformly distributed between 1.2 and 2.0 Myr, tapering to 0 at 0.4 Myr)
Meers Fault	Earthquake recurrence intervals Equation 5.3.3-4	In-cluster data $N = 1, \sum_{i=1}^N t_i + t_0 \text{ uniformly distributed between 2,153 and 2,968 yr}$ Out-of-cluster assessment 200, 350, or 500 kyr cluster recurrence interval
New Madrid Fault System	Earthquake recurrence intervals Equation 5.3.3-4 for Poisson case Equation 5.3.3-9 for renewal model case	Earthquake data defining in-cluster intervals 1811-1812 earthquake sequence AD 1450 earthquake sequence: 95% interval on age 461 to 523 yr BP AD 900 earthquake sequence: 95% interval on age 979 to 1,147 yr BP Out-of-cluster data $N = 1, \sum_{i=1}^N t_i + t_0 = 4,000 \text{ yr}$

RLME Source	Recurrence Method	Recurrence Data
Eastern Rift Margin—South	Earthquake count in a time interval Equation 5.3.3-2	$N = 1, 2, \text{ or } 3, T$ uniformly distributed between 17.7 and 21.7 kyr
Eastern Rift Margin—North	Earthquake count in a time interval Equation 5.3.3-2	$N = 1 \text{ or } 2, T$ uniformly distributed between 12 and 35 kyr
Marianna	Earthquake recurrence intervals Equation 5.3.3-4	$N = 2 \text{ or } 3, \sum_{i=1}^N t_i + t_0$ uniformly distributed between 9.6 and 10.2 kyr
Commerce Fault Zone	Earthquake recurrence intervals Equation 5.3.3-4	$N = 1 \text{ or } 2, \sum_{i=1}^N t_i + t_0$ uniformly distributed between 18.9 and 23.6 kyr
Wabash Valley	Earthquake recurrence intervals Equation 5.3.3-4	$N = 1, \sum_{i=1}^N t_i + t_0$ uniformly distributed between 11 and 13 kyr

**Table 6.1.1-1  
Charlevoix RLME Recurrence Frequency**

<b>RLME Frequency (earthquakes/year)</b>			<b>Weight</b>
<b>Data Set 1</b>	<b>Data Set 2</b>	<b>Data Set 3</b>	
9.3E-03	1.3E-03	9.8E-04	0.101
6.7E-03	8.4E-04	6.7E-04	0.244
4.2E-03	5.7E-04	4.7E-04	0.310
2.2E-03	3.7E-04	3.2E-04	0.244
7.7E-04	1.9E-04	1.8E-04	0.101

**Table 6.1.2-1**  
**Summary of Interpreted Charleston Earthquake Ages and Sizes from**  
**–Contemporary Ages Only” Scenario**

Earthquake	Age (years BP)	No. of Constraining Features	No. of Constraining Ages	SW-NE Extent (km)	Dist. to Energy Center (km)*	Assessment: Regional or Local?
1886	64	—		200	100	Regional
A	536–655	6	7	190	110	Regional
B	982–1,046	7	12	175	110	Regional
C	1,524–1,867	5	5	160	150	Regional
D	3,472–3,559	5	7	100	100	Local?
E	4,864–5,281	1	1	—	90	Local?

\* Assumes approximate center of 1886 Charleston meizoseismal area as energy center.

**Table 6.1.2-2**  
**Summary of Interpreted Charleston Earthquake Ages and Sizes from –All Ages” Scenario**

Earthquake	Age (years BP)	No. of Constraining Features	No. of Constraining Ages	SW-NE Extent (km)	Dist. to Energy Center (km)*	Assessment: Regional or Local?
1886	64	—	—	200	100	Regional
A	536–655	6	7	190	110	Regional
B	982–1,046	8	14	175	110	Regional
C	1,569–1,867	6	7	250	150	Regional
D	3,472–3,559	6	9	190	100	Regional
E	4,821–5,281	2	3	80?	90	Local?

\* Assumes approximate center of 1886 Charleston meizoseismal area as energy center.

**Table 6.1.2-3**  
**Charleston Liquefaction Feature Ages Used to Assess Ages of Prehistoric Earthquakes**

<b>Prehistoric Earthquake</b>	<b>Site ID</b>	<b>Age Type*</b>	<b>Minimum Age (yr BP)</b>	<b>Maximum Age (yr BP)</b>
A	BLUF-C-11	CON	316	680
A	BLUF-B-8	CON	475	655
A	BLUF-A-4	CON	307	905
A	BLUF-A-7	CON	316	678
A	HLYD-125	CON	536	680
A	SP-SPN	CON	317	667
B	CG-1	CON	796	1174
B	HLYD-XVII	CON	662	1356
B	HLYD-XIV	CON	982	1291
B	SP-SPMR-1	CON	690	1056
B	SP-SPMR-2	CON	687	1691
B	SP-BWL	CON	741	1049
B	GTWN-A	CON	663	1315
B	SP-BWR	A	766	1053
B	SP-BWR	B	1141	1383
C	FHS-1	CON	1524	1867
C	SP-SPS	CON	1178	2148
C	OLN-A	CON	794	2679
C	MM-1	CON	1400	2303
C	MB-3	CON	1145	2306
C	BLUF-A-5	A	1569	1969
C	BLUF-A-5	B	2001	2331
D	BLUF-D-14	CON	2880	3835
D	BLUF-D-15	CON	2965	3680
D	TMH-A	CON	2045	4416
D	TMH-C	CON	3415	4075
D	TMH-ARP	CON	3215	3845
D	GPWY-A	A	1870	2152
D	GPWY-A	B	3450	3827
E	GPWY-D	CON	4864	5281
E	TMH-D	A	4821	6176
E	TMH-D	B	5045	8189

\* CON = Contemporary with earthquake; B = before earthquake; A = after earthquake

**Table 6.1.2-4**  
**Charleston RLME Recurrence Frequency for Poisson Model**

RLME Frequency (earthquakes/year)					Weight
Post-2,000 yrs Earthquakes 1886, A, B, and C	Post-5,500 yrs Earthquakes 1886, A, B, and C	Post-5,500 yrs Earthquakes 1886, A, B, C, and D	Post-5,500 yrs Earthquakes 1886, A, B, C, and E	Post-5,500 yrs Earthquakes 1886, A, B, C, D, and E	
4.7E-03	4.7E-03	2.7E-03	1.9E-03	2.2E-03	0.101
3.1E-03	3.1E-03	1.9E-03	1.3E-03	1.5E-03	0.244
2.1E-03	2.1E-03	1.3E-03	9.2E-04	1.1E-03	0.310
1.3E-03	1.3E-03	8.8E-04	6.4E-04	7.8E-04	0.244
6.8E-04	6.8E-04	5.0E-04	3.4E-04	4.6E-04	0.101

**Table 6.1.2-5  
Charleston RLME Recurrence Frequency for Renewal Model**

RLME Frequency (earthquakes/year)					Weight
Post-2,000 yrs Earthquakes 1886, A, B, and C	Post-5,500 yrs Earthquakes 1886, A, B, and C	Post-5,500 yrs Earthquakes 1886, A, B, C, and D	Post-5,500 yrs Earthquakes 1886, A, B, C, and E	Post-5,500 yrs Earthquakes 1886, A, B, C, D, and E	
<b><math>\alpha = 0.3</math></b>					
6.4E-05	6.8E-05	3.5E-07	4.5E-09	1.5E-08	0.101
7.6E-06	8.0E-06	2.5E-08	2.0E-10	8.7E-10	0.244
9.5E-07	1.0E-06	2.2E-09	1.2E-11	7.0E-11	0.310
8.5E-08	9.2E-08	1.4E-10	5.4E-13	4.4E-12	0.244
2.3E-09	2.5E-09	2.7E-12	6.4E-15	8.2E-14	0.101
<b><math>\alpha = 0.5</math></b>					
1.4E-03	1.4E-03	2.2E-04	5.2E-05	7.0E-05	0.101
3.8E-04	3.9E-04	4.5E-05	8.2E-06	1.3E-05	0.244
9.5E-05	9.8E-05	9.3E-06	1.4E-06	2.5E-06	0.310
1.7E-05	1.7E-05	1.4E-06	1.7E-07	3.7E-07	0.244
1.0E-06	1.1E-06	7.6E-08	7.0E-09	2.1E-08	0.101
<b><math>\alpha = 0.7</math></b>					
2.6E-03	2.7E-03	1.0E-03	5.2E-04	5.7E-04	0.101
9.8E-04	9.9E-04	3.3E-04	1.4E-04	1.6E-04	0.244
3.2E-04	3.3E-04	9.5E-05	3.4E-05	4.5E-05	0.310
7.1E-05	7.3E-05	2.0E-05	6.1E-06	9.2E-06	0.244
5.6E-06	5.8E-06	1.5E-06	3.9E-07	7.6E-07	0.101

**Table 6.1.3-1**  
**Range of Cheraw Fault Estimated Magnitudes (M)**

Approach	Rupture Length <sup>1</sup>		Max. Displacement <sup>2</sup>		Average Displacement <sup>3</sup>		Rupture Area <sup>4</sup>			Rupture Area <sup>5</sup>		
	<b>Parameter Value</b>	30 km (18.5 mi.)	46 km (28.5 mi.)	1.6 m (5.2 ft.)	2.6 m (8.5 ft.)	1.1 m (3.6 ft.)	2.1 m (6.9 ft.)	430 km <sup>2</sup> (L = 30 km SD = 13 km Dip = 65°)	1,020 km <sup>2</sup> (L = 46 km SD = 17 km Dip = 50°)	1,321 km <sup>2</sup> (L = 46 km SD = 22 km Dip = 50°)	430 km <sup>2</sup> (30 km × 14.3 km) (assumes 65° dip)	1,020 km <sup>2</sup> (L = 46 km SD = 17 km Dip = 50°)
<b>Estimated Magnitude (M)</b>	6.6/6.6	6.9/6.9	6.8/6.8	6.9/7.0	6.8/7.0	7.0/7.2	6.6/6.7	7.0/7.0	7.1/7.1	7.0	7.4	7.5

<sup>1</sup> Wells and Coppersmith (1994)—Subsurface rupture length (km) to magnitude (M), normal fault/all types

<sup>2</sup> Wells and Coppersmith (1994)—Maximum displacement (m) to magnitude (M), normal fault/all types

<sup>3</sup> Wells and Coppersmith (1994)—Average displacement (m) to magnitude (M), normal fault/all types

<sup>4</sup> Wells and Coppersmith (1994)—Area (km<sup>2</sup>) to magnitude, normal fault/all types

<sup>5</sup> Somerville et al. (2001)—Area (km<sup>2</sup>) to magnitude

**Table 6.1.3-2**  
**Cheraw RLME In-Cluster Recurrence Frequency**

RLME Frequency (earthquakes/year)		Weight
2 Earthquakes in 20–25 ka	3 Earthquakes in 20–25 ka	
2.4E-04	3.1E-04	0.101
1.3E-04	1.9E-04	0.244
7.6E-05	1.2E-04	0.310
3.8E-05	7.2E-05	0.244
1.4E-05	3.2E-05	0.101

**Table 6.1.3-3**  
**Cheraw RLME In-Cluster Slip Rates**

RLME Fault Slip Rate (mm/year)	Weight
0.14	0.185
0.16	0.630
0.19	0.185

**Table 6.1.3-4**  
**Cheraw RLME Out-of-Cluster Recurrence Frequency**

<b>RLME Frequency (earthquakes/year)</b>	<b>Weight</b>
5.0E-06	0.333
2.9E-06	0.334
2.0E-06	0.333

**Table 6.1.3-5**  
**Cheraw RLME Out-of-Cluster Slip Rates**

<b>RLME Fault Slip Rate (mm/year)</b>	<b>Weight</b>
0.0038	0.101
0.0043	0.244
0.0054	0.310
0.0072	0.244
0.011	0.101

**Table 6.1.4-1**  
**Range of Estimated Meers Fault Earthquake Magnitudes (M)**

Approach	Rupture Length			Max. Displacement		Average Displacement		Rupture Area	
	Parameter Value	26 km (16 mi.)	37 km (23 mi.)	67 km (42 mi.)	3.5 m (12 ft.)	5.25 m (17.2 ft.)	1.75 m (5.74 ft.)	3.0 m (9.8 ft.)	390 km <sup>2</sup> (151 mi. <sup>2</sup> )
Estimated Magnitude (M)	~6.7	~6.9	~7.1	7.1–7.2	7.2–7.4	7.1–7.3	7.3–7.5	6.6–7.0	7.1–7.4

**Table 6.1.4-2**  
**Meers RLME In-Cluster Recurrence Frequency**

RLME Frequency (earthquakes/year)	Weight
2.1E-03	0.101
1.2E-03	0.244
6.7E-04	0.310
3.4E-04	0.244
1.2E-04	0.101

**Table 6.1.4-3**  
**Meers RLME Out-of-Cluster Recurrence Frequency**

RLME Frequency (earthquakes/year)	Weight
5.0E-06	0.333
2.9E-06	0.334
2.0E-06	0.333

**Table 6.1.5-1**  
**Preferred Ages for Paleoseismicity in the New Madrid Region<sup>1</sup>**

AD 1811-1812
500 yr BP $\pm$ 150 yr (350–650 yr BP)
1,050 yr BP $\pm$ 150 yr (900–1,200 yr BP)
2,750 yr BP $\pm$ 150 yr; sand blow of this age at only one site (Eaker 2); sand dike at Porter Gap (2,600–2,900 yr BP)
2,902 yr BP $\pm$ 2,138 yr; possibly same as Holbrook's event ~1000 BC or 2,514–3,560 yr BP
4,300 yr BP $\pm$ 150 yr (4,150–4,450 yr BP)

<sup>1</sup> Age in years BP, relative to AD 1950 (see Appendix E)

**Table 6.1.5-2**  
**Magnitude Comparisons for New Madrid 1811-1812 Earthquake Sequence**

Study	NM1	NM2	NM3
Johnston (1996b)	M 8.1 ± 0.3	M 7.8 ± 0.3	M 8.0 ± 0.3
Johnston (pers. comm., Aug. 31, 2004)	M 7.8–7.9	M 7.5–7.6	M 7.7–7.8
Johnston (pers. comm., Feb. 16, 2010)	Currently has no new information that would change his previous estimates. He noted that he is disillusioned with using intensity data to estimate moment magnitude and thinks that overinterpretation of the data using site correction, etc. is a problem.		
Bakun and Hopper (2004b)	M <sub>i</sub> 7.6 ( <b>M</b> 7.2–7.9) (preferred model 3)	M <sub>i</sub> 7.5 ( <b>M</b> 7.1–7.8) (preferred model 3)	M <sub>i</sub> 7.8 ( <b>M</b> 7.4–8.1) (preferred model 3)
	M <sub>i</sub> 7.2 ( <b>M</b> 6.8–7.9) (model 1)	M <sub>i</sub> 7.2 ( <b>M</b> 6.8–7.8) (model 1)	M <sub>i</sub> 7.4 ( <b>M</b> 7.0–8.1) (model 1)
Bakun (electronic comm., Feb. 3, 2010—no change, use entire range of uncertainty cited in Bakun and Hopper, 2004b)	M 6.8–7.9	M 6.8–7.8	M 7.0–8.1
Hough et al. (2000)	<b>M</b> 7.2–7.3 (using isoseismal method of Johnston, 1996) <b>M</b> 7.0–7.3 (using method of Bakun and Wentworth, 1997) <sup>1</sup>	<b>M</b> ~ 7.01 <sup>2</sup> (located on the New Madrid North fault) (using isoseismal method of Johnston, 1996)	<b>M</b> 7.4–7.5 (using isoseismal method of Johnston, 1996)
Mueller and Pujol (2001)	–	–	<b>M</b> 7.2–7.4 (preferred <b>M</b> 7.2–7.3)
Mueller et al. (2004)	<b>M</b> 7.3	<b>M</b> 6.8 (located within the Wabash Valley of southern Illinois/ southern Indiana)	<b>M</b> 7.5
Hough and Page (2011)	<b>M</b> 6.69/6.85 (min) to <b>M</b> 6.85/7.08 (max) (full range of experts) <b>M</b> 6.7 (model 1)/6.9 (model 3) <sup>3</sup>	<b>M</b> 6.72/6.86 (min) to <b>M</b> 6.91/7.09 (max) (full range of experts) <b>M</b> 6.8 (model 1)/7.0 (model 3) (NM location) <sup>3</sup> <b>M</b> 6.5 (model 1)/6.7 (model 3) (IL location near 1968 event) <sup>3</sup>	<b>M</b> 6.83/7.02 (min) to <b>M</b> 7.21/7.50 (max) (full range of experts) <b>M</b> 7.1 (model 1)/7.3 (model 3) <sup>3</sup> Scaling relationships <b>M</b> 6.8 (assume 35 km length, 15 km width, 1 m slip)

<sup>1</sup> Based on intensity values reported in Hough et al. (2000) and Bakun and Wentworth (1997) method as noted in Hough and Page (2011).

<sup>2</sup> The estimated location and magnitude of this earthquake are revised in Mueller et al. (2004).

<sup>3</sup> Using method of Bakun and Wentworth (1997) and published attenuation models; following Bakun et al. (2003) and Bakun and Hopper (2004) these are referred to as models 1 and 3.

**Table 6.1.5-3**  
**Liquefaction Constraints on Age of AD 1450 NMFS RLME**

Liquefaction Feature	Maximum Age (years before 1/1/2011)	Minimum Age (years before 1/1/2011)	Age of AD 1450 RLME (years before 1/1/2011)*							
			351	471	511	556	561	571	590	601
Tyr01-01	711	211								
MarkedT01-01	591	511	X	X						X
MarkedT01-03	591	511	X	X						X
HatchieR31-02	1551	221								
Nodena01-01	561	341						X	X	X
KochD01-01	1021	351								
LittleR09-02	696	466	X							
Eaker01-01	601	271								
Yarbro01-01	591	341								X
Yarbro03-03	591	341								X
Crav01-01	601	331								
ObionR216-02	811	611	X	X	X	X	X	X	X	X
Dodd01-01	721	556	X	X	X					
Cagle01-01	591	321								X
ObionR200-02	711	591	X	X	X	X	X	X	X	
CurrentR02-01	701	561	X	X	X	X				
Wilhelmina01-05	571	471	X						X	X
No. of Samples with Age Range Outside of Specific Age			8	6	4	3	2	3	4	8

\* X indicates sample age range does not include specified date.

**Table 6.1.5-4**  
**Liquefaction Constraints on Age of AD 900 NMFS RLME**

Liquefaction Feature	Maximum Age (years before 1/1/2011)	Minimum Age (years before 1/1/2011)	Age of AD 900 RLME (years before 1/1/2011)*					
			801	1011	1021	1131	1211	1221
CentralD01-01	1221	771						
Eaker03-01	1211	611						X
Eaker03-03	1211	611						X
Eaker02-01	1541	1011	X					
Bugg01-01	1211	1011	X					X
Hueys01-01	1211	1011	X					X
Haynes01-02	1211	611						X
Arch01-01	1351	801						
Dill01-01	1101	521				X	X	X
NewFrnk03-01	1221	1021	X	X				
NewFrnk04-01	1371	1131	X	X	X			
Johnson05-01	1211	1011	X					X
Wilhelmina01-03	1236	1106	X	X	X			
Tow01-01	1472	1020	X	X				
HillH01-01	1221	1011	X					
No. of Samples with Age Range Outside of Specific Age			9	4	2	1	1	7

\* X indicates sample age range does not include specified date.

**Table 6.1.5-5**  
**NMFS In-Cluster RLME Recurrence Frequency—Poisson Model**

RLME Frequency (earthquakes/year)	Weight
6.0E-03	0.101
3.7E-03	0.244
2.4E-03	0.310
1.4E-03	0.244
6.2E-04	0.101

**Table 6.1.5-6**  
**NMFS In-Cluster RLME Recurrence Frequency—Renewal Model**

RLME Frequency (earthquakes/year)			Weight
$\alpha = 0.3$	$\alpha = 0.5$	$\alpha = 0.7$	
3.5E-03	4.8E-03	4.4E-03	0.101
1.1E-03	2.2E-03	2.2E-03	0.244
3.2E-04	8.9E-04	1.0E-03	0.310
6.4E-05	2.6E-04	3.4E-04	0.244
4.7E-06	3.1E-05	4.7E-05	0.101

**Table 6.1.5-7**  
**NMFS Out-of-Cluster RLME Recurrence Frequency—Poisson Model**

RLME Frequency (earthquakes/year)	Weight
1.3E-03	0.101
7.2E-04	0.244
4.2E-04	0.310
2.2E-04	0.244
8.0E-05	0.101

**Table 6.1.6-1**  
**Range of ERM-S Estimated Magnitudes (M)**

Approach	Rupture Length <sup>1</sup>		Max. Displacement <sup>2</sup>		Average Displacement <sup>3</sup>		Rupture Area <sup>4</sup>			Rupture Area <sup>5</sup>		
	<b>Parameter Value</b>	≤80 km (50 mi.)	114 km (71 mi.)	0.5 m (1.5 ft.)	2.1 m (6.9 ft.)	0.5 m (1.5 ft.)	2.1 m (6.9 ft.)	≤1,040 km <sup>2</sup> (L ≤ 80 km SD = 13 km)	1,215 km <sup>2</sup> (L = 80 km SD = 15 km)	1,938 km <sup>2</sup> (L = 114 km, SD = 17 km)	≤1,040 km <sup>2</sup> (L ≤ 80 km SD = 13 km)	1,215 km <sup>2</sup> (L = 80 km SD = 15 km)
<b>Estimated Magnitude (M)</b>	≤7.2/7.2	7.4/7.4	6.6/6.5	7.1/6.9	6.8/6.7	7.3/7.2	≤7.1/7.0	7.1/7.1	7.3/7.3	≤7.4	7.4	7.6

<sup>1</sup> Wells and Coppersmith (1994)—Subsurface rupture length (km) to magnitude (M), strike-slip/all types

<sup>2</sup> Wells and Coppersmith (1994)—Maximum displacement (m) to magnitude (M), strike-slip/all types

<sup>3</sup> Wells and Coppersmith (1994)—Average displacement (m) to magnitude (M), strike-slip/all types

<sup>4</sup> Wells and Coppersmith (1994)—Area (km<sup>2</sup>) to magnitude, strike-slip/all types

<sup>5</sup> Somerville et al. (2001)—Area (km<sup>2</sup>) to magnitude

**Table 6.1.6-2**  
**Range of ERM-N Estimated Magnitudes (M)**

Approach	Rupture Length <sup>1</sup>	Rupture Area <sup>2</sup>			Rupture Area <sup>3</sup>		
Parameter Value	≤73 km (45.5 mi.)	≤949 km <sup>2</sup> (L = 73 km, SD = 13 km)	1,095 km <sup>2</sup> (L = 73 km, SD = 15 km)	1,241 km <sup>2</sup> (L = 73 km, SD = 17 km)	≤949 km <sup>2</sup> (L = 73 km, SD = 13 km)	1,095 km <sup>2</sup> (L = 73 km, SD = 15 km)	1,241 km <sup>2</sup> (L = 73 km, SD = 17 km)
Estimated Magnitude (M)	≤7.1/7.2	≤7.0/7.0	7.1/7.1	7.1/7.1	≤7.3	7.4	7.4

<sup>1</sup> Wells and Coppersmith (1994)—Subsurface rupture length (km) to magnitude (M), strike-slip/all types

<sup>2</sup> Wells and Coppersmith (1994)—Area (km<sup>2</sup>) to magnitude, strike-slip/all types

<sup>3</sup> Somerville et al. (2001)—Area (km<sup>2</sup>) to magnitude

**Table 6.1.6-3**  
**ERM-S RLME Recurrence Frequency**

RLME Frequency (earthquakes/year)			Weight
2 Earthquakes in 17.7–21.7 kyr	3 Earthquakes in 17.7–21.7 kyr	4 Earthquakes in 17.7–21.7 kyr	
3.5E-04	4.3E-04	5.0E-04	0.101
2.1E-04	2.8E-04	3.4E-04	0.244
1.4E-04	1.9E-04	2.4E-04	0.310
8.0E-05	1.2E-04	1.6E-04	0.244
3.6E-05	6.2E-05	9.0E-05	0.101

**Table 6.1.6-4**  
**ERM-N RLME Recurrence Frequency**

RLME Frequency (earthquakes/year)		Weight
1 Earthquake in 12–35 kyr	2 Earthquakes in 12–35 kyr	
2.9E-04	3.9E-04	0.101
1.5E-04	2.2E-04	0.244
8.0E-05	1.3E-04	0.310
4.0E-05	7.2E-05	0.244
1.4E-05	3.2E-05	0.101

**Table 6.1.7-1**  
**Marianna RLME Recurrence Frequency**

RLME Frequency (earthquakes/year)		Weight
3 Earthquakes in 9.6–10.2 kyr	4 Earthquakes in 9.6–10.2 kyr	
6.9E-04	8.4E-04	0.101
4.2E-04	5.5E-04	0.244
2.7E-04	3.7E-04	0.310
1.6E-04	2.4E-04	0.244
7.2E-05	1.2E-04	0.101

**Table 6.1.8-1**  
**Range of Commerce Fault Zone RLME Estimated Magnitudes (M)**

Approach	Rupture Length <sup>1</sup>		Max. Displacement <sup>2</sup>		Average Displacement <sup>3</sup>		Rupture Area <sup>4</sup>			Rupture Area <sup>5</sup>		
	Parameter Value	≤55 km (34 mi.)	120 km (75 mi.)	2.0 m (6.6 ft.)	2.2 m (6.9 ft.)	2.0 m (6.6 ft.)	2.2 m (6.9 ft.)	≤715 km <sup>2</sup> (L ≤ 55 km, SD = 13 km)	975 km <sup>2</sup> (L = 65 km, SD = 15 km)	2,040 km <sup>2</sup> (L = 120 km, SD = 17 km)	≤715 km <sup>2</sup> (L ≤ 55 km, SD = 13 km)	975 km <sup>2</sup> (L = 65 km, SD = 15 km)
Estimated Magnitude (M)	≤6.9/7.0	7.4/7.5	7.0/6.9	7.1/6.9	7.3/7.2	7.3/7.2	≤6.9/6.9	7.0/7.0	7.4/7.3	≤7.2	7.3	7.7

<sup>1</sup> Wells and Coppersmith (1994)—Subsurface rupture length (km) to magnitude (M), strike-slip/all types

<sup>2</sup> Wells and Coppersmith (1994)—Maximum displacement (m) to magnitude (M), strike-slip/all types

<sup>3</sup> Wells and Coppersmith (1994)—Average displacement (m) to magnitude (M), strike-slip/all types

<sup>4</sup> Wells and Coppersmith (1994)—Area (km<sup>2</sup>) to magnitude, strike-slip/all types

<sup>5</sup> Somerville et al. (2001)—Area (km<sup>2</sup>) to magnitude

**Table 6.1.8-2**  
**Commerce Fault Zone RLME Recurrence Frequency**

RLME Frequency (earthquakes/year)		Weight
2 Earthquakes in 18.9–23.6 kyr	3 Earthquakes in 18.9–23.6 kyr	
2.5E-04	3.3E-04	0.101
1.4E-04	2.0E-04	0.244
8.0E-05	1.3E-04	0.310
4.0E-05	7.6E-05	0.244
1.4E-05	3.4E-05	0.101

**Table 6.1.9-1**  
**Liquefaction Evidence for Prehistoric Earthquakes in the Southern Illinois Basin**

Inferred Energy Center for Earthquake(s)	Location	Size and Distribution of Features	Age <sup>1</sup>	Estimated Magnitude	Reference(s)
<b>Lower Wabash Valley</b>					
Vincennes-Bridgeport	~25 km (~15 mi.) west of Vincennes, Indiana	≥0.5 m (≥1.6 ft.) dike width; 115 km (71.5 mi.) minimum to 153 km (95 mi.) maximum distance from inferred energy center	~6,100 ± 200 yr BP	≥ <b>M</b> 7.5–7.8 (magnitude-bound, cyclic stress, and energy stress methods)	Munson et al. (1997) Obermeier (1998) Obermeier et al. (1993)
				<b>M</b> 7.8 (energy-stress) <sup>2</sup>	Pond and Martin (1997)
				<b>M</b> 7.1–7.3 (updated magnitude-bound curve)	Olson et al. (2005b)
				<b>M</b> ~ 7.5 (back-calculated ground motion characteristics from paleoliquefaction effects)	Green et al. (2005)
				<b>M</b> 7.99 ± 0.27 (preliminary results—probabilistic approach using magnitude bounds and back-calculations to address uncertainties).	Olson et al. (2007)

Table 6.1.9-1 (continued)

Inferred Energy Center for Earthquake(s)	Location	Size and Distribution of Features	Age <sup>1</sup>	Estimated Magnitude	Reference(s)
				M ~ 7.5 ± 0.3 Prior distribution from magnitude-bound method combined with likelihood function from sites of observed liquefaction (or no liquefaction) to yield posterior distribution. Considers uncertainties in back-calculation analyses.	Olson (2009)
				≥M 7.0 (115 km epicentral distance); ≥M 7.3 (153 km epicentral distance); (minimum magnitude-bound curve)	Castilla and Audemard (2007)
Skelton	~40 km (~25 mi.) SW of Vincennes, Indiana	≥0.5 m (≥1.6 ft.) dike width; 50–60 km (31–37 mi.) maximum distance from inferred energy center	~12,000 ± 1,000 yr BP	M ~ 7.1 (summary of magnitude-bound and geotechnical analysis results)	Hajic and Wiant (1997)  Obermeier (1998)
				M 7.1–7.3 (magnitude bound)	Munson et al. (1997)
				M 7.3 (energy stress) <sup>2</sup>	Pond and Martin (1997)
				M 6.7 (updated magnitude bound)	Olson et al. (2005b)
				≥ M 6.3 (63 km epicentral distance); (minimum magnitude-bound curve)	Castilla and Audemard (2007)
Single site near	35 km (22 mi.)	Very small and restricted	4,000 ± 500 yr	Near threshold	Munson et al.

Table 6.1.9-1 (continued)

Inferred Energy Center for Earthquake(s)	Location	Size and Distribution of Features	Age <sup>1</sup>	Estimated Magnitude	Reference(s)
Iona, Indiana	SE of Vincennes, Indiana, near Iona	(probably limited to 5 km [3.1 mi.])	BP	( <b>M</b> ~ 5.5–6.0 to <6.7)	(1997) Obermeier (1998)
<b>Central and Southern Indiana</b>					
Vallonia	East Fork valley ~100 km (~62 mi.) east of the Wabash Valley seismic zone	≥0.5 m (1.5 ft.); 36 km (22.5 mi.) maximum distance from inferred energy center	3,950 ± 250 yr BP	<b>M</b> ≥ 6.9 (magnitude bound)	Munson et al. (1997) Obermeier (1998)
				<b>M</b> 7.1 (energy stress) <sup>2</sup>	Pond and Martin (1997)
				<b>M</b> 6.3 (updated magnitude bound)	Olson et al. (2005b)
				≥ <b>M</b> 5.7 (36 km epicentral distance); (minimum magnitude-bound curve)	Castilla and Audemard (2007)
Martinsville-Waverly	~30–50 km (~18–30 mi.) SW of Indianapolis, Indiana (location poorly constrained)	≥0.15 to ≤0.5 m (≥5 to ≤1.6 ft.); 28 km (17.5 mi.) maximum distance from inferred energy center  Geotechnical analyses demonstrate that these features are not associated with the <b>M</b> ~ 7.5 Vincennes	Between 8,500 and 3,500 yr BP	<b>M</b> 6.8 (magnitude bound)	Munson et al. (1997) Obermeier (1998)
				<b>M</b> 6.9 (energy stress) <sup>2</sup>	Pond and Martin (1997)
				<b>M</b> 6.2 (updated magnitude bound)	Olson et al. (2005b)

Table 6.1.9-1 (continued)

Inferred Energy Center for Earthquake(s)	Location	Size and Distribution of Features	Age <sup>1</sup>	Estimated Magnitude	Reference(s)
		earthquake		≥ M 5.5 (28 km epicentral distance); (minimum magnitude-bound curve)	Castilla and Audemard (2007)
Single site near Elнора, Indiana	60 km (37 mi.) E-NE of Vincennes	Limited areal extent	2,000 ± 500 yr BP	M ≥ 5.5–6.0	Munson et al. (1997) Obermeier (1998)
Single site along Indian Creek, Indiana	~50 km (~31 mi.) S-SW of Indianapolis	Single site	~20,000 yr BP	Unknown	Munson et al. (1997) Obermeier (1998)
Ohio River region—Absence of paleoliquefaction in Ohio River sediments along the Indiana-Kentucky and Illinois-Kentucky borders suggests that this area has not experienced severe ground shaking in the past 4,500 years (Munson et al., 1997). However, Munson et al. (1997) suggest that a 5–6 m (16.4–19.7 ft.) thick clay cap may have kept sand dikes from penetrating to levels above the current maintained water level of the Ohio River.					
<b>Central and Southern Illinois</b>					
Springfield	~35 km (~22 mi.) NE of Springfield, Illinois	Maximum dike width 0.4 m (1.3 ft.); 35 km (22 mi.) maximum distance from inferred energy center	One, possibly two, events between 5,960 ± 60 yr BP and 7,380 ± 90 yr BP	M 6.2–6.8	Hajic et al. (1995)
				M 5.5 (second event)	McNulty and Obermeier (1999)
				M 6.2 (updated magnitude bound)	Olson et al. (2005b)
				≥ M 5.7 (35 km epicentral distance); (minimum magnitude-bound curve)	Castilla and Audemard (2007)

**Table 6.1.9-1** (continued)

Inferred Energy Center for Earthquake(s)	Location	Size and Distribution of Features	Age <sup>1</sup>	Estimated Magnitude	Reference(s)
Shoal Creek (Germantown, Illinois)	Centered in vicinity of lower Shoal Creek near its confluence with Kaskaskia River: ~65 km (~40 mi.) E-SE of St. Louis, Missouri. Alternative location: Centralia fault (Du Quoin monocline)	Maximum dike width 1.55 m (5 ft.); 35 km (22 mi.) maximum distance from inferred energy center	~5,670 ± 80 yr BP  4520 BC ± 200 yr	<b>M</b> 6.5 (lower limit)	McNulty and Obermeier (1999)
				<b>M</b> 6.2 (updated magnitude bound)	Olson et al. (2005b)
				≥ <b>M</b> 5.7 (35 km epicentral distance); (minimum magnitude-bound curve)	Castilla and Audemard (2007)
				Alternative scenarios: <b>M</b> 7.0 (Shoal Creek) <b>M</b> 7.5 (Centralia/Du Quoin)	Tuttle, Chester, et al. (1999)
Cache River	Cache River from Sandusky to the Mississippi River	Dike width 1–9 cm (0.4–3.5 in.)	Two ages: maximum age AD 1020–1250 for younger and possibly older event(s)  Age estimates of Middle Holocene liquefaction features are of poor quality (cannot preclude they could be associated with	Unknown  Middle Holocene events could have formed as a result of a very large earthquake originating from a distant source such as the NMSZ or a smaller-magnitude earthquake from a closer source such as the Commerce geophysical lineament.	Chester and Tuttle (2000)  Tuttle (2005b)

Table 6.1.9-1 (continued)

Inferred Energy Center for Earthquake(s)	Location	Size and Distribution of Features	Age <sup>1</sup>	Estimated Magnitude	Reference(s)
			the 4520 BC ± 200 yr (Shoal Creek) event).		
n/a	Big Muddy River	No new sites identified. Geologic conditions not favorable for liquefaction.	n/a	All paleoliquefaction dikes in the region could possibly be induced by paleoearthquakes that occurred near the potential seismogenic sources identified by reanalysis of seismic reflection data. Maximum possible magnitude for a basement-involved fault in the region is between M 6 and just above M 7.	Su and McBride (1999)
<b>Southeastern Missouri</b>					
Big Muddy and Meramec rivers	~30 km (~20 mi.) SW of St. Louis, Missouri	Dikes 0.1–1 cm (.04–.4 in.) wide; maximum dike at MR25W site is 20 cm (7.9 in.) wide	Big Muddy River: post-9070 BC and possibly prior to 4240 BC  Meramec River: post-13,210 BC.  Several features are estimated to have formed during the late Holocene and Holocene. No	Three scenarios: Local, <b>M</b> > 5.2–6.0 Shoal Creek, <b>M</b> 7.0 Centralia fault, <b>M</b> 7.5  Results of liquefaction potential analysis (cyclic stress method using in situ geotechnical testing results for three possible source layers) showed that a local ( <b>M</b> > 5.25–6.0) earthquake would induce liquefaction for the upper and middle layer; a <b>M</b> 6.75 earthquake in Germantown, Illinois (~80 km [~50 mi.] from site) would not induce liquefaction in any layer; a <b>M</b> 7.5 along Centralia fault–Du Quoin monocline (~100 km [~62 mi.] from site) would	Tuttle, Chester, et al. (1999)  Tuttle (2005b)

**Table 6.1.9-1** (continued)

Inferred Energy Center for Earthquake(s)	Location	Size and Distribution of Features	Age <sup>1</sup>	Estimated Magnitude	Reference(s)
			liquefaction features have yet been attributed to the 4,520 ± 200 yr BP (Shoal Creek) earthquake. Maximum age of 20 cm (7.9 in.) wide dike at MR 25W site is 4340–3990 BC. Stratigraphic relations suggest it might be as young as 800 BC.	induce liquefaction in the upper and middle layers; a <b>M</b> 7.8 along the same structure would induce liquefaction in all three layers; a <b>M</b> 8 earthquake produced by northern New Madrid fault would not induce liquefaction.	

<sup>1</sup> Ages given in yr BP are uncorrected radiocarbon ages.

<sup>2</sup> The energy-stress method used by Pond and Martin (1997) is flawed (energy attenuation relations used should not be used for liquefaction analysis and the results are not reliable [S. Obermeier, pers. comm., May 13, 2003]).

**Table 6.1.9-2**  
**Wabash RLME Recurrence Frequency**

RLME Frequency (earthquakes/year)	Weight
4.4E-04	0.101
2.5E-04	0.244
1.4E-04	0.310
7.2E-05	0.244
2.4E-05	0.101

**Table 6.2-1**  
**Alternative Mmax Zonation Models**

Mesozoic Extended—Narrow Model		Mesozoic Extended—Wide Model	
MESE-N	NMESE-N	MESE-W	NMESE-W
AHEX	MidC-A	AHEX	MidC-D
ECC-AM	IBEB	ECC-AM	OKA
ECC-GM	OKA	ECC-GM	
GHEX		GHEX	
RR		RR-RCG	
SLR		SLR	
NAP		NAP	
GMH		GMH	
PEZ-N		IBEB	
		PEZ-W	

**Table 6.3.2-1**  
**Maximum Magnitude Distributions for Mmax Distributed Seismicity Sources**

Weight Assigned to Mmax	Maximum Magnitude for:				
	Study Region	MESE-N	NMESE-N	MESE-W	NMESE-W
0.101	6.5	6.4	6.4	6.5	5.7
0.244	6.9	6.8	6.8	6.9	6.1
0.310	7.2	7.2	7.1	7.3	6.6
0.244	7.7	7.7	7.5	7.7	7.2
0.101	8.1	8.1	8.0	8.1	7.9

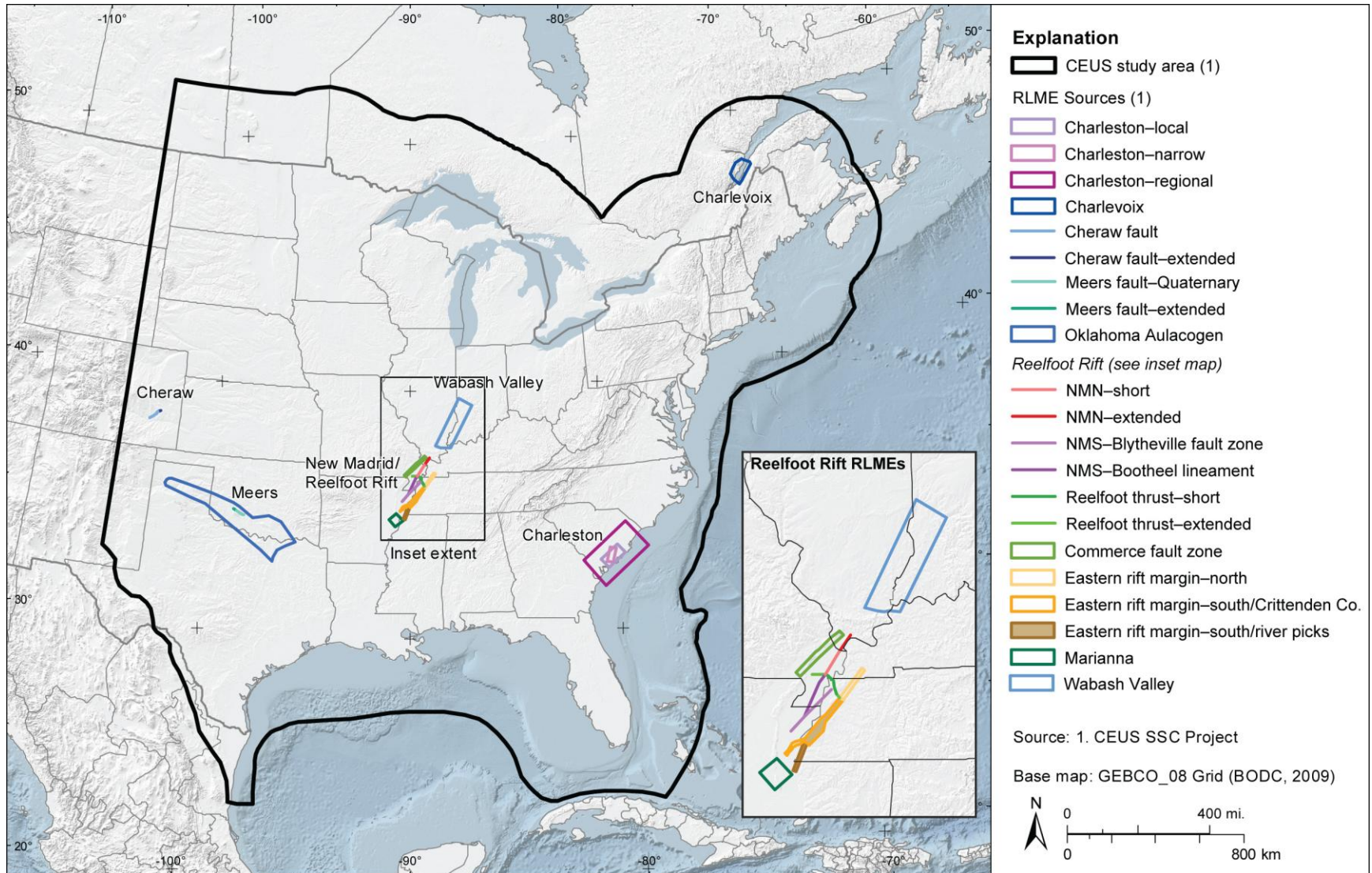


**Figure 6.1-1**  
 Map showing the RLME sources characterized in the CEUS SSC model. Detailed alternatives to the source geometries are shown on figures associated with each RLME discussion.

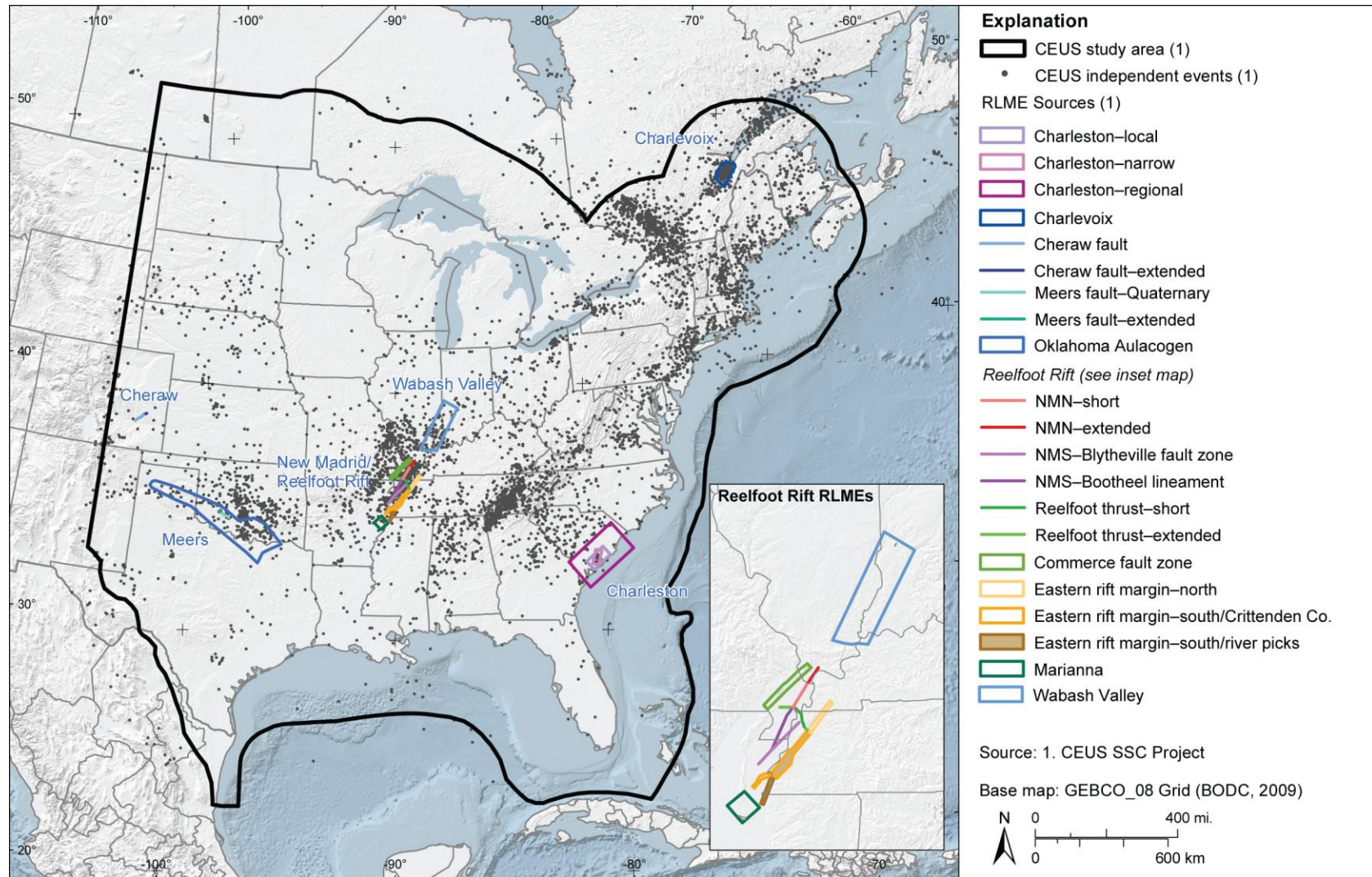


**Figure 6.1-2a**  
 Map showing the RLME sources and seismicity from the CEUS SSC earthquake catalog. Some of the RLMEs occur in regions of elevated seismicity, but others do not.

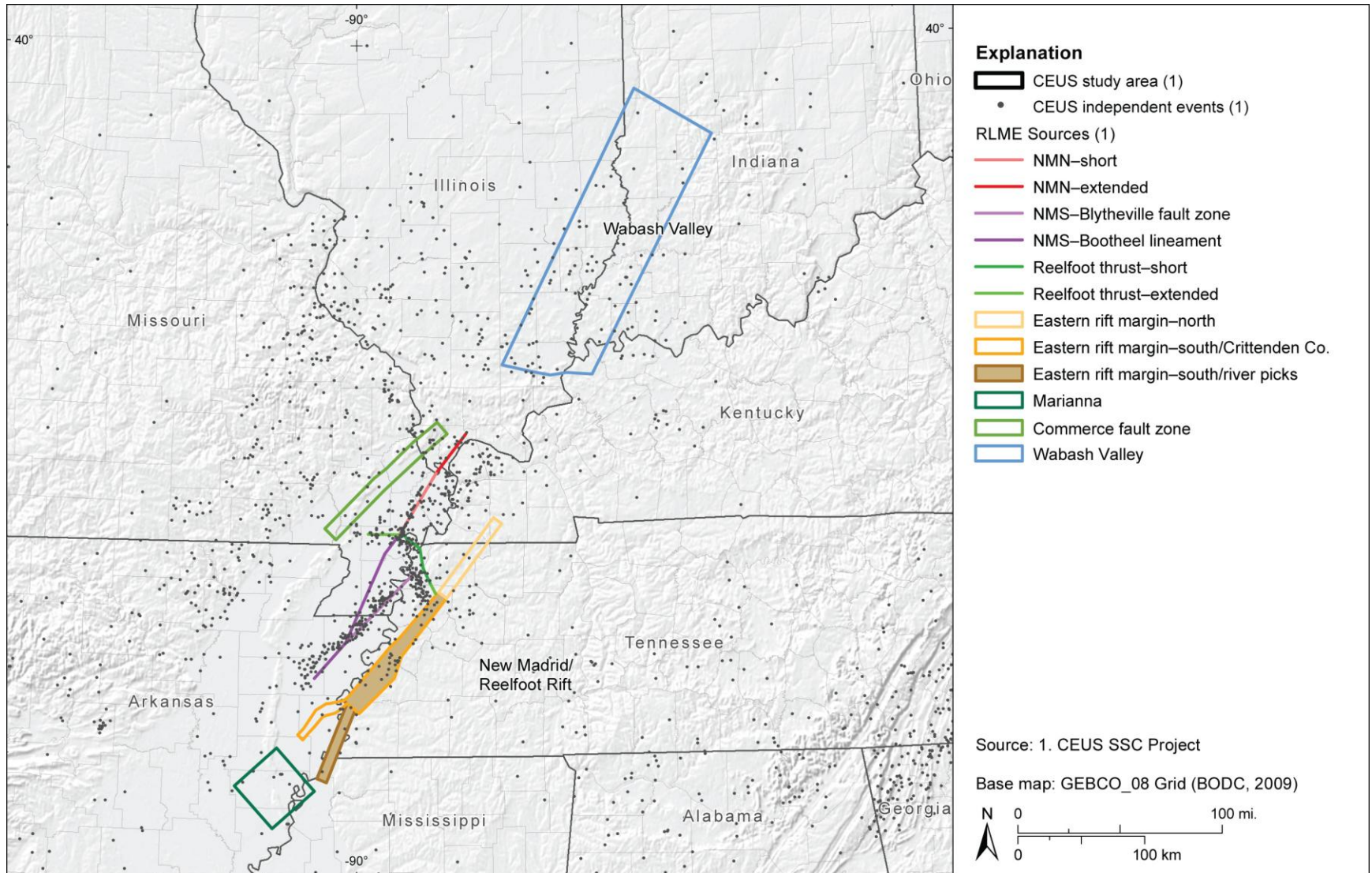
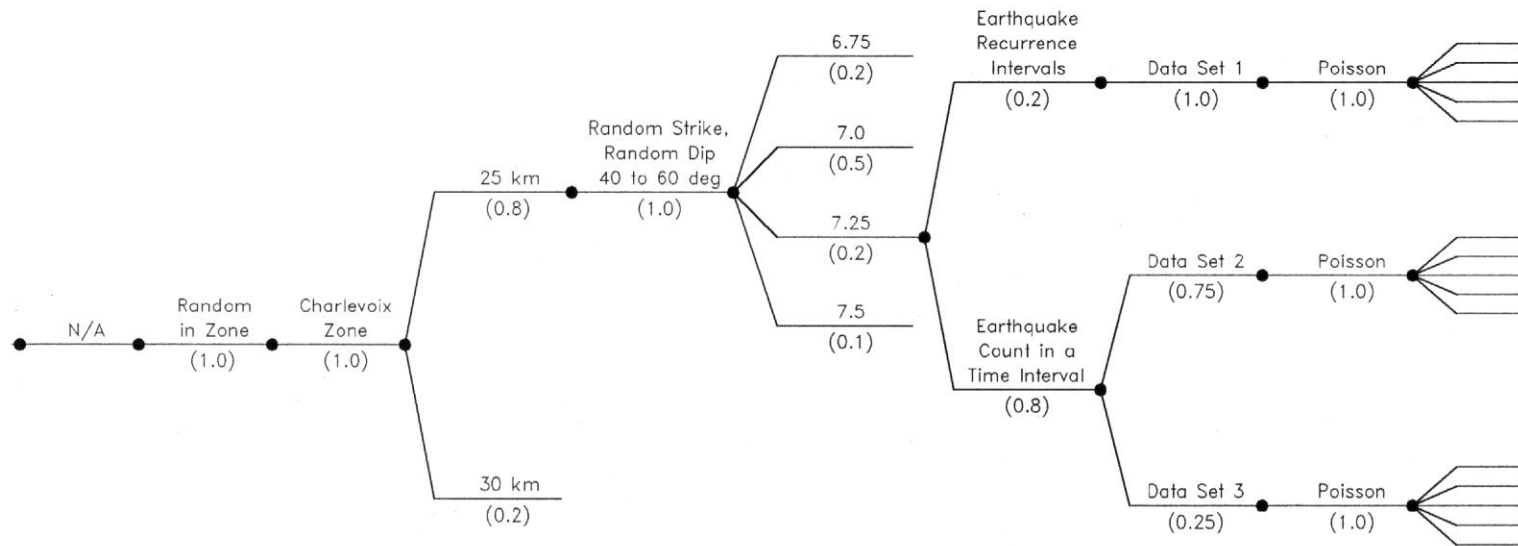


**Figure 6.1-2b**  
 Close-up of the Wabash Valley and New Madrid/Reelfoot Rift RLME sources and seismicity from the CEUS SSC earthquake catalog. Some of the RLMEs occur in regions of elevated seismicity, but others do not.

Chapter 6  
 SSC Model: RLME Sources and Mmax Zones Branch

<i>In or Out of Cluster</i>	<i>Localizing Tectonic Feature</i>	<i>Source Geometry</i>	<i>Seismogenic Crustal Thickness</i>	<i>Rupture Orientation</i>	<i>RLME Magnitude</i>	<i>Recurrence Method</i>	<i>Recurrence Data</i>	<i>Earthquake Recurrence Model</i>	<i>RLME Annual Frequency*</i>
-----------------------------	------------------------------------	------------------------	--------------------------------------	----------------------------	-----------------------	--------------------------	------------------------	------------------------------------	-------------------------------



\*see Table 6.1.1-1

**Figure 6.1.1-1**  
 Logic tree for the Charlevoix RLME source

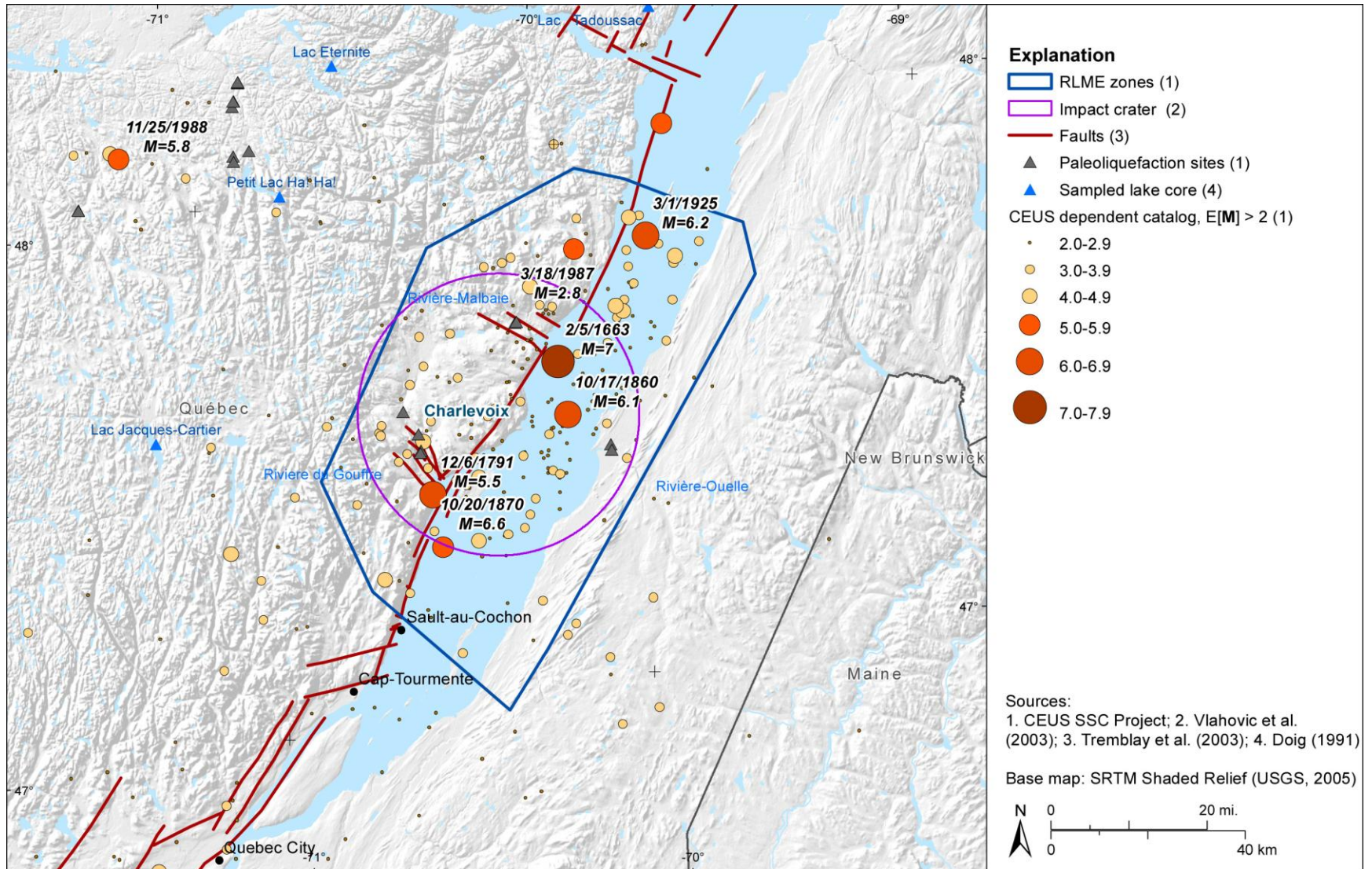


**Figure 6.1.1-2**  
 Seismicity and tectonic features of the Charlevoix RLME

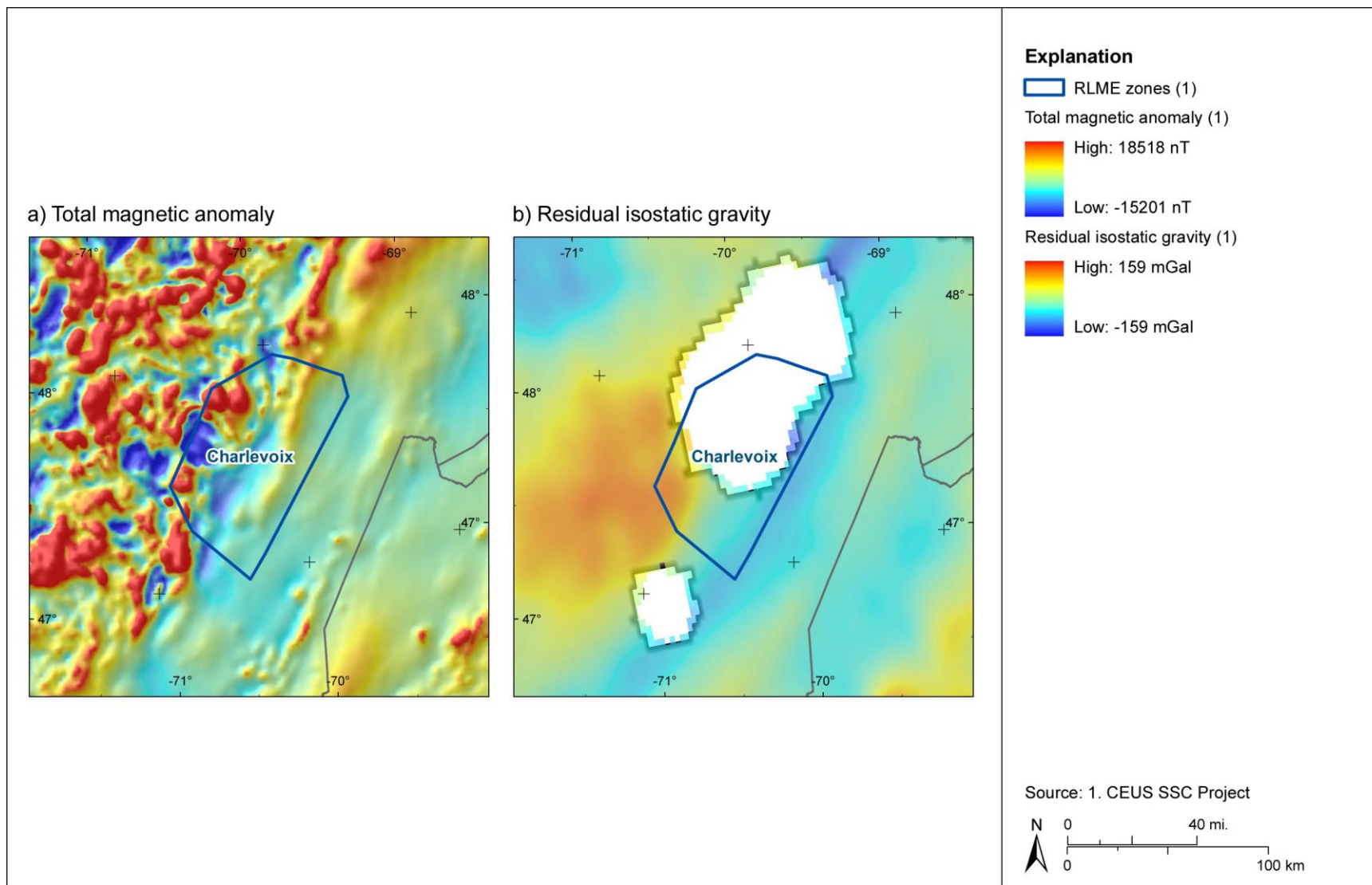


**Figure 6.1.1-3**  
**Magnetic and gravity anomaly maps of the Charlevoix RLME**

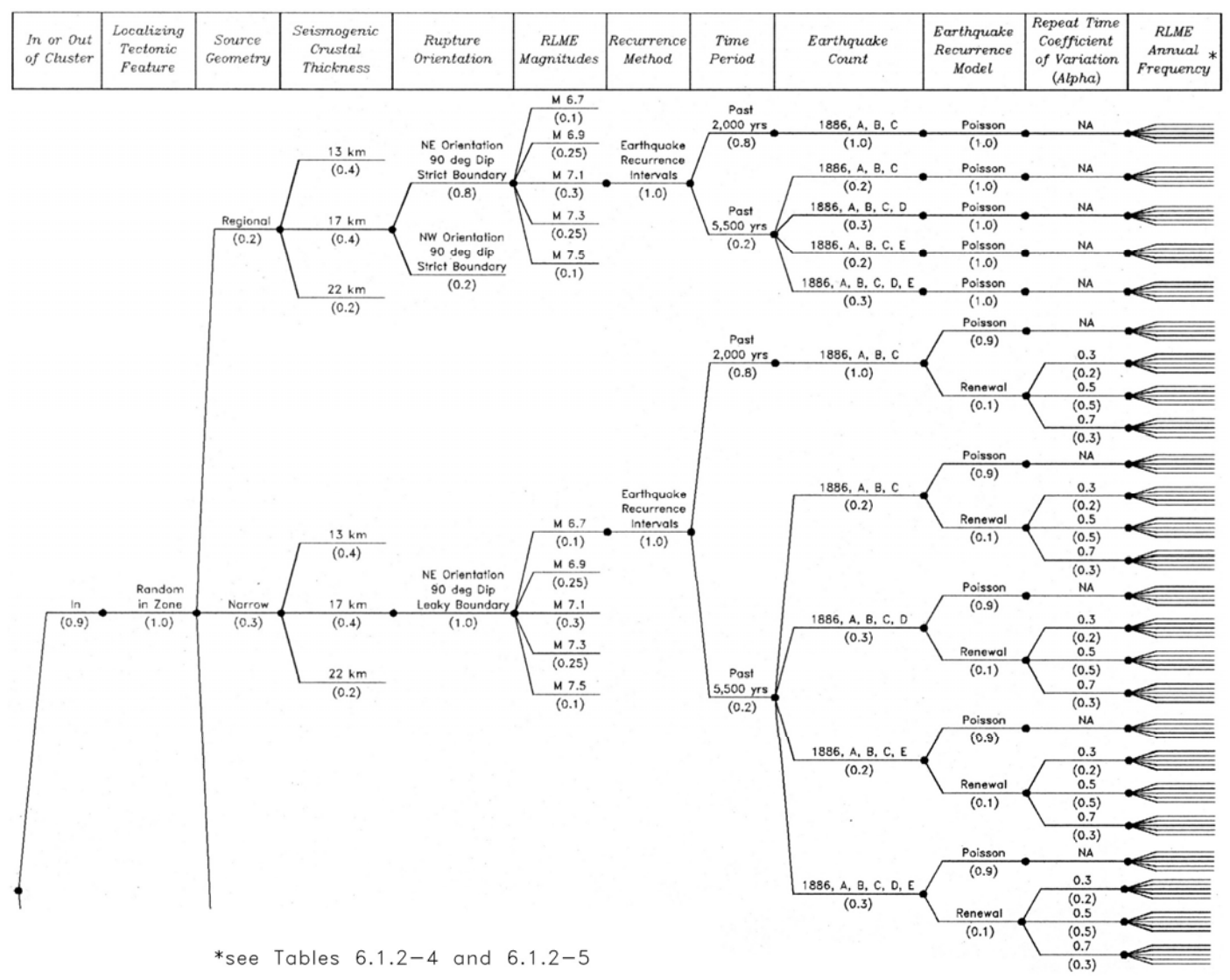
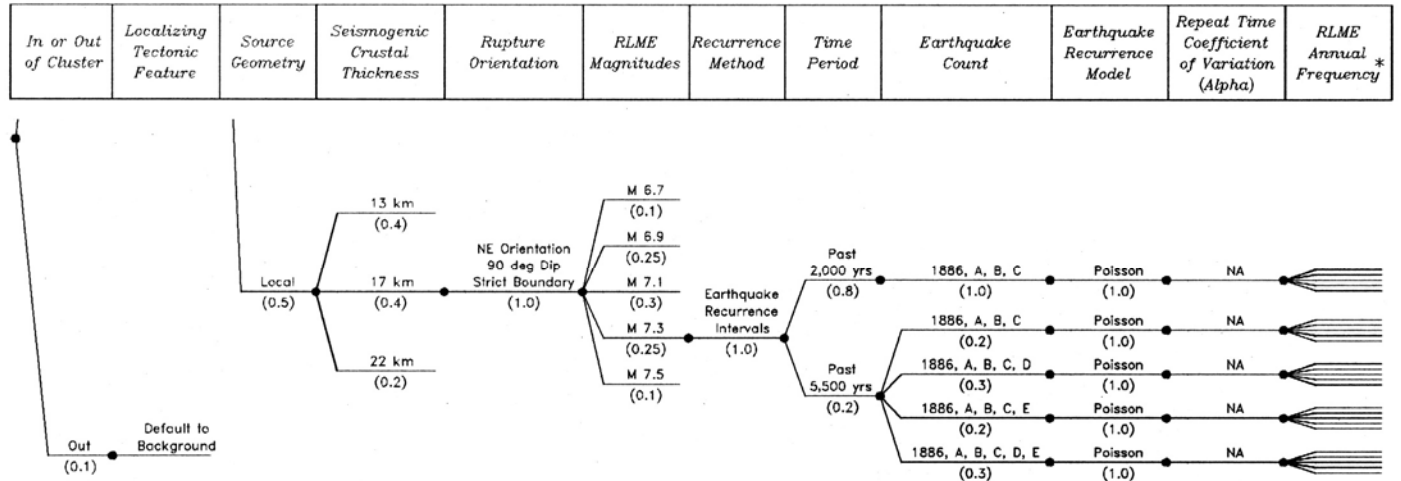


Figure 6.1.2-1a  
Logic tree for the Charleston RLME source

Chapter 6  
 SSC Model: RLME Sources and Mmax Zones Branch



\*see Tables 6.1.2-4 and 6.1.2-5

Figure 6.1.2-1b  
 Logic tree for the Charleston RLME source

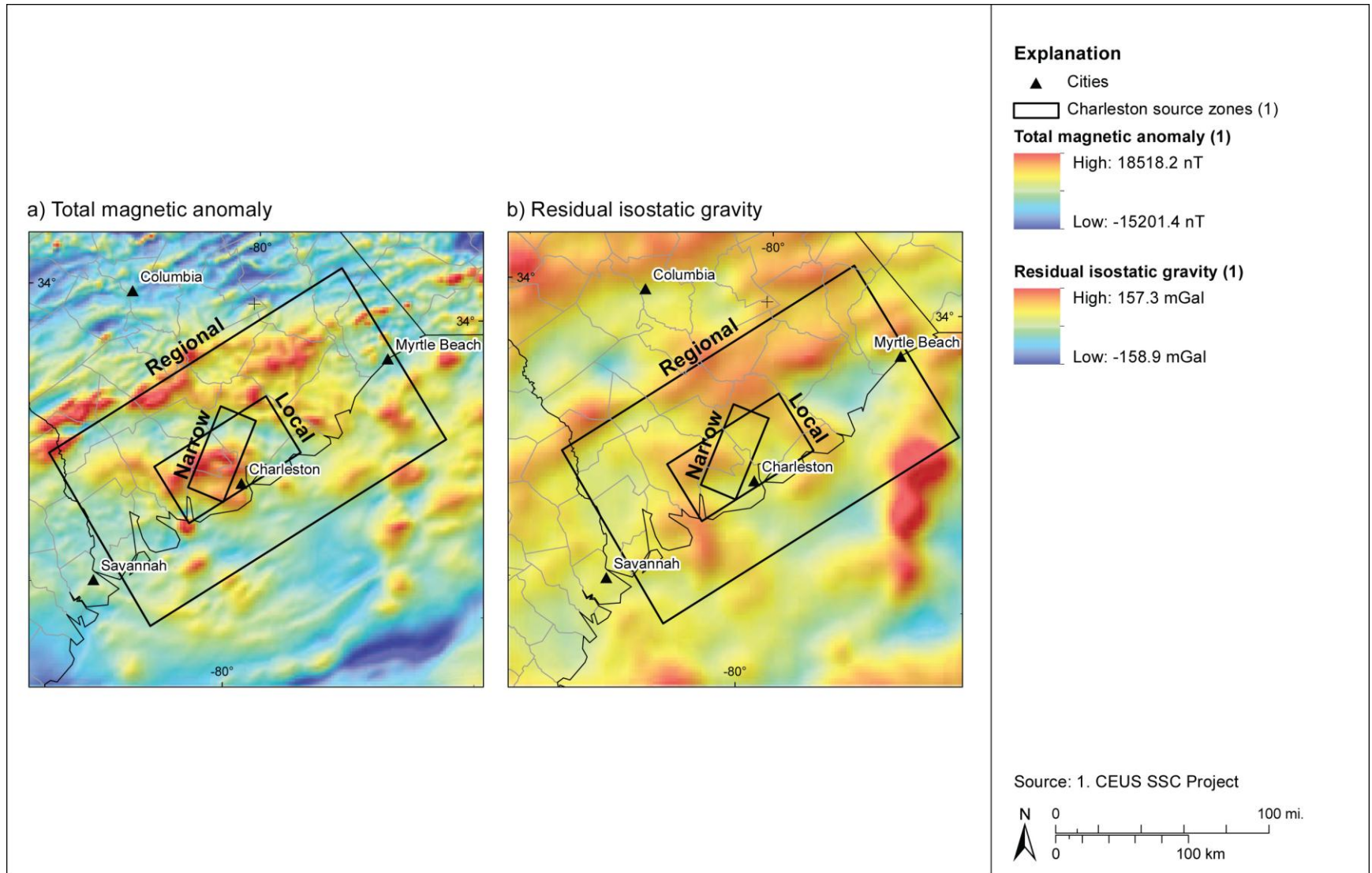


**Figure 6.1.2-2**  
 Charleston RLME source zones with (a) total magnetic anomaly and (b) residual isostatic gravity data

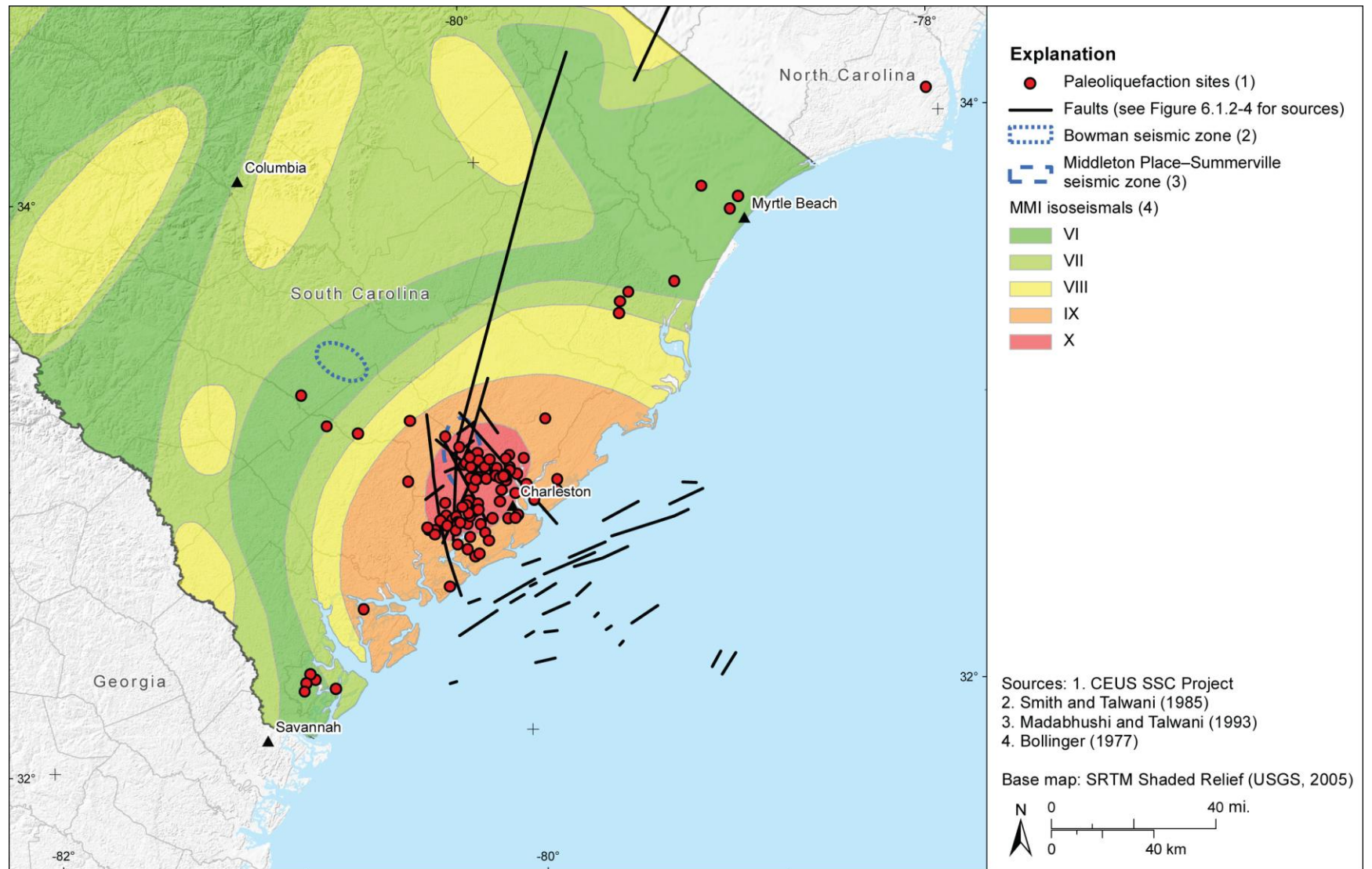


**Figure 6.1.2-3**  
 Postulated faults and tectonic features in the Charleston region

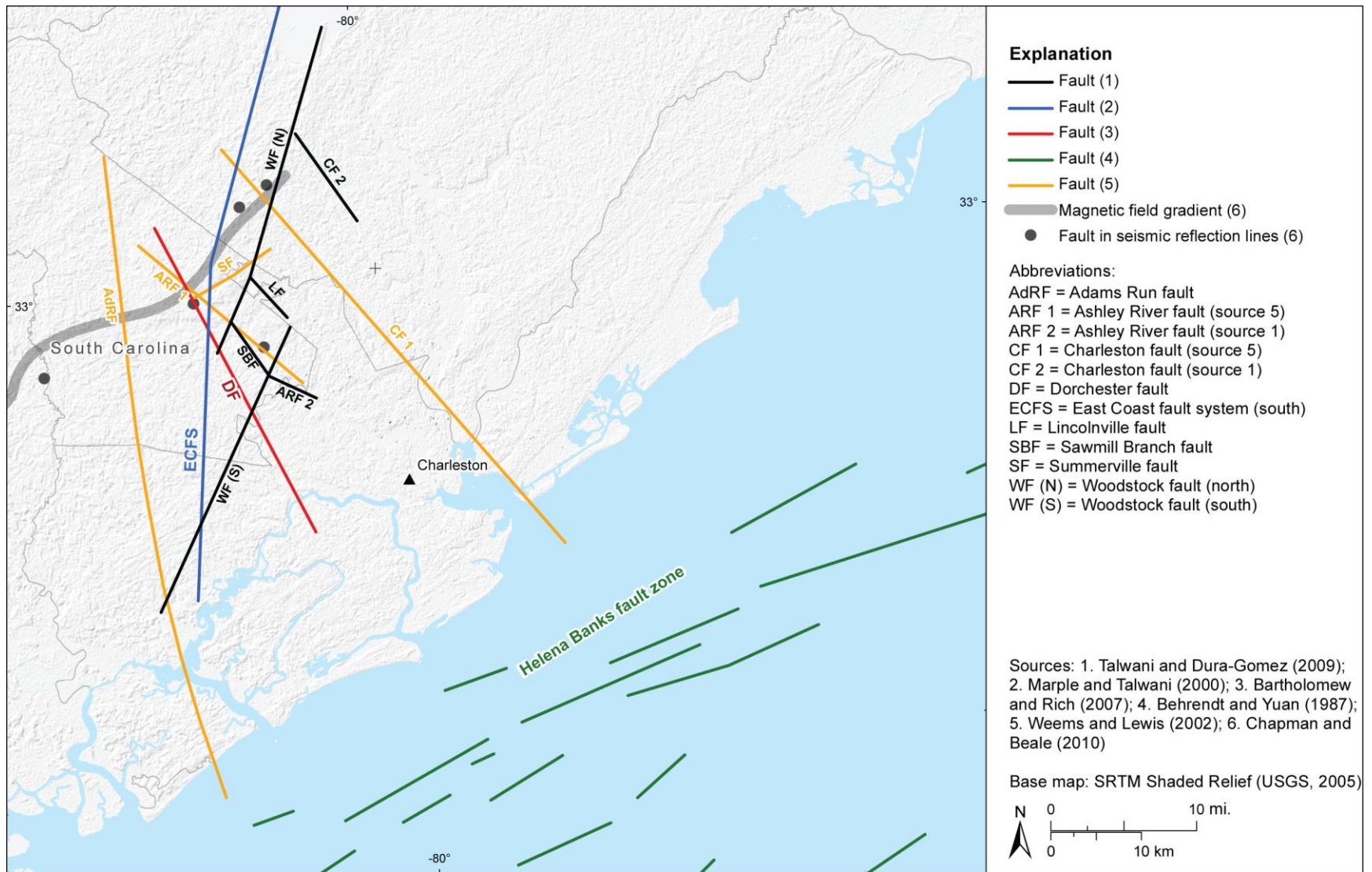


**Figure 6.1.2-4**  
 Postulated faults and tectonic features in the local Charleston area

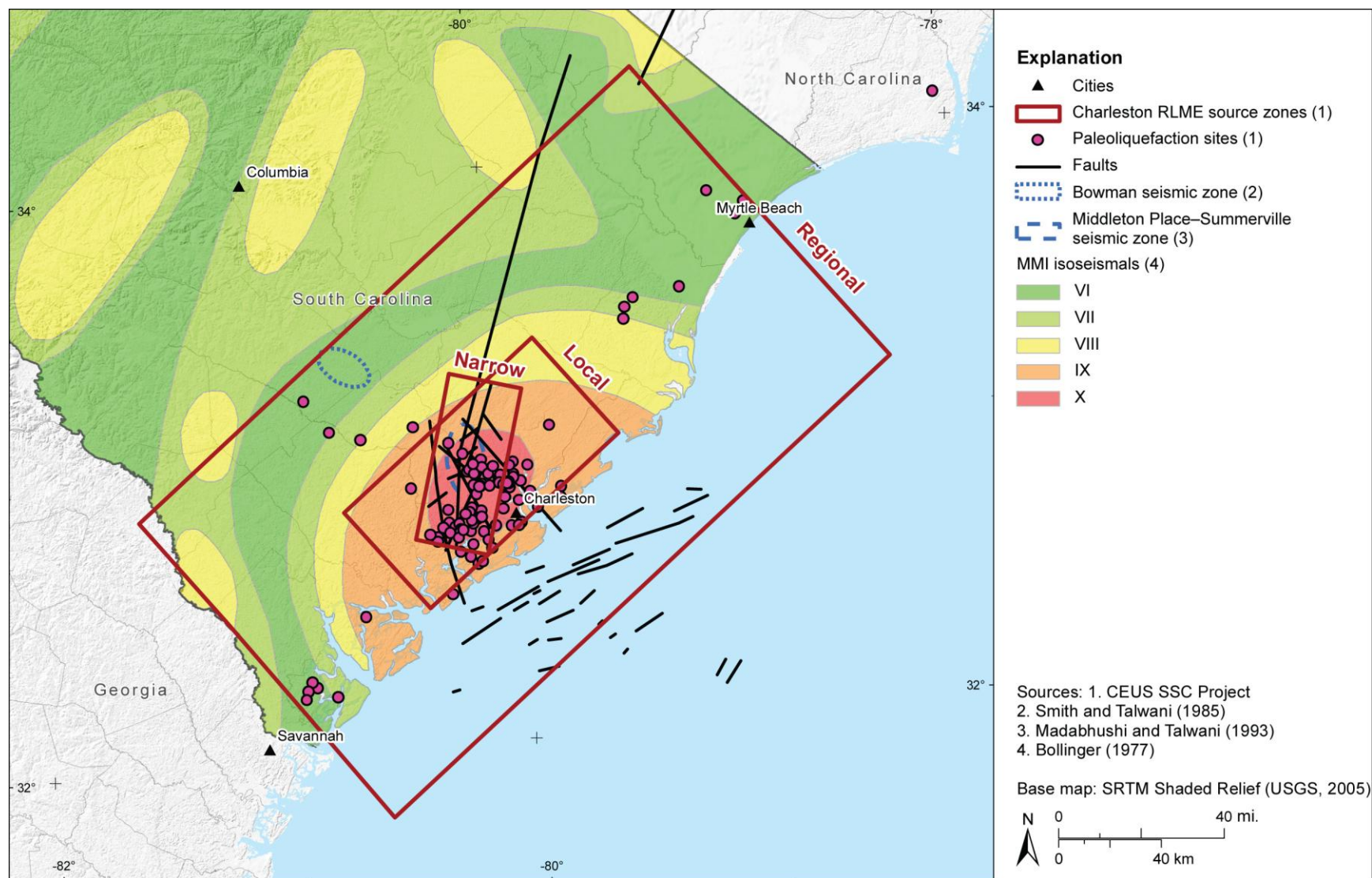


**Figure 6.1.2-5a**  
 Postulated faults and tectonic features in the Charleston region with Charleston RLME source zones

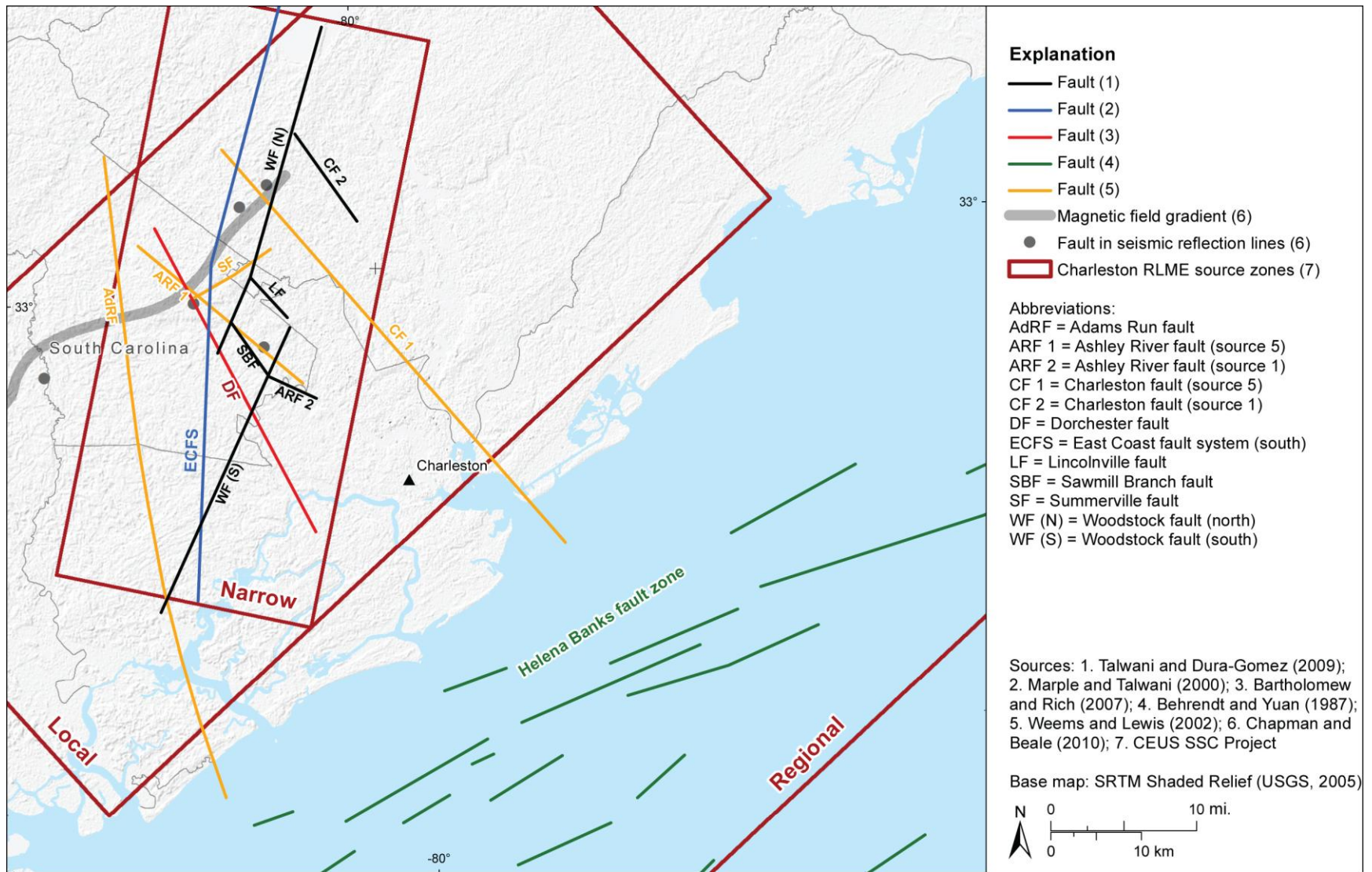


**Figure 6.1.2-5b**  
Postulated faults and tectonic features in the local Charleston area with Charleston RLME source zones

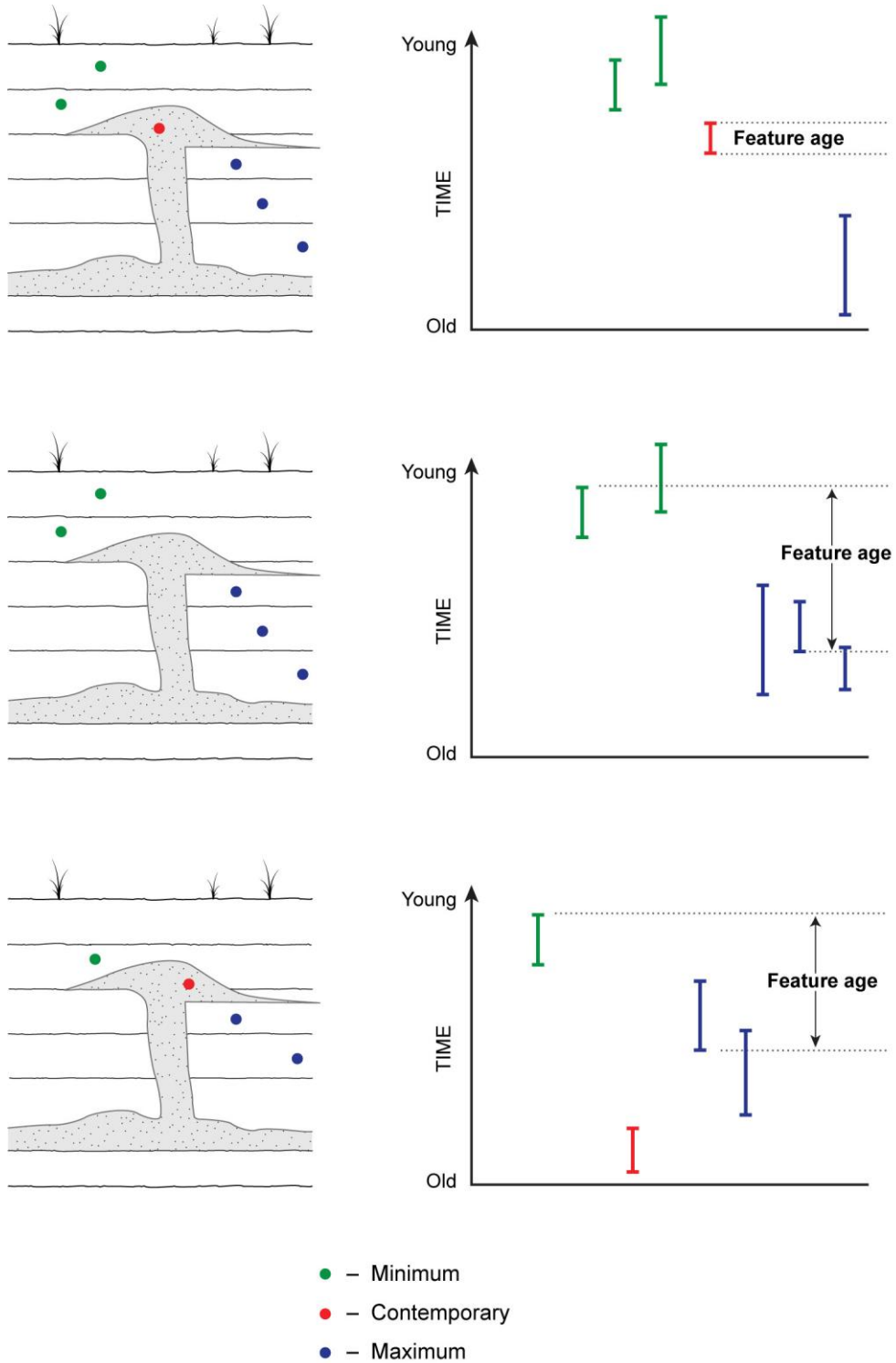


**Figure 6.1.2-6**  
 Schematic diagram showing contemporary, maximum, and minimum constraining age sample locations



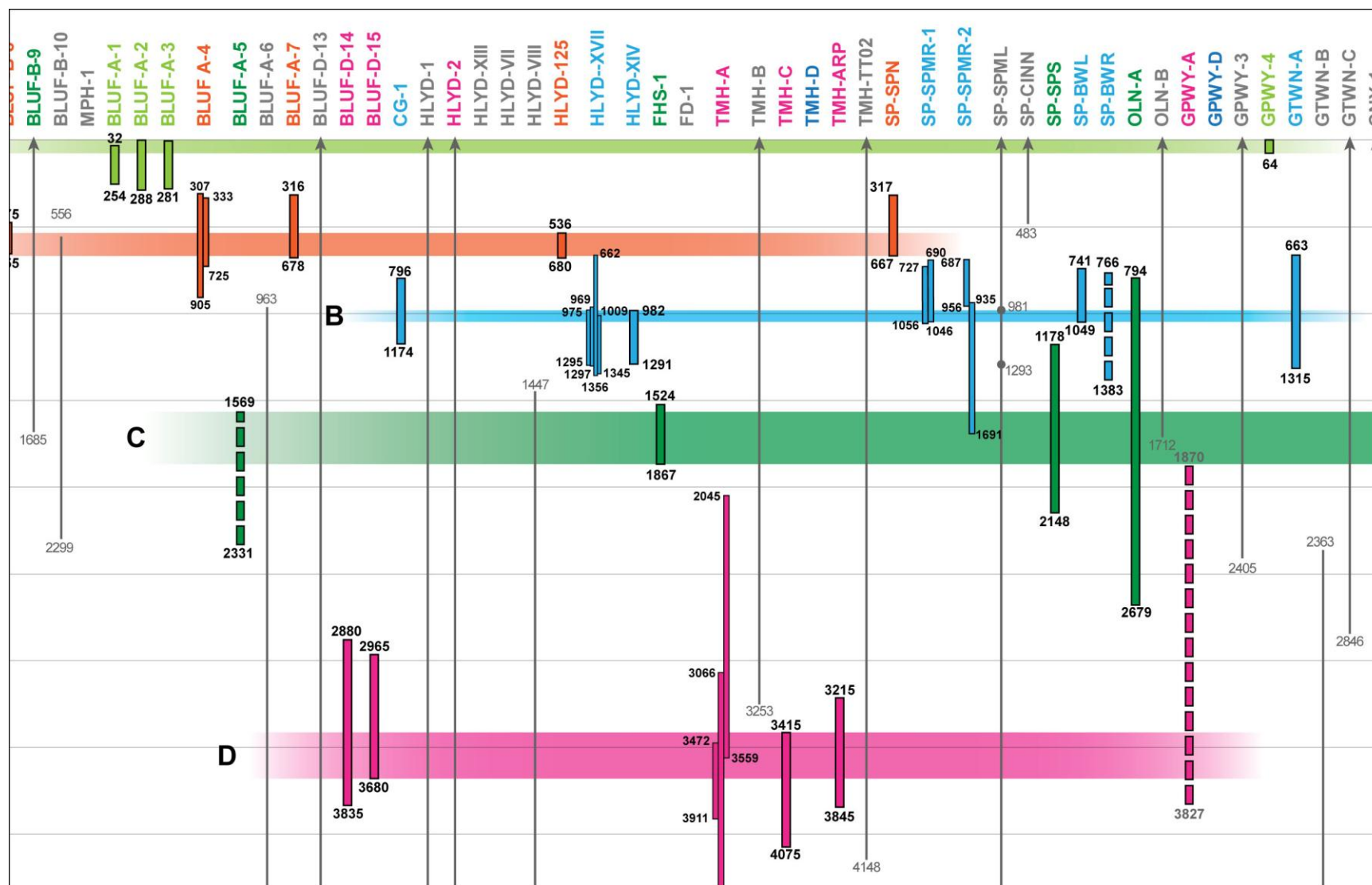
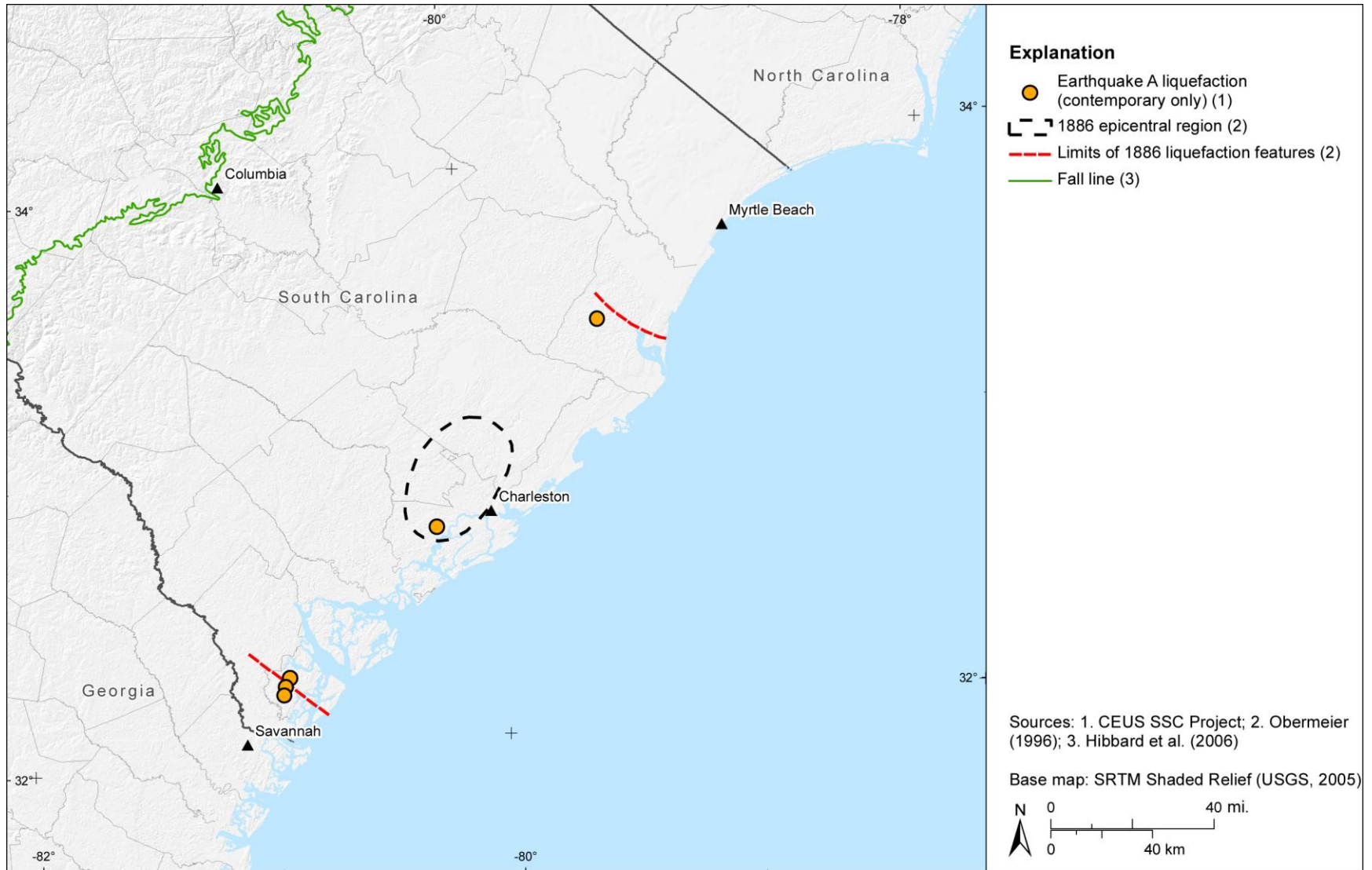
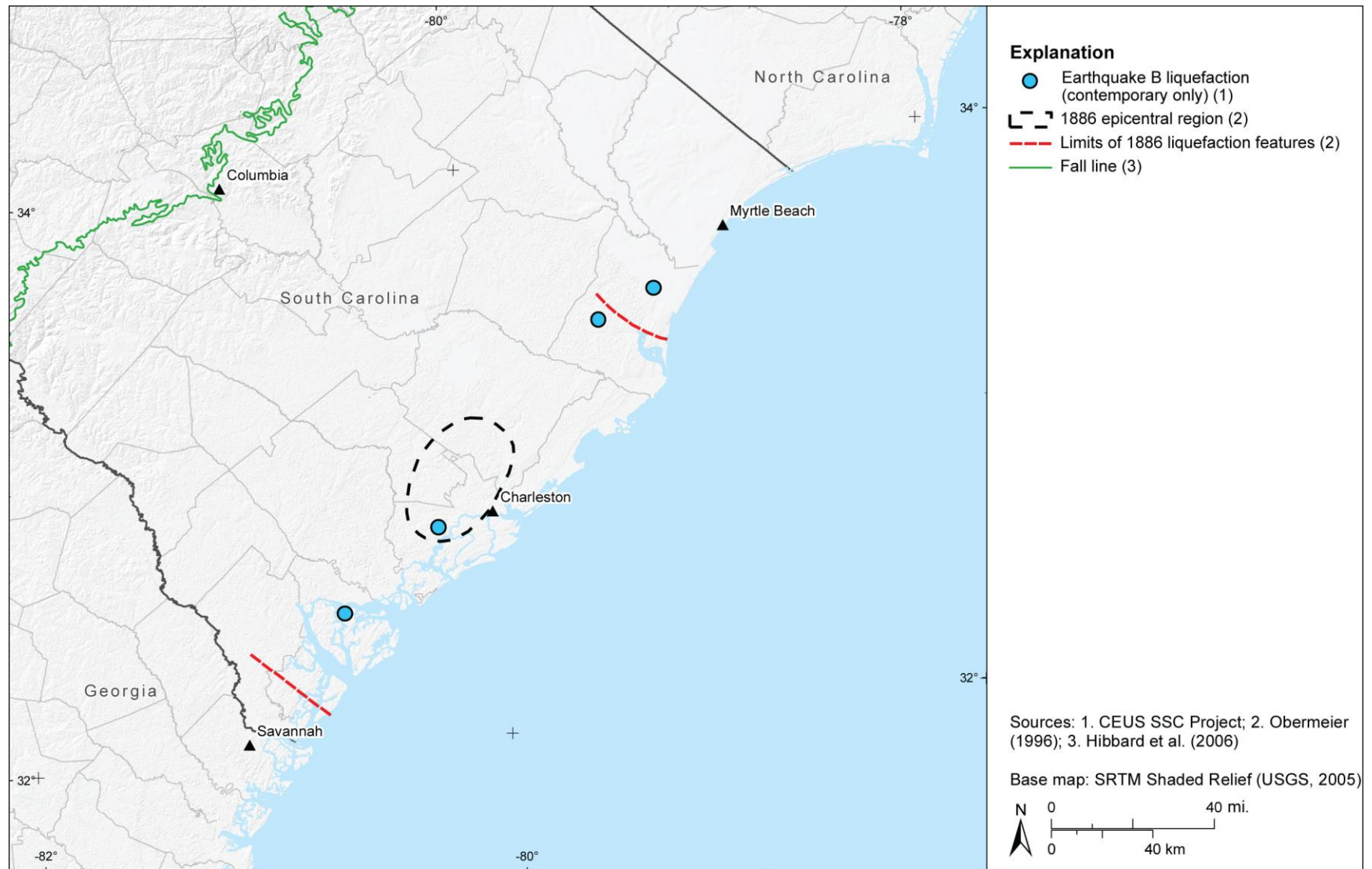


Figure 6.1.2-8  
 Charleston space-time diagram of earthquakes interpreted from paleoliquefaction, all-ages scenario



**Figure 6.1.2-9**  
Distribution of liquefaction from earthquake A, contemporary-ages-only scenario



**Figure 6.1.2-10**  
Distribution of liquefaction from earthquake B, contemporary-ages-only scenario

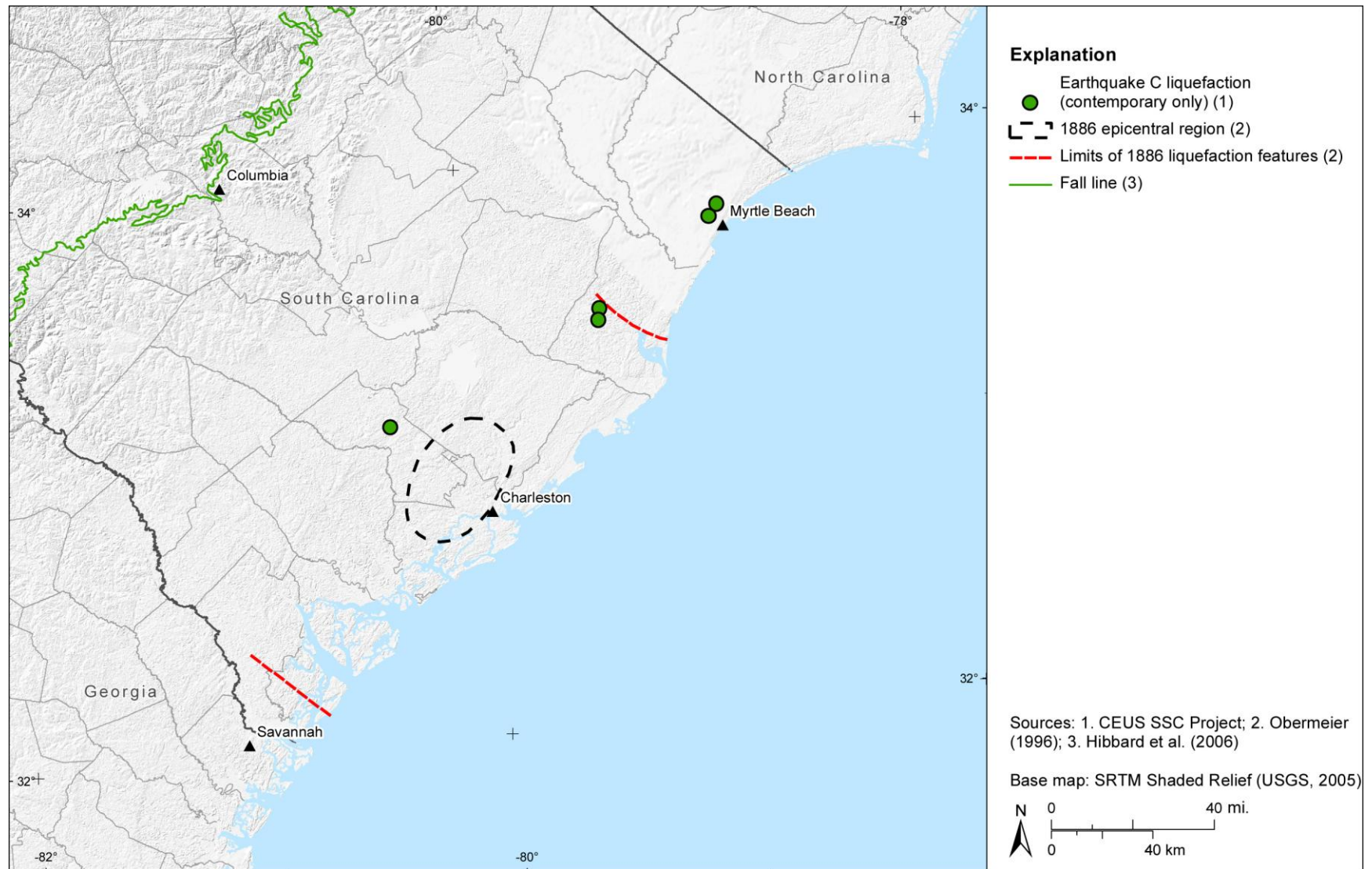


**Figure 6.1.2-11**  
Distribution of liquefaction from earthquake C, contemporary-ages-only scenario

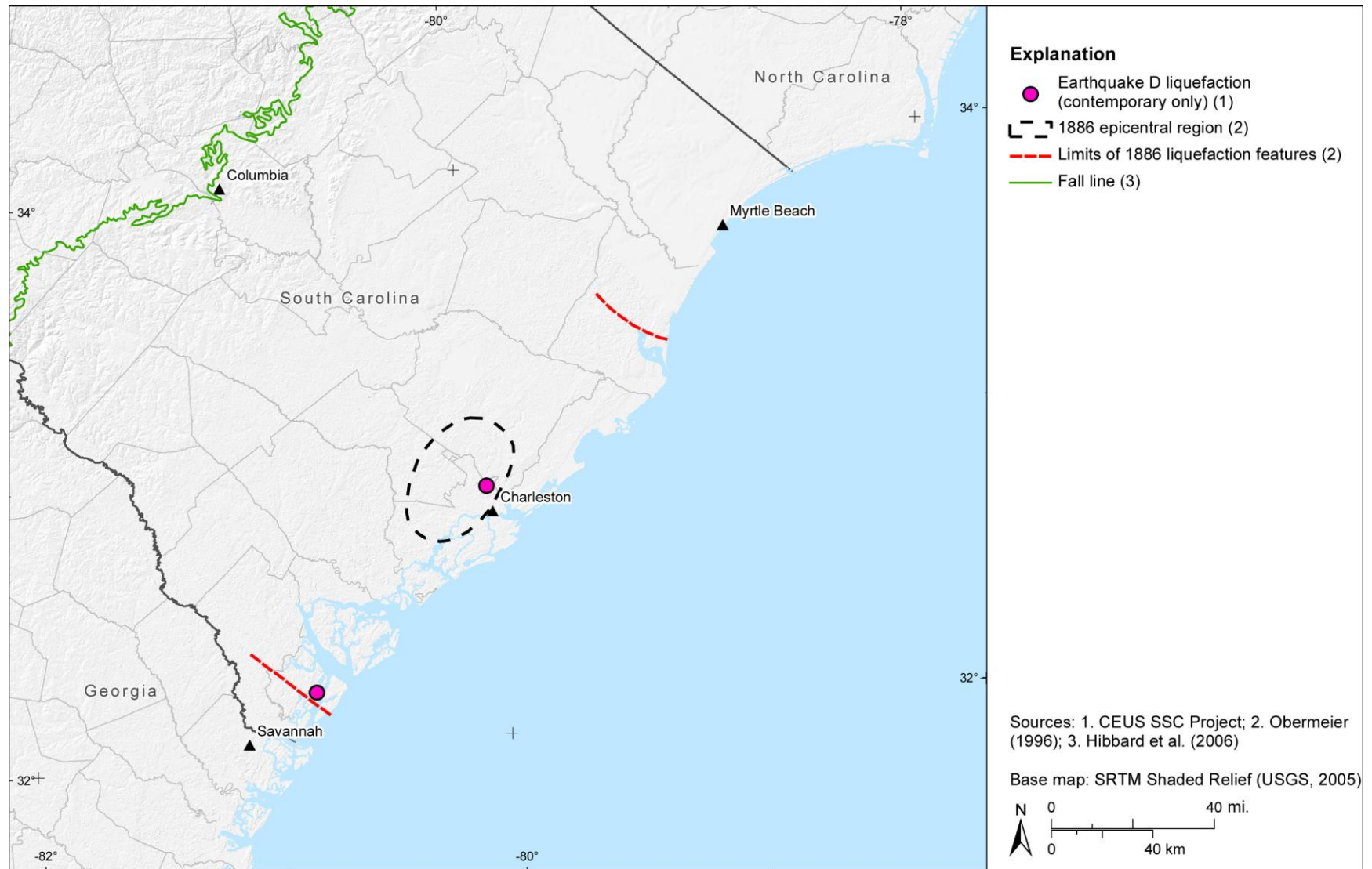


**Figure 6.1.2-12**  
Distribution of liquefaction from earthquake D, contemporary-ages-only scenario

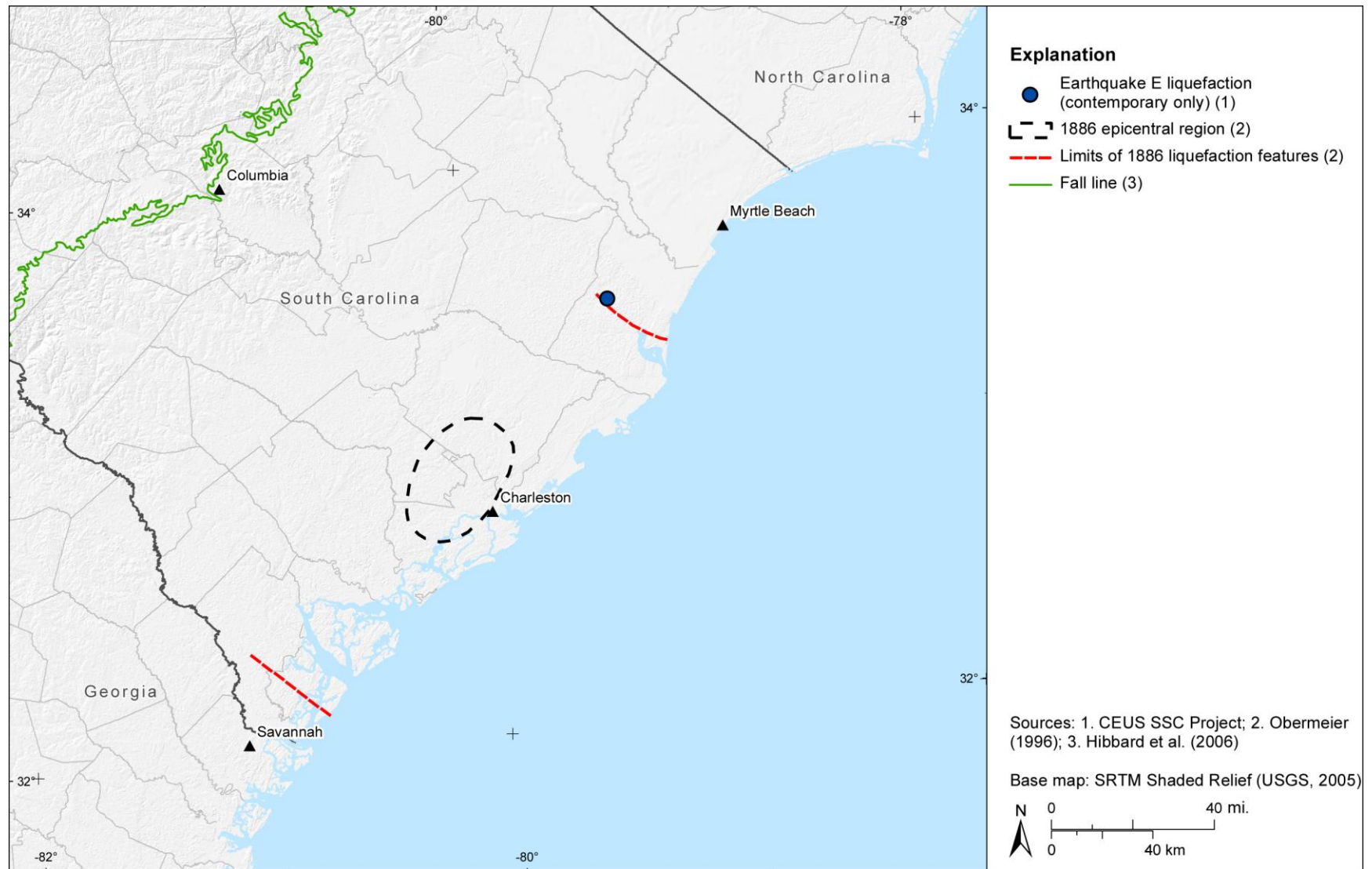


**Figure 6.1.2-13**  
Distribution of liquefaction from earthquake E, contemporary-ages-only scenario

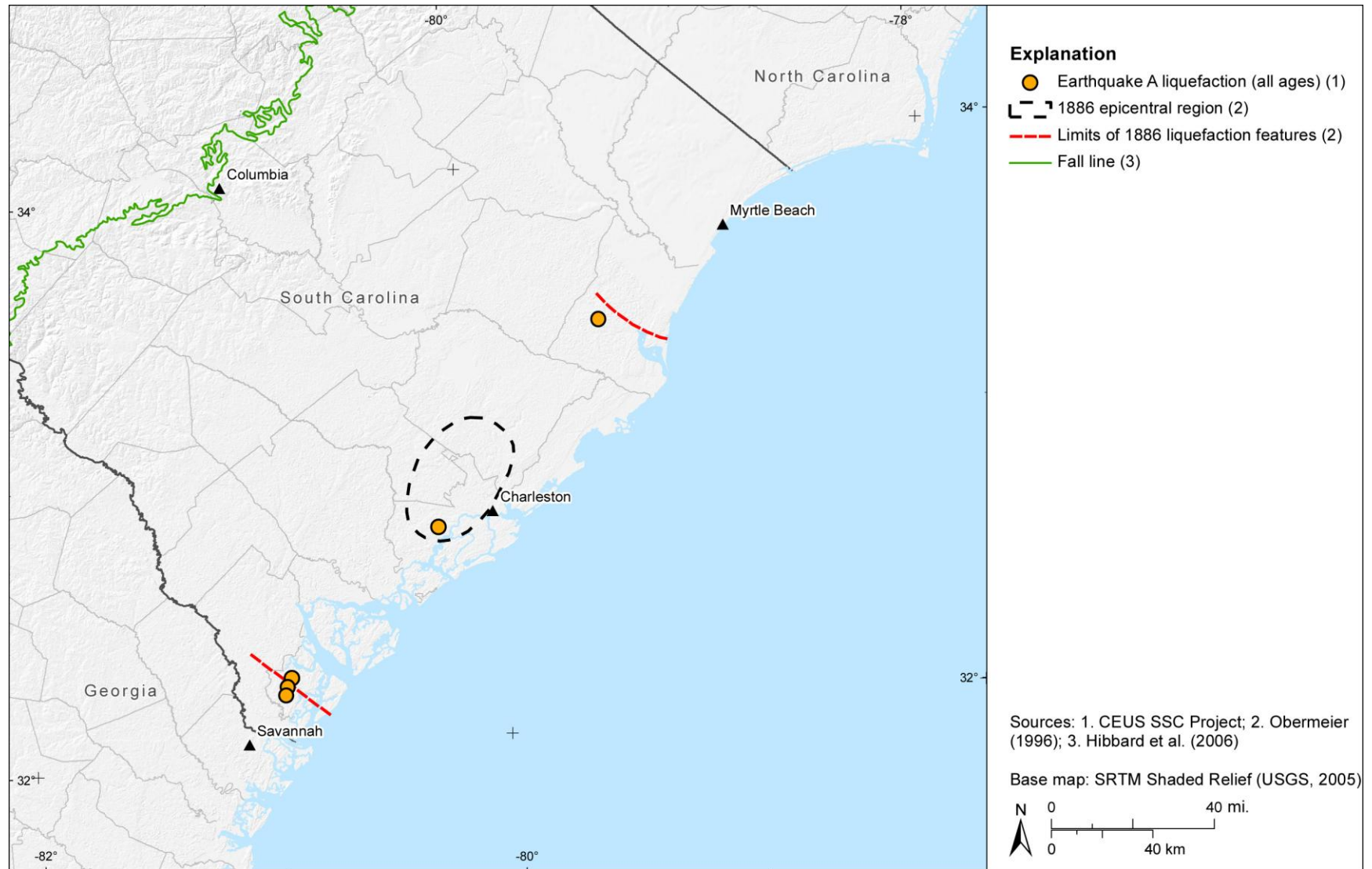


**Figure 6.1.2-14**  
Distribution of liquefaction from earthquake A, all-ages scenario

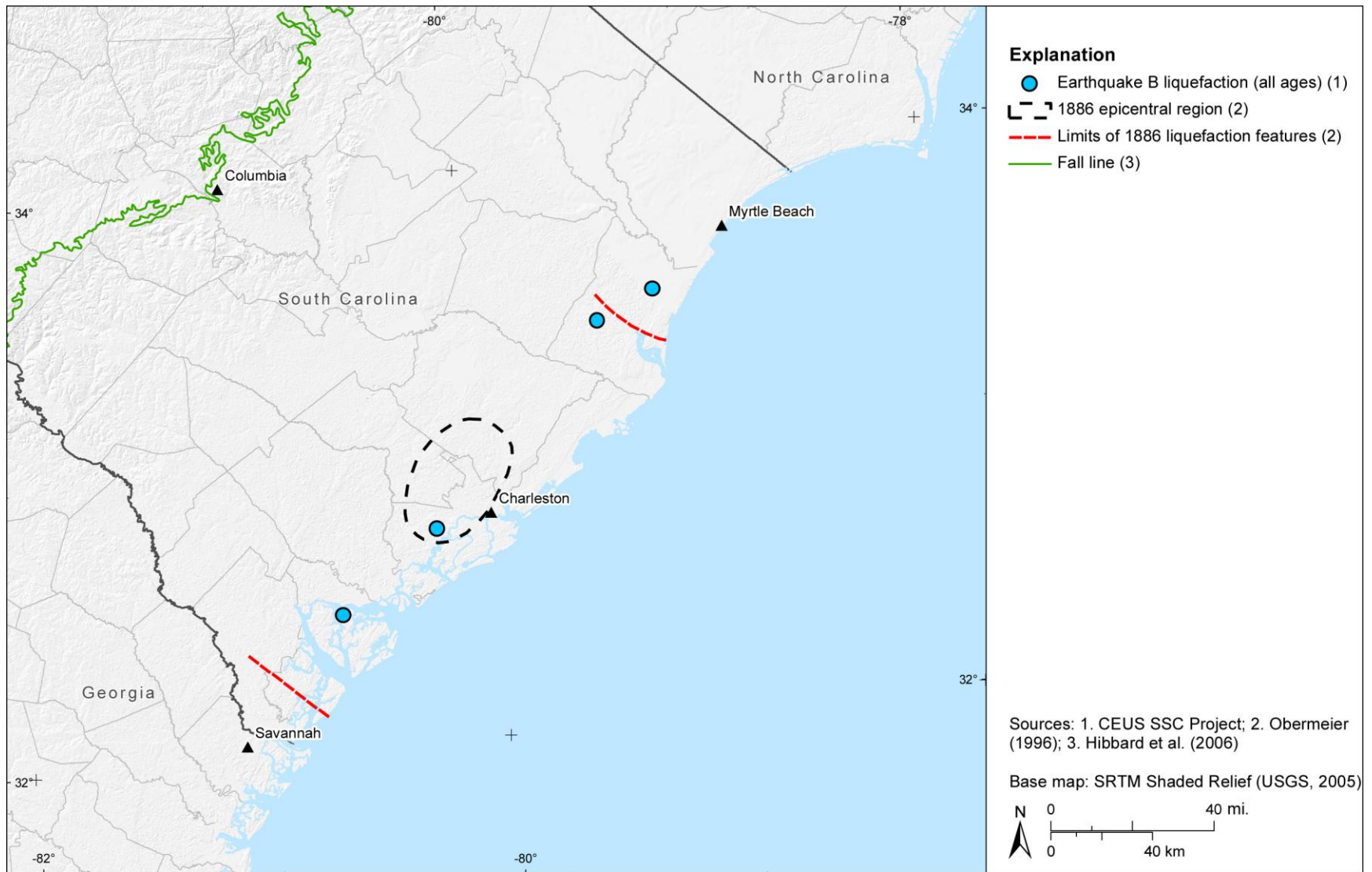


**Figure 6.1.2-15**  
Distribution of liquefaction from earthquake B, all-ages scenario

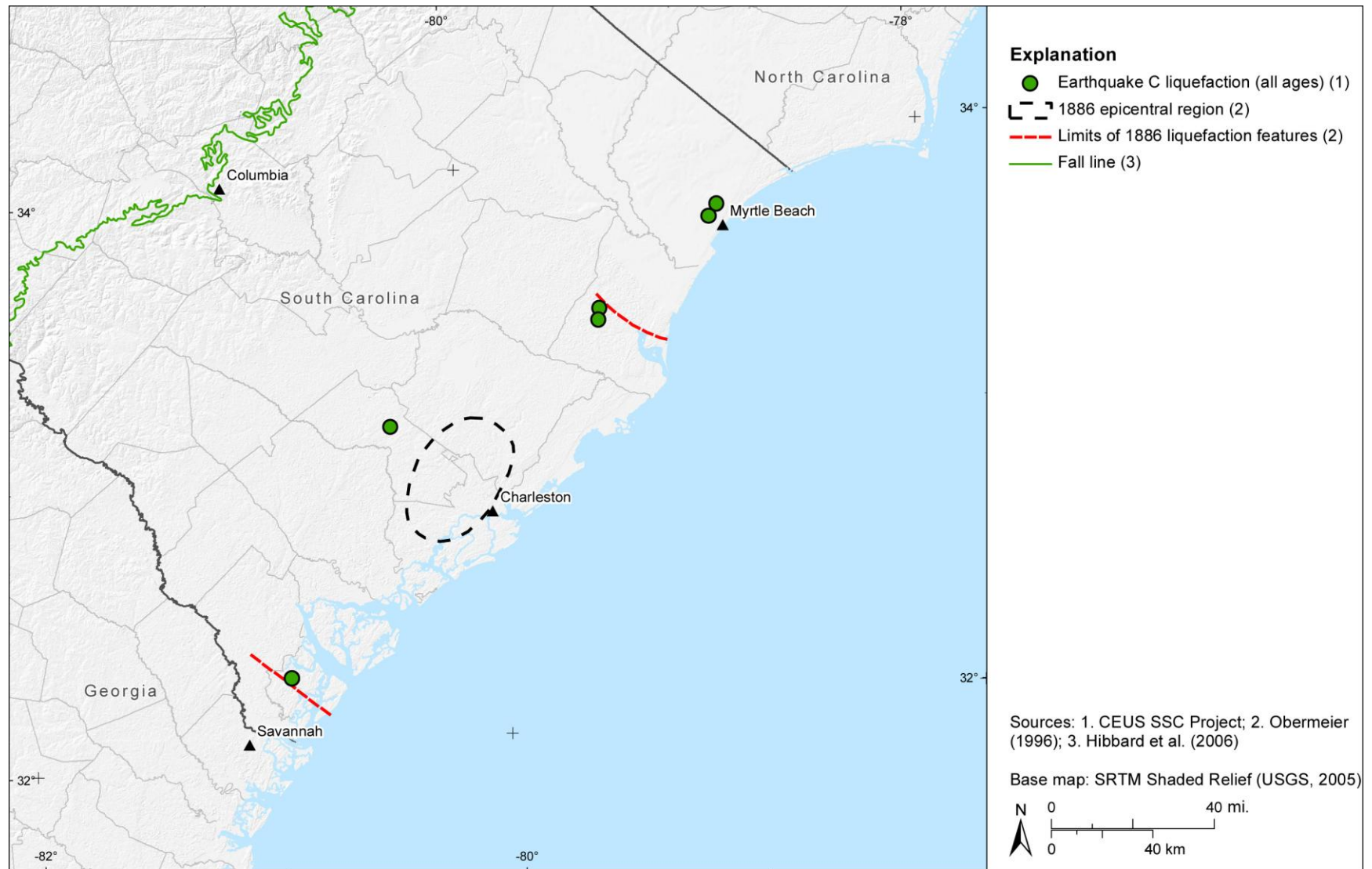


**Figure 6.1.2-16**  
Distribution of liquefaction from earthquake C, all-ages scenario

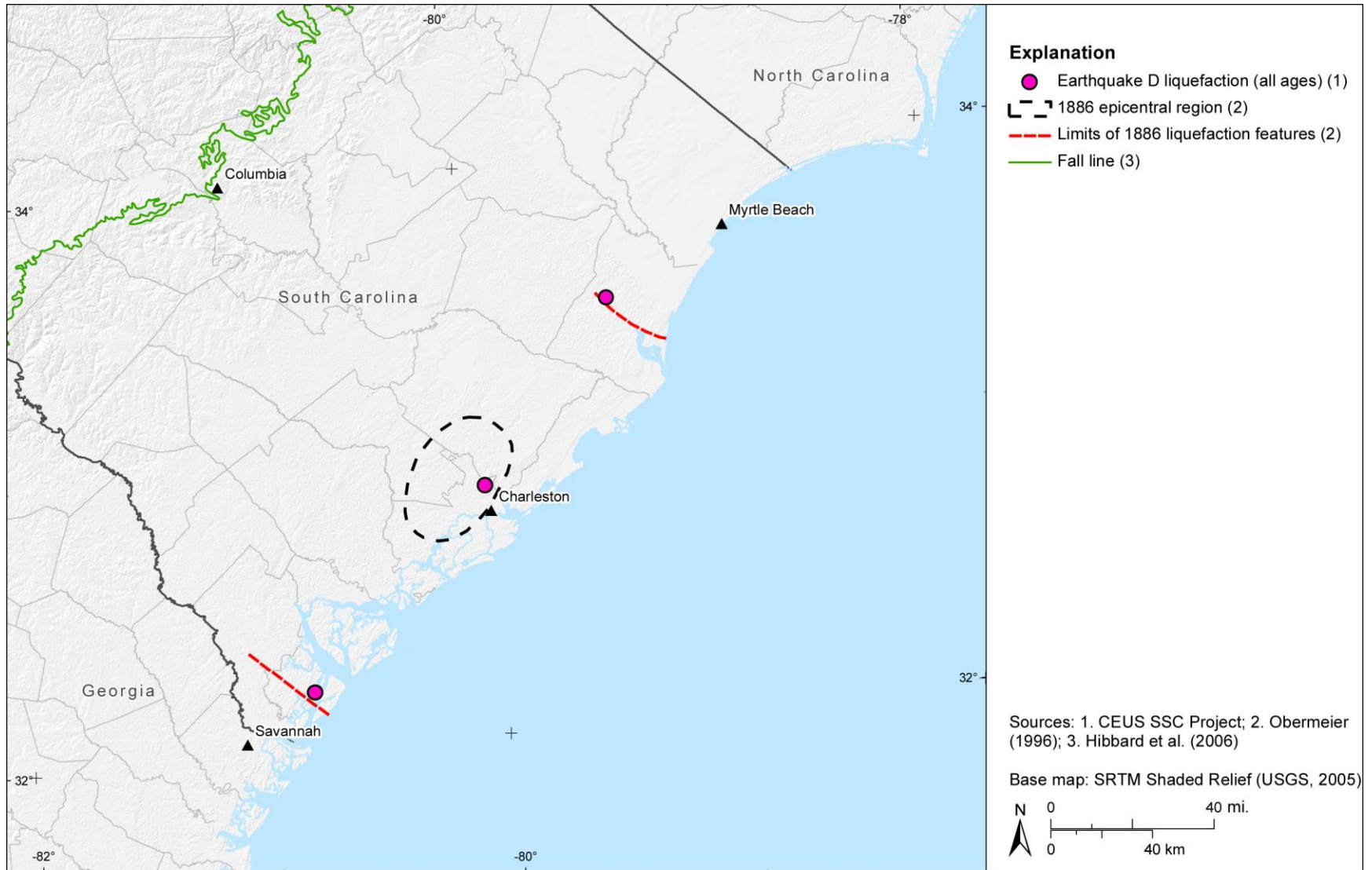


**Figure 6.1.2-17**  
Distribution of liquefaction from earthquake D, all-ages scenario

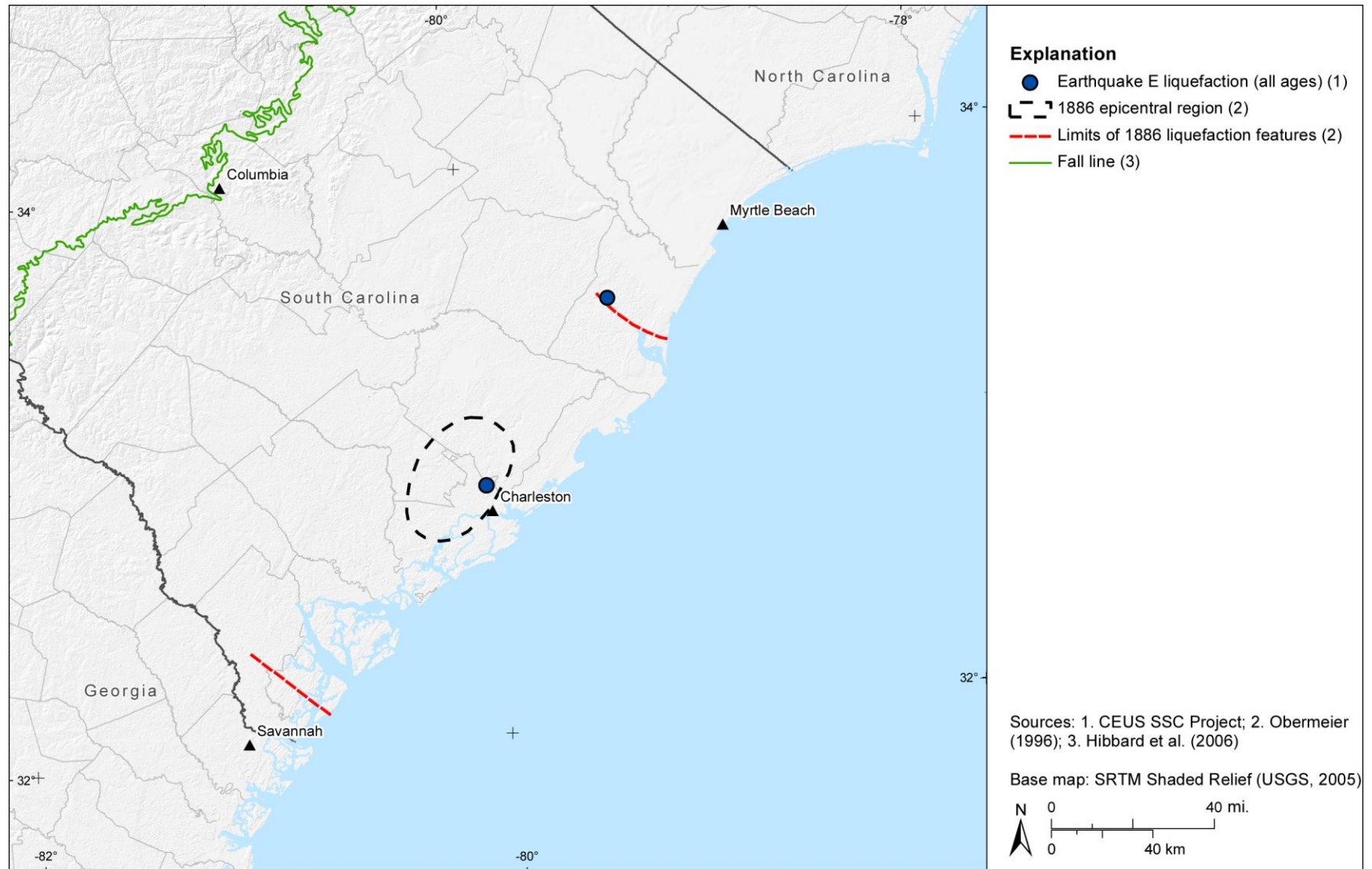


**Figure 6.1.2-18**  
Distribution of liquefaction from earthquake E, all-ages scenario

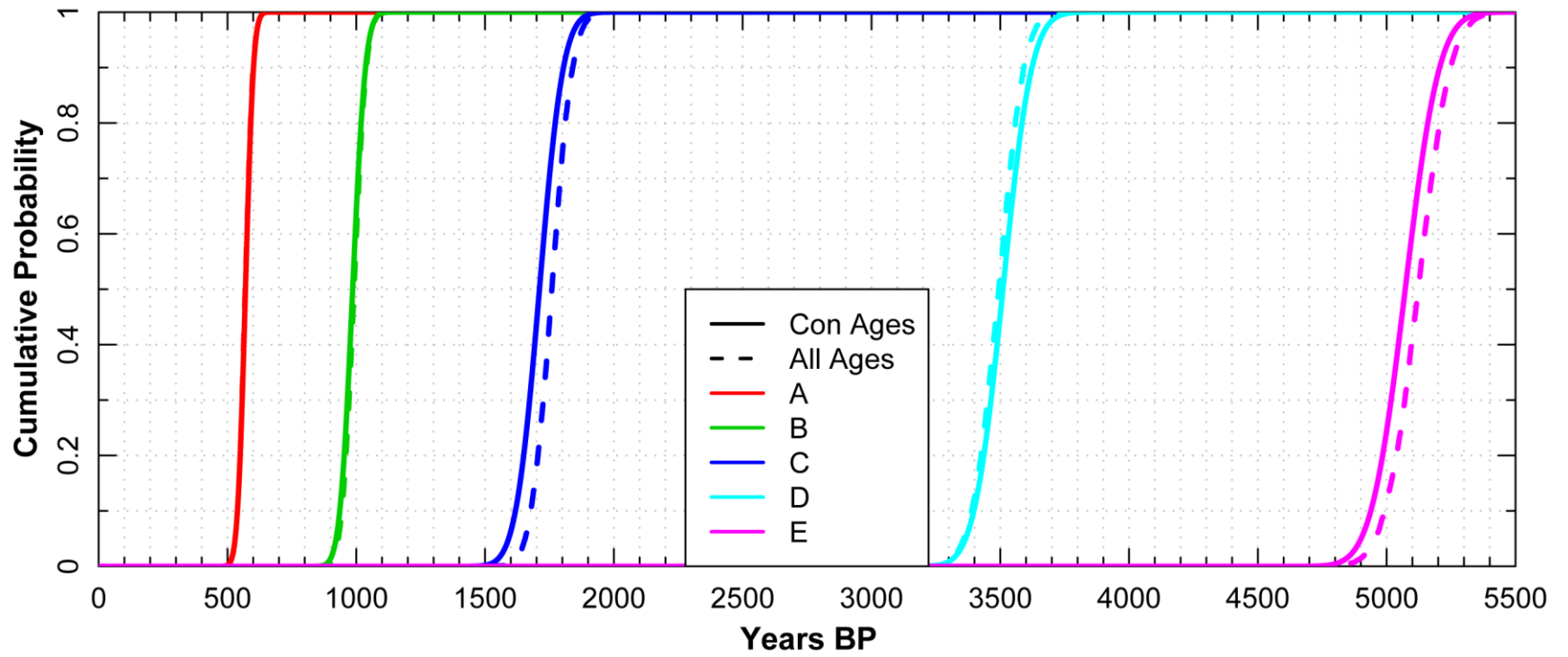
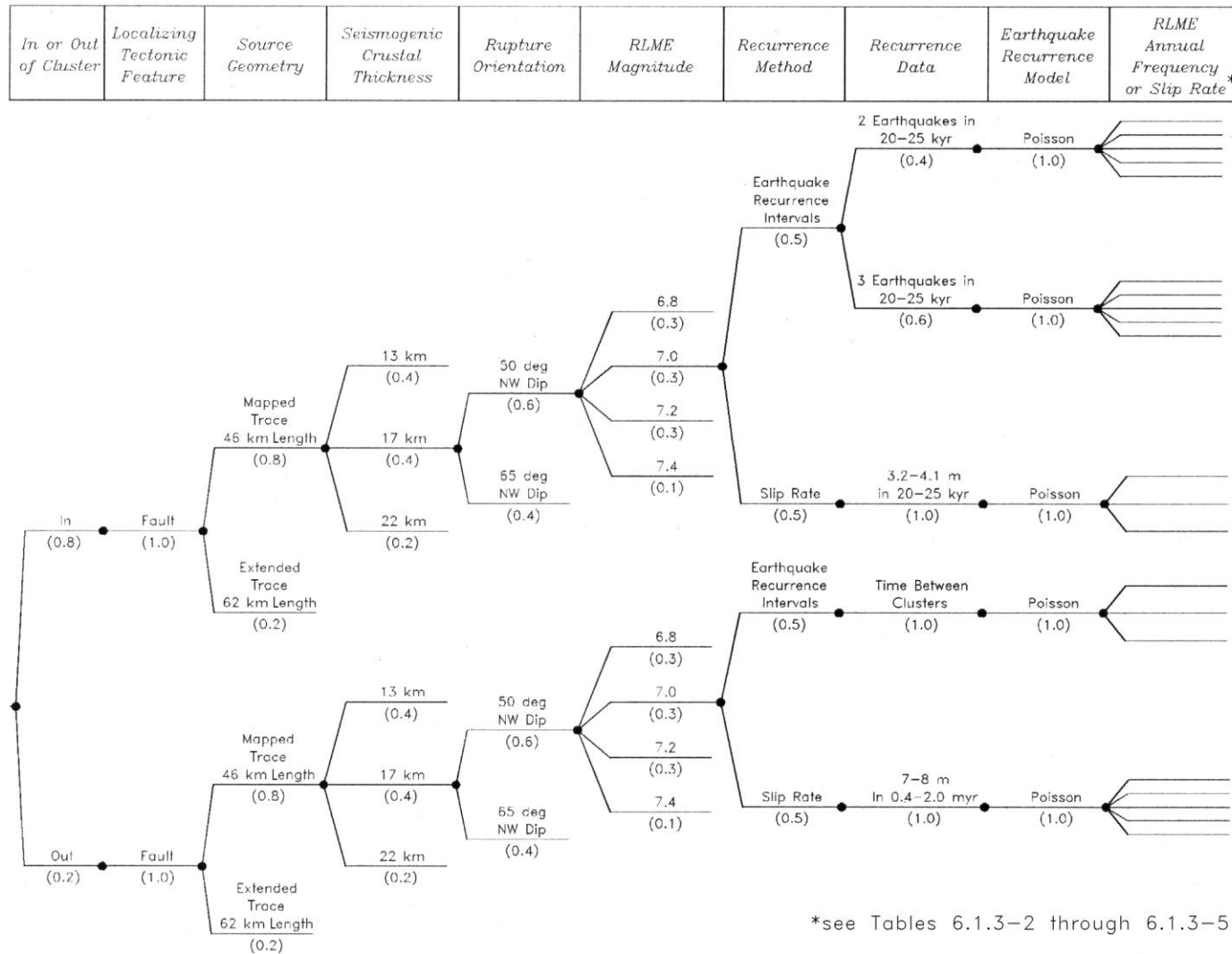
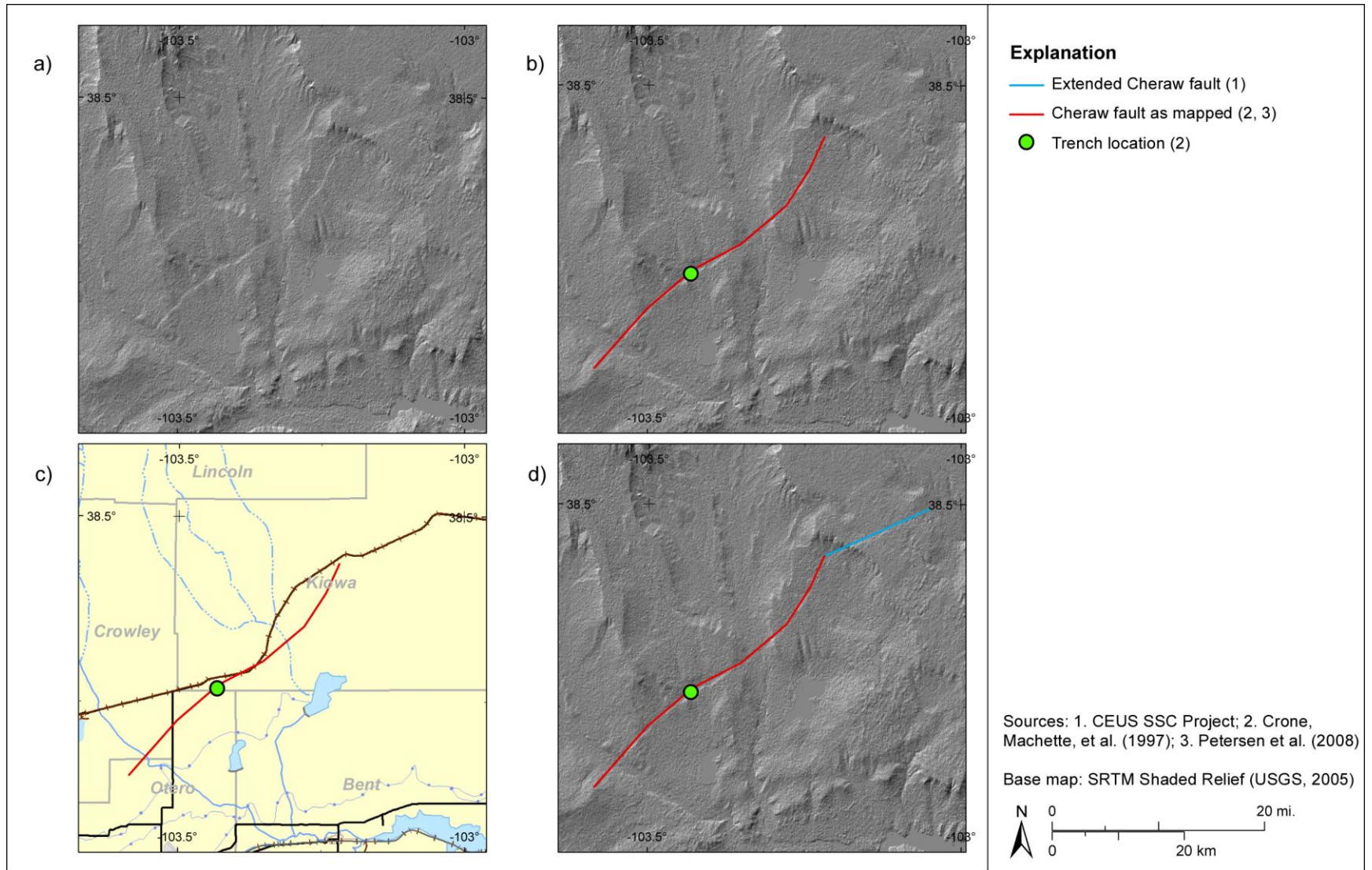


Figure 6.1.2-19  
Uncertainty distributions for the age of Charleston RLMEs

Chapter 6  
 SSC Model: RLME Sources and Mmax Zones Branch



**Figure 6.1.3-1**  
 Logic tree for the Cheraw fault RLME source



**Figure 6.1.3-2**  
Map (c) and hillshade relief images (a, b, and d) showing location of mapped Cheraw fault, possible northeast extension, and paleoseismic locality

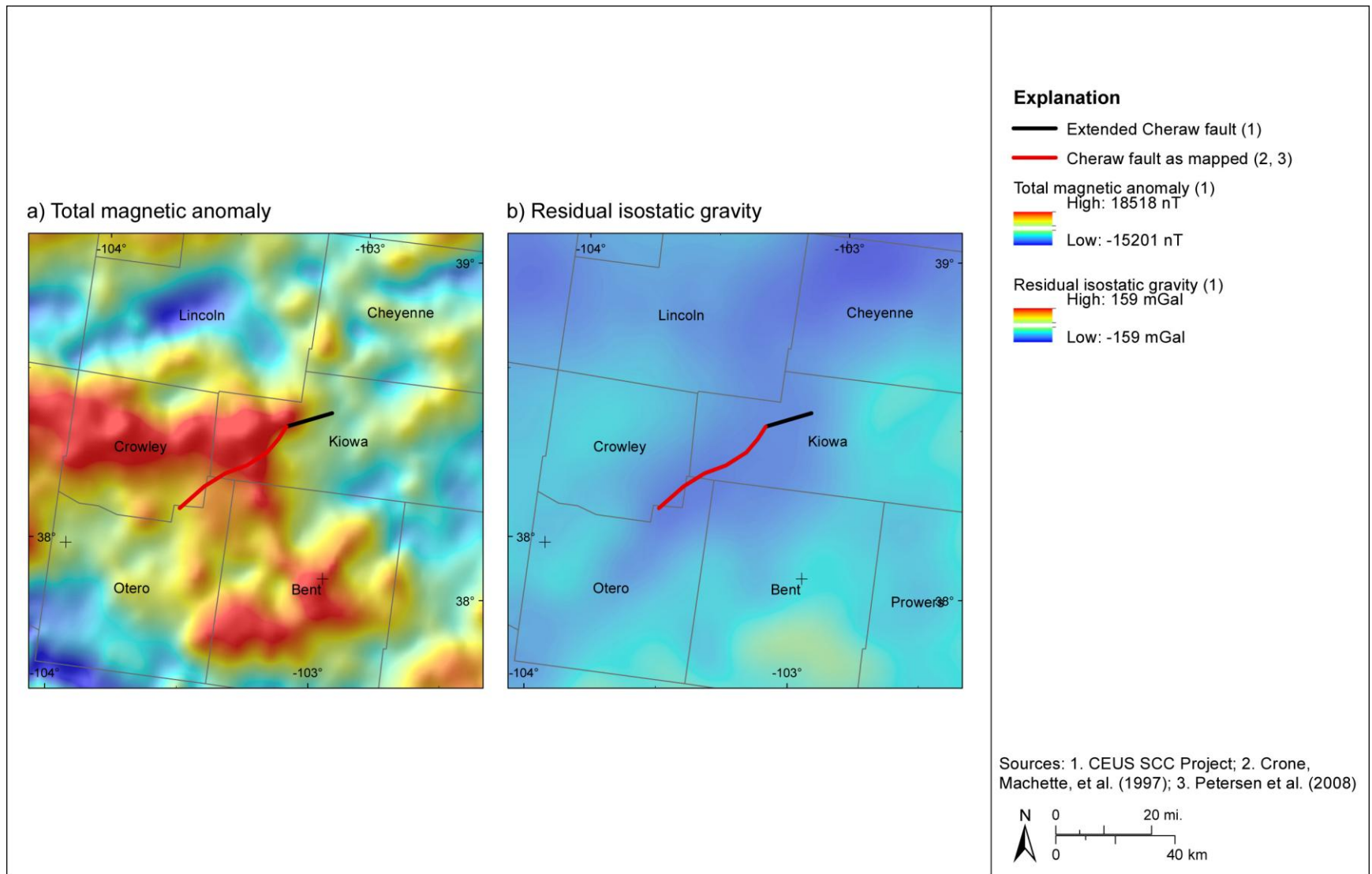


**Figure 6.1.3-3**  
 Cheraw RLME source relative to (a) total magnetic anomaly and (b) residual isostatic gravity data

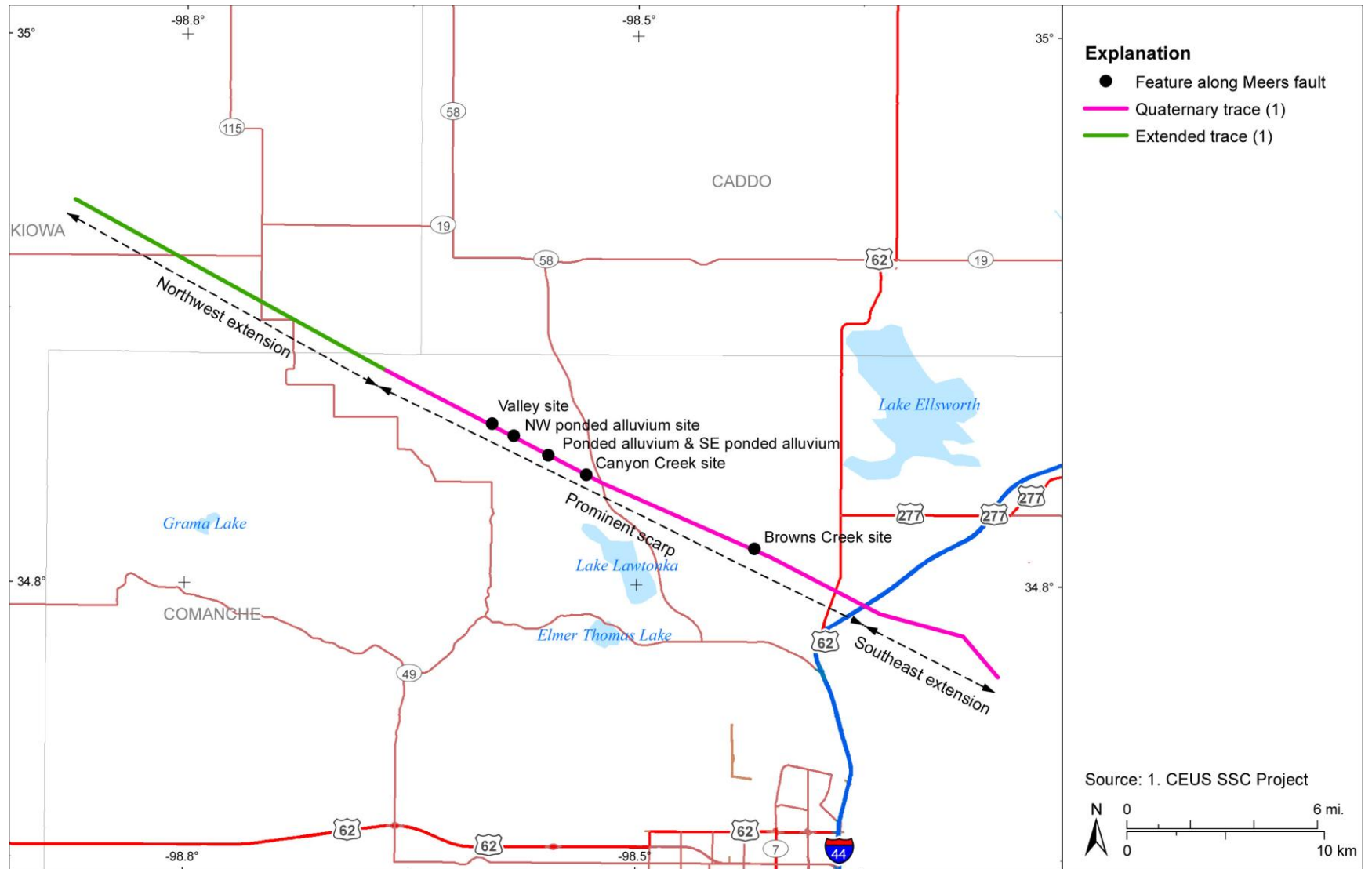


**Figure 6.1.4-1**  
 Meers fault location

Chapter 6  
SSC Model: RLME Sources and Mmax Zones Branch

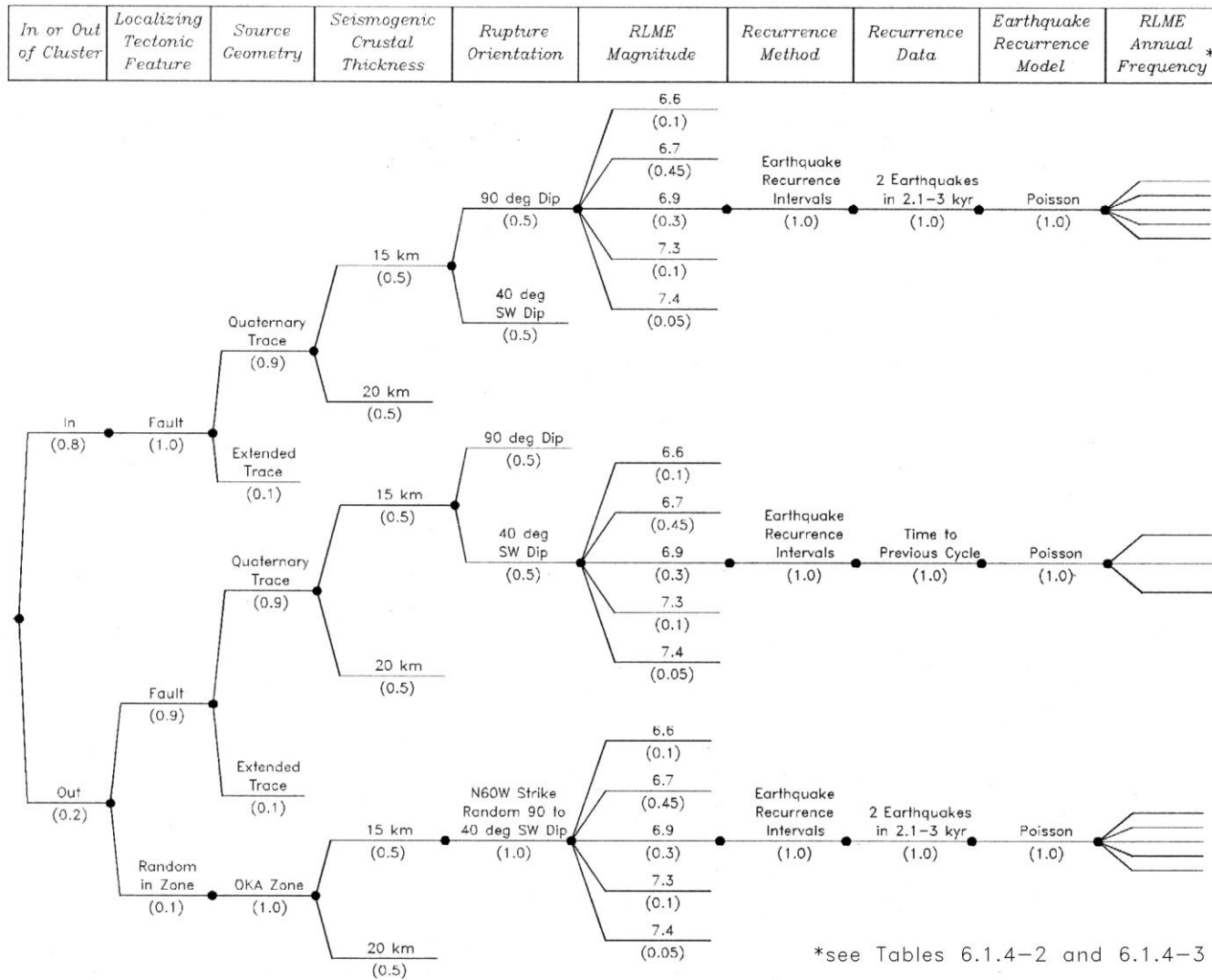
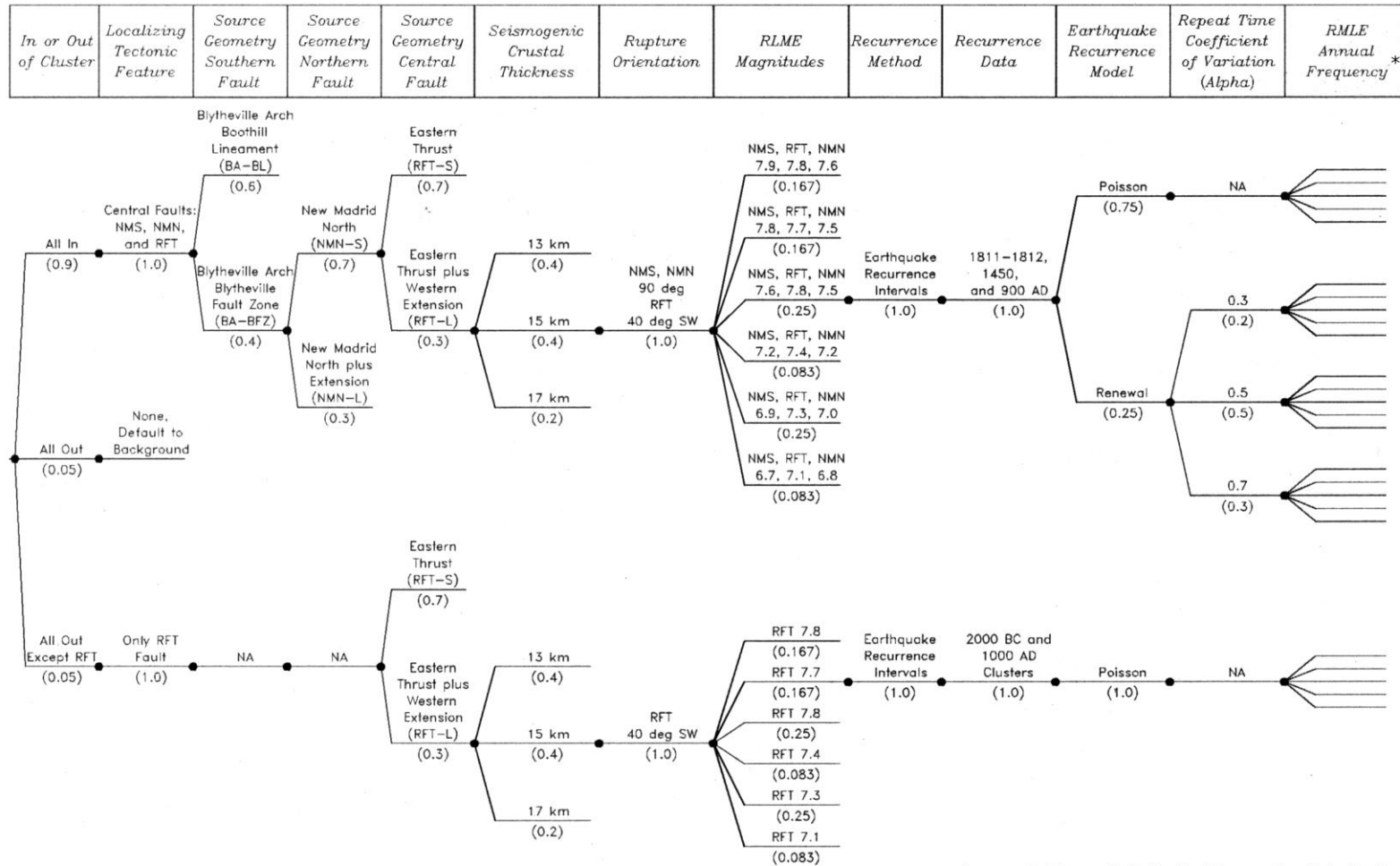
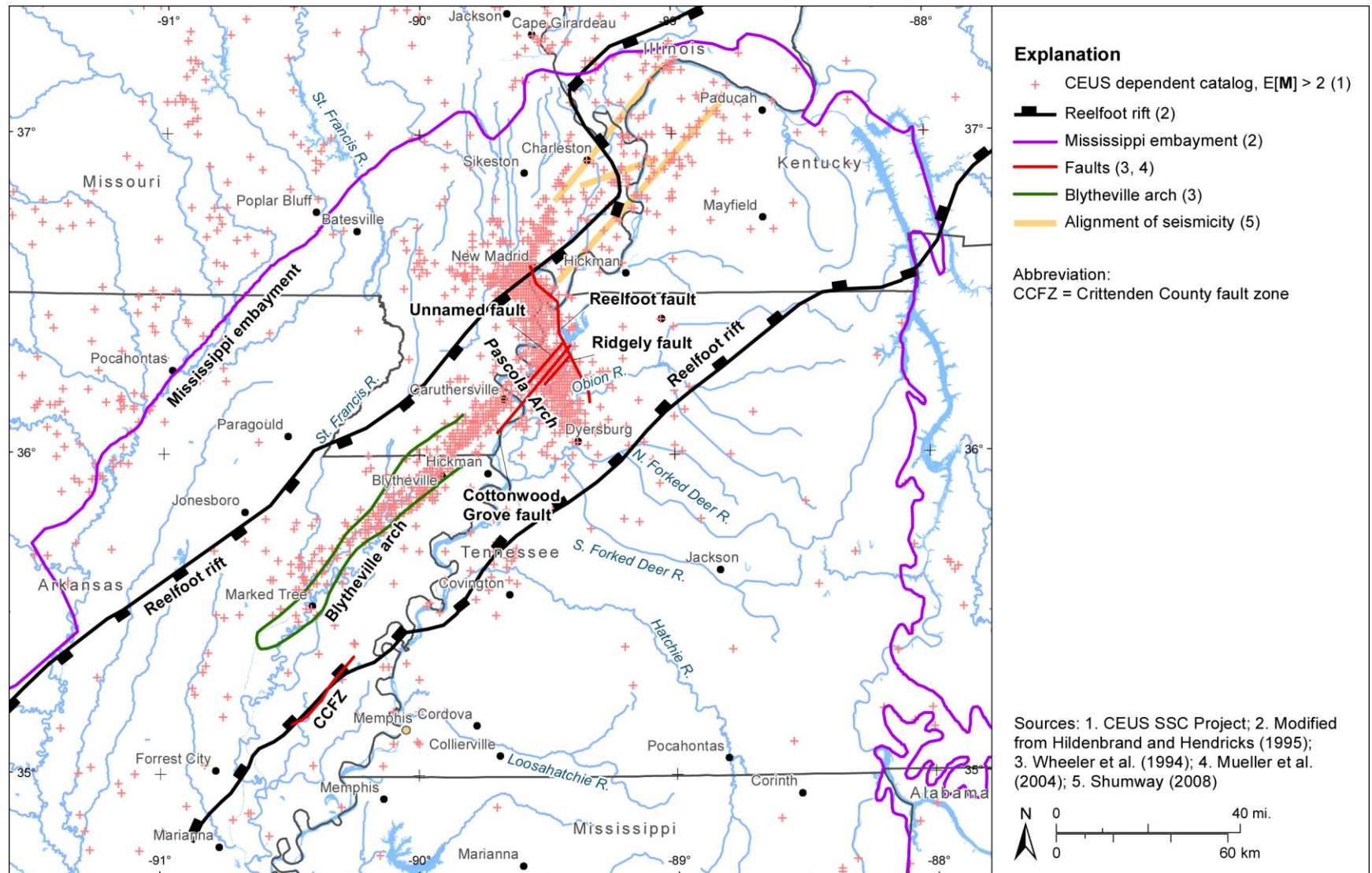


Figure 6.1.4-2  
Logic tree for the Meers fault source



\*see Tables 6.1.5-5 through 6.1.5-7

Figure 6.1.5-1  
Logic tree for the NMFS RLME source



**Figure 6.1.5-2**  
 Map showing seismicity and major subsurface structural features in the New Madrid region

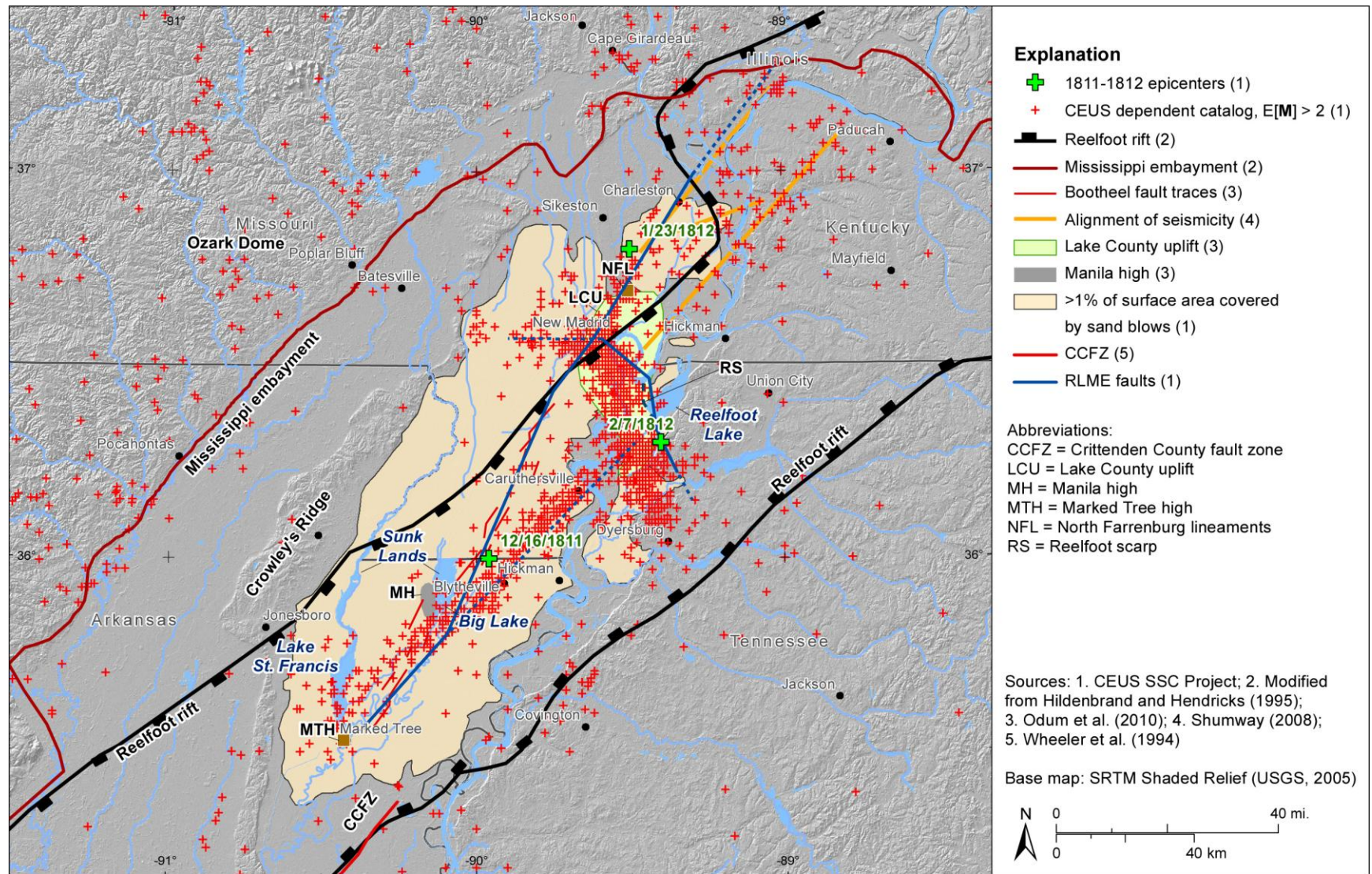


**Figure 6.1.5-3**  
 Map showing geomorphic and near-surface tectonic features in the New Madrid region and locations of NMFS RLME fault sources

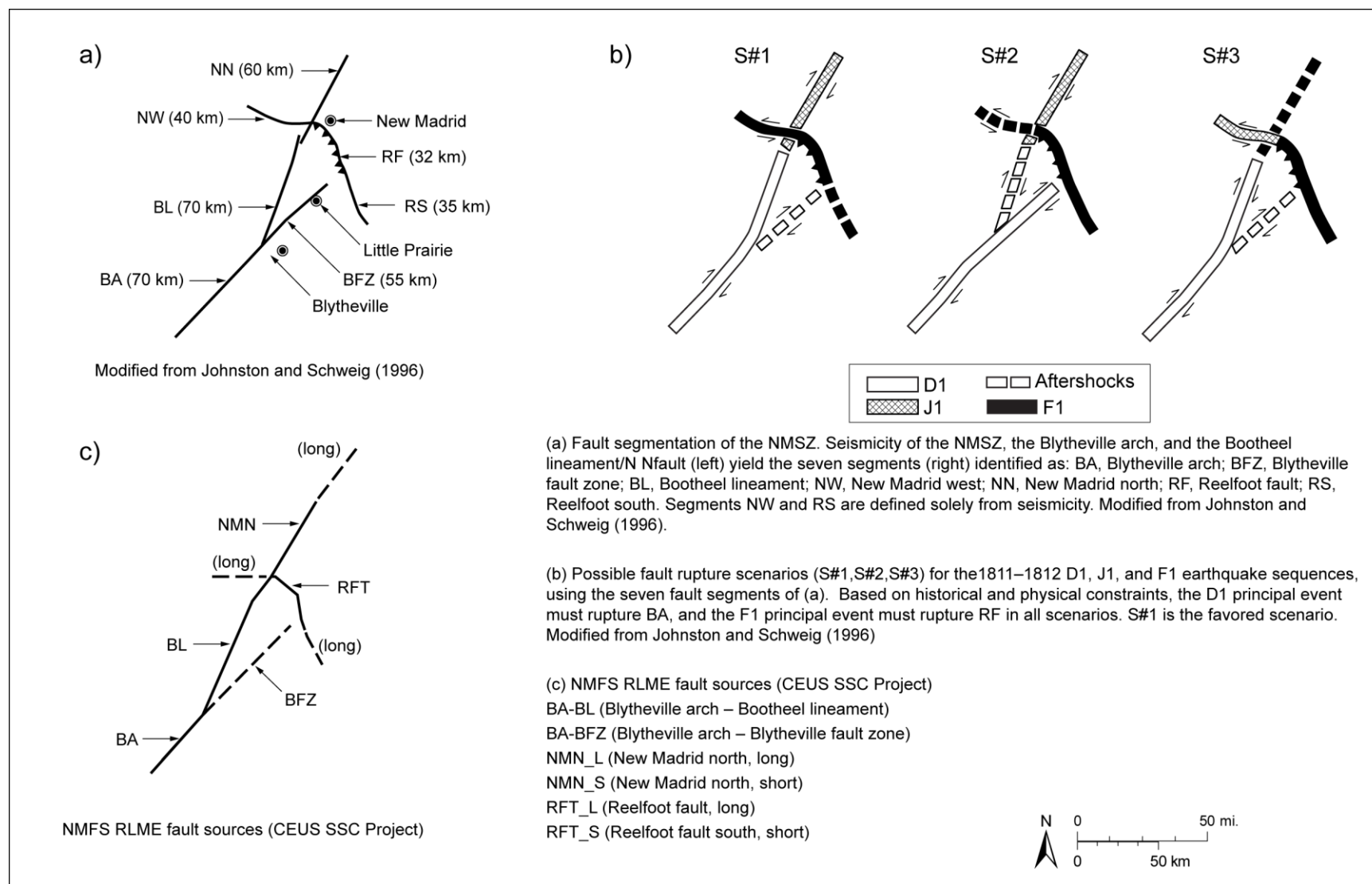


**Figure 6.1.5-4**  
Rupture segments (a) and models (b) for the New Madrid faults from Johnston and Schweig (1996) and (c) the NMFS RLME fault sources

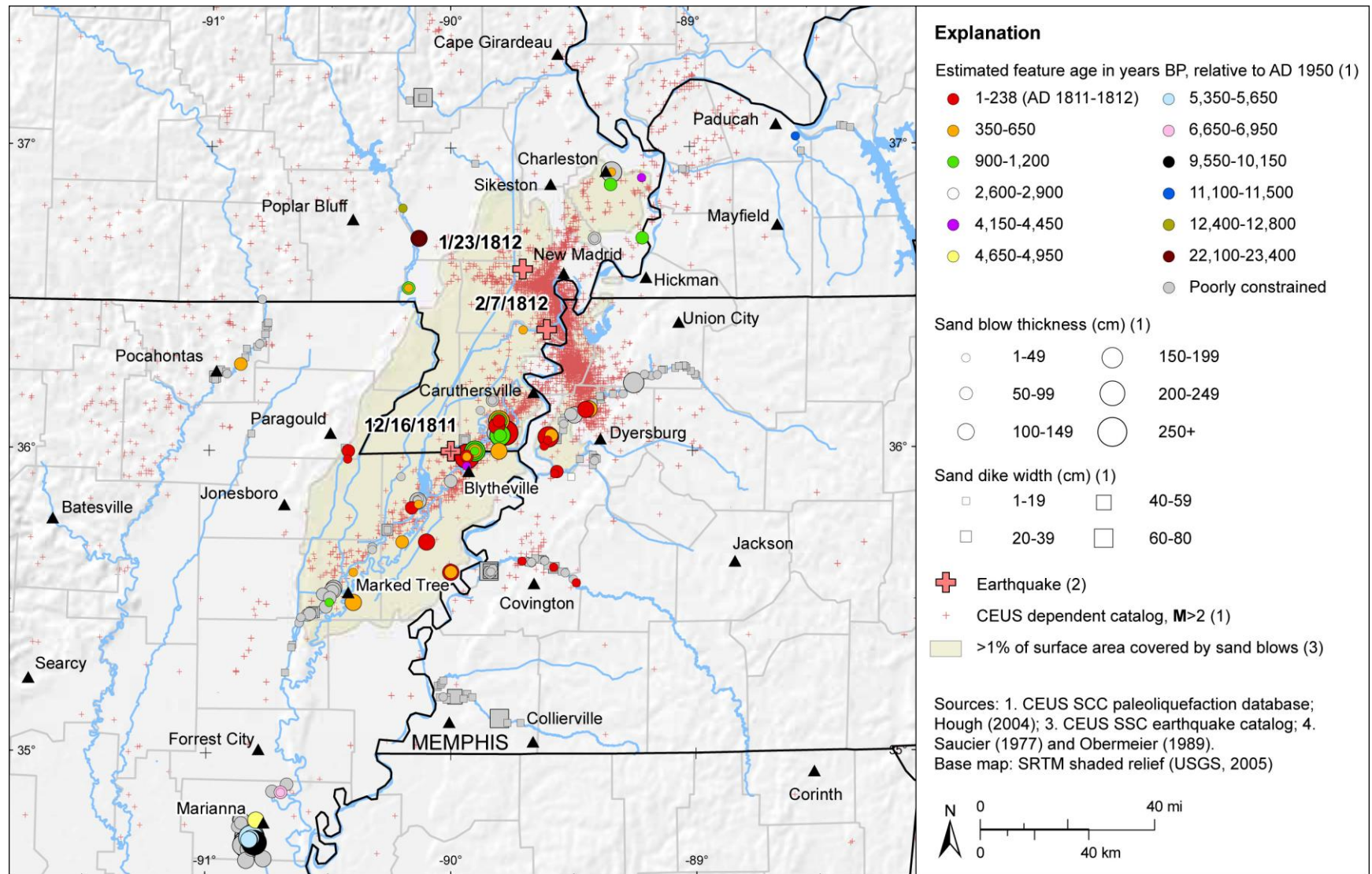


**Figure 6.1.5-5**  
 Map of NMSZ showing estimated ages and measured sizes of liquefaction features

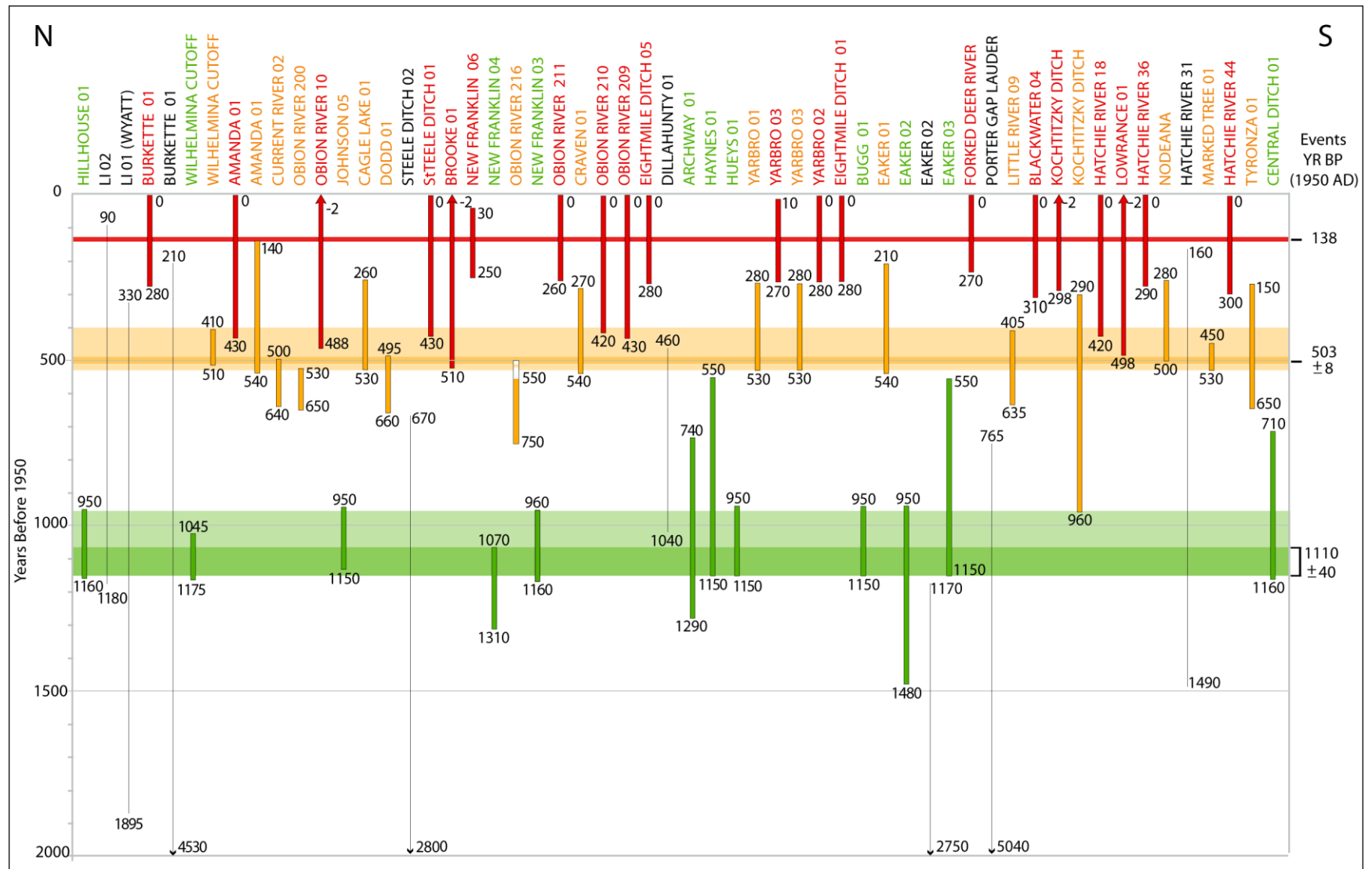


**Figure 6.1.5-6**  
 Earthquake chronology for NMSZ from dating and correlation of liquefaction features at sites (listed at top) along N-S transect across region

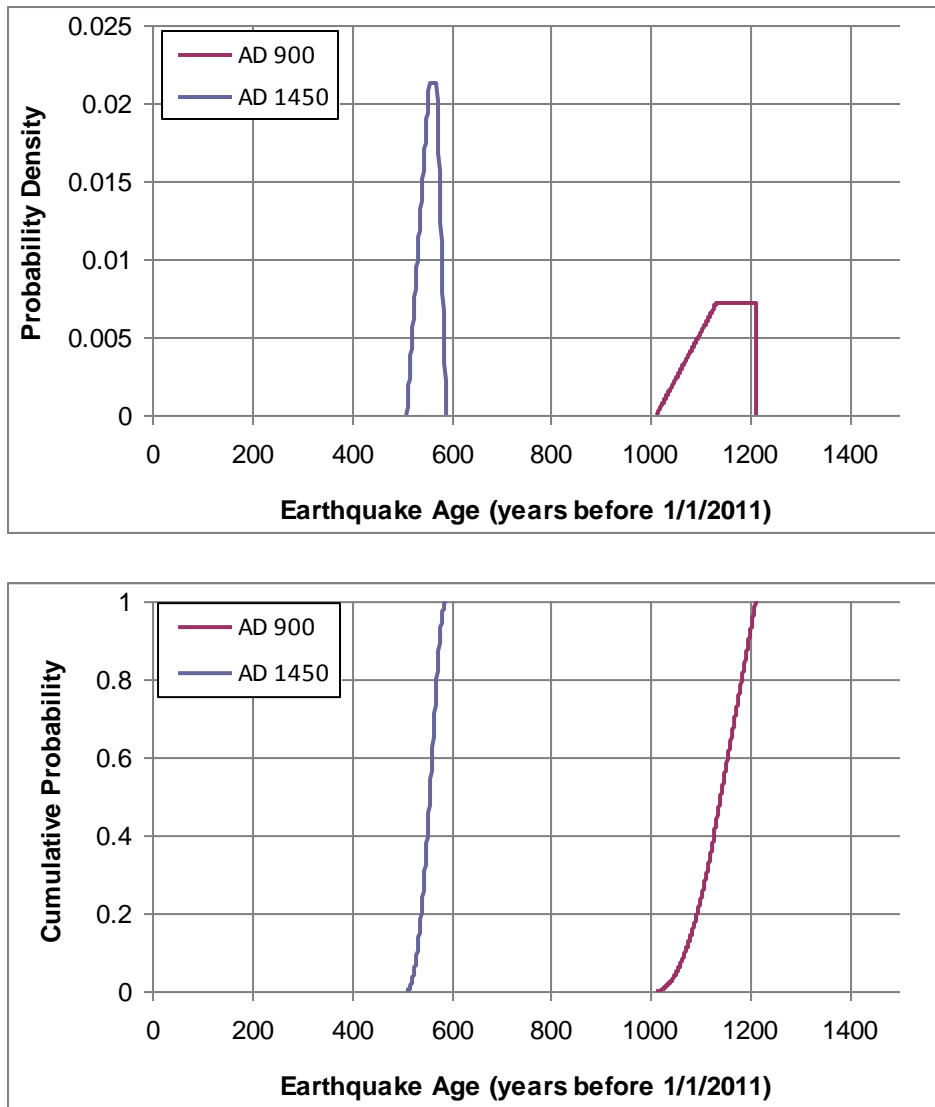
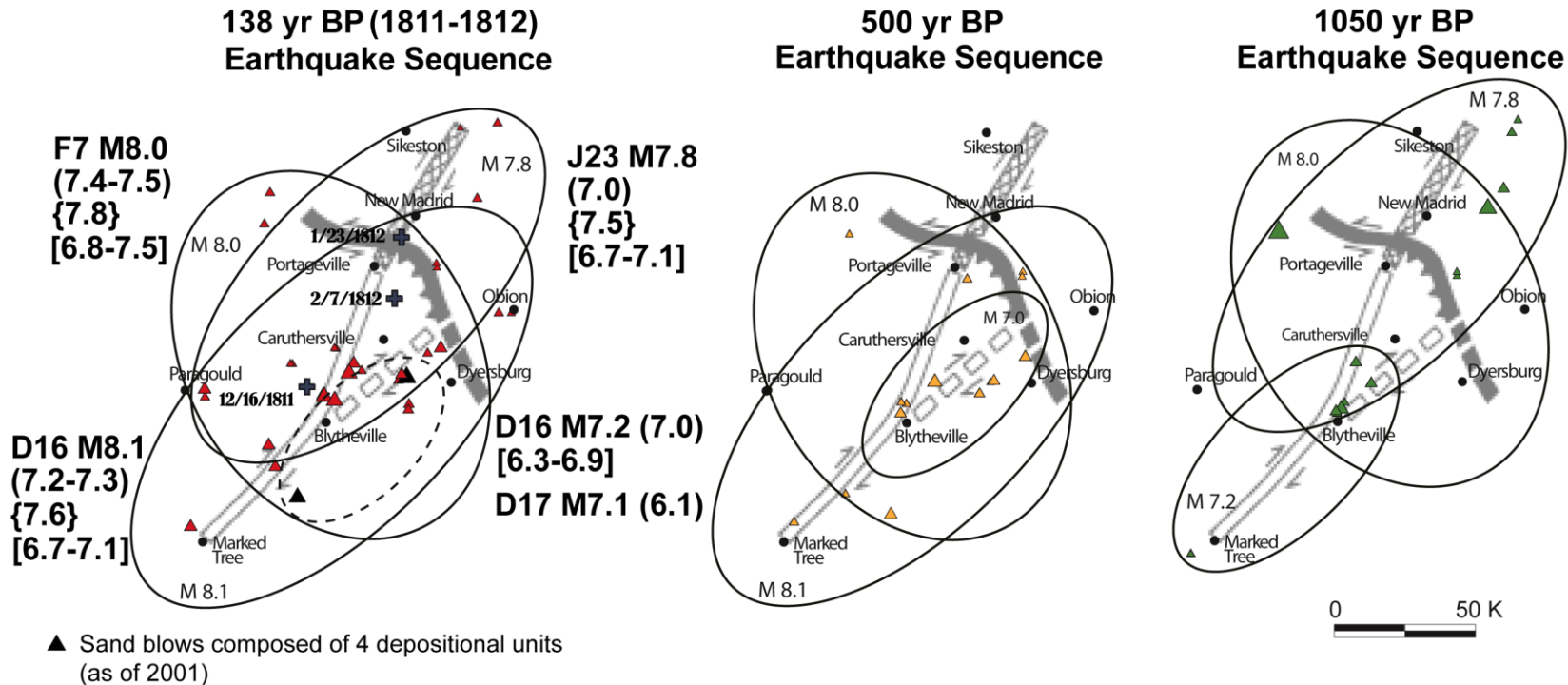


**Figure 6.1.5-7**  
**Probability distributions for the age of the AD 900 and AD 1450 NMFS RLMEs**



**1811-1812 Main Shocks:**  
 D16: December 16, 1811 earthquake  
 J23: January 23, 1812 earthquake  
 F7: February 7, 1812 earthquake

**Estimated Magnitudes:**  
 M 8.0 Johnston and Schweig (1996)  
 (7.4-7.5) Hough et al. (2000); Hough and Martin (2002)  
 {7.8} Bakun and Hopper (2004)  
 [6.8-7.5] Hough and Page (2011)

Source: Modified from Tuttle (2009)

**Figure 6.1.5-8**  
 Liquefaction fields for the 1811-1812, AD 1450, and AD 900 earthquakes as interpreted from spatial distribution and stratigraphy of sand blows

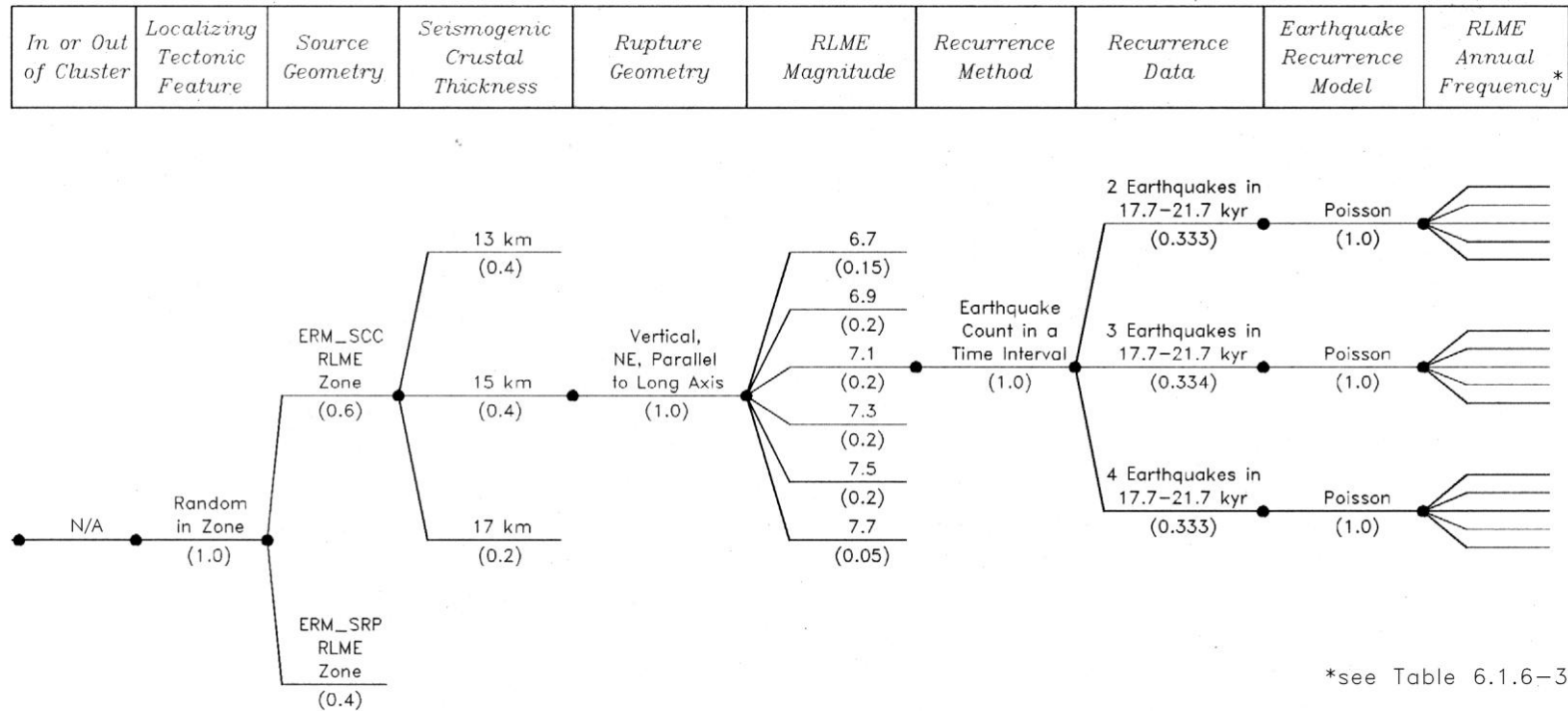
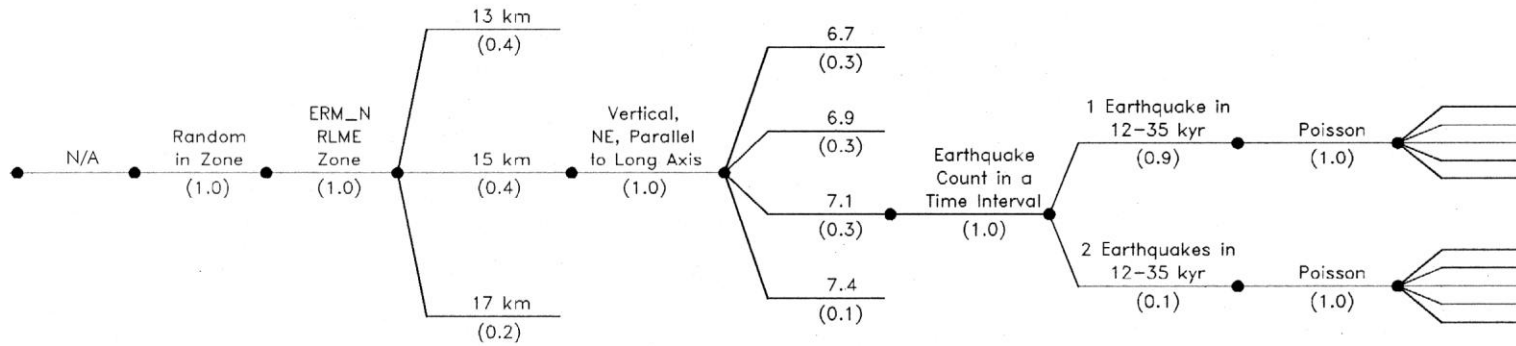


**Figure 6.1.6-1a**  
**Logic tree for the Reelfoot Rift–Eastern Rift Margin South RLME source. Two options for the southern extent of the ERM-S are considered: ERM-SCC includes the Crittenden County fault zone, and ERM-SRP includes the postulated zone of deformation based on fault picks identified in a high-resolution seismic profile along the Mississippi River.**

Chapter 6

SSC Model: RLME Sources and Mmax Zones Branch

<i>In or Out of Cluster</i>	<i>Localizing Tectonic Feature</i>	<i>Source Geometry</i>	<i>Seismogenic Crustal Thickness</i>	<i>Rupture Geometry</i>	<i>RLME Magnitude</i>	<i>Recurrence Method</i>	<i>Recurrence Data</i>	<i>Earthquake Recurrence Model</i>	<i>Equivalent Annual Frequency*</i>
-----------------------------	------------------------------------	------------------------	--------------------------------------	-------------------------	-----------------------	--------------------------	------------------------	------------------------------------	-------------------------------------



\*see Table 6.1.6–4

**Figure 6.1.6-1b**  
**Logic tree for the Reelfoot Rift–Eastern Rift Margin North RLME source**

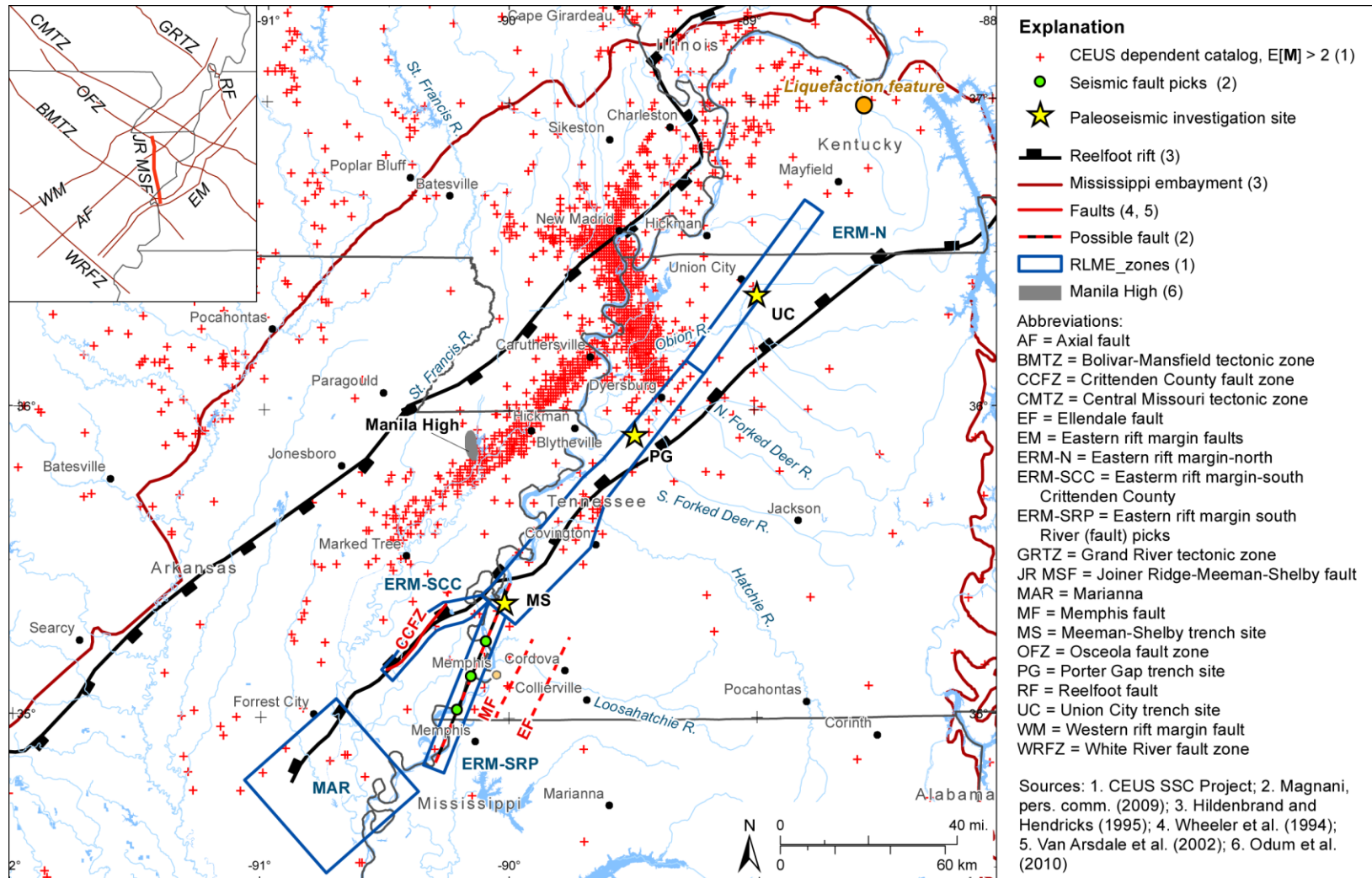


**Figure 6.1.6-2**  
Map showing structural features and paleoseismic investigation sites along the eastern margin of the Reelfoot rift. The inset map shows the locations of inferred basement faults that border and cross the Reelfoot rift (Csontos et al., 2008) and the inferred Joiner Ridge–Meeman-Shelby fault (JR-MSF; Odum et al., 2010).

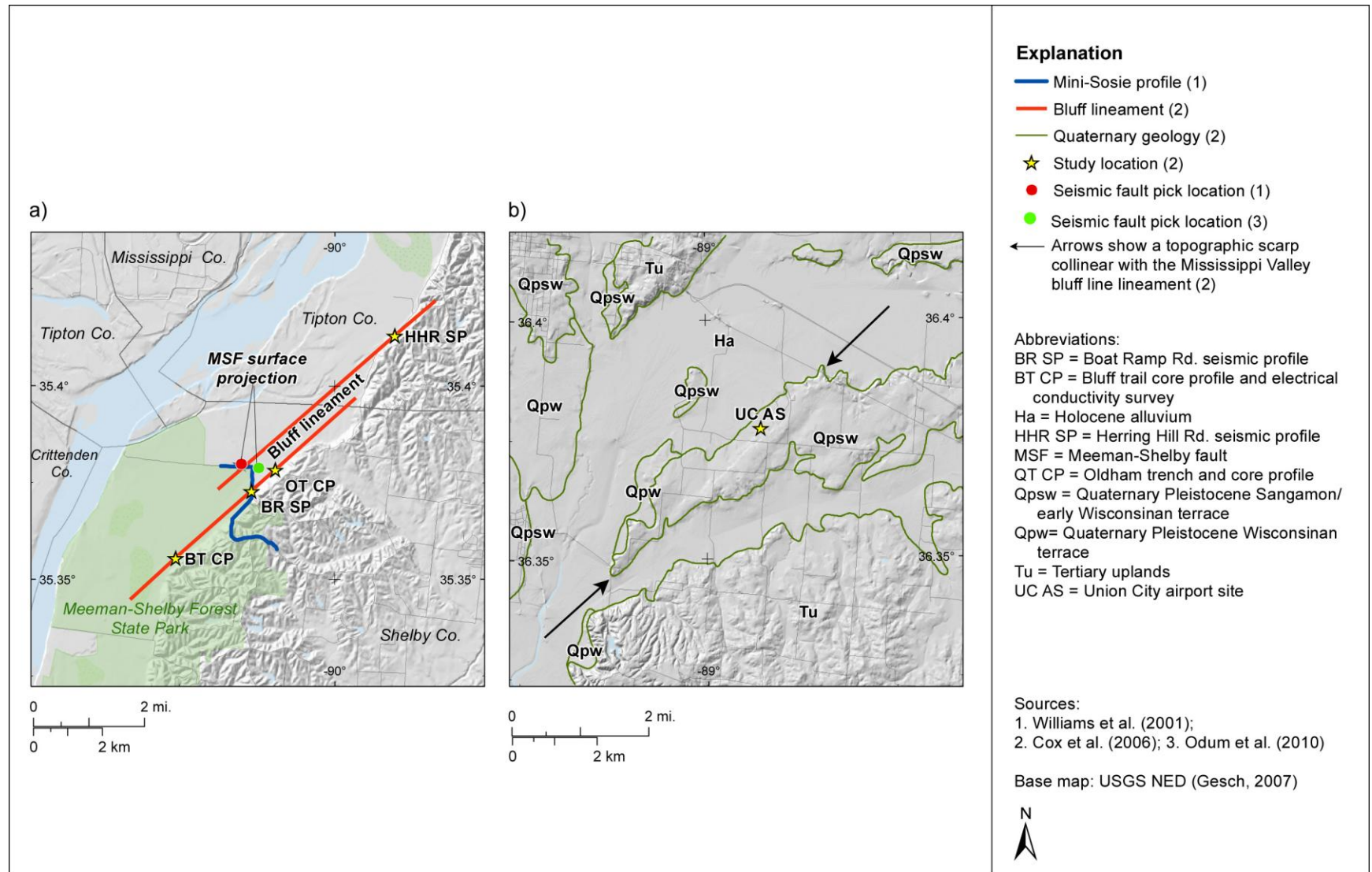


**Figure 6.1.6-3**  
**Maps showing surficial geology and locations of subsurface investigations at (a) Meeman-Shelby Forest State Park locality and (b) Union City site (MSF and UC on Figure 6.1.6-2). Modified from Cox et al. (2006) and Odum et al. (2010).**

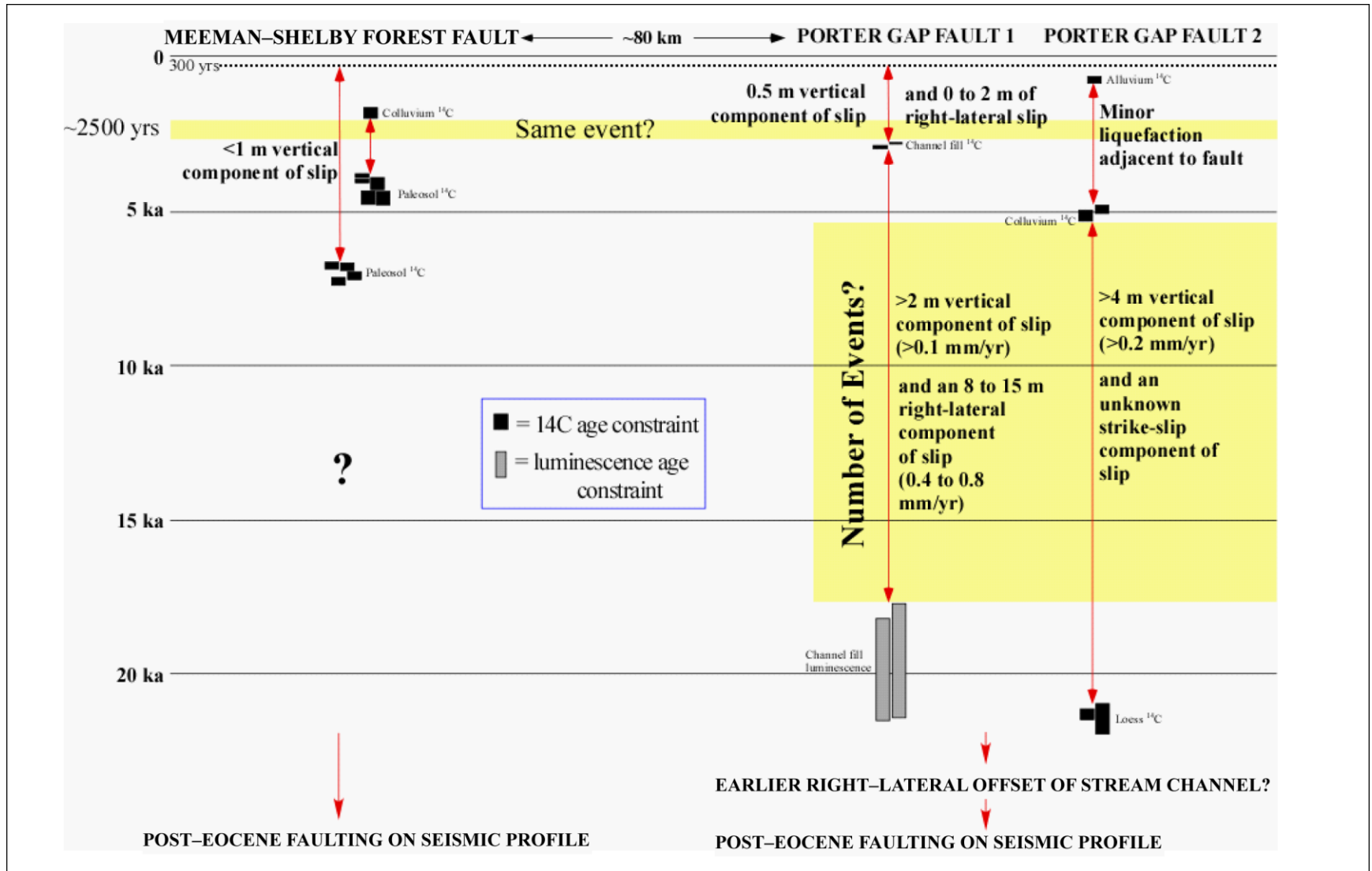
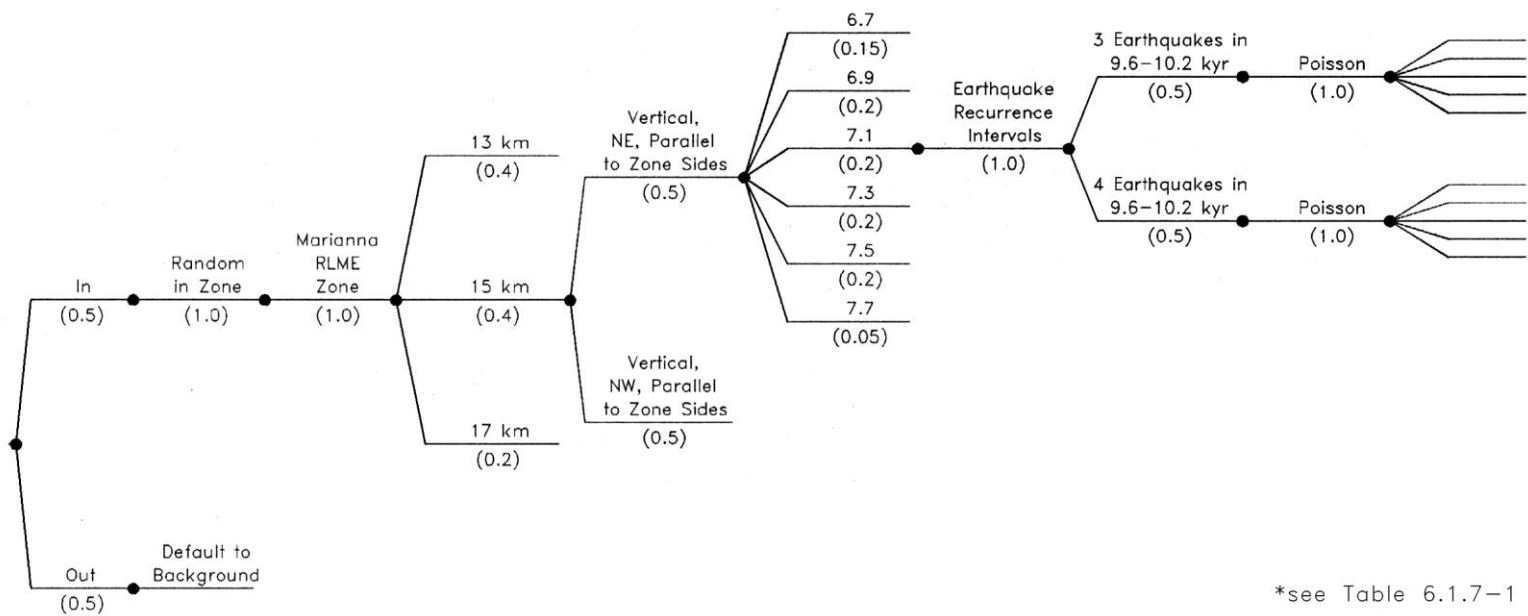


Figure 6.1.6-4  
Figure showing the timing of events along the eastern Reelfoot rift margin. Modified from Cox (2009).

Chapter 6  
 SSC Model: RLME Sources and Mmax Zones Branch

<i>In or Out of Cluster</i>	<i>Localizing Tectonic Feature</i>	<i>Source Geometry</i>	<i>Seismogenic Crustal Thickness</i>	<i>Rupture Geometry</i>	<i>RLME Magnitude</i>	<i>Recurrence Method</i>	<i>Recurrence Data</i>	<i>Earthquake Recurrence Model</i>	<i>RLME Annual Frequency*</i>
-----------------------------	------------------------------------	------------------------	--------------------------------------	-------------------------	-----------------------	--------------------------	------------------------	------------------------------------	-------------------------------



\*see Table 6.1.7-1

**Figure 6.1.7-1**  
 Logic tree for the Reelfoot rift-Marianna RLME source

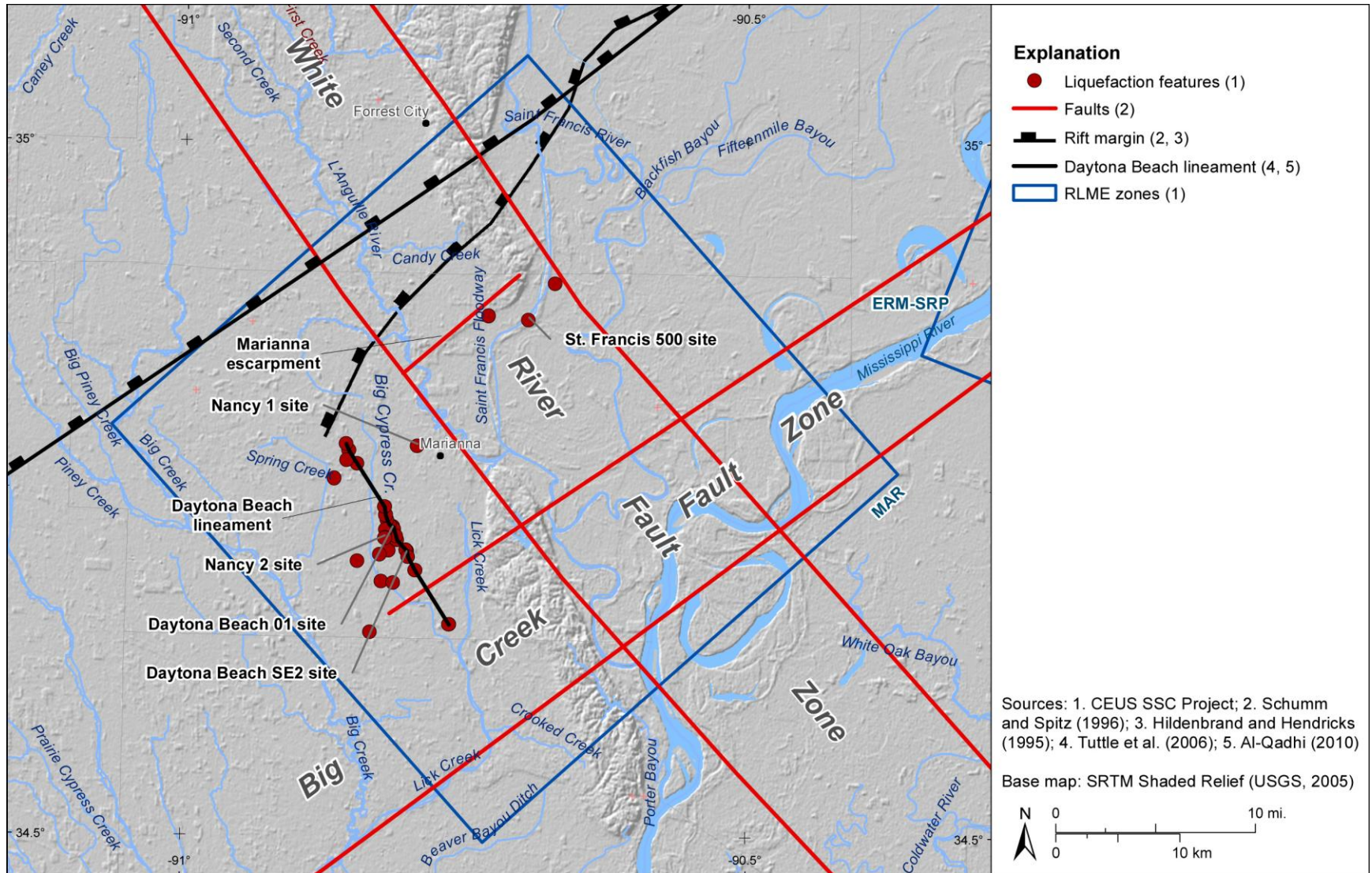


**Figure 6.1.7-2**  
 Map showing tectonic features and locations of paleoliquefaction sites in the vicinity of Marianna, Arkansas

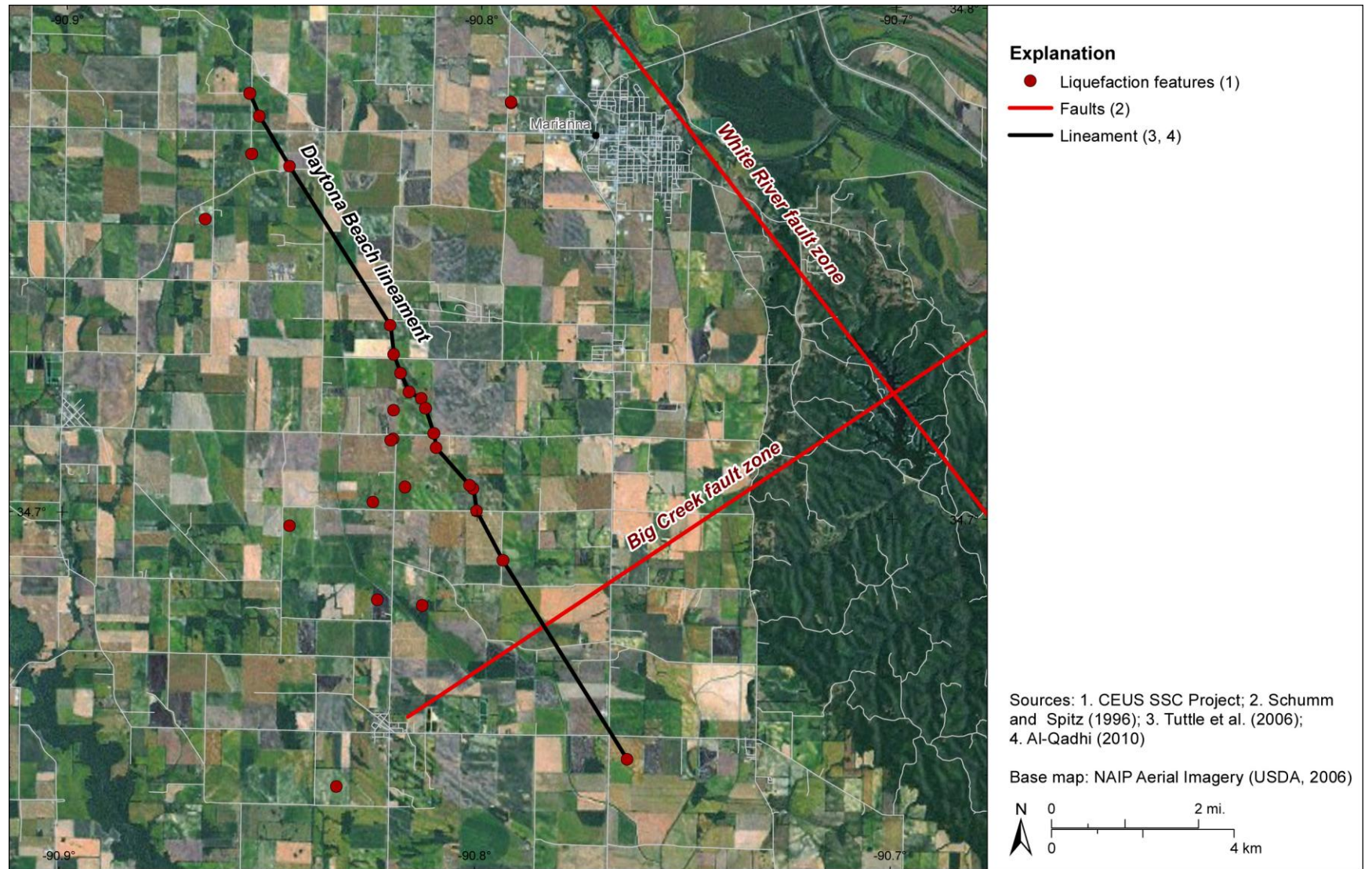
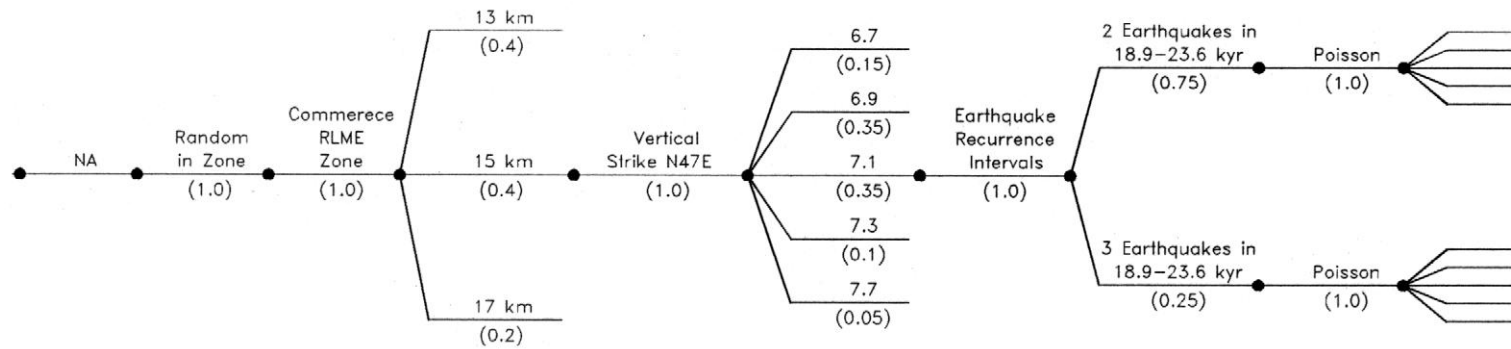


**Figure 6.1.7-3**  
Map showing liquefaction features near Daytona Beach lineament southwest of Marianna, Arkansas

<i>In or Out of Cluster</i>	<i>Localizing Tectonic Feature</i>	<i>Source Geometry</i>	<i>Seismogenic Crustal Thickness</i>	<i>Rupture Geometry</i>	<i>RLME Magnitude</i>	<i>Recurrence Method</i>	<i>Recurrence Data</i>	<i>Earthquake Recurrence Model</i>	<i>RLME Annual Frequency*</i>
-----------------------------	------------------------------------	------------------------	--------------------------------------	-------------------------	-----------------------	--------------------------	------------------------	------------------------------------	-------------------------------



\*see Table 6.1.8-2

**Figure 6.1.8-1**  
 Logic tree for the Commerce Fault Zone RLME source

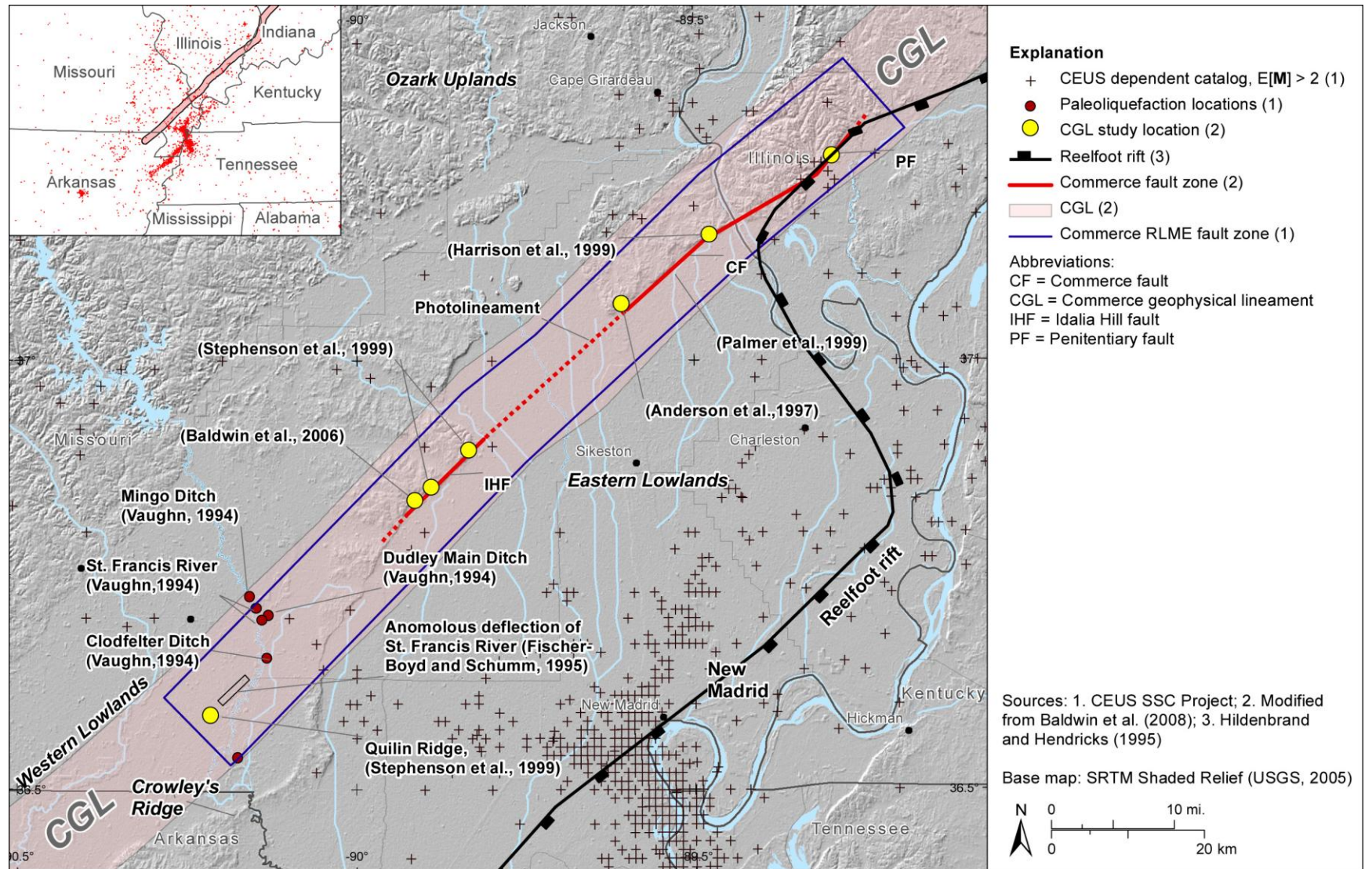


**Figure 6.1.8-2**  
 Map showing tectonic features, seismicity, and paleoseismic localities along the Commerce Fault Zone RLME source

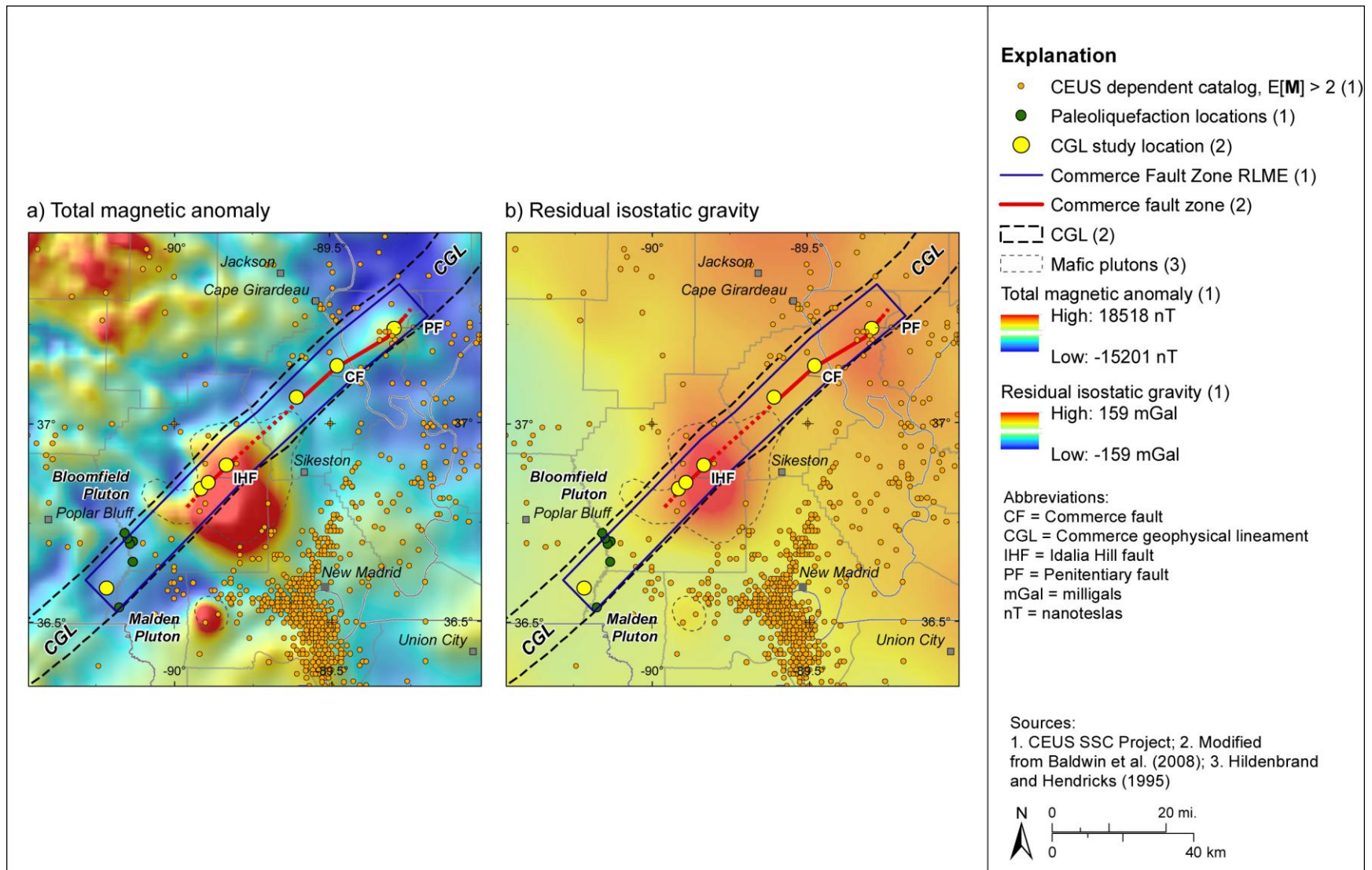
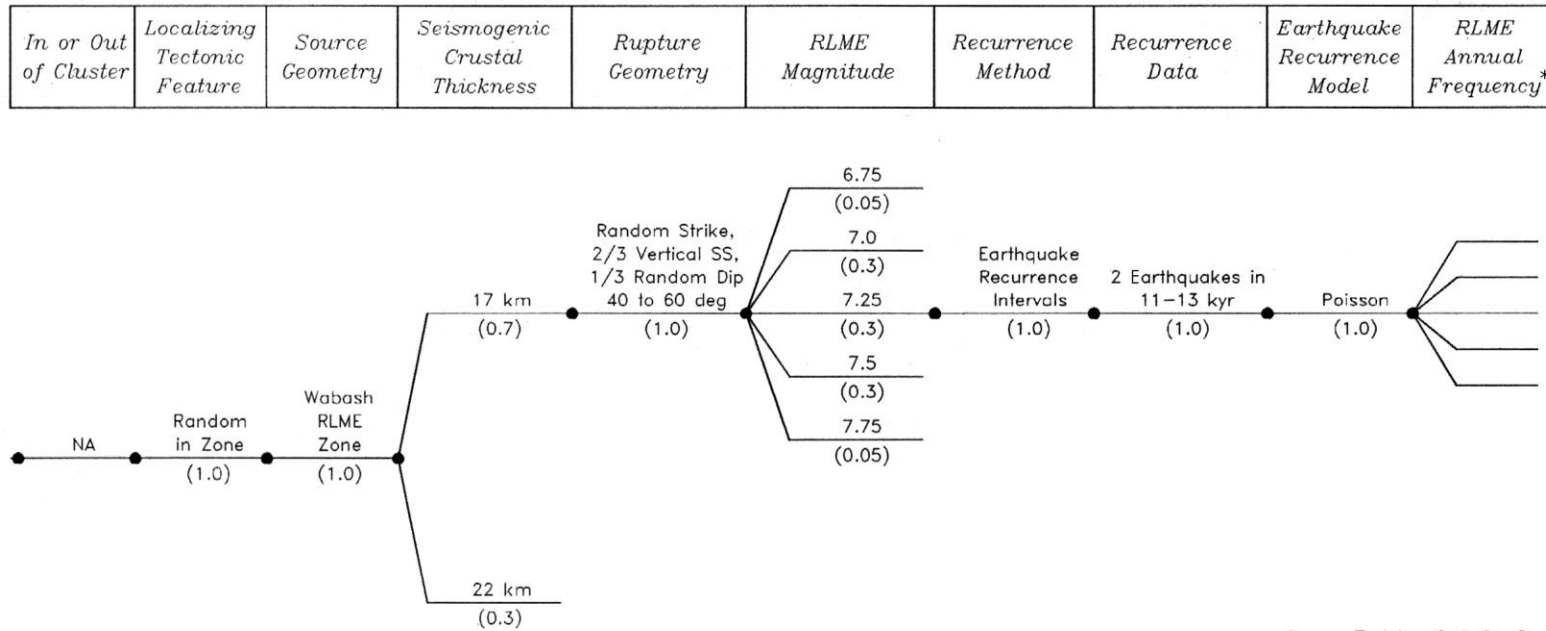


**Figure 6.1.8-3**  
Location of the Commerce geophysical lineament and Commerce Fault Zone RLME source relative to the (a) regional magnetic anomaly map and (b) regional gravity anomaly map





\*see Table 6.1.9-2

**Figure 6.1.9-1**  
 Logic tree for the Wabash Valley RLME source

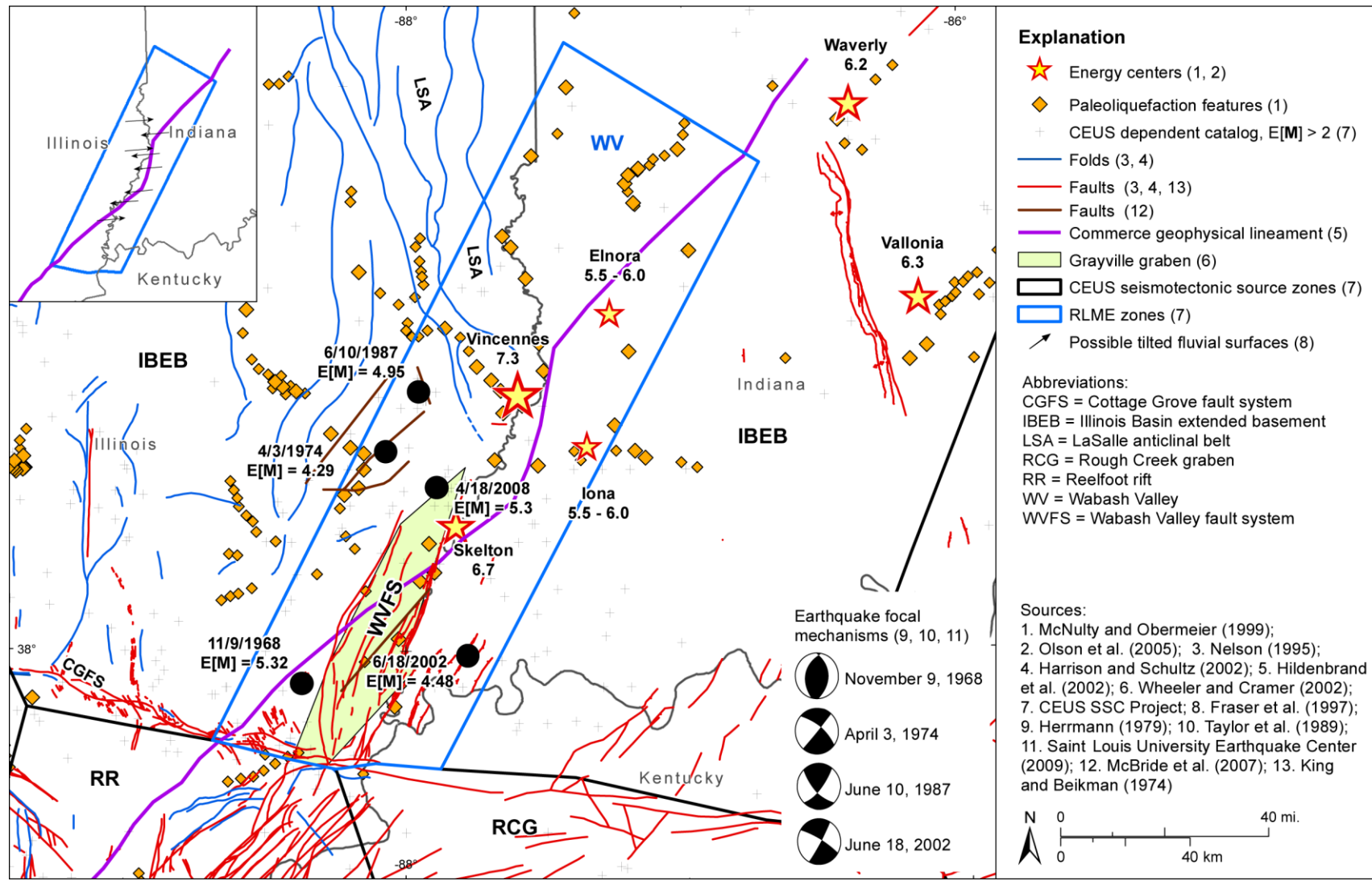


**Figure 6.1.9-2**  
 Map showing seismicity, subsurface structural features, paleoearthquake energy centers, and postulated neotectonic deformation in the Wabash Valley region of southern Illinois and southern Indiana

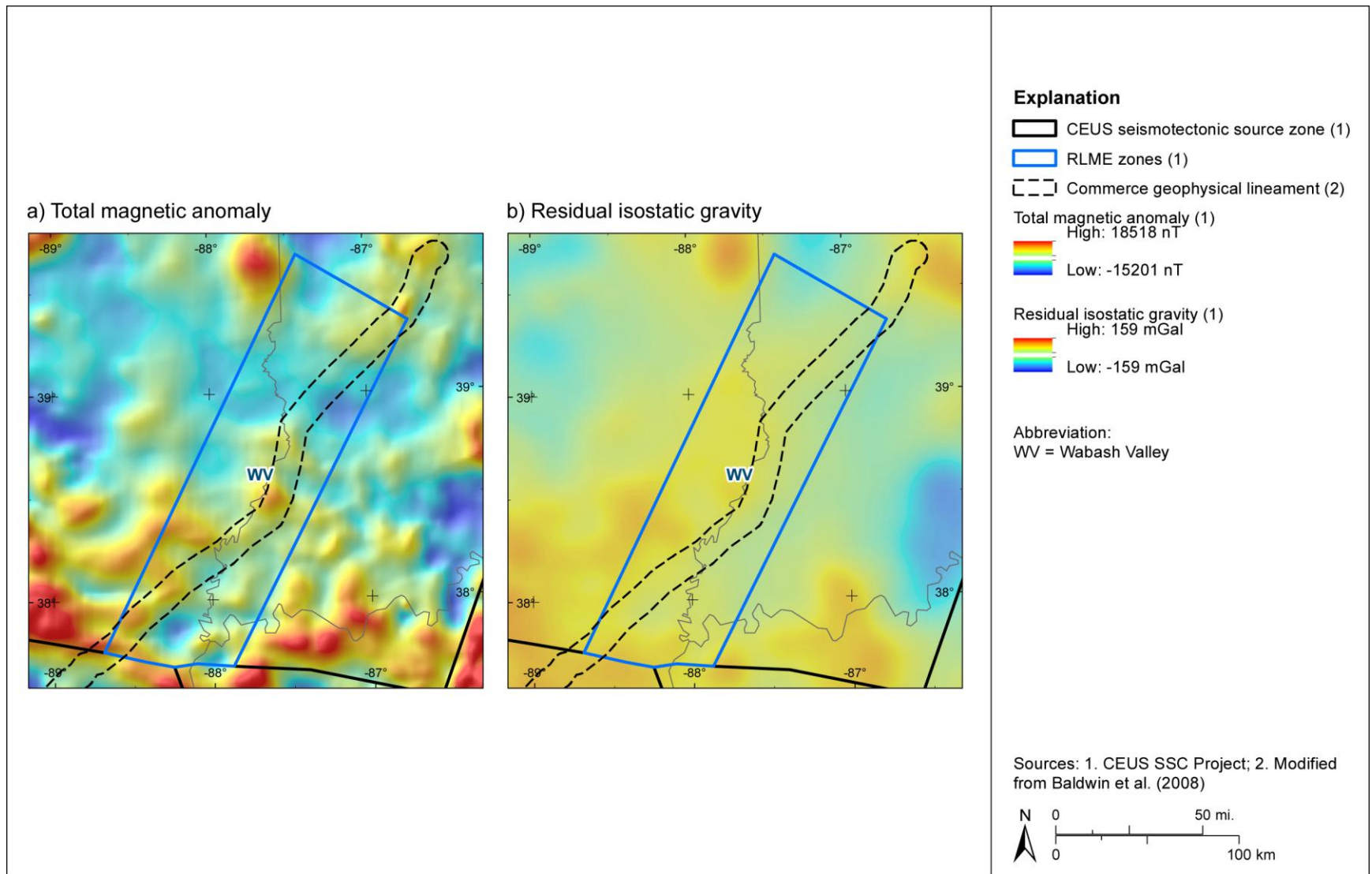


**Figure 6.1.9-3**  
 Wabash Valley RLME source relative to (a) magnetic anomaly, and (b) residual isostatic gravity data

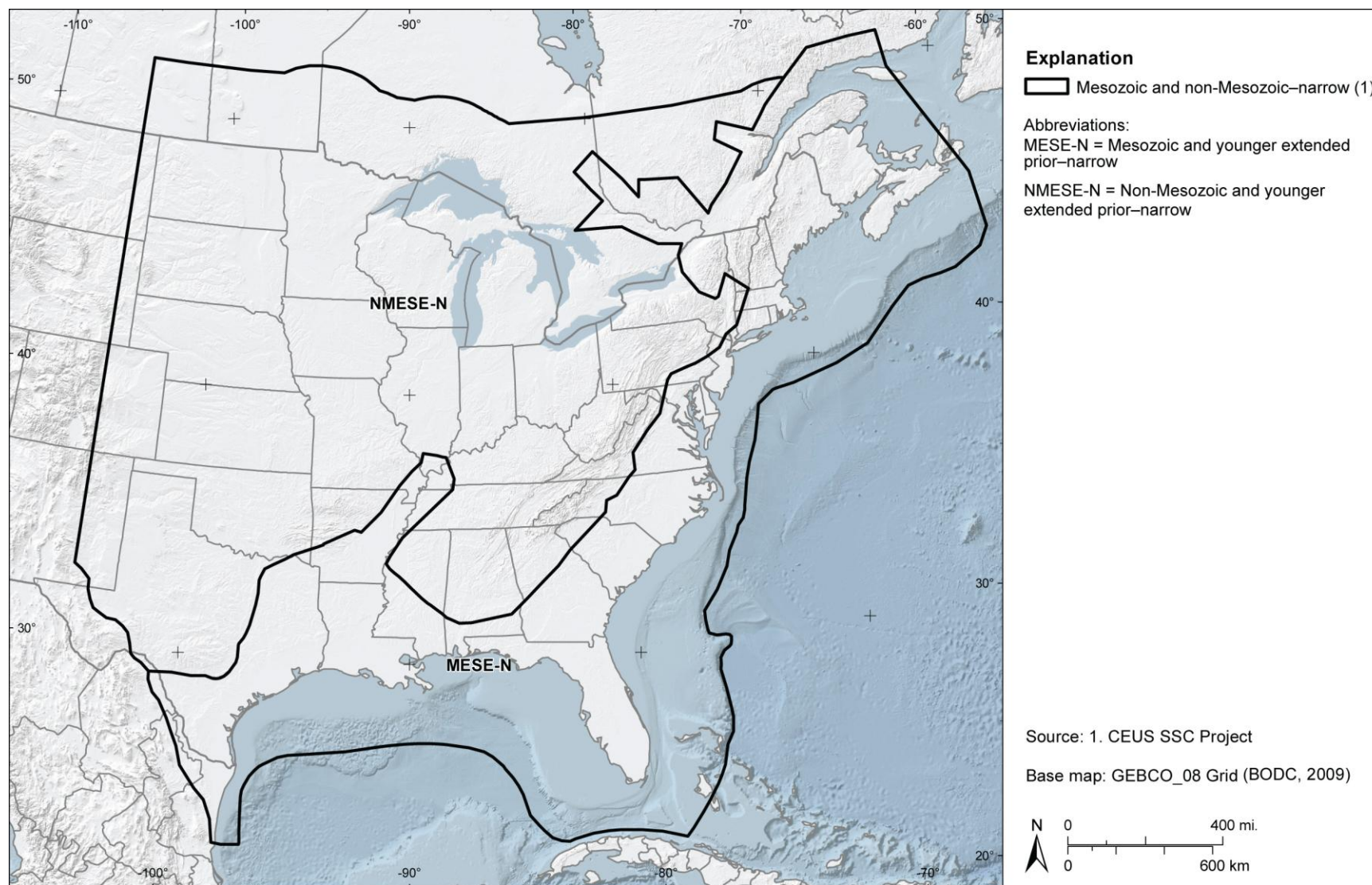


**Figure 6.2-1**  
Map showing the two Mmax zones for the “narrow” interpretation of the Mesozoic-and-younger extended zone

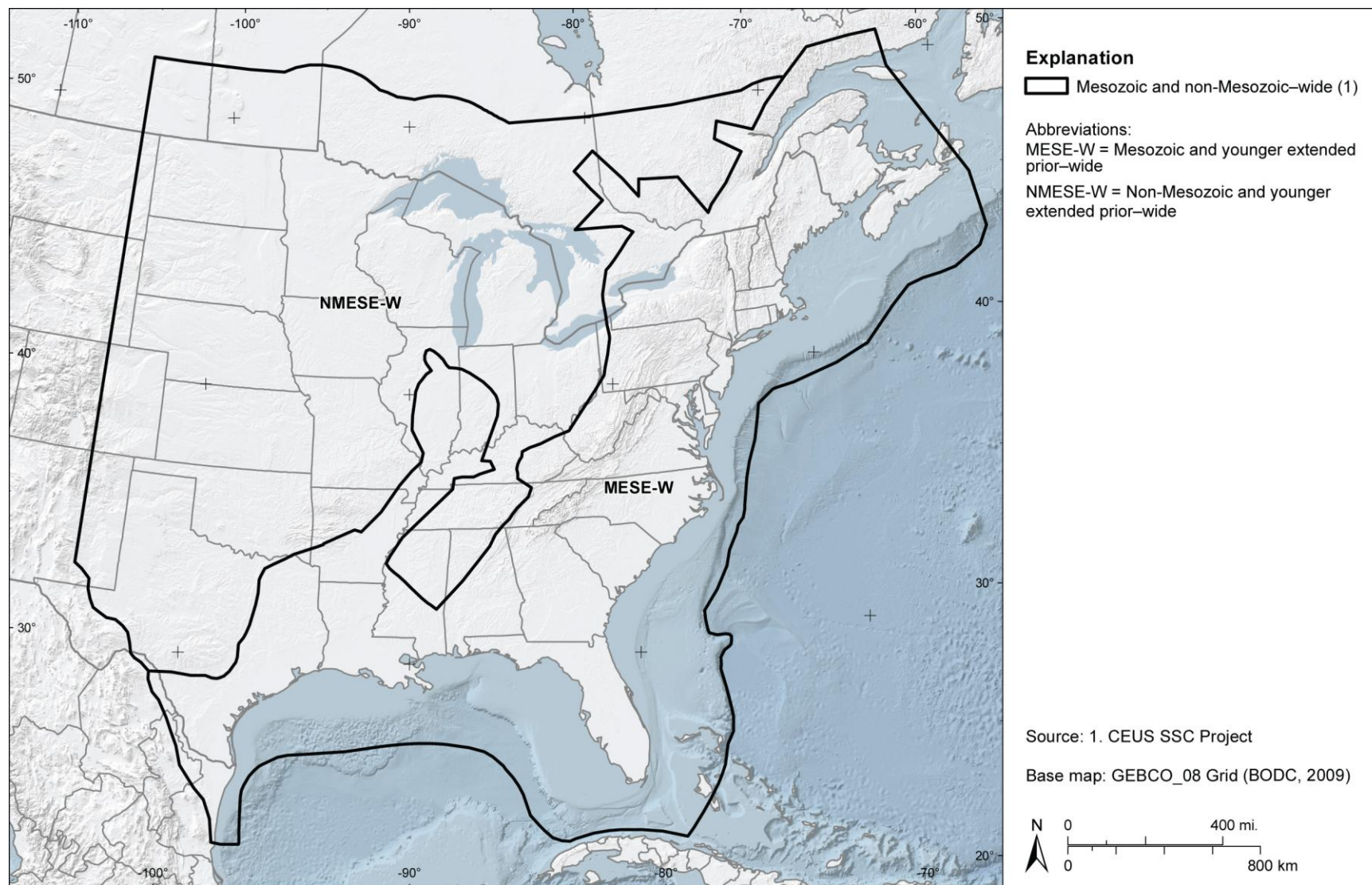


**Figure 6.2-2**  
Map showing the two Mmax zones for the “wide” interpretation of the Mesozoic-and-younger extended zone

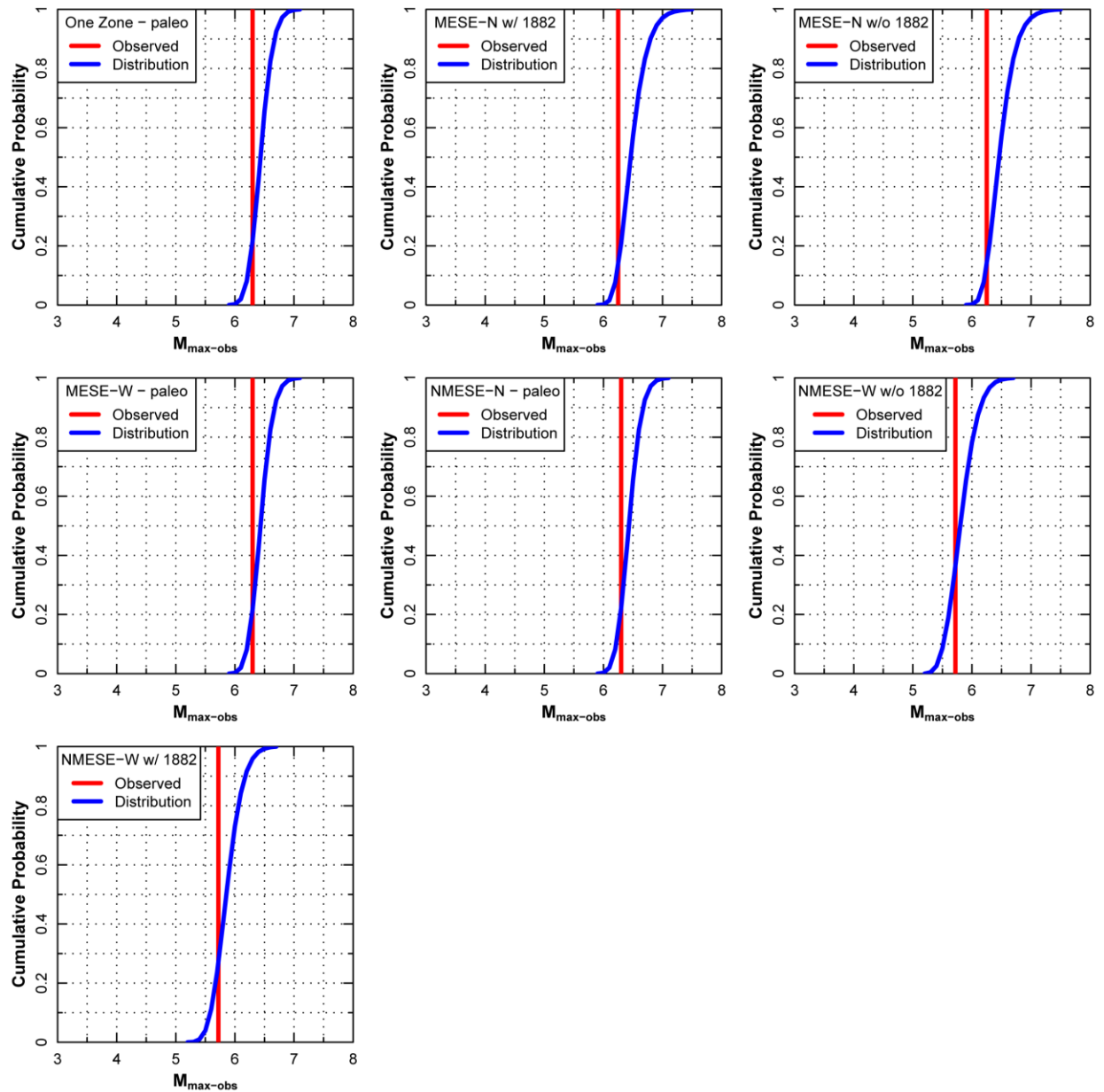


**Figure 6.3.1-1**  
**Distributions for  $m_{\max-obs}$  for the Mmax distributed seismicity source zones**

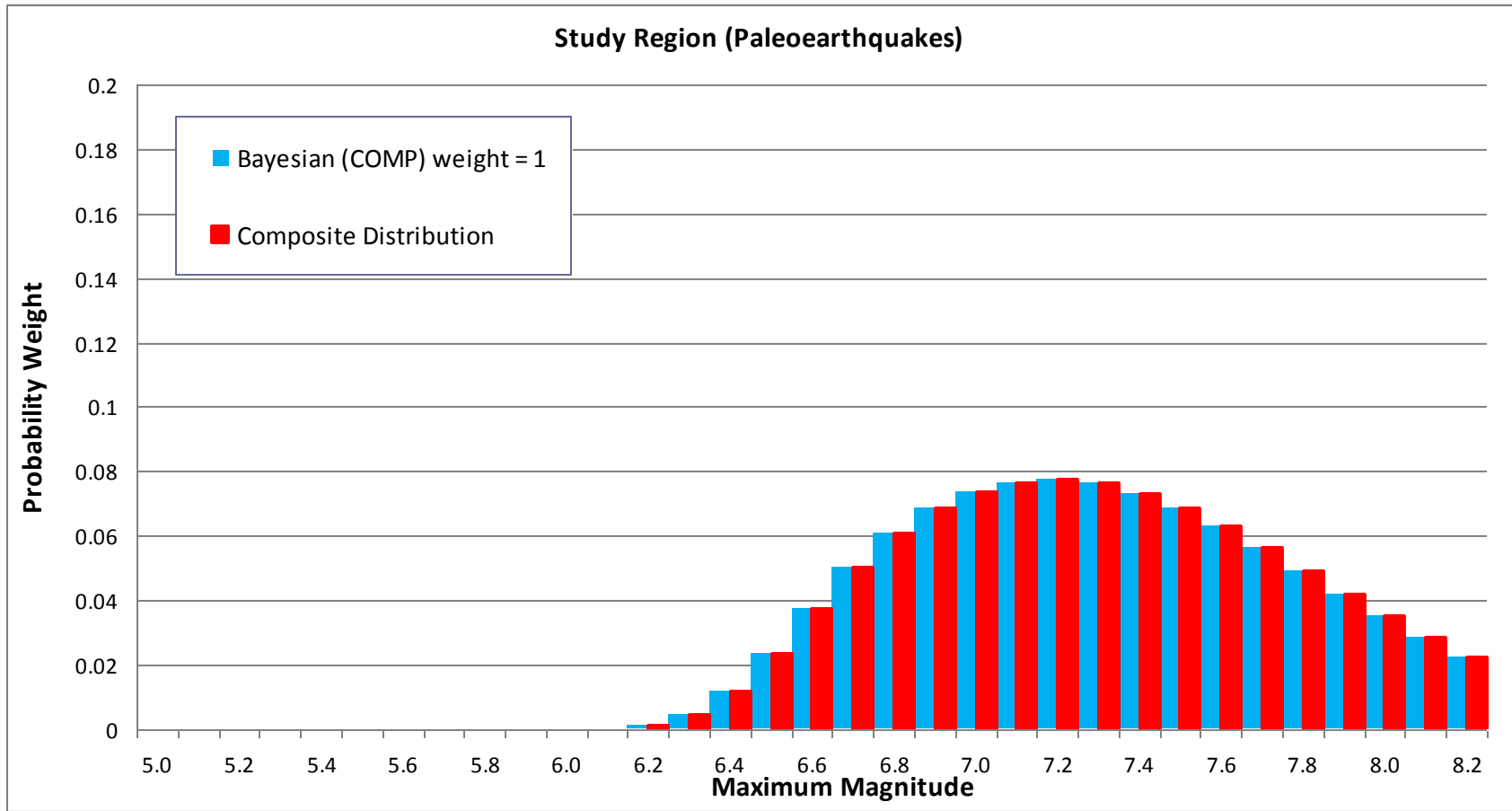


**Figure 6.3.2-1**  
Mmax distributions for the study region treated as a single Mmax zone

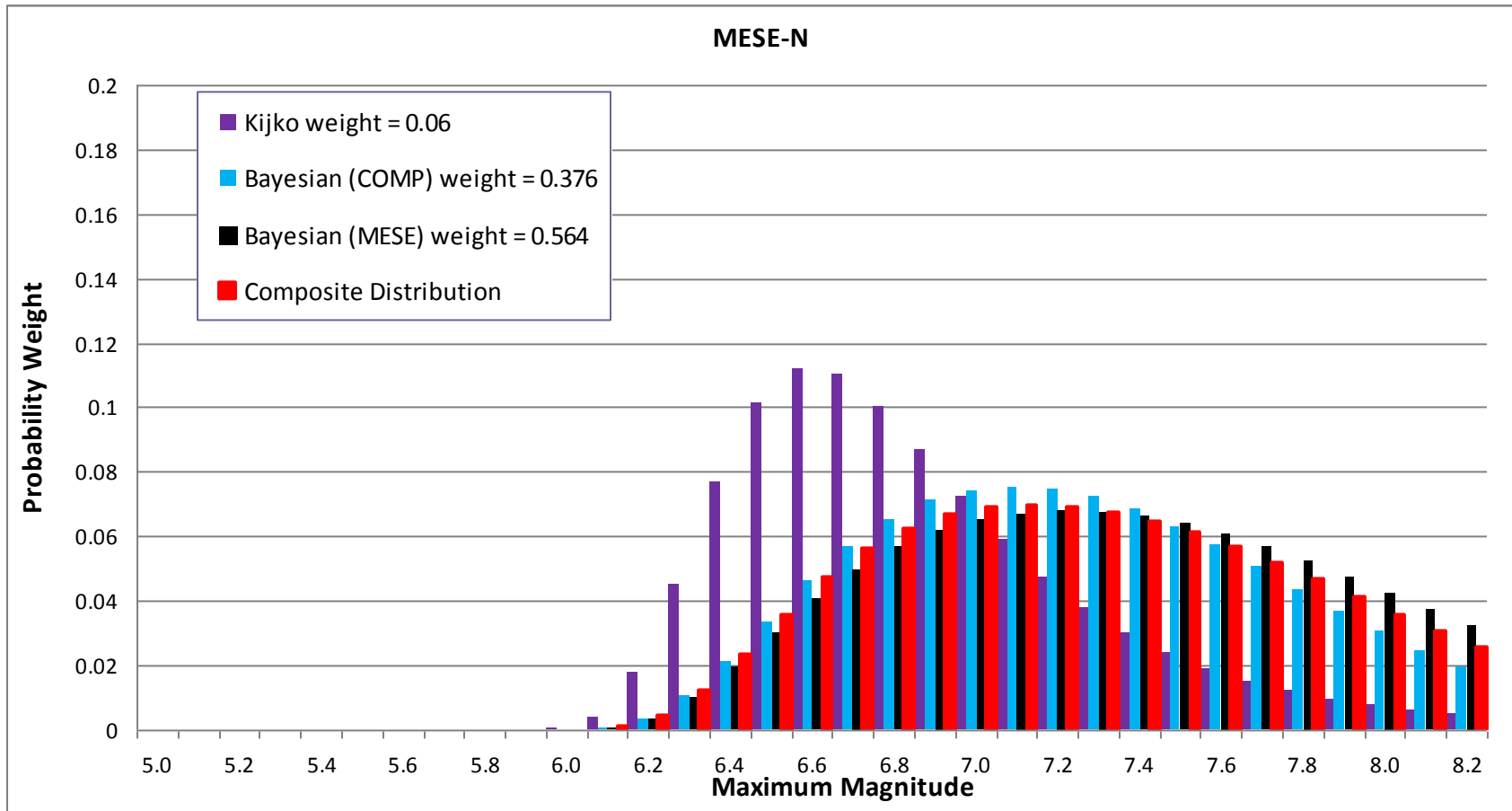


Figure 6.3.2-2  
Mmax distributions for the MESE-N Mmax zone

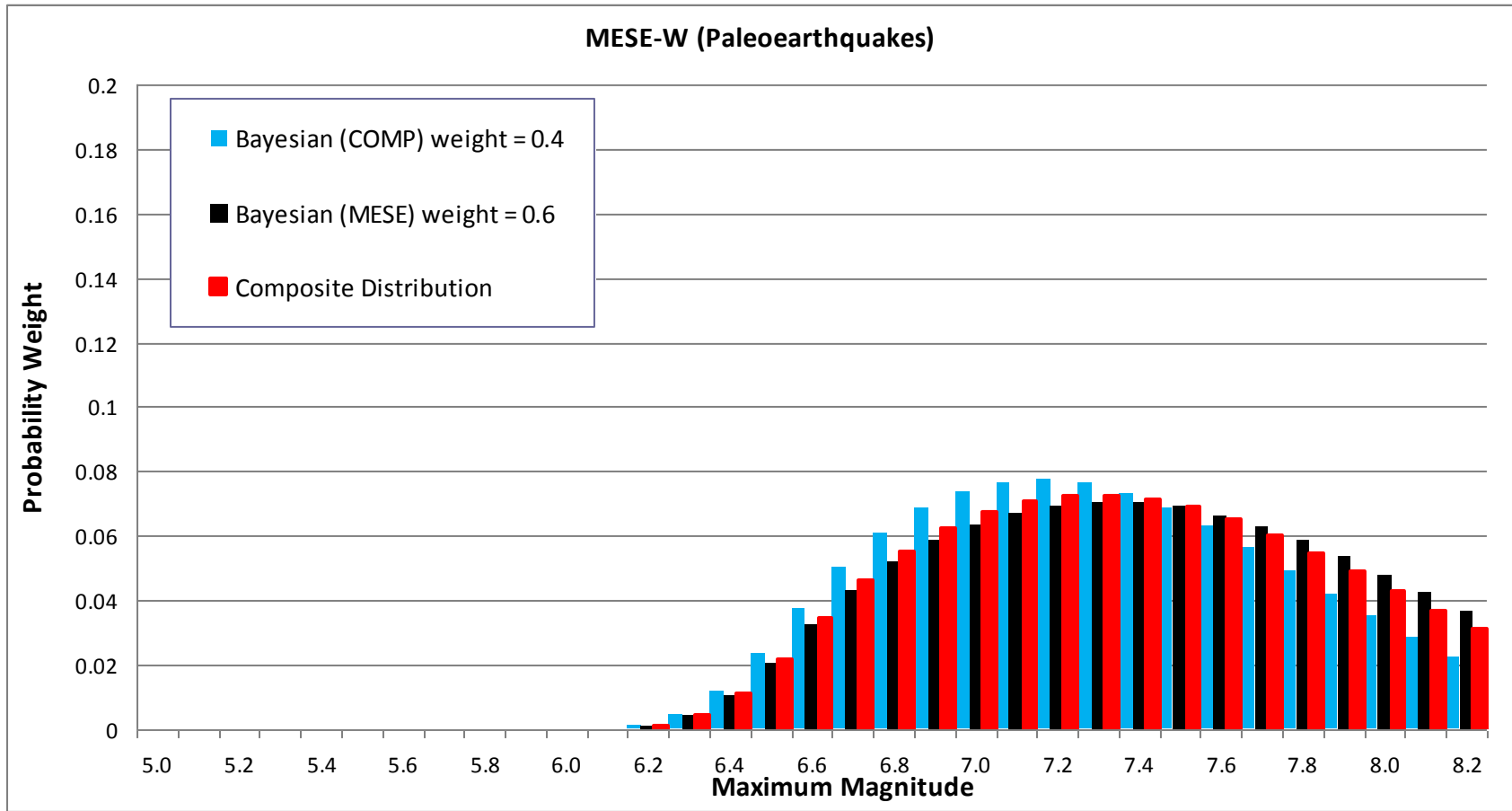


Figure 6.3.2-3  
Mmax distributions for the MESE-W Mmax zone

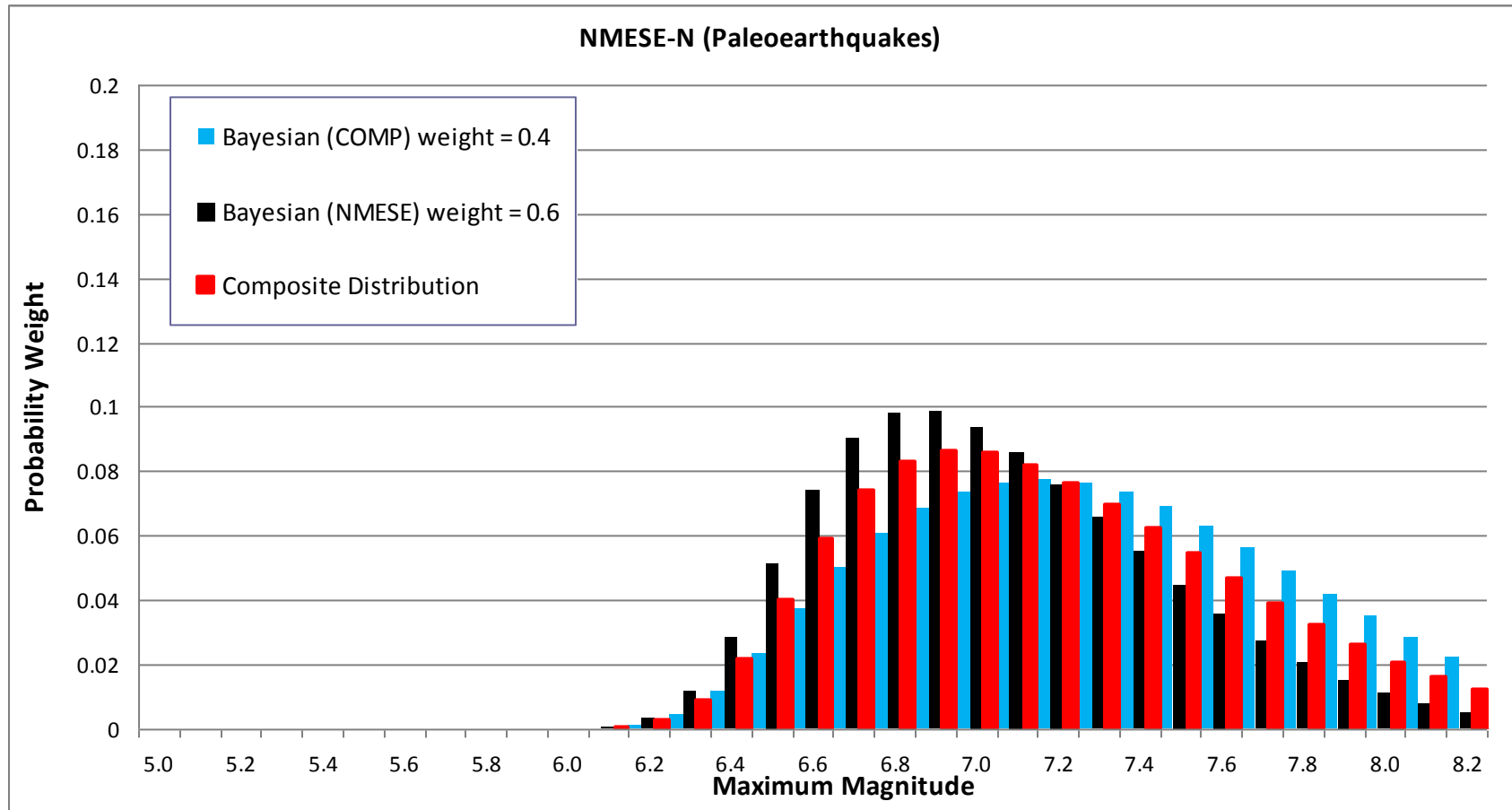


Figure 6.3.2-4  
Mmax distributions for the NMESE-N Mmax zone

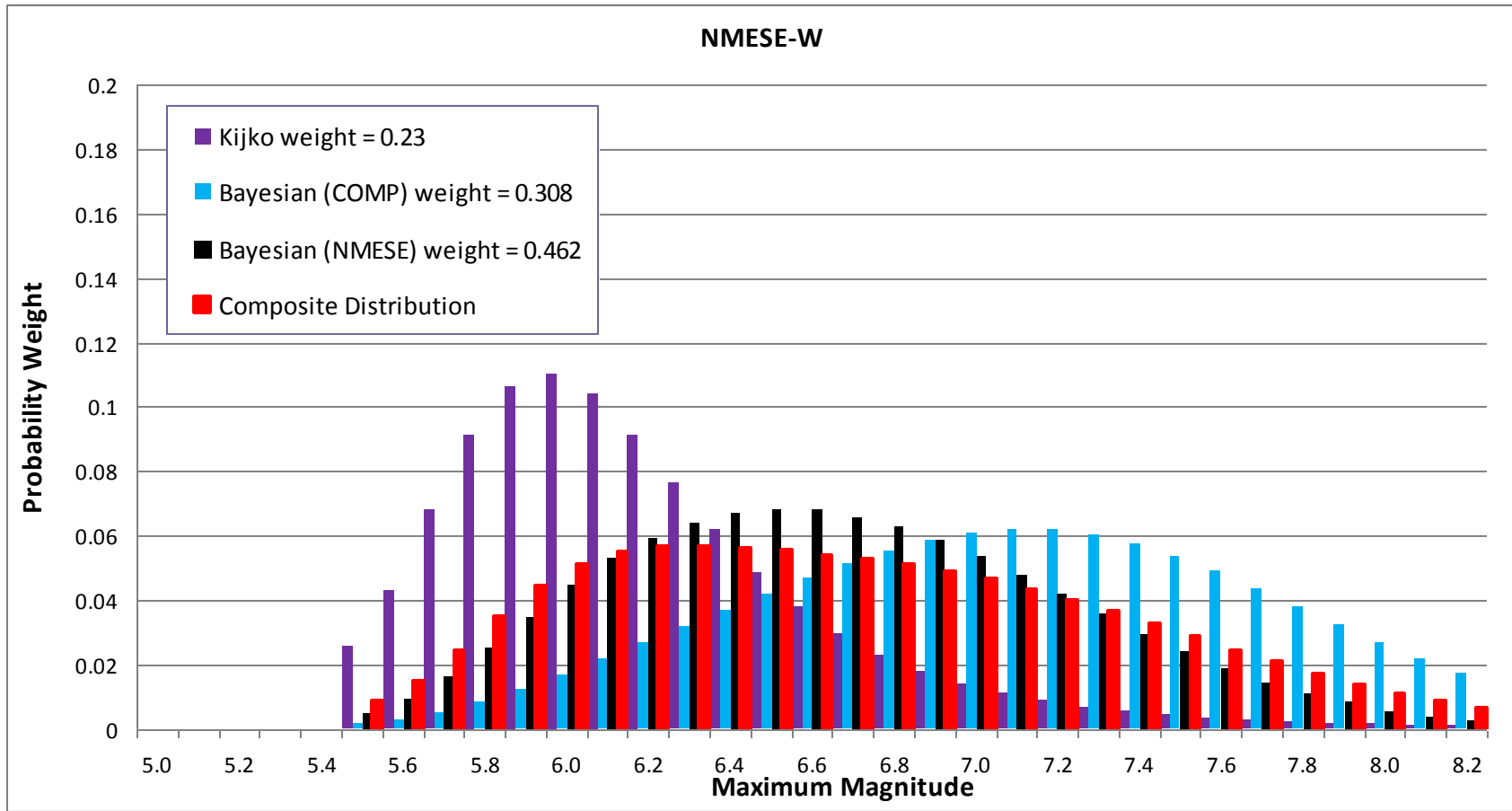
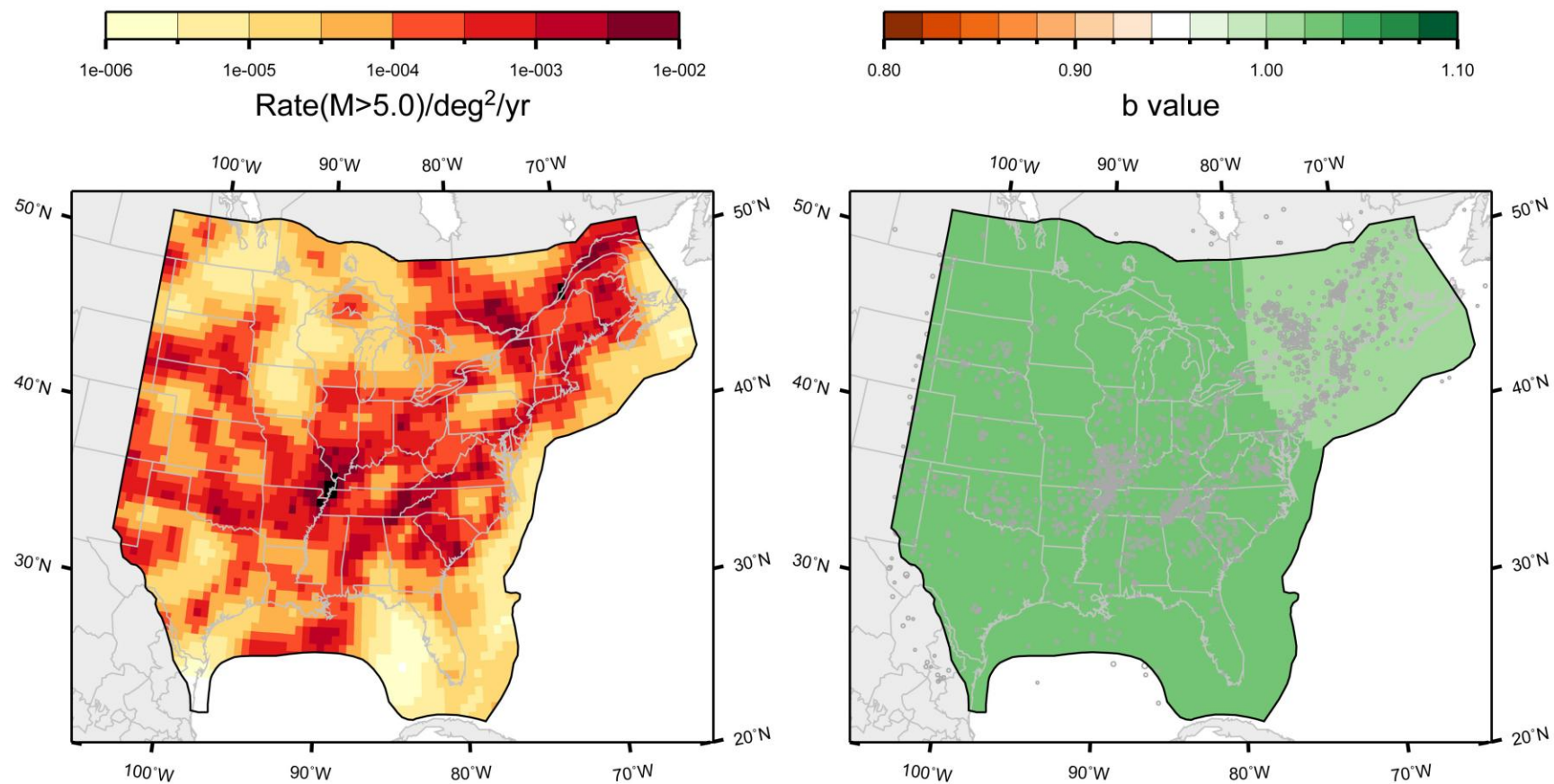
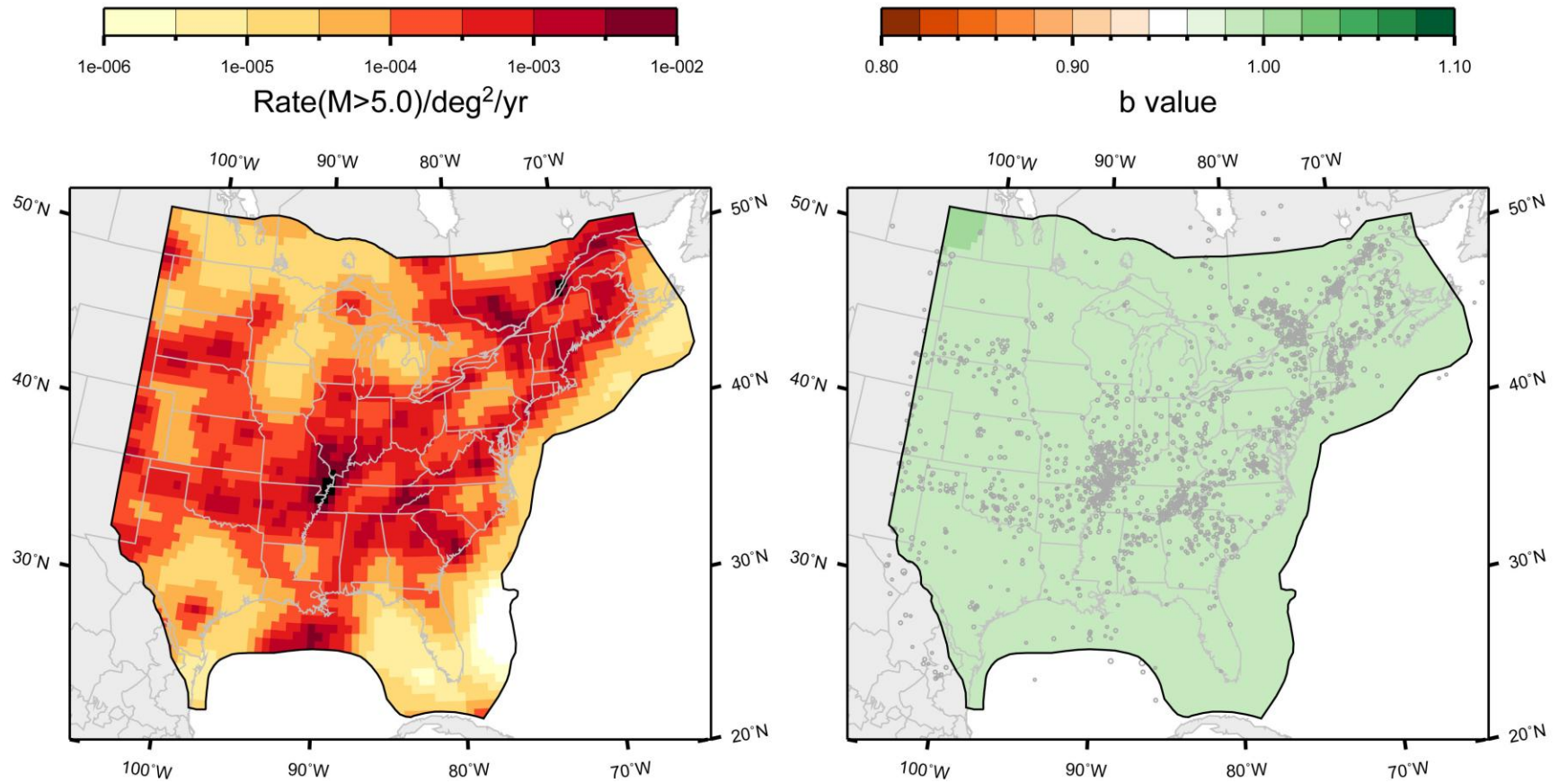


Figure 6.3.2-5  
 Mmax distributions for the NMESE-W Mmax zone



**Figure 6.4.1-1**  
Mean map of rate and  $b$ -value for the study region under the source-zone configuration, with no separation of Mesozoic extended and non-extended; Case A magnitude weights



**Figure 6.4.1-2**  
Mean map of rate and  $b$ -value for the study region under the source-zone configuration, with no separation of Mesozoic extended and non-extended; Case B magnitude weights

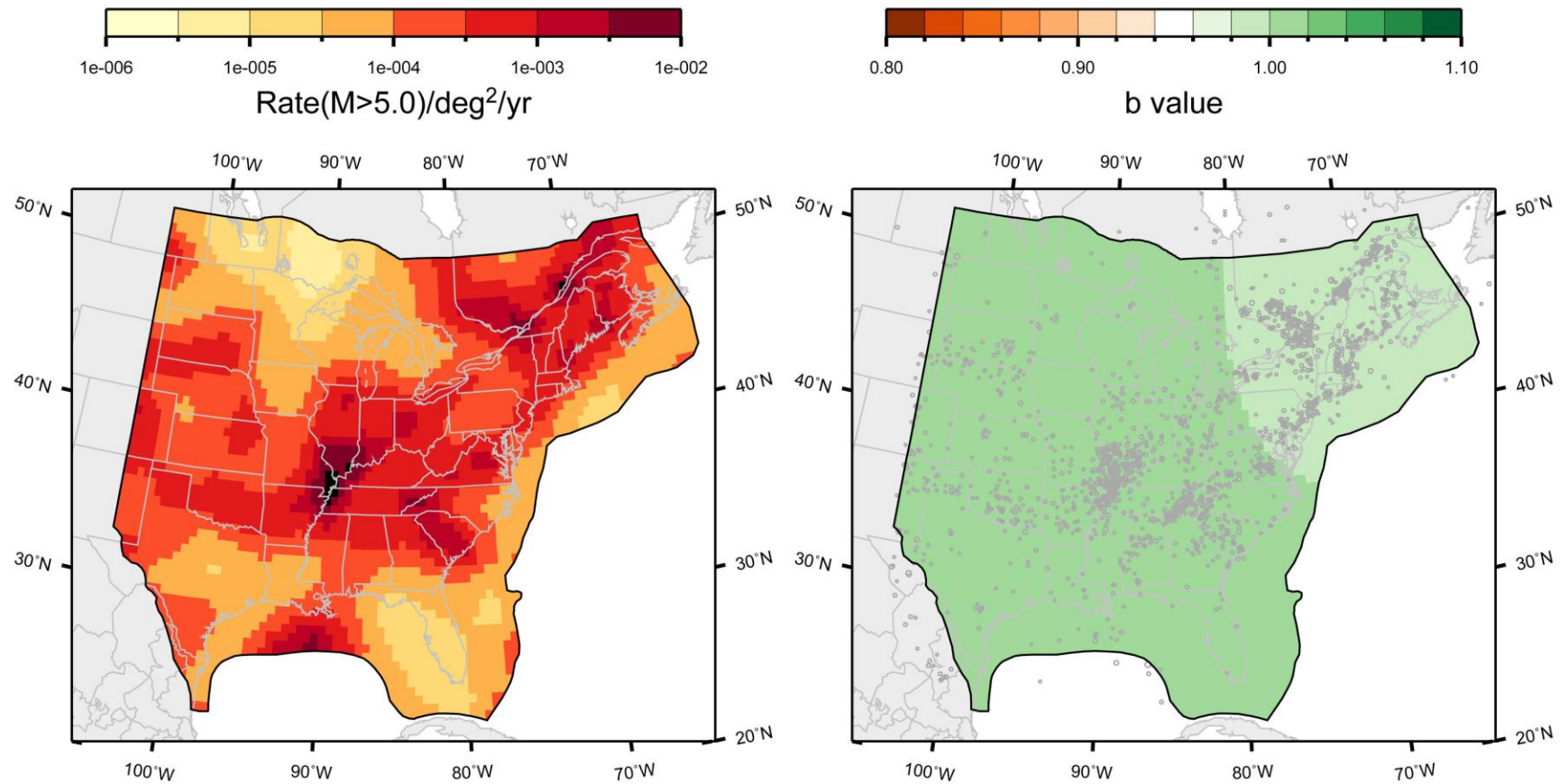


**Figure 6.4.1-3**  
Mean map of rate and  $b$ -value for the study region under the source-zone configuration, with no separation of Mesozoic extended and non-extended; Case E magnitude weights

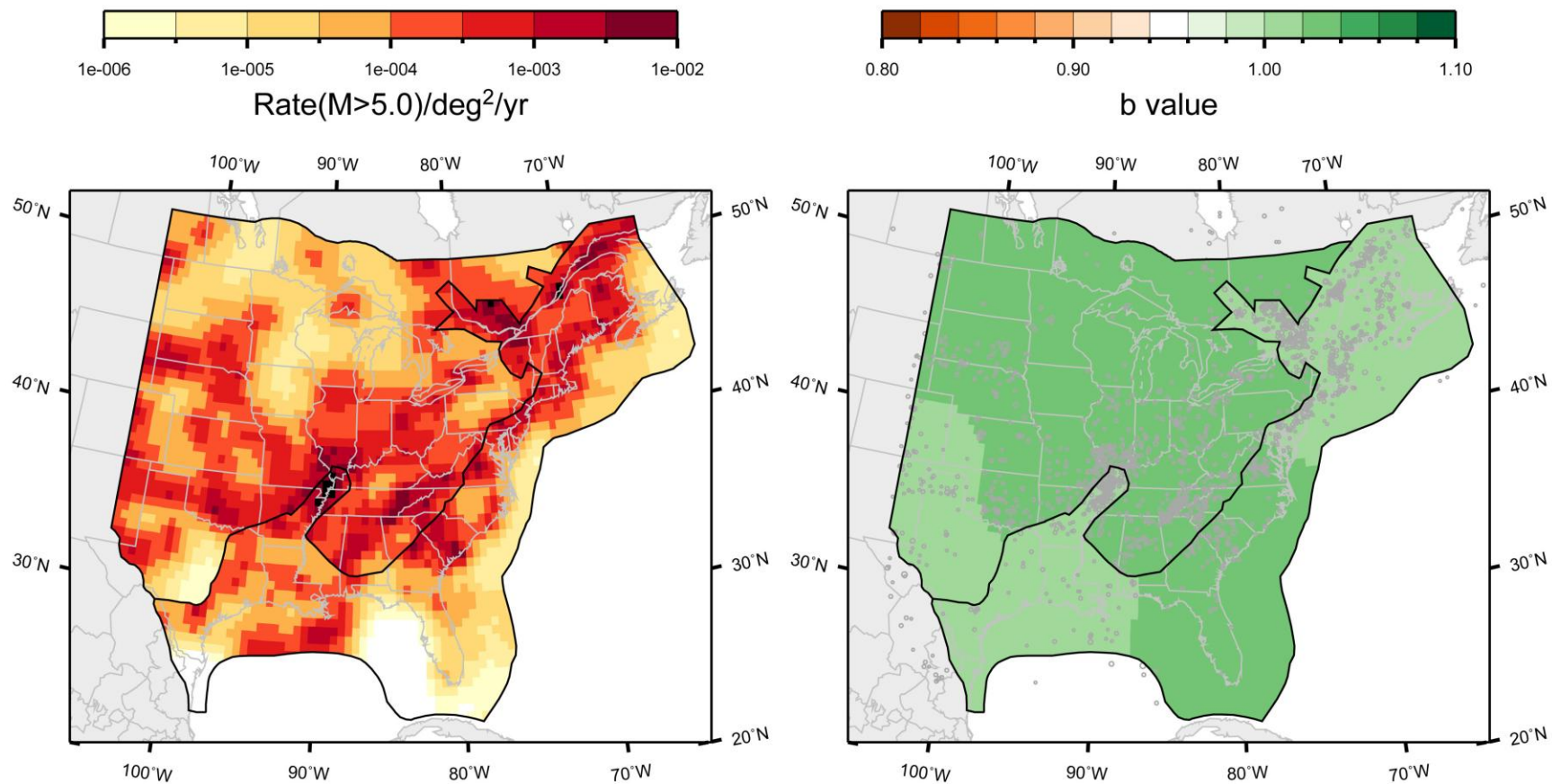


**Figure 6.4.1-4**  
Mean map of rate and *b*-value for the study region under the source-zone configuration, with separation of Mesozoic extended and non-extended, narrow geometry for MESE; Case A magnitude weights

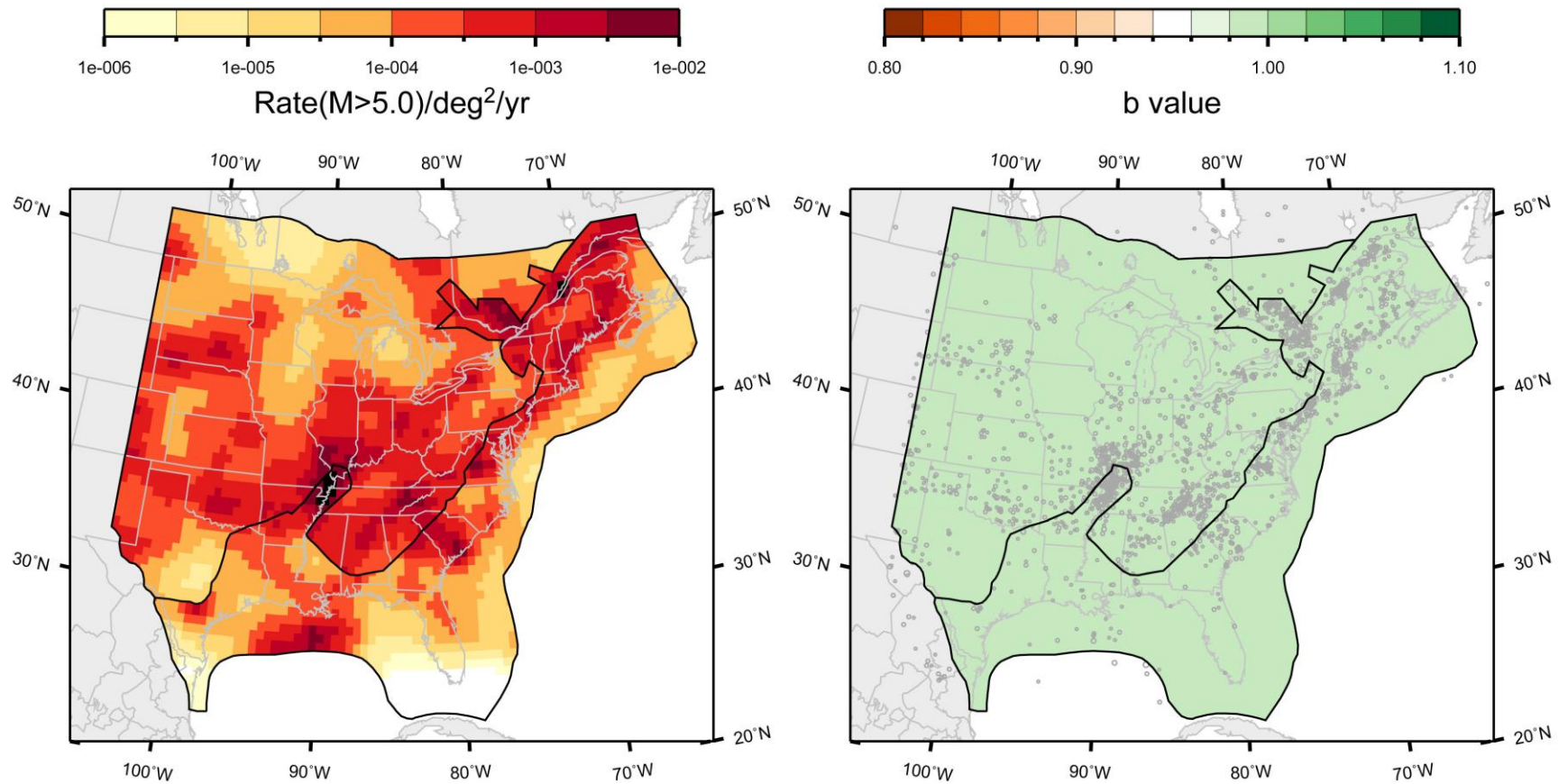


**Figure 6.4.1-5**  
Mean map of rate and *b*-value for the study region under the source-zone configuration, with separation of Mesozoic extended and non-extended, narrow geometry for MESE; Case B magnitude weights

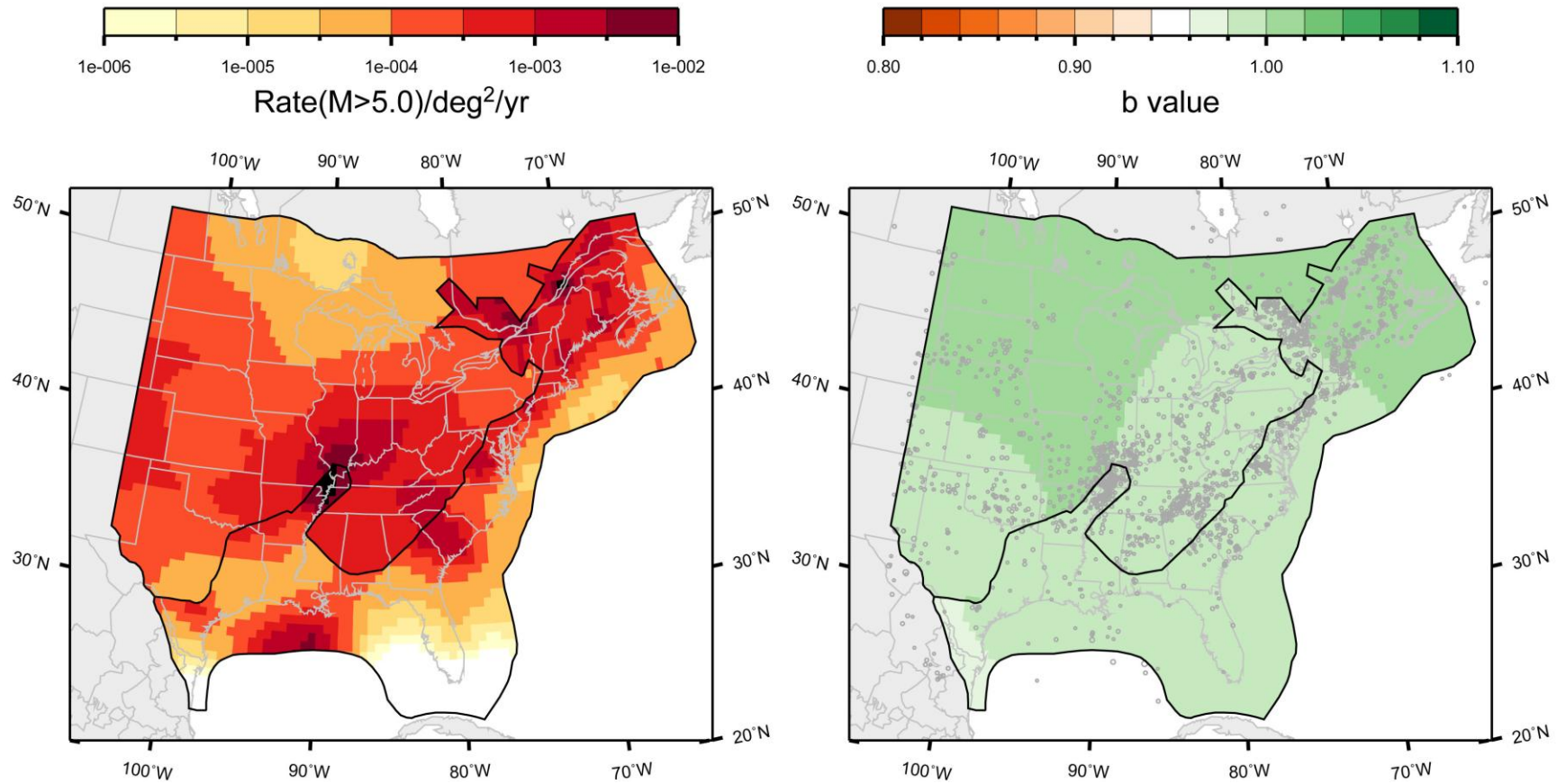


**Figure 6.4.1-6**  
Mean map of rate and *b*-value for the study region under the source-zone configuration, with separation of Mesozoic extended and non-extended, narrow geometry for MESE; Case E magnitude weights

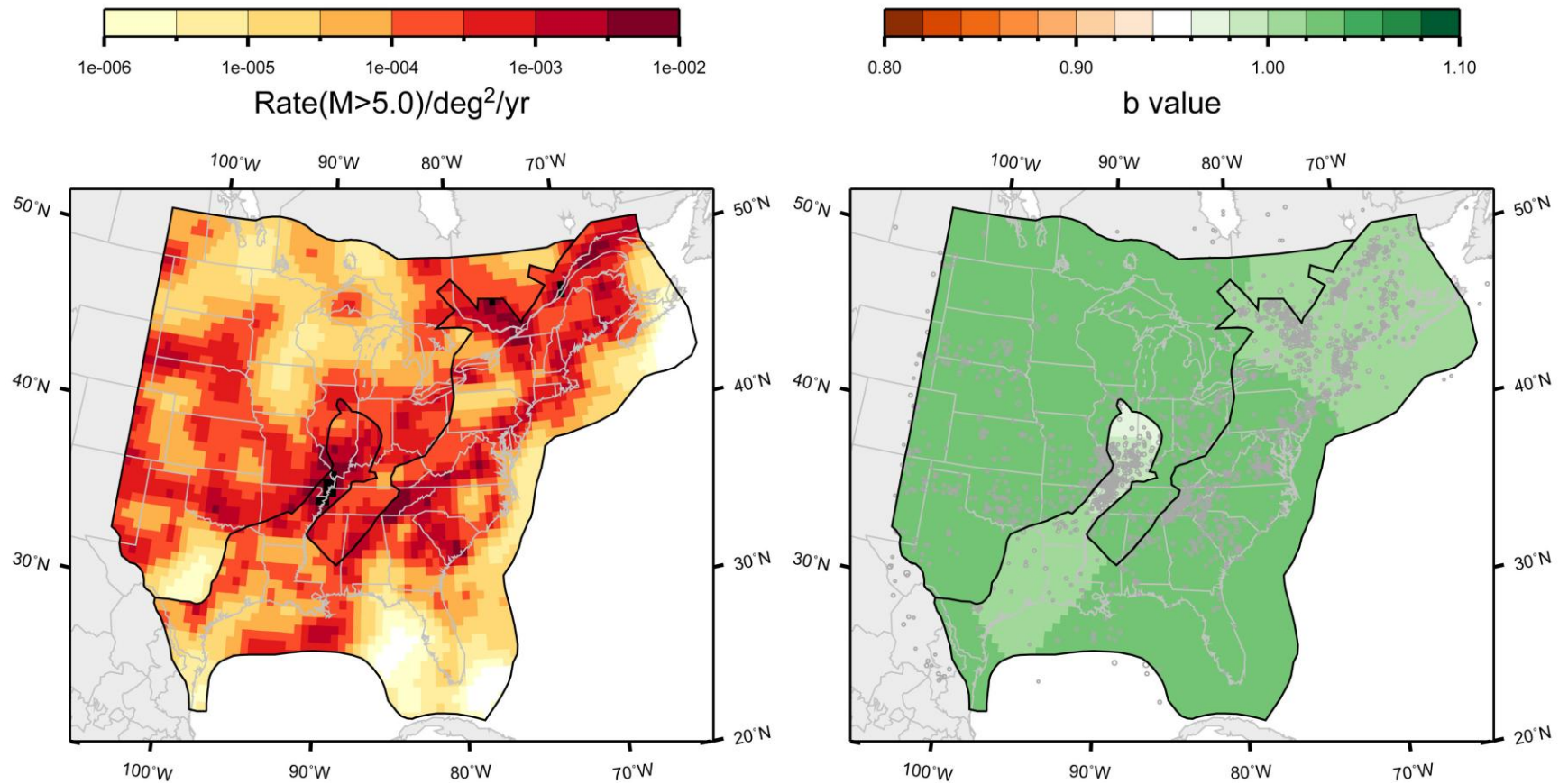


**Figure 6.4.1-7**  
Mean map of rate and  $b$ -value for the study region under the source-zone configuration, with separation of Mesozoic extended and non-extended, wide geometry for MESE; Case A magnitude weights

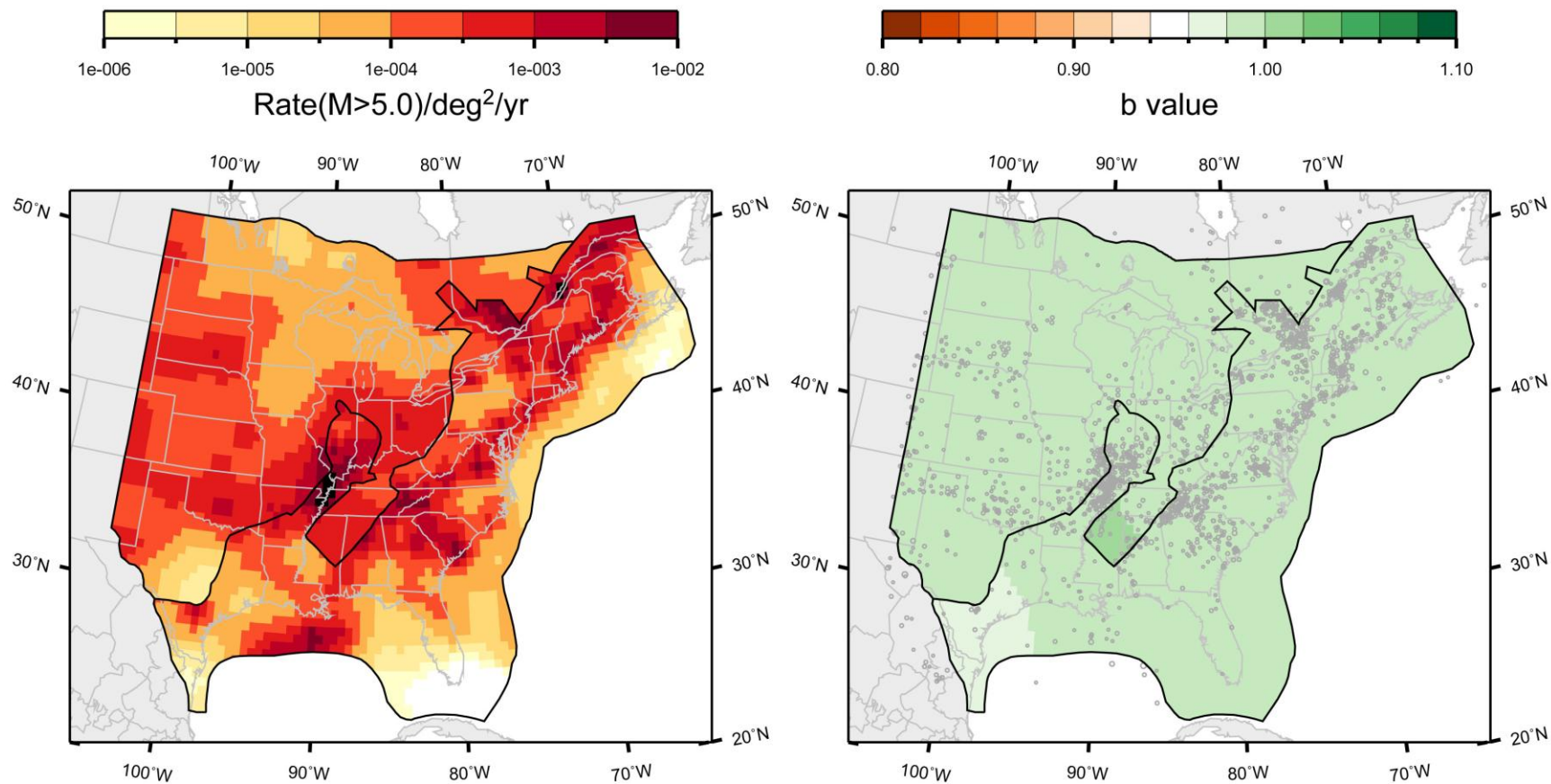


**Figure 6.4.1-8**  
Mean map of rate and  $b$ -value for the study region under the source-zone configuration, with separation of Mesozoic extended and non-extended, wide geometry for MESE; Case B magnitude weights

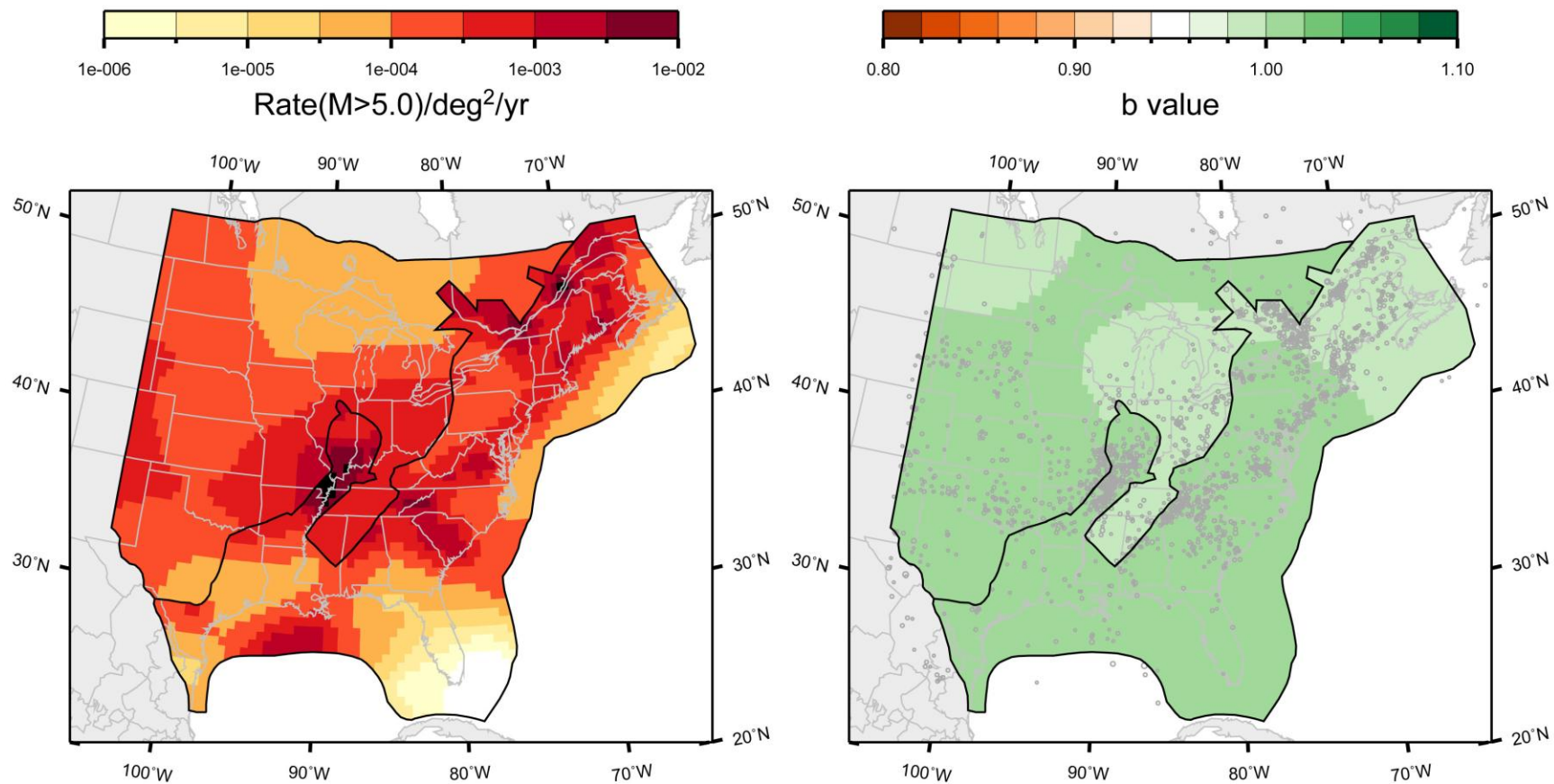


**Figure 6.4.1-9**  
Mean map of rate and  $b$ -value for the study region under the source-zone configuration, with separation of Mesozoic extended and non-extended, wide geometry for MESE; Case E magnitude weights

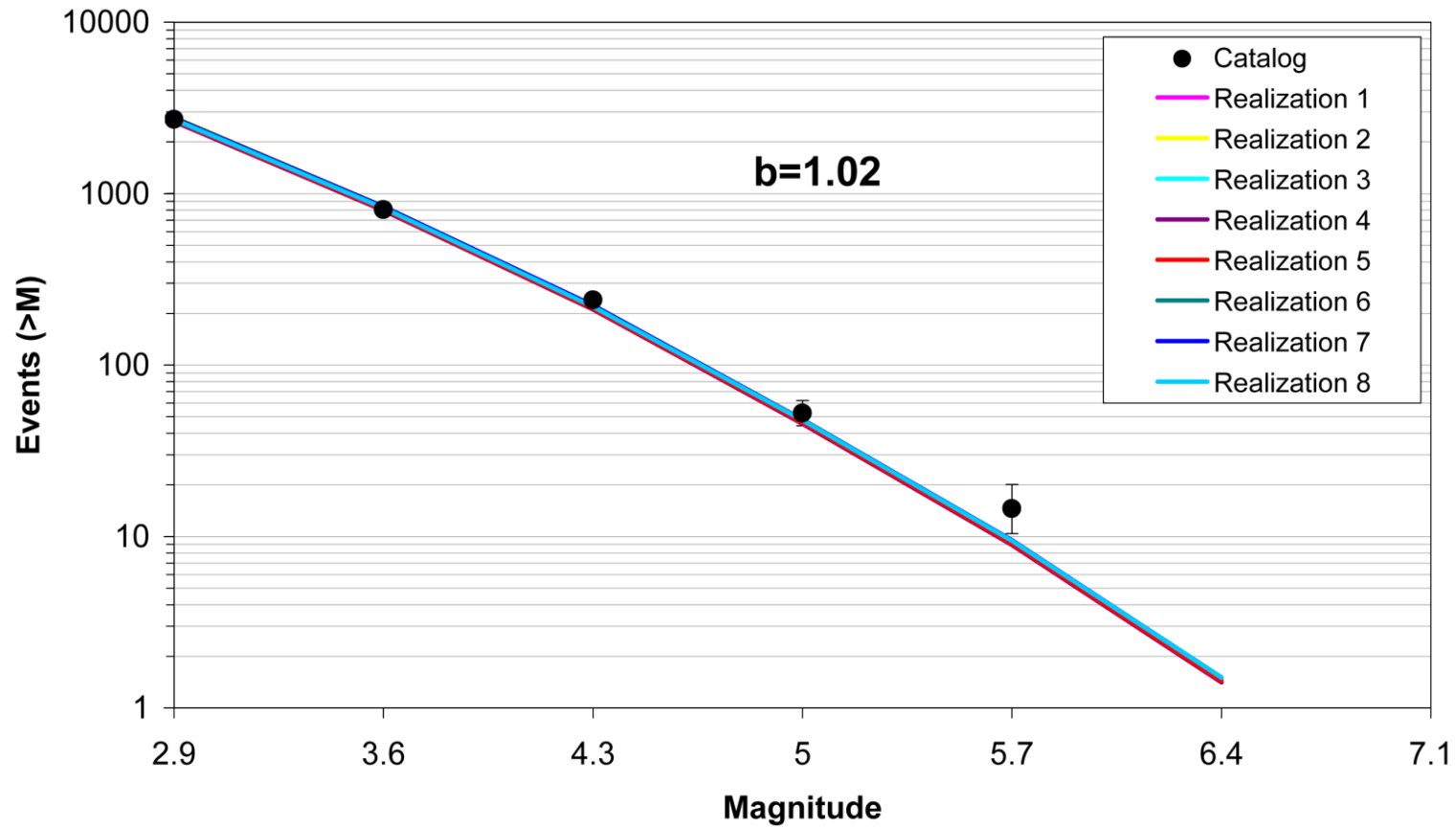


Figure 6.4.2-1  
Comparison of model-predicted earthquake counts for study region using Case A magnitude weights. The error bars represent the 16%–84% uncertainty associated with the data, computed using the Weichert (1980) procedure.

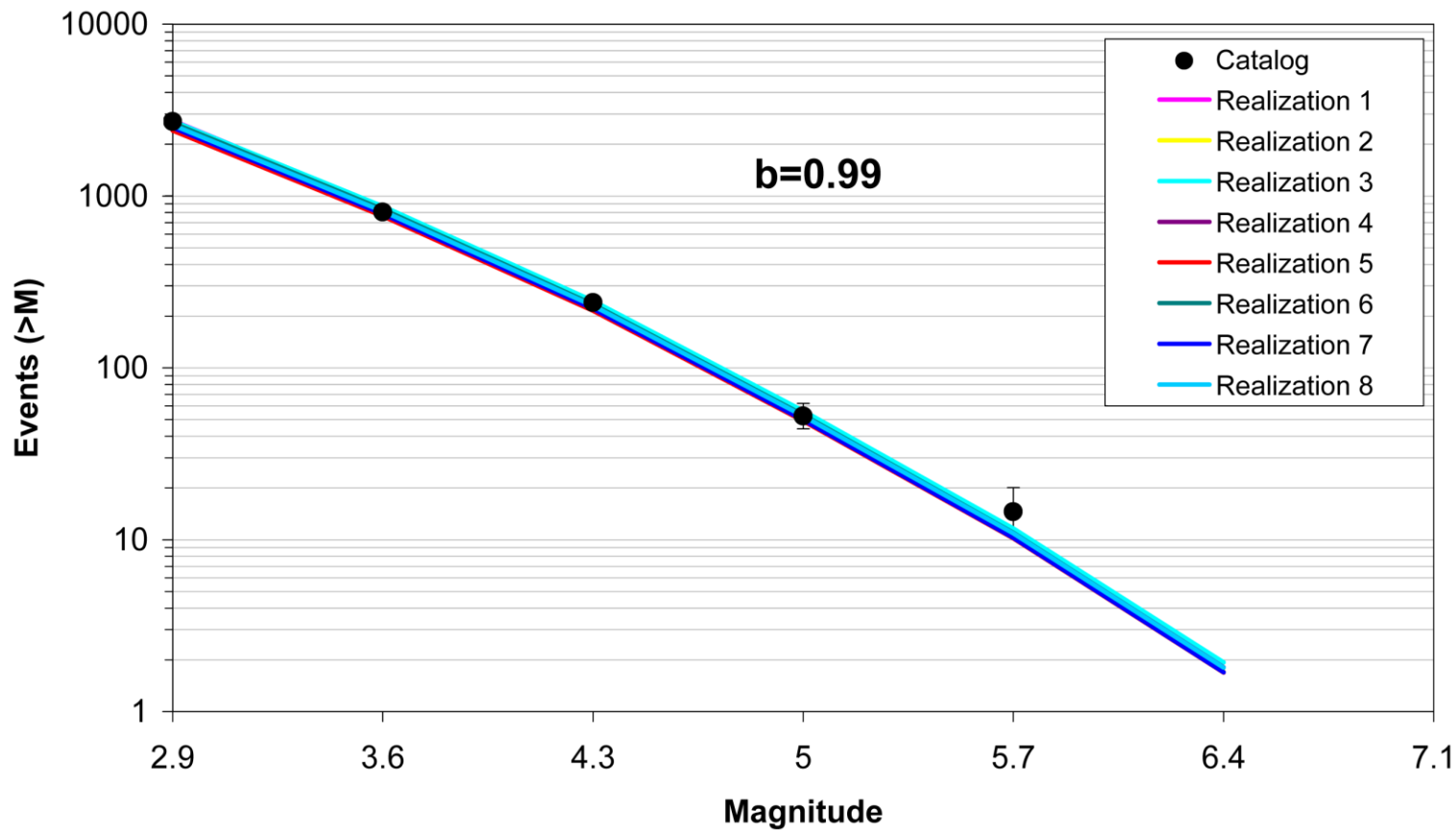


Figure 6.4.2-2  
Comparison of model-predicted earthquake counts for study region using Case B magnitude weights. The error bars represent the 16%–84% uncertainty associated with the data, computed using the Weichert (1980) procedure.

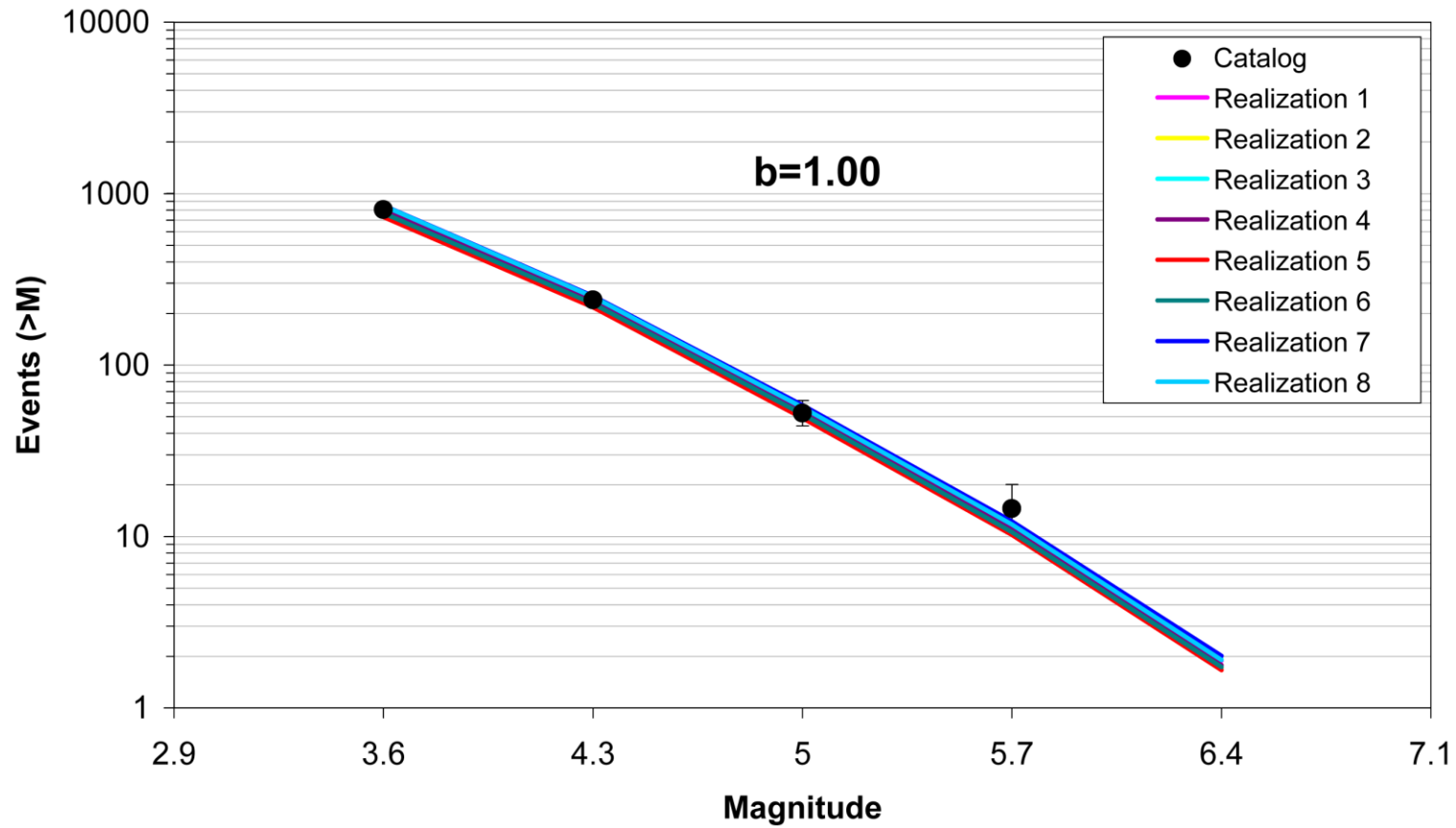


Figure 6.4.2-3  
Comparison of model-predicted earthquake counts for study region using Case E magnitude weights. The error bars represent the 16%–84% uncertainty associated with the data, computed using the Weichert (1980) procedure.

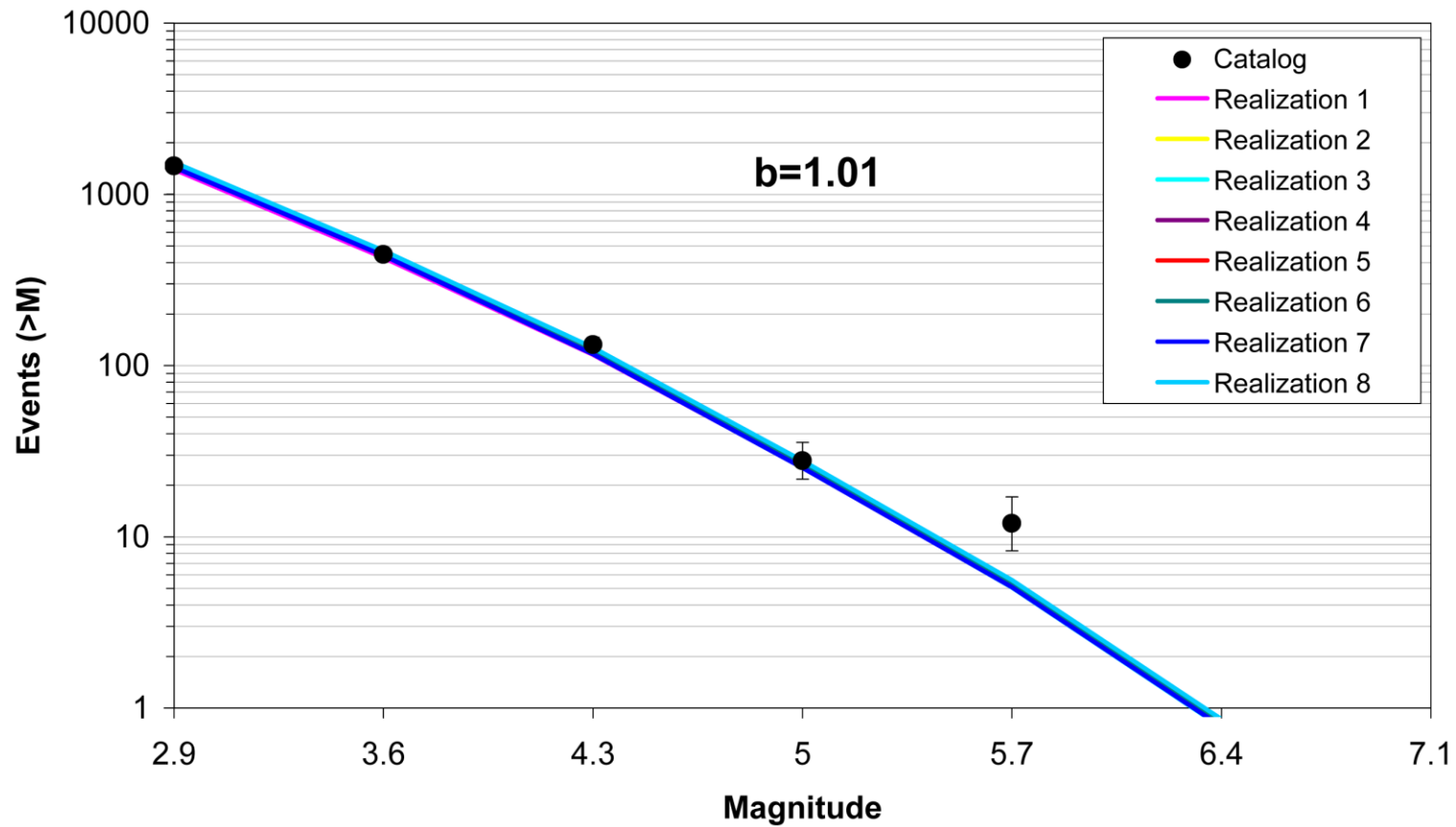


Figure 6.4.2-4  
Comparison of model-predicted earthquake counts for MESE-N using Case A magnitude weights. The error bars represent the 16%–84% uncertainty associated with the data, computed using the Weichert (1980) procedure.

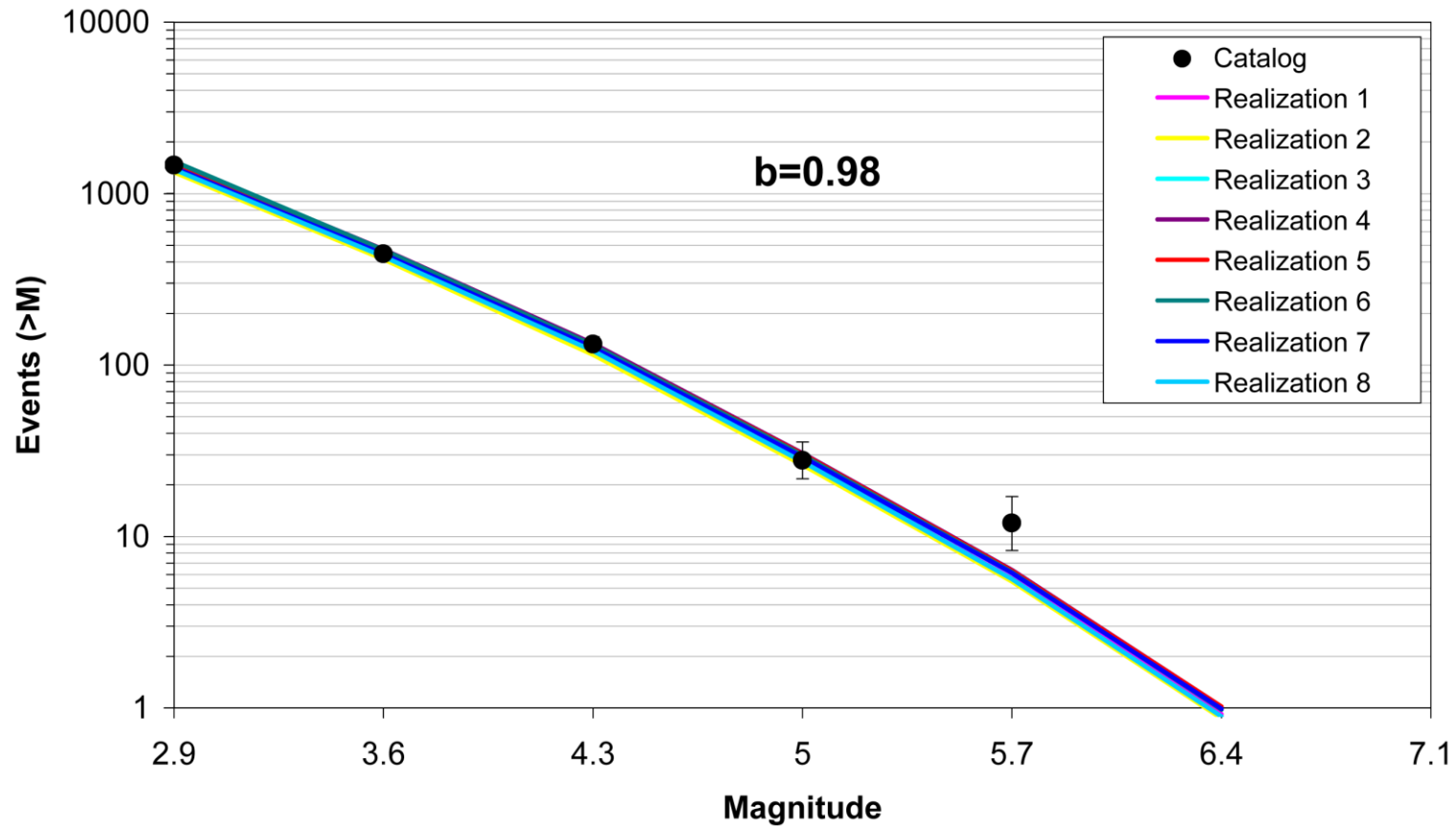


Figure 6.4.2-5  
Comparison of model-predicted earthquake counts for MESE-N using Case B magnitude weights. The error bars represent the 16%–84% uncertainty associated with the data, computed using the Weichert (1980) procedure.

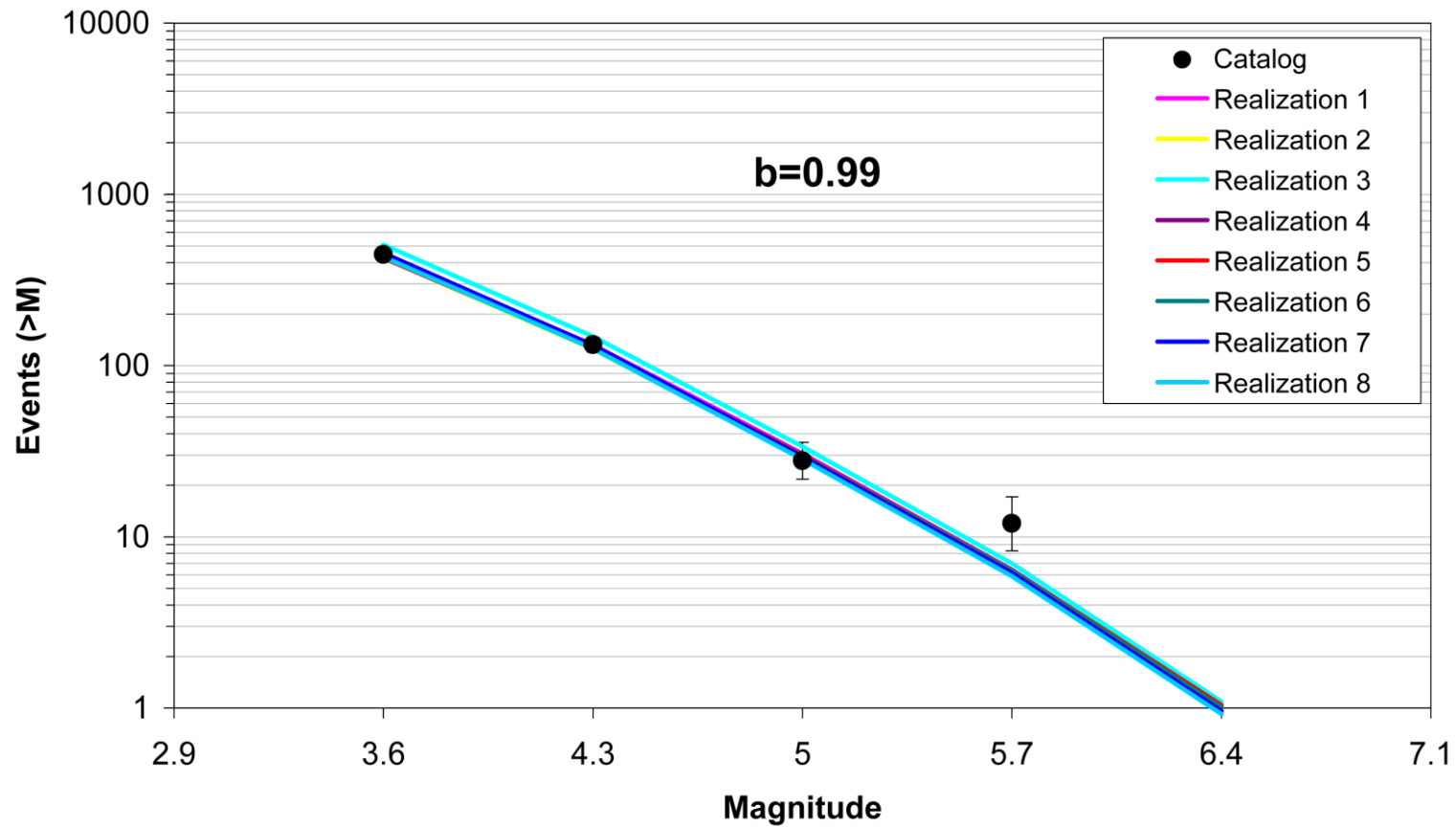


Figure 6.4.2-6  
Comparison of model-predicted earthquake counts for MESE-N using Case E magnitude weights. The error bars represent the 16%–84% uncertainty associated with the data, computed using the Weichert (1980) procedure.

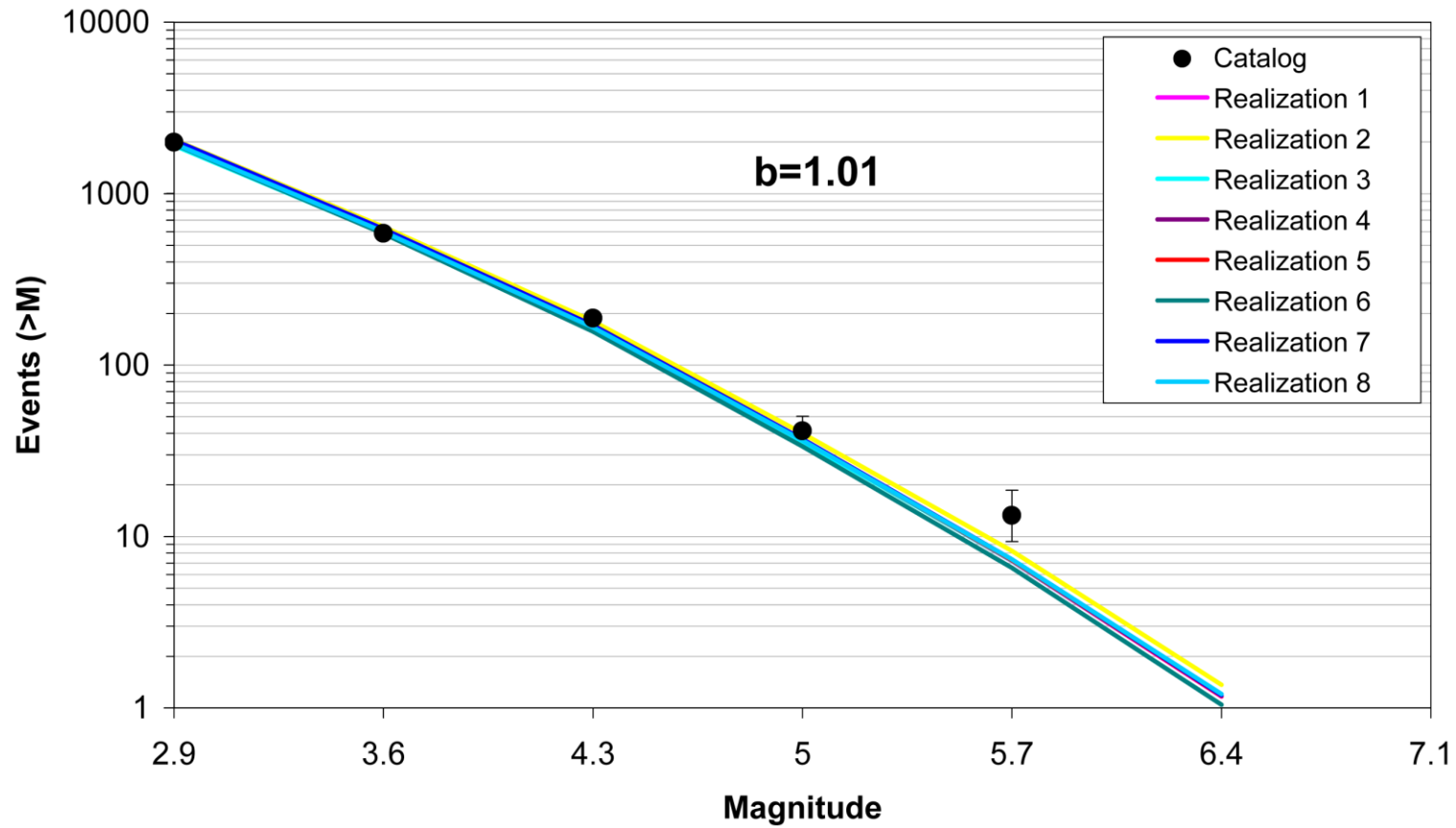


Figure 6.4.2-7  
Comparison of model-predicted earthquake counts for MESE-W using Case A magnitude weights. The error bars represent the 16%–84% uncertainty associated with the data, computed using the Weichert (1980) procedure.

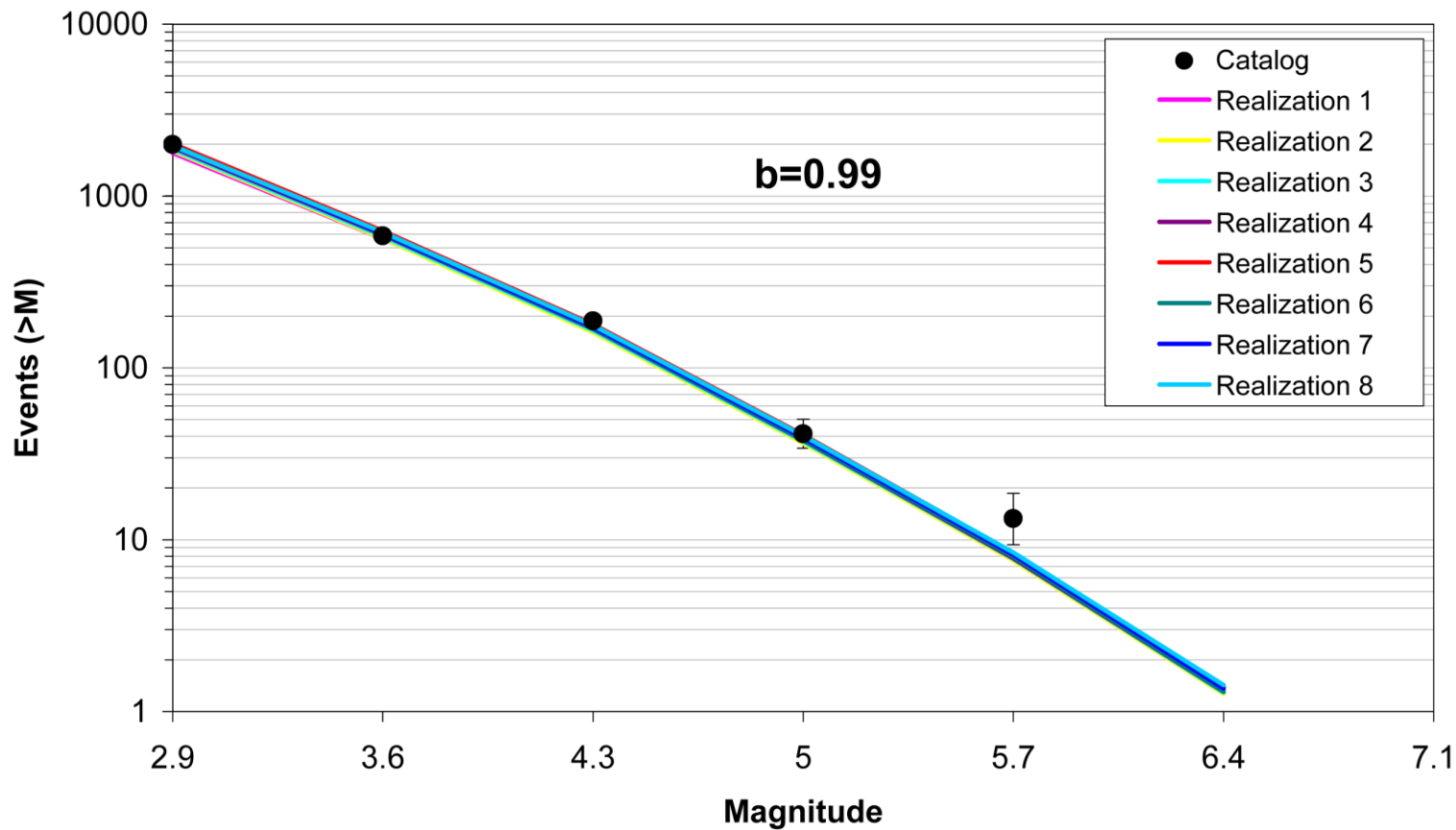


Figure 6.4.2-8  
Comparison of model-predicted earthquake counts for MESE-W using Case B magnitude weights. The error bars represent the 16%–84% uncertainty associated with the data, computed using the Weichert (1980) procedure.

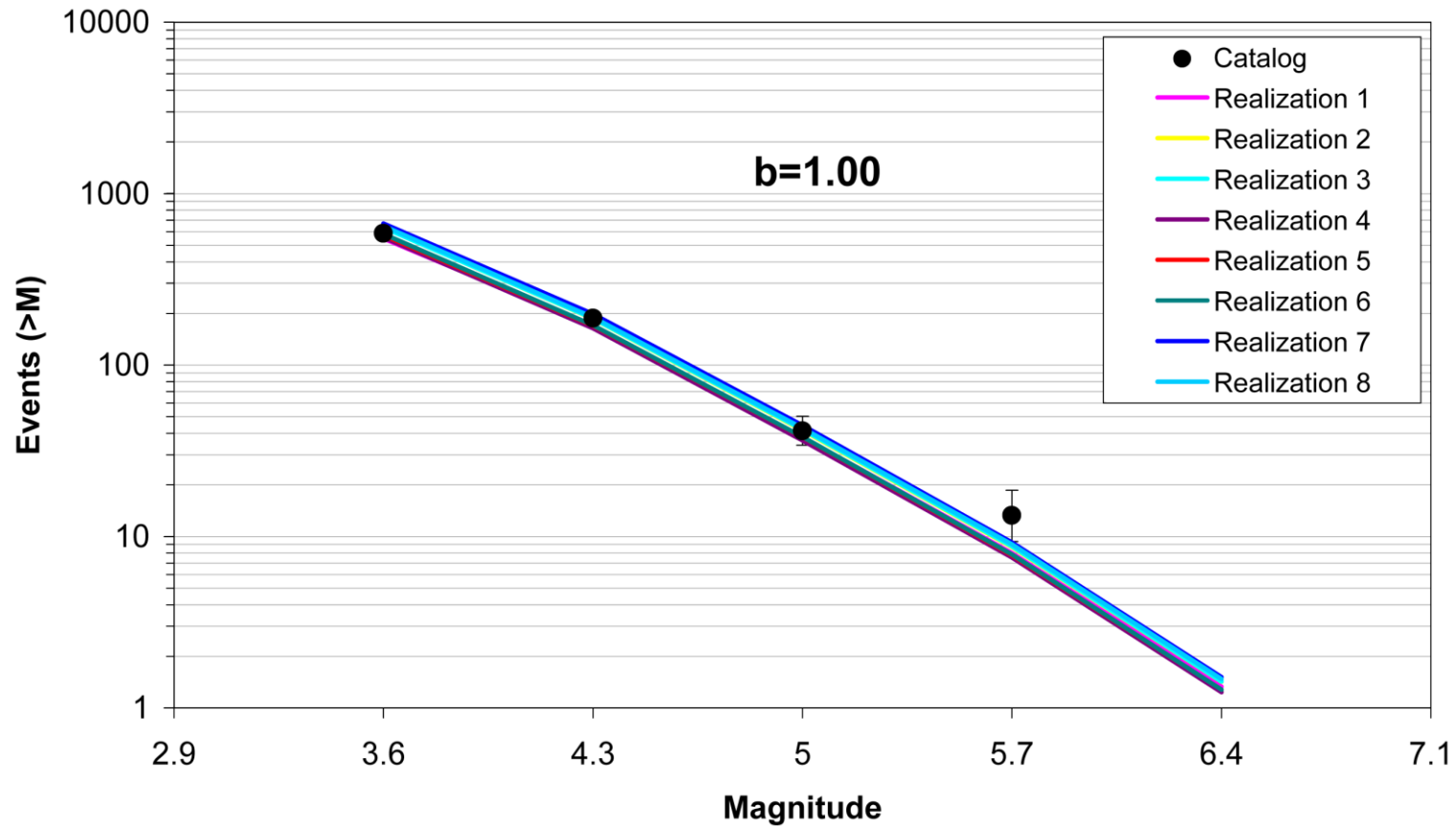


Figure 6.4.2-9  
Comparison of model-predicted earthquake counts for MESE-W using Case E magnitude weights. The error bars represent the 16%–84% uncertainty associated with the data, computed using the Weichert (1980) procedure.

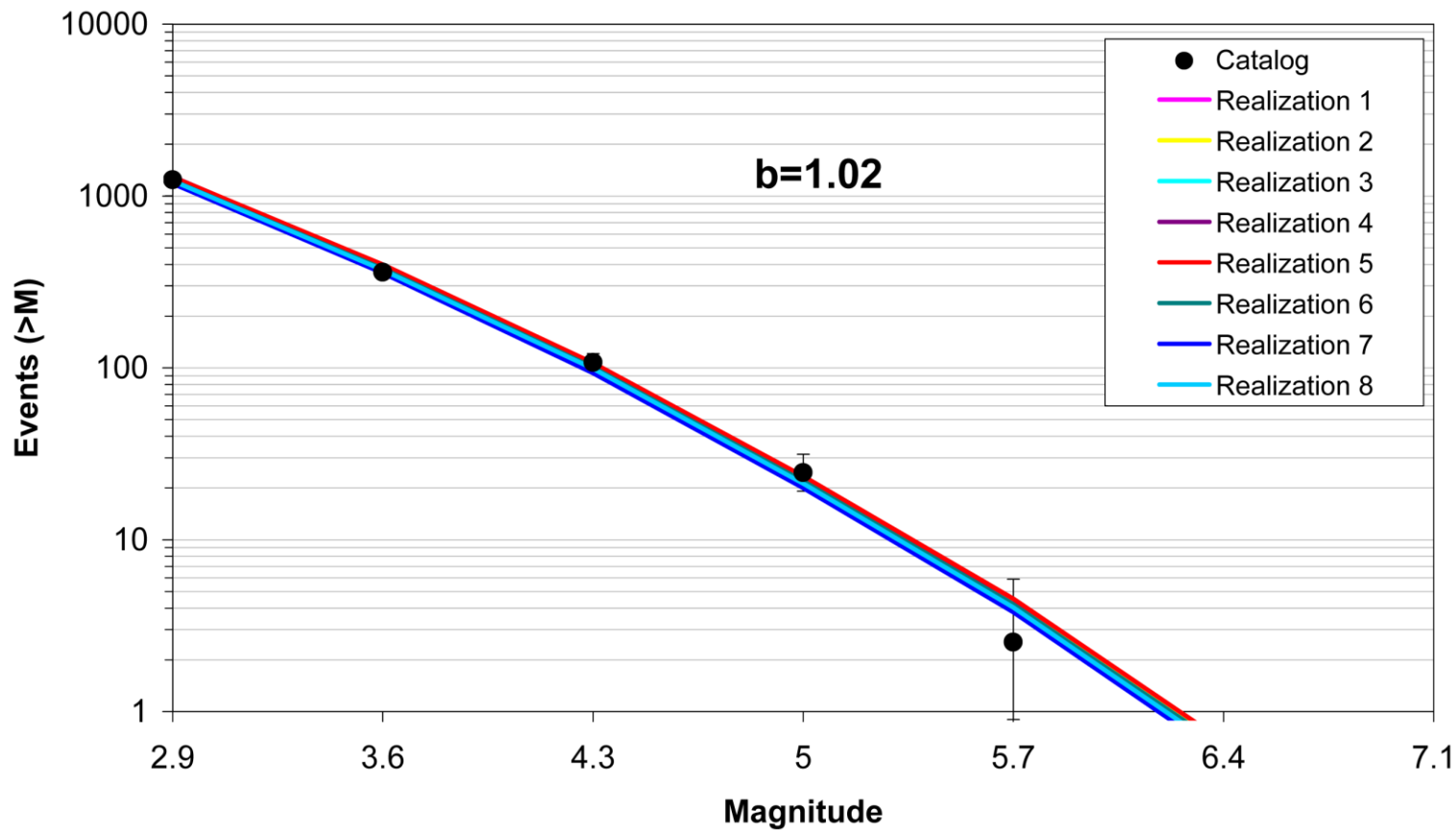


Figure 6.4.2-10  
Comparison of model-predicted earthquake counts for NMESE-N using Case A magnitude weights. The error bars represent the 16%–84% uncertainty associated with the data, computed using the Weichert (1980) procedure.

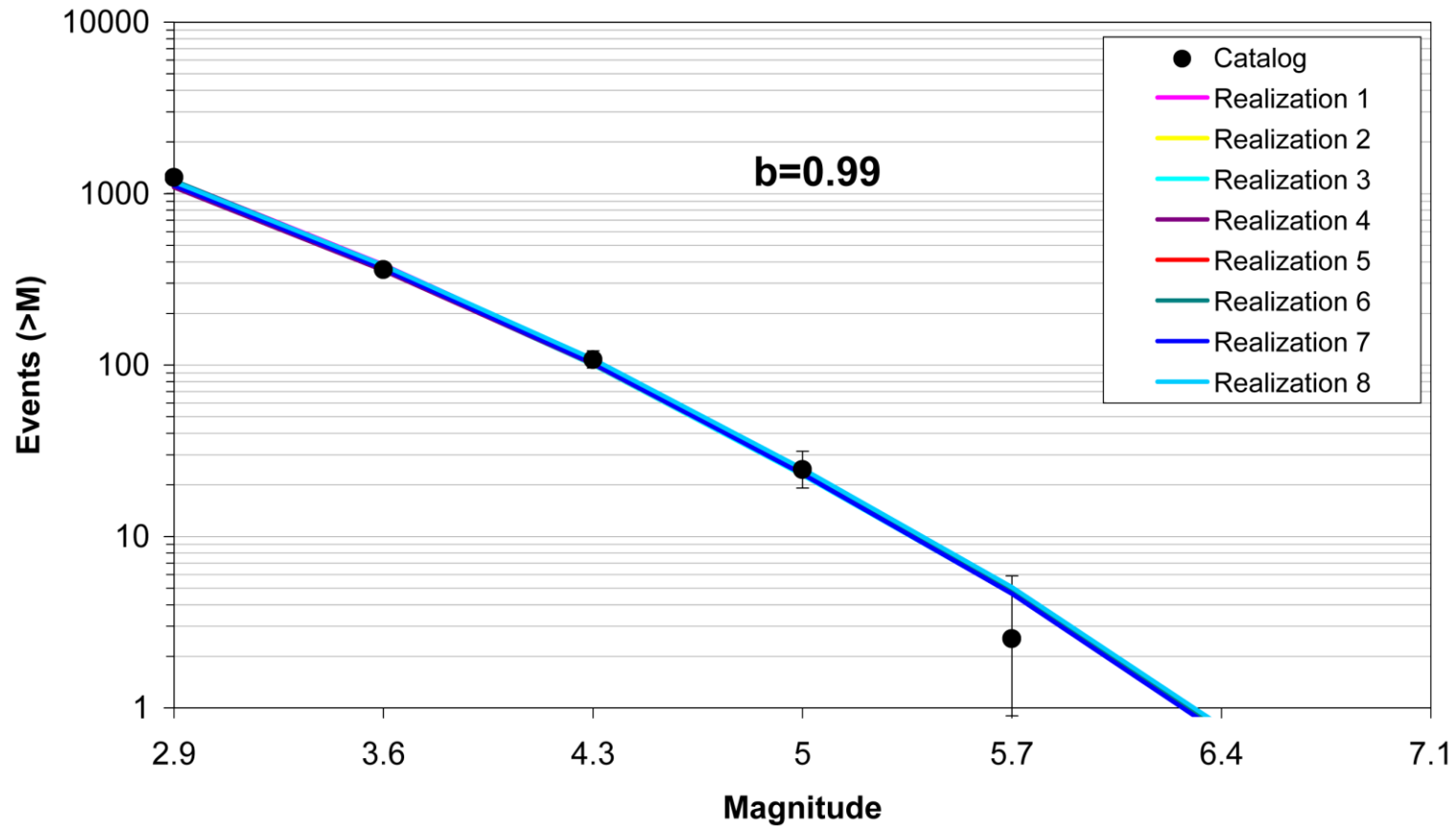


Figure 6.4.2-11  
Comparison of model-predicted earthquake counts for NMESE-N using Case B magnitude weights. The error bars represent the 16%–84% uncertainty associated with the data, computed using the Weichert (1980) procedure.

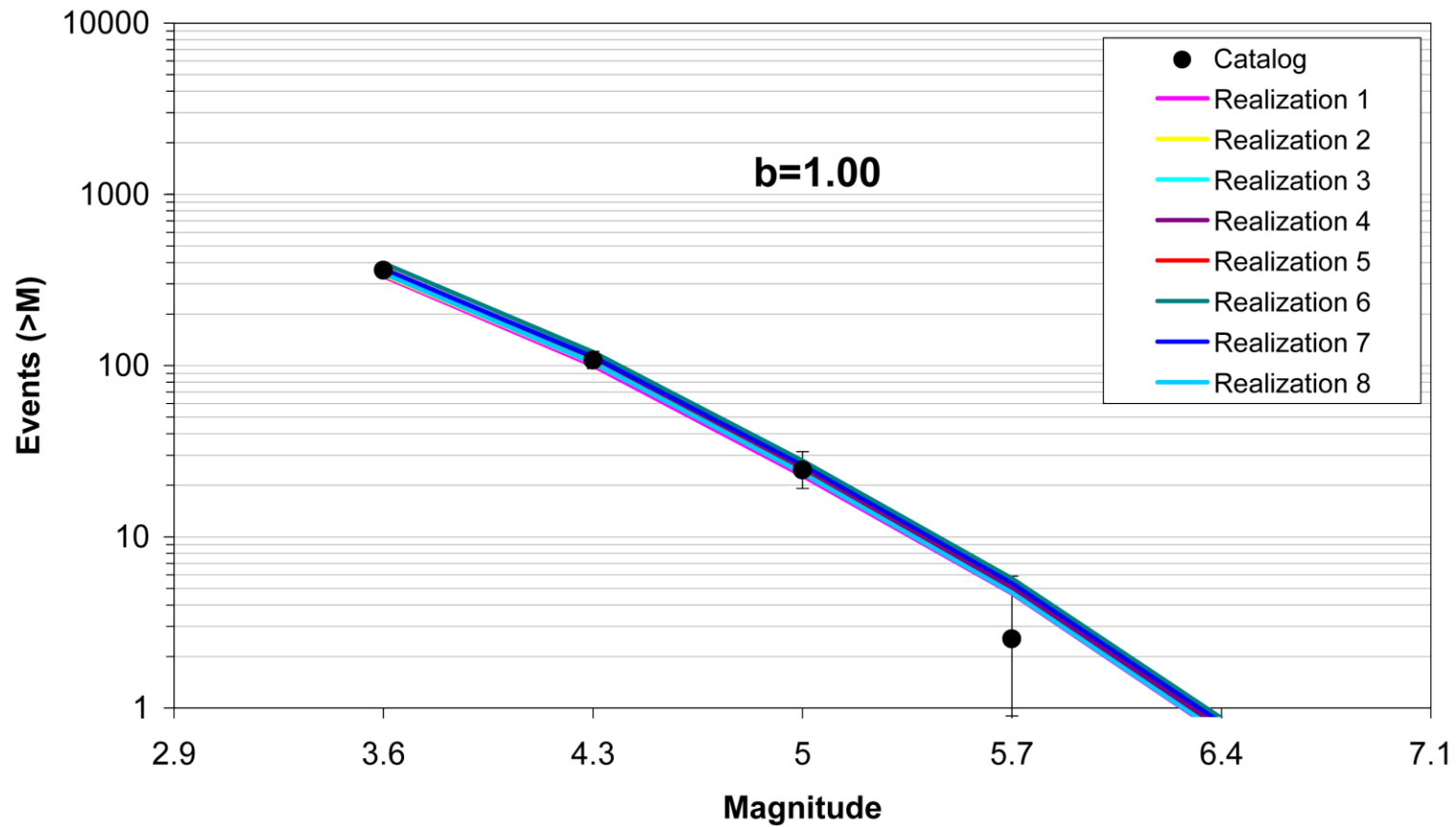


Figure 6.4.2-12  
Comparison of model-predicted earthquake counts for NMESE-N using Case E magnitude weights. The error bars represent the 16%–84% uncertainty associated with the data, computed using the Weichert (1980) procedure.

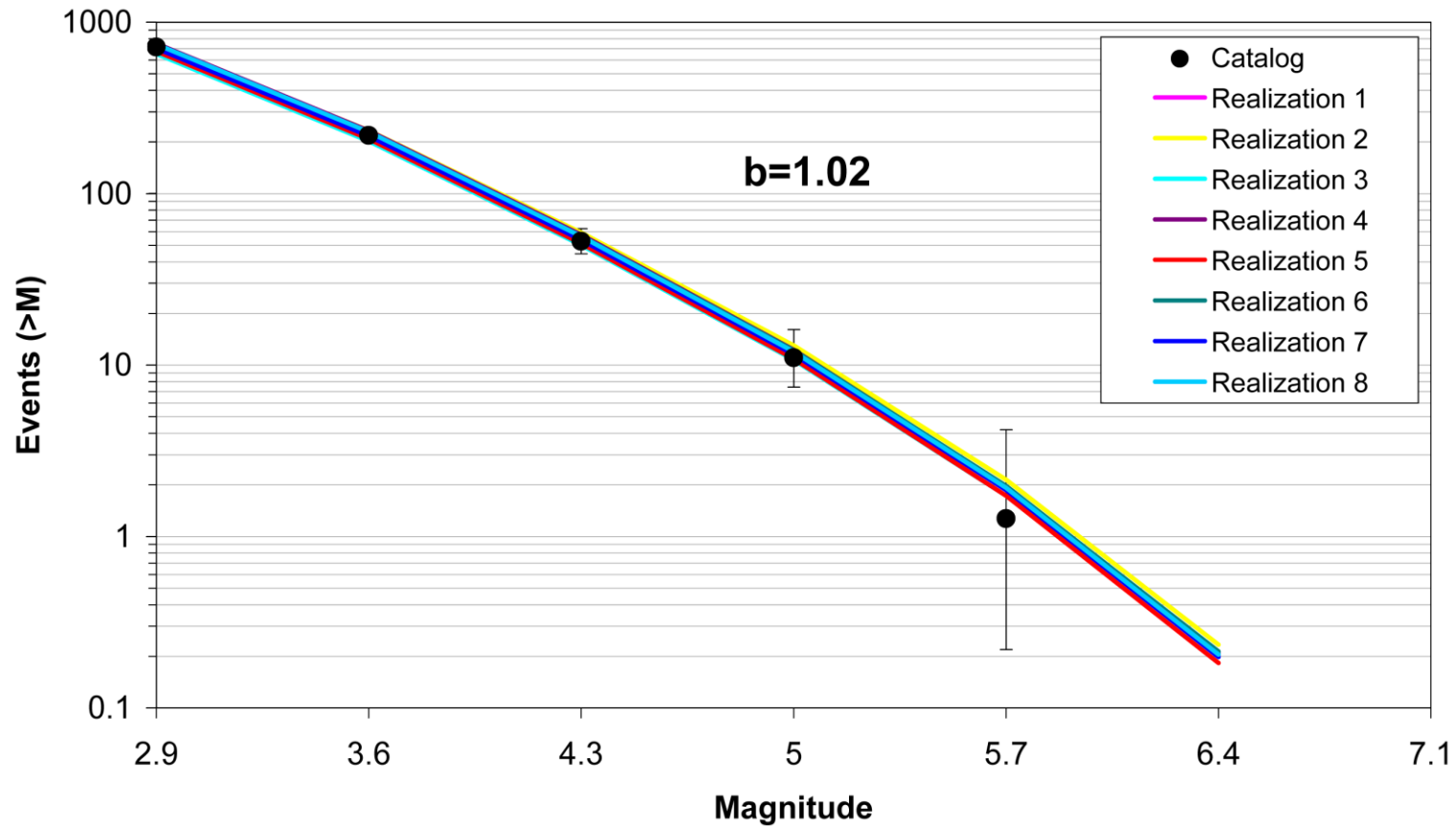


Figure 6.4.2-13  
Comparison of model-predicted earthquake counts for NMESE-W using Case A magnitude weights. The error bars represent the 16%–84% uncertainty associated with the data, computed using the Weichert (1980) procedure.

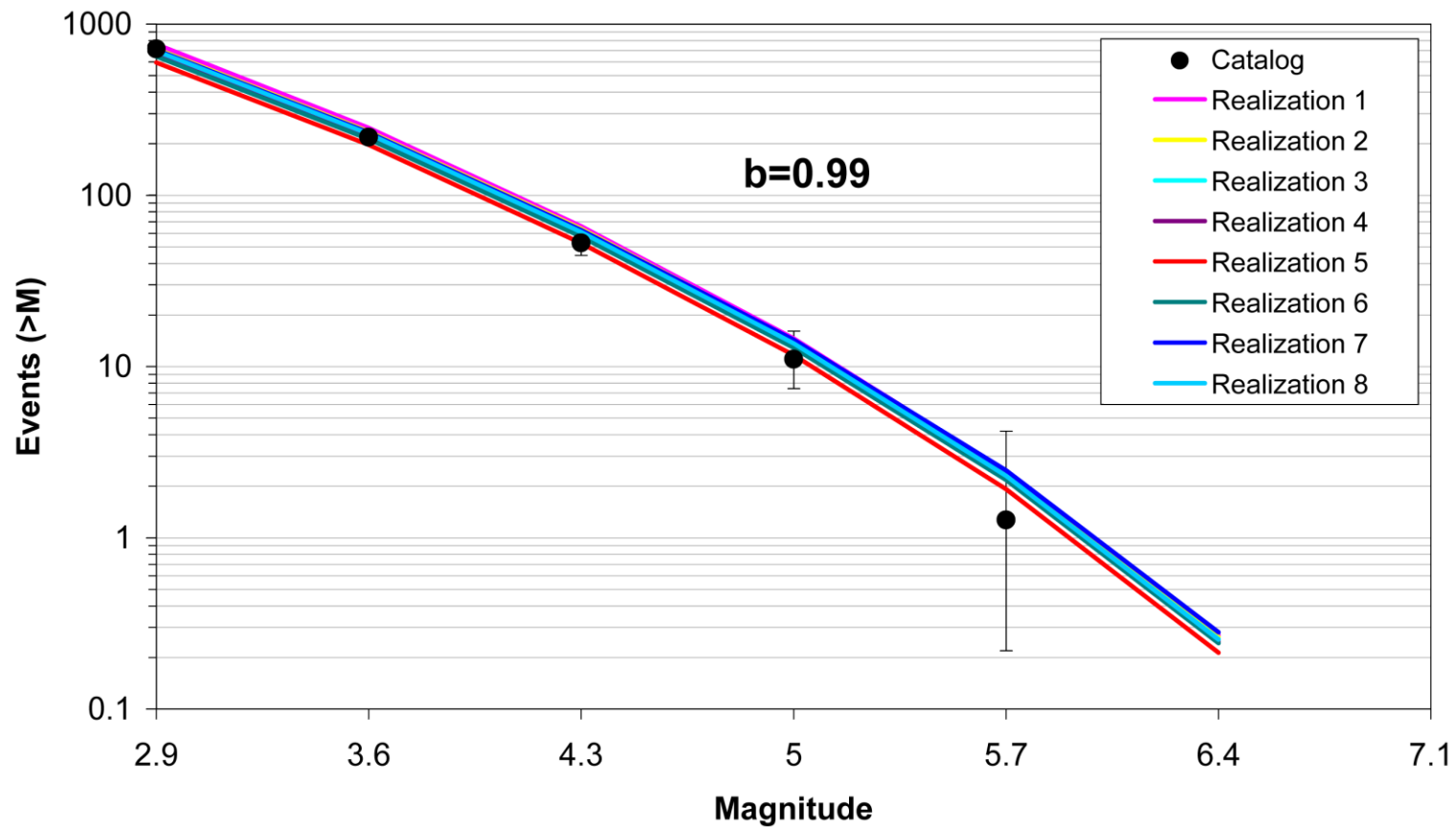


Figure 6.4.2-14  
Comparison of model-predicted earthquake counts for NMESE-W using Case B magnitude weights. The error bars represent the 16%–84% uncertainty associated with the data, computed using the Weichert (1980) procedure.

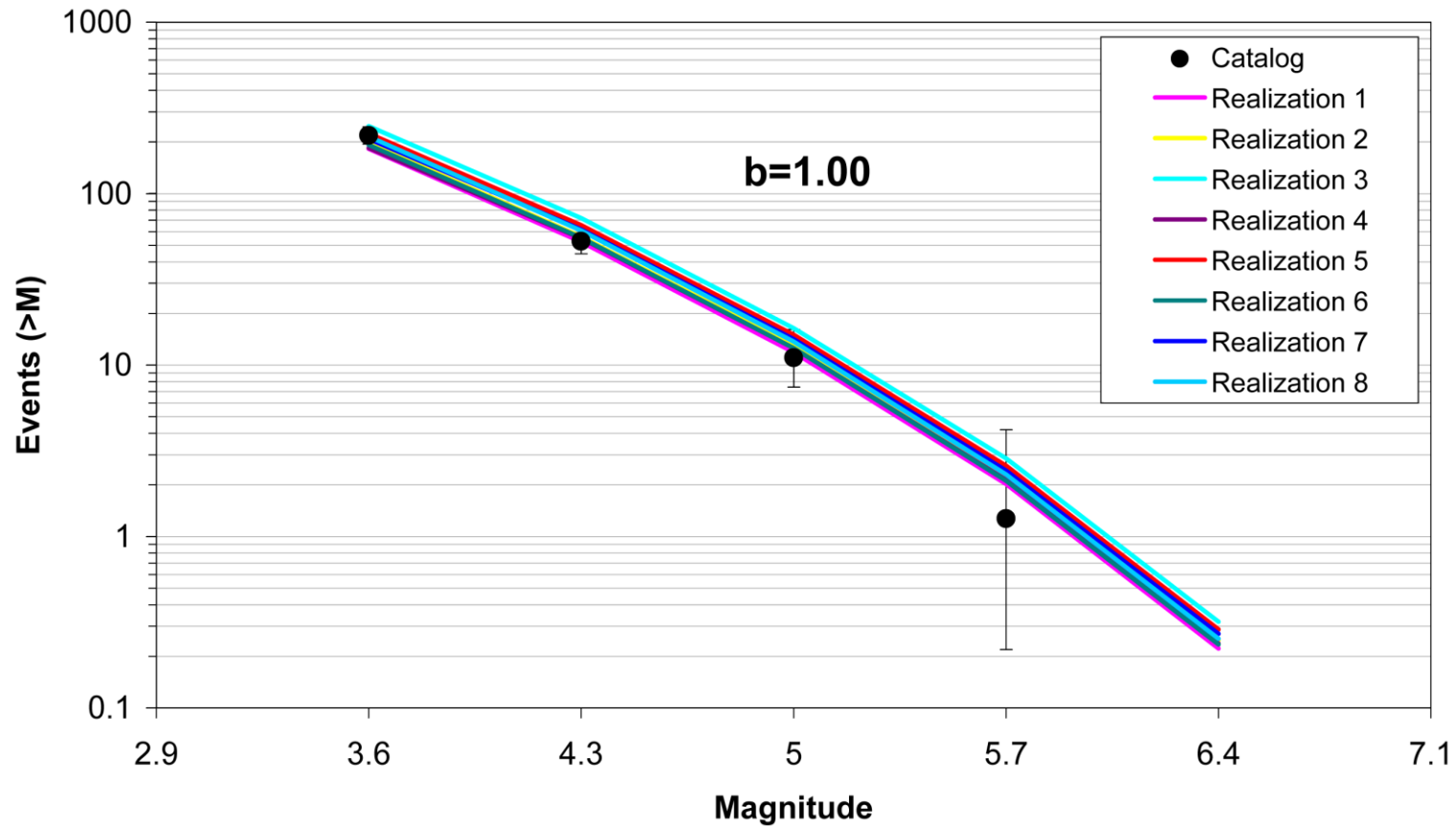


Figure 6.4.2-15  
Comparison of model-predicted earthquake counts for NMESE-W using Case E magnitude weights. The error bars represent the 16%–84% uncertainty associated with the data, computed using the Weichert (1980) procedure.



# 7

## CHAPTER 7

### SSC MODEL: SEISMOTECTONIC ZONES BRANCH

---

As discussed in Section 4.2.1, the conceptual framework for assessing the CEUS SSC model is characterized by two alternative branches of the master logic tree: the Mmax zones branch and the seismotectonic zones branch. The seismotectonic zones branch subdivides the CEUS SSC region according to differences in the seismic source assessment criteria described in Section 4.1.3.3. A common element of both the Mmax zones and the seismotectonic zones branches is the RLME sources. Because the paleoearthquake data that indicate the presence, location, and size of the RLMEs are essentially independent from data used to assess seismotectonic sources, the RLME branch is present in both models. The seismotectonic zones approach allows the incorporation of additional information related to the characteristics of future earthquakes. Therefore, this approach is assessed a higher weight than the Mmax zones approach in the master logic tree, as discussed in detail in Section 4.2.1. An overview of the factors used to identify and characterize the seismotectonic zones is given in Sections 7.1 and 7.2, followed by a detailed discussion of each of these zones in Section 7.3.

#### 7.1 Approaches and Data Used to Define Seismotectonic Zones

The conceptual basis for the seismotectonic zones branch of the master logic tree is that regional differences in characteristics related to recurrence rates, Mmax, future earthquake characteristics, and/or the probability of activity of tectonic features are best addressed by identifying a source zone (see Section 4.1.3.3). Likewise, the regional differences in these characteristics provide the bases for defining individual seismotectonic zones. Although the recurrence rates within the zones are allowed to vary according to the smoothing of observed seismicity, the other characteristics are assumed to be uniform within the zone. For example, a seismotectonic zone may possess characteristics that would lead to a different Mmax than adjacent zones, including a different prior distribution or different maximum observed earthquake. A seismotectonic zone might also be characterized by earthquakes resulting from reverse fault displacement, while adjacent zones might be characterized by larger components of strike-slip displacement. Likewise, a seismotectonic zone might best be characterized as having thicker seismogenic crust than adjacent zones. A seismotectonic zone may also be defined if tectonic features or groups of tectonic features are identified that have a significant probability of activity, but as discussed in Section 4.1.3.3, such features have not been identified on a regional basis as part of this study.

The geometries of the seismotectonic zones are largely a function of the major tectonic domains within which a given SSC characteristic is assessed to be relatively uniform (Figures 7.1-1 through 7.1-4) and different from the characteristics of adjacent zones. In most cases, the characteristics that define the zones are expected differences in future earthquake characteristics

such as rupture orientation, depth distribution, and style of faulting. A summary of the future earthquake characteristics for each seismotectonic zone is given in Table 5.4-2. The boundaries of the seismotectonic zones are derived from interpretations in the literature of regional geophysical, geologic, and tectonic data sets. In addition, data developed as part of the CEUS SSC Project, such as magnetic and gravity data (Figures 7.1-5 and 7.1-6), were examined for defining the zones. As discussed in Section 5.4.7, zone boundaries are defined as being either “leaky” or “strict” with respect to whether future earthquake ruptures are assessed to extend across a zone boundary.

As described in Section 4.1.2.2 and included in Appendices C and D, Data Evaluation and Data Summary tables have been developed for each of the seismotectonic zones. These tables are an important resource for the reader, as they supplement the discussions of each zone given in this section. The Data Summary tables specify the various data sets that were reviewed and considered by the TI Team during the course of its assessments. The Data Evaluation tables provide an evaluation of the quality of the data and the degree of reliance placed by the team on the data during the assessment process. The reader is advised to consult both tables when reviewing the descriptions to better understand how the available data were applied to define the characteristics of each seismotectonic zone. Tables developed for RLME sources are also relevant for some of the seismotectonic zones. Table 7.1-1 shows which table numbers are associated with each of the seismotectonic zones.

To illustrate the definition of a seismotectonic zone by way of a specific example, the St. Lawrence Rift (SLR) seismotectonic zone (discussed in Section 7.3.1 and shown on Figures 7.1-1 and 7.3.1-1) is outlined by the region assessed to be a terrane of known and inferred northeast-trending normal faults that formed parallel to the passive margin of Laurentia during the late Proterozoic–early Paleozoic opening of the Iapetus Ocean and underwent continental extension during the most recent extensional tectonic episode in the Mesozoic. The data considered in the identification and characterization of this zone are presented in Data Summary Table D-7.3.1 (Appendix D), and the data evaluated to provide a basis for characterizing the zone are given in Data Evaluation Table C-7.3.1 (Appendix C). The detailed assessments of the available data for the SLR zone are given in Section 7.3.1, including the basis for identifying the SLR as a seismotectonic zone and the location of the zone boundary (Section 7.3.1.2). The set of future earthquake characteristics for the SLR zone is given in Table 5.4-2. This zone is adjacent to the Northern Appalachian zone to the south and differs from it in the expected strikes of future ruptures and in the thickness of the seismogenic crust. The boundaries to the SLR zone are assessed to be “leaky,” such that future earthquake epicenters would lie within the zone, but ruptures, the strike of which is given in Table 5.4-2 and the length and width of which are magnitude-related (as discussed in Section 5.4), could extend beyond the zone boundaries.

Given the regional nature of the CEUS SSC model and the need for it to be reviewed for possible local refinement for site-specific application (see discussion in Section 4.1.3), the sensitivity to the exact location of seismotectonic zone boundaries is not expected to be large. Therefore, explicit quantification of the uncertainty in zone boundary location is included in the model for only a couple of cases, such as the western boundary of the Paleozoic Extended Crust (PEZ narrow or wide) and the inclusion or exclusion of the Rough Creek graben in the Reelfoot Rift seismotectonic zone (RR-RCG).

It is important to note that, in the discussion of the seismotectonic zones, the TI Team was well aware of previous SSC models developed for the CEUS through the years for both site-specific and regional hazard evaluations. Some of these studies relied on different approaches and criteria for identifying seismic source zones from those used in this study (Section 4.1.3). As a result, it may appear that some of the “tried-and-true” approaches to drawing seismic source zone boundaries have been ignored or not considered in the CEUS SSC Project. For example, the spatial distribution of seismicity is decidedly non-uniform in the CEUS (Figure 7.1-7), and a common approach to identifying seismic sources in some past studies was to enclose zones of concentrated seismicity. Specific examples include the Central Virginia seismic zone and the Eastern Tennessee seismic zone (ETSZ). Acknowledging that these zones of elevated seismicity in the historical period of observation likely represent zones of future elevated rates, the method of implementing this concept in the CEUS SSC model is spatial smoothing of *a*- and *b*-values, rather than drawing source zone boundaries. Further, both the Mmax zones and the seismotectonic zones branches of the master logic tree provide for such smoothing regardless of where source zone boundaries are drawn. Therefore, given that some seismotectonic zones show spatial variations in observed rates of past earthquakes (Figure 7.1-8), these variations are accounted for in the smoothing model.

Another common characteristic of previous SSC models is identifying prominent tectonic features as potential seismic source zones. Examples include the Midcontinent rift, which displays strong gravity and magnetic anomalies, or the numerous Mesozoic extensional faults and basins along the eastern margin of the CEUS. In a general sense, the seismotectonic zones accommodate the regional tectonic domains within which these types of tectonic features occur, provided that they meet the criteria for identifying a seismic source (Section 4.1.3.3). The SLR is defined by a different prior distribution for estimating Mmax from that of some adjacent regions, and the zone encloses the major Paleozoic extensional features of the St. Lawrence rift system. However, the zone boundary is drawn not because it is a tectonic feature, but because of expected differences with adjacent zones in Mmax, as well as other future earthquake characteristics (e.g., style of faulting, rupture orientation, thickness of seismogenic crust).

In contrast, features such as the Midcontinent rift are not assessed to lead to different Mmax or future earthquake characteristics from adjacent regions, nor does the feature have a high probability of activity ( $P_a > 0.5$ ) that could lead to a significant potential hazard. Therefore, using the hazard-informed approach discussed in Section 4.1.3, these types of tectonic features are not called out in the SSC model. Other types of tectonic features that are not identified explicitly are faults and other features that might have local significance, unless there is a clear consensus within the technical community that the feature should be assessed a high  $P_a$  and considered seismogenic. For example, recent and ongoing studies of faults in the vicinity of the ETSZ postulate that these faults are related to the zone either as causative faults or as secondary faults resulting from displacement on faults at depth (see Section 7.3.4). However, these postulated associations are judged to lack definitive support for use in this SSC model as a result of the preliminary nature of the studies. Even the Charleston RLME source characterization does not rely on an individual fault or faults as seismic sources, given the lack of definitive geologic evidence for young faulting in the Charleston area. However, the range of hypotheses for the location of the Charleston source fault is encompassed by the source zones as they are currently defined.

## 7.2 RLME Sources in the Seismotectonic Zones Branch

The RLME sources are described in Section 6.1 under the Mmax zones branch of the master logic tree. Because the RLME sources are defined and characterized by independent paleoseismic data that are not affected by the presence or absence of seismotectonic zones or Mmax zones, they are assumed to exist in exactly the same manner as on the Mmax zones branch of the master logic tree.

## 7.3 Seismotectonic Source Zones

The logic tree structure for the seismotectonic source zones is shown on Figure 7.3-1. The first two levels of the logic tree address the basic source zonation. The first level addresses the location of the boundary between the PEZ and the Midcontinent-Craton (MidC) zone. Characterization of the uncertainty in this boundary parallels the uncertainty in the MESE/NMESE boundary for the Mmax zones and arises from uncertainty in characterizing the western extent of Mesozoic extension. The second level of the logic tree addresses the uncertainty in the eastern extent of the RR zone—whether or not it includes the Rough Creek graben. These two logic tree branches lead to the four alternative seismotectonic zonation configurations shown on Figures 7.1-1 through 7.1-4.

The next level of the logic tree addresses uncertainty in the choice of weights on magnitude ranges used in computing the seismicity rates. These are discussed in Section 7.5.

Descriptions of the individual seismotectonic zones are presented below.

### 7.3.1 St. Lawrence Rift Zone (SLR)

The SLR seismotectonic zone consists of crust initially rifted during the late Proterozoic–early Paleozoic opening of the Iapetus Ocean; faults within the rifted crust were subsequently reactivated during the Paleozoic and Mesozoic. This seismotectonic zone is characterized by elevated rates of seismicity and contains significant historical earthquakes, including the 1935 Timiskaming **M** 6.2 (E[**M**] 6.02)<sup>1</sup> earthquake, the 1988 Saguenay **M** 5.9 (E[**M**] 5.84) earthquake, and historical earthquakes from Charlevoix (Figure 7.3.1-1). Historical earthquakes and paleoseismic evidence suggest that the entire rift system is capable of generating moderate- to large-magnitude earthquakes. Compressional reactivation of favorably oriented Iapetan faults has been postulated as the causal mechanism for several seismically active regions in eastern North America, including the SLR, Charlevoix, and the lower St. Lawrence Valley in Quebec, Canada (Adams and Basham, 1991). As the result of an analysis of earthquakes in stable continental regions (SCRs) worldwide, Johnston et al. (1994) determined that zones of rifted crust in SCRs correlate directly with increased earthquake activity when compared to zones of nonrifted SCRs in regard to number and maximum magnitude of earthquakes. The seismic source

---

<sup>1</sup> Magnitudes are reported in magnitude scale as designated in the cited publication. E[**M**] denotes the value of the expected moment magnitude listed in the CEUS SSC catalog for an earthquake. It is reported to two decimal places to indicate that it is a calculated value. See the discussion in Section 3.3.1.

characterization of the SLR seismotectonic zone is based on a review of published material that is summarized in the Data Summary table for the SLR zone (Appendix Table D-7.3.1). Explicit references and data that were used as the basis for source characteristics of SLR are identified in the Data Evaluation table (Appendix Table C-7.3.1).

### 7.3.1.1 Background

#### 7.3.1.1.1 *Iapetan Rifting*

Breakup of the Mesoproterozoic supercontinent of Rodinia occurred as diachronous rifting along the margins of Laurentia. Rifting began on the western margin of Laurentia between 780 and 680 Ma, and continued to the eastern margin between 620 and 550 Ma from Newfoundland into the southern Appalachian Mountains (Whitmeyer and Karlstrom, 2007), resulting in the opening of the Iapetus Ocean (Faill, 1997a). Kumarapeli (1985) proposed that a mantle plume initiated Iapetan rifting along the Sutton Mountains triple junction, resulting in the development of the St. Lawrence valley system and aulacogens of the Ottawa-Bonnechere and Saguenay grabens (Kumarapeli and Saull, 1966; Kumarapeli, 1985, 1993). Based on geochronological studies of the Sutton Mountains volcanics, Kumarapeli (1993) established the following sequence: (1) rifting initiated at 590 Ma and continued for 35 Myr; (2) rifting ceased about 554 Ma after an outburst of alkaline to transitional basalts at the Sutton Mountains triple junction; and (3) a period of rift-facies clastic sedimentation followed until the rift-drift transition at 550 Ma. Rift-related lava flows (Figure 7.3.1-2) are observed along the entire eastern margin of Laurentia now preserved in Appalachian thrust sheets, including the Skinner Cove Formation of western Newfoundland (McCausland and Hodych, 1998); the Mont St-Anselme Formation and Lac Matapédia flows of Quebec (Hodych and Cox, 2007); the Tibbit Hill Formation of Vermont and Quebec (Kumarapeli et al., 1988); the Pinney Hollow metarhyolite of central Vermont (Walsh and Aleinikoff, 1999); the Caldwell Group lavas of southern Quebec (Bedard and Stevenson, 1999); and the Nassau Formation of eastern New York and western Massachusetts (Ratcliffe, 1987). Major and trace element studies of the lava rocks confirm a mantle source consistent with plume activity (St. Seymour and Kumarapeli, 1995; Abdel-Rahman and Kumarapeli, 1998). Puffer (2002) compiled a database of high field-strength elements for late Neoproterozoic to early Paleozoic flood basalts, revealing that superplume activity peaked at 550 Ma at the Sutton Mountains triple junction. The 564 Ma Catocin Formation of southeastern Pennsylvania and central Virginia and the 758 Ma Mount Rogers Formation of southwestern Virginia and North Carolina and Tennessee record a more complex history of Iapetan rifting in the southeastern United States (Aleinikoff et al., 1995) and are discussed in Section 7.3.4.1.

Iapetan rifting is also recorded by widespread dikes and intrusions throughout the SLR and the Ottawa-Bonnechere and Saguenay aulacogens (Figure 7.3.1-2). The Grenville dike swarm of the Ottawa-Bonnechere graben (Kamo et al., 1995) and the Adirondack dike swarm of New York (Abdel-Rahman and Kumarapeli, 1998) are coeval with the 590 Ma Sutton Mountains volcanism, implying that the dike swarms were emplaced within a relatively short time span at the onset of rifting. Alkalic intrusions within the Ottawa-Bonnechere graben yielding an early Cambrian age of approximately 565 Ma and syn-rift carbonatite complexes of the Saguenay graben dated at 565 Ma support the view that these aulacogens formed as part of a single event (Kumarapeli, 1985). This interpretation is supported by subsequent ages of the 577 Ma Callander

Complex near Lake Nipissing in the western end of the Ottawa-Bonnechere graben (Kamo et al., 1995) and the 564 Ma Mt. Rigaud syenite of Quebec (McCausland and Hodych, 1998). Higgins and van Breemen (1998) attribute the  $565 \pm 4$  Ma Sept Iles layered mafic intrusion of the Gulf of St. Lawrence to emplacement of plume melts along rift faults that developed after emplacement of dike swarms. Additional details are provided in Appendix Table D-7.3.1. This rifted margin is expressed as promontories and embayments defined by northeast-striking normal faults and northwest-striking transform faults along the margins of Laurentia (Thomas, 1991; 2006; Lavoie et al., 2003).

In southeastern Canada, Iapetan rifting is expressed along the St. Lawrence River valley (Section 7.3.1.1.2) and associated with the Ottawa (Section 7.3.1.1.4) and Saguenay (Section 7.3.1.1.5) failed arms, or aulacogens, that formed transverse to the faulted edge of the ancient continental margin (Adams et al., 1995). These aulacogens are defined by zones of approximately east-west-trending normal faults that extend into the Canadian Shield and have not undergone significant total extension (Adams et al., 1995). Large-magnitude earthquakes located within the Charlevoix area (Figure 6.1.1-1) are characterized as part of the Charlevoix RLME seismic source zone (Sections 6.1.1 and 7.3.1.1.3), whereas the moderate-magnitude seismicity at Charlevoix is characterized as part of the SLR seismotectonic zone. Adams et al. (1995) argue that seismicity clusters observed throughout the Iapetan margin are a temporal artifact and characterize the possible future activity of the region by incorporating these clusters into a regional zone. The following subsections address the geologic, geophysical, and seismic characteristics of the crust within the SLR seismotectonic zone, which exhibits variable rates of seismicity.

#### 7.3.1.1.2 St. Lawrence Rift

The late Proterozoic–early Paleozoic St-Laurent fault, which is attributed to opening of the Iapetus Ocean, forms a northeast-trending, southeast-dipping half graben lying along the main axis of the SLR system (Tremblay and Lemieux, 2001). High-resolution seismic profiles in the St. Lawrence estuary indicate that the Laurentian Channel trough transitions from a half graben to a graben structure from southwest to northeast (Tremblay et al., 2003). The St-Laurent fault trends N20 to 50E, dips 60–70 degrees to the southeast (Tremblay and Lemieux, 2001; Tremblay et al., 2003), and is crosscut by the Cap-Tourmente fault at Cap-Tourmente, Quebec. West of Cap-Tourmente, the Montmorency Falls fault occupies the same structural position as the St-Laurent fault, suggesting that they formed as en echelon faults oblique to the axis of the SLR (Tremblay and Lemieux, 2001). The Cap-Tourmente fault possibly represents a transfer fault acting as an oblique relay structure between two longitudinal normal faults (Tremblay and Lemieux, 2001). St. Julien and Hubert (1975) observe that east-west and N30E steeply southeast-dipping normal faults active between late Precambrian and the Late Ordovician times cut Cambrian and Ordovician platform rocks in southwestern Quebec. Results of the Quebec-Maine seismic reflection surveys provide evidence of closely spaced en echelon normal faults with displacements between 200 and 1,000 m (656 and 3,280 ft.), interpreted as fossilized Iapetan growth faults below the Appalachian detachment surface (Spencer et al., 1989). These normal faults are imaged on the northwestern portion of seismic line QM2001 northwest of the Baie-Vert–Brompton line (Spencer et al., 1989).

Multiple phases of reactivation of the SLR are in evidence. The St-Laurent fault crosses the Devonian Charlevoix impact crater without major deflection, suggesting post-impact reactivation (Lemieux et al., 2003). The St-Laurent fault influenced the deposition of Ordovician sediments during late stages of the Taconian orogeny by syndepositional faulting, preserved as major lateral thickness variations within these platform rocks, presence of slump deformation in almost all stratigraphic units, preservation of pseudotachylyte within synsedimentary breccias, and occurrence of fault breccia clasts (Lemieux et al., 2003). Truncation of Devonian impact-related structures by northeast-southwest and northwest-southeast fault sets is consistent with Mesozoic fault reactivation due to rifting of the North Atlantic region (Lemieux et al., 2003). Tremblay et al. (2003) attribute some fault throw along the SLR fault system to opening of the Central Atlantic in the Jurassic and/or seafloor spreading of the North Atlantic during the Cretaceous. Faults located in Quebec near Montreal, where the southern portion of the SLR approaches the Ottawa-Bonnechere graben, provide evidence for northwest-southeast extension associated with the opening of the Iapetus Ocean; west-northwest/east-southeast compression followed by minor north-northwest compression associated with Appalachian thrusting; northeast-southwest and north-northwest/south-southeast extension associated with the opening of the Atlantic-Labrador Ocean; and northeast-southwest compression postdating these events (Rocher et al., 2003).

In addition to large-magnitude historical earthquakes located within the Charlevoix RLME source area (Sections 6.1.1 and 7.3.1.1.3), the September 16, 1732, modified Mercalli intensity (MMI) VIII (E[M] 6.25) Montreal earthquake (Leblanc, 1981) and the September 5, 1944, M 5.8 (E[M] 5.71) Cornwall-Massena earthquake (Bent, 1996b) are also located along the main axis of the SLR.

#### 7.3.1.1.3 *Charlevoix RLME Source*

Adams and Basham (1991) attribute seismicity of the SLR system to earthquakes occurring on rift structures in the regional stress field of southeast-to-east compression, recognizing that a Devonian impact structure also exists in the general area and may be related to the spatial concentration of seismicity in the Charlevoix area. Two major fault orientations (N40-70W and N20-40E) are found outside the Charlevoix impact zone, with minor fault sets trending east to west to N80W and north to south to N20E (Lemieux et al., 2003). Lemieux et al. (2003) observed the largest variation in fault trends within the central portion of the impact crater, which still displayed a dominant northeast-southwest orientation. Lamontagne and Ranalli (1997) attribute large-magnitude Charlevoix earthquakes to reactivation of rift faults in response to the regional stress field. They interpret variations in orientation and style of faulting for small-magnitude earthquakes to reactivation of impact-related faults and fractures in response to local stress and/or strength conditions. In another paper, Lamontagne and Ranalli (1996) attribute earthquakes in the Charlevoix seismic zone to some or all of the following circumstances:

- Fracturing above the brittle-ductile transition at depths of at least 25 km (15.5 mi.).
- High pore-fluid pressure at mid- to lower crustal depths where hydration reactions are not favored.
- Low coefficients of friction related to highly fractured zones at depth, as opposed to thick fault gouges made of clay minerals.

Results of two-dimensional stress modeling account for the spatial pattern of observed seismicity as stress concentration due to the interaction of the crater (local zone of weakness) and rift faults (large-scale weak zone; Baird et al., 2009). Smaller-magnitude, more frequent seismicity occurs within the impact crater, and infrequent larger-magnitude earthquakes are localized along rift faults (Baird et al., 2009). Tuttle and Atkinson (2010) observed paleoliquefaction features in the Charlevoix area—but not to the south in Trois Rivières, Quebec—that suggest stationarity of large-magnitude earthquakes within the Charlevoix RLME seismic source zone. Although the February 5, 1663, **M** 7 (E[**M**] 7.00) and October 20, 1870, **M** 6.5 (E[**M**] 6.55) earthquakes are modeled as RLME in Section 6.1.1, the December 6, 1791, **M** 5.8 (E[**M**] 5.50); October 17, 1860, **M** 6 (E[**M**] 6.08); and March 1, 1925, **M** 6.3 (E[**M**] 6.18) earthquakes do not meet the RLME criterion of exceeding **M** 6.5 and are thus assigned to the SLR seismotectonic zone. The Charlevoix Data Summary and Data Evaluation tables (Tables D-6.1.1 and C-6.1.1) present additional details about the Charlevoix RLME zone.

#### 7.3.1.1.4 Ottawa-Bonnechere Graben

The Ottawa-Bonnechere graben extends for approximately 700 km (435 mi.) into the Canadian Shield (Kumarapeli and Saull, 1966; Kumarapeli, 1985, 1993) from the Sutton Mountains salient of the central Appalachian orogen. The graben is inferred to extend eastward beneath the Appalachian thrust sheets for approximately 30 km (19 mi.) by Kumarapeli (1993), based on observations that the Early Cretaceous Montegian intrusions reported by Foland et al. (1986) are emplaced along the graben faults. Alkalic intrusions within the Ottawa-Bonnechere graben yield an early Cambrian age of approximately 565 Ma (Kumarapeli, 1985). A tholeiitic diabase dike swarm associated with the graben is dated at 590 Ma, implying that the initiation of rifting was a late Proterozoic event (Kumarapeli, 1985).

The faults defining the Ottawa-Bonnechere graben generally strike west-northwest and offset Silurian strata (Forsyth, 1981). Rimando and Benn (2005) report three periods of faulting in Cambro-Ordovician sedimentary rocks within the eastern end of the Ottawa-Bonnechere graben, near Ottawa, Ontario, Canada, as follows:

- The oldest generation of faults, formed in response to a horizontal maximum principal compressive stress ( $\sigma_1$ ) oriented northwest, are kinematically congruent with the compression direction associated with closing of the Iapetus Ocean.
- A second generation of faults, which indicate a west-northwest-oriented  $\sigma_1$ , coincide with emplacement of Cretaceous carbonatite dikes.
- A third generation of faults indicate a southwest-oriented  $\sigma_1$  consistent with the post-Cretaceous stress field for eastern North America.

The Ottawa-Bonnechere graben and associated basement faults acted as localized zones of weakness in the early stage of Cretaceous extension, resulting in reorientation of the regional stress field and formation of the localized zone of north-south-directed extension (Faure et al., 1996b). Results of the 1982 Canadian Consortium for Crustal Reconnaissance Using Seismic Techniques (COCRUST) long-range seismic refraction experiment show a sharp, step-like displacement of the Moho beneath the south shoulder of the Ottawa-Bonnechere graben,

confirming the deep-seated nature of the faults associated with the graben and penetration of mantle melts into the crust (Mereu et al., 1986). In addition, the COCRUST surveys show a poorly defined Moho at unusually shallow depths beneath the graben (Mereu et al., 1986).

Adams and Basham (1991) recognized two distinct bands of seismicity within the Western Quebec seismic zone. They attribute the west-northwest-trending band of seismicity along the Ottawa River between Ottawa, Ontario, and Lake Timiskaming to rift faults of the Ottawa-Bonnechere graben and the more northern band to the Great Meteor hotspot (Section 7.3.2). The second band of seismicity in the Western Quebec seismic zone trends north-northwest, extends from Montreal to the Baskatong Reservoir, and is attributed to crustal fracturing associated with the passage of a Cretaceous hot spot track as discussed in Section 7.3.3. Adams et al. (1995) consider the 1935 **M** 6.2 (E[**M**] 6.02) Timiskaming earthquake, which occurred at a depth of 10 km (6 mi.) near the Quebec-Ontario border, the paradigm earthquake for the Ottawa-Bonnechere graben. The January 1, 2000,  $M_N$  5.2 (E[**M**] 4.62) Kipawa earthquake is located near the 1935 epicenter and exhibits northwest-southeast-striking reverse faults that may be associated with northwest-trending lineaments under Lake Kipawa that have been interpreted as faults (Bent et al., 2002).

In the western portion of the Ottawa-Bonnechere graben, Doig (1991) interprets two paleoearthquakes based on inferred landslide deposits in lakes located near the epicenter of the 1935 Timiskaming earthquake. As discussed in Section 6.1.1.5, this method of interpreting earthquake-induced landslide deposits cannot distinguish between local small-magnitude earthquakes and distant large-magnitude earthquakes, but these results qualitatively suggest that the Ottawa-Bonnechere graben has experienced recurring moderate-magnitude earthquakes. Aylsworth et al. (2000) attribute widespread landsliding and irregular subsidence along the Ottawa River in the eastern portion of the graben to two paleoearthquakes occurring at about 7,060 and 4,550 BP that could be as large as the 1663 Charlevoix (**M** 7) earthquake (Section 7.3.1.3).

#### 7.3.1.1.5 Saguenay Graben

The Saguenay graben, which also represents a failed arm of the Iapetan passive margin (Kumarapeli, 1985), extends into the Precambrian Canadian Shield for approximately 300 km (186 mi.) northwest from the St. Lawrence Valley. The graben margins are defined by the Lac Tchitogama, Ste-Marguerite River, and Lake Kenogami east-west-striking normal faults (Du Berger et al., 1991). Syn-rift carbonatite complexes dated at 565 Ma suggest an early Cambrian age for the Saguenay graben (Kumarapeli, 1985). Some of the graben-bounding faults offset Ordovician limestone by as much as 500 m (1,640 ft.) and are marked by prominent topographic scarps with 100–300 m (328–984 ft.) of relief (Du Berger et al., 1991). Lavoie et al. (2003) attribute middle to late Cambrian debris flow units preserved in southern Quebec and western Newfoundland to reactivation of the Saguenay graben. Longu  p  e and Cousineau (2005) interpret the Anse Maranda Formation as sediments deposited in deep subbasins along a narrow shelf south of the Saguenay graben. Roden-Tice, Brandt, and Tremblay (2009) observe apatite fission-track age discontinuities across the Sainte-Marguerite and Lac Kenogami faults, suggesting Late Triassic to Early Jurassic and Middle Jurassic reactivation, respectively, across the faults. Adams et al. (1995) characterized the 1988 Saguenay **M** 5.9 (E[**M**] 5.84) earthquake,

which occurred at a depth of 27 km (17 mi.), as the paradigm earthquake for the Saguenay graben. Prior to this earthquake, seismicity rates for the Saguenay graben were extremely low (Adams et al., 1995). Paleoliquefaction investigations conducted by Tuttle et al. (1990, 1992) and Tuttle (1994) in the Saguenay graben area revealed liquefaction features within 26 km (16 mi.) of the epicenter of the 1988 Saguenay earthquake, and included evidence for an older earthquake of unknown magnitude occurring at AD 1420 ± 200 yr.

Other investigations also provide geologic evidence for repeated earthquakes in Saguenay. Doig (1998) determined a recurrence interval ranging from 350 to 1,000 years based on evidence of earthquake-induced landslide deposits within lakes near the epicenter of the 1988 Saguenay earthquake. As discussed in Sections 6.1.1.5 and 7.3.1.1.4, these observations are difficult to quantitatively incorporate within recurrence calculations because silt layers may be due to nontectonic landslides, and if they are tectonic, these silt layers can be attributed to either local moderate-sized earthquakes or distant large-magnitude earthquakes. These results do, however, suggest that the Saguenay graben has experienced recurring moderate-magnitude earthquakes. Recent work by Locat (2008) places the 1663 *M* 7 earthquake near Saguenay, based on the distribution of largely undated landslide deposits throughout the region and subaqueous mass movements in the St. Lawrence estuary, Saguenay fjord (Syvitski and Schafer, 1996; Urgeles et al., 2002; St-Onge et al., 2004), and nearby lakes. These studies by Doig (1998), Locat (2008), Syvitski and Schafer (1996), Urgeles et al. (2002) and St-Onge et al. (2004) illustrate the role of landsliding, in addition to liquefaction, as a mechanism for recording paleoearthquakes in the region. As discussed in Section 6.1.1.3, better constraints on timing of earthquakes are required for correlating deformation with specific earthquakes and determining location and magnitude of those earthquakes.

#### *7.3.1.1.6 Lower St. Lawrence*

Adams et al. (1995) attribute aseismic regions that clearly separate seismicity of the Lower St. Lawrence from that in the Charlevoix area as temporal artifacts, and relate the Lower St. Lawrence cluster of seismicity to a separate seismic source zone, the Bas St. Laurent zone in the GSC H model (Adams et al., 1996; Adams and Halchuk, 2003). Lamontagne et al. (2003) propose that this localized Lower St. Lawrence cluster of seismicity occurs in Precambrian basement where intersecting faults may be weakened by crustal fluids, hydrostatic pressure, or fault gouge, and that emplacement of the Sept-Iles layered igneous complex may have further fractured this portion of crust. Lamontagne et al. (2004) attribute the March 16, 1999, *M<sub>N</sub>* 5.1 (*E[M]* 4.45) Côte-Nord earthquake, whose focal mechanisms exhibited northwest-trending nodal planes to rupture of northwest-striking faults associated with magnetic and gravimetric lineaments, as opposed to northeast-southwest-trending rift faults.

#### *7.3.1.1.7 Adirondack Mountains*

Kumarapeli and Saull (1966) interpret fault scarps along the western margin of the Champlain Valley to St. Lawrence rifting. Iapetan normal faults within the Adirondack Mountains occur within the Adirondack dike swarm (Kamo et al., 1995; Figure 7.3.1-2). Kamo et al. (1995) established that the Grenville dike swarm of the Ottawa-Bonnechere graben is coeval with the

590 Ma Sutton Mountains triple junction, and Abdel-Rahman and Kumarapeli (1998) determined that the Adirondack dike swarm of New York is geochemically similar to the Grenville dike swarm, implying that both swarms are coeval and comagmatic with Sutton Mountains volcanism. Focal mechanism interpretations for the April 20, 2002, **M** 5.0 (**E**[**M**] 4.91) Au Sable Forks, New York, earthquake show reverse faulting consistent with reactivation of a north-south-striking structure (Pierre and Lamontagne, 2004; Seeber et al., 2002). The October 7, 1983,  $m_b$  5.1 (**E**[**M**] 4.84) Goodnow, New York, earthquake also is related to reverse faulting oriented north-south (Nábělek and Suárez, 1989). North-south-trending structures in the Lake Champlain area include normal faults associated with Iapetan rifting and high-angle reverse faults associated with Taconic compression (Seeber et al., 2002). Roden-Tice et al. (2000) inferred Late Jurassic exhumation of the High Peaks section of the Adirondack Mountains, which continued along the northern, northwestern, and southwestern margins of the Adirondack Mountains into the Cretaceous, with a suggestion of renewed unroofing in the Eocene. This exhumation is thought to have been accommodated by reverse-slip reactivation of north-northeast-trending normal faults (Roden-Tice et al., 2000). Subsequent work by Roden-Tice and Tice (2005) indicates that differential unroofing in the southeastern Adirondack Mountains and central New England may have been accommodated by Late Cretaceous fault reactivation.

### 7.3.1.2 Basis for Defining Seismotectonic Zone

The SLR seismotectonic zone delineates crust initially rifted during the late Proterozoic–early Paleozoic opening of the Iapetus Ocean and subsequently reactivated during the Mesozoic opening of the Atlantic Ocean, meeting the criterion for separating crust of the SLR on the basis of maximum earthquake magnitude. As discussed in Section 7.3.1.1, although the rates of seismicity vary throughout the rift, moderate- to large-magnitude earthquakes are observed throughout the seismotectonic zone. Previous interpretations of the Iapetan rifted margin (IRM; Wheeler, 1995; Adams et al., 1995) have included crust that is characterized as part of the Northern Appalachian (Section 7.3.3) and Paleozoic Extended Zone (Section 7.3.4) seismotectonic zones. Crust of the SLR seismotectonic zone is distinguished from these two zones on the basis of age, history of reactivation, and earthquake characteristics.

The SLR seismotectonic zone is defined by mantle plume–initiated Iapetan rifting along the Sutton Mountains triple junction (Kumarapeli, 1985, 1993) that resulted in normal faulting along the main axes of the St. Lawrence rift and the Ottawa-Bonnechere and Saguenay grabens (Kumarapeli and Saull, 1966; Kumarapeli, 1985, 1993; Tremblay et al., 2003; Lemieux et al., 2003). The IRM extends south of the SLR and lies buried beneath the Northern and Southern Appalachian Mountains (Wheeler, 1995). Compressional reactivation of favorably oriented Iapetan faults has been postulated as the causal mechanism for several seismically active regions in eastern North America (Adams and Basham, 1991). Adams et al. (1995) observe that seismicity of the IRM is largely expressed as reverse-slip faulting mechanisms in Canada and strike-slip mechanisms in the United States. Faults exposed within the SLR exhibit multiple phases of reactivation, including during the Mesozoic (Tremblay et al., 2003; Lemieux et al., 2003; Rocher et al., 2003; Rimando and Benn, 2005). Faure et al. (2006) observe east-west- and northwest-southeast-oriented extensional stress regions in Quebec based on stress tensor analysis of regional- and mesoscopic-scale faults, which indicate that Mesozoic extension was

widespread and extended at least 400 km (250 mi.) from the Atlantic margin. Apatite fission-track ages from the Adirondack Mountains and New England indicate widespread Mesozoic uplift and erosion that locally display age discontinuities, suggesting reactivation of preexisting structures (Roden-Tice et al., 2000; Roden-Tice and Tice, 2005; Roden-Tice, West, et al., 2009). As presented in Section 7.3.1.1, the presence of moderate- to large-magnitude historical earthquakes and paleoseismic data indicate that the entire rift system is capable of generating moderate to large earthquakes.

### 7.3.1.3 Basis for Zone Geometry

The geometry for the SLR seismotectonic zone incorporates crust exhibiting evidence of Iapetan rifting, either by faulting or intrusion of rift-related volcanic rocks. The spatial extent of dikes and intrusions is generally larger than graben-bounding normal faults (Figure 7.3.1-2). Therefore, the geometry for SLR is modified from the IRM and Adirondack source zones of the GSC regional model (Adams et al., 1996; Adams and Halchuk, 2003) and the IRM boundary by Wheeler (1995) to incorporate the following data sets. The SLR seismic source zone boundary along the Adirondack Mountains and Ottawa-Bonnechere graben incorporates the Sutton Mountains triple junction, Grenville and Adirondack dike swarms, and Iapetan normal faults as mapped by Kamo et al. (1995).

Mapped locations of Iapetan lava flows (McCausland and Hodych, 1998; Hodych and Cox, 2007; Kumarapeli et al., 1988; Walsh and Aleinikoff, 1999; Bedard and Stevenson, 1999; Ratcliffe, 1987) are preserved within Appalachian thrust sheets and therefore do not provide a reliable eastern boundary for the SLR seismotectonic zone. The eastern boundary of the zone coincides with the Baie Verte–Brompton line of Moench and Aleinikoff (2003) to capture normal growth faulting observed below the Appalachian detachment in the northern Appalachians by Spencer et al. (1989). These boundaries are not well-imaged in potential field data (Figure 7.3.1-3). Du Berger et al. (1991) observed that the 1988 Saguenay earthquake is located outside the Saguenay graben. Therefore, the geometry of this graben is modified from that proposed by Higgins and van Breeman (1998) based on the spatial distribution of small-magnitude earthquakes in the dependent earthquake catalog. The main axis of the SLR seismotectonic zone was drawn to include these small-magnitude earthquakes. The northeastern portion of zone is also truncated beyond the edge of the project boundary.

### 7.3.1.4 Basis for Zone Mmax

A paleoseismic study conducted by Aylsworth et al. (2000) in the eastern portion of the Ottawa-Bonnechere graben provides evidence for two moderate- to large-magnitude Holocene earthquakes. Landslide deposits occurring in the Leda Clay, which was deposited in the Champlain Sea, have normalized radiocarbon ages between 1,870 and 5,130 yr BP, with the majority of ages clustering at 4,550 yr BP. This age is significantly younger than paleochannel abandonment, so these landslide deposits are attributed to a paleoearthquake. Disturbed, hummocky terrain exhibiting local relief between 3 and 8 m (9.8 and 26 ft.) is located east of these landslide deposits within the flat erosional plane of the Ottawa River, and is likely related to landsliding. Faulted, upturned, and warped sediment is also exposed for 500 m (1,640 ft.)

along a ditch, and nearby excavations contain sand lenses, a small flame structure, and a sand boil feature. Large patches of sand occur randomly on the surface. All these features have a radiocarbon age of  $7,060 \pm 80$  yr BP.

Based on analogy to the 1663 Charlevoix earthquake, these earthquakes were estimated to represent a magnitude of  $M \geq 7$  (Aylsworth et al., 2000). Subsequent trenching by Aylsworth and Lawrence (2003) documented lateral spreading and deformation of sediments and surface subsidence within a deep bedrock basin (180 m [590 ft.]) at 7,060 yr BP. In one location, 2 m (6.5 ft.) of fluidized sand is interpreted to have been emplaced along a sand dike during an earthquake associated with either ground cracking due to lateral spreading or in situ block rotation (Aylsworth and Lawrence, 2003). Assessing the magnitude and location of the earthquake causing these features is complicated by the observations that fine sand interbedded with the Leda Clay induces lower cyclic resistance and that deep, steep-sided basins amplify ground motions. A comparison with other earthquakes led Aylsworth and Lawrence (2003) to estimate the magnitude of the earthquake to which these features are related to be at least  $M \geq 6.2$ , and likely  $M \geq 6.5$ . The field observations conducted for these studies are consistent with appropriate evidence for paleoliquefaction as outlined in Appendix E. However, geotechnical investigations to constrain the cyclic stress ratio for these materials are required for constraining magnitude and location of these paleoearthquakes. It is also important to understand that these features could be caused by a paleoearthquake located in the SLR or Great Meteor Hotspot (GMH) seismotectonic zones, or that they could be caused by larger, more distant earthquakes associated with the Charlevoix RLME source. Future research may provide information to update the maximum magnitude distributions for these zones.

Given that the magnitude of the largest observed earthquake lies within the range of uncertainty of the magnitudes estimated by Aylsworth and Lawrence (2003),  $M_{max}$  for the SLR seismic source zone was assessed using historical seismicity. The largest observed earthquakes in SLR include the September 16, 1732,  $E[M]$  6.25; March 1, 1925,  $E[M]$  6.18; and November 1, 1935,  $E[M]$  6.08 earthquakes. As part of the EPRI study on earthquakes in SCRs, Kanter (1994) classified the St. Lawrence–Ottawa domain (Domain 227) as a Paleozoic rift that was reactivated in the Cretaceous. Therefore, the maximum magnitude distribution for the SLR seismotectonic zone was determined by applying a Mesozoic and younger prior to the largest observed earthquake. The resulting  $M_{max}$  distribution is presented in Section 7.4.2.

### 7.3.1.5 Future Earthquake Characteristics

Earthquakes in southeastern Canada are classified as mainly thrust earthquakes (Adams et al., 1995; Du et al., 2003). Bent et al. (2003) determined focal mechanisms for  $M > 4$  earthquakes occurring in eastern Canada between 1994 and 2000 and documented the mechanisms as predominantly reverse. Bent (1996a) determined a reverse mechanism for the November 1, 1935,  $m_b$  6.1 Timiskaming earthquake (Figure 7.3.1-1) and preferred a moderately dipping northwest-striking plane. The January 1, 2000,  $M_N$  5.2 ( $E[M]$  4.62) Kipawa earthquake (Figure 7.3.1-1) is located near the 1935 epicenter and exhibits northwest-southeast reverse faults dipping to the northeast (Bent et al., 2002). Du et al. (2003) determined thrust motion along either a southwesterly steeply dipping (68 degrees) or northeasterly dipping (30 degrees) nodal plane for

the Kipawa earthquake. Bent et al. (2003) observed that focal mechanisms in the Western Quebec seismic zone have a strong component of thrust faulting, with at least one nodal plane striking northwest-southeast, consistent with reactivation of the Ottawa-Bonnechere graben. Bent (1996b) determined an oblique thrust mechanism for the September 5, 1944,  $M$  5.8 ( $E[M]$  5.71) Cornwall-Massena earthquake (Figure 7.3.1-1), located at the eastern edge of the Ottawa-Bonnechere graben along the St. Lawrence River. Bent (1996b) could not determine which nodal plane was the fault plane, given that the regional seismicity trend is consistent with the northwest plane, and mapped faults are more consistent with the northeast plane.

Bent et al. (2003) report that mechanisms for the October 22, 1998, and March 16, 1999, Lower St. Lawrence earthquakes (Figure 7.3.1-1) exhibit evidence for oblique-thrust faulting over a wide range of possible dips (30–68 degrees). Lamontagne et al. (2004) favor the northwest nodal plane of the March 16, 1999,  $M_N$  5.1 ( $E[M]$  4.45) Côte-Nord earthquake based on agreement with an alignment of aftershocks. The focal mechanism determined by Du et al. (2003) for this earthquake favors northeast- and southwest-trending nodal planes for this earthquake.

Focal mechanisms for two earthquakes in the Adirondack Mountains indicate north-south-striking nodal planes. Focal mechanisms for the April 20, 2002,  $M$  5.0 ( $E[M]$  4.91) Au Sable Forks, New York, earthquake (Figure 7.3.1-1) show reverse faulting along a north-south-striking nodal plane, with aftershocks indicating an intermediate dip to the west (Seeber et al., 2002). The October 7, 1983,  $m_b$  5.1 ( $E[M]$  4.84) Goodnow, New York, earthquake (Figure 7.3.1-1) also exhibits north-south-striking reverse faults dipping 60 degrees to the west (Nabelek and Suarez, 1989).

Adams and Basham (1991) report that structural complexity in the form of distributed fracturing and ring faulting within the Charlevoix impact crater may be responsible for more varied focal mechanisms within the Charlevoix RLME source. Focal mechanisms for earthquakes of magnitude  $\geq 3$  show reverse faulting, whereas smaller-magnitude earthquakes indicate some strike-slip and normal faulting, suggesting that local stress conditions may affect rupture style (Lamontagne and Ranalli, 1997). Fault plane solutions for recent small earthquakes located within the Charlevoix RLME source are predominantly thrust earthquakes on steeply dipping planes, but there are also a number of earthquakes with a significant strike-slip component, some on northwest-striking planes and some on more shallowly dipping planes (Lamontagne, 1987; Adams et al., 1989; Wetmiller and Adams, 1990). Analysis of rupture directions for two  $M$  4 earthquakes by Li et al. (1995) indicate that focal mechanisms have east-dipping planes. Bent (1992) determined a thrust mechanism for the 1925  $M_S$  6.2 ( $E[M]$  6.18) Charlevoix earthquake with a strike of  $N42^\circ \pm 7^\circ E$ , a dip  $53^\circ \pm 7^\circ$ , and rake  $105^\circ \pm 10^\circ$ , and favors a southeast-dipping solution based on observed seismicity and mapped faults. Dips for fault surfaces related to the January 11, 1986,  $M_N$  4.0 ( $E[M]$  3.40) and the March 18, 1987,  $M_N$  3.3 ( $E[M]$  2.79) earthquakes range between 42 and 59 degrees to the south (Lamontagne and Ranalli, 1997).

Future ruptures occurring in the SLR seismotectonic zone are modeled with two-thirds weight as reverse mechanisms and one-third weight as strike-slip. Given the wide variability in structural orientations and focal mechanisms, the strike of future ruptures contains northeast, northwest, north-south, and east-west alternative orientations with the following percentages: N25E (20%), N40E (20%), N70E (20%), N50W (15%), N70W (15%), N-S (5%), and E-W (5%).

Earthquakes within eastern Canada can have anomalously deep hypocenters compared to the adjacent craton. Bent and Perry (2002) relocated earthquakes in eastern Canada occurring between 1992 and 2000 and concluded that moderate-magnitude earthquakes in the Ottawa-Bonnechere graben have depths in the 11–16 km (7–10 mi.) range but may occur at variable depths in the crust. Hypocentral depths for the 1935 Timiskaming and 1944 Cornwall-Massena earthquakes are 10 and 20 km (6 and 12.5 mi.), respectively (Bent 1996a, 1996b). Bent and Perry (2002) also observed that earthquakes in the Lower St. Lawrence extend to 27 km (17 mi.) in depth. The 1988 Saguenay earthquake was anomalously deep, occurring at a depth of 28 km (17.5 mi.; Somerville et al., 1990). Based on the above information, thickness of seismogenic crust for the SLR seismic source zone is modeled with equal weights at 25 and 30 km (15.5 and 18.5 mi.).

### **7.3.2 Great Meteor Hotspot Zone (GMH)**

The Great Meteor Hotspot (GMH) seismotectonic zone lies within the Western Quebec seismic zone as defined by Adams and Basham (1991). This seismotectonic zone is characterized by moderate seismicity, including the 1975 **M** 4.2 (E[**M**] 4.17) Maniwaki and 1978 **M** 4.1 (E[**M**] 3.82) St. Donat earthquakes (Adams and Basham, 1991); the October 19, 1990, **M** 4.6 (E[**M**] 4.53) Mont-Laurier earthquake (Lamontagne et al., 1994; Du et al., 2003); and the February 10, 1914, **M<sub>L</sub>** 5.5 (E[**M**] 5.10) Saint-André-Avellin earthquake (Bent, 2009; Figure 7.3.2-1). Adams and Basham (1991) have suggested that the band of seismicity north of the Ottawa River within the Western Quebec seismic zone is due to crustal fractures that formed as the North American Plate rode over a Cretaceous hotspot (Crough, 1981).

Section 7.3.2.1.1 presents alternative hypotheses for Cretaceous volcanism, including mantle plume, lithospheric processes, and/or small convection cells. Regardless of the mechanism for Cretaceous volcanism, Sections 7.3.2.1.2 and 7.3.2.1.3 also present evidence of faulting, uplift, and geophysical anomalies associated with Cretaceous alkaline rocks. Ma and Eaton (2007) propose that seismicity of the Western Quebec seismic zone represents blind intrusions associated with entrapment of mantle-derived melt at the transition from kimberlite dikes to plutons of the Monteregian Hills. Modern seismicity may be localized along these intrusions either by weakened faults and shear zones as a result of reheating of the crust by the hotspot track, or by stress concentrations associated with the emplacement of major bodies in more felsic crust (Ma and Eaton, 2007). Elevated seismicity rates are present within Grenville-age crust that lacks Iapetan rifting but exhibits Cretaceous volcanism and reactivation, and these form the basis of the GMH seismotectonic zone.

The source characterization of the GMH seismotectonic zone is based on a review of published material that is summarized in the Data Summary table for the GMH zone (Appendix Table D-7.3.2). Explicit references and data that were used as the basis for source characteristics of GMH are identified in the Data Evaluation table (Appendix Table C-7.3.2).

### 7.3.2.1 Background

#### 7.3.2.1.1 Geological Evidence

Cretaceous volcanism in eastern Canada and New England has been attributed to intrusions along preexisting zones of weakness (McHone, 1996) and movement of the Great Meteor hotspot track (Morgan, 1983; Crough, 1981; Sleep, 1990) beneath eastern North America. (The Great Meteor hotspot is named after the Great Meteor seamount in the central Atlantic Ocean [Morgan, 1983]). Morgan (1983) attributed the age distribution of these rocks to two hotspot tracks passing through New England at different times: the Verde hotspot track at 160 Ma and the Meteor hotspot at about 120 Ma (Figure 7.3.2-2). Geologic evidence for the hotspot (see Appendix Table D-7.3.2) consists of an alignment of mapped alkalic intrusions from the Montereian Hills of Quebec (Poole, 1970) through the White Mountain magma series in New Hampshire (Zartman, 1977), the Cretaceous seamounts of offshore New England (Duncan, 1984), the Corner Rise (recorded when the Mid-Atlantic Ridge crossed over the hotspot), to the Great Meteor seamount (11–17 Ma) in the Central Atlantic (Morgan, 1983; Figure 7.3.2-2). Rock types and chronology of igneous activity related to the GMH can be summarized as follows:

- Alkaline intrusive rocks of the Montereian Hills form circular plugs with steep walls and lacoliths within a 241.5 km (150 mi.) long west-trending line between Montreal and Lake Megantic of Quebec (Poole, 1970). These intrusions range in age from 84 to 123 Ma, with many dates falling between 100 and 115 Ma (Poole, 1970).
- Alkaline rocks of the White Mountain plutonic suite were emplaced over three rather broad pulses of magmatism at 220–235 Ma, 155–200 Ma, and 95–125 Ma, but lack any regular time-transgressive pattern of ages (Zartman, 1977; Figure 7.3.2-2).
- Duncan (1984) observed that radiometric ages for dredged volcanic rocks from seven of the New England seamounts increase in age from the southeast (82.9 Ma for the Nashville seamount) to the northwest (103 Ma for the Bear seamount; Figure 7.3.2-2) and fall within a longer age progression to the Corner seamounts (70–75 Ma).
- Subsequent mapping by Heaman and Kjarsgaard (2000) extended the GMH track to the Rankin Inlet on the west side of James Bay. They identified four periods of kimberlite magmatism (at 196, 180–176, 148–146, and 142–134 Ma) along a northwest-southeast trend from Rankin Inlet through to the Attawapiskat, Kirkland Lake, and Timiskaming fields (Figure 7.3.2-2). These results support a single hotspot track.

McHone (1996) concluded that lithospheric processes were necessary to start and stop the generation of magma from the same source in the mantle. He proposed that heterogeneous source areas, coupled with tectonic reactivation of crustal structures, were required to explain the wide distribution of intrusions in space and time and the different styles of igneous activity expressed onshore and offshore. Heaman and Kjarsgaard (2000) proposed that interaction of the hotspot with thinned continental lithosphere toward the continental margin can account for the transition from kimberlitic dikes to alkaline intrusions east of Montreal. Subsequent synthesis by McHone (2000) attributes Cretaceous magmatism to shallow linear upwelling and convection following Jurassic rifting. Matton and Jebrak (2009) propose that periodic reactivation of deep-

seated preexisting zones of weakness during major stages of Atlantic tectonic evolution, combined with coeval asthenospheric upwelling due to edge-driven convection and continental insulation flow, enhanced the ascent of alkaline magmas. Shallow, small-scale upwelling during periodic structural reactivation provides a better mechanism for Cretaceous alkaline magmas than a mantle plume model (Matton and Jebrak, 2009).

#### 7.3.2.1.2 *Evidence for Reactivation*

Faure et al. (1996b) recognize two distinct phases of Cretaceous extension based on paleostress analysis of Cretaceous dike trends and regional- and mesoscopic-scale faults from the Montereian plutons that differ from regional stress fields related to opening of the Atlantic ocean (Faure et al., 2006). Paleostress analysis of Jurassic normal faults and dike trends in the Quebec and New England Appalachian Mountains distinguishes east-west- and northwest-southeast-oriented extensional stress regimes (Faure et al., 2006). Fault stress tensors indicate that most east-west to east/southeast–west/northwest–oriented stress is found in the Montreal and Gaspé area, possibly related to regional partitioning of stress along north-south-trending structures in the Champlain Lake valley and the northeast-southwest-trending structures of the St. Lawrence rift basin (Faure et al., 2006). An initial Late Triassic east-west extension related to the formation of rift basins in the Bay of Fundy and South Georgia and a later Early Jurassic east/southeast–west/northwest-oriented extension related to the central Atlantic rift system is more consistent with the two-phase rifting models for the opening of the Atlantic Ocean (Faure et al., 2006). Subsequent Cretaceous extension consists of an older widespread northeast-southwest-trending extension and a younger north-south-oriented extension restricted to the Montreal area (Faure et al., 1996b).

Northwest-southeast- to west-northwest-/east-southeast-trending normal faults trend obliquely to the Ottawa-Bonnechere graben and have stress orientations that vary between north/northeast–south/southwest near Ottawa and Montreal and east/northeast–west/southwest in southern Quebec (Faure et al., 1996b). East-west-trending normal faults are predominantly found in the Montreal area and along the axis of the Montereian Hills, have similar orientations to regional Cretaceous dikes, and have crosscutting relationships indicating they are younger than northwest-southeast-trending faults (Faure et al., 1996b). The Ottawa-Bonnechere graben and associated basement faults may have acted as localized zones of weakness in the early stage of Cretaceous extension, resulting in reorientation of the regional stress field and formation of the localized north-south-directed extension (Faure et al., 1996b). Although Faure et al. (1996b) attribute these two Cretaceous extensions to an initial northeast-southwest extension event associated with rifting between Labrador and Greenland at 140 Ma and opening of the South Atlantic at 130 Ma and a subsequent north-south-oriented extension corresponding to global fragmentation of Pangaea when Iberia separated from Newfoundland, Faure et al. (2006) recognize that the lack of Mesozoic rift basins in central New England and Quebec may be due to high topographic elevation induced by a regional thermal event.

Crough (1981) suggests that the passage of the GMH caused a 600 km (373 mi.) wide zone of epeirogeny (broad regional vertical motion) during the Cretaceous and early Tertiary in southeastern Canada and New England, resulting in erosion of at least 1 km (0.6 mi.) in Montreal and as much as 6–7 km (3.7–4.3 mi.) in New England. Recent thermochronology studies provide

evidence for epeirogeny that was accompanied by Late Cretaceous reactivation of faults. Roden-Tice et al. (2000) interpreted two periods of unroofing of the Adirondack Mountains from apatite fission-track dating that must be explained by tectonic denudation processes: Late Jurassic–Early Cretaceous (160–120 Ma) throughout the region and Early–Late Cretaceous (~110–80 Ma) in the southeast. Roden-Tice et al. (2000) support the hypothesis that this Early–Late Cretaceous uplift, contemporaneous with intrusion of the Montereian Hills plutons, can be attributed to differential unroofing resulting from reactivation normal faults. Roden-Tice and Tice (2005) attribute the widespread unroofing during the Middle Jurassic–Late Cretaceous to remnant heating from the GMH track, accommodated by extensional reactivation of faults in the Adirondack Mountains and New Hampshire. Roden-Tice, West, et al. (2009) integrate these results with apatite fission-track ages from northeastern Vermont, New Hampshire, and western Maine and conclude that normal reactivation of orogen-parallel faults accommodating northwest-southeast extension is associated with remnant heating from passage of the GMH during the Late Cretaceous.

### 7.3.2.1.3 Geophysical Evidence

A remnant thermal anomaly is inferred to exist in the upper mantle and lower lithosphere, based on several types of geophysical evidence. Travel-time inversions of teleseismic results from southern Ontario image a low-velocity corridor between 50 and 300 km (31 and 186.5 mi.) depth that crosscuts regional structures of the Grenville province (Rondenay et al., 2000). These results are attributed to a zone of contrasting thermal-compositional-anisotropic properties related to the GMH (Rondenay et al., 2000). Subsequent work by Li et al. (2003) using Rayleigh wave paths confirms the presence of a broad, low-velocity layer in the upper mantle beneath eastern New York and central New England between depths of 60 and 140 km (37 and 225 mi.). This anomaly is interpreted as the lateral contrast between relatively thick lithosphere beneath western New York and Pennsylvania and the warm asthenosphere beneath the thinned New England lithosphere, caused by thermal erosion associated with the Cretaceous hotspot (Li et al., 2003). Crustal thickness and average P-wave and S-wave velocity ( $V_p/V_s$ ) ratio maps derived from teleseismic receiver functions illustrate thin crust (Figure 7.3.2-3) and variable  $V_p/V_s$  ratio northeast of the Ottawa-Bonnechere graben coincident with the Western Quebec seismic zone (Eaton et al., 2006), possibly indicating mafic intrusions within felsic crust (Ma and Eaton, 2007).

### 7.3.2.2 Basis for Defining Seismotectonic Zone

Ma and Eaton (2007) recognize that seismicity cannot be easily correlated with Grenville or Iapetan structures within this zone and conclude that the GMH provides the only compelling explanation for seismicity within the Western Quebec seismic zone. Seismicity may result from either weakened crust caused by reheating or from stress concentrations caused by strength contrasts between mafic and felsic crust (Ma and Eaton, 2007), as indicated by the variable  $V_p/V_s$  observed by Eaton et al. (2006). Crust of the GMH seismotectonic zone is distinguished from the adjacent craton on the basis of Cretaceous volcanism and extension, meeting the criterion for separating crust of the GMH on the basis of maximum earthquake magnitude. GMH crust lacks Iapetan-age faulting and the repeated reactivation expressed within the St. Lawrence rift (SLR)

seismotectonic zone (Section 7.3.1). Additionally, the earthquakes within this seismotectonic zone have a depth distribution similar to the SLR seismotectonic zone. However, earthquakes of the GMH seismotectonic zone exhibit thrust mechanisms with predominantly northwest-striking nodal planes, whereas those of the SLR seismotectonic zone generally exhibit greater variability in the strike of nodal planes and a component of strike-slip faulting. Earthquakes of the Northern Appalachian and Extended Continental Crust–Atlantic Margin seismotectonic zones have shallower depth distributions than the GMH zone.

### 7.3.2.3 Basis for Zone Geometry

The GMH seismotectonic zone lies within the Western Quebec seismic zone, as defined by Adams and Basham (1991), who recognized two distinct bands of seismicity within the Western Quebec zone. One band trends west-northwest along the Ottawa River between Ottawa and Lake Timiskaming, is associated with rift faults of the Ottawa-Bonnechere graben, and is interpreted to be part of the SLR seismotectonic zone (Section 7.3.1). The second band trends north-northwest, extends from Montreal to the Baskatong Reservoir, and is attributed to crustal fracturing associated with the passage of a Cretaceous hotspot track. Ma and Eaton (2007) propose that seismicity of the Western Quebec seismic zone represents blind intrusions associated with entrapment of mantle-derived melt at the transition from kimberlite dikes to plutons of the Montereian Hills. The geometry for the GMH source zone is adopted from the Gatineau (GAT) source zone of the GSC H model (Adams et al., 1996; Adams and Halchuk, 2003) and was compared to data sets listed in the Data Evaluation table (Appendix Table C-7.3.2). Given the uncertainty in a plume model as a mechanism for the cause of Cretaceous volcanism presented in Section 7.3.2.1.1, alternative geometries based on segments of the proposed hotspot track were not considered in the CEUS SSC model.

The geometry of the GMH zone is consistent with a region of thinner crust northeast of the Ottawa-Bonnechere graben observed by Eaton et al. (2006) and with the progressive change from kimberlitic melts in the interior of the craton to more voluminous crustal magmatism as the hotspot interacted with a progressively thinner lithosphere (Ma and Eaton, 2007). Earthquakes of the Kapuskasing cluster, located 100 km (62 mi.) northwest of the zone and separated by an aseismic area, have focal depths (4–20 km [2.5–12.4 mi.]; Figure 7.3.2-3) and mechanisms (reverse with northwest-striking nodal planes) located along strike of the kimberlite dike portion of the hotspot track (Ma et al., 2008). Adams and Basham (1991) postulate that elevated rates of seismicity in western Quebec are due to thermally stressed and fractured crust, whereas plutonism in New England may have healed deep crustal fractures. Therefore, the geometry for the GMH seismotectonic zone encompasses the volume of crust likely to produce frequent moderate earthquakes associated with thermally stressed crust. Gravity and magnetic maps do not correlate well with seismicity and seismogenic structures (Figure 7.3.2-4) given that the mechanisms for earthquakes associated with the GMH track involve thermal weakening.

### 7.3.2.4 Basis for Zone Mmax

No paleoseismic investigations have been performed within the GMH seismotectonic zone. A paleoseismic study conducted by Aylsworth et al. (2000; Figure 7.3.2-1), located south of the

GMH within the SLR seismotectonic zone (Section 7.3.1.3), provided evidence for two moderate- to large-magnitude paleoearthquakes in the Holocene. Subsequent trenching by Aylsworth and Lawrence (2003) documented lateral spreading, surface subsidence, and sediment deformation occurring at 7,060 yr BP. As discussed in Section 7.3.1.3, additional research is required to constrain the location and magnitude of earthquakes causing this deformation. Ma and Eaton (2007) observe that the Mont-Laurier earthquake clusters are located near the paleoseismic investigations along the Ottawa River documented by Aylsworth et al. (2000) and Aylsworth and Lawrence (2003) and may represent persistent aftershocks of past large earthquakes. The maximum observed earthquake for the GMH seismotectonic zone is therefore derived from historical and instrumental earthquakes. The largest observed earthquake within the zone is the February 1914 E[M] 5.10 Saint-André-Avellin earthquake.

Kanter (1994) classified crust of the GMH seismotectonic zone as exposed middle Proterozoic non-extended crust. However, as described above, Cretaceous uplift (Roden-Tice and Tice, 2005; Roden-Tice, West, et al., 2009) and Cretaceous mesoscopic-scale normal faulting (Faure et al., 1996) provide evidence for Mesozoic extension. Therefore, the maximum magnitude distribution for this zone was determined by applying the likelihood function based on the largest observed earthquake to the Mesozoic and younger prior distribution.

#### 7.3.2.5 Future Earthquake Characteristics

The GMH has been associated with clusters of midcrustal seismicity by Ma and Eaton (2007). Ma and Atkinson (2006) attribute the wide hypocentral depth distribution (2–25 km [1.2–15.5 mi.]) for relocated earthquakes in the Western Quebec seismic zone to faults of through-going crustal extent or faults of varying depths in the crust. Ma and Atkinson (2006) also note that the clustering of focal depths at 5, 8, 12, 15, and 22 km (3, 5, 7.5, 9.3, and 13.7 mi.) may reflect layering related to different seismogenic properties within the crust. Ma and Eaton (2007) report that shallow earthquakes with relocated depths less than 8 km (5 mi.) are randomly distributed, with reverse mechanisms that can be attributed to glacial isostatic adjustment. Ma and Eaton (2007) also note that earthquakes with intermediate depths define a linear band of earthquakes, and deep earthquakes (greater than 17 km [10.5 mi.] in depth) are localized as clusters at Maniwaki and Mont-Laurier. Focal depths for this deep zone extend to 30 km (18.5 mi.; CEUS SSC Project earthquake catalog). Seismogenic thickness for the GMH seismotectonic zone is modeled with equal weight for 25 and 30 km (15.5 and 18.5 mi.).

Earthquakes within the GMH seismotectonic zone exhibit reverse mechanisms. Bent et al. (2003) observe that focal mechanisms can be classified as either thrust or oblique-thrust in response to northeast compression. Ma and Eaton (2007) note that these reverse mechanisms have southwest-trending P-axes that change to east-west-trending P-axes in the southern portion of the zone. Bent (1996a) acknowledges that interpreting which nodal plane for mechanisms within the Western Quebec seismic zone corresponds to the fault plane is ambiguous, given that seismicity trends northwest and some mapped structures trend northeast. Mechanisms in the southern part of the Western Quebec seismic zone, corresponding to the Ottawa graben of the SLR seismotectonic zone, display more variability in strike and exhibit more strike-slip behavior (Bent, 1996a) compared to mechanisms of the GMH seismotectonic zone. Lamontagne et al.

(1994) determined a steeply north-dipping, east-west-oriented nodal plane with a reverse mechanism for the October 19, 1990, Mont-Laurier earthquake. Du et al. (2003) observe that mechanisms for earthquakes in the Western Quebec seismic zone have strikes of one of their nodal planes parallel to the general trend of seismicity. Future ruptures are modeled as 100 percent reverse faulting. The strike of ruptures is modeled with three orientations consisting of N50W (0.4), N20W (0.4), and EW (0.2). The dip of ruptures consists of the default characteristics for both styles. Ruptures are allowed to extend beyond the zone boundary. These characteristics are presented in Table 5.4.2.

### **7.3.3 Northern Appalachian Zone (NAP)**

The Northern Appalachian (NAP) seismotectonic zone (Figures 7.3.3-1 and 7.3.3-2), which is characterized by moderate-magnitude, shallow seismicity (Adams et al., 1995), contains crust assembled outboard of the Laurentian margin in the Taconic, Salinian, and Acadian orogenies and deformed by these events and the subsequent Alleghanian orogeny and Mesozoic extension associated with opening of the Atlantic Ocean (see the data summary in Appendix Table D-7.3.2). This seismicity occurs above the continental margin within crust of Appalachian terranes (Spencer et al., 1989).

#### **7.3.3.1 Background**

##### **7.3.3.1.1 Geological Evidence**

Crust of the NAP seismotectonic zone postdates Iapetan rifting. The late Cambrian–Middle Ordovician Penobscottian orogeny amalgamated composite terranes within arcs of the Iapetus Ocean (Murphy and Keppie, 2005). These magmatic arcs, which developed in the late Cambrian within the Theic Ocean, were obducted to the Laurentian margin during the Middle–Late Ordovician Taconic orogeny (Faill, 1997a; Moench and Aleinikoff, 2003). This deformation produced north-south- to northeast-southwest-trending reverse conjugated brittle faults under a pure compressional stress regime late in the development of the orogeny (Faure et al., 2004). This Taconic compressional event also resulted in reactivation of Iapetan faults in the SLR seismotectonic zone as east-northeast/west-southwest dextral and northwest-southeast sinistral faults (Rocher et al., 2003; Faure et al., 2004).

The Late Ordovician–Silurian Salinic orogeny accreted the Gander, Avalon, Nashoba, and Carolina terranes to Laurentia during the closing of the Iapetus Ocean during the Laurentia–Avalonia collision (Murphy and Keppie, 2005). Silurian metamorphism (430–410 Ma) in the northern Appalachian Mountains is attributed to retrograde metamorphism following the main compression event (Tremblay and Castonguay, 2002). Compression of the Salinian orogeny involved southeast-directed transport of the Taconian crustal wedge followed by normal faulting (Saint-Joseph and Baie Verte–Brompton faults) and development of the fault-bounded sedimentary basins of the Connecticut Valley–Gaspé trough (Tremblay and Castonguay, 2002). Tremblay and Pinet (2005) attribute the late-stage extension to supracrustal extensional collapse caused by late-stage delamination of the lithospheric mantle in a southeast-dipping subduction zone.

The Devonian Acadian orogeny has been attributed to either the collision of Avalonia with Laurentia or the accretion of the Meguma terrane; however, recent work indicates that the Meguma terrane is the passive margin on the southern margin of Avalonia (Murphy and Keppie, 2005). Murphy and Keppie (2005) interpreted the Acadian orogeny as forming along an Andean-type margin that possibly overrides a plume and swell. Acadian metamorphism is well dated as 385–375 Ma in the southern part of the Dunnage zone (Tremblay et al., 2000). Deformation from the Acadian orogeny is expressed as east-southeast/west-northwest compression in a transpressional regime producing east-northeast/west-northwest dextral and northwest-southeast sinistral strike-slip faults that crosscut Taconian thrust faults in the Appalachian Mountains of Quebec and New Brunswick (Faure et al., 2004). This deformation also resulted in reactivation of Iapetan structures in the SLR seismotectonic zone (Faure et al., 2004; Rocher et al., 2003).

There is general consensus that the late Carboniferous–Permian Alleghany orogeny was due to terminal collision between Gondwana and Laurentia-Baltica that closed the Rheic Ocean and resulted in the formation of Pangaea (Murphy and Keppie, 2005). The Alleghanian orogeny produced decollement tectonism in the central and southern Appalachian Mountains along with early penetrative shortening, late low-angle thrusts, low-grade metamorphism, and transpressional shear zones. Rocks of the northern Appalachians exhibit relatively high-grade metamorphism of Taconic and Acadian crust and deformation of Appalachian deposits near the Hudson Valley (Faill, 1998). Although no structures within the northern Appalachians have been unequivocally assigned to Alleghanian deformation, brittle faults of the northern Appalachians exhibit three phases of compression: an early north-northwest/south-southeast compression, a north-northeast/south-southwest compression, and a late west-northwest/east-southeast compression (Faure et al., 1996a).

Mesozoic rifting resulted in the breakup of Pangaea. This rifting is associated with the separation of the North American and African plates and produced rift basins along the Atlantic seaboard that are situated landward of the hinge zone of the continental margin. This landward region experienced considerably less crustal thinning than did the region seaward of the hinge zone that includes the deeper marginal sedimentary basins (Klitgord et al., 1988). Faure et al. (2006) identified two phases of extension: an initial Late Triassic east-west extension related to the formation of rift basins in the Bay of Fundy and South Georgia, and Early Jurassic east-southeast/west-northwest extension related to the central Atlantic rift system.

Apatite fission-track ages across the Norumbega fault zone in southern coastal Maine reveal a 30–50 Myr discontinuity, suggesting that this fault shows 2 km (1.2 mi.) of vertical offset in the Late Cretaceous (West and Roden-Tice, 2003). Roden-Tice and Tice (2005) attribute the widespread unroofing during the Middle Jurassic–Late Cretaceous, accommodated by northwest-southeast extensional reactivation of faults in the Adirondack Mountains and New Hampshire, to remnant heating from the Great Meteor hotspot track.

#### 7.3.3.1.2 *Geophysical Data*

Refraction studies across northern New England image crust between 36 and 40 km (22 and 25 mi.) thick from Maine to Vermont (Hughes and Luetgert, 1991; Taylor and Toksöz, 1982), to 44 km (27 mi.) thick in New Brunswick and southeastern Quebec (Taylor and Toksöz, 1982).

Regional seismic profiles of the Quebec-Maine transect image normal faults in the passive margin beneath the master decollement overlain by the St. Lawrence platform and allochthonous continental margin sediments and volcanics accreted during the Taconic orogeny (Stewart et al., 1993). These normal faults do not appear to extend east of the Baie Verte–Brompton line (Stewart et al., 1993).

#### 7.3.3.1.3 Seismicity

Various special studies provide better constraints for historical earthquakes: Leblanc and Burke (1985) determined the location for the March 21, 1904,  $m_{bLg}$  5.9 (E[**M**] 5.73) Passamaquoddy Bay earthquake and three other earthquakes. Burke (2004) revised magnitudes and locations for historical earthquakes within the Central Highlands, Moncton, and Passamaquoddy Bay subzones. He also later provided complete documentation, with felt areas, for all historical earthquakes in New Brunswick (Burke, 2009). Ruffman and Peterson (1988) researched historical earthquakes in Nova Scotia under contract with the Geological Survey of Canada and provided lists of new and fictitious earthquakes. Unfortunately, this study did not provide intensity or felt-area information for determining magnitudes and locations of historical earthquakes, and it could be improved upon with further research.

Ebel (1996) reviewed felt reports in Trois Rivières, Quebec, and Boston, Massachusetts, for the June 11, 1638, earthquake and placed the epicenter within the seismically active part of central New Hampshire with a magnitude of  $6.5 \pm 0.5$  (E[**M**] 5.32). Ebel et al. (1986) analyzed historical seismograms for two earthquakes occurring in December 1940 near Ossipee, New Hampshire: the December 20  $M_L$  5.3 (E[**M**] 5.08) and December 24  $M_L$  5.4 (E[**M**] 5.13) earthquakes. Instrumental seismicity consists of small- to moderate-magnitude earthquakes, including the January 19, 1982,  $M_C$  4.7 (E[**M**] 4.23) Gaza, New Hampshire, earthquake (Brown and Ebel, 1985) and the January 9, 1982,  $m_{bLg}$  5.7 (E[**M**] 5.47) Miramichi earthquake (Wetmiller et al., 1984).

#### 7.3.3.2 Basis for Defining Seismotectonic Zone

Crust of the NAP seismotectonic zone postdates Iapetan rifting and therefore should be excluded from the SLR and PEZ seismotectonic zones. Terranes of this zone formed outboard of the Laurentian margin after Iapetan rifting and were subsequently accreted to the passive margin. Normal faulted basement underlying the Taconic master decollement (St. Julien and Hubert, 1975; Spencer et al., 1989) exhibits an echelon normal faults associated with development of the Iapetan passive margin as interpreted from seismic profiles (Spencer et al., 1989). These normal faults are depicted at the base of the allochthonous continental margin sediments northwest of the Baie Verte–Brompton line. This crust is included within the SLR seismotectonic zone (Section 7.3.1).

Crust of the NAP seismotectonic zone formed in the Paleozoic and experienced multiple phases of extension, including normal faulting in the late stages of the Salinian orogeny (Tremblay and Castonguay, 2002) and extensional reactivation of both the Ammonoosuc fault in the Mesozoic (Moench and Aleinikoff, 2003) and the Norumbega fault zone in the Late Cretaceous (Stewart et

al., 1993; West and Roden-Tice, 2003). Therefore, the NAP seismotectonic zone meets the criterion for application of a Mesozoic and younger prior distribution for maximum earthquake magnitude. Crust of the NAP seismotectonic zone is separated from the Extended Continental Crust–Atlantic Margin (ECC-AM) seismotectonic zone on the basis of lack of Alleghanian structure and Mesozoic rift basins.

The style of extension within the NAP seismotectonic zone differs from the ECC-AM seismotectonic zone (Section 7.3.7) by exhibiting a lack of fault-bounded rift basins. This difference has been attributed to Early Jurassic pluton emplacement associated with the White Mountain magma series in central New England, which created a topographic high that resisted extension (Faure et al., 2006). Roden-Tice, West, et al. (2009) attribute this topographic elevation to regional unroofing during the Cretaceous. Additionally, fault rupture characteristics for the NAP seismotectonic zone are predominantly reverse (Du et al., 2003; Bent et al., 2003), and seismicity of the NAP seismotectonic zone occurs in the upper 10 km (6 mi.) of the crust.

### 7.3.3.3 Basis for Zone Geometry

The geometry for the NAP seismotectonic zone is modified from the Northern Appalachians source zone of the GSC (Adams et al., 1996; Adams and Halchuk, 2003). Adams et al. (1995) characterized this source zone for use in Canadian seismic hazard maps (Adams et al., 1996; Adams and Halchuk, 2003) as extending from the landward limit of Mesozoic extensional faulting to the seaward limit of thinned Grenville crust of the Iapetan passive margin. The northwestern boundary of NAP coincides with the Baie Verte–Brompton line of Moench and Aleinikoff (2003) to restrict Iapetan normal faults below the Taconic decollement to the SLR seismotectonic zone. The southeastern boundary follows the Cobequid-Chedabucto fault system in Nova Scotia (Pe-Piper and Piper, 2004) and the northern limit of the Fundy Basin and Gulf of Maine along coastal Maine (Klitgord et al., 1988), which exhibit clear Mesozoic activity. The southwestern boundary was drawn to exclude the Hartford basin, which falls within the ECC-AM seismotectonic zone. The northeastern boundary of the NAP seismotectonic zone follows the project boundary.

### 7.3.3.4 Basis for Zone Mmax

As part of the EPRI study on earthquakes of stable continental regions, Kanter (1994) classified crust of the NAP seismotectonic zone as exposed Paleozoic non-extended crust. However, as described above, the NAP seismotectonic zone has experienced several contrasting stress regimes, including several phases of extension: Cambrian growth faulting beneath the master decollement (St. Julien and Hubert, 1975; Stewart et al., 1993; Spencer et al., 1989); normal faulting in the late stages of the Salinian orogeny (Tremblay and Castonguay, 2002); extensional reactivation of the Ammonoosuc fault in the Mesozoic (Moench and Aleinikoff, 2003); and recurring movement along the Norumbega fault zone (Stewart et al., 1993; West and Roden-Tice, 2003). Because extension has occurred since the Mesozoic, the maximum magnitude distribution for this zone was determined by applying a Mesozoic and younger extension prior, updated by a likelihood function based on the largest observed earthquake.

There is some uncertainty about the largest observed earthquake within the NAP seismotectonic zone. The largest observed earthquakes include the March 21, 1904, E[M] 5.73, followed by the June 11, 1638, E[M] 5.32 and December 24, 1940, E[M] 5.6 earthquakes. There is also some possibility that the largest observed earthquake in the ECC-AM seismotectonic zone (1755 E[M] 6.10 Cape Ann earthquake) applies to the NAP seismotectonic zone. Bakun et al. (2003) have a preferred location for the 1755 E[M] 6.10 Cape Ann earthquake near the boundary between ECC-AM and NAP, with the area defining 95 percent confidence level for the earthquake location spread across both seismotectonic zones. Ebel (2006a) estimates the location within ECC-AM farther southeast than the Bakun et al. (2003) location based on attenuation of felt effects. Therefore, the probability that the 1755 Cape Ann earthquake modifies the prior for the NAP seismotectonic zone is assigned a weight of 0.4. The resulting Mmax distributions are presented in Section 7.4.2.

### 7.3.3.5 Future Earthquake Characteristics

As noted by Adams et al. (1995), all earthquakes in the NAP seismotectonic zone with known depths are relatively shallow (less than 10 km, or 6 mi.), the prime example being the Miramichi earthquake sequence of 1982 (Wetmiller et al., 1984). Ebel et al. (1986) determined depths of 8 km (5 mi.) for both 1940 earthquakes. Relocating depths of earthquakes within the NAP seismotectonic zone has not been as active an area of research as other seismically active regions of Eastern Canada and the northeastern United States. The default depth distribution as described in Section 5.4 is applied to the NAP seismotectonic zone.

Ebel and Bouck (1988) present focal mechanisms for small to moderate earthquakes occurring in New England between 1981 and 1987. These mechanisms are predominantly reverse with a component of strike-slip. These mechanisms have variable strike directions, including northeast-southwest, northwest-southeast, north-south, and east-west. Synthetic seismograms for the December 20, 1940, Ossipee earthquake provide evidence for a predominantly thrust mechanism with either a north-south- or east-west-striking nodal plane (Ebel et al., 1986). Bent et al. (2003) observe a combination of thrust and strike-slip faulting in mechanisms for the July 14, 1994, and July 15, 1998, New Brunswick earthquakes. Bent et al. (2003) do not observe a consistent trend in stress axes orientation. Both solutions exhibit one west-southwest- to west-striking plane (Bent et al., 2003)—and the 1994 earthquake has one near north-south nodal plane. The June 16, 1995, Lisbon, New Hampshire,  $M_w$  3.7 (E[M] 3.17) and August 21, 1996, Berlin, New Hampshire,  $M_w$  3.4 (E[M] 3.45) earthquakes have predominantly reverse mechanisms with northwest-striking nodal planes. The Lisbon earthquake contains an oblique component (Du et al., 2003). Future ruptures within the NAP seismotectonic zone are modeled with 1/3 weight as strike-slip and 2/3 weight as reverse with default dip characteristics. The distribution for rupture strike is modeled as N50W (20%), NS (20%), N35E (40%), N60E (10%), and EW (10%).

### 7.3.4 Paleozoic Extended Crust (PEZ)

The concept that extended crust may have different seismogenic characteristics (i.e., maximum magnitude and related moment rate) than non-extended or Precambrian rifted crust in SCRs has been applied to the identification and characterization of regional seismic source zones. Based on

a global analysis of earthquakes in SCRs, Johnston et al. (1994) concluded that zones of rifted crust in SCRs exhibit a higher rate of seismic activity, normalized to a given unit area of crust, than nonrifted crust and Precambrian rifts; these zones also have different maximum magnitude priors (see discussion in Section 5.2).<sup>2</sup> This interpretation by Johnston et al. (1994) resulted in efforts to characterize the limit of early Paleozoic (Iapetan) extension within the craton in the CEUS by defining the margin of Iapetan rifting. As characterized by Wheeler (1995), the Iapetan rifted margin (IRM) encompasses that portion of continental crust that includes known and inferred normal faults that formed parallel to the passive margin of Laurentia during the late Proterozoic–early Paleozoic opening of the Iapetus Ocean. Compressional reactivation of favorably oriented Iapetan faults has been suggested as the causal mechanism for several seismically active regions in eastern North America, including Giles County, Virginia, and eastern Tennessee (Bollinger and Wheeler, 1988; Wheeler, 1995; Powell et al., 1994). Adams et al. (1995) observe that seismicity of the IRM is largely expressed as reverse-slip faulting mechanisms in Canada and strike-slip mechanisms in the United States. The IRM concept is incorporated in source characterization for the national seismic hazard maps for the United States (Petersen et al., 2008) and Canada (Adams et al., 1995).

For the CEUS SSC Project, crust of the IRM source zone of Wheeler (1995) and Adams et al. (1995) has been divided into the St. Lawrence rift (SLR; Section 7.3.1); Northern Appalachian (NAP; Section 7.3.3); and Paleozoic Extended Crust (PEZ; this section) seismotectonic zones according to geologic criteria established by this project for separating crust on the basis of Mmax and future earthquake characteristics. The following discussion addresses the geologic, geophysical, and seismic characteristics of the PEZ seismotectonic zone (Figure 7.3.4-1). This discussion, as well as the seismic source characterization of the PEZ, is based on a review of published material, summarized in the Data Summary table for the PEZ (Appendix Table D-7.3.4). Explicit references and data that were used as the basis for source characteristics of PEZ are identified in the Data Evaluation table (Appendix Table C-7.3.4).

#### 7.3.4.1 Background

As discussed in Section 7.3.1.1, breakup of the Mesoproterozoic supercontinent of Rodinia occurred as diachronous rifting along the margins of Laurentia. Rifting began on the western margin of Laurentia between 780 and 680 Ma during opening of the paleo-Pacific Ocean, and resulted in the separation of Australia, Antarctica, south China, and Siberia from Laurentia (Whitmeyer and Karlstrom, 2007). This event also resulted in failed rifting along the eastern margin of Laurentia (Whitmeyer and Karlstrom, 2007), as evidenced by both the continental rift-facies volcanic Mount Rogers Formation of the Virginia/North Carolina Blue Ridge and the largely nonvolcanic Ocoee rift deposits farther to the southwest (Faill, 1997a). Successful rifting of the eastern margin of Laurentia occurred between 620 and 550 Ma and culminated in the rifting of the Argentina Precordillera terrane from the Ouachita embayment (Whitmeyer and Karlstrom, 2007). This second phase of rifting is recorded by the volcanic rocks of the Catoclin

---

<sup>2</sup> As discussed in Section 5.2, analysis of the updated worldwide data set completed for this study suggests that crust extended during the Paleozoic cannot be differentiated from non-extended or Precambrian rifted crust and that the more statistically significant difference is between Mesozoic and younger crust and older extended/nonextended crust.

Formation; sedimentary clastics of the Chilhowee group of Virginia, Maryland, and Pennsylvania (Faill, 1997a); and lavas, dikes, and intrusions formed along the eastern margin of Laurentia extending north to Labrador (Kumarapeli et al., 1988; Kamo et al., 1995; Higgins and van Breemen, 1998; McCausland and Hodych, 1998; Bédard and Stevenson, 1999; Walsh and Aleinikoff, 1999; Hodych and Cox, 2007). Within the PEZ seismotectonic zone, these events occurred 758 Ma for the Mount Rogers Formation and 564 Ma for the Catoclin rift (Aleinikoff et al., 1995; Figure 7.3.4-1).

The IRM is expressed as promontories and embayments defined by northeast-striking normal faults and northwest-striking transform faults along the margins of Laurentia (Thomas, 1991; 2006; Lavoie et al., 2003). The Peters Creek Formation of southeastern Pennsylvania and northern Maryland (Figure 7.3.4-1) may represent deposits transported along an Iapetan rift-related transform fault linking the southern Lynchburg rift basin with a comparable rift basin in southern New England (Valentino and Gates, 1995). The IRM influenced the location of salients and angular recesses during subsequent Appalachian orogenesis and Atlantic rifting (Thomas, 2006). A master detachment separates overthrust Paleozoic Appalachian terranes from the relatively intact continental crust of North America that includes IRM structures (Spencer et al., 1989; Cook et al., 1979; McBride et al., 2005). In the southern Appalachians, the Consortium for Continental Reflection Profiling (COCORP) seismic-reflection data in Tennessee and Georgia show the master detachment to be ~6 km (3.5 mi.) deep at the western flank of the Appalachians and ~10 km (6 mi.) deep in the Piedmont zone, then quickly steepening to ~35 km (22 mi.) deep beneath the peri-Gondwanan Carolina terrane to the east, where it merges with the Moho (Cook et al., 1979; McBride et al., 2005).

The western extent of significant extensional structures associated with the IRM is not well defined. The IRM exhibits some tectonic inheritance from Grenville structures. For example, the trace of the Alabama-Oklahoma transform corresponds to the probable location of a large-scale dextral bend in the Grenville front that subsequently localized the Ouachita salient and Mississippi embayment (Thomas, 2006). The New York–Alabama (NY-AL) lineament represents a crustal-scale right-lateral strike-slip fault that may have formed during either a late postcontractual stage of the Grenville orogeny, Iapetan rifting, or Appalachian orogenesis (Steltenpohl et al., 2010). The NY-AL lineament locally parallels and coincides with linear fault segments that border the Rome trough (Steltenpohl et al., 2010). Rift-parallel graben systems of the Rome trough formed inboard from the rifted margin during late synrift extension (Thomas, 2006) and may represent inboard extension of Iapetan rifting along the Mesoproterozoic East Continent rift basin (Drahovzal, 1997; Stark, 1997). It appears that a part of the fault along the southern margin of the trough was reactivated as a normal fault that underwent west-side-down dip-slip displacement during the formation of the Rome trough (Steltenpohl et al., 2010). To the north, crust northwest of the NY-AL lineament appears to have behaved as a coherent block (Steltenpohl et al., 2010). The Michigan basin experienced late Cambrian–Early Ordovician subsidence that evolved into different styles and geometry of subsidence in response to subsequent Appalachian tectonic events, indicating that Iapetan rifting did not affect the Michigan basin (Howell and van der Pluijm, 1999).

The following subsections present geologic and seismic information for zones of elevated seismicity within the continental crust of the PEZ seismotectonic zone.

### 7.3.4.1.1 Giles County, Virginia, Seismic Zone (GCVSZ)

Earthquake foci at Giles County in southwestern Virginia define a tabular zone that strikes N44°E and dips steeply to the southeast within Precambrian basement lying beneath Appalachian thrust sheets (Bollinger and Wheeler, 1983, 1988). This zone, referred to as the Giles County, Virginia, seismic zone (GCVSZ), is about 40 km (25 mi.) long, 10 km (6 mi.) wide, and 5–25 km (3–15.5 mi.) deep (Bollinger and Wheeler, 1982, 1983; Bollinger et al., 1991). The zone is oriented about 20 degrees counterclockwise from the east-northeasterly trend of the overlying structures in the Valley and Ridge province and subparallel to the northeasterly trend of the central Appalachian structures in the northern part of the state (Bollinger et al., 1991).

Possible differential uplift of Tertiary and younger New River fluvial terraces in southwestern Virginia in the area of the GCVSZ has been postulated as resulting from movement on a series of small faults exposed in the terraces (i.e., the high-angle Pembroke faults of Law et al., 1993). The location and relative displacement of the Pembroke faults is consistent with orientation of the GCVSZ and principal-stress estimates from focal-mechanism studies (Mills, 1986). The Pembroke faults and a broad antiformal fold exposed in unconsolidated fluvial deposits have raised questions about the possibility of surface tectonic faulting that may be related to seismic activity in this region (Bollinger et al., 1992; Law et al., 1993; Robinson et al., 1993). The age of the deformed sediments, which lie at 55 m (180 ft.) above the current level of the New River, is estimated as  $1.5 \pm 0.4$  Ma or  $2.0 \pm 0.4$  Ma based on analysis of cosmogenic  $^{26}\text{Al}$  and  $^{10}\text{Be}$  present in the deposits (Granger et al., 1997; Law et al., 1998). Therefore, the age of this deformation, whether tectonic or nontectonic in nature, is latest Pliocene to Pleistocene.

The east-northeast-/west-southwest-trending antiform in these sediments extends over a horizontal distance of at least 95 m (312 ft.) from limb to limb and plunges 70 degrees toward N64°E. Two grabens are associated with the antiform, one in the hinge zone and one on the south-southeast-dipping limb. The grabens are downward-narrowing structures defined by at least five extensional faults having apparent dip-slip offsets of 1–2.8 m (3.3–9.2 ft.). These faults are marked by 10–20 cm (4–7.8 in.) wide zones of clay-rich infilling. Based on the orientation of striae on surfaces within the fault zones, displacements of 11.4 m (37.4 ft.), 1.84 m (6 ft.), 1.1 m (3.6 ft.), and 3 m (9.8 ft.) are indicated for four of these faults. Judging from electrical resistivity surveys, the major graben is a linear feature that can be traced for a distance of 100–130 m (300–400 ft.). Recent geophysical investigations (Robinson et al., 1993), however, have not been successful in imaging anything below a depth of approximately 35 m (115 ft.), and thus the downdip extent of these structures is unknown. Law et al. (1994) presented three models to explain the formation of the fold and fault structures at this site: landsliding, solution collapse, and basement faulting of tectonic origin. Although some researchers have noted that the correlation between surface faults and subdetachment seismogenic structures may be tenuous or completely lacking (e.g., Chapman and Krimgold, 1994), Law et al. (1994, 1997) concluded from a review of the available data and interpretations that a tectonic origin cannot be ruled out.

Additional geophysical and subsurface investigations of these structures provide further constraints on the origin of the fold and faults. Robinson et al. (2000) show that voids occurring in the terrace sediments may result from cavity collapse in the underlying limestone, and that no

features occur in the limestone basement that correspond to the fold and graben structure in the terrace deposits. Williams et al. (2000) map a linear depression in the limestone bedrock surface that corresponds to the graben in the terrace deposits, and note that the fold and graben structure has a linear nature that is not consistent with a subcircular sinkhole. Law et al. (2000) show that the nature of fine structure in some of the terrace deposits is consistent with sedimentation in a depression formed by limestone solution, followed by inversion to form the anticlinal structure.

These observations appear to indicate that some or all of the observed deformation is nontectonic in origin. Additional surficial mapping by Anderson and Spotila (2001) of fractures in bedrock outcrops shows that the orientation of many small fractures is not consistent with topography or with karst-related subsidence. Anderson and Spotila (2001) note that one set of northeast-trending fractures crosscuts the regional structural trend, is oriented consistent with the trend of the underlying seismic zone, and may be a surface manifestation of rupture in the seismic zone. None of the field evidence, however, provides any direct evidence for Quaternary displacement on these fractures.

#### 7.3.4.1.2 *Eastern Tennessee Seismic Zone (ETSZ)*

The Eastern Tennessee seismic zone (ETSZ) is a well-defined, northeasterly trending belt of seismicity, 300 km (186 mi.) long by less than 100 km (62 mi.) wide, within the Valley and Ridge and Blue Ridge physiographic provinces of eastern Tennessee and parts of North Carolina, Georgia, and Alabama (Johnston et al., 1985; Bollinger et al., 1991; Powell et al., 1994; Chapman et al., 2002). This area is one of the most active seismic regions in eastern North America in terms of the rate of small (i.e.,  $M < 5$ ) earthquakes.

The earthquakes are spatially associated with major potential field anomalies (King and Zietz, 1978; Johnston et al., 1985; Bollinger et al., 1991; Powell et al., 1994; Kaufmann and Long, 1996; Vlahovic et al., 1998; Chapman et al., 2002). For example, the western margin of the ETSZ is associated with a prominent gradient in the total intensity magnetic field marking the NY-AL lineament (Chapman et al., 2002). Alternative structural models have also been postulated to explain the association of seismicity with these anomalies. Powell et al. (1994) proposed that the ETSZ is an evolving seismic zone in which slip on north- and east-striking surfaces is slowly coalescing into a northeast-trending strike-slip zone running along or near the northwest boundary of the Ocoee block in eastern Tennessee. Strike-slip motion would be consistent with both the sharp nature of this boundary, as inferred from its magnetic signature, and the orientation of the boundary in the contemporary stress field. Powell et al. (1994) suggested that the ETSZ seismic activity results from the regional stress field, and the activity is coalescing near the juncture between a relatively weak, seismogenic block (the Ocoee block of Johnston et al., 1985) and the relatively strong crust to the northwest, which may be strengthened by mafic rocks associated with an inferred Keweenaw-age rift (1,100 Ma; Keller et al., 1982). Powell et al. (1994) also noted that the densest seismicity and the largest of the instrumentally located epicenters in the ETSZ generally lie close to and east of the NY-AL magnetic lineament between latitudes 34.3°N and 36.5°N, and west of the Clingman magnetic lineament.

Based on detailed analyses of the pattern and focal mechanisms of earthquakes in the ETSZ, Chapman (1996) and Chapman et al. (1997) present a more refined picture of the nature of

faulting in the region. Using a revised velocity structure model (Vlahovic et al., 1996), focal mechanisms and hypocentral locations were updated. Statistical analysis of trends in the earthquake focal mechanisms suggests that earthquakes occur primarily by left-lateral strike-slip on east-west-trending faults, and to a lesser degree by right-lateral slip on north- and northeast-trending faults. The hypocenters suggest that possible east-west-trending fault sources are up to 50–100 km (31–62 mi.) long and lie east of, but adjacent to, the NY-AL lineament. This more refined picture is consistent with a tectonic model in which seismogenic faulting is localized along a sharp contrast in crustal strength, reflecting competency as represented by the NY-AL lineament.

An alternative model to explain the localization of seismicity in the eastern Tennessee region is given by Long and Kaufmann (1994). After an analysis of the velocity structure of the region, they conclude that the seismically active areas are not apparently constrained by the crustal blocks defined by the NY-AL lineament, but rather their locations are determined by low-velocity regions at midcrustal depths. They suggest that the data support the conjecture that intraplate earthquakes occur in crust that may be weakened by the presence of anomalously high fluid pressures. Their data suggest that only a portion of the NY-AL lineament is consistent with the interpretation of this lineament as a contact between two crustal blocks having different properties.

Steltenpohl et al. (2010) propose in recent work that seismicity of the ETSZ may be localized along a N15°E-trending magnetic low anomaly in the Ocoee block. They observe that seismicity occurs south of the NY-AL lineament and follows this trend within the magnetic anomalies. This anomaly coincides with the subsurface extension of the Amish anomaly beyond the NY-AL lineament and is interpreted to represent metasedimentary gneissic rocks. The modern stress field is compatible with that which initiated dextral motion along the NY-AL lineament. The magnetic grain of the gneissic rocks and depositional anisotropies could control the spatial pattern of modern seismicity, given the lack of known faults.

Chapman et al. (2002) conclude that the linear segments, and the locations of their terminations, may reflect a basement fault structure being reactivated in the modern stress field. They state that physical processes for reactivation of basement faults could involve a weak lower crust and/or increased fluid pressures within the upper to middle crust. There may be a marginal correlation between the seismicity and major drainage pattern and general topography of the region, suggesting a possible hydrological element linkage (Chapman et al., 2002).

#### 7.3.4.1.3 *Clarendon-Linden Fault System*

The Clarendon-Linden fault system is located in upstate New York south of Lake Ontario (Figure 7.3.4-1) and comprises a broad zone of faults with small displacements in lower Paleozoic bedrock. The fault system is at least 77 km (48 mi.) long and 7–17 km (4–10.5 mi.) wide and is spatially coincident with a north-trending geophysical (combined magnetic and gravity) lineament within the basement rock (Fakundiny and Pomeroy, 2002). The fault system extends for approximately 150 km (93 mi.) from just north of the Pennsylvania border (Jacobi and Fountain, 1993) to the north shore of Lake Ontario (Hutchinson et al., 1979).

Closely spaced small-offset step faults characterize the Clarendon-Linden fault system in outcrops of Devonian rocks (Jacobi and Fountain, 1993, 1996, 2002). By integrating surface stratigraphy, structure, soil gas, and lineaments, Jacobi and Fountain (2002) recognized as many as 10 parallel, segmented faults across the fault system in southwestern New York State. The main strand of the Clarendon-Linden fault system is highly segmented, steeply east-dipping in the north and west-dipping in the south, and displays a maximum vertical displacement of about 80 m (262 ft.; Jacobi and Fountain, 1993). Cumulative offset across the Clarendon-Linden fault system is as high as 130–200 m (426–656 ft.), according to well log, outcrop, and seismic data (Jacobi and Fountain, 1996). Forsyth, Milkereit, Zelt, et al. (1994); Milkereit et al. (1992); and Zelt et al. (1994) suggested that the Clarendon-Linden fault system is part of a wider zone of small Paleozoic faults that lie above the crest of a northeast-trending Precambrian bedrock high (i.e., the Iroquoian high).

The Clarendon-Linden fault system is inferred to extend northeastward beneath Lake Ontario, coincident with a bathymetric lineament known as the Scotch Bonnet Rise (Hutchinson et al., 1979). The Scotch Bonnet Rise is a west-facing bedrock ridge that exhibits approximately 20 m (66 ft.) of relief and may be related to faulting (Anderson and Lewis, 1975). Hutchinson et al. (1979) collected seismic data across the Scotch Bonnet Rise and, within the resolution of their data (approximately 2–3 m [6.6–9.8 ft.]), observed no evidence for postglacial Holocene faulting across this feature. Both the Clarendon-Linden fault system and the Scotch Bonnet Rise coincide with the east flank of a magnetic anomaly and the west edge of a series of Bouguer gravity anomalies, both of which can be traced from west-central New York to the north shore of Lake Ontario (Hutchinson et al., 1979).

Deep seismic-reflection data suggest that the Clarendon-Linden fault system is coincident with structures associated with the Elzevir-Frontenac terrane boundary zone of the Grenville province (Milkereit et al., 1992; Zelt et al., 1994; Forsyth, Milkereit, Zelt, et al., 1994; Easton and Carter, 1995). Seismic-reflection profiles show the gently east-dipping ductile thrusts of the Elzevir-Frontenac boundary zone extending up to the Precambrian/Paleozoic contact in the region of the Clarendon-Linden fault system (Forsyth, Milkereit, Zelt, et al., 1994; Jacobi and Fountain, 1996). However, the Precambrian structures do not lead directly to individual Clarendon-Linden faults (Jacobi and Fountain, 1996). The Salmon River fault, which is exposed approximately 30 km (18.5 mi.) north of Lake Ontario, is believed to be the northern extension of the Clarendon-Linden fault system (McFall, 1993). Farther north, the projection of the Clarendon-Linden fault system and Salmon River faults coincide with the Robertson Lake mylonite zone in the Canadian Shield (McFall, 1993; Easton and Carter, 1995). The surface continuity of inferred faults constituting the Clarendon-Linden fault system is not strongly supported by the reprocessed seismic data examined by Ouassaa and Forsyth (2002). Ouassaa and Forsyth (2002) also noted that north-northeast-trending curvilinear magnetic and gravity anomalies parallel, but are not restricted to, the principal trend of the postulated Clarendon-Linden fault system.

The Clarendon-Linden fault system probably represents brittle reactivation of a major Grenville structure (Hutchinson et al., 1979; Seeber and Armbruster, 1995). The detailed map pattern of the Clarendon-Linden fault system shows that the north-south-trending faults comprise numerous short segments connected by oblique northwest-trending transfer faults, similar to that in rift settings (Jacobi and Fountain, 1996). This geometry suggests that the underlying east-dipping

Precambrian thrusts could have acted as a detachment surface, possibly during Iapetan rifting (Jacobi and Fountain, 1996). Culotta et al. (1990) correlated the Clarendon-Linden fault system with a continental-scale magnetic lineament, the Amish anomaly, which is crosscut by the NY-AL lineament (Culotta et al., 1990). This anomaly is interpreted as a major Grenville terrane boundary that separates the Elzevir and Frontenac tectonic blocks (Culotta et al., 1990).

The Clarendon-Linden fault system is associated with a well-defined cluster of seismicity, which is referred to as the Attica seismic zone (Seeber and Armbruster, 1995). This zone contains the 1929  $m_b$  5.2 (E[M] 4.72) Attica earthquake, numerous natural small-magnitude earthquakes, and several induced earthquakes associated with salt brine recovery at Dale, New York (Fletcher and Sykes, 1977). Seeber and Armbruster (1995) suggest that the 1929 earthquake may have been artificially triggered, as the brine fields in Dale were already active in 1929. Dineva et al. (2004) relocated hypocenters from earthquakes occurring between 1990 and 2001 that delineate clusters of earthquakes beneath Lake Ontario. They report that their cluster C is parallel to the Clarendon-Linden fault system but shifted slightly to the southeast by about 4 km (2.5 mi.). During the 1990–2001 recording period for their analysis, Dineva et al. (2004) note that little seismic activity occurred along the Clarendon-Linden fault system, with only two earthquakes near the southern end.

#### 7.3.4.2 Basis for Defining Seismotectonic Zone

As described in Section 7.3.4.1, reactivation of Iapetan rift–related structures has been postulated as a causal mechanism for localizing seismicity in the Appalachian Mountains, St. Lawrence, and eastern Great Lakes regions. Well-documented Iapetan faults that were reactivated during the Mesozoic are included in the SLR seismotectonic zone (Section 7.3.1). Likewise, thinned Iapetan crust under the Atlantic coastal plain that experienced significant extension during the Mesozoic is included in the ECC seismotectonic zone (Section 7.3.7). Postulated Iapetan structures beneath the Appalachian detachment west of the Piedmont gravity anomaly gradient are not easily identified and are interpreted only from limited seismic and borehole information. The PEZ seismotectonic zone encompasses IRM crust in that region, which exhibits some evidence of early Paleozoic rifting or extension.

Extended crust of the PEZ seismotectonic zone does not exhibit clear evidence of rift faulting. The deep seismic data collected in Lakes Ontario and Erie (e.g., Milkereit et al., 1992; Forsyth, Milkereit, Davidson, et al., 1994; Forsyth, Milkereit, Zelt, et al., 1994; Zelt et al., 1994; White et al., 1994) do not show high-angle extensional structures or extensional deformation within the PEZ seismotectonic zone on the scale of the Ottawa graben faults or the St. Lawrence rift faults, providing very strong evidence that a failed rift arm does not extend into the lake. Faulted lower Paleozoic rocks in the northeastern Lake Ontario region (e.g., Grier, 1995; Williams, 1991) generally exhibit maximum offsets on the order of several tens of meters. Normal faulting within the PEZ seismotectonic zone is associated with the Rome trough, Clarendon-Linden fault system, and CMBBZ, which represent extensional reactivation of Grenville structures, as opposed to rift structures.

Because Mesozoic extension within the PEZ seismotectonic zone is equivocal, crust of the SLR, ECC-AM, and ECC-GC seismotectonic zones is separated from the PEZ seismotectonic zone based on the more definitive evidence of Mesozoic extension in those zones. However, it is difficult to preclude that subdetachment structures within the PEZ seismotectonic zone that are currently active were not also reactivated during Mesozoic opening of the Atlantic Ocean (Swanson, 1986; Williams, 1978; Pratt et al., 1988; Cook et al., 1979; McBride et al., 2005). Therefore, the PEZ seismotectonic zone is differentiated from the adjacent Midcontinent-Craton (MidC) seismotectonic zone to accommodate alternative Mmax priors (see discussion in Section 7.3.4.4).

### 7.3.4.3 Basis for Zone Geometry

The PEZ seismotectonic zone characterizes crust extended in the Paleozoic inboard of the rifted margin. Iapetan normal faults likely decrease in size, abundance, and slip gradually and irregularly northwestward into the North American craton over a distance of perhaps 100–200 km (60–120 mi.; Bollinger and Wheeler, 1988). The eastern margin of the Paleozoic Appalachian terranes beneath the detachment corresponds to a gravity anomaly gradient underlying the Piedmont that is inferred to represent thinning of crust (Pratt et al., 1988) (Figure 7.3.4-2). Bollinger and Wheeler (1988) suggested that the steep eastward rise in the Bouguer gravity anomaly field is the eastern limit for the Iapetan normal faults and that most of the faults occur in the relatively intact continental crust of North America west of the gravity anomaly gradient. This gravity anomaly gradient, referred to as the Appalachian (Piedmont) gravity gradient, is interpreted to mark the transition from thick continental to less thick, and possibly more mafic (transitional), crust to the east (James et al., 1968; Kane and Long, 1981; Hatcher and Zietz, 1980; Hutchinson et al., 1983). Wheeler (1996) interprets this boundary as the hinge zone of the IRM. Two alternative geometries are considered for PEZ, namely, the PEZ Narrow and PEZ Wide. The criteria for defining these two alternatives are discussed below.

#### 7.3.4.3.1 PEZ Narrow

The PEZ Narrow (PEZ-N) geometry is defined based on structural and seismologic evidence that provides the most convincing evidence for the presence of Iapetan faults or rift sediments below the detachment (Wheeler et al., 1995). This alternative is given the highest weight (0.8) because of the strength of this evidence. The western boundary of the PEZ-N alternative geometry follows the Birmingham basement fault system in Alabama and the NY-AL lineament to the northeast. Crust northwest of the NY-AL lineament appears to have behaved as a rigid, somewhat coherent block, and its sharp boundary against the anomaly implies the edge of this competent block (Steltenpohl et al., 2010). King and Zeitz (1982) suggested that the lineament acted as buttress during the Paleozoic and limited Appalachian deformation east of it. Seismicity is observed below the detachment in Giles County and eastern Tennessee, supporting the concept that these earthquakes involve reactivation of Iapetan structures below the detachment surface.

#### 7.3.4.3.2 PEZ Wide

The PEZ Wide (PEZ-W) geometry extends to the west to capture additional crust that was extended to a lesser degree during opening of the Iapetan Ocean. Given that Iapetan rift structures and significant extension are assumed to decrease to the west, and the evidence for extensional reactivation is limited, a low weight (0.2) is assigned to the PEZ-W alternative.

The western boundary of the PEZ-W alternative geometry follows the Rome trough in Kentucky and West Virginia and the CMBBZ in Ontario. Wheeler (1995) interpreted the Clarendon-Linden fault system of upstate New York as the westernmost limit of Iapetan faulting in the vicinity of the Great Lakes. The Clarendon-Linden fault system appears to be associated with a Grenville shear zone at depth. Movement along the Clarendon-Linden fault system records Iapetan reactivation (Seeber and Armbruster, 1995) of the Grenville Elzevir-Frontenac boundary zone, indicating the extent of the extensional stress field and not the location of through-going rift faults. Lower Paleozoic extensional reactivation also is exhibited farther west on the CMBBZ (Milkereit et al., 1992; Forsyth, Milkereit, Davidson, et al., 1994). Recent interpretation of seismic lines and regional magnetic data place the western boundary of the CMBBZ on the west side of the Mississauga domain as defined by O'Dowd et al. (2004).

The western boundary of the PEZ-W continues southward to the western margin of the Rome trough, following the Kentucky River fault system (Van Arsdale, 1986, Potter et al., 1995; Steltenpohl et al., 2010). Subsidence of the Rome trough may represent inboard extension of Iapetan rifting along the Mesoproterozoic East Continent rift basin (Drahovzal, 1997). Stark (1997) attributes development of the Rome trough and reactivation of the Kentucky River fault system to reactivation of the East Continent rift complex during Iapetan extension. The western boundary of the Rome trough coincides with the western limit of Grenvillian contractional deformation (i.e., Grenville front) and the eastern boundary of the East Continent rift basin (Drahovzal et al., 1992).

#### 7.3.4.4 Basis for Zone Mmax

Paleoseismic investigations from the Rome trough, eastern Tennessee, and the vicinity of the Clarendon-Linden fault system do not provide evidence for large-magnitude earthquakes in these areas of historically higher seismicity. Van Arsdale and Sergeant (1992) trenched terrace materials along the Kentucky River fault system, which forms the northern boundary of the Rome trough, and observed evidence for folding and faulting within the last five million years, and probably within the last million years. The absence of post-Paleozoic deposits prevents the determination of Mesozoic or Tertiary reactivation (Van Arsdale and Sergeant, 1992). Whisner et al. (2003) performed paleoseismic reconnaissance investigations in a 300 km<sup>2</sup> (186 mi.<sup>2</sup>) area within the most active part of the ETSZ and found no evidence of large prehistoric earthquakes.

An NRC-sponsored research effort was initiated in the ETSZ in the last half of 2009 to help clarify the late Quaternary earthquake history and hazard potential of this seismic zone. At locations east to northeast of Knoxville, Tennessee, with late Quaternary terrace deposits, Vaughn et al. (2010) report the occurrence of outcrop-scale strike-slip, reverse, and normal faults and prevalent fractures; minor paleoliquefaction features; and anomalous fractured and disrupted

features attributed to liquefaction and forceful expulsion of groundwater during one or more major late Quaternary earthquakes. These preliminary observations suggest that the ETSZ has produced surface faulting and generated one or more strong earthquakes during late Quaternary time. However, these preliminary results could not qualify that RLMEs had occurred in the ETSZ, and were therefore insufficient to determine whether the ETSZ could be considered an RLME zone and treated accordingly in the CEUS SSC Project.

A paleoliquefaction study of the Clarendon-Linden fault system was conducted by Tuttle et al. (2002). These investigations observed a lack of earthquake-induced liquefaction features in geologic units susceptible to liquefaction, suggesting that the fault system did not generate large  $M > 6$  earthquakes during the past 12,000 years. Tuttle et al. (2002) conclude that the fault system could have produced small and moderate earthquakes, but probably not large earthquakes during the late Wisconsinan and Holocene. Because this lack of evidence for paleoliquefaction features may not indicate an absence of past earthquakes, the maximum magnitude for the PEZ seismotectonic zone is modeled by historical seismicity.

Paleoseismic investigations in other areas of the PEZ seismotectonic zone have not been carried out. Therefore, the maximum magnitude for PEZ-N and PEZ-W is assessed using historical earthquakes. The largest observed earthquake in the PEZ seismotectonic zone is the 1897 Giles County earthquake (MMI = VIII,  $m_b = 5.7$ ; E[M] 5.91), which occurred within this zone near the Virginia–West Virginia border (Bollinger and Hopper, 1971). The next largest earthquakes are also located near Giles County and include the 1861 E[M] 5.63 and 1852 E[M] 5.21 earthquakes. The largest recorded earthquakes associated with the ETSZ are the 1973  $M_S 4.6^3$  (E[M] 4.01) Maryville, Tennessee, earthquake (Stover and Coffman, 1993) ( $m_b 4.6$ ; Bollinger et al., 1991) and the April 2003  $M 4.6$  (E[M] 4.53) Fort Payne earthquake that occurred in northeastern Alabama near the Georgia border.

A likelihood function based on the moment magnitude of the 1897 Giles County earthquake is used to update two prior distributions representing alternative interpretations of the age of most recent activation of extensional features in the PEZ seismotectonic zone (NMESE and MESE, see Section 5.2). The geometries of the PEZ seismotectonic zone are defined largely by the limit of Iapetan rifting in the late Precambrian and early Cambrian. However, some researchers have suggested that Mesozoic extension continued west into crust of the PEZ seismotectonic zone. Faure et al. (2006) performed paleostress analysis of mesoscopic faults and emplacement of Jurassic dikes in Quebec and New Brunswick and concluded that preexisting Neoproterozoic, Taconic, Acadian, and Alleghanian structures within this zone were reactivated during the opening of the Atlantic Ocean and are kinematically linked to faults bounding Mesozoic basins. This work suggests that Atlantic rifting was a widespread extensional event extending as far as 400 km (244 mi.) into the plate (Faure et al., 2006). Pliocene and younger deformation within Giles County (Law et al., 1993, 1998) and the Rome trough (Van Arsdale and Sergeant, 1992) can be considered a proxy for Mesozoic activity. Therefore, some weight is given to a Mesozoic and younger prior for the PEZ seismotectonic zone. The resulting  $M_{max}$  distributions are presented in Section 7.4.2.

---

<sup>3</sup>  $M_S$  = surface-wave magnitude.

#### 7.3.4.5 Future Earthquake Characteristics

Earthquakes within the PEZ seismotectonic zone exhibit predominantly strike-slip focal mechanisms with a variety of orientations. Therefore, default characteristics for fault orientation are used, but style of faulting parameters is modified to give a higher weight to strike-slip (0.80) than to reverse (0.20) faulting based on the focal mechanism information described below. The default orientations are therefore modeled with the default characteristics for future earthquakes.

Bollinger and Wheeler (1988) propose that earthquakes in Giles County consist of strike-slip faulting below the Appalachian detachment on steeply dipping (>70 degrees) planes. They attribute right-lateral slip on northerly striking nodal planes or left-lateral slip on easterly striking nodal planes (Bollinger and Wheeler, 1988) to a series of down-to-the-east, subdetachment faults associated with Iapetan rifting (Gresko, 1985). The P-axis estimates (i.e., maximum compressive stress axes) are uniformly of a northeasterly (north-northeast to east-northeast) trend with subhorizontal inclination, and are similar to the orientation of P-axis estimates elsewhere in the region (Bollinger and Wheeler, 1988).

Focal mechanisms in eastern Tennessee indicate strike-slip faulting on steeply dipping planes and a uniform regional stress field with horizontal maximum compression trending N70E (Chapman et al., 2002). Most mechanisms involve either right-lateral motion on north-south-oriented planes or left-lateral slip on east-west-oriented planes (Chapman et al., 1997). Chapman et al. (2002) also note that a smaller population shows right-lateral motion on northeasterly trending planes, parallel to the overall trend of the seismicity. The seismicity is not uniformly distributed; rather, epicenters form northeasterly trending en echelon segments (Chapman et al., 2002).

Focal mechanisms near the Great Lakes are also predominantly strike-slip. Herrmann (1978) reported that focal mechanism studies of two shallow (2–3 km, or 1.2–1.9 mi.) earthquakes in 1966 and 1967 in the Attica area suggested that seismicity occurs along approximately north-northeast-trending Clarendon-Linden faults. The 1966 earthquake ( $m_b = 4.6$  [E[M] 4.26]) yielded solutions with one nodal plane striking north-northeast and dipping steeply to the east, and a second striking west-northwest and dipping steeply to the south. If the north-northeast solution is accepted, then the fault motion was primarily right-lateral strike-slip with a reverse component. The 1967 earthquake ( $m_b = 4.4$  [E[M] 4.07]) yielded solutions with one nodal plane striking north-northeast and dipping steeply to the east, and a second west-northwest-striking plane dipping moderately to the south. Again, accepting the north-northeast solution indicates right-lateral and reverse slip on the fault. Herrmann (1978) selected the north-northeast nodal plane as the most likely fault plane solution, based on the well log data (Van Tyne, 1975) indicating north-northeast-trending Clarendon-Linden faults. He noted, however, that the west-northwest trend could not be totally discounted. Kim et al. (2006) determined a predominantly strike-slip double-couple moment tensor with a strike of 8 degrees east of north and dipping to the east (50 degrees) for the August 4, 2004, Lake Ontario earthquake.

Kim et al. (2006) determined a precise hypocentral depth of  $4 \pm 2$  km ( $2.4 \pm 1.2$  mi.) mechanism for the August 4, 2004,  $M_w$  3.1 (E[M] 3.11) earthquake located in Lake Ontario. This shallow depth is consistent with other well-located earthquakes near Lakes Erie and Ontario, including

the 1966 Attica earthquake (2 km [1.2 mi.]); the 1967 Attica earthquake (3 km [1.8 mi.]); the 1998 Pymatuning, Pennsylvania, earthquake (2 km [1.2 mi.]; Du et al., 2003); the 2001 Ashtabula, Ohio, earthquake (2 km [1.2 mi.]); and the 1986 Perry, Ohio, earthquake. These observations suggest a broad-scale strike-slip faulting stress regime with a shallow seismogenic layer in the Erie-Ontario Lowlands. Dineva et al. (2004) provide the depth distribution for relocated hypocenters in the Great Lakes region. These data are consistent with the shallow hypocentral depths mentioned above. However, the entire distribution has a 95th percentile depth of approximately 16 km (10 mi.). Ma and Atkinson (2006) determined focal depths for small to moderate earthquakes in southern Ontario and northern New York that range from 2 to 15 km (1.2 to 9 mi.). Focal depths of most earthquakes in ETSZ range from 5 to 22 km (3 to 13.4 mi.) and lie beneath detached Alleghanian thrust sheets (Vlahovic et al., 1998; Chapman et al., 2002). Therefore, the thickness of seismogenic crust is modeled using the default alternatives.

### **7.3.5 Illinois Basin Extended Basement Zone (IBEB)**

Southern Indiana and southern Illinois are characterized by higher rates of seismicity than adjacent craton regions. Braile et al. (1984) proposed that two branches or arms of the Reelfoot rift, the Wabash Valley and St. Louis arms, extend into southern Indiana and southeast Missouri, respectively. Although subsequent studies (e.g., Wheeler and Cramer, 2002) have demonstrated that highly extended rifted crust does not extend into these regions as far as Braile et al. (1984) proposed, the interpretation of seismic profiles and the mapping and dating of paleoliquefaction features in the southern Illinois basin provide evidence for multiple paleoearthquakes having magnitudes larger than historical earthquakes that have occurred in this region. The two largest paleoearthquakes that appear to be localized within the Wabash Valley are included in the Wabash Valley RLME source zone (Section 6.1.9). Four additional paleoearthquakes estimated to be approximately  $M$  6.2–6.3 are recorded by more widely distributed liquefaction features and inferred energy centers for moderate-sized earthquakes beyond the limits of the Wabash Valley RLME source (Table 6.1.9-1; Figures 7.3.5-1, 7.3.5-2, and 7.3.5-3). These earthquakes are considered in the characterization of the Illinois Basin Extended Basement (IBEB) seismotectonic zone.

An additional energy center near St. Louis, referred to as the Meramec River energy center, is not included in the IBEB zone. The Meramec energy center lies outside the areas of extended Precambrian basement used to define the zone boundaries (Section 7.3.5.3); it has been postulated that paleoliquefaction features here could be the result of smaller ( $M < 6.0$ ) local earthquakes or larger earthquakes ( $M$  7.0–7.5) originating on structures in the southern Illinois region (e.g., the Du Quoin monocline/Centralia fault that lies within the IBEB) (Tuttle, Chester et al., 1999; Tuttle, 2005b). The Wabash Valley RLME source zone as described in Section 6.1.9 is an independent zone that characterizes only RLMEs. Earthquakes of magnitudes less than the RLME maximum magnitude are modeled based on recurrence parameters for the IBEB seismotectonic zone.

### 7.3.5.1 Background

McBride, Hildenbrand, et al. (2002) and McBride et al. (2007) have completed integrated analyses of geophysical, industry seismic reflection profile, and well data to evaluate possible fault sources for historical earthquakes in the southern Illinois basin. These studies suggest that both Precambrian basement and Paleozoic structures within the southern Illinois basin have been reactivated by recent moderate-sized earthquakes, and that to a large degree, Paleozoic structures may be decoupled from deeper seismogenic Precambrian basement structures. Although some historical earthquakes, such as the 1987  $m_b$  5.2 (E[M] 4.95) earthquake, may be associated with a fault-propagation fold representing possible reactivation of a basement fault that originated during the Laramide orogeny), McBride et al. (2007) suggest that a clear association of seismicity with mapped structural trends is not well documented throughout the southern Illinois basin.

McBride et al. (2007) note that the post-Mississippian structure and stratigraphy of the Illinois basin's thick Paleozoic sedimentary section have been investigated using petroleum industry boreholes and limited seismic reflection profiles (e.g., Sexton et al., 1986; Kolata and Nelson, 1991; Bear et al., 1997; McBride and Nelson, 1999). The seismic stratigraphy and composition of the Precambrian basement upper crust have been less well characterized (Pratt et al., 1992; Van Schmus et al., 1996; Potter et al., 1997; McBride and Kolata, 1999; McBride et al., 2003), and thus the deep structure of the basin remains poorly understood.

Historical epicenter relocation studies by the USGS, based on the method of Bakun and Wentworth (1997), have repositioned moderate- to large-magnitude earthquakes over or near major structural axes in the southern Illinois basin (e.g., Du Quoin monocline; Cottage Grove fault system; La Salle anticlinal belt) (Bakun et al., 2003; Bakun and Hopper, 2004a).

The Du Quoin monocline has been suggested by some researchers (Su and McBride, 1999; Tuttle, Chester, et al., 1999; Tuttle, Schweig, et al., 2005) as a possible causative source for the earthquake that resulted in the paleoliquefaction features in the Shoal Creek–Kaskaskia River region of south-central Illinois.

Other prehistoric earthquakes, such as the Springfield paleoearthquake, cannot be readily correlated to mapped structures in the Paleozoic cover rocks, but may be associated with a magnetic anomaly (Figure 7.3.5-3).

### 7.3.5.2 Basis for Defining Seismotectonic Zone

The following observations suggest that there are fundamental differences in the crust underlying the southern Illinois basin that will influence the maximum magnitude and future earthquake characteristics relative to the surrounding regions:

- There is evidence of several moderate-sized paleoearthquakes and higher rates of instrumental seismicity in parts of this region that are not recognized in the adjoining craton regions.

- The southern part of the Illinois basin is one of the most structurally complex areas of the Midcontinent (McBride et al., 2007). McBride et al. (2007) note that (1) Proterozoic rift faults distinct from those bounding the Grayville graben (in the Wabash Valley RLME source zone [Section 6.1.9]) are imaged in Precambrian basement rock below a thick sequence of Precambrian layered volcanic rocks; (2) the circular to oval pattern of the sequences in plan view argue against a linear rift geometry and is instead suggestive of a large rhyolitic collapsed caldera complex; and (3) newly observed mantle reflectivity beneath the Illinois basin indicates significant upper-mantle heterogeneity compared with other parts of the United States studied using reflection methods. These observations suggest that crust beneath the Illinois basin is distinct from that of the neighboring craton.
- An extensive series of moderately dipping reflectors interpreted to be faults is present in the basement. The 1968  $m_b$  5.5 earthquake may have occurred in response to reactivation of one of these inferred faults.
- Association of dipping crustal reflectors and gently arched Paleozoic strata suggests an additional, but limited, degree of Phanerozoic (post-Precambrian) reactivation of structures spatially associated with the strongly deformed deep structure. Moderate-sized historical earthquakes that appear to be spatially associated with Precambrian basement faults and with Paleozoic faults suggest continued reactivation of older basement features as well as younger Paleozoic structures (McBride et al., 2007).
- Stresses induced by Mesozoic rifting possibly extended into the southern Illinois basin, resulting in reactivation of deep structures. This concept was initially postulated by Braile et al. (1984). Although evidence for Mesozoic rifting is primarily limited to reactivation of basement structures in the Grayville graben (included in the Wabash Valley RLME source, Section 6.1.9), more distal effects cannot be ruled out. The IBEB is defined in part to allow for use of both the non-Mesozoic and younger extended (NMESE) and the Mesozoic and younger extended (MESE)  $M_{max}$  prior distributions in the assessment of maximum magnitude.

Multiple hypotheses have been presented to explain the localization and high rates of Holocene activity within the adjacent Reelfoot rift and the New Madrid region to the south (see Section 6.1.5). Some of these mechanisms may also apply to the southern Illinois and southern Indiana region, as follows:

- The presence of intrusive rocks in the Precambrian basement may cause a local stress concentration.
- Glacial unloading at the close of the Wisconsinan increased seismic strain rates in the region.
- Descent of the ancient Farallon slab into the deep mantle beneath central North America as inferred from high-resolution seismic tomography induces a highly localized flow and stresses in the Midcontinent.
- This region, like the NMSZ, may be a lithospheric weak zone on the edge of a high-velocity lithospheric block that transfers stress to the upper crust when loaded, thus leading to repeated shallow earthquakes.

None of the individual characteristics alone are sufficient to define the IBEB as a separate seismotectonic zone. However, when considered in combination, they support the contention that the IBEB has different seismogenic characteristics and possibly a different  $M_{max}$  prior compared with the neighboring regions.

The IBEB source zone is defined to characterize sources of moderate- to large-magnitude earthquakes (excluding those attributed to the Wabash RLME source) that may occur on deep structures in the Precambrian basement and in as Paleozoic faults that extend into the overlying Paleozoic sedimentary rocks.

### 7.3.5.3 Basis for Zone Geometry

The roughly oval-shaped Illinois basin, overlying parts of Illinois, Indiana, western Kentucky, and southeastern Missouri, contains as much as 7,000 m of Cambrian through Pennsylvanian sedimentary rock units (Buschbach and Kolata, 1991; Nelson, 1995; Figure 7.3.5-2). The basin is bisected by the La Salle anticlinal belt and the Wabash Valley fault system, both of which have expression in the Paleozoic strata.

The extent of the older Precambrian basement structural features is less well known. McBride, Hildenbrand, et al. (2002) identify a proto-Illinois basin based on interpretation of geopotential field data; petroleum industry borehole logs (Buschbach and Kolata, 1991); and deep crustal seismic data. McBride et al. (2001) report that the first vertical derivative of the reduced-to-pole magnetic intensity anomaly map shows a subdued magnetic intensity character associated with the Proterozoic rifting and/or layered volcanic sequences in Precambrian basement as inferred from deep seismic reflection profiles. The pattern continues to the north and east beyond the limits of the deep reflection profile data. The margins of the layered volcanic sequences, especially to the south and west, are marked by prominent coincident closed-contour magnetic and gravity anomalies, which reflect, at least in part, mafic igneous source intrusions that may be related to the original thermal event that produced the Proterozoic Eastern Granite-Rhyolite province (1,480–1,450 Ma; McBride et al., 2001) (Figure 7.3.5-3). Other researchers (e.g., Pratt et al., 1992; Baranoski et al., 2009, Drahovzal, 2009) have identified rift basin sediments in the Precambrian basement below the Paleozoic cover rocks in southern Illinois and southern Indiana. Drahovzal et al. (1992) characterize these basement rocks as the western part of the East Continent rift basin. Baranoski et al. (2009) also interpret clastic rift basins associated with the East Continent rift basin under most of the southern Illinois basin and a basaltic rift basin extending into northern Illinois (Figure 7.3.5-2).

The boundaries of the IBEB are drawn to roughly encompass the various interpretations of basement rift sediments and the areas where moderate-sized prehistoric earthquakes have been identified from paleoliquefaction studies. Because the boundary of the IBEB is not well defined by these data and its exact geographic location is uncertain, it is treated as “leaky,” such that ruptures that nucleate within the zone may also propagate outside the uncertain geographic boundary of the source zone.

#### 7.3.5.4 Basis for Zone Mmax

The Mmax distribution for the IBEB uses only the Bayesian approach, as outlined in Section 5.2. The three largest historical earthquakes recorded within the zone are the September 27, 1891, E[M] 5.52; August 15, 1891, E[M] 4.97; and April 18, 2008, E[M] 5.30 earthquakes. Four prehistoric earthquakes inferred from the paleoliquefaction studies have estimated magnitudes that are larger than the historical earthquakes. These are the ~M 6.3 Vallonia, ~M 6.2 Shoal Creek, ~M 6.2 Springfield, and M 6.2 Waverly earthquakes (Figure 7.3.5-1; Table 6.1.9-1).

For the Bayesian approach, three alternative priors are considered: COMP, a composite (weight of 0.4); NMESE, non-Mesozoic and younger extended (weight of 0.48); and MESE, Mesozoic and younger extended (weight of 0.12). The NMESE prior is given a high weight (0.48) based on the lack of evidence for Mesozoic mafic intrusions and significant Mesozoic or younger extension throughout the IBEB zone. Less weight is given to the possibility that stresses associated with Mesozoic extension in the adjacent Reelfoot rift may have propagated into the IBEB zone, giving rise to some reactivation of structures in both the Precambrian basement and the overlying Paleozoic cover. The COMP prior also is given a relatively high weight (0.4) based on the uncertainty in the characteristics that influence maximum magnitude. The prior distribution in each case is truncated and modified based on the evidence for the four moderate-sized paleoearthquakes (M 6.2–6.3) in the zone that are not modeled as RLMEs. Due to the uncertainty in the sizes of these paleoearthquakes, which are based primarily on the magnitude-bound curve presented by Olson et al. (2005b), a sigma of 0.25-magnitude units is used in the development of an updated likelihood function. The derived Mmax distribution for IBEB is presented in Section 7.4.2.

#### 7.3.5.5 Future Earthquake Characteristics

Characteristics for future earthquake ruptures in the IBEB source zone are given in Table 5.4-2. The aleatory variability in the future earthquake characteristics assigned to the IBEB is based on the following:

- Consideration of focal mechanisms in the southern Illinois basin region, which are a mixture of interpreted north-northeast-trending strike-slip and reverse mechanisms (Taylor et al., 1989; McBride, Hildenbrand, et al., 2002; McBride et al., 2007; Larson, 2002; Hamburger et al., 2008; Larson et al., 2009; Withers et al., 2009; Yang et al., 2009).
- Orientations of mapped Paleozoic structures (Nelson, 1995).
- Orientations of Precambrian basement faults and inferred structures (McBride et al., 2007).

The expected style of faulting and fault dip vary with the fault orientation and are inferred based on comparison to focal mechanisms and fault geometry, which is also inferred based on analysis of seismic profiles and seismicity data. The majority of earthquakes having well-constrained focal mechanisms show strike-slip movement. Therefore, strike-slip behavior overall is judged to be more likely. However, reverse faulting mechanisms for historical earthquakes also have been associated with reactivated Precambrian basement and Paleozoic structures (McBride et al., 2007).

The depth of future ruptures is based on reported depths of seismicity within the IBEB (Taylor et al., 1989; McBride, Hildenbrand, et al., 2002; McBride et al., 2007; Hamburger et al., 2008; and Yang et al., 2009). The deepest well-constrained earthquake hypocenters in the Fairfield basin, a relatively deep part of the Illinois basin, are located at depths of 20–22 km (12.4–13.7 mi.; (McBride et al., 2007; Yang et al., 2009). However, the average depth throughout the IBEB zone based on other historical earthquakes may be less. Therefore, a range of values from 13 to 22 km (8 to 13.7 mi.) is used to model the average seismogenic depth within the zone.

### **7.3.6 Reelfoot Rift Zone (RR)**

The Reelfoot Rift (RR) seismotectonic zone beneath the northern Mississippi embayment is interpreted as a Cambrian aulacogen (Ervin and McGinnis, 1975; Thomas, 1991). The crystalline basement rocks defining the rift have been mapped from gravity, magnetic, and seismic refraction and reflection data, as well as from subsurface information derived from a few deep petroleum exploration wells (Hildenbrand, 1982; Mooney et al., 1983; Hildenbrand and Hendricks, 1995; Langenheim and Hildenbrand, 1997; Dart and Swolfs, 1998; Parrish and Van Arsdale, 2004; Csontos et al., 2008; Csontos and Van Arsdale, 2008). The RR zone includes the Reelfoot graben as defined by gravity, magnetic, and seismic data, as well as the regions marginal to the rift graben where crustal extension also is indicated by secondary structures and Mesozoic mafic and ultramafic plutons (Hildenbrand and Hendricks, 1995).

RLME sources within the RR zone are independent sources that characterize only RLMEs; these sources include the New Madrid Fault System (NMFS; Section 6.1.5), Eastern Rift Margin (ERM; Section 6.1.6), Marianna (MAR; Section 6.1.7), and Commerce Geophysical Lineament (CGL; Section 6.1.8) RLMEs.

The source characterization of the RR described in the following text is based on a review of published material outlined in the Data Summary table for the Reelfoot Rift–New Madrid Fault System (Appendix Table D-6.1.5-1). Explicit references that were used as the basis for source characteristics are identified in the Data Evaluation table for the RR zone (Appendix Table C-7.3.6).

#### **7.3.6.1 Background**

##### **7.3.6.1.1 Evolution of the Reelfoot Rift**

Csontos et al. (2008) outline the major tectonic events and evolution of the Reelfoot rift. The following observations are primarily summarized from Csontos et al. (2008) and cited references:

- The Reelfoot rift graben structures are part of the Reelfoot rift–Rough Creek graben–Rome trough intracratonic rift zone that formed during the disassembly of Rodinia and opening of the Iapetus Ocean in late Proterozoic time (Thomas, 1976; 2006). Rifting may have been initiated by an upwelling mantle plume that developed along terrane boundaries (Dart and Swolfs, 1998). Alternatively, the Reelfoot rift may be a consequence of right-lateral strike-

slip motion along a northwest-oriented transform fault that formed the Paleozoic continental margin of southeastern Laurentia (Thomas, 1991).

- An anomalously dense layer is present at the base of the crust and thickens beneath a broad northeast-trending graben that formed during the initial stages of Iapetan rifting. The thickest part of the anomalous crust underlies the region of greatest seismic activity within the geographic limits of the Reelfoot rift (Hildenbrand, 1982).
- Cambrian Reelfoot rifting occurred primarily along large normal faults that appear to become listric with depth (Nelson and Zhang, 1991). However, the straight margin faults suggest that the northeast-trending rift structures originated as strike-slip faults (Hildenbrand, 1985).
- A maximum of 7 km (4.3 mi.) of sediment accumulated in the Reelfoot graben during rifting that continued into middle Cambrian time, while outside the rift only 1.5 km (0.9 mi.) of contemporary sediments accumulated. Regional subsidence and sedimentation continued during the late Cambrian–Middle Ordovician time (Dart and Swolfs, 1998). From Middle Ordovician to Pennsylvanian time, subsidence and uplift alternated due to distal effects of the Taconic, Acadian, and Alleghanian orogenies.
- Structural reactivation of the Reelfoot rift began during the late Paleozoic with the assembly of Pangaea (Thomas, 1985). An unconformity atop the Paleozoic rock units represents mid-Cretaceous uplift and erosion. Sense of slip along many preexisting normal faults within the Central United States was inverted to reverse slip during the Paleozoic collisional processes (Marshak and Paulsen, 1996).
- Cox and Van Arsdale (1997, 2002) proposed that the regional mid-Cretaceous uplift and subsequent subsidence of the Mississippi embayment occurred as the North America Plate drifted over the Bermuda hotspot.
- Late Cretaceous and Cenozoic sediments record transgressive-regressive sequences within the Mississippi embayment trough (Thomas, 1985).
- Fluvial erosion and deposition during the Pliocene resulted in deposition of the Upland Complex, a terrace of the ancestral Mississippi-Ohio River system (Van Arsdale et al., 2007). Crowley's Ridge formed from erosion of the Western Lowlands by the ancestral Mississippi River, erosion of the Eastern Lowlands by the ancestral Ohio River, and Quaternary reactivation of ridge-bounding faults (Van Arsdale et al., 1995).
- Repeated periods of glacial meltwater escape, sea-level change, loess deposition, and structural deformation have produced various river terraces, river courses, lakes, and areas of warping during the Quaternary (Autin et al., 1991; Schweig and Van Arsdale, 1996). Four processes affected base level through the Quaternary: glacio-eustatic sea-level changes, variations in rates and patterns of sediment yield, climatic changes, and tectonic activity.
- The principal seismic activity within the upper Mississippi embayment currently is interior to the Reelfoot rift along the NMSZ.

### 7.3.6.1.2 Major Structures

Major basement structures and tectonic features associated with the Reelfoot rift graben are shown on Figure 7.3.6-1; structural and tectonic features inferred from interpretation of geopotential field data (gravity and magnetic) are shown on Figure 7.3.6-2. Using a structure-contour map and a three-dimensional computer model of the top of the Precambrian crystalline basement, Csontos et al. (2008) show the Reelfoot rift to consist of two major basins, separated by an intrarift uplift, that are further subdivided into eight subbasins bounded by northeast- and southeast-striking rift faults, some of which have been reactivated as reverse or oblique-slip faults.

Tectonic landforms within the central Mississippi River valley are directly linked to the underlying Reelfoot rift faults (Figure 7.3.6-1; Mihills and Van Arsdale, 1999; Csontos et al., 2008; Csontos and Van Arsdale, 2008). Recent seismologic, geologic, and geophysical studies have associated some of these basement faults within the NMSZ with large-magnitude historical earthquakes that occurred in 1811 and 1812. These faults are referred to as the New Madrid fault system (NMFS). Quaternary displacement also has been documented along the Eastern Rift margin (Cox, Van Arsdale, and Harris, 2001; Cox, Van Arsdale, et al., 2001; Cox et al., 2006); Western Rift Margin (Van Arsdale et al., 1995; Baldwin et al., 2005); Axial fault (Van Arsdale, 1998; Guccione et al., 2000); Reelfoot fault (Russ, 1982; Kelson et al., 1996; Mueller et al., 1999; Van Arsdale et al., 1999; Champion et al., 2001); and Fluorspar Area fault complex (Nelson et al., 1997; Nelson, Denny et al. 1999; McBride, Nelson, and Stephenson, 2002; SAIC, 2002; Woolery et al., 2009). In addition, the Lake County uplift, which is essentially coincident with the seismicity between the central and northern 1811-1812 earthquakes shown on Figure 7.3.6-1, the Reelfoot Lake basin, the southern half of Crowley's Ridge, the Big Lake and Lake Saint Francis Sunlands area, and Joiner Ridge are interpreted to be tectonic or tectonically influenced landforms (Csontos et al., 2008).

NMSZ faults have also modified Mississippi River gradients and influenced sedimentary processes during the Quaternary (Schumm and Spitz, 1996; Spitz and Schumm, 1997; Guccione, Mueller, et al., 2002; Guccione, 2005; Holbrook et al., 2006). Johnston and Schweig (1996) have proposed that the Bootheel lineament produced one of the major earthquakes of the 1811-1812 sequence. Guccione et al. (2005) confirmed Quaternary displacement along the Bootheel lineament and suggested the feature should be referred to as a fault. However, Csontos (2007) mapped the Precambrian basement unconformity and the Pliocene-Pleistocene unconformity surfaces within the Reelfoot rift, and sees no evidence of vertical displacement or hypocenter alignment along the Bootheel fault. This lack of vertical displacement may be due to a very young Bootheel fault with relatively minor displacement, or the actual fault displacement may be primarily strike-slip.

The NMFS, Quaternary active faults along the northwestern and southeastern margins of the zone (i.e., the ERM and CGL fault zones, respectively), and unknown structures in the southern part of the rift near Marianna, Arkansas, are characterized as RLME sources (NMFS, ERM, MAR, and CGL RLME sources; Figure 6.1-1). Section 6.1 provides a detailed description of these RLME sources.

The Fluorspar Area fault complex (FAFC) structures, which originated as normal faults during latest Proterozoic and early Cambrian time coincident with the formation of the northeast-trending faults associated with the Reelfoot rift, have experienced periodic reactivation in post-Pennsylvanian, pre-Cretaceous, and late Neogene–Quaternary time (Nelson, Denny, et al., 1999; McBride, Nelson, and Stephenson, 2002). The FAFC structures were very active, with evidence for large-magnitude earthquakes as reflected by surface manifestation of faulting as far back as latest Pleistocene (Nelson, Denny, et al., 1999; McBride, Nelson, and Stephenson, 2002). Despite efforts to identify and document evidence for Holocene activity on several of the FAFC structures, no convincing evidence of Holocene activity has been identified on any of the faults (E. Woolery, pers. comm., February 9, 2010). Reported evidence supporting Holocene displacement on one of the major faults within this system, the Barnes Creek fault (SAIC, 2002), is very equivocal based on the following observations:

- There is an apparent absence of faulting observed in the upper younger deposits (i.e., presence of only a fracture).
- The origin of the observed fracture is uncertain (e.g., possibly related to roots).
- There is an absence of distinct stratigraphic evidence for Holocene displacement on this fault and other faults within the FAFC (WLA, 2006; E. Woolery, pers. comm., February 9, 2010).

There also is a general lack of paleoliquefaction evidence for large-magnitude earthquakes in the northern Reelfoot rift that cannot be attributed to the New Madrid earthquakes. Older, weathered paleoliquefaction features in western Kentucky to the east of the FAFC appear to have formed within the past 4,850 years (WLA, 2006; Appendix E). An older earthquake, the source of which has not been determined, is recorded by older paleoliquefaction features dated at 11,300 yr BP  $\pm$  200 yr (Appendix E). Rupture along the northern Eastern Rift margin fault, or along one of the Wabash Valley fault zone structures (e.g., the Hovey Lake fault) that exhibit evidence for possible latest Pleistocene displacement, is considered to be a likely source of the earthquake that produced these older paleoliquefaction features.

Because of the lack of definitive evidence for Holocene or latest Pleistocene faulting of the FAFC, McBride, Nelson, and Stephenson (2002) propose a dynamic structural model that suggests a mechanism by which seismicity and active (Holocene) faulting have shifted within the central Mississippi Valley, away from the FAFC, over the last several ten thousand years. There is no evidence to indicate that the FAFC should be modeled as an RLME source, and a seismicity-based estimate of recurrence on the FAFC is consistent with the latest Pleistocene/Holocene record.

Quaternary reactivation of faults bounding Crowley's Ridge, a topographic ridge that spans the western margin of the Reelfoot rift in northeastern Arkansas and southeastern Missouri, is inferred from interpretation of high-resolution geophysical data and geomorphic relationships (Van Arsdale et al., 1992, 1995). Van Arsdale et al. (1995) infer that the faults bounding the ridge likely are right-lateral strike-slip faults that appear to have been active in late Wisconsinan time. This ridge, which is subparallel to the CGL in northeastern Missouri, diverges in trend from the CGL in northeastern Arkansas (Figure 7.3.6-1). Because no definitive evidence for recurrent late Pleistocene deformation has been identified along Crowley's Ridge, if faults

bounding this ridge are active, they may have much lower slip rates than faults identified in the Thebes Gap/Benton Hill region. Therefore, potential slip on faults along Crowley's Ridge is represented by earthquakes occurring in the RR seismotectonic or Mmax zone.

Other structures postulated as potential Quaternary neotectonic features (e.g., Joiner Ridge [Csontos et al., 2008] and a north-northwest-trending Meeman-Shelby fault–Joiner Ridge boundary fault [Odum et al., 2010]) also do not offer sufficient evidence to be modeled as RLME sources.

#### 7.3.6.2 Basis for Defining Seismotectonic Zone

The following observations suggest that there are fundamental differences in the crust underlying the RR that will influence maximum magnitude and future earthquake characteristics relative to the surrounding regions:

- The RR graben structures were reactivated during Mesozoic rifting and experienced Mesozoic and younger plutonic activity. The extended crust within and adjacent to the central rift basin contrasts with the surrounding, more stable non-extended crust.
- The higher rate of seismicity within the RR and the occurrence of multiple Quaternary active faults and tectonic landforms within the RR, in addition to the identified RLME sources, suggest that tectonic strain has been localized within and adjacent to the rift. Multiple hypotheses have been presented to explain the localization and high rates of Holocene activity within the rift and the New Madrid region (see Section 6.1.5).
- The RR is expected to have distinct differences in future earthquake characteristics compared to surrounding regions. For example, focal depths for a well-located earthquake in the RR show that the seismogenic crust is not as deep as in parts of the Illinois Basin Extended Basement (IBEB) seismotectonic zone to the north. Detailed seismic surveys (e.g., Pratt, 2009), studies of the crustal architecture of the basin, and deformation of the Pliocene–Pleistocene unconformity surface (Csontos et al., 2008) provide specific information about the orientation of structures that may have experienced Quaternary reactivation, and this information can be used to differentiate the earthquake characteristics for the RR (Section 7.3.6.5) from the default values used for the adjacent Midcontinent-Craton (MidC) and Extended Continental Crust–Gulf Coast (ECC-GC) zones.

#### 7.3.6.3 Basis for Zone Geometry

The first branch of the RR logic tree (Figure 7.3-1) addresses the uncertainty about the inclusion of the Rough Creek graben (RCG) into the RR source zone. The RCG represents the eastward extension of extensional deformation related to formation of the intracontinental rift system during Precambrian to earliest Cambrian rifting of North America (Braile et al., 1982, 1986; Kolata and Nelson, 1991). Initial development involved strike-slip and extensional faulting related to the development of the Reelfoot rift, probably in latest Proterozoic or early Cambrian time. Some of the structures may have been reactivated in post-Pennsylvanian time, probably during the late Paleozoic Ouachita orogeny (Kolata and Nelson, 1991). The RCG is bounded on

the north by the south-dipping, listric Rough Creek fault and on the northwest by the Shawneetown fault (Nelson and Lumm, 1987; Kolata and Nelson, 1991). The southern boundary approximately follows the Pennyrite fault system (Nelson and Lumm, 1987), which forms the southern margin to the Paleozoic syn-rift deposits (Kolata and Nelson, 1991). The RCG in western Kentucky is structurally connected to the northern portion of the RR that includes the Fluorspar area of southern Illinois (Soderberg and Keller, 1981; Kolata and Nelson, 1991; Potter and Drahovzal, 1994). Wheeler (1997), however, defines a boundary in this region between the RCG and the Reelfoot rift/Fluorspar area based on changes in the strikes of single large faults, the location of a Cambrian transfer zone, and the geographic extent of alkaline igneous rocks that provide three independent estimates of the location of a structural boundary between the rift and graben.

Faults associated with the RCG show strong evidence for initiation during late Proterozoic–Cambrian Iapetan-phase rifting and reactivation during the mid to late Paleozoic Appalachian–Ouachita orogeny (Heyl, 1972; Soderberg and Keller, 1981; Thomas, 1991; Noger, 1988, Kolata and Nelson, 1991; Potter et al., 1995). Mesozoic activity on RCG faults also is suggested by post-Permian displacements and regional correlation of extensional deformation associated with post-Permian to pre-Cretaceous rifting of the Pangaea continental landmass (Kolata and Nelson, 1991). However, the lack of clearly associated alkaline igneous rocks of Mesozoic age in the RCG (Wheeler, 1997) suggests that Mesozoic reactivation of deep-penetrating faults was limited.

Based on these observations, lower weight (0.333) is given to the inclusion of the RCG in the RR zone and higher weight (0.667) is given to limiting the RR to the more seismically active part of the rift that also experienced greater Mesozoic extension.

#### 7.3.6.4 Basis for Zone Mmax

The Mmax distribution for the RR is based on the two approaches outlined in Section 5.2: the Bayesian approach and the Kijko [2004] approach. For the Bayesian approach, the Mesozoic and younger prior is used in addition to the composite prior. The prior is truncated by the two largest historical earthquakes recorded within the zone: the January 5, 1843, and October 31, 1895 earthquakes, which are interpreted to be **M** 6 (E[**M**] 6.00) earthquakes (Bakun et al., 2003). The 1811-1812 sequence of earthquakes and other large-magnitude prehistoric earthquakes recognized in the RR are included in the characterization of the RR RLME sources (NMFS, ERM, MAR, and CGL).

The weights for the Bayesian and Kijko approaches for the RR zone and the weighted composite posterior maximum-magnitude probability distribution for the RR zone are presented in Section 7.4.2.

### 7.3.6.5 Future Earthquake Characteristics

Characteristics for future earthquake ruptures in the RR source zone are given in Table 5.4-2. The aleatory variability in the future earthquake characteristics assigned to the RR is based on the following:

- Consideration of focal mechanisms (Zoback, 1992; Shumway, 2008).
- Orientations of RLME fault sources and faults that do not meet the criteria for RLME sources but have evidence of reactivation in the Quaternary (e.g., the north-northeast-trending FAFC faults, the north-trending faults bounding the southern part of Crowley's Ridge).
- Orientations of basement faults and inferred structures that deform the Pliocene-Pleistocene unconformity (Csontos et al., 2008).

The expected style of faulting varies with fault strike and is inferred based on comparison to focal mechanism and fault geometry interpreted from seismic profiles and seismicity data. The majority of earthquakes having well-constrained focal mechanisms show strike-slip movement (Zoback, 1992; Shumway, 2008). Therefore, strike-slip behavior is judged to be more likely. Faults and postulated structures with trends subparallel to the Reelfoot thrust fault, however, are expected to behave as reverse faults in the present tectonic stress environment.

Seismogenic depth is based on reported depths of seismicity within the RR (Zoback, 1992; Chiu et al., 1992, 1997; Herrmann and Ammon, 1997; Mueller and Pujol, 2001; Shumway, 2008; Csontos and Van Arsdale, 2008). In the central and northern part of the rift, seismicity is observed at depths between 5 and 15 km (3.1 and 9.3 mi.); (Chiu et al., 1992; Shumway, 2008). Along the southeastern margin of the rift, seismicity is slightly deeper, with earthquakes recorded between 13.9 and 22.8 km (8.6 and 14.2 mi.). The average depth of seismicity across the entire zone, which takes into account uncertainties in the velocity model and measurements, is considered to range from 13 to 17 km (8 to 10.6 mi.).

Specific parameters and weights used to characterize future ruptures in the RR are given in Table 5.4-2.

### **7.3.7 Extended Continental Crust–Atlantic Margin Zone (ECC-AM)**

The Extended Continental Crust–Atlantic Margin (ECC-AM) seismotectonic zone was defined to include the region characterized by the presence of extended continental crust developed during Mesozoic rifting along the Atlantic Ocean basin margin. This seismotectonic zone extends from Georgia to Nova Scotia and includes onshore portions of the Piedmont and Coastal Plain provinces as well as most of the offshore continental shelf region (Figures 7.3.7-1 and 7.3.7-2).

Breakup of the supercontinent of Pangaea and formation of the Atlantic Ocean basin in the Triassic and Jurassic produced the present-day passive Atlantic margin, which can be divided into three general zones based on several characteristics, including crustal structure, composition, and thickness. These zones, from west to east are (1) rifted and extended continental crust

beneath the Piedmont, Coastal Plain, and continental shelf; (2) a 50–100 km wide (31–62 mi.) zone of highly extended transitional crust; and (3) mafic oceanic crust lying beneath the continental rise (Klitgord et al., 1988; Holbrook, Reiter, et al., 1994). The ECC-AM seismotectonic zone includes only the rifted and extended portion of the continental crust. The narrow zone of highly extended transitional crust is included in the AHEX seismotectonic zone (see Section 7.3.8).

This chapter discusses the geologic, seismic, and geophysical characteristics of the ECC-AM seismotectonic zone. The information presented is based on a review of the published material summarized in the Data Summary table for the ECC-AM and the AHEX seismotectonic zones (Appendix D, Table D-7.3.7). Explicit references and data that were used as the basis for source characteristics of the ECC-AM are identified in the Data Evaluation table of Appendix C (Table C-7.3.7).

### 7.3.7.1 Background

#### 7.3.7.1.1 *Crustal Structure*

A distinguishing structural feature of the Mesozoic extended crust within the ECC-AM is that it includes an older, east-dipping Paleozoic master basal detachment surface separating overthrust Paleozoic Appalachian terranes from the underlying rocks of the North American craton. For example, in the southern Appalachian Mountains, the Consortium for Continental Reflection Profiling (COCORP) seismic reflection data from Tennessee and Georgia show the master detachment to be ~6 km (~3.5 mi.) deep at the western flank of the mountains (west of ECC-AM), ~10 km (~6 mi.) deep in the Piedmont, and then quickly steepening to ~35 km (~22 mi.) depth beneath the peri-Gondwanan Carolina terrane to the east, where it merges with the Moho (Cook et al., 1979; McBride et al., 2005). In general, therefore, Paleozoic thrust sheets above the master detachment surface change across the Appalachian orogenic belt in the ECC-AM from dominantly “thin-skinned” in the west over the North American craton, to dominantly “thick-skinned” in the accreted terranes to the east over the cratonic margin (Klitgord et al., 1988).

The formation of the Appalachian orogen in the Paleozoic was followed in the Mesozoic by extension that resulted in formation of the present-day Atlantic Ocean. Extension occurred primarily in the eastern foothills of the Appalachian Mountains, the Piedmont, and Coastal Plain regions as the rifting propagated southward, initiating the separation of North America and Africa in Late Permian time. Continued rifting in the Late Triassic created elongate, northeast-trending rift basins, primarily as half grabens, from the Gulf of Mexico to the Grand Banks (Figure 7.3.7-1). A second phase of rifting in the Early Jurassic opened extensional marginal basins, such as the offshore Carolina and Baltimore Canyon troughs, as the extensional onshore basins ceased to be active (Klitgord et al., 1988). Generally, bounding faults of Mesozoic extensional basins follow the crustal fabric of the Paleozoic orogenies, and several Mesozoic normal faults have been demonstrated to be reactivated Paleozoic thrust faults (Withjack et al., 1998).

During most of the Late Triassic, onshore half grabens were created that are bounded by faults extending into the lower crust, except along the northeast Atlantic margin, where rift basins tend to be local, rather than widespread, and bounded by listric normal faults (Manspeizer et al., 1989; Withjack et al., 1998). This difference between basins in the northeast and southeast of the ECC-AM has been attributed to Early Jurassic pluton emplacement associated with the White Mountain Magma Series in central New England, which created a topographic high that may have resisted extension (Faure et al., 2006). Roden-Tice, West, et al. (2009) attribute this topographic elevation to regional unroofing during the Cretaceous, resulting from passage of the Great Meteor hotspot (see Section 7.3.2). As a result, the southeast portion of the ECC-AM underwent a relatively greater degree of extension, and faults extended to lower crustal levels.

#### 7.3.7.1.2 Geophysical Anomalies

Given the presence of the relatively shallow Appalachian thrust sheets in the western parts of the ECC-AM, geophysical markers may provide the best means to define deep structural boundaries along the Atlantic margin and the ECC-AM. Gravity anomaly profiles across the Appalachian Mountains show a gravity anomaly low in the Valley and Ridge province, with a parallel gravity anomaly high in the Piedmont (Hutchinson et al., 1983; Karner and Watts, 1983; Cook, 1984). Pratt et al. (1988) concluded that this gravity anomaly gradient, when combined with geophysical data documenting an eastward-shallowing Moho and east-dipping reflectors, represents a thinning of continental crust toward the inferred late Precambrian–early Paleozoic continental margin lying beneath the Piedmont and marks the location of a Taconic collision zone at depth. Pratt et al. (1988) propose that this buried margin has persisted as a zone of weakness, which could explain the spatial correlation of the Piedmont gravity anomaly high with Mesozoic rift basins from Massachusetts to southern Georgia (Swanson, 1986; Hutchinson et al., 1986; Williams, 1978; Pratt et al., 1988). In either case, the Appalachian gravity anomaly gradient appears to define a fundamental structural boundary that is the western limit of thinned, extension-dominated crust lying east of the Appalachian Mountains.

The East Coast magnetic anomaly (ECMA) is a major geophysical feature of the North American Atlantic margin, extending from Georgia to Nova Scotia (Figure 7.3.7-3). Combined multichannel and wide-angle seismic studies of the Atlantic margin have shown that the ECMA is spatially correlated with a zone of transitional igneous crust, largely comprised of basalts and mafic intrusions, marking the seaward transition from rifted continental crust to mafic oceanic crust that extends along the entire Atlantic margin (Austin et al., 1990; Holbrook, Purdy, et al., 1994; Holbrook, Reiter, et al., 1994; LASE Study Group, 1986; Trehu et al., 1989). The magnetic anomaly that defines the ECMA changes trend offshore of Georgia. This east-west-trending onshore portion of the magnetic anomaly has been identified as the Brunswick magnetic anomaly (BMA; Figure 7.3.7-3). The BMA cuts across the South Georgia rift, as well as several other pre-Cretaceous features, suggesting that it must be related to a deeper and older structure (Daniels et al., 1983). COCORP seismic reflection data, combined with magnetic anomaly modeling results, suggest that this structure is either a subducted slab, or subcontinental mantle, trapped during the Alleghanian collision (McBride and Nelson, 1988). The BMA therefore demarcates the structural boundary between the North American craton and the Florida–South Georgia microcontinent, known as the Suwannee, or Wiggins-Suwannee, suture.

### 7.3.7.1.3 Major Structures

The ECC-AM includes an abundance of major shear zones and faults, most of which are related to the Paleozoic accretion of terranes during the Appalachian orogenies. Prominent examples are the Brevard fault zone, a largely strike-slip fault in Georgia, South Carolina, and North Carolina that transported west-directed thrusts to the southwest along the Inner Piedmont during the Neocadian and Alleghanian orogenies; the Central Piedmont suture of Georgia, the Carolinas, and Virginia that was the possible Alleghanian thrust ramp for the Carolina terrane; and the East Piedmont fault system, which bounds the Alleghanian metamorphic core of the southern Appalachian Mountains (Hatcher et al., 2007).

Mesozoic normal faults bound the rift basins throughout the ECC-AM (Figure 7.3.7-1). The location and geometry of these rift basins are interpreted to have been controlled mainly by existing Paleozoic structures, which were reactivated as brittle normal faults when the Mesozoic extension direction was at a high angle to the preexisting fault (Cook et al., 1981; Schlische, 1993). The East Piedmont fault system, for example, was the dominant structure controlling basin development in the southern Appalachians, forming the Danville, Farmville, and Richmond basins (Swanson, 1986). Rift basins of the northern Appalachian Mountains, such as the Gulf of Maine and Fundy Basin, can be similarly correlated with specific reactivated Paleozoic faults (Swanson, 1986).

Cretaceous and younger faults within the ECC-AM are predominantly oriented north-south to northeast-southwest (Prowell, 1988). Prowell (1988) indicates that post-Cretaceous movement on these faults is reverse slip, with limited evidence for strike-slip movement. Within the ECC-AM source zone, several northeast-striking reverse fault zones in fault systems have experienced Cenozoic activity (Prowell, 1983, 1988; Wentworth and Mergner-Keefer, 1983). Some of these include the Stafford fault system in northeastern Virginia (Mixon and Newell, 1977; Newell, 1985; Pavich et al., 1989); the subsurface Brandywine fault system in southwestern Maryland (Jacobein, 1972); the Belair fault zone in eastern Georgia (Prowell and O'Connor, 1978; Bramlett et al., 1982); the Everona–Mountain Run fault zone and the Dutch Gap fault in Virginia (Pavlides et al., 1983; Prowell, 1988; Pavlides, 1994); the Hares Crossroads fault in North Carolina (Prowell, 1983); and the Cooke and offshore Helena Banks faults (Behrendt et al., 1983) near Charleston, South Carolina. These faults typically strike north to northeast, exhibit steep dips, and displace sedimentary rocks of Late Cretaceous–Miocene (100–5.3 Ma) age. Individual vertical fault zone displacements generally are tens of meters, with a maximum cumulative offset of as much as 80 m (262.5 ft; Prowell, 1988). The available stratigraphic data generally show greater displacement on older units, indicating progressive displacement through time. Vertical slip rates range from 0.0003 to 0.0015 meters per thousand years (m/ka) during the past 110 Ma, averaging 0.0005 m/ka (Prowell, 1988).

The occurrence of late Cenozoic movement along the faults mapped in the ECC-AM is difficult to assess because of poor exposure, lack of suitable stratigraphy, relatively small displacements, and low slip rates on these faults. Possible Quaternary displacement on north- and northeast-striking faults appears to be reverse slip. However, the available evidence for postulated Quaternary movement provides little constraint on possible strike-slip movement. For example, possible Pleistocene (1.8 Ma to 11 ka) activity is suggested on the Everona–Mountain Run fault

zone in central Virginia based on displacement of gravel deposits considered to be of late Cenozoic or Pleistocene age (Pavrides et al., 1983; Pavrides, 1994; Crone and Wheeler, 2000). Geomorphic relationships (Mayer and Wentworth, 1983) and possible faulted fluvial terraces at Fredricksburg, Virginia, along an extension of the Stafford fault system (Darton, 1950) may indicate post-Pliocene movement (post–1.8 Ma). There is no direct evidence, however, for Quaternary movement on any of the strands of the Stafford fault system. Furthermore, activity of these north- to northeast-striking reverse faults is difficult to reconcile with the observed northeast-southwest orientation of contemporary maximum horizontal compressive stress for the Atlantic Coastal Plain defined by Zoback and Zoback (1989) and Zoback (1992).

#### 7.3.7.1.4 Seismicity

Like most of the CEUS, seismicity within the ECC-AM is spatially variable, with moderate concentrations of earthquake activity separated by areas of very low seismicity. The most prominent of these zones of seismicity are located in the Central Virginia seismic zone and the greater New York City–Philadelphia area. To a lesser degree, these prominent zones include clusters of seismicity in the Charleston, South Carolina, area; the Piedmont region of South Carolina and Georgia; and New England (Figure 7.3.7-2). As characterized by Bollinger et al. (1991), hypocenters in the Atlantic Coastal Plain are distributed throughout the upper 13 km (8 mi.) of crust where focal mechanisms indicate a north-northeast maximum horizontal compressive stress. The largest earthquake within the ECC-AM is the 1886 Charleston earthquake. Due to the strong paleoliquefaction evidence for RLMEs in the Charleston area, a separate RLME seismic source zone is defined for Charleston (see Section 6.1.2).

The Central Virginia seismic zone (CVSZ) is an area of persistent seismic activity in the Piedmont province of Virginia, extending approximately 120–150 km (75–93 mi.) west of Richmond with a north-south width of about 100 km (62 mi.). The relative paucity of paleoliquefaction features along the coastlines and riverways of Virginia makes it unlikely that the CVSZ has produced  $M > 7$  earthquakes in the last 5,000 years (Obermeier and McNulty, 1998). The largest historical earthquake in this zone is the 1875 Goochland County earthquake, with a reported intensity of MMI VII and an estimated magnitude of  $m_b$  5.0 (Bollinger and Hopper, 1971). In general, however, the CVSZ is defined by small, shallow earthquakes, three-quarters of which occur at depths  $< 11$  km (7 mi.; Bollinger and Sibol, 1985). As the southern Appalachian detachment is at least 12 km (7.5 mi.) deep in this part of the Piedmont (Keller et al., 1985; de Witt and Bayer, 1986), CVSZ seismicity is interpreted to occur on the Paleozoic and Mesozoic faults that lie above the Precambrian basement. Outside the CVSZ, the broad pattern of seismicity in eastern North America suggests an aseismic upper crust and the occurrence of strike-slip faulting below the Appalachian detachment, with focal mechanisms yielding a northeast-southwest orientation for the maximum horizontal compressive stress. This stress orientation is consistent with the ridge-push forces resulting from continuous seafloor spreading at the mid-Atlantic ridge, which Zoback and Zoback (1989) proposed as the origin of the contemporary regional stress field in the CEUS.

For the New York–Philadelphia region, Sykes et al. (2008) used historical earthquake catalogs with their own instrumentally located earthquake database to compile a history of seismicity covering the years 1677–2006. Sykes et al. (2008) find earthquakes to be concentrated in mid-

Proterozoic to Ordovician terranes bordering the Newark basin, with hypocenters tracing out northeasterly swaths that roughly parallel the trend of the Appalachian Mountains. The most active of these zones is a 35 km (22 mi.) wide belt east and southeast of the Newark basin, which is the location for the largest historical earthquake in this region (i.e., a magnitude 5.25, a felt magnitude of Sykes that relates felt area to  $m_{bLg}$ ). Of the 383 earthquakes in the Sykes et al. (2008) local catalog, 95 percent occurred at depths shallower than 12.5 km (8 mi.). Both the New York–Philadelphia region and CVSZ are characterized by a majority of earthquakes occurring at depths shallower than the Appalachian detachment, in contrast to the deeper levels of seismicity in the Eastern Tennessee and Giles County seismic zones, which occur nearly exclusively below the detachment surface. Both of these seismic zones are located within the Paleozoic Extended Crust (PEZ) seismotectonic source (see Section 7.3.4). As is the case in the CVSZ, specific faults responsible for seismicity around the Newark basin are not well defined. However, focal mechanisms around the Newark basin conform to the broad stress field found throughout the Atlantic margin and are consistent with a  $N64^{\circ}E$  orientation of maximum horizontal compressive stress (Sykes et al., 2008).

Northeastern Massachusetts, southeastern New Hampshire, and southernmost Maine have experienced many small, and several moderate, earthquakes during the past 400 years. The two most notable earthquakes, the 1727 felt-area magnitude 5.5 Newburyport and the 1755  $M$  6.1 ( $E[M]$  6.10) Cape Ann earthquakes in Massachusetts, induced liquefaction and caused damage to buildings (Ebel, 2000, 2001). During a paleoseismology study in the Newburyport area in the late 1980s, Tuttle and Seeber (1991) found both historical and prehistoric liquefaction features. The historical features were attributed to the 1727 earthquake, and the prehistoric features were estimated to have formed during the past 4,000 years. More recent searches for earthquake-induced liquefaction features in the region yielded only one small sand dike (Tuttle, 2007, 2009). The limited paleoliquefaction features in New England, which do not provide sufficient information to characterize the recurrence, geometry, or  $M_{max}$  parameters of the ECC-AM seismotectonic source, are further discussed in Appendix E.

#### 7.3.7.2 Basis for Defining Seismotectonic Zone

The basis for defining the ECC-AM seismotectonic zone centers primarily on the assessments of Johnston et al. (1994) that Mesozoic and younger extended crust has produced all  $M \geq 7$  stable craton earthquakes worldwide, and that extended or rifted crust may provide a basis for differentiating  $M_{max}$ . In this study of global earthquakes and SCR tectonic domains, Johnston et al. (1994) found that the subdivision between rifted and nonrifted crust is significant and that SCR earthquake activity is concentrated in extended crust. As presented in Section 5.2, the SCR database and analysis of the data given in Johnston et al. (1994) was updated as part of the CEUS SSC Project. This updated analysis supports the basis for separating Mesozoic and younger extended crust to establish a prior distribution of  $M_{max}$ . The statistical significance for this separation, however, is not strong.

Defining the ECC-AM as a seismic source also differentiates it from adjoining regions of the crust that appear capable of producing different  $M_{max}$  earthquakes or future earthquake rupture characteristics. For example, the ECC-AM is separated from the ECC-GC (Gulf Coast) because

the structural grain of the two seismotectonic zones is different and will likely give rise to different future rupture characteristics (e.g., particularly rupture orientation). Crust of the ECC-AM seismotectonic zone is separated from Mesozoic extended crust of the Northern Appalachian (NAP) seismotectonic zone (Section 7.3.3) because of both the lack of rift basins expressed in the NAP and the multiple phases of reactivation and differences in future earthquake rupture characteristics.

### 7.3.7.3 Basis for Geometry

The geometry of the ECC-AM is based on the concept of including those portions of crust that underwent significant Mesozoic extension expressed as rifting. The geometry of the ECC-AM zone is similar to the Eastern Seaboard domain defined by Kanter (1994), which includes extended Paleozoic basement of the eastern United States and Nova Scotia as well as the continental shelf. The western boundary of the ECC-AM, which is defined by the Piedmont (Appalachian) gravity anomaly gradient (e.g., Bollinger and Wheeler, 1988; Figure 7.3.7-3) and corresponds closely to the Piedmont/Avalon terrane boundary of Williams and Hatcher (1983), generally follows the western edge of the Triassic-Jurassic onshore basins or the boundaries of the structural blocks in which they occur. In New England and eastern New York, the western boundary of the ECC-AM incorporates crust that has experienced Cretaceous uplift west of the Hartford basin (Roden-Tice and Tice, 2005) and deep-velocity anomalies associated with the Cretaceous Great Meteor hotspot (Li et al., 2003). Across Nova Scotia, the ECC-AM western boundary generally follows the Cobequid-Chedabucto fault system (Pe-Piper and Piper, 2004; Murphy and Keppie, 2005). The eastern boundary of the ECC-AM follows the western margin of the ECMA. The southern boundary of the ECC-AM generally follows the Brunswick magnetic anomaly (BMA), which marks the Wiggins-Suwannee suture (Hatcher et al., 2007).

### 7.3.7.4 Basis for Mmax

As with all seismotectonic zones defined for the CEUS-SSC Project, the Mmax distribution for the ECC-AM is derived using two different approaches (see Section 5.2). For the Bayesian approach, both the Mesozoic and younger extended (MESE) and composite (COMP) priors are used for this seismotectonic zone because the zone is defined by the presence of extended continental crust that was rifted during Mesozoic extension. The Kijko method was also used to assess Mmax for the ECC-AM. These methods are discussed further in Section 5.2, and the Mmax distributions and weighting schemes for ECC-AM are presented in Section 7.4.

The largest observed earthquake in the ECC-AM seismotectonic zone is the 1755 **M** 6.1 (E[M] 6.10) Cape Ann, Massachusetts, earthquake. However, there is some uncertainty as to whether this earthquake occurred in the ECC-AM since it lies near the boundary between the ECC-AM and the NAP zones. As shown on Figure 7.3.7-4, the location preferred by Bakun et al. (2003) lies within the ECC-AM, but the area defining a 95 percent confidence level for the earthquake location straddles the seismotectonic boundary. A study by Ebel (2006a) estimates the location within the ECC-AM farther southeast from the Bakun et al. (2003) preferred location (Figure 7.3.7-4). The Bakun et al. (2003) model addresses uncertainty by mapping the 67 percent and 95

percent confidence levels for its location, whereas the Ebel study (2006a) provides only an estimated epicentral area.

The uncertainty in location of the 1755 Cape Ann earthquake is included in this assessment of Mmax by assigning a 0.6 weight for a location within the ECC-AM, and a corresponding 0.4 weight that the earthquake is located not in the ECC-AM but farther north in the NAP. The higher weight is assigned for the location within the ECC-AM since the more recent study by Ebel (2006a) places the earthquake within the ECC-AM. Therefore, the Cape Ann earthquake is used (with a weight of 0.6) to represent the largest earthquake within the ECC-AM. The next largest earthquake within the ECC-AM is the E[M] 5.32 earthquake that occurred on June 11, 1638. This earthquake, which is located farther offshore than the 1755 Cape Ann earthquake, is also used (with a weight of 0.4) to represent the largest earthquake within the zone.

#### 7.3.7.5 Future Earthquake Characteristics

The future rupture characteristics assigned to the ECC-AM seismotectonic zone are listed in Table 5.4-2. For the ECC-AM, the sense of slip, rupture dip, and source boundaries are assigned default characteristics (Tables 5.4-1 and 5.4-2). The characteristics of seismogenic crustal thickness and rupture orientation are assigned unique values for ECC-AM. The extended continental crust within the ECC-AM is assigned a greater seismogenic thickness than the more highly extended transitional crust of AHEX because the crustal thickness defined by depth to the Moho is distinctly greater in the ECC-AM. Seismogenic thickness values of 13, 17, and 22 km (8, 10.5, and 13.5 mi.) are assigned weights of 0.6, 0.3, and 0.1, respectively, for the ECC-AM. In contrast, the adjacent highly extended AHEX is assigned seismogenic thickness values of 8 and 15 km (5 and 9.5 mi.) with equal weights as discussed in Section 7.3.8. The ECC-AM distribution reflects a greater seismogenic thickness than the AHEX, but a slightly lesser thickness than most of the more cratonward seismotectonic zones which have default seismogenic thickness distributions of 13, 17, and 22 km (8, 10.5, and 13.5 mi.), with weights of 0.4, 0.4, and 0.2, respectively (Table 5.4-1). The rupture orientation distribution assigned to the ECC-AM modifies the weights of the default orientations of N50°W, N-S, N35°E, N60°E, and E-W (Table 5.4-1) such that most of the weight is given to the north and northeast orientations. For the ECC-AM, the individual weights assigned to the rupture orientations of N50°W, N-S, N35°E, N60°E, and E-W are 0.1, 0.2, 0.4, 0.2, and 0.1, respectively (Table 5.4-2).

#### 7.3.8 Atlantic Highly Extended Crust Zone (AHEX)

The Atlantic highly extended crust (AHEX) seismotectonic zone represents the region of highly extended crust that is the transition between the extended, thick continental crust of the ECC-AM and the significantly thinner mafic oceanic crust of the Atlantic Ocean basin. This zone lies entirely offshore and approximately follows the continental shelf edge from Georgia to Nova Scotia (Figure 7.3.7-1).

Extension during the Triassic and Jurassic rifting of the Atlantic Ocean basin produced the relatively broad zone of extended continental crust of the ECC-AM and the adjacent narrow AHEX zone of highly extended transitional crust that was more intensely modified by rifting.

The greater amount of rifting in the 50–100 km (31–62 mi.) wide AHEX zone resulted in a greater thinning of the crust and the introduction of significant components of new igneous material, largely basalts, and mafic intrusions (Klitgord et al., 1988; Holbrook, Reiter, et al., 1994).

This chapter discusses the geologic, seismic, and geophysical characteristics of the AHEX seismotectonic zone. The information presented is based on a review of the published material summarized in the Data Summary table for both the ECC-AM and AHEX seismotectonic zones (Appendix D, Table D-7.3.7). Explicit references and data that were used as the basis for source characteristics in the AHEX are identified in the Data Evaluation table of Appendix C (Table C-7.3.7).

#### 7.3.8.1 Basis for Defining Seismotectonic Zone

Following the methodology for defining seismotectonic zones (see Chapter 4), the AHEX seismotectonic zone is included as a zone distinct from the ECC-AM zone because the AHEX zone is expected to exhibit a lesser seismogenic thickness to influence future earthquake characteristics. The sparse seismicity in the AHEX does not allow seismogenic thickness, and hence, dimensions of future ruptures, to be characterized directly from the depths of recorded earthquakes. Rather, the crustal thickness defined by depth to the Moho provides the best proxy for assessing seismogenic thickness compared with that of the adjacent extended continental crust. The eastward-thinning wedge of highly extended transitional crust that characterizes the AHEX zone is significantly thinner than the approximately 35–40 km thick (21.5–25 mi.) extended continental crust of the adjacent ECC-AM seismotectonic zone. Crustal-scale seismic-reflection profiles derived from multichannel and wide-angle seismic studies offshore of South Carolina (Holbrook, Purdy, et al., 1994), Virginia (Holbrook, Reiter, et al., 1994), and Nova Scotia (Funck et al., 2004) indicate that the AHEX zone ranges in thickness from about 15 to 30 km (9.5 to 18.5 mi.). The decreasing crustal thickness away from the continent strongly argues that the seismogenic thickness (typically thinner than the crust or depth to the Moho) should also be thinner in the AHEX than in the ECC-AM. These same studies also reveal that the zone of transitional crust of the AHEX zone corresponds to the strong positive East Coast magnetic anomaly (ECMA). As shown on Figure 7.3.8-1, Holbrook, Purdy, et al. (1994) and Holbrook, Reiter, et al. (1994) interpret the eastern limit of rifted continental crust to correspond to the western margin of the ECMA, and the western limit of oceanic crust to correspond to the eastern margin of the ECMA. In seismic Line 801 from Holbrook, Reiter, et al. (1994), located on Figure 7.3.8-1, the AHEX zone beneath the ECMA is interpreted as comprising rift-related basalts and mafic intrusive rocks up to 25 km (15.5 mi.) thick (Holbrook, Reiter, et al., 1994, Figure 15).

Crust of the AHEX seismotectonic zone is also compositionally different than the extended continental crust of the ECC-AM. The more mafic composition of the AHEX is defined by the ECMA, a major geophysical feature of the North American Atlantic margin, extending from Georgia to Nova Scotia (Figure 7.3.7-3). Combined multichannel and wide-angle seismic studies of the Atlantic Ocean margin have shown that the ECMA is spatially correlated with a zone of transitional igneous crust, marking the seaward transition from rifted continental crust to mafic

oceanic crust that extends along the entire Atlantic margin (Austin et al., 1990; Holbrook, Purdy, et al., 1994; Holbrook, Reiter, et al., 1994; LASE Study Group, 1986; Trehu et al., 1989), implying that the basalts and underlying mafic intrusives produce the high magnetic values of the anomaly (Talwani et al., 1992). The ECMA is interpreted as the result of rift-related magmatism during the first pulse of seafloor spreading (Sheridan et al., 1993; Holbrook, Purdy, et al., 1994; Holbrook, Reiter, et al., 1994; Talwani et al., 1995; Oh et al., 1995; Talwani and Abreau, 2000). The ECMA therefore marks a profound geological boundary beyond which very little continental crust occurs (Holbrook, Reiter, et al., 1994).

#### 7.3.8.2 Basis for Geometry

The boundary of the AHEX was largely defined based on the location of the ECMA. This magnetic anomaly corresponds to the highly extended transitional crust comprising the AHEX (Figure 7.3.8-1). The western margin of the AHEX corresponds to the seaward extent of continental crust that was rifted and extended in the Mesozoic, and the eastern margin of AHEX corresponds to the landward extent of oceanic crust. Although the boundary of the AHEX is generally well defined by high total magnetic values (Figure 7.3.8-1), the boundary is gradational, and thus local uncertainty about the location of the boundary between AHEX and ECC-AM seismotectonic zones could be on the order of tens of kilometers.

#### 7.3.8.3 Basis for Mmax

The Mmax distribution for the AHEX was developed using the Bayesian approach, which uses global prior distributions developed for SCRs (see Section 5.2). Because the AHEX is defined as highly extended transitional crust that was rifted during Mesozoic extension, the Mesozoic and younger extended prior (MESE) is used for this zone with the composite prior (COMP). The Kijko method was not used for the AHEX due to the low number of earthquakes observed within the zone. The largest observed earthquake within the AHEX is the September 24, 1996, E[M] 2.89 earthquake. The derived Mmax distributions for the AHEX are presented in Section 7.4.

#### 7.3.8.4 Future Earthquake Characteristics

The future rupture characteristics assigned to the AHEX seismotectonic zone are listed in Table 5.4-2 and, with the exception of seismogenic thickness and rupture orientation, are the same as those assigned to the ECC-AM. The more highly extended transitional crust within the AHEX is assigned two equally weighted seismogenic thicknesses of 8 and 15 km (5 and 9.5 mi.), which reflects a shallower seismogenic thickness than that for the ECC-AM. These values are estimates of seismogenic thickness that are not well constrained by data. Because large faults within this zone likely formed during extension and are therefore likely to be oriented parallel to the long axis of the zone and perpendicular to the maximum extension direction, a distribution of rupture directions that are asymmetrically weighted in favor of northeast-striking (i.e., N25°E and N60°E) ruptures was assigned for the AHEX, while also allowing for ruptures striking north-south, east-west, and N50°W (Table 5.4-2).

### **7.3.9 Extended Continental Crust–Gulf Coast Zone (ECC-GC)**

The breakup of the supercontinent of Pangaea and the formation of the Gulf of Mexico in the Triassic and Jurassic resulted in the development of three large crustal domains in the Gulf of Mexico region. From north to south, these domains are thick transitional crust, thin transitional crust, and newly formed oceanic crust (Buffler and Sawyer, 1985; Marton and Buffler, 1994; Salvador, 1991a, b; Sawyer et al., 1991). The Extended Continental Crust–Gulf Coast (ECC-GC) seismotectonic zone is the thick transitional crust domain (Figure 7.3.9-1). The thin transitional crust domain, the Gulf Highly Extended Crust (GHEX) seismotectonic zone, is discussed in Section 7.3.10.

The thick transitional crust domain within the Gulf of Mexico region represents continental crust that was thinned during the opening of the Gulf of Mexico. In general, the thick transitional crust is characterized by basement highs (e.g., Sarasota arch, Middle Ground arch, Wiggins uplift, Monroe uplift, Sabine uplift) and intervening lows (e.g., South Florida basin, Tampa embayment, Apalachicola basin, Mississippi Salt basin, North Louisiana Salt basin, East Texas basin) that occur along the Gulf margin from Florida to Texas (Sawyer et al., 1991). Crustal thicknesses within the thick transitional crust vary between approximately 20 and 40 km (12 and 25 mi.), with the thinnest crust occurring within the basement lows, and the thicker, relatively less extended crust occurring in association with the basement highs.

Most of the mid-Jurassic and younger subsidence and sedimentation within the thick transitional crust domain occurred in the basement lows, as reflected by the thick salt deposits that occur in many of these basins (Buffler and Sawyer, 1985; Marton and Buffler, 1994; Sawyer et al., 1991). Combined with the thin transitional crust to the south (discussed in Section 7.3.10), the total amount of thinning of continental crust in Gulf region is thought to have accommodated 50 percent of the relative plate motion during the rifting of Pangaea and opening of the Gulf of Mexico (Dunbar and Sawyer, 1987). Despite the significant amount of extension that has occurred in the thick transitional crust domain, very few accommodating structures have been identified, in part due to masking by the thick sedimentary sequence that overlies the area of extended crust (Buffler and Sawyer, 1985; Marton and Buffler, 1994; Sawyer et al., 1991).

The source characterization of the ECC-GC described in the following text is based on a review of published material (see Appendix Table D-7.3.9). Explicit references that were used as the basis for source characteristics are identified in Appendix Table C-7.3.9.

#### **7.3.9.1 Basis for Defining Seismotectonic Zone**

Following the methodology for defining seismotectonic zones presented in Chapter 4, the ECC-GC is defined as a distinct seismotectonic zone because it is anticipated that this zone will have an  $M_{max}$  distribution different from that of neighboring zones. In particular, the ECC-GC has experienced Mesozoic extension and thus the appropriate  $M_{max}$  prior is different from that applicable to other regions of the CEUS that have not experienced Mesozoic extension. The ECC-GC zone is defined as distinct from the equivalent zone along the Atlantic margin (i.e., the Extended Continental Crust–Atlantic Margin seismotectonic zone, or ECC-AM, as discussed in

Section 7.3.7), based on differences in expected future rupture characteristics. In particular, the dominant structural grain for the ECC-AM is roughly north-northeast and subparallel to the margin of Mesozoic extension along the East Coast, regional structures in the Appalachian orogen, and the modern Atlantic coastline. There is no preferred dominant structural grain in the ECC-GC because there is considerable variability and uncertainty in the orientation of structures that accommodated the opening of the Gulf of Mexico (see Section 7.3.9.4).

The ECC-GC is also distinguished from the highly extended crust to the south, which lies within the GHEX zone, as discussed in Section 7.3.10, based on a difference in expected future earthquake characteristics. This difference is related to the interpretation that the GHEX seismotectonic zone is characterized by a thinner seismogenic crust than the ECC-GC zone because the GHEX zone is more highly extended (see Sections 7.3.7.10.4 and 7.3.7.9.4).

### 7.3.9.2 Basis for Zone Geometry

#### 7.3.9.2.1 Southern Boundary

Most of the southern boundary of the ECC-GC zone, from west Texas to the eastern Gulf of Mexico, is defined as the transition between thick and thin transitional crust domains (Figure 7.3.9-1). In general, the boundary between these domains is not well defined because of the lack of a clear distinction in geologic characteristics of the two domains, and because of the difficulty in observing geologic differences between the zones due to the thick accumulation of sediment deposited atop the rifted Mesozoic crust. Some of the fundamental geologic differences between the thick and thin transitional crust domains are as follows:

- The thin transitional crust has undergone more extension.
- The thin transitional crust has been thinned more uniformly, as opposed to the basin-and-uptilt style of extension in the thick transitional crust.
- The pattern of magnetic anomaly trends within the thin transitional crust are roughly margin-parallel, as opposed to margin-perpendicular in the thick transitional crust domain (e.g., Figure 7.1-5; Buffler and Sawyer, 1985; Marton and Buffler, 1994; Sawyer et al., 1991).

In many places along the Gulf margin, these geologic contrasts are coincident with a hinge zone in the basement topography, marking where the shallow-dipping basement of the less subsided, thick transitional crust abuts the more subsided and more steeply dipping thin transitional crust. This hinge zone correlates with the location of an Early Cretaceous carbonate platform that rimmed the Gulf of Mexico basin (Buffler and Sawyer, 1985; Harry and Londono, 2004; Sawyer et al., 1991). Presumably, the location of the platform reflects the contrast in subsidence between the thick and thin transitional crust domains. This platform has been called upon by many authors to infer the location of the boundary between thick and thin transitional crust (Buffler and Sawyer, 1985; Ewing and Lopez, 1991; Harry and Londono, 2004; Marton and Buffler, 1994; Sawyer et al., 1991).

Given the lack of readily identifiable and distinct geologic differences between the thick and thin transitional crust domains, there is considerable uncertainty in the location of this boundary.

Therefore, the interpretation of the thick to thin transitional crust boundary presented by Sawyer et al. (1991) is used for defining the southern boundary of the ECC-GC; the uncertainty in the location of this boundary is on the order of 50–100 km (31–62 mi.).

South of Florida, the southern boundary of the ECC-GC zone is defined by the location of the Nortecubana fault along the north coast of Cuba. This fault marks the former suture zone of the Caribbean and North American plates and thus delineates the southern limit of Mesozoic extension within the Gulf of Mexico at this longitude (Kanter, 1994). This fault system was active until about Middle Eocene time, and it accommodated relative convergence of the Bahama platform and Cuba (Gordon et al., 1997). The current boundary between the Caribbean and North American plates is on the southern side of Cuba.

#### 7.3.9.2.2 *Western Boundary*

The western boundary of the ECC-GC zone is defined as the easternmost extent of the Gulf of Mexico coastal plain as determined by the onset of topographic relief associated with the Sierra Madre Oriental, the Coahuila folded province, and other topographic features of the eastern Mexico peninsula (Figure 7.3.9-1). Uncertainty in this boundary is on the order of several to tens of kilometers (several to tens of miles) at most, given that it is relatively well defined based on topography. The Sierra Madre Oriental and the Coahuila folded province are structural domains produced by Laramide-age fold-and-thrust tectonics, and they exhibit some evidence of Tertiary extension associated with development of the Basin and Range and the Rio Grande rift (Cook et al., 1979; Dickerson and Muehlberger, 1994; Gray et al., 2001; Murray, 1961).

#### 7.3.9.2.3 *Eastern Boundary*

Some researchers consider the eastern limit of transitional crust associated with the opening of the Gulf of Mexico to be delineated by the northwest-trending Bahamas fracture zone that extends from roughly the southeastern tip of the Florida peninsula to the northwest part of the Gulf of Mexico. This interpretation is largely based on (1) the extent of Mesozoic volcanic rocks observed in wells in southern Florida; (2) distinct boundaries seen in the gravity and magnetic anomalies of Florida; and (3) the presence of the Suwannee terrane, a relatively unextended portion of the African continent that was accreted to North America during the rifting that formed the Atlantic Ocean and Gulf of Mexico, between the Bahamas fracture zone and southern Georgia (Marton and Buffler, 1994; Salvador, 1991a; Sawyer et al., 1991; Thomas, 2006).

In spite of this tectonic interpretation, the eastern boundary of the ECC-GC zone is defined as the edge of the Atlantic margin continental shelf and the Blake plateau (Figure 7.3.9-1), and thus includes the Suwannee terrane within the ECC-GC. The decision to include the Suwannee terrane, all of Florida, and parts of southern Georgia in the ECC-GC is based on the following considerations:

- Mesozoic extension is documented within these regions (e.g., rifted crust off eastern Florida, the Apalachicola basin, and the South Georgia rift) (Daniels et al., 1983; Kanter, 1994; Klitgord et al., 1984).

- A boundary between the ECC-GC and ECC-AM occurs along the Wiggins-Suwannee suture that represents the late Alleghanian suture separating the southern Appalachians from Gondwana (African-affinity rocks). This suture marks the southern termination of the dominant Appalachian structural grain and subsequent northeasterly striking structures that formed or reactivated during Mesozoic rifting of the Atlantic.

Given the different orientations of spreading between the Atlantic and Gulf and the dominant northeast structural grain of the Appalachians, it is anticipated that the Suwannee terrane, all of Florida, and parts of southern Georgia will likely have future earthquake rupture characteristics more similar to other portions of the ECC-GC than to the ECC-AM (see Section 7.3.9.2.4).

#### 7.3.9.2.4 Northern Boundary

The northern boundary of the ECC-GC is intended to represent the northernmost extent of Mesozoic crustal thinning associated with the rifting of Pangaea and the opening of the Gulf of Mexico. The northernmost extent of Mesozoic extension is roughly coincident with the edge of Iapetan margin that formed during Paleozoic extension (within approximately 100 km, or 62 mi.; Thomas, 1988, 2006). However, there is considerable variability in the relative location of the Paleozoic and Mesozoic extensional boundaries. In Texas, the location of both boundaries is not well defined. Faulting of Mesozoic-aged basement is hypothesized by some to have extended as far north as the Balcones fault zone in central Texas (Collins, 2004; Pindell et al., 2000; Sawyer et al., 1991), but some interpretations of the edge of Iapetan margin are gulfward of this fault zone (see Wheeler and Frankel, 2000, and references therein). In this region, the northern edge of the ECC-GC is defined as the edge of the Iapetan margin by the USGS in its national seismic hazard maps (Petersen et al., 2008; Wheeler and Frankel, 2000) for the following reasons:

- There is considerable uncertainty in the boundary of Mesozoic rifting in the region.
- In many other locations along the Gulf of Mexico, structures associated with the Iapetan margin localized Mesozoic extension (Sawyer et al., 1991; Thomas, 1988).
- This boundary lies within the zone of Mesozoic rifting proposed by different researchers (e.g., Kanter, 1994; Pindell and Kennan, 2001; Pindell et al., 2000; Sawyer et al., 1991).

At the longitude of Arkansas and Louisiana, the Southern Arkansas fault zone is commonly interpreted as the northern extent of transitional crust, based on the presence of Triassic-age red beds that fill grabens associated with the fault zone (Sawyer et al., 1991; Thomas, 1988). In this region, however, the northern boundary of the ECC-GC zone is drawn farther north, encompassing more of southern Arkansas and abutting the southern extents of the Oklahoma Aulacogen (OKA) and RR seismotectonic zones. The source zone is extended north of the South Arkansas fault zone for several reasons:

- There is evidence of Late Cretaceous volcanism north of the fault zone and south of the Reelfoot rift that, while not related to the Mesozoic opening of the Gulf of Mexico, suggests that this region has undergone deformation more recently than the Midcontinent-Craton seismotectonic zone to the north (Baksi, 1997; Byerly, 1991; Hendricks, 1988; Hildenbrand and Hendricks, 1995).

- It does not seem tectonically reasonable to have a relatively thin sliver of crust without Mesozoic extension sandwiched between the northern extent of the ECC-GC zone and the southern extent of the Reelfoot rift zone, both of which are zones with Mesozoic extension.
- It does not seem appropriate to include the potential liquefaction features discussed by Cox and other researchers (Cox, 2009; Cox et al., 2007; Cox, Larsen, Forman, et al., 2004) within the Midcontinent-Craton seismotectonic zone when, if these features represent actual paleoseismic earthquakes, they may be related to reactivation of Mesozoic and Paleozoic structures (e.g., Alabama-Oklahoma transform fault; see Section 7.3.9.5; Gordon and Cox, 2008; Thomas, 1988; Thomas, 2006).

From Mississippi to western Alabama, the boundary of the ECC-GC zone is defined by the location of the Alabama-Oklahoma transform, a transform fault originally formed during the opening of the Iapetus Ocean and later reactivated during the Mesozoic opening of the Gulf of Mexico and the Atlantic Ocean (Sawyer et al., 1991; Thomas, 1988). The location of this boundary is relatively well known based on its expression in magnetic anomaly data.

From Alabama to Georgia, the northern boundary of the ECC-GC is defined by the late Alleghanian Wiggins-Suwannee suture, which underlies the South Georgia rift basin and approximately coincides with the Brunswick magnetic anomaly (BMA; McBride and Nelson, 1988; McBride et al., 2005; Hatcher et al., 2007). This suture represents the southern termination of the dominant Appalachian structural grain and subsequent structures that formed or reactivated during Mesozoic rifting of the Atlantic.

In general, the entire northern boundary of the ECC-GC is not well defined, and uncertainty in the location of the boundary is on the order of 50–100 km (31–62 mi.).

### 7.3.9.3 Basis for Zone Mmax

As with all the seismotectonic zones, the Mmax distribution for the ECC-GC is derived using two different approaches (see Section 5.2). For the Bayesian approach, the MESE and COMP priors are used for this seismotectonic zone because the zone geometry is defined by the extent of Mesozoic extension. For both approaches, three weighted alternative characterizations are used to represent uncertainty in the largest observed earthquake within the zone, as follows:

- Alternative 1: The largest observed earthquake is the October 22, 1882, E[**M**] 5.58 earthquake.
- Alternative 2: The largest observed earthquake is the October 24, 1997, **M** 4.9 E[**M**] 4.88 earthquake.
- Alternative 3: The largest observed earthquake is the potential paleoearthquake identified from the studies of Cox and other researchers and is characterized with a potential magnitude distribution of 5.0 (0.1), 5.5 (0.4), 6.0 (0.4), and 6.5 (0.1) (see discussion in Section 7.3.9.5).

Alternative characterizations 1 and 2 represent the use of historical and instrumental seismicity to define the largest observed earthquake, and Alternative 3 represents the use of paleoseismicity

to define the largest observed earthquake within the zone. For this project, 0.2 weight is given to using the potential paleoearthquake as the largest observed earthquake within the zone (see Section 5.2), so Alternative 3 is given 0.2 weight in truncating the prior. Alternatives 1 and 2 combined are given the remaining 0.8 weight, and individually they are weighted 0.4 each. The October 22, 1882, E[M] 5.58 earthquake is the largest earthquake in the zone, and the October 24, 1997, E[M] 4.884.9 earthquake is the second largest earthquake within the zone. The even weighting between the two alternative characterizations reflects the observation that the October 22, 1882, E[M] 5.58 earthquake occurs close to the eastern edge of the OKA zone boundary (see Figure 7.3.11-1), and that there is significant uncertainty in its location because the location is based on historical accounts. Similar to the treatment of this earthquake for the OKA zone (see Section 7.3.11.3), the possibility that this earthquake occurred outside the ECC-GC zone is captured with the 0.4 weight on the October 24, 1997, E[M] 4.88 earthquake as the largest in the zone.

It should be noted that for the Alternative 3 case where the maximum observed magnitude is based on the potential paleoearthquake, the magnitude distribution for maximum observed earthquake needs to take into account the probability that the largest historical earthquake is either the 5.58 or 4.9. Taking this weighted historical earthquakes into account, the actual maximum observed magnitude distribution for Alternative 3 is 5.0 (0.05), 5.5 (0.2), 5.58 (0.25), 6.0 (0.4), 6.5 (0.1).

The final Mmax distribution for the zone is presented in Section 7.4

#### 7.3.9.4 Future Earthquake Characteristics

Future earthquakes within the ECC-GC are modeled using the default characteristics for the CEUS, with the exception of the strike of fault ruptures and weighting of seismogenic thickness values. It is anticipated that future moderate to large earthquakes will most likely occur along preexisting basement structures associated with the opening of the Gulf of Mexico, and the two types of structures most likely to be reactivated are normal faults roughly perpendicular to the rifting direction that accommodated the extension, and transform faults subparallel to the rifting direction that accommodated differential spreading rates. However, there is considerable uncertainty in the orientation of these structures throughout the ECC-GC zone because there are several kinematic models for opening of the Gulf of Mexico, all of which imply different orientations for the two fault types, and, in general, each of the models has internal variation in orientation of the two fault types within different regions of the ECC-GC zone (e.g., the western vs. eastern Gulf of Mexico) (Anderson and Schmidt, 1983; Buffler and Sawyer, 1985; Buffler et al., 1980; Dunbar and Sawyer, 1987; Hall et al., 1982; Hall and Najmuddin, 1994; Klitgord et al., 1984; Marton and Buffler, 1994; Pindell, 1985, 1993; Pindell and Kennan, 2001; Pindell et al., 2006; White, 1980). Combining the uncertainty from these two factors, it is difficult to identify a preferred range of orientations, so the expected strike of future ruptures within the ECC-GC is modeled as randomly oriented.

### 7.3.9.5 Possible Paleoliquefaction Features in Arkansas, Louisiana, and Mississippi

Cox and other researchers (Cox, 2002, 2009; Cox, Forman, et al., 2002; Cox, Harris, et al., 2004; Cox and Larsen, 2004; Cox, Larsen, Forman, et al., 2004; Cox, Larsen, and Hill, 2004; Garrote et al., 2006; Cox et al., 2007; Cox and Gordon, 2008; Gordon and Cox, 2008) have conducted several studies in the southeastern Arkansas, northeastern Louisiana, and western Mississippi (ALM) areas, investigating what they interpret to be paleoliquefaction features possibly related to moderate to large earthquakes occurring along the Saline River fault zone in southern Arkansas. Collectively, this group of proposed paleoliquefaction features is referred to as the ALM features. Briefly, the basis for the researchers' interpretation is as follows:

- They observed roughly circular sandy deposits in aerial photographs throughout the Arkansas and Mississippi river valleys between southeastern Arkansas and northeastern Louisiana that they interpret to be seismically induced sand blows.
- They trenched sandy deposits at seven locations, and within the trenches they interpret multiple sand-venting episodes that can be correlated between trench sites based on stratigraphic relationships observed in the trenches, and dating of the sand units.
- They proposed that there is evidence of Quaternary fault rupture in the Saline River area along the trend of the Oklahoma-Alabama transform, a transform boundary during the Paleozoic rifting related to opening of the Iapetus Ocean and the Mesozoic rifting that formed the Gulf of Mexico.

As part of the CEUS SSC Project, the results of the studies by Randel Cox (University of Memphis) and his colleagues were evaluated to determine whether there was evidence of either RLMEs, and thus evidence for a RLME source zone, or of a single Quaternary earthquake that would impact the determination of the maximum observed earthquake within the ECC-GC zone.

To establish whether the proposed ALM paleoliquefaction data supported the presence of an RLME source, criteria established as part of the CEUS SSC Project were used for identifying earthquake-induced liquefaction features. These criteria focus on the identification of sand blows, sand-blow craters, and sand dikes because these features are the only reliable indicators of earthquake-induced liquefaction. Characteristics of these liquefaction features are described in Appendix E. With these criteria, project team members evaluated in detail the ALM features presented by Cox and other researchers. This evaluation included reviews of published papers, including trench logs; conversations with Cox; and reviews of original field notes, field trench logs, and field photographs taken by Cox as part of the various studies.

The conclusions of the evaluation are as follows:

- There is no unequivocal evidence for repeated large earthquakes in the exposures.
- There is little, if any, unequivocal evidence for large ( $M > 6$ ) earthquakes in the studied exposures.
- The best evidence for a paleoearthquake is a possible small (<6 cm wide) feeder dike shown in the field logs and on photographs of the Portland, Arkansas, trench site. It remains unclear

whether this possible small dike is the result of (1) a moderate-magnitude local earthquake, (2) a larger, more distant earthquake, or (3) non-earthquake processes. Other small sand dikes may occur in other trenches.

In summary, the conclusion was made that the paleoliquefaction data from the ALM region are preliminary and do not provide adequate evidence for a source of RLMEs in the ALM area. Therefore, an RLME source zone is not defined based on the ALM features.

The studies of Cox and other researchers were also evaluated to determine whether they provided evidence of any Quaternary paleoearthquakes that would impact the characterization of the ECC-GC zone. Following from the methodology of using the maximum observed earthquake within a seismotectonic zone in defining the Mmax distribution, a paleoearthquake magnitude could define the largest observed earthquake. As stated above, the possible sand dike in the Portland trench is the strongest evidence for a paleoearthquake within the ALM region. In general, the magnitude threshold for liquefaction is about **M** 5. The magnitude threshold in Holocene fluvial deposits in the Mississippi River floodplain is about **M** 6.3 (i.e., the magnitude of the 1895 Charleston, Missouri, earthquake). Therefore, a local earthquake in the magnitude range of **M** 5 to 6.5 could be responsible for the formation of the sand dike.

Based on our evaluation of the uncertainty in this possible magnitude, the magnitude of the paleoearthquake was characterized using the following magnitude distribution: **M** 5.0 (0.1), **M** 5.5 (0.4), **M** 6.0 (0.4), and **M** 6.5 (0.1). This magnitude distribution is one of the options used in truncating the Mmax prior for the zone (see Section 7.3.9.3). The apparent lack of unequivocal liquefaction features at other sites across the ALM region argues against a large local earthquake. Alternatively, the Portland sand dike could be the result of a large distant earthquake, perhaps centered near Marianna, Arkansas.

The Quaternary fault rupture in the Saline River area as proposed by Cox et al. (2000) was not considered in developing estimated paleoearthquake magnitudes because it is not thought that there is strong evidence for Quaternary fault rupture at that location. This appraisal of the evidence for Quaternary activity is based on (1) the fact that the faults described by Cox et al. (2000) are all relatively small displacement fault splays that have evidence of Eocene offsets, and at best equivocal evidence of Pliocene to Pleistocene offsets; and (2) the fact that there has been no additional published research conducted to support Quaternary offsets along these faults (e.g., Wheeler, 2005).

### **7.3.10 Gulf Coast Highly Extended Crust Zone (GHEX)**

The breakup of the supercontinent of Pangaea and the formation of the Gulf of Mexico in the Triassic and Jurassic resulted in the development of three large crustal domains in the Gulf of Mexico region. From north to south, these domains are the thick transitional crust, the thin transitional crust, and the newly formed oceanic crust (Buffler and Sawyer, 1985; Marton and Buffler, 1994; Salvador, 1991a, 1991b; Sawyer et al., 1991). The Gulf Highly Extended Crust (GHEX) seismotectonic zone is the thin transitional crust domain (Figure 7.3.10-1).

The thin transitional crust within the Gulf of Mexico region represents continental crust that has undergone considerable thinning associated with the opening of the Gulf of Mexico. In contrast to the thick transitional crust that is 20–40 km (12.5–25 mi.) thick (see Section 7.3.9), the thin transitional crust is generally 8–15 km (5–9.3 mi.) thick (Sawyer et al., 1991). This relatively thin crust subsided more quickly than the thick transitional crust during and following the opening of the Gulf of Mexico allowing for the deposition of thick nonmarine and marine sediments, including the salt deposits that are characteristic of the Gulf of Mexico region. These thick sedimentary sequences—and in particular, the salt deposits—have made it difficult to seismically image geologic structures that may have accommodated the extension of the thin transitional crust (Buffler and Sawyer, 1985; Marton and Buffler, 1994; Sawyer et al., 1991). However, magnetic data suggests that structures within the thin transitional crust are generally oriented parallel to the trend of the Gulf margin (Sawyer et al., 1991).

The source characterization of the GHEX seismotectonic zone described in the following text is based on a review of published material; these same materials were also used for Section 7.3.9 Extended Continental Crust—Gulf Coast (see Appendix Table D-7.3.9). Explicit references that were used as the basis for source characteristics are identified in Appendix Table C-7.3.9.

#### 7.3.10.1 Basis for Defining Seismotectonic Zone

Following the methodology for defining seismotectonic zones (see Chapter 4), the GHEX zone is included as a zone distinct from the ECC-GC zone because the GHEX zone is expected to have different future earthquake characteristics. In particular, based on the reduced crustal thickness of the GHEX zone (8–15 km [5–9.3 mi.]), the seismogenic thickness of the zone should be less than that of the ECC-GC zone.

#### 7.3.10.2 Basis for Zone Geometry

The boundaries of the GHEX seismotectonic zone are defined by the boundary between the thin and thick transitional crust (see Section 7.3.9.2 for discussion of this boundary) and the boundary between the oceanic crust and the thin transitional crust (Figure 7.3.10-1). The oceanic-transitional crust boundary of Bird et al. (2005) defines the zone because it is one of the more recent interpretations of the crustal extent that takes into account the latest data, and because it is within the range of extents estimated by previous researchers (e.g., Buffler and Sawyer, 1985; Hall and Najmuddin, 1994; Marton and Buffler, 1994; Pindell et al., 2000; Sawyer et al., 1991).

#### 7.3.10.3 Basis for Zone Mmax

As with all the seismotectonic zones, the Mmax distribution for the GHEX zone is derived using two different approaches (Section 5.2). However, the Kijko approach was given zero weight for this zone because of the low *P*-value (see Section 5.2.1.3). For the Bayesian approach, the MESE and COMP priors are used because the zone geometry is defined by the extent of Mesozoic extension. Two weighted magnitudes are used to represent uncertainty in the largest earthquake occurring within the zone.

The largest earthquake from the catalog within the zone is the February 10, 2006, E[M] 4.85 earthquake, referred to as the Green Canyon earthquake. The earthquake occurred along the Sigsbee escarpment off Louisiana. Nettles (2007) has interpreted this earthquake as a gravity-driven landslide based on the lack of high-frequency energy in the waveforms, slow rise time, preliminary focal mechanism determinations, and location on the Sigsbee escarpment. Preliminary conclusions of Dellinger et al. (2007a, b) also support this interpretation, but these studies acknowledge that neither a consensus nor conclusive interpretation of the earthquake mechanism has been determined. Furthermore, efforts to relocate the earthquake cannot constrain the depth of the earthquake to within the range expected for a landslide mechanism (Dewey and Dellinger, 2008), and there have been no peer-reviewed studies of the earthquake published in the scientific literature.

In addition to the February earthquake, the September 10, 2006, E[M]5.82 earthquake occurred just outside the zone by approximately 15 km (9 mi.; Figure 7.3.10-1). The magnitudes of these two earthquakes are equally weighted as the maximum observed earthquake within the zone for the following reasons:

- There is uncertainty in whether or not the February earthquake was caused by a landslide or discrete fault rupture.
- There is considerable uncertainty in the exact location of the oceanic-transitional crust boundary (e.g., Bird et al., 2005; Buffler and Sawyer, 1985; Hall and Najmuddin, 1994; Marton and Buffler, 1994; Pindell et al., 2000; Sawyer et al., 1991).
- Given that uncertainty, it is possible that the September earthquake occurred in transitional, and not oceanic, crust.

The final Mmax distribution for this zone is presented in Section 7.4.

#### 7.3.10.4 Future Earthquake Characteristics

Future earthquakes within the GHEX seismotectonic zone are modeled with the default characteristics for the CEUS with the exception of the strike of fault ruptures and the seismogenic thickness of crust within the zone. Similar to the ECC-GC zone, it is likely that future moderate to large earthquakes will occur along preexisting basement structures associated with the opening of the Gulf of Mexico, and the structures most likely to be reactivated are normal faults roughly perpendicular to the rifting direction (i.e., roughly parallel to the coastline) that accommodated the extension and transform faults subparallel to the rifting direction (i.e., roughly perpendicular to the coastline) that accommodated differential spreading rates. However, there is considerable uncertainty in the orientation of these structures throughout the GHEX zone because there are several kinematic models for the opening of the Gulf of Mexico, all of which imply different orientations for the two fault types, and in general, each of the models has internal variation in the orientation of the two fault types within different regions of the ECC-GC zone (e.g., the western vs. eastern Gulf of Mexico) (Anderson and Schmidt, 1983; Buffler and Sawyer, 1985; Buffler et al., 1980; Dunbar and Sawyer, 1987; Hall et al., 1982; Hall and Najmuddin, 1994; Klitgord et al., 1984; Marton and Buffler, 1994; Pindell, 1985, 1993; Pindell and Kennan, 2001; Pindell et al., 2006; White, 1980). Combining the uncertainty from these two

factors, it is difficult to identify a preferred range of orientations, so the expected strike of future ruptures within the GHEX zone is modeled as randomly oriented.

The large amounts of crustal thinning in the GHEX zone has resulted in crustal thicknesses for the thin transitional crust that are generally between 8 and 15 km (5 and 9.3 mi.; Sawyer et al., 1991). Because of this thinning, the seismogenic thickness of the crust within the zone should be less than the default values for the CEUS. For the GHEX zone the seismogenic thickness is assumed to be limited by the approximate crustal thickness (i.e., 8–15 km [5–9.3 mi.]). For simplicity and because the crustal thickness is not uniformly known within the GHEX zone, these two end-member seismogenic thicknesses are weighted evenly.

### **7.3.11 Oklahoma Aulacogen Zone (OKA)**

The Oklahoma aulacogen (OKA) seismotectonic zone (Figure 7.3.11-1) is interpreted as a failed rift arm that formed in the late Proterozoic to early Cambrian. Many of the original rift-related structures were subsequently reactivated and/or overprinted during the late Paleozoic Ouachita orogeny. The geologic history of the aulacogen generally is represented as consisting of four phases (Gilbert, 1983b; Keller and Stephenson, 2007; McConnell and Gilbert, 1990; Perry, 1989):

1. The initial late Proterozoic–early Cambrian rifting and associated magmatism.
2. A period of post-rift subsidence in the middle Paleozoic.
3. Compressional deformation associated with the late Paleozoic Ouachita orogeny.
4. Mesozoic and Cenozoic stability with the exception of the noted Quaternary slip observed on the Meers fault.

The main stage of rifting that led to the breakup of Rodinia along what is now the eastern margin of North America occurred between approximately 620 Ma and 550 Ma (Thomas, 2006; Whitmeyer and Karlstrom, 2007). Within this stage of large-scale rifting, the initiation of extension within the OKA is marked by the intrusion of rift-related basaltic magma at approximately 600 Ma (Gilbert, 1983b; McConnell and Gilbert, 1990). Magmatism associated with aulacogen formation continued until approximately 500 Ma (Gilbert, 1983b). The rifting presumably was accommodated along a series of normal faults approximately parallel to the trend of the aulacogen, but the original extensional faults have been either masked or reactivated during subsequent tectonic events, making identification of rift-related faults difficult (Brewer et al., 1983; Gilbert, 1982; Gilbert, 1983b; Keller and Stephenson, 2007; Perry, 1989).

During the middle Paleozoic (Cambrian through early Mississippian), the region surrounding the aulacogen was tectonically stable and characterized by subsidence that initiated significant basin deposition in the present-day Anadarko basin (Perry, 1989). This period of tectonic quiescence ended in the late Paleozoic during the Pennsylvania Ouachita orogeny that marked the closing of the Iapetus Ocean and the formation of the supercontinent Pangaea. In the region of the Oklahoma aulacogen, the Ouachita orogeny led to the formation of the Wichita, Arbuckle, and Amarillo uplifts, which partially were accommodated along reactivated normal faults from the original aulacogen formation. These uplifts and related structures now overprint the structural

expression of the aulacogen (Brewer, 1982; Brewer et al., 1981; Brewer et al., 1983; Good et al., 1984; Perry, 1989). Since the cessation of the Ouachita orogeny, the region surrounding the OKA has been tectonically stable with the exception of the Quaternary activity observed on the Meers fault (Crone and Luza, 1990; Gilbert, 1983a; Swan et al., 1993; see Section 6.1.4). No other faults associated with the Wichita, Arbuckle, and Amarillo uplifts or the OKA have demonstrated Quaternary activity.

The source characterization of the OKA described in the following text is based on a review of published material (see Appendix Table D-6.1.4). Explicit references that were used as the basis for source characteristics are identified in Appendix Table C-6.1.4.

#### 7.3.11.1 Basis for Defining Seismotectonic Zone

Following the CEUS SSC methodology for defining seismotectonic zones (see Chapter 4), the OKA is included as a distinct zone because we expect it to have distinct differences in future earthquake characteristics compared to surrounding regions. Compared to the default future earthquake characteristics applied to the CEUS in our model, we expect the OKA to have the following differences:

- Style of faulting: Left-lateral oblique-reverse fault dominated by strike-slip motion based on the observed slip of the Meers fault (see Section 6.1.4).
- Strike of ruptures:  $N60^{\circ}W \pm 15^{\circ}$  based on the observed strike of faults in the Wichita, Arbuckle, and Amarillo uplifts (e.g., Ham et al., 1964; Texas BEG, 1997).

The basis for defining the distinct future earthquake characteristics for the aulacogen is the observation of the characteristics of the Quaternary activity on the Meers fault, a fault within the Wichita frontal fault system (see Section 6.1.4). Despite the lack of evidence for any Quaternary activity on any other geologic structures within the aulacogen, the strong structural expression of the aulacogen and uplifts indicates that any future moderate to large earthquakes in the aulacogen are likely to have characteristics similar to those of the Meers fault.

#### 7.3.11.2 Basis for Zone Geometry

The geometry of the OKA seismotectonic zone is defined to envelop the extent of (1) the aulacogen as defined by gravity and magnetic anomaly data (CEUS SSC gravity and magnetic anomaly data; Figure 7.3.11-1); and (2) mapped faults related to the Arbuckle, Amarillo, and Wichita uplifts (e.g., Ham et al., 1964; Texas BEG, 1997). The southeastern extent of the zone is defined by the limit of crustal thinning associated with the Mesozoic opening of the Gulf of Mexico. This envelope is meant to capture both the region of crust that was the center of rifting and magmatism during the opening of the aulacogen, and faults within this potentially weakened crust and associated with the Arbuckle, Amarillo, and Wichita uplifts and the Ouachita orogeny. Given the uncertainty in the extent of the aulacogen and the uplift-related faults, there is considerable uncertainty in the boundary of the OKA. It is not possible to quantify this uncertainty, but it is likely on the order of 50 km (31 mi.) or more.

It should be noted that the OKA zone was not extended into New Mexico, Colorado, and Utah despite evidence for magmatism and geopotential anomalies in these regions that have been attributed to the Cambrian rifting of the OKA (e.g., Keller and Stephenson, 2007; Larson et al., 1985). The decision to limit the OKA source zone to the extent presented here was based on the lack of evidence for Quaternary faulting within the New Mexico, Colorado, and Utah regions of Cambrian rifting; the fact that the Arbuckle, Amarillo, and Wichita uplifts do not extend that far; and the fact that most of these regions are outside of the study area.

#### 7.3.11.3 Basis for Zone Mmax

As with all the seismotectonic zones, the Mmax distribution for the OKA zone is derived using two different approaches (see Section 5.2). However, for this zone, the Kijko approach was given zero weight because of the low  $P$ -value (see Section 5.2.1.3). For the Bayesian approach, the NMESE and COMP priors are used for this zone due to the absence of Mesozoic extension within the OKA. Two weighted scenarios are used to represent uncertainty in the largest earthquake observed within the zone. The largest earthquake within the zone is the July 30, 1925, E[M] 5.24 earthquake (Figure 7.3.11-1). However, the October 22, 1882, E[M] 5.58 earthquake is located just to the west of the zone and likely has significant uncertainty in its location because that location is based on historical accounts. To capture the possibility that the 1882 earthquake did occur within the OKA zone, two equally weighted options for the largest observed earthquake in the zone are considered: E[M] 5.58, based on the 1882 earthquake, and E[M] 5.24, based on the 1925 earthquake. The final Mmax distribution for this zone is presented in Section 7.4.2.

#### 7.3.11.4 Future Earthquake Characteristics

As described above, we model future earthquakes within the OKA seismotectonic zone using the default characteristics for the CEUS, as discussed in Section 5.4, with the exception of the style of faulting and rupture strike. Default values are used because there is little to no information to strongly support alternative values. Based on the observations of Quaternary slip on the Meers fault, the style of faulting for future earthquakes within the OKA is constrained to be left-lateral, oblique-reverse fault dominated by strike-slip motion (see Section 6.1.4). Based on the observed orientation of faulting associated with the Wichita, Arbuckle, and Amarillo uplifts, the strike of future ruptures within the OKA is constrained to be parallel to the long axis of the zone (e.g., Ham et al., 1964; Texas BEG, 1997).

### 7.3.12 Midcontinent-Craton Zone (MidC)

The continental interior (Midcontinent-Craton), which consists of those regions that have not been incorporated into Phanerozoic orogens of the continental margin, comprises two geologic provinces: the Canadian Shield, where Precambrian metamorphic and igneous basement rocks crop out at the ground surface, and the platform, where Precambrian basement rocks lie beneath a veneer of sedimentary strata (Marshak and Paulsen, 1997).

The following text provides a discussion of the geologic, seismic, and geophysical characteristics of the Midcontinent-Craton (MidC) seismotectonic zone. This discussion, as well as the seismic source characterization of the MidC, is based on a review of published material that is summarized in the Data Summary table for the MidC zone (Appendix Table D-7.3.12). Explicit references and data that were used as the basis for source characteristics of MidC are identified in the Data Evaluation table (Appendix Table C-7.3.12).

### 7.3.12.1 Background

#### 7.3.12.1.1 Precambrian Crustal Basement Structure

The Central United States is underlain by several Precambrian terranes, including the Superior province (2,700 Ma); Penokean orogen (1,880–1,830 Ma); Northern Central Plains orogen (1,880–1,700 Ma); Southern Central Plains orogen (1,700–1,600 Ma); Eastern Granite-Rhyolite province (1,470 ± 30 Ma); Southern Granite-Rhyolite province (1,370 ± 30 Ma); Midcontinent rift system (1,100–1,000 Ma); and Grenville province (1,100–800 Ma; Atekwana, 1996; Van Schmus et al., 1996).

Whitmeyer and Karlstrom (2007) present a plate-scale model for the Precambrian growth and evolution of the North American continent. The core of the North American continent, including the Canadian Shield, was formed in the Paleoproterozoic (1,600–2,500 Ma) by plate collisions. The thick, buoyant, and compositionally depleted mantle lithosphere that now underlies North America, although dominantly of Archean (>2,500 Ma) age, took its present shape due to collisional orogenesis and likely has a scale of mantle heterogeneity similar to that exhibited in the overlying crust.

In marked contrast, the lithosphere of southern North America (i.e., much of the continental United States) was built by progressive addition of a series of dominantly juvenile volcanic arcs and oceanic terranes accreted along a long-lived southern (based on present coordinates) plate margin. The lithospheric collage that formed from dominantly juvenile terrane accretion and stabilization (1,800–1,000 Ma) makes up about half of the present-day North American continent. Throughout—and as a result of—this long-lived convergent cycle, mantle lithosphere below the accretionary provinces was more hydrous, fertile, and relatively weak compared to mantle lithosphere under the Archean core.

Mooney and Ritsema (2009) hypothesize that greater lithospheric strength correlates with lower rates of continental crustal seismicity and with lower maximum magnitude. They suggest that high lithospheric S-wave velocities that are typical of cratonic lithosphere correspond to high integrative lithospheric strength. By comparing global maps of S-wave velocity anomalies at a depth of 175 km (108 mi.) and the moment magnitudes of earthquakes in the overlying crust, Mooney and Ritsema (2009) conclude that the maximum magnitude for SCRs underlain by S-wave velocity anomalies of >3.5 percent, which includes a large portion of the Archean- and Neoproterozoic-age Precambrian continental interior of the CEUS, appears to be **M** 7. Analysis of the magnitudes of earthquakes in stable continental regions worldwide indicates that a broader range of magnitudes may better represent the uncertainty in maximum magnitude (Section 5.2).

### 7.3.12.1.2 Major Precambrian Basement Structures

Major Precambrian basement features have been interpreted by various workers based on interpretation of geologic data from drilling, deep crustal seismic profiles, and interpretation of geopotential field data (e.g., Braile et al., 1986; Pratt et al., 1989; Atekwana, 1996; Marshak and Paulsen, 1997). Sims et al. (2005) present a preliminary structure map of Precambrian basement rocks based on interpretation of geologic and magnetic data (Figure 7.3.12-1). They suggest that the systematics of major regional post-assembly Precambrian basement structures throughout the continental United States point to a common causal mechanism for their development. A major driving force for plate movement is deep-mantle flow resulting from seismic anisotropy beneath the continents and mechanical coupling and subsequent shear between the lithosphere and asthenosphere. Two orthogonal sets of shear zones and faults are predominant in the continent: (1) northeast-striking partitioned ductile shear zones and (2) northwest-trending strike-slip ductile-brittle faults (Sims et al., 2005).

The northeast-striking shear zones are interpreted by Sims et al. (2005) as resulting from northwest-southeast shortening, apparently formed during the interval 1,760–1,700 Ma. The northwest-trending (1,700–1,500 Ma) transcurrent fault system consists of west-northwest to northwest synthetic faults and northerly trending antithetic transfer faults. The deformation during this interval is attributed to transpressional-transensional deformation (i.e., strike-slip deformation that deviates from simple shear because of a component of shortening or extension orthogonal to the deformation zone). The northeast- and northwest-oriented shears and faults mimic orthogonal teleseismic images of the upper mantle. These structures were reactivated during the Mesoproterozoic (1,000–1,600 Ma) and later times. The kinematics of regional Precambrian basement structures within the continental United States suggest that deformation since at least early Proterozoic time has been predominantly transpressional. Transcurrent lithospheric structures formed during Proterozoic mantle deformation are oriented obliquely to the southwestward (absolute) motion of the North American Plate. Stress caused by traction between the asthenosphere and lithosphere during the southwestward drift focused on preexisting block boundaries that have repeatedly reactivated basement zones of weakness, thus localizing sedimentation, magmatism, and generation of ore deposits (Sims et al., 2005).

Marshak and Paulsen (1997) identified similar north-northeast and west-northwest trends that break up the continental interior of the United States into roughly rectangular blocks. They refer to these as the Midcontinent fault and fold zones and suggest that the current intraplate stress field of North America is sufficient to cause slight movements of crustal blocks in the interior, thereby triggering seismicity. Marshak and Paulsen (1997) also note that differential epeirogenic movements (the gradual uplift, subsidence, or tilting of broad areas relative to their surroundings) have affected sedimentary thicknesses and facies throughout the region. These movements occurred episodically through the Phanerozoic (post-Precambrian), giving rise to reactivated regional-scale (>200 km [ $>124$  mi.] diameter) basins, domes, and arches.

### 7.3.12.1.3 Geophysical Anomalies

As noted by Hinze and Hildenbrand (1988), information on the crystalline crust of the Eastern United States from direct observations, drilling, and sparse crustal seismic studies is limited.

Regional gravity and magnetic anomaly data provide more uniform coverage and can be used to estimate the strength of the crust and lithosphere and to map and characterize (1) zones of weakness such as paleorifts, sutures, and faults; (2) regions of potential stress amplifications such as plutons and irregularities in fault zones; and (3) basement terranes of generally consistent structural pattern that may delimit coherent regional seismic zones.

Some of the more prominent geophysical anomalies are shown on Figures 7.3.12-1 and 7.3.12-2, including the Midcontinent gravity high associated with the Midcontinent rift (Hinze et al., 1997); gravity and magnetic anomalies associated with the East Continent rift basin (Drahovzal et al., 1992); geophysical lineaments such as the Commerce geophysical lineament (CGL; Langenheim and Hildenbrand, 1997; Hildenbrand and Hendricks, 1995); the south-central magnetic lineament (SCML; Hildenbrand et al., 1983); and the neodymium (Nd) isotopic boundary (also referred to as the St. Charles lineament [SCL]), which probably represents the southeast limit of Paleoproterozoic crust (Van Schmus et al., 1996; Harrison and Schultz, 2002; Van Schmus et al., 2007); and sutures such as the Great Lakes tectonic zone (GLTZ), Spirit Lake tectonic zone (SLTZ), Eau Plain shear zone (EP), and Niagara fault zone (NF; Hinze, 1996; Van Schmus et al., 2007).

#### 7.3.12.1.4 Seismicity

Seismicity within the MidC zone is spatially variable, with moderate concentrations of earthquake activity separated by areas of very low seismicity. Previously recognized zones of seismicity are the Anna seismic zone in Ohio, the Northeast Ohio seismic zone, and a zone of moderate seismicity in the vicinity of the Nemaha ridge in Kansas (Figure 7.3.12-3). Reconnaissance paleoliquefaction surveys conducted to date have not identified evidence for large-magnitude ( $M > 7$ ) earthquakes in these zones. Preliminary conclusions from these studies, which are discussed in the following descriptions of the zones, are that  $M > 7$  earthquakes probably have not occurred in these regions in the past few thousand years. Moderate-sized earthquakes ( $M 6$  to  $< M 7$ ), however, cannot be precluded based on the extent and completeness of the surveys and the existing geologic characteristics (e.g., liquefaction susceptibility, quality of exposure, age of deposits). The available information does not support defining RLME sources associated with these zones of more concentrated seismicity.

**Anna Seismic Zone**—This zone, also called the Western Ohio seismic zone, coincides with northwest-southeast-trending basement faults associated with the Fort Wayne rift (Figure 7.3.12-2) in Shelby, Auglaize, and nearby counties (Hansen, 1993; Baranoski, 2002). Ruff et al. (1994) attribute seismicity to the Anna-Champaign, Logan, and Auglaize faults. This zone has produced at least 40 felt earthquakes since 1875, including earthquakes in 1875, 1930, 1931, 1937, 1977, and 1986 that caused minor to moderate damage (Hansen, 1993). The July 12, 1986, earthquake near the town of St. Marys in Auglaize County was the largest earthquake to occur in the zone since 1937 (Hansen, 1993). For the 1986 magnitude ( $m_b$ ) 4.5 ( $E[M]$  4.37) earthquake, Schwartz and Christensen (1988) determined a hypocenter of 5 km (3 mi.) and a focal mechanism (strike =  $25^\circ$ , dip =  $90^\circ$ , rake =  $175^\circ$ ) representing mostly strike-slip, with a small oblique component approximately parallel to the Anna-Champaign fault and a nearly horizontal  $P$ - (maximum compressive stress) axis oriented east-northeast. The earthquake produced a MMI VI intensity (Schwartz and Christiansen, 1988). Obermeier (1995) investigated stream banks in

the vicinity of Anna, Ohio, and portions of the Auglaize, Great Miami, Stillwater, and St. Marys rivers and found no evidence of paleoliquefaction features indicative of a magnitude 7 earthquake in the past several thousand years. Obermeier (1995) noted that although there was sufficient outcrop to preclude with some confidence an earthquake larger than magnitude 7, the paucity of outcrop did not preclude the possibility of prehistoric earthquakes of lower magnitudes. Crone and Wheeler (2000) designated the Anna seismic zone a Class C feature<sup>4</sup> based on the occurrence of significant historical earthquakes and the lack of paleoseismic evidence.

**Northeast Ohio Seismic Zone**—This zone, also called the Ohio-Pennsylvania seismic zone, defines an approximately 50 km (30.5 mi.) long, northeast-southwest-trending zone of earthquakes south of Lake Erie on the Ohio-Pennsylvania border (Dineva et al., 2004). The largest historical earthquake in this zone was the January 31, 1986,  $m_b$  5.0 (E[M] 4.65) earthquake located about 40 km (25 mi.) east of Cleveland in southern Lake County, Ohio. The earthquake produced MMI VI to VII at distances of 15 km (9 mi.) from the epicenter (Nicholson et al., 1988). Aftershocks with magnitudes ranging from 0.5 to 2.5 and focal depths ranging from 2 to 6 km (1.2 to 3.7 mi.) occurred in a tight cluster about 1 km (0.6 mi.) wide and oriented north-northeast. Focal mechanisms represent predominantly oblique, right-slip motion on nearly vertical planes oriented N15° to 45°E, with a nearly horizontal *P*-axis consistent with the modern stress regime (Nicholson et al., 1988).

The January 31, 1986, earthquake and aftershocks were within 12 km (7.3 mi.) of deep waste-disposal injection wells, and the earthquake sequence is possibly due to injection activities at the wells that reactivated favorably oriented preexisting fractures (Nicholson et al., 1988). However, the relative distance of the wells from the earthquake cluster (12 km [7.3 mi.]), as well as the lack of large numbers of earthquakes that are typical of induced sequences, a history of small to moderate earthquakes in the region preceding well activities, and the attenuation of the pressure field with distance from the wells—all argue for a natural origin for the earthquakes (Nicholson et al., 1988).

Nicholson et al. (1988) observe that the 1986 cluster is coincident with a N40°E trending gravity and magnetic anomaly. Seeber and Armbruster (1993) and Dineva et al. (2004) also associate the Northeast Ohio seismic zone with the Akron magnetic boundary, which is also called the Akron magnetic anomaly or lineament (Figure 7.3.12-2). Seeber and Armbruster (1993) speculate that the Akron magnetic boundary may be associated with the Central Metasedimentary Belt boundary zone as a continental-scale Grenville-age structure. Since the Akron lineament is imaged as ductile shear zones on regional seismic lines and no structures are observed in the overlying Paleozoic sediments, Seeber and Armbruster (1993) acknowledge that the geometry of brittle faulting within or near this ductile deformation may have a complex relationship with the geometry of these shear zones.

In 1987, the first in a series of earthquakes continuing to 2003 occurred within the Northeast Ohio seismic zone near Ashtabula in Ashtabula County, Ohio, northeast of the 1986 earthquakes

---

<sup>4</sup> See Section 4.1.3.3 for definition of fault and feature categories used by the USGS to characterize Quaternary and possible Quaternary features in the CEUS.

(Nicholson et al., 1988; Seeber and Armbruster, 1993; Hansen et al., 2001; Seeber et al., 2004). The largest earthquakes in the sequence include an initial  $m_{bLg}$  3.8 (E[**M**] 3.61) earthquake on July 13, 1987; a  $m_{bLg}$  2.6 foreshock earthquake on January 19, 2001; a  $m_{bLg}$  4.3 (E[**M**] 3.86) earthquake on January 26, 2001, which had an MMI of VI; followed by a  $m_{bLg}$  3.0 (E[**M**] 2.92) earthquake on June 3, 2001, and a  $m_{bLg}$  2.4 earthquake on June 5, 2001 (Hansen et al., 2001). The latest subsequence started in July 2003 with a  $m_{bLg}$  2.5 earthquake (Seeber et al., 2004)

Seeber et al. (2004) discuss these fore-/main-/aftershock sequences and interpretations of these earthquakes using information obtained from three short-term deployments of portable seismographs (in 1987, 2001, and 2003) and from regional broadband seismograms. The main observations and conclusions from this analysis are as follows:

- A persistent earthquake sequence in northeast Ohio includes multiple, distinct fore-/main-/aftershock sequences that illuminate two nearly vertical, east-trending faults approximately 4 km (2.5 mi.) apart. The first motions are consistent with left-lateral strike-slip movement on an east-west-striking fault. The seismicity is closely associated with injection of waste fluid in the basal Paleozoic formation from 1986 to 1994.
- All the earthquakes originated from a relatively small area (~10 km [~6 mi.] wide) and are assumed to form a single sequence of casually related earthquakes.
- Felt earthquakes started in 1987, a year after the onset of injection. At that time, earthquakes were located 0.7–2.0 km (0.4–1.2 mi.) from the injection site. Seismicity continued and in 2001, five and a half years after the end of injection, hypocenters were then 5–9 km (3–5.6 mi.) from the injection site. The only known episode of seismicity in Ashtabula is closely associated with the 1986–1994 Class 1 injection, and the pattern of hypocenters is consistent with one expected for the high pore-pressure anomaly spreading from the injection site.
- This spatial and temporal correlation is strong evidence that the seismicity was triggered by the injection.

A paleoseismic liquefaction field study along two of the larger drainages in northeast Ohio, the Grand River and the Cuyahoga River, was conducted by Obermeier (1995) and involved reconnaissance along approximately 25 km (7.6 mi.) of stream bank. No evidence of liquefaction was observed along either transect. Although the scarcity of suitable exposures precludes definitive statements about prehistoric earthquakes, this led Crone and Wheeler (2000) to classify the Northeast Ohio seismic zone as a Class C feature. Conditions and ages of the sediment encountered along each of these rivers as noted by Obermeier (1995) were summarized in the report, as follows:

- Radiocarbon data from along the Grand River show that many of the exposures searched are at least 2,000 years old. Many others are probably mid-Holocene in age, based on depth and severity of weathering. A few scattered sites are earliest Holocene in age. Liquefaction susceptibility at many of the sites examined is at least moderate.
- Numerous exposures along the Cuyahoga River are at least a few thousand years in age, and scattered exposures are up to 8,000 years old, based on radiocarbon data. Conditions are favorable for forming liquefaction effects at many places.

- It is unlikely that sediments exposed in a sand pit near the Ashtabula-Trumbull county line experienced strong ground shaking through most or all of Holocene time. The groundwater table has probably been shallow enough through all or much of the Holocene to provide conditions favorable to liquefy the thick sand deposits overlain by a silt cap that are exposed in the quarry walls.

**Nemaha Ridge–Humboldt Fault Seismic Zone**—Historical felt earthquakes and instrumentally recorded microseismicity are loosely associated with basement structures in northeastern Kansas. Wheeler and Crone (2001) note that two damaging earthquakes in 1867 (Wamego earthquake) and 1952, which were assigned magnitudes of  $M$  5.54 and  $M$  5.66, respectively, by Johnston (1994), occurred in the vicinity of the Humboldt fault zone on the Nemaha uplift. Niemi et al. (2004) and Bakun and Hopper (2004a) also suggest a possible association of the 1867 Wamego earthquake with the basement Nemaha Ridge–Humboldt fault structures, which lie to the east and roughly parallel to the Proterozoic Midcontinent rift system. Seeber and Armbruster (1991) assigned the 1867 earthquake a magnitude of 5.2. Bakun and Hopper (2004a) assign a magnitude ( $2\sigma$  range) of  $M_I$  4.9 (4.5–5.2) to the earthquake. The 1867 and 1952 earthquakes are assigned magnitudes of  $E[M]$  5.50 and  $E[M]$  5.29 in the CEUS SSC Project catalog.

Niemi et al. (2004) conducted field reconnaissance investigations to evaluate evidence for paleoliquefaction in the epicentral region of the 1867 Wamego earthquake. Field investigations confirm that sedimentary deposits with moderate liquefaction susceptibility are present in the vicinity of Wamego and Wabaunsee, Kansas, the preferred source location of the 1867 Wamego earthquake. Soft-sediment deformation features, including flame and dish structures, are present in late Holocene floodplain deposits of the Kansas River and appear to be concentrated in the horseshoe bend region of the Kansas River near Wamego and Wabaunsee, Kansas. Results of the reconnaissance suggest that liquefaction features (e.g., clastic dikes), which may be attributed to seismically induced liquefaction, are present but may not be pervasive in this region. Niemi et al. (2004) concluded from the results of their reconnaissance that these data suggest that the 1867 Wamego earthquake with a reported magnitude of 5.2 (Seeber and Armbruster, 1991) may characterize the seismic source in this region. Although the available data suggest that the earthquake that triggered the paleoliquefaction features could have been close to the threshold-sized earthquake that may trigger paleoliquefaction (approximately  $M$  5.4–5.8; Olson et al., 2005), the available data do not preclude the possibility that the earthquake was larger. There is not sufficient information at this time to characterize an RLME source associated with the Nemaha Ridge–Humboldt fault region.

### 7.3.12.2 Basis for Defining Seismotectonic Zone

The MidC seismotectonic zone represents continental crust that has not experienced Mesozoic or younger crustal extension. Defining the MidC seismotectonic zone centers primarily on the concept that continental crust that has not experienced Mesozoic or younger crustal extension will have a different maximum magnitude probability than crust that has experienced Mesozoic or younger extension (Johnston et al., 1994; see also updated analysis in Section 5.2).

The MidC zone is also defined as a seismic source in part to differentiate it from some adjoining regions of the crust that are interpreted as producing different future rupture characteristics. For example, the trend of future ruptures in the adjoining Illinois Basin Extended Basement (IBEB), Reelfoot Rift (RR), and Oklahoma Aulacogen (OKA) seismotectonic zones reflects preferred orientations of structures in those zones, which differ from the trend of ruptures modeled for the MidC.

#### 7.3.12.3 Basis for Zone Geometry

Four alternative geometries are considered based on alternative geometries of adjacent zones. These are shown on Figure 7.3.12-4. The northern and western boundaries of all alternative MidC zones are the study region boundaries. The eastern boundary is defined by either the western boundary of the Paleozoic Extended Crust (PEZ) and RR wide or narrow geometries (see Sections 7.3.4 and 7.3.5, respectively). The southern boundary west of the RR is defined by the northern boundary of the Extended Continental Crust–Gulf Coast (ECC-GC) and OKA seismotectonic zones (Sections 7.3.9 and 7.3.11, respectively).

#### 7.3.12.4 Basis for Zone Mmax

The Mmax distribution for the MidC source zone is based on the two approaches, Kijko (2004) and Bayesian, as outlined in Section 5.2.

For the Kijko approach, the *P*-values for the four MidC alternative geometries (MidC-A, MidC-B, MidC-C, and MidC-D) are all 0.03; therefore, in all cases this approach is weighted 0.24.

For the Bayesian approach, both the composite (COMP) prior and the non-Mesozoic and younger extension (NMESE) prior are used; the NMESE is selected based on the evidence for no Mesozoic or younger extension in the craton region of the Midcontinent. The priors are truncated and modified using the likelihood function based on the largest historical earthquakes recorded within the zone: the May 16, 1909, E[M] 5.72; November 15, 1877, E[M] 5.50; and March 28, 1964, E[M] 4.84 earthquakes. The location of the largest earthquake in this zone, the May 16, 1909, E[M] 5.72 earthquake at a latitude/longitude intersection in eastern Montana near the Canadian border suggests this earthquake is poorly constrained.

The weights for Kijko and Bayesian approaches for the RR zone also are discussed in Section 7.4.2, and the weighted composite posterior maximum-magnitude probability distribution for the RR zone is provided in Section 7.4.2. The derived Mmax distributions for the MidC seismotectonic zone are presented in Section 7.4.2.

#### 7.3.12.5 Future Earthquake Characteristics

The MidC seismotectonic zone uses default characteristics for future rupture characteristics listed in Table 5.4-2. The MidC zone encompasses a large intracratonic region characterized by

deeply buried Precambrian structures for which independent interpretational constraints are limited. The available data for the CEUS on style of faulting, focal mechanisms, and depth of well-constrained earthquakes used to develop the “default” characteristics as outlined in Table 5.4-1 include information from the MidC region.

## 7.4 Maximum Magnitude Distributions for Seismotectonic Distributed Seismicity Sources

This section presents the maximum earthquake magnitude (Mmax) distributions for the seismotectonic distributed seismicity sources. The methodology used to develop these distributions is presented in Section 5.2.1. The steps involved in the process are identification of the maximum observed earthquake in each distributed seismicity source (described in Section 7.4.1) and then application of the quantitative approaches developed in Section 5.2.1 to produce the composite Mmax distributions (described in Section 7.4.2).

### 7.4.1 Maximum Observed Earthquake Magnitude

The maximum observed earthquake magnitude,  $m_{\text{max-obs}}$ , represents the largest non-RLME earthquake observed to have occurred with each source. The value of this magnitude is used in developing the likelihood function for the Bayesian Mmax approach (Section 5.2.1.1) and is a parameter of the Kijko approach (Section 5.2.1.2). Two resources are used to assess  $m_{\text{max-obs}}$ . One is the CEUS SSC Project catalog developed for this study (Chapter 3) and the other is identified paleoearthquakes that are not treated as RLMEs. The latter consist of the four non-RLME paleoearthquakes that have been identified in the IBEB seismotectonic zone and the potential liquefaction earthquake in the ECC\_GZ zone. These earthquakes are discussed in Sections 7.3.5.4 and 7.3.9.5 for the IBEB and ECC\_GC zones, respectively. The largest non-RLME historical earthquakes identified in the CEUS SSC Project catalog for each seismotectonic source zone are described in Section 7.3 in the subsection for each zone.

Uncertainty in  $m_{\text{max-obs}}$  was incorporated into the Mmax assessment using the procedure described in Section 5.2.1.1.6. The uncertainties in the magnitudes for the catalog of historical earthquakes or paleoearthquakes for each source were used to develop simulated catalogs of earthquake magnitudes. The largest values for each simulation were then used to develop a distribution for  $m_{\text{max-obs}}$ . Figure 7.4.1-1 shows the resulting distributions for  $m_{\text{max-obs}}$ . The blue curve on each plot shows the distribution developed for  $m_{\text{max-obs}}$ , and the red vertical line indicates the nominal observed magnitude. The phrase “paleo” in a plot legend (see IBEB on Figure 7.4.1-1) indicates that the set of paleoearthquakes is the controlling set for determining  $m_{\text{max-obs}}$  and was the set used to develop the Mmax distributions. For a number of zones, alternative earthquake catalogs (as indicated in the plot legends) were used to address the uncertainty in assigning particular earthquakes to the zone.

## 7.4.2 Mmax Distributions

Mmax distributions were developed for each seismotectonic distributed seismicity source using the Bayesian and Kijko methods. For the Bayesian Mmax approach, the alternative priors described in Section 5.2.1.1 were used. Figures 7.4.2-1 through 7.4.2-17 show the resulting Mmax distributions obtained by each method. Indicated in the legend of each figure are the weights assigned to the individual Mmax methods following the weighting approach described in Section 5.2.1.1. The final weighted composite distributions are indicated by the thick red bars on each plot.

The weights assigned to the Kijko method are tabulated below. In general, the numbers of earthquakes in many of the seismotectonic source zones are too few to allow weight to be applied to the Kijko method.

<b>Seismotectonic Source Zone</b>	<b>Weight Assigned to Kijko Method</b>
AHEX	0
ECC_AM	0.05
ECC_GC	0
GHEX	0
GMH	0
IBEB	0
MidC-A	0.24
MidC-B	0.24
MidC-C	0.24
MidC-D	0.24
NAP	0
OKA	0
PEZ_N	0
PEZ_W	0.01
RR	0
RR_RCG	0.07
SLR	0.02

The continuous distributions shown on Figures 7.4.2-1 through 7.4.2-17 were used to construct five-point discrete approximations for use in hazard analyses. The resulting Mmax distributions are listed in Table 7.4.2-1.

## 7.5 Recurrence Parameters

The recurrence parameters (i.e., rate and  $b$ -values) for the seismotectonic zones were calculated using the methodology and parameters described in Section 5.3.2. Briefly, this methodology divides the source zone into cells of dimensions a quarter or half degree and then calculates the rate and  $b$ -value in each cell using the likelihood function of the data in that cell together with penalty functions that tend to smooth the cell-to-cell variation in the rate or the  $b$ -value, as discussed in Section 5.3.2.1. In addition, this procedure characterizes epistemic uncertainty in the recurrence parameters by generating eight alternative maps of the recurrence parameters.

### 7.5.1 Rate and $b$ -Value Maps for Single Zone and Two Zones

Figures 7.5.1-1 through 7.5.1-12 show the mean recurrence maps for the four alternative configurations of the seismotectonic zones' distributed seismicity source zones and the three choices of magnitude weights (i.e., Cases A, B, and E presented in Section 5.3.2.2). Maps of the calculated uncertainties in recurrence parameters, as well as alternative recurrence maps that represent that uncertainty (eight alternative maps for each source-zone configuration), are shown in Appendix J.

The SLR zone exhibits lower  $b$ -values than other zones. This zone was fit using somewhat different smoothing parameters, as described in Section 5.3.2.

### 7.5.2 Comparison of Recurrence Parameters to Catalog

Figures 7.5.2-1 through 7.5.2-51 compare the expected counts from the recurrence maps for each source zone to the observed earthquake counts within the zone. The error bars on the data represent the 16–84 percent range of statistical uncertainty in the counts and are calculated using the approach by Weichert (1980). Each of the eight curves represents expected counts (i.e., rate times equivalent period of completeness) for one of the eight equally weighted alternative maps, taking  $M_{max}$  into account.

These comparisons indicate a good agreement between predicted and observed rates. For some zones, such as ECC\_AM, the recurrence model over- or underestimates the observed rates for a magnitude bin, but these discrepancies are not unexpected in bins with low earthquake counts.

These comparisons also illustrate the effect of earthquake counts on rate uncertainty at the source-zone scale. The eight alternative curves are nearly identical for MidC-A (Figures 7.5.2-19 through 7.5.2-21), which has hundreds of earthquakes in the low-magnitude range. In contrast, the eight curves differ by a factor of 2 to 5 for OKA (Figures 7.5.2-35 and 7.5.2-36), which has earthquake counts more than one order of magnitude lower. The results for OKA also illustrate the effect of the magnitude weights on the uncertainty in rates. The behavior of the uncertainty in rate at smaller scales is similar to that observed in these figures and is shown more clearly in the maps showing uncertainty (see Appendix J).

**Table 7.1-1**  
**Data Summary and Data Evaluation Tables for Seismotectonic Zones in Appendices C and D**

<b>Section</b>	<b>Source (with Acronym)</b>	<b>Data Table</b>
7.3.1	St. Lawrence Rift (SLR)	C-7.3.1, D-7.3.1
7.3.2	Great Meteor Hotspot (GMH)	C-7.3.2, D-7.3.2
7.3.3	Northern Appalachian (NAP)	C-7.3.3, D-7.3.3
7.3.4	Paleozoic Extended Crust (PEZ)	C-7.3.4, D-7.3.4
7.3.5	Illinois Basin Extended Basement (IBEB)	C-7.3.5, D-6.1.9
7.3.6	Reelfoot Rift Zone (RR)	C-7.3.6, D-6.1.5
7.3.7	Extended Continental Crust–Atlantic Margin (ECC-AM)	C-7.3.7, D-7.3.7
7.3.8	Atlantic Highly Extended Crust (AHEx)	C-7.3.7, D-7.3.7
7.3.9	Extended Continental Crust–Gulf Coast (ECC-GC)	C-7.3.9, D-7.3.9
7.3.10	Gulf Coast Highly Extended Crust (GHEx)	C-7.3.9, D-7.3.9
7.3.11	Oklahoma Aulacogen (OKA; incl. Meers Fault)	C-6.1.4, D-6.1.4
7.3.12	Midcontinent-Craton (MidC)	C-7.3.12, D-7.3.12

**Table 7.4.2-1**  
**Maximum Magnitude Distributions for Seismotectonic Distributed Seismicity Sources**

Weight	Maximum Magnitude for:												
	AHEX	ECC_AM	ECC_GC	GHEX	GMH	IBEB	MidC-A, MidC-B, MidC-C, and MidC-D	NAP	OKA	PEZ_N and PEZ_W	RR	RR_RCG	SLR
0.101	6.0	6.0	6.0	6.0	6.0	6.5	5.6	6.1	5.8	5.9	6.2	6.1	6.2
0.244	6.7	6.7	6.7	6.7	6.7	6.9	6.1	6.7	6.4	6.4	6.7	6.6	6.8
0.310	7.2	7.2	7.2	7.2	7.2	7.4	6.6	7.2	6.9	6.8	7.2	7.1	7.3
0.244	7.7	7.7	7.7	7.7	7.7	7.8	7.2	7.7	7.4	7.2	7.7	7.6	7.7
0.101	8.1	8.1	8.1	8.1	8.1	8.1	8.0	8.1	8.0	7.9	8.1	8.1	8.1

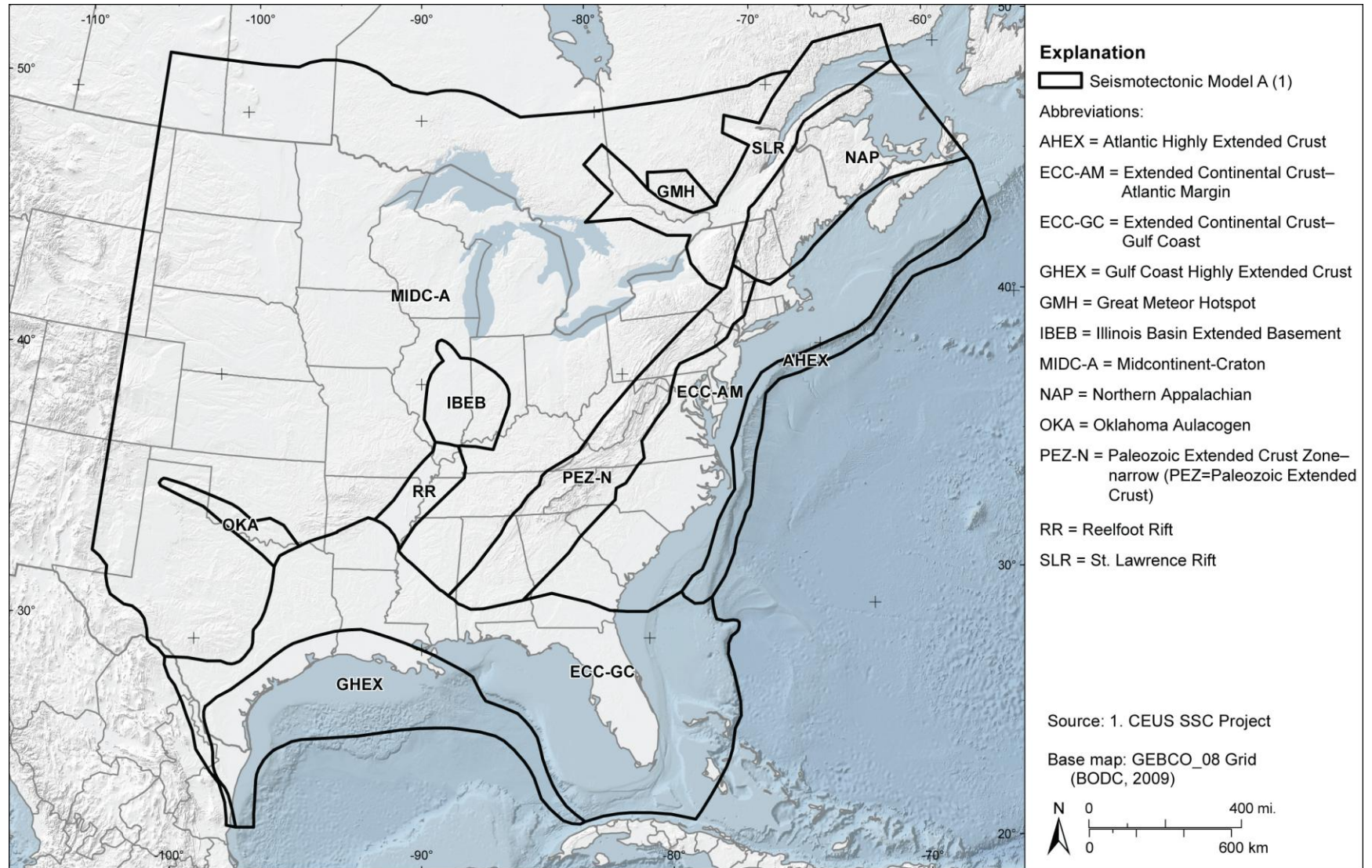


**Figure 7.1-1**  
 Seismotectonic zones shown in the case where the Rough Creek graben is not part of the Reelfoot rift (RR) and the Paleozoic Extended Crust is narrow (PEZ-N)

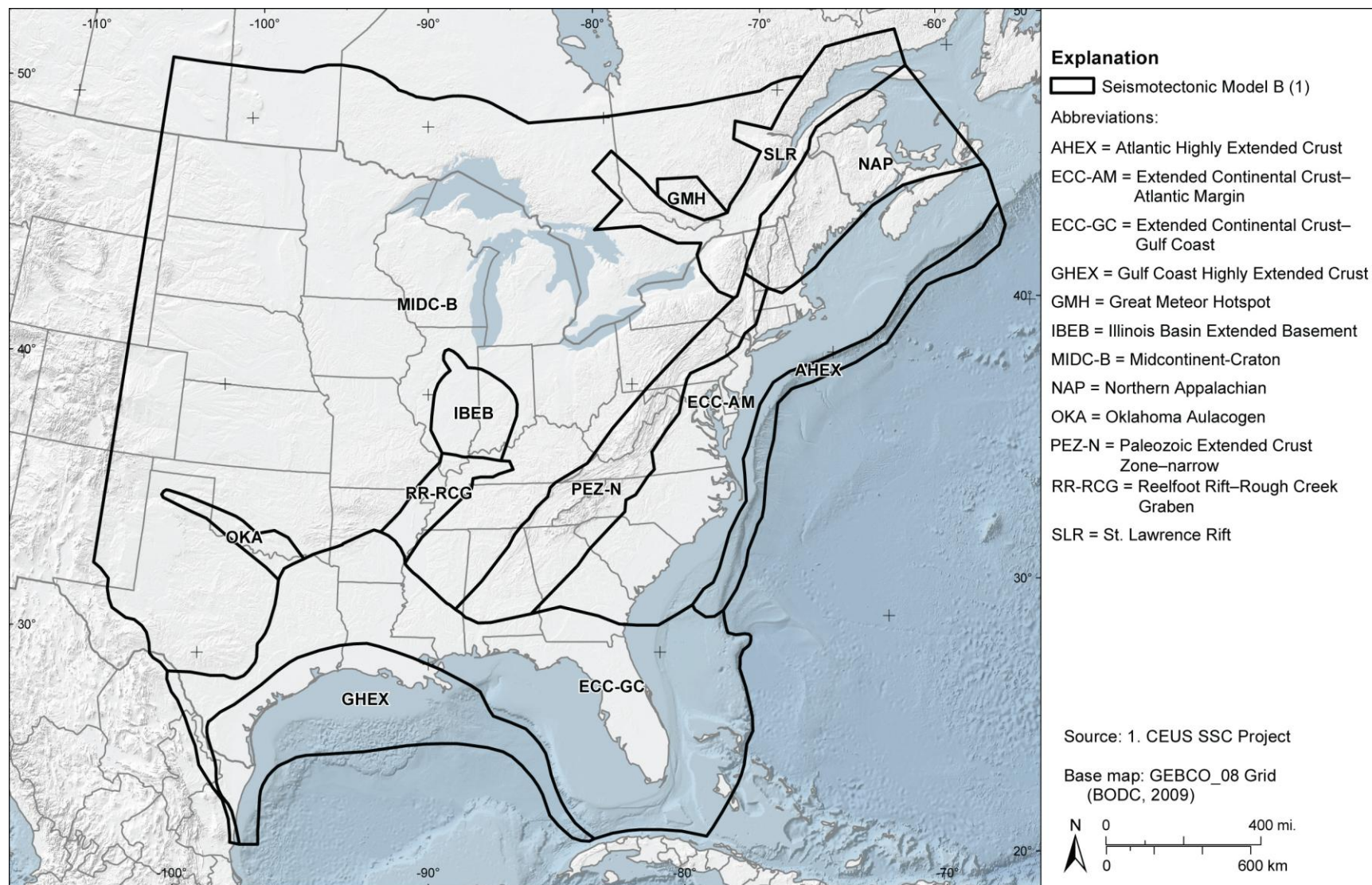


**Figure 7.1-2**  
 Seismotectonic zones shown in the case where the Rough Creek graben is part of the Reelfoot rift (RR\_RCG) and the Paleozoic Extended Crust is narrow (PEZ-N)

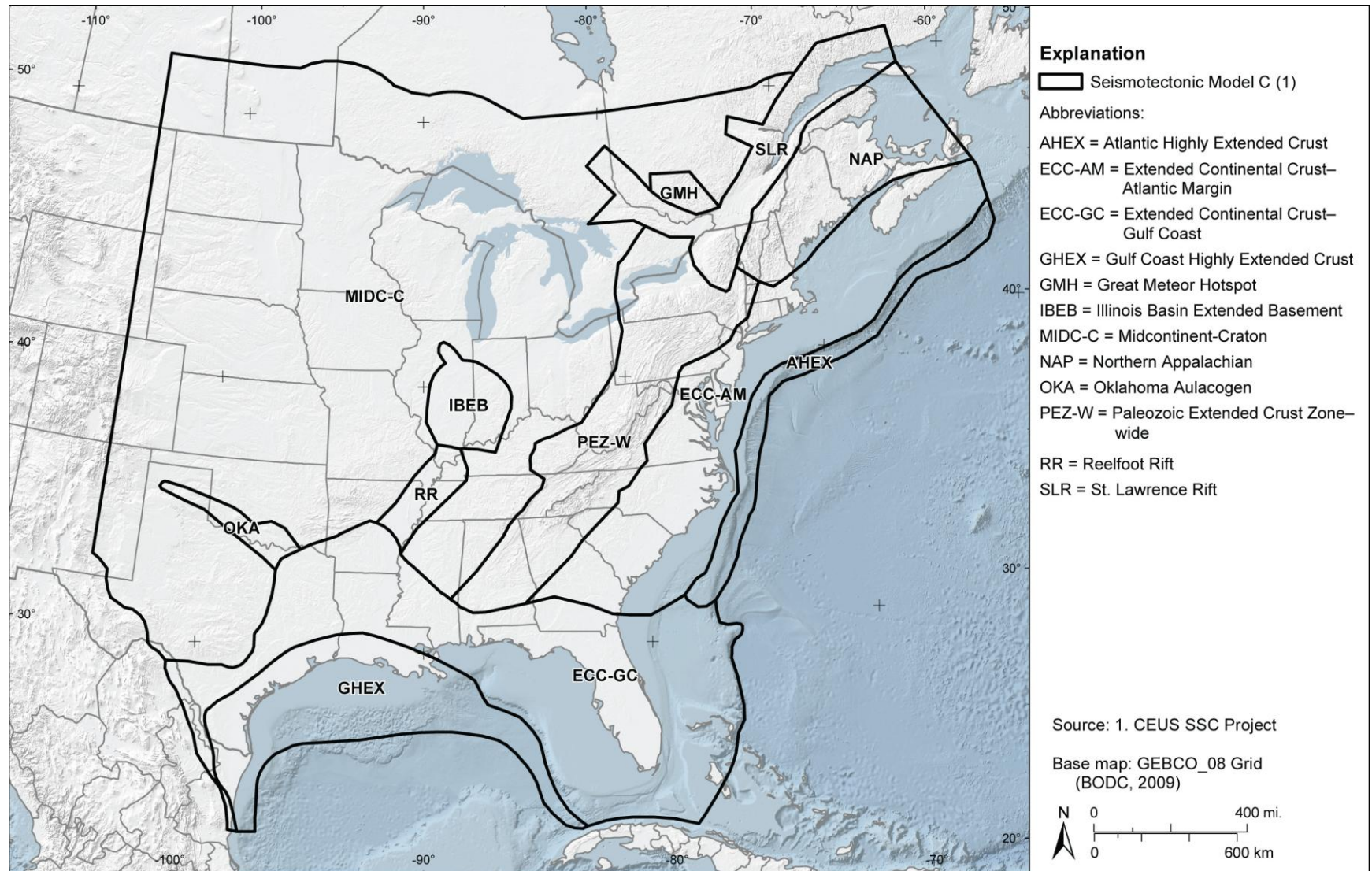


**Figure 7.1-3**  
Seismotectonic zones shown in the case where the Rough Creek graben is not part of the Reelfoot rift (RR) and the Paleozoic Extended Crust is wide (PEZ-W)

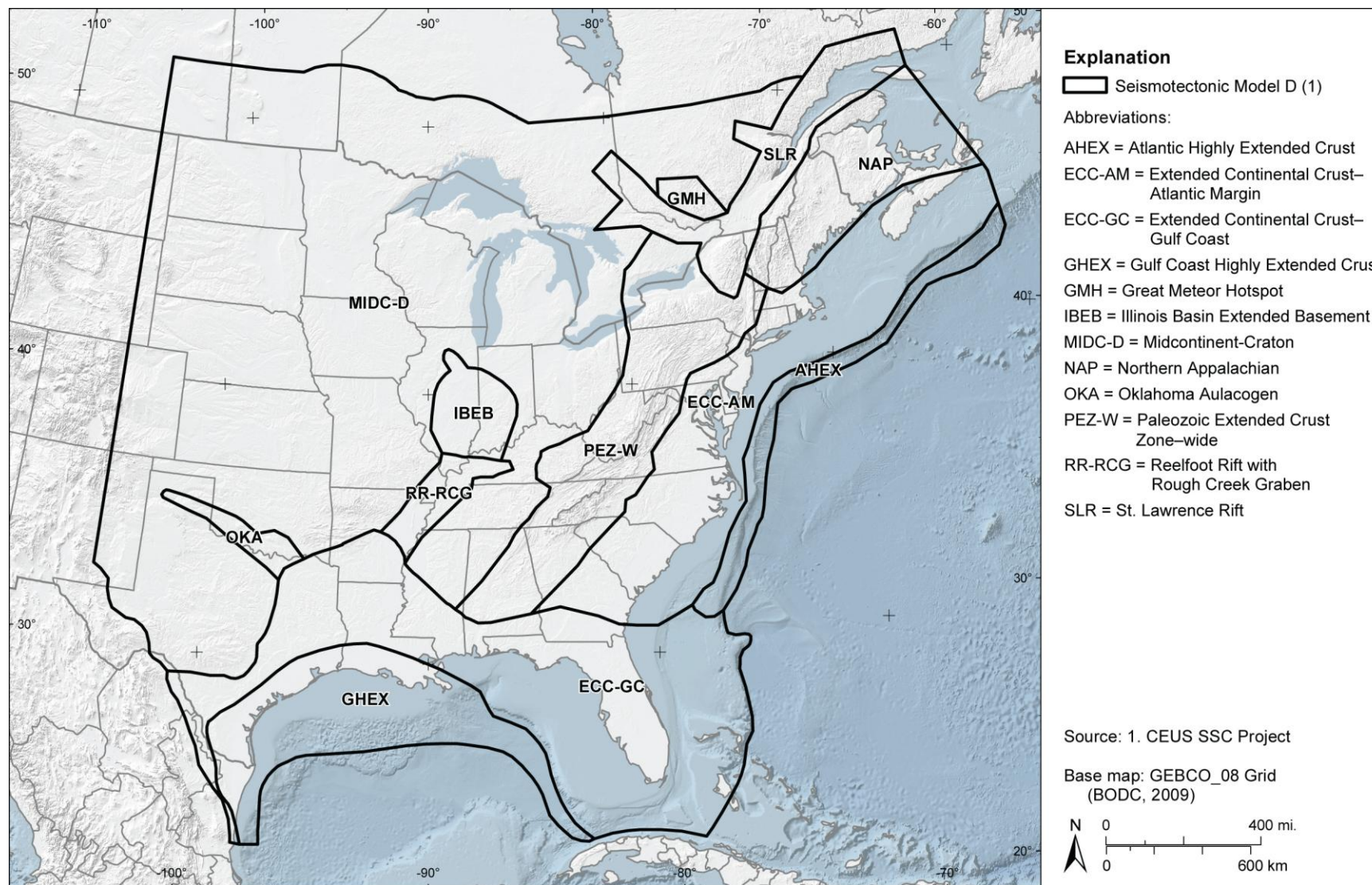


**Figure 7.1-4**  
 Seismotectonic zones shown in the case where the Rough Creek graben is part of the Reelfoot rift (RR\_RCG) and the Paleozoic Extended Crust is wide (PEZ-W)

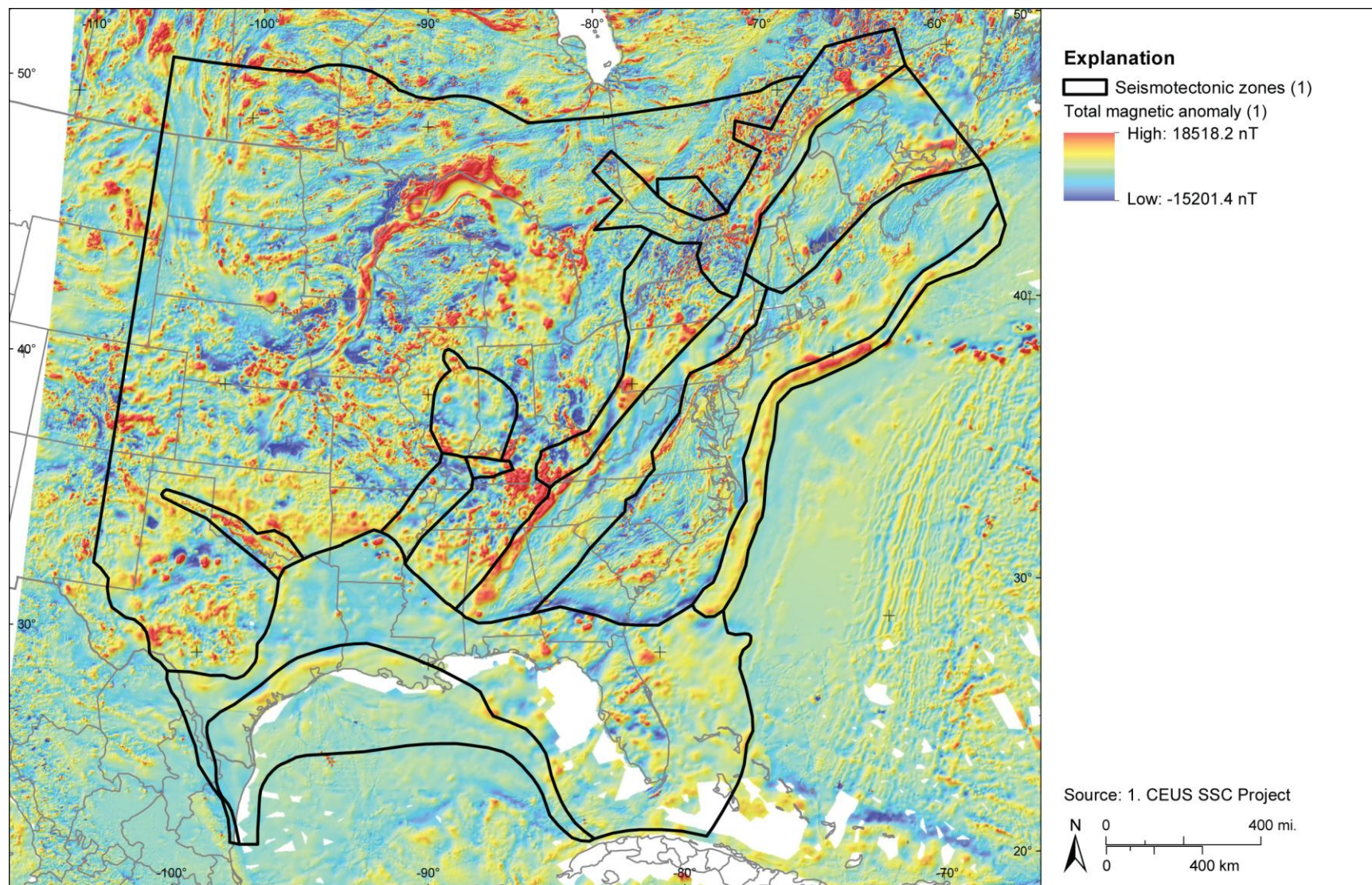


**Figure 7.1-5**  
Example of comparing seismotectonic zones with magnetic map developed as part of the CEUS SSC Project

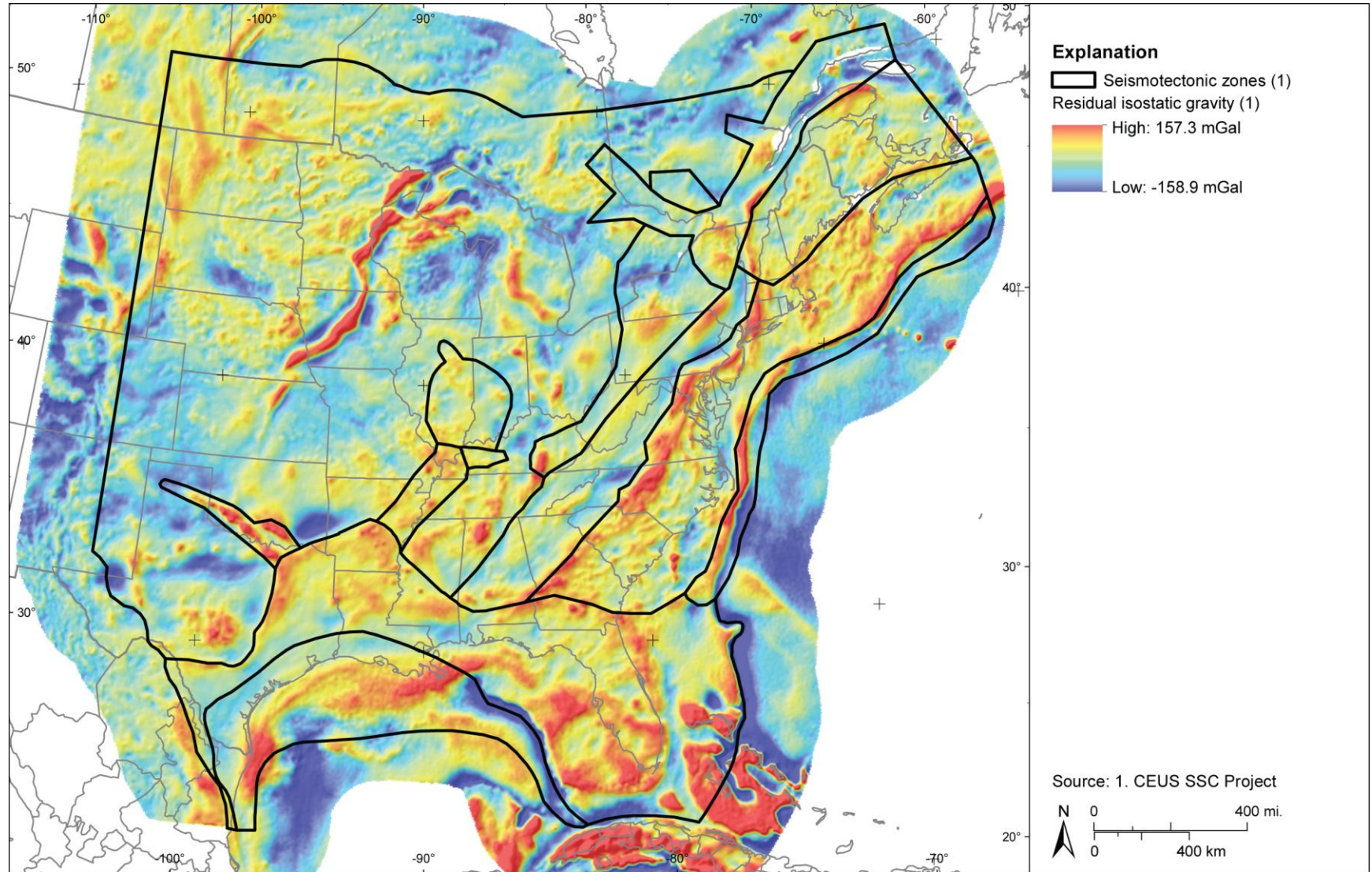


**Figure 7.1-6**  
Example of comparing seismotectonic zones with isostatic gravity map developed as part of the CEUS SSC Project

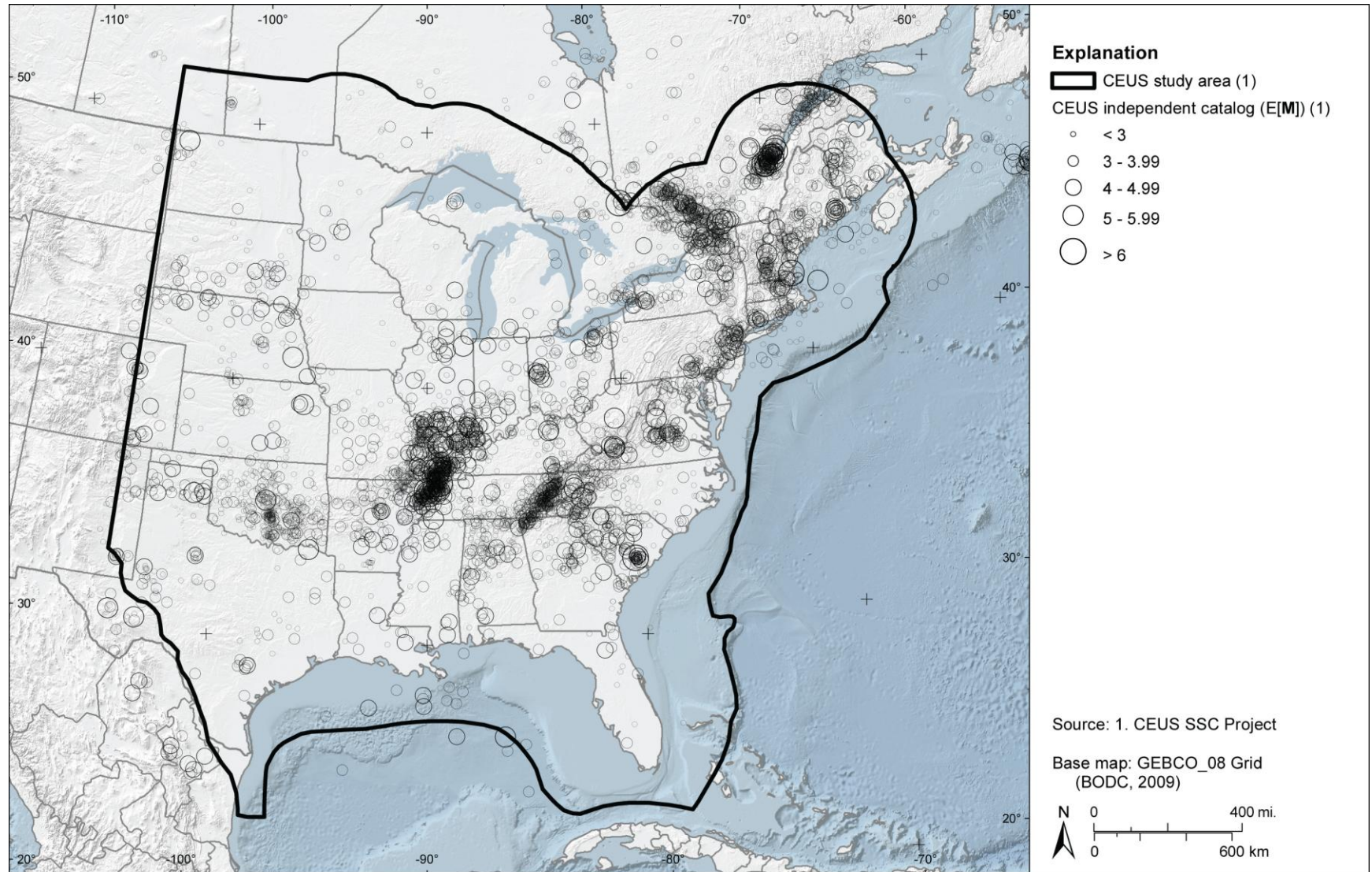


**Figure 7.1-7**  
Map of seismicity based on the earthquake catalog developed for the CEUS SSC Project

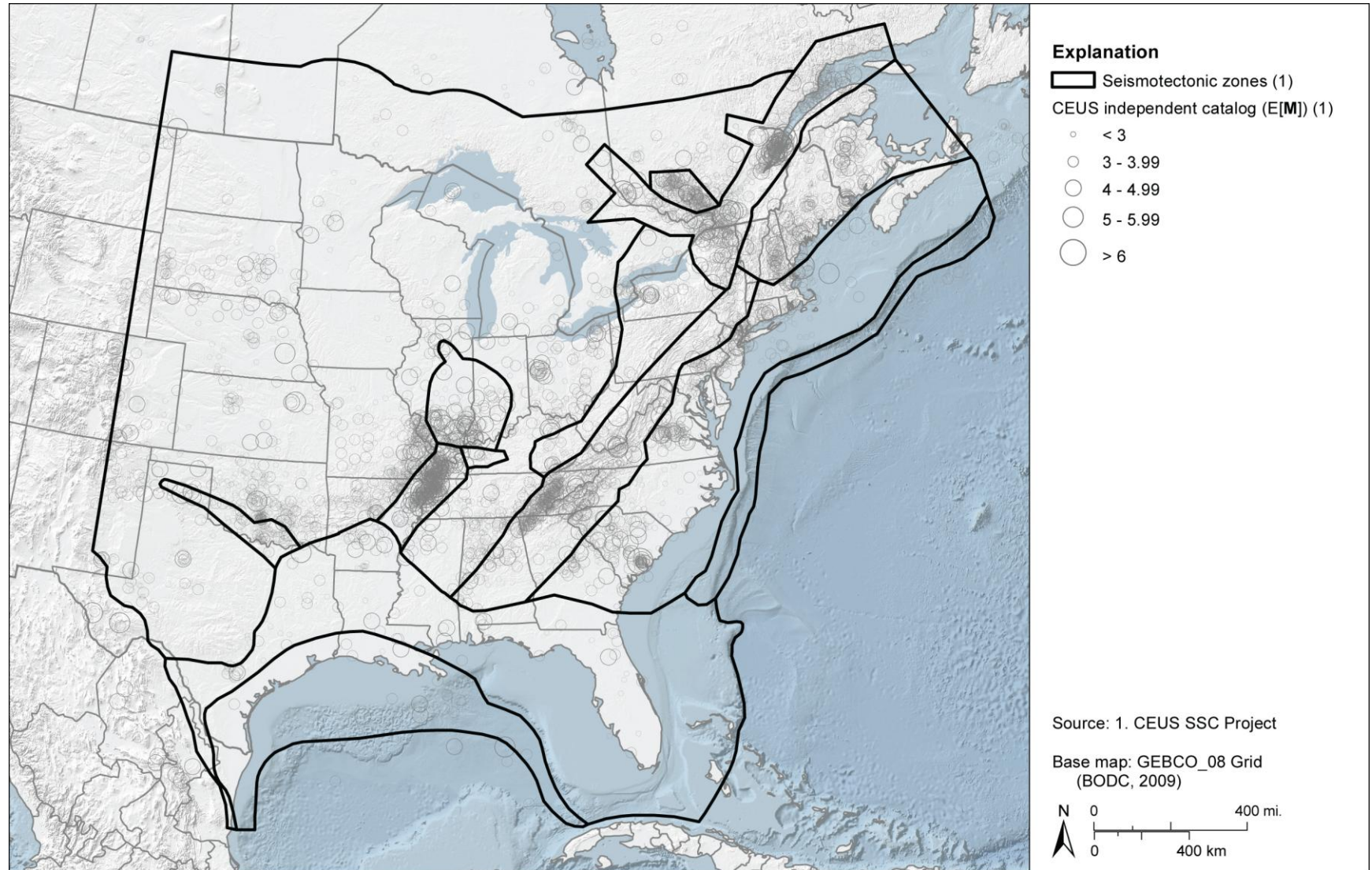


**Figure 7.1-8**  
Map showing example comparison of seismotectonic zones with seismicity. Note the non-uniform spatial distribution of seismicity within the zones. Spatial smoothing of  $a$ - and  $b$ -values accounts for these spatial variations.

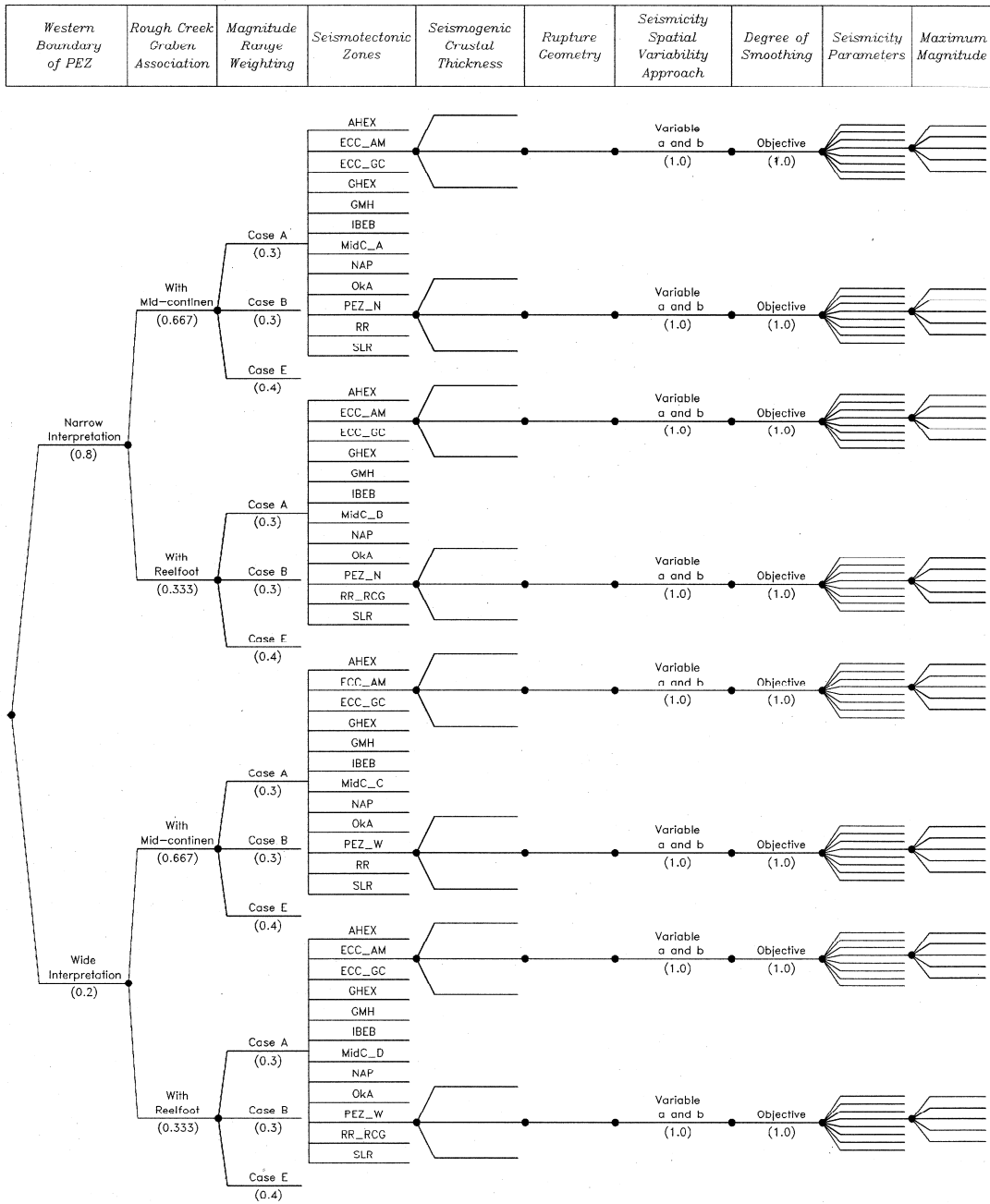
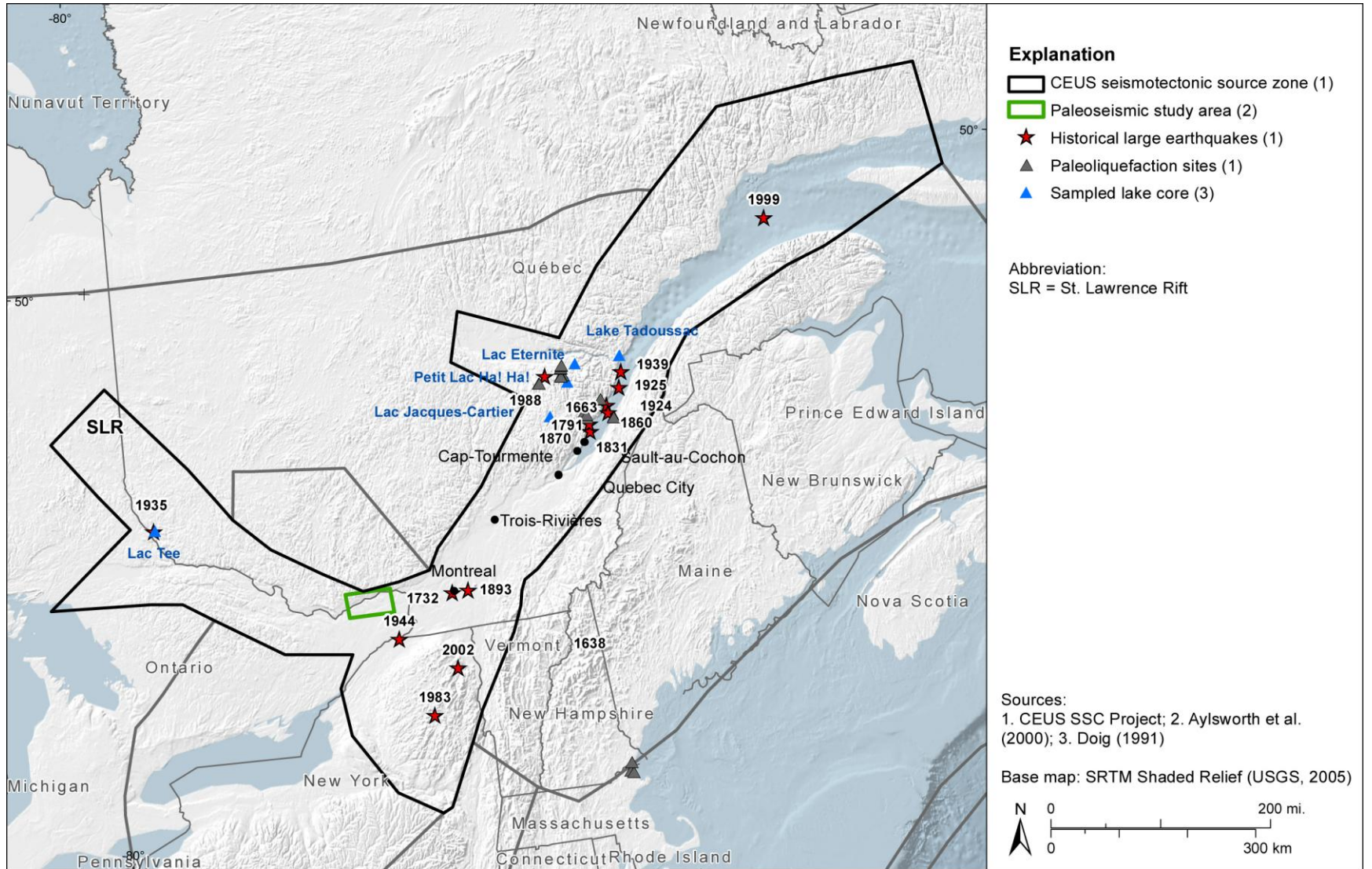
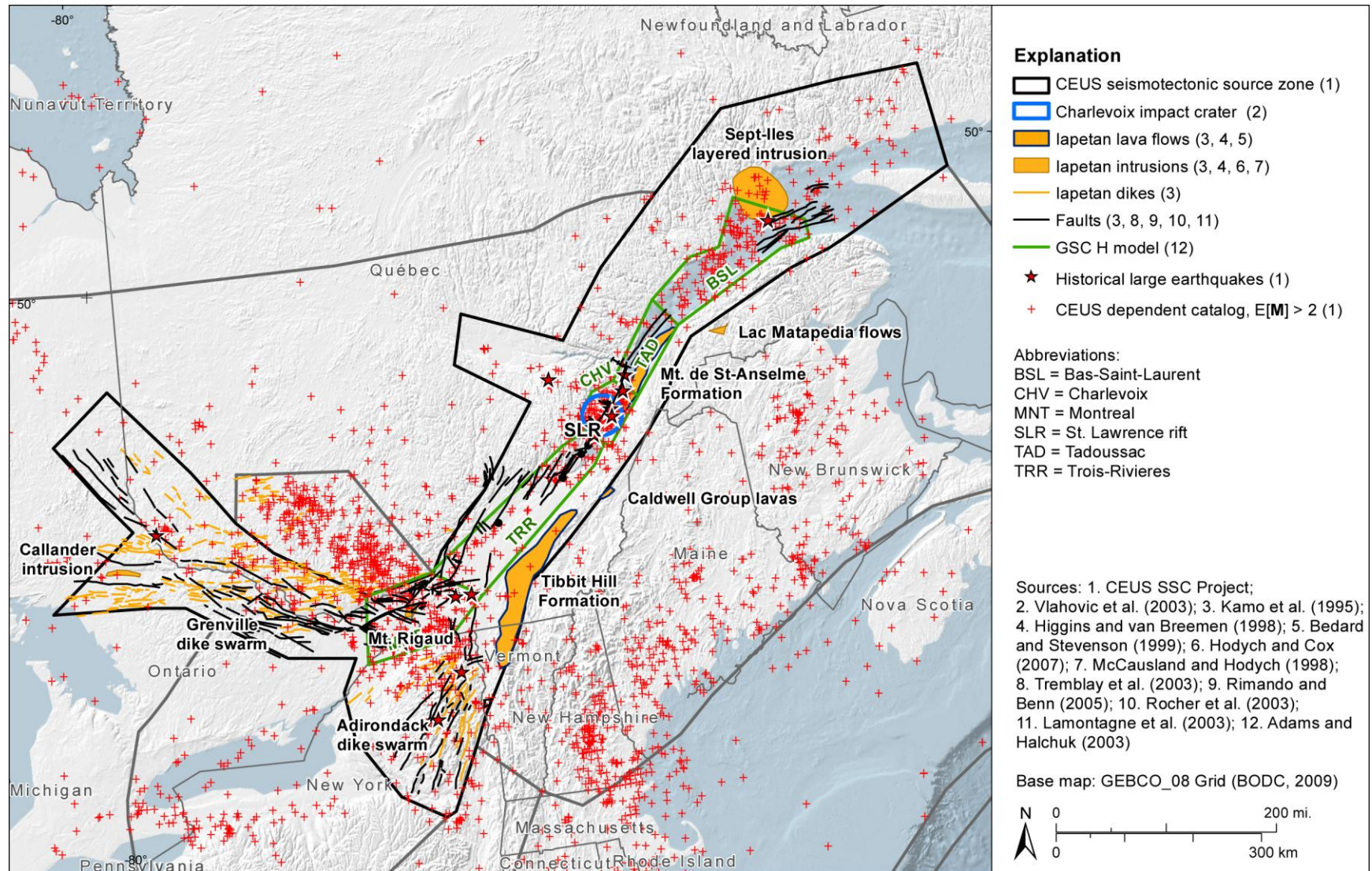


Figure 7.3-1  
Logic tree for the seismotectonic zones branch of the master logic tree



**Figure 7.3.1-1**  
 Significant earthquakes and paleoseismology of the SLR seismotectonic zone



**Figure 7.3.1-2**  
Tectonic features of the SLR seismotectonic zone

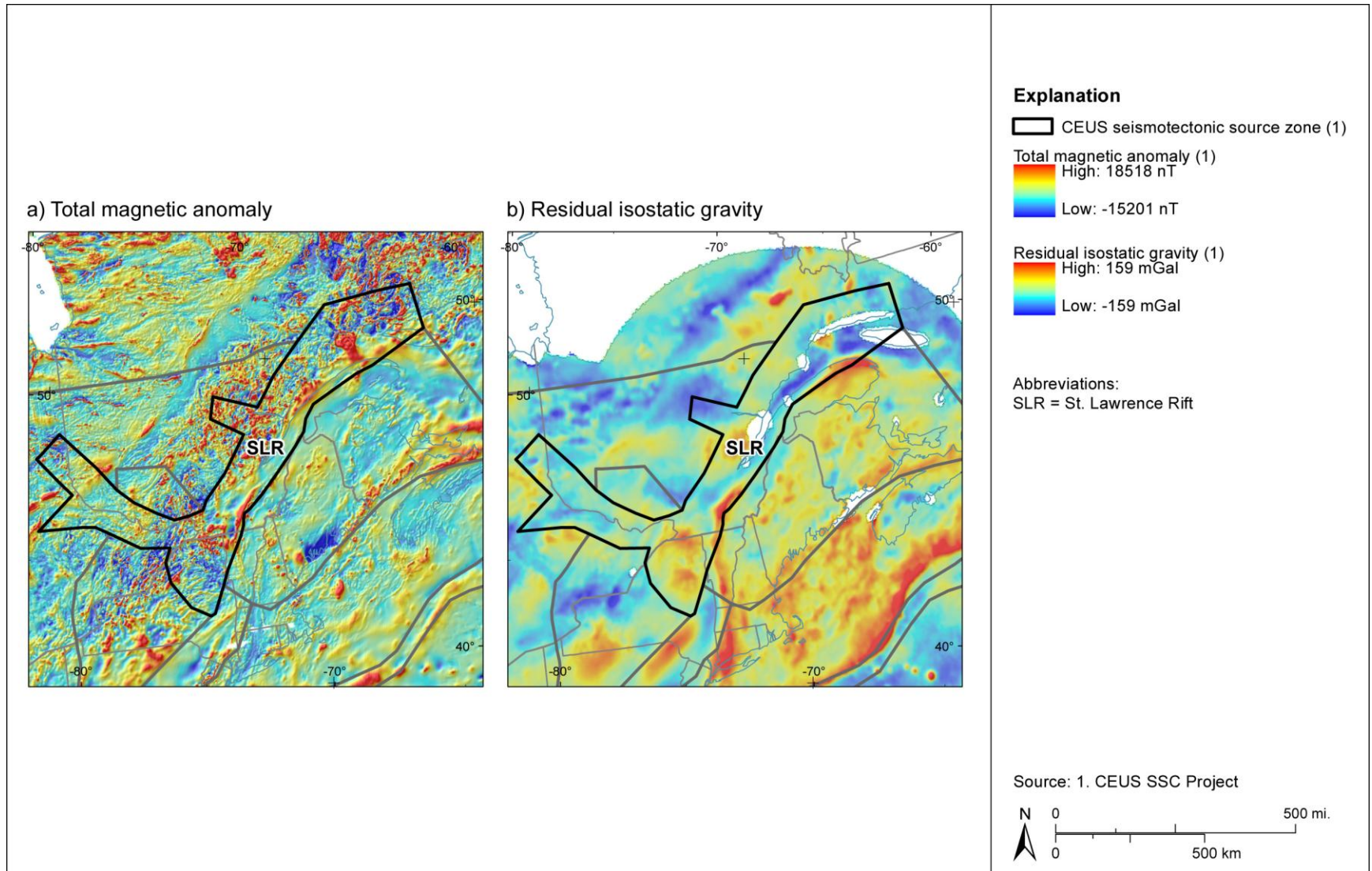


**Figure 7.3.1-3**  
**Magnetic and gravity anomaly maps of the SLR seismotectonic zone**

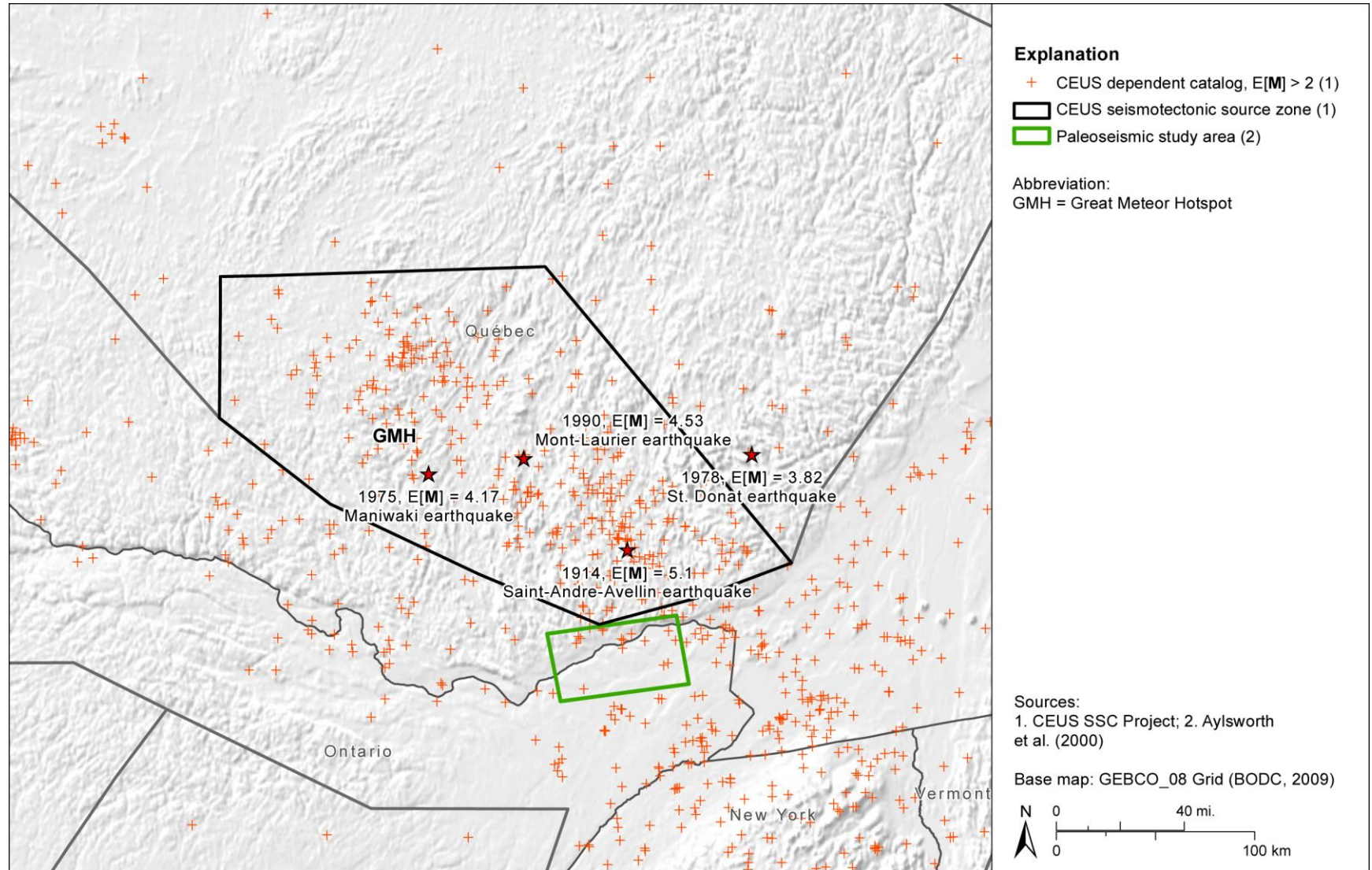


**Figure 7.3.2-1**  
Significant earthquakes and paleoseismic study area in the region of the GMH seismotectonic zone

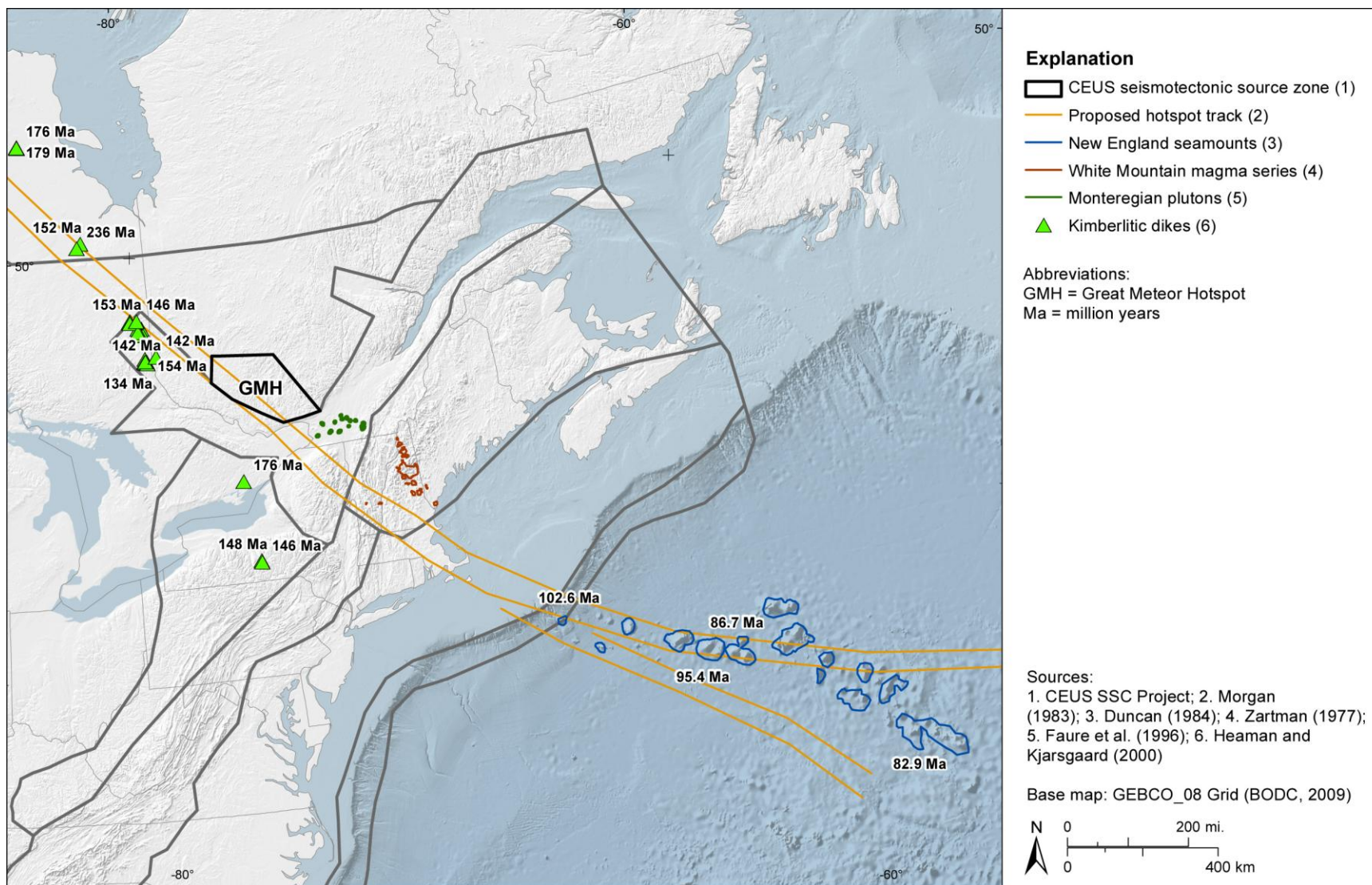


**Figure 7.3.2-2**  
 Igneous rocks attributed to the GMH seismotectonic zone

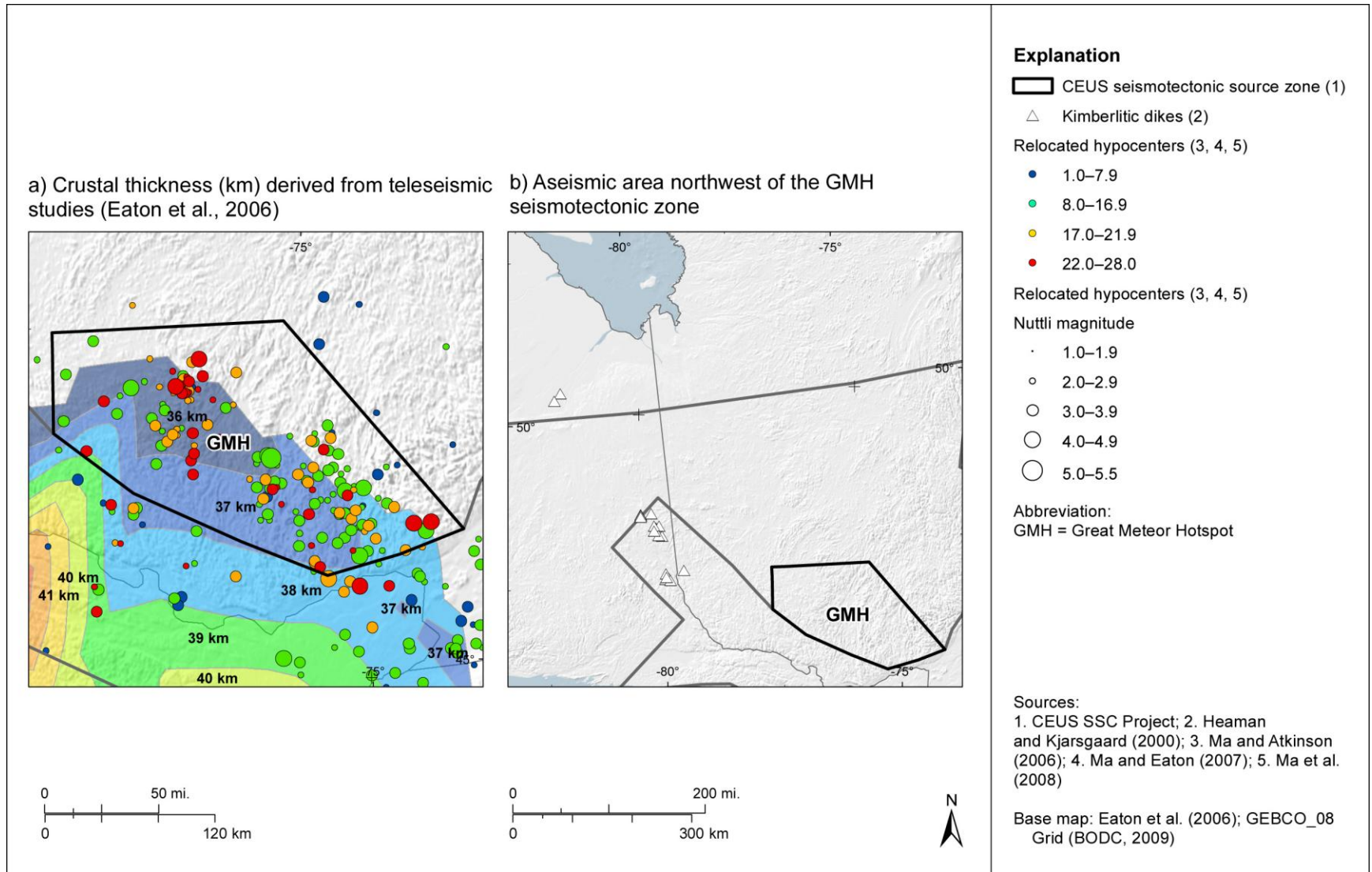


**Figure 7.3.2-3**  
 Relocated hypocentral depths and crustal depth of the GMH seismotectonic zone

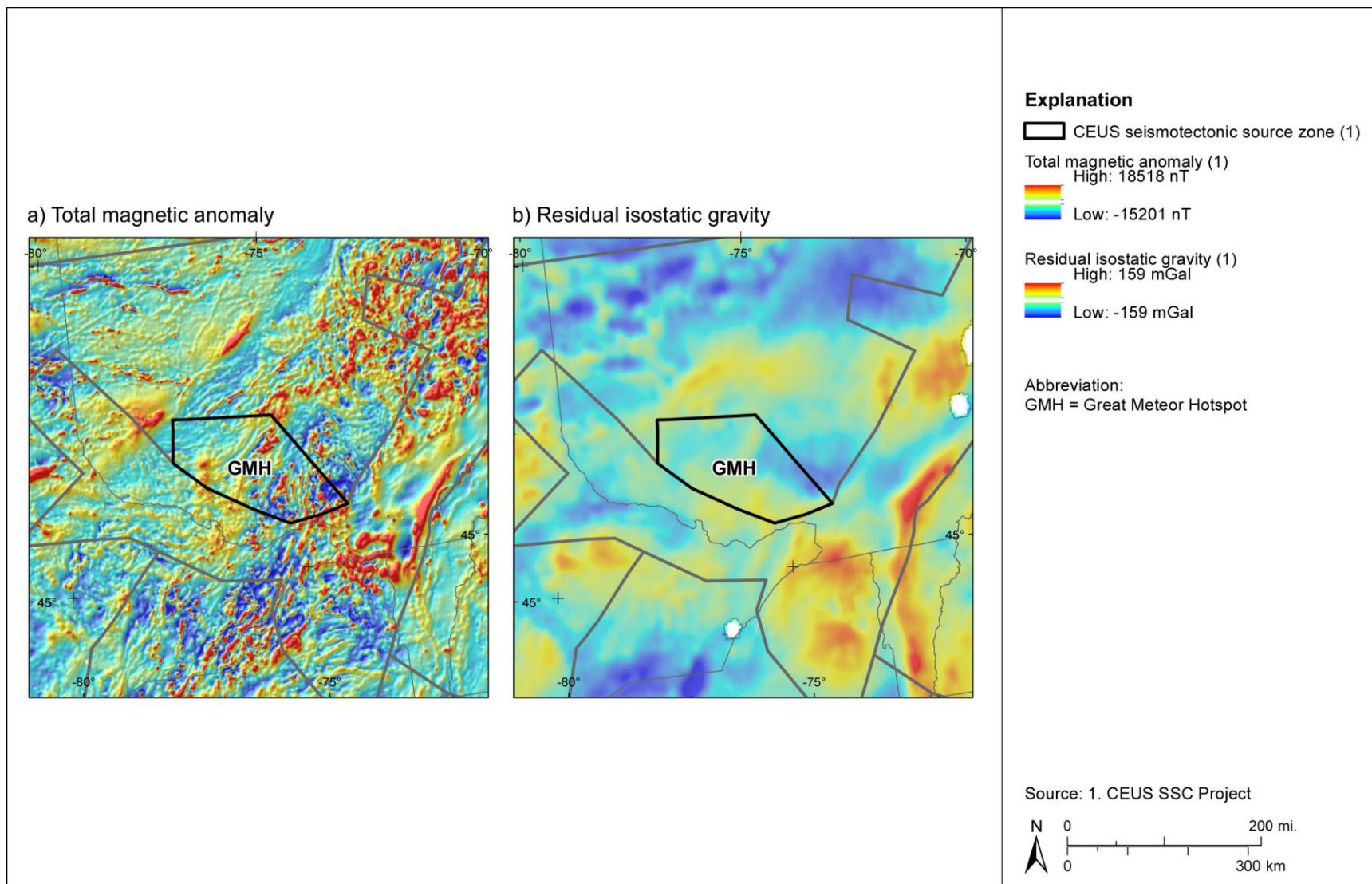


**Figure 7.3.2-4**  
Magnetic and gravity anomaly maps of the GMH seismotectonic zone

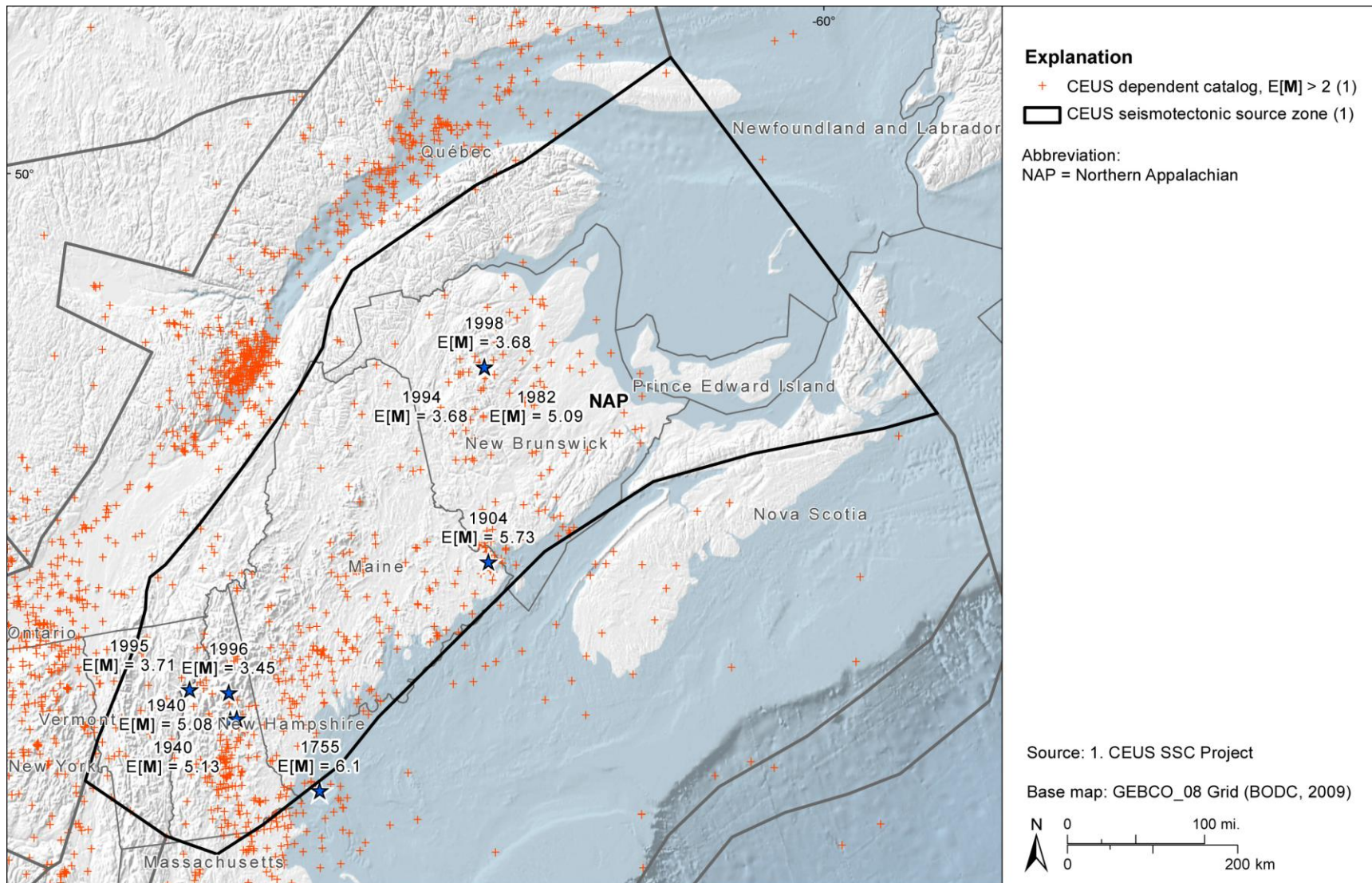


**Figure 7.3.3-1**  
 Seismicity of the NAP seismotectonic zone

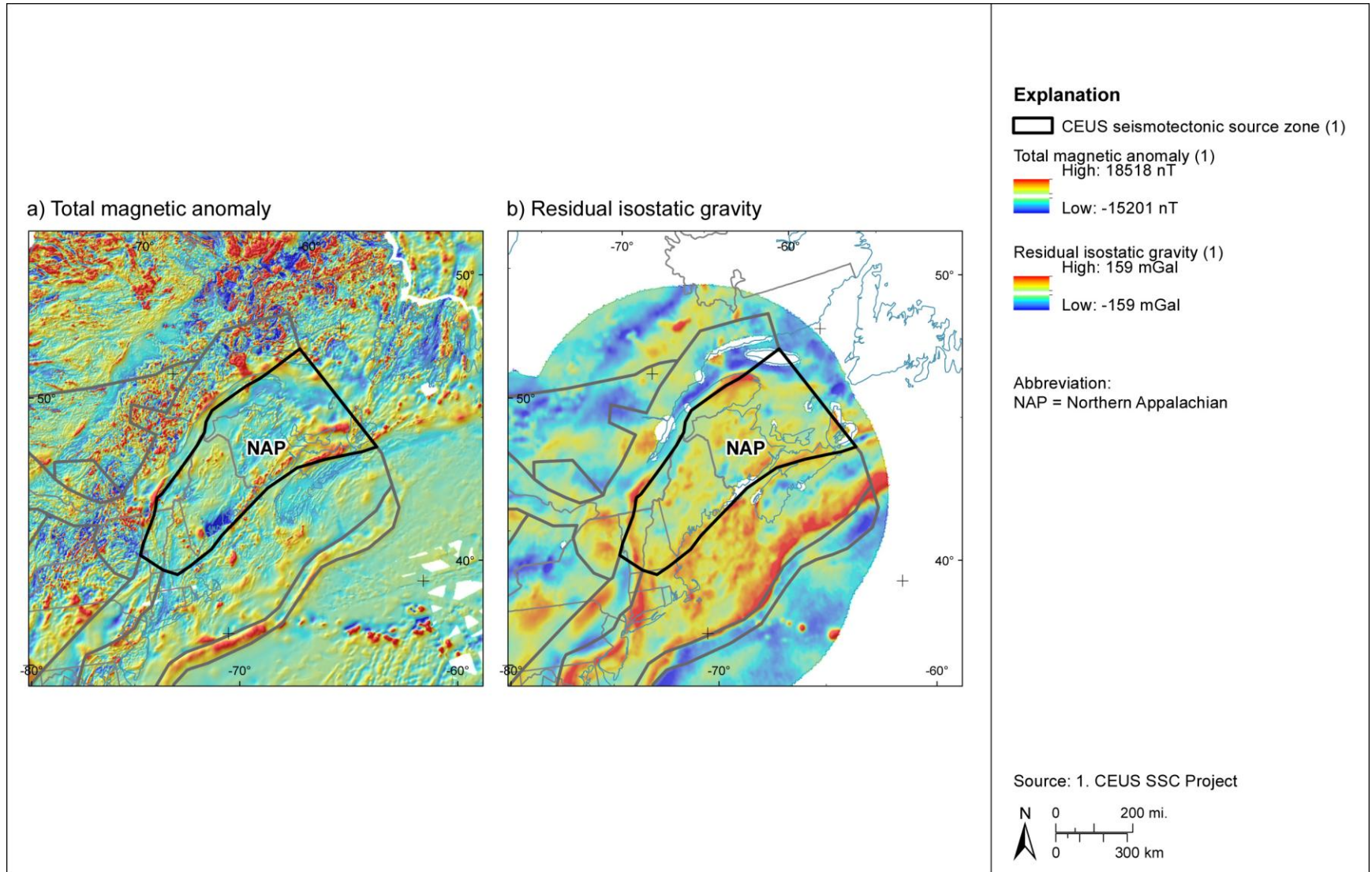


**Figure 7.3.3-2**  
**Magnetic and gravity anomaly maps of the NAP seismotectonic zone**

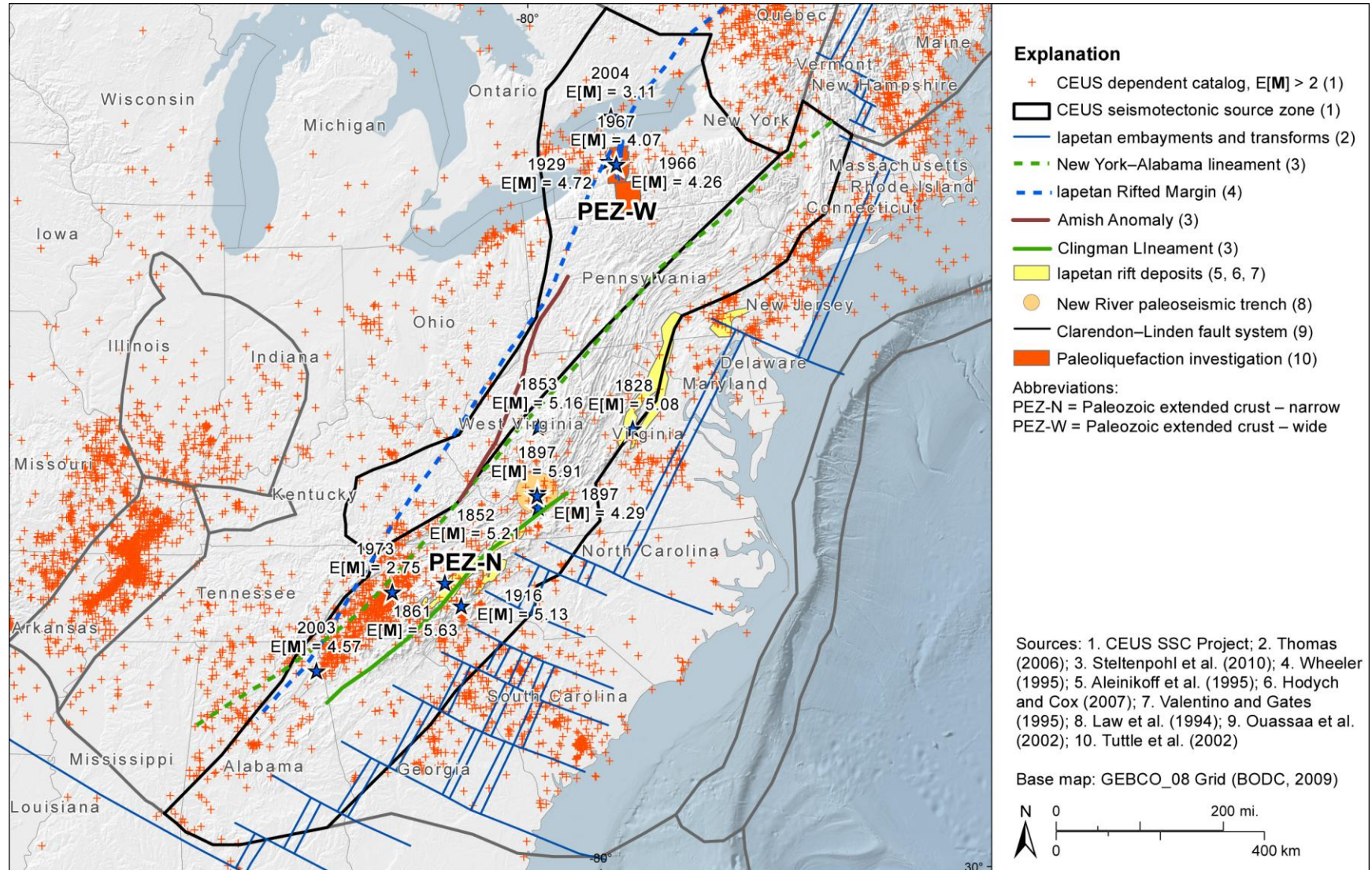


**Figure 7.3.4-1**  
Seismicity and tectonic features of the PEZ seismotectonic zone

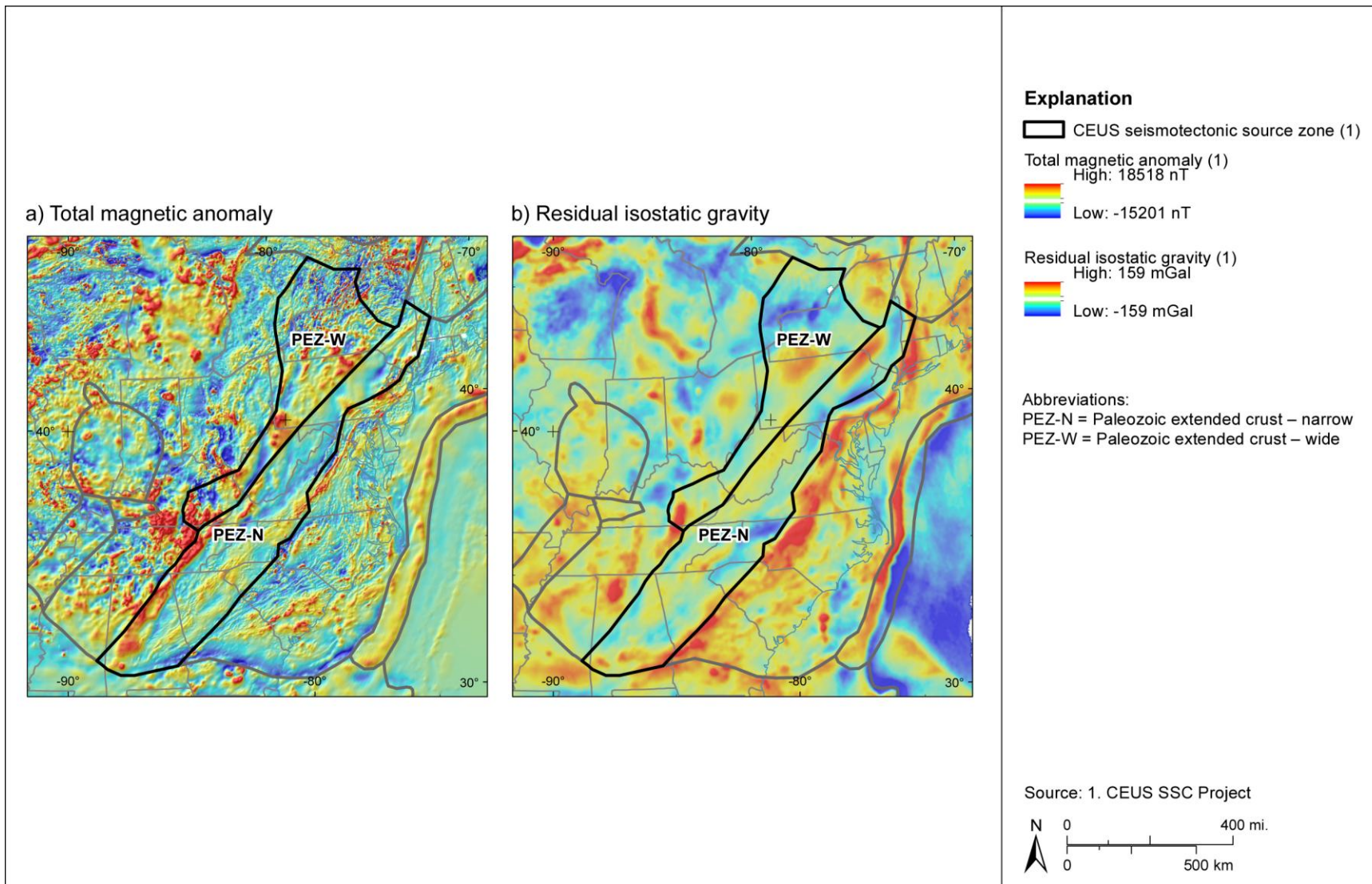


**Figure 7.3.4-2**  
**Magnetic and gravity anomaly maps of the PEZ seismotectonic zone**

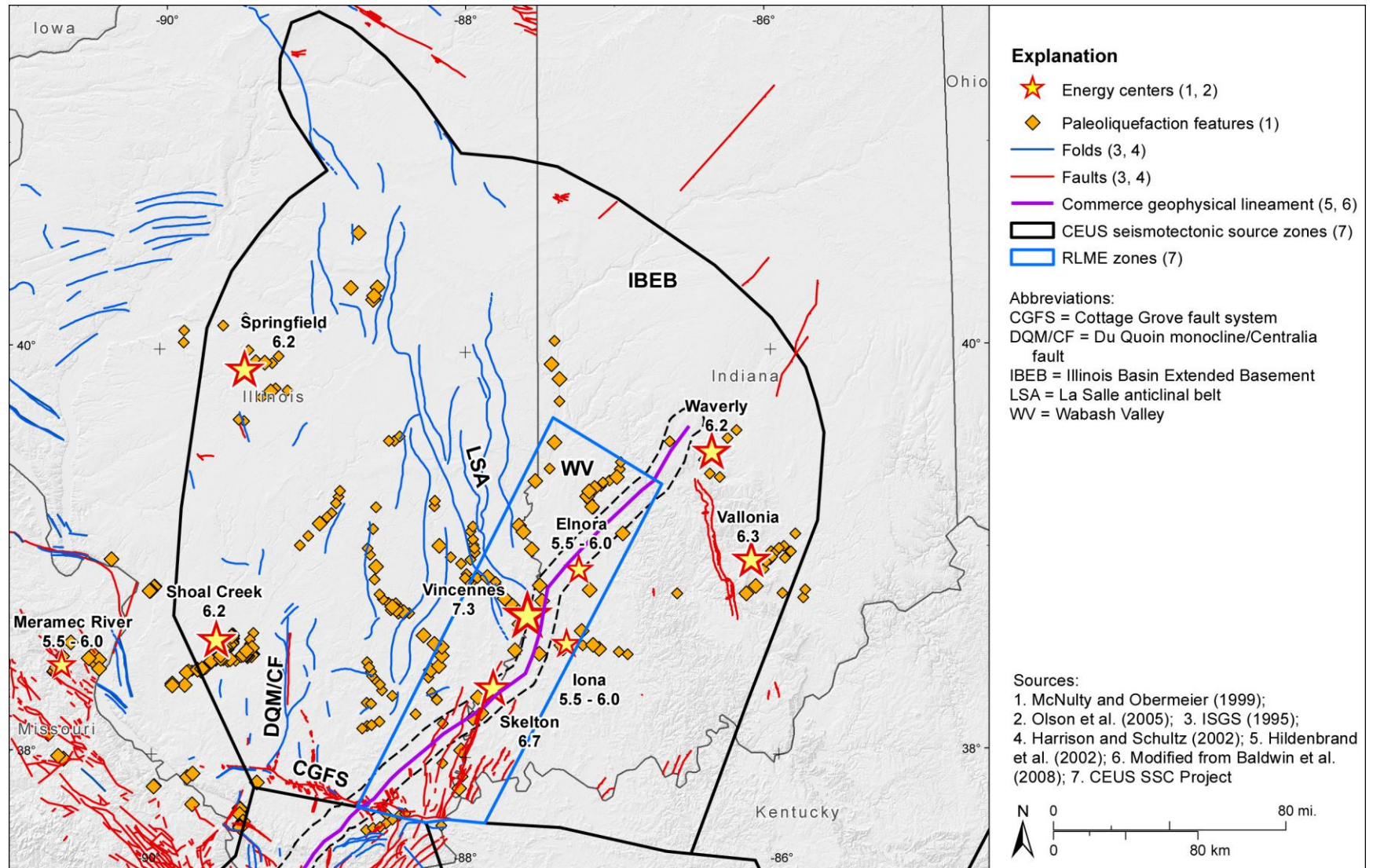


**Figure 7.3.5-1**  
Map showing seismicity, subsurface Paleozoic and basement structures, and postulated energy centers for prehistoric earthquakes

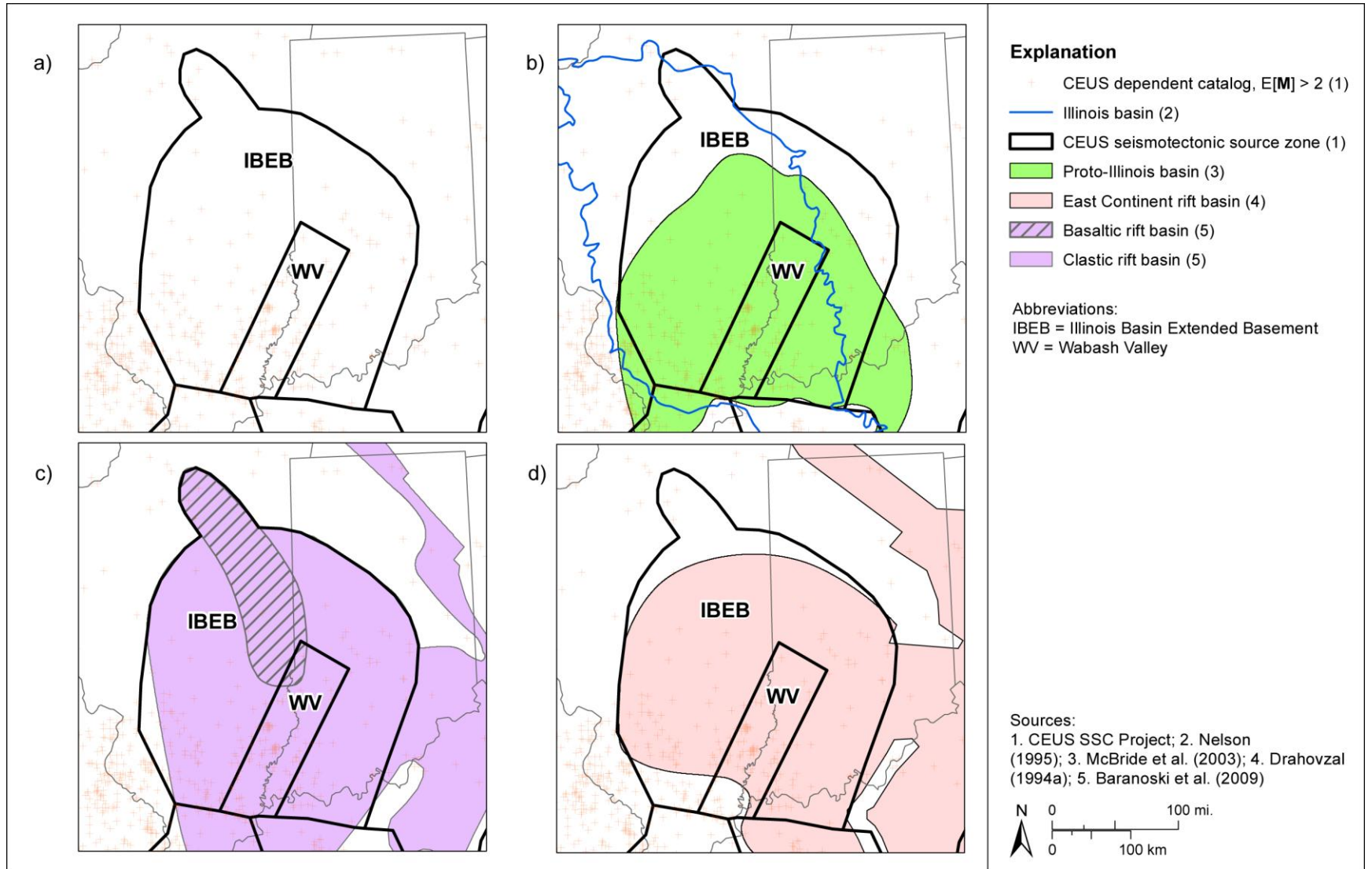


**Figure 7.3.5-2**  
Map showing alternative boundaries for Precambrian (proto-Illinois basin) rift basins

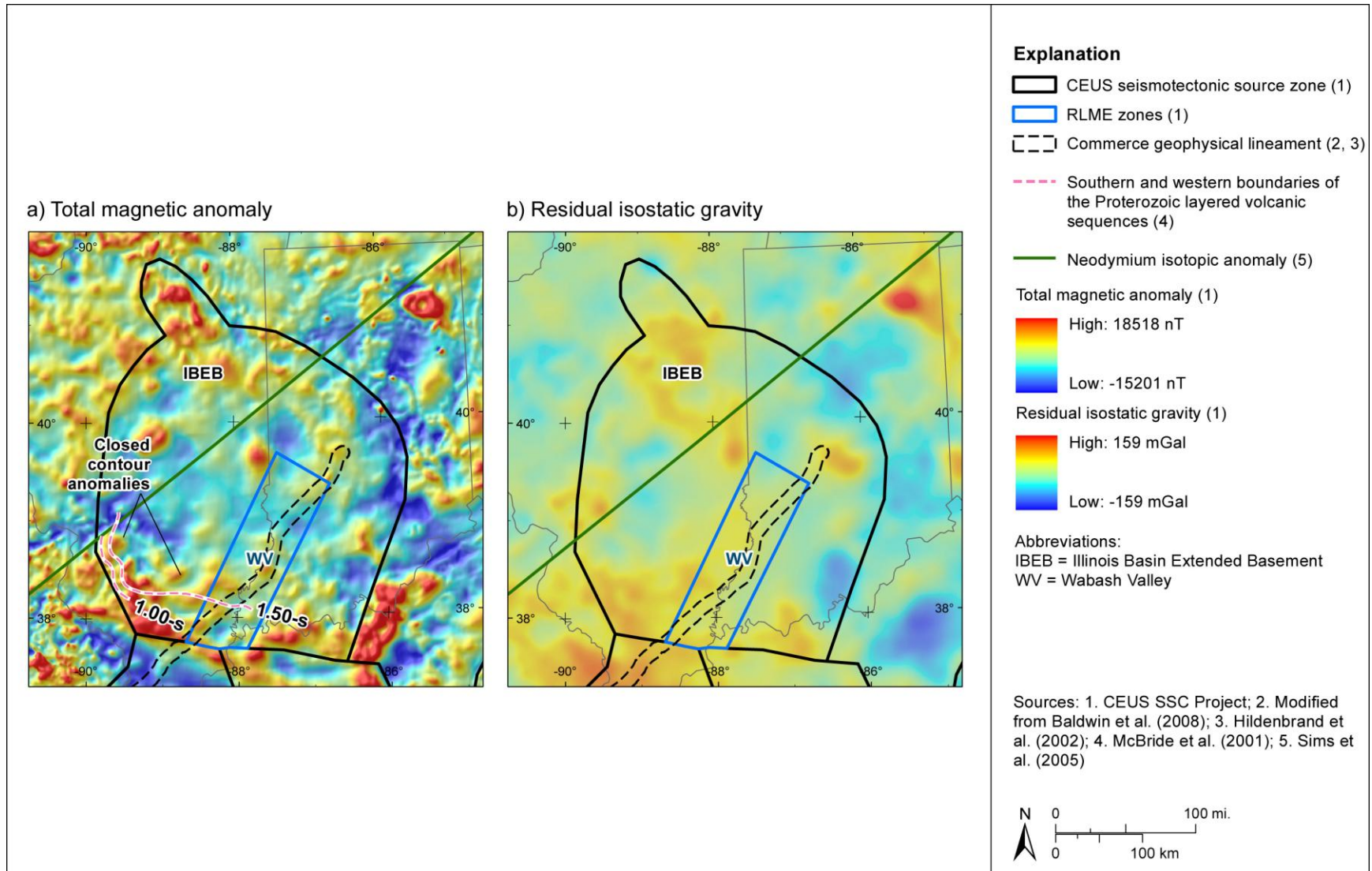


**Figure 7.3.5-3**  
 Maps showing the IBEB source zone boundaries, seismicity, and prehistoric earthquake centers relative to (a) regional magnetic anomalies and (b) regional gravity anomalies

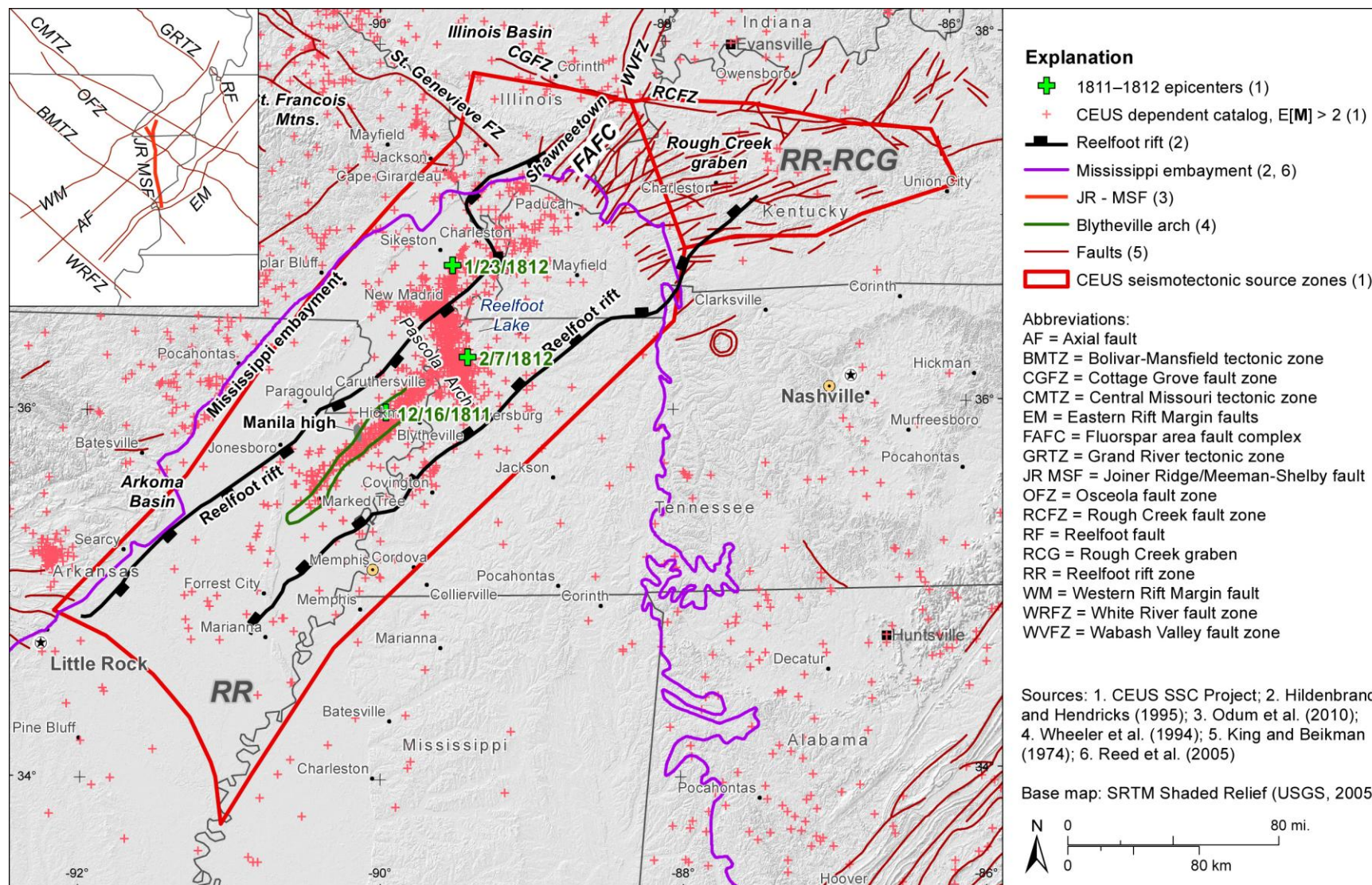


**Figure 7.3.6-1**  
 Map of seismicity and geomorphic features and faults showing evidence for Quaternary neotectonic deformation and reactivation. Inset map shows basement structures associated with the Reelfoot rift.

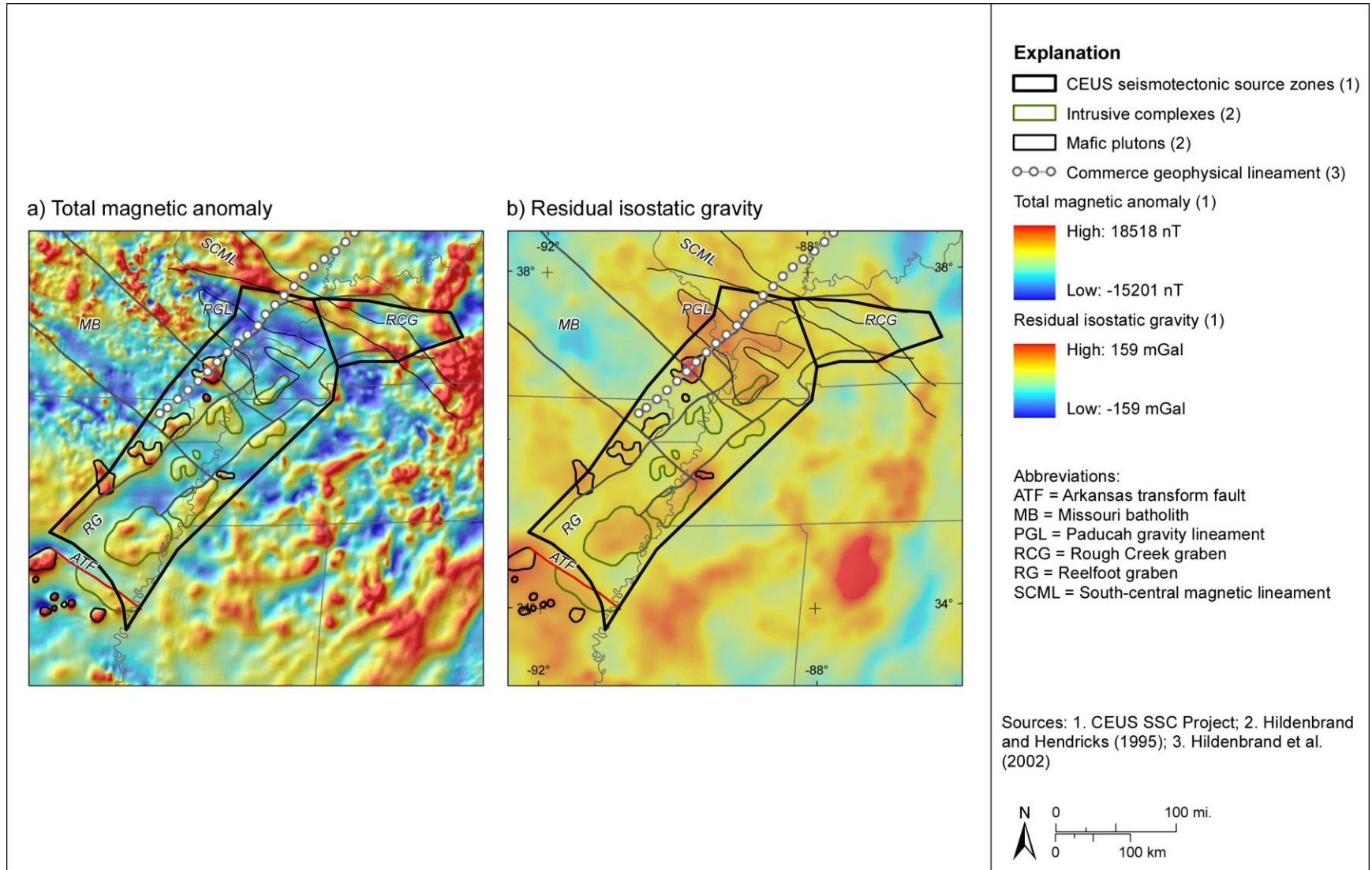


**Figure 7.3.6-2**  
 Maps showing geophysical anomalies in the Reelfoot rift region

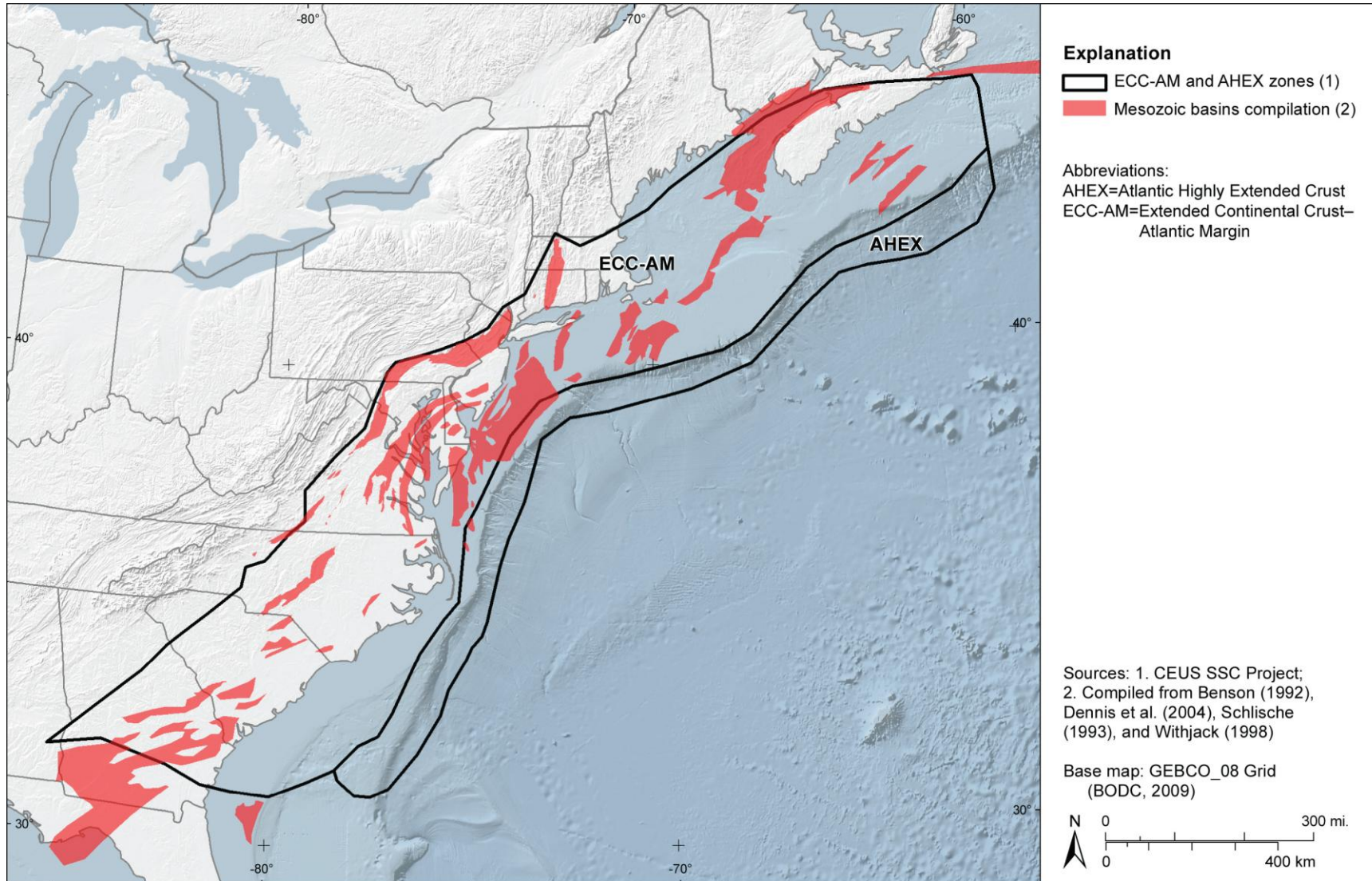


**Figure 7.3.7-1**  
**Mesozoic basins within the ECC-AM zone**

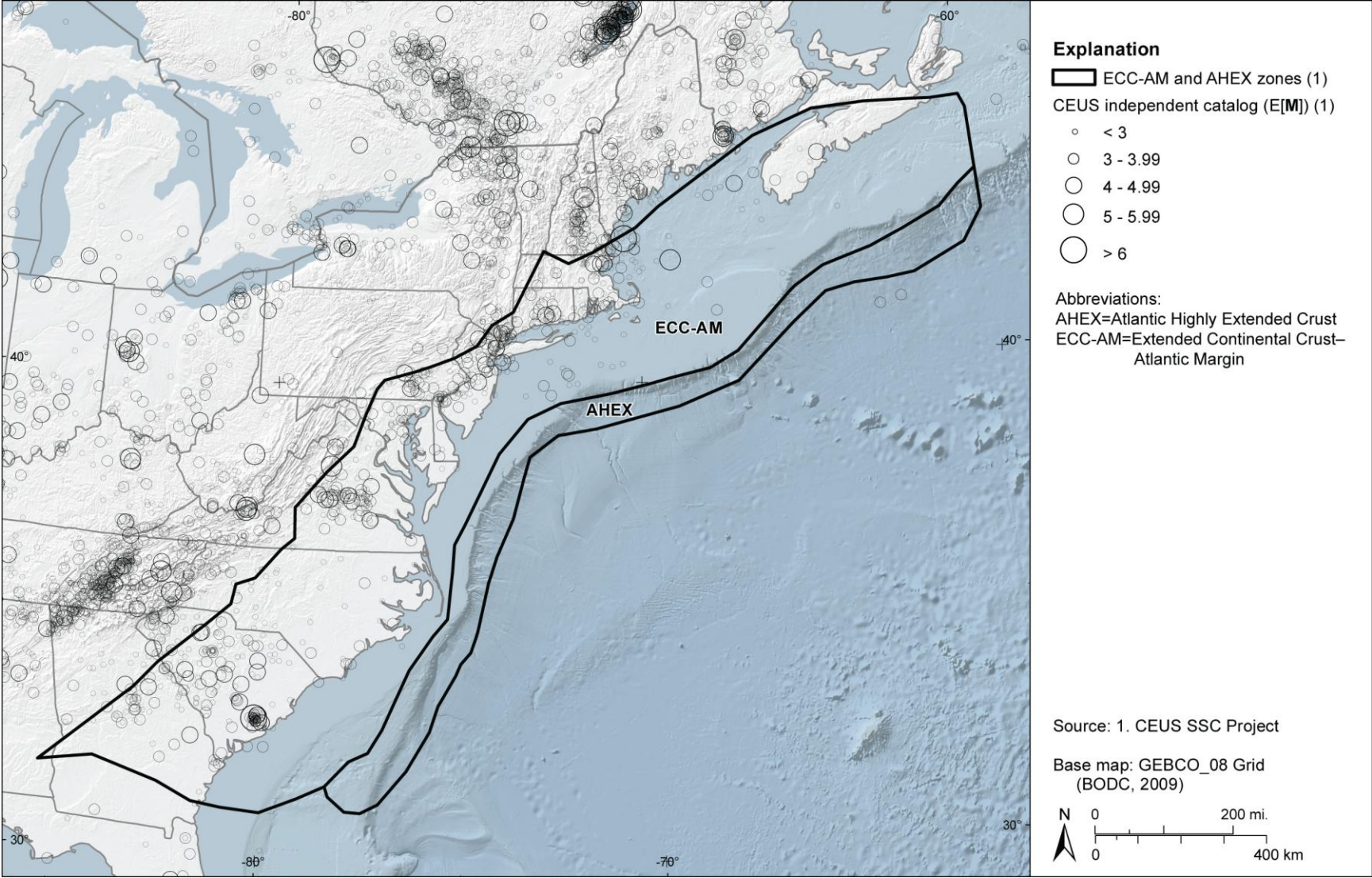


**Figure 7.3.7-2**  
Seismicity within the ECC-AM and AHEX zones

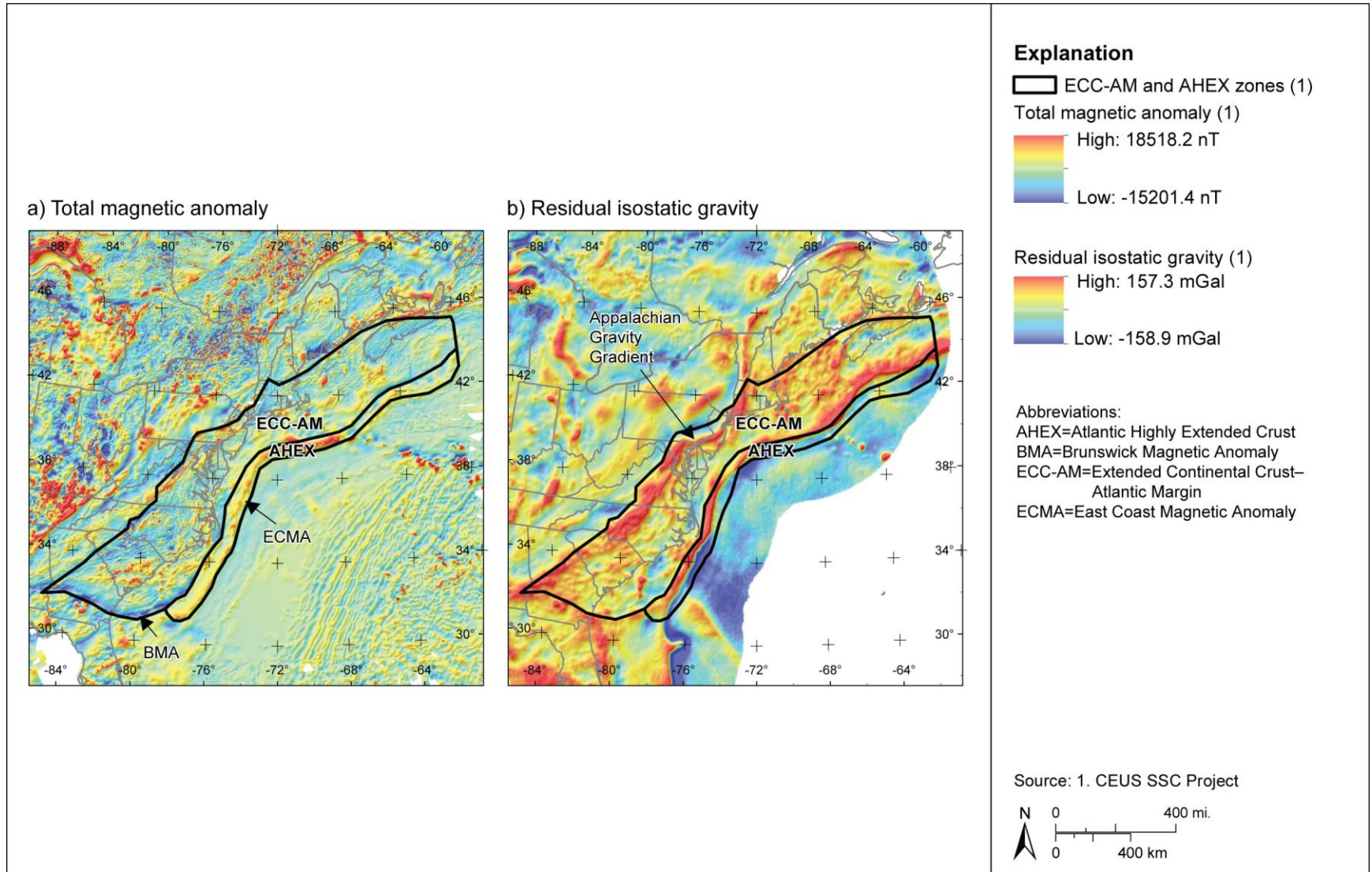


**Figure 7.3.7-3**  
 Magnetic and gravity data for ECC-AM and AHEx zones

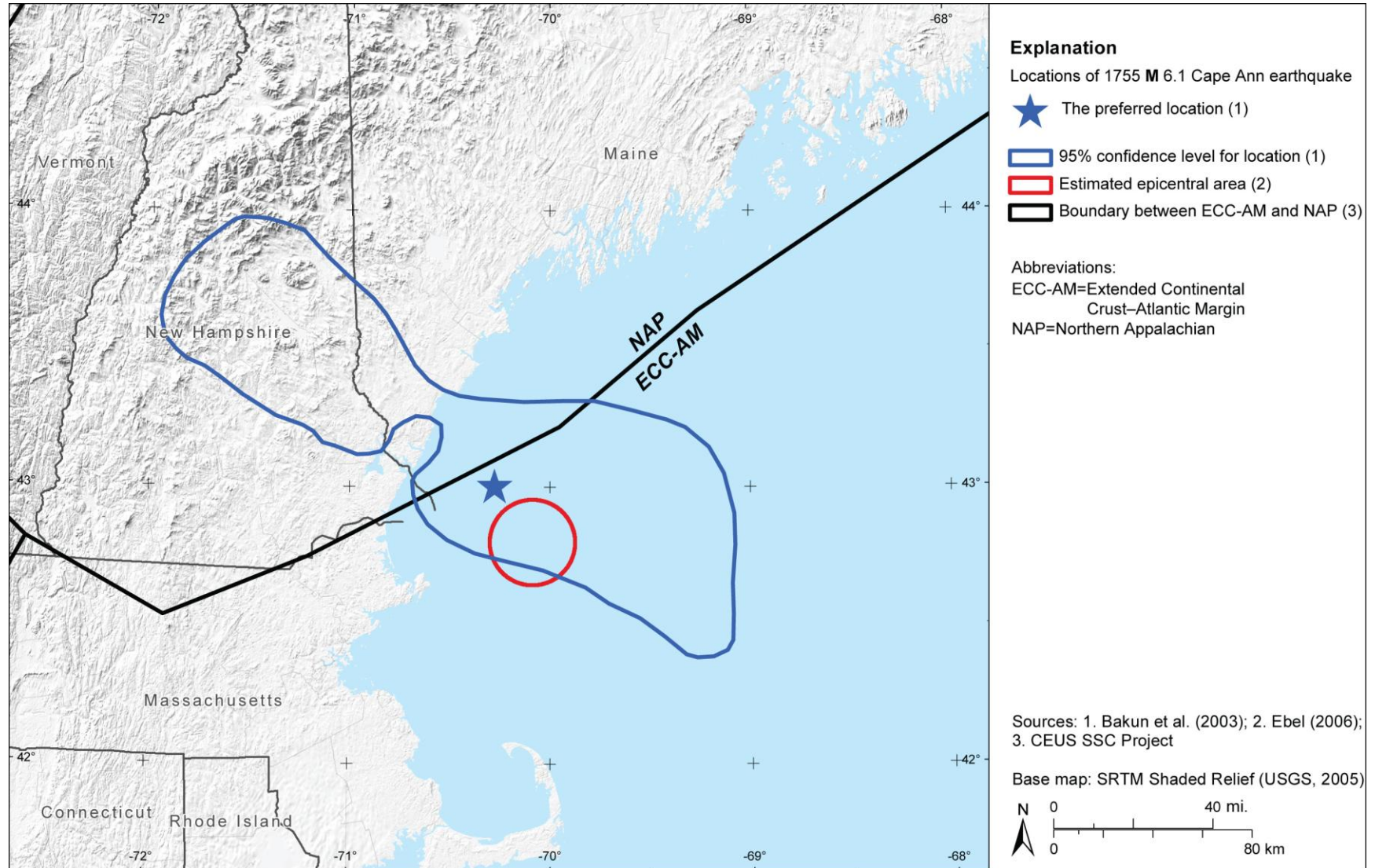


**Figure 7.3.7-4**  
 Estimated locations of the 1755 M 6.1 Cape Ann earthquake

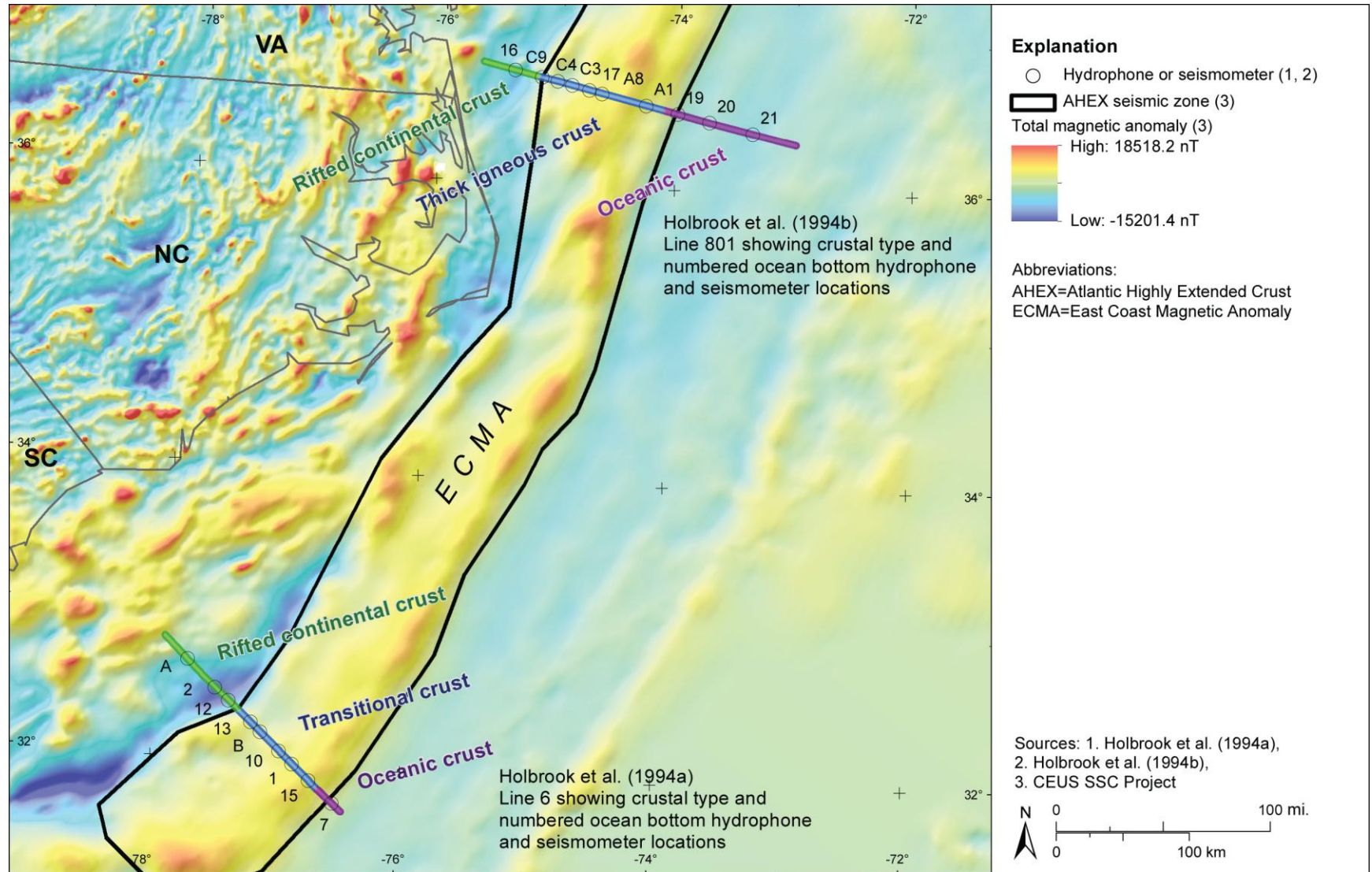


**Figure 7.3.8-1**  
 Correlation of interpreted transitional crust with the East Coast magnetic anomaly

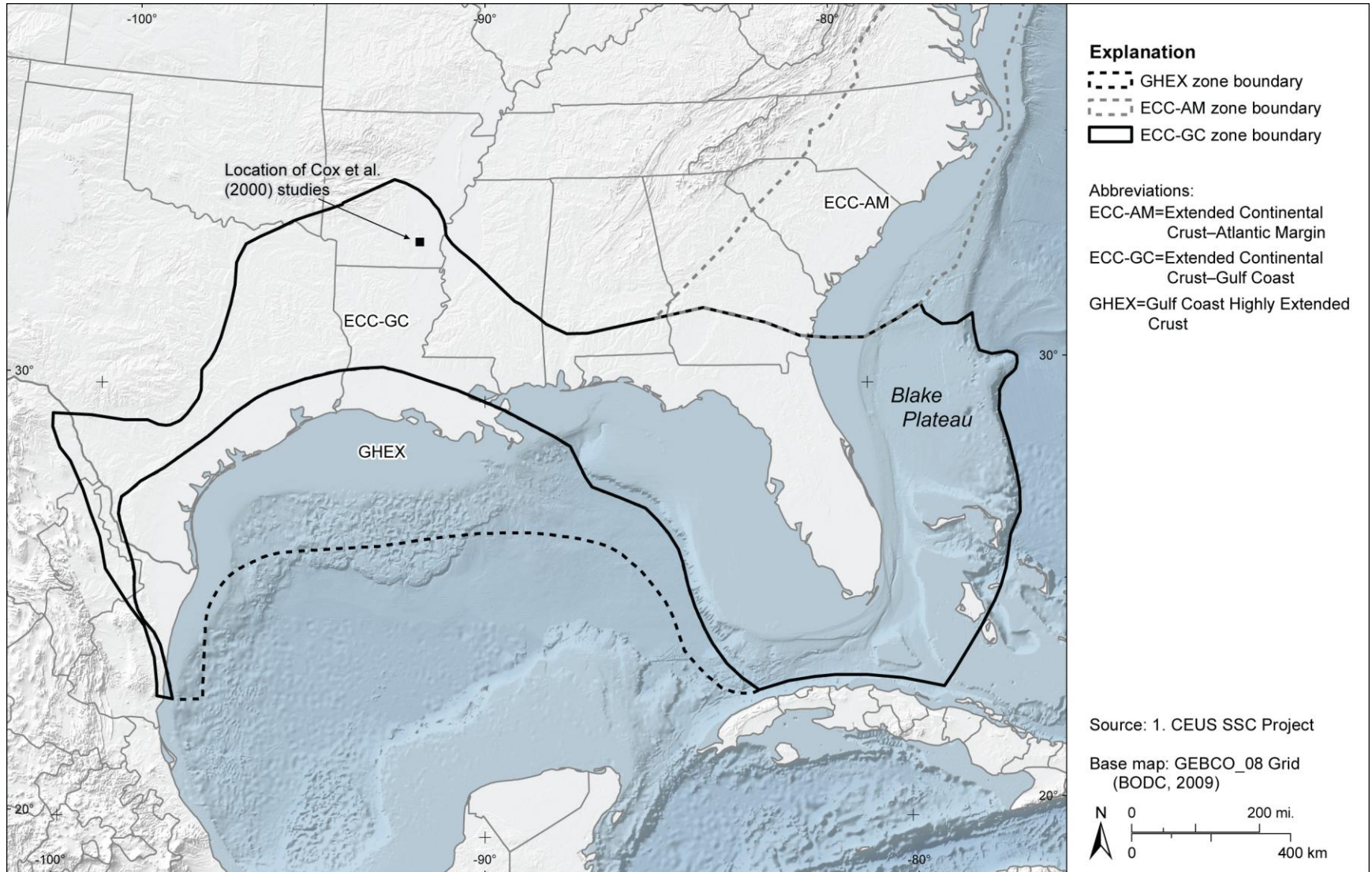


**Figure 7.3.9-1**  
The ECC-GC seismotectonic zone

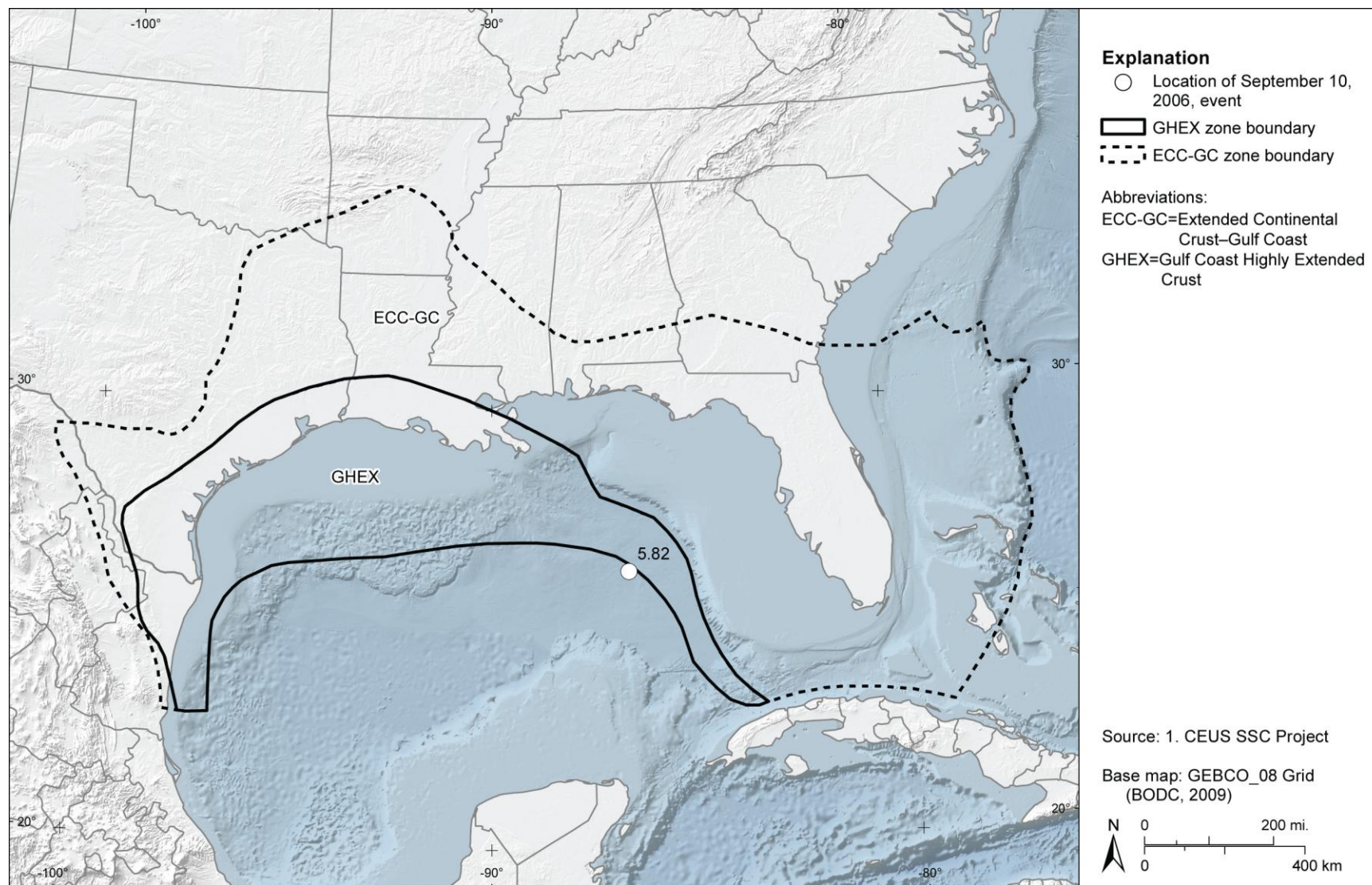


**Figure 7.3.10-1**  
**The GHEX seismotectonic zone**

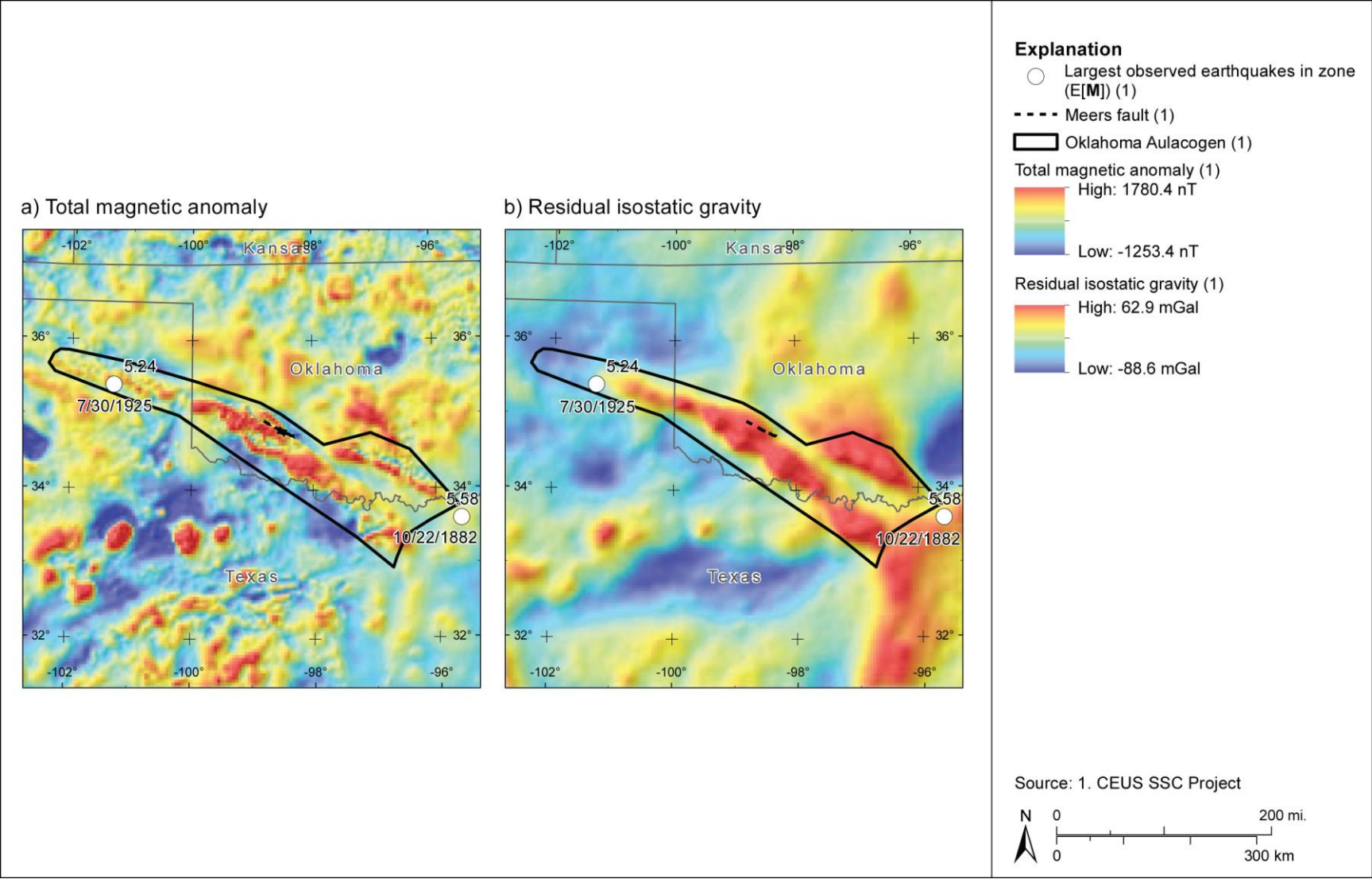


**Figure 7.3.11-1**  
 The OKA seismotectonic zone and regional gravity and magnetic data

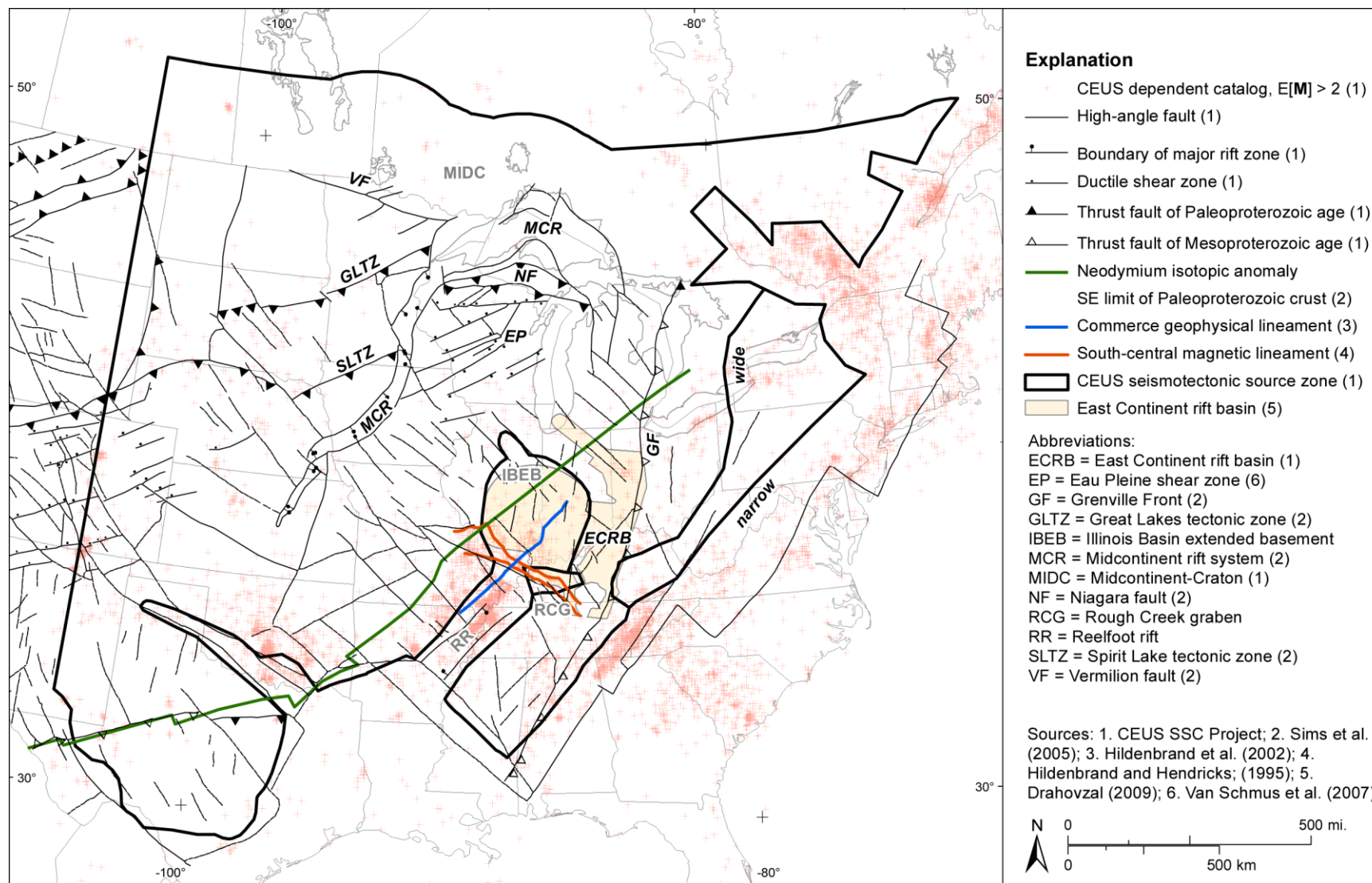


**Figure 7.3.12-1**  
 Simplified tectonic map showing the distribution of principal basement faults, rifts, and sutures in the Midcontinent

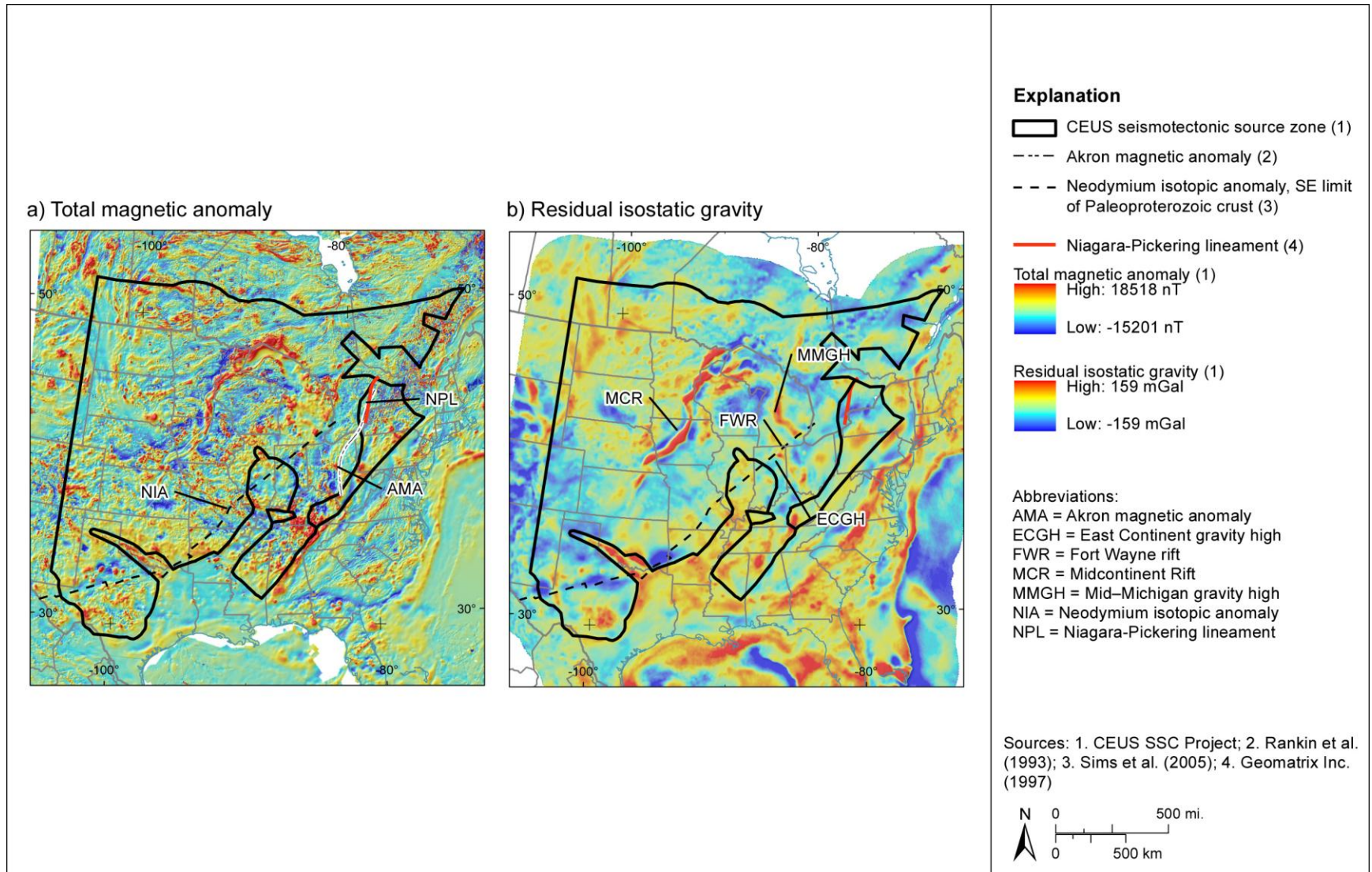


**Figure 7.3.12-2**  
 Maps showing major basement structural features relative to (a) regional magnetic anomalies and (b) regional gravity anomalies

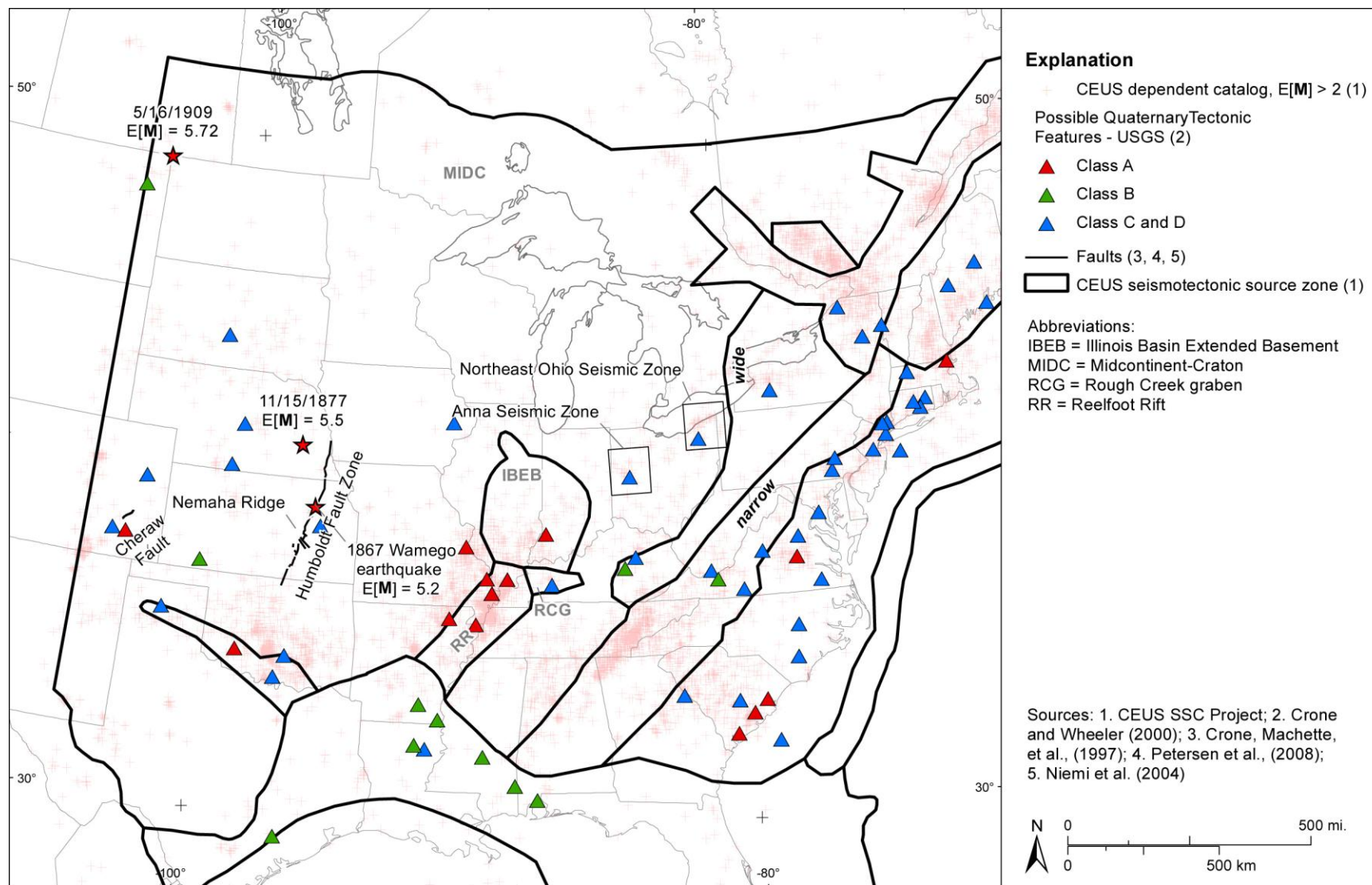


**Figure 7.3.12-3**  
 Seismic zones and maximum observed earthquakes in the MidC zone

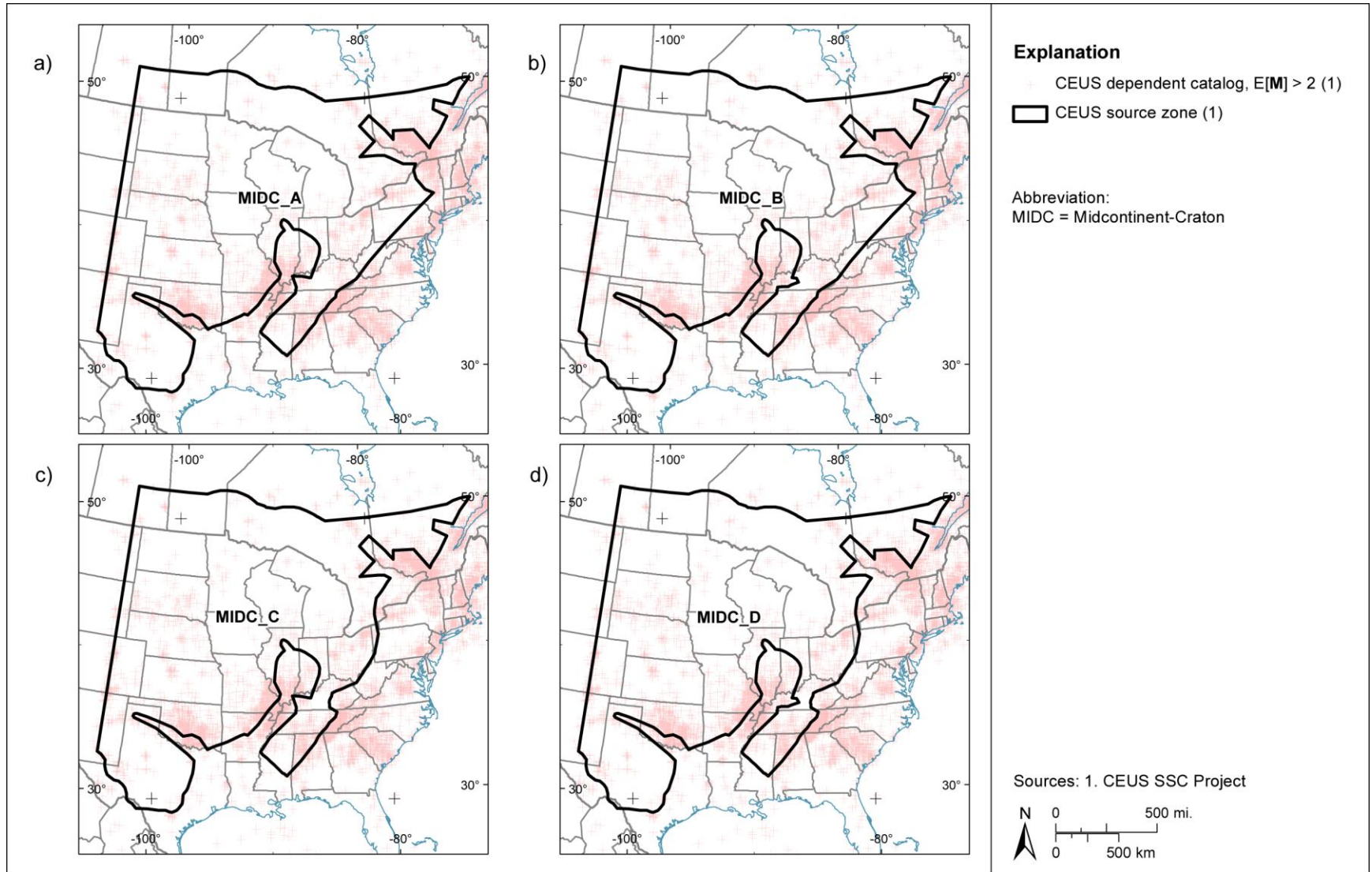


**Figure 7.3.12-4**  
Alternative MidC source zone configurations

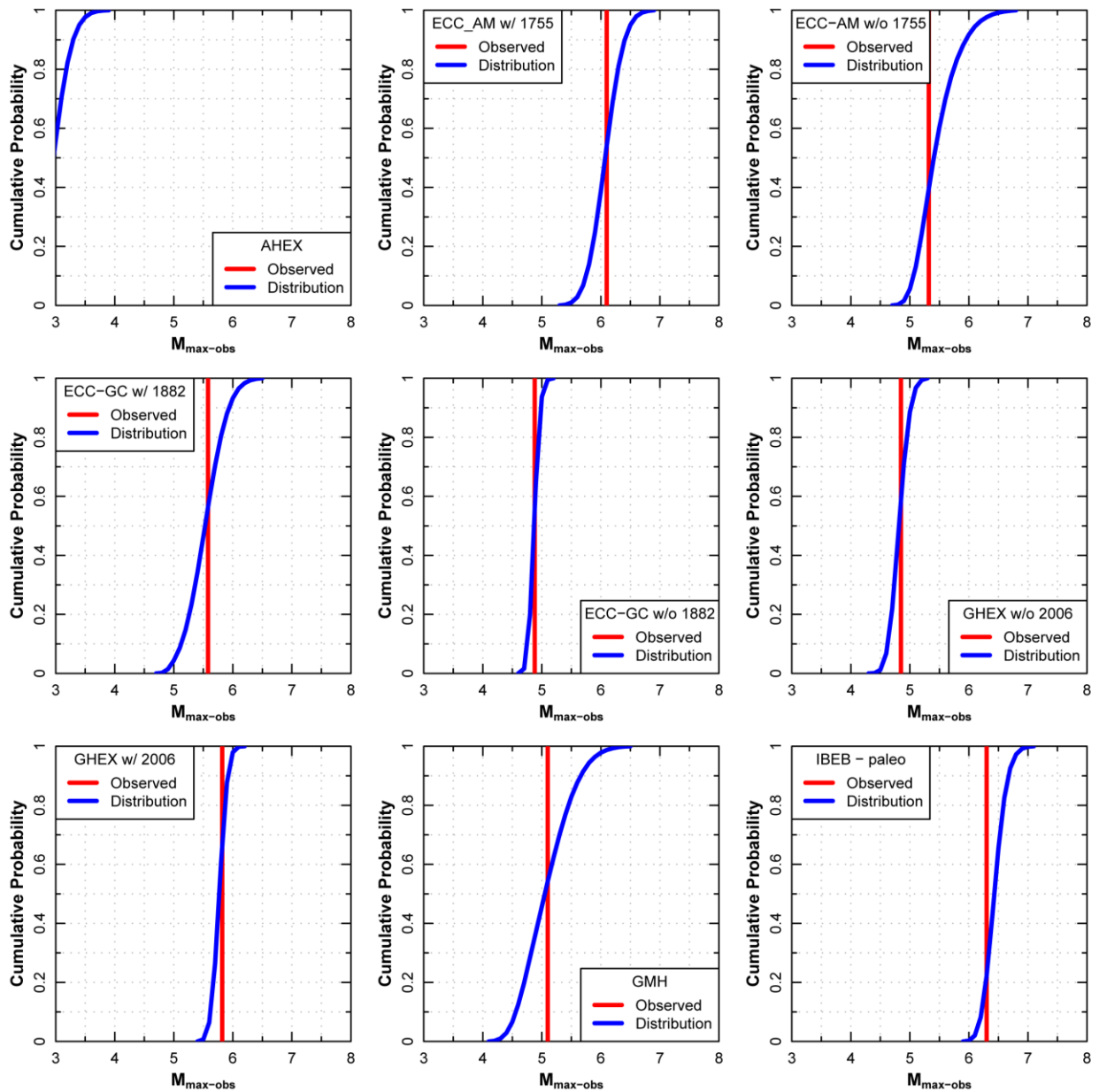


Figure 7.4.1-1 (1 of 3)  
 Distributions for  $m_{\max-obs}$  for the seismotectonic distributed seismicity source zones

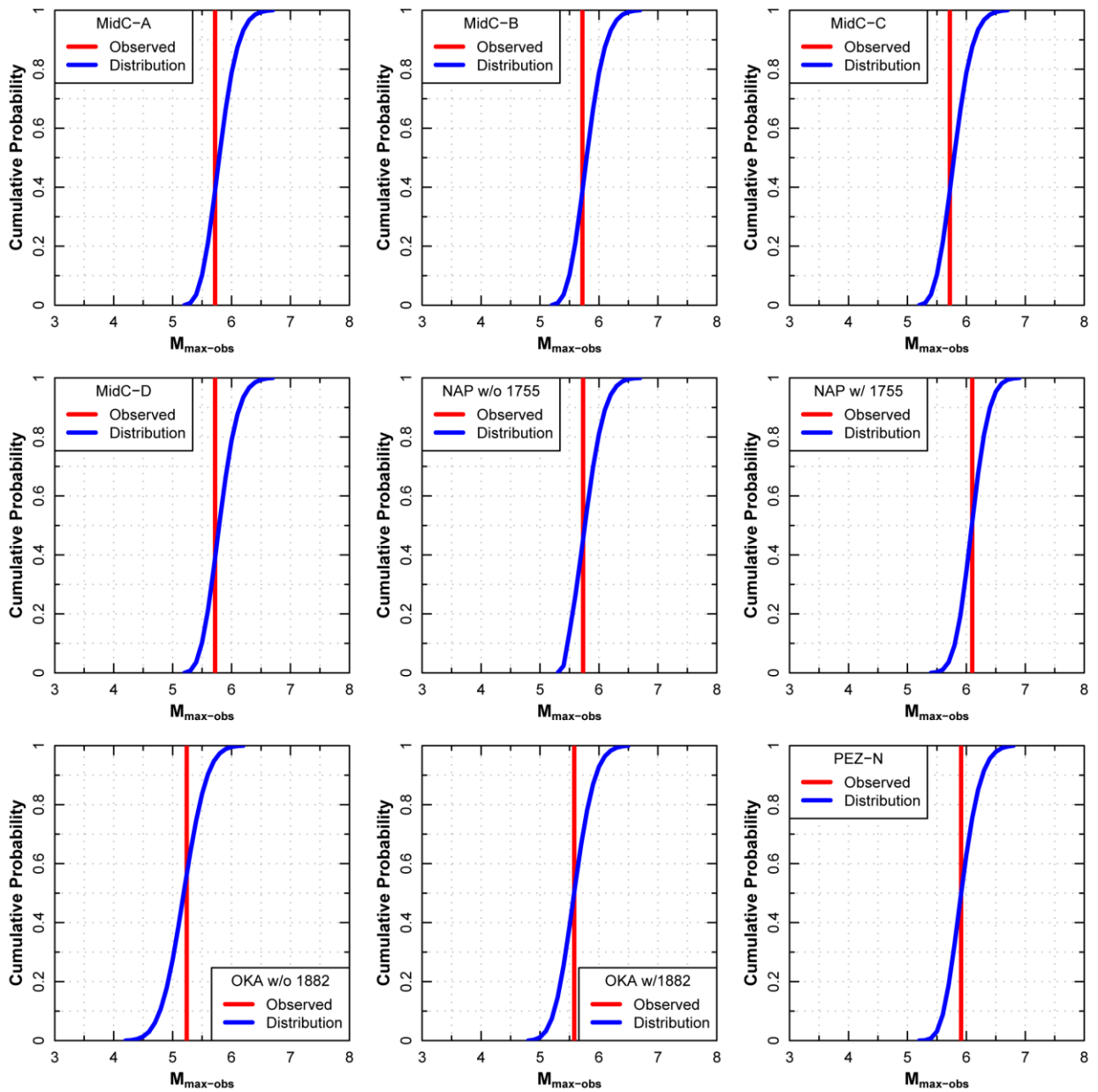
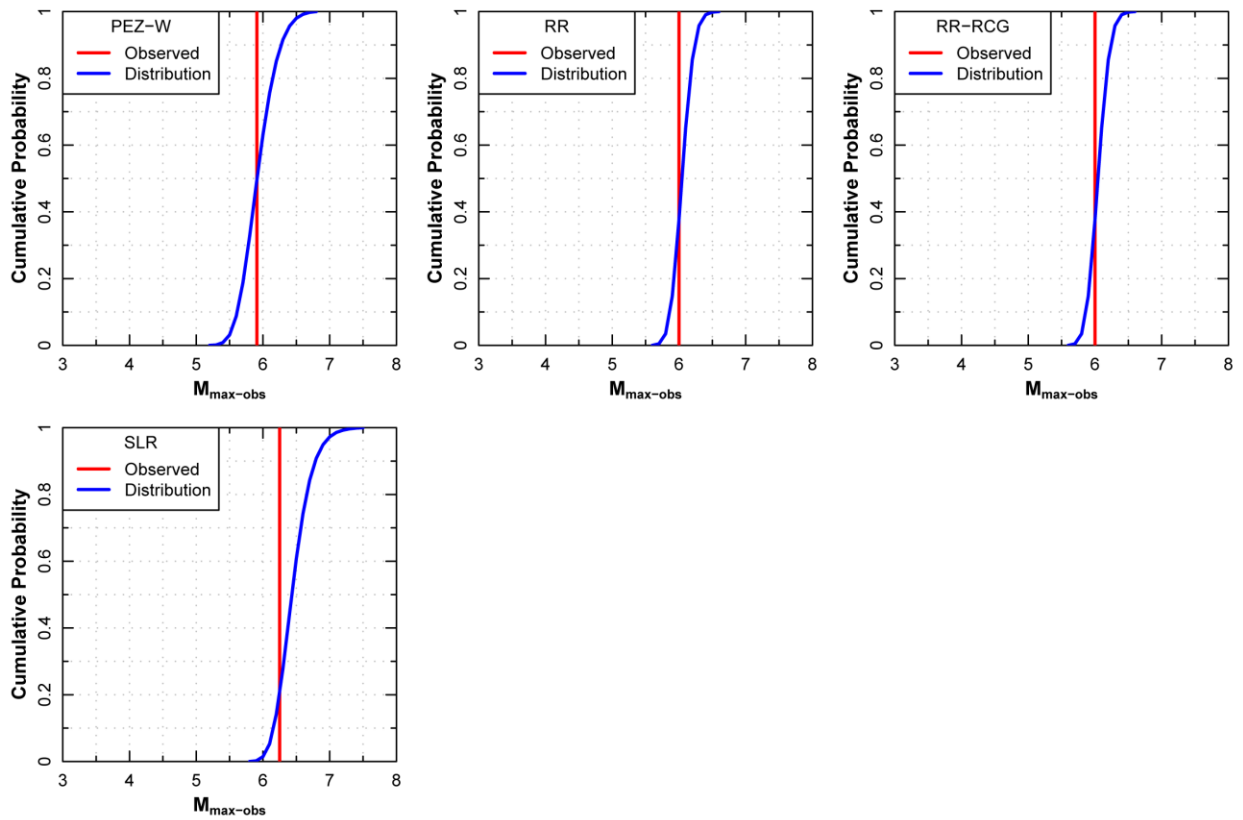


Figure 7.4.1-1 (2 of 3)  
Distributions for  $m_{\max-obs}$  for the seismotectonic distributed seismicity source zones



**Figure 7.4.1-1 (3 of 3)**  
**Distributions for  $m_{\max-obs}$  for the seismotectonic distributed seismicity source zones**

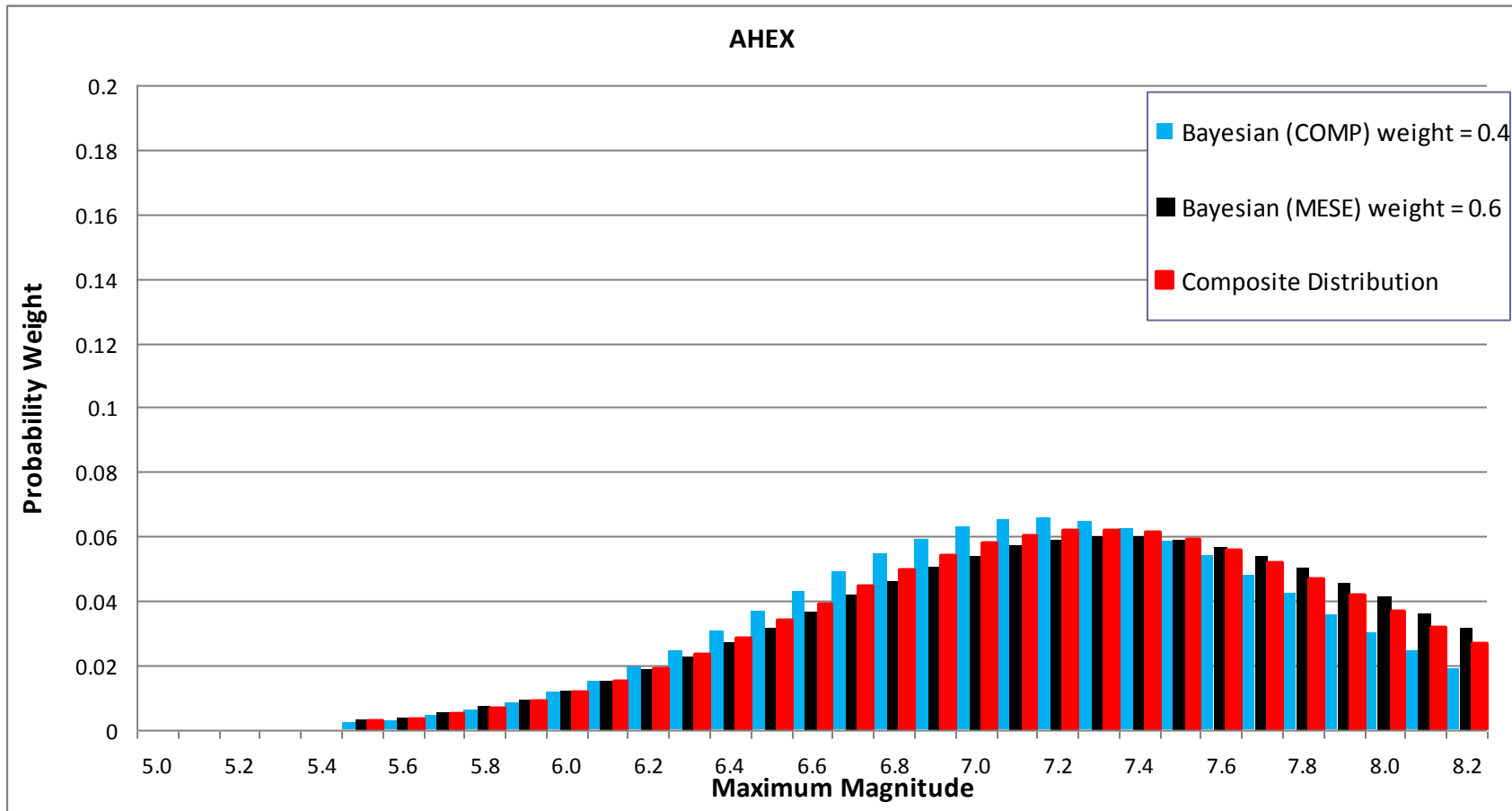


Figure 7.4.2-1  
Mmax distributions for the AHEX seismotectonic zone

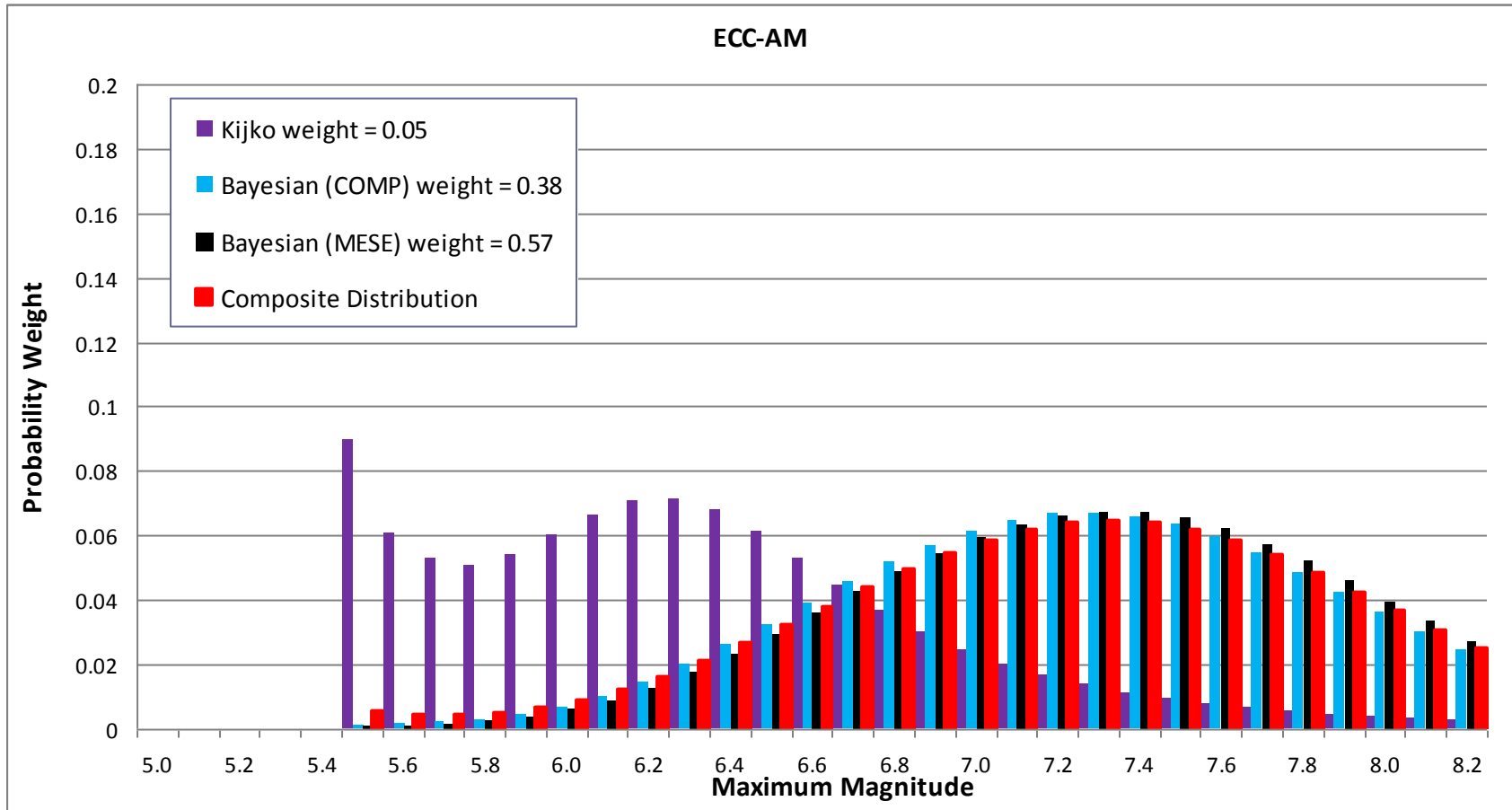


Figure 7.4.2-2  
Mmax distributions for the ECC\_AM seismotectonic zone

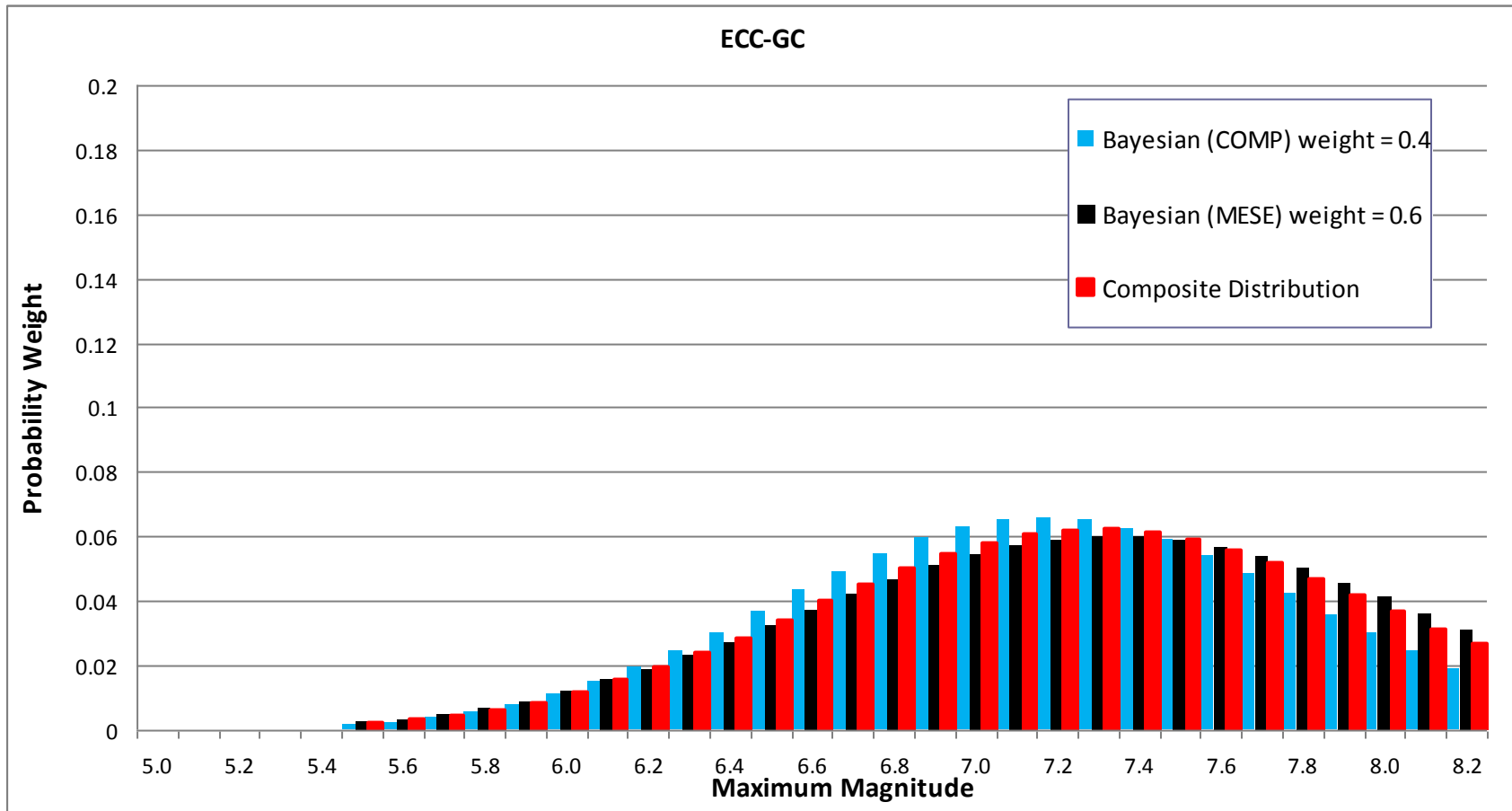


Figure 7.4.2-3  
Mmax distributions for the ECC\_GC seismotectonic zone

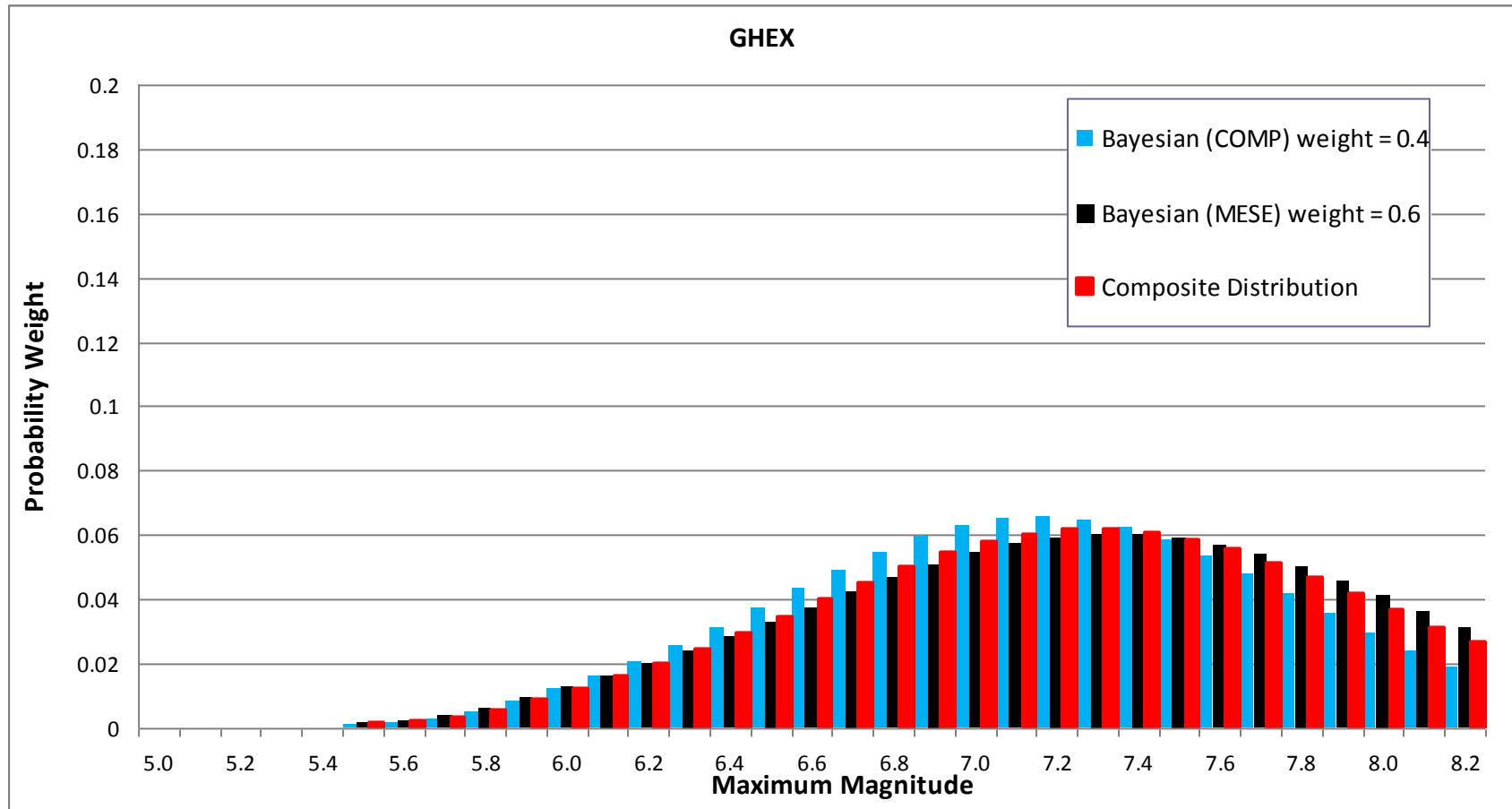


Figure 7.4.2-4  
Mmax distributions for the GHEX seismotectonic zone

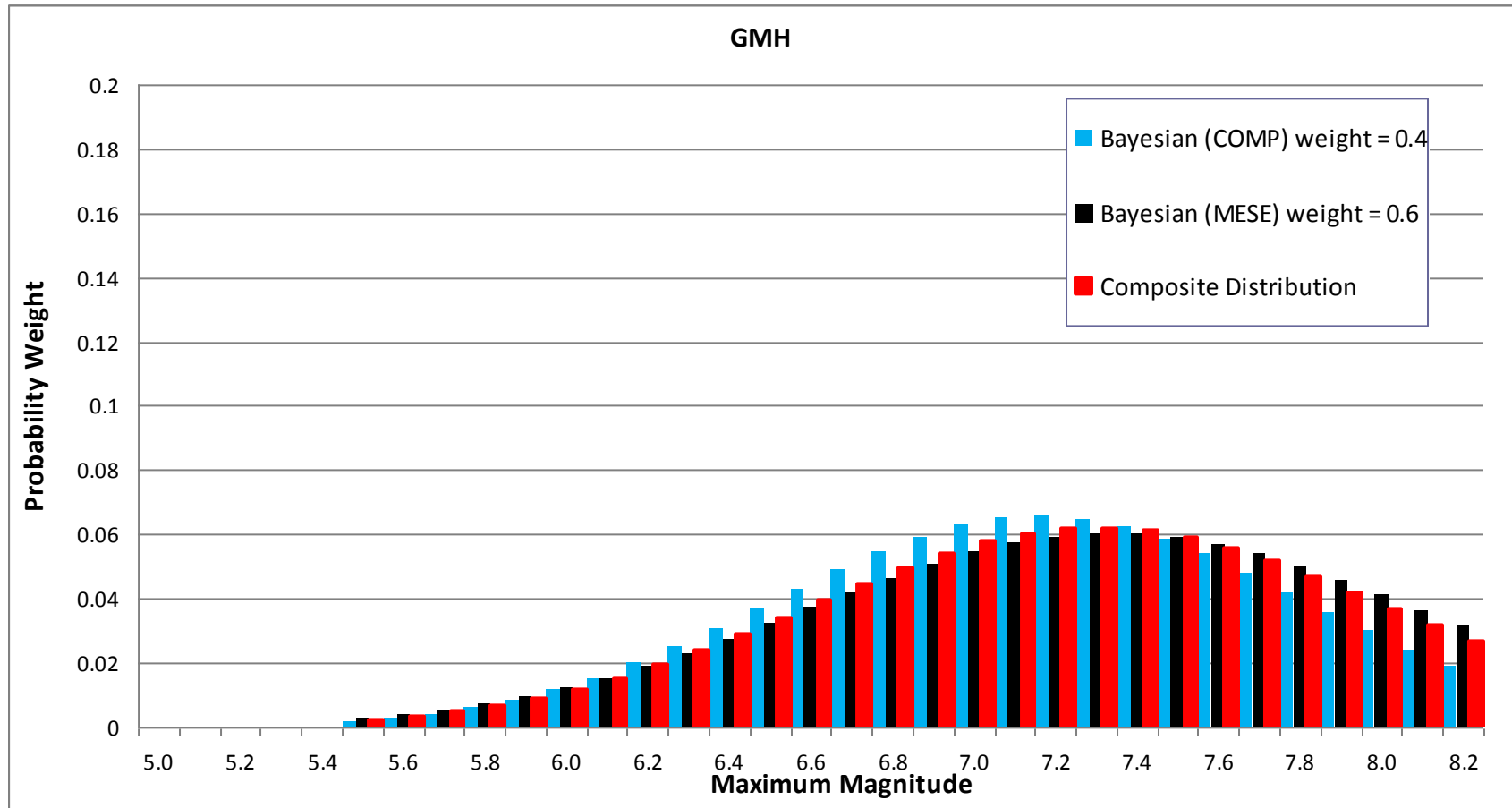


Figure 7.4.2-5  
Mmax distributions for the GMH seismotectonic zone

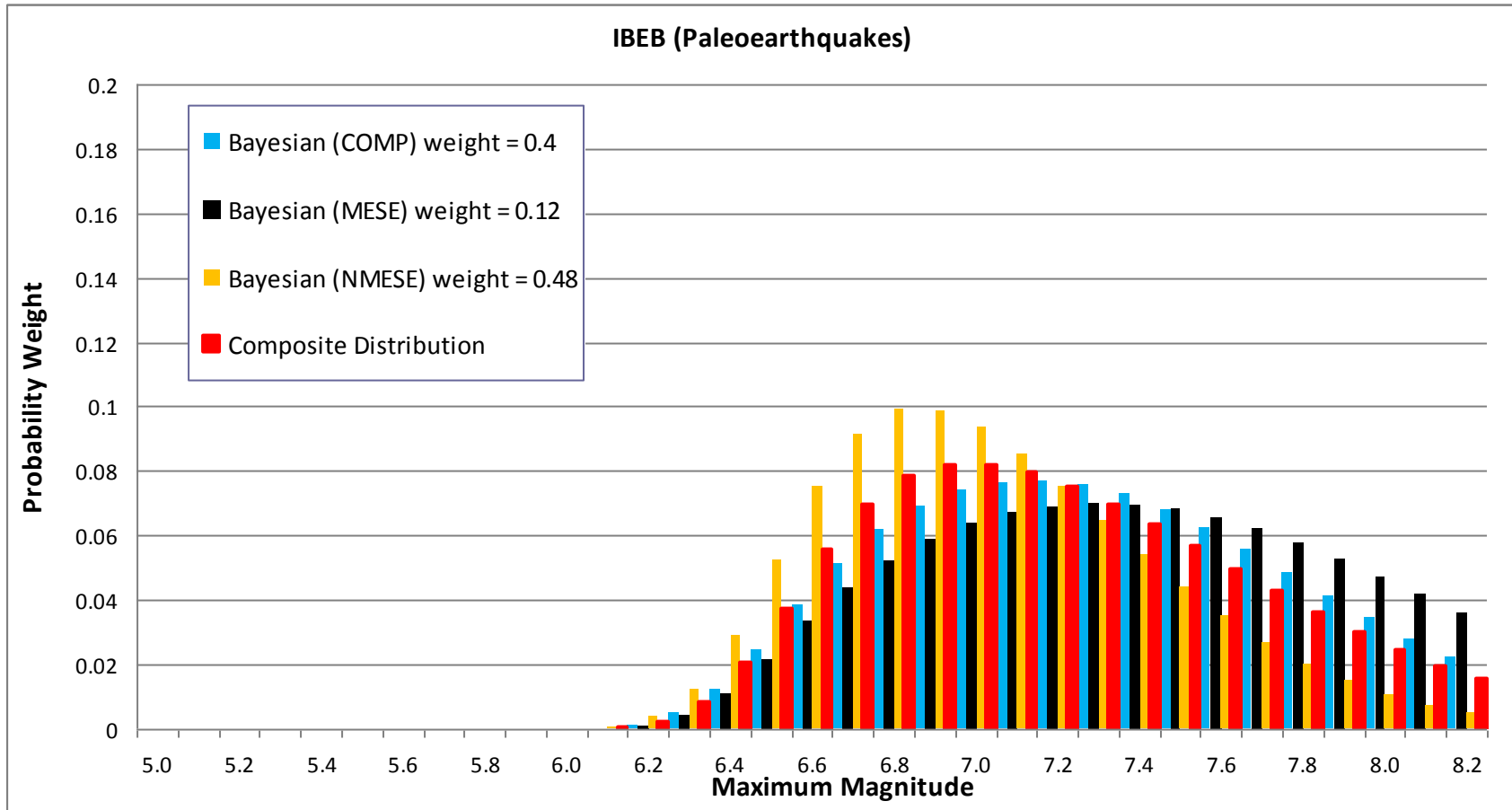


Figure 7.4.2-6  
Mmax distributions for the IBEB seismotectonic zone

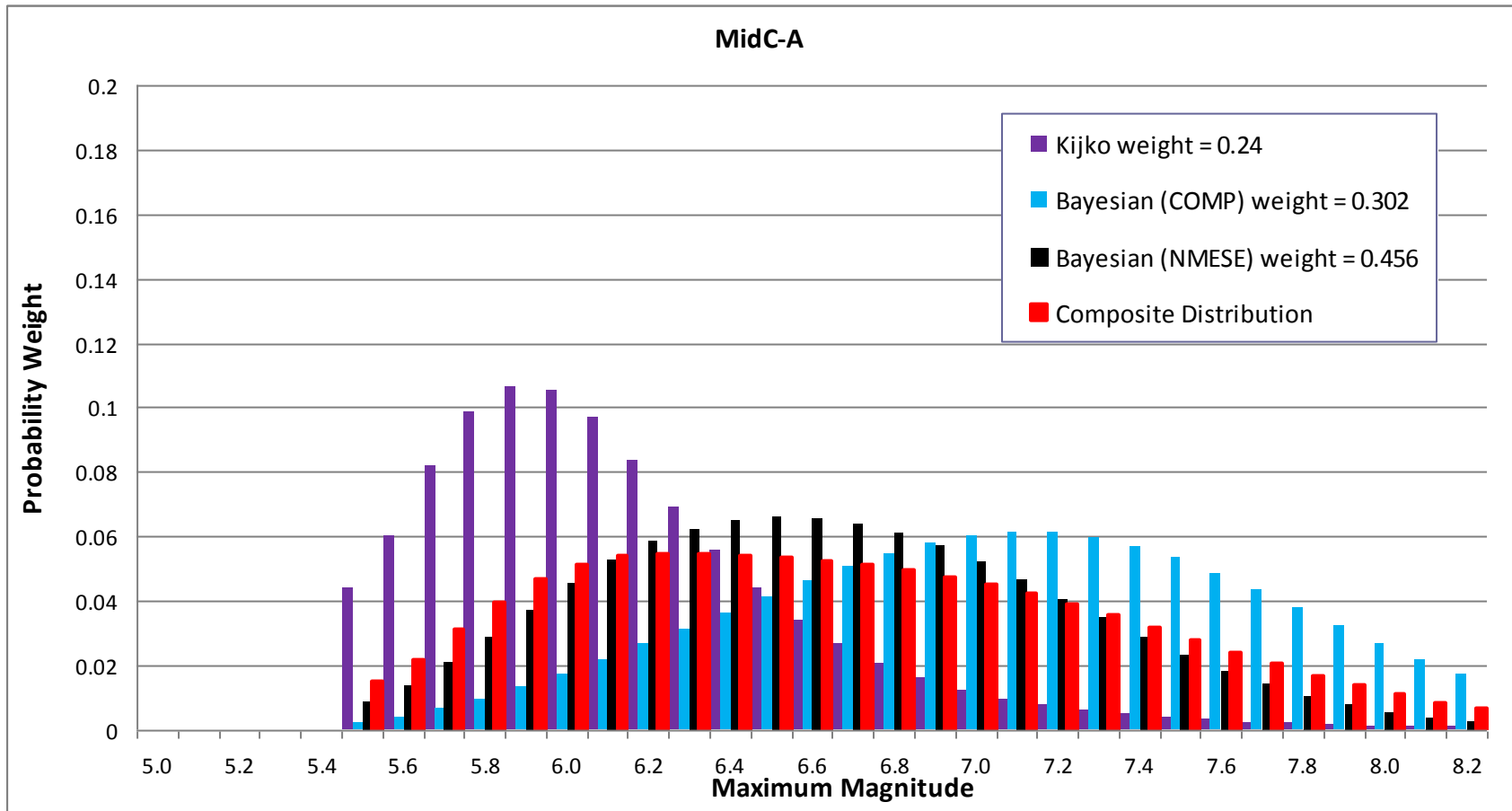


Figure 7.4.2-7  
Mmax distributions for the MidC-A seismotectonic zone

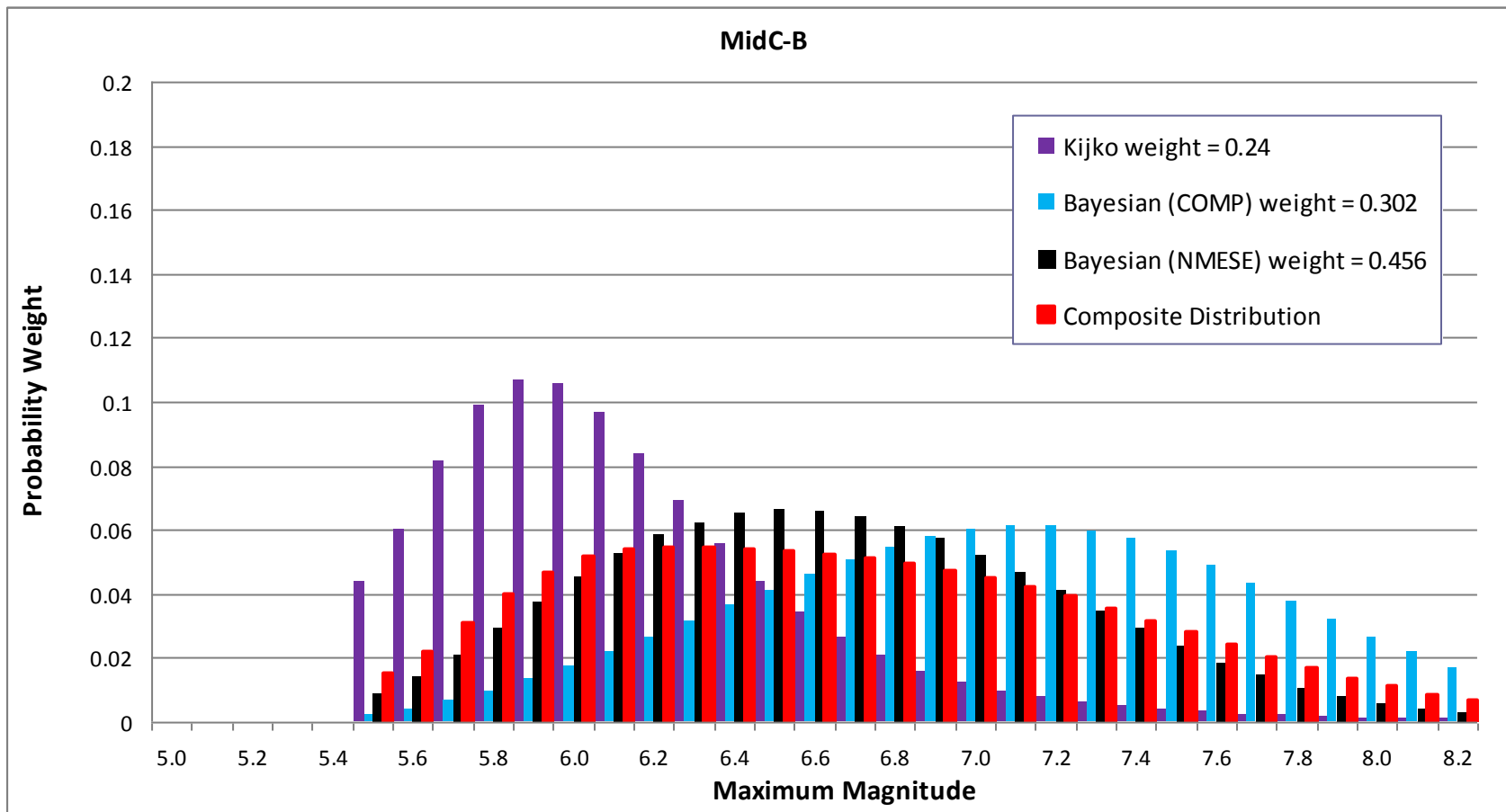


Figure 7.4.2-8  
Mmax distributions for the MidC-B seismotectonic zone

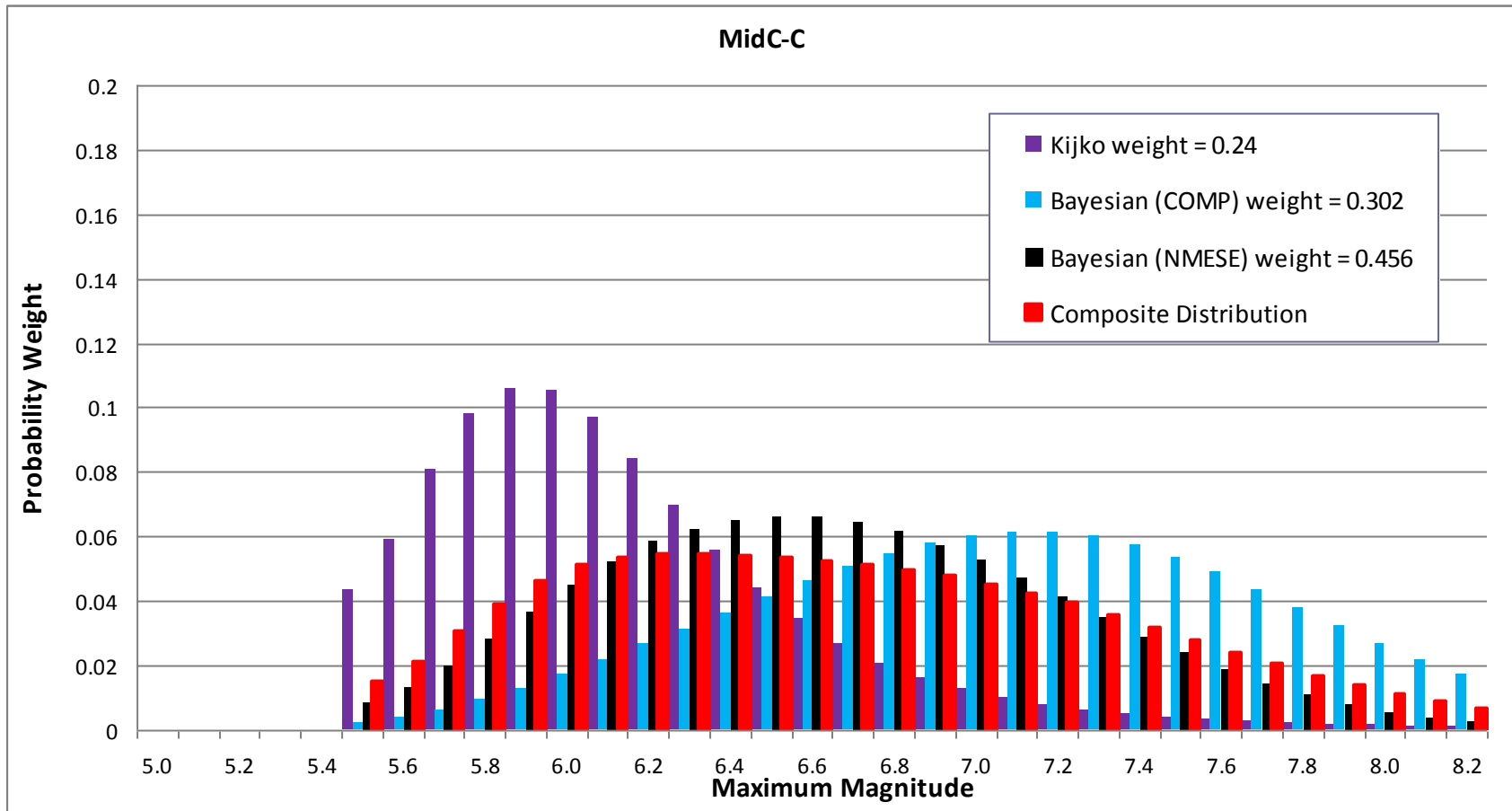


Figure 7.4.2-9  
Mmax distributions for the MidC-C seismotectonic zone

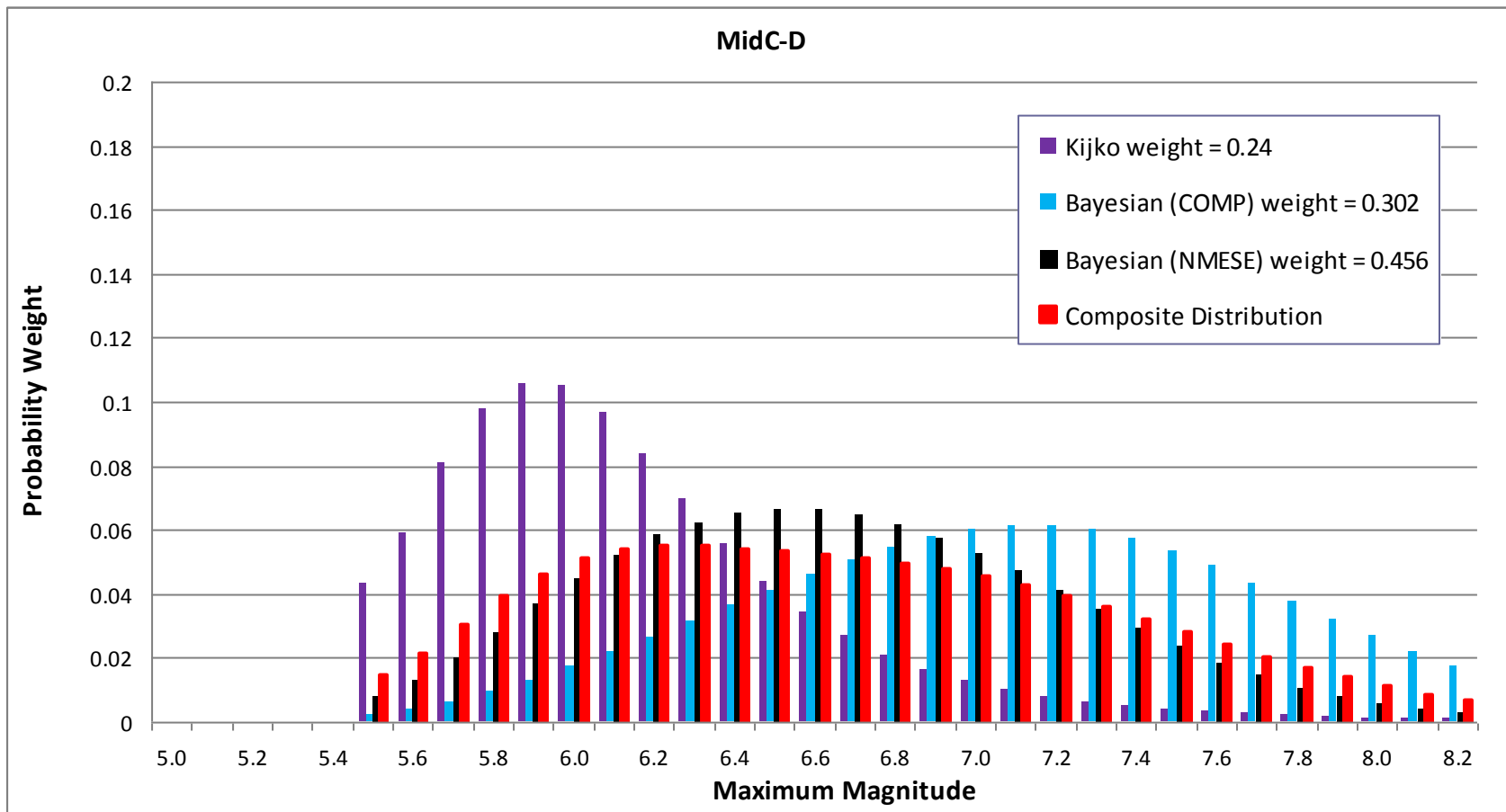


Figure 7.4.2-10  
Mmax distributions for the MidC-D seismotectonic zone

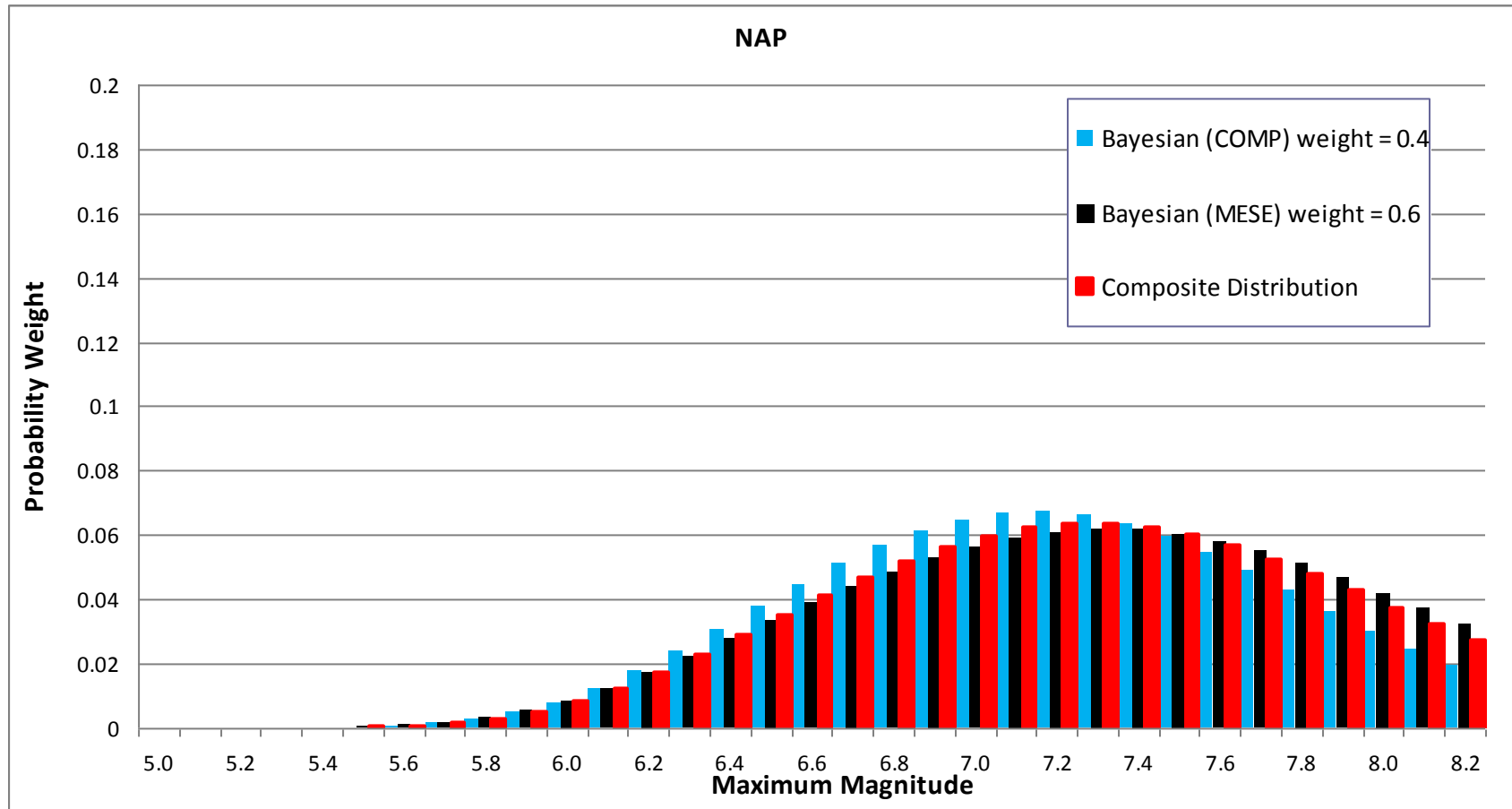


Figure 7.4.2-11  
Mmax distributions for the NAP seismotectonic zone

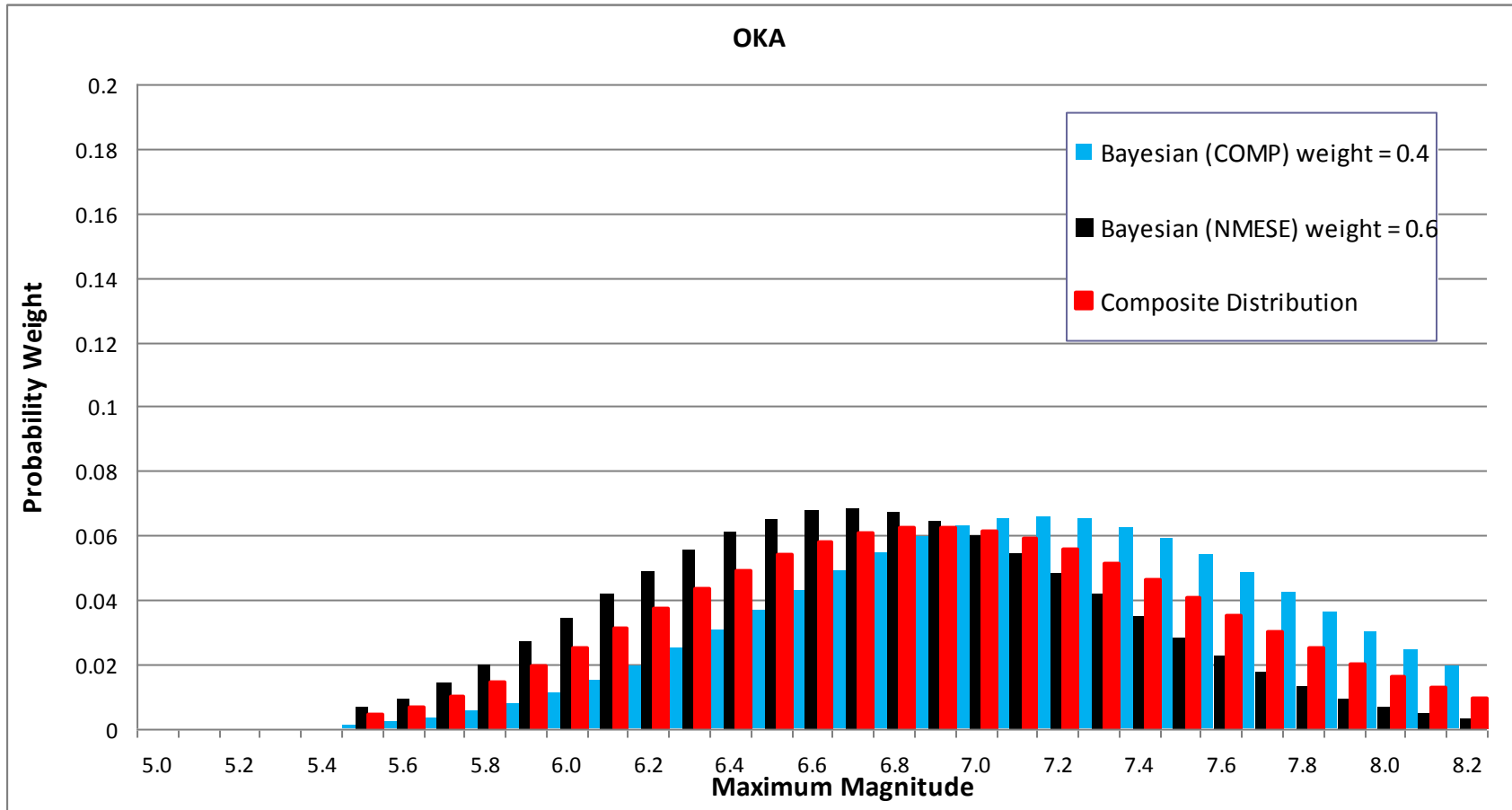


Figure 7.4.2-12  
Mmax distributions for the OKA seismotectonic zone

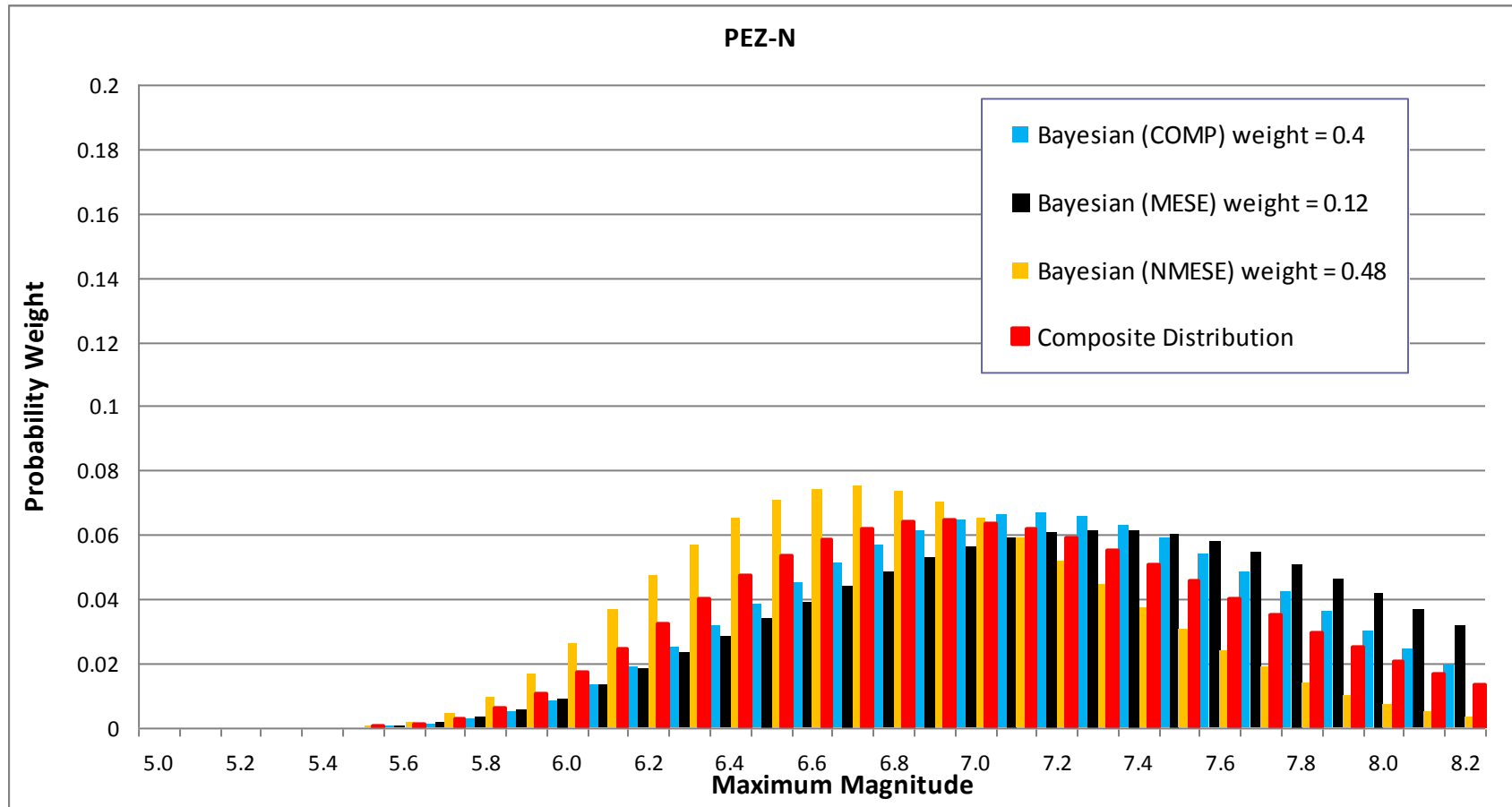


Figure 7.4.2-13  
Mmax distributions for the PEZ\_N seismotectonic zone

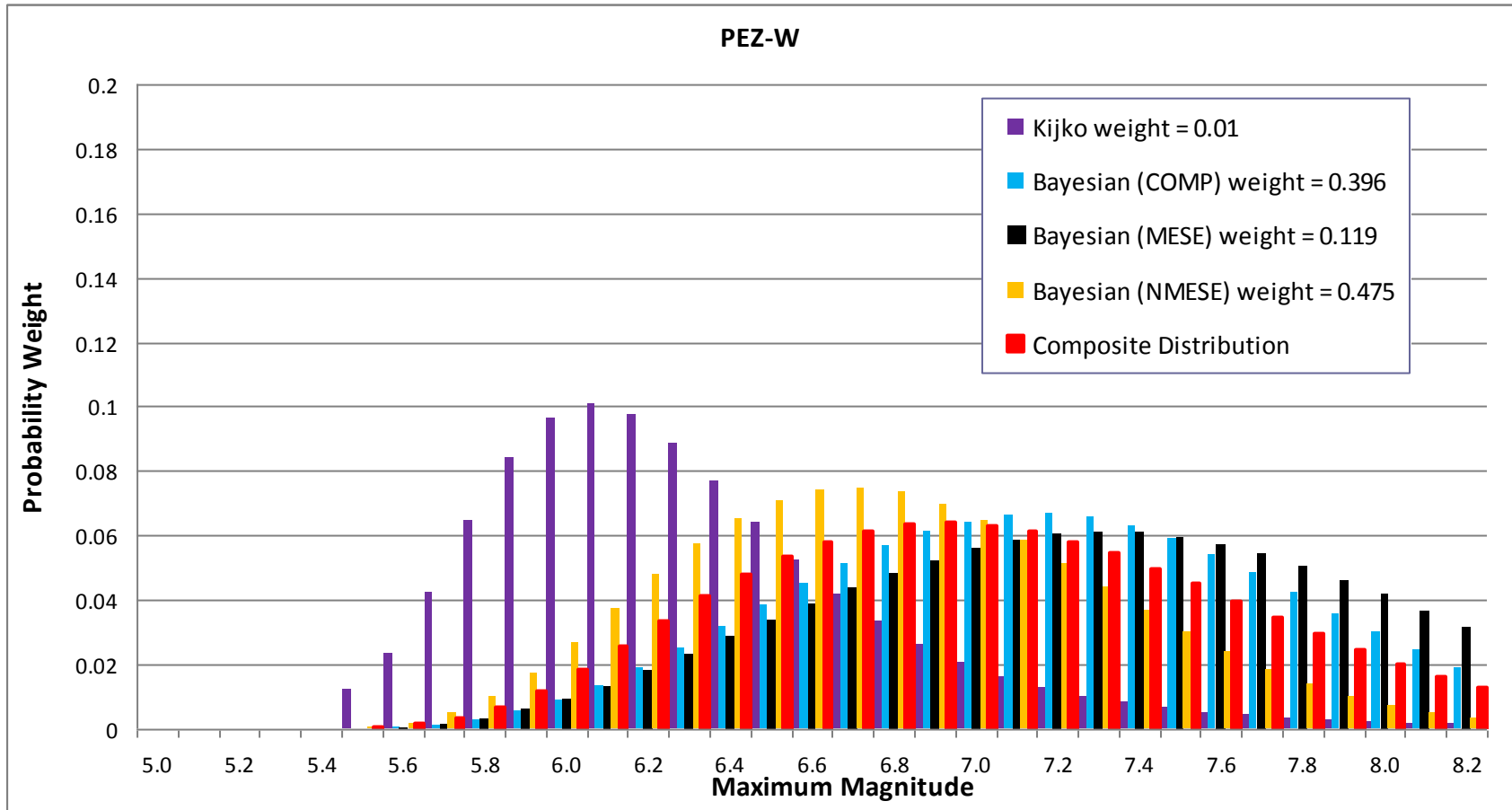


Figure 7.4.2-14  
Mmax distributions for the PEZ\_W seismotectonic zone

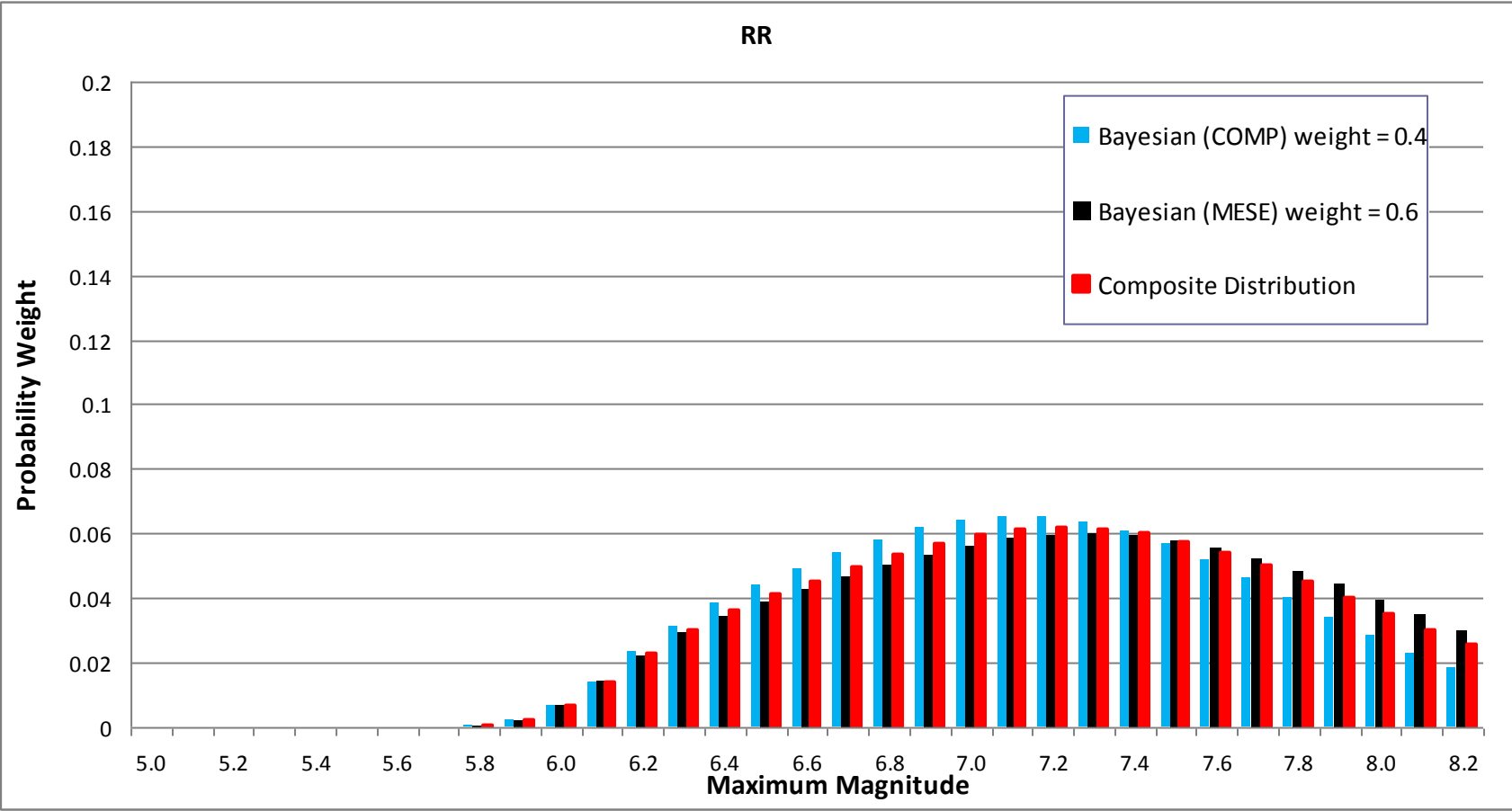


Figure 7.4.2-15  
Mmax distributions for the RR seismotectonic zone

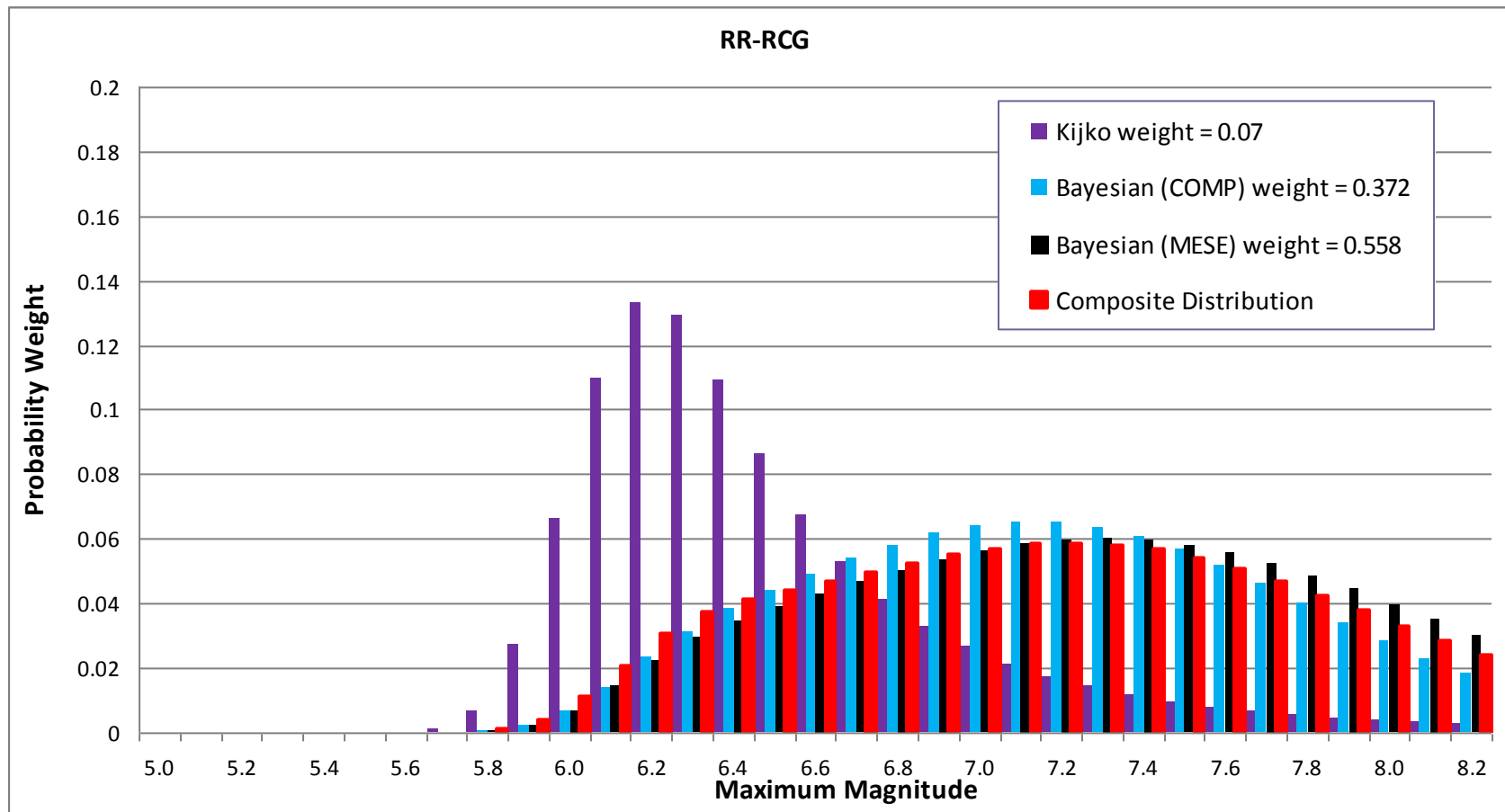


Figure 7.4.2-16  
Mmax distributions for the RR\_RCG seismotectonic zone

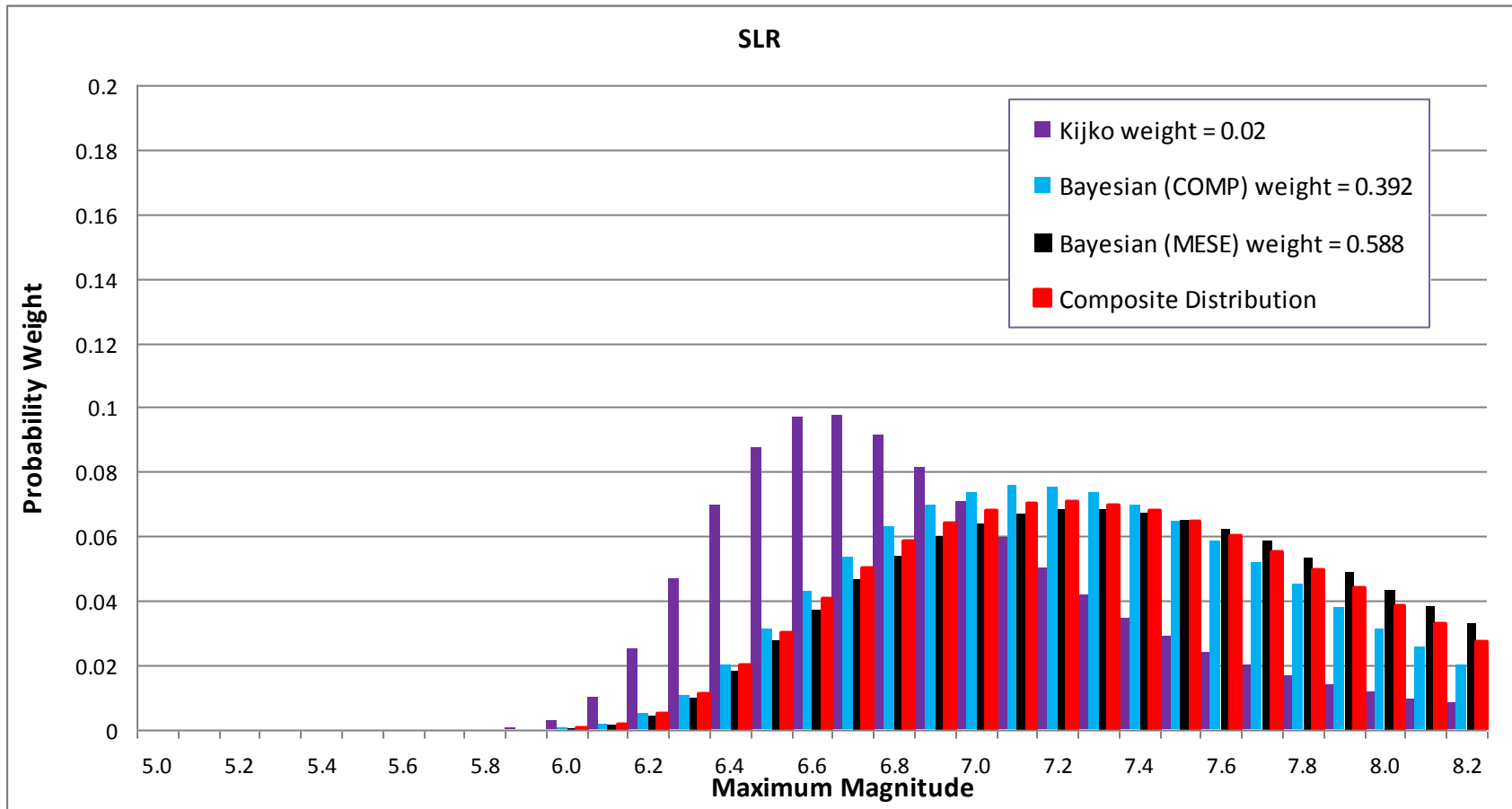
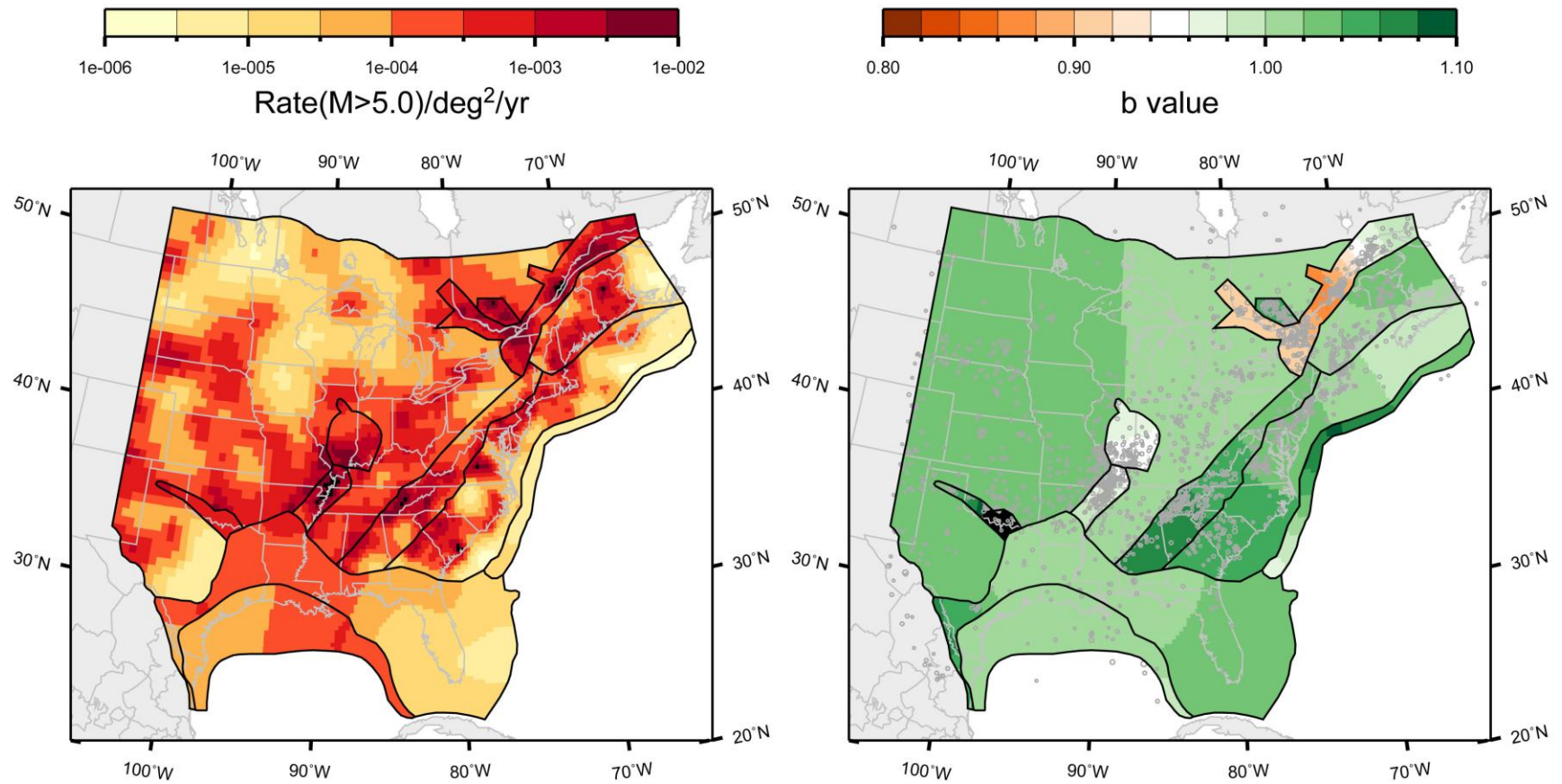
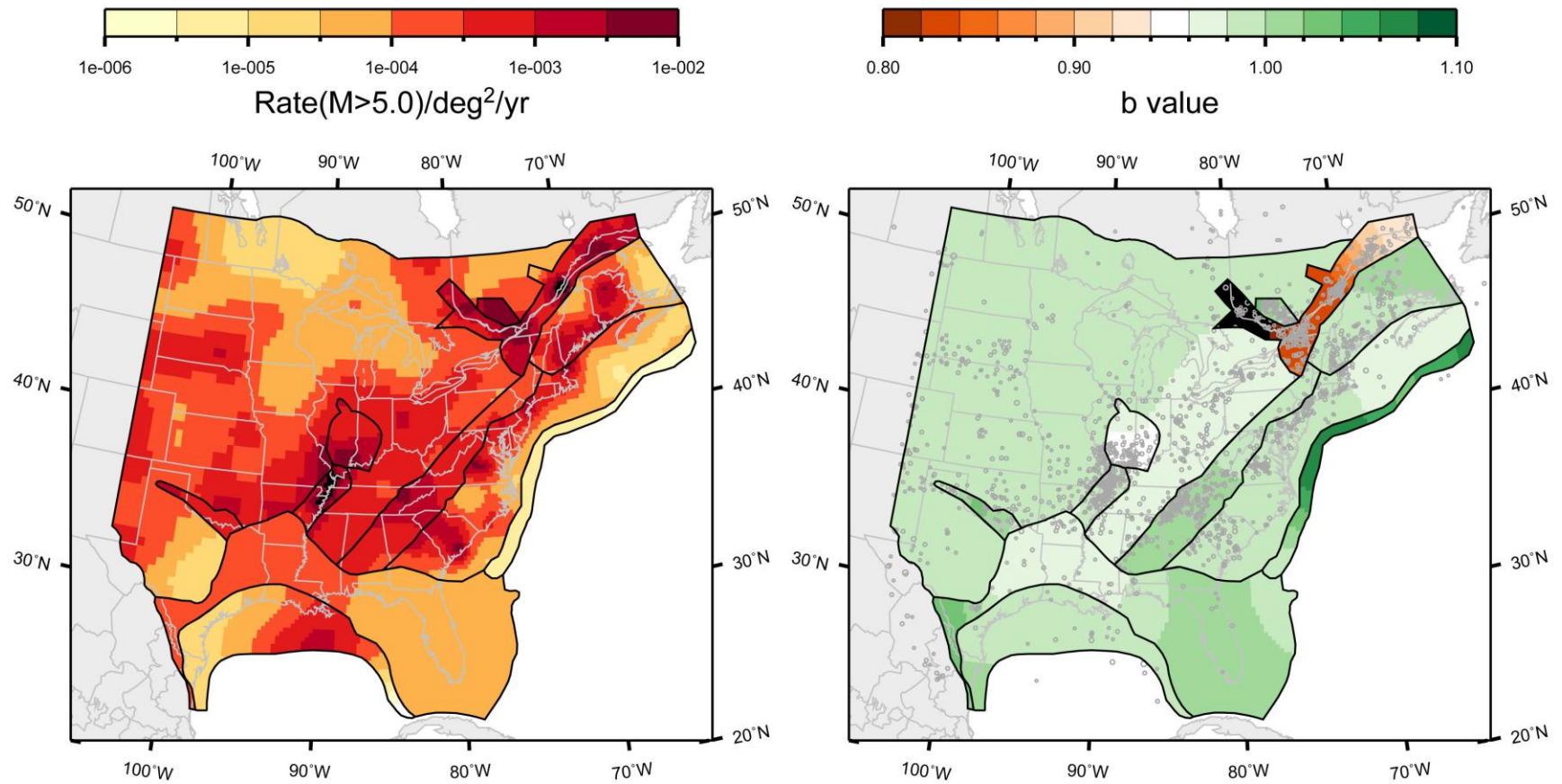


Figure 7.4.2-17  
Mmax distributions for the SLR seismotectonic zone



**Figure 7.5.1-1**  
Mean map of rate and *b*-value for the study region under the source-zone configuration with narrow interpretation of PEZ, Rough Creek graben associated with Midcontinent; Case A magnitude weights



**Figure 7.5.1-2**  
Mean map of rate and *b*-value for the study region under the source-zone configuration with narrow interpretation of PEZ, Rough Creek graben associated with Midcontinent; Case B magnitude weights

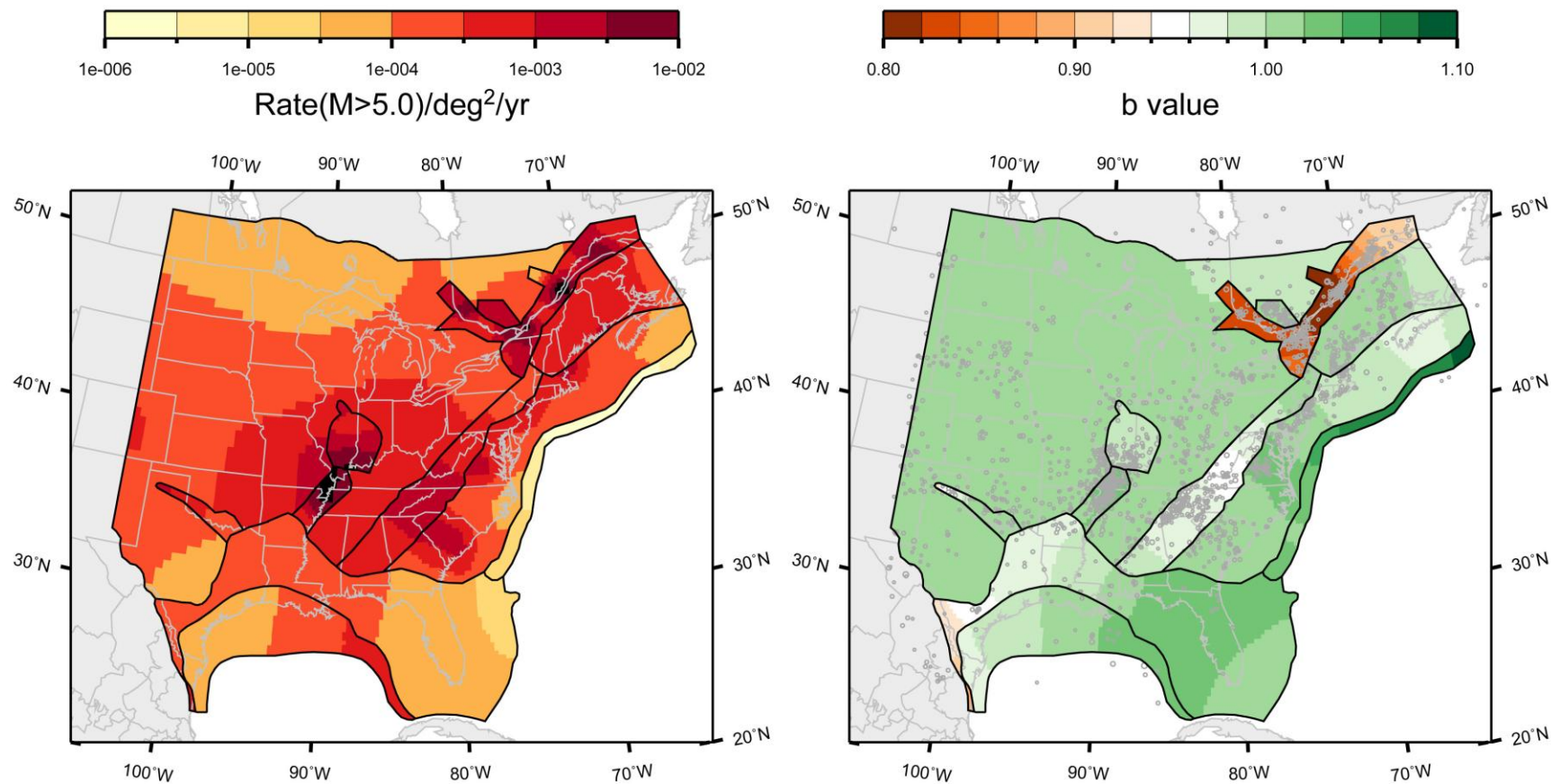


**Figure 7.5.1-3**  
Mean map of rate and *b*-value for the study region under the source-zone configuration with narrow interpretation of PEZ, Rough Creek graben associated with Midcontinent; Case E magnitude weights

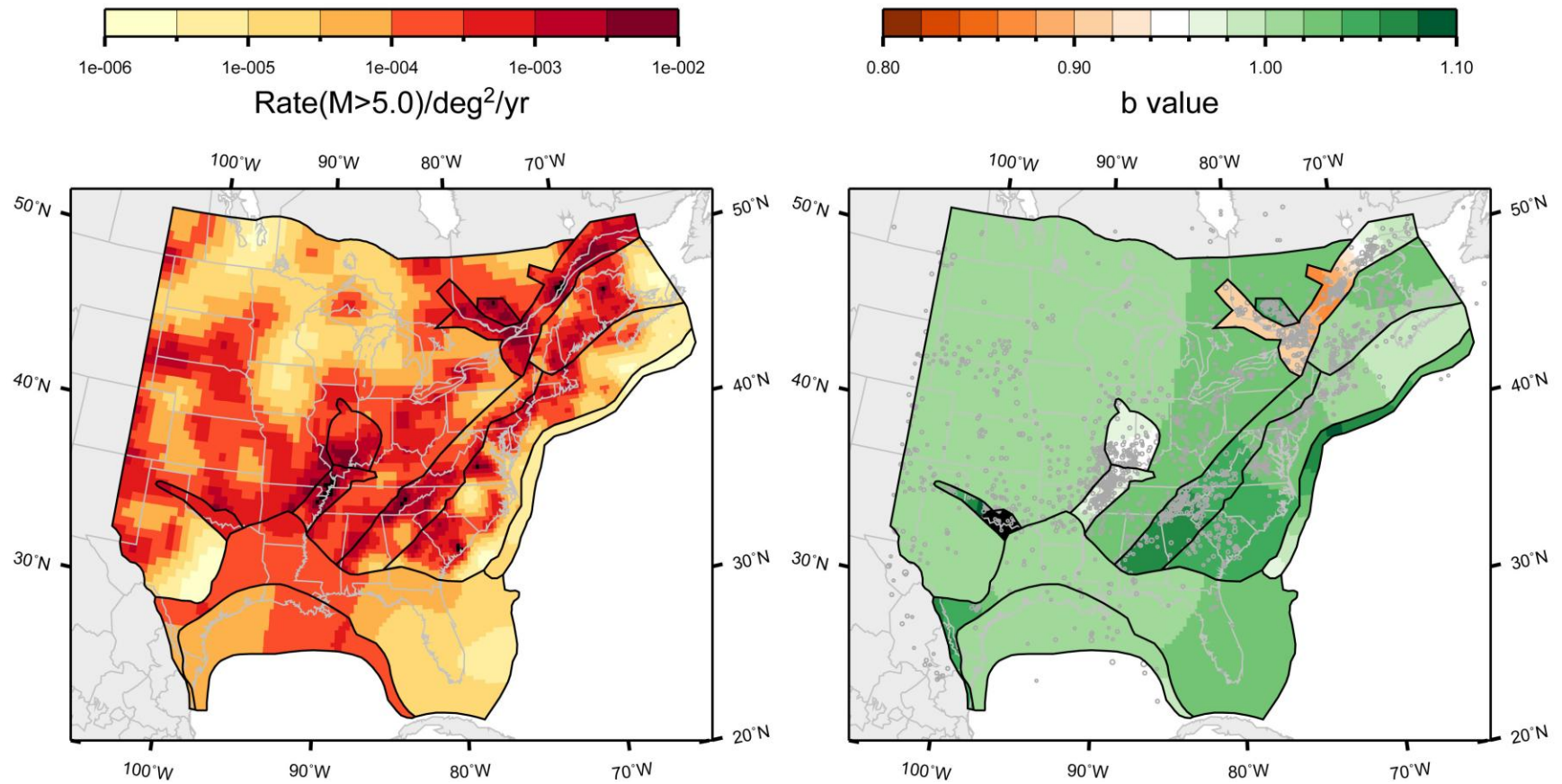


**Figure 7.5.1-4**  
Mean map of rate and *b*-value for the study region under the source-zone configuration with narrow interpretation of PEZ, Rough Creek graben associated with Reelfoot rift; Case A magnitude weights

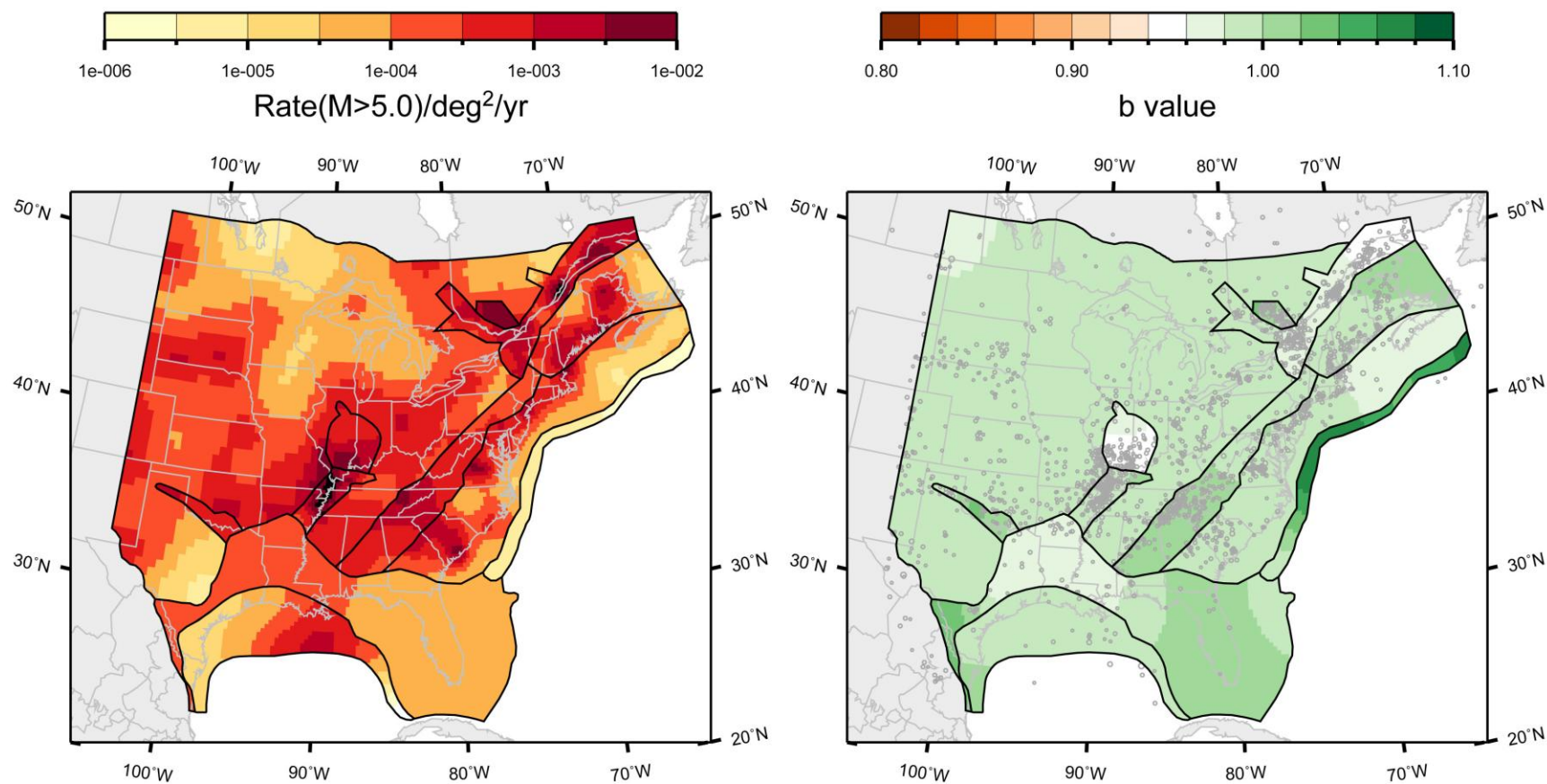


**Figure 7.5.1-5**  
Mean map of rate and *b*-value for the study region under the source-zone configuration with narrow interpretation of PEZ, Rough Creek graben associated with Reelfoot rift; Case B magnitude weights

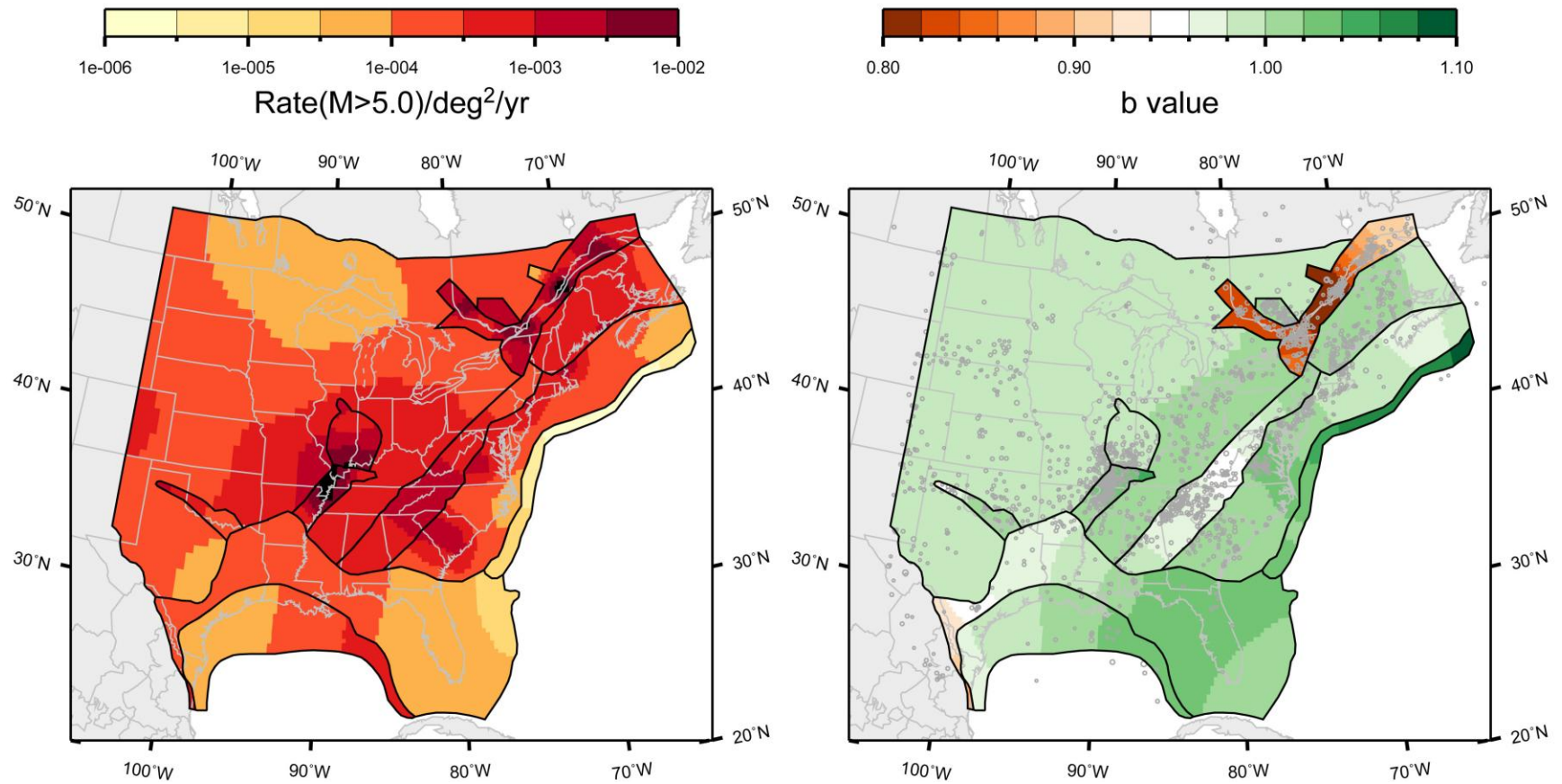


**Figure 7.5.1-6**  
Mean map of rate and  $b$ -value for the study region under the source-zone configuration with narrow interpretation of PEZ, Rough Creek graben associated with Reelfoot rift; Case E magnitude weights

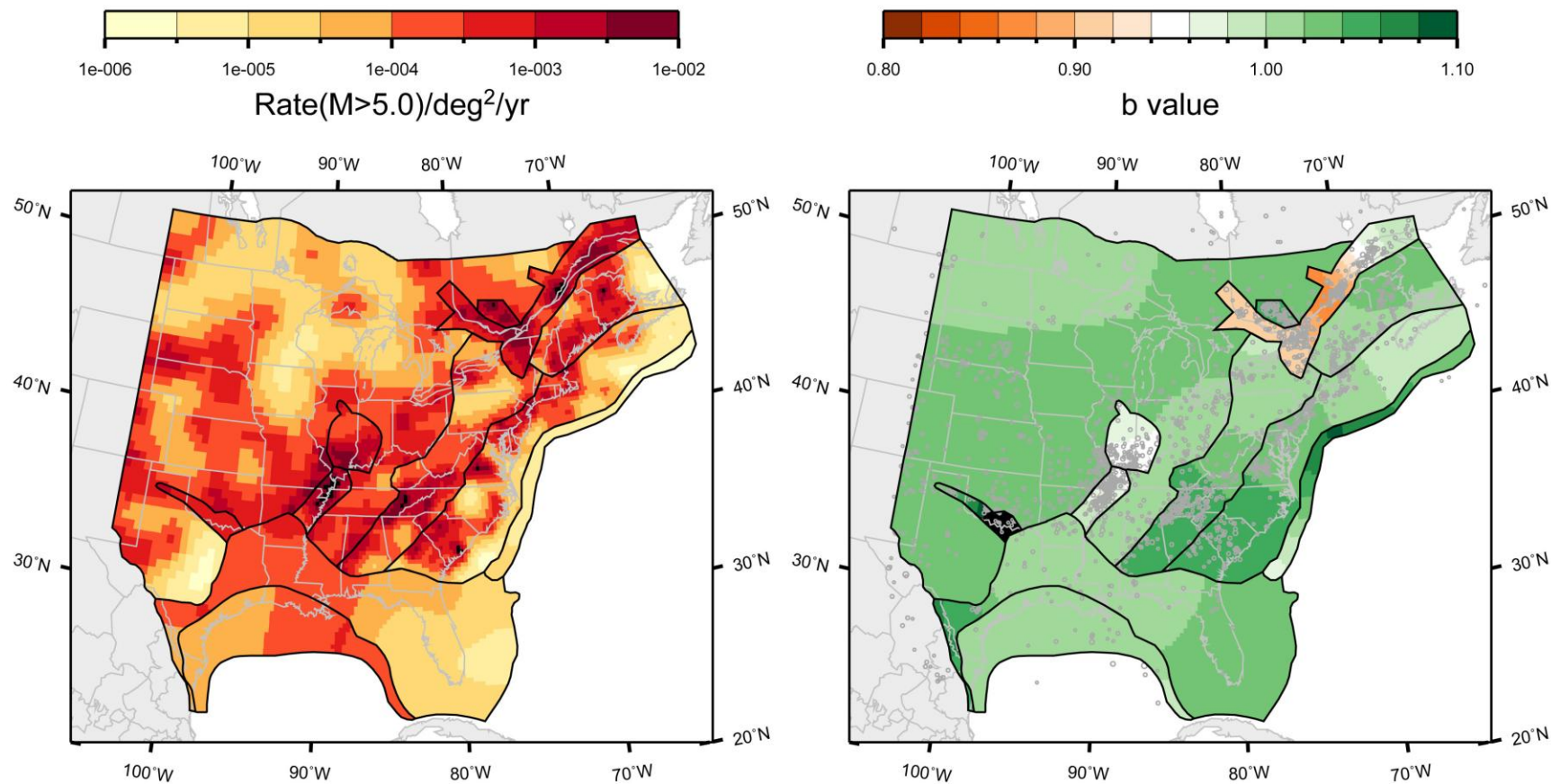


**Figure 7.5.1-7**  
Mean map of rate and *b*-value for the study region under the source-zone configuration with wide interpretation of PEZ, Rough Creek graben associated with Midcontinent; Case A magnitude weights

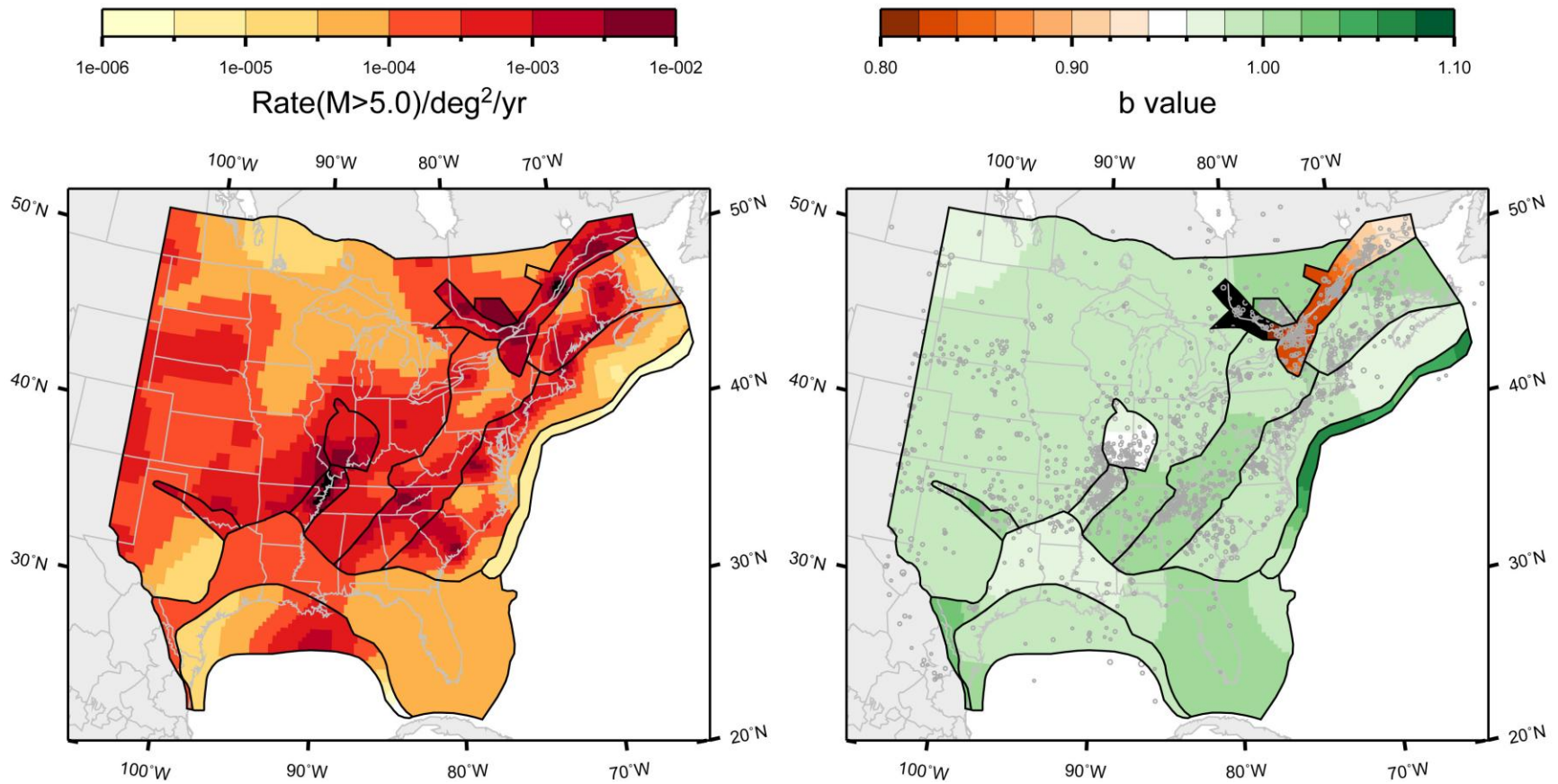


**Figure 7.5.1-8**  
Mean map of rate and  $b$ -value for the study region under the source-zone configuration with wide interpretation of PEZ, Rough Creek graben associated with Midcontinent; Case B magnitude weights

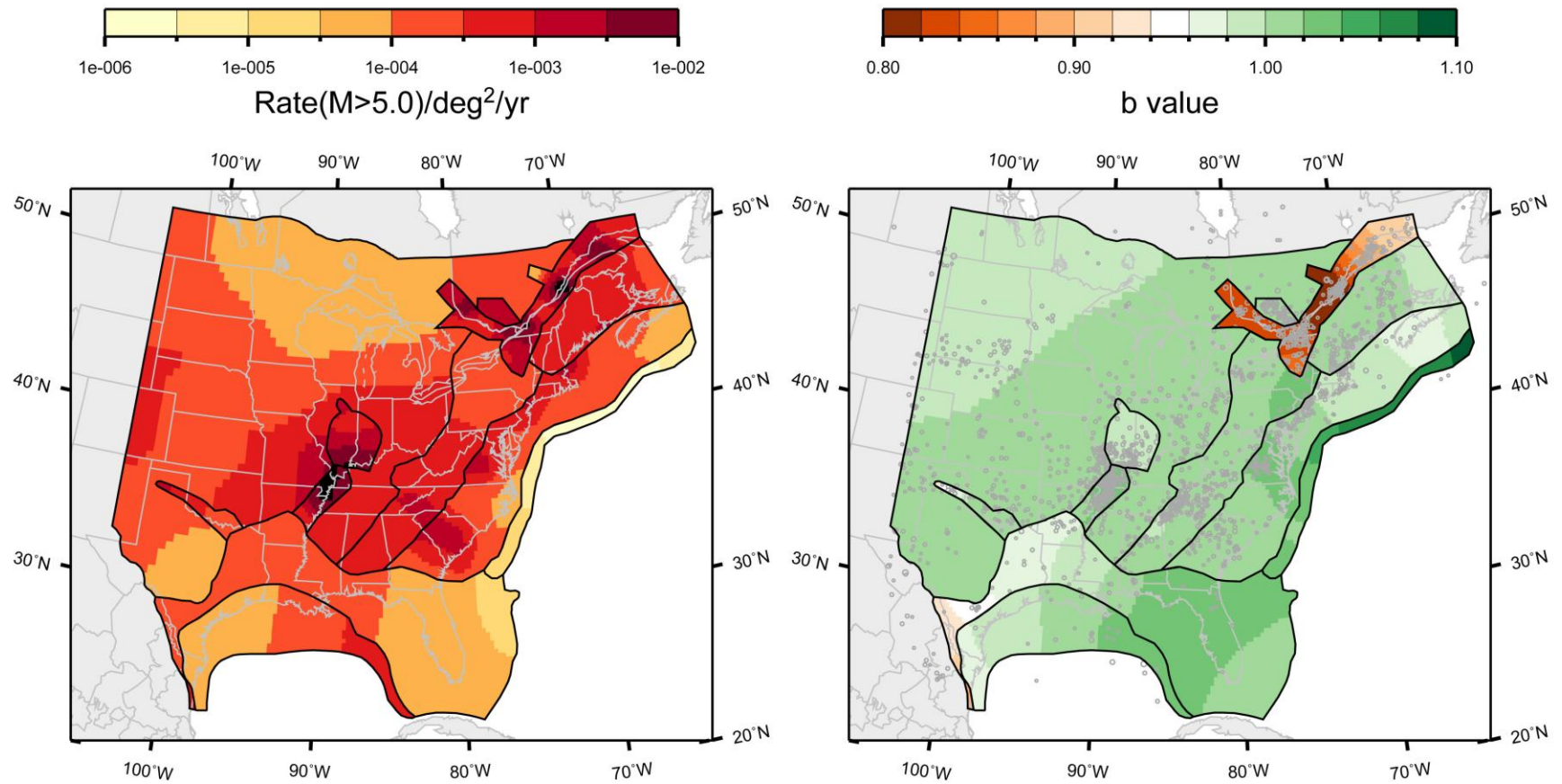


**Figure 7.5.1-9**  
Mean map of rate and *b*-value for the study region under the source-zone configuration with wide interpretation of PEZ, Rough Creek graben associated with Midcontinent; Case E magnitude weights

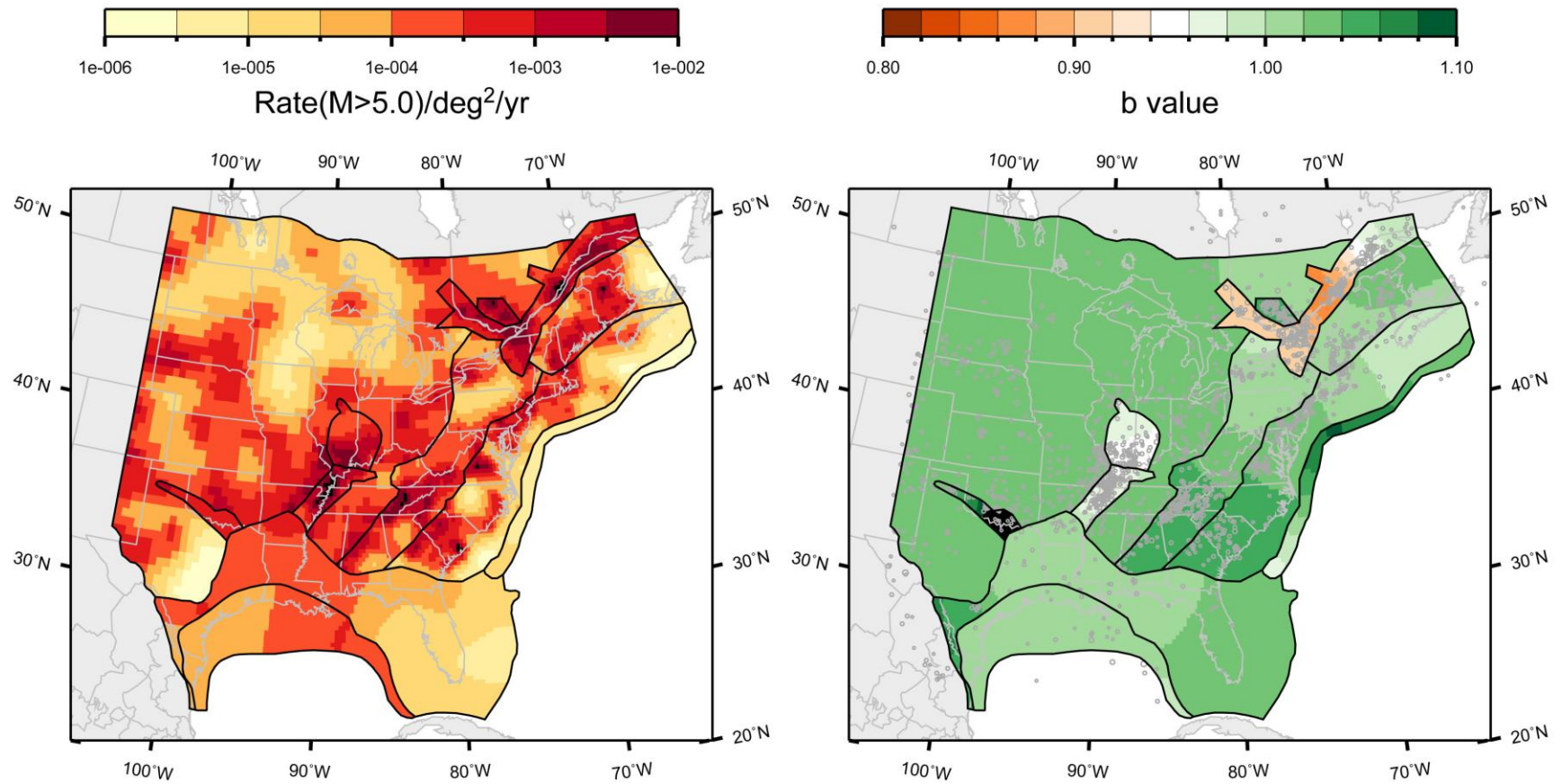


**Figure 7.5.1-10**  
Mean map of rate and *b*-value for the study region under the source-zone configuration with wide interpretation of PEZ, Rough Creek graben associated with Reelfoot rift; Case A magnitude weights

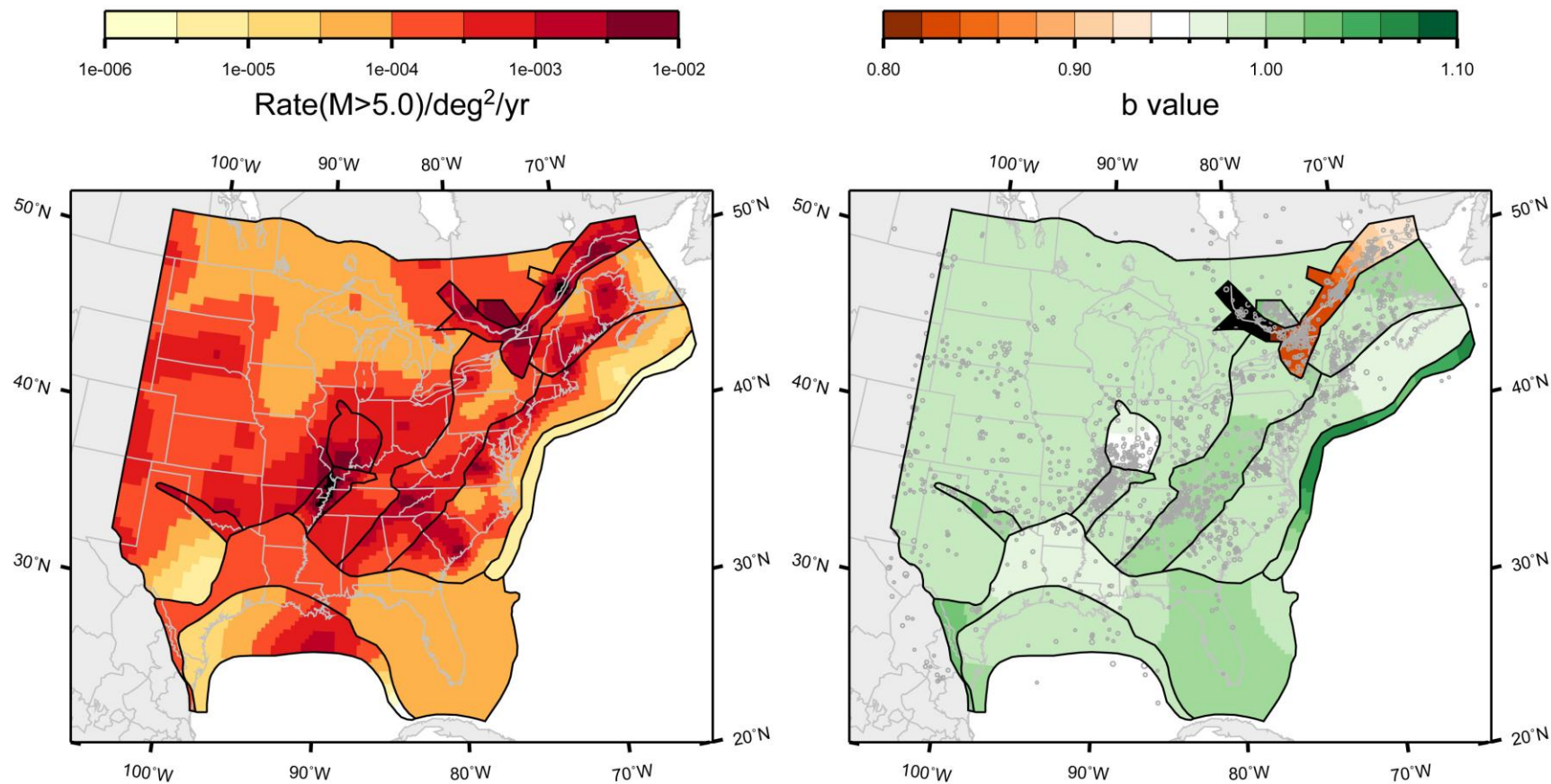


**Figure 7.5.1-11**  
Mean map of rate and *b*-value for the study region under the source-zone configuration with wide interpretation of PEZ, Rough Creek graben associated with Reelfoot rift; Case B magnitude weights

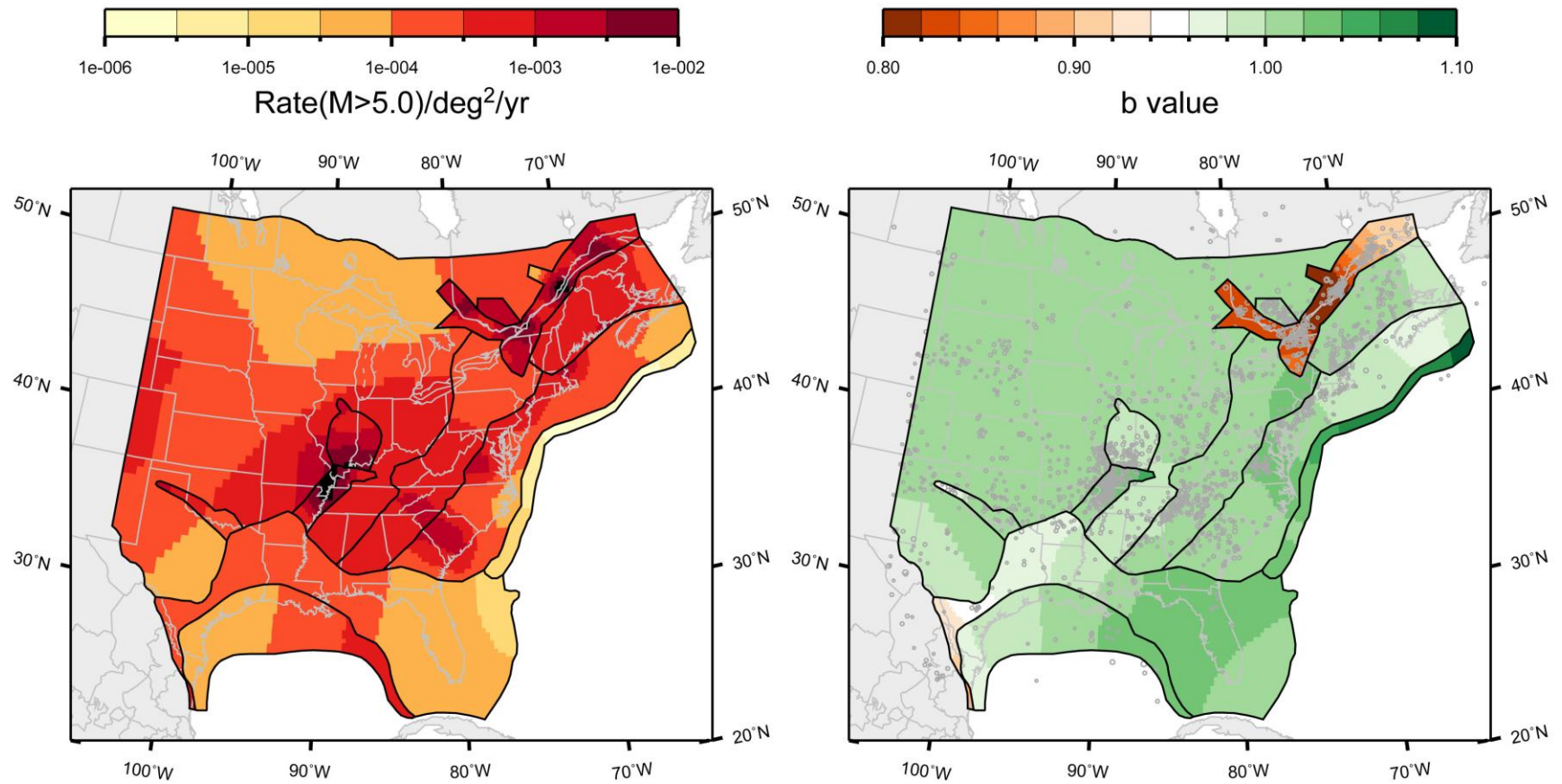


**Figure 7.5.1-12**  
Mean map of rate and  $b$ -value for the study region under the source-zone configuration with wide interpretation of PEZ, Rough Creek graben associated with Reelfoot rift; Case E magnitude weights

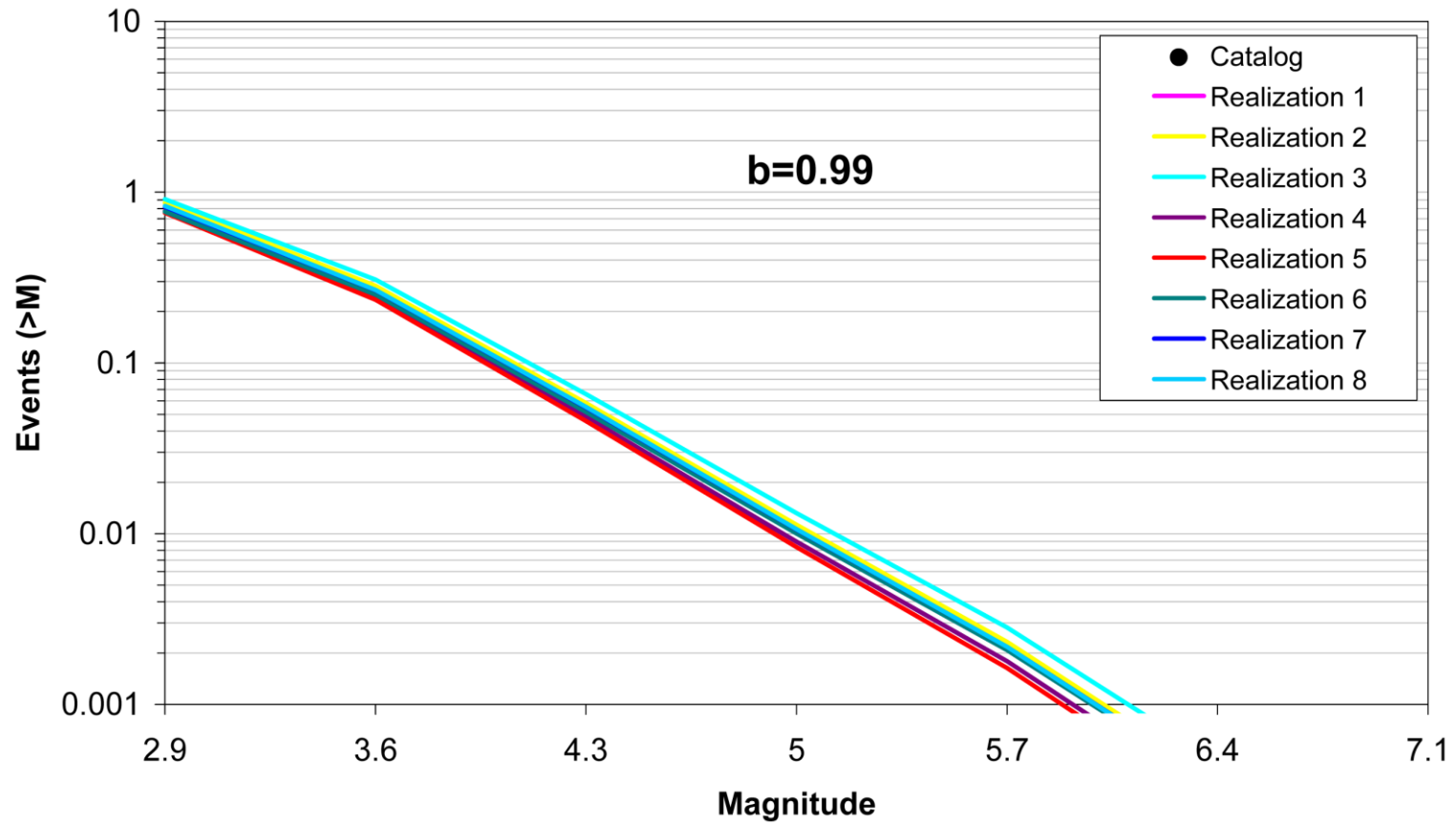


Figure 7.5.2-1  
Comparison of model-predicted earthquake counts for AHEX using Case A magnitude weights. No earthquake counts are shown because this source zone contains no seismicity.

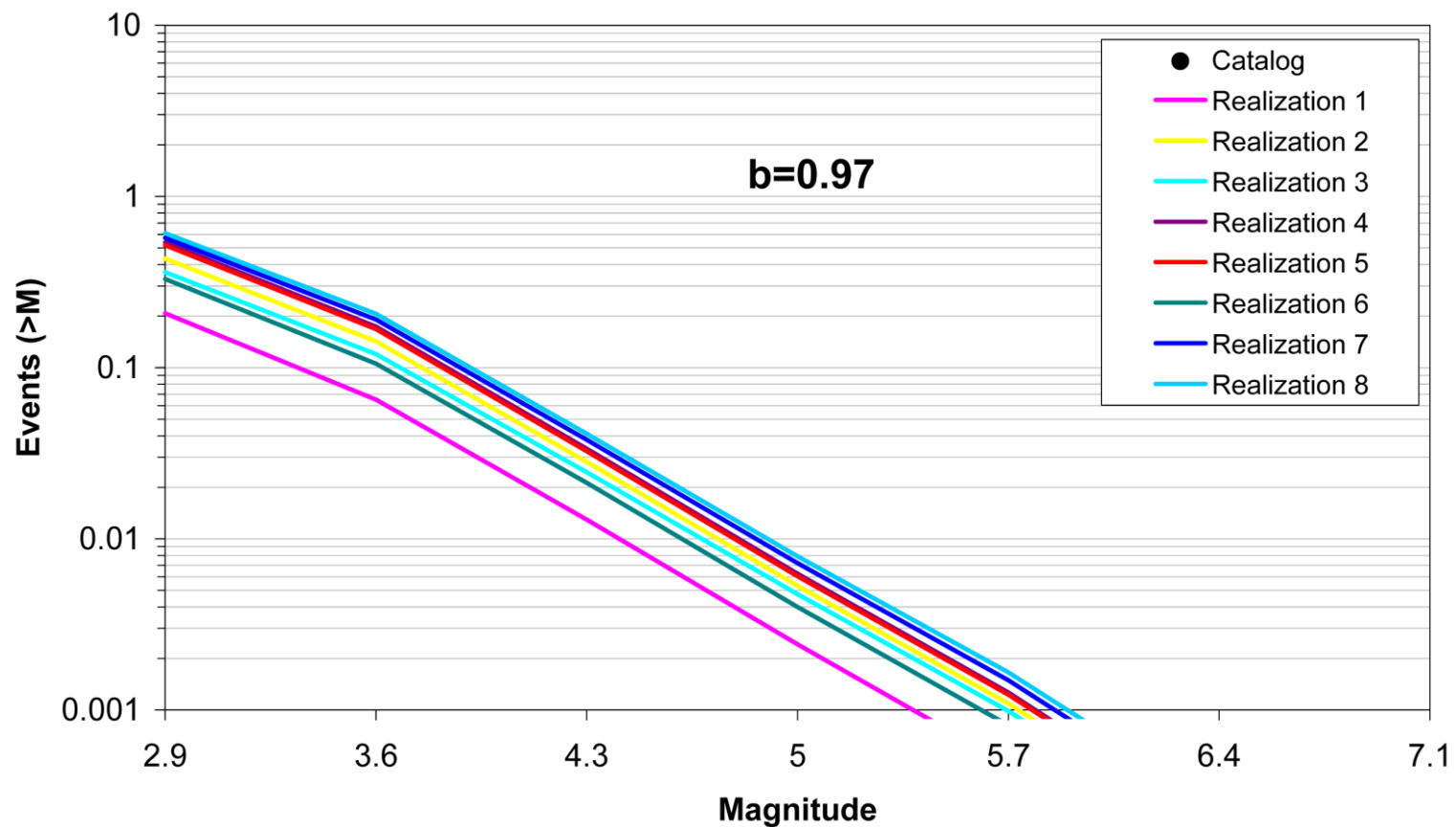


Figure 7.5.2-2  
Comparison of model-predicted earthquake counts for AHEX using Case B magnitude weights. No earthquake counts are shown because this source zone contains no seismicity.

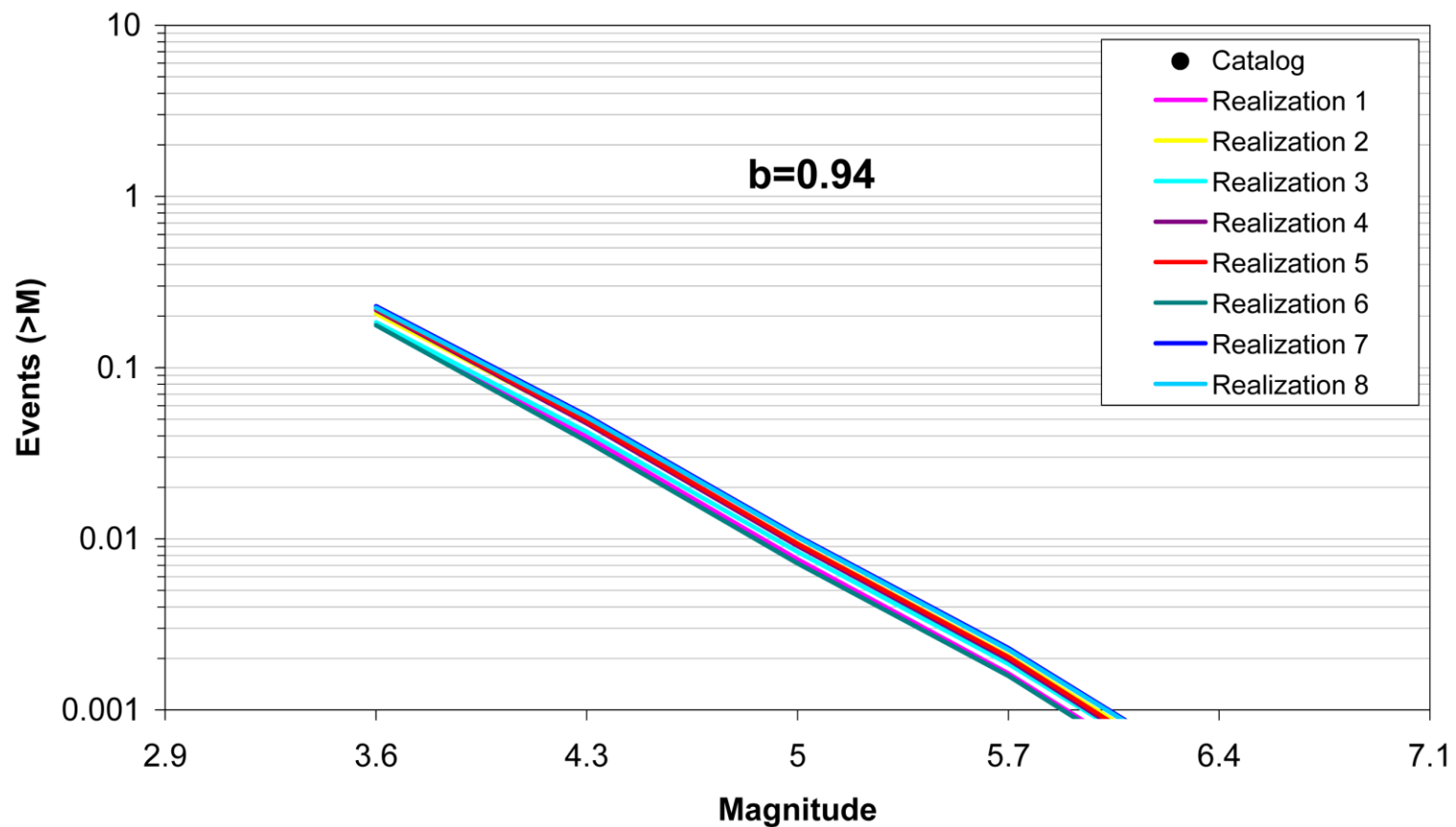


Figure 7.5.2-3  
Comparison of model-predicted earthquake counts for AHEx using Case E magnitude weights. No earthquake counts are shown because this source zone contains no seismicity.

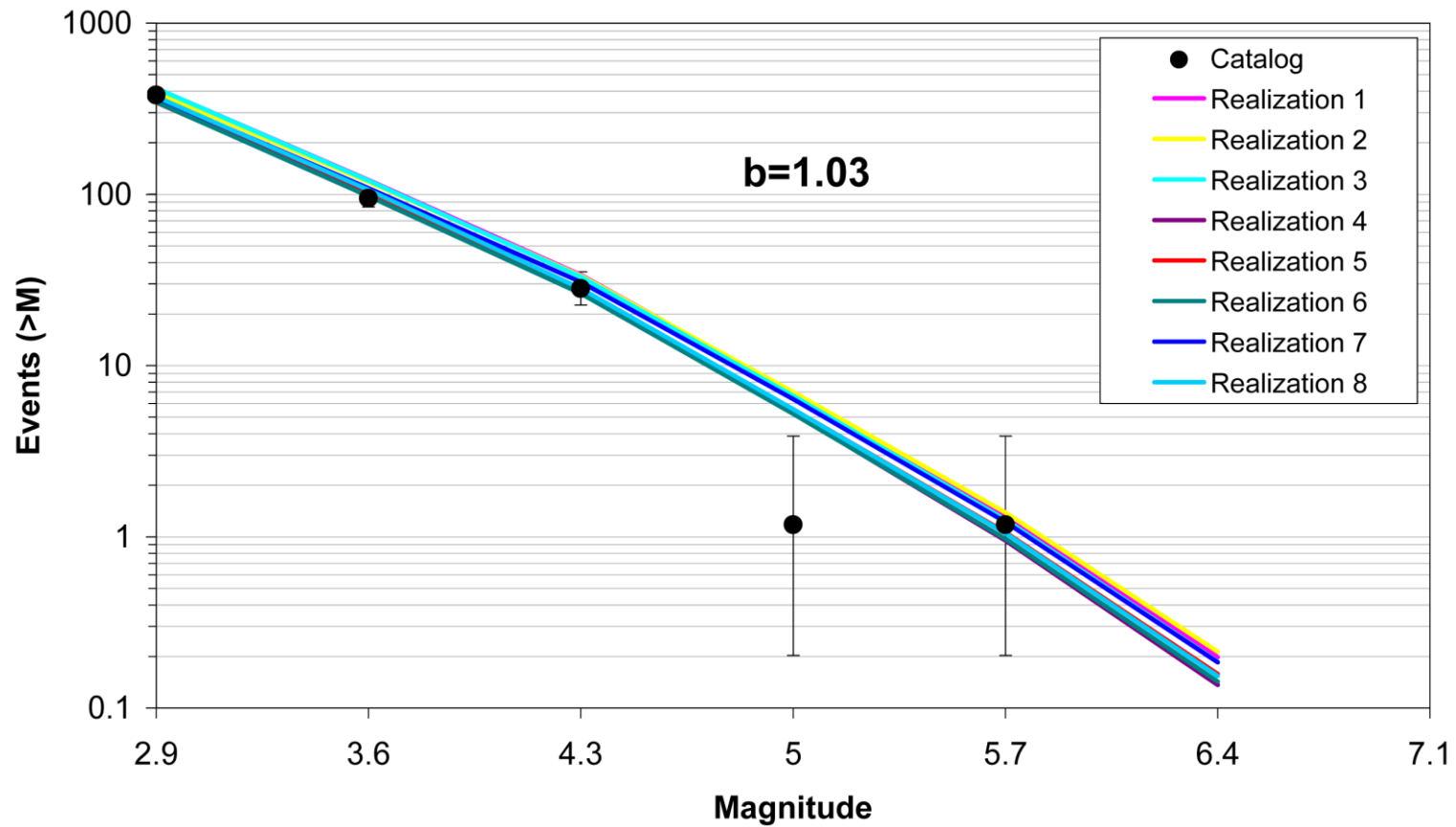


Figure 7.5.2-4  
Comparison of model-predicted earthquake counts for ECC\_AM using Case A magnitude weights. The error bars represent the 16%–84% uncertainty associated with the data, computed using the Weichert (1980) procedure.

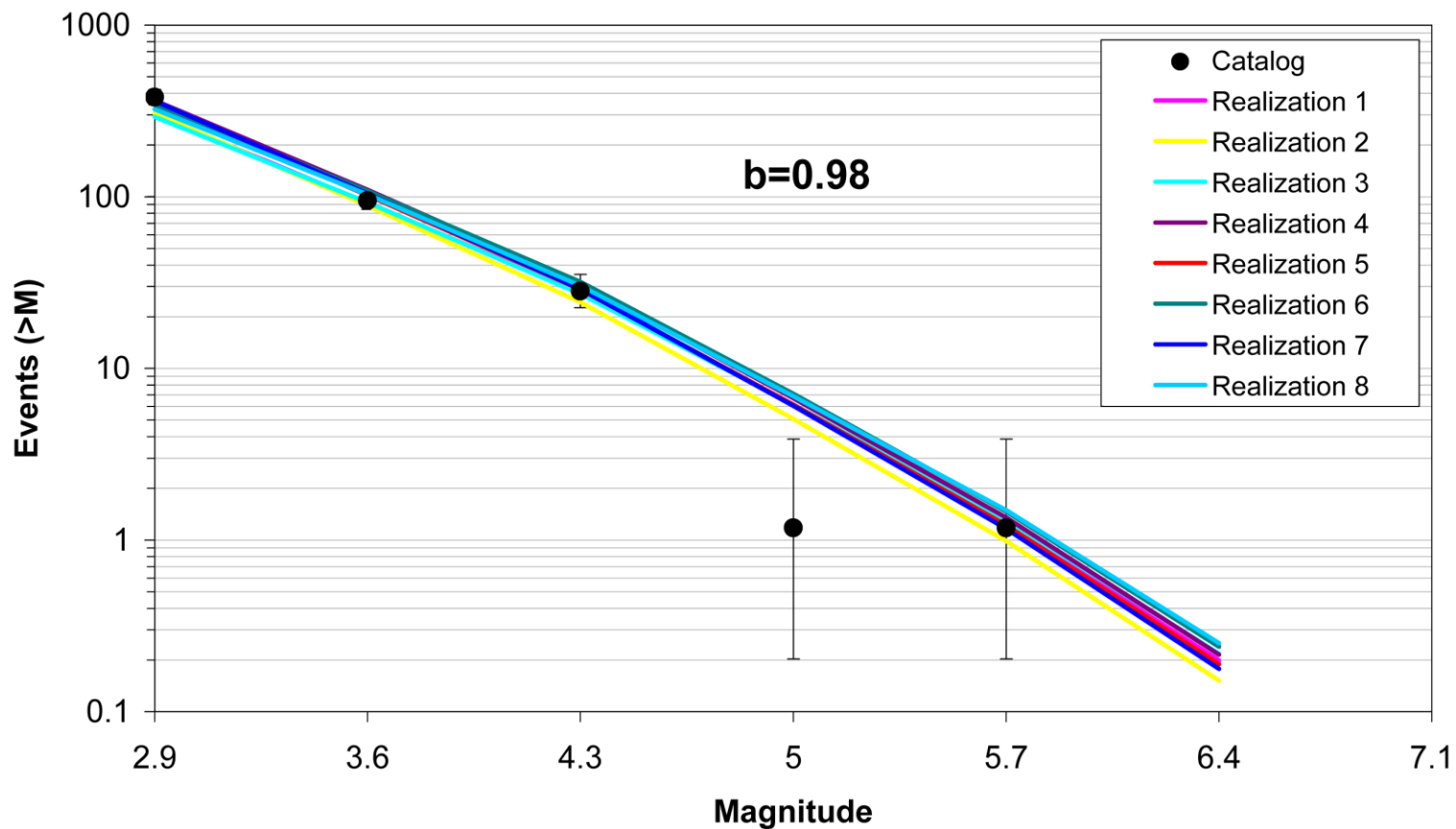


Figure 7.5.2-5  
Comparison of model-predicted earthquake counts for ECC\_AM using Case B magnitude weights. Error bars as in Figure 7.5.2-4.

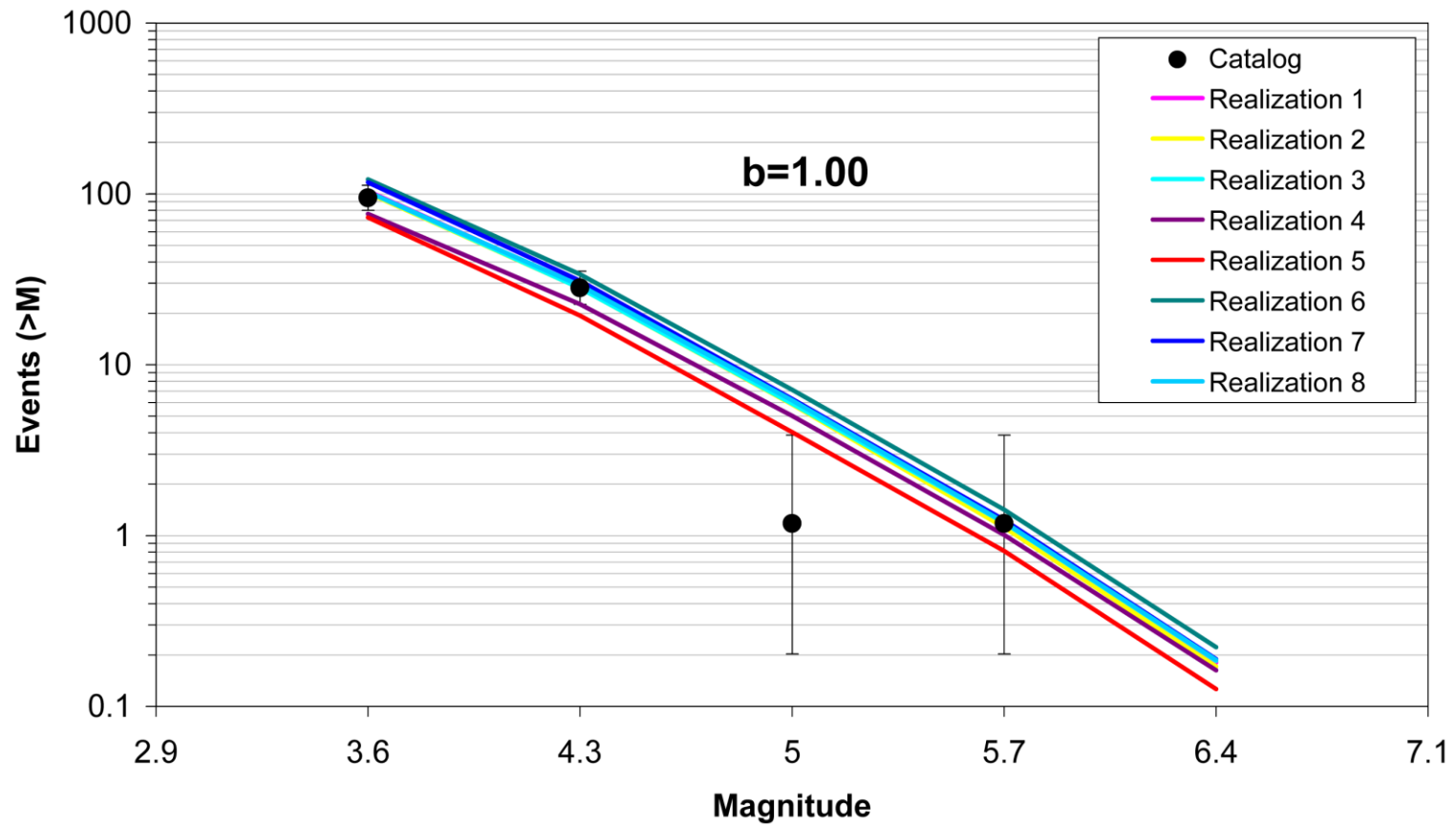


Figure 7.5.2-6  
Comparison of model-predicted earthquake counts for ECC\_AM using Case E magnitude weights. Error bars as in Figure 7.5.2-4.

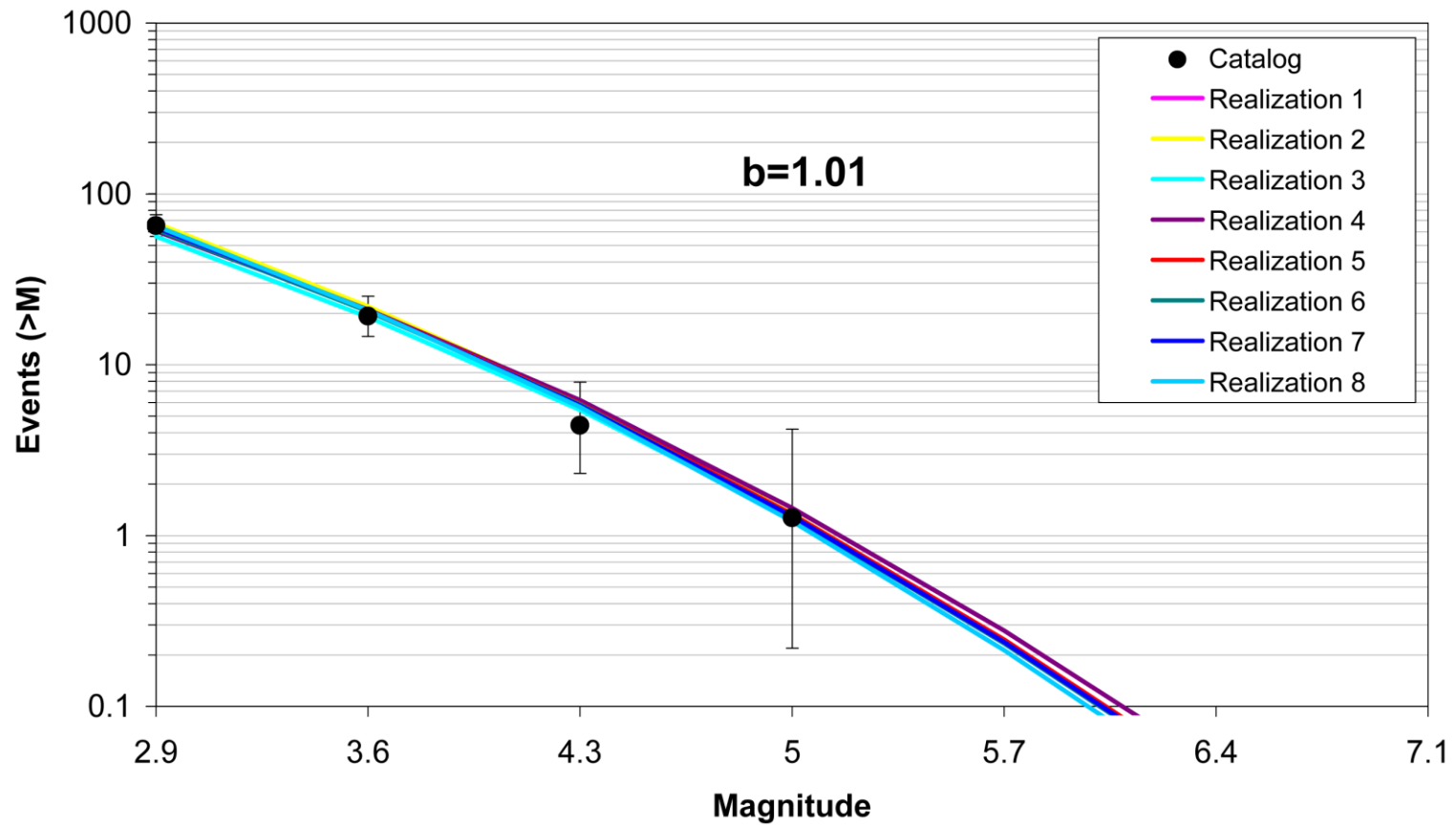


Figure 7.5.2-7  
Comparison of model-predicted earthquake counts for ECC\_GC using Case A magnitude weights. Error bars as in Figure 7.5.2-4.

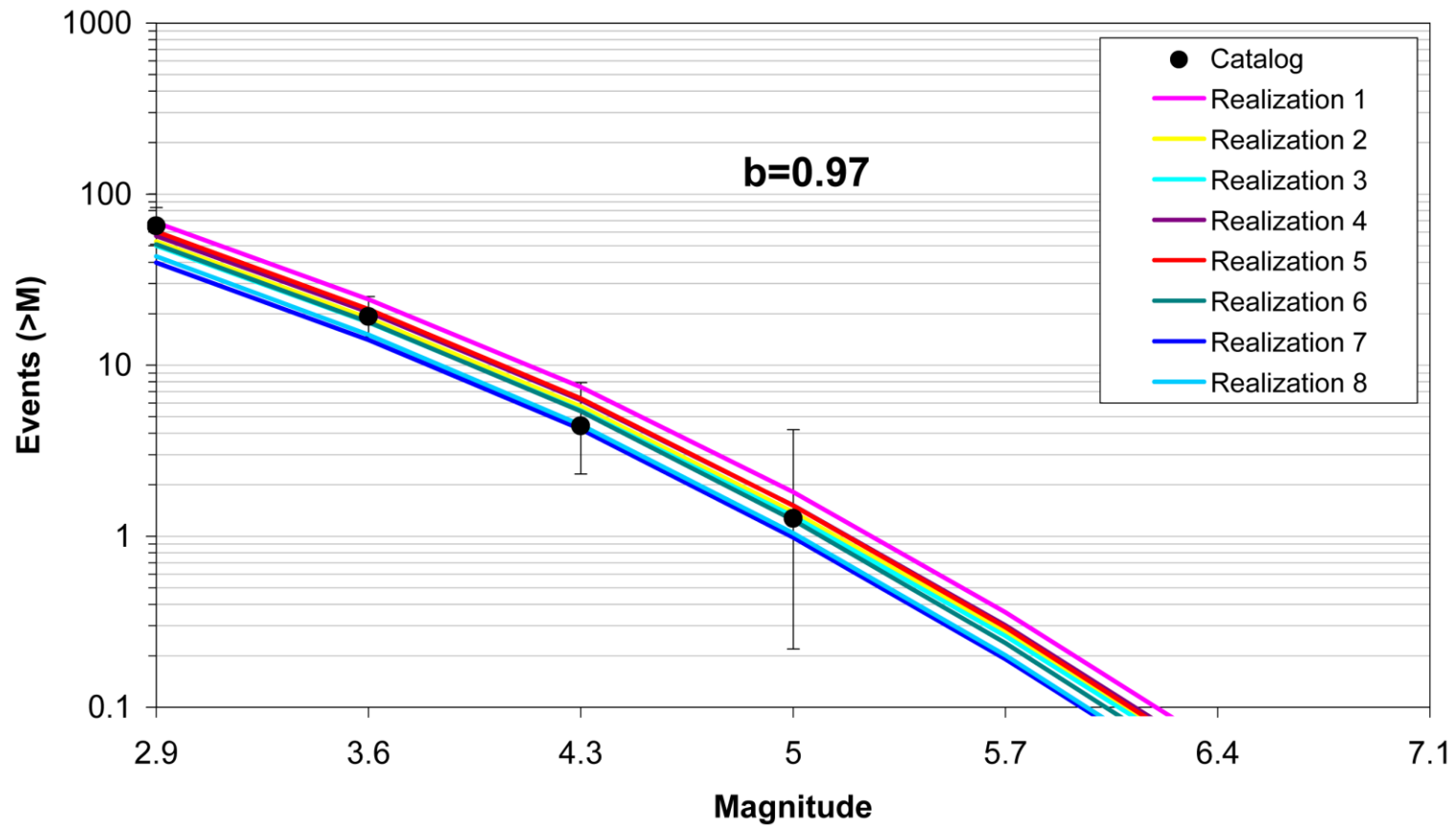


Figure 7.5.2-8  
Comparison of model-predicted earthquake counts for ECC\_GC using Case B magnitude weights. Error bars as in Figure 7.5.2-4.

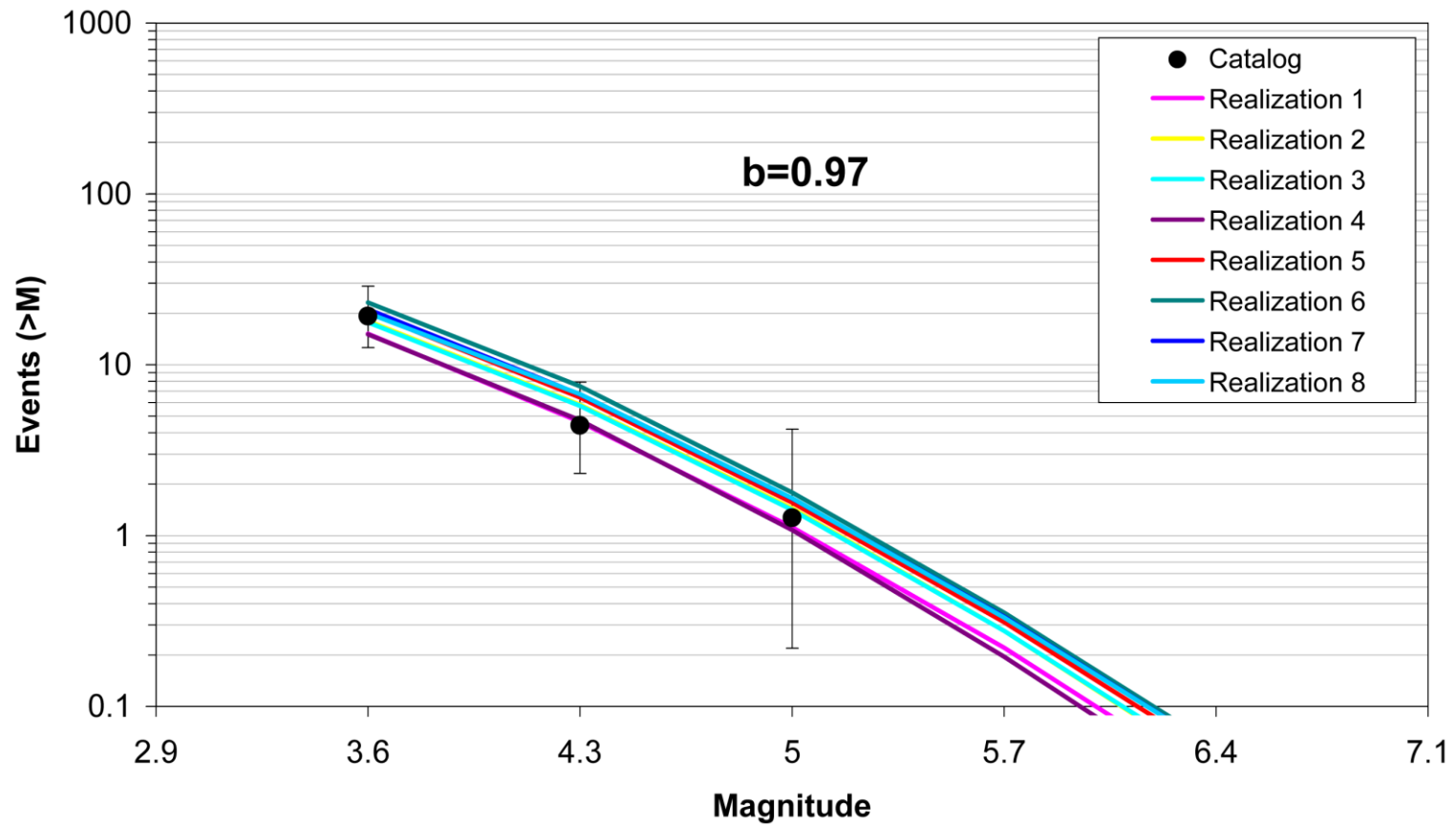


Figure 7.5.2-9  
Comparison of model-predicted earthquake counts for ECC\_GC using Case E magnitude weights. Error bars as in Figure 7.5.2-4.

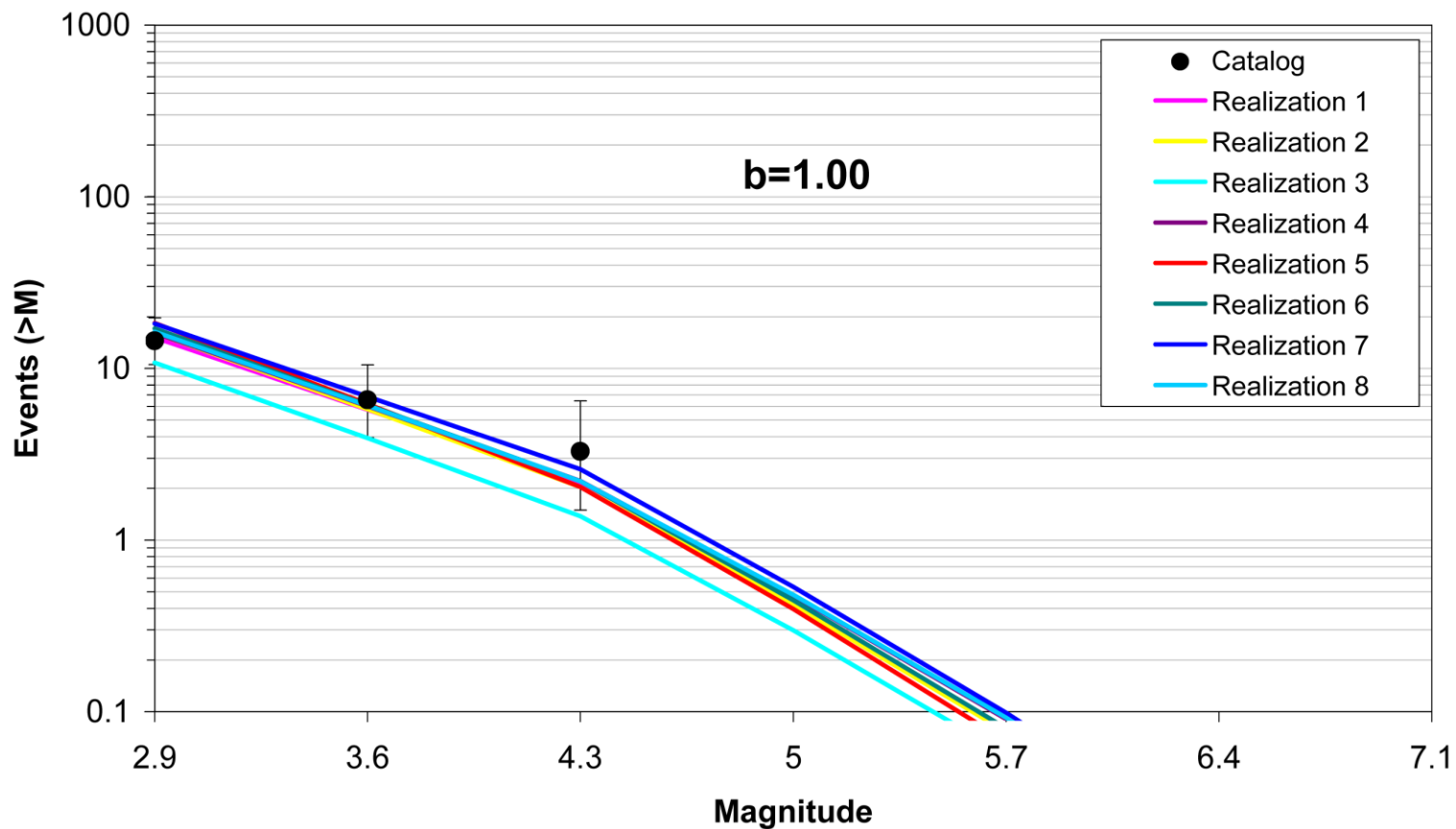


Figure 7.5.2-10  
Comparison of model-predicted earthquake counts for GHEX using Case A magnitude weights. Error bars as in Figure 7.5.2-4.

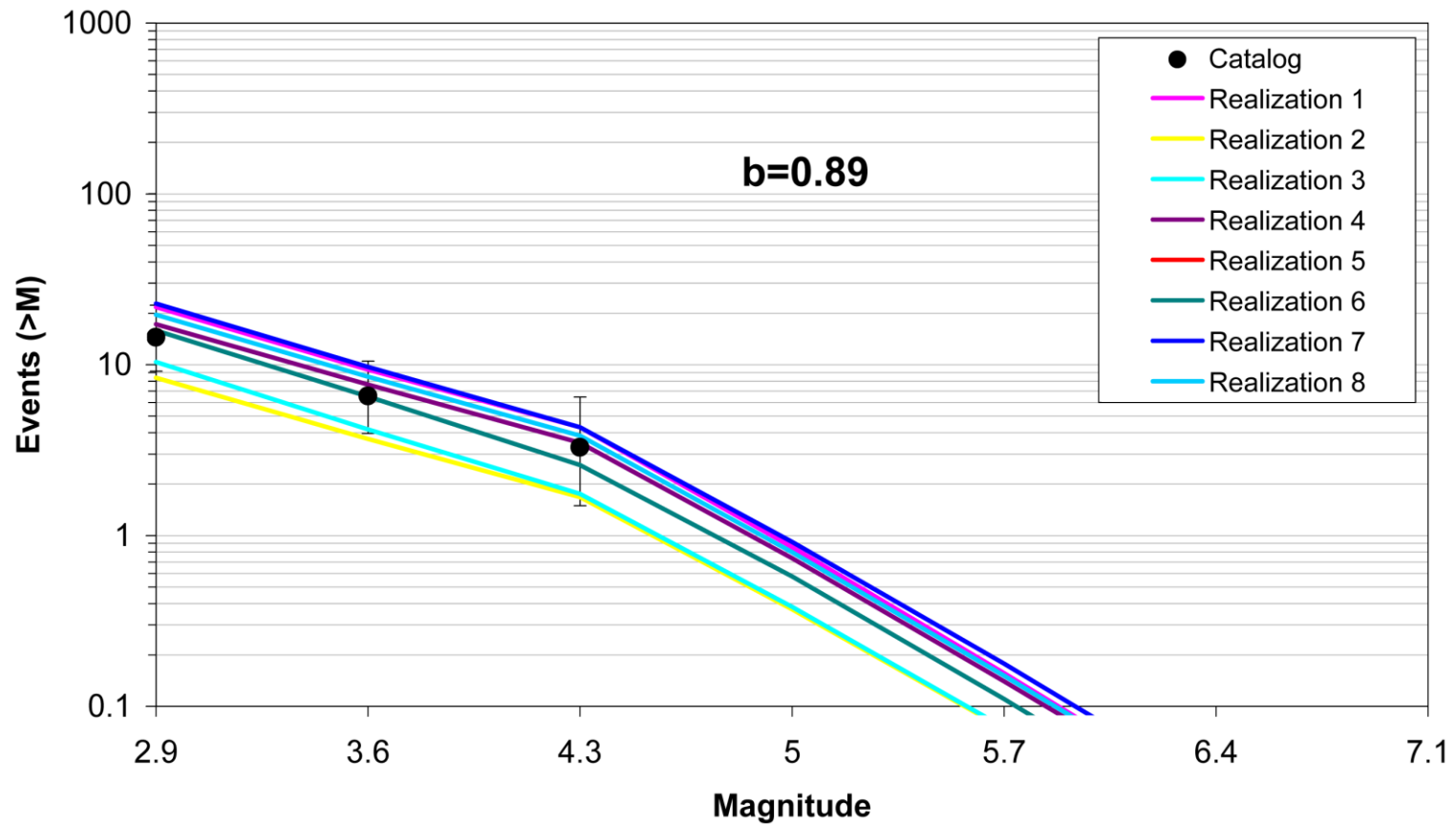


Figure 7.5.2-11  
Comparison of model-predicted earthquake counts for GHEX using Case B magnitude weights. Error bars as in Figure 7.5.2-4.

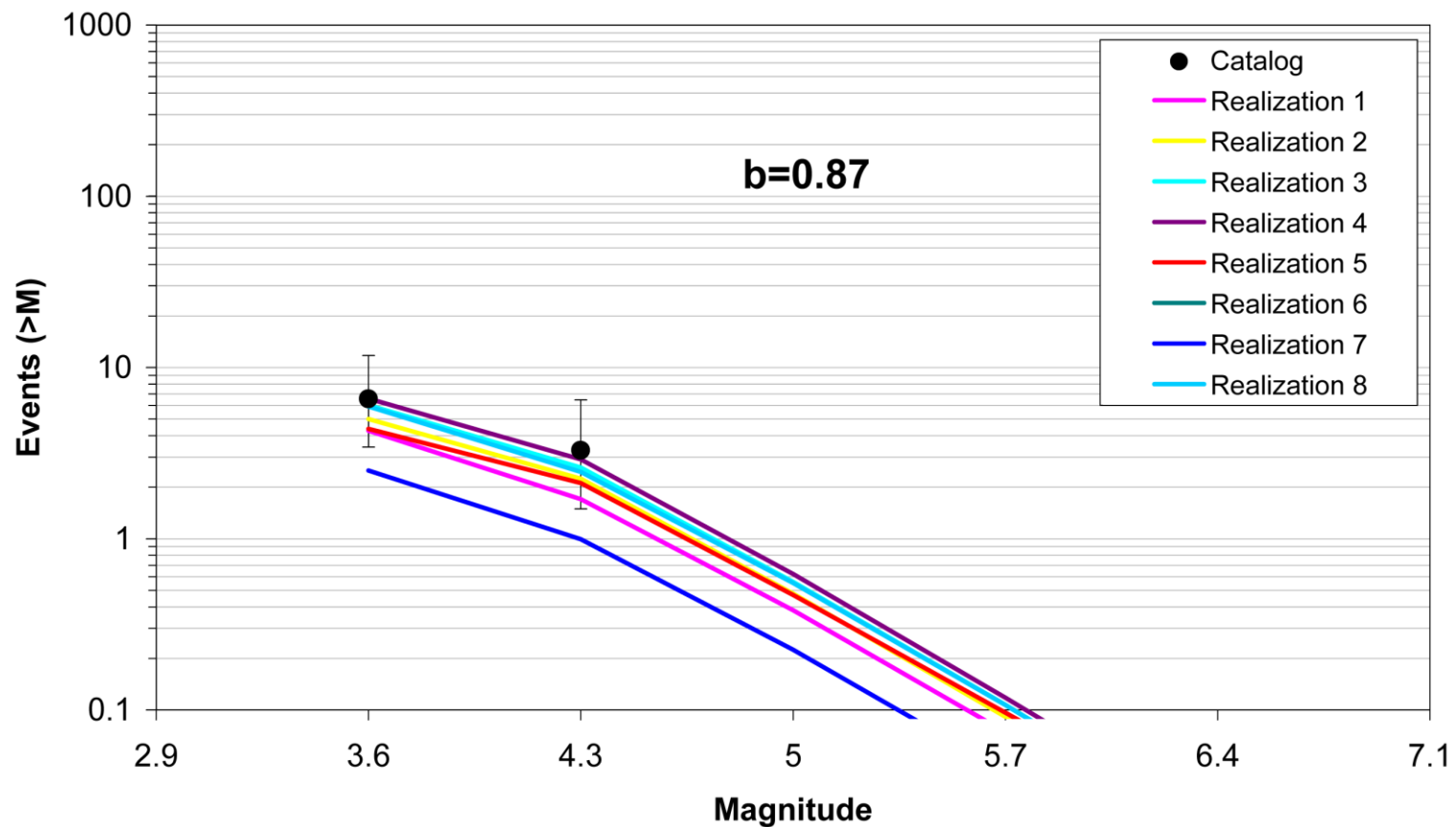


Figure 7.5.2-12  
Comparison of model-predicted earthquake counts for GHEX using Case E magnitude weights. Error bars as in Figure 7.5.2-4.

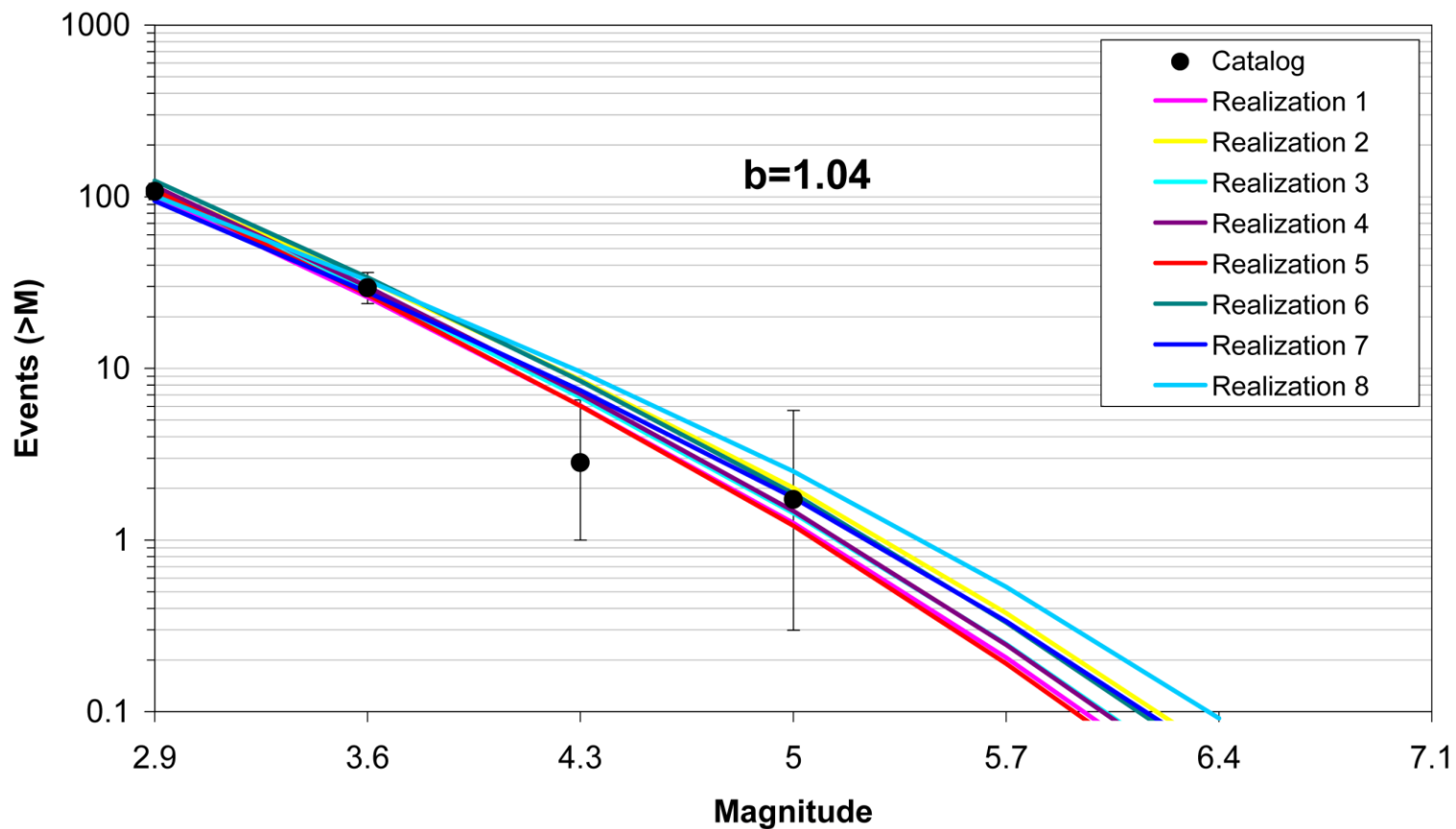


Figure 7.5.2-13  
Comparison of model-predicted earthquake counts for GMH using Case A magnitude weights. Error bars as in Figure 7.5.2-4.

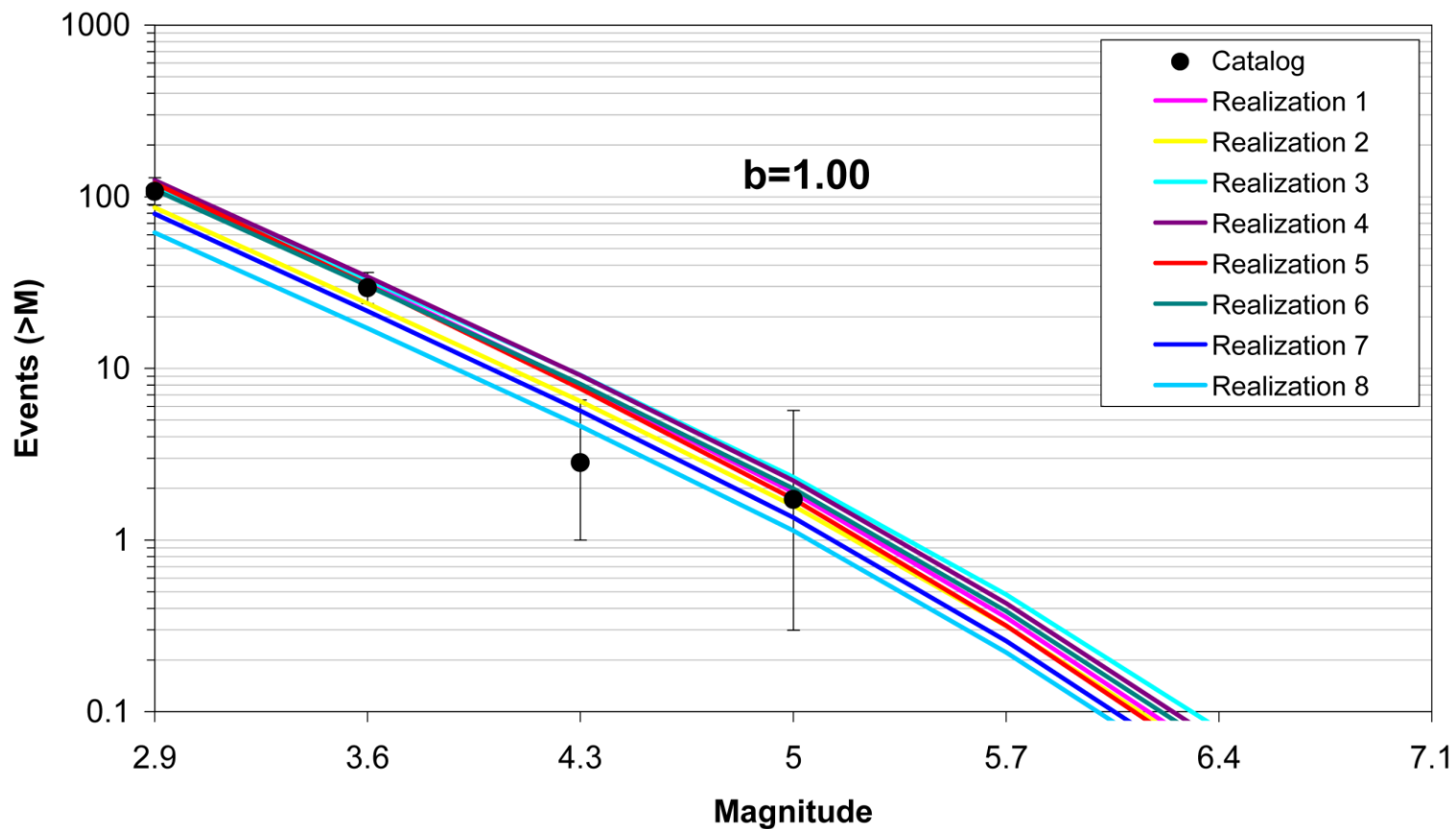


Figure 7.5.2-14  
Comparison of model-predicted earthquake counts for GMH using Case B magnitude weights. Error bars as in Figure 7.5.2-4.

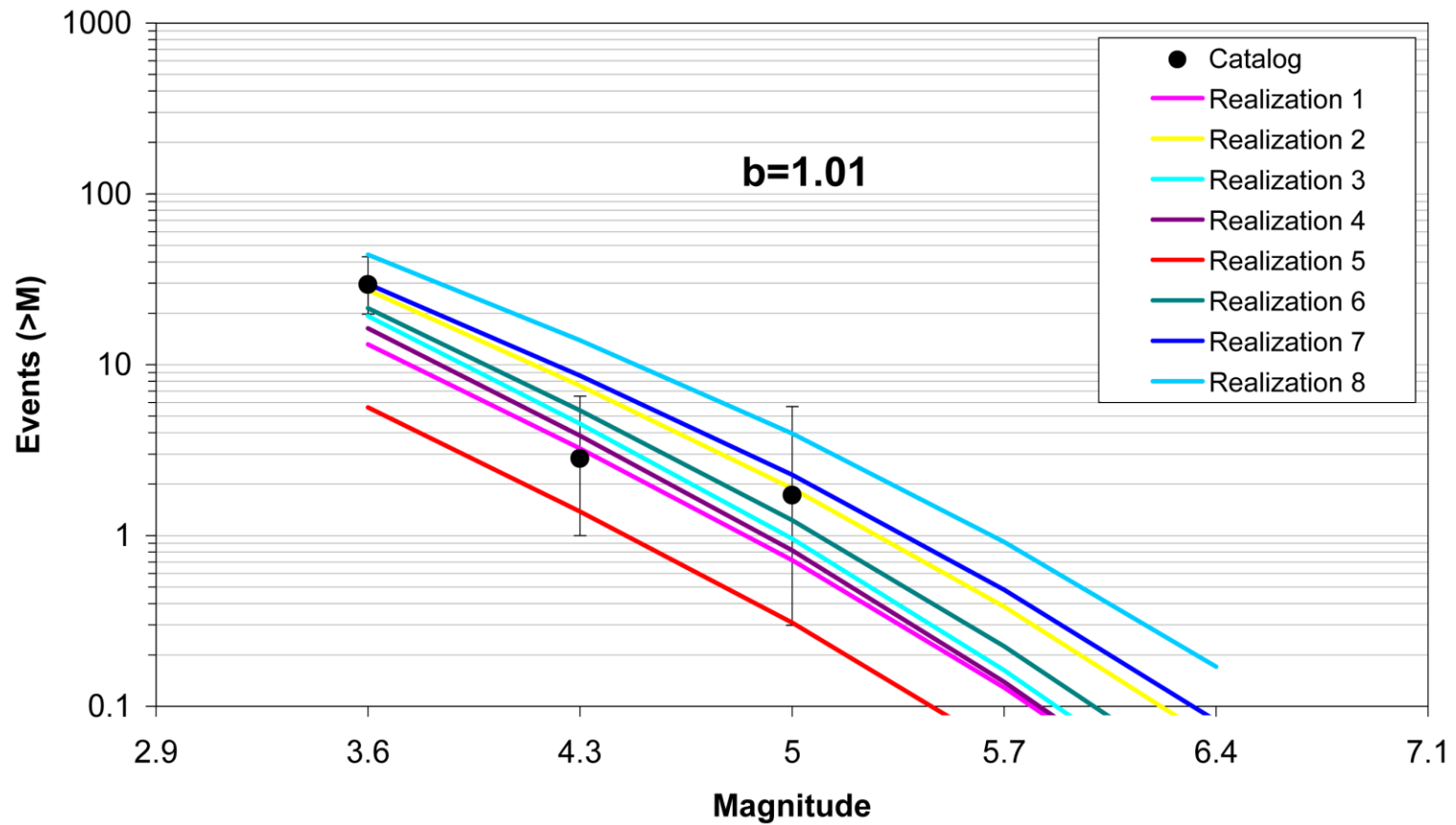


Figure 7.5.2-15  
Comparison of model-predicted earthquake counts for GMH using Case E magnitude weights. Error bars as in Figure 7.5.2-4.

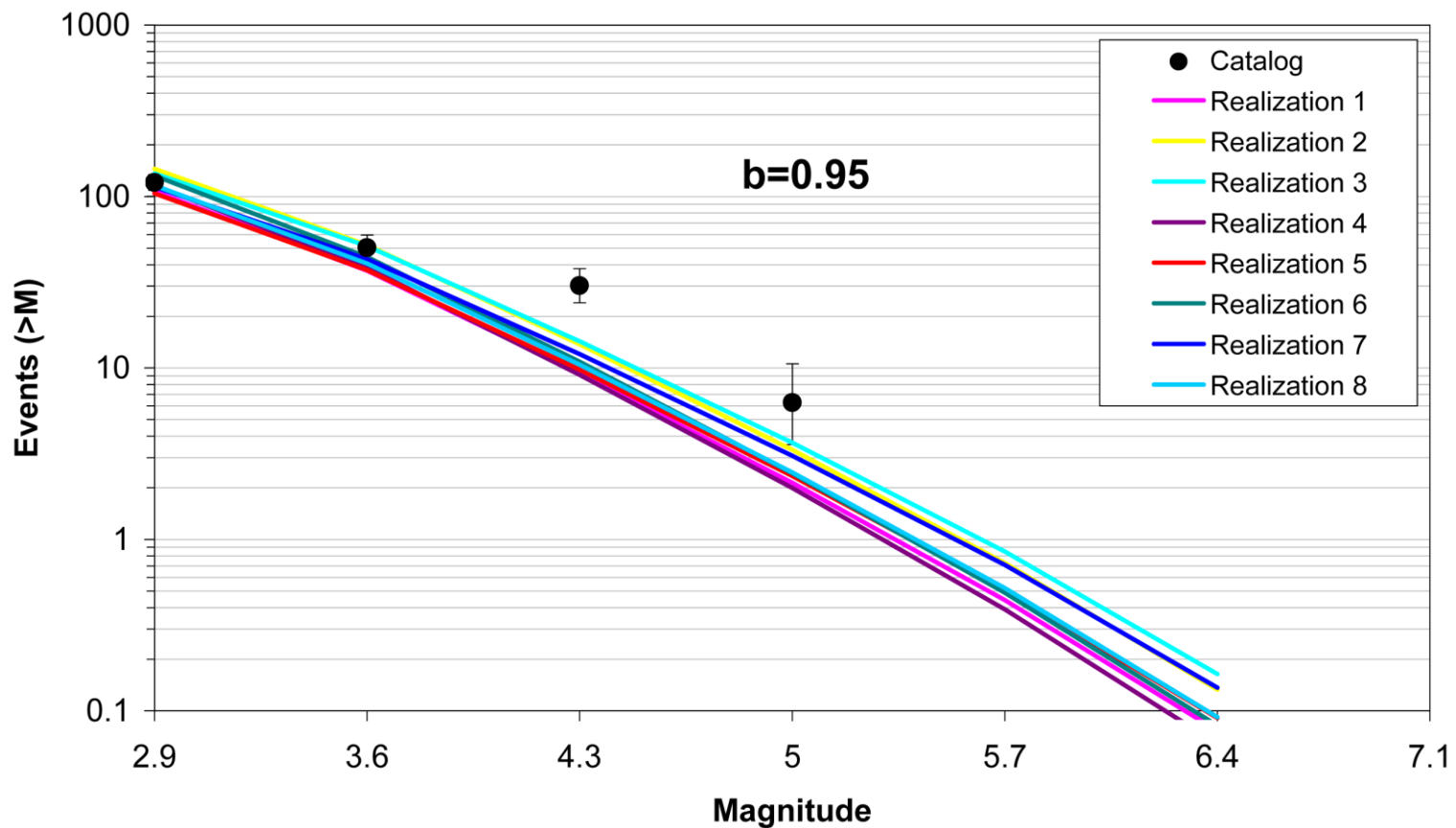


Figure 7.5.2-16  
Comparison of model-predicted earthquake counts for IBEB using Case A magnitude weights. Error bars as in Figure 7.5.2-4.

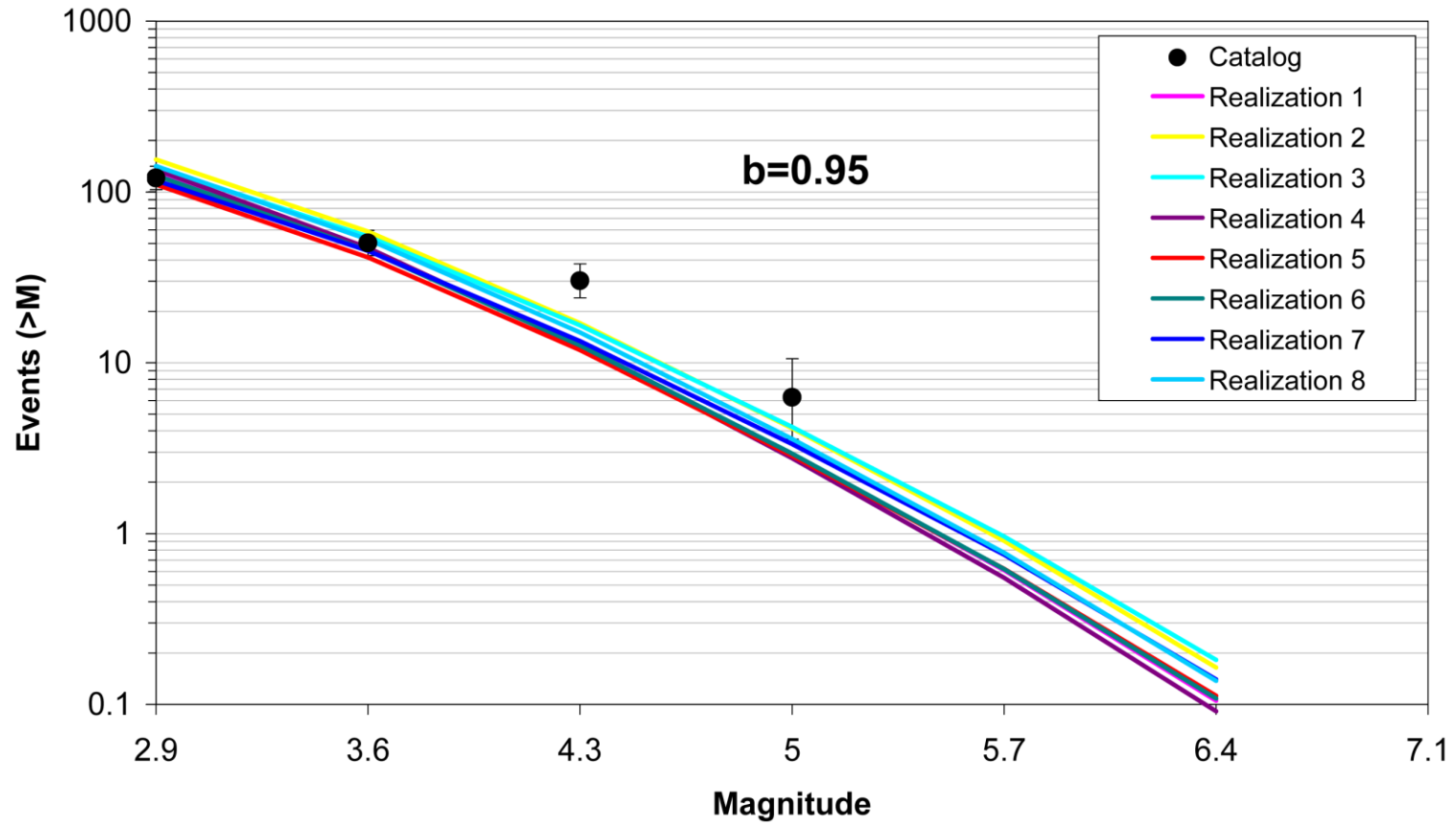


Figure 7.5.2-17  
Comparison of model-predicted earthquake counts for IBEB using Case B magnitude weights. Error bars as in Figure 7.5.2-4.

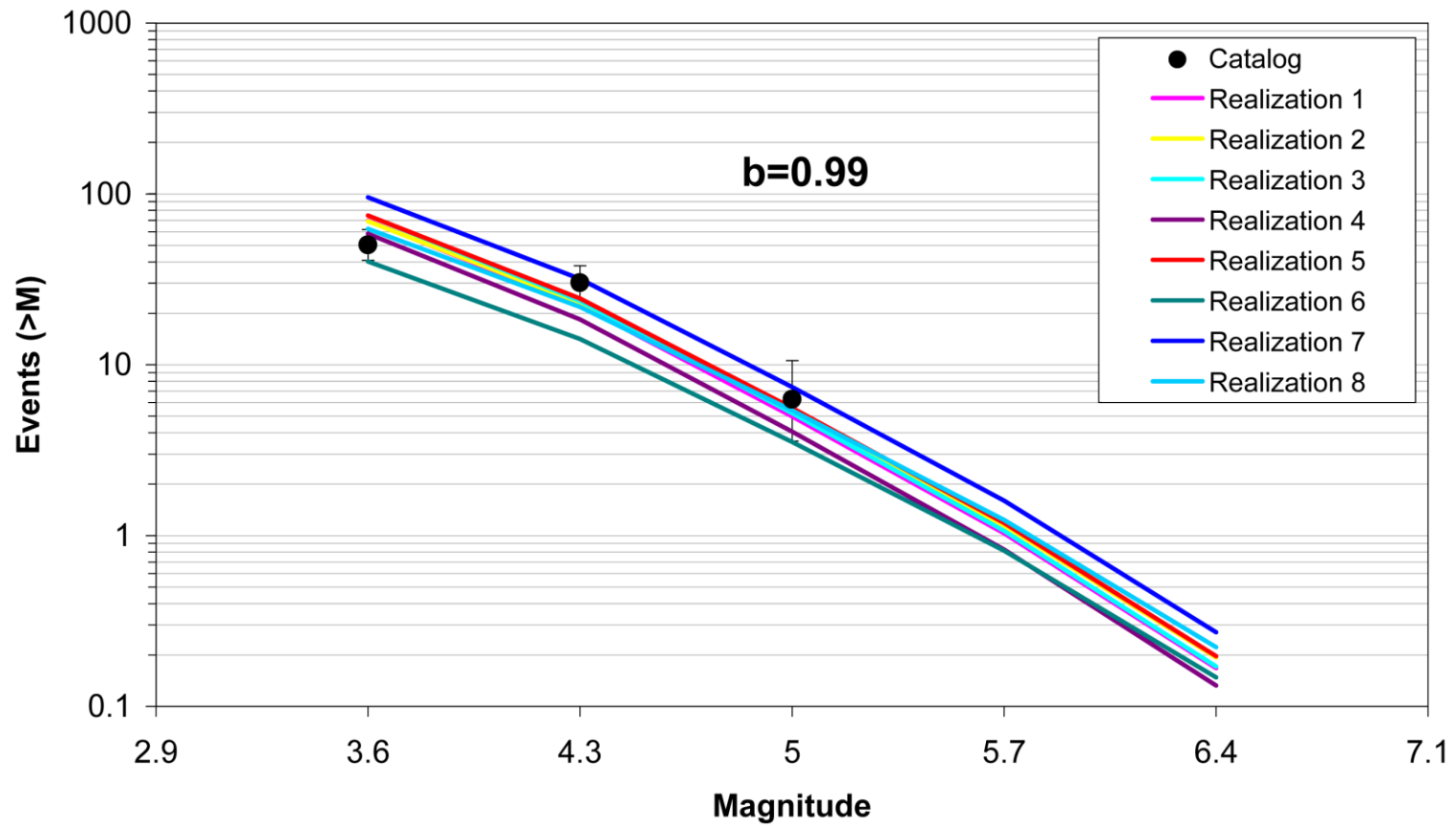


Figure 7.5.2-18  
Comparison of model-predicted earthquake counts for IBEB using Case E magnitude weights. Error bars as in Figure 7.5.2-4.

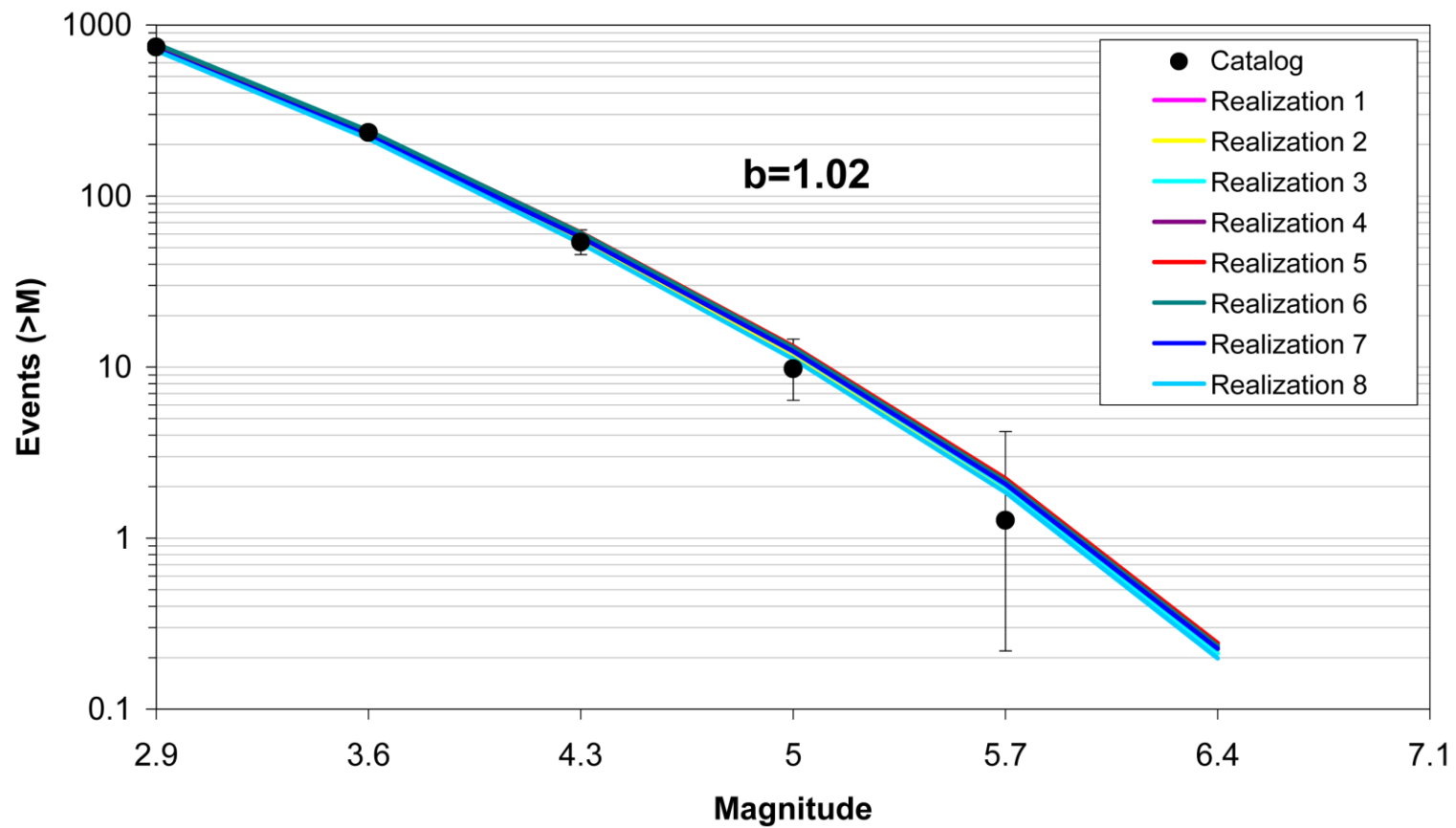


Figure 7.5.2-19  
Comparison of model-predicted earthquake counts for MidC-A using Case A magnitude weights. Error bars as in Figure 7.5.2-4.

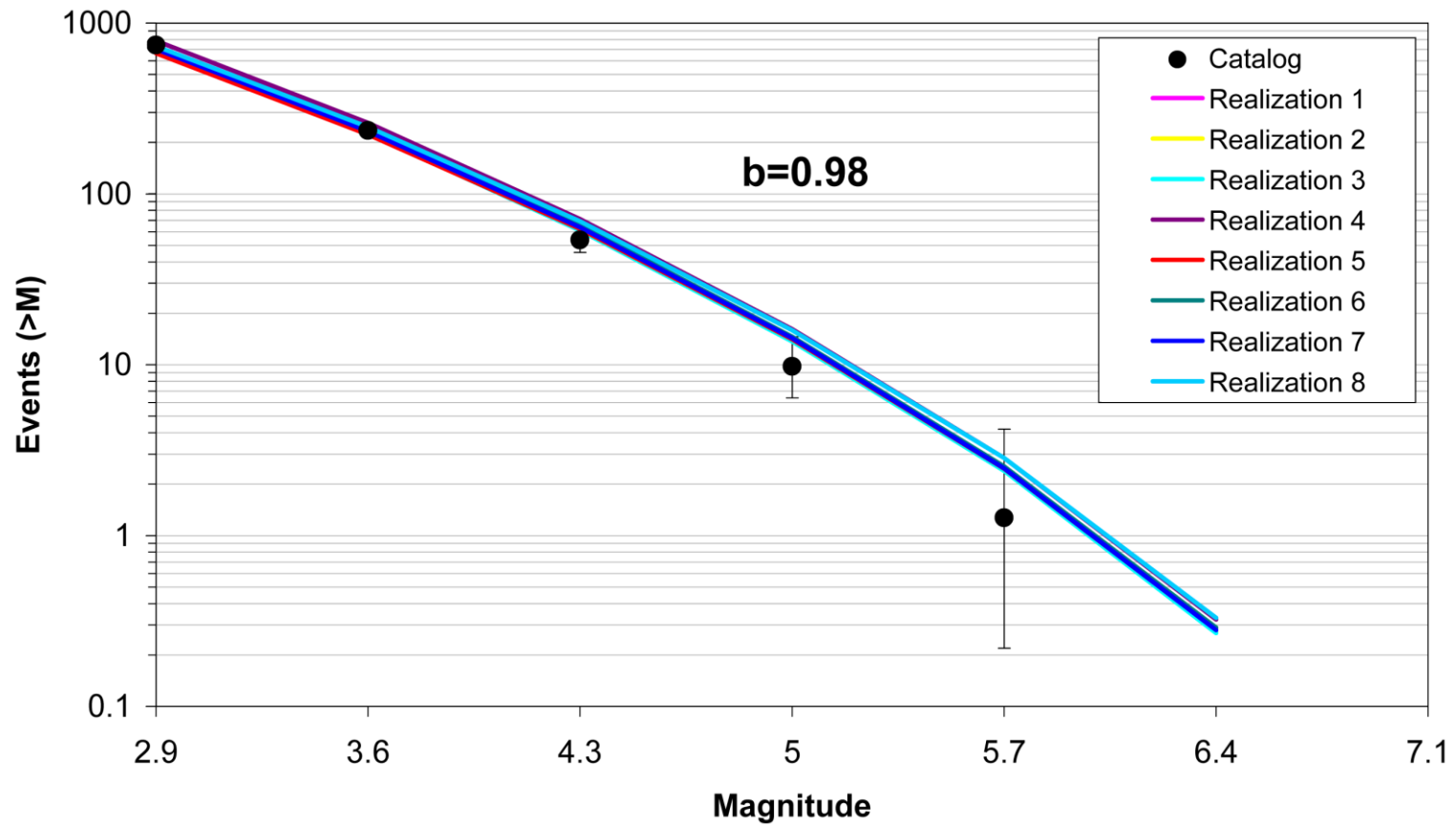


Figure 7.5.2-20  
Comparison of model-predicted earthquake counts for MidC-A using Case B magnitude weights. Error bars as in Figure 7.5.2-4.

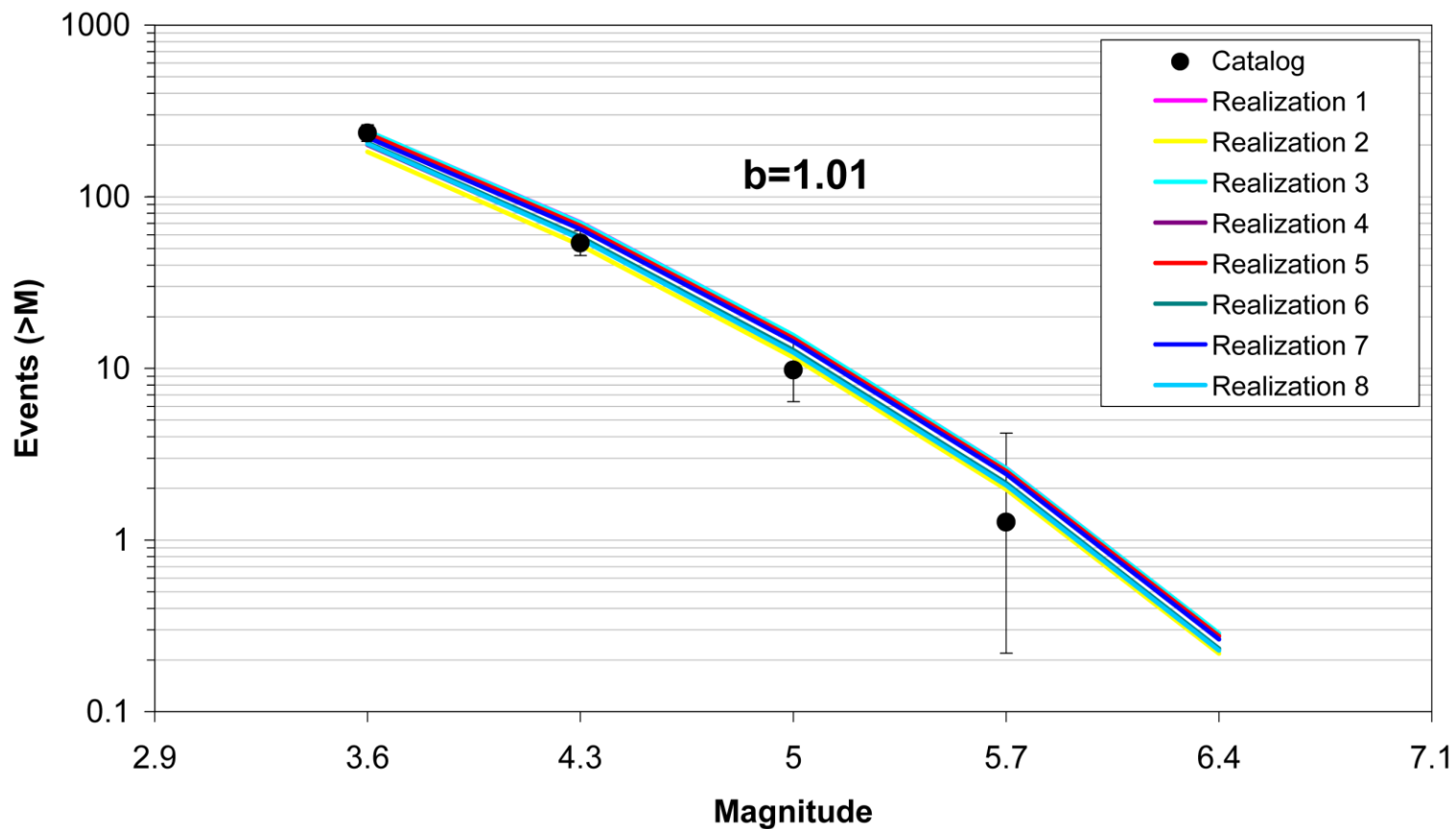


Figure 7.5.2-21  
Comparison of model-predicted earthquake counts for MidC-A using Case E magnitude weights. Error bars as in Figure 7.5.2-4.

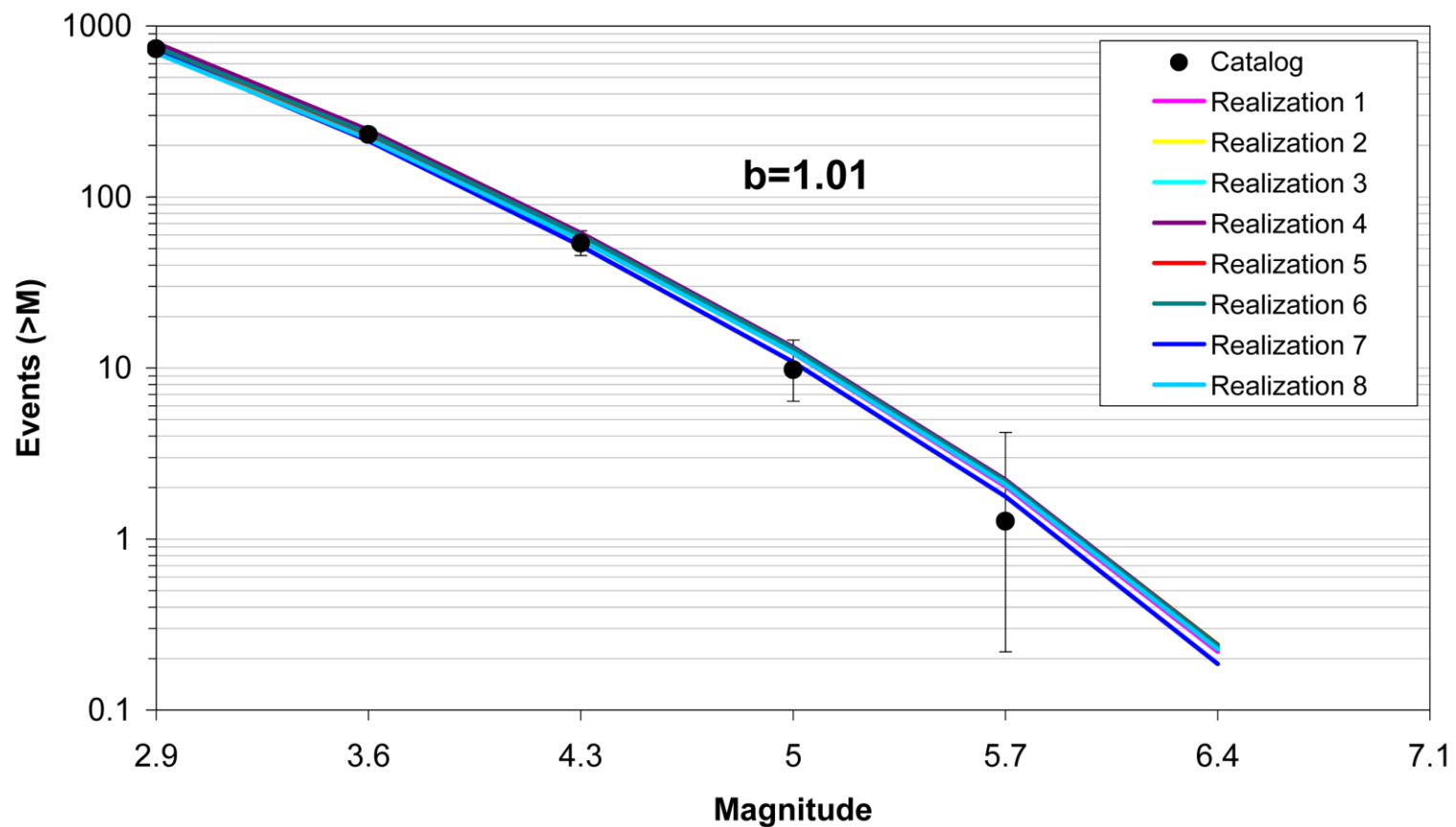


Figure 7.5.2-22  
Comparison of model-predicted earthquake counts for MidC-B using Case A magnitude weights. Error bars as in Figure 7.5.2-4.

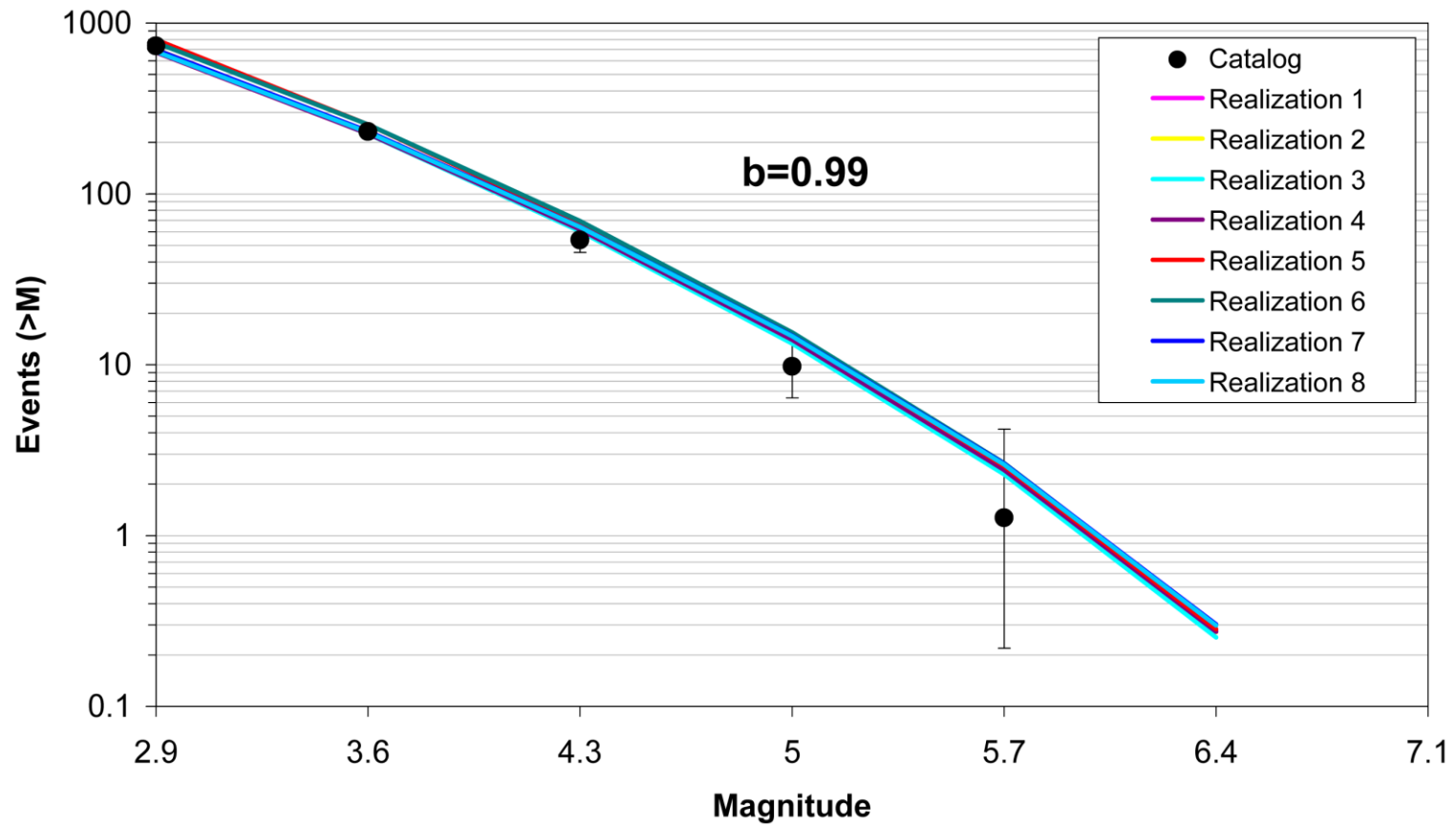


Figure 7.5.2-23  
Comparison of model-predicted earthquake counts for MidC-B using Case B magnitude weights. Error bars as in Figure 7.5.2-4.

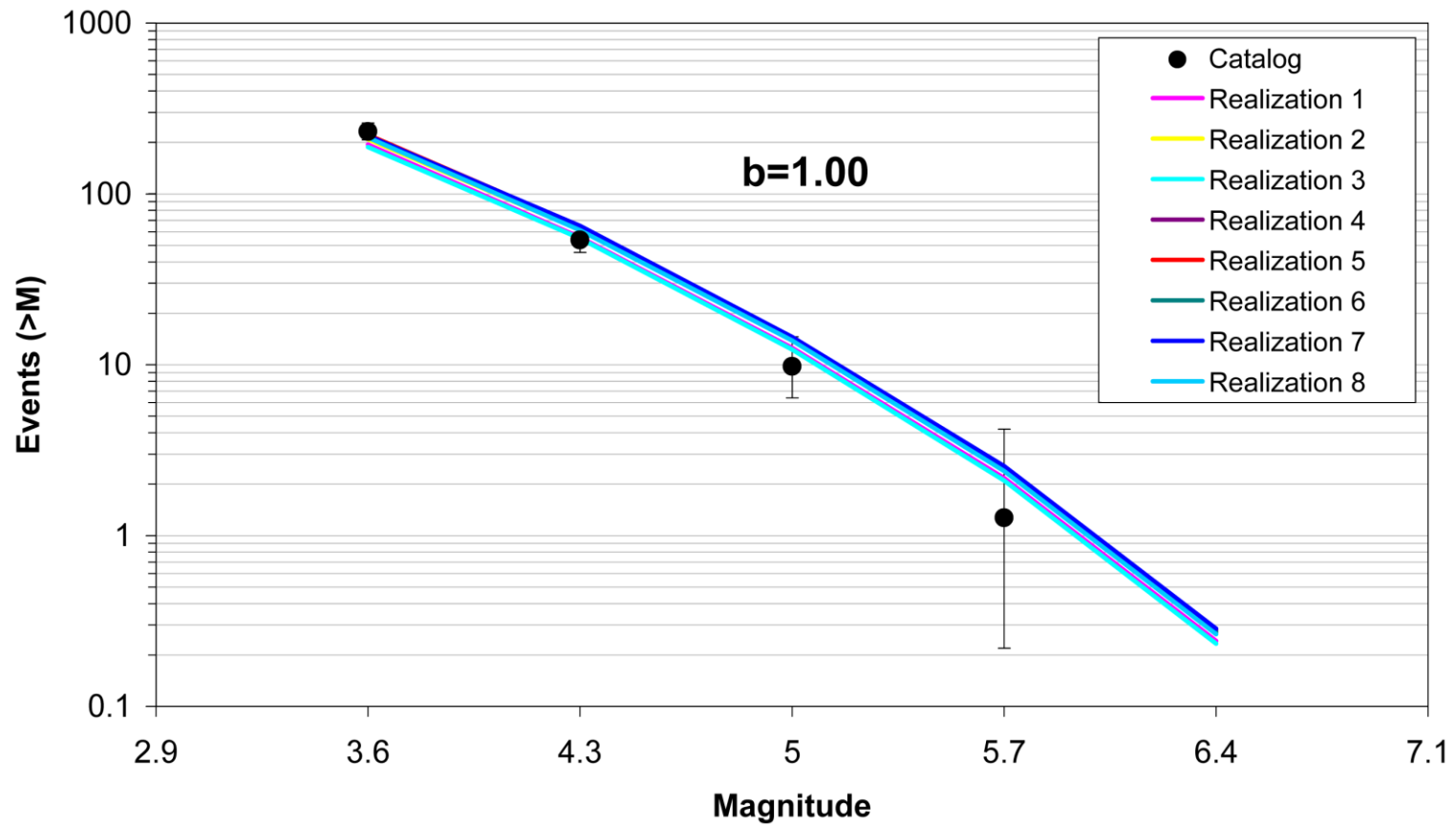


Figure 7.5.2-24  
Comparison of model-predicted earthquake counts for MidC-B using Case E magnitude weights. Error bars as in Figure 7.5.2-4.

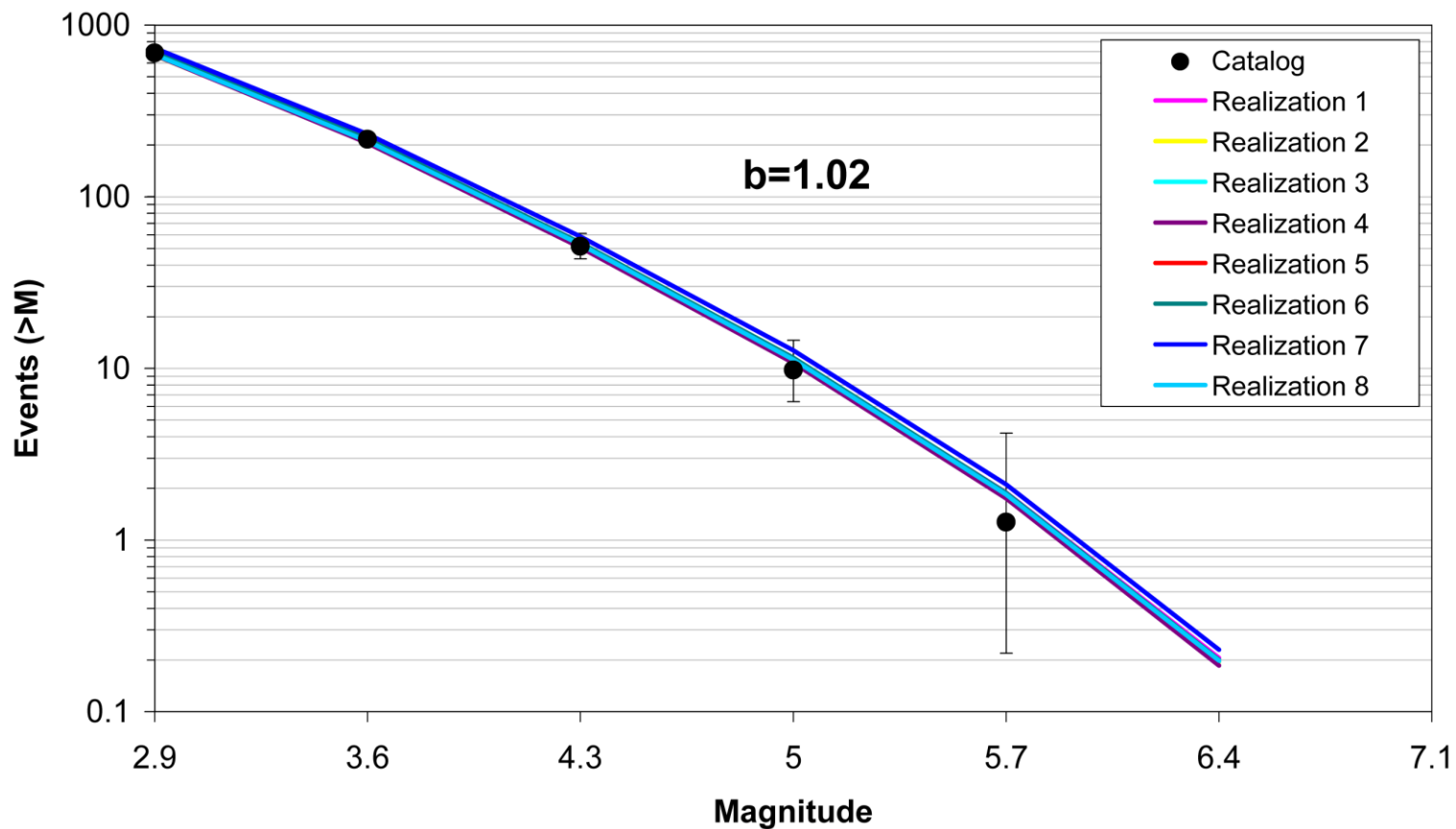


Figure 7.5.2-25  
Comparison of model-predicted earthquake counts for MidC-C using Case A magnitude weights. Error bars as in Figure 7.5.2-4.

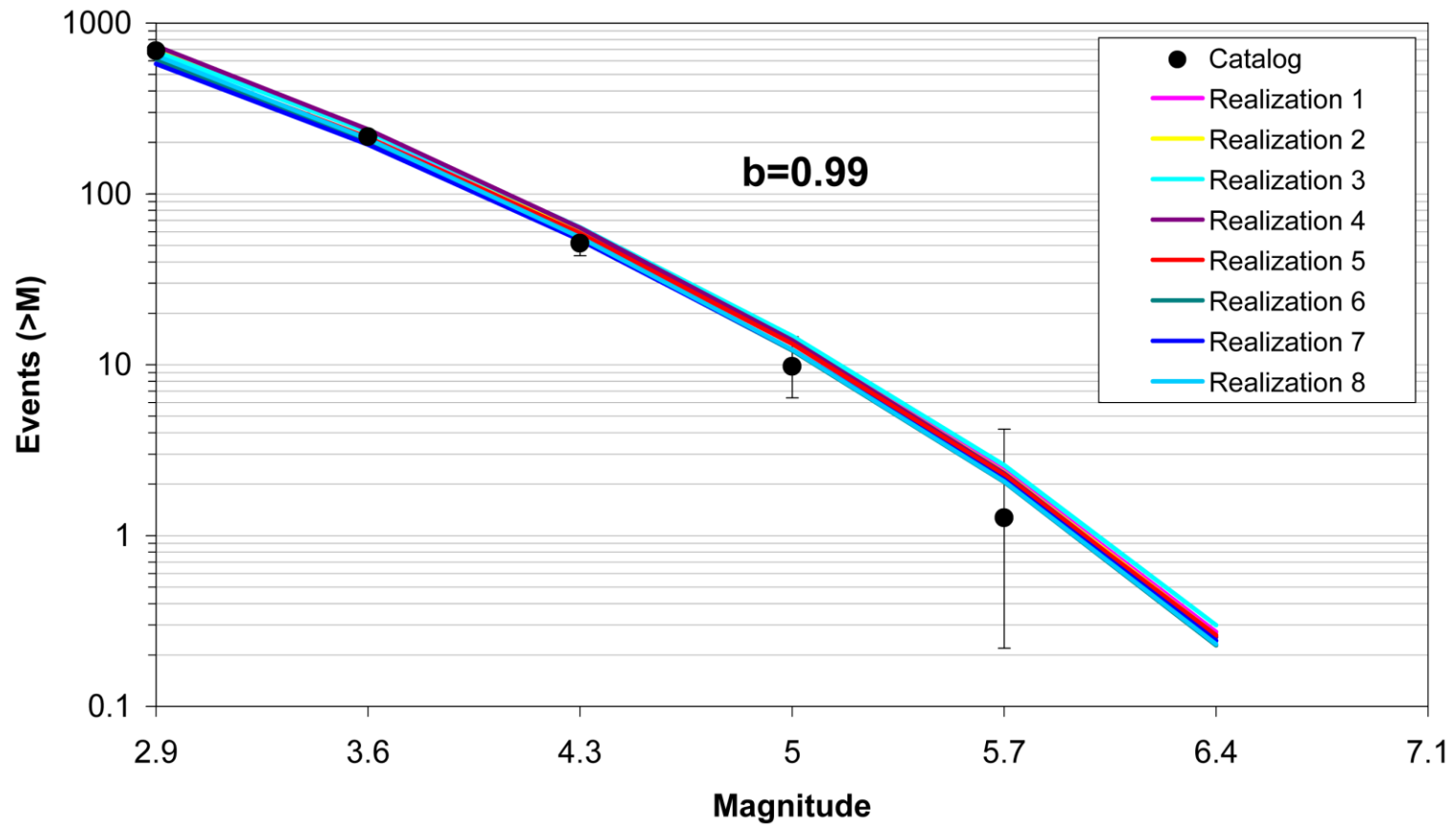


Figure 7.5.2-26  
Comparison of model-predicted earthquake counts for MidC-C using Case B magnitude weights. Error bars as in Figure 7.5.2-4.

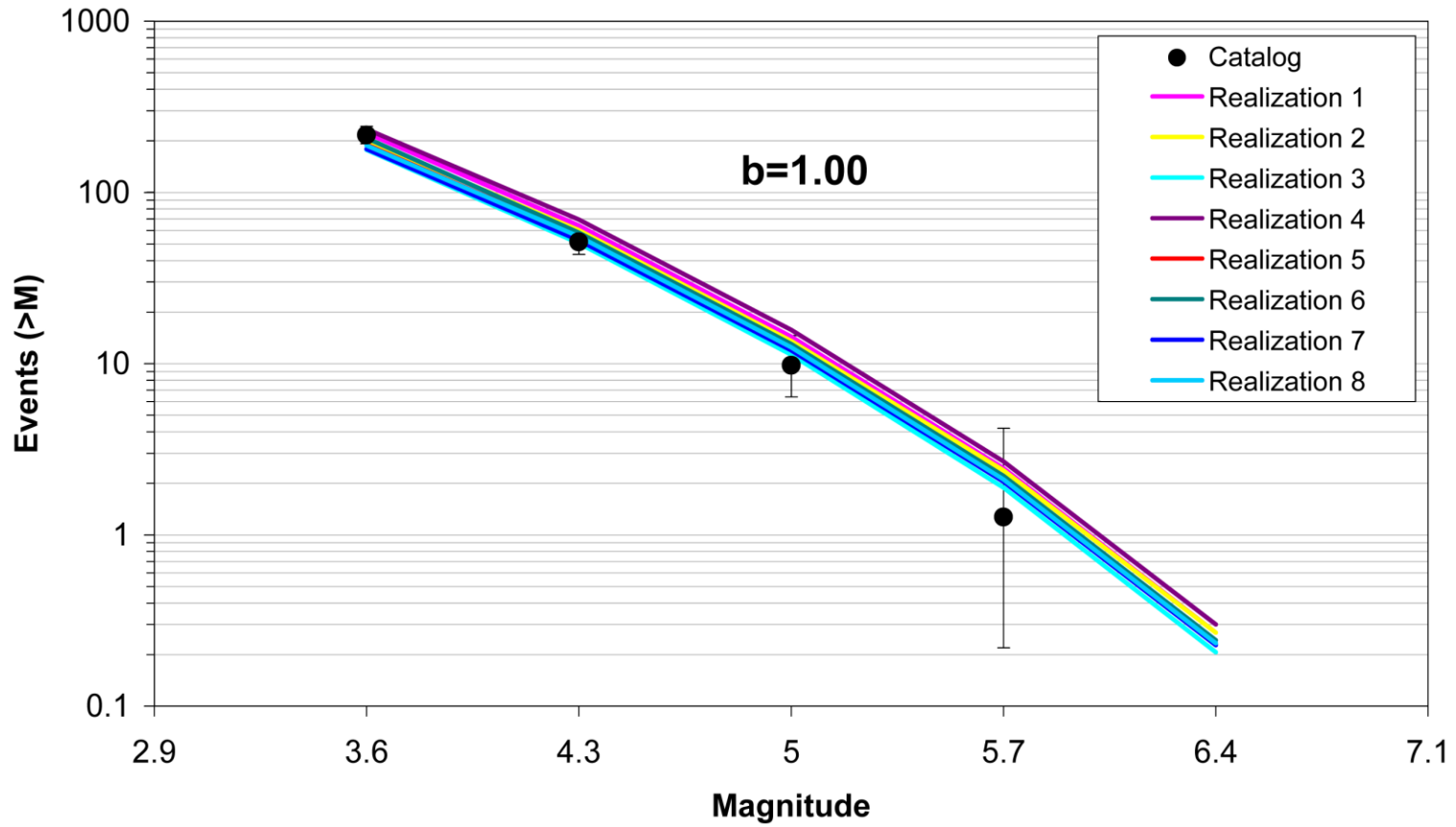


Figure 7.5.2-27  
Comparison of model-predicted earthquake counts for MidC-C using Case E magnitude weights. Error bars as in Figure 7.5.2-4.

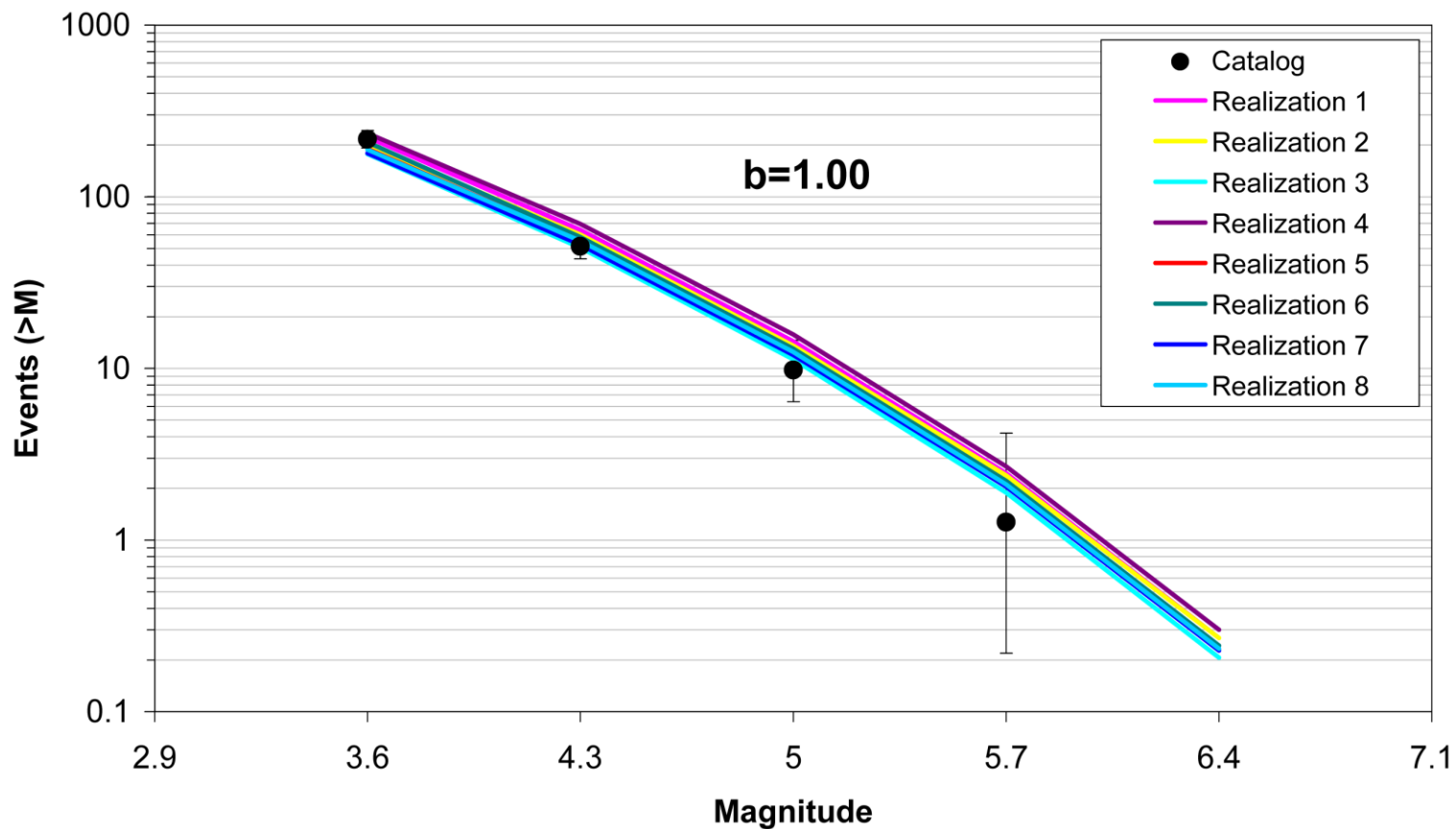


Figure 7.5.2-28  
Comparison of model-predicted earthquake counts for MidC–D using Case A magnitude weights. Error bars as in Figure 7.5.2-4.

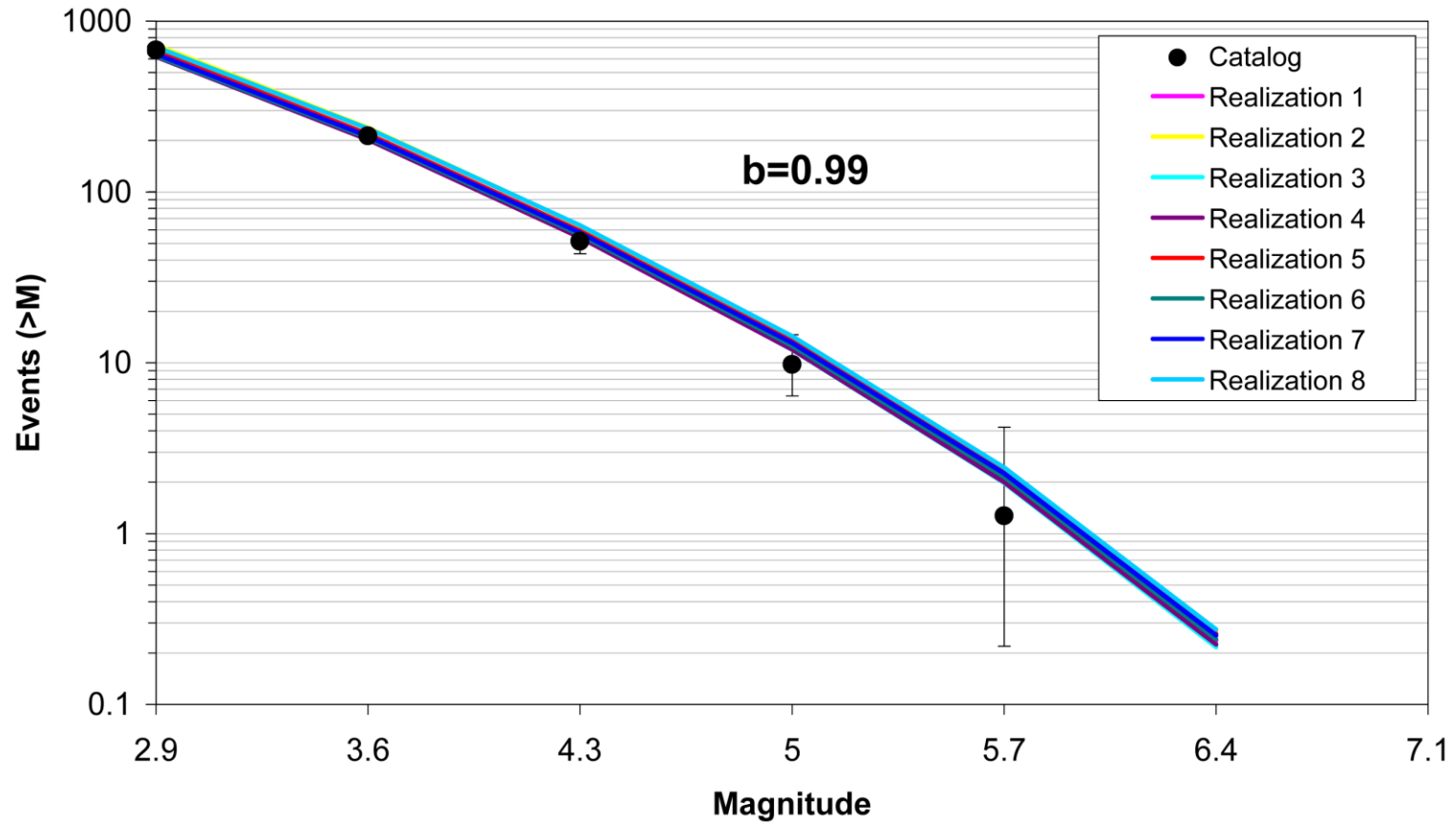


Figure 7.5.2-29  
Comparison of model-predicted earthquake counts for MidC–D using Case B magnitude weights. Error bars as in Figure 7.5.2-4.

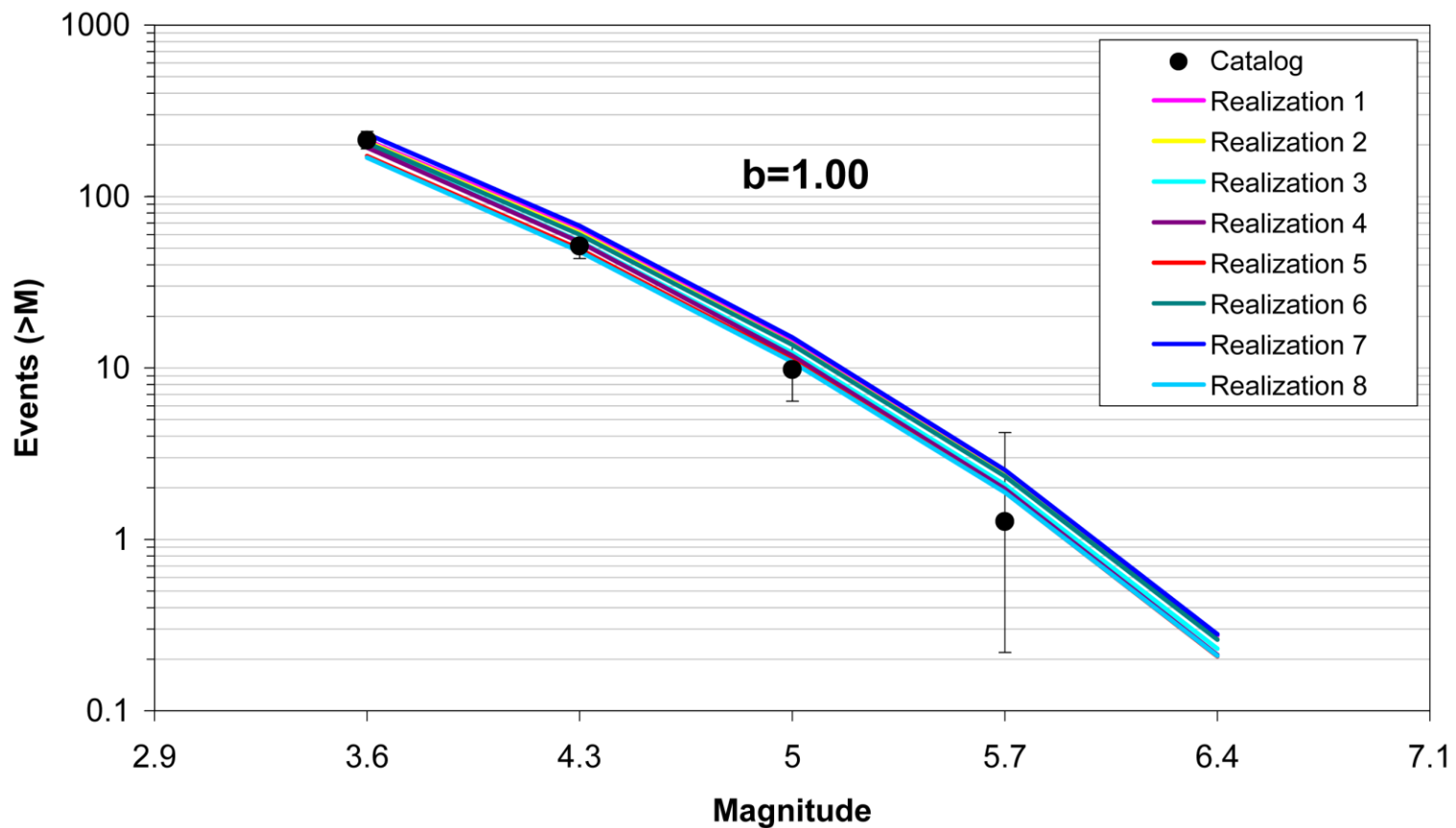


Figure 7.5.2-30  
Comparison of model-predicted earthquake counts for MidC–D using Case E magnitude weights. Error bars as in Figure 7.5.2-4.

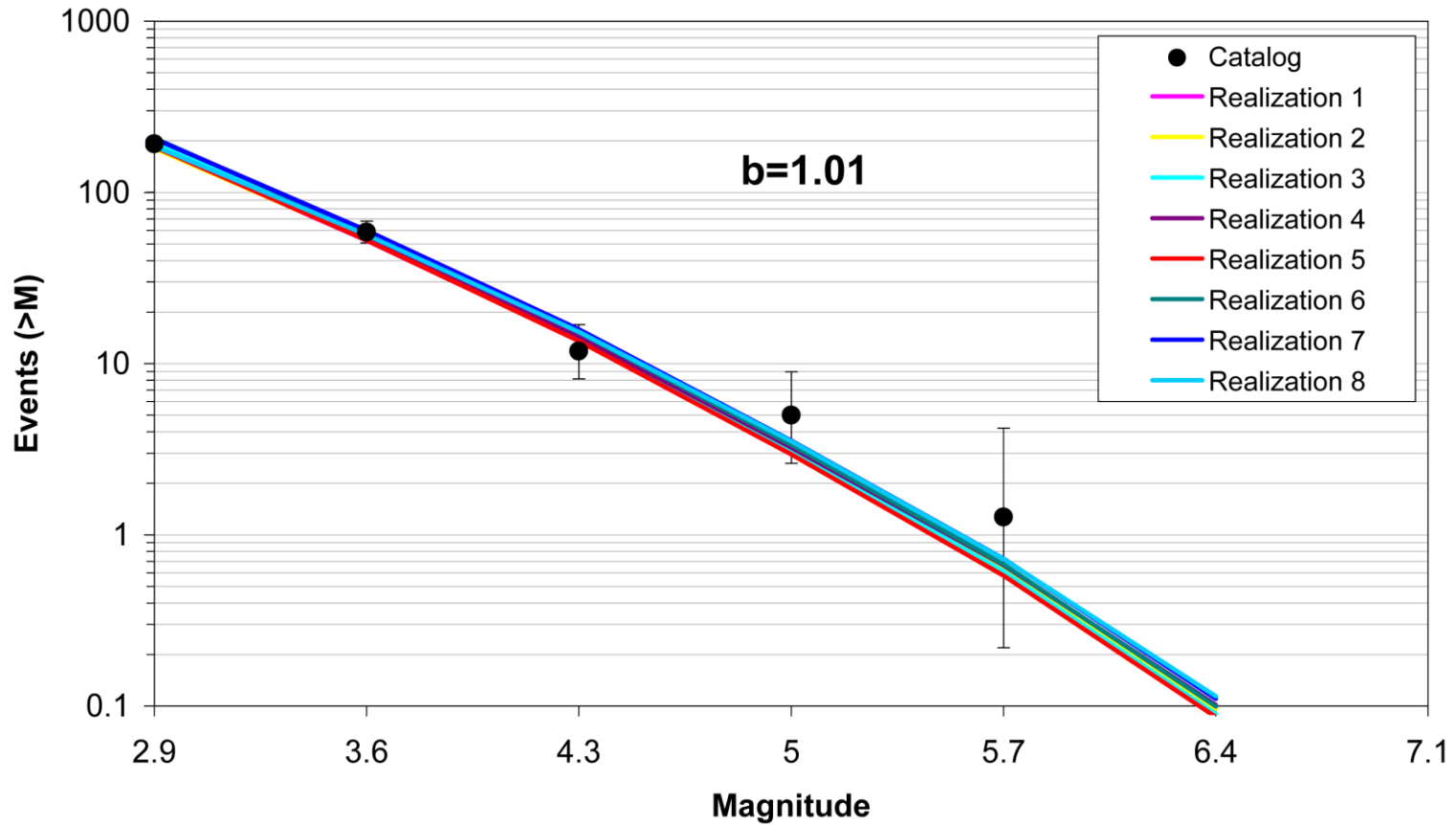


Figure 7.5.2-31  
Comparison of model-predicted earthquake counts for NAP using Case A magnitude weights. Error bars as in Figure 7.5.2-4.

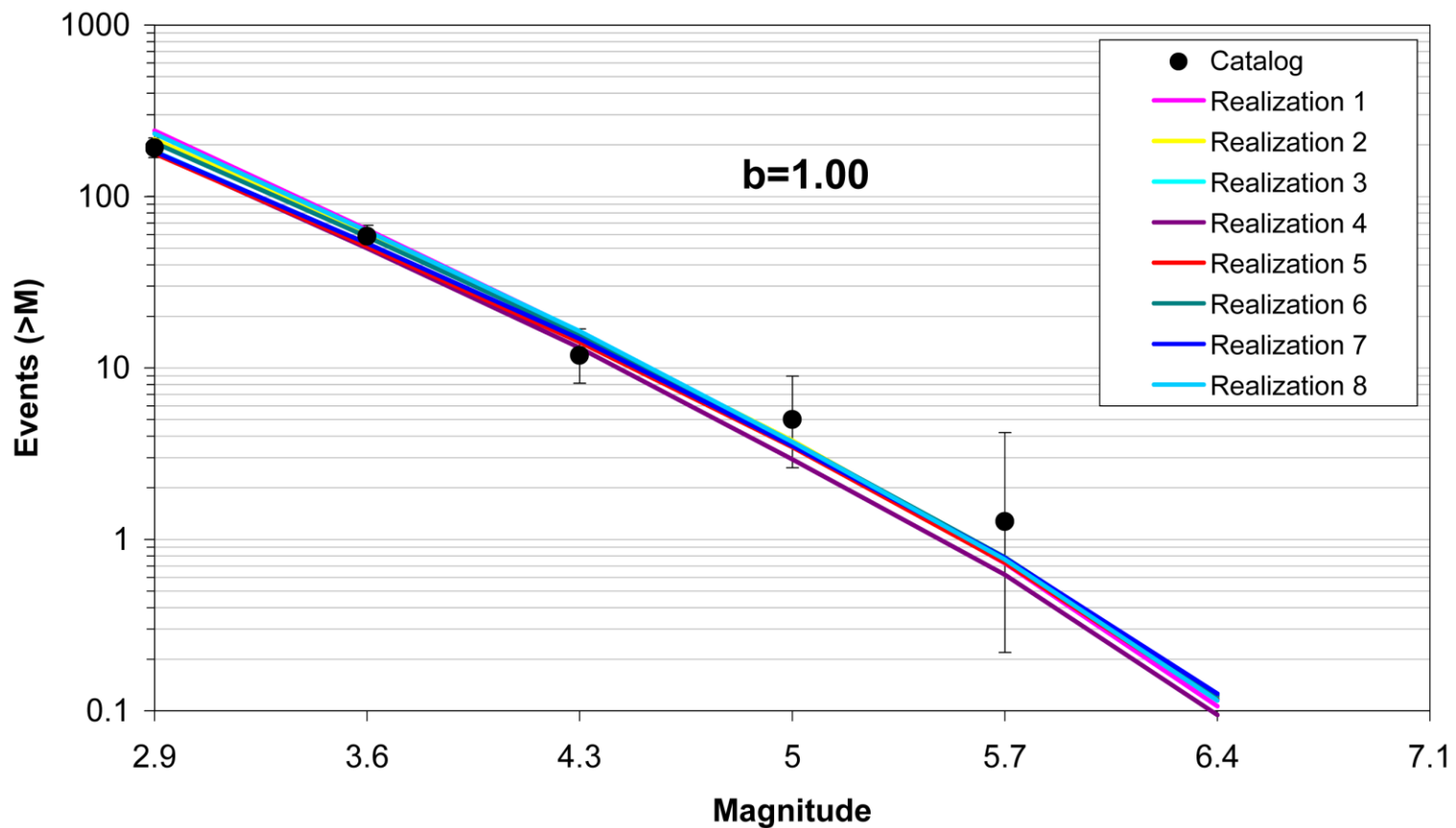


Figure 7.5.2-32  
Comparison of model-predicted earthquake counts for NAP using Case B magnitude weights. Error bars as in Figure 7.5.2-4.

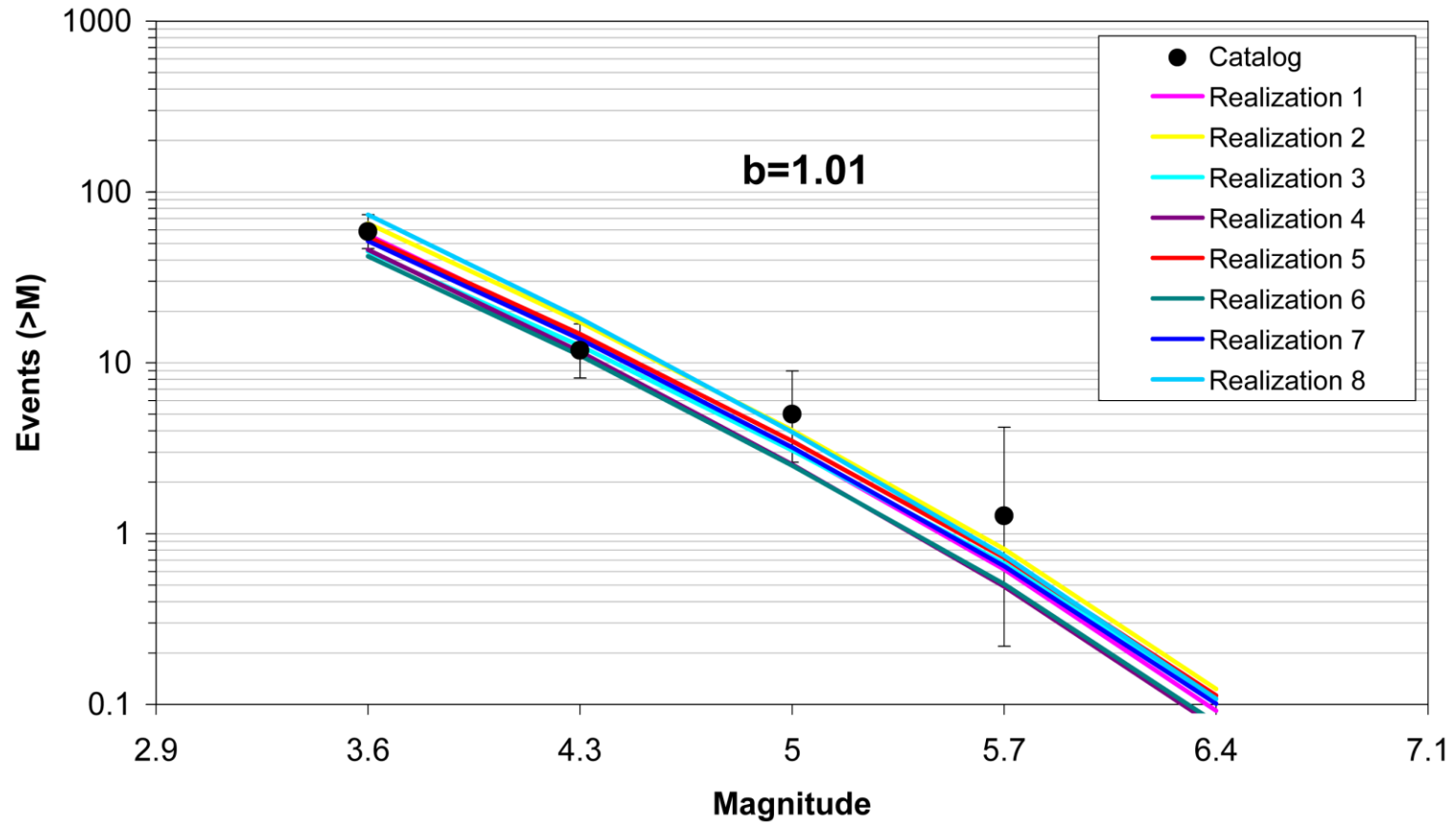


Figure 7.5.2-33  
Comparison of model-predicted earthquake counts for NAP using Case E magnitude weights. Error bars as in Figure 7.5.2-4.

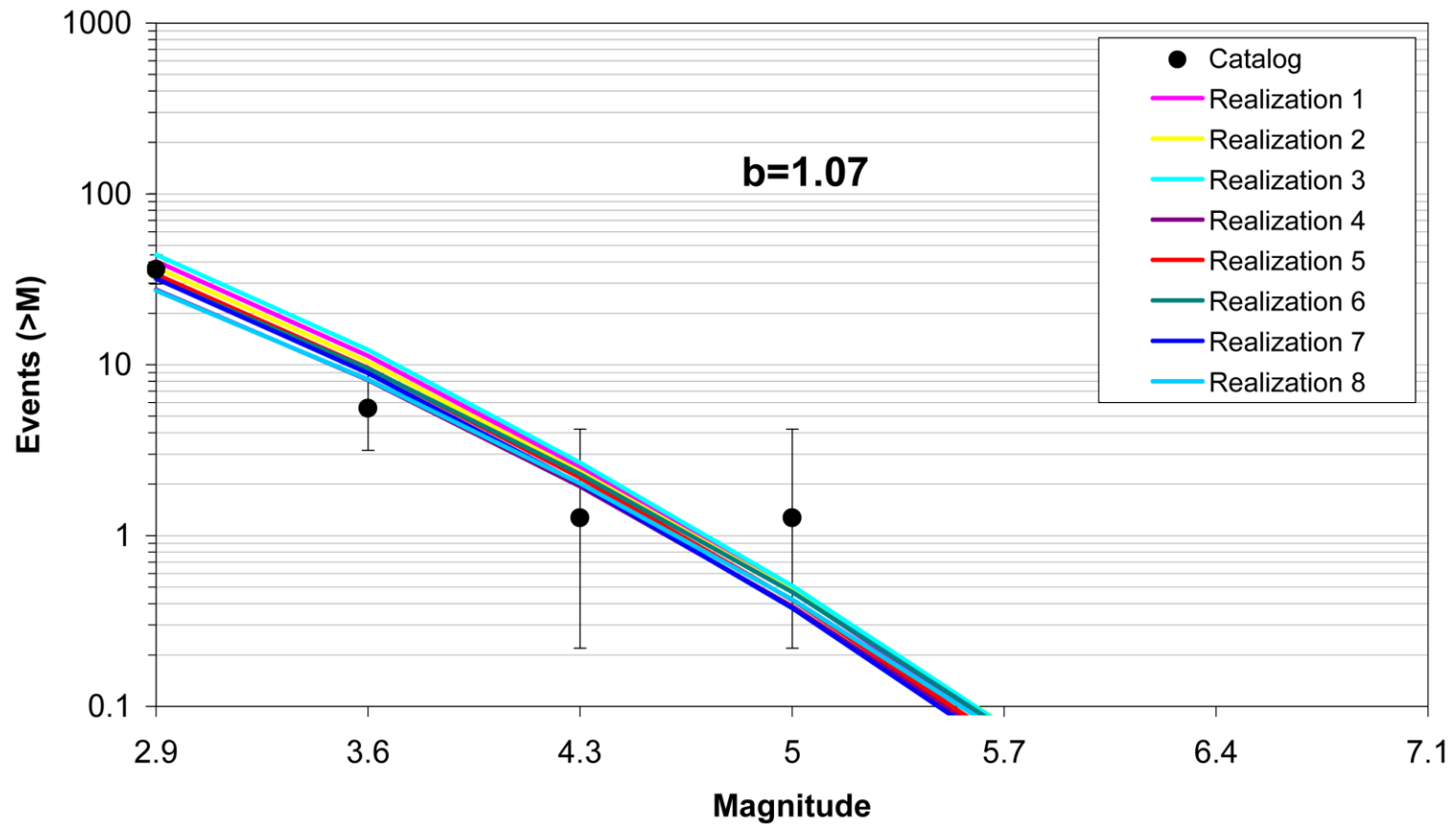


Figure 7.5.2-34  
Comparison of model-predicted earthquake counts for OKA using Case A magnitude weights. Error bars as in Figure 7.5.2-4.

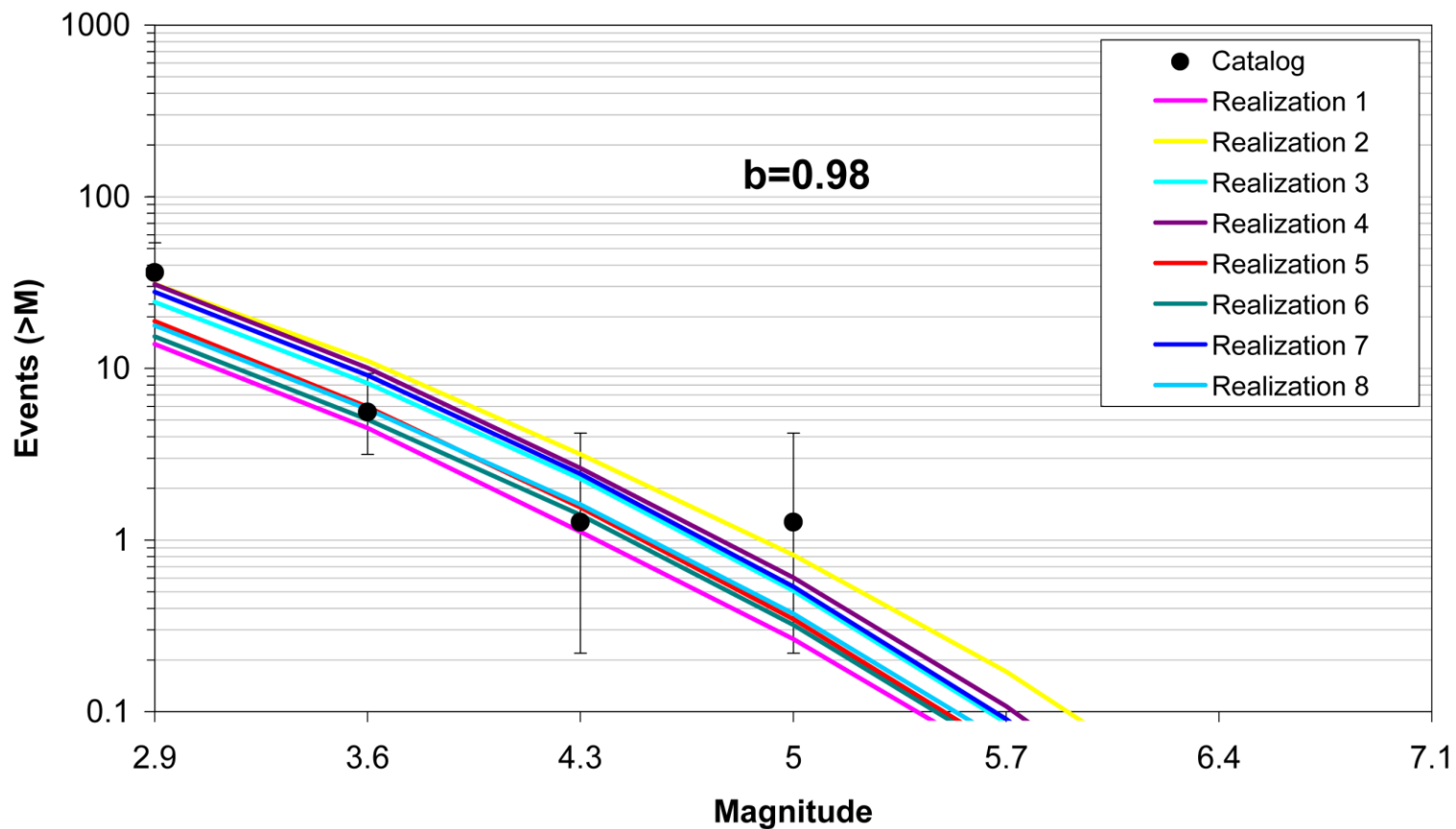


Figure 7.5.2-35  
Comparison of model-predicted earthquake counts for OKA using Case B magnitude weights. Error bars as in Figure 7.5.2-4.

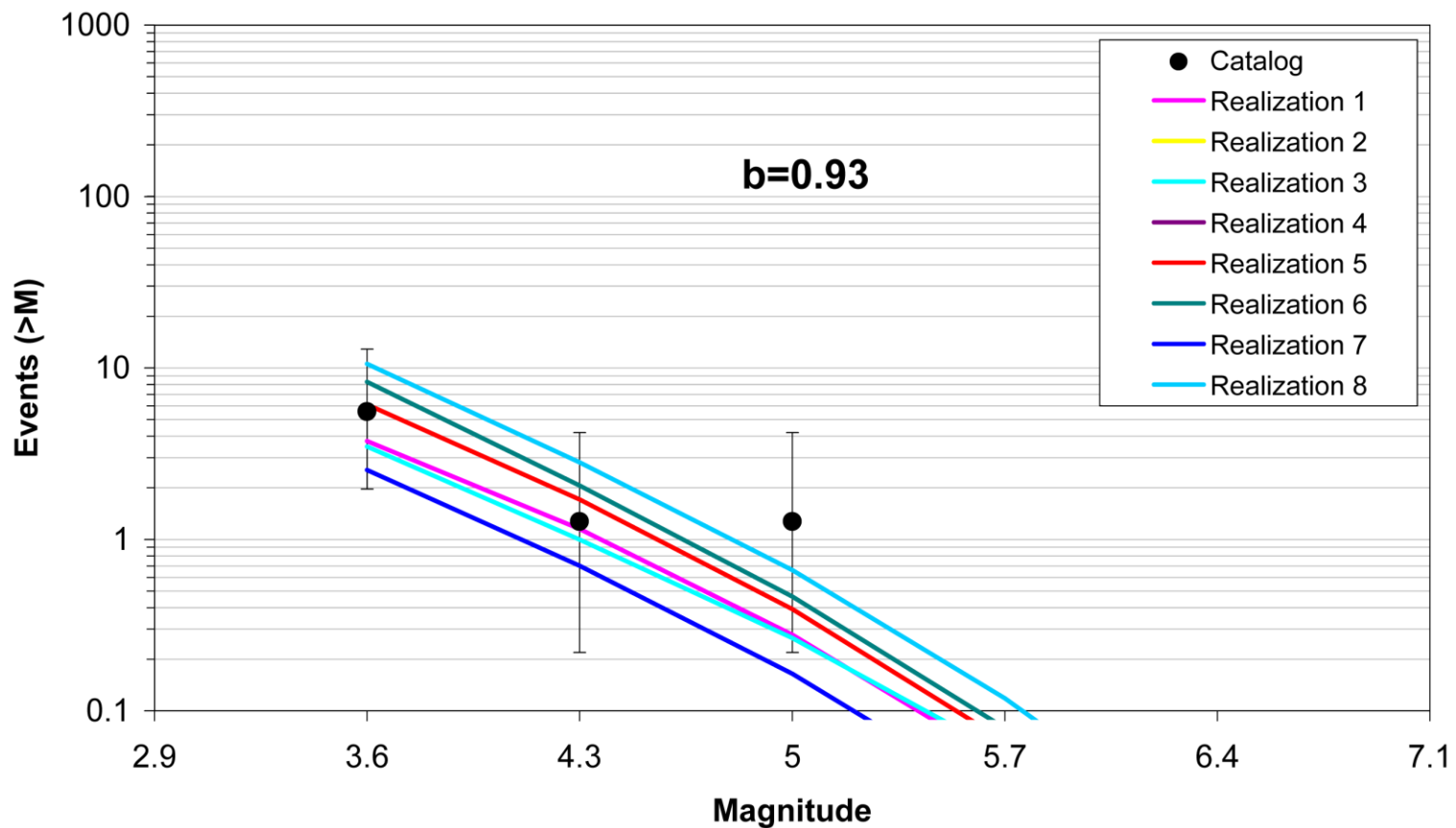


Figure 7.5.2-36  
Comparison of model-predicted earthquake counts for OKA using Case E magnitude weights. Error bars as in Figure 7.5.2-4.

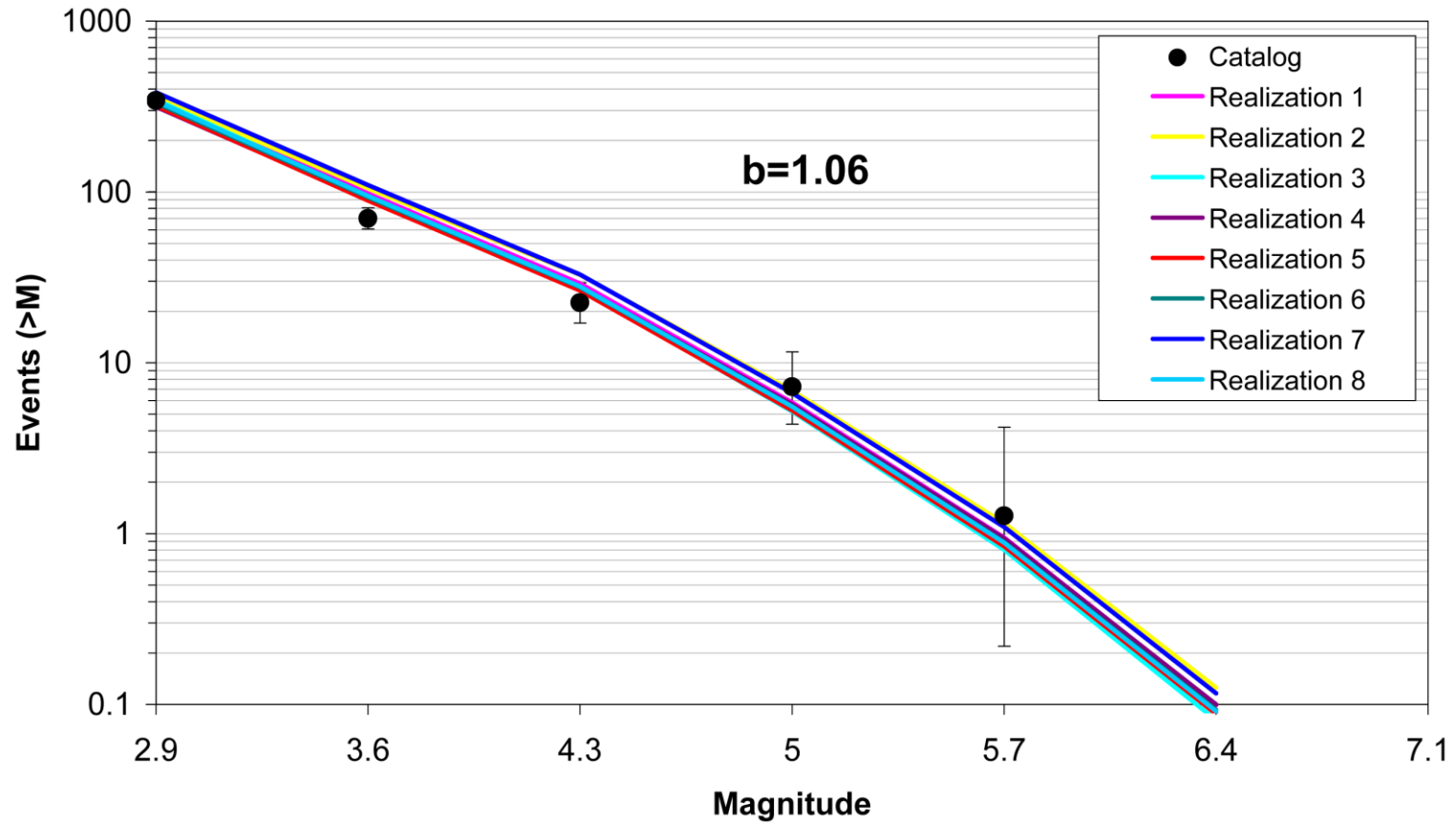


Figure 7.5.2-37  
Comparison of model-predicted earthquake counts for PEZ\_N using Case A magnitude weights. Error bars as in Figure 7.5.2-4.

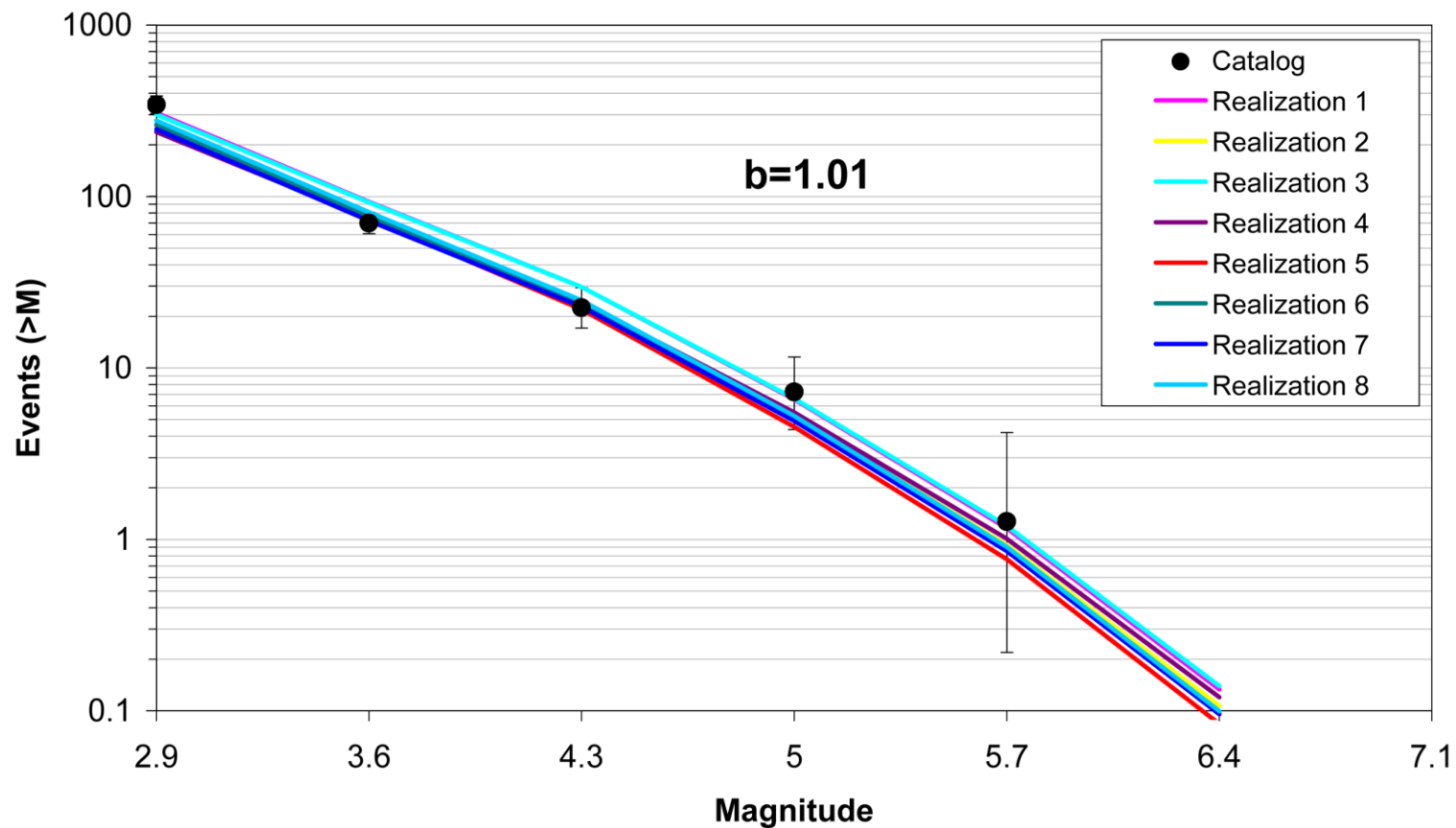


Figure 7.5.2-38  
Comparison of model-predicted earthquake counts for PEZ\_N using Case B magnitude weights. Error bars as in Figure 7.5.2-4.

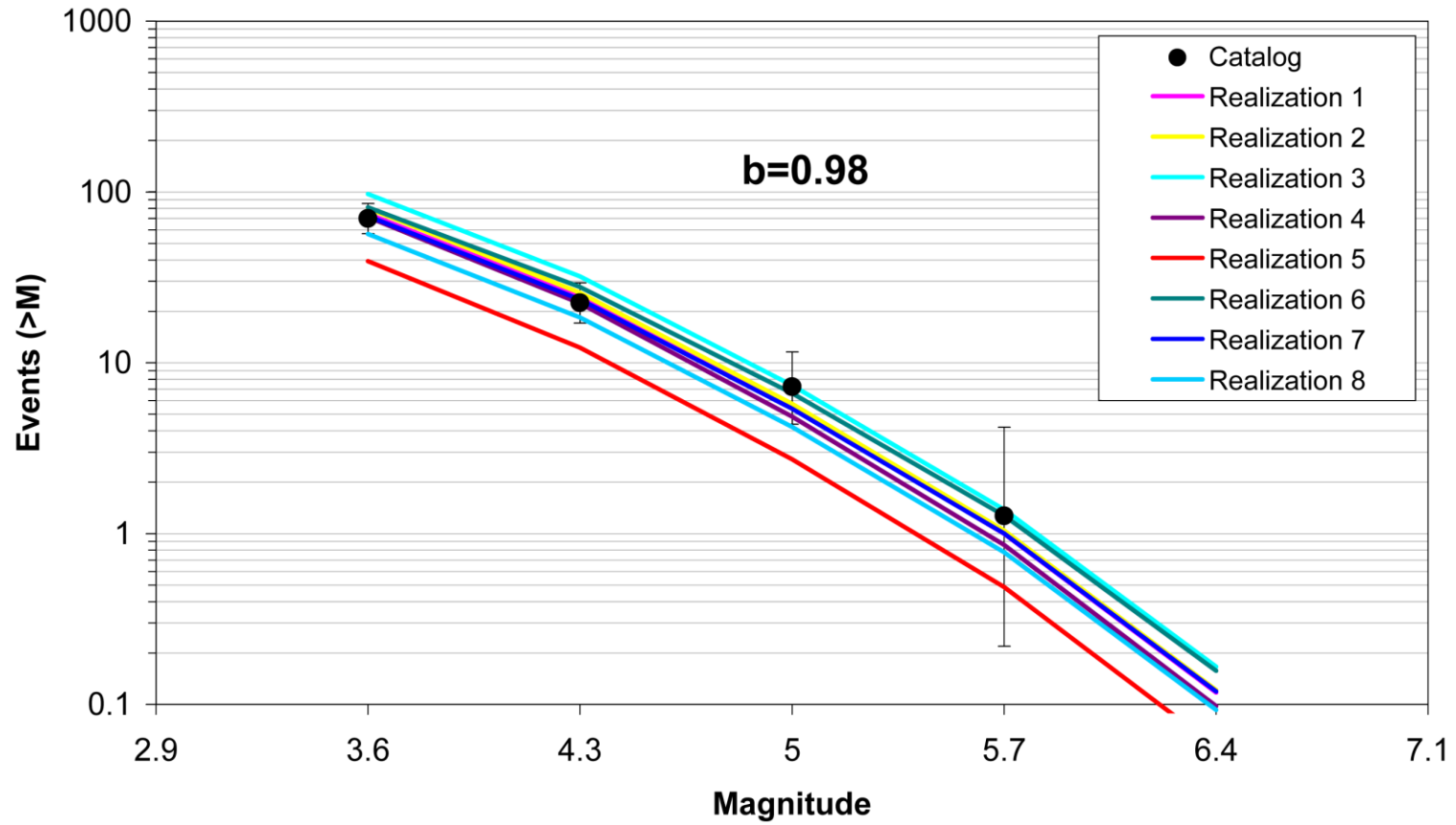


Figure 7.5.2-39  
Comparison of model-predicted earthquake counts for PEZ\_N using Case E magnitude weights. Error bars as in Figure 7.5.2-4.

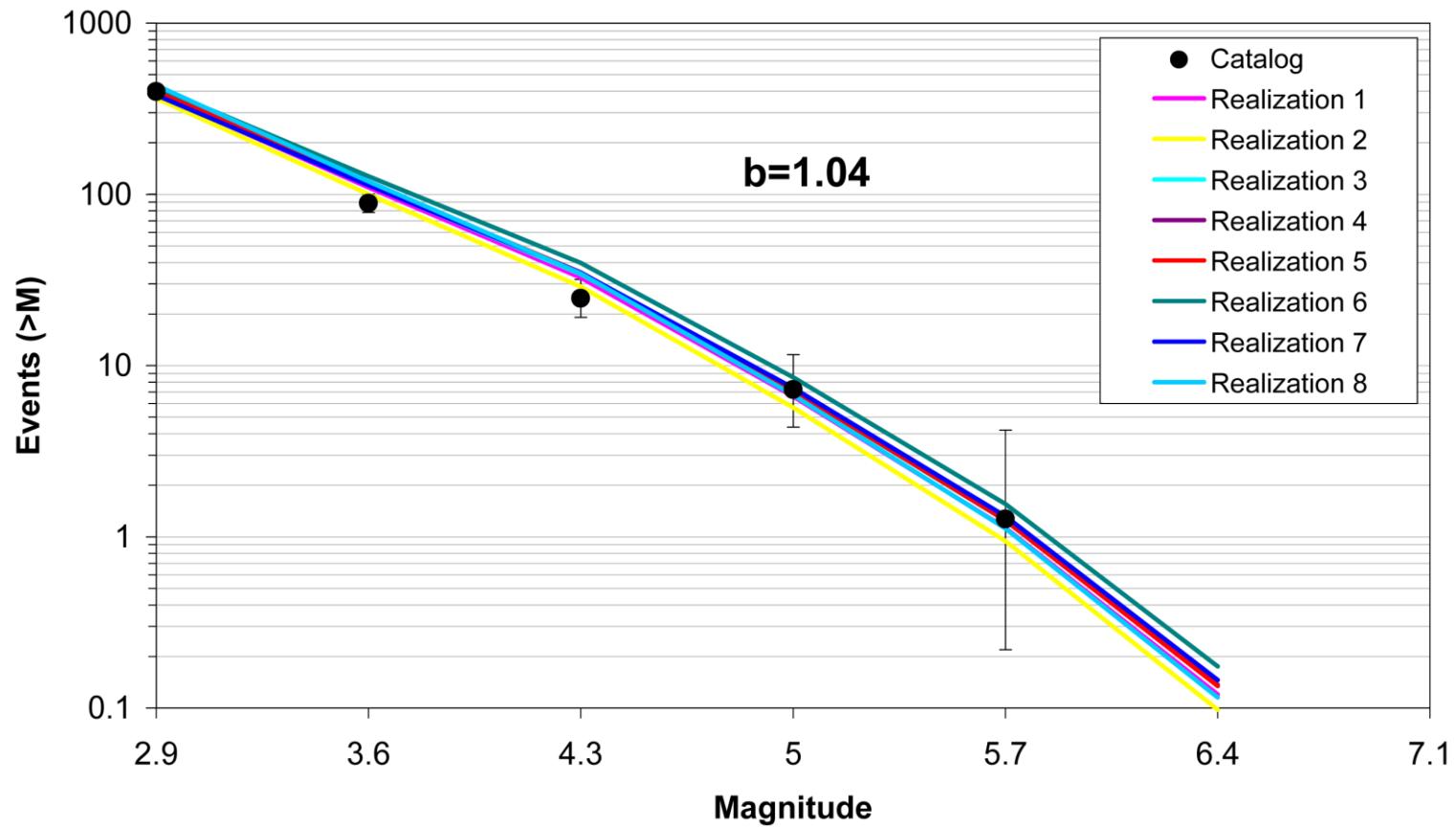


Figure 7.5.2-40  
Comparison of model-predicted earthquake counts for PEZ\_W using Case A magnitude weights. Error bars as in Figure 7.5.2-4.

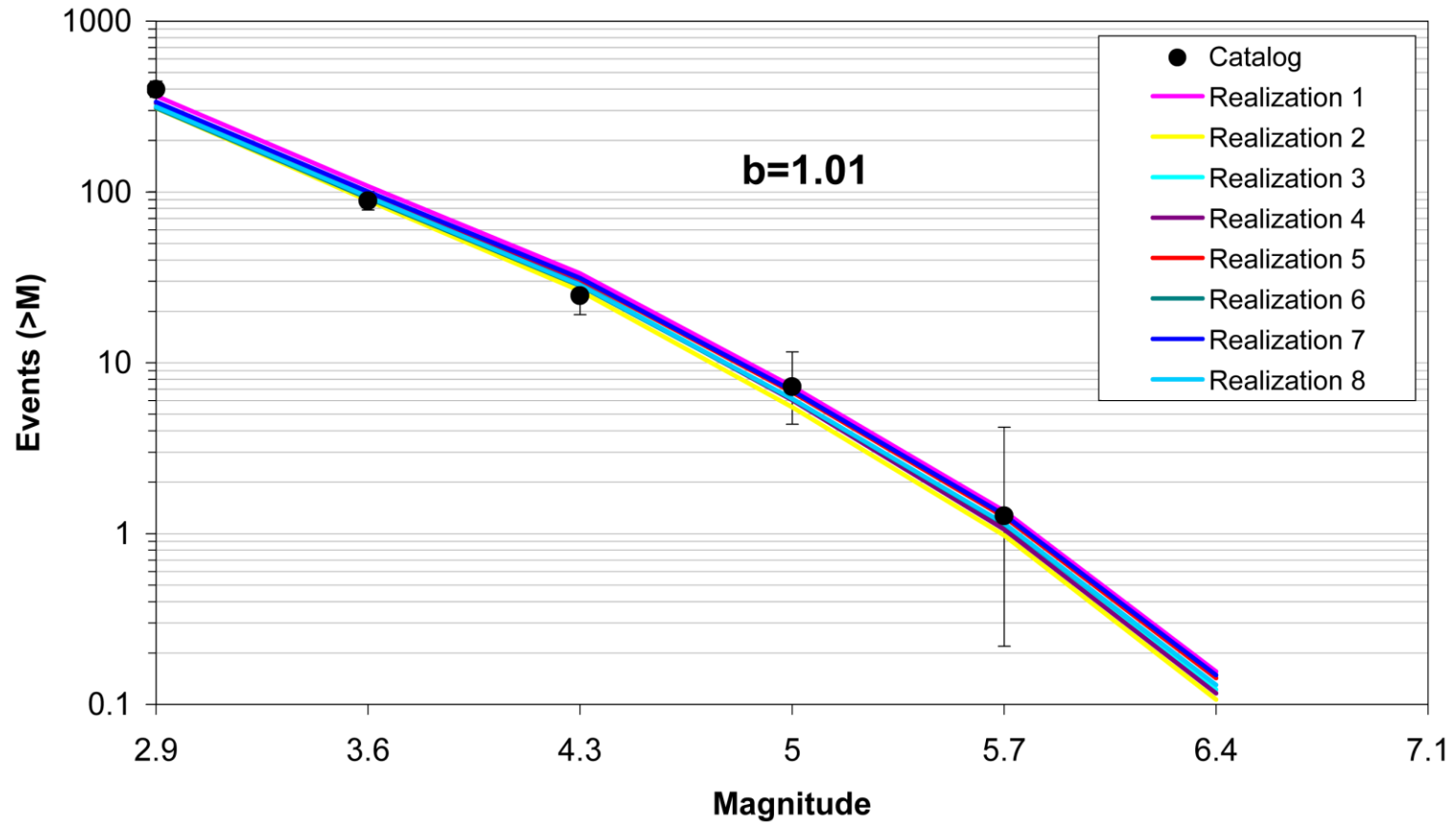


Figure 7.5.2-41  
Comparison of model-predicted earthquake counts for PEZ\_W using Case B magnitude weights. Error bars as in Figure 7.5.2-4.

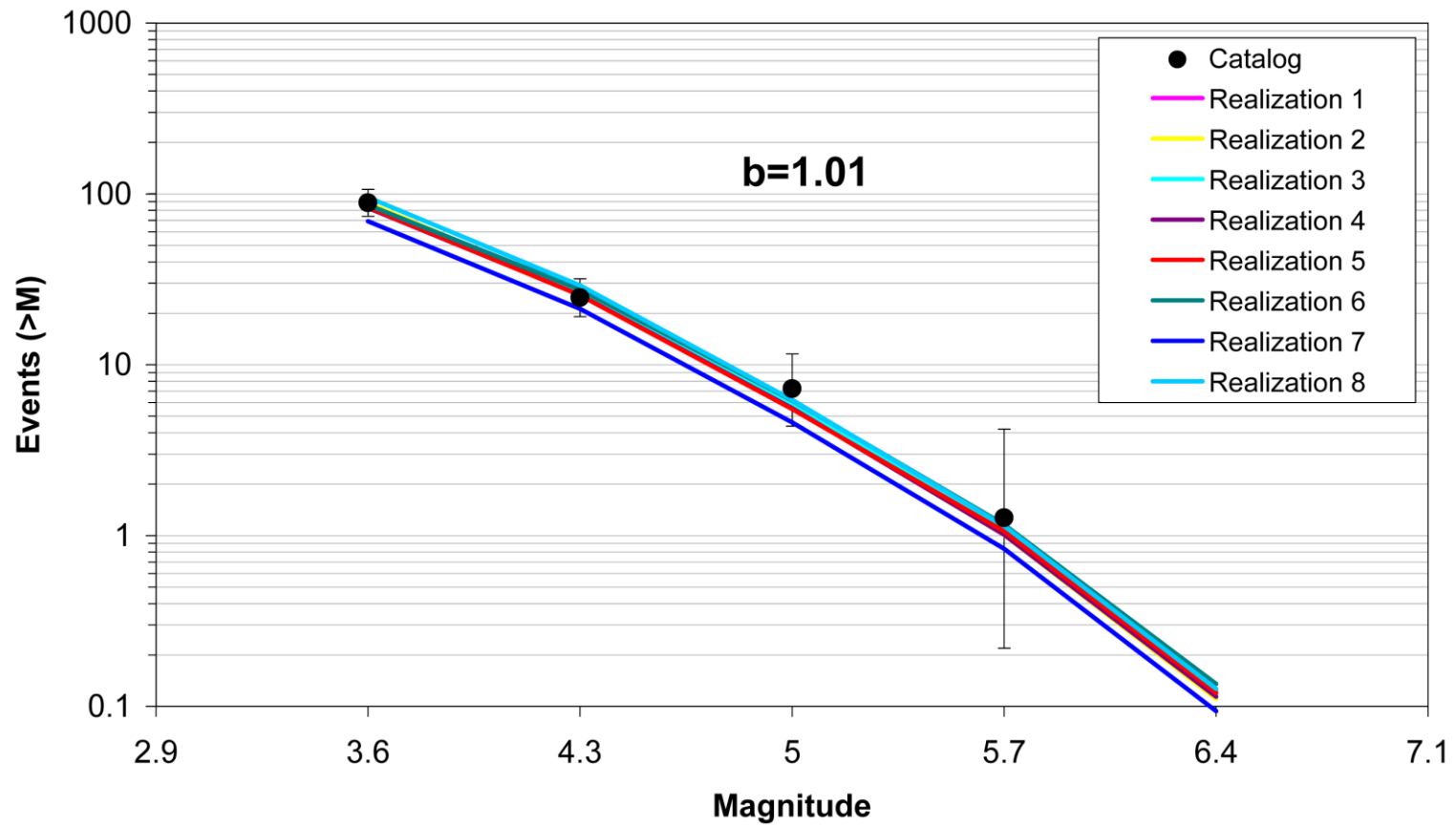


Figure 7.5.2-42  
Comparison of model-predicted earthquake counts for PEZ\_W using Case E magnitude weights. Error bars as in Figure 7.5.2-4.

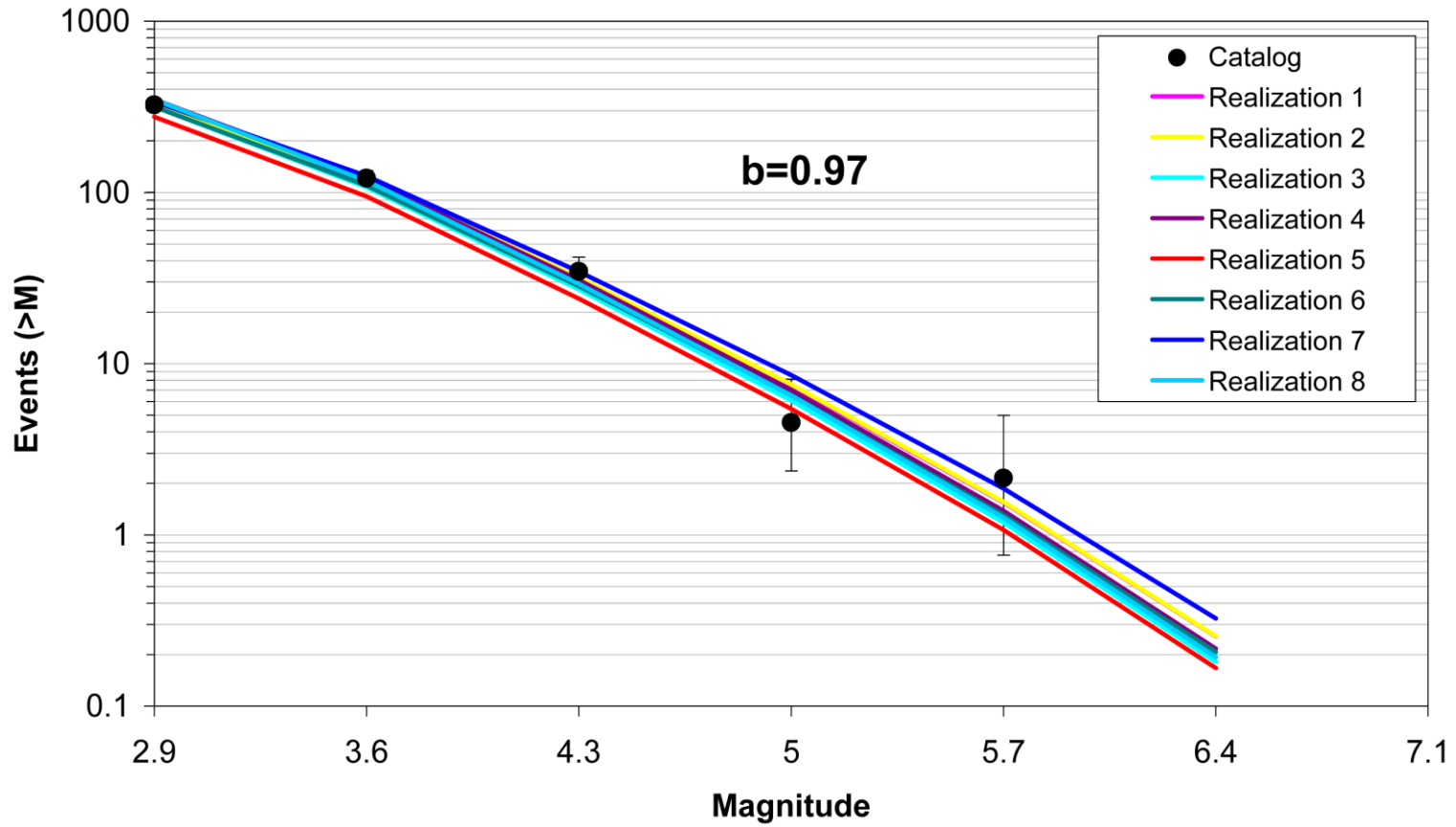


Figure 7.5.2-43  
Comparison of model-predicted earthquake counts for RR using Case A magnitude weights. Error bars as in Figure 7.5.2-4.

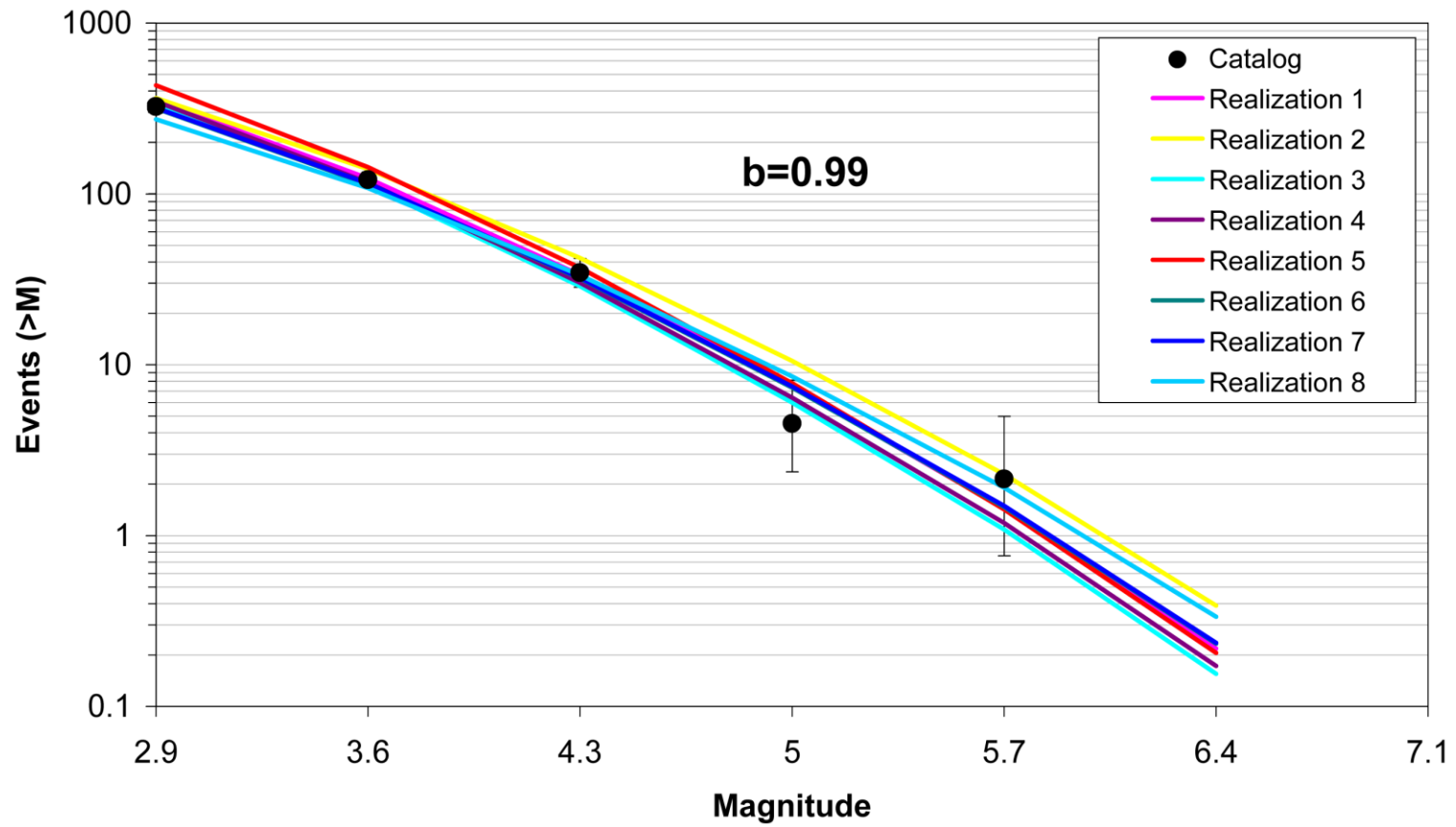


Figure 7.5.2-44  
Comparison of model-predicted earthquake counts for RR using Case B magnitude weights. Error bars as in Figure 7.5.2-4.

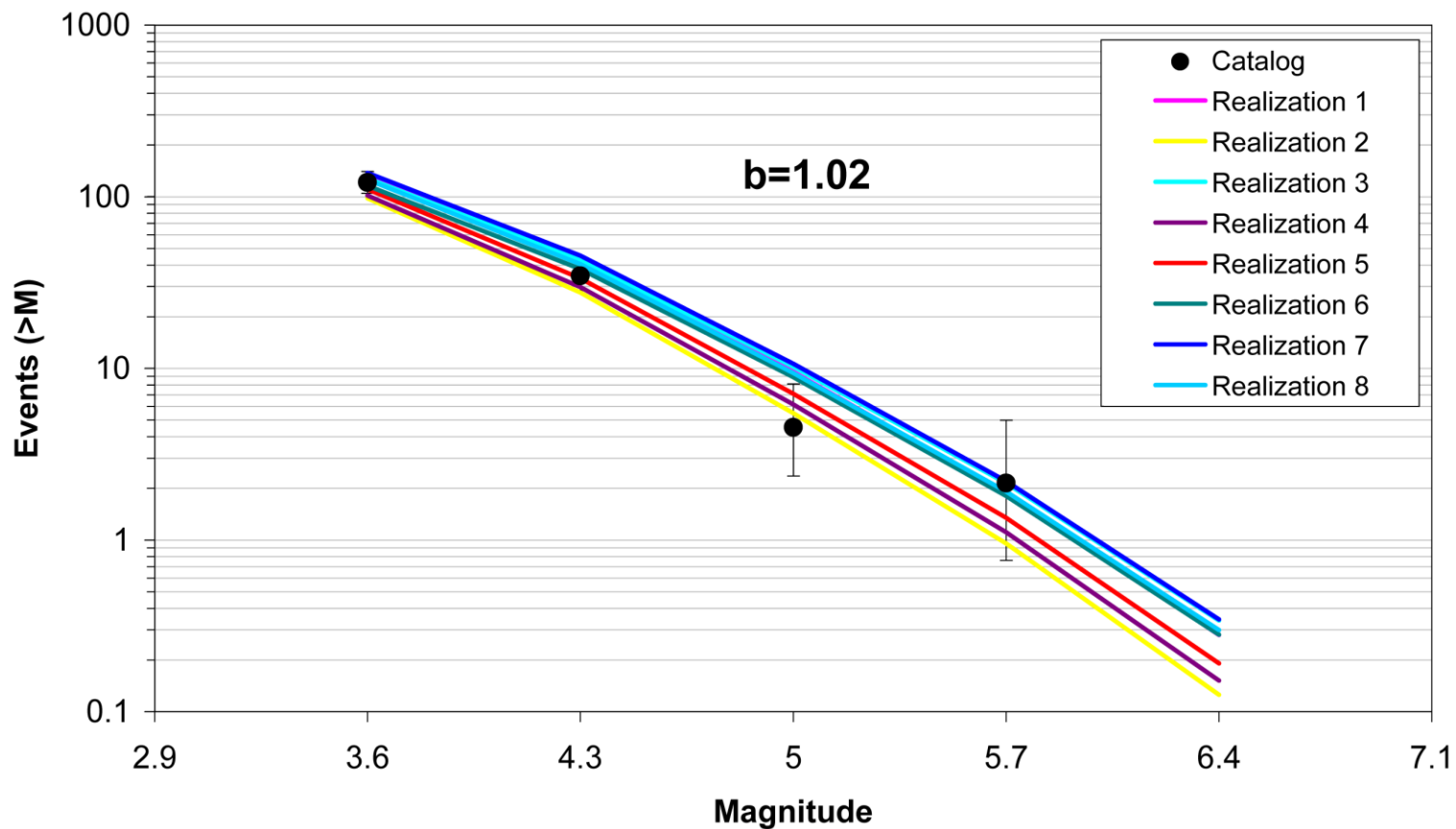


Figure 7.5.2-45  
Comparison of model-predicted earthquake counts for RR using Case E magnitude weights. Error bars as in Figure 7.5.2-4.

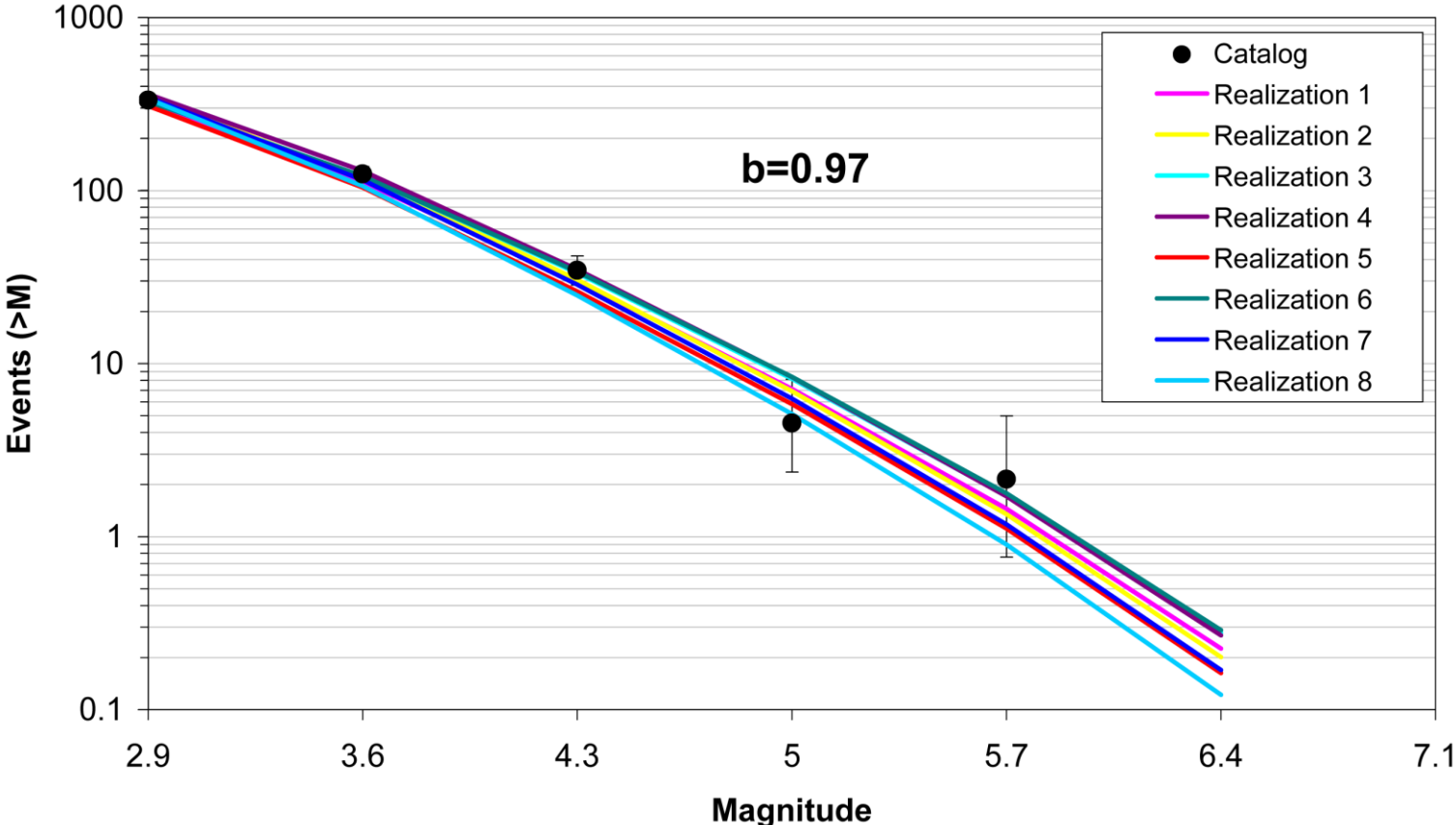


Figure 7.5.2-46  
Comparison of model-predicted earthquake counts for RR\_RCG using Case A magnitude weights. Error bars as in Figure 7.5.2-4.

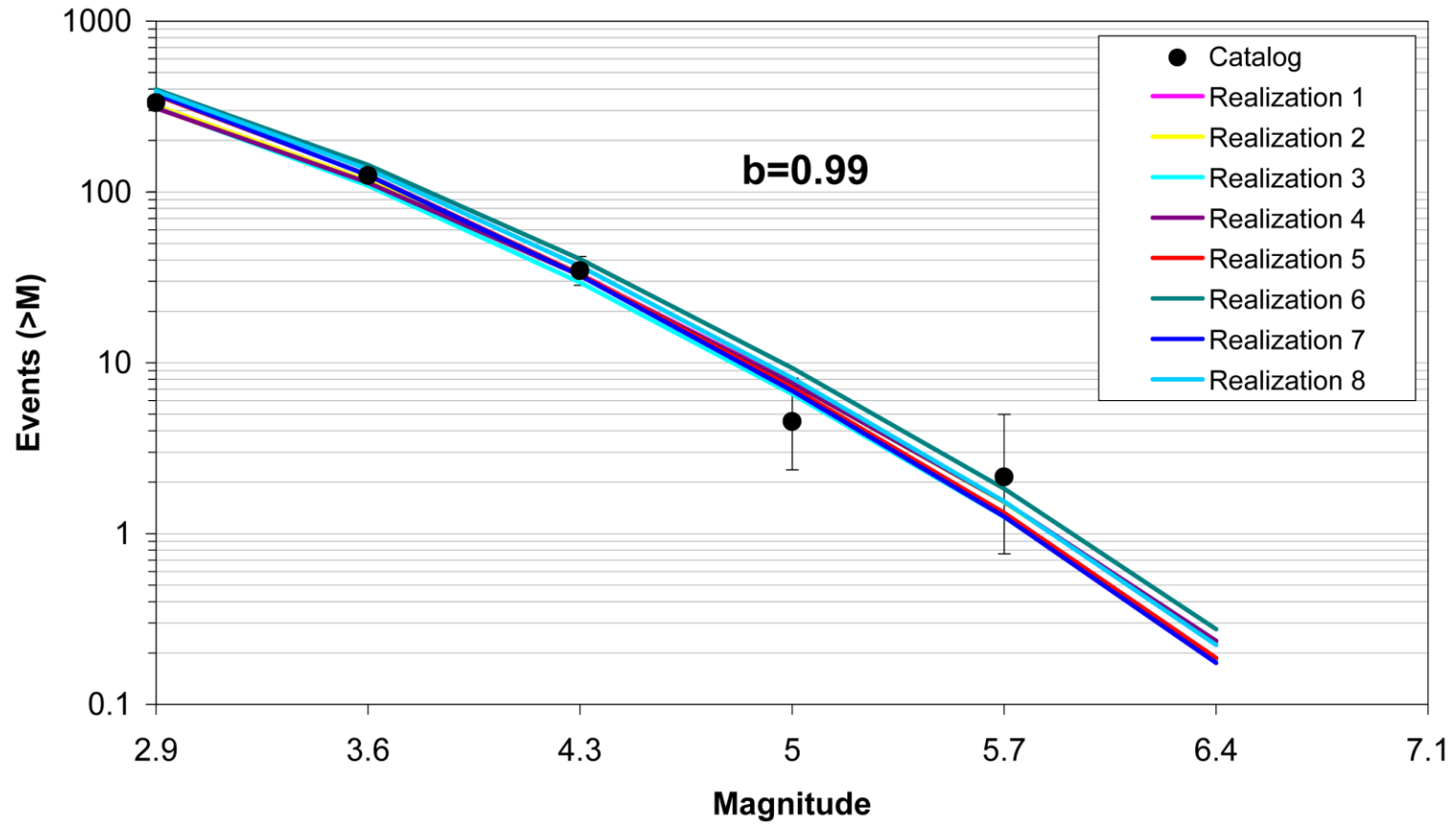


Figure 7.5.2-47  
Comparison of model-predicted earthquake counts for RR\_RCG using Case B magnitude weights. Error bars as in Figure 7.5.2-4.

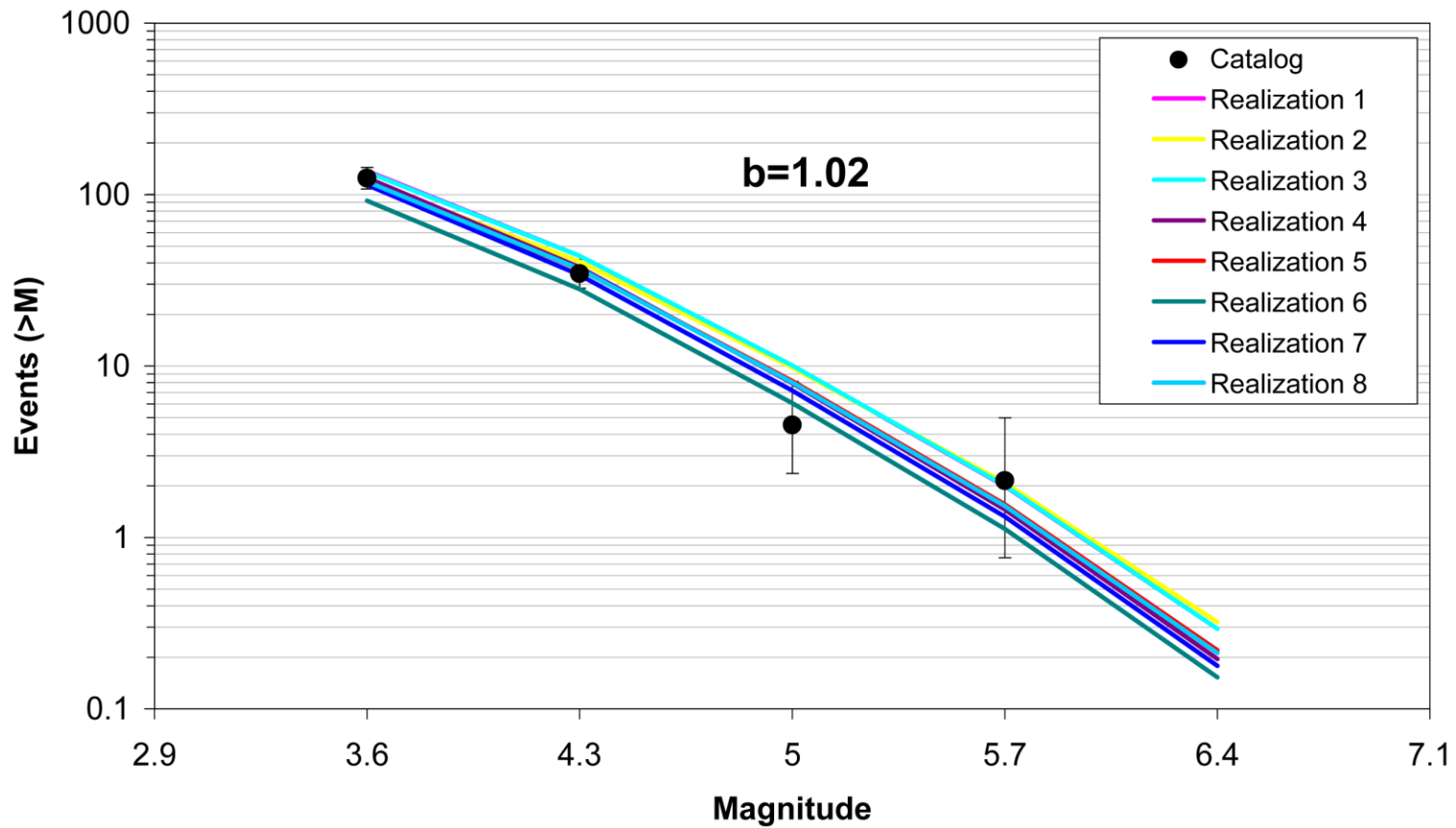


Figure 7.5.2-48  
Comparison of model-predicted earthquake counts for RR\_RCG using Case E magnitude weights. Error bars as in Figure 7.5.2-4.

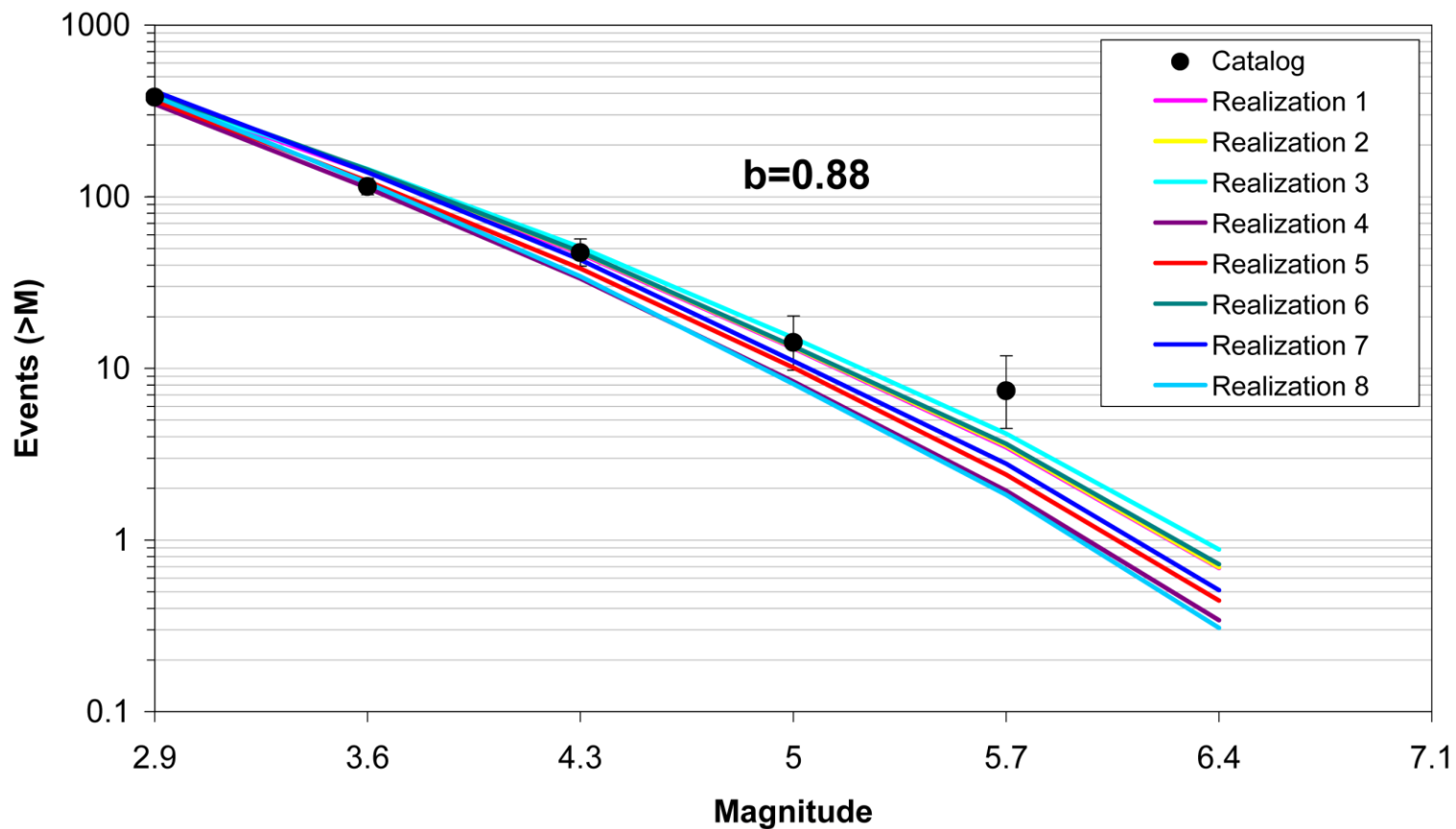


Figure 7.5.2-49  
Comparison of model-predicted earthquake counts for SLR using Case A magnitude weights. Error bars as in Figure 7.5.2-4.

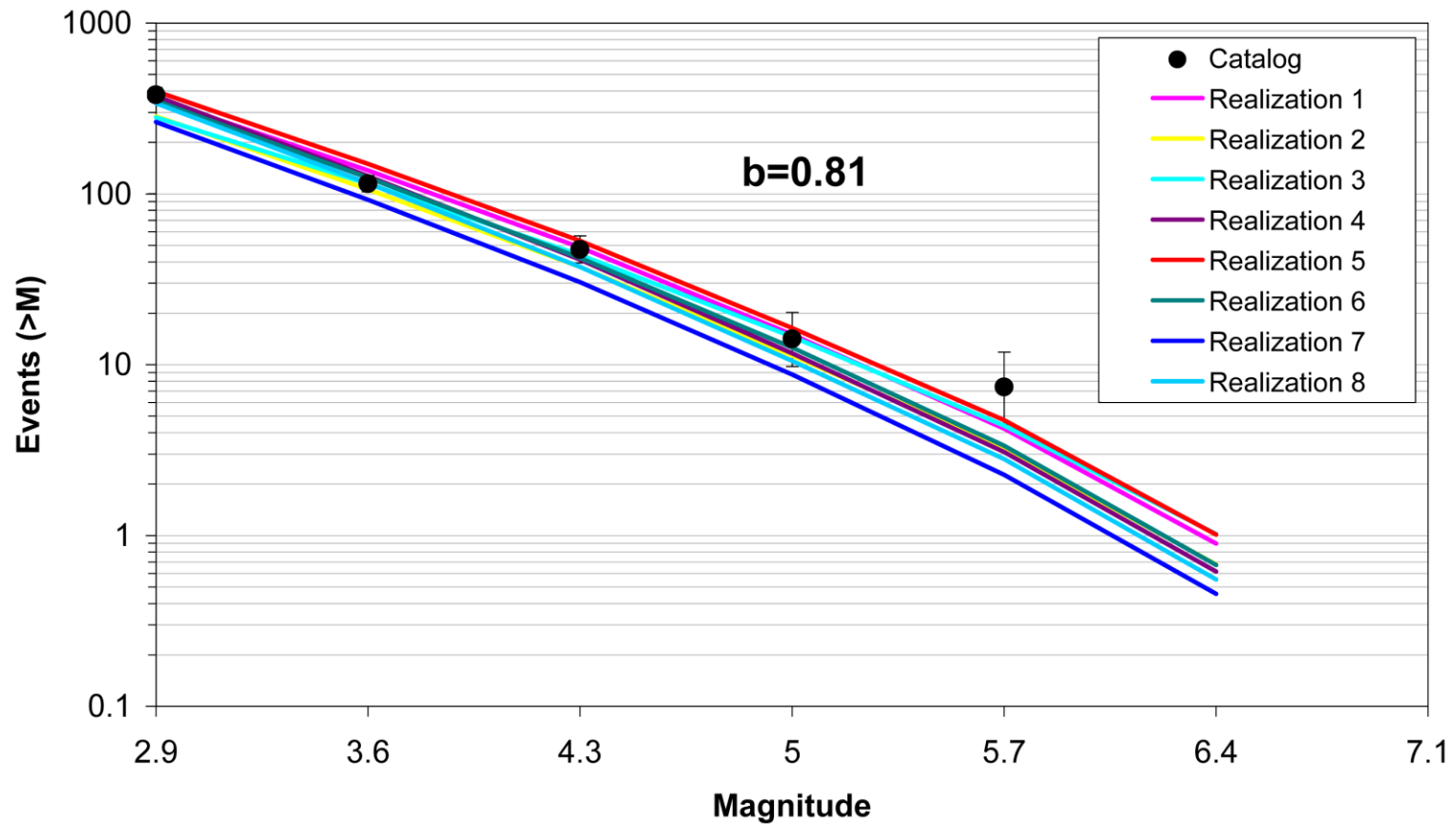


Figure 7.5.2-50  
Comparison of model-predicted earthquake counts for SLR using Case B magnitude weights. Error bars as in Figure 7.5.2-4.

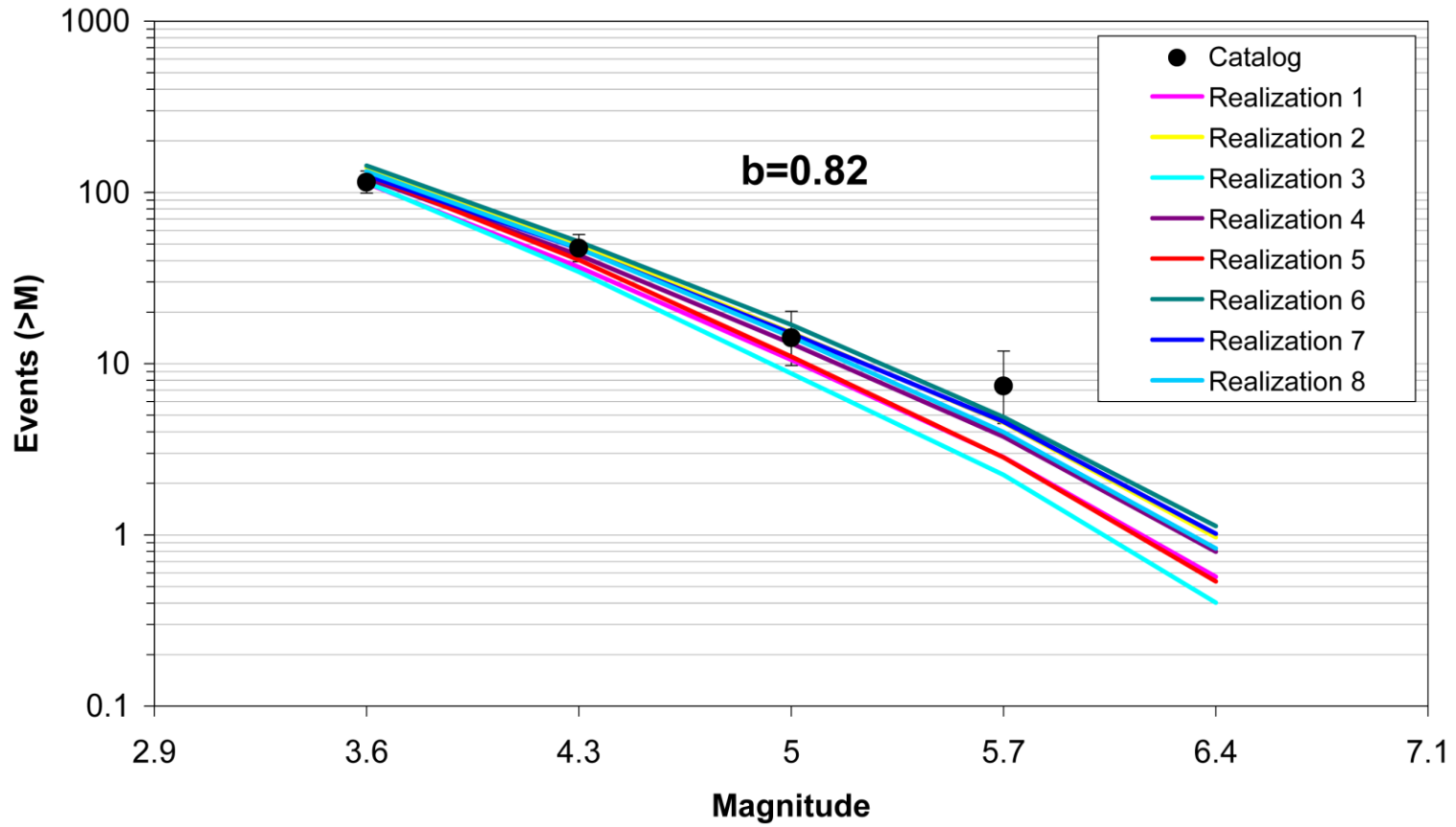


Figure 7.5.2-51  
Comparison of model-predicted earthquake counts for SLR using Case E magnitude weights. Error bars as in Figure 7.5.2-4.

**BIBLIOGRAPHIC DATA SHEET**

(See instructions on the reverse)

NUREG-2115  
Vol. 2

2. TITLE AND SUBTITLE

Central and Eastern United States Seismic Source Characterization for Nuclear Facilities  
Volume 2: Chapters 5 to 7

3. DATE REPORT PUBLISHED

MONTH

YEAR

January

2012

4. FIN OR GRANT NUMBER

K6877

5. AUTHOR(S)

G. Stirewalt (NRC), L. Salomone (Savannah River Nuclear Solutions, LLC), S. McDuffie (DOE), K. Coppersmith (Coppersmith Consulting, Inc), Fugro William Lettis & Associates, Inc.: C. Fuller, R. Hartleb, W. Lettis, S. Lindvall, R. McGuire, G. Toro, D. Slayter, R. Cumbest, A. Shumway, F. Syms, AMEC Geomatrix, Inc: L. Glaser, K. Hanson, R. Youngs, S. Bozkurt, V. Montaldo Falero, R. Perman, R. McGuire (Risk Engineering), M. Tuttle (M. Tuttle & Associates)

6. TYPE OF REPORT

Technical

7. PERIOD COVERED (Inclusive Dates)

8. PERFORMING ORGANIZATION - NAME AND ADDRESS (If NRC, provide Division, Office or Region, U.S. Nuclear Regulatory Commission, and mailing address; if contractor, provide name and mailing address.)

U.S. Nuclear Regulatory Commission, Office of Nuclear Regulatory Research, Washington DC 20555  
U.S. Department of Energy, 1000 Independence Avenue SW, Washington DC 20585  
Electric Power Research Institute, 3420 Hillview Avenue, Palo Alto, CA 94304

9. SPONSORING ORGANIZATION - NAME AND ADDRESS (If NRC, type "Same as above"; if contractor, provide NRC Division, Office or Region, U.S. Nuclear Regulatory Commission, and mailing address.)

U.S. Nuclear Regulatory Commission, Office of Nuclear Regulatory Research, Washington DC 20555  
U.S. Department of Energy, 1000 Independence Avenue SW, Washington DC 20585  
Electric Power Research Institute, 3420 Hillview Avenue, Palo Alto, CA 94304

10. SUPPLEMENTARY NOTES

11. ABSTRACT (200 words or less)

This report describes a new seismic source characterization (SSC) model for the Central and Eastern United States (CEUS). It will replace the Seismic Hazard Methodology for the Central and Eastern United States, EPRI Report NP-4726 (July 1986) and the Seismic Hazard Characterization of 69 Nuclear Plant Sites East of the Rocky Mountains, Lawrence Livermore National Laboratory Model, (Bernreuter et al., 1989). The objective of the CEUS SSC Project is to develop a new seismic source model for the CEUS using a Senior Seismic Hazard Analysis Committee (SSHAC) Level 3 assessment process. The goal of the SSHAC process is to represent the center, body, and range of technically defensible interpretations of the available data, models, and methods. Input to a probabilistic seismic hazard analysis (PSHA) consists of both seismic source characterization and ground motion characterization. These two components are used to calculate probabilistic hazard results (or seismic hazard curves) at a particular site. This report provides a new seismic source model.

12. KEY WORDS/DESCRIPTORS (List words or phrases that will assist researchers in locating the report.)

Probabilistic seismic hazard analysis (PSHA)  
Seismic source characterization (SSC)  
Seismic source characterization model  
Central and Eastern United States (CEUS)

13. AVAILABILITY STATEMENT

unlimited

14. SECURITY CLASSIFICATION

(This Page)

unclassified

(This Report)

unclassified

15. NUMBER OF PAGES

16. PRICE





